Proceedings of the International Symposium on Seawater Drag Reduction

22-23 July 1998
Newport, Rhode Island

DISTRIBUTION STATEMENT A
Approved for Public Release
Distribution Unlimited

DTIC QUALITY INSPECTED 4

19990504 000

FOREWORD

The International Symposium on Seawater Drag Reduction (ISSDR), held in Newport, RI, on 22-23 July 1998, focused on drag reduction methods applicable primarily in the seawater environment. The symposium was jointly sponsored by the Office of Naval Research (including ONR's European Office), the Naval Sea Systems Command, the Defense Advanced Research Projects Agency, the Naval Surface Warfare Center—Carderock Division, the American Society of Mechanical Engineers and the Naval Undersea Warfare Center—Newport Division.

The call for ISSDR papers resulted in an overwhelming response from around the world. Accepted papers represent authors from 11 different countries and include contributions from the government sector, private industry, and academia. The resulting proceedings volume offers a comprehensive collection of the latest thinking on seawater drag reduction from leaders of the international drag reduction community. Papers are grouped in this volume in the following categories:

- drag reduction - historical overview
- wall turbulence physics
- drag reduction physics
- seawater physics
- turbulent drag reduction methods—including compliant coating, spanwise fluid motion and wall motion, polymer, microbubble, electromagnetic, and biology based methods

One of the fundamental advances in the study of turbulence over the last five decades has been the discovery that turbulence production and self-sustainment in a boundary layer are organized phenomena and not entirely random processes. A principal objective of this symposium and proceedings was to promote a closer coupling of these wall turbulence physics fundamentals to drag reduction methodologies, while also seeking to increase awareness of the challenges unique to seawater drag reduction, and encouraging wider and more extensive discussion in the drag reduction community of the potential applicability to seawater vehicles.

ACKNOWLEDGMENTS

A sincere thank you goes to the members of the Steering, Executive, and Technical Committees; the session chairpersons; the staff of the Surface Warfare Officers School; and the administrative team at Systems Resource Management, Inc. Their hard work and dedication ensured that both the symposium and proceedings reflected the highest standards of professionalism and intellectual achievement in the field of drag reduction. The names and organizations of these distinguished professionals follow.

Dr. James C. S. Meng
Symposium Chairperson

STEERING COMMITTEE

Dr. John Sirmalis, *Naval Undersea Warfare Center*

RADM Michael Coyle, *Naval Sea Systems Command*

Mr. Robert Draim, *Naval Sea Systems Command*

Mr. Timothy Douglass, *Program Executive Office, Undersea Warfare*

RADM Charles Young, *Naval Sea Systems Command*

Dr. Spyridon Lekoudis, *Office of Naval Research*

Dr. Theo Kooij, *Defense Advanced Research Projects Agency*

CAPT Brian Wegner, *Naval Sea Systems Command*

Mr. Art Spero, *Naval Sea Systems Command*

Mr. James Thompson, *Program Executive Office, Undersea Warfare*

Dr. Richard Vogelsong, *Office of Naval Research*

EXECUTIVE COMMITTEE

Mr. Dennis Bushnell, *National Aeronautics and Space Administration - Langley*

Mr. James Fein, *Office of Naval Research*

Dr. Louis Goodman, *Office of Naval Research*

Dr. Thomas Huang, *Naval Surface Warfare Center, Carderock Division*

Mr. Gary Jones, *Defense Advanced Research Projects Agency*

Dr. James McMichael, *Defense Advanced Research Projects Agency*

Dr. Richard Nadolink, *Naval Undersea Warfare Center, Division Newport*

CDR Steven Petri, *Naval Sea Systems Command*

Dr. Patrick Purtell, *Office of Naval Research*

Dr. Edwin Rood, *Office of Naval Research*

TECHNICAL COMMITTEE

Dr. Rudolph Bannasch, *Technische Universitat Berlin, Germany*

Dr. Dietrich Bechert, *Technische Universitat Berlin, Germany*

Prof. Herman Branover, *Ben Gurion University, Israel*

Dr. Kwing-So Choi, *University of Nottingham, UK*

Dr. Steven Deutsch, *Applied Research Lab/Penn State University, USA*

Dr. Robert Mons, *Northrop Grumman, USA*

Dr. Mark Savill, *University of Cambridge, UK*

Dr. Promode Bandyopadhyay, *Naval Undersea Warfare Center, Division Newport, USA*

Dr. Peter Hendricks, *Naval Undersea Warfare Center, Division Newport, USA*

Dr. Stephen Huyer, *Naval Undersea Warfare Center, Division Newport, USA*

Dr. William Keith, *Naval Undersea Warfare Center, Division Newport, USA*

Mr. Richard Philips, *Naval Undersea Warfare Center, Division Newport, USA*

Dr. Howard Schloemer, *Naval Undersea Warfare Center, Division Newport, USA*

TABLE OF CONTENTS

DRAG REDUCTION - HISTORICAL OVERVIEW

Polymer Solution Effects on Turbulent Friction Mechanisms 1
J.W. Hoyt - *San Diego State University*

Drag Reduction "Designer Fluid Mechanics" - Aeronautical Status and Associated Hydrodynamic Possibilities (an "embarrassment of technical riches") 7
D. Bushnell - *NASA - Langley Research Center*

European Drag Reduction Research - Recent Developments and Current Status 13
K.S. Choi - *The University of Nottingham*

Drag Reduction Research in Japan 19
K. Watanabe - *Tokyo Metropolitan University*

WALL TURBULENCE PHYSICS

Near Wall Turbulence: A Remembrance of Steve Kline 29
B. Cantwell - *Stanford University*

Vortex Packets and the Structure of Wall Turbulence 33
R. Adrian, S. Balachandar - *University of Illinois at Urbana-Champaign*

Vortex Development and Interactions in Turbulent Boundary Layers: Implications for Surface Drag Reduction 39
C. Smith - *Lehigh University*

Coherent Structures, Self-Sustaining Process and Bifurcations in Shear Flows 47
F. Waleffe - *University of Wisconsin-Madison*

Detection of Transition and Flow Bifurcation Regions on A Hydrofoil Using Hot-Film Constant Voltage Anemometry 53
S. Mangalam, G. Sarma, R. Pfouts, T. Kwa - *Tao Systems, Inc.*, J. Casper, M. Wallace, H. Moghadam - *Newport News Shipbuilding*, R. Nigon - *Naval Surface Warfare Center, Carderock Division*

Measured Wall Pressure Signatures of Turbulence Producing Structures 63
S. Russell - *Naval Surface Warfare Center, Carderock Division*

Streamfunction - Vorticity Calculations of Navier-Stokes Equations As A Tool For High Accuracy Study of Pressure - Tension Relation 73
M. Zakharenkov - *Central Aero-Hydrodynamic Institute*

Frequency-Wavenumber Spectral Measurement of Turbulent Boundary Layer Wall Pressure 83
M. Pognant - *MS L.A.I.A.T. - Université de Toulon*, G. Giovannelli, B. Forestier - *I.R.P.H.E., France*

High Reynolds Number Turbulent Flows 89
A. Smits - *Princeton University*, M. Zagarola - *Creare, Inc.*

DRAG REDUCTION PHYSICS

The Lamb Vector and Its Divergence in Turbulent Drag Reduction 99
C. Crawford, H. Marmanis, G. Karniadakis - *Brown University*

Role of Helicity and Chirality in Drag Reduction in Turbulent Flows 109
S. Moiseev, O. Chkhetiana - *Space Research Institute, Moscow*,
H. Branover, A. Eidelman, E. Golbraikh - *Ben-Gurion University*

Methods of Influence on Coherent Vortical Structures of A Boundary Layer 113
V. Babenko - *National Academy of Sciences, Kiev*

Drag Reduction with Submerged Ribs and its Mechanism in A Turbulent Boundary Layer Over D-Type Roughness 121
S. Mochizuki, H. Osaka - *Yamaguchi University*

A New Approach to Drag Reduction 127
A. Cotel - *University of Manitoba,* R. Breidenthal - *University of Washington*

Direct Numerical Simulations of Drag Modifications Using Randomized Force Fields 131
R. Dahlburg, W. Sandberg, R. Handler - *Naval Research Laboratory,*
L. Sirovich - *Brown University*

Adaptive Feed-Forward Control of Turbulent Boundary Layers 135
K. Breuer, R. Rathnasingham, K. Amonlirdviman - *Massachusetts Institute of Technology*

Flow Management Using Inherent Transition and Receptivity Features 143
N. Yurchenko - *National Academy of Sciences, Kiev,* R. Rivir - *Wright-Patterson Air Force Base*

SEAWATER PHYSICS

In-Situ Estimation of the Abundance and Sizes of Particulates in the Sea 149
D. Holliday - *Tracor Aerospace*

Biofouling Control: A Critical Component of Drag Reduction 155
G. Swain - *Florida Institute of Technology*

Environmental Factors For Ocean Bubbles 163
J.Hanson - *The Johns Hopkins University/Applied Physics Laboratory*

A Boat-Mounted Foil to Measure the Drag Properties of Antifouling Coatings Applied to Static Immersion Panels 169
B. Kovach, G. Swain - *Florida Institute of Technology*

The Effect of Biofilms on Turbulent Boundary Layer Structure 175
M. Schultz, G. Swain - *Florida Institute of Technology*

TURBULENT DRAG REDUCTION METHODS: COMPLIANT COATINGS

Recent Advances in the Use of Compliant Walls for Drag Reduction 185
P. Carpenter - *University of Warwick, U.K.*

Recent Developments in Interference Analysis of Compliant Boundary Action on Near-Wall Turbulence 189
B. Semenov, A. Semenova - *Siberian Branch of Russian Academy of Sciences*

Compliant Coatings: The Simpler Alternative 197
M. Gad-el-Hak - *University of Notre Dame*

Drag Reduction of the Ocean Surface by the Surface Waves 205
A. Benilov - *Stevens Institute of Technology*

Blubber and Compliant Coatings for Drag Reduction in Fluids: V. Driving Point Shear Impedance Measurements on Compliant Surfaces 211
E. Fitzgerald - *Johns Hopkins University,* J. Fitzgerald - *Kildare Corporation*

Blubber and Compliant Coatings for Drag Reduction in Fluids: VI. Rotating Disc Apparatus for Drag Measurement on Compliant Layers 215
J. Fitzgerald, J. Martin, E. Modert - *Kildare Corporation*

Interface Waves on A Compliant Coating Bounded by A Fluid Flow and Their Excitation by Acoustic Resonance 219
H. Uberall - *Catholic University of America,* W. Madigosky - *A&T, Inc.*

Analysis of Evolution of Disturbances in Channel Flow Over A Wavy Wall 225
D. Riahi - *University of Illinois at Urbana-Champaign*

TURBULENT DRAG REDUCTION METHODS: SPANWISE FLUID MOTION & WALL MOTION

The Mechanism of Turbulent Drag Reduction with Wall Oscillation 229
K.S. Choi, B. Clayton - *University of Nottingham, U.K.*

On the Physics of Skin Friction Reduction Through Wall Oscillation 237
M. Dhanak, C. Si - *Florida Atlantic University*

Local Oscillating Blowing in A Turbulent Boundary Layer 241
S. Tardu - *Laboratoire des Ecoulements Géophysiques et Industriels*

Drag Reduction Through the Near Wall Vortex System Management 249
Y. Savchenko - *Institute of Hydromechanics of Ukrainian National Academy of Sciences*

Boundary Layer Control at Wave-Like Swimming 257
L. Koryenna - *Institute of Hydromechanics of Ukrainian National Academy of Sciences*

Substitution of Rolling for Slipping as an Effective Mechanism of Decreasing Hydrodynamic Drag 263
V. Merkulov - *Siberian Branch of the Russian Academy of Sciences*

TURBULENT DRAG REDUCTION METHODS: POLYMER

The Combination of Polymer, Compliant Wall, and Microbubble Drag Reduction Schemes 269
B. Semonov - *Siberian Branch of the Russian Acadeny of Sciences*

Similarities and Differences in Drag Reduction Behavior of High Polymer and Surfactant Solutions 277
J. Zakin, Z. Lin - *The Ohio State University*, J. Myska - *Czech Academy of Sciences*

Drag Reducing Additive for Recirculating Hydronic Systems: Full-Scale System Engineering Analysis and Field Test 281
K. Gasljevic, K. Hoyer, E. Matthys - *University of California, Santa Barbara*

Practical Applications of Dilute Polymer Additives for Water Craft 289
T. Kowalski - *University of Rhode Island*

Experimental Research of the Influence of Conditions of Polymer Admission to the Boundary Layer on A Drop of Turbulent Friction 295
V. Pogrebnyak - *Ecological Center of Scientific and Applied Researches*, Y. Ivanyuta - *A.N. Krylov Central Research Institute*

Drag Reduction Dynamics 299
V. Kulik - *Russian Academy of Sciences*

On the Hydrodynamical Smoothness in Polymer Solutions 305
W. Amfilokhiev, K. Mazaev - *Saint-Petersburg State Marine Technical University*

TURBULENT DRAG REDUCTION METHODS: MICROBUBBLE

Experimental Evidence for a Link Between Microbubble Drag Reduction Phenomena and Periodically Excited Wall-Bounded Turbulent Flow 313
M. Guin - *The Johns Hopkins University*, H. Kato - *The University of Tokyo*, Y. Takahashi - *IHI Ltd.*

Role of Bubble Injection Technique Drag Reduction 319
R. LaTorre - *University of New Orleans*, V. Babenko - *National Academy of Sciences, Kiev*

Optimization of the Distributed Gas Injection into A Turbulent Boundary Layer for the Drag Reduction 327
V. Bogdevich, L. Maltzev, A. Maluga - *Siberian Branch of the Russian Academy of Sciences*

Effect of Microbubble Distribution on Skin Friction Reduction 331
Y. Kodama - *Ship Research Institute, Tokyo*

Combined Polymer and Microbubble Drag Reduction 335
R. Philips, J. Castano, J. Stace - *Naval Undersea Warfare Center Division Newport*

Microbubble Formation and Splitting in a Turbulent Boundary Layer for Turbulence Reduction 341
J. Meng, J. Uhlman - *Naval Undersea Warfare Center Division Newport*

TURBULENT DRAG REDUCTION METHODS: ELECTROMAGNETIC DRAG REDUCTION

Engineering Insight of Near-Wall Microturbulence for Drag Reduction and Derivation of a Design Map for Seawater Electromagnetic Turbulence Control 359
J. Meng - *Naval Undersea Warfare Center Division Newport*

Experiments on Turbulent Channel Flow with Electromagnetic Turbulence Control 369
X. Fan, G. Brown - *Princeton University*

Drag Reduction Experiments on a Small Axisymmetric Body in Saltwater Using Electromagnetic Microtiles 373
P. Bandyopadhyay, J. Castano, D. Thivierge, W. Nedderman - *Naval Undersea Warfare Center Division Newport*

MHD Turbulence Experiments, Drag Reduction and Application to Non-MHD Flow 379
A. Eidelman, H. Branover, E. Golbraikh, - *Ben Gurion University,* S. Moiseev - *Space Research Institute, Moscow*

Drag Reduction by Electro-Magnetic Forces 385
V. Merkulov - *Siberian Branch of the Russian Academy of Sciences*

Electromagnetic Effects on Low Speed Coherent Structures Embedded in A Wall Layer 389
J.P. Thibault, V. Botton, L. Rossi - *PAMIR Team, LEGI, France*

Some Results on Electromagnetic Control of Flow Around Bodies 395
T. Weier, G. Gerbeth, G. Mutschke, U. Fey - *MHD Dept., Forschungszentrum Rossendorf,* O. Posdziech - *Inst. Aerospace Eng., TU Dresden,* O. Lielausis, E. Platacis - *Institute of Physics Riga, Latvia*

Analysis and Finite Element Simulation of MHD Flows, with an Application to Seawater Drag Reduction 401
A. Meir, P. Schmidt - *Auburn University*

Lorentz Force Modeling in EMHD Turbulence Control: DNS Studies 407
Y. Du, C. Crawford, G. Karniadakis - *Brown University*

Fundamental Studies on Active Control of Large Scale Coherent Structures in Channel Turbulence 413
P. O'Sullivan, S. Biringen - *University of Colorado at Boulder*

Interactive Electro-Magnetohydrodynamic Control of Near-Wall Streaks 419
S. Snarski - *Kohler, WI*

TURBULENT DRAG REDUCTION METHODS: BIOLOGY BASED DRAG REDUCTION

Dolphin Drag Reduction: Myth or Magic 429
J. Fein - *Office of Naval Research*

Hydrodynamics of Wave-Like Curvature on Bodies of Swimming Animals 435
R. Bannasch - *Technische Universität Berlin*

Imaginative Solutions by Marine Organisms for Drag Reduction 443
F. Fish - *West Chester University*

On Biological Foundations of Dolphin's Control of Hydrodynamic Resistance Reduction 451
V. Babenko, A. Yaremchuk - *National Academy of Sciences, Kiev*

Hydrobionics Principles of Drag Reduction 453
V. Babenko - *National Academy of Sciences, Kiev*

Phased Vortex Seeding for Thrust Modulation in a Rigid Cylinder with Flapping Foil Thrusters 457
P. Bandyopadhyay, J. Castano, W. Nedderman, D. Thivierge - *Naval Undersea Warfare Center Division Newport*

Drag Reduction and Turbulence Control in Swimming Fish-Like Bodies 463
M. Wolfgang, S. Tolkoff, A. Techet, D. Barrett, M. Triantafyllou, D. Yue, F. Hover - *Massachusetts Institute of Technology,* M. Grosenbaugh, W. McGillis - *Woods Hole Oceanographic Institution*

Flow Separation Control By Means of Flapping Foils 471
M. Platzer - *U.S. Naval Postgraduate School,* J. Lai - *Australian Defence Force Academy,* C. Dohring - *German Armed Forces University*

The Vorticity Control Unmanned Undersea Vehicle - A Biologically Inspired Autonomous Vehicle 479
J. Anderson - *Charles Stark Draper Laboratory*

A Fast-Starting and Maneuvering Vehicle, the ROBOPIKE 485
J. Kumph, M. Triantafyllou - *Massachusetts Institute of Technology*

INDEX BY AUTHOR NAME 491

Drag Reduction - Historical Overview

19990504 000

POLYMER SOLUTION EFFECTS ON TURBULENT FRICTION MECHANISMS

J.W. Hoyt
Professor Emeritus, Mechanical Engineering
San Diego State University
San Diego, CA 92182-1323

Abstract – In discussing the prospects for reducing the turbulent-friction drag, it seems important to first try to understand where the friction arises. Such a basic and fundamental knowledge is still elusive. This paper is intended as a basis for discussion, at least, of the known components of turbulent friction as they pertain to flat-plate and external flows. Experimental results illustrating the various components of turbulent drag are drawn from the literature, together with some new data.

I. INTRODUCTION

The question of "where does the turbulent drag arise?" is one of the most fundamental problems in fluid mechanics, and one of the least understood. Turbulence has attracted the attention of some of the world's greatest scientists over the last hundred years or so, and yet our understanding is far from complete. If substantial progress is to be made in reducing the friction on vehicles of various kinds, deeper understanding of the fundamentals of turbulent flow seems essential.

Nevertheless, a great amount of information is available. With new experimental and computational tools, the last few years have given much greater insight into the details of turbulent flow over plates and surfaces. The new information has occasioned some friendly controversy, and authorities can differ strongly on basic turbulent flow mechanisms. Some of these differences will be discussed here.

If we restrict our attention to smooth plates, contributors to the overall resistance or drag include:

- Fluid viscosity
- Reynolds stresses
- Coherent structures
  - Streaks
  - Vortices
- Pressure fluctuations

Each of these resistance components will be examined to show, if possible, avenues of approach which might lead to significant drag reduction.

II. FLUID VISCOSITY

The shear stress appears in both laminar and turbulent flow as:

$$\tau = \mu \partial u/\partial y \qquad (1)$$

Obviously, reducing the viscosity, μ, would reduce the friction. For a vehicle operating in seawater, the viscosity could be reduced by heating the seawater flowing over the body, or by introducing a second fluid of lower viscosity around the hull. Experiments using air exuded around the surface show a reduction in overall resistance but this may be due to other interactions as will be described below. In any event, the resistance due to fluid viscosity becomes insignificant compared to other components of the drag as the Reynolds number is increased to values typical of vehicle applications.

III. REYNOLDS STRESSES

To provide insight into more significant elements of the turbulent friction, it is useful to write the x-direction term of the incompressible, steady, Navier-Stokes (or momentum) equation:

$$\rho[u(\partial u/\partial x) + v(\partial u/\partial y) + w(\partial u/\partial z)] = -\partial P/\partial x + \mu[\partial^2 u/\partial x^2 + \partial^2 u/\partial y^2 + \partial^2 u/\partial z^2] \qquad (2)$$

But now we find that the viscosity term (with μ) is inadequate for turbulent motion and resort to a strategy proposed by Osborne Reynolds over 100 years ago. We replace the velocity quantities by a mean or average value, plus a fluctuating velocity whose mean is zero, but whose square or product is, of course, not zero. Thus:

$$u = \overline{u} + u' \qquad v = \overline{v} + v' \quad \text{and} \quad w = \overline{w} + w'$$

where the overbar indicates averaged quantities.

When these values are introduced into the Navier-Stokes equations, and time averaged again, additional terms of the form:

$$-\rho[\partial \overline{u'^2}/\partial x + \partial \overline{u'v'}/\partial y + \partial \overline{u'w'}/\partial z] \qquad (3)$$

appear. Among the new time-averaged quantities, the term $-\rho\overline{u'v'}$ is believed to be of major importance, and having the units of a stress, is usually called the Reynolds stress. (The overbar will be dropped in all further discussion, but the time-averaged concept still applies.)

In order to contribute to the resistance, the fluctuating quantities themselves must be on average negative. Modern instrumentation can detect quantities such as u'v', and show that in fact u'v' is strongly negative. Figure 1 shows measurements of u'v', where the fluctuating velocity values have been weighted by the frequency of their occurrence and plotted as a function of their respective signs. The strongly negative quadrants 2 and 4 show that the overall sign of the fluctuating quantities is negative.

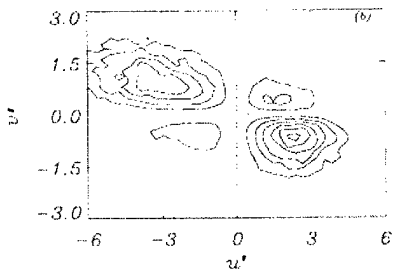

Figure 1: Fluctuating velocities u'v', weighted by how frequently they occur. Turbulent boundary layer: $Re_\theta = 1070$; $y^+ = 35$. (From Ong [1].)

The maximum values of u'v' occur well away from the wall, at y^+ = around 30, where $y^+ = y\,u^*/\nu$, with u^* the friction velocity and ν the kinematic viscosity. Figure 2 shows how, in a plot of shear stress as a function of distance from the wall in a channel, the Reynolds stress forms most of the total stress, other stresses including the viscous stress (1) presumably contributing the remainder. The distribution of stresses found in a channel may be expected in the turbulent boundary layer.

In the momentum equation (3), the y derivative of u'v' forms the resistance component; hence changing the slope of the Reynolds stress term, as well as its value, offers an opportunity for substantial drag reduction. This has been exploited in drag reduction by polymer solutions and fiber suspensions.

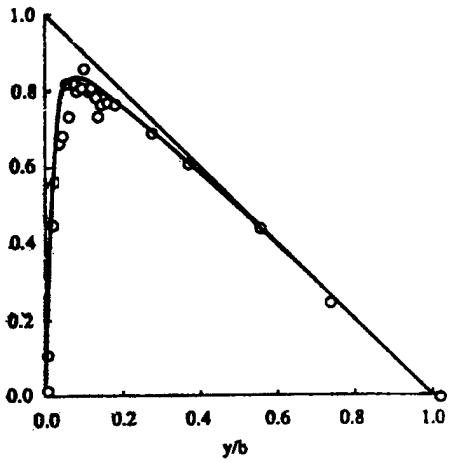

Figure 2. Total shear stress as function of distance from wall to center of water channel, with u'v' data points. (From Willmarth *et al.* [2].)

Polymer additives seem to inhibit both u' and v' and decreases their correlation, as can be seen from Figures 3-5. The astonishing thing is that the Reynolds stress can be reduced almost to insignificance, but the drag reduction, (around 60% in this experiment), seems nowhere near as large. This action of polymer additives (and also fiber suspensions and possibly microbubbles [3]) appears to be a result of physically disrupting the interaction between the vertically-moving and the axially-moving fluctuating velocities. Putting it more scientifically, the axial to transverse velocities become decorrelated.

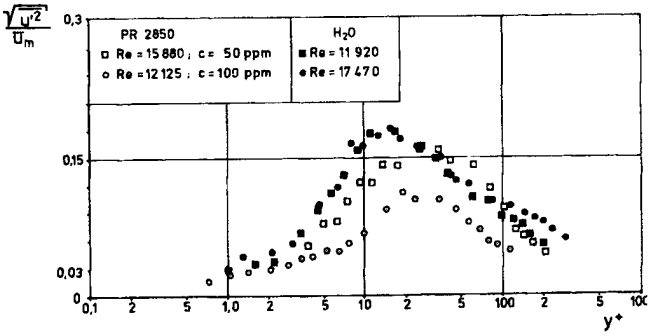

Figure 3. Fluctuating axial velocities – polymer solution flow compared with water. (From Gampert & Delgado [4].)

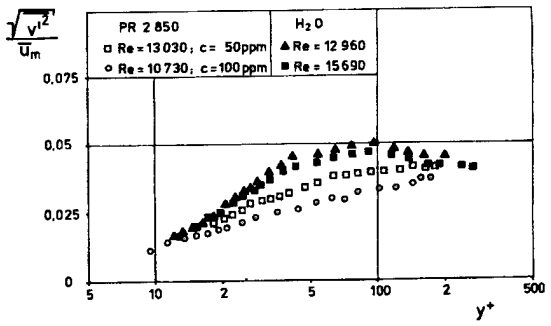

Figure 4. Fluctuating vertical velocities – polymer solution flow compared with water. (From Gampert & Delgato [4].)

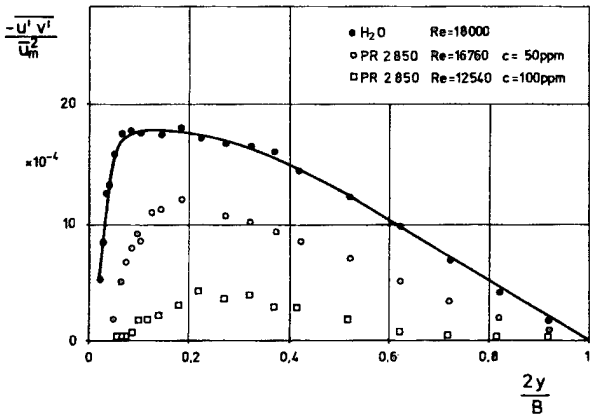

Figure 5. Reynolds stress for water and polymer solutions, plotted across the half-width of the channel. (From Gampert & Delgado [4]

Results similar to those obtained by Gampert & Delgado [4] have also been obtained by Willmarth *et al.* [2] and Bewersdorff [5], among others. Hence the large decrease in u'v' in polymer solution flow must be taken as a fact. The resistance or drag reduction is not as great as the decrease in the fluctuating u'v' component in channel flow.

One interpretation of this result would be to recognize that the u'v' fluctuations are not created spontaneously (i.e. of their own accord) but are the result of other, larger-scale motions in the boundary layer. If the fluctuating velocities are suppressed, these larger motions are still there requiring energy to drive them. Thus the coherent structures could easily be the reason that drag decrease does not mirror the decrease in fluctuating velocities. In pipe flow, where drag reductions approaching 80% have been measured with polymers, coherent structures are limited in growth by the pipe size, and thus may contribute less to the resistance.

Nevertheless, spectacular drag reductions have been achieved on flat plates immersed in polymer solutions. Figure 6 shows results of a test by Levy and Davis [6] on a 1 m long plate, where more than 60% drag reduction was obtained in a high-speed towing tank.

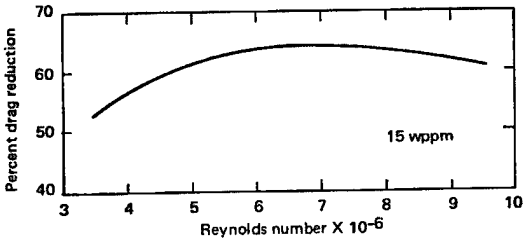

Figure 6. Drag reduction on a flat plate towed in 15 ppm poly(ethylene oxide). (From Levy & Davis [6].)

IV. COHERENT STRUCTURES - STREAKS

The flow region nearest the wall is dominated by structures which, when made visible with dye, appear as low-speed axial streaks, occurring quite densely but randomly and then lifting up and quickly disappearing. The sketch below is widely accepted as a possible mechanism for the production of the streaks, but how the vortices are formed, and whether they occur before, together with, or after the streaks appear is a topic of current discussion. The spacing between

streaks is $\lambda^+ = \lambda u^*/\nu = 100$ for Newtonian fluids, but in polymer solutions, λ^+ becomes substantially larger (Donohue *et al,* [7]). The streaks terminate by lifting away from the wall, oscillating, then "bursting" (Klein *et al.* [8]). The burst rate is reduced in polymer solutions [7] by 50% or more. The bursting is believed to be a major source of the u'v' fluctuating velocities, occurring as it does at $y^+ = 30$-35. Following the burst, "sweeps" [8] of new, higher-speed fluid enters the region. The action of polymer solutions to influence the streak spacing, burst rate, and fluctuating velocities appears to be responsible for their powerful drag-reducing ability.

Riblets are small V-shaped grooves either machined or applied as a plastic sheet coating, with the grooves extending in the axial flow direction. The riblets appear to dampen the lateral motion and spreading of the low-speed streaks. As explained in the excellent review article by Walsh [9], drag reductions of around 8% seem obtainable if the groove size is properly tailored to the flow. On an actual torpedo-like test vehicle, drag reductions of around 8% were found when suitable riblets were applied [10]. Drag reductions of the same magnitude are also found in riblet-lined pipes.

There have been several studies of the combination of riblets and polymer solutions in pipes. Anderson *et al.* [11], Koury & Virk [12], and later Mizunuma *et al.*[13] found a synergistic effect under certain conditions. Indeed, based on their experiments, Koury & Virk suggest that riblets and polymers reduce drag by separate mechanisms.

V. COHERENT STRUCTURES - VORTICES

Horseshoe or hairpin shaped vortices were originally described by Theodorsen [14] in 1952. Only recently have reliable experimental methods of visualizing these structures become available. From these newer studies it appears that the turbulent boundary layer is dominated by vortex-like motions. In fact, Zhou *et al.* [15] believe that the low-speed streaks are also the result of vortex action, as shown in Figure 7. Similar views have been expressed by Smith & Walker [16].

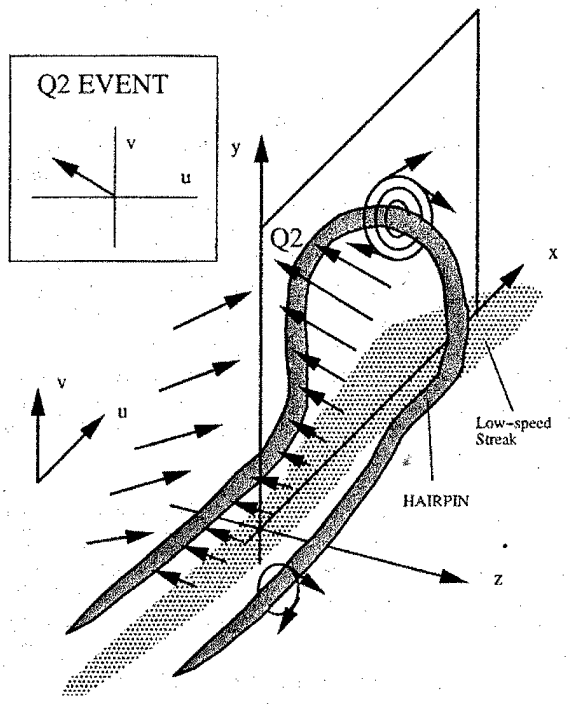

Figure 7. Sketch showing proposed action of hairpin vortices in forming low-speed streaks. As the vortex moves in the x direction, quadrant 2 u'v'events take place. (From Zhou *et al.* [15].)

In contrast to earlier suggestions in the literature that horseshoe vortices were rather rare in the boundary layer, Zhou *et al.* [15] using particle-image-velocimetry find the hairpin vortex to be the most frequently recurrent pattern in the boundary layer. Velocity vector plots show the vortices can extend in height some 30% above the top of the log layer. The vortices can appear singly or in "packets" of two or more. Figure 8 gives some of the results reported by Zhou *et al.* [15].

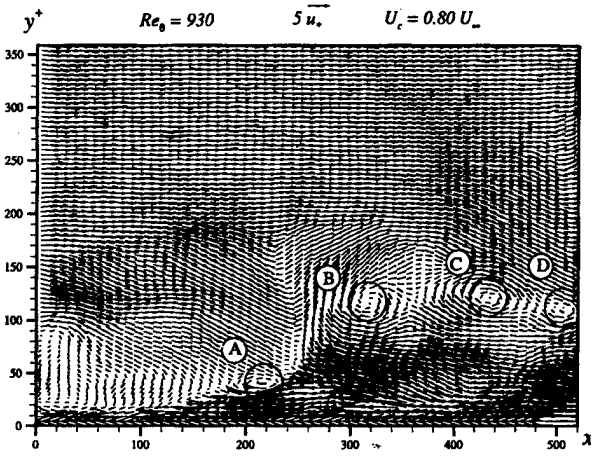

Figure 8. PIV velocity plot showing cross-section through a series of hairpin vortices. Velocities corresponding to 80% of the free-stream velocity have been subtracted from all vectors. (From Zhou *et al.* [15].)

There appear to be no data on the effect of polymers on the hairpin vortices. However, in the course of experimental proposals to use "heterogeneous" drag reduction involving discharge of threads of concentrated polymer solution into flowing water, a new method of visualizing the coherent structures was discovered (Hoyt & Sellin [17]). The technique involves discharging a tracer consisting of a mixture of shear-thickening surfactant, high extensional viscosity polymer, and white emulsion paint into the lower region of the boundary layer. Vortices and other coherent structures pick up the tracer and transport it downstream, giving a visual record of the boundary-layer activity. This simple technique is very effective in bringing out details of the vortex activity, as can be seen in Figure 9.

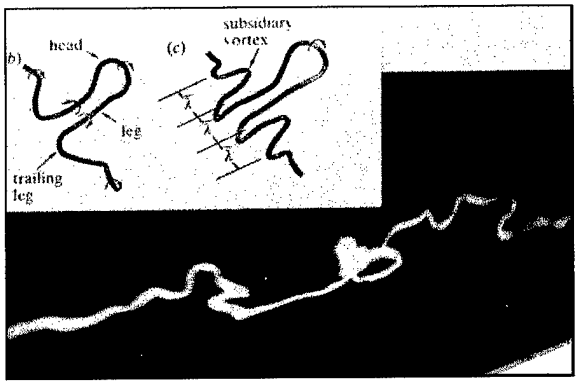

Figure 9. Horseshoe vortices revealed by the tracer (From Hoyt & Sellin [18]), compared with a computer simulation of a line vortex in a shear layer by Smith *et al.* [19]. Flow is left to right.

Extensive computer processing of a numerically simulated turbulent boundary layer has also revealed similar structures, thus implying that they somehow evolve as a solution of the Navier-Stokes equations. Chacin *et al.* [20] show a side view of some of these structures, which can be compared with video frames of a side view of the tracer in the boundary layer of a flat plate in Figure10.

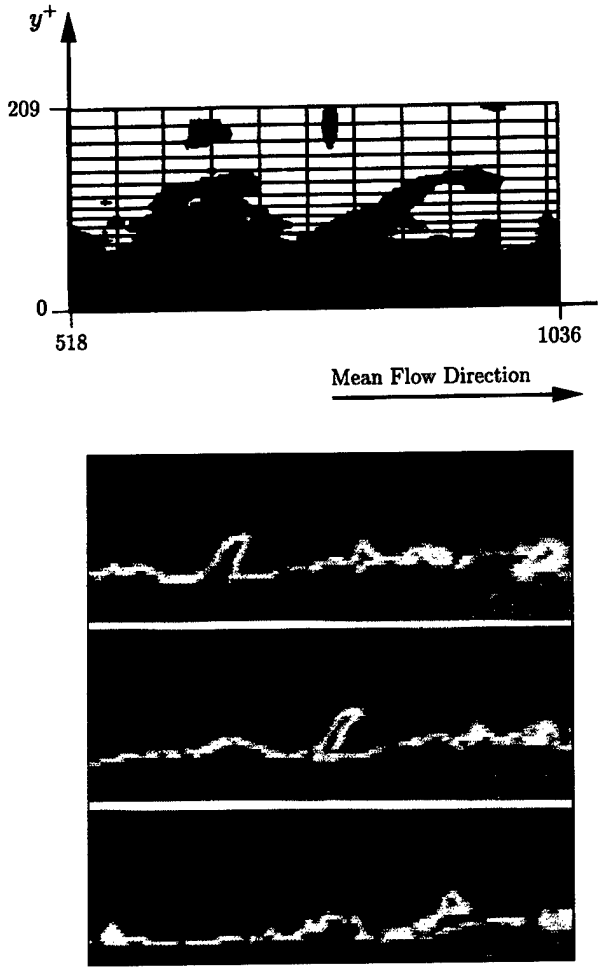

Figure 10. Computational result (above) from Chacin *et al.* [20] compared with video frames (taken 0.24 sec apart) of tracer activity. Both show side views of large structures. Portions of the bottom scene (Hoyt & Sellin [18]) resemble the computational result. The actual height of the structure in the center video is ~ 0.021 m ($y^+ \sim 270$).

Control of these large structures should lead to significant drag reduction. Large-Eddy Breakup Devices (LEBU's) have been successful in reducing the skin friction immediately behind the devices, but unfortunately create a drag themselves which cancels out most of any benefit thus obtained. The excellent review of Anders [21] shows, however, that skin friction reductions approaching 40% could be obtained, thus revealing the large contribution of the coherent structures to turbulent friction

VI. PRESSURE FLUCTUATIONS

It is a familiar occurrence that turbulent flow over a surface creates audible noise. The noise is caused by, or related to, surface pressure fluctuations. Early pressure measurements found that the smaller the pressure transducer, the more intense the signal, thus indicating that the source was small. Further, the pressure signals seemed to be correlated for short distances downstream, but not at all in the spanwise direction. Thus the pressure fluctuations seem to be connected to some boundary-layer event.

Smith & Walker [16] suggest that the pressure disturbances are caused by vortices (the spanwise portion of hairpin structures closest to the surface), which induce the low-speed streaks to abruptly erupt. Barker [22] in an elegant experiment, also suggested that eruption of the low-speed streaks provided the pressure-fluctuation source. Barker also investigated the effect of polymers on the pressure fluctuations, finding, as shown in Figure 11, a significant reduction with polymers present.

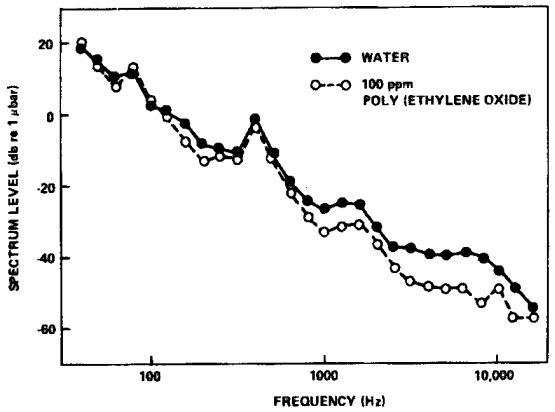

Figure 11. Radiated noise reduction observed with polymer solution on a plate. (From Barker [22].)

Similar noise reduction effects of polymers in turbulent flow have been noted by Brady [23] and others using rotating cylinders

VII. SUMMARY

From experimental results extending over the last 30 years, estimates (possibly very rough) of the smooth-plate turbulent-friction budget can be made:

- 50-60% Reynolds stresses, based on the $\rho u'v'$ reduction observed with drag-reducing polymers
- 20-30% coherent structures, based on LEBU results, and observation of their pervasive nature in the boundary layer
- 6-8% near-wall spanwise motions, based on reductions observed with riblets
- ½% viscous stress (projecting laminar-flow equations)
- ½% noise production (guess)
- 10-20% interactions of the above, and unknown

Much of the above has been derived from the many extensive experiments with polymer additives, which seem to affect both the fluctuating velocities and the spanwise distribution of the low-speed streaks. New observations of the coherent structures emphasize their importance in the turbulent-friction budget.

The scenario for production of turbulent friction on a flat plate moving through the water appears to be:

Viscous stresses → streaks + vortices + $\rho u'v'$ → bursts + horseshoes + $\rho u'v'$ + sweeps → large eddies → dissipation via Kolmogorov → heat

The shear stress at the wall must be the summation of all the above. Intervention at critical junctures by whatever means should lead to substantial drag reduction.

ACKNOWLEDGEMENT

The development of the flow tracer for visualizing coherent structures in the flow has been sponsored by the National Science Foundation under Grants CTS-9411980, CTS-9508409 and CTS-9713857. This technical and financial support is gratefully appreciated.

REFERENCES

1. L. Ong "Visualization of turbulent flows with simultaneous velocity and vorticity measurements", Ph..D. dissertation, University of Maryland, College Park, MD, 1992.

2. W.W. Willmarth, T. Wei & C.O. Lee "Laser anemometer measurements of Reynolds stress in a turbulent channel flow with drag reducing polymer additives" *Physics of Fluids* **30**, 933-935, 1987.

3. C.L. Merkle & S. Deutsch "Drag reduction in liquid boundary layers by gas injection" in D.M. Bushnell & J.N. Hefner, eds. *Viscous Drag Reduction in Boundary Layers,* Progress in Astronautics and Aeronautics **123**, AIAA, 351-412, 1990.

4. B. Gampert & A. Delgado "Laser-Doppler-anemometer measurements in turbulent flow of viscoelastic fluids" in *International Symposium on Laser Anemometry, ASME,* 143-150, November, 1985.

5. H.-W. Bewersdorff "Heterogene Wiederstandsverminderung bei turbulenten Rohrströmungen" *Rheologica Acta* **23**, 522-543, 1984.

6. J. Levy & S. Davis "Drag measurements on a thin plate in dilute polymer solutions" *International Shipbuilding Progress* **14**, 166, 1967.

7. G.L. Donohue, W.G. Tiederman & M.M. Reischman "Flow visualization of the near-wall region in a drag-reducing channel flow" *J. Fluid Mechanics* **56**, 559-575, 1972.

8. S.J. Kline, W.C. Reynolds, F.A. Schraub & P.W. Runstadler "The structures of turbulent boundary layers" *J. Fluid Mechanics* **95**, 741-773, 1967.

9. M.J. Walsh "Riblets" in D.M. Bushnell & J.N. Hefner, eds. *Viscous Drag Reduction in Boundary Layers*, Progress in Astronautics and Aeronautics **123**, AIAA, 203-261, 1990.

10. M.C. Gillcrist & L.W. Reidy "Drag and noise measurements on an underwater vehicle with a riblet surface coating" in R.H.J. Sellin & R.T. Moses, eds. *Drag Reduction in Fluid Flows*, Ellis Horwood Ltd., Chichester, 99-106, 1989.

11. G.W. Anderson, J.J. Rohr & S.D. Stanley "The combined drag effects of riblets and polymers in pipe flow" *Journal of Fluids Engineering* **115**, 213-221, 1993.

12. E. Koury & P.S. Virk "Drag reduction by polymer solutions in a riblet-lined pipe" *Applied Scientific Research* **54**, 323-347, 1995.

13. H. Mizunuma, K. Ueda & Y. Yokouchi "Synergistic effects in turbulent drag reduction by riblets and polymer additives" in J.W. Hoyt *et al.*, eds. *Proceedings of the Fluids Engineering Division Summer Meeting* **2**, *Turbulence Modification and Drag Reduction,* 107-114, 1996.

14. T. Theodorsen "Mechanism of turbulence" *Proceedings of the 2nd Midwestern Conference on Fluid Mechanics,* Ohio State University, Columbus, Ohio, 1952.

15. J. Zhou, C.D. Meinhart, S. Balachandar & R.J. Adrian "Formation of coherent hairpin packets in wall turbulence" in R.L. Panton, ed. *Self-Sustaining Mechanisms of Wall Turbulence,* Computational Mechanics Publications, Southampton, 109-134, 1997.

16. C.R. Smith & J.D.A. Walker "Sustaining mechanisms of turbulent boundary layers: the role of vortex development and interactions" in R.L. Panton, ed. *Self-Sustaining Mechanisms of Wall Turbulence,* Computational Mechanics Publications, Southampton, 13-47, 1997.

17. J.W. Hoyt & R.H.J. Sellin "A turbulent-flow dye-streak technique" *Experiments in Fluids* **20**, 38-41, 1995.

18. J.W. Hoyt & R.H.J. Sellin "Three-dimensional visualization of large structures in the boundary layer" *submitted, 1998.*

19. C.R. Smith, J.D.A. Walker, A.H. Haidari & U. Sobrun "On the dynamics of near-wall turbulence" *Phil. Trans. R. Soc. London A* **336**, 131-175, 1991.

20. J.M. Chacin, B.J. Cantwell & S.J. Kline "Study of turbulent boundary layer structure using the invariants of the velocity gradient tensor" *Experimental Thermal and Fluid Science* **13**, 308-317, 1996.

21. J.B. Anders Jr. "Outer-layer manipulators for turbulent drag reduction" in D.M. Bushnell & J.N. Hefner, eds., *Viscous Drag Reduction in Boundary Layers,* Progress in Astronautics and Aeronautics, **123**, AIAA, 263-284, 1990.

22. S.J. Barker "Radiated noise from turbulent boundary layers in dilute polymer solutions" *Physics of Fluids* **16**, 1387, 1973.

23. J.F. Brady "An experimental study of the vibration, noise, and drag of a cylinder rotating in water and certain polymer solutions" Ph.D. Thesis, University of Rhode Island, 1973.

DRAG REDUCTION "DESIGNER FLUID MECHANICS"--AERONAUTICAL STATUS AND ASSOCIATED HYDRODYNAMIC POSSIBILITIES
(an "embarrassment of technical riches")

Dennis M. Bushnell
Chief Scientist
NASA - Langley Research Center
11 Langley Boulevard, MS 110
Hampton, Virginia 23681-0001
d.m.bushnell@larc.nasa.gov

Abstract - Paper addresses aeronautical drag reduction areas, purposes and approaches and provides a status regarding both individual and combinational techniques. Emphasis is placed upon emerging/re-emerging approaches and consequent near(er) and far(ther) term techniques of potential interest for hydrodynamic applications. Paper considers mitigation/amelioration technologies for pressure drag, drag-due-to-lift, wave drag and viscous drag.

I. INTRODUCTION

Drag per se is among the major requisites for energy utilization by humankind in the 20th Century, the most blatant examples being vehicles of all types (land, sea, air) and pipeline transport. Drag is usually dissected into the major components of pressure or form drag, drag-due-to-lift, wave drag and attached friction or viscous drag. Which particular components are present/dominant is a function of the particular application and extant design sophistication.

Due to their extreme importance (tens of billions of dollars/year) drag reduction techniques and technology have been worked for essentially the entire 20th Century--this is far from a new area of engineering research and development. Considerable progress has been made, primarily in the minimization of form or pressure drag [e.g., refs. 1 and 2]. The other drag sources have also been worked by the research community but, as a general statement, there are few (and these usually quite limited) examples of deployed drag reduction approaches for friction drag, drag due to lift and wave drag other than simple "shape change." There are a great many techniques extant in terms of invention and technical evaluation success but from a technology viewpoint they simply have not offered enough payoff in the "real world" of economics and the "illities." [ref. 3]

General characteristics of those drag reduction approaches which, at least thus far, have "transitioned" from the laboratory to application include simplicity, very favorable economics, generally passive/rigid/retrofittable, reliable/"foolproof," well-understood and simulatable in laboratory facilities at application scale/conditions. [ref. 3]

The course of drag reduction research has historically been one of "ebb and flow," with the more active periods corresponding to the conjunction of the emergence of some new technical opportunities/ inventions/approaches to the problem and reemphasis of various societal (including military) requirements for drag reduction. We are currently entering again into such a conjunction, this time engendered by a combination of economic/ affordability/ environment drivers and the computing/ electronics/smart structures/ miniaturization "revolutions."

The purpose of the present paper is to briefly summarize the status of drag reduction research and technology in each of the drag component areas within the aeronautical world [see also refs. 4-9] and provide, as a surrogate for a conclusions section, a summary of emerging approaches and "best bets" for hydrodynamic R&D/application.

II. PRESSURE/FORM DRAG REDUCTION (SEPARATION/VORTEX CONTROL)

As a general rule, pressure or form drag is, or has the potential to be, the largest of the drag components when exacerbated by steady or dynamic large scale flow separation. A remnant of pressure drag exists even in fully attached flow, due to surface decambering by the attached viscous flow. However, this level is relatively benign, the order of 20 percent or less of the integrated skin friction, and is addressable via either boundary layer thinning or systems approaches (especially propulsive synergisms). Separated flow is the major pressure drag problem area and therefore separated flow control, for both 2-D and 3-D separated flows, is the key R&D arena for pressure drag reduction. 3-D separation can be either "closed" (e.g., analogous to the 2-D case) or open--the latter resulting in organized, generally longitudinal, vorticity and requiring vortex control [e.g., refs. 10 and 11] which therefore becomes a subset of separation control. Canonical approaches to separation control include mitigation of imposed/causative pressure gradients, removal of near wall low momentum fluid, addition of higher momentum fluid into the wall region and/or imposition of a wall "slip layer." Classical approaches to longitudinal vortex control include minimization of causative transverse pressure gradients, production of spatially-phased counter vorticity, segmented vorticity production, setup/excitation of vortex instability modes, control vortices to interact with/alter the vortex and energy extraction from the vortex.

The importance of separation control was recognized early on in aviation and assiduously developed and practiced for the fixed-wing aircraft cruise condition in essentially two stages--addressing first large scale separated regions and later, in a stage called "drag cleanup," smaller scale separated flow regimes associated with skin roughness and waviness, appurtenances and intersection regions. The dominant approach was to remove/mitigate the pressure gradients responsible for the flow separation via geometry alterations, resulting in"streamlining"/smooth(er) surfaces and fillets [e.g., refs. 10 and 12]. A variant of this approach was also utilized for "high lift"--variable geometry (slats and flaps).

Over the years a multitude of other separation control approaches have been invented/discovered, researched and in some specific instances, applied. These include blown flaps for fighters, imbedded boundary layer vortex generators (control by vortices, ref. 10, see also ref. 13), circulation control [ref. 14], base burning (for projectiles), "fences" and passive bleed. An enduring large scale vortex generator separation control approach has been the use of leading edge extensions etc. for improved fighter agility [ref. 10]. All of these approaches satisfy the, at least thus far, common characteristics of deployed drag reduction devices stated previously.

This almost century-long increasing attention to detail has reduced the pressure or form drag on aircraft to a level which is, in the aggregate, the order of half or less of the other drag components. For modern transport aircraft at the cruise condition, the drag breakdown is approximately 45 percent skin friction, 40 percent drag due to lift and 15 percent pressure drag--made up of attached flow "decambering," "crud drag" associated with residual skin roughness and antennas, joints, windshield wipers, intersections, etc. as well as some small "accepted" level of shock wave drag at the higher (subsonic) speeds.

It should be noted that the list of alternative, and generally in some manner "active," separation control approaches studied is quite extensive (e.g., trapped/stabilized transverse vortices [refs. 15-17], pneumatic/ actuated strake vortex control [ref. 10], passive porous wall control of wave-induced separation, spanwise blowing, pulse blowing [refs. 18-21], mission-adaptive wings, jet vortex generators, etc. etc.). As noted previously historically there has been a strong penchant to eschew, operationally, such active approaches in favor of passive ones--based upon valid systems/ application metrics rationale.

III. DRAG-DUE-TO-LIFT REDUCTION

The status of drag--due-to-lift reduction for aircraft parallels that of form drag reduction--the (linear) theoretically obvious and easily

implemented have been adopted. A major difference is a relative lack of a significant (in the aggragate) research program to examine the multitudinous alternative approaches [see ref. 9]. What is nearly universally employed are the tenants of planar inviscid theory which dictate an elliptic span load for DDL minimization on finite span wings. The other obvious approach, again from simple theory, is increased span--obviously limited by structural considerations. "Winglets," "non-planar" wing-tip devices (essentially thrust-producing end plates) are often employed either in lieu of increased span or to mitigate the effects of a non-optimal (tip-loaded) span load distribution. There are a host of passive tip approaches to extract energy from the tip vortex which have been looked at/studied somewhat but, at this point, not employed--e.g., tip turbines, vortex diffuser vanes and tip "sails" or "feathers." Configurational approaches such as ring/joined wings and mass transfer (porous tips, tip injection) have also been found effacious in the laboratory--but are not yet employed.

In short, as in flow separation control, there is an "embarrassment of riches" in the DDL reduction arena, via non-planer lifting surfaces, energy/thrust extraction from the vortex, alteration of the boundary conditions at/ "elimination" of the tip region and creative propulsion integration. However, again none but the simplest, most straightforward is actually utilized or indeed even studied/optimized in sufficient depth to allow a rational systems evaluation for aeronautical applications.

IV. WAVE DRAG REDUCTION (VOLUME AND LIFT)

(Shock) wave drag is a potentially serious wing drag component for high subsonic speed transports and accounts for the order of a third of the drag of a "well-designed" supersonic transport. Again, there are a plethora of drag reduction approaches, [e.g., ref. 9] varying from simple/simplex to complex/multidisciplinary--and again the simpler methods are the ones which are utilized. These include, from linear theory, shock strength mitigation approaches such as wing sweep, area ruling, extended lifting line (onto the fuselage) along with leading edge "thrust," wing twist/warp and reduced thickness and flow angle(s). More recently non-linear theory, e.g., CFD, has been utilized to wring another 10 percent or so from such optimizations.

In addition to these "usual" wave drag reduction methods there is a wealth of "non-conventional" mainly non-utilized approaches including nose spikes, fluid or particle injection, focusing lasers, heat addition, nose blunting ("works" due to presence of over-expansion), "star-bodies" and passive bleed.

There also exists another whole class of alternative approaches to wave drag reduction based upon multi-body favorable interference, the well known "Busemann Bi-plane" being the reducio-ad-absurdum example. Variants include ring wings and, for lifting configurations, the parasol wing. Separated flow control for shock boundary layer interactions regions is probably required to accrue the full benefits of favorable wave interference. Many of these unconventional approaches offer major potential benefits. [ref. 9]

V. ATTACHED VISCOUS DRAG REDUCTION

Obvious zeroth order approaches to viscous drag reduction include smooth(er) surfaces, reduced wetted area and extended regions of laminar, as opposed to turbulent, flow. In the "air world" a recent method of accomplishing the former is to utilize engine thrust vectoring or load alleviation to allow reductions in control surface "acreage." Alternatively, blended wing body/spanloader configurations can, in the limit, obviate a fuselage per se and the associated wetted area/friction drag.

The methodology for transition delay, usually termed laminar flow control or LFC, differs between 2-D and 3-D flows. The latter exhibit boundary layer crossflow which necessitates some type of active (suction is the usual "approach"-of-choice) control whereas in 2-D (including axisymmetric) flows significant drag reduction is usually available via (favorable) pressure gradient tailoring (so-called "natural" laminar flow). Multitudinous flight (and laboratory) studies are available for both "natural" and controlled LFC/transition extension--up to Reynolds numbers greater than 50×10^6 , and, as for many of the other drag reduction arenas/concepts--the approaches "work," technically. Thus far only the simple, more robust "natural" approach is used, often inadvertently, on lower speed aircraft where the wings are largely "2-D"/unswept. The economics of controlled LFC are, at least thus far, evidently not favorable in the air world--even through the technology has been amply "demonstrated" in flight and "production" surface smoothness is now compatible with maintenance of laminar flow.

Turbulent drag reduction is a much studied and, in spite of some significant technical successes, much ignored area of research in terms of "air world "applications. Technically (as opposed to technologically) successful approaches to TDR include riblets, slot injection/wall wake (steady state or dynamic), Stratford closure(s), surface heating [refs. 22, 23], nose "swords," normal injection, (spanwise) oscillatory wall motions, [refs. 24-33] "inplane" or convex longitudinal streamline curvature and relaminarization via massive suction. None of these are, at this point, applied in the air world although riblets have been employed in several Olympic sporting events, the America's Cup races and are evidently to be offered on the Airbus A340 and used on some U.S. military aircraft to save the weight and cost of paint as well as provide drag reduction. Refs.6, 8, 9 and 34-37 provide useful entre into the literature in this arena.

VI. EMERGING AERONAUTICAL DRAG REDUCTION APPROACHES

There are two general areas of increasing activity in the arena of aeronautical drag reduction. Neither of these can, at this point, be termed even technically (let alone technologically) successful but both have sufficient degrees of freedom and promise to bear watching.

The first of these is the use of surface-distributed Mems or Mems-like active sensing/logic/actuator devices to either establish an alternative (lower drag) set of dynamic motions near the wall or, more usually, to sense and attempt to invert/subvert the "pre-burst" wall dynamics. This approach is currently a collective "gleam-in-the eye" with some limited initial successes but truly immense practical difficulties [refs.38-55]. This area is actually a subset of a broader emerging technology termed smart structures/materials. All of the major technology-related Government Agencies/Departments have significant, and in many cases coordinated research programs in smart materials/structures--which can be employed either to control body/surface motions directly or used for flow control via such motions [e.g., refs. 56-62]. Propulsion applications of this technology are relatively far advanced [e.g., refs.63-66]. Aero applications include high lift, vortex control, buffet control, noise alleviation, vehicle health monitoring/ healing, control(s) and viscous drag reduction.

The other general approach which is enjoying increased activity is work at the systems/configuration level utilizing synergisms. [e.g., refs. 8 and 67] Suggestions in this arena include (1) multi-stage aircraft of various persuasions (especially supersonic). (2) strut-braced aircraft with tip engines to simultaneously reduce DDL up to 50 percent and thin and unsweep the wing to allow extensive "natural" laminar flow as well as providing major structural weight reductions (also applicable to supersonic cruise machines), (3) blended wing body/spanloader aircraft which, in the limit, effectively obviate the fuselage wetted area/associated skin friction, (4) reverse delta wing supersonic cruise configurations to provide extensive natural laminar flow, (5) wing/body propulsion system synergisms which generate large additional "static pressure thrust" forces (and increased propulsive efficiency) which act to cancel a sizable fraction of the body/wing drag (ala Goldschmeid), (6) a front-mounted "windmill" which reduces the momentum flux/drag over the vehicle and then redeposits the momentum into the wake (e.g., the momentum is simply extracted at the front and reinserted at the back allowing the viscous drag to be reduced in between), and (7) large(r) diameter bodies--providing reduced surface area/drag per unit of volume, which can/may require flow separation control "at cruise."

Additional "newer" aero drag reduction approaches/research are, in many cases, problematical in terms of technological and, in many cases even technical feasibility. Probably the most highly developed, feasible and interesting of these is active (but not reactive) "synthetic jets" for thrust vectoring [ref. 68], vortex control and other flow control applications [e.g., ref. 69]. There is a recent paper [ref. 70] which indicates that implanted (as opposed to flowing [e.g., ref. 71, 35] fibers/particulates can provide a net drag reduction whereas conventional wisdom/previous experience indicates drag increases. There is also some recent work on an old concept--(downstream) moving walls [ref. 72]. There are obvious, potentially large, skin friction reductions associated with such (flow-driven) wall motions, but the implementation issues are formidable. There is now some recent further indication that a 3-D wall mini-to-micro roughness can provide

turbulent drag reductions the order of that available from riblets [ref. 73, see also ref. 8]. And, finally, there is even some indication that passive compliant walls are again being looked at for the turbulent case [refs. 74, 75]. Observed drag reductions for the latter are relatively modest and their existence is somewhat surprising in view of previous research. This area probably deserves another round of checks, rechecks and double checks for accuracy as well as alternative explanations for the observations obtained.

VII. SUGGESTIONS REGARDING HYDRODYNAMIC DRAG REDUCTION/FLOW CONTROL

The following suggested approaches are based upon study of aero drag reduction techniques and subsequent extrapolation into the hydrodynamics arena with some initial consideration given to "real world" hydrodynamic operational issues such as bio-fouling , etc. Current and projected Naval hydrodynamic requirements are set forth, for example in refs. 76, 77 [see also ref. 79]. Previous/in some cases similar applications of aero drag reduction/flow control research to hydrodynamics include refs. 78-80. There are obvious physical differences between aerodynamics and hydrodynamics which provide major drag reduction opportunities in the hydro arena which are essentially unavailable to the aero world. These include turbulent drag reduction via polymers/surfactants, microbubbles/2 phase flow, electromagnetics and perhaps even compliant walls (the latter possibly enabled by the closer inertia/frequency match between water and vehicle surface dynamics compared to the air case).

VIII. HYDRO RESEARCH SUGGESTIONS

- Thrust vectoring for control/perhaps employing circulation control and/or trailing edge trim tabs on pump jet stators [see refs. 81-84, also ref. 14]
- "Free-wheeling" device ahead of the propulsor to "homogenize" the propulsor inflow, also large eddy break-up devices (viscous flow embedded airfoils) for same purpose [e.g., ref. 85, also ref. 35]
- Shorter/large(r) diameter bodies (with "cruise" separation control for efficient body closure)--reduced wetted area/skin friction for a given volume. Alternatively--multi-stage vehicles (especially for weapons, UUV's)
- Automatic controls for operation in the doubly stratified, (thermal, salinity) sheared water column to reduce 3-D flow generation/vortex drag/signatures engendered by body motion(s) and control surface motions/excursions
- Polymers/surfactants with replenishment via on-board culturing of zo and phyto plankton filtered from seawater coolant. [see ref. 86 for interesting comments on polymers, also ref. 35]
- Supercavitation
- MHD, multitudinous variants including parallel DC magnetic field which "monodimensionalizes" the turbulence/allows attainment of any friction drag level from turbulent to laminar [refs. 87-101]
- Continuous surface curvature in 3-space to minimize longitudinal vortex generation/drag (including obviation of "bilge vortices"), see ref. 10
- Active body vortex control (e.g., via deployed micro VG's) to counter/alter body motion induced vorticity/provide enhanced maneuverability
- Nose region "natural" and/or "heated" laminar flow control
- Design water intakes/outlets synergistically with body hydrodynamics e.g., cooling water injection into tip regions to reduce DDL/control tip vortex generation, slot injection drag reduction
- "Bionic" (e.g., derived from shark/fish study) non-biocide anti-biofouling approaches to reduce residual "crud drag" (estimated to be order of 15 percent to 20 percent of total submarine body drag)
- Favorable wave interference (e.g., utilizing catamaran hulls, swath supports) for surface wave drag reduction/partial "cancellation"
- Examination of potential impact of altered hull-water-air interface (e.g., via passive porous surfaces, steam/bubble layers, etc.) upon surface wave drag
- Active/smart/brilliant materials for (quasi-steady) localized flow optimization (on-going)
- "Afterburner" for burst speed (to counter drag/reduce size of propulsion system-- if propulsion system originally sized for burst speed metric). Hydrogen/oxygen rocket is obvious possibility as fuel is"available" from seawater (process/store /replenish during normal "cruise")
- "Controlled"/localized cavitation to obtain turbulent drag reduction via "microbubble"/flow density reduction [see ref. 35] while obviating direct air pumping/on-board storage penalties. Involves utilization of one or more of the following: micro roughness, increased air entrainment at bow, hydrophobic surface coatings, wall heating, acoustic fields and MHD/EHD as well as overall pressure distribution to enhance micro-cavitation/promote "filmboiling"
- Large scale fillets (as obtained from studies of shark dorsal fin-body intersection regions) for obviation of intersection region "necklace vortices" [ref. 12]
- "Goldschmeid" integrated/shrouded propulsor/body design to obtain additional, synergistic "static pressure thrust" thereby reducing net drag
- Serrated trailing edges to reduce wake deficits [ref. 102, 103]
- Dynamic segmented trim tabs slaved to stanchion internal stress field to reduce/eliminate oscillatory lift on pump jet shroud [see also ref. 104]
- A "manta-ray" configuration with much greater agility/L/D during maneuver and extensive laminar leading edges allowing reduced self noise and larger array gain for passive acoustic sensors [e.g., ref. 105]
- (Dynamic) ring vortices for torpedo defense

IX. AN ADDITIONAL NOTE REGARDING SCALING/ EVALUATION OF "DIFFERENT" APPROACHES

It should be noted that, once shed, organized longitudinal vorticity behavior appears to be highly Reynolds number dependent even at high Reynolds number, probably due to the streamline-induced curvative influences upon the imbedded turbulence fields [ref. 10]. Since such vortical entities have zeroth-to-first order influence(s) upon control(s) and signature(s), as well as powering and sensors, it is essential that Reynolds number scaling issues of flow control/drag reduction approaches be investigated. Current shortfalls in turbulence modelling (and DNS/LES) technology for such flows on actual "real world" configurations for at sea/at speed conditions precludes anything other than an experimental approach to such scaling issues.

Efficient/effective/"useful" examination of drag reduction approaches, especially in terms of ship (as opposed to localized) performance and potential side effects/problems requires the timely development of a small physical scale (for initial and test cost/productivity rationales) and "full scale Reynolds number" experimental capability. There are currently two disparate candidate approaches--a highly pressurized gas facility and a liquid Helium (Helium I NOT Helium II, e.g., a Navier-Stokes fluid, order of 2.3 to 4.5∞ K). The former passes the "giggle factor" test better and has somewhat less stringent model smoothness requirements but does not, as of yet, provide as high a Reynolds number as the latter. A strength of the liquid Helium approach is effective utilization of magnetic suspension to enable perhaps more accurate measurements of powering, control and signature(s).

Until such a relatively inexpensive "whole vehicle" high Reynolds number test capability is made available/utilized much of the drag reduction technical research will remain just that--research. Applications involving significant deviation from current paradigms are simply too risky/expensive given the current experimental facility/approach suite [ref. 3].

X. REFERENCES

1. Gad-el-Hak, Mohamed, and Bushnell, Dennis M. "Separation Control: Review," Journal of Fluids Engineering, March 1991, Vol. 113, pp. 5-30.

2. Viswanath, P. R., "Flow Management Techniques for Base and Afterbody Drag Reduction," Prog. Aerospace Sci., Vol. 32, pp. 70-129. 1995.

3. Bushnell, Dennis M., "Application Frontiers of 'Designer Fluid Mechanics'--Visions versus Reality or *An Attempt to Answer the Perennial Question 'Why Isn't It Used?'*" AIAA 97-2110, 28TH

AIAA Fluid Dynamics Conference, 4th AIAA Shear Flow Control Conference, June 29-July 2, 1997, Snowmass Village, CO.
4. "Drag Reduction Devices for Aircraft," 1910900 NTIS Accession Number: PB96-863576/XAB, National Technical Information Service, Springfield, VA, February 1996.
5. Poisson-Quinton, Ph., "Flow Control Systems Around Airplanes," Francaise de Mecanique, No. 2, 1995, p. 127-137.
6. Joslin, Ronald D., "Overview of Laminar Flow Control," NASA/RP-97-1407, December 1997.
7. Gad-el-Hak, Mohamed, "Modern Developments in Flow Control," Appl. Mech. Rev., Vol. 49, No. 7, July 1996, pp. 365-379.
8. Bushnell, Dennis M., "Viscous Drag Reduction in Aeronautics," ICAS '94 Guggenheim Lecture, ICAS Paper 94.-0.1, pp. 1-24.
9. Bushnell, Dennis M., "Supersonic Drag Reduction," AIAA 21st Fluid Dynamics, Plasma Dynamics and Lasers Conference, June 18-20, 1990, Seattle, WA, AIAA 90-1596.
10. Bushnell, Dennis M., "Longitudinal Vortex Control--Techniques and Applications, The 32nd Lanchester Lecture, Aeronautical Journal, October 1992, pp. 293-312.
11. Zhuang, F. G., "Vortex Control Technology," ICAS Proceedings, September 20-25, 1992, 18th Congress of the International Council of the Aeronautical Sciences, Beijing, People's Republic of China, pp. XXXI-XLI.
12. Lakshmanan, B., Tiwari, S. N., "Study of Supersonic Intersection Flowfield at Modified Wing-Body Junctions," AIAA Journal, V. 31, No. 5, May 1993, pp. 877-883.
13. Lin, John C., Robinson, Stephen K., McGhee, Robert J., Valarezo, Walter O., "Separation Control on High-Lift Airfoils Via Micro-Vortex Generators," Journal of Aircraft, Vol. 31, No. 6, Nov-Dec 1994, pp. 1317-1323.
14. Nielsen, Jack N. (Compiler), Proceedings of the Circulation-Control Workshop 1986, NASA Conference Publication 2432, February 19-21, 1986.
15. Juhasz, Albert J., and Smith, John M., "Performance of High-Area-Ratio Annular Dump Diffuser Using Suction-Stabilized-Vortex Flow Control," NASA Technical Memorandum X-3535, May 1977.
16. Woollett, Richard R., "Preliminary Investigation of Short Two-Dimensional Subsonic Diffusers," NACA Research Memorandum RM E56C02, May 25, 1956.
17. Haight, Charles H., "Experimental Mating of Trapped Vortex Diffusers with Large Area Ratio Thrust Augmentors," Final Report June 1973 - January 1974, ARL TR 74-0115, AD-A003493, September 1974.
18. Wygnanski, I., and Seifert, A., "The Control of Separation by Periodic Oscillations, AIAA 94-2608, 18th AIAA Aerospace Ground Testing Conference, June 20-23, 1994, Colorado Springs, CO.
19. Masuda, Shigeaki, Obi, Shinnosuke and Aoki, Kenta, "Control of Turbulent Separating and Reattaching Flow by Periodic Perturbations," Turbulence Control, FED Vol. 193, 1994 ASME Fluids Engineering Division Summer Meeting, Lake Tahoe, Nevada, June 19-23, 1994.
20. Seifert, A., Bachar, T., Koss, D., Shepshelovich, M., and Wygnanski, I., "Oscillatory Blowing: A Tool to Delay Boundary-Layer Separation," AIAA Journal, Vol. 31, No. 11, November 1993, pp. 2052-2060.
21. Seifert, A., Darabi, A., and Wygnanski, I., "Delay of Airfoil Stall by Periodic Excitation," Journal of Aircraft, Vol. 33, No. 4, July-August 1996, pp. 691-698.
22. Kazakov, A. V., Kogan, M. N., and Kuryachii, A. P., "Reduction of Turbulent Friction under Local Surface Heating," Journal of Applied Mechanics and Technical Physics, Vol. 37, No. 6, 1996, pp. 832-838.
23. Kazakov, A. V., Kogan, M. N., and Kuryachii, A. P., "The Effect of the Thermal Properties of a Body Being Flown about on Friction and Heat Transfer under Conditions of Local Heat Input to a Turbulent Boundary Layer," High Temperature, Vol. 35, No. 1, 1997, pp. 58-63.
24. Laadhari, F., Skandaji, L., and Morel, R., "Turbulence Reduction in a Boundary Layer by a Local Spanwise Oscillating Surface," Phys. Fluids 6 (10), October 1994, pp. 3218-3220.
25. Akhavan, R., Jung, W., Mangiavacchi, N., "Control of Wall Turbulence by High Frequency Spanwise Oscillations," AIAA 93-3282, AIAA Shear Flow Conference, July 6-9. 1993, Orlando, FL.
26. Hu, H.-C., and Kelly, R. E., "Stabilization of Longitudinal Vortex Instabilities by Means of Transverse Flow Oscillations," Phys. Fluids 9 (3), March 1997.
27. Trujillo, Steven M., Bogard, David G., Ball, Kenneth S., "Turbulent Boundary Layer Drag Reduction Using an Oscillating Wall," A97-33308, AIAA Shear Flow Control Conference, 4th, Snowmass Village, Co., June 29-July 2, 1997, 11 pp.
28. Baron, Arturo and Quadrio, Maurizio, "Turbulent Drag Reduction y Spanwise Wall Oscillations," Applied Scientific Research 55: 311-326, 1996.
29. Miyake, Yutaka, Tsujimoto, Koichi, Takahashi, Masayuki, "On the Mechanism of Drag Reduction of Near-Wall Turbulence by Wall Oscillation," Transactions of the Japan Society of Mechanical Engineers, Part B, Vol. 63, No. 605, January 1997, pp. 16-23.
30. Baron, A., and Quadrio, M., "Turbulent Drag Reduction by Spanwise Wall Oscillations," Appl. Sci. Res., Vol. 55, No. 4, pp. 311-26.
31. Satake, Sin-ichi, Kasagi, Nobuhide, "Turbulence Control with Wall-Adjacent Thin Layer Damping Spanwise Velocity Fluctuations," International Journal of Heat and Fluid Flow, Vol. 17, No. 3, June 1996, pp. 343-352.
32. Choi, Kwing-So, Roach, Paul E., DeBisschop, Jean-Robert, Clayton, Brian R., "Turbulent Boundary-Layer Control by Means of Spanwise-Wall Oscillation," 97-1795, AIAA Fluid Dynamics Conference, 28th, Snowmass Village, Co., June 29-July 2, 1997, 9 pp.
33. Akhavan, R., Jung, W. J., Mangiavacchi, N., "Turbulence Control in Wall-Bounded Flows by Spanwise Oscillations," Advances in Turbulence IV (A95-20275 04-34), Fluid Mechanics and Its Applications, Vol. 18, 1993, pp. 299-303 and Applied Scientific Research, Vol. 51, No. 1-2, 1993, pp. 299-303.
34. Bechert, D. W., Bruse, M., Hage, W., Van der Hoeven, J. G. T., and Hoppe, G., "Experiments on Drag-Reducing Surfaces and their Optimization with an Adjustable Geometry," Journal of Fluid Mechanics, 1997, Vol. 338, pp. 59-87.
35. Bushnell, Dennis M., and Hefner, Jerry N. (Editors), Viscous Drag Reduction in Boundary Layers, Vol. 123, Progress in Astronautics and Aeronautics, 1990.
36. Choi, K-S, Prasad, K. K., and Truong, T. V. (Editors), Emerging Techniques in Drag Reduction, 1996, Mech. Engng. Publications Ltd., London.
37. "Special Course on Skin Friction Drag Reduction," AGARD Report 786, March 1992.
38. Gunzburger, Max D. (Editor), Flow Control, The IMA Volumes in Mathematics and its Applications--Volume 68, 1995, Springer-Verlag.
39. Fan, Xuetong, Hofman, Lorenz, and Herbert, Thorwald, "Active Flow Control with Neural Networks," AIAA Paper 93-3273, AIAA Shear Flow Conference, Orlando, FL, July 6-9, 1993.
40. Kimura, Motoaki, Tung, Steve, Ho, Chih-Ming, Jiang, Fukang, Tai, Yu-Chong, "MEMS for Aerodynamic Control," AIAA Paper No. 97-2118, AIAA Fluid Dynamics Conference, 28th, Snowmass Village, Co, June 29-July 2, 1997. 9 pp.
41. Koumoutsakos, Petros, Bewley, Thomas R., Hammond, Edward P., Moin, Parviz, "Feedback Algorithms for Turbulence Control--Some Recent Developments," AIAA Paper 97-2009, AIAA Fluid Dynamics Conference, 28th, Snowmass Village, Co., June 29-July 2, 1997, 13 p.
42. Choi, H., Moin, P., Kim, J., "Active Turbulence Control for Drag Reduction in Wall-Bounded Flows," Journal of Fluid Mechanics, Vol. 262, p. 75-110, March 10, 1994.
43. McMichael, James M., "Progress and Prospects for Active Flow Control Using Microfabricated Electromechanical Systems (MEMS), AIAA Paper No. 96-0306, AIAA Aerospace Sciences Meeting and Exhibit, 34th, Reno, NV, January 15-18, 1996, 21 p.
44. Ho, Chih-Ming, Tung, Steve, Tai, Yu-Chong, "Interactive Control of Wall Structures by MEMS-based Transducers," Advances in Turbulence VI: Proceedings of the 6th European Turbulence Conference, Lausanne, Switzerland, July 2-5, 1996.
45. Choi, H., Moin, P., Kim, J., "Active Turbulence Control for Drag Reduction in Wall-Bounded Flows," Journal of Fluid Mechanics, Vol. 262, March 10, 1994, pp. 75-110.
46. Carlson, H. A., Lumley, J. L., "Active Control in the Turbulent Wall Layer of a Minimal Flow Unit," Journal of Fluid Mechanics, Vol. 329, December 25, 1996, pp. 341-71.
47. Ho, Chih-Ming, Tai, Yu-Chong, "REVIEW: MEMS and its Applications for Flow Control," Journal of Fluids Engineering,

Transactions of the ASME, Vol. 118, No. 3, September 1996, pp. 437-446.
48. Parekh, D. E., Agarwal, R. K., "Control of Transitional and Turbulent Flows," Proceedings of the 1996 ASME Fluids Engineering Division Summer Meeting (Part 2 of 3), San Diego, CA, 1996.
49. Joslin, R. D., Nicolaides, R. A., Erlebacher, G., Hussaini, M. Y., Gunzburger, M. D., "Active Control of Boundary-Layer Instabilities: Use of Sensors and Spectral Controller," AIAA Journal, Vol. 33, No. 8, August 1995, pp. 1521-3.
50. Ho, Chih-Ming, "Control of Fluid Flows by Micro Transducers," MHS '96, Proceedings of the Seventh International Symposium on Micro Machine and Human Science, pp. 29-33.
51. Rathnasingham, R., Breuer, K. S., "System Identification and Control of a Turbulent Boundary Layer," Physics of Fluids, Vol. 9, No. 7, July 1997, pp. 1867-9.
52. Moin, P., "Active Turbulence Control in Wall Bounded Flows Using Direct Numerical Simulation," AD-A267 261, N94-17286, November 6, 1992.
53. Jacobson, Stuart A., and Reynolds, William C., "Active Control of Boundary Layer Wall Shear Stress Using Self-Learning Neural Networks," AIAA 93-3272, AIAA Shear Flow Conference, Orlando, Fl, July 6-9, 1993.
54. Gad-el-Hak, Mohamed, "Interactive Control of Turbulent Boundary Layers: A Futuristic Overview," AIAA Journal, Vol. 32, No. 9, September 1994, pp. 1753-1765.
55. Moin, P., and Bewley, Thomas, "Feedback Control of Turbulence," Appl Mech Rev, Vol. 47, No. 6, Part 2, June 1994, pp. S3-13.
56. Hardy, Robin C., and Simpson, Joycelyn O. (Editors), Proceedings of the 4th Annual Workshop: Advances in Smart Materials for Aerospace Applications, NASA Conference Publication 10185, March 1996.
57. Quackenbush, T. R., Bilanin, A. J., McKillip, R. M., "Vortex Wake Control Via Smart Structures Technology," Proceedings of the SPIE--the International Society for Optical Engineering Conference, Vol. 2721, pp. 78-92.
58. Barrett, Ron, Farokhi, Saeed, "Subsonic Aerodynamics and Performance of a Smart Vortex Generator System," Journal of Aircraft, Vol. 33, No. 2, March-April 1996, pp. 393-398.
59. Saddoughi, S. G., "Experimental Investigations of On-Demand Vortex Generators," NTIS Accession Number: N95-22451/5/XAB, December 1994, 7 pp.
60. Austin, Fred, Siclari, Michael J., Van Nostrand, William, Weisensel, G. N., Kottamasu, Vishnu, Volpe, Giuseppe, "Comparison of Smart-Wing Concepts for Transonic Cruise Drag Reduction," Smart Structures and Materials 1997: Industrial and Commercial Applications of Smart Structures Technologies; Proceedings of the Meeting, San Diego, CA, March 4-6, 1997, pp. 33-40.
61. Loewy, Robert G., "Recent Developments in Smart Structures with Aeronautical Applications," American Institute of Aeronautics and Astronautics, 1997, (A97-29150), 55 pp.
62. Sater, Janet M. (Editor), "Smart Structures and Materials 1997: Industrial and Commercial Applications of Smart Structures Technologies; Proceedings of the Meeting, San Diego, CA, March 4-6, 1997," 490 pp.
63. de Jager, Bram, "Rotating Stall and Surge Control: A Survey," Proceedings of the 1995 34th IEEE Conference on Decision and Control, Part 2 of 4, New Orleans, LA.
64. "Sensing, Actuation, and Control in Aeropropulsion," Proceedings of the SPIE--The International Society for Optical Engineering, Vol. 2494.
65. Day, I. J., "Review of Stall, Surge and Active Control in Axial Compressors," Eleventh International Symposium on Air Breathing Engines, September 20-24, 1993, Tokyo, Japan, pp. 97-105.
66. Dugundji, J., Epstein, A. H., Garnier, V., Greitzer, E. M., Guenette, G., Paduano, J., Silkowski, P., Simon, J., Valavani, L., "A Progress Report on Active Control of Flow Instabilities: Rotating Stall Stabilization in Axial Compressors," AIAA-89-1008, AIAA 2nd Shear Flow Conference, March 13-16, 1989, Tempe, AZ.
67. Bushnell, Dennis M., "Frontiers of the 'Responsibly Imaginable' in (Civilian) Aeronautics, AIAA Paper 98-0001, 1998 AIAA Dryden Lecture presented at the 36th Aerospace Sciences Meeting and Exhibit, January 12-15, 1998, Reno, NV.
68. Smith, Douglas R., Parekh, David E., Kibens, Valdis, Glezer, Ari, "Thrust Vectoring with Hybrid Synthetic Jet Actuators," Proceedings of the 1997 ASME Fluid Engineering Division Summer Meeting, FEDSM'97, Part 8 of 24, Vancouver, Can.
69. Roos, Frederick W., "Synthetic-Jet Microblowing for Vortex Asymmetry Management on a Hemisphere-Cylinder Forebody," AIAA Paper 97-1973, AIAA Shear Flow Control Conference, 4th, Snowmass Village, Co, June 29-July 2, 1997, 5 pp.
70. Takata, Tashi, Kyogoku, Keiji, Nakahara, Tsunamistu, "Turbulent Drag Reduction (Effect of Implanted Fiber)," Transactions of the Japan Society of Mechanical Engineers, Part B, Vol. 62, No. 596, April 1996, pp. 1383-1387.
71. Wamser, C., Lykossov, V. N., "On the Friction Velocity During Blowing Snow," Contributions to Atmospheric Physics, Vol. 68, No. 1, pp. 85-94.
72. Bechert, D. W., Hage, W., and Brusek, M., "Drag Reduction with the Slip Wall," AIAA Journal, Vol. 34, No. 5: Technical Notes, pp. 1072-1074.
73. Sirovich, L., and Karlsson, S., "Turbulent Drag Reduction by Passive Mechanisms," Nature, Vol. 388, August 21, 1997, pp. 753-755.
74. Lee, T., Fisher, M., and Schwarz, W. H., "Investigation of the Stable Interaction of a Passive Compliant Surface with a Turbulent Boundary Layer," Journal Fluid Mechanics, Vol. 257, 1993, pp. 373-401.
75. Choi, K.-S., Yang, X., Clayton, B. R., Glover, E. J., Atlar, M., Semenov, B. N., and Kulik, V. M., "Turbulent Drag Reduction Using Compliant Surfaces," Proc. R. Soc. Lond. A, 1997, 453, pp. 2229-2240.
76. Technology for the United States Navy and Marine Corps, 2000-2035--Volume 6 Platforms, National Academy Press, Washington DC, 1997.
77. " DOD Compiles Submarine Technology Program Wish List," Aerospace Daily, November 27, 1996, pp. 312-313.
78. Moore, K. J., Jones, Gary, and Ndefo, Ejike, "Vortex Control in Submarine Design," Royal Institute of Naval Architects Symposium, May 13-15, 1991, London UK.
79. Bushnell, Dennis M., and Donaldson, C. D., "Control of Submersible Vortex Flows," NASA Technical Memorandum 102693, June 1990.
80. Report on the DARPA Advanced Flow Control Techniques Workshop, November 19-22, 1991.
81. Gal-Or, Benjamin, "Civilizing Military Thrust Vectoring Flight Control," Aerospace America, Vol. 34, No. 4, April 1996, pp. 20-21.
82. Schneider, W. E., "Marine Propulsion Unit with Controlled Cyclic and Collective Blade Pitch," Patent-5 249 992.
83. Flynn, Billie, Smith, Rogers E., Schneider, Ed, "Thrust Vectoring: A New Dimension," Canadian Aeronautics and Space Journal, Vol. 41, No. 4, December 1995, 7 pp.
84. Czarnowski, J., Cleary, R., Kreamer, B., "Exploring the Possibility of Placing Traditional Marine Vessels Under Oscillating Foil Propulsion," Proceedings of the 1997 7th International Offshore and Polar Engineering Conference, Part 2 of 4, Honolulu, HI.
85. Sluchak, Vladimir, "The Thin Ring Wing as a Means of Flow Improvement Upstream of a Propeller," SNAME Propellers/Shafting '97 Symposium, September 23-24, 1997, Virginia Beach, VA.
86. Motier, John F., Chou, Lu-Chien, Kommareddi, Nagesh, "Commercial Drag Reduction Past, Present and Future," American Society of Mechanical Engineers, Fluids Engineering Division FED, Vol. 237, No. 2, 1996, pp. 229-234.
87. Krakov, M. S., and Nikiforov, I. V., "Control of Flow Separation in a Plane Channel by Means of a Magnetic Fluid," Magnetohydrodynamics, Vol. 26, No. 4, October-December 1990, pp. 469-74.
88. Crawford, Catherine H., and Karniadakis, George Em, "Reynolds Stress Analysis of EMHD-Controlled Wall Turbulence. Part 1. Streamwise Forcing," Phys. Fluids 9 (3), March 1997, pp. 788-806
89. Meng, James C. S., "Magnetohydrodynamic Boundary Layer Control System," Patent Number 5,273,465, December 28, 1993.
90. Henoch, C., and Stace, J., "Experimental Investigation of a Salt Water Turbulent Boundary Layer Modified by an Applied Streamwise Magnetohydrodynamic Body Force," Phys. Fluids 7 (6), June 1995.
91. Meng, James C. S., Huyer, Stephen A., Castano, John M., Thivierge, Daniel P., Hendricks, Peter J., "Experimental Study of the Spanwise Vortex Resonance Hypothesis for Turbulent Drag Reduction

Over a Flat Plate in Salt Water," NUWC-NPT Technical Report 10,680, March 1, 1997.
92. Meng, J. C. S., "Wall Layer Microturbulence Phenomenology and a Markov Probability Model for Active Electromagnetic Control of Turbulent Boundary Layers in an Electrically Conducting Medium," NUWC-NPT Technical Report 10,434, June 1, 1995.
93. Cattaneo, Fausto, "On the Effects of a Weak Magnetic Field on Turbulent Transport," The Astrophysical Journal, 434:200-205, October 10, 1994.
94. Meng, James C. S., "Active Turbulence Control Using Microelectrodes, Permanent Magnets in Microgrooves," Patent Number 5,359,951, November 1, 1994.
95. Meng, J. C. S., Henoch, C. W.,, and Hrubes, J. D., "Seawater Electromagnetohydrodynamics: A New Frontier," Magnitnaya Gidrodinamika Conference, Vol. 30, No. 4, October-December 1994, pp. 483-506.
96. Kral, Linda D., and Donovan, John F., "Numerical Simulation of Turbulence Control Using Electromagnetic Forces," American Society of Mechanical Engineers, Fluids Engineering Division FED, Vol. 237, No. 2, 1996, pp. 319-329.
97. Choi, Haecheon, Lee, Donghoon, Lim, Junwoo, and Kim, John, "Control of Near Wall Streamwise Vortices Using an Electromagnetic Force in a Conducting Fluid," AIAA Paper 97-2059, AIAA Shear Flow Control Conference,, 4th, Snowmass Village, CO, June 29-July 2, 1997, 12 pp.
98. Krakov, M. S., and Kamiyama, S., "Steady Flow Past a Circular Cylinder Coated with Magnetic Fluid: Flow Structure, Drag Reduction and Coating Deformation," Journal of Fluid Mechanics, Vol. 295, July 25, 1995, pp. 1-22.
99. Budingen, G. V., Frenzel, H., Steger, R., Vorwerk, J., Brunn, P. O., "Simultaneous Drag Reduction and Heat Transfer Enhancement for Slit Flow by Means of Coating One Wall with a Magnetic Fluid," Journal of Intelligent Material Systems and Structures, Vol. 5, No. 6, November 1994, pp. 776-86.
100. Zhang, W., Diamond, P. H., "Turbulence Suppression and Drag Reduction by External Magnetic Field, Proceedings of International Sherwood Fusion Theory Conference, Dallas, TX, March 14-16, 1994.
101. Orlandi, P., "Drag Reduction in Turbulent MHD Pipe Flows," NTIS Accession Number: N19970014679/XAB, December 1996, 10 pp.
102. Hunter, Craig, Delore, Pasquale, and Presz, Walter M., "Drag Reduction and Wake Minimization on Marine Vehicles," Final Report, Office of Naval Research, Grant No. 0014-89-J-1883, AD-A241 270, July 1991.
103. Vijgen, P., Howard, F. G., Bushnell, D. M., Holmes, B. J., "Serrated Trailing Edges for Improving Lift and Drag Characteristics of Lifting Surfaces," U.S. Patent 5,088,665, 1992.
104. Akin, O., and Rockwell, D., "Actively Controlled Radial Flow Pumping System; Manipulation of Spectral Content of Wakes and Wake-Blade Interactions," Transactions of the ASME, Journal of Fluids Engineering, Vol. 116, No. 3, September 1994, pp. 528-37.
105. August, Henry, Carapezza, Edward, "Ring Wing for an Underwater Missile," AIAA Atmospheric Flight MEchanics Conference, Monterey, CA, August 9-11, 1993, Technical Paper A93-4830120-08.

EUROPEAN DRAG REDUCTION RESEARCH – RECENT DEVELOPMENTS AND CURRENT STATUS

Kwing-So Choi
Department of Mechanical Engineering
The University of Nottingham
Nottingham NG7 2RD, United Kingdom
kwing-so.choi@nottingham.ac.uk

Abstract - The recent developments and current status of the drag reduction research in Europe have been described here with an overview of European Research Community on Flow, Turbulence and Combustion (ERCOFTAC) where a large amount of research work has been coordinated. The research activity in Europe is unique in a sense that the research areas are diverse with a mixture of new and traditional themes. This is due to various funding mechanisms available in Europe mainly through national funding schemes in each country. There is an obvious disadvantage in this arrangement, however, that it is difficult to gather momentum on a particular work as the research funds are spread very thinly across Europe. ERCOFTAC's main aim is, therefore, to stimulate coordinated European-wide research efforts on special topics in flow, turbulence and combustion. The European Drag Reduction Meetings, which are organised as a part of activities within ERCOFTAC's Drag Reduction Special Interest Group have been a driving force for research coordination on drag reduction within Europe.

I. INTRODUCTION

The purpose of this paper is firstly to give an overview of European Research Community on Flow, Turbulence and Combustion (ERCOFTAC) where a large amount of research work has been coordinated in recent years. The *Drag Reduction* Special Interest Group is one of well established research groups within ERCOFTAC, which has organised 10 specialised meetings – European Drag Reduction Meetings - on drag reduction since 1986. Initially the European Drag Reduction Meeting was a very informal gathering of only a dozen or so researchers, and most of discussions were centred around the use of passive devices, such as riblets and LEBUs and their results. As the time goes by, this informal meeting has developed to a semi-formal meeting of delegates from all over the Europe, including researchers from Russia, Ukraine and Czech Republic.

Secondly, a description of recent developments and current status of the drag reduction research in Europe is given with a view to highlight the efforts expended by the European researchers in recent years. Discussions of some of the recent results on riblets, compliant coating, drag reduction in nature, polymer additives and wall oscillation are given with an emphasis on the drag-reduction mechanisms involved. Some descriptions on the emerging techniques for drag reduction such as passive porous surface and slip wall are also given. It is not within the scope of this paper, however, to summarise all the recent research activities on drag reduction in Europe. Therefore, the discussions of some of the topics, such as the polymer additives for drag reduction, are limited only to those presented at the European Drag Reduction Meetings.

II. ERCOFTAC

The ERCOFTAC (European Research Community on Flow, Turbulence and Combustion) Association was created as an international association with scientific objectives according to Belgian law on June 3, 1988 in Paris. The main objectives of ERCOFTAC are:

- to promote joint efforts of European research institutes and industries who are active in all aspects of flow, turbulence and combustion, with the objective of exchanging technical and scientific information concerning basic and applied research and the development, validation and maintenance of numerical codes and databases
- to promote centres, called ERCOFTAC Pilot Centres, in many European countries to act as centres for collaboration, stimulation and application of research
- to promote industrial application of research by means of novel kinds of collaborations between industry, governments, professional societies and research groups
- to stimulate, through the creation of Special Interest Groups, well-coordinated European-wide research efforts on specific topics in flow, turbulence and combustion
- to stimulate the creation of advanced training activities in all fields related to flow, turbulence and combustion.

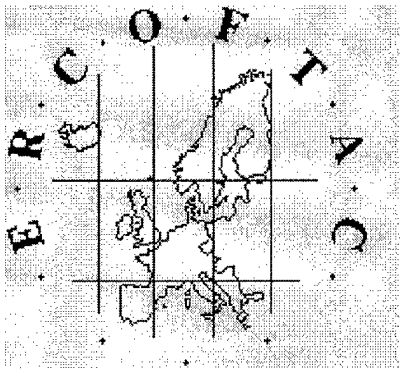

ERCOFTAC membership is open to research groups in academic or governmental organisations and to industrial corporations located in the EC and EFTA countries. The ERCOFTAC Association is managed by the Managing Board which is composed of elected representatives of the voting members. The Managing Board elects among its members the Executive Committee composed of the Chairman, two Vice Chairmen and the Treasurer. Either the Chairman or the two Vice Chairmen are from industry. The Executive Committee is responsible for the daily course of affairs. The General Assembly established the Scientific Programme Committee, which recommends the research goals of ERCOFTAC and proposes special activities. The Managing Board has recently approved the creation of an Industrial Advisory Committee, which advises the Board on matters of Industrial relevance.

The ERCOFTAC Pilot Centre network forms one of the pillars of the ERCOFTAC Association. ERCOFTAC Pilot Centres are composed of ERCOFTAC members in a region or a country. ERCOFTAC Pilot Centres coordinate the research in flow, turbulence and combustion on a regional or national scale, while at the same time being linked to all other Pilot Centres via the ERCOFTAC Pilot Centre network. In 1997, the following 16 ERCOFTAC Pilot Centres exist: Belgium, France PEPIT, France South, France West, Germany North, Germany South, Germany West, Greece, Italy, Netherlands, Nordic, Portugal, Spain, Switzerland, UK North and UK South.

ERCOFTAC Special Interest Groups form the second pillar of the Association. ERCOFTAC Special Interest Groups are composed of ERCOFTAC members working together on a well-defined specific topic on flow, turbulence and combustion. Activities of Special Interest Groups are organising workshops, comparison of codes, exchange of research results, creation of experimental and/or numerical data bases, organisation of courses, etc. ERCOFTAC Special Interest Groups are associated with at least two Pilot Centres, and have an international organising committee.

Currently, ERCOFTAC Special Interest Groups exist on the following topics. The numbers are specific to each individual group and those groups not listed here have ceased their activities.

1. Large Eddy Simulation
2. Turbulent Boundary Layers
3. Identification Schemes for Eddy Structures in Free Turbulent Shear Flows
4. Turbulence in Compressible Flows
5. Atmospheric Boundary Layer Turbulence and Diffusion over Complex Terrain
6. Turbulence and Dispersion in Urban Atmosphere
7. Atmospheric Dispersion
8. Turbomachinery
10. Laminar to Turbulent Transition and Retransition
12. Dispersed Turbulent Two Phase Flow
13. Grid Generation and Adaptivity
14. Stably Stratified and Rotating Turbulence
15. Turbulence Modelling
17 Shock/Boundary Layer Interaction
19. Parallel Computing in CFD
20. Drag Reduction
21. Vortex Dynamics
24. Variable Density Turbulent Flows
25. CFD for Ship Hydrodynamics
28. Aerodynamics and Steady State Combustion in Furnaces and Combustion Chambers
30. Wind over Waves
32. Particle Image Velocimetry
33. Laminar-Turbulent Transition Mechanisms, Prediction and Control
101. Quality and Trust in Industrial CFD

Flow, Turbulence and Combustion (formally *Applied Scientific Research*) is an international journal published in association with ERCOFTAC. Further details of ERCOFTAC Association can be found on World Wide Web (http://imhefwww.epfl.ch/lmf/ERCOFTAC/).

III. DRAG REDUCTION SPECIAL INTEREST GROUP

Drag Reduction Special Interest Group (SIG) is one of the founding groups of ERCOFTAC Association when it was established in 1988, although a drag reduction group in Europe existed before then. A coordination of experimental, numerical and analytical research into drag reduction and flow management using passive and active techniques is carried out by the group, which include riblets, LEBUs, polymer additives, compliant coating, boundary layer structures and drag reduction mechanisms. The Group's main objectives are:

- to bring together active researchers in an area of drag reduction and flow management to discuss the latest results
- to identify area of passive and active devices in terms of industrial applications and technology transfer
- to encourage collaborations among researchers in Europe

The International Organising Committee of Drag Reduction SIG consists of:

D.W. Bechert, DLR, Germany
K.-S. Choi, University of Nottingham, U.K. (convenor)
E. Coustols, ONERA/CERT, France
P. Luchini, University of Milan, Italy
K. K. Prasad, T.U. Eindhoven, The Netherlands
A.M. Savill, University of Cambridge, U.K.
T.V. Truong, EPFL, Switzerland

Recent meetings were held in 1993 in Lausanne, Switzerland (8th European Drag Reduction Meeting and Workshop on Drag-reduction Mechanisms) and in 1995 in Naples, Italy (9th European Drag Reduction Meeting and Workshop on Active Control). The last meeting (10th European Drag Reduction Meeting) was held in 1997 in Berlin, Germany. Several publications [1-4] were made as a result of these meetings. The latest monograph "Emerging Techniques in Drag Reduction" (edited by K.-S. Choi, K.K. Prasad and T.V. Truong) was published in June 1996 by Mechanical Engineering Publication. Reports on these meetings as well as the activities on drag reduction can be found in ERCOFTAC Bulletin.

IV. EUROPEAN DRAG REDUCTION RESEARCH

Riblets

The study of riblets has been one of the focused research activities in turbulent drag reduction in the last two decades. There is still so much interest in this passive device in Europe in controlling turbulent as well as laminar boundary layers. At the University of Nottingham, studies were conducted in a low-speed boundary layer tunnel to investigate a heat-transfer enhancement over the heated riblet surface and a delay in transition to turbulence of laminar boundary layer by riblets. The results of heat-transfer measurement over the heated triangular riblets [5-7] indicate that the heat transfer coefficient is increased as much as 10% within the drag-reducing regime of riblets, say $s^+ < 30$. This apparent breakdown of the Reynolds analogy seems to result from a difference in the turbulence length scale of momentum and thermal boundary layers due to their difference in initial conditions and molecular diffusivities. It has been demonstrated that the transition to turbulence of an excited laminar boundary layer over the riblet surface can be delayed very significantly [8]. The growth rate of the momentum thickness during the non-linear stage of the transition has been reduced over the riblet surface accompanied by a reduction in the turbulence intensity. The shape factor of the boundary layer over the riblet surface is lower, supporting that the rate of transition has indeed been reduced. It seems that the mechanism of transition delay by riblets is similar to that of turbulent drag reduction, where the longitudinal grooves interact with the legs of hairpin vortices to hinder their development.

A research group at DLR Berlin has been investigating riblets for turbulent drag reduction using an oil channel, which is accurate to ±0.3% of the measured drag force [9-12]. A considerable improvement in drag reduction was obtained in recent years by optimising the shape of riblets systematically. They have tested riblets of many configurations including triangular, semi-circular, blade, "brother and sister" and three-dimensional riblets. As a result, the maximum drag reduction as much as 10% can be achieved. Bechert and his colleagues have tested a combination of blade riblets and "ejection" slits in an effort to increase the amount of drag reduction further more. It was expected that the fluctuating pressures in a turbulent boundary layer drive the fluid in and out of small slits like a jet flow, thereby generating a thrust force. With this configuration of riblets, a maximum drag reduction of nearly 9% was achieved.

The technique and theoretical explanation for riblet optimisation is described by a group of researchers at the University of Milan [13-16], who suggested that the drag reduction can be maximised by increasing the difference in protrusion height between the longitudinal and cross flows. This will maximise the impedance to the cross flow with a minimum drag on the longitudinal flow. Luchini also investigated the effects of riblets on the boundary layer stability. His results using the e^N method show that the Tollmien-Schlichting (T-S) waves over the triangular riblet surface are found to be excited at a lower critical Reynolds number. The conditional analysis of ejections in the turbulent boundary layer over riblets was carried out by Baron and Quadrio [17-19], who confirmed that the frequency of ejections is increased and the duration reduced by the presence of riblets. They observed that the average number of ejections in each burst is greater over riblets than that over a flat plate.

Experimental studies of riblets in laminar boundary layers have been carried out by a group at the Institute of Theoretical and Applied Mechanics, Russia [20-23]. The experimental results show that the riblets can delay the transformation of the Λ-vortices into turbulent spots and shift the point of transition further downstream. When the riblets are used in the linear stage of transition, the growth rate of T-S waves is increased agreeing well with the numerical results obtained by Luchini. The effectiveness of riblets in controlling the transitional three-dimensional flow was also investigated by Kozlov and his colleagues. This was carried out by exciting the streamwise vortices in the swept-wing boundary layer using a vortex generator. The results seem to indicate that the riblets can suppress the development of laminar-turbulent transition of three-dimensional boundary layers. It was also demonstrated experimentally that the riblets can substantially affect the way the vortices develop in the wake behind a single roughness element, leading to a delay in transition to turbulence.

Effectiveness of riblets in turbulent boundary layers under pressure gradient was investigated at the Delft University of Technology. Through a direct measurement of drag and velocity, DeBisschop and Nieuwstadt [24] were able to show that a greater drag reduction of up to 13% can be obtained by using riblets in a boundary layer under an adverse pressure gradient. This is to confirm the result of previous study by Choi [25] who carried out a detailed measurement of velocity profiles of turbulent boundary layer over a riblet surface under different pressure gradient conditions.

Review papers on riblets were written by many researchers [26-29].

Compliant coating

A research group at the University of Warwick has been engaged in the study of compliant coating in delaying transition of boundary layers to turbulence [30-35]. They demonstrated that in theory, at least, substantial transition delays were possible with Kramer's coatings. This numerical study was supported by a series of towing tank experiments by Gaster [36]. Recent effort has been directed towards the optimisation of compliant coating for maximum reduction in skin-friction drag, such as by using multiple compliant panels and anisotropic coatings. Effects of compliant rotating disc on the boundary-layer transition were also investigated by the same group. It was shown that a compliant wall has a stabilising effect on the Type I inviscid instability, while the Type II viscous instability is stabilised only when the compliance of the wall coating is increased. Although the experimental work was not conclusive in showing an increase in the critical Reynolds number with compliant rotating disc, there was an indication that this can be done with an increase in the wall compliance.

Over the past forty years, there have been intensive investigations into the use of compliant coating to obtain *turbulent* drag reduction in boundary-layer flows. Although positive results were found in some of the studies carried out in Russia, none of these had been successfully validated by independent researchers. Recently, a series of tests were carried out at the University of Nottingham to verify the experimental results of Semenov and Kulik [37-39], who successfully demonstrated the ability of compliant coatings in reducing the skin-friction drag and surface-flow noise in a turbulent boundary layer. The results obtained by Choi *et al.* [40, 41] clearly demonstrate that the turbulent skin friction is reduced for one of the compliant coatings tested, indicating a drag reduction of up to 7 percent within the entire speed range of the tests. The intensities of skin-friction and wall-pressure fluctuations measured immediately downstream from the compliant coating show reductions in the intensities of up to 7 percent and 19 percent, respectively. The results also indicate reductions in turbulence intensity by up to 5 percent across almost the entire boundary layer. Furthermore, an upwards shift of the logarithmic velocity profile is evident indicating that the thickness of the viscous sublayer is increased as a result of turbulent drag reduction by the compliant coating.

Drag reduction in nature

Experimental studies on live penguins were carried out by Bannasch [42, 43] at the Technical University of Berlin with measurements using life-sized models in a water tank. An axisymmetric body based on three medium-sized penguin species was found to be an excellent low-drag laminar body. When the transition from laminar to turbulent flow was triggered at 5 % of the body length, the surface drag coefficients remained even lower than those of a turbulent flat plate of equal length, and they declined at a higher rate with increasing Reynolds numbers. Viscous drag was reduced by the characteristic "stepwise" pressure and the velocity distribution developed along the multiple-curved (wave-like) contour of that body. Turbulent velocity fluctuations in the boundary layer remained at a low level even with the rigid model. The wavy contour and compliant wall of penguin body are considered to be the main reasons for the excellent swimming efficiency. In most cases, a regular pattern of transverse waves (wavelength of 2 -3 cm) was observed over the plumage.

A passive flow-separation control method to mimic the bird feathers was tested in a wind tunnel at DLR Berlin [12]. The results of the test of self-activated movable flap over a laminar wing section revealed that the maximum lift of the airfoil was increased by 20% without perceivable deleterious effects under cruise condition. This was confirmed by a flight test with a motor glider by recording the reduction in minimum speed before stall. Replica of shark skin was tested in a Berlin Oil Channel for turbulent drag reduction [12]. For this experiment, 800 individually movable scales were carefully produced and they were anchored on adjustable springs. This allowed each artificial scale to move freely, interacting with the near-wall flow field of the turbulent boundary layer. Although there were obvious difficulties in optimizing all the parameters involved in this experiment, Bechert and his colleagues were able to obtain a modest drag reduction of 3%. The same group has tested the hairy surfaces for drag reduction [12], which were exhibited by otters and sea leopards. Again only a marginal drag reduction (1.5%) was observed when the hairs were placed either on the flat surface or very close to it.

Polymer additives

A series of experiments were carried out by Choi and his colleagues [44-46] using a towing tank at British Maritime Technology, where a combined use of riblets with polymer coating was investigated for turbulent drag reduction. A one-third scale model of America's Cup winning yacht, the Australia II was used for this test and the total hydrodynamic resistance was measured at various towing speeds. The results indicated that the riblets/polymer combination offered an overall improvement in drag reduction characteristics over either riblets or polymer coating alone, with a maximum reduction in total flow resistance of 3.5% at $s^+ = 8$ ($Re = 3.8 \times 10^6$).

Drag reduction mechanism of turbulent boundary layers with polymer additives has been studied recently. Orlandi [47] investigated into the constitutive equation of dilute polymer solution, relating the elongation viscosity to the local flow properties. Here, the viscosity of the solution becomes large when the strain rate is greater than the vorticity. The accuracy of this method was tested against other numerical methods. The study at the Delft University of Technology involved a direct numerical simulation and Laser Doppler anemometry of a turbulent pipe flow with polymer additives [48]. The results show that the viscous anisotropic stresses introduced by extended polymers play a key role in the drag reduction.

Wall oscillation

Laadhari and his colleagues [49] at Ecole Centrale de Lyon carried out an experimental study to look at the problem of spanwise-wall oscillation in a turbulent boundary layer. This is to experimentally confirm the results of recent direct numerical simulation suggesting that the turbulent skin-friction drag can be reduced by a wall oscillation. With detailed measurements using hot-wire anemometry they were able to show that the mean velocity gradient of the boundary layer is reduced near the oscillating wall. They also demonstrated that there are reductions in turbulence intensities, suggesting that the skin-friction drag of the turbulent boundary layer may be reduced by the spanwise-wall oscillation.

An investigation into the changes in the turbulent boundary-layer structure with a spanwise-wall oscillation was carried out by Choi *et al.* [50, 51] at the University of Nottingham using hot-wire anemometry and flow visualization Their results clearly indicate that the logarithmic velocity profiles are shifted upwards and turbulence intensities reduced by the spanwise-wall oscillation. When the wall oscillation was optimised with a non-dimensional wall speed, the skin-friction reductions as much as 45% were observed within five boundary layer thicknesses downstream of the start of wall oscillation. The mechanism of drag reduction seems to strongly relate to the spanwise vorticity generated by the periodic Stokes layer over the oscillating wall, which affects the boundary layer profile by reducing the mean velocity gradient within the viscous sublayer. The longitudinal vortices in the near-wall region are also realigned into the spanwise direction, reducing the intensity of streamwise vorticity fluctuations across the boundary layer.

The effect of wall-oscillation amplitude on the total energy balance was investigated by Baron and Quadrio at the University of Milan using a direct numerical simulation [52]. Although no net savings were found when the amplitude of wall oscillation was greater than $3Q_x/8h$, net energy savings were obtained at smaller amplitudes. Here, Q_x is the flow rate and h is the half height of turbulent channel flow. Indeed, there was up to 10% of net energy saving at the wall-oscillation amplitude of $Q_x/4h$. This study was carried out at a fixed non-dimensional period of $T^+ = 100$, therefore there may be a scope of further net energy savings. They also confirmed the basic conclusions of earlier numerical study.

An experimental study of turbulent pipe flows was conducted by Choi and Graham [53] with a view to reduce the friction drag by

oscillating a section of the pipe in a circumferential direction. The results indicated that the friction factor of the pipe is reduced by as much as 25% as a result of active manipulation of near-wall turbulence structure by circular-wall oscillation. An increase in the bulk velocity was clearly shown when the pipe was oscillated at a constant head, supporting the measured drag reduction in the present experiment. The percentage reduction in pipe friction was found to be better scaled with the non-dimensional velocity of the oscillating wall than with its non-dimensional period, confirming a suggestion [50, 51] that the drag reduction seem to be resulted from the realignment of longitudinal vortices into circumferential direction by the wall oscillation.

Direct numerical simulation of turbulent flow in a rotating pipe was carried out by Orlandi at the University of Rome [54, 55]. A drag reduction was observed accompanied by a reduction of turbulent kinetic energy when the pipe rotates about its axis, which seems to result from the modification of the vortical structure near the wall. A spiral motion is seen in the flow at high pipe rotation, transporting the streamwise vorticity away from the wall. The DNS results were used to study how the hilicity fluctuations, turbulent energy production and dissipation change as the solid body rotation is applied to the pipe flow. The results seem to suggest that the energy dissipation takes place in the region where the helicity density is very low.

DNS studies conduced at the University of Madrid on turbulent boundary layer structure [56-58] seem to suggest that there is a regenerating cycle of quasi-streamwise vortices (QSVs). This cycle is local to the near-wall region and does not depend on the outer boundary-layer structure. The wall turbulence is maintained by this regenerating cycle where QSVs extract energy from the mean flow to create the near-wall streaks, and these streaks in turn give rise to the quasi-streamwise vortices. Since QSVs are directly responsible for the turbulent skin-friction drag, attempts have been made to weaken these vortices to obtain a drag reduction. Jimenez and Pinelli suggested that any part of this regenerating cycle can be interrupted for a drag reduction, which is similar to an argument previously put forward by Choi [59]. An oscillating velocity was applied to the near-wall streaks of the boundary layer in an effort to disturb the cycle. This brought a decay of the streaks and laminarisation of the boundary layer, supporting the hypothesis being made. This numerical experiment is reminiscent of the spanwise–wall oscillation of the turbulent boundary layer, which gave a turbulent drag reduction of up to 45%. Preliminary results suggest that the relevant time scales of this numerical experiment are comparable to those of spanwise-wall oscillation.

Passive porous surface

A group at the University of Warwick investigated into the effects of passive porous walls on laminar-turbulent transition [60, 61]. This is the first combined theoretical and experimental study of the effects of such walls similar to those found over wings and in other aeronautical applications. The theoretical work suggested that passive porous walls with the appropriate characteristics could have a markedly favourable effect on transition, provided that the streamwise pressure gradient is not adverse. Broadly, this conclusion holds for both two-dimensional flows and the three-dimensional flows over infinitely swept wedges, the latter being a simple model flow representative of flows over swept wings.

The experiments carried out by Carpenter and Porter did not provide a completely reliable test of the theoretical predictions. They did, however, lead to the discovery of a novel phenomenon. For sufficiently porous walls and when a certain threshold flow speed had been exceeded, strong highly-coherent structures were self-excited in the boundary layer. These appeared to have the form of Λ-vortices. This phenomenon is very robust and could not be suppressed by modifying the cavity's trailing edge, installing baffles or changing the cavity depth. A simple theoretical model and the experimental evidence suggest that the generation of the coherent disturbances is due to a feedback mechanism, where the fluctuations of cavity air mass generate pressures in phase with the disturbance generated at the leading edge of the panel.

Slip wall

For rigid bodies immersed in a flow, the non-slip condition must hold on the wall surface. The basic idea pursued by Bechert at DLR Berlin was to release this non-slip condition in order to reduce drag [62]. This was attempted with a rolling belt driven by the wall shear stress of the boundary layer itself. Drag measurement of the slip wall in an oil channel suggests that there is as much as 9% of net drag reduction. The system has a further scope for optimization, therefore, it may be possible to achieve a greater drag reduction by improving the mechanism.

V. CONCLUSIONS

The recent developments and current status of the drag reduction research in Europe have been described here with an overview of European Research Community on Flow, Turbulence and Combustion (ERCOFTAC) where a large amount of research work has been coordinated. The research activity in Europe is unique in a sense that the research areas are diverse with a mixture of new and traditional themes. This is due to various funding mechanisms available in Europe mainly through national funding schemes in each country. The obvious disadvantage for this arrangement is that it is difficult to gather momentum on a particular work as the research funds are spread very thinly across Europe. ERCOFTAC's main aim is, therefore, to stimulate coordinated European-wide research efforts on special topics in flow, turbulence and combustion, in which drag reduction is one of well established subject areas.

The author would like to acknowledge the support from the Leverhulme Trust.

VI. REFERENCES

1. Coustols, E., "Turbulence Control by Passive Means", Kluwer, 1990.
2. Choi, K.-S., "Recent Developments in Turbulence Management", Kluwer, 1991.
3. Prasad, K.K., "Further Developments in Turbulence Management", Kluwer, 1993.
4. Choi, K.-S. *et al.*, "Emerging Techniques in Drag Reduction", Mechanical Engineering Publications, 1996.
5. Choi, K.-S., "Breakdown of the Reynolds Analogy over Drag-reducing Riblets Surface", *Appl. Sci. Res.*, **51**, 1993, 149-155.
6. Choi, K.-S. and Orchard, D.M., "The Structure of Thermal Boundary Layer over Drag-reducing Riblets", *Proc. 10th European Drag Reduction Meeting*, Berlin, 1997.
7. Choi, K.-S. and Orchard, D.M., "Turbulence Management Using Riblets for Heat and Momentum Transfer", *Int. J. Exp. Thermal Fluid Sci.*, **15(2)**, 1997, 109-124.
8. Starling, I. and Choi, K.-S. "Non-linear Laminar-Turbulent Transition over Riblets", *Proc. Laminar Flow Workshop*, Queen Mary and Westfield College, London, 1997.
9. Bechert, D.W. *et al.*, "The Berlin Oil Channel for Drag Reduction Research", *Exp. in Fluids*, **12**, 1992, 251-260.
10. Bruse, M. *et al.* "Experiments with Conventional and with Novel Adjustable Drag-reducing Surfaces" in *Near-wall Turbulent Flows* (eds. R.M.S. So *et al.*) Elsevier, 1993, pp. 719-738.
11. Bechert, D.W. *et al.*, "Experiments on Drag-Reducing Surfaces and their Optimisation with an Adjustable Geometry", *J. Fluid Mech.* **338**, 1997, 59-87.
12. Bechert, D.W., "Biological Surfaces and their Technological Application – Laboratory and Flight Experiments on Drag Reduction and Separation Control", *AIAA Paper* 97-1960, 1997.
13. Luchini, P. *et al.*, "Resistance of a Grooved Surface to Parallel Flow and Cross-flow", *J. Fluid Mech.* **228**, 1991, 87-109.
14. Luchini, P. *et al.*, "Viscous Eddies over a Grooved Surface Computed by a Gaussian-Integration Galerkin Boundary-Element Method", *AIAA J.* **30(8)**, 1992, 2168-2170.
15. Luchini, P. and Trombetta, G., "Effects of riblets upon flow stability", *Appl. Sci. Res.* **54**, 1995, 313-321.
16. Luchini, P., Pozzi, A., "Computation of Three-dimensional Stokes Flow over Complicated Surfaces (3D Riblets) using a Boundary-Independent Grid and Local Corrections", 10th European Drag Reduction Meeting, Berlin, 1997.
17. Baron, A., "On the Boundary Layer/Riblets Interaction Mechanisms and the Prediction of Turbulent Drag Reduction", *International J. Heat Fluid Flow*, **14**, 1993, 324-332.
18. Baron, A. and Quadrio, M., "Turbulent Boundary Layer over Riblets: Conditional Analysis of Ejection-like Events", *International J. Heat Fluid Flow*, **18(2)**, 1997, 188-196.

19. Baron, A. and Quadrio, M., "On The Accuracy of Wall Similarity Methods in Determining Friction Velocity over Smooth and Ribletted Surfaces", *J. Fluids Engr., Trans. ASME*, **119(4),** 1997, 1009-1011.
20. Grek, G.R. *et al.*, "Experimental Study of the Influence of Riblets on Transition", *J. Fluid Mech.* **315,** 1996, 31-49.
21. Grek, G.R. *et al.*, "Effects of Riblets on Vortex Development in the Wake Behind a Single Roughness Element in the Laminar Boundary Layer on a Flat Plate", *La Recherche Aérospatiale*, **1**, 1996, 1-9.
22. Boiko, A.V. *et al.*, "Transition Control By Riblets in a Swept Wing Boundary Layer with an Embedded Streamwise Vortex", *European J. Mechanics, B/Fluids*, **16(4),** 1997, 465-482.
23. Kozlov, V.V., "Effect of Riblets on Flow-structures at Laminar-turbulent Transition and Simulation of their Influence on Turbulent Boundary Layer", *Proc. 10th European Drag Reduction Meeting*, Berlin, 1997.
24. DeBisschop, J.R. and Nieuwstadt, F.T.M., "Turbulent Boundary Layer in an Adverse Pressure Gradient", *AIAA J.* **34(5),** 1996, 932-937.
25. Choi, K.-S., "Effects of Longitudinal Pressure Gradients on Turbulent Drag Reduction with Riblets" in *Turbulence Control by Passive Means* (ed. E. Coustols), Kluwer, 1990, pp. 109-121.
26. Coustols, E. and Savill, M., "Turbulent Skin-Friction Drag Reduction by Active and Passive Means", AGARD Report 786, 1992.
27. Coustols, E., "Riblets: Main Know and Unknow" in *Emerging Techniques in Drag Reduction* (eds. K.-S. Choi *et al.*), Mechanical Engineering Publications, 1996.
28. Choi, K.-S., "Turbulent Drag Reduction Strategies" in *Emerging Techniques in Drag Reduction* (eds. K.-S. Choi *et al.*), Mechanical Engineering Publications, 1996.
29. Tardu, S.F. "Coherent Structure and Riblets", *Appl. Sci. Res.* **54,** 1995, 349-385.
30. Lucey, A.D. and Carpenter, P.W., "A Numerical Simulation of the Interaction of a Compliant Wall and Inviscid Flow", *J. Fluid Mech.*, **234**, 1992, 121-146.
31. Carpenter, P.W., "Optimisation of Multiple-Panel Compliant Walls for Delay of Laminar-Turbulent Transition", *AIAA J*, **31**, 1993, 1187-1188.
32. Dixon, A.E. *et al.*, "Optimisation of Viscoelastic Compliant Walls for Transition Delay", *AIAA J.*, **32**, 1994, 256-267.
33. Davies, C. and Carpenter, P.W., "Numerical Simulation of the Evolution of Tollmien-Schlichting Waves", *J. Fluid Mech.* **335**, 1997, 361-392.
34. Cooper, A.J. and Carpenter, P.W., "Stability of Rotating-disc Boundary-layer Flow over a Compliant Wall. Part 1. Type I and II Instabilities", *J. Fluid Mech.* **350**, 1997, 231-259.
35. Cooper, A.J. and Carpenter, P.W., "Stability of Rotating-disc Boundary-layer Flow over a Compliant Wall. Part 2. Absolute Instability", *J. Fluid Mech.* **350**, 1997, 261-270.
36. Gaster, M., "Is the Dolphin a Red Herring?" in *Turbulence Management and Relamianalisation* (eds. H.W. Liepmann and R. Narasimha), Springer-Verlag, 1987, pp. 285-304.
37. Kulik, V.M. *et al.*, "Experimental Investigation of One-layer Viscoelastic Coatings Action on Turbulent Friction and Wall Pressure Pulsations" in *Recent Developments In Turbulence Management* (ed. K.-S. Choi), Kluwer, 1991, pp. 263-289.
38. Semenov, B.N., "On Conditions of Modelling and Choice of Viscoelastic Coatings for Drag Reduction" in *Recent Developments in Turbulence Management* (ed. K.-S. Choi), Kluwer, 1991, pp. 241-262.
39. Kulik, V.M. and Semenov, B.N., "The Measurement of Dynamic Properties of Viscoelastic Materials for Turbulent Drag Reduction" in *Emerging Techniques in Drag Reduction* (ed. K.-S. Choi *et al.*), Mechanical Engineering Publications, 1996, pp. 207-217.
40. Choi, K.-S. *et al.*, "Experiments on Turbulent Drag Reduction using Compliant Surface", *Proc. 1st Int. Conf. on Flow Interaction*, Hong Kong, 1994.
41. Choi, K.-S. *et al.*, "Turbulent Drag Reduction using Compliant Surfaces", *Proc. Royal Society, Ser. A.*, **453**, 1997, 2229-2240.
42. Bannasch, R., "Hydrodynamics Of Wave-like Curvature on Bodies of Swimming Animals", *Proc. International Symposium on Seawater Drag Reduction*, Newport, RI, 1998.
43. Bannasch, R., "Experimental Investigations on the Boundary Layer Development in Swimming Penguins: Mechanisms of Drag Reduction and Turbulence Control", *Proc. 10th European Drag Reduction Meeting*, Berlin, 1997.
44. Choi, K.-S. *et al.*, "Tests of Drag Reducing Polymer Coated on Riblet Surface", *Appl. Sci. Res.* **46,** 1989, 209-217.
45. Choi, K.-S. et al., "Drag Reduction with a Combined Use of Riblets and Polymer Coating" in *Drag Reduction in Fluid Flows* (eds. R.H.J. Sellin and R.T. Moses), Ellis Horwood, 1989, pp. 271-277.
46. Choi, K.-S., "Drag Reduction by Riblets for Marine Applications", *Trans. Royal Inst. Naval Arch.*, Part B, **133,** 1991, 129-143.
47. Orlandi, P., "Tentative Approach to the Direct Simulation of Drag Reduction by Polymers", *J. Non-Newtonian Fluid Mech.* **60(2/3),** 1995, 277-301.
48. DenToonder, J.M.J. *et al.*, "Drag Reduction by Polymer Additives in a Turbulent Pipe Flow", *J. Fluid Mech.* **337,** 1997, 193-231.
49. Laadhari, F. *et al.*, "Turbulence Reduction in a Boundary Layer by a Local Spanwise Oscillating Surface", *Phys. Fluids*, **A6(10),** 1994, 3218-3220.
50. Choi, K.-S. *et al.*, "Turbulent Boundary-Layer Control by Means of Spanwise-wall Oscillation", AIAA Paper **97-1795**, presented at the 28th AIAA Fluid Dynamics Conf., Snowmass, Co., USA, 1997.
51. Choi, K.-S. *et al.*, "Turbulent Boundary-Layer Control by Means of Spanwise-Wall Oscillation", to appear in *AIAA J.*, 1998.
52. Baron, A., and Quadrio, M., "Turbulent Drag Reduction by Spanwise Wall Oscillations", *Appl. Sci. Res.*, **55**, 1996, 311-326.
53. Choi, K.-S. and Graham, M., "Drag Reduction of Turbulent Pipe Flows by Circular-wall Oscillation", *Phys. Fluids*, **10(1)**, 1998, 7-9.
54. Orlandi, P. and Fatica, M., "Direct Simulations of Turbulent Flow in a Pipe Rotating about its Axis", *J. Fluid Mech.* **343,** 1997, 43-72.
55. Orlandi, P., "Helicity Fluctuations and Turbulent Energy Production in Rotating and Non-Rotating Pipes", *Phys. Fluids* **9(7),** 1997, 2045-2056.
56. Jimenez, J. and Pinelli, A., "Controlling the Structures of the Turbulent Wall Region", *Proc. Euromech Colloquium - 361*, Berlin, 1997.
57. Jimenez, J. and Pinelli, A., "Wall Turbulence: How It Works and How to Damp It", *AIAA Paper* 97-2112, 1997.
58. Jimenez, J. and Pinelli, A., "The Role of Coherent Structure Interactions in the Regeneration of Wall Turbulence", *Proc. 7th European Turbulence Conference*, Saint Jean Cap Ferrat, France, 1998.
59. Choi, K.-S., "Near-wall Structure of Turbulent Boundary Layer with Riblets", *J. Fluid Mech.*, **208**, 1989, 417-458.
60. Carpenter, P.W. and Porter, L.J., "Further Developments in the Use of Passive Porous Walls for Drag Reduction", *Proc. 9th European Drag Reduction Meeting*, Naples, 1995.
61. Carpenter, P.W., "The Feasibility of Using Passive Porous Walls for Drag Reduction" in *Emerging Techniques in Drag Reduction* (eds. Choi, K.-S. *et al.*), Mechanical Engineering Publications, 1996.
62. Bechert, D.W. *et al.*, "Drag Reduction with The Slip Wall", *AIAA J.* **34(5),** 1996, 1072-1074.

DRAG REDUCTION RESEARCH IN JAPAN

Keizo Watanabe
Department of Mechanical Engineering
Tokyo Metropolitan University
1-1, Minami Ohsawa, Hachiooji-shi, Tokyo, 192-0397
keizo@ecomp.metro-u.ac.jp

Abstract - This paper is a review of recent water drag reduction research and its practical applications proposed in Japan. The methods of drag reduction which are the subjects of this research are surfactant additives, bubble mixing and highly water-repellent walls. Problems that may arise in industrial applications are examined.

I. INTRODUCTION

Since the reduction of friction in turbulent flow was first achieved by Toms [1] in 1948, much of the reported work on drag reduction has been related to hydrodynamic drag reduction using polymer additives. In spite of extensive research on drag reduction, industrial applications are few because of the degradation of polymer solutions, such as the breakdown of polymer molecules by mechanical shearing of the flow fields. Of the various types of drag forces which arise, viscous, or skin friction, drag is one of the most significant. The reduction of drag is important from the point of view of conserving energy.

After the oil shock in 1970, drag reduction research led to the discovery of new merits in application, and new drag reduction techniques were reported. For example, the effects of longitudinally ribbed surfaces on drag were studied in an attempt to contain wall bursts, and the results indicated that drag reductions as large as 7% occur with certain V-groove riblets.

Drag reduction has recently been associated with the reduction of carbon gas emissions which are linked to global warming, and industrial application of drag reduction for such purposes has been expected.

In this paper, the current research on drag reduction in Japan is reviewed and potential industrial applications are surveyed and future research directions are discussed.

II. CLASSIFICATION OF DRAG REDUCTION

We can classify drag reduction according to the flow behavior and the method used, as shown in Fig. 1. It is well-known that hydrodynamic drag reduction using a mixture of bubbles and fine solid particles is achieved through laminar flow control, wherein the transition from laminar to turbulent flow is delayed such that it occurs at a higher Reynolds number. Generally, examination of the characteristics of drag reduction and fluid flow is required to enable the application of drag reduction to fluid engineering technology.

In many of these practical applications, the importance of polymer degradation has been recognized but only a limited amount of data on it is available. Thus there are high expectations from the methods which involve surfactant addition, bubble mixtures and highly water-repellent coatings for drag reduction.

III. APPLICATION OF DRAG REDUCTION

(1) Surfactant additives

Experimental results on drag reduction by the addition of surfactants have been reported for a method of predicting the drag that reduces pipe flow [2], the characteristics of low-speed streaks in turbulent channel flow [3], the flow resistance and heat transfer of cold water pipe flow [4] and the possibility of actively controlling reduced drag flow [5]. Although work on the characteristics of surfactant solutions is still basic, it is necessary to develop new surfactant additives in order to use high-density thermal energy transportation in a wide-area energy supply network system.

It is important to create a municipal energy system with low environmental load to allow the coexistence of urban as well natural environments along with human activity. Under these circumstances, the energy supply network system, The Eco-Energy City Project which is part of the New Sunshine Project of the Agency of Industrial Science and Technology within the Ministry of International Trade and Industry, is being developed in Japan [6]. The New Energy and Industrial Technology Development Organization (NEDO) assigned the research and development to the Energy Conservation Center, Japan, for the period from fiscal 1993 to 2000. Thus we anticipate a practical application of surfactant solutions for reduction of the pumping costs of the transport station in this system.

Figure 2 shows the schematic of one possible example for such a reduction of pumping energy costs in this project. The development of a vacuum thermally-insulated heat transport piping system will enable high-efficiency heat transport and help realize the cascade use of heat in industrial areas and the transport of heat derived from waste heat to heat-requiring areas, thus contributing to the effective use of waste heat while promoting energy-savings and reducing environmental problems. As described above, the practical application of drag reduction by surfactant addition is related

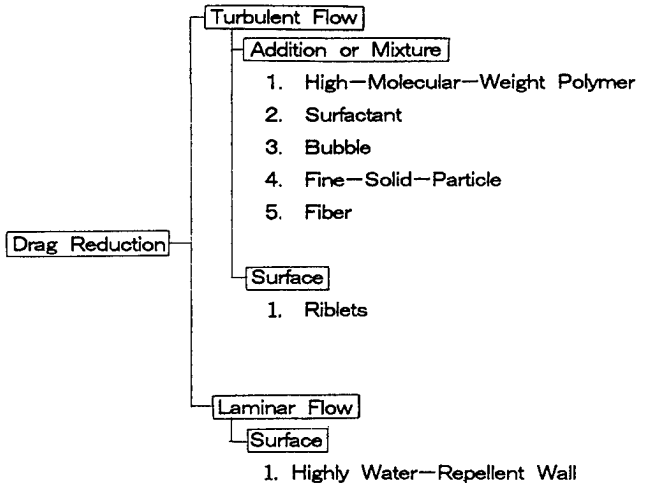

Fig. 1 Classification for Drag Reduction

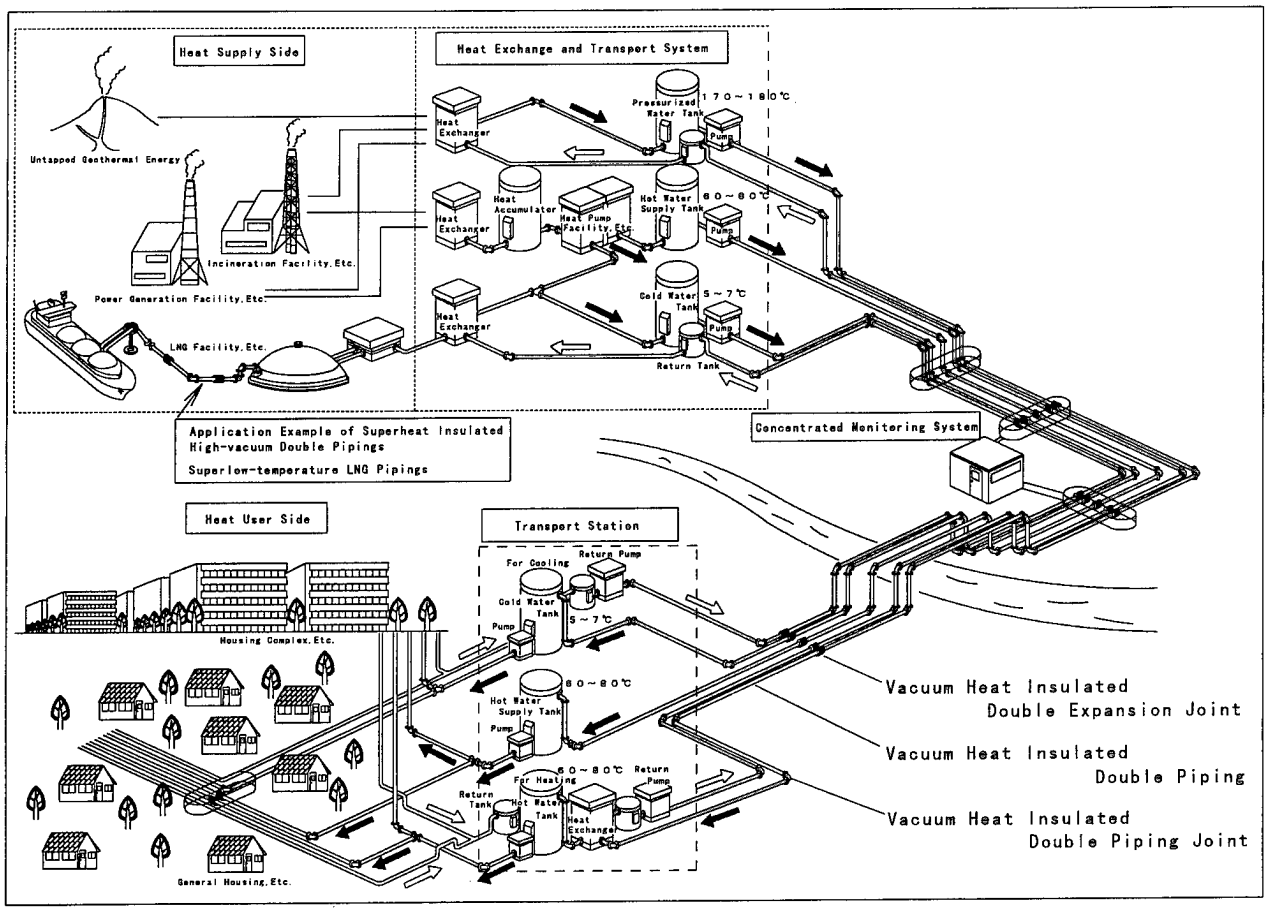

Fig. 2 Heat Transport Systems with Vacuum Thermally-Insulated Heat Transport [6]

to the reduction of the pressure loss of waste heat 200℃ or lower, from various sources, during its transport to areas requiring heat, through the use of highly-insulated heat transport piping.

It is well-known that special kinds of surfactants that form rodlike micelles, are also effective for the drag reduction of turbulent flow. However, there is the problem that the water mixed with such a surfactant cannot be discarded freely because of its toxicity and the corrosive property of halide ions.

If new surfactants which can prevent the aggregation of ice and plugging due to ice slurry in pipes, can be developed, they may be put to use for easy heat storage at low temperatures as well as high-density thermal energy transportation, in the future.

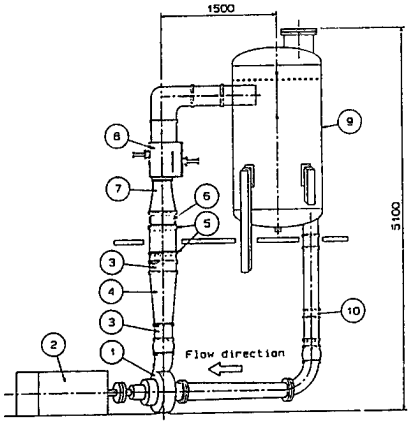

1.Pump 2.Motor 3.Honeycomb 4.Diffuser
5.Gauze screen 6.Bubble generator 7.Nozzle
8.Reservoir tank 9. Orifice

Fig. 3 Test Tunnel [7]

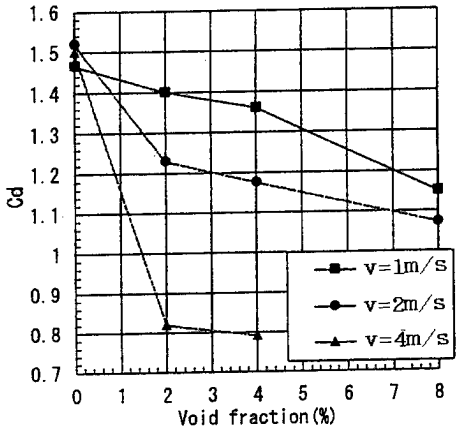

Fig. 4 Drag Coefficient Distribution Associated with Void Fraction [7]

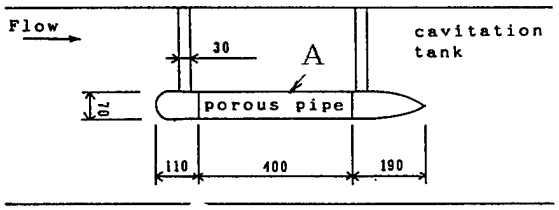

Fig. 5 Schematic of 3-Dimensional Models [10]

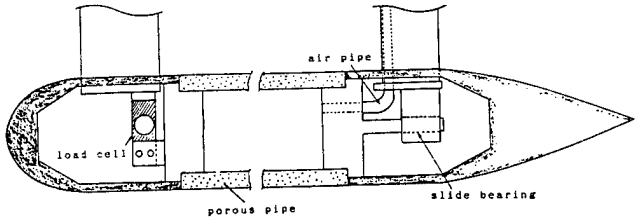

Fig. 6 Details of Part A in the Model [10]

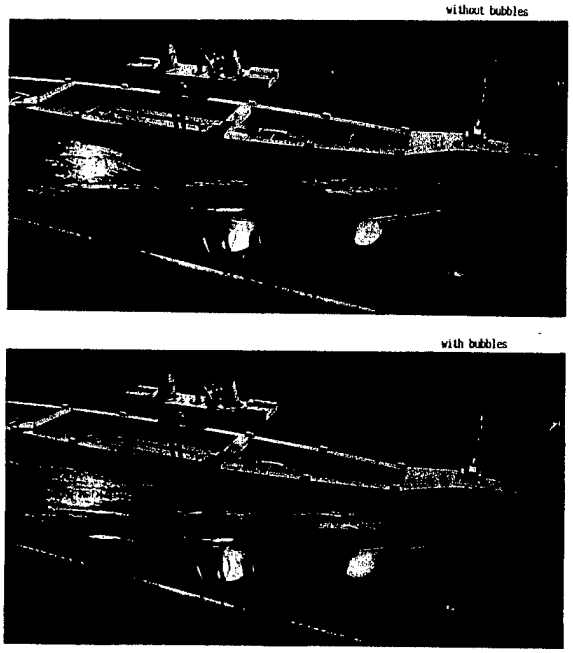

(top : without bubbles, bottom : with bubbles
flow rate : 6.5×10^{-4} m³/s, gauge pressure : 2 kgf/cm², F_n=0.281(1.6 m/s)

Fig. 7 Bow Wave Patterns around Navigating Ship [10]

(2) Bubble mixing or injection

The study of drag reduction of a bubbly flow has been reported for flows around a circular cylinder [7] . Figures 3 and 4 show the test tunnel used in the experiment and the experimental result of drag coefficient distribution associated with void fraction, respectively. The diameter of the test cylinder is 20mm and the experiment was performed in the regions where the Reynolds number was in the

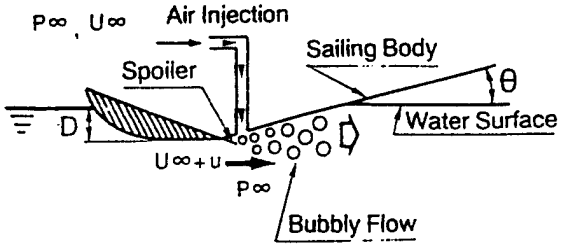

Fig. 8 Principle of Drag Reduction for the Model [11]

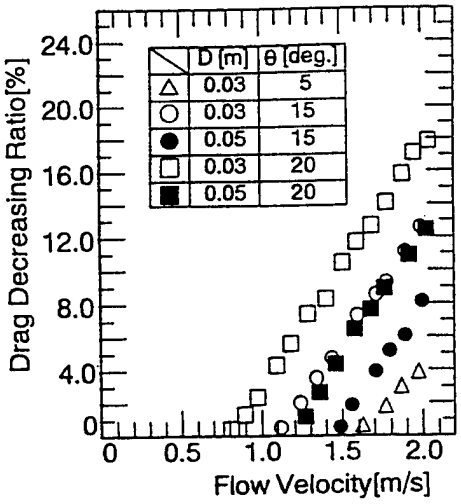

Fig. 9 Drag Reduction Ratio [11]

range of 1.1×10^{4} to 3.5×10^{5} and the void fraction was is the range of 0 to 8%. In Fig.4, a drag reduction of up to 50% is shown at a velocity of 4m/s and a void fraction of 4%. The reduction occurs in the unstable laminar boundary layer and the point of separation of the flow around the circular cylinder then moves downstream from the midsection due to bubble mixing. In the case of for fine solid particle suspensions, it has been reported that a similar drag reduction phenomenon occurs in flows around a sphere [8] or a circular cylinder [9] in dilute carbon black suspensions.

We can expect the practical application of the injection of microbubbles into, or covering microbubbles over the surface, of, a body immersed or floating in fluid flow, for drag reduction. Doi et al. [1 0] formed a microbubble covering by injecting air through a porous pipe with pore size of 15 μ m.

Figures 5 and 6 show the overall view of the 3-dimensional model of a cylindrical body and the details of the experimental apparatus, respectively. In Fig. 5, microbubbles are injected through the porous pipe, and the drag of the model is measured by a load cell which is set at the column as shown in Fig. 6. They studied the effects of the microbubble injection on wave-making resistance by visualizing the bow wave patterns. Figure 7 shows these bow wave patterns around the bows of a navigating ship model in a towing tank. There are very few differences observed between the wave patterns of Figs 7(a) and 7(b). They reported that it is possible to reduce the resistance of a 3-dimensional body by using microbubbles if the body is well covered by microbubbles. They found that the local frictional resistance is reduced by more than 20% when microbubbles cover the body, although the wave-making resistance increases slightly when microbubbles are injected. The total resistance is reduced by more than 5%.

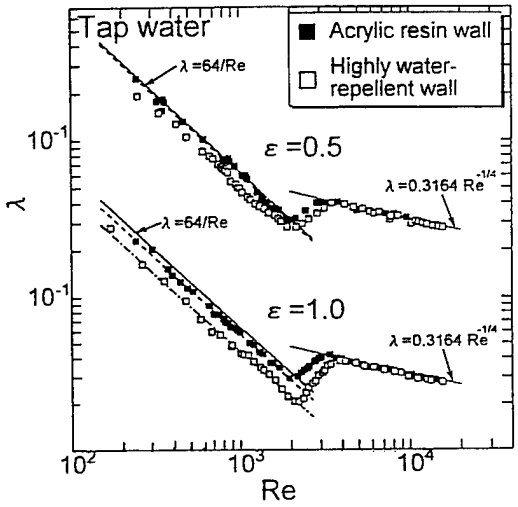

Fig. 10 Friction Factor of Duct [13]

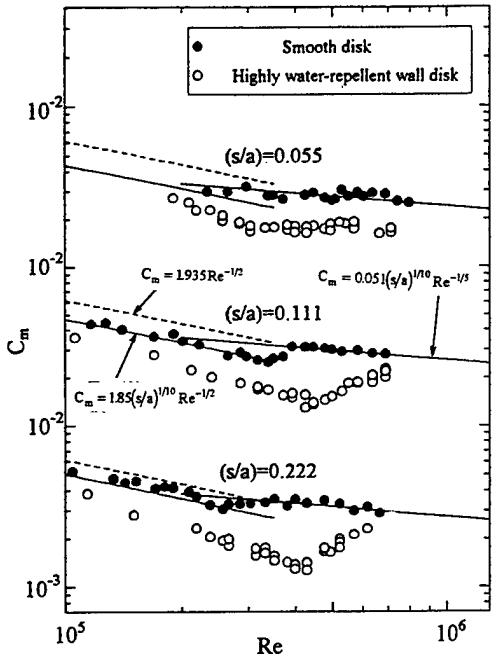

Fig. 11 Moment Coefficient of an Enclosed Rotating Disk [14]

On the other hand, the expansion of air entrained in the water flow generates a high-speed two-phase water jet and drag reduction of a ship's hull is caused by this reaction force. Therefore, fluid drag can be reduced without the addition of external energy. The principle of drag reduction of a ship's hull, which is achieved by injecting air under atmospheric pressure into the water flow, has been proposed by Tsutahara and Sakamoto [11] . The principle of drag reduction in the proposed model is shown in Fig. 7. Although the principle of the acceleration of water flow is similar to that in an underwater ramjet [12] , it has not been reported in the literature as a drag reducing system.

Their experimental setup consists of a spoiler located at the bottom of the propulsion equipment, a sailing body and an air injection nozzle as shown in Fig. 8. Three types of sailing bodies with different spoilers were set in

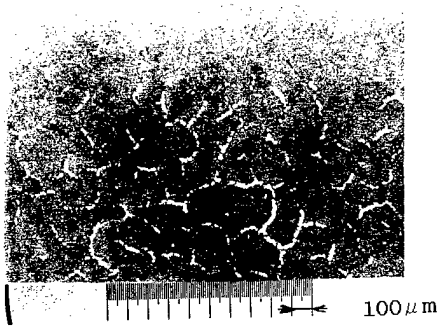

(a)

(b)

Fig. 12 Micrographs of the Highly Water-Repellent Wall

a towing tank, and the amount of drag reduction was determind using various parameters such as sailing velocity, opening angle of the rear plate, and the depth of the sailing body in the water. Figure 9 shows an example of the experimental results. It is seen that the drag decreases monotonically with increasing sailing velocity and increasing opening angle of the rear plate.

(3) Highly water-repellent wall

The initial experiments to clarify laminar skin friction reduction were conducted in the spring of 1994 by Watanabe et al. [13] using ducts with highly water-repellent walls. Figure 10 shows an example of the experimental results of the friction factor obtained in the study. λ and Re are the friction factor of the duct and the Reynolds number, respectively. ε is the aspect ratio, and its value for a square duct is ε=1. It was seen that drag reduction occurs in the laminar region and the drag reduction ratio of the square duct is about 22%.

Figure 11 shows the experimental results of moment coefficient of an enclosed rotating disk [14] with highly water-repellent wall in tap water. In the case of the highly water-repellent wall disk, the moment coefficient decreased compare with that of smooth plane disk, and the value of drag reduction rate increases progressively with increasing the clearance ratio (s/a). We can reduce the disk friction loss of an impeller and the skin friction of casing of a turbomachine by applying the highly water-repellent coating.

The aim of the experiment was to investigate what kind of solid surface would exhibit fluid slip with significantly less skin friction than a smooth wall. In general, the largest contact angles recorded for a smooth surface are 112° ~115° . Thus we need a useful method for producing a

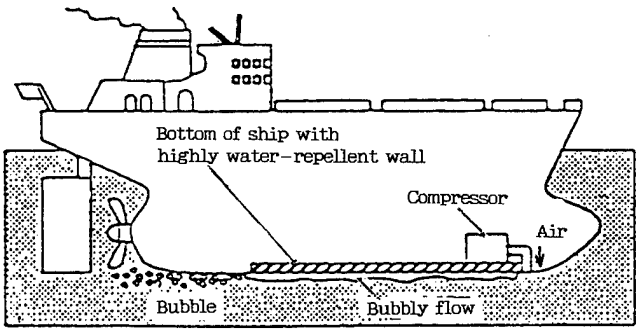

Fig. 13 Model of Drag Reduction Systems for a Ship [18]

surface with a contact angle of 120° or larger, since it is necessary not only to reduce the free surface energy but also to change the surface morphology. Figures 12(a) and 12(b) show micrographs of the tested highly water-repellent wall obtained using a microscope and a SEM. The surface has many narrow grooves that increase the water repellency.

Drag reduction of a circular pipe [15] and two coaxially rotating cylinders [16] has been reported. Then, it was experimentally shown that fluid slip [17] occurs at the wall. We conclude that fluid slip described in that paper occurs due to the existence of air in the grooves, as shown in Fig. 6(b). In other words, water cannot come into contact with the wall because of the surface tension when air exists in the grooves. Thus it can be inferred that drag reduction is poor in the case of the flow of surfactant solutions having low surface tension.

Since certain highly water-repellent walls can reduce laminar flow friction in both internal and external flows, it is expected that they would affect the heat exchanger or the ship's performance. For the heat exchanger of a car, down-sizing and efficient operation are necessary to reduce fuel consumption. Since flow in the tube of the heat exchanger is laminar, the industrial application of coatings is well within the bounds of the possibility of efficiency improvement.

A practical application in the case of an external flow is for the reduction of the skin friction which contributes to about 60% of the total drag, of a ship. Greater drag reduction in the friction of a ship may be achieved with a system that combines bubbly flow for the bottom of a ship with highly water-repellent walls. Figure 13 shows a model of drag reduction for such a system [18] developed by Mitsui Engineering & Shipbuilding Co.. The bottom of the ship is coated with a highly water-repellent material and air is supplied by a compressor located in the ship. Tests using a model have been carried out, and the performance test for a real ship may be conducted in two or three years. Although the problem of coating durability still remains, drag reduction of a ship is one of the interesting potential applications of drag reduction techniques.

IV. CONCLUSIONS

Drag reduction techniques have been applied to few industrial applications because the utility is still limited in terms of the flow range or the cost performance. Surfactant addition or bubble mixing in liquids and the use of highly water-repellent walls can be expected to be increasingly applied to industrial and actual flow fields in the future. However, it must be emphasized that we should also develop and study effective new drag reduction methods.

V. REFERENCES

1. B.. A. Toms "Some Observations on the Flow of Linear Polymer Solution through Straight Tube at Large Reynolds Numbers", Proceedings of the First International Congress on Rheology, July 1948.
2. H. Usui, T. Itoh and T. Saeki "Drag Reduction Pipe Flow of Surfactant Solutions", Proceedings of the ASME Fluids Engineering Division, FED-Vol. 237, July 1996 pp. 159-163.
3. M. Itoh, S. Imao and K. Sugiyama "Characteristics of Low-Speed Streaks in the Flow of Drag-Reducing Surfactant Solution", Transaction of the JSME, Series B, Vol. 63, No. 605, August 1997, pp.40-46 (in Japanese).
4. H. Iaba and N. Haruki "Flow Resistance and Heat Transfer Characteristics of Cold Water Pipe Flow with Surfactant for Cold Heat Energy Transport", Transaction of the JSME, Series B, Vol. 63, No. 608, October 1997, pp. 1336-1343 (in Japanese).
5. Y. Kawaguchi et al. "Active Control of Turbulent Drag Reduction in Surfactant Solutions by Wall Heating", Proceedings of the ASME Fluids Engineering Division, FED-Vol. 237, July 1996 pp. 47-52.
6. Report on Element Technology Development Program, NEDO & ECC, 1997.
7. Y. Ichikawa, K. Sugiyama and Y. Matsumoto "Characteristics of Bubbly Flow around a Circular Cylinder", Proceedings of Symposium on Multiphase Flow '95, July 1995, pp. 132-135 (in Japanese).
8. K. Watanabe and H. Kui "Drag of a Sphere in High-Reynolds-Number Range in Water/Fine Solid Particle Suspension", Proceedings of the ASME Fluids Engineering Division, FED-Vol. 221, August 1995, pp.127-132.
9. K. Watanabe, Y. Chang and T. Fujita "Drag Reduction in Flow Past a Circular Cylinder in Water/Fine Solid Particle Suspension", Trans. of the JSME, Series B, November 1996, Vol. 62, No. 603, pp. 3818-3823 (in Japanese).
10. Y. Doi, K. Mori and T. Hatta "Frictional Drag Reduction by Microbubbles", Journal of Soc. Naval Arch. of Japan, July 1991, Vol. 170. pp. 55-63 (in Japanese).
11. M. Tsutahara and M. Sakamoto M. "Study of Drag Reduction on Ship Hull by Expansion of Entrained Air in Water Flow", Trans. of the JSME, Series B, Vol. .61, No. 586, June 1995, pp. 2088-2094 (in Japanese).
12. E. Motlard and C. J. Shoemaker "Preliminary Investigation of an Underwater Ramjet Powered by Compressed Air", NASA Tech. N., D-991, 1961, pp.1-36.
13. K. Watanabe, Yanuar, K. Okido and H. Mizunuma "Drag Reduction in Flow through Square and Rectangular Ducts with Highly Water Repellent Wall", Proceedings of the ASME Fluids Engineering Division, FED Vol. 237, July 1996, pp. 115-119.
14. K. Watanabe and S. Ogata "Drag Reduction for a Rotating Disk with Highly Water Repellent Wall", Proceedings of the ASME Fluids Engineering Division, FEDSM-3380, June 1997, pp. 1-5.
15. K. Watanabe, Yanuar and H. Udagawa "Drag Reduction of Newtonian Fluids in a Circular Pipe with Highly Water Repellent Wall", Proceedings of 3rd International Symposium on Performance Enhancement for Marine Applications, May 1997, pp. 157-162.
16. K. Watanabe and T. Akino "Drag Reduction in Laminar Flow between Two Coaxial Cylinders", Proceedings of the ASME Fluids Engineering Division, June 1998, pp. 1-6.
17. K. Watanabe, Yanuar and H. Mizumuma "Slip of Newtonian Fluids at Solid Boundary", Proceedings of International Conference on Fluid and Thermal Energy Conversion '97, July 1997, pp. 401-406.
18. Asahi Shinbun, March 27, 1997 (in Japanese).

Wall Turbulence Physics

Steve Kline 1922 - 1997

Near wall turbulence: a rememberance of Steve Kline

by

Brian Cantwell
Department of Aeronautics and Astronautics
Stanford University
Stanford, CA 94305

Abstract

I would like to thank the organizers of this meeting for inviting me to speak on the subject of wall turbulence and in memory of my good friend and Stanford colleague Steve Kline. My presentation today is not intended to be a tribute to Steve. For that I highly recommend the article by Bob Dean which appeared in the March 1998 issue of the Journal of Fluids Engineering [1]. I could not be more eloquent! Rather, I would like to use the opportunity to recall my acquaintance with Steve Kline and his work on wall turbulence and to review our common and differing views of the subject.

Our acquaintance

It is fitting that Steve Kline is remembered at a meeting where the subject is that which was nearest and dearest to his heart. Steve made pioneering contributions to our knowledge of the stability of flow in wide angle diffusers and the development of standards for measurement accuracy. His fluid mechanics film on flow visualization is one of the classics. In his later years he wrote prolifically and provocatively on the relationship between innovation and technology. But it was the structure of turbulence near a wall which held his constant interest for over forty years virtually up to the last days before his death. Watching him struggle through his difficult illness over the past several years, with his health improving at times and then worsening, I was convinced that part of the reason he survived so long was simply that he still had work to do - the problem of turbulence was not yet solved! At one point about a year and a half ago I visited him at home during a particularly bad stretch. He had called me on a Sunday afternoon and asked me to come over not, it turned out, to commiserate about his illness but to discuss a series of technical reports written by an young entrepreneur whom he had been mentoring. At the end of an afternoon of technical discussions we said our goodbyes and I think both of us felt that we would not see each other again. In fact he rallied from that episode and I visited him several more times in similar circumstances until his death about a year later. Throughout this difficult period I could not help but stand in amazement at his tenacious dedication to his research.

I first got to know Steve when I came to Stanford in 1978. He was in the throes of organizing a follow-on to the 1968 Stanford Conference on turbulent boundary layers - the first Kline olympics [2]. The new conference had a much more ambitious theme to consider: the computation of complex turbulent flows. As always, Steve was thinking in totally new ways and he conceived a conference which which would actually run over two years with data presented in the first conference and computed results presented a year later, including computations of hidden cases with data which was to be taken in the intervening year. The result was the 1980-81 Stanford-AFOSR Conference on Complex Turbulent Flows - the second Kline olympics [3]. One of Steve's requirements for the conference was the creation of a digital data library of critically evaluated cases which was also a relatively new idea at the time. The results of the conference were mixed. What was clear was that, at that point in time, there was no way to fully distinguish between model errors and numerical errors. Grids were too coarse and solvers did not have adequate accuracy. So the original goal to evaluate models was never realized. Nevertheless the conference presented a clear picture of the state-of-the-art at the time and Kline's ideas about zonal modeling which were set forth at that conference have wound their way into many of the advances in turbulence modeling since that time. Both the 68 and 80-81 conferences were quintessential examples of Steve's intellectual leadership. This is where his loss will be felt most acutely by the turbulence community.

Kline's work on near wall turbulence

Although I met Steve in 1978, I knew of his work much earlier. Don Coles and I had been doing some research at Caltech on turbulent spots, measuring the ensemble-averaged large scale structure [4]. In the process, we did some visualization and scaling of the sublayer streaks beneath the spot. Don referred to the normalization of the sublayer structure as "Kline scaling" and I was prompted to go back and read Kline's classic 1959 and 1967 papers on the visualization of the sequence of events surrounding bursting [5], [6]. The results of this work are well known to everyone

here and so I will not spend a lot of time repeating them. Kline's sketches of what they saw in their visualizations have been reproduced in a number of papers including by 1981 Annual Reviews paper [7]. Rather, I would like to take the opportunity to briefly consider what the real significance of this work was and why it inspired so much research that followed. In the mid 1950's the prevailing picture of turbulence was in fact no picture at all! What I mean by this is that no one had seriously considered that turbulence might be something that was picturable. Townsend had used correlation data to sketch the mean large scale motion in shear layers and wakes and deserves credit as the first to clearly show that part of the turbulent motion is coherent. But Kline went a step further and recognized that the instantaneous motion was an important object of study. He had developed hydrogen bubble visualization methods was able to use this technique to discover basic flow elements of turbulence in the sublayer. Kline was willing to directly address the dynamics of turbulent motion on its own terms. This was a turning point in turbulence research which then began to emphasize the use of visualization as a primary measurement tool. This emphasis persists today in the way we use DNS data and PIV measurements to enhance our understanding of the physics of turbulence.

During the 1960's and 70's dozens of papers were published devoted to the visual identification of turbulent structure in an effort to fill out and unambiguously define the picture of wall structure and especially the dynamics of the bursting process which was known to be a primary contributer to the Reynolds stress in the near wall region. A wide variety of techniques were developed, some based on direct visualization, some on sophisticated methods of processing records of instantaneous velocity data. By the late 1970's low Reynolds number simulation data began to be available. But as the research proliferated a variety of competing pictures of the turbulent motion began to emerge. By the mid 1980's it was clear that the whole effort was not converging. Researchers looking at the same flow were seeing different things and having a hard time understanding one another. The whole subject was in danger of descending to the level of what Feynman once called "cargo cult science" where, in the absence of fundamental understanding, the mere association of events in time or space is used to infer cause and effect.

This prompted Kline in the late 1980's to undertake, with his student Steve Robinson, a study of all the different pictures that people were using. The idea was to reconcile them and to see if, at the end of the day, one overall picture would emerge. The first step was to survey all the workers in the field and to produce a kind of taxonomy of turbulent structure. At first I had misgivings about the whole approach which looked to me like science carried out by vote. In fact they carried out a rigorous study and in the end a good many scientific issues were resolved. They included in their study the turbulent boundary layer simulation data of Phillipe Spalart [8] which was just then becoming available. This gave them access to quantitative information of a kind which had never been available before to an experimentalist like Steve. Difficult to measure field variables such as vorticity and pressure could be analyzed in a variety of new ways. The upshot of this work was an updated picture of turbulent wall structure in the form of streamwise leaning arches of low pressure [9]. In the most symmetric cases the feet of the arch attached to the wall with the head leaning downstream near the edge of the layer. In a few instances both feet could be observed but in most cases the arch tended to be unsymmetrical with one foot at the wall and the termination of the opposite foot some distance away from the wall. This was the first work I am aware of that used in-situ static pressure to identify the basic flow structure. One of the big advantages of this approach was that pressure, like vorticity, did not suffer from the lack of Galilean invariance which tended to plague visualizations of the velocity field.

Recent work

However this was not altogether satisfying to Steve who felt that any identifier of the flow structure had to be non-local in nature and based in some way on an integration of the velocity field. In his view the pressure was an outcome of some, as yet undefined, dynamical process. This led him to focus his interest on bringing a rigorous definition to the concept of a vortex. To pursue this problem he took on two new PhD students who were to follow the work of Steve Robinson. In the early 1990's he began working with Luis Portela and then a couple of years later Juan Chacin came on board. Both continued to study the Spalart boundary layer simulation, in effect rerunning the simulation as various ideas were tried.

About three years ago, as his health began to fail, Steve recognized that he would not be able to provide adequate advising and he asked Jim Johnston, Peter Bradshaw and me to help. Peter and Jim helped advise Luis and I advised Juan. The effect of this was to put the two of them on somewhat separate tracks toward the PhD. Luis continued to focus on flow patterns near the wall and the question of defining a vortex while Juan began to investigate the structure of the velocity gradient tensor near the wall. The results of both of these studies are reported in the recent volume on Self-Sustaining Mechanisms in Wall Turbulence [10], [11].

Chacin's research led to what I consider to be an important advance in the identification of turbulent wall structure. Following some earlier work by Blackburn et al [12], he found that the cubic discriminant of the velocity gradient tensor provided a very useful, Galilean invariant, scalar descriptor of the flow structure especially near the wall where visualizations of the

vorticity and dissipation and especially the velocity field are full of ambiguities and very difficult to interpret [13], [14]. But I could never convince Steve of the value of this approach which he regarded as a "point method" lacking the non-local character he deemed essential. We argued the point back and forth several times and in the end we simply agreed to disagree. I miss those debates, I wish I could work on him just once more.

References

1. Bob Dean "A tribute to Steve Kline", *J. Fluids Eng.* Vol. 120, March 1998, pp 2-3.

2. S. Kline, M. Morkovin, G. Sovran and D. Cockrell, Proceedings: Computation of turbulent boundary layers - 1968 AFOSR-IFP-Stanford conference Vol I.

3. S. Kline, B. Cantwell, and G. Lilley 1981. Proceedings: 1980-81 AFOSR - HTTM - Stanford conference on complex turbulent flows.

4. B. Cantwell, D. Coles and P. Dimotakis, 1978. Structure and entrainment in the plane of symmetry of a turbulent spot, *J. Fluid Mech.* 87: 641-72.

5. S. Kline and P. Runstadler 1959. Some preliminary results of visual studies of the flow model of the wall layers of the turbulent boundary layer. *Trans ASME Series E* 2: 166-70.

6. S. Kline, W. Reynolds, F. Schraub and P Runstadler 1967. The structure of turbulent boundary layers. *J. Fluid Mech.* 30: 741-73.

7. B. Cantwell 1981. Organized motion in turbulent flow. *Ann. Rev. Fluid Mech.* 13:457-515.

8. P. Spalart 1986. Direct simulation of a turbulent boundary layer up to $Re\theta$ =1410. *J. Fluid Mech.* 187:61-98

9. S. Robinson 1991. The kinematics of turbulent boundary layer structure. NASA TM 103859.

10. S. Kline and L. Portela 1997. A view of the structure of turbulent boundary layers. In self sustaining mechanisms of wall turbulence. *Adv. in Fluid Mech. 15*, ed. by R. Panton , Comp. Mech. Inc.

11. B. Cantwell, J. Chacin and P. Bradshaw 1997. On the dynamics of turbulent boundary layers. In self sustaining mechanisms of wall turbulence. *Adv. in Fluid Mech. 15*, ed. by R. Panton , Comp. Mech. Inc.

12. H. Blackburn, N. Mansour and B. Cantwell 1996. Topology of fine scale motions in turbulent channel flow. *J. Fluid Mech.* 310: 269-292.

13. J. Chacin, B. Cantwell and S. Kline 1996. Study of turbulent boundary layer structure using the invariants of the velocity gradient tensor. *J. Exp. Thermal Fluid Sci.* 13: 308-317.

14. J. Chacin and B. Cantwell 1997. Study of turbulence structure using the invariants of the velocity gradient tensor. Report TF-70, Flow physics and computation division, dept. of Mech. Eng., Stanford Univ.

VORTEX PACKETS AND THE STRUCTURE OF WALL TURBULENCE

Ronald J. Adrian
Department of Theoretical and Applied Mech.
University of Illinois at Urbana-Champaign
216 Talbot Lab, Urbana, IL 61801
r-adrian@uiuc.edu

S. Balachandar
Department of Theoretical and Applied Mech.
University of Illinois at Urbana-Champaign
216 Talbot Lab, Urbana, IL 61801
s-bala@uiuc.edu

Abstract - Experimental evidence in low to moderate Reynolds number wall flows shows that hairpin vortices (including asymmetric inclined vortices) occur in groups that propagate as a whole with relatively slow dispersion. These groups, or "packets", grow upwards from the buffer layer to about one-half of the thickness of the boundary layer. Direct numerical simulations of the growth of a single hairpin eddy in a clean background flow show how these packets may be formed in the near wall (low Reynolds number) region by a viscous autogeneration mechanism that is similar in many regards to the mechanism proposed by Smith and co-workers [1]. The organization of hairpin eddies into packets and the interactions of those packets is an important feature of wall turbulence that provides a new paradigm by which many seemingly unconnected aspects of wall turbulence can be explained. These include the inordinately large amount of streamwise kinetic energy that resides in very long streamwise wavelengths, the occurrence of multiple Q2 events per turbulent burst, the formation of new streamwise vorticity, and the characteristic angles of inclination of fronts. The autogeneration process may also explain the formation of long quasi-streamwise vortices in the buffer layer and the associated low-speed streaks.

I. INTRODUCTION

Hairpin shaped vortices are thought by many to be a central feature of turbulent wall layers. An idealized hairpin vortex consists of a pair of counter-rotating quasi-streamwise vortices that are tilted upwards along the downstream direction and a hairpin head that connects to the quasi-streamwise vortices at their downstream ends, as shown in Figure 1. Hairpin vortices observed in experiments and computations seldom possess perfect spanwise symmetry; more often they are asymmetric, left- or right-handed cane-like vortices, which consist of a head, a neck and one dominant quasi-streamwise leg [2,3]. Nevertheless, a picture of the turbulent wall layer as a distribution of hairpin vortices provides a reasonable model for many of the flow features that have been observed and documented in the past (c.f. [4] for example.).

In the streamwise wall normal (x-y) plane, the velocity signature of a hairpin vortex is characterized by a circular vortex core and a strong outward pumping of low momentum fluid. This hairpin vortex signature is relatively insensitive to the degree of asymmetry of the hairpin. Recent PIV measurements [5-7] in a turbulent boundary layer over a range of Reynolds numbers clearly show numerous hairpin vortex signatures within the boundary layer, providing strong evidence that the turbulent wall layer at moderate Reynolds numbers is thickly populated with hairpin vortices.

In the experimental measurements cited above the hairpin vortices were often observed to occur one behind the other as a train in the streamwise direction forming a coherent group or packet of hairpin vortices. Although the shapes and sizes of the packet varied, the tendency to form group of hairpins was observed at all instances. The streamwise coherence of the near-wall hairpin vortices persisted even at higher Reynolds numbers. The hairpin vortices within a packet were observed to work cooperatively passing low-speed fluid from the downstream most vortex to its upstream neighbor and so on over several hairpin vortices to form a low-speed streak of length significantly longer than a single hairpin vortex. As a result, transport properties, such as Reynolds stresses, of the packet could significantly exceed a simple sum of the contribution from each individual hairpin within the packet. Thus the arrangement of hairpin vortices into packets with definite distribution of size, age and spatial separation has a potentially large effect on the overall momentum and heat transport from the wall. For instance, significant drag reduction can be anticipated by disturbing the streamwise alignment of hairpins within a packet.

The present paper will focus on the following issues: (a) A brief review of all experimental evidence supporting the existence of hairpins; (b) a review of computational results on the autogeneration of new hairpin vortices; (c) explanation on the basis of the hairpin packet paradigm of experimental observations that cannot be explained by single hairpin models;(d) the implications of hairpins occurring as packets, instead of being randomly scattered throughout the boundary layer.

Hairpin vortices have a long history. Theodorsen [8] was the first to suggest the importance of hairpin-type vortices in turbulent wall layers. His original proposal consisted of horseshoe vortices with omega-shaped head and neck region that extended spanwise to form spanwise vortex legs. The visualization experiments of Head and Bandyopadhyay [9] inferred that stretched vortex loops (or hairpin vortices) inclined at about 45° are a major component of the turbulent wall layer. There are two major pieces of experimental evidence showing that hairpins occur in groups. First, the side view smoke flow visualizations of Head and Bandyophadhyay [9] revealed large scale structures, inclined at a characteristic angle of about 20°, that marked the outer edge of the turbulent boundary layer. They inferred that this structure was a group of individual hairpin vortices, each stretching from the wall to the outer edge of the boundary layer, Figure 2(a). (See also the model of Bandyopadhyay [10]) The angle of envelope of the group was approximately 18°. Second, based on experimental observations of hydrogen bubble pattern in the near-wall region of a low Reynolds number turbulent boundary layer, Smith [11] reported that the results are consistent with at least three hairpin vortices forming with alignment along the streamwise direction, Figure 2(b). Subsequent work by Smith and coworkers demonstrated the formation of sequences of hairpins by a stationary hemispherical bump on the wall [12,13] and by impulsive injection of fluid [14] in a laminar boundary layer. More recent direct numerical simulations by Zhou, Adrian & Balachandar [15] and Zhou, Adrian, Balachandar & Kendall [16] on the evolution of a single initial hairpin vortex in a unidirectional mean turbulent channel flow have identified the mechanistic details behind the autogeneration of secondary hairpin vortices in the near-wall region leading to the formation of a hairpin packet. A significant outcome of these simulations is that new hairpins are formed both on the upstream and downstream sides of the initial hairpin resulting in a half-diamond or tent-like hairpin packet. This shape for the hairpin packet is consistent with recent experimental measurements [7] schematically represented in Figure 2c. The computations also show that the autogeneration process is robust and occurs more readily in the case of an asymmetric initial hairpin, eventually forming a staggered array of one-sided hairpin vortices. This is in accordance with the predominantly one-sided hairpins noted by Guezennec & Choi [2] and Robinson [3].

II. EXPERIMENTAL EVIDENCE FOR PACKETS

The velocity signature of a hairpin vortex in a spanwise-wall normal (y-z) plane passing through the quasi-streamwise vortex legs is characterized by a pair of counter rotating vortices pumping fluid away from the wall. On the other hand, in a streamwise-wall normal (x-y) plane the hairpin vortex is characterized by (a) a strong outward pumping of low momentum fluid on the in-board side of the quasi-streamwise vortices. This quadrant-two (Q2) flow encounters the high-speed free-stream and forms a shear layer which is inclined 45° to the horizontal; and (b) closed/spiraling streamlines corresponding to the circular vortex core of the hairpin head in a frame of reference traveling downstream with the hairpin vortex.

The schematic shown in Figure 1 clearly illustrates the typical hairpin vortex signature in the x-y plane, provided it passes between the quasi-streamwise legs. However, it must be emphasized that this hairpin signature is relatively insensitive to the degree of asymmetry of the hairpin. The hairpin vortex signature will then allow reasonably accurate identification of hairpin vortices from quantitative measurement of the velocity field within the turbulent wall layer. It should be emphasized that the Q2 vectors exhibit a maximum somewhere below the vortex head and that it is characteristic of the combined induction associated with the proximity of the vortex head and legs. This peak in the Q2 velocity provides a clear evidence for the existence of a three-dimensional vortex, as a two-dimensional vortex, such as a vortex line, is in general incapable of generating such a local velocity maximum.

Figure 3a shows a velocity vector plot in the streamwise-wall normal (x-y) plane obtained from high resolution PIV measurement of a zero

pressure gradient boundary layer with $Re_\theta = 1015$ [7]. A constant convection velocity of $U_c = 0.91U_\infty$ (U_∞ is the free stream velocity) has been subtracted from the streamwise velocity in order to bring out the packet of hairpins, whose heads are clearly identified in the figure. The hairpins within the packet are observed to extend from the wall up to $y/\delta \approx 0.5$ to 0.6, where δ defines the edge of the boundary layer. From the convection velocity it can be inferred that the hairpin packet propagates along the streamwise direction at 0.6 to 0.9 U_∞. The PIV measurements cover a wide streamwise range of up to 3.0δ and over this extended streamwise range Tomkins [7] observed different geometric shapes for the hairpin packet including: uninterrupted streamwise growth, sawtooth shape, half-diamond or tent shape and constant height. Figure 3a might fit the description of a packet of constant height. In the case a ramp-like envelope for the hairpin packet, as in uninterrupted growth, sawtooth and half-diamond shape, the mean angle of the ramp is observed to be about 15°, which is consistent with earlier observations of Head & Bandyopadhyay [9]. Furthermore, over the Reynolds number (Re_θ) range form 1000 to 7705, the packet is observed to contain from about 4 hairpins to as many as nine hairpins.

The cooperative action of the streamwise aligned hairpins within the packet can be clearly observed in figure 3a as the zone of strong negative velocity that lies below the hairpin vortex heads. This zone of low momentum also exists at higher Reynolds numbers, as shown in figure 3b for $Re_\theta = 7705$ but is restricted closer to the wall in terms of outer units. At higher Reynolds number multiple zones of almost uniform momentum can be observed [5,6]. The interface between any two adjacent zones is marked by a sequence of vortex cores, which contributes to the near uniform velocity jump across them. These vortex cores can be identified as the heads of nearly streamwise aligned hairpin vortices and thus the interface between the different uniform momentum zones can be interpreted as the envelop of a hierarchical hairpin packet.

The uniform momentum zone observed close to the wall in figures 3a and 3b extends over more than one thousand viscous wall units along the streamwise direction. While it resembles the low speed streak that occurs in the buffer layer, it is a new and quite distinct phenomenon as it occurs well above the buffer layer and extends past the logarithmic layer [6]. However the low momentum zones are associated with near wall streaks, since the hairpin vortices and hairpin packets are believed to grow out of the near-wall streaks, at least in the first zone closest to the wall. The packets are also not the conventional bulges, but the largest packets in the hierarchy of hairpin packets might cause the bulges. The organization of the bulges appears to be less coherent than the packets, suggesting that the packets interact in a complex way.

III. GENERATION OF HAIRPIN VORTEX PACKETS

The frequent occurrence of vortex packets in the experiments requires explanation. The kernel experiments of Acarlar & Smith [12,13] followed the process of continuous generation of a train of hairpin vortices behind a hemispherical bump in a laminar boundary layer. Subsequent experiments by Haidari & Smith [14] considered the more relevant case of a single hairpin vortex generated by an impulsive injection of fluid into the boundary layer and the subsequent generation of secondary hairpins to form a packet. This process of initial hairpin formation from fluid injection and its subsequent evolution and formation of additional vortical structures was studied numerically by Singer & Joslin [17]. Based on the experimental observations and inviscid computations, Smith *et al.* [1] offered a conceptual inviscid model for the mechanism by which new hairpins can be naturally generated out of a single hairpin. While the above cited investigations all pertain to the formation of a hairpin packet in a laminar boundary layer flow, the experimental evidence [6,7,9,11] suggests that once a hairpin is formed by a localized, low momentum agency near the wall, it can, under a range of circumstances, proceed to generate a sequence of new vortices forming a coherent packet of hairpin vortices. A fundamentally similar general mechanism may occur in turbulent flow as well, but if so, it needs to be understood in that context.

The numerical simulations of the growth of a single hairpin vortex in the background of a low Reynolds number unidirectional mean turbulent channel flow [15,16] offer additional insight into the mechanisms, which could explain the formation of new hairpin vortices, and their spatial arrangement into packets. These studies differ from the work described above in that the initial field was a viscous, hairpin vortex-like structure that was extracted from the full two-point turbulent correlation tensor of a $Re_\tau = 180$ channel flow direct numerical simulation of Kim, Moser and Moin [18] by the process of stochastic estimation (c.f. [19]), rather than created by external forcing. By appropriately choosing the event vector in the stochastic estimation process, the structure of the initial vortex can be varied over a wide range in a systematic manner to represent form an idealized symmetric hairpin to a more realistic asymmetric or one-sided hairpin.

Zhou *et al.* [15,16] considered both symmetric and asymmetric Q2 event vectors given by a second quadrant velocity ($u = \alpha\sqrt{1-\beta^2}\,u_m$, $v = \alpha\sqrt{1-\beta^2}\,v_m$, $w = \beta\left(u_m^2 + v_m^2\right)^{1/2}$) specified at a single point within the channel. Here (u_m, v_m) is chosen to maximize the product $u_m v_m$ weighted by the probability density of its occurrence $f(u_m, v_m)$ and thereby maximize the contribution to mean Reynolds shear stress. The factor α is a scaling factor, which determines the vortical strength of the initial structure relative to the vorticity of the mean flow. The factor β is the asymmetry parameter; $\beta = 0$ corresponds to a symmetric event and results in an initial symmetric hairpin. For a representative Q2 event, the stochastic estimation process guarantees that the initial field possessed the correct length scales, shape, and vorticity distribution of a typical Q2 structure. Thus we believe that the initial hairpin structure is more representative of the hairpin vortices observed in real turbulence.

Further, the background flow in which the hairpin vortex is embedded is chosen to be a unidirectional flow obtained from the mean streamwise velocity profile of $Re_\tau = 180$ channel flow direct numerical simulation [18], rather than a Poiseuille flow. This difference at first glance might seem not so important; however, in the case of the turbulent mean flow profile the mean shear is predominantly contained close to the channel walls within approximately 25% of the channel half height ($y^+ < 45$), whereas in the case of a plane Poiseuille flow the mean shear extends over the entire channel. As a result the peak shear in the case of the mean turbulent profile is about factor four greater than that of the Poiseuille flow. A delicate balance between the self-induced velocity that tends to curl up the vortex and the influence of the mean shear, which tends to stretch the hairpin vortex, governs the evolution of the hairpin vortex. Thus differences in the mean background flow will have a strong influence on the dynamics of the initial hairpin vortex and the formation of the hairpin packet. In particular, the impact on the spatial and temporal scales of the resulting structure is likely to be strong.

In a real turbulent boundary layer the formation and evolution of the hairpin packet occurs in the presence of other hairpin packets, vortical debris, outer layer perturbations and so on. These disturbances are in deed collectively responsible for the mean turbulent profile, but of course in a time-averaged sense. The rational for using the unidirectional mean turbulent profile as the background flow is to account for the influence of the other turbulent structures at least in a statistical sense, and at the same time maintain the hairpin evolution simple and controlled so as to be able to follow it in close detail without any clutter from other vortical structures.

The simulations were performed at a Reynolds number of $Re_\tau = 180$ in a box of streamwise (x) wall normal (y) and spanwise (z) size 4π, 2 and $4\pi/3$ respectively. The iso-surface of the imaginary part of the eigenvalue of the velocity gradient tensor [16] is used to visualize vortices in the present study.

Time evolution of both symmetric and asymmetric initial structures were followed in detail with a direct numerical simulation. In both cases the quasi-streamwise vortices quickly lift away from the boundary due to mutual induction and the lift-up is the strongest at the downstream end. Simultaneously a shear layer forms where the Q2 velocity encounters the mean flow. Spanwise vorticity associated with this shear layer quickly rolls-up and forms a compact spanwise vortex located just above the downstream end of the quasi-streamwise vortices. By $t^+ \approx 25$ the rolled-up spanwise vortex viscously connects with the lifted quasi-streamwise vortices to form a hairpin structure. The geometry of this vortex resembles in appearance the hairpin vortices observed in many experiments. Figure 4a shows the hairpin-like vortex at $t^+ = 27$ that resulted from an asymmetric initial structure with y_m^+=30, α=2 and β=0.5. Apart from the hairpin vortex, marked by the head and an asymmetric pair of quasi-streamwise vortices on the upstream side of the hairpin head, a pair of vortical tongues can be seen on the downstream side of the head. These

vortical tongues will later develop into new downstream hairpin vortices that will form part of the hairpin packet.

The head of the primary hairpin vortex continues to lift up into a near vertical orientation and also grows wider evolving into the characteristic Ω-shape. Simultaneously the quasi-streamwise legs stretch and form a kink as a result of mutual induction and interaction with the head. A shear layer forms above the kink and quickly intensifies. Subsequently the upstream portion of the quasi-streamwise legs detach from the primary hairpin at the kink and merge with the rolled up shear layer to form a secondary hairpin which remains distinct from the primary hairpin.

This process of new hairpin generation continues along similar lines both upstream and downstream of the primary hairpin resulting in a hairpin packet, which is shown in Figure 4b and 4c at $t^+ \approx 144$. The envelope of the packet of hairpin vortices has a tent like appearance with an approximate angle of 10° upstream and 7° downstream of the primary vortex. The velocity signature of the computed hairpin packet qualitatively compares with the PIV measurements similar to those shown in figure 3. However discrepancies exist since the computed hairpins are separated along the streamwise direction about 200-450 viscous wall units, while in the experiments the distance between hairpins is observed to be around 100-150 viscous units.

The effect of asymmetry on the evolution of hairpin vortices is also investigated by systematically increasing the β parameter from 0. It is observed that the process by which new hairpins are autogenerated remains qualitatively the same as in the symmetric case. Thus the formation of a coherent hairpin packet is a robust mechanism active under a wide range of conditions. However, the asymmetric hairpins are one-sided and the packet consists of a streamwise train of alternating left and right handed one-sided hairpins that are staggered along the span. Both the symmetric and asymmetric cases display a threshold behavior; hairpins only above a certain threshold initial amplitude result in the autogeneration of new hairpins and formation of a hairpin packet. The threshold amplitude is observed to decrease with the degree of asymmetry suggesting that asymmetric hairpins are more likely to autogenerate and form hairpin packets than the idealized symmetric ones. This result is in total agreement with the experimental and computational observation of predominantly one-sided hairpins.

IV. SINGLE HAIRPIN PARADIGM

Here we will consider significant experimental and computational observations that are consistent with the picture of the turbulent boundary layer populated with a forest of symmetric and cane-type hairpins.

1) The often observed quasi-streamwise vortices, hairpin shape and horseshoe (omega) shaped vortices, one-sided cane type vortices are all part of the same entity at various stages of their evolution and with different degree of asymmetry.

2) The range of hairpin vortex angle from 15°-75° (with 45° being more typical) is consistent with the range of angles observed from the quasi-streamwise vortices to the hairpin head. Furthermore, the tilt or angle of the hairpin head is a strong function of its location; the head takes a near vertical orientation in the outer regions of the boundary layer, while near the wall it takes a more conventional 45° angle.

3) The experimentally observed inclined internal shear layers can be explained on the basis of the Q2 fluid pumped by the hairpin encountering the free stream flow.

IV. HAIRPIN PACKET PARADIGM

One must appeal to a coherent packet of streamwise aligned hairpin vortices in order to consistently explanation other experimental and computational observations of the past. Below we list all the important features that can be explained on the basis that the boundary layer is made up of hairpin packets.

• *Low-Speed Streaks*

1) The cooperative Q2 pumping of the near-wall fluid by the streamwise aligned hairpin vortices explain the very long (more than 1000 wall units) low-speed streaks.

2) The spanwise staggering of the one-sided hairpins in the asymmetric case explain the often observed spanwise jogging of the low-speed steaks.

3) Recent measurements by Meinhart & Adrian [5] indicate that the low-speed streaks are not limited to the buffer-layer, but extend into the log-layer as well. Streamwise aligned hairpin vortices that extend into the log-layer, through their combined induced velocity can explain the long log-layer low-speed streaks.

4) The packet paradigm also explains the long tail observed in the u-correlation [20,21].

• *Burst Process*

1) There is similarity to the POD results of Sirovich [22], in which the most important modes are the streamwise independent modes that hug close to the walls. These modes correspond to the streamwise aligned quasi-streamwise legs of the hairpins and the resulting long low-speed streaks. We interpret the propagating modes that trigger the onset of burst-like activity to be the projections of the hairpin heads.

2) The streamwise arrangement of the hairpin vortices is in agreement with the measurements of [23-25], where the near-wall burst process was observed to be typically made up of multiple Q2 events. In this sense the hairpin packet constitutes a burst.

3) The adjacency of hairpins within the packet results in strong internal shear layers where the induced downflow (Q4) from the upstream vortex head meets the low-speed upflow (Q2) induced by the downstream vortex. This Q2/Q4 stagnation point flow provides convincing evidence for the VITA signature, often used to identify burst process.

4) The conventional view of the burst process as wavy oscillation of the low-speed streaks and Q2 eruption t the end also fits into the framework of hairpin packet. While the low-speed (Q2) pumping of the downstream hairpins are somewhat mitigated by the corresponding Q4 induced velocity of their upstream neighbors, the low-speed pumping of the chronologically last upstream-most hairpin remains unopposed and in fact is reinforced by its downstream neighbors.

• *Structure and Symmetry*

1) Preference for cane-shaped one-sided hairpins in the experimental [2] and computational results [3] can be explained on the basis that the autogeneration of new hairpins is much more robust and readily occurring when they are asymmetric.

2) Often observed inline alignment of the streamwise vortices is due to the quasi-streamwise legs of the streamwise aligned hairpins within the packet.

3) In the event of strong asymmetry, only the alternative quasi-streamwise legs are significant - the packet is made up of alternating sequence of right and left handed canes. If one confines attention to only the near wall region ($y^+ < 60$) the behavior of the packet is very similar to that proposed by [26].

• *Hierarchy of Packets*

1) Recent PIV measurements [7] over a range of Reynolds numbers show velocity signature that is consistent with a picture of the turbulent boundary layer made up of hierarchy of hairpin packets that travel downstream coherently.

2) We believe that the hydrogen bubble measurements of [11] and the smoke visualizations of Head & Badyopadhyay [9] extract the near-wall and outermost groups of hairpins, respectively. This suggests the presence of hairpin packets right from the near-wall region to the outermost reaches of the boundary layer.

3) The outer scale structures such as the backs and bulges are consistent with a large-scale hairpin packet that extends into the outer layer.

4) The scaling of different quantities on inner, outer and mixed scales is compatible with the notion of a hierarchy of hairpin packets.

5) The smallest near-wall hairpin packet provides adequate explanation for the buffer-layer behavior. The nesting of smaller packets within larger ones, which are within even larger ones, and so on may explain the log-layer.

6) The hierarchy of packets can explain Robinson's observation that the buffer-region contains predominantly quasi-streamwise vortices, the log-region contains both quasi-streamwise vortices and hairpin heads and the wake-region contains mostly hairpin heads.

VI. IMPLICATIONS OF PACKET PARADIGM

Implications of the hairpin packet paradigm for prediction, control and modeling of turbulent boundary layer are very many. The

superposition of the induced fields of the streamwise-aligned hairpins result in a strong Q2 velocity due to the "solenoid effect". This cooperative action leads to a potentially very large increase in momentum and heat transport from the wall. For example, the total Reynolds stress of N incoherently distributed (spatially uncorrelated) hairpin vortices is simply N times the individual contribution arising from the Q2 pumping of each of the hairpin. On the other extreme, if the N hairpins are perfectly overlaid (perfect correlation) the resulting total Reynolds stress is N^2 times the individual contribution. The Reynolds stress contribution of a real hairpin packet is likely to scale somewhere in between and depend critically on the strength and spatial scales of the hairpin packet.

The above observation suggests that boundary layer models that are based on a hierarchy of random distribution of hairpins as in Perry *et al.* [4] have many of the ingredients necessary for an accurate description of the turbulent boundary layer, except for the coherence of hairpins within a packet. In a similar manner the phenomenological semi-Markov model of the turbulent boundary layer [27] does not fully account for the spatial coherence within the hairpin packet. By incorporating this important feature the predictive capability of these models can be significantly advanced.

Hairpin packets also provide exciting possibilities for the control of boundary layer turbulence and hence drag management. One simple conceptual approach to drag reduction is to delay the formation of secondary and subsequent vortices and thereby increase the streamwise spacing between the hairpins within the packet. The resulting reduced cooperation among the hairpins will significantly cut down the Reynolds shear stress and the momentum transfer. Recent results by Sirovich and coworkers [22] indicate that reasonable drag reduction can be achieved by random distribution of roughness elements. They hypothesized that the roughness elements disturb the propagating modes and thereby control the bursting process. An alternative, but certainly related, viewpoint will be that the roughness elements adversely affect the hairpin generation process and mitigate the internal coherence within packets.

Experimental and computational evidence [12-17] suggests that many types of low momentum events at the wall can create a succession of hairpins. This along with [22] can be taken to suggest that by appropriate surface excitation, for example by momentum addition to overcome a local low momentum event the hairpin formation process can be controlled to reduce drag. Such exciting possibilities must be pursued in the future.

VII. REFERENCES

[1] Smith, C. R., Walker, J. D. A., Haidari, A. H., & Sobrun, U. "On the dynamics of near-wall turbulence", *Phil. Trans. of Roy. Soc. London A*, **336**, 131-175, 1991.

[2] Guezennec, Y. G. & Choi, W. C. "Stochastic Estimation of coherent structures in turbulent boundary layers". In *Proc. Zoran P. Zaric Memorial International Seminar on Near Wall Turbulence, May 1988* (ed. S. J. Kline, N. H. Afgan), pp. 420-436. New York: Hemisphere, 1989.

[3] Robinson, S. K. "Coherent motions in the turbulent boundary layer", *Ann. Rev. Fluid Mech.* **23**, 601-639, 1991.

[4] Perry, A. E., Henbest, S. & Chong, M. S. "A theoretical and experimental study of wall turbulence", *J. Fluid Mech.* **165**, 163-199, 1986.

[5] Meinhart, C. D. & Adrian, R. J. "On the existence of uniform momentum zones in a turbulent boundary layer", *Phys. Fluids* **7**, 694-696, 1996.

[6] Meinhart, C. D. & Adrian, R. J. "The coherent structure of the overlap region in the turbulent boundary layer", (manuscript in preparation), 1998.

[7] Tomkins, C. D. "A particle image velocimetry of coherent structures in a turbulent boundary layer", *M.S. Thesis*, University of Illinois, Urbana, Illinois, 1998.

[8] Theodorsen, T. "Mechanism of turbulence". In *Proc. Second Midwestern Conf. of Fluid Mechanics*, pp. 1-19. Ohio State University, Columbus, Ohio, 1952.

[9] Head, M. R. & Bandyopadhyay, P. "New aspects of turbulent boundary layer structure", *J. Fluid Mech.* **107**, 297-338, 1981.

[10] Bandyopadhyay, P. "Large structure with a characteristic upstream interface in turbulent boundary layers", *Phys. Fluids* **23**, 2326-2327, 1980.

[11] Smith, C. R. "A synthesized model of the near-wall behavior in turbulent boundary layers". In *Proc. Eighth Symp. on Turbulence* (ed. G. K. Patterson & J. K. Zakin). University of Missouri-Rolla. Dept. of Chem. Engng., Rolla, Missouri, 1984.

[12] Acarlar, M. S. & Smith, C. R. "A study of hairpin vortices in a laminar boundary layer. Part 1. Hairpin vortices generated by a hemisphere protuberance", *J. Fluid Mech.* **175**, 1-41, 1987a.

[13] Acarlar, M. S. & Smith, C. R. "A study of hairpin vortices in a laminar boundary layer. Part 2. Hairpin vortices generated by fluid injection", *J. Fluid Mech.* **175**, 43-83, 1987b.

[14] Haidari, A. H. & Smith, C. R. "The generation and regeneration of single hairpin vortices", *J. Fluid Mech.* **277**, 135-162, 1994.

[15] Zhou, J., Adrian, R. J. & Balachandar, S., "Autogeneration of near wall vortical structure in channel flow", *Phys. Fluids*, **8**, 288-291, 1996.

[16] Zhou, J., Adrian, R. J., Balachandar, S., & Kendall, T. M. "Mechanisms for generating coherent packets of hairpin vortices in channel flow" submitted to *J. Fluid Mech.*, 1998.

[17] Singer, B. A. & Joslin, R. D. "Metamorphosis of a hairpin vortex into a young turbulent spot", *Phys. Fluids* **6**, 3724-3736, 1994.

[18] Kim, J., Moin, P., & Moser, R. D. "Turbulent statistics in fully developed channel flow at low Reynolds number", *J. Fluid Mech.* **177**, 133-166, 1987.

[19] Adrian, R. J. "Stochastic Estimation of the Structure of Turbulent Fields". In *Eddy Structure Identification* (ed. J. P. Bonnet), pp. 145-196. Berlin: Springer, 1996.

[20] Townsend, A.A "The structure of turbulent shear flow", Cambridge University Press, 1976.

[21] Grant, H. L. "The large eddies of turbulent motion", *J. Fluid Mech.*, **4**, 149-190, 1958.

[22] Sirovich, L. "Dynamics of coherent structures in wall turbulence". In *Self Sustaining Mechanisms of Wall Turbulence*. (ed. R.L. Panton), pp. 333-364, Computational Mechanics Publications, Southampton, UK.

[23] Bogard, D. G. & Tiederman, W. G. "Burst detection with single-point velocity measurements", *J. Fluid Mech.* **162**, 389-413, 1986.

[24] Luchik, T. S. &. Tiederman, W. G. "Timescale and structure of ejections and bursts in turbulent channel flows", *J. Fluid Mech.* **174**, 529-552, 1987.

[25] Tardu, F. "Characteristics of single and clusters of bursting events in the inner layer. Part 1: Vita events", *Exp. Fluids*, **19**, 112-124, 1995.

[26] Jeong, J. & Hussain, F. "On the identification of a vortex", *J. Fluid Mech.* **285**, 69-94, 1995.

[27] Meng, J. C. S. "Wall layer microturbulence Phenomenological model and a semi-Markov probability predictive model for active control of turbulent boundary layer". In *Self Sustaining Mechanisms of Wall Turbulence*. (ed. R.L. Panton), pp. 201-252, Computational Mechanics Publications, Southampton, UK.

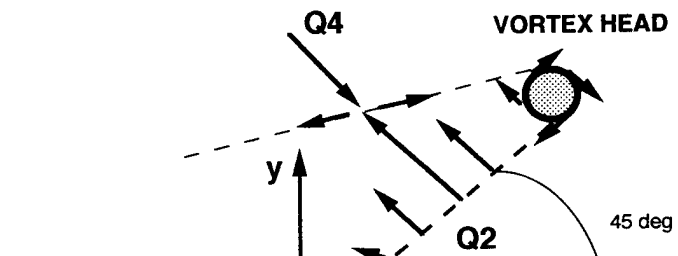

Figure 1. Schematic of a hairpin vortex and associated flow field properties that form the signature of a hairpin on the x-y plane.

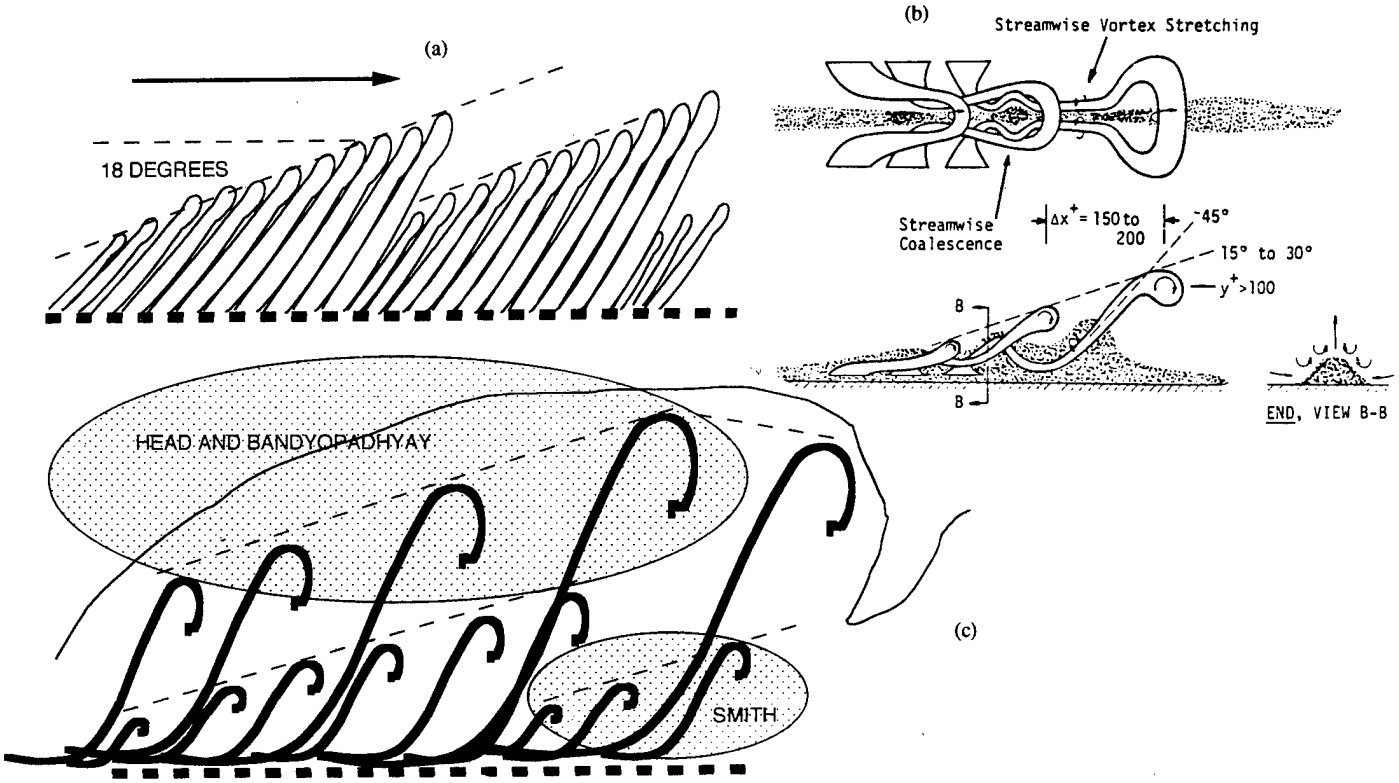

Figure 2. Hairpin packet models. (a) Head and Bandyopadhyay [9]; (b) Smith [11]; (c) Hierarchy of packets as observed in [7].

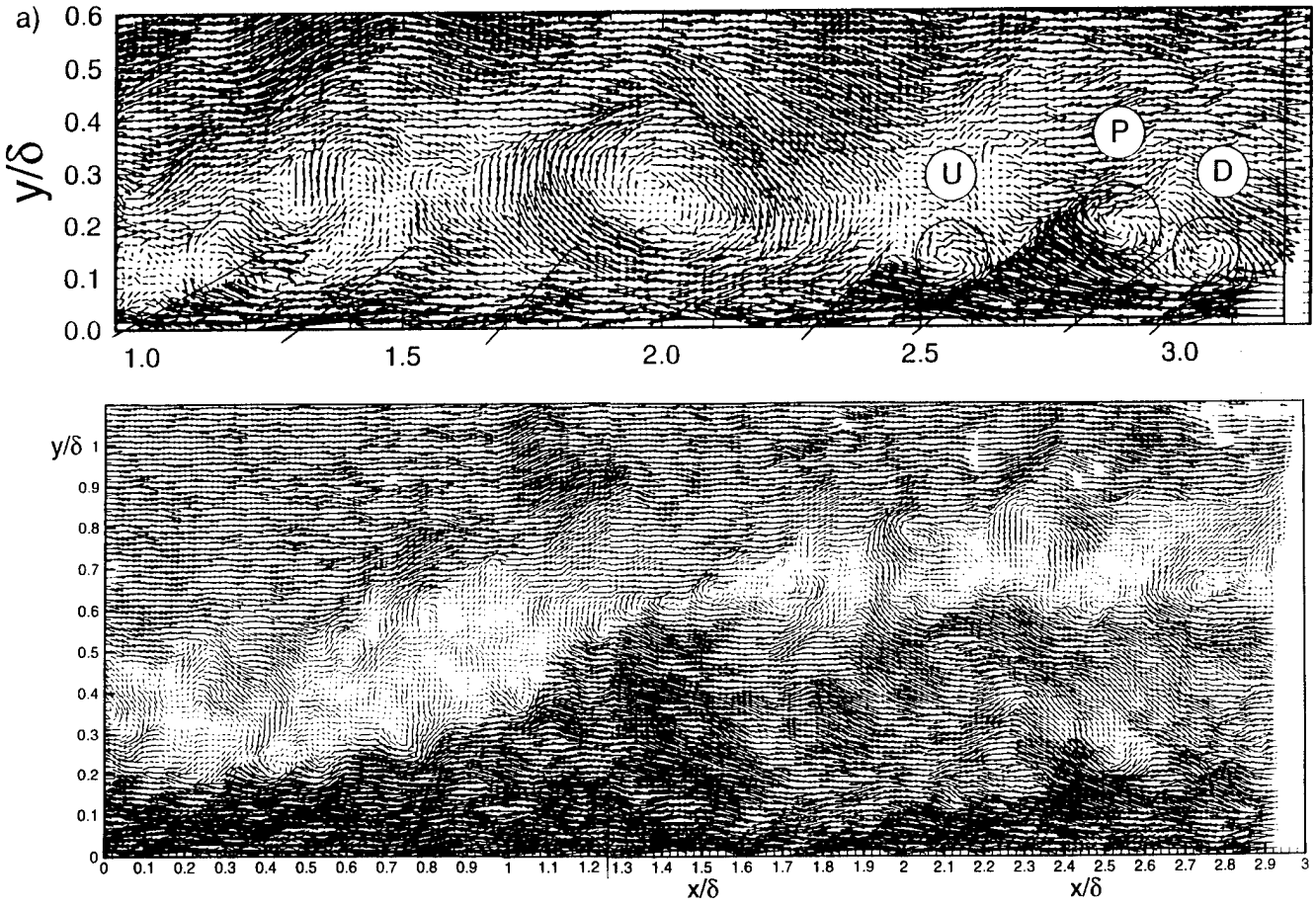

Figure 3. PIV measurements of instantaneous velocity fields in the x-y plane of a turbulent boundary layer. (a) Re_θ=1015; (b) Re_θ=7705.

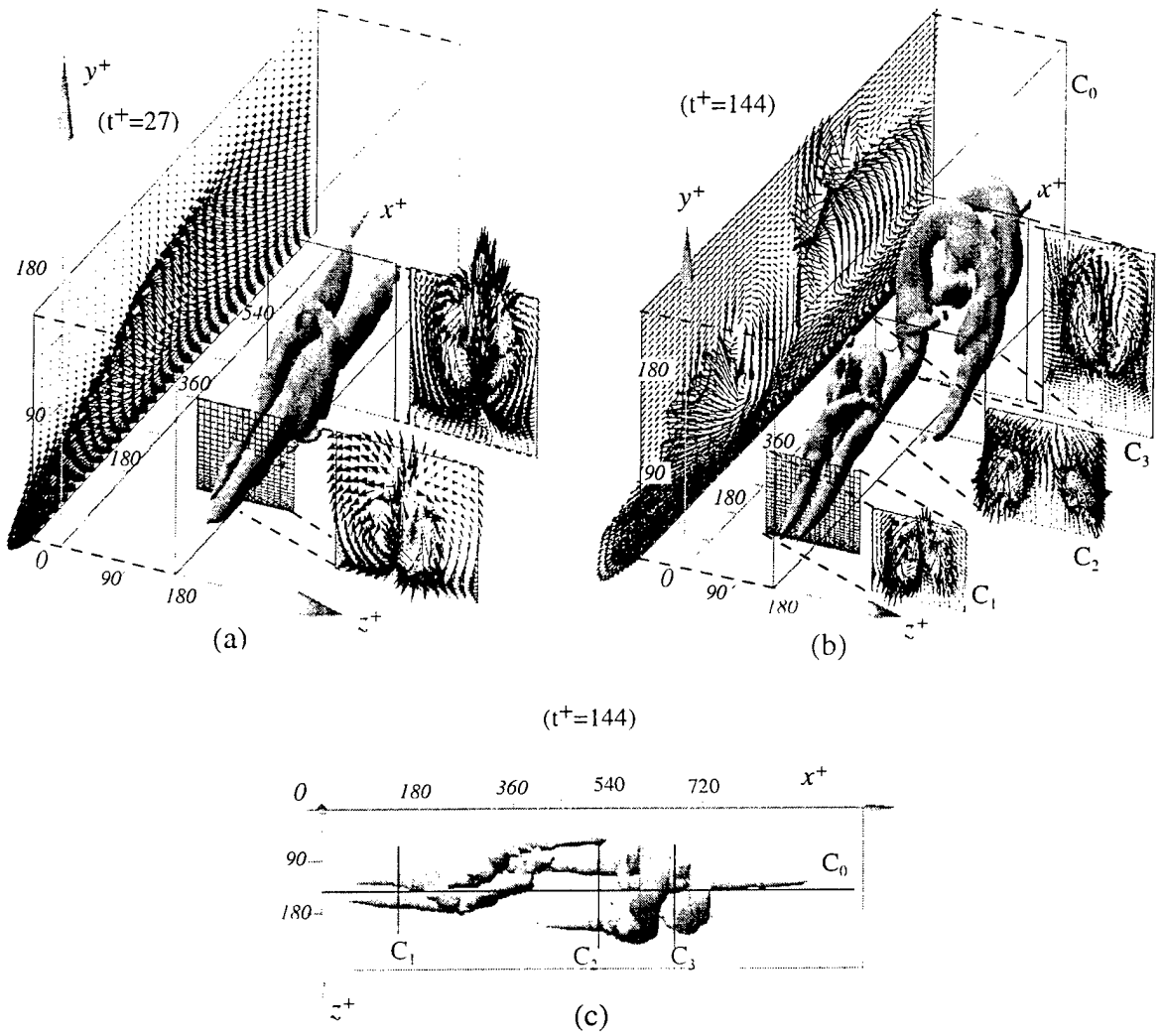

Figure 4. Hairpin packet that evolves from an asymmetric initial disturbance; (a) Perspective view, $t^+ = 27$; (b) Perspective view, $t^+ = 144$; (c) Top view, $t^+ = 144$; (*From Zhou, et al. [16]*).

VORTEX DEVELOPMENT AND INTERACTIONS IN TURBULENT BOUNDARY LAYERS: IMPLICATIONS FOR SURFACE DRAG REDUCTION

Dr. Charles R. Smith
Department of Mechanical Engineering and Mechanics
19 Memorial Drive West
Lehigh University
Bethlehem, PA 18015
crs1@lehigh.edu

Abstract - Ultimately, control of turbulent boundary layers must center around the selected modification of the flow structure of the turbulence, or the conditions which give rise to the flow structure. The present paper examines the particular importance of vortices, and their role in generating and maintaining turbulence production in a turbulent boundary layer. A conceptual model is outlined illustrating how vortex interactions with both other vortices and the bounding surface control the processes of fluid, momentum, and energy transport, and ultimately surface drag. The implications of these vortical processes on approaches to drag reduction/control are discussed.

I. INTRODUCTION

A variety of flow structures have been suggested as important in the development and regeneration of turbulent boundary layers. We now know, through a number of detailed experimental, computational, and analytical studies, that vortex deformation and evolution play a dominant role in creating and sustaining "turbulence," and that these vortical processes give rise to the deterministic "structure" of irregular, but repetitive, spatial-temporal flow patterns such as low-speed wall "streaks," wall region "bursts," "ejections," and "sweeps" which characterize near-wall turbulence. These characteristic patterns are what have been perceived as the "coherent structure" of a turbulent boundary layer. The majority of these flow patterns are now understood to be associated with some form of vortex structure, from streamwise and transverse vortices to multiple hairpin-like vortices. Excellent experimental and computational studies[1-26] have provided detailed correlation, assessment, and categorization of the myriad three-dimensional patterns, or flow structure of turbulent boundary layers, and the relation of such flow structure to the presence and interaction of vortices.

The present paper provides an overview of the hypothesized behavior of vortices in sustaining and developing a turbulent boundary layer, focussing on how vortices and vortex interactions control the process of momentum exchange, energy extraction from the mean flow, and maintenance of the turbulence process. The characteristic patterns of behavior that have been observed and detected in turbulent boundary layers are discussed first, leading to a discussion of the role of vortices in the physical processes giving rise to those patterns. The manifold importance of vortices, and their role in generating and maintaining turbulence are examined. Finally, a conceptual model of wall turbulence based on vortex interactions and development is presented, and the implications of this model in developing rational methods for surface drag reduction and/or control of a turbulent boundary layer is discussed.

II. PATTERNS OF BEHAVIOR

Prior to the late 1950s, turbulent boundary layers were studied as if they were random velocity fluctuations riding on an otherwise time-averaged flow. However, numerous studies[2,3,5,6,9] over the past forty years have revealed that turbulent boundary layers display irregular, but repeatable, *patterns of behavior* in time and space which are reflective of the processes of turbulence generation and regeneration. These repetitive patterns were originally detected by the use of various flow visualization techniques, such as dye and hydrogen bubbles, but similar patterns have been subsequently detected using direct velocity measurement and computation techniques as well. The most organized of these patterns are found nearest the solid boundary, or wall, and have been characterized by such terms as low-speed wall "streaks," and fluid "ejections," "sweeps," and "bursts." These patterns are intermingled with patterns which relate to apparent vortices of manifold descriptions. These patterns reflect the presence of vortices that appear generally more coherent in proximity to the wall, and appear to evolve into increasingly more complex amalgamations of vortices with increasing distance above the surface. Well removed from the wall, large patterns of somewhat organized vortical fluid described as "bulges"[10,11] appear to be the dominate flow pattern near the edge of the boundary layer.

Low-speed wall streaks[9,12,13] are the most pervasive turbulent flow pattern adjacent to a bounding surface. Figure 1 shows the appearance of these low-speed streaks in a water flow visualized by lines of hydrogen bubble markers created using a pulsed electrolysis process. These flow patterns develop very close to the surface (about $y^+ = yu_\tau/\nu < 25$, where y is distance above the surface and $u_\tau = \sqrt{\tau/\rho}$ is the shear velocity), appearing as narrow, closely-spaced regions of low-speed fluid, interspersed between regions of higher-speed flow. The consensus is that this pattern of alternating high-speed/low-speed flow reflects low-speed fluid, originally very close to the surface, which is moving away from the surface in narrow, low-speed bands, and being replaced by high-speed fluid inflows in regions flanking the low-speed bands.

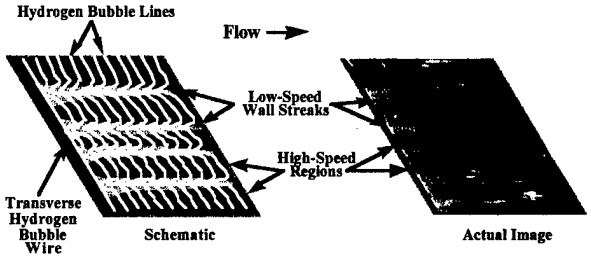

Figure 1. Visualization of low-speed streak pattern beneath a turbulent boundary layer

When one considers that the processes of turbulence create significant fluid and momentum exchange, resulting in elevated shear stress at the wall, it is clear that the streak pattern is reflective of Nature's mechanism for effecting this momentum exchange process. The fluid flowing closest to a surface is of course the most strongly affected by viscous shear, which redistributes momentum, dissipates energy, and causes the continued development of the boundary layer. Nature's problem is how to reenergize this viscously-retarded boundary layer and keep it moving. This is accomplished in a laminar flow through viscous diffusion, until the boundary layer develops to a thickness where this process of viscous diffusion of momentum becomes unstable, and a more effective method of momentum transport becomes necessary. It is the generation of turbulence, following this boundary layer destabilization, that is Nature's vehicle for infusing momentum and energy back toward the wall. The alternating high/low speed streak surface pattern reveals the grand plan of turbulence for implementing this momentum/energy infusion: via lateral, extended regions of surface fluid/momentum exchange.

This surface fluid exchange process is not a steady process, but occurs in an intermittent, somewhat chaotic manner, with low-speed fluid from the wall streaks suddenly rising away from the surface and "ejecting" into the passing flow[3]. The reason for intermittent energy/momentum transport via these ejection events, rather than a smooth transport process, is generally a result of the repetitive breakdown of the low-speed streaks. Since these streaks are local momentum deficit regions surrounded by higher-speed flows, local inflectional velocity profiles develop at the interface between the outward growing, low-velocity streaks and the higher-velocity surrounding flow, as shown in Figure 2 from a study of Kim et al.[3]. These local inflectional regions are inherently unstable, resulting in the subsequent breakdown of the streak, and the observed intermittent ejection of the low-speed fluid into the outer flow. A

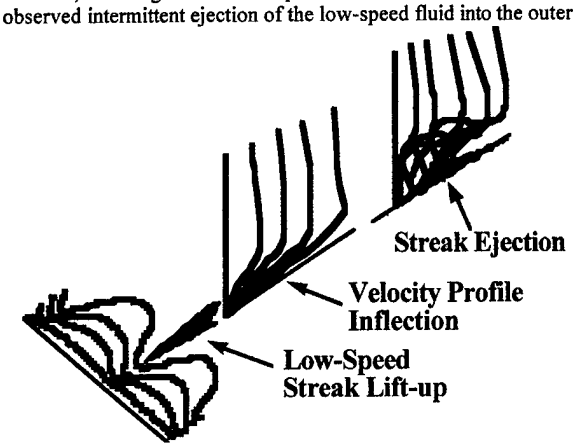

Figure 2. The original streak ejection process of Kim et al.[3]

side-view schematic of this process, shown in Figure 2, illustrates how this ejection was originally observed. To balance this ejection of low-speed fluid, continuity considerations require that a portion of the high-speed outer fluid replace the ejected fluid, which appears as a "sweep" of higher-speed fluid moving inward toward the surface, as shown in Figure 3. Physically, this sweep process brings new, higher-momentum fluid into close proximity of the surface, re-energizing the flow near the surface.

These intermittent ejections and sweeps of fluid are cumulatively the

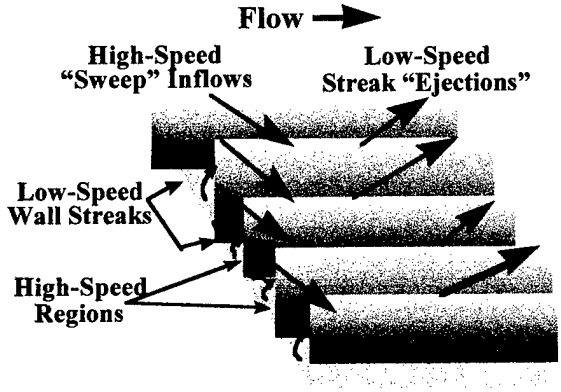

Figure 3. Surface fluid/momentum exchange via low-speed streak ejections and consequent high-speed inflows

agents of a more encompassing process termed "bursting." Originally, the term bursting came from the visual appearance of localized regions of fluid appearing to "burst" rapidly upward from near the boundary[3]. However, over the years turbulent bursting has also become associated with measured "bursts" of fluid momentum (and the commensurate generation of Reynolds stresses), which consist of the transport of both *low momentum fluid away from the surface* through the streak ejections, and *high momentum fluid toward the surface* by the inward sweeps of fluid, as illustrated in Figure 3.

Remarkably, the streak pattern reflecting this surface momentum exchange is extremely repetitive and persistent, demonstrating a consistency in pattern over a broad range of Reynolds numbers[9,12,13]

Figure 4 is a graph from Klewicki, which demonstrates that the average nondimensional spacing between the low-speed streaks is astoundingly consistent at $\lambda^+ = \bar{\lambda} u_\tau / \nu \approx 100$ (where $\bar{\lambda}$ is the average spacing between the streaks) over Reynolds numbers ranging from low-speed water flows[13] to atmospheric-scale boundary layers[12]. However, it is to be emphasized that these fluid/momentum exchange processes, while somewhat organized immediately adjacent to the surface, become quite irregular

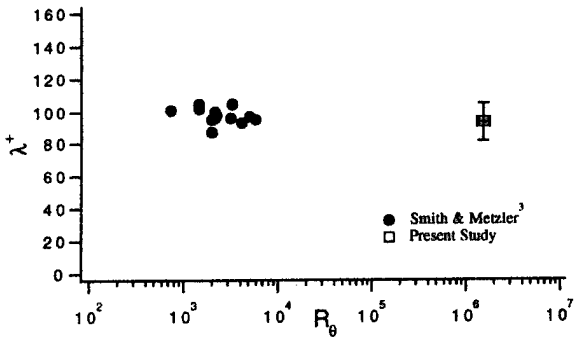

Figure 4. Average low-speed streak spacing in turbulent boundary layers. Dark symbols, water channel flow; open symbol, atmospheric flow. (Klewicki et al.[12])

within a very narrow distance from the surface, with the spanwise regularity of the process degenerating rapidly.

The presence of vortices in a turbulent boundary layer was hypothesized, among others, by Theodorsen[8] and Townsend[14] from theoretical arguments, and Kim et al.[3], Head and Bandyopadhyay[2], and Smith[6] from visualization studies. However, the evaluation by Robinson[5] of an early Navier-Stokes spatial-temporal numerical simulation of a low Reynolds number turbulent boundary layer[10], clearly began to illustrate the manifold presence of vortices in boundary layers, and their interrelationships with other turbulence patterns. Using isosurfaces of low pressure to indicate the presence of rotational vortices, Robinson was able to demonstrate through both dynamic simulations and statistical assessments, that there appeared to be two predominant types of vortex structures populating a turbulent boundary layer: horseshoe-shaped vortices (often termed "heads") that tend to be oriented transverse to the flow, and quasi-streamwise vortices (often referred to as "tilted streamwise vortices"), that extend in a predominantly streamwise direction. Figure 5 is a summary schematic of the type of the generic three-dimensional vortex patterns Robinson detected near the surface within a turbulent boundary layer. Often there seemed to be a connection between the two types of vortices, with the streamwise vortices appearing to be a streamwise extension (termed a "leg") of a horseshoe head. When

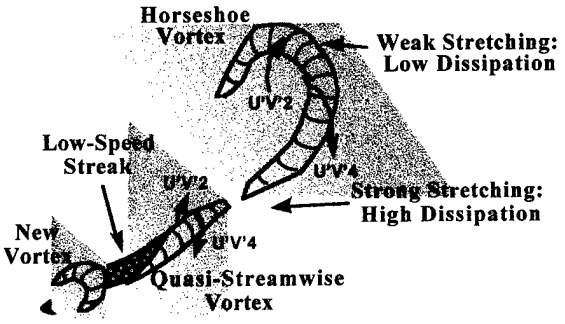

Figure 5. Summary of generic vortex topologies and juxtaposed behavior established for a low Re turbulent boundary layer computational simulation (after Robinson[5]).

combined, a head and *two legs* are often termed a "hairpin" vortex; the more predominant pattern of a head plus *a single leg* is often termed a one-legged "hairpin."

Robinson observed that vortices appear in myriad sizes, but it is the ones nearest the surface that seemed to be associated with the characteristic turbulence patterns (i.e. low-speed streaks, ejections,

sweeps) and statistical processes (generation of Reynolds stress). Interestingly, the horseshoe-type vortices seem to predominate in the region away from the surface, and the quasi-streamwise vortices are dominate in the near-wall region (about $y^+ = yu_\tau / \nu \approx 100$). And while both types of vortices seem to be associated with the generation of local Reynolds stresses (i.e. local momentum exchange), it is the quasi-streamwise vortices that are most associated with the low-speed streaks, and generation of "new" vortices.

Well removed from the bounding surface, the flow becomes quite complex, with the flow well above the surface dominated by highly-contorted collections of vortical fluid extending to the outer edges of the boundary layer. These patterns are generally referred to as turbulent "bulges"; a smoke visualization illustrating these bulges[10] is shown in Figure 6. It has been demonstrated that these bulges are somehow centrally involved in the accretion or engulfment of higher-velocity fluid at the edge of the boundary layer[11], which helps facilitate the momentum exchange process in turbulent boundary layers. And while at low

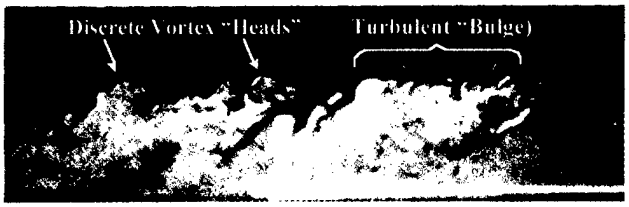

Figure 6. Smoke visualization of turbulent boundary layer bulges (Falco[10])

Reynolds numbers these bulges appear to consist of essentially the horseshoe vortex elements observed by Robinson, these bulges can grow to substantial scale, and apparently unfathomable complexity, such that they dominate almost all of the boundary layer for the high Reynolds number boundary layers encountered in practical aerodynamic and hydrodynamic flows.

III. PROCESSES

In a recent article on the sustaining mechanisms of turbulent boundary layers, turbulence pioneer Steve Kline[16] pointed out that, "two central questions must be answered: (i) what are the [flow] structures that extract energy from the mean flow and convert it into turbulent fluctuations? (ii) how are these turbulence-producing structures created and maintained?" He hypothesizes that the tilted streamwise vortices near the wall, and the head vortices in the outer flow, as described by Robinson[5], provide the mechanistic answers to these questions. However, while generally agreeing with this hypothesis, if one is to make use of flow structure information for turbulence drag reduction/control it is important to understand the dynamics of vortices that support Kline's hypothesis, and to examine how these vortex dynamics both relate to the patterns discussed in the first section of this paper, and are intimately involved in the sustaining nature of turbulence. This section briefly examines the processes of vortex deformation, vortex-vortex interaction, vortex-surface interactions, and vortex regeneration, pointing out how these processes relate to the development and maintenance of turbulent boundary layers. For a more detailed discussion and review of these concepts, the reader is referred to Smith et al.[7] and Doligalski et al.[1].

Evolution of Vortices in a Shear Flow: Clearly, the boundary layer of a turbulent flow is an environment of relatively high streamwise shear. This raises the question of how vortices evolve in the presence of this high shear. To address this question, Hon and Walker[17] considered the evolution of a three-dimensional distortion in an otherwise two-dimensional inviscid line vortex located in a shear layer near a bounding surface, or wall. They noted that when the fluid above the wall moves with a uniform speed, any distortion in a straight vortex appears to gradually spread along the length of the vortex, but does not amplify. However, when the vortex is located within a *shear flow*, a distortion in the line vortex immediately starts to amplify and grow as a result of Biot-Savart effects, displaying the temporal development shown schematically in Figure 7. From the initial distortion (the form of distortion is not critical, if it is small), a vortex head quickly develops and rises from the surface, as shown, bending backward in the shear flow. Concurrently, vortex legs evolve and move progressively toward the surface. As time advances, the vortex head moves farther from the wall, while the legs continue to approach the wall. As a result, the streamwise extent of the distortion continually increases. As shown, the original disturbance also *spreads laterally*, producing vortex structures termed "subsidiary vortices". These subsidiary vortices are produced through the interaction with the background shear flow, which induces a spreading of the disturbance in both the streamwise and spanwise directions, yielding a characteristic

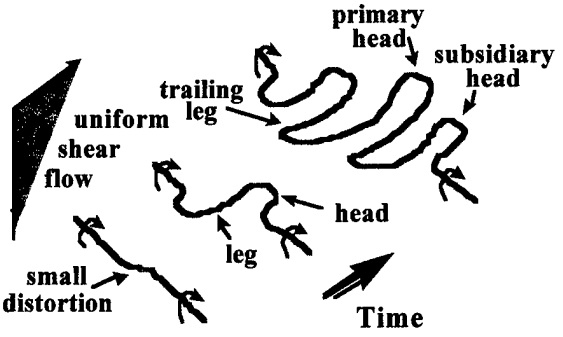

Figure 7. Generic deformation in a uniform shear flow of an inviscid line vortex with a *small* initial deformation

"hairpin" shape. Note that the characteristic spacing of the spanwise legs is dependent on the vortex strength and background shear.

Because most distortions in the vorticity field of a turbulent boundary layer are expected to be asymmetric, results have been obtained by Smith et al.[7] for a variety of such situations, with the generic behavior illustrated in Figure 8. Here the initial configuration is an inviscid line vortex *strongly displaced* near the center. As shown, in this case a "one-legged" or asymmetric hairpin vortex evolves from the distortion in the vortex, with a single leg developing and moving toward the surface. With advancing time, the disturbance expands in both the streamwise and spanwise directions as subsidiary hairpin-shaped structures form (although not as definitively as for the symmetric, small-deformation case). Again, the

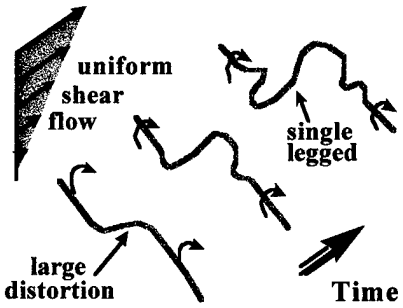

Figure 8. Generic distortion in a uniform shear flow of an inviscid line vortex with a *large* initial deformation

lateral spacing of the subsidiary hairpins is found to be highly dependent on the level of background shear.

In a turbulent boundary layer, the background shear is the largest at the wall, but then rapidly diminishes outside of the near-wall layer. Consequently, as a hairpin-shaped vortex develops in this environment, the legs of the vortex *squeeze together* as they penetrate toward the wall, whereas the head *expands* as it moves away from the wall[7]. This process is similar to that noted by Robinson[5], where vortex heads were observed to (1) send legs down toward the surface, and (2) have a greater spanwise extent with distance from the surface.

If one considers that a turbulent boundary layer contains myriad advected, 3-D vortices in continual asymmetric distortion, the behavior of the inviscid line-vortex simulations are quite instructive as to how vortices in turbulence behave. Near the wall, boundary layer vortices are expected to be of relatively small spanwise extent and varying strengths, and strongly influenced by their immediate neighbors. As they deform, each of the vortices produces leg-like extensions which propagate *toward* the wall. In the complex mutual interactions near the wall, the legs of relatively *weak* vortices will either intertwine with their stronger neighbors

or dissipate as they penetrate the viscous flow close to the surface. On the other hand, *strong* vortices will successfully approach the surface and undergo a process of vortex surface interaction (which is discussed later).

In contrast, the natural tendency for the vortex heads is to rise and expand laterally in the shear flow as they migrate away from the tangle of vorticity near the surface and into zones of decreased shear. In addition to lateral expansion, the heads of the vortices are hypothesized to undergo a process of vortex coalescence and reinforcement as the upward-migrating vortices closely approach one another. This coalescence of multiple hairpin-type vortices in a shear flow into larger flow structures has been has been simulated[7] and is depicted schematically in Figure 9. As suggested by the schematic, a group of distorted vortices soon start to intertwine and amalgamate, producing an asymmetric hairpin vortex structure of larger spanwise scale. Note that only a slight degree of

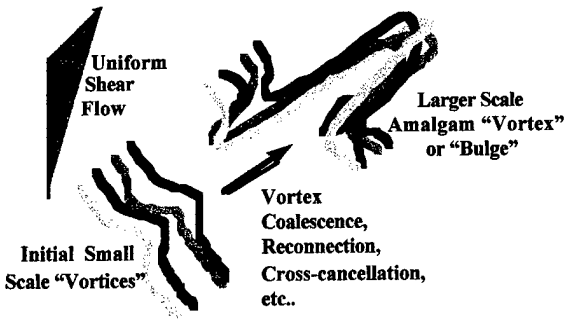

Figure 9. Generic schematic of the amalgamation of a sequence of initially distorted line vortices in a shear flow

asymmetry in the initial vortices leads to the evolution of a strongly asymmetric vortex entanglement.

However, inviscid simulations employing the Biot-Savart law must be viewed cautiously in extension to real, viscous situations, since such simulations must generally be terminated when two vortex cores move into close proximity. A number of studies have shown (e.g. Zhou et al.[18]) that when vortices come into close approach, the vortex cores can and will break and reconnect, which cannot be described by a Biot-Savart simulation. The probability is that the processes of vortex reconnection, coalescence, and annihilation (cross-cancellation of vorticity (or vorticies) of opposite sign) will all lead to migration of vortices away from the surface and their growth into larger vortex structures. In fact, recent PIV results obtained by Adrian[20] at high Reynolds numbers suggest that the large outer-region structures may indeed be composed of a more or less organized coalescence of smaller vortical flow structures (a process suggested by Falco[10]; c.f. Figure 6)

Vortex-Surface Interaction and Vortex Regeneration: The development of the previously discussed low-speed streaks, and their subsequent breakdown and eruption from the wall can be explained by the viscous response of the fluid near a wall to the passage of wall-region vortices. This type of generic response is demonstrated in a number of fundamental experimental and theoretical "kernel" studies, including the motion induced by a two-dimensional vortex translating above a wall[1,7,19]. These studies illustrate that when a vortex is brought into close proximity of a surface, a sequence of events is initiated which results in a discrete eruption of wall-layer fluid, which can culminate in the generation and ejection of a new vortex. The following summarizes the sequence of events that occurs due to strong vortex interaction with a wall.

Figure 10 illustrates the basic surface-eruption processes created by a two-dimensional vortex advecting in a uniform flow above a wall[19]. When viewed by an observer moving with the vortex, the instantaneous streamlines associated with the inviscid flow near the wall will appear generically as sketched in Figure 10(a); note that the details of the vortex core geometry and the motion inside the core are not important. As the vortex moves, a thin unsteady boundary layer must develop in order to satisfy the no-slip condition at the wall. Characteristic velocity and pressure distributions (as viewed advecting with the vortex) are impressed on the viscous fluid layer [Figure 10(b)]. It is the imposition of the adverse portion (on the trailing, or upflow side of the vortex) of this translating pressure gradient that stimulates the subsequent interaction process. The presence of the local adverse pressure gradient causes the formation of a moving zone of separation within the boundary layer which grows rapidly normal to the wall. If the vortex is sufficiently strong and close to the surface, the boundary-layer fluid beneath the vortex will rapidly focus into a narrow band and appear to leave the wall as a sharply-focused fluid spike[19], as shown in Figure 10(c). This process is generically known as an "unsteady separation," which implies a process in which an initially thin boundary layer grows rapidly outward and interacts strongly with the external flow. In physical terms, the fluid particles just above the wall are significantly compressed by the opposing inertia and pressure-gradient

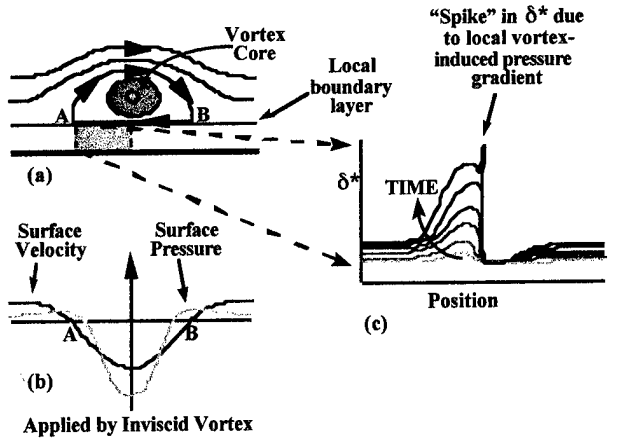

Figure 10. Schematic of the generic interaction of a vortex in close proximity to a surface with the viscous wall layer.

forces, causing a rapid vertical extension of the fluid. Thus, the presence of the leg vortices moving wallward in a turbulent boundary layer provide the stimulus for these types of surface interactions, which are essentially the low-speed streaks and surface ejections discussed in section II.

An important effect of this compression process is a local concentration of the local boundary layer vorticity into a relatively narrow band. Under normal circumstances, vorticity diffuses slowly outward from the wall in response to a pressure distribution imposed at the outer edge of the boundary layer, such that at any instant the vorticity field is relatively smooth. However, once an event of the type illustrated in Figure 10 occurs, the vorticity field is concentrated locally into a double-sided shear layer which moves rapidly away from the wall. Note that the generation of the truly eruptive events requires a *strong* interaction process that will generally occur only when a strong vortex is brought into close proximity of a wall. Relatively weak vortices, or vortices which are farther removed from the wall, may cause boundary-layer growth, but such growth will be much more gradual and no eruptive response occurs[1,19].

The three-dimensional response of a viscous wall layer due to an advecting three-dimensional vortex, such as the vortices depicted in Figures 7 and 8, is rather more complicated than two-dimensional situations[1]. An eruption stimulated by a three-dimensional vortex tends to develop as a ridge in the surface fluid, the shape of which depends on the portion of the vortex in proximity to the wall. A rapid outward penetration of fluid will initiate from such a ridge, with the furthest penetration occurring at the point of closest approach by the vortex. These eruptive tongues of fluid have been illustrated to roll rapidly over into vortices[1,7], starting from the point of highest penetration and rolling progressively outboard.

This process of vortex regeneration is illustrated using an asymmetric hairpin vortex, since we assume that most wall-region vortices are asymmetric with one dominant trailing leg, as Robinson[5] observed. As sketched in Figure 11, an asymmetric hairpin vortex can potentially generate surface-layer separations both behind the head and immediately inboard of the leg. Note that in the region immediately behind the vortex head, a *streamwise* region of adverse pressure gradient develops, which is very similar to that produced by the two-dimensional vortex shown in Figure 10. In addition, a local *spanwise* adverse pressure gradient also develops on the upflow side of the dominant vortex leg. In general, the adverse pressure gradient associated with the vortex head is often weak, and may not stimulate an interaction, since the head moves away from the wall and outward in the shear flow. In contrast, the vortex leg moves progressively closer to the wall, which intensifies the spanwise adverse pressure gradient generated by the leg.

As indicated in Figure 11(a), separation initiates along U-shaped fronts, with the tip of the ejected tongue originating somewhere near the base of the U and moving outward. As this ejected tongue penetrates regions of increased streamwise velocity, the tongue rolls up into a new

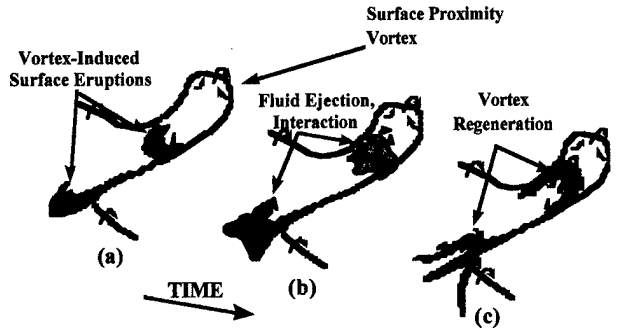

Figure 11. Generation of secondary vortices by vortex-surface interaction for an asymmetric wall-region vortex.

hairpin-like vortex as shown in Figure 11(b) and 11(c). In the final stage of this *viscous-inviscid* interaction, the erupting ridge completely detaches from the surface layer and a new *secondary* hairpin vortex is formed. The displacement of fluid outward by this eruption/vortex formation process is countered by an inflow of faster-moving fluid from immediately upstream due to continuity considerations. As discussed in section II, this inward movement of fluid appears as a "sweep" of fluid bringing higher-momentum fluid to the wall.

Note that the events shown in Figure 11 occur intermittently, over very short time scales (relative to that of the overall motion of the vortex),

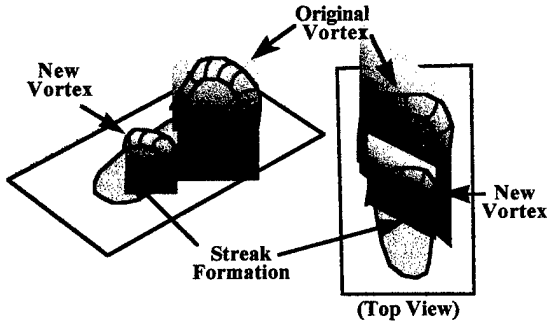

(a) Symmetric Regeneration

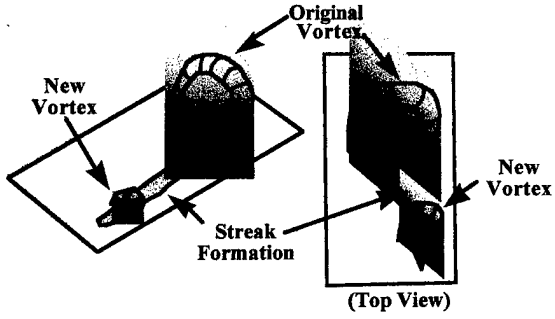

(b) One-Sided Regeneration

Figure 12. Schematic of regeneration of hairpin-like vortices in the near-wall region (modified from Robinson[5])

and that the eruptive events will (generally) not occur simultaneously near the head and leg. Note also, that for the less common case of a symmetric hairpin-type vortex, the process shown in Figure 11 is essentially the same except that the eruptive activity associated with the vortex head is expected to be much more significant.

The process outlined here is consistent with the description of Robinson[5] of the evolution of "new vortical arches" (i.e. new hairpin vortices) near "quasi-streamwise" vortices (c.f. Figure 5), as illustrated in Figure 12. Similar to Figure 11, Robinson identifies two types of regeneration, that he refers to as (1) symmetric and (2) one-sided regeneration, depending on whether the process occurs respectively behind the vortex head or adjacent to the leg, with the one-sided regeneration by far the more common process.

The regenerative process outlined in Figure 11 was clearly observed by Haidari and Smith[21], who observed that the production of new hairpin-type vortices quickly leads to the streamwise and spanwise spread of turbulent-like disturbances in an otherwise laminar boundary layer. This spreading is the result of an ever-expanding sequence of wall-layer eruption/hairpin generation cycles, which promote continued streamwise and spanwise growth. Eventually, a large structure similar to a turbulent spot evolves from a single hairpin vortex[21,25].

In a turbulent boundary layer, newly-created vortices may intertwine with the parent vortex or neighboring vortices as discussed in section II. Alternatively, new vortices can act to induce further eruptions downstream, thereby perpetuating the generation of additional hairpin-like vortices. Note that only those vortices strongest and closest to the wall will induce eruptions. Robinson[5] detected that only a fraction (perhaps less than fifty percent) of lifted streaks roll up to form a new vortex, with the rest appearing to dissipate and disappear.

In end-view visualization studies of the turbulent near-wall[7,22], visualization material introduced immediately upstream has been shown to concentrate into intermittent spanwise regions, which sporadically erupt in thin spires of fluid which often penetrate outward on the order of $y^+ \approx 100$. These spires are believed to be the eruptive regions shown in Figure 11, and are coincident with the ubiquitous low-speed streaks. Consequently, these eruptive plumes are the fundamental way in which fluid and momentum from the wall region is exchanged with the outer part of the flow and turbulence is sustained.

IV. A CONCEPTUAL MODEL

Based the vortex processes discussed in section III, a conceptual model is hypothesized, illustrating how vortex development and interactions sustain and maintain a turbulent boundary layer. The key element in this model is the understanding of the behavior of three-dimensional, hairpin-type vortices in proximity to a surface.

From the previous discussion, it is clear that once vortex deformation develops, most likely due to transition of a laminar boundary layer, or from external vorticity contamination, hairpin-like vortices will develop in the shear layer near a surface. Once these three-dimensional vortices are present, they are able to (1) regenerate *new* vortices through an interaction with the viscous wall layer, (2) interact with other three-dimensional vortices to yield larger-scale flow structures, and (3) facilitate the transfer of energy and momentum within the turbulent boundary layer. The following description, in conjunction with Figures 13 and 14, summarizes the key aspects of a vortex-based conceptual model both for the transport processes in the near-wall region, and for the development of outer-region flow structures.

- Low-speed streaks are generated by the interaction of a passing streamwise or hairpin-like vortex with wall-region fluid, and comprise a narrow spire of low-speed fluid lifted from the wall. If the original vortex is strong, this can precipitate a burst event wherein, a streak in proximity to the vortex penetrates the outer flow (i.e. erupts), destabilizes, and rolls over into a secondary hairpin-like vortex via a viscous/inviscid interaction, resulting in the ejection of a portion of the streak into the outer region. If the vortex is weak, a streak may form, but the vortex action may be insufficient to create a local breakdown and subsequent formation of a secondary hairpin vortex. In this latter case, a streak will either diffuse or be acted upon by subsequent streamwise or hairpin-like vortices (generated independently upstream), which can cause a *refocusing* of the original streak. Vortex interaction with an existing streak can cause the original streak to develop further (possibly through combination or amalgamation with other adjacent streaks) until a subsequent eruption occurs.

- A "burst" is conceptualized as the local breakdown and ejection into the outer region of wall-layer fluid essentially comprising a low-speed streak; this breakdown is a form of localized unsteady separation, precipitated by a local adverse pressure gradient created by an advecting wall-region vortex. The ejection associated with this burst can result in the formation of one or more secondary hairpin-like structures in the immediate wake of the initial vortex via a viscous/inviscid interaction; a

burst may also occur well behind the initial vortex due to the stimulation of a breakdown by the passage of a subsequent vortex[21]. In either case, the result is the rapid ejection of fluid from a streak into the outer flow, regenerating other hairpin-type flow structures.

• A "sweep" is the three-dimensional inflow of high-speed fluid from the outer region due to both the formation and presence of hairpin-like vortices. This process takes conceptually two forms: 1) During the formation stage, when low-speed fluid is ejected outward from a streak, an inflow of higher-speed fluid will occur near the plane of symmetry of the streak, resulting in the local recovery of the mean velocity profile[23], which will appear and be detected as a local acceleration of the flow; 2) Alternatively, higher-speed fluid will be induced toward the wall on the

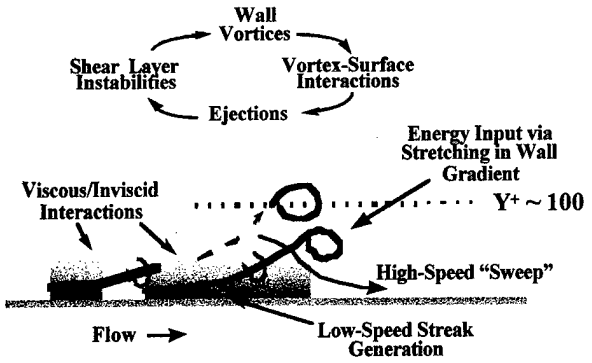

Figure 13. Generalized processes of near-wall turbulence generation.

wallward-rotating portion of either a quasi-streamwise vortex or a leg of a hairpin-like vortex; this can result in the observation (visual studies) or detection (fixed probe studies) of what appears as an accelerated "sweep" type behavior[5].

• As illustrated in Figure 13, the processes occurring in the near-wall are cyclical, although not periodic. Wall-region vortices interact with and precipitate ejections of wall-region fluid, which subsequently roll up to form new vortices through viscous/inviscid interactions with the higher-speed, outer-region fluid. This process defines a continuing cycle which perpetuates both the elements which sustain turbulence (i.e. three-dimensional vortices), and the process for their generation (i.e. viscous/inviscid interactions).

• The engine that powers the turbulence regeneration process and is necessary to sustain the energy transfer from the free-stream to the near-wall is three-dimensional vortex stretching in the local velocity gradient. As suggested originally by Theodorsen[8], the formation of hairpin-like vortices provides the logical mechanism for achieving this energy transfer process in the near-wall region, with the energy input to the hairpin vortices supplied by the free-stream work done during vortex stretching in the local velocity gradient. Note that during rapid stretching in the local velocity gradient, the angular momentum (proportional to ωr^2) in a tilted streamwise vortex or leg of a hairpin-like vortex will be roughly conserved, while the energy (proportional to $\omega^2 r^2$) will increase significantly as the vortex tube narrows. Note also that this narrowing of a vortex tube sharply increases the radial velocity gradients within the vortex tube, which strongly elevates viscous dissipation (proportional to the square of the velocity gradient in the tube); as is characteristic of turbulence, this dissipation will thus be highest in regions of high shear, such as in the vicinity of the wall.

• As Figure 14 shows, the process of growth to a fully-turbulent boundary layer can be explained by the proximity of multiple hairpin-like vortices in different phases of development, which creates a condition conducive to three-dimensional vortex amalgamation and coalescence. This process of amalgamation, demonstrated in both simulations[7] (c.f. Figure 9) and experiments[24], suggests that local collections of hairpin-like vortices can intertwine and interact to yield essentially a hairpin-like structure of somewhat larger scale. Recent studies[21,25] have observed the development of just such an amalgamation process, tracking the controlled evolution of a single hairpin vortex into a multi-hairpin, turbulent spot-like structure. This suggests that the outer region of a turbulent boundary layer can evolve from hairpin-like vortex structures, and that the large, arch-type vortices[5] observed in the outer region of turbulent boundary layers are essentially amalgams of initially smaller, deformed vortices; recent

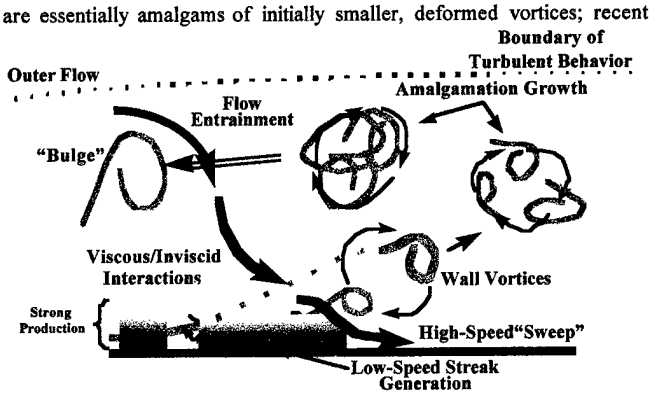

Figure 14. Conceptual model of turbulence regeneration, amalgamation, and evolution of outer-region structures

PIV results by Adrian[20] strongly support this interpretation (note also the discrete-appearing vortices in Figure 6).

• Since the larger outer-region structures directly interface with the free-stream flow, they play an instrumental part in inducing the flow of higher-speed fluid toward the wall (i.e. intermittent engulfment) along a tortuous gauntlet of vortex-induced motions, terminating in a "sweep" motion at the wall, as shown in Figure 14. However, despite the overall size and strength of these outer structures, the stretching mechanism for energy transfer to these larger-scale vortical structures is strongly diminished because of the weak mean-velocity gradient in the outer region. Following an initially strong energy input to the initial vortex scales near the wall, these outer structures will basically "evolve" to larger and larger scales, but with no significant additional energy input, eventually succumbing to slow, viscous dissipation. The outer part of the boundary layer may thus be regarded as a "graveyard" for vorticity, where the cumulative remnants of deformed wall-region vortices pass through a complicated process of dissipation, diffusion and mutual cancellation, similar to the hierarchy model of Perry and Chong[4]

As a cautionary note, one should recognize that the above hypotheses on the mechanisms of energy exchange and growth of a turbulent boundary layer are based on studies which have been done primarily at low Reynolds number and on smooth walls. Thus, although one presumes that the basic processes outlined above should maintain in general, caution needs to be exercised when extrapolating these processes to the very high Reynolds number behavior encountered for flows over aircraft or large ships, or in environmental circumstances where roughness is particularly important, such as flows in rivers or in the atmospheric boundary layer. Indeed, the earlier cited work of Klewicki et al.[12] in the near wall of a true atmospheric boundary layer, indicates that the non-dimensional spacing of streaks measured at high Reynolds numbers is consistent with the spacing originally established for low Reynolds number flows. However, Klewicki also notes several variations in local turbulence statistics from accepted low Reynolds number flows, such as reduced levels of local velocity fluctuation. It is unclear whether such differences indicate that a growth in boundary layer scale results in a small modification of the energy exchange process outlined above, or a substantive change in the physical processes hypothesized from the low Reynolds number studies.

One must remember that at high Reynolds numbers the outer region turbulent bulges will dominate almost the entire boundary layer, and contain almost all the momentum and energy. It thus stands to reason that the outer region must play a role in the turbulence regeneration process. If the near-wall structure, as Klewicki shows us, is essentially canonical even at very high Reynolds numbers, the best guess is that the outer region structure acts as a *modulator* of the near-wall response. As Meinhart and Adrian[26] have shown, the outer region of a turbulent boundary layer often displays large areas of almost constant velocity, separated by irregular interfaces. If such is the case, the possible effect on the turbulence regeneration process may be through a modulation of the wall processes by the application of a lower-frequency pressure variation on the near-wall by the outer flow variations. However, it is expected that the character of the physical regeneration process at the wall will remain unchanged. The implications of these variations, and whether they

indicate significant changes in the turbulent energy exchanges process at high Reynolds number is a particularly important area for future research.

IV. IMPLICATIONS FOR DRAG REDUCTION/CONTROL

The reduction of turbulent surface drag requires a reduction in the level of momentum exchange at the wall, which in turn requires a reduction of the bursting activity near the wall. In principle this may be accomplished either by reducing the number of low-speed streaks (i.e. "burst" sites) adjacent to the wall or by increasing the cycle time for the momentum exchange bursting process. Considering the vortex dynamics described above, it is clear that to accomplish this, one must generally inhibit the interaction of the near-wall vortices with the retarded near-wall flow. Since these vortices generate the low-momentum streaks and eventually provoke an eruption to produce new hairpin-like vortices, this cyclical momentum exchange process might be interrupted in at least two ways. The first is to provide mechanisms which inhibit the viscous-inviscid interaction by interfering with the capability of the vortices to focus low-momentum fluid at the wall and generate eruptions. The second is to maintain the streaks in a stable state for a longer period. The first of these approaches is clearly the mechanism implemented by streamwise surface riblets, which have been shown to be effective in reducing surface drag by up to 10%[27]. The riblets inhibit lateral flow near the surface, reduce the capacity of wall-region vortices to generate low-momentum streaks, and thus retard the wall vortex regeneration process; this is evidenced by an increase in streak spacing[28], which suggests reduced momentum exchange. Passive modification of surface topography to interfere with the vortex interaction process is therefore a viable approach for reducing the local momentum exchange process, and thus surface drag. The recent success with streamwise fences and shark scale-like surface modifications are other examples of this approach[27].

The maintenance of streak stability is a more tenuous approach, since this entails a delicate balance between the inherent stability of the low-speed streak and the amplitude of the destabilizing pressure perturbations in the outer flow. The injection of a polymer into the near-wall of the boundary layer is an example where streak stability is increased by addition of an external additive, as evidenced by wider streak spacing and reduced bursting activity. It is speculated that polymer addition may either affect the streak stability directly, by inhibiting lateral concentration of fluid by the hairpin vortices, or indirectly, by providing a region which is locally more viscous, which (1) more effectively damps external perturbations (thus retarding streak breakdown) and (2) dissipates the energy in the hairpin vortices generated by the breakdowns, thus weakening the vortex strength of the hairpin vortices and inhibiting their effectiveness in perpetuating the vortex regeneration cycle.

With regard to active control, one must again somehow modify the streak development process, force the wall flow toward uniformity, and thus reduce the development of the eruptive wall-region momentum exchange. Distributed wall suction is successful, since it essentially removes the inner layer of low-momentum fluid. Magnetic effects apply a body force that inhibits movement normal to the surface, and thus restricts the development of low-momentum streaks. The concept of generation of opposite sign vortices near the surface by surface actuators, with the intent of effecting vorticity "cancellation" of the strength (and thus the regenerative capabilities) of the wall-region vortices, is somewhat dubious. It is unclear that such actuators are capable of generating sufficiently "clean" streamwise vortices to effect a cancellation process. And if such vortices can be effectively generated juxtaposed to the existing wall vortices, it is not clear that a cancellation process will occur, as opposed to some other form of induced motion. Of course, one must also account for the momentum lost during the generation process due to the form drag of the actuator, which raises questions of net drag reduction.

The possibility for drag reduction/control by manipulation of the outer region, either passively or actively, does not seem to hold much promise, since this region is effectively an inactive participant in the turbulence generation process. While outer-region splitter plates and airfoils have shown that they can have a temporary effect on modifying surface drag, this is probably due to a modulation of the local surface pressure, which only affect the near-wall turbulence regeneration process adjacent to the control device. And as has been shown, when device drag effects are accounted for, the net system drag will always increase.

ACKNOWLEDGEMENTS

I would like to thank the AFOSR for their extended support. I would also like to thank Dr. J.D.A. Walker for his long-standing collaboration and insight. And finally, I would like to express my life-long admiration and thanks to Dr. Steve Kline for his insight, inspiration, encouragement, mentorship, and guidance. He will be greatly missed.

REFERENCES

1. Doligalski, T.L., Smith, C.R., and Walker, J.D.A. "Vortex interactions with walls," *Ann. Rev. Fluid Mech.*, 26, 573-616, 1994.
2. Head, M.R. and Bandyopadhyay, P. "New aspects of turbulent boundary layer structure, *J. Fluid Mech.*, 107, 297-338, 1981.
3. Kim, H.T., Kline, S.J., and Reynolds, W.C. "The production of turbulence near a smooth wall," *J. Fluid Mech.*, 50, 133-160, 1971.
4. Perry, A.E. and Chong, M.S. "On the mechanisms of wall turbulence," *J. Fluid Mech.*, 119, 173-217, 1982
5. Robinson, S.K. "Coherent motions in the turbulent boundary layer," *Ann. Rev. Fluid Mech.*, 23, 601-639, 1991.
6. Smith, C.R. "A synthesized model of the near-wall behavior in turbulent boundary layers," In *Proc. 8th Biennial Symp. on Turb.*, Zakin, J.L. & Patterson, G. (Ed), U. of Missouri-Rolla, 299-327, 1984.
7. Smith, C.R., Walker, J.D.A., Haidari, A.H. and Sobrun, U. " On the dynamics of near-wall turbulence," *Phil. Trans. Roy. Soc. Lond. A.*, 336, 131-175, 1991.
8. Theodorsen, T. "Mechanism of turbulence," In *Proceedings Second Midwestern Conference on Fluid Mechanics*, Bull. No. 149, Ohio State University, Columbus, Ohio, 1952.
9. Kline, S.J., Reynolds, W.C., Schraub, F.A. & Runstadler, P.W. "The structure of turbulent boundary layers," *J. Fluid Mech.*, 95, 741-773, 1967.
10. Falco, R.E. "Coherent motions in the outer region of turbulent boundary layers," *Phys. Fluids*, 20, S124, 1977.
11. Kovasznay, L.S.G., Kibens, V., and Blackwelder, R.F. "Large-scale motion in the intermittent region of a turbulent boundary layer," *J. Fluid Mech.*, 41, 283-325, 1970.
12. Klewicki, J.C., Metzger, M.M., Kelner, E., and Thurlow, E.M. "Viscous sublayer flow visualization at $Re_\theta \approx 1{,}500{,}000$," *Phys. Fluids*, 7, 857-865, 1995
13. Smith, C.R and Metzler, S.P. "The characteristics of low-speed streaks in the near-wall region of a turbulent boundary layer," *J. Fluid Mech.*, 129, 27-54, 1983..
14. Townsend, A.A. *The structure of turbulent shear flow*, Second Edition, Cambridge University Press,150-158, 1976.
15. Spalart, P.R. "Direct simulation of a turbulent boundary layer up to $Re_\theta \approx 1410$," *J. Fluid Mech.*, 187, 61-98, 1988.
16. Kline, S.J. & Portela, L.M. "A view of the structure of turbulent boundary layers," in Self-Sustaining Mech. of Wall Turb., R.L. Panton, ed., Comp. Mech. Pubs., Boston, 165-180, 1997
17. Hon, T.L. and Walker, J.D.A. "Evolution of hairpin vortices in a shear flow," *Computers and Fluids*, 20, 343-358, 1991.
18. Zhou, J, Meinhart, C.D., Balanchandra, S., Adrian, R.J. "Formation of coherent hairpin packets in wall turbulence" in Self-Sustaining Mech. of Wall Turb., R.L. Panton, ed., Comp. Mech. Pubs., Boston, 109-134, 1997.
19. Peridier, V.J., Smith, F.T. & Walker, J.D.A. "Vortex-induced boundary-layer separation. Part 2. Unsteady interacting boundary-layer theory," *J. Fluid Mech.*, 232, 133-165, 1991.
20. Adrian, R.J. Private communication, 1998.
21. Haidari, A.H. and Smith, C.R. " The generation and regeneration of single hairpin vortices," *J. Fluid Mech.*, 277, 135-162, 1994.
22. Wallace, J.M. and Balint, J.L. " Flow visualization study of the effects of trip type on the structure of the turbulent boundary layer," Video Tape, Turbulence Laboratory, University of Maryland, 1990.
23. Lu, L.J. and Smith, C.R. "Use of flow visualization data to examine spatial-temporal velocity and burst-type characteristics in a turbulent boundary layer," *J. Fluid Mech.*, 232, 303-340, 1991.
24. Gretta, W.J. and Smith, C.R. "The flow structure and statistics of a passive mixing tab," *ASME J. Fluid Engng.*, 115, 225-263, 1993.
25. Singer, B.A. and Joslin, R.D. "Metamorphosis of a hairpin vortex into a young turbulent spot," *Phys. Fluids.*, 6, 3724-3730, 1994.
26. Meinhart, C.D. & Adrian, R.J. "On the existence of uniform momentum zones in a turbulent boundary layer," Phys. Fluids, 7, 694-696, 1995.
27. Bechert, D.W., Bruse, M., Hage, W., & Van Der Hoeven, J.G.T., "Experiments on drag-reducing surfaces and their optimization with an adjustable geometry," *J. Fluid Mech.*, 338, 59-87, 1997.
28. Bacher, E.V. & Smith, C.R. "Turbulent Boundary-Layer Modification by Surfac Riblets",*AIAA J.*, 24, 8, 1382-1385, 1986.

COHERENT STRUCTURES, SELF-SUSTAINING PROCESS AND BIFURCATIONS IN SHEAR FLOWS

Fabian Waleffe
Departments of Mathematics and Engineering Physics
Center for Mathematical Sciences
University of Wisconsin-Madison
Madison WI 53706-1388
waleffe@math.wisc.edu

Abstract: Experiments and simulations have revealed the existence of *Coherent Structures* in the near-wall region of turbulent shear flows. A complete *self-sustaining process* responsible for the origin of those structures is briefly reviewed. The process consists of streamwise rolls that create streaks whose instability directly feeds back onto the rolls. The understanding of that process is used to calculate exact hidden steady states of the Navier-Stokes equations that are strikingly similar to the observed coherent structures. The self-sustaining process thus appears to be fundamental to the physics of near-wall turbulence. Its elucidation and characterization should provide a solid basis for the development of turbulence models and control strategies.

I. INTRODUCTION

This work presently focuses on fundamentals of wall turbulence physics and in particular on the physical origin of the observed coherent structures (CS). The objective is to establish the complete dynamical and mathematical characterization of a nonlinear, three-dimensional, self-sustaining process (SSP) suggested by many experimental observations. Instead of directly trying to model the observations, the strategy has been to take clues from those observations to extract a fundamental nonlinear process from the Navier-Stokes equations. One of the most surprising results of this approach is the calculation of hidden ordered solutions that are intimately linked to the coherent structures. The calculation of these steady and other periodic or nearly-periodic solutions provide a solid foundation for the notion of "active motions" in the near-wall layer that can be completely and rigorously separated from the "inactive motions". A fundamental understanding of the physics of near-wall turbulence is essential to the development of *robust* turbulence models and *optimum* control strategies. Turbulence models of the "K-Epsilon" type, for instance, require a variety of drastic and ad hoc adjustments (*e.g.* wall functions) in order to recover adequate near-wall behavior, that are symptomatic of an incomplete understanding of the wall layer dynamics. The elucidation of the SSP should remedy that unsatisfactory aspect of turbulence models.

With respect to drag reduction, this work and observations suggest that much of the "turbulent" drag actually results from the coherent motions. Indeed, the disorder characteristic of turbulence may actually *reduce* the drag that would result from the the 3D ordered steady solutions such as those discussed below. The characterization of the SSP, and low-order models of that process in particular, should thus be critical to the development of active control strategies.

II. COHERENT STRUCTURES

Coherent structures in the near-wall region of turbulent shear flows were first revealed by visualization experiments about three decades ago [1]. Many analyses of experiments and computer simulations have educed the typical structures and shown their relationship not only with the increased drag on the wall, but also with the maintenance of turbulence itself. A sketch of the typical coherent structure is shown in Fig. 1 [4,5]. This sketch summarizes a series of analyses of a well-known database of computer generated turbulent channel flows [6]. Experimental visualizations (*e.g.* [2,3]) often emphasize symmetric structures known as *hairpin vortices*, as opposed to the staggered vortices of Fig. 1. Although the numerical and theoretical evidence tend to favor the asymmetric structure of Fig. 1, and there has been much debate over which structure predominates, the underlying physical processes are in fact essentially identical. The existence of two types of structures is closely related to the existence of two modes of instability of wakes: sinusoidal and varicose [9,11,12]. The beautiful sketches of the generation and regeneration of hairpin vortices in Acarlar & Smith [2] were in fact most inspiring to this author, as was the theoretical work of Benney [16] on a "mean flow-first harmonic theory".

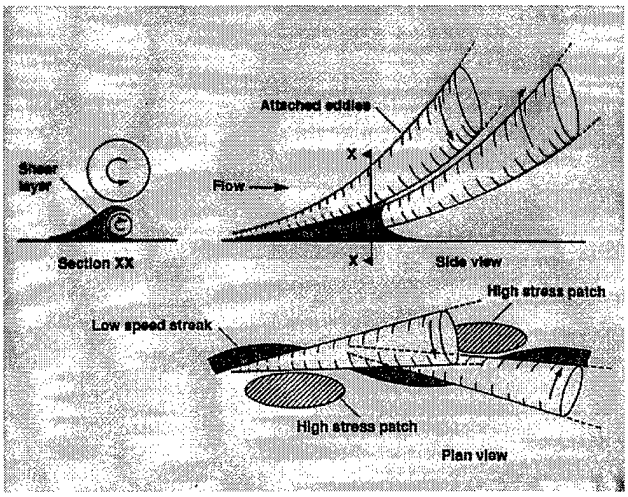

FIG. 1. Sketch of the coherent structure educed from DNS data, from Ref. [4], see also [5].

III. SELF-SUSTAINING PROCESS

A complete, three-dimensional, self-sustaining process (SSP) responsible for the coherent structures has been stud-

ied [7–12]. For the case of plane parallel shear flow in the x direction between two walls located at $y = \pm 1$, the process can be seen as consisting of the interaction between three elements: streamwise rolls, streaks and a streak instability. The streamwise rolls $[0, V(y,z), W(y,z)]$ redistribute the mean momentum $[\bar{U}(y), 0, 0]$ to create a spanwise modulation of the streamwise velocity known as streaks $[U(y,z) - \bar{U}(y), 0, 0]$ (these fields maybe time-dependent but t is kept implicit). The resulting spanwise inflections drive a three-dimensional instability leading to the development of a sinusoidal modulation in the streamwise direction of the form $e^{i\alpha x}\mathbf{v}(y,z) + c.c.$. The nonlinear quadratic interaction of the latter with its conjugate, *i.e.* $\mathbf{v}(y,z)\mathbf{v}^*(y,z)$ feeds back on the x-averaged flow. This feedback is the direct and primary effect of nonlinearity (together with the generation of an $e^{2i\alpha x}$ harmonic).

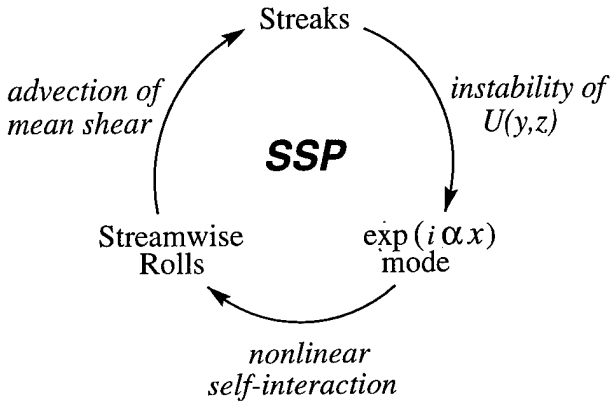

FIG. 2. The self-sustaining process.

The full equations for the x-averaged flow consist of one equation for the streaky flow $\overline{u}^x = U(y,z)$ and one equation for the streamwise rolls which can be represented in terms of a streamfunction $\Psi(y,z)$ with $\overline{v}^x = V(y,z) = \partial_z \Psi$, $\overline{w}^x = W(y,z) = -\partial_y \Psi$. These equations read respectively

$$\frac{\partial U}{\partial t} + V\frac{\partial U}{\partial y} + W\frac{\partial U}{\partial z} - \frac{1}{R}\nabla^2 U = F(y) - \frac{\partial \overline{u'v'}^x}{\partial y} - \frac{\partial \overline{u'w'}^x}{\partial z} \qquad (1)$$

$$\frac{\partial}{\partial t}\nabla^2\Psi + J(\nabla^2\Psi, \Psi) - \frac{1}{R}\nabla^4\Psi = \frac{\partial^2}{\partial y \partial z}(\overline{w'w'}^x - \overline{v'v'}^x) + \left(\frac{\partial^2}{\partial y^2} - \frac{\partial^2}{\partial z^2}\right)(\overline{v'w'}^x) \qquad (2)$$

where the primed variables are the x-dependent fluctuations with $\overline{u'}^x = \overline{v'}^x = \overline{w'}^x = 0$. It has been demonstrated elsewhere [8,9,11] that the nonlinear interaction of the streaky flow eigenmode $e^{i\alpha x}\mathbf{v}(y,z)$ with its complex conjugate $e^{-i\alpha x}\mathbf{v}^*(y,z)$ leads to Reynolds stresses $\overline{u'v'}^x$, $\overline{u'w'}^x$ whose net effect is to extract energy from the streaks while the net effect of the stresses $\overline{v'v'}^x$, $\overline{v'w'}^x$ and $\overline{w'w'}^x$ is to regenerate the streamwise rolls. It is noteworthy that the stresses $\overline{u'v'}^x$, $\overline{u'w'}^x$ put energy back into the mean shear $\bar{U}(y)$. Energy and momentum are extracted from the mean shear by the x-independent components: $[U(y,z) - \bar{U}(y)]V(y,z)$ averaged over z. The overbar denotes an average over both x and z.

The term $F(y)$ in the $U(y,z)$ equation represents a steady deterministic forcing that maintains the shear flow (*e.g.* $F(y) = constant$ for plane Poiseuille flow). In this paper, $F(y) = 0$ and the shear flow is maintained by the boundary conditions (namely imposed stress at the walls) but other $F(y)$ have also been considered such as $F(y) \propto \sin \pi y/2$ with free-slip boundary conditions (*i.e.* $\partial u/\partial y = \partial w/\partial y = v = 0$ at $y = \pm 1$). Imposed stress can be seen as a limit case of the body force situation in which the forcing consists of Dirac delta functions localized at the plates: $F(y) = 2R^{-1}[\delta(y-1) - \delta(y+1)]$. For imposed stress, one steady solution of the Navier-Stokes equations has the plane Couette flow form, $U(y) = y$, and is linearly stable for all Reynolds numbers. Many other linearly stable plane parallel shear flows $U(y)$ can be constructed by proper choices of $F(y)$ [13].

IV. HIDDEN STEADY STATES

Numerical simulations [7,8], a stability analysis [9,11] and a low-order model [10,11] have been used to study the SSP. Here, the existence of steady states that are remarkably similar to the coherent structure of Fig. 1 is shown for the case of plane Couette flow with imposed stress at the wall, corresponding to the boundary conditions $\partial u/\partial y = 1$, $\partial w/\partial y = v = 0$ at $y = \pm 1$. The steady states are exact solutions of the Navier-Stokes equations for incompressible flow with no turbulence model and no approximations, except for negligible error from numerical truncation of the modal expansions. Similar steady solutions exist for no-slip (imposed velocity) boundary conditions. The imposed stress boundary condition is instructive because it eliminates several potential mechanisms for the origin of the coherent structures. Viscous instabilities leading to growing Tollmien-Schlichting waves cannot occur [13] for instance, and the viscous rebound mechanism [14] cannot operate either.

The velocity field is expanded into Fourier modes in all 3 directions. The expansion is truncated to keep only the Fourier modes with indices (l,m,n) in directions x, y, z respectively, that satisfy

$$\left(\left|\frac{l}{L_T+1}\right|^p + \left|\frac{m}{M_T+1}\right|^p + \left|\frac{n}{N_T+1}\right|^p\right)^{1/p} < 1$$

with $p = 1, 2, \infty$. Resolutions that provide converged results on the scale of the plots (errors of less than 1%) are, for instance, $[L_T, M_T, N_T] = [11, 25, 11]$ for $p = 1$ (1256 degrees of freedom), and $[8, 20, 8]$ for $p = 2$ (1764 degrees of freedom) (Fig. 4 results). The Fourier expansion in the wall-normal direction is not asymptotically satisfactory as it lead only to algebraic scaling (error $O(m^{-4})$ as $m \to \infty$). However, for the low truncations to which we are limited for the continuation procedure, the Fourier expansion may actually be superior to an asymptotically exponential expansion in Chebyshev modes. The better accuracy of the Fourier expansion for low truncations (*i.e.* $M_T < 25$) was verified for the linearized vertical vorticity equation (the "Squire equation").

The procedure to compute steady states consists in calculating a solution of the steady Navier-Stokes equations by

Newton's method. The key issue is to generate a suitable initial guess. A good initial guess is provided by a "mean field" approach [9,11] based on the self-sustaining process, where the mean field consist of a steady x-averaged streaky flow and streamwise rolls $[U(y,z), V(y,z), W(y,z)]$. The mean field is constructed by picking the weakest streamwise rolls $[0, V(y,z), W(y,z)]$ that create the largest streaks, holding the rolls steady and computing the corresponding steady streaky flow $[U(y,z), 0, 0]$ which is the solution of the linear advection-diffusion equation $V\partial U/\partial y + W\partial U/\partial z = R^{-1}\nabla^2 U$. A linear eigenvalue analysis of the streaky flow [9,11] is then employed to locate the streamwise wavenumber α at which the streaky flow is marginally stable and to compute the corresponding neutral eigenmode $e^{i\alpha x}\mathbf{v}(y,z) + c.c.$. The nonlinear interaction of that mode with its conjugate has been shown to properly feed back on the streamwise rolls. The amplitude of that eigenmode can then be chosen so as to exactly balance the viscous dissipation of the streamwise rolls (Eqn. (6) in [11]). This procedure provides an initial guess good enough for the calculation of an exact steady solution of the incompressible Navier-Stokes equations by Newton's method.

The steady solutions come in pairs. They arise "out of nowhere" through a *saddle-node* bifurcation as for the simple ODE $\dot{y} = (R - R_c) - y^2$ which has no fixed point for $R < R_c$ but two fixed points for $R > R_c$. The solutions are referred to as "upper" and "lower branch solutions" based on the amplitude of the modulation in x (Fig. 3). Both solutions look alike as they result from the same self-sustaining process. The upper branch has a more pronounced waviness in x but weaker streaks than the lower branch. For $\alpha = 0.48$ and spanwise wavenumber $\gamma = 1.50$, the 3D steady states do not exist below $R \approx 144$. This is not the smallest Reynolds number at which such steady states exist. The absolute smallest R has not been fully calculated yet but appear to be around 110 for the optimum α and γ. Figure 4 shows the upper branch steady state at $R = 150$ for $\alpha = 0.48$ and spanwise wavenumber $\gamma = 1.5$. The maximum velocity components at the mid-plane $y = 0$ (xz cut) are $\max(u) = 0.29$, $\max(v) = 0.07$, $\max(w) = 0.11$, and at the mid-section $x = \pi/\alpha$ (yz cut) they are 0.75, 0.06 and 0.12, respectively. The similarity with the sketch of the coherent structures in Fig. 1 is striking. The wavy low-speed streak and the staggered vortices are clearly recognizable. It is remarkable that such strong similarity occurs in spite of the facts that Fig. 1 is a sketch of an ensemble average of snapshots of a turbulent channel flow with no-slip at the walls at $R_* = 180$ while the steady solution of Fig. 4 is an exact steady state occupying the full channel with imposed stress at the walls at $R_* = \sqrt{150} \approx 12.25$. The friction Reynolds number $R_* = u_* h/\nu$ is based on the friction velocity $u_*^2 := \nu dU/dy|_{wall}$ and the half-channel width h. The mean flow for the steady state of Fig. 4 is shown in Fig. 5. The maximum velocity is less than half the maximum velocity in the basic laminar flow plane Couette flow $U(y) = y$.

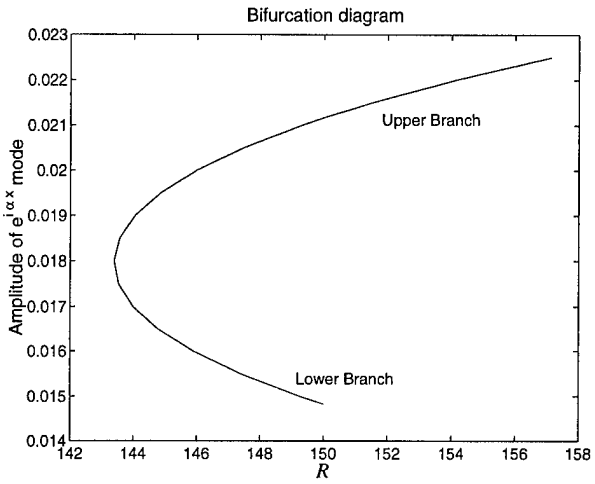

FIG. 3. Bifurcation diagram for 3D, nonlinear steady states at $\alpha = 0.48$ and spanwise wavenumber $\gamma = 1.5$.

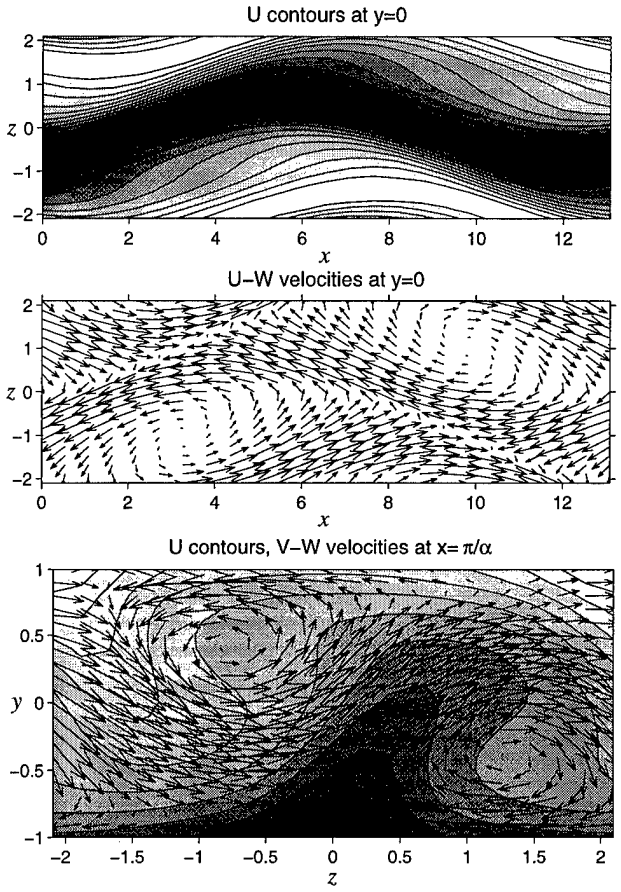

FIG. 4. Cuts through exact upper branch steady solution at $R = 150$, $\alpha = 0.48$, $\gamma = 1.5$. Compare xz cuts to 'Plan View' in Fig. 1 and yz cut to 'Section XX' in Fig. 1.

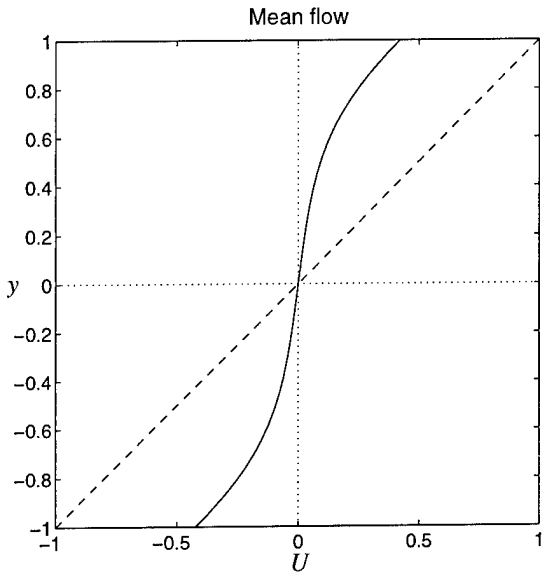

FIG. 5. Mean flow $\bar{U}(y)$ for upper branch steady state (solid) and basic steady state $U(y) = y$ (dashed).

Such steady solutions appear to exist for forcings $F(y)$ in (1) that are sufficiently localized near the walls in which case the mean shear $d\bar{U}/dy$ of the steady streaky flow $U(y, z)$ is wiped out in the center of the channel (Fig. 5). For the sinusoidal forcing $F(y) = \pi^2/(4R) \sin \pi y/2$, there are apparently no steady states. Spurious steady states can be found that do not converge as the truncation is increased. For that sine forcing the mean shear of the streaky flow remains close to sinusoidal and is thus maximum at the center of the channel. The bifurcation from purely streamwise flow then occurs through a subcritical Hopf bifurcation, hence we expect that a saddle-node bifurcation of cycles takes place with sine forcing (*i.e.* wall-bounded Kolmogorov flow). The low-order model developed earlier [9,11] is still expected to apply but the variable "W" should be reinterpreted as the amplitude of the cycle in such cases.

Similar steady state solutions exist for the regular plane Couette flow with no-slip boundary conditions. Such solutions have been calculated by other authors recently, either by continuation of wavy Taylor-Couette vortices in rotating plane Couette flow [17,18] or of wavy convection rolls in sheared convection [19]. The exact nature of the boundary conditions, imposed velocity or imposed stress, thus does not have much effect on the steady states. This is probably because the self-sustaining process responsible for those solutions is essentially nonlinear and inertial. In fact, the present evidence is that even the critical Reynolds numbers for existence of the 3D steady states are very close, within 10% of each other, for both types of boundary conditions. In contrast, the critical Rayleigh number in Rayleigh-Bénard convection with free-slip boundary conditions is about 657 and thus significantly different from the critical value of 1708 with no-slip boundary conditions.

V. BRIEF DISCUSSION

The 3D steady solutions have been dubbed "hidden" because they are unstable. Hence they cannot be observed in physical experiments or through numerical simulations of the time-dependent Navier-Stokes equations. Preliminary analyses indicate that the lower branch of solutions is a "saddle point" (i.e. a linear stability analysis of that solution always yields one positive real eigenvalue) as expected from a saddle-node bifurcation. The upper branch, however, is not the expected stable node. Instead, it would appear as an unstable node (two positive real eigenvalues) near onset and quickly turn into an unstable spiral as the Reynolds number is increased. This behavior is in agreement with that seen in a related low-order model [11]. The strong similarity with the observed coherent structures suggests however, that the steady solutions may be central to our understanding of turbulence in shear flows in spite of their instability, or perhaps because of it. These solutions may for instance provide the "backbone" for strange attractors. This would mean that although the flow does not settle onto a steady state, it fluctuates around or between them. This is also suggested by the numerical simulations analyzed in Ref. [8]. Although the solutions herein have been calculated at low Reynolds numbers, there is no evidence that these solutions cease to exist for larger Reynolds number. In fact, a simple asymptotic argument suggests that the solutions exist for all Reynolds numbers above their (finite) critical value. Figure 5 shows that these ordered steady states have strongly *decreased* flow velocity for imposed drag (or *increased* drag for imposed velocity) as compared to the basic laminar shear flow. Thus, in agreement with research on coherent structures, the "turbulent" drag probably results from the hidden ordered solutions (the "active motions") while the disorder itself results from the transient instabilities (the "inactive motions") of those sustained ordered states and in fact probably reduce the maximum drag achievable by the coherent motions.

The existence of these hidden steady states is remarkable and should have fundamental implications for the nature of turbulence and its onset in shear flows. The calculation of these steady states provide an excellent objective verification of the validity of the Self-Sustaining Process. From an applications point of view, the derivation of simplified models, such as the low-order model or the mean field approach [10,11] sufficiently sophisticated to faithfully capture the self-sustaining process promises to lead to robust turbulence models. Simplified models could also be incorporated into prediction and control strategies in order to reduce drag. As discussed above, controlling the coherent motions allowed by the SSP appear to be the key to drag reduction.

ACKNOWLEDGEMENTS

The author is grateful to the MIT Research Support Committee for financial support from the MIT Sloan fund and to Derek Stretch for providing Fig. 1.

REFERENCES

1. S.J. Kline, W.C. Reynolds, F.A. Schraub & P.W. Runstadler "The structure of turbulent boundary layers," *J. Fluid Mech.* **30**, 741-773 (1967).

2. Acarlar, M.S. and Smith, C.R., "A study of hairpin vortices in a laminar boundary layer," *J. Fluid Mech.* **175**, pp. 1-41 and 43-83 (1987).

3. Head, M.R. and Bandyopadhyay, P. "New aspects of turbulent boundary layer structure," *J. Fluid Mech.* **107**, 297-338 (1981).

4. D.D. Stretch, "Automated pattern eduction from turbulent flow diagnostics," *Annual Research Briefs-1990*, Center for Turbulence Research, Stanford U.

5. J. Jeong, F. Hussain, W. Schoppa & J. Kim "Coherent structures near the wall in a turbulent channel flow," *J. Fluid Mech.* **332**, 185-214 (1997).

6. J. Kim, P. Moin & R. Moser, "Turbulence statistics in fully developed channel flow at low Reynolds number," *J. Fluid Mech.* **177**, 133-166 (1987).

7. F. Waleffe, J. Kim and J. Hamilton, "On the origin of streaks in turbulent shear flows", in *Turbulent Shear Flows 8: selected papers from the Eighth International Symposium on Turbulent Shear Flows, Munich, Germany, Sept. 9-11, 1991*, F. Durst, R. Friedrich, B.E. Launder, F.W. Schmidt, U. Schumann, J.H. Whitelaw, Eds., pp. 37-49, Springer-Verlag, Berlin, 1993.

8. J. Hamilton, J. Kim and F. Waleffe, "Regeneration mechanisms of near-wall turbulence structures," *J. Fluid Mech.* **287**, 317-348 (1995).

9. F. Waleffe, "Hydrodynamic stability and turbulence: beyond transients to a self-sustaining process," *Studies in Appl. Math.*, **95**, 319-343 (1995).

10. F. Waleffe, "Transition in shear flows. Nonlinear normality versus non-normal linearity," *Phys. Fluids*, **7**, 3060-3066 (1995).

11. F. Waleffe, "On a self-sustaining process in shear flows," *Phys. Fluids*, **9**, 883-900 (1997).

12. F. Waleffe and J. Kim, "How streamwise rolls and streaks self-sustain in a shear flow," in *Self-Sustaining Mechanisms of Wall Turbulence*, R.L. Panton, Ed., pp. 309-332, Computational Mechanics Publications, Southampton UK and Boston USA, August 1997.

13. Lou Howard has proven stability under no-stress boundary conditions for $U(y) = y$, $1 - y^2$ and $\sin \pi y/2$ (September 1997, private communication).

14. J. Jimenez & P. Orlandi "The rollup of a vortex layer near a wall," *J. Fluid Mech.* **248**, 297 (1993).

15. D. Meksyn & J.T. Stuart, "Stability of viscous motion between parallel planes for finite disturbances," *Proc. Roy. Soc. London A*, **208**, 517-526 (1951).

16. D.J. Benney, "The evolution of disturbances in shear flows at high Reynolds numbers," *Stud. Appl. Math.* **70**, 1-19 (1984).

17. M. Nagata "Three-dimensional finite-amplitude solutions in plane Couette flow: bifurcation from infinity," *J. Fluid Mech.* **217**, 519-527 (1990).

18. A. Conley, "New plane shear flows," *Ph.D. Thesis, California Institute of Technology*, H. B. Keller, advisor (1994).

19. Clever, R.M. and Busse, F.H. "Three-dimensional convection in a horizontal layer subjected to constant shear," *J. Fluid Mech.* **234**, 511-527 (1992).

DETECTION OF TRANSITION AND FLOW BIFURCATION REGIONS ON A HYDROFOIL USING HOT-FILM CONSTANT VOLTAGE ANEMOMETRY

S.M. Mangalam, G.R. Sarma
R.A. Pfouts, and T.S. Kwa
tao@taosystem.com
Tao Systems, Inc.
471 McLaws Circle, Ste. A
Williamsburg, VA 23185

J.H. Casper casper_jh@nns.com
M.A. Wallace wallace_ma@nns.com
H.E. Moghadam
Newport News Shipbuilding
Bldg. 600 4101 Washington Ave.
Newport News, VA 23607

R. Nigon nigon@oasys.dy.navy.mil
NSWC, Carderock Division
9500 MacArthur Blvd.
Code 5600
West Bethesda, MD 20817

Abstract - The potential for global measurement of surface shear stress characteristics with a large number of water-proofed, micro-thin, multi-element hot-film sensor arrays operated by a Constant Voltage Anemometer (CVA) instrumentation system was successfully demonstrated in tests carried out on a 6"-chord NACA 0012 hydrofoil model in the NSWC's 24" water tunnel up to speeds of 7 knots at 0°, 5°, and 10° angles-of-attack. The hydrofoil model was instrumented with an 80-element hot-film sensor array extending from about 30% chord on the lower surface to the trailing-edge on the upper surface. Pressure distribution on the hydrofoil model was obtained with differential pressure gages. Boundary-layer characteristics measured with hot-film sensors were in good agreement with numerical simulations obtained with Reynolds-Averaged Navier-Stokes (RANS) equations and boundary-layer integral methods. The experimental approach described in this paper will be useful for the development and evaluation of various sea-water drag reduction methods.

The classical sequence of phenomena associated with the laminar-to-turbulent transition was very clearly demonstrated in these experiments. The laminar region was characterized by very low amplitude signals followed by the birth of turbulent bursts, their growth, rapid multiplication, and final break-down in the transition region. These classical features were clearly observed in raw, unprocessed signals themselves which were displayed in real time on the computer screen. The transition region was demarcated by the unmistakable presence of large amplitude fluctuations which were orders of magnitude higher than the laminar signal. One of the interesting observations in these experiments was the consistent presence of 'laminar bursts' in the turbulent region mirroring the 'turbulent bursts' in the laminar region. It is conjectured that they arise as a result of laminar separation, transition in the separated shear layer, and subsequent turbulent reattachment which may bring a few 'laminar bursts' from the outer layer to the solid boundary of the model. The leading-edge stagnation, flow separation, and reattachment points were characterized by the presence of a local minimum (cusp) in the mean voltage distribution of signals from sensors located in these bifurcation regions. The bifurcation regions were also identified by the presence of phase reversal signatures in signals from sensors located across the critical region.

I. INTRODUCTION

Identification and characterization of hydrodynamic flow features such as transition, separation, and turbulence around model hulls and control surfaces are critical in the evaluation of the performance of new designs incorporating sea-water drag reduction technology and in validating computational fluid dynamic (CFD) codes. Flush-mounted array of micro-thin hot-film sensors have been used extensively in aero- and hydrodynamic measurements [1-8] to characterize viscous phenomena. The formation of bubbles at high currents, corrosion and degradation of sensors due to electro-chemical reactions, and electrical conductivity of the fluid medium are some of the problems associated with the operation of sensors in water. These problems have resulted in less extensive use of hot-film sensors in hydrodynamic measurements. The need to obtain high sensitivity (without losing bandwidth) at low currents (to prevent bubble formation) and the high power requirements resulting from high thermal conductivity of water are some of the problems associated with the operation of the anemometer. In addition to these problems, the experimenter also faces the possibility of losing sensors due to burn-out and damage from particles present in the flow. There is a need to develop effective water-proofed shear-stress sensors and a suitable instrumentation system to operate them over long periods of testing. The following discussions are based on work recently conducted to demonstrate the use of advanced techniques (developed in aerodynamic measurements) in hydrodynamic test environment. Tests were carried out at the Naval Surface Warfare Center's Carderock facility on a NACA 0012 hydrofoil model instrumented with an array of water-proofed hot-film sensors and differential pressure gages. NASA Langley Research Center provided the technical know-how and assistance in water-proofing the sensors for long-duration applications.

II. TEST OBJECTIVE

The objective of the experiment was threefold:

- Assess the effectiveness of chemical coating on hot-film sensors to insure extended sensor life in under-water applications,
- demonstrate the use of CVA to operate hot-film sensors in water to obtain high sensitivity at low sensor currents (to avoid bubble formation and erosion through electrolysis), and
- detect critical hydrodynamic viscous phenomena such as the boundary-layer transition, flow separation, and flow reattachment regions and compare results with computational predictions.

III. TEST SET-UP AND TEST CONDITIONS

The test model was a 6"-chord, 14"-span hydrofoil with NACA 0012 airfoil section equipped with ten pressure taps that were evenly spaced along the chord of the model to make pressure measurements using the Micro Switch pressure gages. The pressure tubes were 1/16-inch stainless steel tubes having an inside diameter of 1/32 inches. An array of 80-element micro-thin hot-film sensors was glued on to the hydrofoil. The sensor elements were aligned along the centerline of the hydrofoil and extended from about 30% chord location on the lower surface to the trailing edge of the upper surface. The sensor elements were spaced 0.1 inch apart in the chordwise direction (1.66% chord). Holes were punched in the substrate material to expose the pressure orifices to the flow. A special breakout box was used to connect all the 80 sensors from the hydrofoil and connect them to 16-channel CVA instrumentation system in groups of 16 sensors. The output from each of the 16-channel CVA was taken to an auto-zero unit which was used to create a level reference voltage (zero volt) for all the sensors.

A schematic of the instrumentation system is shown in Fig. (1). Tests were conducted in the 24" water tunnel facility at the Carderock Division of Naval Surface Warfare Center. The hydrofoil was tested at 0°, 5°, and 10° angles-of-attack. The free-stream velocity was varied from 1 to a maximum of 7 knots for the lower two angles but restricted to 6 knots for the highest angle because of concern for the structural integrity of the hydrofoil model. Test data was acquired with a 16-channel tape recorder as well as with a 16-channel analog-to-digital converter operated by a laptop personal computer. Data was sampled at 50 Hz with a minimum of 512 and a maximum of 4096 samples for each realization. Over 150 test runs were made at the above test conditions and the experiment was completed in less than two days. On-line display of the test data was accomplished with Tao Systems' data acquisition and analysis software.

Hot-Film Sensors

The hot-film sensors were designed and fabricated by Tao Systems, Inc. The nickel sensor elements were typically about 0.25 microns thick with a nominal cold resistance of about 6 Ohms. The hot-film sensors and copper leads on a polyimide substrate were coated with chemicals to provide electrical insulation for under-water applications. The water-proofing with chemicals was carried out with the support of technical know-how from NASA Langley Research Center. The coated sensor was submerged in water and operated by CVA for many weeks before tests were conducted in the water tunnel. Simultaneously, tests were also conducted on uncoated sensors to evaluate the impact of water on the performance and life of sensors. Preliminary studies also showed that CVA was able to provide high sensitivity without causing problems such as bubble formation. Various combinations of hot-film sensors, in batches of 16, were connected to the 16-channel CVA system and data recorded at different test conditions. In spite of the chemical coating, the signal levels obtained on CVA were large, even with a unity gain, and the maximum sensitivity was in excess of one (1) volt/knot at one knot. Not a single sensor was burnt or damaged in these tests.

Constant Voltage Anemometer

The Constant Voltage Anemometer system has been described in a number of recent publications [9-13]. Constant Current and Constant Temperature Anemometers (CCA and CTA) are the other two types of anemometers used extensively in dynamic measurements. As the name implies, the sensor is maintained at a constant voltage (Fig. 2). The voltage level maintained across the sensor determines the current through the sensor and is used for ohmic heating of the sensor. The thermal gradient between the sensor and the fluid medium results in heat transfer by convection. The changes in sensor temperature due to convection results in changes in sensor resistance and corresponding changes in sensor current is measured across a large resistor R_2.

The output voltage from the CVA is a measure of the convective heat transfer (and conduction losses to the substrate) from the surface hot-films which can be directly related to surface shear stress. Hence the output voltage is expected to be small in laminar boundary layers and high in turbulent boundary layers. The output voltage will also be small when the convective heat transfer and the corresponding shear stress is small as in flow bifurcation regions (leading-edge stagnation point, flow separation and flow reversal regions). In order to effectively detect various critical flow features, the CVA system is equipped with an auto-zero unit which creates a level initial (reference) voltage for all the sensors. Subsequently, the output voltage at any test condition is an indication of relative change in shear stress from the reference condition. The CVA instrumentation system, since it operates on a constant voltage basis, does not suffer from the adverse impact of EMI and RFI, cable length (capacitance) does not pose any operational problems (such as instability or oscillations), has high sensitivity and large bandwidth even at low currents. It is fully automated and requires no critical adjustments.

IV. TEST TECHNIQUES & NUMERICAL SIMULATIONS

Detection of Boundary Layer Transition

Heated element sensors have been used extensively since their introduction by Ludwig [14] and subsequent pioneering work by Liepmann and Skinner [15] who established mathematical expressions relating convective heat transfer and surface shear stress to the measured electrical output from anemometers. In addition to their use in measuring surface shear stress distribution, heated element sensors have also been used extensively in flow diagnostics. Typically the heated elements are operated at elevated temperatures to enable heat transfer to take place from the sensor to the fluid. The convective heat loss experienced by the sensor results in change in the sensor temperature and hence its electrical resistance. This change in electrical properties is used as a measure of the state of the boundary layer. The changes are minimal in a laminar boundary layer. Transition is characterized by the generation of large disturbances that result in large convective heat transfer and when these large eddies breakdown to smaller eddies (turbulent flow), the heat transfer is relatively less compared to the peak transition but significantly higher in the turbulent region than in the laminar boundary layer.

The most commonly used quantifiable criteria to identify laminar-to-turbulent transition region are:

- A significant increase in signal amplitude (dc+ac) and RMS voltages compared to the output voltage in the laminar region.
- A sharp increase in intermittence factor (a self-normalized measure of the turbulence level of the signal, [16-17]) from close to zero in the laminar region to nearly one in the fully turbulent flow.

In addition to these methods, one could also identify boundary-layer transition from power spectra of signals. In the interest of brevity, the present paper describes transition process by observing the raw signals and their RMS distribution.

Detection of Flow Bifurcation Regions

Flow bifurcates at a number of points along the surface of a body in motion. For a two-dimensional body, the streamlines bifurcate first at the leading-edge where the surface streamlines diverge in two opposite directions across the stagnation point Fig. (3). At flow separation, the surface streamlines converge towards each other from two opposite directions. The situation at the flow reattachment point is similar to the leading-edge stagnation point, with the surface streamlines diverging away from each other. One common feature for flow bifurcation regions is that the flow stagnates at these critical points where the convective heat transfer and surface shear stress reach a local minimum and increase monotonically both upstream and downstream of these locations. In terms of hot-film measurements, the sensors located at these points can be looked at as local 'hot-spots' because the fluid convects less heat away from them than from their neighboring sensors which are 'cooler'. In electrical terms, the sensors located at the 'hot-spots' have higher resistance and hence the CVA voltage output from them will exhibit a local minimum. Another property exhibited by the signals from sensors across the bifurcation point is the presence of a phase reversal signature (PRS) caused by the characteristic unsteadiness associated with the flow at these locations [18].

Analytical/Computational Predictions for NACA 0012

Since this experiment was the first attempt to demonstrate the use of water-proofed multi-element hot-film sensors to simultaneously detect transition as well as all the bifurcation points on a hydrofoil model, boundary-layer theory and computational simulations were chosen to serve for the validation of the test results. These numerical simulations were used to predict the locations of separation and transition as a function of chord length. No attempt was made to predict reattachment point. The test cases discussed in this section are: $\alpha = 0°$,

U_∞ = 7 knots; : $\alpha = 5°$, U_∞ = 7 knots; and $\alpha = 10°$, U_∞ = 6 knots. These cases represent the highest free-stream speeds obtained in experiments.

These NACA 0012 [19] test cases have been analyzed in two ways: by boundary-layer integral methods accompanied with empirical formulations, and by numerical solutions of the Reynolds-Averaged Navier-Stokes (RANS) equations. Two-dimensional, steady-state flow conditions were assumed in these computations. The flow separation points were deduced from an inspection of the velocity distribution within the boundary layer of a RANS solution since a 2D separation must be accompanied by flow reversal. Boundary-layer integral methods [20] were applied for the prediction of laminar separation and transition to turbulence.

V. TEST RESULTS

Test Conditions: $\alpha = 0°$, U_∞ = 7 knots (Re = 5.41 x 10^5)

Inspection of the tangential velocity distribution from the RANS solution at one point off the surface ($y^+ = 1$) revealed no flow reversal occurring before the trailing edge, at approximately x/c = 0.99. This value is consistent with the prediction of the boundary-layer integral method which determines the location of the turbulent separation at x/c = 0.998. However, the experimental measurements did not extend to the trailing edge of the hydrofoil. The momentum thickness θ and velocity at the edge of the boundary layer U_e, from the boundary-layer integral method were used to determine laminar-to-turbulent transition with the Michel criterion [21]. For incompressible flows about airfoil shapes, transition is predicted when

$$Re_\theta > 1.174\,(1 + 22{,}400 / Re_x)\, Re_x^{0.46}$$

where $Re_\theta = U_e\, \theta / \nu$ and $Re_x = U_e\, x / \nu$. For the 7-knot case the chord-Reynolds number is 5.46 X 10^5, and the Michel criterion predicts transition at x/c = 0.567.

Figures (4) and (5a) show time series signals (output voltage) obtained from sensors at various chord locations at a free-stream velocity of 7 knots and $\alpha = 0^0$. The first indication of the presence of a turbulent 'burst' is observed at about 13.4% chord. The number of such bursts and their amplitude begins to increase gradually in the beginning, up to about 46% chord, and explosively beyond 50% chord, reaching a peak at about 56% chord. The flow is practically fully turbulent beyond this point.

The RMS distribution is shown in Fig. (5b) for the same test conditions. The different symbols indicate different batches of sensors used to acquire data over the test region. The laminar region appears to extend from the leading edge to about 10% chord beyond which the RMS value begins to increase gradually from the low laminar values. The rate of increase is dramatic beyond about 40% chord, reaching a peak at about 55% chord. As observed in the raw signals, the peak RMS (peak transition) occurs at about 56% chord. Computational results using boundary-layer integral methods predicted transition location at 56.7% chord for the given test conditions, showing that the measured data are in excellent agreement with CFD.

We can observe an interesting feature in the raw signals in the pre-transitional and post-transitional regions: the 'turbulent' bursts in the laminar region appear as mirror images of the 'laminar' bursts in the turbulent region. For greater clarity, the data have been plotted in Fig. (4) for individual sensors in order to clearly show the disturbances levels relative to the mean voltage. In the predominantly laminar region, the sensors experience intermittent turbulent eddies observed as 'bursts' which 'ride' on top of the flat laminar signal. In the transition region (approximately, $0.45 \leq x/c < 0.58$), the disturbances are evenly distributed about the mean voltage level. In the immediate post-transitional region, the mean voltage level itself is relatively higher than the laminar region and the disturbances are primarily below the flat peak, indicating that the flow is primarily turbulent with relatively high rate of heat transfer by convection but occasionally interrupted by the lower heat transfer rates caused by vertical convection of relatively smoother (laminar) flow from the outer edge of the boundary layer. Such a behavior could also exist immediately downstream of the reattachment region of a laminar separation bubble. This phenomenon needs to be studied more systematically.

Figure (5c) shows the CVA output voltage distribution in the leading-edge region for the above test conditions. The sensor located exactly at the leading edge was destroyed during the installation of sensors on the model. The voltage distribution exhibits a cusp at x/c = 0.0365 indicating that the model was initially at a negative angle-of-attack to the flow.

Test Conditions: $\alpha = 5°$, U_∞ = 7 knots

The boundary-layer integral method predicts separation for this test case to occur at x/c = 0.109. Transition is predicted with the Michel criterion to occur at x/c = 0.171.

Raw signals and RMS distributions at $\alpha = 5°$ are shown in Fig. (6). The transition region between the laminar and turbulent boundary layers is clearly observed between 16%-20% chord. This chord location for transition again agrees very well with the theoretical predictions. Compared to the zero-degree angle-of-attack case, where the transition was located at 56% chord, the transition region at $\alpha = 5°$, U = 7 knots moved upstream, as expected.

Figure (6c) shows the mean voltage distribution in the leading-edge region at this test condition. Figure (6b) shows the corresponding RMS distribution. A significant drop in mean voltage at about 10% chord indicates flow separation at this location. Numerical simulations also predicted laminar flow separation to occur at about 10.9% chord. At this location we observe a sharp rise in the RMS distribution. Thus, we can conclude that boundary-layer transition takes place rapidly downstream of the separation point, with the peak occurring at about 20% chord. The next minimum in the mean output voltage occurs at about 28% chord, indicating a turbulent reattachment region of the separation bubble. The RMS distribution also indicates the completion of the transition process and the beginning of a fully turbulent boundary layer downstream of this chord location. Thus, the laminar separation bubble extended from 10% chord to about 28% chord at the above test conditions.

Phase Reversal Signatures

The disturbance amplitude of signals from the hot-film sensors located in the bifurcation region was extremely low compared to other regions. The extremely low noise levels of the CVA system made it possible to measure even a couple of millivolts but, unfortunately, the data acquisition system had only about 4 millivolts resolution. On the other hand, the disturbance amplitude in the transition region sometimes exceeded 2.5 volts. Hence, in order to adequately cover such a large change in voltage levels the test set up will require modifications for future experiments. Incidentally, this is not a problem but a luxury we have to deal with because of the very low noise and high sensitivity of the CVA instrumentation system.

Since the data acquisition system was unable to resolve the very low level of fluctuations in the signals near bifurcation regions, it was not possible to clearly obtain phase reversal signatures in all the cases. However, at low speeds, the unsteadiness in the water tunnel free-stream was sufficient to create large-scale, low-frequency fluctuations in the flow at these critical points. For example, (Fig. 7) shows the mean voltage distribution from sensors located between 25% and 36% chord, indicating that the local minimum in the mean output voltage occurs near 31.72% chord. Raw signals from sensors located in this region Fig. (7) are clearly out of phase with each other indicating the presence of a bifurcation point between them. The RMS voltage levels at these locations (not shown here) are low and indicate a laminar separation between these two sensor locations. Figure (8) shows similar plots for the reattachment region with a clear PRS observed in signals from neighboring sensors. It is worth noting that while the signals from

sensors across the separation point are both indicative of a laminar flow, the sensor signals at reattachment indicate turbulent flow.

Test Conditions: $\alpha = 10°$, $U_\infty = 6$ knots

The chord-Reynolds number for this test case is 4.69×10^5. The boundary-layer integral method predicts separation for this test case to occur at x/c = 0.008. However, this method is not capable of predicting reattachment. Figure (9) depicts the tangential velocity distribution from the RANS solution at one point off the surface. The flow reversal in the 2-6% chord region is indicative of a separation region. Transition is predicted to occur at x/c = 0.06.

The mean voltage distribution shown in Fig. (10c) shows that the leading-edge stagnation point is at about 6% chord on the lower surface. Laminar flow separation occurred practically at the leading-edge of the hydrofoil followed by rapid transition to turbulence near 5% chord. Flow reattachment appears to take place near 9% chord. As in the previous test case, the flow separation and reattachment points also coincide with the beginning and end of transition to turbulence as shown by the raw signals and RMS distribution Figs. (10a,b). Again, the agreement with theoretical predictions is excellent.

VI. CONCLUSIONS

- Water-proofed, micro-thin, multi-element hot-film sensors were successfully used in water-tunnel tests on a hydrofoil model. Not a single sensor was burnt or damaged in the experiment.
- Tao Systems' Constant Voltage Anemometry system was successfully used to operate these sensors in water to obtain high sensitivity at low sensor currents without bubble formation and erosion through electrolysis.
- Advanced flow diagnostics techniques were successfully used for the detection of critical boundary-layer characteristics such as transition, flow separation, and flow reattachment regions.
- Computational results showed very good agreement with test results.
- The low noise feature of the CVA made it possible to measure the very low fluctuating signal levels (of the order of 2 mV) present in the bifurcation region and the high sensitivity provided extremely large signals in the transition region. Additional work is required to properly accommodate this wide range of signal levels in future experiments.

VII. ACKNOWLEDGMENT

A number of new techniques were tried in this experiment which could not have been made possible without the participation and help received from many individuals. We sincerely acknowledge the help received from Dave Bochinski and Dave Fishpaw of NSWC, Jim Bartlett of NASA Langley Research Center, and Bob Lankes of Tao Systems, Inc., for their assistance at various stages of this experiment.

VIII. REFERENCES

1. W. Bechteler, H. B. Kleeberg, H. Teichmann, and H. J. Vollmers "Application of Hot-Film Probes for Measurement of Wall Shear Stress in Water", *Institut fur Wasserwesen,* Germany 1992.

2. B. J. Bellhouse and D. L. Schultz "Determination of Mean and Dynamic Skin Fricion, Separation, and Transition in Low Speed Flow With a Thin-film Heated Element", *Journal of Fluid Mechanics,* Vol. 24, pt. 2, 1966.

3. H. H. Bruun "Hot Wire Anemometry, Principles and Signal Analysis", *Oxford University Press,* 1995.

4. R. Houdeville and J. C. Juillen "Skin Friction Measurement With Hot Elements", *in VKI Lecture Series 1989-05, Measurement Techniques in Aerodynamics,* April 1989.

5. S. M. Mangalam, J. P. Stack, and W. G. Sewall "Simultaneous Detection of Separation and Transition in Surface Shear Layers. Fluid Dynamics of Three-Dimensional Turbulent Shear Flows", *AGARD CP-438,* 1988.

6. S. M. Mangalam, G. R. Sarma, and S. Kuppa "Quantitative Flow Diagnostics Techniques for Unsteady Aerodynamics", *PICAST2-AAC6 International Conference,* Australia, 1995.

7. S. M. Mangalam, G. R. Sarma and T. R. Moes "In Flight Shock Detection Using Hot-Film Sensors and Constant Voltage Anemometer System", *To be presented at the 21st Congress of ICAS,* Melbourne, Australia, Sep. 1998.

8. V. A. Sanborn "Resistance Temperature Transducers", *Metrology Press,* 1972.

9. G. Comte-Bellot "Hot Wire Anemometry", *Handbook of Fluid Dynamics,* ed. R. W. Johnson, CRC Press, 1998.

10. M. S. Kegerise and E. F. Spina "A Comparative Study of Constant Voltage and Constant Temperature Hot-Wire Anemometer in Supersonic Flows", *3rd International Symposium on Thermal Anemometry,* San Diego, CA., July 1996.

11. M. A. Kegerise "A Study of the Constant Voltage Hot-Wire Anemometer", *M. S. Thesis, Syracuse University,* 1997.

12. G. R. Sarma "Analysis of a Constant Voltage Anemometer Circuit", *IEEE/IMTC Conference,* May 1993.

13. G. R. Sarma "Transfer Function Analysis of the Constant Voltage Anemometer", *Review of Scientific Instruments,* to be published June, 1998.

14. H. Ludwig "Instrument for Measuring the Wall Shearing Stress of Turbulent Boundary Layers", *NACA TM-1284,* 1950.

15. H. W. Liepmann and G. T. Skinner "Shearing Stress Measurements by Use of a Heated Element", *NACA TN-3268,* 1954.

16. S. Dhawan and R. Narasimha "Some Properties of Boundary Layer Flow During the Transition from Laminar to Turbulent Motion", *Journal of Fluid Mechanics,* Vol. 3, pt. 4, pp.418-436, January 1958.

17. S. P. Schneider "Improved Methods for Measuring Laminar-Turbulent Intermittency in Boundary Layers", *Experiments in Fluids 18,* pp. 370-375, 1995.

18. S. M. Mangalam "Instrumentation System for Determining Flow Stagnation Points", *US Patent No. 5,218,863.* June 1993.

19. I. H. Abbott and A. E. Von Doenhoff "Theory of Wing Section" *Dover Publications, Inc.* 1959

20. J. Moran "Theoretical and Computational Aerodynamics", *New York: John Willey and Sons,* 1984.

21. R. Michel "Etude de la Transition sur les Profiles d'Aile", *ONERA Report 1-1578A,* 1951.

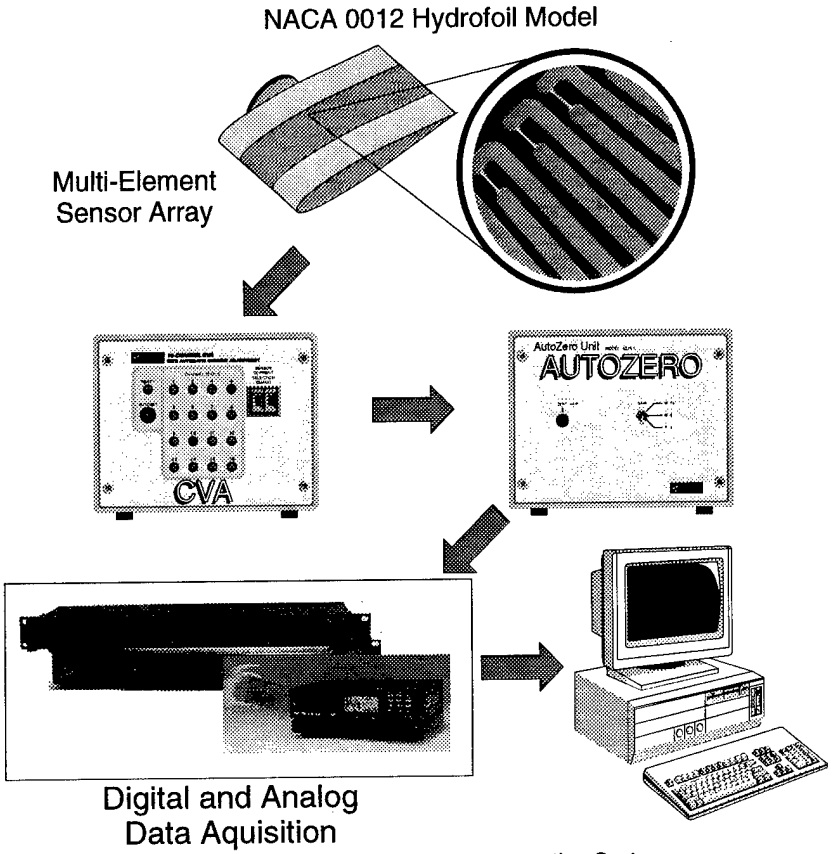

Fig. 1 - Schematic of the Hot-Film Instrumentation System

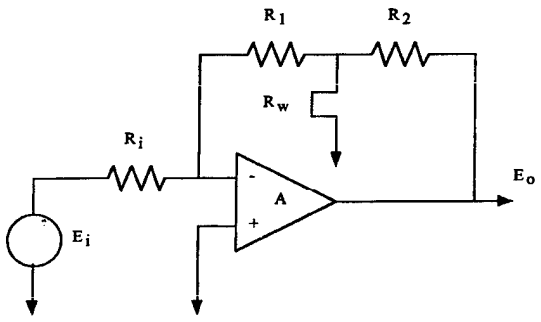

Fig. 2 Basic Constant Voltage Circuit

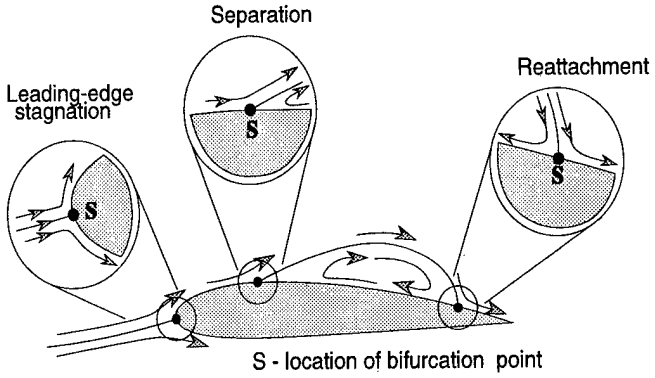

Fig. 3 Flow Bifurcation Region

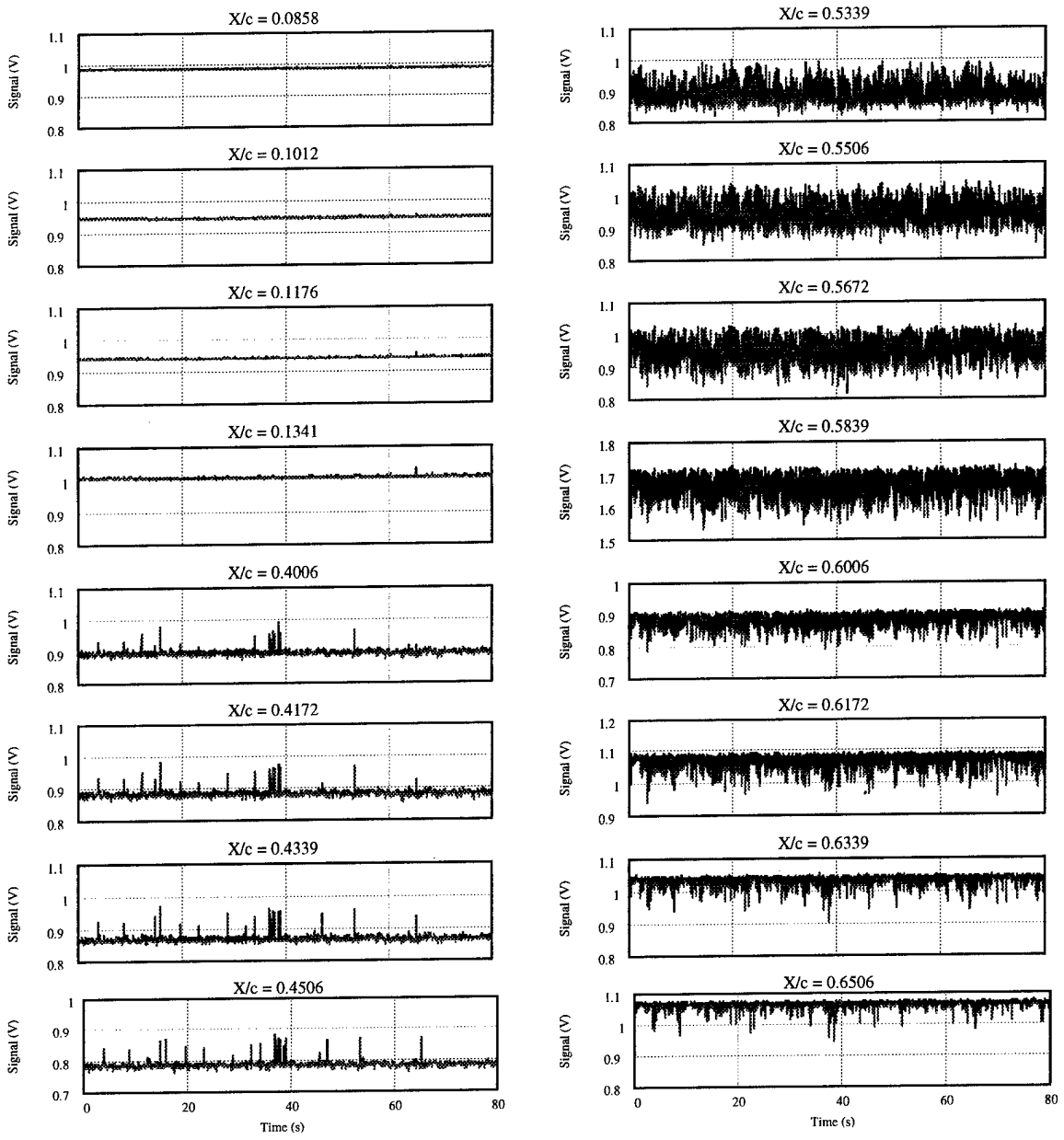

Fig. 4 Raw CVA output signals from various sensors. $\alpha = 0°$, $U_\infty = 7$ knots

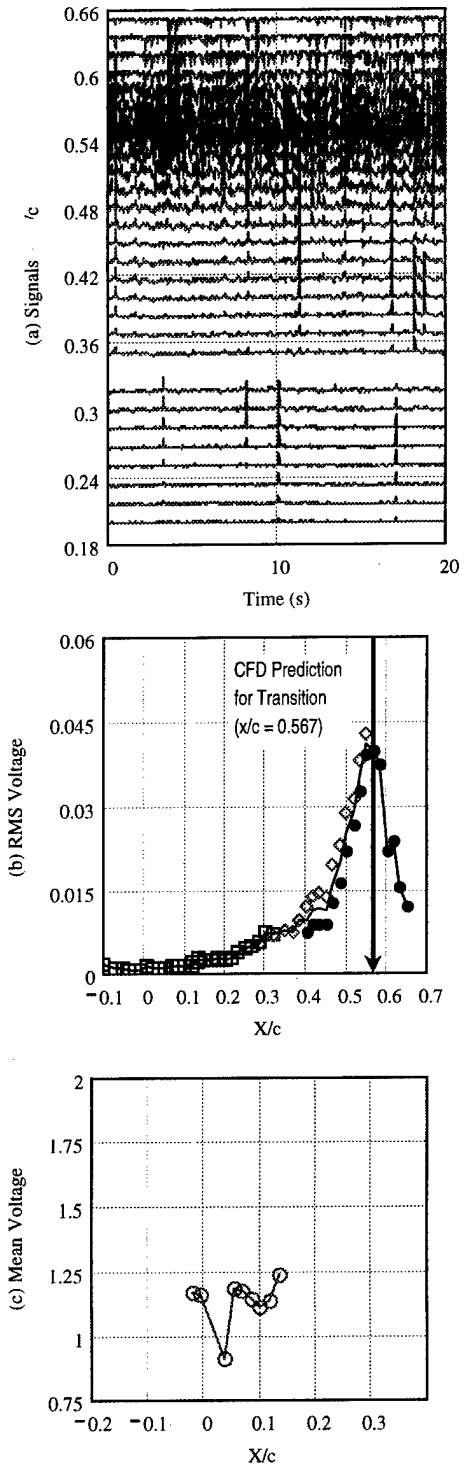

Fig. 5

Raw Signals, RMS and Mean Output Voltages.
α=0°, U_∞ =7 knots.

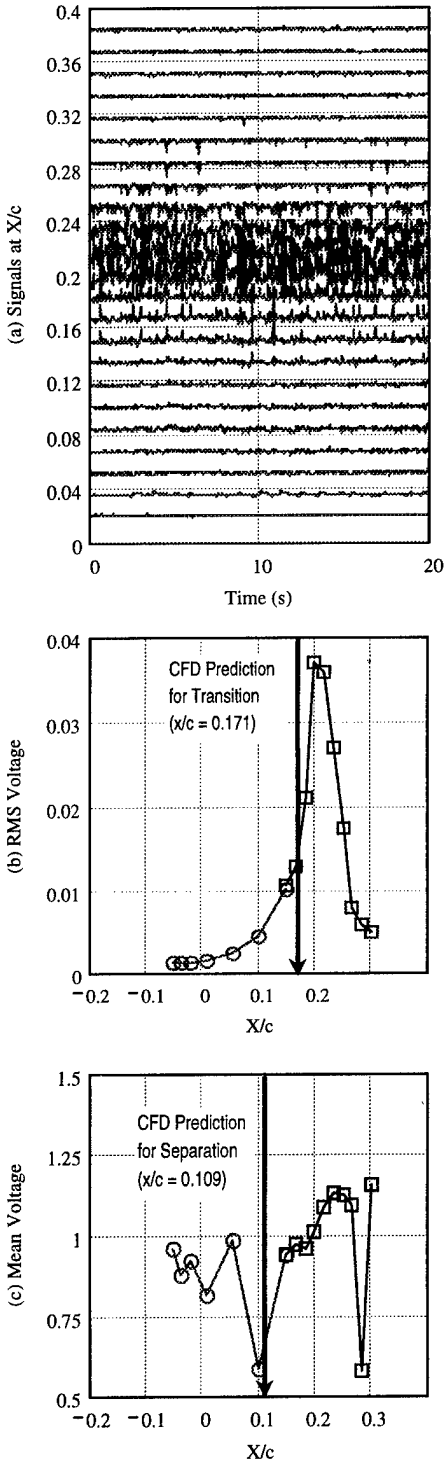

Fig. 6

Raw Signals, RMS and Mean Output Voltages.
α=5°, U_∞ =7 knots.

Mean Voltage Distribution at Separation. $\alpha = 5°$, $U_\infty = 1$ knot

Fig. 7

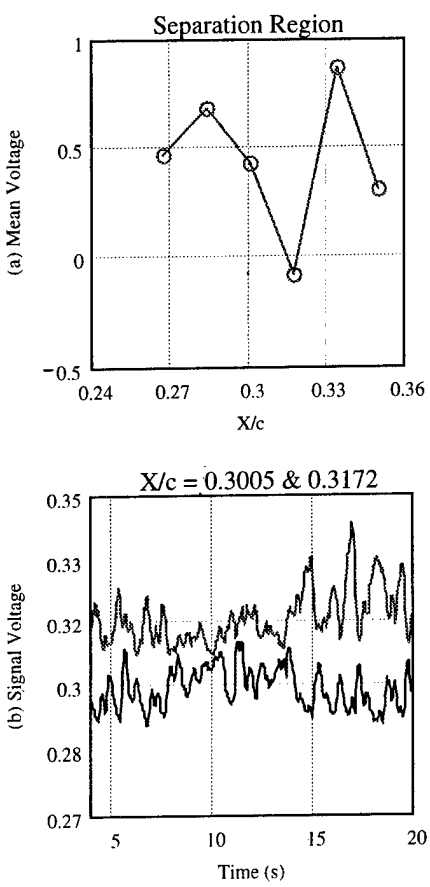

Mean Voltage Distribution at Reattachment. $\alpha = 5°$, $U_\infty = 1$ knot

Fig. 8

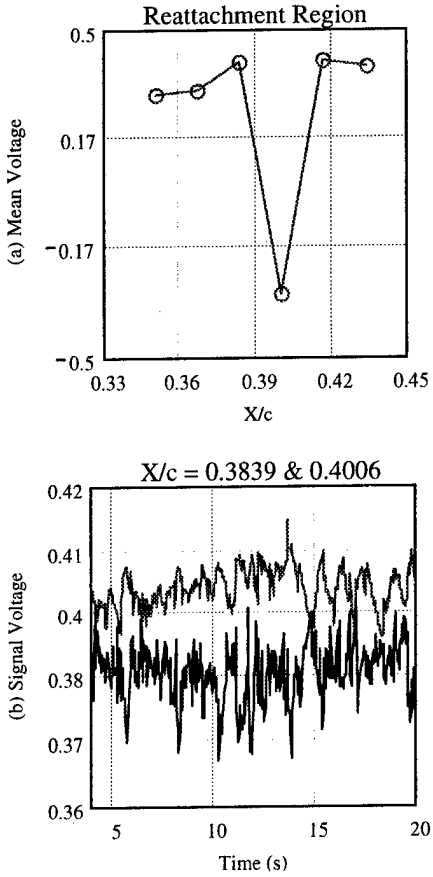

Fig. 9 RANS Solution for $\alpha = 10°$, $U_\infty = 6$ knots

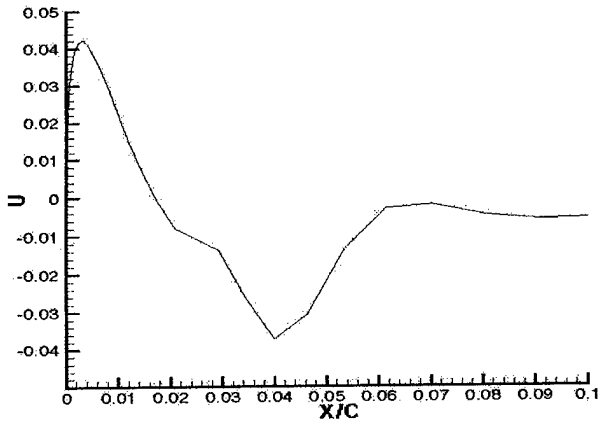

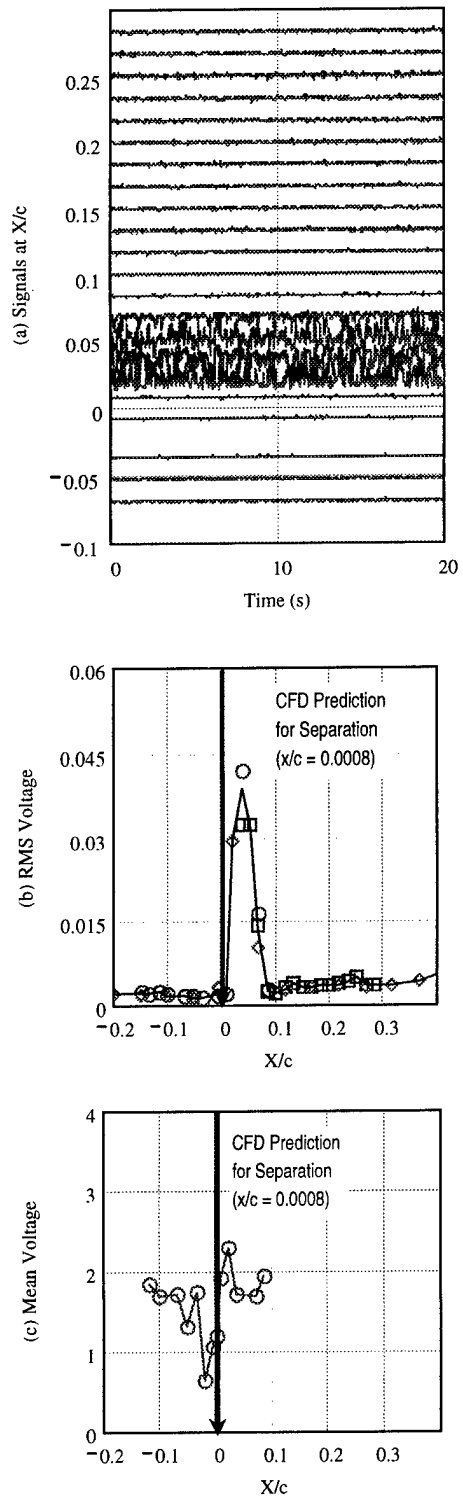

Fig. 10
Raw Signals, RMS and Mean Output
Voltages $\alpha = 10°$, $U_\infty = 6$ knots

MEASURED WALL PRESSURE SIGNATURES OF TURBULENCE PRODUCING STRUCTURES

Steven J. Russell
Naval Surface Warfare Center
Carderock Division, Code 725
9500 MacArthur Blvd
West Bethesda, MD 20817-5700
srussell@oasys.dt.navy.mil

Abstract - An extensive database of simultaneously obtained wall pressure and velocity measurements was acquired for a high Reynolds number, equilibrium turbulent flow. These data were obtained in both streamwise and spanwise measurement planes using an array of wall pressure transducers. Analyses of these data were performed to examine the spatial extent and convective features of turbulence producing structures.

Several signal processing techniques were shown to extract detailed structural features of the turbulent motions. These techniques included digital band-pass filtering to discriminate between turbulent scales and a localized variance method for the detection of clusters of high frequency turbulent activity.

Cross-spectral, cross-correlation, and conditional sampling methods applied to these data clearly show the dynamic relationships between coherent turbulent motions as well as their induced wall pressure signatures. Both pressure-velocity correlation results and conditionally averaged maps of the flow field sampled on peak wall pressure events, reveal a consistent correlation between large scale motions and near-wall, small scale turbulent production activity. The large scale vortical motions (or shear layers) extend across the turbulent boundary layer and exhibit Reynolds stress (turbulent production) characteristics. These findings are consistent with many of the proposed conceptual models of organized motions.

I. INTRODUCTION

Active turbulence control schemes, whether for drag reduction, noise/vibration reduction, or other purposes, must tackle the turbulence production process. Since turbulence is inherently self-sustaining, to disrupt its effect on a body, an active control method must be developed which affects the production chain. The purpose of this investigation is to examine the dynamic relationships between coherent motions related to turbulent production in a boundary layer. This is achieved by measuring the spatial and temporal characteristics of these structures as seen in their velocity and wall pressure statistics. If a model for the wall pressure signature of these motions could be defined, turbulent production events could then be identified using pressure sensors as part of the detection loop of a control system.

An explicit criterion for turbulent production or "active" motions can be established by examining the equation for the turbulence kinetic energy:

$$\frac{DK_T}{Dt} = -\overline{u_i u_j}\frac{\partial U_i}{\partial x_j} - \nu\overline{\frac{\partial u_i}{\partial x_j}\frac{\partial u_i}{\partial x_j}} - \frac{\partial}{\partial x_j}\left[\overline{K_T u_j} + \frac{\overline{p u_j}}{\rho} - \nu\frac{\partial K_T}{\partial x_j}\right] \qquad (1)$$

where D/Dt is the substantial derivative, ρ is the density, and p is the fluctuating pressure. Overbars represent time averages. The focus of this investigation is the first term, turbulence production, characterized by the interaction of the Reynolds stress $-u_iu_j$ with the mean shear gradient. In the flow field studied in this investigation, positive production occurs when $u < 0$, and $v > 0$ or $u > 0$, $v < 0$, which correspond to the second and fourth quadrants of the u-v plane. These motions are commonly referred to as Q2 and Q4 motions, or ejections and sweeps of fluid. The wall pressure signatures of these active motions are the focus of this investigation and are measured using an array of flush-mounted pressure transducers.

II. BACKGROUND

Recent research in the field of turbulent boundary layers, numerical and experimental, has yielded a multitude of descriptions or models of the turbulence production process and the structures involved. Robinson[1] compiled a summary of turbulent structures identified by the turbulence community in the last 40 years and divided them into eight categories:

- Low speed streaks in the viscous sublayer.
- Lifting and ejection of these streaks.
- Subsequent sweep of high speed fluid inward.
- Vortical structures of varying form.
- Sloped near-wall shear layers with high spanwise vorticity.
- Near wall pockets swept clean of marker fluid (splats).
- δ-scale motions capped by the inner/outer interface.
- Shear layer backs of these motions.

Two fundamental questions that have challenged researchers are: which of these inner and outer layer structures play the dominant role in the physical mechanism governing turbulence, and to what extent do these structures interact during these production and maintenance processes? Since nearly 80 percent of turbulence energy is produced during the quasi-periodic burst/sweep events,[2] disrupting this process is the key to active control. If a link could be established between the near wall, turbulent production events and other larger scale structures in the outer flow (shear layers, backs, etc.) then detection of the large scale structures could be used to predict or pinpoint turbulent production events.

Many researchers have proposed models which describe the kinematic and dynamic processes of turbulence production. Theodorsen[3] first proposed a horse shoe or hairpin-like vortex model based on the vorticity transport form of the Navier-Stokes equations. Willmarth and Tu[4] proposed a model for the average near wall eddy structure based on space time correlations between wall pressure and velocity. Again, the hairpin vortex was the dominant theme; however, they extended the influence of the vortex to the outer edge of the boundary layer. Offen and Kline[5], Hinze[6], and many others suggested similar models based on the lift up and ejection of horseshoe-like vortical structures in the near wall region of the turbulent boundary layer. A relationship between coherent outer motions and near wall turbulence production was presented by Praturi and Brodkey[7] where near wall ejections were induced by the passage of δ-scale shear layers. Falco[8] also suggested that large scale outer structures affect but do not govern near-wall production. Thomas and Bull[9] demonstrated that near wall, high frequency activities were associated with the passage of large-scale organized flow structures by correlating filtered pressure and velocity data.

Kline[10] reviewed the results of several DNS studies and found that two types of vortices are found to be "central structures"

- inner layer: tilted streamwise vortices (legs)
- outer layer: transverse vortices (heads)

The two forms overlap in the log-law region of the boundary layer. Kline further concluded that these structures are strongly related to the production process. Robinson[11] attributes most of the eight structures listed earlier to these vortical structures, including the δ-scale shear layers. Many other models with similar features have been proposed which share a common theme; that is, sweeps and ejections play significant roles in maintaining turbulence and that hairpin-like vortices appear to be the dominant structures.

Farabee[12] showed that high-frequency pressure fluctuations were associated exclusively with sources near the wall. Farabee also demonstrated the influence of large scale, outer layer disturbances on the low frequency pressure fluctuations as well as on the value of the RMS wall pressure. Karangelen[13] confirmed that large amplitude wall pressure events are footprints of the near-wall bursting cycle.

Wilczynski's[14] analysis suggested that positive and negative peak wall pressure events are often components of the ejection/sweep, or burst cycle. Johannson, Her, and Haritonidis[15] also found that negative wall pressure peaks were associated with sweep-like motions. Schewe,[16] who visually tracked pressure producing structures in time records from an array of pressure transducers, attributed them to sources near the wall ($y^+<21$). Kammeyer[17] observed the presence of an inclined vortical structure associated with large amplitude pressure events.

Repeatedly, structures associated with turbulence production have been demonstrated to impart a pressure signature at the wall. The primary intent of the experiments documented here was to measure the spatial extent of both the structures in the boundary layer and that of their induced wall pressures. Through various signal processing techniques, a correlation between large and small scale turbulent motions was also uncovered which is consistent with many of the turbulent boundary layer models discussed above.

III. THE EXPERIMENT

The experiments in this investigation were conducted in the Catholic University of America (CUA) Low Noise Flow Facility shown schematically in figure 1.

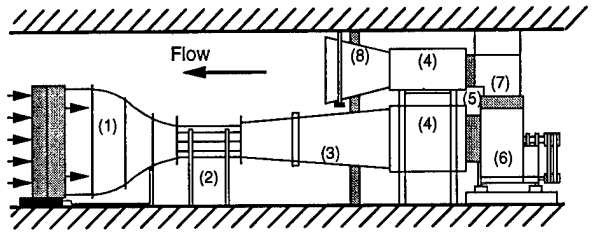

Figure 1. CUA Low Noise Flow Facility features (1) inlet section (2) test section (3) diffuser (4) muffler (5) coupler (6) blower/motor (7) turn vanes (8) return duct

All experiments in this investigation were conducted with an equilibrium turbulent boundary layer and a free stream velocity of approximately 16 m/s (50 ft/s). Detailed boundary layer characteristics are given in table I. Wall pressure measurements were made using Endevco model 8507-C2 piezo-resistive pressure transducers, which are described in detail in Russell.[18] Boundary layer characteristics were measured using a TSI type 1261 A-T1.5 miniature boundary layer probe. All two-component velocity measurements were made with a TSI type 1249 A-10 miniature "X" probe. The data acquisition system is described in detail in Kammeyer.[17]

Parameter	SI	English
Freestream Velocity, U_0	15.33 m/s	50.28 ft/s
Shear Velocity, u_τ	0.59 m/s	1.93 ft/s
u_τ/U_0	0.038	
Boundary Layer Thickness, δ	2.73 cm	1.075 in
Viscous TBL Thickness, δ^+	1026	
Displacement Thickness, δ^*	0.49 cm	0.195 in
Momentum Thickness, θ	0.34 cm	0.133 in
Reynolds No., Re_τ	3364	
Shape Factor, H	1.4606	
C_f, calculated	0.00285	
C_f, measured	0.00295	

Table I. Boundary Layer Parameters

The purpose of the wall pressure array was to track and measure the spatial extent of near wall turbulent structures. To resolve the small scales at which these structures exist, the sensing diameter of the transducer had to be minimized ($d^+=39$). The orientations of the wall pressure arrays are shown in figure 2.

Two sets of experiments were performed. The first set involved the exclusive measurement of fluctuating wall pressure with both streamwise and spanwise transducer arrays. The second set of experiments involved the simultaneous measurement of pressure and velocity. Figure 2 also illustrates the orientation of the hot wire system during the velocity surveys. To map the flow field in the X-Y plane, three different cross-wire surveys were conducted downstream of the

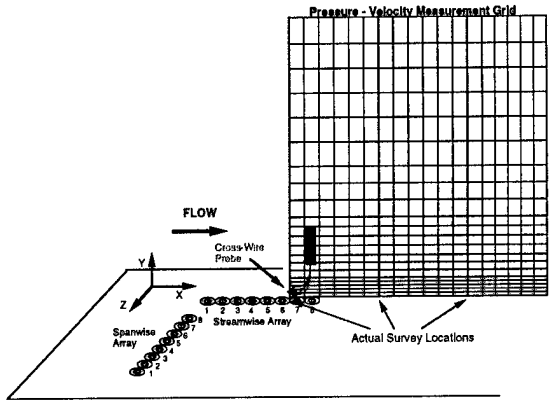

Figure 2. Sensor Configuration During Wall Pressure and Velocity Measurements.

streamwise transducer array. The result was a rectangular grid (18 x 30) at which wall pressure and velocity signals could be simultaneously sampled and compared using correlation and conditional sampling techniques. A similar grid (10 x 30) was generated in the Y-Z plane using the spanwise transducer array. In each of the experiments, the pressure and velocity signals were sampled simultaneously at a rate of 32,768 Hz for a period of 10 seconds.

Facility noise as well as transducer noise were first removed by filtering with a broadband, band-pass digital filter (filter 0). Based on the behavior of velocity spectra measured outside the boundary layer (see Russell[18]) a filter was chosen to remove the scales associated with the outer "irrotational bulge." These motions were assumed to be passive since no conclusive evidence exists that these structures are associated with turbulent production. This band-pass filter (filter 1) had cutoff frequencies of 100 and 300 Hz. A third filter was chosen with cutoff frequencies of 300 and 1200 Hz (Farabee's[12] "universal" range). Finally, a high frequency band-pass filter was chosen which best duplicated the performance of Kammeyer's[17] wavelet filter. This frequency range was shown by Kammeyer to capture the near-wall burst/sweep activity. The three filters are listed in table II. Figure 3 shows the spectral effect of these filters on a typical wall pressure signal.

Filter Number	Frequency Band (Hz)	Spectral Region
0	100-5000	Broadband
1	100-300	"Mid"
2	300-1200	"Universal"
3	1200-5000	"High"

Table II. Bandpass Filter Break Frequencies

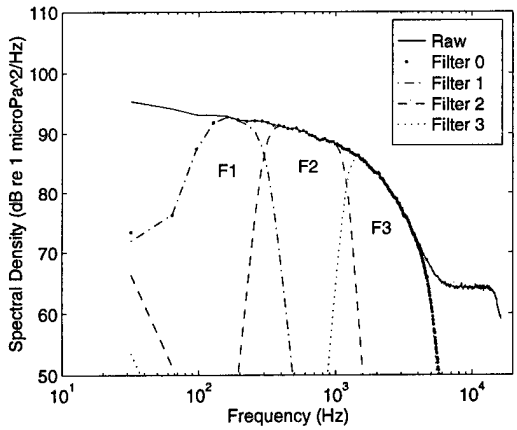

Figure 3. The Spectral Effects of Band-Pass Filters on a Typical Wall Pressure Signal (U_0=15.3 m/s)

Another form of scale discrimination or filtering was applied to pressure and velocity signals in an attempt to detect turbulent events. This was the Variable Interval Time Average or VITA function, (Blackwelder[19]) which is a measure of the localized variance of a signal over a time window, T_v, an adjustable integration time. T_v can be changed to fit the time scales of the events of interest, allowing the VITA method to be applied to velocity and pressure signals which have been band-pass filtered.

IV. SPACE TIME CHARACTERISTICS OF THE WALL PRESSURE FIELD

Signals from the streamwise and spanwise wall-pressure arrays were analyzed for information about the space-time characteristics of the wall pressure field. These methods included spectral analysis, cross-correlation measurements, and conditional sampling. The results successfully demonstrate the spatial extent of the wall pressure signatures of organized structures. Correlation and conditional sampling results are also presented for both the streamwise and spanwise transducer arrays.

Streamwise Correlation Results

The correlation coefficient, $R_{pp}(\tau)$, was computed between the upstream-most transducer (p1) and each of the remaining transducers in the streamwise array (p1 to p8). This computation was made over a segmented time span, ΔT, and then repeated for successive time spans until the end of the time record was reached. The individual correlation functions were then ensemble averaged. Typical results of this computation are shown in figure 4 for time records that were subjected to filters 0,1,2 and 3.

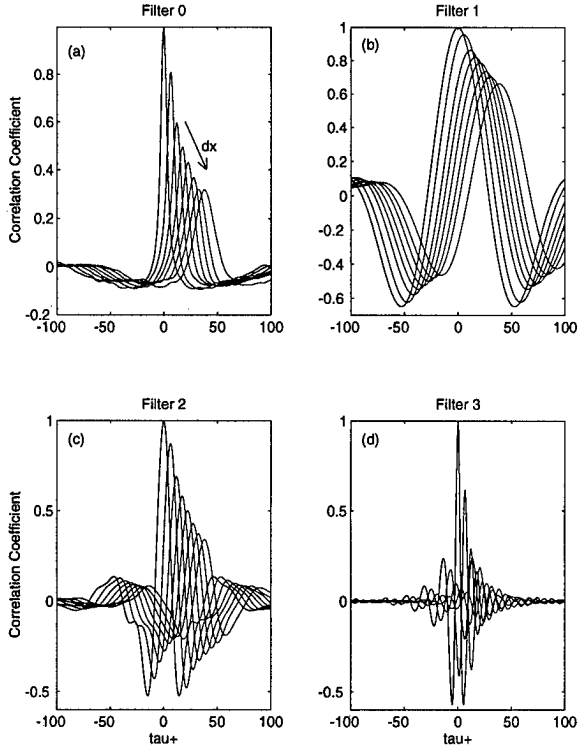

Figure 4. The ensemble averaged correlation function between transducer pairs in the streamwise array, (a) unfiltered, (b) filter 1, (c) filter 2, (d) filter 3.

Figure 4a shows $R_{pp}(\tau)$ for wall pressure time records subjected to filter 0, which is the baseline data, free from background and electrical noise, hereafter referred to as "unfiltered" data. Several distinctive features of these data are worth noting. First, the exponential decay with streamwise distance of the magnitude of the maximum correlation is consistent with the exponential decay of the coherence function seen by other investigators.[12,18] Second, as the separation distance between the transducers is increased, the width of the correlation function broadens. This is also consistent with the spectral results which showed the measured influence of the large scale, low frequency pressure fluctuations increases with transducer separation, ie., the turbulent structures which remain well correlated across the length of the array define the shape of the correlation function between first and last transducers.

The cross-correlation function computed for signals subjected to filter 1 are shown in figure 4b. The shape of $R_{pp}(\tau)$ changes dramatically when only a narrow band of frequencies is considered. The overall shape of the correlation is quite different. Rather than the pulse-like shape of the broad band (filter 0) correlation function, $R_{pp}(\tau)$ for the low frequency (filter 1) appears more wave-like. By removing the high frequency components of the wall pressure signal, a physically relevant correlation function of the pressure sources due to the irrotational flow is exposed. The same general trend is observed as the filter cutoff frequencies are increased (filters 2 and 3).

The spatial decay rates of the maximum cross-correlation for each of the filters tested are re-plotted versus streamwise distance in figure 5a. It is clear from these curves that the decay rate of $R_{pp}(\tau)_{max}$ of the wall pressure signals is highly dependent on the filtering applied. From these data it would appear that high frequency (filter 3) wall pressure activity is only correlated out to one half the boundary layer thickness ($\delta/2$) in the streamwise direction.

The convection velocity of the wall pressure field can be computed from the time delay between peaks in the correlation functions and the separation distance between the transducers. Results of this computation, using the upstream-most transducer as the reference, are shown in figure 5b. The slightly rising convection velocity with transducer spacing is also consistent with Farabee's spectral results. More important however, is the variation of U_c with the choice of filtering. U_c computed from broadband data (filter 0) as well as that from filters 2 and 3 appear to collapse on each other. The scales associated with filter 1, those in the outer-irrotational flow, convect at consistently higher velocities across the array. It appears that the scales associated with filters 2 and 3 convect at approximately the same speed and this speed corresponds to that measured by cross-correlation functions of the broad-band, (filter 0) data.

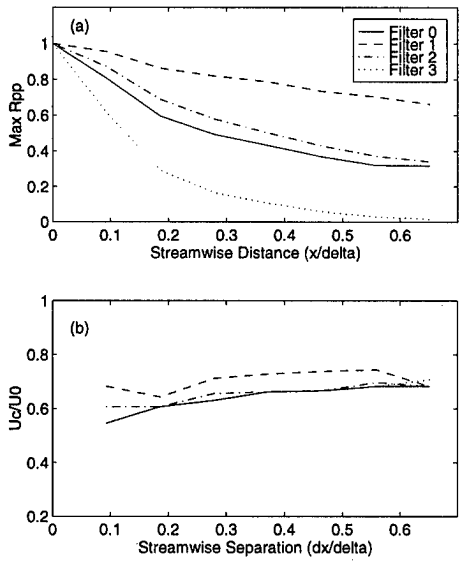

Figure 5. Convective features of the cross-correlation function for the streamwise array, (a) mean decay of peak correlation coefficients, (b) convection velocity based on mean time between peaks.

As shown in figure 5a, the magnitude of the cross-correlation of the high frequency wall pressure signal decays rapidly with transducer separation. These pressure signatures are generally attributed to burst events in the near wall region. This would suggest that the spatial influence of the ejection/sweep processes are limited to 3 or 4 transducer spacings in the streamwise direction. However, this is not the case. The spatial influence of these near wall structures is much larger. A shortcoming of the standard cross-correlation function is that it fails to illustrate the true influence of these scales because the pressure signature of these structures changes rapidly as they convect.

A more appropriate method of measuring the spatial influence of these burst events is to correlate the wall pressure signals based on a measure of the localized energy contained in clusters of these short time events.

Figure 6 shows the normalized correlation between the VITA functions at two streamwise transducers computed exclusively from filter 2 and filter 3 wall pressure signals. The results for filter 2-filter 2 and filter 3-filter 3 correlations show consistently strong correlations over the spatial extent of the streamwise array for both the pressure signatures of the larger scale structures (filter 2) and the near-wall burst events (filter 3).

By comparing figure 4d and figure 6b an important feature of high frequency wall pressure signals is revealed. That is, the appearance of individual near-wall burst events in the wall pressure signal is distorted as it convects downstream, deteriorating the temporal correlation between transducers. However, the cluster of turbulent activity associated with the event, identified in the VITA calculation of the signal's variance, remains well correlated as it convects the length of the transducer array. And as shown in figure 5b, this cluster of burst activity appears to convect with the same speed as the larger structures captured by filter 2.

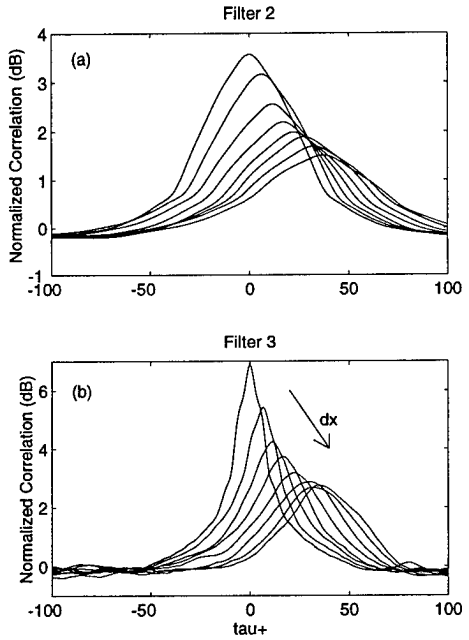

Figure 6. Normalized correlation based on the localized variance (VITA) functions of filtered wall pressure signals from the streamwise array, (a) filter 2, (b) filter 3.

Streamwise Conditional Sampling Results

Conditional sampling and ensemble averaging of wall pressure peak events can also yield information on the spatial and convective properties of the wall pressure field, however, with this approach, the intermittent, high amplitude wall pressure fluctuations can be extracted from the total signal and examined for their own spatial and convective features.

Conditional sampling results from the streamwise array are shown in figure 7. Wall pressure signals from each transducer were conditionally sampled based on the detection of peak events (k=+3) occurring at the upstream-most transducer (p1). The signals from each of the transducers were then ensemble averaged over a fixed time window centered at the peak detection time. This computation was performed on time records that were subjected to filters 0,1,2, and 3. The conditionally averaged event shapes at each of the eight transducers in the array are shown in separate plots for each of the filtered time records. The average shape of the events is similar to the shape of the corresponding correlation functions in figure 4. The broadening and exponential decay of the filter 0 event shapes as well as the clarifying effect of the other filters is similarly reflected in these data.

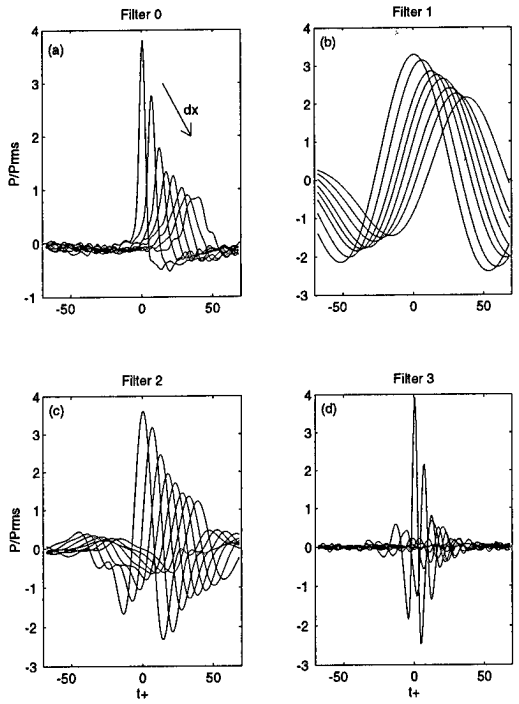

Figure 7. Downstream wall pressure signals conditionally averaged on peak wall pressure events (k=+3) at the first transducer in the streamwise array, (a) unfiltered, (b) filter 1, (c) filter 2, (d) filter 3.

The mean convection velocity, U_c, can also be determined by measuring the time delay between peaks in the conditionally averaged event shapes. The results for each of the four filters is shown in figure 8. The collapse of the filter 2 and filter 3 curves on the filter 0 curve is not as apparent as with correlation results, however, the events sampled in the filter 1 time records do appear to convect consistently faster than the events detected in the other (high frequency) signals.

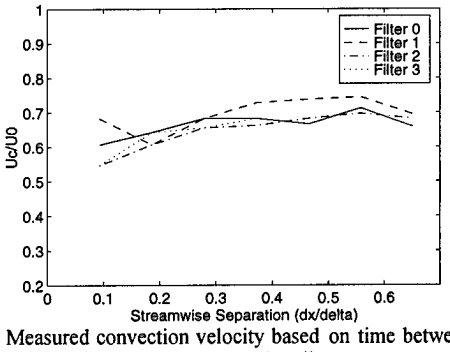

Figure 8. Measured convection velocity based on time between peaks in the streamwise conditionally averaged wall pressure events.

The convection velocity results presented so far (cross-correlation, and conditional sampling) consistently show that wall pressure events associated with the scales defined by filters 2 and 3 have similar convection velocities (U_c/U_0) of between 0.55 and 0.7. This places the center of these pressure sources at ($50<y^+<250$), the log-law region of the boundary layer.

Spanwise Conditional Sampling Results

To illustrate the spanwise extent of the wall pressure field, results from the spanwise conditional sampling experiments are presented. Absent the convective effects, the conditionally averaged event shapes resemble the shapes of the streamwise conditional averages in figure 7. However, rather than view the event shapes in the time domain, it is possible to project the event shapes onto the X-Z plane using Taylor's hypothesis. By assuming a frozen, convecting pressure field, the conversion from time to space is accomplished simply via the average measured convection velocity by $X^+=U_c^+t^+$. The wall pressure signals

for each transducer in the spanwise array (p1 to p8) were conditionally sampled and ensemble averaged on the detection of peak events (k=+3) at p4, a transducer at the center of the array. Time was converted to space using the average convection velocities, computed for each filter from the streamwise cross-correlation results. Contour plots from the resulting ensemble averaged event shapes (P/P_{rms}) are shown in figure 9. The streamwise (x^+) scale of the filter 1 curve has been expanded to accommodate the large streamwise extent of the wall pressure events detected in that signal. The average spatial extent of high amplitude wall pressure events from the unfiltered (filter 0) do not appear elongated in the streamwise direction like those of Kim[20] for a simulated channel flow, however, they do exhibit the same nominal spatial extent.

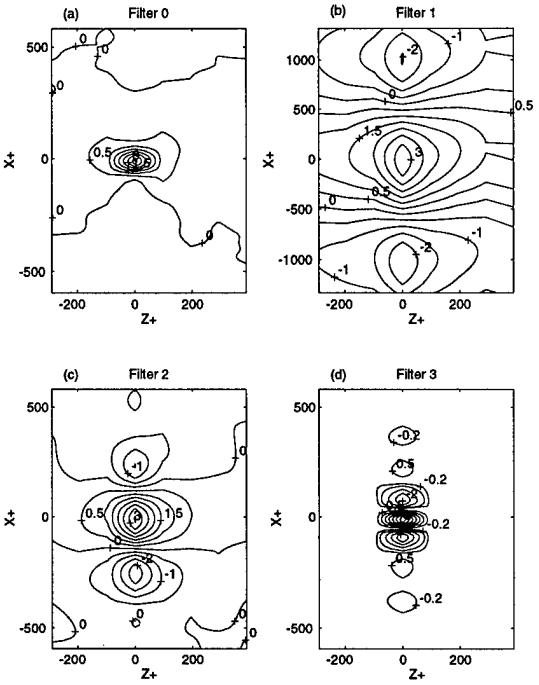

Figure 9. Contours of spanwise wall pressure signals conditionally averaged on peak wall pressure events at P4 (k=+3), (a) unfiltered, (b) filter 1, (c) filter 2, (d) filter 3.

Examining the data in figure 9 collectively, one sees the complexity of the turbulent wall pressure field. Clearly, the wall pressure signal is composed of many large and small scale events. The wall pressure signatures of these events varies greatly with the filtering performed on the original signal. Not suprisingly, the wall pressure events associated with scales characteristic of the irrotational flow (filter 1) have a much larger spatial extent than the streamwise or spanwise dimensions of the transducer array, and yet, the events detected in the filter 3 data are nearly too small to resolve with the transducer array used.

Correlation of Large and Small Scale Structures

The possibility that large scale (filter 2) and small scale (filter 3) wall pressure signatures are correlated was suggested by their matched convection velocities. Several of the turbulence production models discussed in Section II are based on this type of correlation in which there is a causal relationship between large and small scale turbulent activity. Thomas and Bull,[9] for example, correlated the passage of large scale, inclined shear layer with small scale, near wall, turbulent production activity. The relationship between the scales in the wall pressure field are now examined using the cross-correlation and conditional sampling methods already demonstrated.

Streamwise VITA correlation results presented earlier illustrated that small scale events occur in clusters of large amplitude positive and negative peaks, and that while the pattern of peaks in the cluster changes significantly as it convects, the cluster itself remains generally intact. Figure 10 shows the normalized correlation of the low and high frequency wall pressure VITA functions (filter 2-filter 3) between the transducers. There appears to be consistent correlation between activity in the filter 2 signal of the upstream-most transducer, and high frequency (filter 3) activity at the downstream transducers in the array, the magnitude of which decays very gradually with transducer separation. *This qualitative observation of the strong VITA correlations between the filtered signals suggests that the filter 2 and filter 3 wall pressure activity appear to be components of composite footprint of a single, organized turbulent motion.* This behavior is also illustrated by examining sample time records from the wall pressure array.

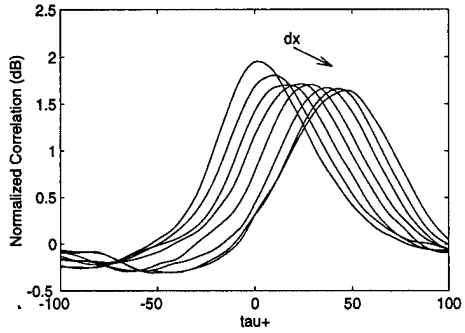

Figure 10. Normalized correlation based on the localized variance (VITA) functions of filter 2 wall pressure at P1 and downstream (P1-P8) filter 3 wall pressure

A sample window of simultaneous wall pressure time records from the streamwise array is shown in figure 11. In this sample there are obvious regions or clusters of high frequency activity (filter 3) which appear to convect at approximately the same speed as the peaks in the lower frequency signal (filter 2). At each of the downstream transducers, the turbulent clusters seen in the high frequency signal appear to be slightly preceded by high amplitude positive peaks in the low frequency signal. Thomas and Bull[9] observed the same behavior in high and low pass filtered wall pressure signals.

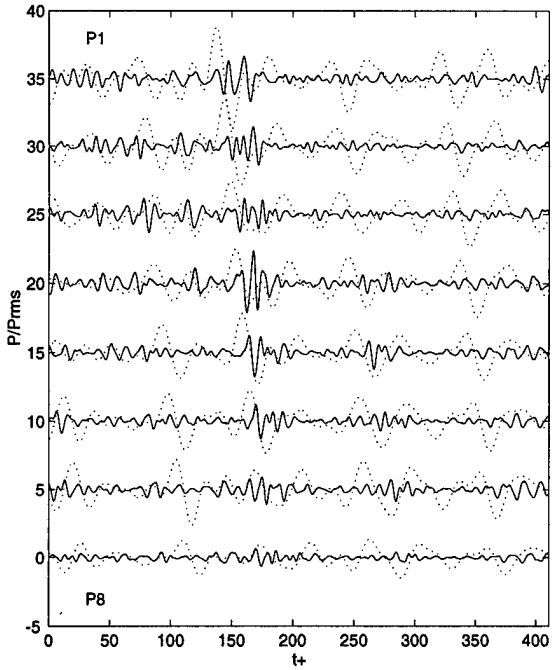

Figure 11. Sample filtered wall pressure time records from the streamwise array (P1 to P8): ..., filter 2; ---, filter 3.

As one would expect based on the streamwise correlation results, the low frequency event shapes appear almost frozen as they convect across the entire span of the array, whereas, the peaks within the high frequency clusters do not retain their shape as the cluster convects. Nonetheless, the high frequency cluster remains generally intact.

The low and high frequency VITA functions for each transducer in the streamwise array are shown in figure 12. The time sample shown is the same as that in figure 11. The low and high frequency events seen in the time records are successfully captured by the corresponding VITA functions. As observed in the raw time records, the high and low frequency VITA functions indicate a time lag between peak low frequency and peak high frequency wall pressure activity. This suggests that the large scale component of the structure passes over the transducers ahead of the small scale component. The signature of the large scale head and small scale legs of an inclined hairpin vortex, for example, would satisfy this description.

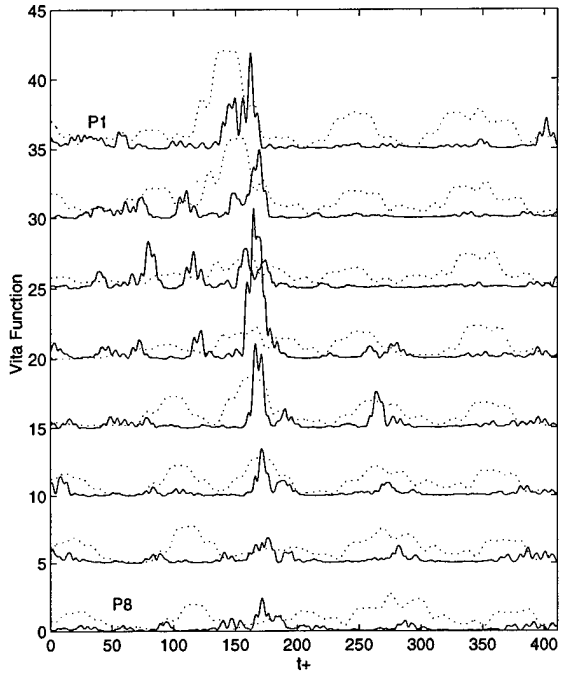

Figure 12. Sample VITA functions of the wall pressure time records shown in figure 11: ..., filter 2; ---, filter 3.

Although the sample time records in figure 11 are typical of the entire time record collected, the illustration of a single event is not sufficient to draw general conclusions. Therefore, conditional sampling methods were also applied to the filter 2 and filter 3 wall pressure time records. Figure 13 shows the ensemble averaged data from the high frequency (filter 3) wall pressure time records of the first four transducers in the streamwise array based on the detection of low frequency (filter 2) high amplitude (k=+3) peak events in the upstream-most transducer. These data confirm the correlation results in figure 10 as well as the temporal information observed in the time

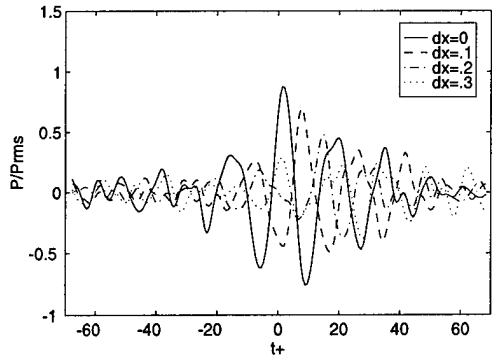

Figure 13. Downstream filter 3 wall pressure signals conditionally averaged on peak events in upstream, filter 2 wall pressure signal, (k=+3)

records and the VITA functions. There is a clear correlation between low frequency peak events and high frequency wall pressure activity across the array. On average, the peak high frequency activity occurs slightly after the low frequency peak has passed, shown by the offset of the dx=0 peak from $t^+=0$.

Collectively, the wall pressure findings reveal a consistent phase relationship between large and small scale wall pressure activity. This phase relationship supports the idea that, in many cases, small and large scale wall pressure activity are components of the wall pressure signature of a single, large scale, turbulent structure. The small scale activities were characterized by intermittent, convecting clusters of peaks which evolved over the spatial extent of the array. The large scale activity accompanying the small scale events, resembled a frozen, convecting wave train, which maintained its shape as it traversed the length of the streamwise array. The large scale wave trains were less intermittent than the high frequency events and usually contained 2 or more peaks and axis crossings. This feature made them well suited to VITA detection.

V. IDENTIFICATION OF FLOW STRUCTURES

This section contains the results from the simultaneous measurements of the flow field and wall pressure signatures. The objective here was to identify the distinct flow structures whose wall pressure signatures were measured with the array. These flow structures are defined using the same analysis tools previously employed including cross-correlation, and conditional sampling, applied to both velocity and pressure data.

The physical extent of the pressure-producing structures can be illustrated by measuring both the spectral and temporal cross-correlation between wall pressure and streamwise (u), as well as wall normal (v) components of velocity at locations across the boundary layer. These findings are presented in Russell.[18] Many of the same flow characteristics can also be derived from the results of the conditional sampling experiments conducted. In this section the results of experiments in which u and v are conditionally sampled based on wall pressure peak events are presented. From these results, a composite picture of the average pressure producing flow structures is inferred. In addition, by conditionally sampling high frequency velocity signals on low frequency wall pressure events, the correlation between large and small scale structures seen in the wall pressure data is illustrated in the ensemble averaged flow field.

Two basic techniques for flow field visualization are used. The first technique utilizes the entire array of transducers to produce a database of pressure and velocity time records in the streamwise measurement grid. At each station in the streamwise measurement grid, the velocity vectors (u and v) are sampled at times corresponding to large amplitude wall pressure events ($k = \pm 2$) at location $(x^+,y^+)=(0,0)$. The velocity samples are then ensemble averaged. Vector or 'quiver' plots of the average velocities are then plotted in a map in which the quivers are physically located at the measurement position (x^+,y^+) relative to the fixed reference pressure transducer. The flow fields depicted represent flow patterns downstream of the transducer array.

The second technique uses a single pressure transducer and a single velocity (u,v) survey. For this technique, in which the ensemble averaged velocity time records are played back, an effective streamwise (x) axis is computed from an assumed convection velocity ($x^+=U_c^+t^+$). The average velocity time record from each y location in the survey is then vector plotted at that y location. The " Taylor plots" created using this method are based on an assumption of a frozen, convecting flow field which changes negligibly in the time window viewed. This technique has the distinct advantage of an essentially unlimited streamwise resolution, limited only by the sample time ($1/f_s$) and will prove to have an advantage in visualizing the small scale, near-wall, filter 3 flow structures. The quivers in these flow maps are scaled, i.e., normalized by the local RMS fluctuating velocity value. The purpose of the scaling is to better visualize the weaker large scale outer structures which are characterized by velocity excursions far less violent than the near wall structures associated with large amplitude wall pressure events.

Flow Field "Mapping" Results

The four conditionally averaged flow field maps in figure 14 show the filter 0 (unfiltered) average flow field conditionally sampled on filter 2 and filter 3 positive and negative peak wall pressure events.

The positive pressure event in figure 14a is characterized by a reverse flow and ejection motion, whereas the negative pressure event in figure 14b is characterized by a sweep, which happens to follow a negative shear stress and ejection motion. The coupling of the positive and negative peaks as components of the total footprint of large scale ejection/sweep type motions is clearly demonstrated in these data.

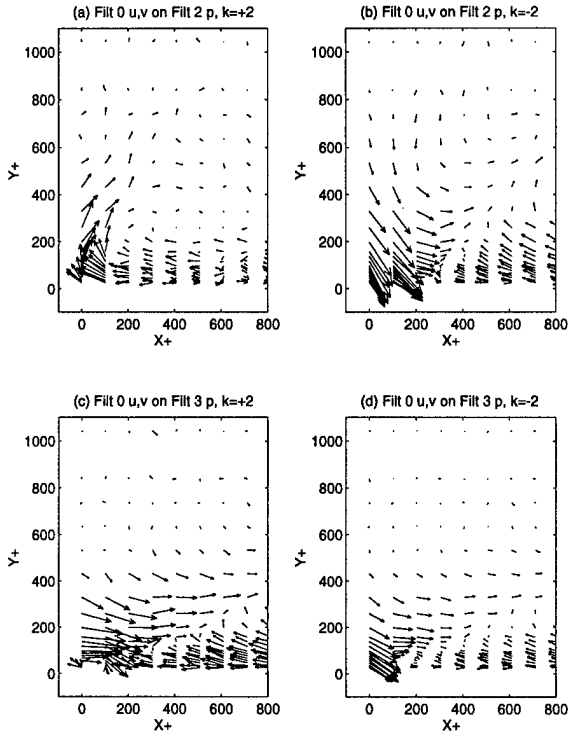

Figure 14. Unfiltered average flow field conditionally sampled on filter 2 and filter 3 positive and negative peak wall pressure events

The maps in figure 14c and d similarly illustrate a relationship between large and small scale structures. In these figures, the unfiltered flow field is conditionally averaged on filter 3, positive and negative wall pressure events. Two important features should be noted. The first is the familiar large scale, near-wall shear stress region which extends far beyond the streamwise extent of the plots (out to at least x^+ of approximately 1800). The large scale sweep of fluid, coupled with the near wall shear stress region combine to form an inclined shear layer across the boundary layer. This large scale shear layer, by virtue of its strong presence in these data, is correlated with high frequency (filter 3) wall pressure activity.

The second observation is of activity in the near-wall region ($y^+<100$ and $x^+<200$). Upon close examination of figures 14c and d in this region, the near wall turbulent structure associated with the filter 3 wall pressure event is visible. The first two x locations of velocity vectors in figure 14c indicate a small ejection (Q2) and sweep (Q4), respectively. Since the scale of these structures are on the order of the transducer spacing, their detailed shape is not clear, however, they clearly contain Q2 and Q4 motions. The flow field associated with a negative pressure event shown in figure 14d contains further evidence of the small scale structure at $x^+ \sim 200$. In this figure, the rotational motion of the structure is weakly visible. It appears as though the small scale structure rotates clockwise as it is swept along by the large scale shear layer. The resemblance between figures 14c and d is strong, and they appear only to differ by a finite phase shift. Though the small scale activity may have a larger vertical and streamwise extent than is indicated in figures 14c and d, the dominance of the large scale shear layer in these data appears to have a masking effect on it. It is hoped that by removing the large scale component of the velocity signals, a more refined image of these near wall structures will be revealed.

The velocity data presented in figure 15 are subject to the same filtering as the wall pressure on which their sampling was based. Figures 15a and b show the filter 2 average flow field conditionally sampled on filter 2, positive and negative, peak wall pressure events; while figures 15c and d show the filter 3 average flow field conditionally sampled on filter 3, positive and negative, peak wall pressure events. The filter 2 flow structures are nominally consistent with the unfiltered flow results in figures 14a and b. However, the filtered flow field reveals a more organized, inclined structure, exhibiting the same ejection type motion. It also exhibits a near-wall "splat" feature at $x^+ \sim 400$ for the positive peak pressure detection in figure 15a which appears to be a component of the ejection/sweep process for structures of filter 2 scale.

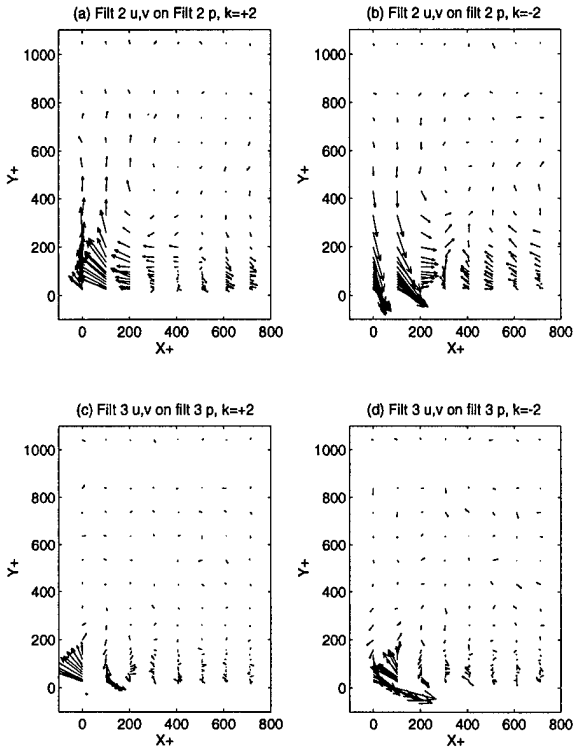

Figure 15. Filter 2 and filter 3 average flow fields conditionally sampled on positive and negative peak wall pressure events

The average flow field downstream of filter 2 negative wall pressure events, depicted in figure 15b, contains the characteristic sweep motion above the reference transducer. This is followed downstream by an ejection which occurs upstream of a region of strong near wall negative shear stress. These motions combine to form an inclined shear layer similar to that seen in the filter 0 (unfiltered) flow fields.

The unfiltered flow results in figures 14c and d, showed small scale near wall ejection/sweep motions associated with high frequency wall pressure fluctuations associated with the passage of larger scale motions. By removing the larger scales from the velocity signals, a clearer image of the small scale motions is revealed. This is illustrated in figures 15c and d. The average filter 3 flow field associated with a positive peak pressure consists of a strong Q2 ejection directly above the transducer and a simultaneous Q4 sweep of fluid at the next transducer (100 viscous units downstream). Similarly, the negative wall pressure event consists of a sweep and ejection motion in the opposite order.

Since filter 3 peak events were shown to occur in clusters, one would expect to see a multitude of ejections and sweeps in figures 15c and d. These data do indicate the presence of additional near-wall organized activity, however, the resolution of the measurement grid, combined with the short correlation lengths of these scales, make it difficult to map the entire cluster of activity. An alternative method is needed to view the near wall turbulent activity with greater resolution.

Flow Field Visualization Using Taylor's Assumption

The Taylor method was employed to both qualify the results from the flow field mapping technique and to provide better resolution of the small scale turbulent motions. The flow fields shown in figure 16

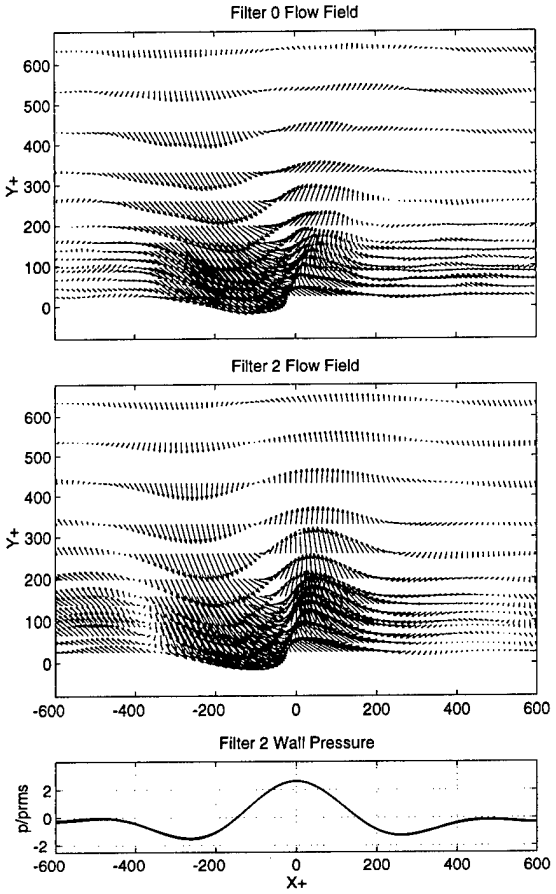

Figure 16. Taylor plot of unfiltered and filter 2 flow fields conditionally sampled on filter 2 positive peak wall pressure events

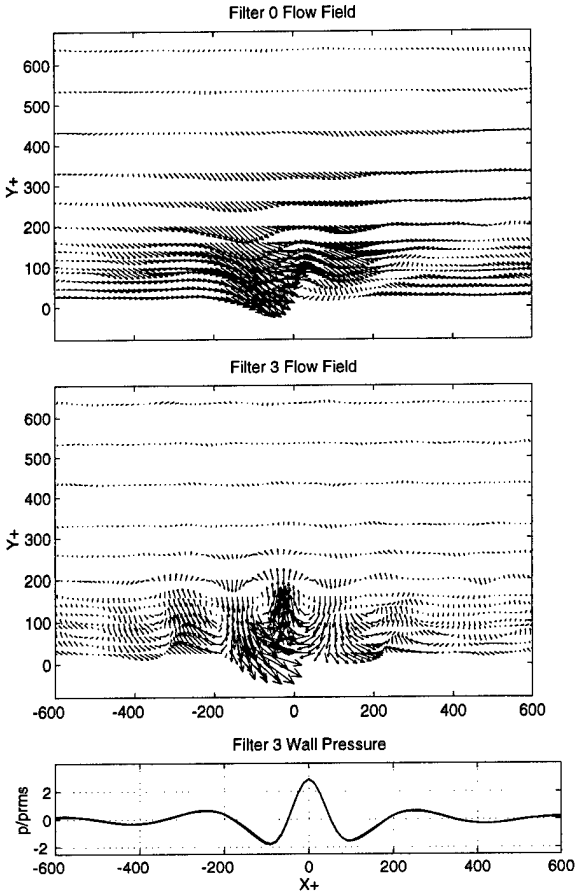

Figure 17. Taylor plot of unfiltered and filter 3 flow fields conditionally sampled on filter 3 positive peak wall pressure events.

are a Taylor plot of the filter 0 (unfiltered) and filter 2 average flow fields conditionally sampled on filter 2, positive (k=+2), peak wall pressure events. The ensemble averaged filter 2 wall pressure signature is shown at the bottom of the figure. The general features of the downstream unfiltered and filter 2 flow fields ($x^+ > 0$) in these figures are consistent with the equivalent flow maps in figures 14a and 15a. This observation confirms that the turbulent motions isolated by filter 2 remain generally intact as they convect the span of the streamwise array. Furthermore, by viewing the filtered flow field with the enhanced streamwise resolution of this method, the rotational features of these structures is revealed, as are the rotating secondary motions upstream and downstream of the primary structure. Hence, rather than the large scale, inclined shear layer as this motion appears in the unfiltered flow maps (figure 14), by filtering, the vortical characteristics of these structures are revealed. It is possible that the backs of these vortical structures comprise the shear layers described by other investigators.

As observed in the flow field maps, the temporal increases in pressure are associated by ejection motions, while a drop in pressure signifies an inrush or sweep of fluid toward the wall. These motions may be associated with the passage of counter rotating vortical structures, or alternatively, the vortical structures could be a product of the mean flow interaction with the ejection/sweep process. This relationship cannot be determined from these data.

The two flow fields shown in figure 17 are the filter 0 and filter 3 averaged flow fields conditionally sampled on filter 3, positive, peak wall pressure events. The ensemble averaged unfiltered flow field in figure 17 is nearly identical to that measured by Laadhari etal.[21]

The Taylor plots clearly allow a much improved view of the small scale rolling vortical structure below the shear layer in the unfiltered flow field. Filtering the flow field data reveals the small scale vortical structures which are masked by the large scale motions in the unfiltered data. As many as six, counter-rotating near-wall vortical structures can be identified in the filter 3 flow field. The wall pressure signature of these motions also follows the ejection and sweep pattern demonstrated by the larger scale motions.

To further illustrate the correlation between large scale motions and small scale, near-wall turbulent activity, figure 18 shows the filter 3 average flow field conditionally sampled on filter 2 positive wall pressure events. There are obvious regions of organized activity, primarily ejection and sweep type motions depicted in these data. These data confirm what was generally observed in the wall pressure time records. That is, not all low frequency (filter 2) peak events are accompanied by clusters of high frequency (filter 3) activity, however, a sufficient number are to produce the patterns shown in figure 18.

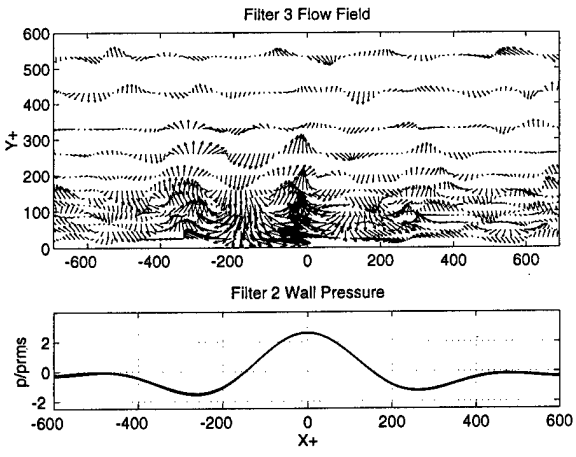

Figure 18. Taylor plot of filter 3 flow field conditionally sampled on filter 2 positive peak wall pressure events

VI. CONCLUSIONS

The distinct features of the "total" wall pressure footprint of the small and large scale turbulence producing structures are not easily defined. Based on the results of this investigation, it is clear that a simple characteristic signature of a turbulent producing structure is not feasible. A hierarchy of structures that induce wall pressure signatures exists within and outside of the boundary layer, however, because the large and small scale structures appear to convect together, the total streamwise spatial influence of the large and small scale motions are comparable.

Although dominant Reynolds stress production has been historically found to occur near the wall, the large scale structures across the boundary layer associated with mid frequency wall pressure peak events were shown to exhibit similar Q2/Q4 motions and, more importantly, appear to be coupled to the near wall burst events.

From a turbulence control or drag reduction standpoint, the results of this investigation are promising. Since the focus of any active control technique would most likely be to affect the near-wall, small scale production motions, the findings associated with these scales are of primary interest. The occurrence of these motions in clusters (best visible in a filtered time record) indicates the advantage of a VITA type detection criteria. Since these motions were also shown to occur simultaneously with large scale, inclined vortical structures or shear layers, the possibility is raised of an early warning mechanism based on the detection of large scale motions. These large scale motions were successfully tracked in this investigation using conventional wall pressure transducers.

VII. NOMENCLATURE

C_f coefficient of skin friction
d diameter
f function or frequency, Hz
f_s sampling frequency
H conventional shape factor, δ^*/θ
K_T turbulence kinetic energy $(u_1^2+u_2^2+u_3^2)/2$
p fluctuating pressure
Re_θ Reynolds number based on momentum thickness
t_ν viscous time scale, ν/u_τ^2
u fluctuating streamwise velocity
u_τ shear velocity, $(\tau_w/\rho)^{1/2}$
U mean streamwise velocity
U_c streamwise convection velocity
U_0 freestream velocity
v fluctuating wall-normal velocity
V mean wall normal velocity
x,y,z streamwise, wall-normal & transverse coordinates
δ boundary layer thickness, where $U=.99U_0$
δ^* boundary layer displacement thickness
θ boundary layer momentum thickness
k peak-event detection threshold (P/P_{rms})
ν kinematic viscosity
ρ density
τ_w wall shear stress
ω frequency, rad/s
τ time delay used in correlation functions
$(\,)^+$ quantity scaled on viscous variables

VIII. REFERENCES

1. S.K. Robinson "Coherent Motions in the Turbulent Boundary Layer", *Annu. Rev. Fluid Mech..*, 23:601-639, 1991.

2. W. W. Willmarth and S. S. Lu, "Structure of the Reynolds Stress Near the Wall", *J. Fluid Mech.*, 55:65-92, 1972.

3. T. Theodorsen, "Mechanism of Turbulence", In *Proc. Midwest Co nf. Fluid Mech.* 2nd, pages 1-18, 1952.

4. W. W. Willmarth and B. J. Tu, "Structure of Turbulence on the Boundary Layer Near the Wall", *Phys. Fluids*, 10:134-137, 1967.

5. G. R. Offen and S. J. Kline, "A Proposed Model of the Bursting Process in Turbulent Boundary Layers", *J. Fluid Mech.*, 70:209-228, 1975.

6. J. O. Hinze, "*Turbulence*", McGraw Hill, New York, 1975.

7. A. K. Praturi and R. S. Brodkey, "A Stereoscopic Visual Study of Coherent Structures in a Turbulent Shear Flow", *J. Fluid Mech.*, 89:251-272, 1978.

8. R. E. Falco, "New Results, a Review and Synthesis of the Mechanism of Turbulence Production in Boundary Layers and its Modification", AIAA Paper No. 83-0377, 1983.

9. A. S. W. Thomas and M. K. Bull, "On the Role of Wall-Pressure Fluctuations in Deterministic Motions in the Turbulent Boundary Layer", *J. Fluid Mech.*, 128:283-322, 1983.

10. S. J. Kline, "Boudary Layer Structure - a Summary", In Turbulence Research - Joint AFOSR/ONR Grantee and Contractors Meeting, pages 157-173, Illinois Institute of Technology, Fluid Dynamics Research Center, 1992.

11. S. K. Robinson, "Kinematics of Turbulent Boundary Layer Structure", Ph.D. thesis, Stanford University, 1990.

12. T. M. Farabee, "An Experimental Investigation of Wall Pressure Fluctuations Beneath Non-Equilibrium Turbulent Flows", Technical Report DTNSRDC-86/047, 1986.

13. C. C. Karangelen, "Temporal and Spectral Features of Wall Pressure Fluctuations Beneath a Turbulent Boundary Layer", Ph.D. thesis, The Catholic University of America, 1991.

14. V. Wilczynski, "Organized Turbulent Structures and their Induced Wall Pressure Fluctuations", Ph. D. thesis, The Catholic University of America, 1992.

15. A. V. Johansson, J. Her, and J. H. Haritonidis, "On the Generation of High-Amplitude Wall Pressure Peaks in Turbulent Boundary Layers and Spots", *J. Fluid Mech.*, 175:119-12, 1987.

16. G. Schewe, "On the Structure and Resolution of Wall-Pressure Fluctuations Associated with Turbulent Boundary Layer Flow", *J. Fluid Mech.*, 134:311-328, 1983.

17. M. Kammeyer, "An Experimental Investigation of Organized Turbulent Motions and Wall-Pressure Fluctuations in Complex Flows", Ph.D. theses, The Catholic University of America, 1995.

18. S. J. Russell, "Wall-Pressure Signatures of Organized Turbulent Motions", NSWCCD-TR-97/009, 14 July 1997.

19. R. F. Blackwelder and R. E. Kaplan, "On the Wall Structure of the Turbulent Boundary Layer", *J. Fluid Mech.*, 76:89-112, 1976.

20. J. Kim, "On the Structure of Pressure Fluctuations in Simulated Turbulent Channel Flow", *J. Fluid Mech.*, 205:421-451, 1989.

21. F. Laadhari, R. Morel, and E. Alcaraz, "Combined Visualization and Measurements in Transitional Boundary Layers", *Eur. J. Mech., B/Fluids*, 13 No. 4:473-489, 1994.

STREAMFUNCTION - VORTICITY CALCULATIONS OF NAVIER-STOKES EQUATIONS AS A TOOL FOR HIGH ACCURACY STUDY OF PRESSURE -TENSION RELATION

Mickael N. Zakharenkov
Central Aero-Hydrodynamic Institute
140160 Zhukovsky, Moscow region, Russia
Fax:(095)5564337

Abstract - This paper considers the problems of streamfunction -vorticity formulation of Navier-Stokes equations. This is shown that the boundary condition for vorticity which had been assessed many authors as "artifical" boundary condition is really a total combination of the no-slip boundary conditions (b.c.). and some differential conditions outcoming from a continuation of governing equations onto the boundary. This conditions are necessary for all high accuracy numerical algorithms. Two-parameters approximating formula for the boundary vorticity is described and containes the parameter optimizing the calculations. The no-slip and slip-boundary conditions on the wall are in the problem statement. The pressure uniqueness condition is incorporated into proposed algorithm. The formulation of necessary boundary differential conditions is spreaded to velocity-pressure form of N-S eqs. The influence of multidipole far field flow asimptotic on the viscous flow around an airfoil is considered. The thermodynamically closed boundary condition on the trailing edge of an airfoil is discussed in connection with such phenomena as a surface vorticity waves, vortex/momentum/heat spots generation.

1. INTRODUCTION

The problem of accuracy study of pressure-tension relation have the fundamental significans in the theory of moving bodies and closely related with the problems of drag reduction. We can take as an example the known Stokes law formulated as the relation between the tangential velocity on the body and stress tensor [1]:

$$\lambda' \mathbf{V}_\tau' = \mathbf{j}\, \tau_s' \qquad (1)$$

where $\mathbf{V}_\tau'$ is a tangential velocity vector on the wall s , $\mathbf{j}$ is the unit vector in the direction of $\mathbf{V}_\tau'$, τ_s' is the component of wall-shear stress in the direction of $\mathbf{V}_\tau'$, λ' is the slip coefficient.

This relation corresponds to no-slip boundary condition for $\lambda' = \infty$, the perfect slip relalizes at $\lambda' = 0$, and the slip occures at $0 < \lambda' < \infty$ .The discussion of physical and theoretical reasons for condition (1) is in [1]. The cases of new rheological laws when the polymers (or some pollutions) are inserted into the thin layer near the body (for drag reduction purposes) can be formulated in the similar form. We must note, that even for high speed flows the slip condition is a basic law for the boundary conditions formulation [2, 3]. On this reason the study of the viscous flow with the boundary condition (1) have the wide application and may be easily continued onto a more complex flows.

The numerical realization of the law (1) proposed by Lugt et al. [1] and formulated in a more common form in Section 4 of this paper shows that the right connection of wall-shear stress on the body surface with the boundary vorticity (vortex in 3-D case) defines the high demands to the vorticity calculations. Consequently, the usage of vorticity as a basic term in N-S equations formulation is very desirable. On the contrary, the veloicity-pressure formulation must be complicated by some differential conditions which are necessary for thoroughly approximation of law (1) on the surface.

The boundary condition for the pressure on the wall is the second known "artifical" boundary condition as well as a boundary vorticity condition [4, 5]. These condition is commonly derived as a consequence of continuation of momentum equations onto the boundary. This had been shown by Zakharenkov [6] that the pressure boundary condition in a numerical formulation is completly analogous to the vorticity condition.

In other hand, we have the necessity to know both the pressure and vorticity on the wall because the integral characteristics: drag, lift, moment of force - are in interest for practice. In such situation we have not doubts that if the mentioned above boundary conditions are well posed then we must employ them in the process of solution of N-S eqs. formulated in any form, at least at the final stage of boundary vorticity and pressure calculations. Moreover, we must study is it possible to employ the solution where this conditions are not incorporated into a numerical algorithm. As a common case the problem of high accuracy study of pressure-vorticity relations on the wall is formulated.

2. PROBLEM STATEMENT

For viscous incompressible flow the problem statement is wellknown and is described elsewhere. The usage of integrating function for continuity equation fulfillment is recomendated by theory because this allows us to eliminate this equation from numerical solution. Let us introduce stream function Ψ and vorticity Ω by relations

$$V_\xi = -H^{-1}\,\partial\Psi/\partial\eta\ ,\ V_\eta = H^{-1}\,\partial\Psi/\partial\xi\ ,$$
$$\Omega = H^{-2}[-\partial(HV_\xi)/\partial\eta + \partial(HV_\eta)/\partial\xi] \qquad (2)$$

where $H^2 = (\partial x/\partial\xi)^2 + (\partial y/\partial\xi)^2$ is the Jacobian of transformation from Cartesian coordinate (x, y) to curvilinear orthogonal coordinates (ξ, η). The coordinate η is a cyclic one, and ξ is orthogonal to the body and η coordinate; V_ξ and V_η are the velocity components in (ξ, η). coordinates.

Introduction of stream function fulfilles the continuity equation and (2) gives us the relation

$$\Delta\Psi = H^2\,\Omega \qquad (3)$$

where Δ is the Laplace operator.

The Navier-Stokes equations in Gromeka-Lamb form are

$$\partial p/\partial\xi = \mathrm{Re}^{-1}\partial\Omega/\partial\eta - \partial(\Psi/\partial t)/\partial\eta - \partial(V^2/2)/\partial\xi + \Omega\partial\Psi/\partial\xi \qquad (4.1)$$
$$\partial p/\partial\eta = -\mathrm{Re}^{-1}\partial\Omega/\partial\xi + \partial(\Psi/\partial t)/\partial\xi - \partial(V^2/2)/\partial\eta + \Omega\partial\Psi/\partial\eta \qquad (4.2)$$

where $\mathrm{Re} = U_\infty\, c/\nu$, U_∞ is the freestream velocity, c is the airfoil chord, ν is the coefficient of kinematic viscosity.

The known transformations of eq. (4) lead to vorticity transport equation

$$H^2\,\partial\Omega/\partial t + \partial\Psi/\partial\eta\,\partial\Omega/\partial\xi - \partial\Psi/\partial\xi\,\partial\Omega/\partial\eta = \mathrm{Re}^{-1}\Delta\Omega \qquad (5)$$

and Poisson equation for the pressure

$$\Delta(p+V^2/2) = \partial\Omega/\partial\xi\,\partial\Psi/\partial\xi + \partial\Omega/\partial\eta\,\partial\Psi/\partial\eta + H^2\Omega^2 \qquad (6)$$

© Michael N.Zakharenkov 2 April 1998

The boundary conditions on the wall s will be formulated for common law (1) in the Section 4. Hear, the case of no-slip condition gives

$$V_\xi = -H^{-1}\,\partial\Psi/\partial\eta = 0\,,\ V_\eta = H^{-1}\,\partial\Psi/\partial\xi = 0 \qquad (7)$$

The far-field flow asimptotic is used for the numerical formulation of boundary conditions on the outer boundary s_∞ of computational domain (the "O" type mesh is considered which is obtained by mapping of an airfoil onto the circle

$$\partial\Psi/\partial\xi = \partial x/\partial\xi\sin\alpha - \partial y/\partial\xi\cos\alpha - R_\infty^{-1}[\,D_x^1\sin(\eta-\alpha) + D_y^1\cos(\eta-\alpha)] + \sum_{k=2}^{5} D_x^k \sin k(\eta-\alpha) + \sum_{m=2}^{5} D_y^m \cos m(\eta-\alpha) - \Gamma/2\pi + \ldots \qquad (8)$$

$$\partial\Omega/\partial\xi = 0 \qquad (9)$$

where α is the angle of attack, D_x^k, D_y^m are intensities of multidipole terms, Γ is the velocity circulation around an airfoil at a large distance (on s_∞) from it, R_∞ is the radius of a circle in a mapped plane. The source terms are included into (8) too, but are omitted here because the study presented below is restricted by given form (8) only.

The initial condition are follows. The body and fluid are in the rest.

$$\Psi(0, x, y)=\Omega(0, x, y) = 0 \qquad (10)$$

The study of abrupt start of the body and slowly start of the body in fluid had been considered in [7,8]. This study shows that the flow characteristics are the same in a both cases after a some short time period after start. On this reason there are not considered the cases of initial conditions with the given vortex sheet on the airfoil at the start which is recomendated by Ghia et al. [9].

3. NUMERICAL ALGORITHM

The widespread numerical code is employed for solution of eqs.(2), (3), (5) with boundary conditions (7)-(9). The ADI method [10] is used for solution of eq.(5) and the direct method [11] is used for solution of eq.(3). The last method employes the expansion into a trigonometrical polynom in coordinate η, Fast Fourier Transformation and Thomas algorithm. The method of solution of decoupled equations (3), (5) is very suitable in this case, because the eq.(3) is solved exactly and this allow us to eliminate the distortions in stream-function calculation which are very dangerous to the main idea of introduction of the stream function: the continuity equation must be fulfilled exactly. Any error in stream function calculation leds to violation of continuity equation and as it will be shown below to hardly assessing errors in a vorticity-pressure relation on the wall.

The second derivatives in (3), (5) and the velocity components in (5) are approximated by central differences. The one-sided upwind differences approximate the first vorticity derivatives in (5), for example

$$\partial[(\partial\Psi/\partial\xi)\Omega]/\partial\eta|_j = \{3(\partial\Psi/\partial\xi)_j\Omega_j + [3(\partial\Psi/\partial\xi)_{j+1} + (\partial\Psi/\partial\xi)_j]\Omega_{j+1} - (\partial\Psi/\partial\xi)_{j+1}\Omega_{j+2}\}/2h_\eta \qquad (11)$$

The approximation (11) is near to proposed in [12] which reveals the property of enstrophy coservation in the flow.

The boundary condition $\Psi_s = 0$ ($V_\xi|_s = 0$) and (8) are used for solution of eq.(3). The given velocity (or relation (1) on the wall) and (9) are used as a boundary condition for eq.(5).

The iteration process couples eqs.(3) and (5) into the system and simultaneously solves thoroughly the vorticity-pressure relations on the wall which will be described in the next Section.

4. VORTICITY-PRESSURE RELATIONS ON THE WALL

Let us consider the law (1) as a some relation known from practice. Then, follow to Lugt et al. [1] we can write the expression to the vorticity and shear stress

$$\Omega = H^{-2}[-\partial(HV_\xi)/\partial\eta + \partial(HV_\eta)/\partial\xi] = H^{-2}\Delta\Psi \qquad (12)$$

$$\tau = \partial(V_\xi/H)/\partial\eta + \partial(V_\eta/H)/\partial\xi \qquad (13)$$

where $\tau=(c/\mu U_\infty)\tau^*$, μ is the coefficient of dynamic viscosity.

Taking into account relation (2) and condition $V_\xi|_s = 0$ we rewrite eq.(1) as

$$\lambda V_\eta = \partial(H^{-2}\partial\Psi/\partial\xi)/\partial\xi \qquad (14)$$

or, taking into consideration (12)

$$\lambda H^{-1}\partial\Psi/\partial\xi|_s=\partial\Psi/\partial\xi|_s\partial(1/H^2)/\partial\xi+\Omega \qquad (15)$$

The known two-parameter fomula for condition $\partial\Psi/\partial\xi|_s = HV_\eta|_s$ is described in [6,8,13] and has the form

$$HV_\eta|_s = \partial\Psi/\partial\xi|_s = -H^2E\Omega_s + h_\xi^{-2}\sum_{j=0}^{3} K_j\Psi_j + h_\xi(2h_\xi-\alpha)/3!\ \partial^3\Psi/\partial\xi^3|_s + 2h_\xi^2(6h_\xi-\beta)/4!\ \partial^4\Psi/\partial\xi^4 + \ldots \qquad (16)$$

where $E=(6\alpha-\beta)/22$ is the Tarunin' parameter, K_j are defined by expressions in [6, 8, 13], α and β are parameters (we do not change the original notation α in (16) because it is difficult to mix this parameter with the angle of attack introduced in eq.(8)).

After some transformations we obtain the formula for boundary vorticity

$$\{H^2E+[\lambda H^{-1}-\partial(1/H^2)/\partial\xi]^{-1}\}\Omega_s = h_\xi^{-2}\sum_{j=0}^{3} K_j\Psi_j + h_\xi(2h_\xi-\alpha)/3!\ \partial^3\Psi/\partial\xi^3|_s + 2h_\xi^2(6h_\xi-\beta)/4!\ \partial^4\Psi/\partial\xi^4 + \ldots \qquad (17)$$

and for tangential velocity on the body

$$V_\eta|_s = \Omega_s[\,\lambda + H^{-3}\partial H^2/\partial\xi]^{-1} \qquad (18)$$

Finally, the derivative $\partial^3\Psi/\partial\xi^3|_s$ in (17) must be expressed as

$$\partial^3\Psi/\partial\xi^3|_s = \partial(H^2\Omega)/\partial\xi|_s - \partial^2(HV_\eta)/\partial\eta^2|_s \qquad (19)$$

where $\partial(H^2\Omega)/\partial\xi|_s = (-3H^2_S\,\Omega_s + 4H^2_1\Omega_1 - H^2_2\Omega_2)/2h_\xi$

For given value of slip coefficient λ the formulae (17)-(19) allow us to calculate vorticity and tangential velocity on the surface of a flown body. The pressure on the wall can be calculated from eqs.(4) when the Ψ and Ω are known. This was shown by Zakharenkov [14, 16] that two pressure distribution on the **s**, the first one obtained by integrating eq.(4.1) from **s** to s_∞ and the second one obtained by integration eq.(4.2) along **s** may not be in concidence for a common solution of eqs.(3),(5). On this reason the corrector stage of algorithm consists in the calculation of p_0 from (4.1) and in the usage of expression (k is the index of iterations):

$$\partial\Omega/\partial\xi^{k+1}|_s=(-3\Omega^k{}_s+4\Omega^{k+1}{}_1-\Omega^{k+1}{}_2)/2h_\xi = \mathrm{Re}[-\partial p_0/\partial\eta + \partial(\partial\Psi/\partial\xi)^k/\partial t - \partial(V^2{}_s/2)^k/\partial\eta]|_s \qquad (20)$$

(obtained from (4.2)) as the boundary condition for eq.(5).The alternating predictor-corrector iterations calculate the (17)-(19) and use (17) as a b.c. for eq.(5) at the first stage, and calculate (17),(18),(20) and use (20) as a b.c. for eq.(5) at the second stage. The six-eight iterations are sufficient. The convergence of procedure is shown by Zakharenkov

[15]. This algorithm ensures the pressure uniqueness on the wall. The pressure uniqueness n the flow field may be controlled by integrating eqs.(4) and by comparision of p_0 from (4.1) and p_1 from (4.2) on the coordinate lines $\xi = \xi_i$.

The vorticity dissipation in the wake is the next dangerous phenomenon which can desturbs the pressure field. This problems is solved analogously to SIMPLE procedure for pressure correction. The dissipating vorticity may be reconstracted at a mesh nodes in the far wake due to the two rules. This stage of corrector algorithm consists, in the first, the pressure uniqueness on coordinate lines $\xi = \xi_i$. is verified, in the second, the integral law of vorticity conservation in the flowfield leds to condition that the integral of vorticity along line $\xi = \xi_i$. conserves its value in far wake flow (for all $j > j_0$) for positive and negative vorticity separately (condition of vorticity neutralitty in the steady wake flow). This algorithm ensures that the pressure compatibility condition, see [16], is really fulfilled. In this procedure the N-S eqs. in form (4) are solved correctly. Therefore, the eq.(6) which is derivative form of eq.(4) will be fulfilled automatically if we carry out properly the differentiation of eq.(4).

The last remark touch upon the problem of pressure boundary condition on the wall. The eq.(6) is often used instead of continuity equation (taking into account that the continuity equation is used for simplification of eq.(6) after differentiation of eq.(4)). But this procedure rises the issue is the continuity equation ensured really? This problem may be solved directly by properly formulation of pressure boundary condition, see [6], which is necessary for solution of eq.(6). The final form of this condition (for no-slip case) is

$$0 = \partial V_\xi/\partial\xi = - H^2 E \partial^2 V_\xi/\partial\xi^2|_s + h_\xi^{-2} \sum_{j=0}^{3} Kj(V_\xi)_j + O(h^2_\xi) =$$

$$- H^2 E \mathrm{Re}(\partial p/\partial\xi)|_s + h_\xi^{-2} \sum_{j=0}^{3} Kj(V_\xi)_j + O(h^2_\xi) \qquad (21)$$

The relation (21) incorporates the next conditions: (i) continuity equation is hold on the wall (this is correct procedure if we admit the differentiation of (4) and any kind of discretization of governing equations); (ii) the continuation of momentum equation onto the wall. The parametrization of (21) is attained analogously to vorticity boundary condition [13].

In such a way we must solve the known momentum equations and eq.(6) (if the velocity-pressure form of N-S eqs. is used), with b.c. (21) and carry out the pressure correction in the wake. For stream-function and vorticity form of N-S eqs. we solve the vorticity transport eq.(5), the eq.(3), satisfy b.c.(17)-(19), corrects solution by employing (20) as a b.c. for eq.(5), and reconstruct vorticity in the far wake flow (if its necessary, see Section 5). This two approaches are similar. I find the advantage in the stream-function and vorticity formulation because the continuity equation is fulfilled exactly, the second order approximation for vorticity is achived by employing of simple finite-difference scheme. The same level of solution accuracy demands the third (fourth-) order approximation of governing equation in the velocity-pressure formulation.

5. RESULTS OF CALCULATIONS

Three groups of results may be distinguished for viscous incompressible flow around an airfoil/body. The first ones are classic and directed to verification of algorithm and to study of basic properties of the viscous flow around a body. The second ones deal with the new physical phenomena which are revealed by analysis of computational results. The third group of results is pointed out for assessment of correctness of problem statement and for study of the problem to what extend the model of incompressible medium is equivalent to a problems under study?

The volume of a single paper does not sufficient for complete description of all results from this list. On this reason the presentation of results from the first group are limited by a few examples. The mesh used in calculations have 128 or 256 nodes in η-coordinate and 80 or 400 nodes in ξ -coordinate. The outer region is on the ten (or more) airfoil chords. The mesh is compressed to an airfoil by the transformation $\xi = d\ \mathrm{tg}(\pi\vartheta/2)$ where $d=0.5$ for $N_\xi=80$ and $d=0.25$ for $N_\xi=400$. The first mesh will be mentioned as a normal mesh and the second one as a fine mesh. The flow around airfoil NACA0012 is studied.

In Fig. 1 the pressure coefficient $Cp = - (p-p_0)/0.5\rho U_\infty$ and surface vorticity are presented for the flow at Re=10,000, $\alpha=5°$ (no-slip boundary conditions), the normal mesh, the predictor-corrector algorithm. The $D_x^k = D_y^m = 0$ and the Fig. 1a, b, c corresponds to the values of circulation Γ are equal to 0, -0.21, -0.4. This results show that a pressure uniqueness on the wall is fulfilled (the solid line corresponds to p_1 and the dotted line corresponds to p_0). This is essential that solution at $\Gamma = 0$ exists. The airfoil lift L at $\Gamma = 0$ is equal nearly to $L^p/2$ (see [14]), where L^p is the value of lift obtained for a potential ideal flow at $\alpha=5°$. The maximum of lift obtained in [14] is attained at $\Gamma = - 0.21$ and is equal to $C_L = L/_0.5\rho U^2_\infty = 0.55$ (when the predictor stage of Ω_S calculation had been used only). This value of lift is near to experimental result [17]. The lift calculated for p_0 in this case is equal to 0.49. The predictor-corrector algorithm singles out the lift value equals 0.49 for a given value of $\Gamma=-0.21$.

The problem of lift maximum is very complex. The results of Huang et al. [18] show that the lift may be significantly larger if the single vortex is posed near the airfoil in diffusor part at leeward side of an airfoil. There are the lines of equilibrium positions of centre of this single vortex. This vortex can exist due to a flow separation. The computational simulation in viscous incompressible flow confirms the possibility of such flow at Re=10,000, $\alpha=5°$, $D_y^1=4$, see [19, 20, 21]. The lift is increased significantly. The problem of an aerodynamical hysteresis arises in this connection, see [22].

The second group of results is presented by the study of surface vorticity waves. In Fig. 2 the relative surface vorticity (the relative vorticity is defined as a difference between vorticity at two time moments t1 and t2) is shown for t1-t2=0.1, Re=10,000, $\alpha=5°$. The vorticity waves are born at the leading edge, move to separation point at leeward side of an airfoil, intensify in separation region and greatly grow in the region near a trailing edge (TE). At windward side of an airfoil the vorticity waves move to a trailing edge and amplify at a small region near TE. Two vorticity waves having a different sign of vorticity run into each other at the TE (theangle of TE is not zero for NACA0012 airfoil). This process borns the large pressure impulse in incompressible flow at the TE. The point of zero vorticity oscillates in the region of two neighbouring mesh nodes on an airfoil surface (one of this nodes consides with TE). The flow is locally unsteady. We discuss the possible temperature process at this region in Section 6 and substantiate the realty of unsteady behavior of the flow in this phenomenon.

The multidipole asymptotic used in (8) as a far boundary condition for the velocity plays a decisive role in a number of critical physical processes near an airfoil in the stream [22]. We can consider the perturbation of upcoming flow (or surrounding flow) as the perturbation of coefficients at multidipole terms in (8). This problem had been considered by Zakharenkov in [21]. The predictor stage only had been employed in [21]. This is done because the problem of pressure uniqueness is related with the assignment of far field boundary condition, see Badr et al. [23]. This had been shown in [21] that for NACA0012 airfoil at Re=10,000 and $\alpha=5°$ the pressure uniqueness on the wall cannot be achieved by variation of parameters of (8). On this reason the errors in calculation of pressure-vorticity relation on the airfoil are picked out as a main reason. The employment of predictor-corrector algorithm eliminates this errors and results presented in [21] are verified because the pressure distributions corresponding to p_0 are conserved. In Fig. 3a, b, c the pressure distribution and in Fig. 3d,e,f the surface vorticity which correspond to the flow patterns in Fig. 4 (Fig.4a, b, c are streamlines, d, e, f are the lines of equal values of vorticity) are shown for the variation of a single dipole term in (8): Fig. 3a) $Dy^1 = 4$, b) $Dx^2 = 78$, c) $Dy^2 = -64$. For the case $Dy^1=4$ the results corresponds to predictor-corrector algorithm calculations. The variation of this coefficients only changes the flow pattern significantly. Variation of Dy^1 and $Dx^2<0$ coefficients provokes the strong separation. Variation of $Dx^2>0$ coefficient moves the separation point on the airfoil toward TE and conserves the form of flow separation

which can be characterized as a weak separation. Variation of Dy^2 term effects the width and thickness of separation zone and suppress the fluctuation of vorticity field near the trailing edge. In connection with a surface vorticity waves generation we can conclude that the presence of Dy^2 dipole field suppress the amplification of vorticity waves.

The effectivness of predictor-corrector algorithm for calculation of unsteady flow at Re=10,000 is shown in [15] and is confirmed herein by presentation of the pressure coefficient in Fig. 3a for Dy^1=4. The next example is in Fig. 5, where a,b) presents the pressure coefficient and c,d) is the surface vorticity at Re=1,000, α=5°, Dy^1=24 for two time moments t1=39.25, t2=42.25. The streamlines and lines of equal values of vorticity are presented on Fig. 6a, b and Fig. 6c, d correspondingly. The massive flow separation is visible in Fig.6. The uniqueness of pressure distribution along an airfoil is correctly fulfilled.

The unsteady flow in the region of TE can be characterized by formation of vortex spots, see [24, 25]. The running one into another of two surface vorticity waves (see Fig.2) is the reason of oscillation of point of zero vorticity. This process leds to complex phenomenon which shaw itself in the vorticity field. The new vortex patterns which are intermediate between vortex waves and a vorticies are generated. This vortex patterns are shown for Re=30,000 and α=0 at Fig. 7 where the lines of equal relative vorticity are shown for t1-t2=0.06 . The fine mesh is used for calculations at Re=30,000. The correspondence between a trailing edge vortex spots generation and fluctuations of lift and drag coefficients is picked out in [24, 25]. For zero angle of attack this correspondence is conserving and may be interpritated as a periodical drag accumulation which leds to the shedding of vortex spots.

The influence of slip-condition on the viscous flow characteristics is interested as a process of possible drag reduction. Simultaneously we obtaine an interesting case of the flow in vicinity of TE. If we take into account that vorticity at the TE (or near TE) must be zero and look on the formulae (17),(18), then we can conclude that the tangential velocity at the TE is zero even for slip-condition. In this case the increase of friction in the inner layers of the viscous flow near the trailing edge is possible because the friction about the surface is reduced and the last one may be unsufficient to establish the tangential velocity to be a zero at the TE. In Fig. 8 the pressure, tangential velocity and vorticity distribution along the airfoil are presented for the flow at Re=10,000, α=5°, λ=3,000 (Γ=-0.21). The streamlines and the lines of equal vorticity are shown in Fig.9. The drag coefficient component due to pressure C_{DP} and one due to friction C_{Df} for no-slip condition are equal to 3.4794*10-2 and 2.7247*10-2 correspondingly. For slip condition at λ=3.000 this components are equal to 4.0883*10-2 and 2.6748*10-2 correspondingly. The fluctuations of C_D are conserving. The slip along the surface decreases the friction drag and increases the pressure drag components. The perfect slip at λ=0 is attainable for a small Reynolds number only (Re=200 in [1]). This is because the surface vorticity grows essentially with Re increasing, and the tangential velocity (related with surface vorticity by expression (18)) achieves a too large values.

6. DISCUSSION

The results presented in a previous Section show the wide possibilities for the study of different complex flows around a body at Reynolds number up 100,000. But the number of complex phenomena in the regions of leading and trailing edges of the body initiates us to improve the problem statement.The refined problem statement includes the study of heat process in a boundary layer and a possible viscous-temperature dependence. We can write the heat transport equation in the form

$$DT/Dt = 1/Pr\ !/Re\ \Delta T + Ec\ 1/Re\ \Phi \qquad (22)$$

where T is temperature, Pr is the Prandtl number, Ec is the Eckert number and the dissipation function Φ takes the form, see [26]

$$\Phi = 2(\partial^2\Psi/\partial x\partial y)^2 + (\Omega - 2\partial^2\Psi/\partial x^2)^2 \qquad (23)$$

The number of boundary conditions for eq.(22) on a wall are possible. The continuation of eq. (22) onto the wall can not be employed for every kind of boundary conditions. But we can consider such continuation as a special b.c. when we have not the confidence in any other relation on a wall. Then for a steady flow (at a no-slip conditions) we obtaine on the wall y=0 the relation

$$1/Pr\ 1/Re\ \Delta T + Ec\ 1/Re\ (H^2\Omega_S)^2 = 0 \qquad (24)$$

which at the points where Ω_S=0 simplifies to ΔT=0. This is essential that the last relation is hold for a very small region near the TE on the centreline (c.l.) of the wake where Ω = 0.

This means that near the trailing edge where a convective heat transfer and vorticity are equal to zero the realization of (24) demands for a "O" type computational mesh the fulfillment of condition

$$\partial^2 T/\partial\eta^2|^{upper}_{S,\,c.l} = \partial^2 T/\partial\eta^2|^{lower}_{S,\,c.l.} \qquad (25)$$

The eq. (25) is additional differential relation which must be fulfilled in computations. But this relation may be a great restrictive (see discussion of analogous problem for a boundary vorticity at the vertex in [4]). For example, the process of running one into another of two surface vorticity waves (while such processes is initiated by any way) leds to a large growth of local friction on the surface and to a corresponding growth of heat. This is preferably to suppose that the heat transfer in the region of TE is unsteady in this case. The similar analysis is correct for a boundary vorticity. There are not an evident physical mechanism which stabilizes the flow in the region of TE if any perturbation initiates the spots generation.

The heat transfer from TE should be essentially easy if the tangential velocity at the TE is not zero *then the convective transfer is possible(. We can consider as an example of such boundary condi..on the slip-condition obtained for large velocity in [2]

$$u_X(x, 0) = f(T)(A\partial u/\partial y|_S + B\varphi(T)\partial\ lnT/\partial x) \qquad (26)$$

where f(t) φ(t) are known functions on temperature, A and B are some constants defined in [2] and others papers.

This relation admits the non-zero tangential velocity at the TE even at zero value of vorticity ($\partial u/\partial y|_S$ = 0). Moreover, the tangential velocity may be different if we consider the limits upon upper and lower surface of an airfoil. The uniqueness of tangential velocity at the TE puts the additional condition which may be employed for example for the determination of velocity circulation around an airfoil. The necessity to take into account the viscosity-temperature dependence become evident

The theoretical and computational results show the wide possibilities for application of proposed numerical algorithm to the problem of drag reduction. The new rheological laws may be easily incorporated into the problem statement including the boundary conditions on the wall. The inclusion of heat calculation and viscosity-temperature dependence which are conducted in a present time supposes a more realistic computational results.

The inclusion of any additional turbulence model is practicable. The correct pressure-vorticity relations on the body surface is the most attractive property of proposed approach for solution of Navier-Stokes equations.

REFERENCES

1. H.J.Lugt and S.Ohring "Laminar flow behavior under slip-boundary conditions," The Physics of Fluids, Vol.18, No.1, January, pp.1-8, 1975.
2. M.N.Kogan "The dynamics of rarefied gas," Moscow: "Nauka", 1967 (in Russian).
3. M.A.Reynolds, J.J.Smolderen "Profile measurements in the Knudsen layer for the Kramers problem," for Karman an Institute for fluids Dynamics, 1974.
4. P.J.Roach "Computational Fluid Dynamics," Hermosa publishers, Albuquerque, NM, 1976.
5. S.Sundaresan and S.M.Deshpander "On pressure compatibility condition in numerical simulation of incompressible viscous flows using primitive variable formulation," In Book of Briefs 1st International Conference on Numercical Methods in Fluid Dynamics, June 24-28, 1996, Monterey, California, pp.118-119, 1996.

6. M.N.Zakharenkov "Singularities of finite-difference scheme for two-dimensional Navier-Stokes equations solution connected with the boundary conditions statement on a solid surface", Zurnal Vychislitel'noj Matematiki i Matematicheskoj Fiziki, 30, 8, 1224-1236, 1990 (in Russian).
7. H.J.Lugt, H.J.Haussling "The acceleration of thin cylindrical bodies in a viscous fluid," Journal of Applied Mathematics, V.45, pp.1-6, 1978.
8. M.N.Zakharenkov "On the approximation of the boundary condition for vorticity," In Sbornik Chislennye Metody Mehaniki Sploshnoj Sredy, 13, 2, pp.61-81, Novosibirsk, 1982 (in Russian).
9. K.N.Ghia, G.A.Osswald, U.Ghia "Analysis of two-dimensional incompressible flow past airfoils using unsteady N-S equations," In Numerical and Physical Aspects of Aerodynamic Flows III. Ed. by Tuncer Cebeci, 1986.
10. A.A.Samarsky "Theory of difference schemes," Moscow: "Nauka", 1977 (in Russian).
11. D.Potter "Numerical Methods in Physics," Moscow:"Mir", 1975 (Translation from English into Russian).
12. B.Engquist, S.Osher "One-sided difference approximations for nonlinear conservation laws," Mathematics of Computations, V.36, No.154, pp.321-351, 1981.
13. M.N.Zakharenkov "Approximation of the boundary condition for vorticity at a solid body surface in the analysis of the Navier-Stokes equation," In Sbornik Chislennye Metody Mehaniki Sploshnoj Sredy, 11, 7, pp.56-74, Novosibirsk, 1980 (in Russian).
14. M.N.Zakharenkov "Far-field boundary conditions for a viscous incompressible flow past a profile," Matematicheskoe Modelirovanie, 2, pp. 3-18, 1990 (in Russian).
15. M.N.Zakharenkov "Pressure uniqueness for solution of Navier-Stokes equations in terms of stream function and vorticity," Matematicheskoe Modelirovanie, V.10, No.1, pp. 3-10, 1998 (in Russian).
16. S.Abdallah "Numerical solution for pressure Poisson equation with Neumann boundary condition using a non-staggered grid," Int. Journal of Computational Physics, 70, pp.182-192, 1987.
17. Tuncer Cebeci, L.W.Carr, H.M.Jang "An iterative boundary-layer procedure for oscillating airfoils including transition effects," AIAA-89-0020, 27th Aerospace Sciences Meeting, January 9-12, Reno, Newada, 1989.
18. M.-K.Huang, C.-Y.Chow "Trapping of a Free Vortex by Joukovski Airfoils," AIAA Journal, V.20, No.3, pp.292-298, 1982.
19. M.N.Zakharenkov "The calculation of a separated flow around a trailing edge of an airfoil," Preprint TsAGI No.4, 1991, Moscow: Central Aero-Hydrodynamic Institute (in English, translation from Russian 1990).
20. M.N.Zakharenkov "Unsteady incompressible viscous flow past an airfoil," Arch.Mech, V.42, No.4-5, pp.609-615, 1990.
21. M.N.Zakharenkov "Influence of multidipole asymptotics of far field (employing as a boundary condition) onto the flow separation in the problem of viscous incompressible flow around an airfoil," In Akustika neodnorodnyh sred-IV, 28-31 May 1996, Novosibirsk (in Russian).
22. M.N.Zakharenkov "Simulation of airfoil aerodynamic hysteresis for flight safety problems," 4th International conference "Aircraft and Helicopters diagnostics. AIRDIAG'95. Warsaw, 6-7 December 1995. Air Force Institute of Technology.-ITWL/Informator ITWL wewn 338/96, Warsaw, 1996.
23. H.M.Bard and S.C.R.Dennis "Time-dependent viscous flow past an impulsively started rotating and translating circular cylinder," J.fluid Mechanics, 158, pp.447-488, 1985.
24. M.N.Zakharenkov "Small-scale vortex structures in numerical solutions of two-dimensional Navier-Stokes equations," Preprint TsAGI No.69, Moscow:Central Aero-Hydrodynamic Institute, 1993 (In Russian and in English).
25. M.N.Zakharenkov "Generation of vortices and vortex spots - spots of momentum loses, in the viscous flow around an airfoil," In Scientific Papers of International symposium on ship hydrodynamics devoted to 85th anniversary of bithday of A.M.Basin, pp.450-470, 1995 (in Russian).
26. H.Schlichting "The theory of boundary layer," Moscow:"Nauka", 1974 (Translation from German into Russian).

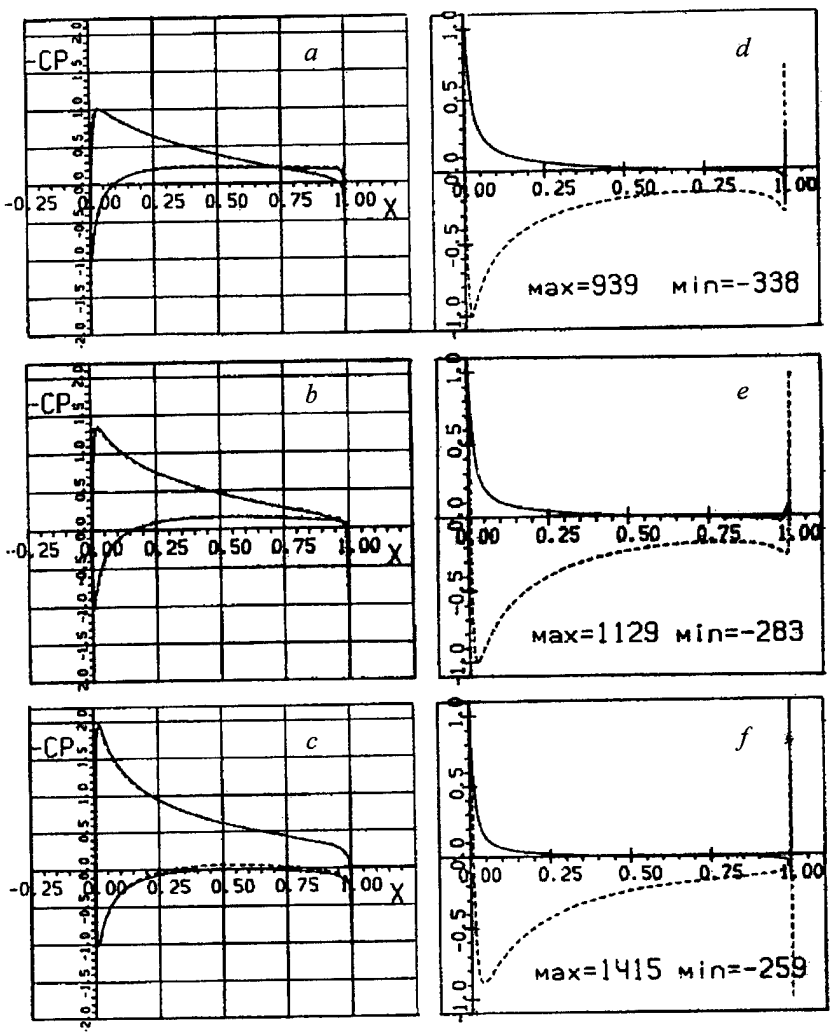

Figure 1. C_p - a, b, c) and vorticity - d, e, f) along the NACA0012 airfoil surface at Re = 10,000, $\alpha = 5°$ for circulation $\Gamma = 0, -0.21, -0.4$ cofrespondingly.

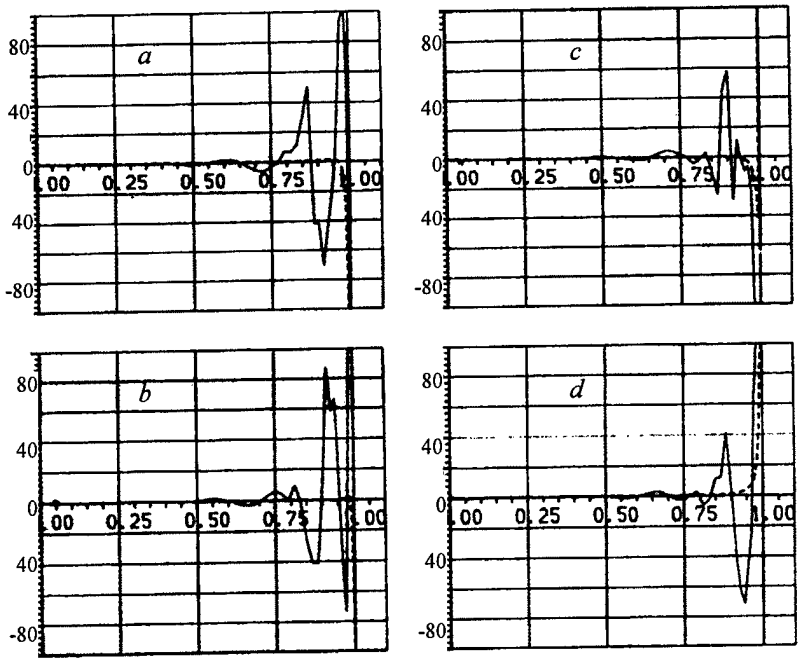

Figure 2. The waves of surface relative vorticity at Re = 10,000, $\alpha = 5°$ shown with time increment $\delta t = 0.1$.

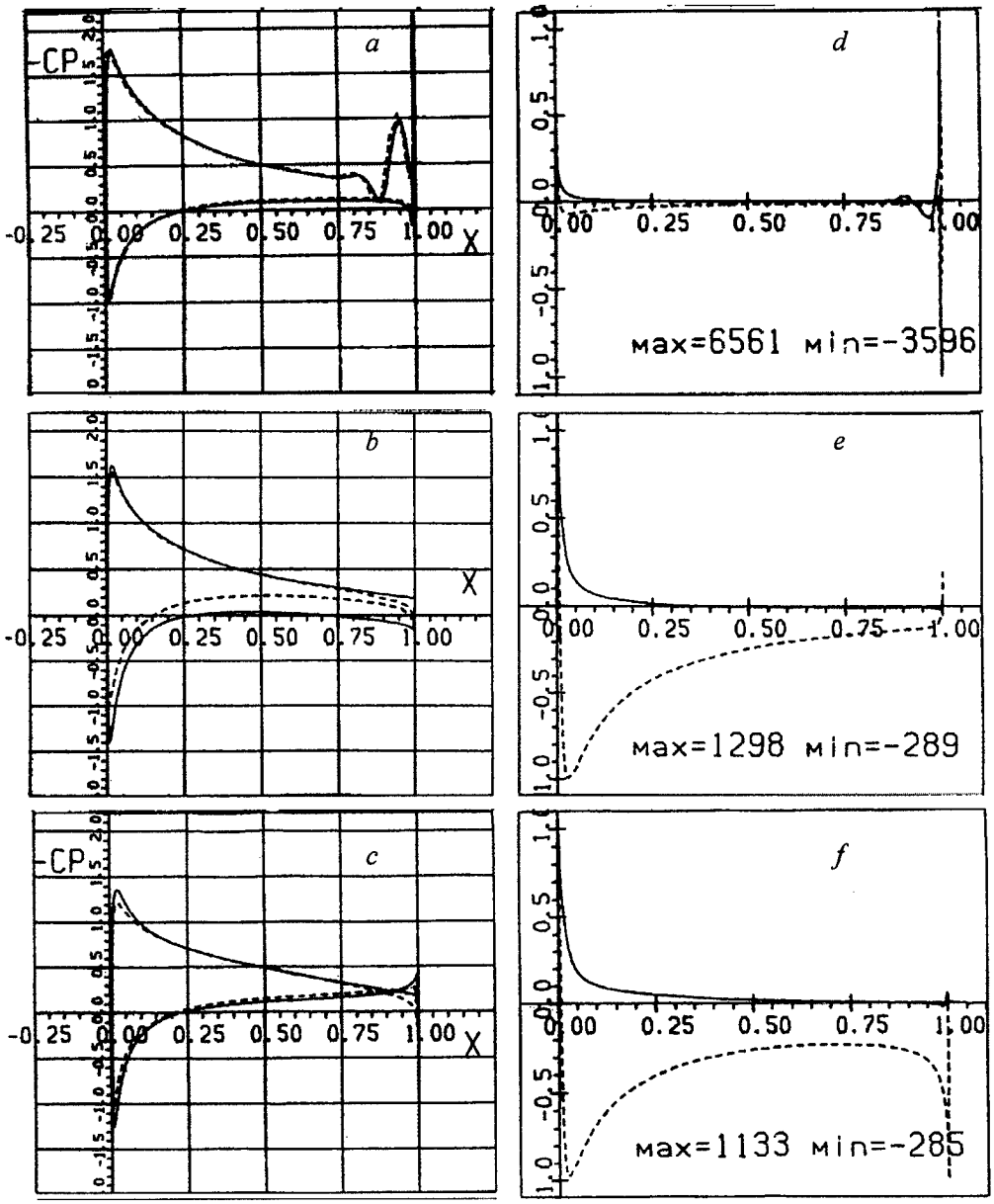

Figure 3. C_p – a, b, c and surface vorticity – d, e, f corresponding to the flow disturbed by multidipole perturbations: a, d – D_y^1=4; b, e – D_x^2=78; c, f – D_y^2=-64.

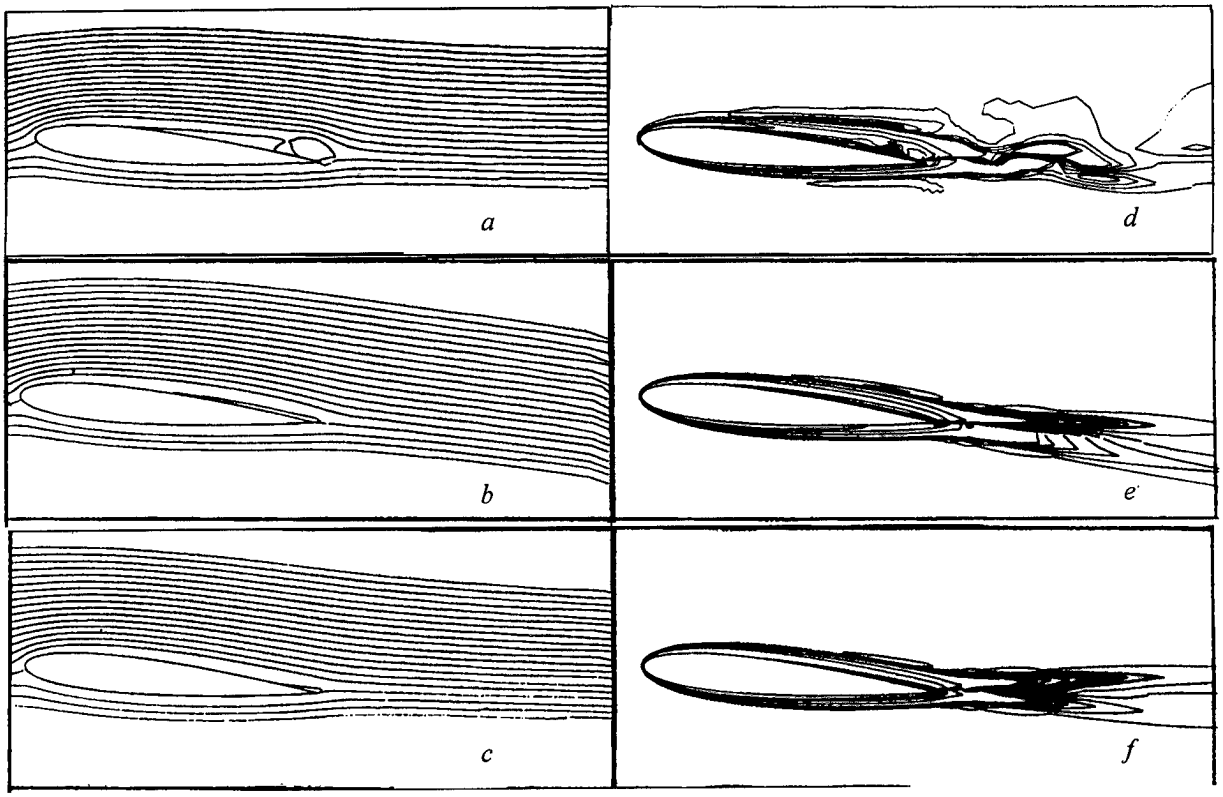

Figure 4. a, b ,c - streamlines, d, e, f - the lines of equal values of vorticity corresponding to multidipole perturnbations listed in Fig. 3

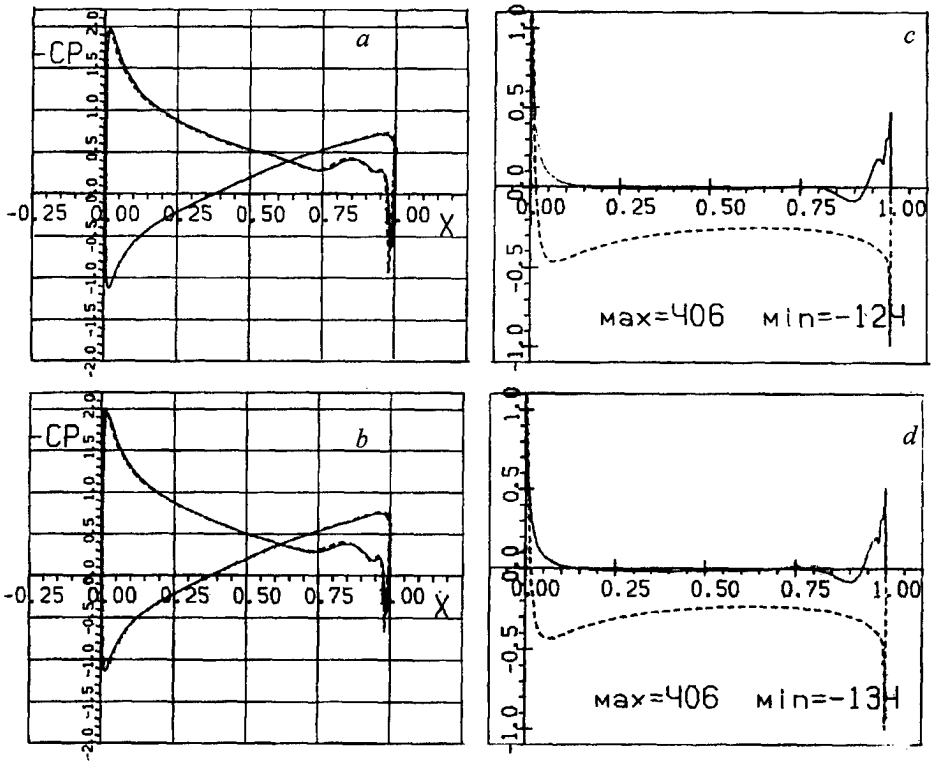

Figure 5. C_p on NACA0012 airfoil at Re=1,000, $\alpha = 5°$, $\Gamma = -0.20$, $D_y^1 = 24$. a, c – t = 39.25 ; b, d – t = 42.25.

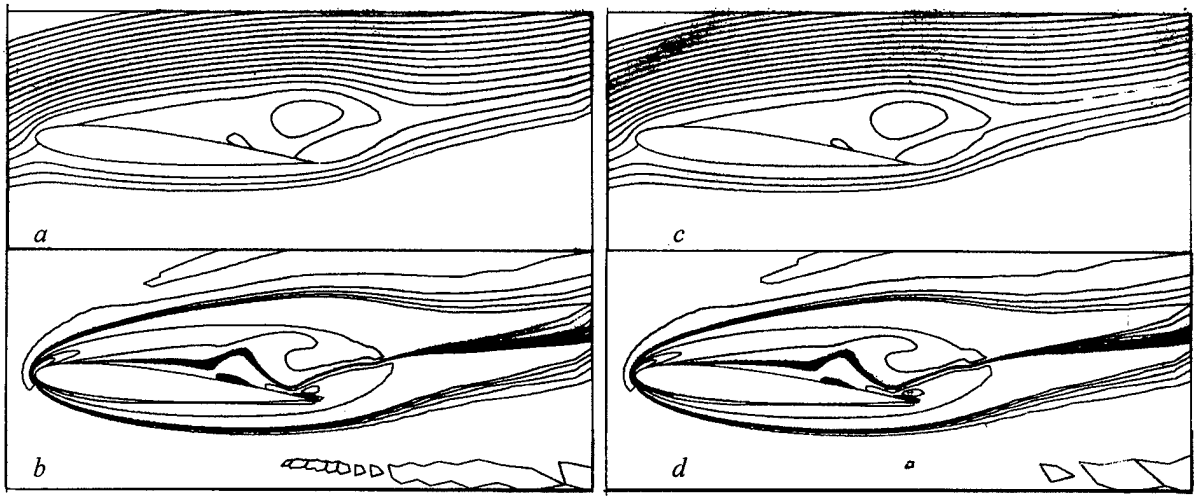

Figure 6. a,c - streamlines, b, d - the lines of equal values of vorticity. a, b - t = 39.25 ; c, d - t = 42.25.

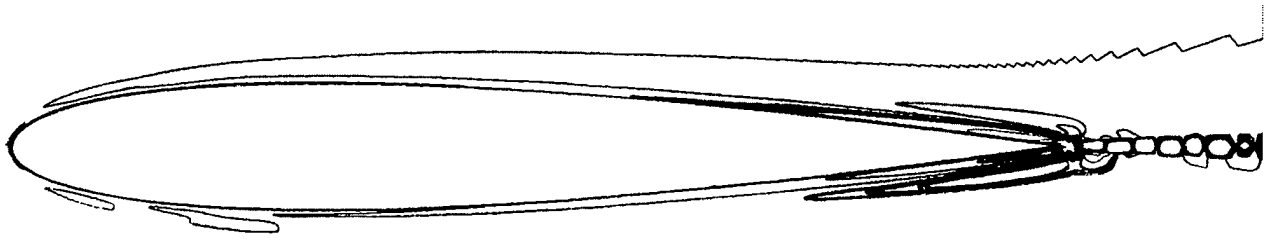

Figure 7. The lines of equal values of relative (time increment is equal to 0.06) vorticity around NACA0012 airfoil at Re=30,000, $\alpha = 0$ shown with the step $\delta\Omega = 0.125$.

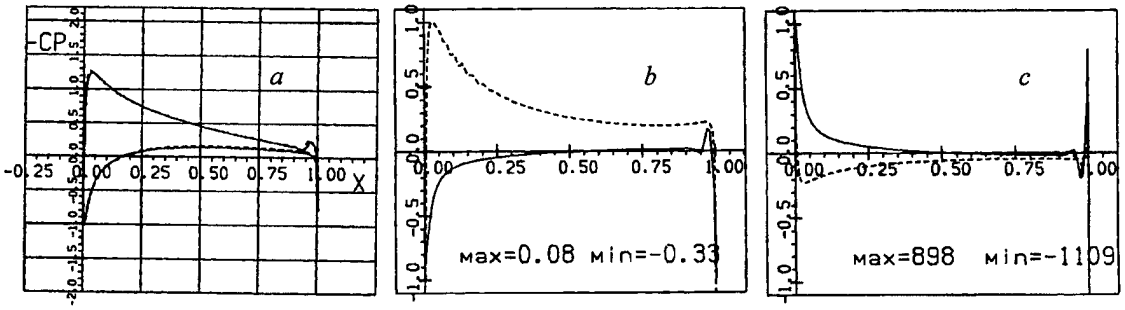

Figure 8. a) - C_p, b) - tangential velocity , c) surface vorticity on NACA0012 airfoil at Re=10,000, $\alpha = 5°$, $\lambda = 3000$.

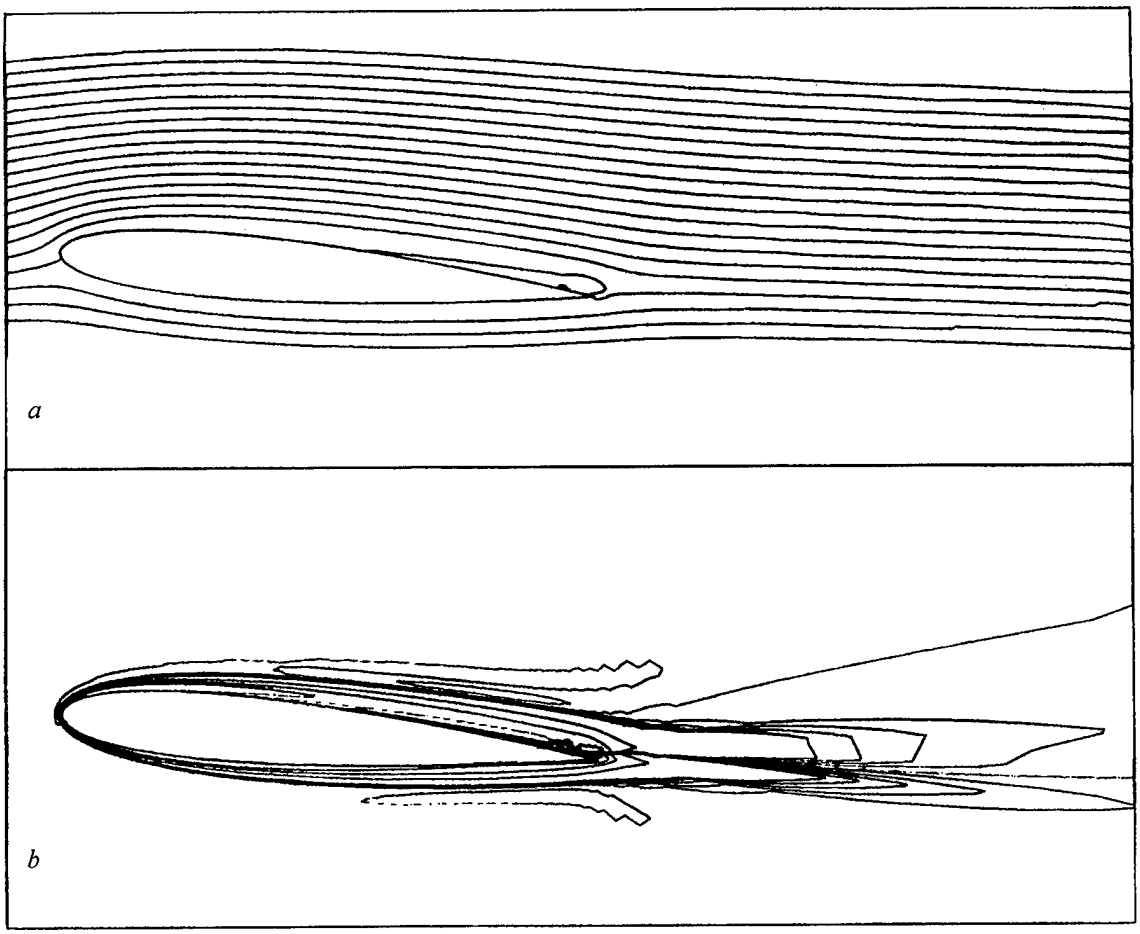

Figure 9. Streamlines a) and lines of equal vorticity b) around NACA0012 airfoil at Re=10,000, $\alpha = 5°$, $\lambda = 3000$.

FREQUENCY-WAVENUMBER SPECTRAL MEASUREMENT OF TURBULENT BOUNDARY LAYER WALL PRESSURE.

M. Pognant (1), G. Giovannelli (2) and B.E. Forestier (2)

(1) MS L.A.I.A.T. Université de Toulon, LA GARDE – FRANCE
(2) I.R.P.H.E – UMR 6594 CNRS, MARSEILLE – France

Abstract
The wavevector-frequency spectral estimation of wall pressure fluctuations by means of multiple Fourier transform processing of multi point data is discussed. This study brings up front the interest to probe the pressure field using pinhole transducers with a sensor spacing as small as possible. The investigations are carried beneath a turbulent boundary layer for a Reynolds number Re_x of 2,9 10^6. Fluctuating pressure measurements are made synchronously at sixteen equally spaced points. The convective ridge and the acoustic peak due to the background noise generated by the wind tunnel form the dominant energy contributions to the wall pressure spectrum. The spectral level at low wavenumbers has been previously evaluated in [1]. We use both these experiments in the subconvective domain and the present measurements in the convective part to fit the parameters of Chase's model of the ω-k spectrum. We show that the bias introduced by the discrete Fourier transform estimation on Chase's model integrated over the transverse wavenumbers is about 5 dB. The addition of Chase's model and the acoustic contamination of the facility is close to experimental frequency-wavenumber spectral densities.

NOMENCLATURE

N	number of sensors
r_x	sensor spacing
x/c	abscissa normalized by the long model
k	wavevector (k_x,k_z) in the wall plane
Δk	wavenumber resolution
k_N	Nyquist wavenumber
f	frequency
ω	circular frequency $\omega=2\pi f$
f_N	maximum frequency
$\Phi_{pp}(\omega)$	frequency spectral density
$\Phi_{pp}(\mathbf{k},\omega)$	wavenumber-frequency spectrum
δ	boundary layer thickness
δ*	boundary layer displacement thickness
ν	cinematic viscosity
U_∞	free stream velocity
U_c	convection velocity
U_τ	friction velocity
Re_x	Reynolds number $Re_x=xU_\infty/\nu$
Re_τ	Reynolds number $Re_\tau=\delta U_\tau/\nu$
$(\,)^m$	measured quantity

I. INTRODUCTION

Properties of fluctuating pressure in fully developed turbulent boundary layer flow at low Mach numbers are important in various aero and especially hydrodynamic applications. Many investigations examine changes in the fluctuating wall pressure field by the presence of LEBU, riblet surface or by the introduction of polymers. The performance enhancement addressed in these investigations is often the control of turbulent wall pressure fluctuations which are primary self and radiated noise source for undersea vehicles. It rapidly appears that the wavevector-frequency spectrum is suitable for description of the wall pressure field. In this paper, the ω-k spectrum is obtained by means of multiple Fourier transform processing of multi-point pressure data. If we desire measure the spectral modifications in the ω-k domain, it seems necessary to proceed the understanding of the limitations and the performance of the Discrete Fourier Transform (DFT) estimation.

II. ESTIMATION OF THE WAVENUMBER-FREQUENCY SPECTRUM

The recovery of the wavenumber spectrum at a given frequency is governed by the separation r_x between the centers of adjacent sensors according to the familiar Shannon's theorem. The Nyquist wavenumber $k_N=\pi/r_x$ and maximum frequency $f_N=U_c/2r_x$ can be putted back to $2k_N$ and $2f_N$ if the ω-k spectrum is predominantly one-sided i.e. if we suppose that the spectrum is highly attenuated above the convective ridge. Otherwise, there is no possible compromise ([2]) between an efficient low pass filtering (large sensor) of the convective part a nd limited wavenumber aliasing range (small spacing). Owing to these constraints, the pressure field is probed in this study using pinhole transducers of small size.

II.1 Boundary filter

A boundary filter is conceived to sample, spatially and temporally, the pressure fluctuation signals beneath a turbulent boundary layer for obtain the wavevector-frequency distribution of the pressure field. The difficulties for the computation of the actual spectrum $\Phi_{pp}(\mathbf{k},\omega)$ from a series of determinations of the measured spectrum $\Phi^m_{pp}(\mathbf{k},\omega)$ have been presented by [3]. In the temporal domain, the sampling frequency and the number of samples as numerous as desired and the filter can be approximated by a Dirac distribution. In the spatial domain, sensors are few and the separation distance is imposed by their size.

II.1.1 Relation between the actual and the measured ω-k spectra

For an array of N transducers in the x direction, the relation between the true and the measured spectra at steering

longitudinal wavenumber k_{x_0} and frequency ω_0 according to [3] is not explicit. If we consider punctual sensors, the integration over the transverse wavenumbers of this relation is given by :

$$\Phi_{pp}^{m}(k_{x_0},\omega_0) = 4\pi^2 \frac{r_x}{N} \int_{-\infty}^{+\infty} \Phi_{pp}(k_x,\omega_0) \left|A(k_x - k_{x_0})\right|^2 dk_x \quad (1)$$

where the multiplicity of sensors is accounted by the wavenumber filter shape function classically defined by :

$$\left|A(k_x - k_{x_0})\right|^2 = \left|\sum_n S_n \exp\left(-in(k_x - k_{x_0})r_x\right)\right|^2 \quad (2)$$

where S_n are the coefficients of the DFT filter shape for the window function.
If N is large, the window bandwidth is narrow. For an uniform window, we obtain the following usable relation :

$$\Phi_{pp}(k_{x_0},\omega_0) = \frac{N^2}{8\pi^3} \Phi_{pp}^{m}(k_{x_0},\omega_0) \quad (3)$$

III. MODELS OF THE WALL PRESSURE SPECTRUM

We present briefly the two main models of the wall pressure spectrum.

The Corcos model [4] is based on the similarity properties of the covariance of the pressure field. He made the assumption that the cross density function could be written in a separable form where the coherence loss of pressure sources is approximated by exponential decay functions. The decay constants γ_x and γ_z are respectively 0,2 and 0,8 in our study.

Chase [5] published a descriptive model of the turbulent boundary layer wall pressure spectrum established by its relation to the fluctuating velocity filed. The mathematical model for the wavevector-frequency spectrum in the incompressive inviscid domain is the sum of two components relative to the mean shear-turbulence and turbulence-turbulence interactions. At high frequencies defined by $\omega\delta^*/U_c >> 4$ or $\omega\delta/U_\tau >> 100$, the integration over wavenumbers gives an ω^{-1} evolution for $\Phi_{pp}(\omega)$. This model has been fitted by Chase on the experimental data of [6] : h=3, $C_M h$=0,466, $C_T h$=0,014 and b=0,75. h fixes the wavenumber dispersion of the energy around the convective ridge. The spectral maximum is determined by the constant C_M. The spectral level at low wavenumbers is proportional to $C_T h^3$. The parameter $C_T h$ has been estimated in [1] from acceleration spectra measurements at the center of two plates excited by a turbulent boundary layer in a hydrodynamic tunnel. The mean value which results of this experimental study is 0,12 with h=3 and is eight times as much as the value issued from the data of [6]. Its validity is discussed in [1].

IV. EXPERIMENTAL SET UP

The investigations were conducted in the elliptical open wind tunnel of I.R.P.H.E. in Marseille. The dimensions of the test section are 3,3×2,2 m². The measurement device is located at x/c=0,65 from the leading edge of the 5,4 m long, 0,8 m diameter axisymmetrical model. The wall pressure fluctuations are measured using 2,5 mm diameter piezoelectric ENDEVCO transducers whose sensing area is reduced by placing a cap perforated with a 0,3 mm diameter hole in its center. The extinction frequency of the single point spectrum given by $\omega\nu / U_\tau^2 \approx 2{,}5$ is 5,6 kHz. The Helmholtz resonance frequency for the pinhole system is next to 9,6 kHz. Measurements are unaffected by spatial averaging for f<7,6 kHz for a 12 m/s free stream velocity. The frequency response of each transducer has been tested using Bruel & Kjaer source delivering a white noise from 50 Hz to 10 kHz. The comparison between the response with and without the pinhole cap shows that the instrumental cut off frequency is 4 kHz. Pressure measurements are made synchronously at sixteen equally 3 mm spaced points. The Nyquist wavenumber k_N is 1047 m^{-1} and the frequency f_N is 1,2 kHz ($U_c \approx 0{,}6U_\infty$). The filter bandwidth Δk is equal to 131 m^{-1}. By assuming that the energy is not truncated and the number of transducers is sufficient, we use the practical relation (3) in order to estimate the ω-k spectrum. The ω-k spectrum is computed from the periodogram method. 64 blocs of 1024 temporal points for each sensor are recorded with an uniform window using a 10 kHz sampling frequency after low pass filtering at the Nyquist frequency of 5 kHz. The resulting frequency resolution is 4,88 Hz. The time-series are digitally filtered by applying a low pass filter of 80 dB/octave. The cross spectral density matrix is computed from 32 averages of 1024 points and the ω-k spectra are represented using a Fourier interpolation with 64 points.

V. EXPERIMENTAL RESULTS

V.1 Flow mean properties

Mean characteristics of the turbulent boundary layer obtained from the velocity profile measurements are recapitulated on table 1. The ratio of the boundary layer thickness to the radius a is small (δ/a=0,18) and therefore effects of transverse curvature are negligible.

δ	$10^3 C_f$	U_τ	τ_w	$10^{-6} Re_x$	$10^{-3} Re_\tau$
mm		m/s	Pa		
67,8	2,84	0,45	0,26	2,9	2,12

Table 1 : flow mean properties

V.2 Wavenumber-frequency spectra of the wall pressure field

The experimental spectral densities as a function of the longitudinal wavenumber k_x are reported in figure 1 for various frequencies. The structure of the spectral density exhibits a dominant ridge corresponding to convection of turbulent pressures. The convective ridge becomes broader and its amplitude decreases as the frequency increases. Owing to the resolution Δk equal to 131 m^{-1}, the acoustic peak, due to the background noise generated by the wind tunnel, is always centered around k_x=0 m^{-1}. The difference between the acoustic and convective levels is never higher than 5 dB and therefore, the acoustic contribution may contaminate the low wavenumber domain. At low frequencies, the two peaks are close and tend to disjoint as the frequency increases.

The basic DFT filter shape for the uniform window presents a difference of 13 dB between the main lobe and the highest side lobe localized at $k_x = \pm 200 m^{-1}$. The ripples observed at proximity of the acoustic peak and especially at $k_x = -200 m^{-1}$, are interpreted as acoustic energy leaking out by the side lobes of the

wavenumber filter shape function. The distortions located in the vicinity of the two peaks are probably due to acoustic and convective energy intercepted by the side lobes. Above $0{,}8f_N$, the sidelobe leakage is concealed by the first effects of spectral aliasing.

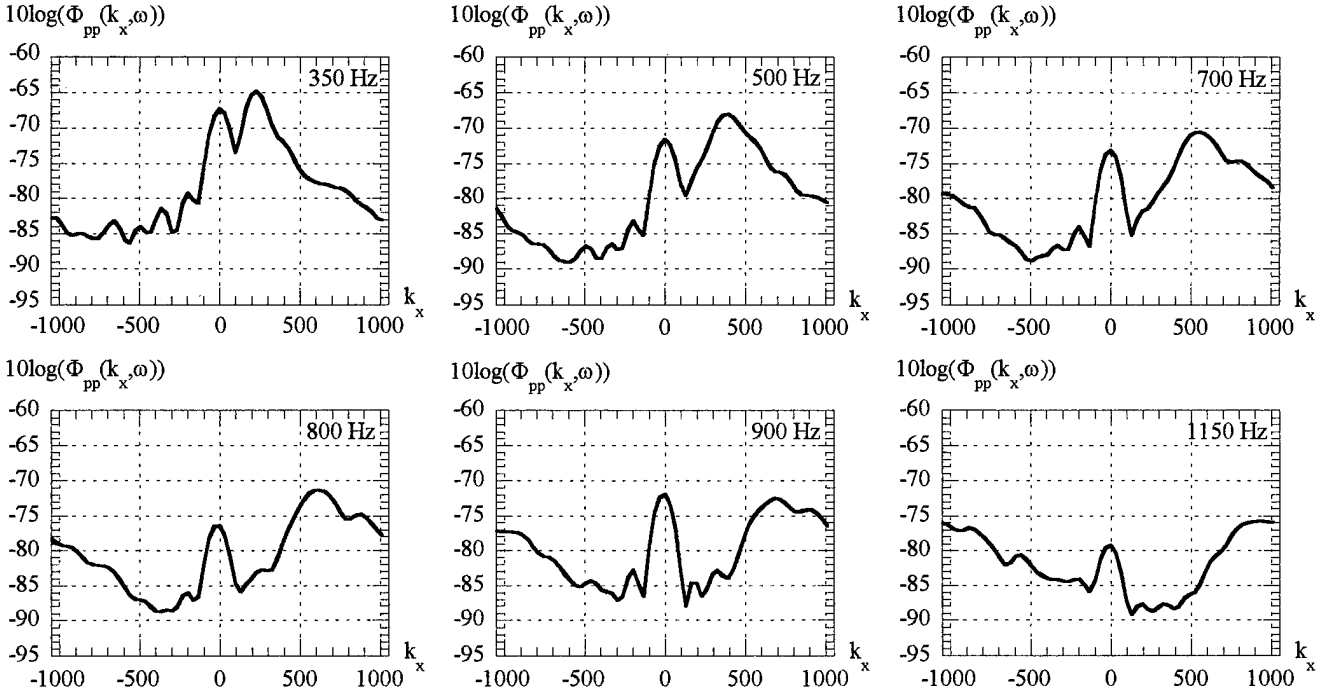

Figure 1 : experimental spectral densities measured from the synchronous method by sixteen equally spaced transducers beneath a turbulent boundary layer for various frequencies ($f<f_N$).

VI. PERFORMANCE OF THE DFT ESTIMATION FOR THE CORCOS AND CHASE MODELS

For the Chase model, the correlation matrix is obtained by inverse 512-point Fourier transform over the longitudinal wavenumbers. The frequency-wavenumber spectrum is computed with 16 points in order to take into account the same bias as the experimental estimation. h and $C_M h$ parameters fit on our experimental results for a frequency of 700 Hz (figure 2) situated at the middle of the ω^{-1} behavior of the auto spectrum. The values obtained for h and $C_M h$ are respectively 4,9 and 0,85 and remain superior to 3 and 0,466 recommended by Chase with the data of [6]. But in the approach [6], the major part of the convective contribution is filtered.

The performance of the periodogram with the Fourier transform estimator is shown in figure 3 for the Chase and Corcos models at $\omega\delta^*/U_\infty \approx 4$ (900 Hz).

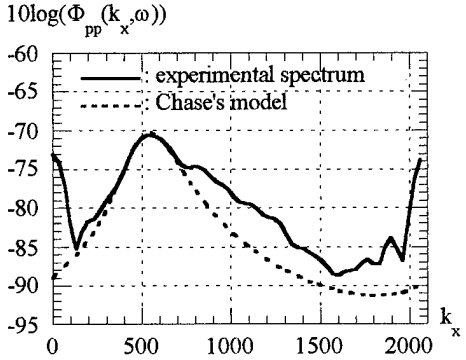

Figure 2 : determination of the Chase model parameters h and $C_M h$ at 700 Hz.

The values of $C_T h$ equals to 0,014 for the measurements of [6] and 0,12 for the data issued from [1] with h=3 are respectively adjusted at $5{,}25\ 10^{-3}$ and 0,045 with h=4,9 in order to follow the subconvective level proportional to $C_T h^3$, predicted by the Chase model.

The bias, at $k_z=0\ m^{-1}$, introduced by the DFT for a linear array of 16 points equally 3 mm spaced is about 17 dB if $C_T h=5{,}25\ 10^{-3}$ and is reduced to 9 dB for $C_T h=0{,}045$ (figure 3a).

The difference between the convective and subconvective levels decreases when the Chase model is integrated over k_z, whereas it remains constant for a model of rectangular product form as the Corcos spectrum. This difference is about 29 dB for the figure 3a and 23 dB for the figure 3b with $C_T h=0{,}045$.

For the k_z- integrated Chase's model, the error due to the low number of sensors is 12 dB for $C_T h=5{,}25\ 10^{-3}$ and 5 dB if $C_T h=0{,}045$ (figure 3b). The spectral fidelity of conventional beamforming using the Chase model with $C_T h=0{,}045$ is reasonably correct.

It is clear that the subconvective level comparatively to the spectral maximum is imposed by the filter shape function. For an uniform window, the difference between the main and the highest side lobes is 13 dB. The ratio between the convective level to the corresponding subconvective level predicted by the Corcos model is 14 dB (Figure 3c). The DFT estimation is thus accurate for the Corcos model.

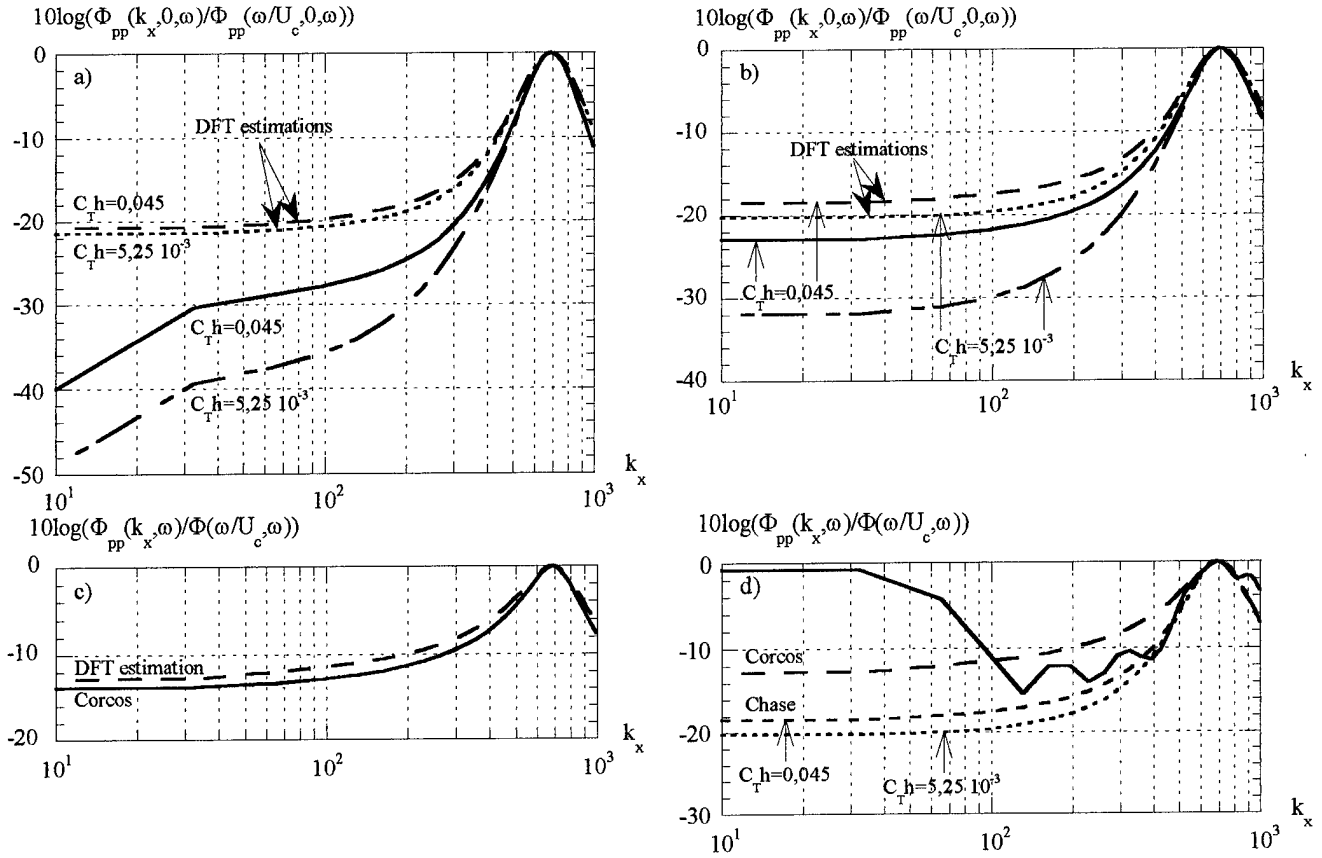

Figure 3 : bias introduced by the DFT estimation at $\omega\delta^*/U_\infty \approx 4$ (900 Hz) a) on Chase's model at $k_z=0$, b) on the k_z-integrated Chase's model c) on the Corcos model ; d) comparison between the Chase and Corcos models estimated by DFT and the experimental density.

When the parameter $C_T h$ grows from 5,25 10^{-3} to 0,045 the subconvective level increase resulting from the periodogram beamforming method is merely 1,8 dB. The DFT estimation on Chase's model is close to the experimental ω-k spectrum (figure 3d). The acoustic contamination of the facility can explain the difference between the experimental and computed spectra. When the Corcos model is used, the low wavenumber level is overestimated.

We model the acoustic contamination of the facility. This external contribution is seen as a plane wave propagating in the streamwise direction. We add this excitation on Chase's spectrum. The model is confronted figure 4 to the experimental densities.

The evaluation of the parameters h and $C_T h$ carried at 700 Hz is satisfactory for all frequencies included to the –1 slope of the frequency spectrum. The differences between the experimental and predicted convective levels are very slight. Otherwise, the wavenumber dispersion of the energy around the convective maximum is correctly reproduced by the model. We show that the DFT estimation on the integrated model is close to experimental frequency-wavenumber spectral densities for frequencies inferior to $0{,}8f_N$ (960 Hz). At 1000 Hz and 1150 Hz, the aliasing energy predicted by the model remains slightly inferior to the experimental one. The figure shows that the periodogram beamforming method is adequate as an estimate of the experimental wavenumber spectrum. The disymmetry of the convective ridge observed in experimental densities is questionable.

VII. CONCLUSION

According to the Shannon theorem and given that the sensitive sensor size cannot act as a pre-filter to attenuate the convective region of the ω-k spectrum [2], the sensor spacing in our study is as reduced as possible. Moreover, for a sufficient number of sensors and for a very small sensitive sensor surface, there is a simple relation between the actual and the measured spectra. Consequently, we probe the pressure field using pinhole transducers.

In the convective region, the DFT method is adequate for the determination of the spectral maximum reached at about $k_x=\omega/U_c$ and the dispersion of the energy around ω/U_c. The convective parameters h and $C_M h$ of the Chase model obtained from our experimental results are 4,9 and 0,85.

The subconvective level, previously evaluated in [1], is 9 dB higher than the measured one by [6]. These experiments lead to a parameter $C_T h$ of about 0,045 for the present study. In this case, the DFT estimation follows the general trend of the k_z-integrated Chase model quite well. Otherwise, the experimental spectra are correctly reproduced by the sum of the integrated Chase model and the acoustic contribution expected from a sixteen sensor beamformer. The acoustic contamination is responsible for a slight rise of the subconvective level, about 3 dB. We propose to infer an approximation of the ratio between the convective to the subconvective levels from the model. This ratio is about 23 dB.

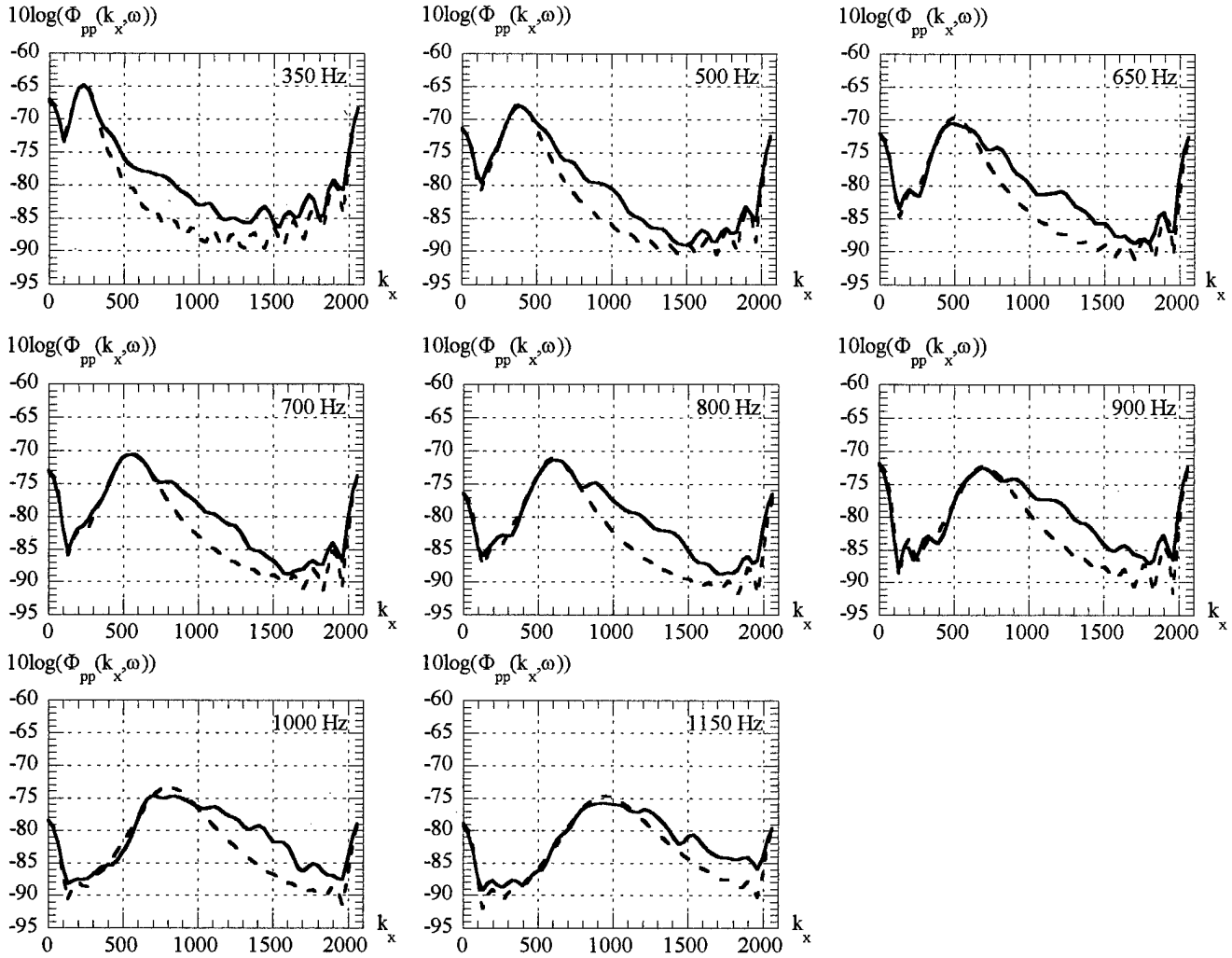

Figure 4 : comparison between the experimental densities measured with the synchronous method (———) and the computed spectra from the addition of Chase's model and the acoustic contamination (- - - -).

AKNOWLEDGEMENTS

This work was supported by the Centre d'Etude et de Recherche en Détection Sous-Marine (C.E.R.D.S.M) at the Direction des Constructions Navales (D.C.N.). Dr Giangreco C. is gratefully acknowledged.

REFERENCES

1. G. Giovannelli, A. Iddir and B.E. Forestier "Effets d'une couche limite turbulente sur le comportement vibroacoustique d'une plaque bafflée couplée à une cavité", Actes du 4ième congrès français d'acoustique, April 1997 pp. 1023-1026.

2. G.H Wakefield and M. Kaveh "Frequency-wavenumber spectral estimation of the wall-pressure field beneath a turbulent boundary layer", ASME, Shear Flow-Structure Interaction Phenomena, A. Akey and M. Reischman eds., 1985.

3. G. Maïdanik and D.W. Jorgensen "Boundary wave-vector filters for the study of the pressure field in a turbulent boundary layer", Journal of the Acoustical Society of America, 42 (2), 1967, pp. 494-501.

4. G.M. Corcos "The structure of the turbulent pressure field in boundary layer flows", Journal of Fluid Mechanics, 18, 1964, pp. 353-378.

5. D.M. Chase "The wavevector-frequency spectrum of pressure on a smooth plane in turbulent boundary layer flow at low mach number, Journal of the Acoustical Society of America, 90 (2) 1991, pp. 1032-1040.

6. N.C. Martin and P. Leehey "Low wavenumber wall pressure measurements using a rectangular membrane as a spatial filter", Journal of Sound and Vibration, 52 (1), 1977, pp. 95-120.

HIGH REYNOLDS NUMBER TURBULENT FLOWS

Alexander J. Smits
Mechanical and Aerospace Engineering
Princeton University
Princeton, New Jersey 08544-0710
asmits@princeton.edu

Mark V. Zagarola
Creare Inc.,
P.O. Box 71,
Hanover, NH 03755
mvz@creare.com

Abstract - New scaling laws for the mean velocity profiles in pipe flow and boundary layers are discussed. These laws are based on recent measurements in the Superpipe facility over a very wide Reynolds number range. For the inner layer scaling, a power law was found for the overlap region of the mean velocity profile at low Reynolds numbers, and both a power law and log law region at high Reynolds numbers. The power law with empirical constants determined from pipe flow data was also in good agreement with boundary layer data. For the outer layer scaling, a new outer velocity scale given by $U_{CL} - \bar{U}$ was proposed for the pipe flow and $U_\infty \delta^*/\delta$ was proposed for boundary layers. These scales collapse the pipe and boundary layer data considerably better than the conventionally-used friction velocity, over very wide ranges in Reynolds number.

1 Introduction

The behavior of turbulence at high Reynolds number is interesting from a fundamental point of view, in that most theories of turbulence make very specific predictions in the limit of infinite Reynolds number. From a more practical point of view, there exist many applications that involve turbulent flow where the Reynolds numbers are extremely large. For example, large vehicles such as submarines and commercial transports operate at Reynolds numbers based on length of the order of 10^9, and industrial pipe flows cover a very wide range of Reynolds numbers up to 10^7. Some typical values are given in table 1, where Re_ℓ is Reynolds number based on length given by

$$Re_\ell = \frac{\rho U_\infty \ell}{\mu} = \frac{U_\infty \ell}{\nu},$$

where ρ is the density, ℓ is the length, U_∞ the speed, μ is the dynamic viscosity and ν is the kinematic viscosity. Similarly, Re_δ is based on U_∞ and the expected maximum value of the boundary layer thickness, Re_D is based on the average velocity $\bar{U}$ and the pipe diameter, and

$$Re_\tau = \frac{D u_\tau}{\nu},$$

where u_τ is the friction velocity ($= \sqrt{\tau_w/\rho}$, τ_w is the shear stress at the wall). The examples listed in table 1 are of engineering interest, but very important applications pertain to atmospheric and other geophysical flows where extremely high Reynolds numbers are the rule rather than the exception.

To model the behavior of high Reynolds number turbulence it is often necessary to extrapolate laboratory results obtained at considerably smaller Reynolds numbers. This scaling process is fraught with uncertainty, as we shall see, even for relatively simple flows such as pipe flows. Here, we present some observations regarding the Reynolds number dependence of turbulent pipe and boundary layer flows, based on recent experimental evidence obtained at Princeton and elsewhere. Here, we concentrate on the mean flow scaling.

2 Scaling of the Mean Flow

For wall-bounded turbulent shear flows, the shape of the mean velocity profile, or equivalently, the relative fraction of the flow occupied by the inner and outer regions, changes with Reynolds number. If the Reynolds number is large enough, it is usually assumed that the interaction between these regions vanishes because of the disparity of length scales, and consequently, independent similarity solutions may exist for each region. Therefore, most theoretical treatments start by dividing the flow into an inner and outer region. For each region, a length and velocity scale may be defined. The velocity scale in the near-wall region is typically taken to be the friction velocity. The length scale associated with the inner region is then the kinematic viscosity ν divided by the friction velocity, ν/u_τ. For the outer region, the velocity scale is also typically taken to be the friction velocity, although this has long been the source of controversy ([1], [2]), and the length scale is taken to be the radius of the pipe R or the boundary layer thickness δ.

Using dimensional analysis, the scaling for the inner region is

$$U^+ = f\left(y^+\right), \tag{1}$$

where f represents the functional dependence in the inner region [3]. Here, $U^+ = U/u_\tau$, $y^+ = y u_\tau/\nu$, y is the distance from the wall, and U is the mean velocity in the

	$Re_\ell \times 10^{-6}$	$Re_\delta \times 10^{-5}$
Submarine	1000	700
Aircraft carrier	2500	1400
Boeing 747	560	400

	$Re_D \times 10^{-6}$	$Re_\tau \times 10^{-5}$
Water main	60	15
Natural gas main	40	10

Table 1: Typical Reynolds numbers encountered in practice.

streamwise direction. Equation 1 is known as the "law-of-the-wall" and is valid only in the inner region. It can be shown from the Navier-Stokes equation that f is linear near the wall, and we may expect that equation 1 is valid further from the wall than the linear region but not into the outer region (that is, equation 1 will hold for $0 < y^+ \ll R^+$, where $R^+ = Ru_\tau/\nu$).

The dimensionless scaling law for the outer region is

$$\frac{U_{CL} - U}{u_0} = g(\eta), \tag{2}$$

where g represents the functional dependence in the outer region, and for a pipe $\eta = y/R$ and U_{CL} is the centerline velocity. The parameter u_0 is the outer velocity scale. If $u_0 = u_\tau$, then equation 2 is known as the "defect-law" [3]. Equation 2 is valid only in the outer region where viscosity is not important (that is, equation 2 will hold for $0 \ll \eta < 1$).

Equations 1 and 2 are based on the assumption that R^+ is large enough for both regions to be independent of Reynolds number. If we assume that an intermediate region exists where both scaling laws are valid, then we can define two different matching conditions.

By matching the velocity gradients given by equations 1 and 2, we find

$$y^+ f' = -\Lambda \eta g', \tag{3}$$

where the differentiation in equation 3 is with respect to the dependent variables and Λ is the ratio of the outer to inner velocity scales, u_0/u_τ. If $u_0 = u_\tau$, then equation 3 is the same relation used by Millikan (1938) to derive the classical logarithmic overlap region.

Alternatively, if we simultaneously match the velocities and velocity gradients, the matching condition is

$$y^+ \frac{f'}{f} = -\frac{\eta g'}{\frac{U_{CL}}{u_0} - g}. \tag{4}$$

Equation 4 is the same relation used by George *et al.* [2] with $u_0 = U_\infty$ to support their assertion that the overlap region in a boundary layer is given by a power law.

At low Reynolds numbers that are still high enough that an overlap region exists, we expect that Λ depends on R^+. At these Reynolds numbers, equation 3 does not define an overlap region that is independent of R^+, but equation 4 does. By integrating equation 4, the velocity profile in this region can be written using inner layer variables as

$$U^+ = C_1 \left(y^+\right)^\gamma. \tag{5}$$

3 Turbulent Pipe Flow

To verify these scaling concepts, pipe flow measurements were obtained in the Princeton/DARPA/ONR Superpipe apparatus which can achieve a range of Reynolds numbers spanning three orders-of-magnitude. The facility uses compressed air as the working fluid to achieve very high Reynolds numbers at a reasonable cost. A closed-loop system was built with the test pipe located inside high-pressure piping (see figure 1). The test pipe had a nominal diameter of 129 mm, with a length-to-diameter ratio of 200. Further details of the facility are given in [1] and [4].

The results show that the values of C_1 and γ were independent of Reynolds number and equal to 8.70 and 0.137, respectively (see figure 2a). Equation 5 with these constants was shown to be in excellent agreement with pipe flow data for $60 < y^+ < 500$ or $y^+ < 0.15R^+$, the outer limit depending on whether R^+ is greater or less than 9×10^3 [5]. With these limits, a power law can exist only if $R^+ > 400$.

At even higher Reynolds numbers, it was shown that u_0/u_τ approaches a finite limit [1]. For this case, equation 3 also gives an overlap region which is independent of Reynolds number. Equation 3 can be set equal to a constant (typically $1/\kappa$) and integrated to give the classical log law which can be written in terms of inner scaling variables as

$$U^+ = \frac{1}{\kappa} \ln y^+ + B. \tag{6}$$

The values of κ and B were shown to be 0.436 and 6.15, and as shown in figure 2b this log law is in excellent agreement with experimental pipe flow data for $600 < y^+ < 0.07R^+$ [5]. With these limits, a log law can exist only if $R^+ > 9 \times 10^3$ which is a very large Reynolds number compared to most laboratory flows.

For the preceding argument to be valid, u_0 must be proportional to u_τ at high Reynolds number. The correct velocity scale for the outer region was shown to be the velocity deficit in the pipe, or $U_{CL} - \bar{U}$, where $\bar{U}$ is the average velocity, which is a true outer velocity scale, in contrast to the friction velocity which is a velocity scale associated with the inner region which is "impressed" on the outer region [1]. The comparisons with the data are shown in figure 3. As expected on the basis of the argument given here, the collapse of the data for $y/R > 0.1$ using u_0 is considerably better than that using u_τ.

4 Turbulent Boundary Layers

The preceding analysis for pipe flow may also hold for boundary layers if the centerline velocity is replaced by the freestream velocity and the radius is replaced by the boundary layer thickness [6]. Here we also assume that the streamwise dependence of the velocity profile is properly accounted for by our choice of length and velocity scales. An outer velocity scale equivalent to $U_{CL} - \bar{U}$ can be expressed using boundary layer parameters as follows.

$$\begin{aligned} u_0 &= U_\infty - \bar{U} = \frac{U_\infty}{\delta} \int_0^\infty \left(1 - \frac{U}{U_\infty}\right) dy \\ &= U_\infty \frac{\delta^*}{\delta}. \end{aligned} \tag{7}$$

This new outer velocity scale can be accurately determined from the velocity profiles, in contrast to the friction velocity u_τ which is not easily measured accurately in a boundary layer. The new outer velocity scale is related to the Clauser or Rotta thickness Δ which is given by

$$\Delta = \int_0^\infty \frac{U_\infty - \bar{U}}{u_\tau} dy = \delta^* \sqrt{\frac{2}{C_f}},$$

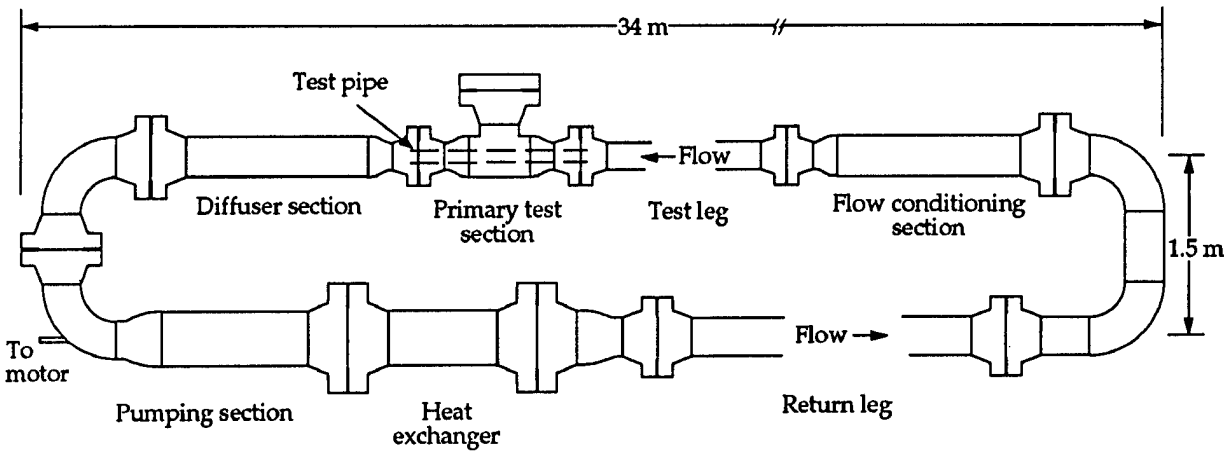

Figure 1: The layout of the SuperPipe facility. The flow direction is counter-clockwise.

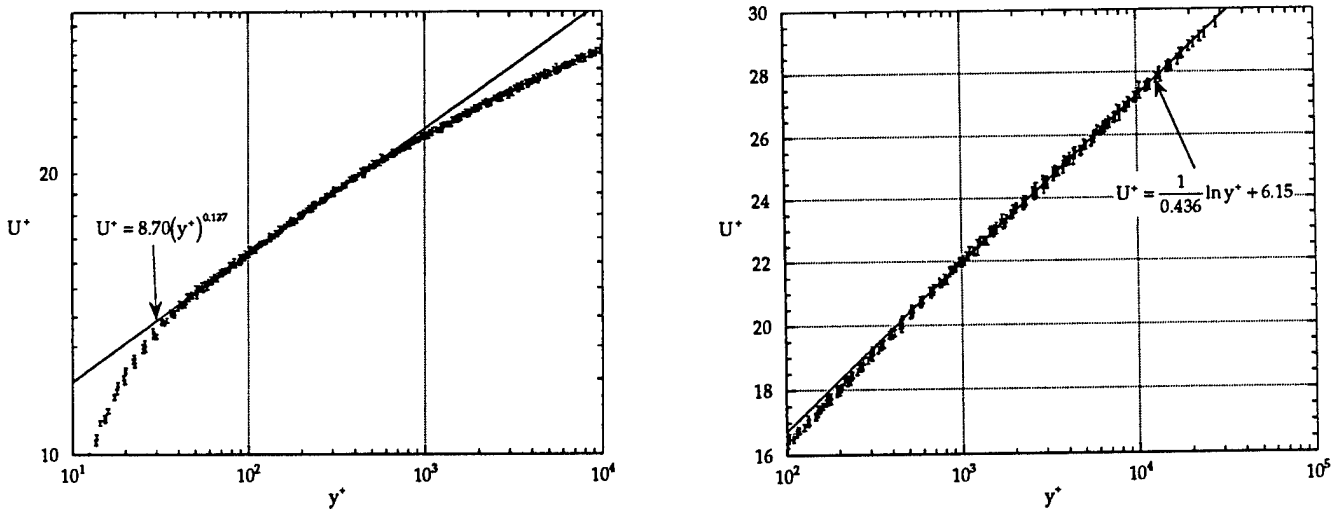

Figure 2: Pipe flow velocity profiles normalized using inner scaling variables for 26 different Reynolds numbers between 31×10^3 to 35×10^6 [1]. (a) Log-log plot; (b) Linear-log plot.

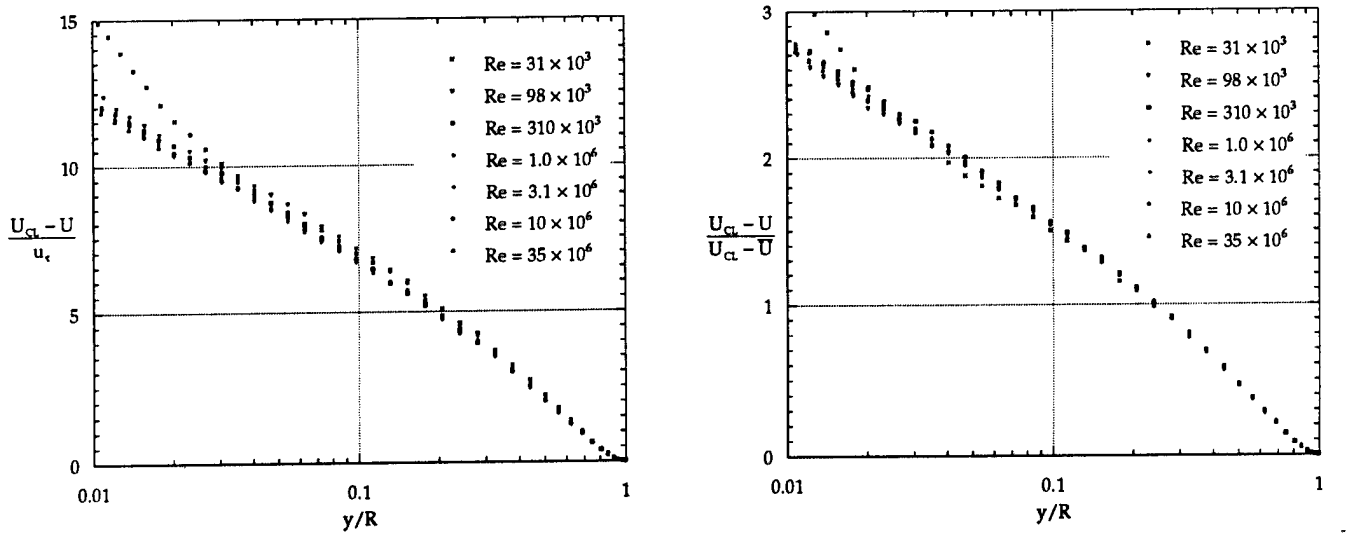

Figure 3: Pipe flow velocity profiles for Reynolds numbers between 31×10^3 to 35×10^6 [1]. (a) Normalized using the conventional outer velocity scale; (b) Normalized using the proposed new outer velocity scale.

so that

$$u_0 = U_\infty \frac{\delta^*}{\delta} = u_\tau \sqrt{\frac{2}{C_f}} \frac{\delta^*}{\delta} = u_\tau \frac{\Delta}{\delta}. \qquad (8)$$

At high Reynolds numbers, we can expect that $u_0 \propto u_\tau$, or equivalently $\delta^*/\delta \propto \sqrt{C_f}$, (or $\Delta \propto \delta$) for a logarithmic overlap region to exist (the skin friction coefficient $C_f = 2(u_\tau/U_\infty)^2$).

A very rough basis for comparison between pipe and boundary layer flows is to estimate the equivalent momentum thickness of a fully-developed pipe flow at about 1/10th the radius, so that the equivalent value of $Re_\theta \approx Re_D/20$. However, comparisons between boundary layers and pipe flows must be made very carefully. Even though a similar scaling may exist for boundary layers and pipe flow, we can not expect the functional form of the velocity profiles in the outer region $g(\eta)$ to be the same since the equations of motion and the boundary conditions are different. This is true even in the infinite Reynolds number limit. Furthermore, any limit that depends on Reynolds number (R^+ or δ^+) may be different due to the differences in the outer region ($\delta^+ = \delta u_\tau/\nu$). These limits include the Reynolds number at which complete similarity exists in the outer and inner region, the outer limit of the power law or log law, and the Reynolds number at which the overlap regions appear. Conversely, the equations of motion and boundary conditions of the inner region are the same for both flows in the infinite Reynolds number limit, and we may therefore expect that the functional form of the velocity profiles in the inner region $f(y^+)$ are the same.

Data from three separate boundary layer investigations were used for the comparison presented here (see table 2). The data from Purtell *et al.* [7] spanned the range $470 < Re_\theta < 5,100$ ($220 < \delta^+ < 1,700$); the data from Smith [8] spanned the range $4,600 < Re_\theta < 13,00$ ($1,500 < \delta^+ < 4,000$); and the data from Fernholz *et al.* [9] provided the data at $Re_\theta = 21,000$ and 58,000 ($\delta^+ = 6,900$ and 18,000).

Profile #	Re_θ	δ^+	Reference
1	470	220	[7]
2	500	220	[7]
3	700	290	[7]
4	1.0×10^3	390	[7]
5	1.3×10^3	470	[7]
6	1.8×10^3	650	[7]
7	2.8×10^3	970	[7]
8	3.5×10^3	1.2×10^3	[7]
9	4.1×10^3	1.4×10^3	[7]
10	4.6×10^3	1.5×10^3	[8]
11	5.0×10^3	1.6×10^3	[8]
12	5.1×10^3	1.7×10^3	[7]
13	5.4×10^3	1.7×10^3	[8]
14	5.9×10^3	1.8×10^3	[8]
15	6.9×10^3	2.1×10^3	[8]
16	7.7×10^3	2.3×10^3	[8]
17	9.1×10^3	2.7×10^3	[8]
18	10×10^3	3.1×10^3	[8]
19	12×10^3	3.5×10^3	[8]
20	13×10^3	4.0×10^3	[8]
21	21×10^3	6.9×10^3	[9]
22	58×10^3	18×10^3	[9]

Table 2: Boundary layer data sources.

In figure 4, the velocity profiles reported in [7], [8] and [9] are shown normalized by inner layer variables. The data at lower values of δ^+ (profiles 1 to 5 in table 2) are not shown since it is doubtful that a universal overlap region exists at these Reynolds numbers ($\delta^+ < 500$). The power law established from pipe flow data is also shown, as are the regions marking a ±3% error in u_τ (representing a best estimate for the uncertainty in u_τ). For all profiles except

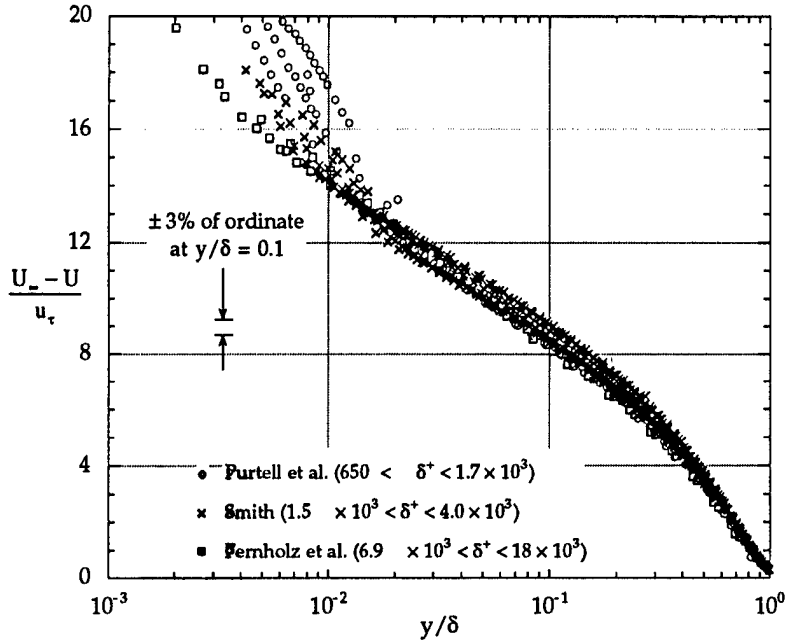

Figure 5: Boundary layer velocity profiles normalized using traditional outer scaling variables.

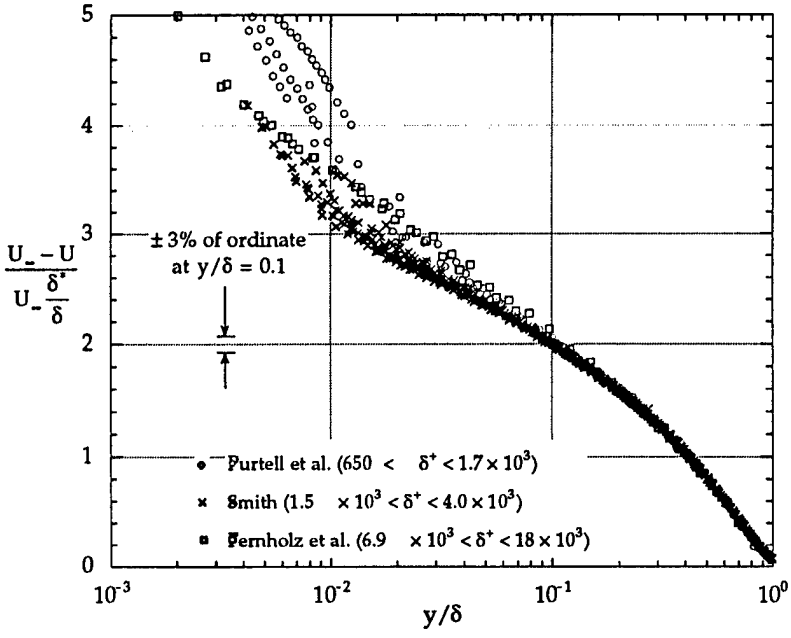

Figure 6: Boundary layer velocity profiles normalized using proposed outer scaling variables.

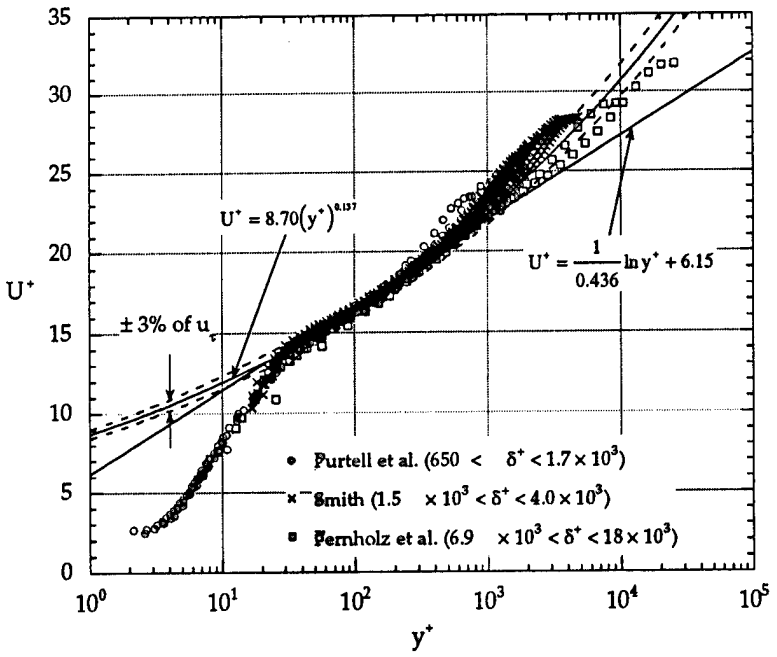

Figure 4: Boundary layer velocity profiles normalized using inner scaling variables.

at the highest Reynolds number, the data are nominally within ±3% of the power law for some range of y^+ and deviate from the curve in the inner region where viscosity dominates and in the outer region where the inner scaling no longer holds. At the highest Reynolds number, the data near the wall deviates from the other profiles by more than 3%, but this perhaps can be attributed to an error in position since the five points nearest to the wall are all within 1 mm of the wall. The log law established from pipe flow data is also shown in figure 4. According to the analysis of pipe flow data, the log law should be apparent only at the highest Reynolds number since a log law should not exist until δ^+ is of order 10^4. The uncertainty in the friction velocity prevents us from drawing any definitive conclusions here, but a power law with $C_1 = 8.70$ and $\gamma = 0.137$ seems to be in good agreement with these boundary layer data.

In figures 5 and 6, the velocity profiles are normalized by the conventional outer velocity scale, u_τ, and the proposed outer velocity scale $U_\infty \delta^*/\delta$, respectively. In each figure, error bars are shown which represent a ±3% uncertainty of the ordinate at $y/\delta = 0.1$. When normalizing the wall-normal position in the outer region, the length scale was taken to be the boundary layer thickness at $0.99U_\infty$, although it was found that the profiles collapsed equally well when using the displacement thickness or momentum thickness. Regardless of the length scale used, the collapse is poor in the outer region for the profiles normalized by u_τ and much improved for $y/\delta > 0.07$ and for $650 < \delta^+ < 18 \times 10^3$ when using $U_\infty \delta^*/\delta$.

5 Discussion

From the analysis given here, and the experiments in the Superpipe facility for Reynolds numbers ranging from 31×10^3 to 35×10^6, Zagarola & Smits [1] proposed a new scaling for the mean velocity profile of fully-developed pipe flow. Zagarola & Smits [6] recently extended this analysis to turbulent boundary layers, and using data over a large range of Reynolds numbers ($650 < \delta^+ < 18 \times 10^3$ or $4.6 \times 10^3 < Re_\theta < 58 \times 10^3$) suggests that it is in good agreement with experiment. For pipe flow and boundary layers, the new scaling leads to a power law for the overlap region of the mean velocity profile at low Reynolds numbers, and both a power law and log law region at high Reynolds numbers. The power law with empirical constants determined from pipe flow data was in good agreement with boundary layer data, at least within the uncertainties in the data, specifically the value of the friction velocity. The proposed scaling requires a new outer velocity scale given by $U_{CL} - \bar{U}$ for the pipe flow and $U_\infty \delta^*/\delta$ for boundary layers.

6 Outlook for the Future

Work is continuing on measurements of the turbulence intensities, structure functions, space-time correlations and structure angles. We hope to report soon on the applicability of the new scaling suggested here to the turbulence data.

In addition, we are currently constructing a High Reynolds Number Testing Facility (HRTF) using compressed air as the working fluid and featuring a Magnetic Suspension Balance (MSB). The work is supported by ONR through the DURIP program. The facility is designed to study lift and drag, wake formation and decay, unsteady flows typical of maneuvering vehicles, turbulence in boundary layers and wakes, all at Reynolds numbers typical of full-scale ships, submarines, torpedoes and airplanes (up to length Reynolds number of 176×10^6). Its

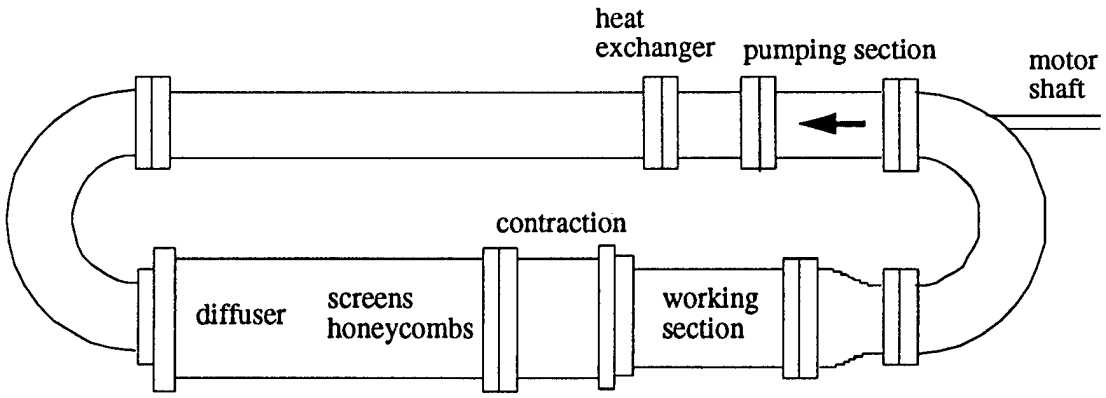

Figure 7: Schematic of the new High Reynolds Number Testing Facility at Princeton.

design is largely based on the Superpipe apparatus (see figure 1), and also uses compressed air as its working fluid. A plan view of the new facility is shown in figure 7. Such a facility is not currently available anywhere in the world, and it is expected to provide vital new data on the performance of submarines and torpedoes, as well as providing a new capability for minimizing risks in the development of new and innovative vehicles.

Acknowledgments

The research in high Reynolds number flows is supported by ONR through grants N000014-92-J-1796, N000014-97-1-0618, and N000014-98-1-0325, monitored by Dr. L.P. Purtell.

References

[1] M.V. Zagarola and A.J. Smits. Scaling of the mean velocity profile for turbulent pipe flow. *Physics Review Letters*, **78** (2), 239–242, 1997.

[2] George, W.K., Castillo, L., & Knecht, P. The zero pressure-gradient turbulent boundary layer. Technical Report No. TRL-153, S.U.N.Y. Buffalo, 1996.

[3] Schlichting, H. *Boundary-Layer Theory.* McGraw-Hill, 1987.

[4] M.V. Zagarola. *Mean flow scaling in turbulent pipe flow.* Ph.D. Thesis, Princeton University, 1996.

[5] Zagarola, M.V. & Smits, A.J., 1998 Mean flow scaling of turbulent pipe flow. Submitted for publication.

[6] M.V. Zagarola and A.J. Smits. A new mean velocity scaling for turbulent boundary layers. *ASME Paper FEDSM98-4950*, 1998.

[7] Purtell, L.P., Klebanoff, P.S. & Buckley, F.T. Turbulent boundary layers at low Reynolds number *Phys. Fluids*, **24** (5), 802–811, 1981.

[8] Smith, R.W. Effect of Reynolds number on the structure of turbulent boundary layers. Ph.D. Thesis, Princeton University, Princeton, NJ, 1994.

[9] Fernholz, H.H., Krause, E., Nockemann, M., & Schober, M. Comparative Measurements in the canonical boundary layer at $Re_{\delta 2} \leq 6 \times 10^4$ on the wall of the German-Dutch Windtunnel. *Phys. Fluids*, **7** (6), pp. 1275–1281, 1995.

Drag Reduction Physics

THE LAMB VECTOR AND ITS DIVERGENCE IN TURBULENT DRAG REDUCTION

C. H. Crawford, H. Marmanis and G. E. Karniadakis
Center for Fluid Mechanics
Division of Applied Mathematics
Brown University

email: (H. Marmanis - marmanis@cfm.brown.edu); (G. Karniadakis - gk@cfm.brown.edu)

Abstract We analyze high-resolution numerical data bases for a turbulent channel flow with one wall formed by streamwise aligned V-grooves (riblets). The simulations cover a range of R_τ from 140 to 200, and are based on parallel spectral element-Fourier discretizations. In order to study the effect of different geometries on the drag, we have used various heights and widths for the riblets. The fact that the divergence of the Reynolds stress tensor equals the average Lamb vector motivates us to write the Reynolds stress gradient that dominates over a flat wall, i.e. $\partial(\overline{u'v'})/\partial x_2$, as the sum of the streamwise component of the Lamb vector and the spanwise variation of the turbulent stress $T_3 = \partial(\overline{u'w'})/\partial x_3$. The streamwise component of the Lamb vector consists of a vortex stretching term, i.e. $\overline{w'\omega_2'}$, and a vortex transport term. By studying spanwise locations, from groove valley to tip, we find that an increase of the vortex stretching term is associated with an increase of the Reynolds stress and shear stress. For a smooth wall T_3 is zero, but for the non-smooth wall it achieves large positive and negative values at the valleys and the tips of the roughness elements, respectively. The above analysis suggests two ways of reducing the drag: The first is to prevent the appearance of normal vorticity, and the second to create valleys at the wall so that the T_3 component becomes negative. In addition to this standard approach, we invoke the concept of turbulent charge, which is by definition the divergence of the Lamb vector. We present the spatial distribution of this quantity and analyze its connection to the problem of drag reduction.

I. INTRODUCTION

The current status of developing means of turbulent drag reduction is based largely on identifying, and following the evolution of the so-called coherent structures. These structures, however, are arbitrary in the sense that their selection as structures is subjective, based primarily on visualization, and outside the framework of a turbulence theory. Their spatial distributions are not quite clear and vary considerably in time, covering a large range of scales that generally increases with distance from the wall. Thus it is not surprising that the description of their interaction, and thereby the solution of the problem, is far from complete. If we consider the effect of non-smooth surfaces ([37], [8]), we will certainly have to modify our structures in a way that depends on the particular geometrical characteristics of the surface and it is not known a priori. This naturally raises the following question: Even if a model involving all these features and structures is completed, will it be able to be used robustly and efficiently in practical applications? We will not attempt to answer this question, but we shall present an alternative in the description of turbulent boundary flows that invokes the structure of the Lamb vector and its divergence.

We shall consider a channel geometry with one wall smooth and the opposite wall mounted with longitudinal riblets, so that we are able to make a simultaneous study of the flow over both flat and deformed walls. This type of geometry was first introduced in [11] and was used in subsequent more systematic studies of drag reduction in the work of [12], [8], and [19]. In order to obtain very accurate *vorticity* fields, our new numerical data bases were built at a *higher* resolution than in the previous studies of [12] and [8]. We shall encounter flow quantities that involve derivatives of the velocities even higher than the first, therefore high accuracy is required in order to obtain reliable numerical results. By using a vector identity, we can express the divergence of the Reynolds stress tensor as being equal to the average Lamb vector (i.e. $\overline{\mathbf{l}} = \overline{\omega \times \mathbf{u}}$). This motivates us to write the Reynolds stress gradient that dominates over a flat wall, i.e. $\partial(\overline{u'v'})/\partial x_2$, as the sum of the streamwise component of the Lamb vector and the spanwise variation of the turbulent stress $T_3 = \partial(\overline{u'w'})/\partial x_3$. The streamwise component of the Lamb vector consists of a vortex stretching term, i.e. $\overline{w'\omega_2'}$, and a vortex transport term, i.e. $\overline{v'\omega_3'}$. By studying spanwise locations, from groove valley to tip, we found that an increase of the vortex stretching term is associated with an increase of the Reynolds stress and shear stress. It is well-known that in the case of the smooth wall T_3 is zero due to the statistical homogeneity in the spanwise direction. For the non-smooth wall, however, it achieves large positive and negative values at the valleys and the tips of the roughness elements, respectively. The above analysis suggests two ways of reducing the drag: The first is to prevent the appearance of normal vorticity and the second to create valleys at the wall, so that the T_3 component becomes negative.

In addition to this standard approach, we invoke the concept of *turbulent charge*, which is by definition the divergence of the Lamb vector. We present the spatial distribution of this quantity and analyze its connection to the problem of drag reduction. The difference between the two approaches is fundamental. On the one hand, the coherent structures of vorticity are investigated in the hope that they will provide the ground for the formulation of a turbulence theory [23]. However, as we have already mentioned these structures are intensely three-dimensional and their identification is mainly based on visualization techniques, which are restricted to low Reynolds numbers. Moreover, even if their identification was an easy task, the classification of all advected structures by modes and parameter size would be necessary before any reasonable theory could be developed. Considering the large number of these structures, this would be an immensely arduous task that would result in a theory of dubious effectiveness. On the other hand, the turbulent charge is an essential element of a new theory of turbulence [34] and the fact that it does have a characteristic structure is more than promising. The advantage of thinking in terms of this quantity is that it represents, in the physical space, the tendency of the energy to "clump" at some regions where its value is positive, and to leave some other regions where its value is negative; the stronger the tendency, the greater the magnitude of the divergence. Hence, if the turbulent charge is negative at some region, it means essentially that at these regions we have dissipation of kinetic energy into heat, and therefore the link between the turbulent charge and drag force is physically clear.

The paper is organized as follows: In section II we discuss the simulation parameters. In section III we present a summary of vorticity statistics for three cases (A, B and C) that we have considered. Case A corresponds to a 5% drag reduction on the deformed wall, case B represents a 10% drag increase, and case C corresponds to a 2% drag reduction. In section IV we present numerical evidence that the stretching component of the Lamb vector is responsible for most of the drag. We also show that the T_3 component changes sign and results in drag reduction, as we go from the tip to the valleys. In section V we examine the relation between drag reduction and the distribution of turbulent charge. In section VI we summarize our results.

II. SIMULATION PARAMETERS

The simulations presented here were based on spectral element-Fourier discretizations. Detailed resolution tests and a complete validation can be found in [16]. Both spatial and temporal resolution employed are higher than in previous studies [12], [8], [19]. For example, the time step is an order of magnitude smaller than the one used in [8]. The details of the spectral element-Fourier method can be found in [24] and recent developments of spectral elements on unstructured meshes in [40]. All simulations were performed *in parallel* on the IBM SP2 (thin nodes) with one or a group of Fourier modes assigned to a processor; a typical run requires 4 to 5 seconds per time step. The details of the parallel implementation are presented in [15].

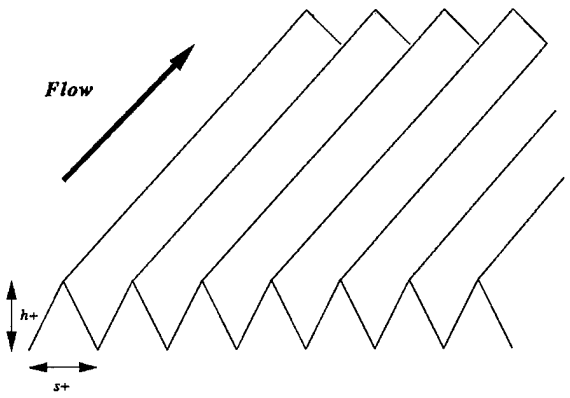

Figure 1: Geometry for streamwise aligned grooves. The flow direction is denoted by x_1, the normal direction by x_2, and the spanwise direction by x_3.

The roughness elements are streamwise aligned grooves aligned in the flow direction as shown in figure 1; such a surface modification has been shown to reduce the shear stress in turbulent flows by several researchers, including the experiments of [52], [33], [49], [44], and the simulations of [12], [8], and [19]. These triangular grooves are characterized by their height and span in wall units h^+ and s^+, respectively. Grooves with $h^+ = s^+ \leq 20$ have been shown to reduce drag while those with $h^+ = s^+ > 20$ have been shown to increase drag.

For these simulations, the computational domain was a channel consisting of a smooth upper wall and a non-smooth lower wall. The flow is perpendicular to the $(x_2 - x_3)$ planes, which are discretized with spectral elements. Along the flow direction x_1, Fourier expansions are employed. With this type of domain, statistics on both the smooth wall and the non-smooth wall can be computed simultaneously for comparison. Our results also indicate that the presence of the grooves did not effect the smooth wall statistics in these simulations. We choose two cases with groove heights in the drag reducing range and one case with relatively large grooves, i.e. in the drag increasing range. Table I summarizes the cases studied.

A summary of the computational domain dimensions for each study is shown in table II; in each case, 10 grooves were used on the bottom wall. As with previous channel studies the flow is periodic in the x_1 and x_3 directions and no-slip boundary conditions are used on the upper and lower walls. In the final simulations, 240 spectral elements were used with 11 × 11 grid points in each element and with 32 Fourier modes in the streamwise discretization. Table III gives a summary of the resolution for each case; these values can be compared with tables 2 and 3. In all our cases $\Delta x_1 = 0.0877$, the maximum $\Delta {x_2}^+$ was less than seven, and the maximum $\Delta {x_3}^+$ was less than three for both the smooth and non-smooth walls. The time-step used was $\Delta t U_l/\delta = 0.005$, and the flow was driven by a constant flow rate, Q, based on the channel cross-sectional area and the equivalent laminar centerline velocity U_l.

Case	h^+	s^+	Re	Re_τ (u-l)	$Drag$
A	17.70	20.41	4280	181 - 177	-5%
B	31.01	35.66	3280	148 - 155	+10%
C	18.57	21.42	3280	144 - 143	-2%

Table I: Summary of streamwise aligned groove cases studied. Shown are the geometrical parameters, Reynolds numbers for the upper (u) and lower (l) walls, as well as the drag decrease (-%) or increase (+%) observed. Re is Reynolds number based on centerline velocity U_l and half-channel width δ, while Re_τ is based on the skin-friction velocity u_τ and δ.

Case	L_{x_1}	L_{x_2}	L_{x_3}	$L^+_{x_1}$	$L^+_{x_2}$	$L^+_{x_3}$
A	5.61	2.05	1.15	1018	372	209
B	5.61	2.1	2.3	830	311	340
C	5.61	2.065	1.5	808	297	216

Table II: Summary of turbulent grooved channel domain for all cases studied. Shown are the computational domain dimensions (L) in global and wall units for the streamwise (x_1), normal (x_2), and spanwise (x_3) directions. Note that the wall unit normalization uses the non-smooth wall span-averaged skin friction velocity.

We define an average quantity as an average in time *and* space. Spatial averages are constructed by collapsing three-dimensional time-averaged data onto a two-dimensional, single "master groove". Note that in time-averaging, samples of the data are taken at *every* time-step in the integration of the Navier-Stokes equations, no time-steps are skipped. The initial condition for all three cases came from previous turbulent channel data used in [14]. These flow fields were already turbulent and the velocity and pressure data was simply interpolated spectrally onto the new mesh. The simulations were run for more than 700 non-dimensional time units (tU_l/δ). The accuracy of the simulation was monitored using the global momentum error, which was bounded by $O(10^{-6})$ in all cases [16].

III. REYNOLDS STRESS AND VORTICITY STATISTICS

Results are presented in global coordinates, i.e. normalization with U_l and δ, as well as wall coordinates, i.e. normalization

Case	Δx_2	Δx_3
A	0.0011 - 0.0373	0.0019 - 0.0085
B	0.0011 - 0.0364	0.0038 - 0.0170
C	0.0011 - 0.0371	0.0024 - 0.0111

Table III: Summary of turbulent grooved channel grid spacing for all cases studied. Shown are the computational grid spacings in global units for both the smooth and non-smooth walls.

with u_τ and δ. Grooved wall quantities are normalized by the span-averaged $u_{\tau,sp}$ and the non-smooth wall x_2^+ is defined as $x_2^+ = u_{\tau,sp}(x_2 - x_{2\ v.o.})/\nu$, where $x_{2\ v.o.}$ is the virtual origin (see [16]). We present data in this section for cases A and B to contrast the statistics of a drag decreasing configuration (A) and a drag increasing configuration (B). Data for case C can be found in [16]. The non-smooth wall statistics are compared to the smooth wall statistics of the same case; this prevents any confusion in plots concerning known Reynolds number effects ([53], [43], [3]) as demonstrated in figure 2 for the Reynolds stress. Note that in this plot the DNS data from [8] at $Re_\tau = 180$ is closest to our DNS channel data at $Re_\tau = 200$. The agreement is fortuitous and it may be due to the rather low resolution in the *streamwise* direction used in their study as compared to the data shown here. More specifically, it was demonstrated in [16] that under-resolved simulations (in the streamwise direction) tend to overpredict the Reynolds stress.

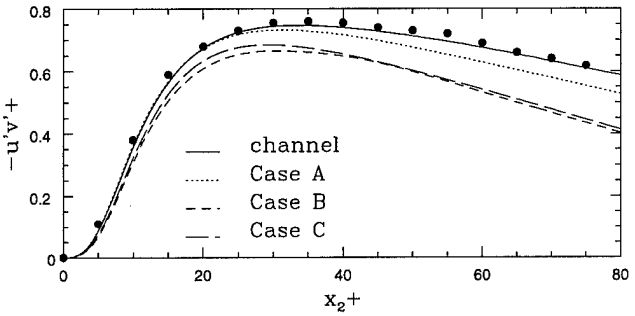

Figure 2: Profiles at the *smooth* wall of the the Reynolds stress $-\overline{u'v'}^+$ plotted in wall coordinates for the channel ($Re_\tau \approx 200$), case A ($Re_\tau \approx 180$), case B ($Re_\tau \approx 150$), and case C ($Re_\tau \approx 150$). Points are from the DNS data of Choi, et. al. 1993 ($Re_\tau \approx 180$).

Reynolds shear stress profiles normalized by U_l and u_τ are shown in figures 3 and 4. For case A, there is a slight increase in the peak Reynolds stress as profile location moves from the groove valley to the groove tip. In [36], experiments showed that the Reynolds stress was increased in profiles taken from the groove valley to the groove tip as well. In case B, the increase in peak magnitude is more pronounced as the profile spanwise location changes. In case A there has been a reduction in the peak Reynolds stress as compared to the smooth wall. In case B, the Reynolds stress peak has been increased. These trends for drag reducing and drag increasing cases in triangular grooves have been reported in [44], [12], and [8]. For case A, in plots using wall coordinates, the difference between the non-smooth wall and the smooth wall remains almost constant out to $x_2^+ = 80$. For case B, however, the non-smooth wall and smooth wall data become quite similar for $x_2^+ \geq 40$. From these same figures, we also observe that the Reynolds ($-\overline{u'v'}^+$) stress at the groove tips has been decreased for case A but increased for case B. Previous work in [16], [8], [12] has also shown that the spanwise and normal turbulence intensities decrease in drag decreasing configurations and increase in drag increasing configurations. These combined findings have been used to propose a possible mechanism for drag reduction. The hypothesis is that the reduction of spanwise motions causes near wall bursts to take place prematurely leading to reductions in their duration and intensity, and therefore reductions in turbulent shear stress [10].

Figures 5, 6, and 7 show profiles of root-mean-square vorticity fluctuations normalized in wall variables ($\omega_{rms}^+ = \omega_{rms}\nu/(u_\tau^2)$). The x_2^+ at the non-smooth wall is measured from the virtual origin. In both case A and case B, all components of the vorticity intensities show maximum values at the groove tips. For the streamwise vorticity in case A, the maximum $(\omega_1)_{rms}^+$ has been reduced as compared to the smooth wall. The opposite is true with case B, where $(\omega_1)_{rms}^+$ has been dramatically increased. This leads to speculation concerning the strength and structure of the streamwise vortices at the non-smooth wall. In [28], the

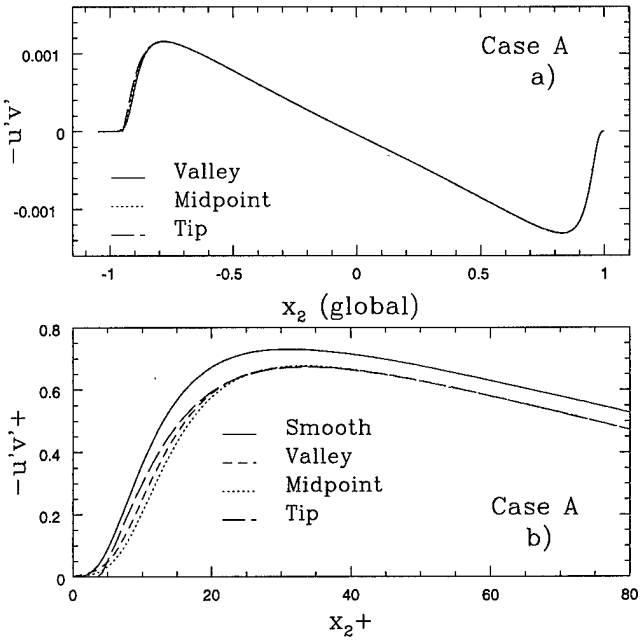

Figure 3: Reynolds stress profiles plotted in a) global and b) wall coordinates for case A.

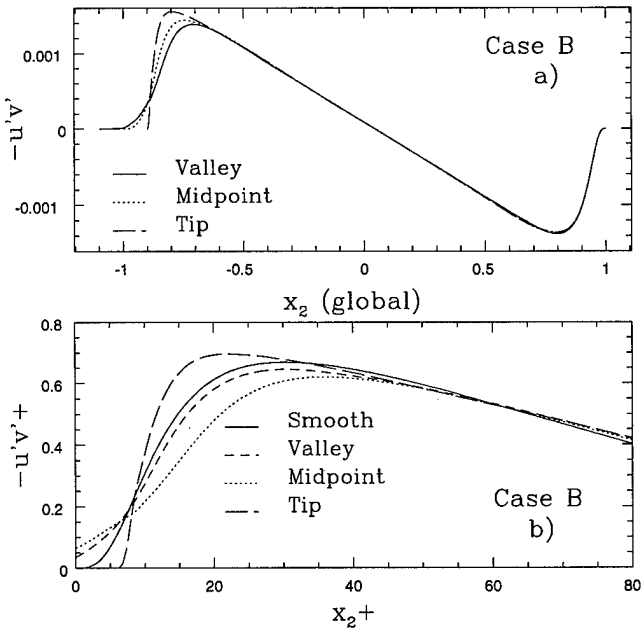

Figure 4: Reynolds stress profiles plotted in a) global and b) wall coordinates for case B.

center of the streamwise vortex was postulated to coincide with the local maximum in a profile of $(\omega_1)_{rms}$ data. Using such a criterion, we see that for cases A and B at the smooth wall, the center of the streamwise vortex is between $x_2^+ \approx 15-20$, in good agreement with [28]. For case A, where the maxima for the data has not changed significantly due to spanwise plotting location for $x_2^+ \geq 12$, the streamwise vortical structure would be located at $x_2^+ \approx 20$. This is in good agreement with [8] for a similar non-smooth wall. For case B, it is difficult to discern where the maximum is for the non-smooth wall data, as the three profiles continue to change for $x_2^+ \geq 20$. The relative strength of the streamwise vortices can be deduced from these plots as well. The peak $(\omega_1)_{rms}$ at the smooth wall for case A is larger than the peak $(\omega_1)_{rms}$ for case B at the smooth wall, thus showing that as the Reynolds number increases the strength of the streamwise vortices increases, a Reynolds number effect also found in [4]. The reduction in the $(\omega_1)^+_{rms}$ for the non-smooth wall in case A indicates that the strength of the vortices has been reduced, while the increase in the $(\omega_1)^+_{rms}$ for case B indicates that the strength of the vortices has been increased.

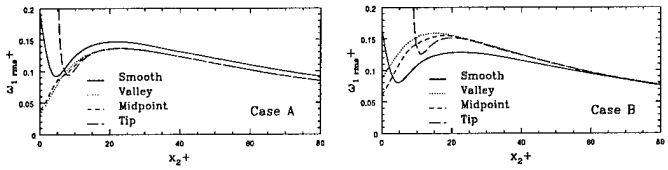

Figure 5: Profiles of root mean square streamwise vorticity plotted in wall coordinates for cases A and B.

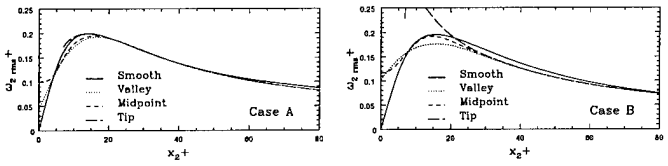

Figure 6: Profiles of root mean square normal vorticity plotted in wall coordinates for cases A and B.

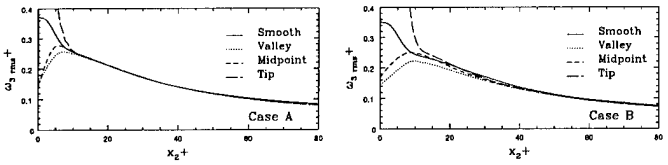

Figure 7: Profiles of root mean square spanwise vorticity plotted in wall coordinates for cases A and B.

We make one final comment on the smooth wall data presented in this section. At the beginning of this section the point was made that the presence of the non-smooth wall did not effect the smooth wall data. The results from this section (especially for case B –also C not shown here) demonstrate the validity of this statement. The average difference in the turbulence intensities between cases B and C is 2%; the average difference in the Reynolds stress is less than 4%. Such differences could be attributed to the slight differences x_2-x_3 plane resolution at the smooth wall for each case. In cases B and C at the smooth wall, the x_2 resolution does not change. However, the Δx_3 grid spacing for case B is larger than that of case C (see table III). Results from the channel resolution study in [16] indicate that as the spanwise resolution increases (decreasing Δx_3), the Reynolds stress magnitude increases. In figure 2, we see that case B has lower values for $-\overline{u'v'}^+$ than case C – the trend that we expect from the resolution study. We also note that time-averaging effects could be responsible for 1% differences in the data ([16]).

IV. LAMB VECTOR AND REYNOLDS STRESS ANALYSIS

The Lamb vector has not been studied as extensively as vorticity, especially for turbulent flows. In the context of fixed points of the Euler equations, Kraichnan & Panda [31] introduced a decomposition of the Lamb vector into a potential and a solenoidal part, and compared their magnitudes. A large potential part implies a high probability for the Fourier image of the Lamb vector and the wave vector $\mathbf{k}$ to be aligned, and the argument made is that purely kinematic properties of turbulent flows can lead to reduction of their nonlinearity. In the context of Reynolds stress modeling, Wu *et al.* [55] have examined the relation between the Lamb vector and the Reynolds stress tensor and concluded that the problem of modeling turbulent force exclusively amounts to modeling the mean turbulent Lamb vector. In a recent attempt to study the problem of turbulence, Marmanis [34] has introduced a closed set of equations that involve the mean vorticity and the mean Lamb vector. His closure is based on the identification of certain nonlinear quantities as sources for the mean fields. We will use one of these sources in the next section and suggest how we can employ them in turbulence control.

For the case of our channel, the Navier-Stokes equations written for the mean streamwise component of the velocity involve explicitly the streamwise component of the Lamb vector. We will assume that the streamwise direction is homogeneous as far as the kinetic energy is concerned, i.e. $\partial\langle \mathbf{u}\cdot\mathbf{u}\rangle/\partial x = 0$, and write the equation in the following form

$$\frac{\partial\langle u\rangle}{\partial t} = -\langle l_x\rangle - \langle \frac{\partial}{\partial x}\frac{p}{\rho}\rangle + \nu\nabla^2\langle u\rangle\,, \qquad (1)$$

where l_x is the streamwise component of the Lamb vector, and we used $\langle \ldots \rangle$ to denote any appropriate averaging operator. This equation immediately shows that the Lamb vector is the most important agent of turbulence; without its presence the above equation would describe simply a Stokesian flow. Hence the analysis of the Lamb vector can explicitly provide ways of altering the mean flow. In particular, the streamwise component of the averaged Lamb vector in our channel can be written as

$$\overline{l_x} = \overline{v'\omega_3'} - \overline{w'\omega_2'}\,, \qquad (2)$$

and the terms $\overline{v'\omega_3'}$ and $\overline{w'\omega_2'}$ are called vortex transport and vortex stretching terms, respectively.

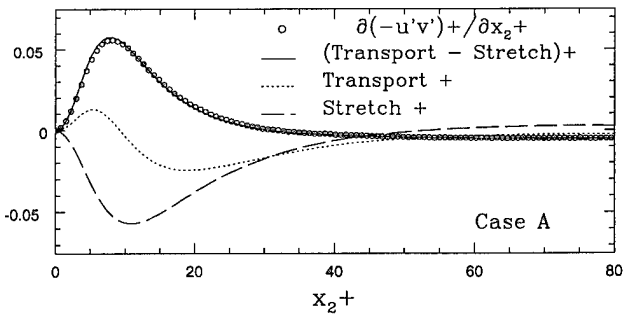

Figure 8: Profiles of the transport $(\overline{v'\omega_3'}^+)$ and stretching $(\overline{w'\omega_2'}^+)$ terms and Reynolds stress derivative for case A at the *smooth* wall. The circles correspond to direct differentiation of Reynolds stress while the solid line corresponds to the sum of all contributions.

Figure 8 shows the transport and stretching terms, as well as the Reynolds stress derivatives in wall units (ν/u_τ^3) at the smooth wall for case A. This plot demonstrates numerically that, for a smooth wall, the stretching term is the dominant contribution to the positive Reynolds stress derivative for $x_2^+ \leq 20$. The results of [29] also showed that the stretching term contribution was greater than the transport term from $10 \leq x_2^+ \leq 20$ in a zero-pressure gradient flat plate turbulent boundary layer flow at $Re_\theta = 2870$.

The appearance of the Lamb vector in equation (1) implies that the lamb vector is directly associated with the Reynolds

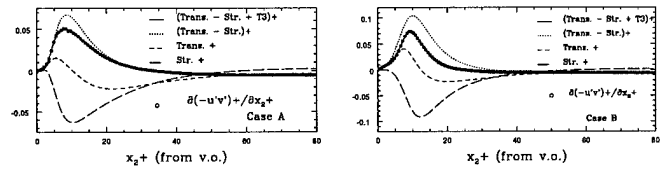

Figure 9: Profiles of the transport $\overline{v'\omega_3'}^+$, stretching $\overline{w'\omega_2'}^+$, and turbulent stress derivative terms $\partial(-\overline{u'v'}^+)/\partial x_2^+$, $\partial\overline{u'w'}^+/\partial x_3^+ = T_3$ for cases A and B at the non-smooth wall. Note that x_2^+ is measured from the virtual origin.

stress tensor. In fact, the lamb vector is the divergence of the Reynolds stress tensor minus the gradient of the kinetic energy per unit density. This is proved easily, by employing a well-known vector identity regarding the Lamb vector, i.e.

$$\frac{\partial(\overline{u_j u_i})}{\partial x_j} = -\overline{l_i} + \frac{1}{2}\frac{\partial(\overline{u_j u_j})}{\partial x_i}. \qquad (3)$$

If we assume homogeneity, as we did before, in the streamwise direction ($\partial/\partial x_1 = 0$) and set $i = 1$, we get the following equation for the Reynolds stress,

$$\frac{\partial(-\overline{u'v'})}{\partial x_2} = \overline{v'\omega_3'} - \overline{w'\omega_2'} + \frac{\partial(\overline{u'w'})}{\partial x_3} = l_x + T_3, \qquad (4)$$

and if we also assume homogeneity in the spanwise direction ($\partial/\partial x_3 = 0$) we get,

$$\frac{\partial(-\overline{u'v'})}{\partial x_2} = \overline{v'\omega_3'} - \overline{w'\omega_2'} = l_x, \qquad (5)$$

where the last equality is due to equation (2). Note that the r.h.s. of this equation is the same as the r.h.s. of (2), which is merely the definition of the Lamb vector.

Figure 9 shows the transport, stretching, and turbulent stress derivative terms, given in equation (4), for profiles from the non-smooth wall virtual origin in cases A and B (case C is similar to A). At the non-smooth wall the stretching term remains dominant over the transport term, and the $T_3 = \partial\overline{u'w'}^+/\partial x_3^+$ term is in competition with the term $\partial(-\overline{u'v'}^+)/\partial x_2^+$, which is the only term of the divergence of the Reynolds stress that survives in the smooth wall case.

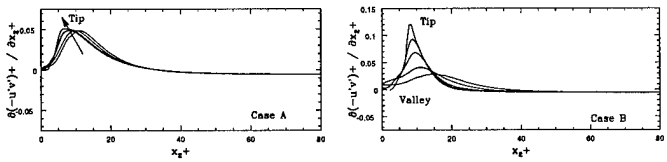

Figure 10: Profiles of the Reynolds stress derivative, $\partial(-\overline{u'v'}^+)/\partial x_2^+$, for cases A and B at the non-smooth wall.

Our results have shown that peaks in the Reynolds stress profile increase as profiles are taken from the groove valley to the groove tip. Profiles of the *derivatives* of the Reynolds stress for cases A and B are shown in figure 10. For each case, $\partial(-\overline{u'v'}^+)/\partial x_2^+$ increased in peak magnitudes from profiles taken at the groove valley to profiles taken at the groove tip. Note that in case B, the magnitude of $\partial(-\overline{u'v'}^+)/\partial x_2^+$ has been increased by more than a factor of two compared to case A as well as the corresponding smooth wall. This quantity shows the first *substantial* (more than 10% or 20%) statistical difference between the smooth wall and the non-smooth wall as well as among the three non-smooth wall cases. Figure 11 shows that the wall shear stress increases in magnitude from the groove valley to the groove tip. This quantity also shows a substantial increase in magnitude as the spanwise location within the groove is varied. It seems likely, then, that understanding the changes that occur in the terms of equation (4) may provide an understanding to the shear stress modification found in these geometries.

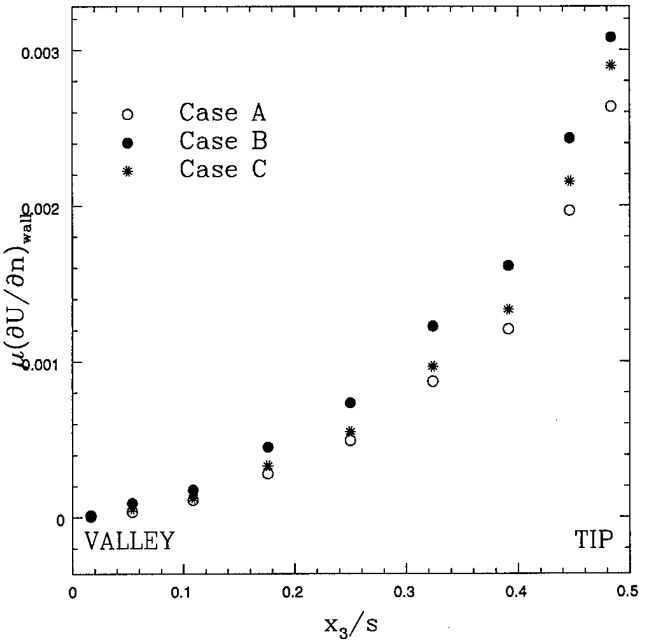

Figure 11: Wall mean shear stress in global variables plotted along the master groove from valley to tip for cases A, B, and C. Note that the spanwise position has also been normalized by the groove spanwise length-scale, s.

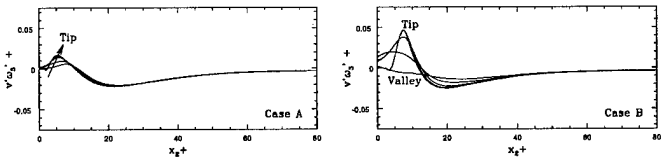

Figure 12: Profiles of the transport term, $\overline{v'\omega_3'}^+$, for cases A and B at the non-smooth wall.

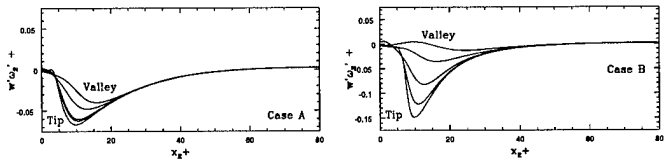

Figure 13: Profiles of the stretching term, $\overline{w'\omega_2'}^+$, for cases A and B at the non-smooth wall.

Figure 12 shows $\overline{v'\omega_3'}^+$ plotted for cases A and B. Profiles are taken at five positions along the groove from the valley to the tip. In all cases, the magnitude of $\overline{v'\omega_3'}^+$ increases from the groove valley to the groove tip, with the largest increase coming in case B. The values for case B at the tip are more than a factor of two greater than the other non-smooth wall cases as well as the smooth wall. The transport terms at the groove tip for case A (similarly for C) show a small increase compared to the smooth wall data. Figure 13 shows $\overline{w'\omega_2'}^+$ plotted for cases A and B. As with the transport terms, the magnitude of the $\overline{w'\omega_2'}^+$ peaks are largest in profiles taken at the tips. The position of the peak value also changes with the profile location. The stretching term at the tip for case B is more than twice that of the smooth wall or the other non-smooth wall cases (note the change in axis limits needed). However, the data for case B also shows that deep within the groove valleys, the stretching term is almost zero.

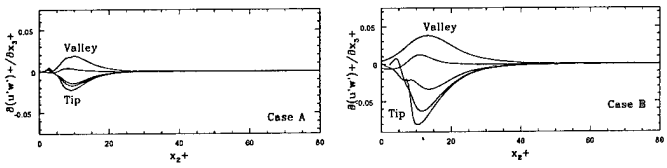

Figure 14: Profiles of spanwise derivatives of the turbulent stress, $\partial\overline{u'w'}^+/\partial x_3^+$, for cases A and B at the non-smooth wall.

Figure 14 shows $T_3 = \partial\overline{u'w'}^+/\partial x_3^+$, plotted at the different spanwise locations of the riblet, for cases A, B, and C; at the smooth wall this term is zero. These plots show that below the groove midpoint $\partial\overline{u'w'}^+/\partial x_3^+$ is positive and works to increase the gradient in the Reynolds stress. This behavior in $\partial\overline{u'w'}^+/\partial x_3^+$ could be related to secondary motion within the groove ([44]). Above the midpoint, $\partial\overline{u'w'}^+/\partial x_3^+$ is negative and works to decrease the gradient of the Reynolds stress. Again, case B shows the largest positive values for $\partial\overline{u'w'}^+/\partial x_3^+$ within the groove valleys and the largest negative values at the groove tip.

In order to determine what the relationship between T_3 and the secondary motion is, we looked at spanwise (w) and normal (v) velocity vector plots from ensemble averages constructed from the entire simulation time of each case on the two-dimensional master groove. At the smooth wall, averages of w and v are zero; close to the non-smooth wall, w and v have non-zero means which are $O(10^{-3})$ smaller than the mean streamwise velocity for all cases. Figure 15 shows these vector plots for the near-wall portion of half the master groove domain for cases A and B. Note that these vector plots are symmetric about $x_3 = x_{3,tip}$. We see that in each case, there exists a roll-like structure between the groove valley and tip. The scaling of these structures in wall units can be determined from the groove height and span dimensions given in wall units as shown in table I. The centers of these structures appear to be at $x_2^+ \approx 10$ above the groove virtual origin, slightly closer to the wall than the streamwise vorticity rolls found at canonical smooth walls, [28].

Profiles of $\partial\overline{u'w'}^+/\partial x_3^+$ that originate near the groove valley go through a *downward* motion region of this secondary structure (vectors pointing towards the groove wall). Profiles that originate near the groove tip go through an *upward* motion region of the structure (vectors pointing away from the groove wall). Profiles that originate near the groove midpoint go through the *core* of the structure. Therefore, positive values of $\partial\overline{u'w'}^+/\partial x_3^+$ correspond to the downward motion of fluid towards the wall; negative values of $\partial\overline{u'w'}^+/\partial x_3^+$ correspond to fluid being transported away from the wall. This observation is consistent with the observations in [14] for smooth walls and groove walls. In that work, an inrush of fluid towards the wall was determined to *increase* the shear stress at the wall and fluid motion away from the wall was determined to *decrease* the shear stress at the wall. Since positive $\partial\overline{u'w'}^+/\partial x_3^+$ increases the gradients of the Reynolds stress and negative $\partial\overline{u'w'}^+/\partial x_3^+$ decreases the gradients of Reynolds stress, the same conclusions about the mean secondary motion at the non-smooth wall in these plots can be made here. Overall, case B shows the largest positive values for $\partial\overline{u'w'}^+/\partial x_3^+$ within the groove valleys and the largest negative values at the groove tip.

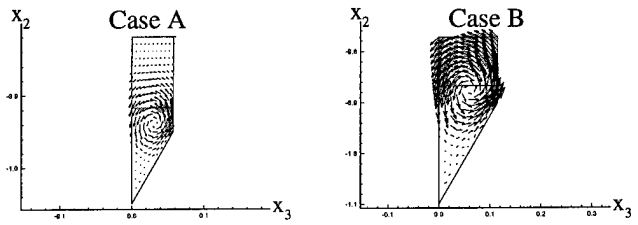

Figure 15: Mean spanwise and normal velocity vectors at the master groove for case A (left) and B (right). The ensemble mean was constructed from 25 samples taken over the entire simulation time. The axis dimensions are in global units. The domain shown is the near-wall region of one half of the master groove.

V. THE DIVERGENCE OF THE LAMB VECTOR AND DRAG REDUCTION

Previous works in the area of turbulence control based their concepts primarily on observation. That is, the concepts involved have been introduced by visualization of the flow and have been selected due to their spatial structure; no matter how arbitrarily the latter is defined. The notion of the *turbulent charge* [34], which is by definition the divergence of the Lamb vector, originates from a theory of turbulence that seeks a closed set of equations involving only the vorticity and the Lamb vector. The terms that cannot be explicitly expressed as a function of either the vorticity or the Lamb vector are gathered together and treated as sources. This leads to a set of equations that are linear in their prime variables. Of course, the determination of the sources needs to be done outside this model system. Whenever the sources are given as an input to the system, the system responds according to the model equations. Herein, we do not attempt to engage the above mentioned theory in the calculation of the drag. Nevertheless, it turns out that these sources have remarkable properties, which deserve some attention in the context of turbulent drag reduction.

The divergence of the Lamb vector is a completely kinematic quantity. Its relation to the dynamics can be obtained by applying the divergence operator on both sides of the Navier-Stokes. For an incompressible fluid we get

$$\nabla \cdot \mathbf{l}(\mathbf{x},t) = -\nabla^2 \Phi, \qquad (6)$$

where Φ is the Bernoulli energy function (i.e. $\Phi = (u^2/2) + p/\rho$). Therefore, the divergence of the Lamb vector is connected with the "curvature" of the Bernoulli energy function. It follows that the turbulent charge is endowed with a clear physical meaning: It represents the tendency of the energy to concentrate at some regions where its value is positive, and to be destroyed at some other regions where its value is negative; the stronger the tendency, the greater the magnitude of the divergence. In the case where the Laplacian is zero, the energy has no curvature at all and its density arranges itself so as to average out the differences imposed by the boundary conditions. Notice that for an incompressible Newtonian fluid, the divergence of the Lamb vector is the same for both the inviscid and the viscous case; this is evident from direct calculation of the equations. In what follows, we consider this quantity for the case of the channel, and examine a reasonable explanation of drag reduction in terms of its spatial distribution.

The importance of the turbulent charge lies on its property to be located in a very narrow region close to the wall. Indeed, it is well-known that in wall-bounded turbulent flows, there is a region near the wall where viscous effects dominate. This viscous layer that extends up to $y^+ \approx 5$ is the region in space where most of the energy is dissipated, consequently we would expect the

turbulent charge to be negative there and achieve its maximum value exactly at the wall, i.e. $y^+ = 0$. In the area just above the viscous layer ($5 \leq y^+ \leq 20$), the turbulent motion becomes intense and tends to accumulate the energy of the mean flow there. The rates of energy production and dissipation in these two regions are much larger than those anywhere else in the flow. This implies that the distribution and the magnitude of the turbulent charge should be nearly independent of the weaker motion in the center of the channel, and they should be determined by the gross energetics and the geometry of the wall. In figure (16) we present the spatial distribution of the turbulent charge, in the case of a flat smooth wall. It should be noted that even without averaging, the distribution of the turbulent charge does not change in time, it is only its magnitude that varies in time. This is essentially a numerical verification of our plausible qualitative argument given above.

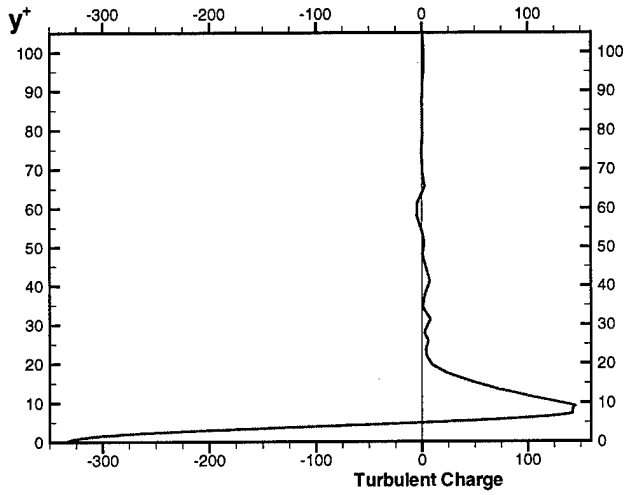

Figure 16: Mean profile of the turbulent charge in the channel (Re=5000). We measure the normal distance in wall units and show only half the channel.

The question that naturally arises is: How do geometric modifications of the wall change the turbulent charge distribution ? We can show analytically that if we require the enstrophy, i.e. ω^2 and the strophokinesis, i.e. l^2, to be finite along the tips of the riblets, then the vorticity and the Lamb vector will behave singularly at these tips. This is confirmed in figure (17) where the turbulent charge is again calculated and shown to be concentrated at the tips of the riblets. This means that most of the dissipation takes place in the neighborhood of the tips, since the turbulent charge achieve its maximum negative value there. The areas of positive charge just above the tips drain the kinetic energy from the mean flow and pass it to the areas of negative charge at the tips.

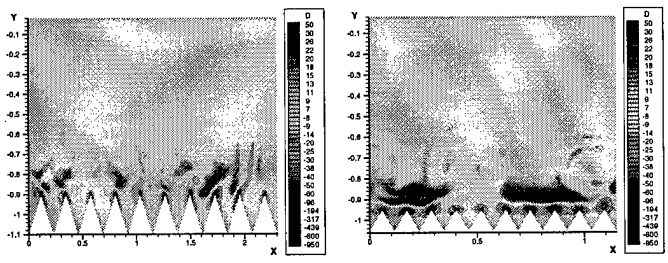

Figure 17: Turbulent charge distributions over the streamwise riblets.

The same figure shows two different cases, one where the drag is reduced (case A) and another where the drag is increased (case B). Can we explain, at least qualitatively, the different effect of the riblets on the drag by examining the structure of the turbulent charge? We believe that the answer is affirmative. The reason is that, although both cases exhibit the singular behaviour at the tips, the case where the drag is reduced exhibits a "cloud" of negative charge that bridges the maxima of the neighboring tips and consequently it hides the valleys of the riblets from the rest of the flow. This layer of negative charge that covers the riblets forms a pseudo-wall, so to speak, and essentially reduces the height of the channel. Moreover, the average thickness of this negative layer is greater than the one that corresponds to a flat wall. This means that the Reynolds number has been effectively reduced. On the other hand, the case where drag has increased is lacking this negative cloud. Therefore, the effectively laminar canals formed by the valleys of the riblets and the negative cloud, in the drag reducing case, do not exist here. This implies that the kinetic energy accumulated above the tips can be disposed of between the riblets, in the valleys. In fact, the situation is even worst in the cases where the singularity increases so much that the Reynolds number is effectively increased. A rule of thumb, according to the above analysis, would be as follows: Edges are good (i.e. drag reducing) if they can form a uniform layer of negative turbulent charge whose thickness is greater, and its magnitude is smaller, than their corresponding quantities in the flat wall case. For this to be accomplished, the key parameters are the angle of the edge at the tip and the spacing between the tips. The angle determines the magnitude of the singularity, which is worst for the degenerate case of a one-dimensional riblet and decreases monotonically as the angle between the sides of the riblet increases. These conclusions are supported by experimental evidence [5].

VI. SUMMARY

We have presented two different scenarios regarding the nature of turbulent drag reduction in wall-bounded flows with riblets. The first is related to the decomposition of the Lamb vector into two components and their relation to the Reynolds stress tensor. This analysis suggests that the stretching term $\overline{w'\omega_2'}$ is the dominant contribution to the drag force. It also provides an explanation regarding the role of bumps and dents to the shear stress distribution. Bumps like the tips of the riblets increase locally the shear stress ($T_3 < 0$ whereas dents like the valleys decrease it ($T_3 > 0$).

The second scenario involves the concept of turbulent charge, i.e. $\nabla \cdot \mathbf{l}$. This quantity identifies the regions of space where most of the energy is dissipated and the regions of space where most of the turbulent kinetic energy is generated. The spatial distribution of this quantity is very simple and therefore it is simple to model. Drag reduction is associated with a redistribution of the turbulent charge due to the geometrical modifications. A reasonable argument on why this happens has been given and found to be in agreement with experiments. The advantage of the latter approach is that study of local solutions for a particular geometry can give an immediate answer and lead to an optimization algorithm regarding the best (i.e. most drag reducing) geometrical shape.

Acknowledgments

This work was partially supported by the Department of Energy and the National Science Foundation. Computations were performed on the IBM SP2 at the Cornell Theory Center, the Maui High Performance Computing Center, and the Center for Fluid Mechanics at Brown University.

References

[1] ACARLAR, M.S. & SMITH, C.R. 1987a A study of hairpin vortices in a laminar boundary layer. Part 1. Hairpin vortices generated by a hemisphere proturbance. *J. Fluid Mech.* **175**, 1.

[2] ACARLAR, M.S. & SMITH, C.R. 1987b A study of hairpin vortices in a laminar boundary layer. Part 2. Hairpin vortices generated by fluid injection. *J. Fluid Mech.* **175**, 43.

[3] ANTONIA, R.A., TEITEL, M.,KIM, J. & BROWNE, L.W.B. 1992 Low-Reynolds number effects in a fully developed turbulent channel flow. *J. Fluid Mech.* **236**, 579.

[4] ANTONIA, R.A. & KIM, J. 1994 Low-Reynolds-number effects on near-wall turbulence. *J. Fluid Mech.* **276**, 61.

[5] BECHERT, D. W. & BARTENWERFER, M. The viscous flow on surfaces with longitudinal ribs, *J. Fluid Mech.* **206**, 105-129..

[6] BERNARD, P.S., THOMAS, J.M. & HANDLER, R.A. 1993 Vortex dynamics and the production of Reynolds stress. *J. Fluid Mech.* **253**, 385.

[7] BROWN, G.L. & THOMAS, A.S.W. 1977 Large structure in a turbulent boundary layer. *Phys. Fluids* **10**, S243.

[8] CHOI, H., MOIN, P. & KIM, J. 1993 Direct numerical simulation of turbulent flow over riblets. *J. Fluid Mech.* **255**, 455.

[9] CHOI, K.S. 1989 Near-wall structure of a turbulent boundary layer with riblets. *J. Fluid Mech.* **208**, 417.

[10] CHOI, K.S. 1993 Turbulence structure revisited; Results and implications from riblets research. In *International Conference on Near-Wall Turbulent Flows.* Tempe, Arizona. eds. Speziale, C.G. & Launder, B.E.

[11] CHU, D.C. & KARNIADAKIS, G.E. 1991 Numerical investigation of drag reduction in flow over surfaces with streamwise aligned riblets. *AIAA-91-0518.*

[12] CHU, D.C. & KARNIADAKIS, G.E. 1993 The direct numerical simulation of laminar and turbulent flow over riblets. *J. Fluid Mech.* **250**, 1.

[13] COLES D.E. 1978 A model for flow in the viscous sublayer. *Coherent Structures of Turbulent Boundary Layers,* (ed. C.R. Smith & D.E. Abbot). AFOSR/Lehigh University Workshop, Dept. of Mech. Engng. & Mech., Bethlehem, PA.

[14] CRAWFORD, C.H. 1994 The structure and statistics of turbulent flow over riblets. *M.S.E. Thesis* Princeton University.

[15] CRAWFORD, C.H., EVANGELINOS, C., NEWMAN, D.J. & KARNIADAKIS, G.E. 1995 Parallel benchmarks of turbulence in complex geometries. Presented at *Parallel CFD 1995* and *Computer and Fluids*, vol. 25, p. 677, 1996.

[16] CRAWFORD, C.H. 1996 Direct numerical simulation of near-wall turbulence: Active and passive control. *PhD Dissertation*, Princeton University.

[17] CRAWFORD, C.H. & KARNIADAKIS, G.E. 1997 Reynolds stress analysis of EMHD-controlled wall turbulence: Part I: Streamwise forcing. *Physics of Fluids*, **9**(3), 788.

[18] DEISSLER, R.G. 1969 Direction of maximum turbulent vorticity in shear flow. *Phys. Fluids.* **12**, 426.

[19] GOLDSTEIN, D., HANDLER, R. & SIROVICH, L. 1995 Direct numerical simulation of turbulent flow over a modeled riblet covered surface. *J. Fluid Mech.* **302**, 333.

[20] HAIDARI, A.H. & SMITH, C.R. 1994 The generation and regeneration of single haipin vortices. *J. Fluid Mech.* **277**, 135.

[21] HAMA, F.R. 1962 Progressive deformation of a curved vortex filament by its own induction. *Phys. Fluids* **5**, 1156.

[22] HEAD, M.R. & BANDYOPADHYAY, P.R. 1981 New aspects of turbulent boundary layer structure. *J. Fluid Mech.* **107**, 297.

[23] HUSSAIN, A.K.M.F. 1986 Coherent structures and turbulence *J. Fluid Mech.* **173**, 303-356.

[24] HENDERSON, R.D. & KARNIADAKIS, G.E. 1995 Unstructured spectral element methods for simulation of turbulent flows. *J. Comp. Phys.* **122**, 191.

[25] KASAGI, N., SUMITANI, Y., SUZUKI, Y. & IIDA, O. 1995 Kinematics of the quasi-coherent vortical structure in near-wall turbulence. *Int. J. Heat and Fluid Flow* **16**, 2.

[26] KIDA, S. & TANAKA, M. 1994 Dynamics of vortical structures in a homogeneous shear flow *J. Fluid Mech.* **274**, 43.

[27] KIM, J. & MOIN, P. 1986 The structure of the vorticity field in turbulent channel flow. Part 2. Study of ensemble average fields. *J. Fluid Mech.* **162**, 339.

[28] KIM, J., MOIN, P. & MOSER, R. 1987 Turbulence statistics in fully developed channel flow at low Reynolds number. *J. Fluid Mech.* **177**, 133.

[29] KLEWICKI, J.C. 1989 Velocity-vorticity correlations related to the gradients of Reynolds stresses in parallel turbulent wall flows. *Phys. Fluids* **1**, 1285.

[30] KLINE, S.J. & ROBINSON, S.K. 1989 Quasi-coherent structures in the turbulent boundary layer. Part 1, Status report on a community-wide summary of the data. In *Near Wall Turbulence.* eds. Kline, S.J. & Afgan, N.H.

[31] KRAICHNAN, R.H. & PANDA, R. 1988 Depression of nonlinearity in decaying isotropic turbulence, *Phys. Fluids* **31**, 2395.

[32] LAUNDER, B.E. & LI, S.-P. 1992 A prediction of riblet behavior with a low-Reynolds number k-ϵ model. *Aeronautical Journal* November 1992, 354.

[33] LIU, K.N., CHRISTODOULOU, C., RICCIUS, O. & JOSEPH D.D. 1990 Drag reduction in pipes lined with riblets. *AIAA J.* **28**, 1967.

[34] MARMANIS, H. 1998 Analogy between the Navier-Stokes equations and Maxwell's equations: Application to turbulence, *Phys. Fluids* (in print)

[35] MOIN, P. & KIM, J. 1985 The structure of the vorticity field in turbulent channel flow. Part 1. Analysis of instantaneous fields and statistical correlations. *J. Fluid Mech.* **155**, 441.

[36] PARK, S.-R. & WALLACE, J.M. 1993 Flow field alteration and viscous drag reduction by riblets in a turbulent boundary layer. *AIAA-93-3256.*

[37] PERRY, A.E., LIM, K.L. & HENBEST S.M. 1987 An experimental study of the turbulence structure in smooth- and rough-wall boundary layers. *J. Fluid Mech.* **177**, 437.

[38] RAJAEE, M., KARLSSON, S. & SIROVICH, L. 1995 On the streak spacing and vortex roll size in a turbulent channel flow. *Phys. Fluids* **7**, 2439.

[39] ROBINSON, S.K. 1991 Coherent motions in the turbulent boundary layer. *Ann. Rev. Fluid Mech.* **23**, 601.

[40] SHERWIN, S.J. & KARNIADAKIS, G.E. 1995 A triangular spectral element method; Applications to the incompressible Navier-Stokes equations. *Comp. Meth. Appl. Mech. Engr.*, **123**, 189.

[41] SMITH, C.R. & METZLER, S.P. 1983 The characteristics of low-speed streaks in the near-wall region of a turbulent boundary layer. *J. Fluid Mech.*, **129**, 27.

[42] SMITH, C.R. 1996 Coherent flow structures in smooth wall turbulent boundary layers: Facts, Mechanisms, and Speculation. In *Coherent Flow Structures in Open Channels,* eds. Ashworth, P.J., Bennett, S.J., Best, J.L. & McLelland, S.J. *John Wiley & Sons Ltd.*, 1.

[43] SREENIVASAN, K.R. 1990 The turbulent boundary layer. In *Frontiers in Experimental Fluid Mechanics.* ed. Gad-el-Hak, M., 159.

[44] SUZUKI, Y. & KASAGI, N. 1993 Drag reduction mechanism on micro-grooved riblet surface. In *International Conference on Near-Wall Turbulent Flows.* Tempe, Arizona. eds. Speziale, C.G. & Launder, B.E.

[45] TAYLOR, G.I. 1932 Diffusion by continuous movements. In *Proceedings of the London Mathematical Society, Series 2.* **20**.

[46] TENNEKES, H. & LUMLEY, J.L. 1972 *A First Course in Turbulence.* The MIT Press.

[47] THEODORSEN, T. 1952 Mechanism of turbulence. In *Proceedings of the 2nd Midwestern Conference on Fluid Mechanics, Bull. No. 129.* Ohio State University, Columbus, Ohio.

[48] TOWNSEND, A.A. 1976 *The Structure of Turbulent Shear Flow.* Cambridge University Press.

[49] VUKOSLAVCEVIC, P., WALLACE, J.M. & BALINT, J.-L. 1992 Viscous drag reduction using streamwise aligned riblets. *AIAA J.* **30**, 1119.

[50] WALLACE, J.M., ECKELMANN, H. & BRODKEY, R.S. 1972 The wall region in turbulent shear flow. *J. Fluid Mech.* **54**, 39.

[51] WALLACE, J.M. 1982 On the structure of bounded turbulent shear flow: A personal view. *Developments in Theoretical and Applied Mechanics, XI*, 509.

[52] WALSH, M.J. 1990 Riblets. In *Viscous Drag Reduction in Boundary Layers, Progress in Astronautics and Aeronautics.* eds. Bushnell, D. & Hefner, J. **123** 203.

[53] WEI, T. & WILLMARTH, W.W. 1989 Reynolds-number effects in the structure of turbulent flow. *J. Fluid Mech.* **204**, 57.

[54] WILLMARTH, W.W. & TU, B.J. 1967 Structure of turbulence in the boundary layer near the wall. *Phys. Fluids* **10**, S134.

[55] WU, J.Z., ZHOU, Y. & WU, J.M. 1996 Reduced stress tensor and dissipation and the transport of Lamb vector, *ICASE* Rept. 96-21.

ROLE OF HELICITY AND CHIRALITY IN DRAG REDUCTION IN TURBULENT FLOWS

S. Moiseev, H. Branover*, O. Chkhetiani, A. Eidelman*, E. Golbraikh*
Space Research Institute, Profsoyuznaya st., 84/32, 117810 Moscow, Russia
moiseev@mx.iki.rssi.ru
*Center for MHD Studies, Ben-Gurion University of the Negev, P.O.B.653, Beer-Sheva 84105, Israel
eidel@bgumail.bgu.ac.il

Abstract - The behavior of Reynolds stresses in the mean velocity equation of a turbulent flow is studied. We have derived an expression of turbulent viscosity for the case where the initial small-scale turbulence is helical. The helicity decreasing turbulent viscosity leads to a slow-down of the direct energy transfer and to the formation of an inverse one. Formation of intermittent mode of helical turbulence leading to the localization of turbulent regions, as observed in wakes, is also studied. This effect is enhanced in magnetohydrodynamic flows under an external magnetic field. We also discuss general problems connected with so called chirality and its consequences for turbulent motions. The studied phenomena alter energy transfer and dissipation in turbulent seawater and affect hydrodynamic drag of moving bodies.

1. Introduction

An essential drag reduction in turbulent liquid flow with small amounts of certain polymers was observed about 50 years [1]. Further investigations have shown a considerable drag reduction when adding 2.5-10 ppm of certain polymers [2] or 2-3 orders larger amount of surfactants [3] to the liquid flow. Although the properties of the two mentioned additives are rather different, their common basic property is an ultimate drag reduction value reaching ~ 60-70% in both cases! Note that drag reduction is also achievable, if the turbulence is affected in an entirely different way, namely, in magneto-hydrodynamic (MHD) flow. In this case, turbulence control is realized at the expense of electromagnetic forces arising at the interaction of a conductive liquid flow with the magnetic field. Here, just as in case of additives, the same drag reduction value of 60-70% is achievable [4, 5]. MHD flow investigated at a laboratory represents a convenient object for studying the properties of flows with a reduced drag.

Since it is just in the boundary layer, not far from the wall, that the main part of turbulence energy is generated and dissipated, - the understanding of the processes in this flow region represents the key to the problem. Visual observations, beginning with [6, 7], point to a helical character of motion in this region. Recent progress in the study of helical turbulence makes it possible to develop an adequate physical model and, hence, a mathematical description of the influence of drag reducing additives on the turbulent motion.

Not only visual studies demonstrating the helical character of the motion, but also important integral properties of flows with reduced drag, inherent to helical turbulence, are considered below. Changes in the shape of turbulence spectrum caused by a decrease in the small-scale motion energy and growth of the large-scale motion energy, which are observed in drag-reduced flows, are also inherent to helical turbulence due to the inverse energy transfer [8]. The decrease in Reynolds stresses noted in drag-reduced flows is also characteristic of helical turbulence possessing a reduced effective viscosity [9].

Despite a large number of encouraging experiments, the absence of an adequate physical model prevents a significant progress in this field. This circumstance negatively affects the attempts of using geometrical means of turbulence control, such as riblets and outer boundary layer (OBL) devices. Riblets lead to a drag reduction of <10% in case of a successful choice of their parameters. But we should emphasize an encouraging result reported in [10]: turbulent friction on the surface located downstream in the vicinity of OBL device was reduced by 50%. However, in this and other experiments, the change in net friction losses including OBL device overflow losses fluctuate about zero. The study of OBL devices action on turbulent friction gives qualitatively different results even within the same laboratory. We believe that the understanding of helical turbulence properties will make the basis of more efficient decisions in turbulence control by geometrical means.

2. Turbulent viscosity

Helical turbulence occupies a special position among the variety of turbulent motions. Helicity

$$H = \int_V (\mathbf{u} \cdot \omega) dV$$

(here u is the velocity and ω = rot **u** is the vorticity), being a second invariant of Euler's equation, just as energy [11], has a great influence on the evolution and stability of turbulent and laminar flows [12]. Apparently, helicity is one of the main sources of magnetic fields generation and maintaining in astrophysical objects [13]. Possibly, helical mechanism is responsible for the generation of some intense large--scale geophysical vortices, such as typhoons and tornado [14, 15].

Many properties of systems, having helicity are explained by that the last effectively reduces action of nonlinear processes responsible for the transfer and the redistribution of energy between various scales.

Numerous investigations of the properties of helical turbulence [16, 17] also demonstrate that non-zero helicity leads to the decrease in the energy flux from large to small scales. One of the principal parameters connected with the energy flux from larger to smaller scales is turbulent viscosity. Hence, its magnitude should decrease with decreasing direct energy cascade. Additionally, the decrease of energy transfer should lead to another energy redistribution between different scales involved in turbulent motions.

To study mean helicity effect on turbulent viscosity value in a flow, we consider incompressible turbulent fluid flow and examine the stability of initial turbulent field $\mathbf{u}^{(0)}$ with zero mean flow to the weak large-scale inhomogeneous disturbances. We write the total perturbed velocity **u** as a sum $\mathbf{u} = \langle \mathbf{u} \rangle + \mathbf{u}^{(0)} + \mathbf{u}^{(1)}$, where $\langle \mathbf{u} \rangle$ is the mean part of the disturbance and $\mathbf{u}^{(1)}$ is the fluctuational part of disturbance, with $\mathbf{u}^{(1)} \ll \mathbf{u}^{(0)}$, $\langle \mathbf{u} \rangle \ll \langle (\mathbf{u}^{(0)})^2 \rangle^{1/2}$. One can derive a system of equations for $\mathbf{u}^{(1)}$ and $\mathbf{u}^{(0)}$ from the Navier-Stokes equation for the total velocity **u**

$$\frac{\partial \mathbf{u}}{\partial t} - \nu \Delta \mathbf{u} = -\frac{1}{\rho} \nabla p - (\mathbf{u} \cdot \nabla \mathbf{u}) + \mathbf{F}$$

$$\nabla \cdot \mathbf{u} = 0$$

where p is pressure, **F** is an external force, ρ and ν are, respectively, the fluid density and viscosity.

The evolution of the initial turbulent field $\mathbf{u}^{(0)}$ is described by equations

$$\frac{\partial \mathbf{u}^{(0)}}{\partial t} + \left(\mathbf{u}^{(0)} \cdot \nabla\right) \mathbf{u}^{(0)} - \nu \Delta \mathbf{u}^{(0)} = -\frac{1}{\rho} \nabla p^{(0)} + \mathbf{F}^{(0)} \qquad (1)$$

$$\nabla \cdot \mathbf{u}^{(0)} = 0, \ \left\langle \mathbf{u}^{(0)} \right\rangle = 0.$$

where $p^{(0)} = p - \langle p \rangle - p^{(1)}$ is the initial pressure fluctuation and $\mathbf{F}^{(0)} = \mathbf{F} - \langle \mathbf{F} \rangle$, $\langle \mathbf{F}^{(0)} \rangle = 0$ is the external random force sustaining the turbulent field. Correlational properties of $\mathbf{u}^{(0)}$ we'll discuss later.

For weak disturbances of the velocity we have linearized equations:

$$\frac{\partial \langle \mathbf{u} \rangle}{\partial t} - \nu \Delta \langle \mathbf{u} \rangle = -\frac{1}{\rho} \nabla \langle p \rangle - \left\langle (\mathbf{u}^{(0)} \cdot \nabla) \mathbf{u}^{(1)} \right\rangle - \left\langle (\mathbf{u}^{(1)} \cdot \nabla) \mathbf{u}^{(0)} \right\rangle + \langle \mathbf{F} \rangle , \qquad (2)$$

$$\nabla \cdot \langle \mathbf{u} \rangle = 0,$$

$$\frac{\partial \mathbf{u}^{(1)}}{\partial t} - \nu \Delta \mathbf{u}^{(1)} =$$

$$-\frac{1}{\rho}\nabla p^{(1)} - (\langle \mathbf{u} \rangle \cdot \nabla)\,\mathbf{u}^{(0)} - \left(\mathbf{u}^{(0)} \cdot \nabla\right)\langle \mathbf{u} \rangle$$

$$-\left(\left(\mathbf{u}^{(0)} \cdot \nabla\right)\mathbf{u}^{(1)} + \left(\mathbf{u}^{(1)} \cdot \nabla\right)\mathbf{u}^{(0)}\right. \qquad (3)$$

$$\left. - \left\langle (\mathbf{u}^{(0)} \cdot \nabla)\mathbf{u}^{(1)} \right\rangle - \left\langle (\mathbf{u}^{(1)} \cdot \nabla)\mathbf{u}^{(0)} \right\rangle\right),$$

$$\nabla \cdot \mathbf{u}^{(1)} = 0\,, \left\langle \mathbf{u}^{(1)} \right\rangle = 0$$

where <p>, $p^{(1)}$ are average pressure and a weak disturbance of the pressure, respectively.

Let us introduce the following notations

$$Q_{ij}^{00}(x', t', x, t) = \left\langle u_i^{(0)}(x', t') u_j^{(0)}(x, t) \right\rangle$$

$$Q_{ij}^{10}(x', t', x, t) = \left\langle u_i^{(1)}(x', t') u_j^{(0)}(x, t) \right\rangle$$

$$Q_{ijk}^{100}(x'', t'', x', t', x, t) = \left\langle u_i^{(1)}(x'', t'') u_j^{(0)}(x', t') u_k^{(0)}(x, t) \right\rangle$$

To study the behavior of Reynold's stress tensor and turbulent viscosity, we apply the procedure suggested by Krause and Rudiger [18]. Multiplying (3) by $\mathbf{u}^{(0)}(x', t')$ and averaging, we obtain:

$$\left(\frac{\partial}{\partial t} - \nu\Delta\right) Q_{ij}^{10}(x, t, x', t') =$$

$$-\frac{1}{\rho}\frac{\partial}{\partial x_i} P_j^{10}(x, t, x', t') -$$

$$\frac{\partial}{\partial x_k}\left(\langle u_k(x, t)\rangle\, Q_{ij}^{00}(x, t, x', t')\right. \qquad (4)$$

$$\left. + \langle u_i(x, t)\rangle\, Q_{kj}^{00}(x, t, x', t')\right) -$$

$$\frac{\partial}{\partial x_k}\left(Q_{ikj}^{100}(x, t, x, t, x', t') + Q_{ikj}^{100}(x, t, x, t, x', t')\right)$$

where $P_j^{10}(x, t, x', t') = \langle p^{(1)}(x, t)\, u_j^{(0)}(x', t')\rangle$.

The equation of the third moments may be derived in a similar way. For the sake of simplicity, we assume hereinafter that the original turbulence is of Gaussian character. In this case

$$\left(\frac{\partial}{\partial t} - \nu\Delta\right) Q_{ipj}^{100}(x, t, x', t', x'', t'') =$$

$$-\frac{1}{\rho}\frac{\partial}{\partial x_i} P_{pj}^{100}(x, t, x', t', x'', t'') -$$

$$\frac{\partial}{\partial x_k}\left[\left(Q_{ikpj}^{1000}(x, t, x, t, x', t', x'', t'') + \right.\right. \qquad (5)$$

$$Q_{kipj}^{1000}(x, t, x, t, x', t', x'', t'')) -$$

$$\left.\left.(Q_{ik}^{10}(x, t, x, t) + Q_{ki}^{10}(x, t, x, t))\, Q_{pj}^{00}(x', t', x'', t'')\right]\right.$$

Here

$$P_{pj}^{100}(x, t, x', t', x'', t'') = \left\langle p^{(1)}(x, t) u_p^{(0)}(x', t') u_j^{(0)}(x'', t'') \right\rangle.$$

The account for the correlation time finiteness in turbulence may be realized in various ways leading to similar results. In the present paper, an analog of Orszag approximation [19] studied by Vainshtein in the theory of MHD-dynamo [13, 20] for the second moments has been applied to close the series of equations (4).

Fourth order correlation moments can be represented as a sum:

$$Q_{ikpj}^{1000}(x, t, x, t, x', t', x'', t'') =$$

$$Q_{ik}^{10}(x, t, x, t) Q_{pj}^{00}(x', t', x'', t'') +$$

$$Q_{ip}^{10}(x, t, x', t') Q_{kj}^{00}(x, t, x'', t'')$$

$$+ Q_{ij}^{10}(x, t, x'', t'') Q_{kp}^{00}(x, t, x', t') +$$

$$Q_{ikpj}^{1000}(x, t, x, t, x', t', x'', t'')_{cum},$$

where $Q_{ikpj}^{1000}(x, t, x, t, x', t', x'', t'')_{cum}$ is a cumulant.

Let us make the following substitution of coordinates:

$$x \to x + \xi, x' \to x + \xi', x'' \to x,$$

$$t \to t + \tau, t' \to t + \tau',\ t'' \to \tau$$

then $\partial/\partial x_i \to \partial/\partial \xi_i$ and we derive an expression for the third moment from the equation (5):

$$Q_{ipj}^{100}(x + \xi, t + \tau, x + \xi', t + \tau', x, t) =$$

$$Q_{ipj}^{100}(\xi, \tau, \xi', \tau', x, t) =$$

$$-\tau^* \nabla_k \Pi_{im}(Q_{pm}^{10}(\xi, \tau, \xi', \tau') Q_{kj}^{00}(\xi, \tau, x, t) \qquad (6)$$

$$+ Q_{mj}^{10}(\xi, \tau, x, t) Q_{kp}^{00}(\xi, \tau, \xi', \tau') +$$

$$Q_{kp}^{10}(\xi, \tau, \xi', \tau') Q_{mj}^{00}(\xi, \tau, x, t) +$$

$$Q_{kj}^{10}(\xi, \tau, x, t) Q_{mp}^{00}(\xi, \tau, \xi', \tau'))$$

Here $\Pi_{im} = \delta_{im} - \nabla_i \nabla_m / \Delta$ is the projection operator. Relaxation time τ^* can be estimated as:

$$\tau^* \approx \mu L_{tur} / E_{tur}^{1/2},$$

where L_{tur} is the integral scale of turbulence, E_{tur} is the mean energy of turbulent motion, μ is a constant. Relaxation time is a open parameter here, but under simplifying assumptions, it can be determined from the functional equation [20]. In the present problem, turbulence is affected by a weak large-scale disturbance becoming weakly inhomogeneous and weakly anisotropic. Turbulent relaxation time is less that the characteristic evolution time of perturbation, so a quasi stationary moments distribution is established in the system. In this paper this question is not discussed.

Additionally, we have noted that analogous closure methods are used in phenomenological theories of turbulence [20, 21, 22]. It turns out that the 3rd order moments calculated in this approximation describe correlation properties of different turbulent flows with the same value of numeric constant $\mu \approx 0.44$ [22].

The equation (4) for the second moments contains a combination $\nabla_p(Q_{ipj}^{100} + Q_{pij}^{100})$, and since $\nabla_p \Pi_{pm} = 0$, the term involving third moments will be of the following form

$$\tau^* \nabla_k \nabla_p \Pi_{im}(Q_{mp}^{10}(\xi, \tau, \xi', \tau') Q_{kj}^{00}(\xi, \tau, x, t)$$

$$+ Q_{mj}^{10}(\xi, \tau, x, t) Q_{kp}^{00}(\xi, \tau, \xi', \tau') +$$

$$Q_{kp}^{10}(\xi, \tau, \xi', \tau') Q_{mj}^{00}(\xi, \tau, x, t) + \qquad (7)$$

$$Q_{kj}^{10}(\xi, \tau, x, t) Q_{mp}^{00}(\xi, \tau, \xi', \tau'))$$

We assume that the external random force $\mathbf{F}^{(0)}$ has sustained the initial small--scale turbulent field $\mathbf{u}^{(0)}$ in stationary state with the properties of homogeneity, isotropy and non--zero helicity. The extremely interesting problem of the mirror symmetry breaking in fluid dynamics we did not discuss in this paper. In this case a two-point correlator $Q_{ij}^{00}(x, t, \xi, \tau)$ has the following form [23]

$$Q_{ij}^{00}(x, t, \xi, \tau) = A(\xi, \tau)\delta_{ij} + \qquad (8)$$

$$B(\xi, \tau)\xi_i \xi_j + C(\xi, \tau)\varepsilon_{ijk}\xi_k$$

$$\xi = |x - x'|\,, \tau = |t - t'|\,.$$

where ε_{ijk} is an entirely antisymmetric tensor. $A(\xi, \tau)$, $B(\xi, \tau)$ are scalar functions. $C(\xi, \tau)$ is a pseudoscalar function ($C(|\xi|, \tau) = -C(|-\xi|, \tau)$). Applying the incompressibility condition (3) and taking into account that

$$Q_{kp}^{00}(\xi - \xi', \tau - \tau')_{\xi' \to \xi, \tau' \to \tau} \to A(0, 0)\delta_{kp} \qquad (9)$$

$$\nabla_k Q_{mp}^{00}(\xi - \xi', \tau - \tau')_{\xi' \to \xi, \tau' \to \tau} \to C(0, 0)\varepsilon_{mpk}$$

we obtain from (7) the following expression at $\xi' \to \xi$ and $\tau' \to \tau$ transition:

$$\tau^*\Pi_{im}(\nabla_k Q^{10}_{mp}(\xi,\tau,\xi,\tau)\nabla_p Q^{00}_{kj}(\xi,\tau,\mathrm{x},t)+ \quad (10)$$
$$\Delta Q^{10}_{mj}(\xi,\tau,\mathrm{x},t)A(0,0)+$$
$$Q^{10}_{kp}(\xi,\tau,\xi,\tau)\nabla_k\nabla_p Q^{00}_{mj}(\xi,\tau,\mathrm{x},t)+$$
$$C(0,0)\varepsilon_{mpk}\nabla_p Q^{10}_{kj}(\xi,\tau,\mathrm{x},t))$$

Assuming that spatial and temporal scales of the mean inhomogeneity exceed greatly the turbulent field correlation length and time, we may take Taylor series expansions of $Q_{ij}^{10}(\xi, \tau, \xi, \tau)$ and $\langle u_i(\xi, \tau)\rangle$ in powers of ξ. Restricting ourselves by the first order terms, we obtain

$$Q^{10}_{ij}(\xi,\tau,\xi,\tau) \cong Q^{10}_{ij}(\mathrm{x},t,0,0) + \xi_l \frac{\partial Q^{10}_{ij}(\mathrm{x},t,0,0)}{\partial x_l} \quad (11)$$

$$\langle u_i(x+\xi,t+\tau)\rangle = \langle u_i(\mathrm{x},t)\rangle + \xi_l \frac{\partial \langle u_i(\mathrm{x},t)\rangle}{\partial x_l}$$

Substituting (11) into (10), and the result of it - into (4), we derive the equation for the second moments

$$\left[(\frac{\partial}{\partial\tau} - (\nu+\nu_t^0)\Delta)\delta_{ik} - \alpha\varepsilon_{ipk}\nabla_p\right] Q^{10}_{kj}(\xi,\tau,\mathrm{x},t) =$$
$$\langle u_p(\mathrm{x},t)\rangle \nabla_p Q^{00}_{ij}(\xi,\tau,\mathrm{x},t) - \quad (12)$$
$$\frac{\partial}{\partial x_p}\langle u_i(\mathrm{x},t)\rangle Q^{00}_{pj}(\xi,\tau,\mathrm{x},t) -$$
$$\frac{\partial \langle u_p(\mathrm{x},t)\rangle}{\partial x_s}\xi_s\nabla_p Q^{00}_{ij}(\xi,\tau,\mathrm{x},t)+$$
$$\tau^*\nabla_p\{\frac{\partial}{\partial x_p}Q^{10}_{ip}(\mathrm{x},t,0,0)Q^{00}_{kj}(\xi,\tau,\mathrm{x},t)$$
$$+\frac{\partial Q^{10}_{kp}(\mathrm{x},t,0,0)}{\partial x_s}\nabla_k(\xi_s Q^{00}_{ij}(\xi,\tau,\mathrm{x},t))$$
$$+Q^{10}_{kp}(\mathrm{x},t,0,0)\nabla_k Q^{00}_{ij}(\xi,\tau,\mathrm{x},t)\}$$

where $\nu_t^0 = A(0, 0)\tau^*$ and $\alpha = C(0, 0)\tau^*$.

A similar equation arises in the theory of magnetic dynamo, when using KIyatskin-Tatarski's method [21]. However, in the present case, additional terms arise in the right-hand part, proportional to one-point moments of disturbed turbulence. They make the problem self-consistent.

Solving Eq. (12) for $Q_{ij}^{10}(x, t, 0, 0)$ one obtains the following expression for turbulent viscosity (coefficient at $\Delta\langle\mathbf{u}\rangle$):

$$\nu_t = \{1+$$
$$\frac{\tau^*}{15}\int_{k_{tur}}^{\infty}\int_0^{\infty}\exp(-\nu_t^0 k^2\tau)(2E_f(k,\tau)\mathrm{Ch}(\alpha k\tau)$$
$$+\frac{H_f(k,\tau)}{k}\mathrm{Sh}(\alpha k\tau))dkd\tau\}^{-1}\times$$
$$\frac{2}{5}\int_{k_{tur}}^{\infty}\int_0^{\infty}\exp(-\nu_t^0 k^2\tau)\{[E_f(k,\tau) \quad (13)$$
$$+\frac{k}{3}\frac{\partial E_f(k,\tau)}{\partial k}]\mathrm{Ch}(\alpha k\tau) -$$
$$[\frac{2}{3}\frac{H_f(k,\tau)}{k} - \frac{1}{6}\frac{\partial H_f(k,\tau)}{\partial k}]\mathrm{Sh}(\alpha k\tau)\}dkd\tau$$

where $E_f(k, \tau)$ and $H_f(k, \tau)$ are related to symmetric and antisymmetric parts of Fourier-transform of the undisturbed turbulence correlator

$$\widehat{Q}^{00}_{ij}(\mathrm{k},\tau) = \frac{E_f(k,\tau)}{4\pi k^2}(\delta_{ij} - \frac{k_i k_j}{k^2}) \quad (14)$$
$$-i\frac{H_f(k,\tau)}{8\pi k^4}\varepsilon_{ijl}k_l$$

where

$$|H_f(k,\tau)| \le 2kE_f(k,\tau). \quad (15)$$

In particular,

$$A(0,0) = \int E_f(k,0)dk, \quad (16)$$
$$C(0,0) = \frac{1}{6}\int H_f(k,0)dk$$

As Eq. (13) shows, helicity, in fact, decreases turbulent viscosity.

Considering the correlator's time dependence in the form $(\beta\tau_{cor})\exp(-\beta|\tau|)$, where both τ_{cor} and τ^* are determined by the characteristic scale and the energy of turbulent motion, we obtain, after integrating with respect to time

$$\nu_t = [1+\frac{\beta\tau^*\tau_{cor}}{15}\int_{k_{tur}}^{\infty}\frac{(2E_f(k)(\nu_t^0 k^2+\beta)+\alpha H_f(k))}{(\nu_t^0 k^2+\beta)^2-\alpha^2k^2}dk]^{-1}\times$$
$$\frac{2(\beta\tau_{cor})}{5}\int_{k_{tur}}^{\infty}\{[E_f(k) \quad (17)$$
$$+\frac{k}{3}\frac{\partial E_f(k)}{\partial k}](\nu_t^0 k^2+\beta)[(\nu_t^0 k^2+\beta)^2-\alpha^2k^2]^{-1} -$$
$$\alpha k[\frac{2}{3}H_f(k) - \frac{1}{6k}\frac{\partial H_f(k)}{\partial k}][(\nu_t^0 k^2+\beta)^2-\alpha^2k^2]^{-1}\}dk$$

It can be easily shown that the transition to δ-correlated process ($\beta \to \infty$) under the condition of finite τ_{cor} and τ^* does not result in the disappearance of the helicity contribution to the turbulent viscosity, as it would be in case of initially postulated δ-correlated character. It is finite and determined by intrinsic turbulence characteristics.

3. Intermittency in helical turbulent flow

It is well-known that turbulent wakes at the motion of bodies in seawater persist for a long time. Below we consider one of possible mechanisms of turbulent wakes formation in the presence of non-zero helicity and its fluctuations. According to the theory of mean magnetic field generation in the mode of so called rapid dynamo [24], preferential growth of higher moments of the velocity and magnetic field fluctuations lead to large-scale field breaking. This phenomenon is observed, for instance, in the velocity field of magnetohydrodynamic helical turbulence [29].

On the other hand, since seawater represents a heavily stratified medium, and at the overflow of bodies strong shear flows are formed in it, we can say that equations for mean velocity fields are formally similar to equations of dynamo type. In fact, an equation of a vortex $\omega = \mathrm{rot}\,\mathbf{u}$ in an incompressible fluid

$$\frac{\partial\omega}{\partial t} = rot[\mathrm{v}\times\omega] + \nu\Delta\omega \quad (18)$$

is formally similar to magnetic field equation

$$\frac{\partial \mathrm{B}}{\partial t} = rot[\mathrm{v}\times\mathrm{B}] + D\Delta\mathrm{B} \quad (19)$$

However, as noted in [13], the formal similarity of these equations does not imply identical behavior of ω and **B**. On the other hand, in an inhomogeneous helical medium of seawater type, dynamo-type equation can also take place, i.e.

$$\frac{\partial\langle\mathrm{u}\rangle}{\partial t} = C\ rot\langle\mathrm{u}\rangle + \nu\Delta\langle\mathrm{u}\rangle \quad (20)$$

If the helicity in a given system is fluctuating, then it is necessary to study in this case the influence of so called multiplicative noise on the evolution of the non-equilibrium system [25]. Systems with multiplicative noise include those where random fluctuations of the system parameters at the expense of external energy multiplied by some magnitude Characterizing the state of the system exert the most considerable influence. If we present helicity in Equation (20) in the form $C = C_o + C'$, where C' are helicity fluctuations, then the equation

$$\frac{\partial\langle\mathrm{u}\rangle}{\partial t} = (C_o + C')\ rot\langle\mathrm{u}\rangle + \nu\Delta\langle\mathrm{u}\rangle \quad (21)$$

will also fall into the category of equations with multiplicative noise. We can readily show that the equation (21) leads to the

following expression for higher moments (of the order of n) of the velocity field

$$\frac{\partial}{\partial t}\left\langle \prod_{e=1}^{n} u_e \right\rangle = \tag{22}$$

$$D\left\langle \sum_{l=1}^{n}\sum_{m=1}^{n}\prod_{\substack{f=1\\ f\neq e\\ g\neq m}}^{n} u_e (rot\ \mathbf{u})_f (rot\ \mathbf{u})_g \right\rangle$$

where D is defined as $< C'(t)\ C'(t')> = D\delta(t - t')$, and for the chosen velocity component

$$\frac{\partial}{\partial t}\langle u_e^n \rangle \sim Dn^2 \langle u_e^{n-2}(\nabla_j u_k)(\nabla_j u_k)\rangle \tag{23}$$

i.e. higher moments grow proportionally to the square of their order.

As established in [24], preferential growth of higher moments of a random velocity field represents a transition of a turbulent field to intermittency, i.e. to breaking. Thus, the expression (23) points out that the presence of helicity fluctuations leads the system to an intermittent turbulent field. Simultaneously, as shown earlier, turbulent viscosity in the present system decreases, which also contributes to intermittency enhancement.

Thus, in case of bodies moving in seawater, we should emphasize the following: if a wake with a fluctuating mean helicity can be formed behind the body, then it should be expected that the turbulent wake will become strongly intermittent just due to helical turbulence properties.

One of promising trends in the study of seawater as a medium with peculiar symmetry properties is the study of its chiral properties.

The chirality phenomenon is connected with a global violation of mirror symmetry in a system under study. In this sense, helicity is a particular case of chirality. Chirality is a wide-spread property observed in quantum physics and in solid state physics. It is noteworthy that chirality is intrinsically present in practically all organic substances, including living matter. Chirality of seawater results from the latter. In fact, it is well-known that seawater contains a large amount of biomass, which imparts chiral properties to seawater. On the other hand, salts containing in
seawater make it a well-conductive medium. As is known [26], at the interaction of media without a symmetry center with an external source of light, current structures are formed in a conductive medium. In turn, as demonstrated in [27], chiral conducting turbulent medium (in any case, the seawater surface layer) may lead to the growth of mean electric field. On the other hand, the same currents generate a ponderomotive force, which forms nonzero mean helicity in a turbulent medium [28]. Hence, due to chiral properties of seawater, it can be practically always considered helical in the surface layer. Motions of bodies in it represent large-scale disturbances, and we, thus, come back to the problems discussed in the previous sections.

4. Conclusion

We have computed turbulent viscosity of a flow involving small-scale helical turbulence and a weak large-scale disturbance. When computing higher moments, finite correlation time is taken into account within Orszag's approximation. It is shown that in this case turbulent viscosity is
considerably decreased in the mean flow.

One of helical turbulence modes is intermittent. This mode is realized at the increase of helicity of motion and its fluctuations. Such a mode of flow entails preferential growth of higher velocity moments and localization of turbulent regions.

The study of these phenomena directly affects the mode of turbulent motions changing their structure and, hence, energy transfer and dissipation determining hydrodynamic drag.

References

1. Toms, B.A. 1949. Some observations on the flow of linear polymer solutions through straight tubes at large Reynolds numbers. Proc. of the 1st Internat. Rheology Congress, II, Part 2 (North-Holland, Netherlands), 135-142.

2. McComb, W.D. and Rabie, L.H. 1982. Local drag reduction due to injection of polymer solutions into turbulent flow in a pipe. Part 1: Dependence on local polymer concentration. Part 2: Laser-Doppler measurements of turbulent structure. AIChE J., v. 28, 547-565.

3. Dobrychenko, V.M., Lobachev, V.G., Povkh, I.L. and Eidelman, A.E. 1976. Drag reduction by liquid thickening surfactant admixtures. J. of Engineereing Physics, v. 30, No. 2. Transl. of: Inzhenerno-Fizicheskii Zhurnal, v. 30, No. 2, 240-245.

4. Klebanoff, P.S. and McMichael, J.M. 1976. On MHD pipe flow. Proc. Bat-Sheva Internat. Seminar on MHD-Flows and Turbulence, Beer-Sheva. John Wiley, N.Y., p. 73.

5. Branover, H. 1978. Magnetohydrodynamic flow in ducts. J. Wiley & Sons, N.Y., 290 pp

6. Corino, E.R. and Brodkey, R.S. 1969. A visual investigation of the wall region in turbulent flow. J. Fluid Mech., v. 37, p. 1, 1-30.

7. Kline, S.J., Reynolds, W.C., Schraub, F.A. and Runstadler, P.W. 1967. The structure of turbulent boundary layers. J. Fluid Mech., v. 30, p. 4, 741-773.

8. Chkhetiani, O.G., Moiseev, S.S., Petrosyan, A.S. and Sagdeev, R.Z. 1993. The inverse energy cascade and self-organization in homogeneous turbulent shear flow. Applied Sci. Research, v. 51, 67-72.

9. Belyan, A.V., Moiseev, S.S. and Chkhetiani, O.G. 1994. On turbulent viscosity in helical turbulence. Dokl. Akad. Nauk, v. 334, No. 1, 34-36.

10. Yajnik, K. S. and Acharaya, M. 1976. Structure and mechanisms of turbulence, Vol. 1, Lecture notes in Physics 76 (Springer, N.Y.), p. 249 (from Balakumar, P. and Widnall, S.E., 1986).

11. Moffatt, H.K. 1969. The degree of knottedness of tangled vortex lines. J. Fluid Mech., v. 35, p. 1, 117-129.

12. Moffatt, H.K., Tsinober, A. 1992. Helicity in laminar and turbulent flow. Annu. Rev. Fluid Mech., v. 24, 281 - 312.

13. Vainstein, S.N., Zeldovich, Ya.B. and Ruzmaikin, A.A. 1980. Turbulent Dynamo in Astrophysics. Moscow:\ Nauka (in Russian).

14. Moiseev, S.S., Sagdeev, R.Z., Tur, A.V., Khomenko, G.A. and Yanovskii, V.V. 1983. Theory of the origin of large-scale structures in hydrodynamic turbulence. Sov. Phys. JETP, v. 58, No 6, 1149-1153.

15. Khomenko, G.A., Moiseev, S.S. and Tur, A.V. 1991. The hydrodynamical alpha-effect in a compressible medium. J. Fluid Mech. v. 225, 355-369.

16. Chkhetiani, O.G., Moiseev, S.S., Petrosyan, A.S. and Sagdeev, R.Z. 1994. The large scale stability and self-organization in homogeneous turbulent shear flow. Physica Scripta, v. 49, 214 - 220.

17. Levich, E., Shtilman, L.and Tur, A.V. 1991. The origin of coherence in hydrodynamical turbulence. Physica A, v. 176, 241-296.

18. Krause, F. and Rudiger, G. 1974. On the Reynolds stresses in mean-field hydrodynamics. I. Incompressible homogeneous isotropic turbulence. Astron. Nachr., v. 295, No. 2, 93-99.

19. Orszag, S.A. 1970. Analytical theories of turbulence. J. Fluid Mech., v. 41, p. 2, 363-386.

20. Vainshtein, S.I. 1983. Magnetic fields in space. Moscow: Nauka, (in Russian).

21. Klyatskin, V.I. and Tatarsky, V.I. 1972. Statistical theory of the light propagation in turbulent medium. Izv. VUZov. Radiofizika, v. 15, 1433-1442.

22. Launder, B.E., Reece, G.J. and Rodi, W. 1975. Progress in the development of a Reynolds-stress turbulence closure. J. Fluid Mech., v. 68, p. 3, 537-566

23. Batchelor, G.K. 1953, The theory of homogeneous turbulence. Cambridge Univ. Press, L.

24. Molchanov, S.A., Ruzmaikin, A.A. and Sokolov, D.D. 1985. Kinematic dynamo in a random flow. Sov. Phys.: Uspekhi, v. 145, No. 4, 593-627.

25. Moiseev, S.S., Chkhetiani, O.G. and Shavva, I.I. 1990. On the effects of fluctuational "negative viscosity" in some problems of plasma physics and hydrodynamics", Preprint of Space Research Institute No. 1667.

26. Sturman. B.I. and Fridkin, V.M. 1992. Photogalvanic effect in media without a symmetry center and related phenomena", Moscow, "Nauka", 208 pp.

27. Belyan, A.V., Moiseev, S.S., Pungin, V.G. and Chkhetiani, O.G. 1997. Anomalous growth of electric fields in a chiral medium. Moscow, Space Research Institute Preprint No. 1999.

28. Chkhetiani, O.G., Moiseev, S.S.and Golbraikh, E. 1997. On helicity generation in shear turbulent MHD\ flows (in press, JETP)

29. Eidelman, A., Branover, H., Golbraikh, E. and Moiseev S. MHD turbulence experiments, drag reduction and application to non-MHD experiments. Proc. Seawater Drag Reduction Symp.

METHODS OF INFLUENCE ON COHERENT VORTICAL STRUCTURES OF A BOUNDARY LAYER

Viktor V. Babenko

Department of Hydrobionics and Boundary Layer Control, Professor, Dr.Tech.Sc., Head of Department, 8/4, Zheliabov str., 252057, Kiev, Ukraine, E-mail: vb@bionics.kiev.ua

A study was made of the mechanisms of coherent structure formation in boundary layer during laminar-turbulent transition. Coherent structure features under mentioned types of external disturbabces are analyzed. A special attention was payed to the study of the vortex form character. There were elicited three forms of vorticity associated with the characteristic stages of a traditional boundary layer. A model of the disturbing motion development for characteristic transition stages with and without mentioned disturbing factors is presented. Similar to the vortex development in a transitional boundary layer there were considered disturbance structures in a wall region of the turbulent boundary layer. Mechanisms of the coherent structure development and interaction along the boundary layer thickness were investigated. A table accumulates some methods of the active control of the bo-undary layer flow character including local separations and separating flows. They are methods of coherent structure introduction and control, methods of wall jets including the polymer solution delivery, vibration methods, plane oscillation methods. Experiments were carried out using tellurium-method, thermo- and laser anemometry both for a flat plate in a low-turbulence hydrodynamic bench and for three-dimensional bodies.

Actual problem is study of regularities of coherent structures generation in turbulent boundary layer and determination of mutual influence of vortical coherent structures in near-wall and outer regions. Such research permits us to substantiate the mechanisms of control of coherent structures in boundary layer, on which basis one can work out the methods of their control. It is known fact that turbulence production in boundary layer exists mainly in near-wall region which coherent structures are characterized by stastically alternated in transverse direction longitudinal areas of low-speed and high-speed fluid. In near-wall region there are other coherent formations like "pockets" and Kline's vortices too. However, still here is not clear understanding of spatial character of the coherent structures and their dependence both between each other and on coherent structures of outer part of boundary layeris subjected to disturbances of difeerent type from outer and inner boundaries. Let the disturbances to be called deteriorating factors in comparison with idealized conditions for flat palte flowing by indisturbed flow. The basic idea of present investigations is based on resukts of experimental research that have allow us to put forward the hypothesis that viscous sublayer of turbulent boundary layer can be represented as quasi-laminar boundary layer. In 1980 we put forward the hypothesis [1] that in viscous sublayer of turbulent boundary layer development of coherent structures happens approximately in the same way as in transitional boundary layer with influence of deteriorating factors. Since measuring in viscous sublayer is difficult then taking into account mentioned hypothesis it is enough to learn the development of coherent structures in transitional boundary layer when it is subjected to influence of deteriorating factor, for example in form of increased turbulence of free stream and vibration of flowing surface. Really, increased vortical disturbances, which are in outer part and in the core of turbulent boundary layer, influence the viscous sublayer from iuter side. To model this situation one should, in transitional boundary layer, create the increased turbulence of free stream or disturb outer boundary layer by plane of three-dimensional finite disturbances. From another side, permanent bursts of deccelerated fluid from viscous sublayer create as if the extra disturbances from the lower boundary of viscous sublayer. This may be modelled in transitional boundary layer by means of generation of vibration of flowing boundary.

This fundamental idea is being illustrated on fig. 1. In lower part of the figure there is schematic picture of structure of development of disturbing motion at different stages of transitional boundary layer development. Shown in viscous sublayer of turbulent boundary layer is disturbances development pattern which is analog to and characteristic for transitional boundary layer. Besides, through the thickness of turbulent boundary layer there are generated three areas of coherent vortical structures. This is large vortices in outer part, ordered vortical systems in buffer zone and systems of vortices in viscous sublayer.

In upper part of the figure there is distribution of friction coefficient corresponding to vortical coherent structures of boundary layer at different stages of transition. Dotted lines denote measurements of longitudinal pulsative velosity at different stages of transition by other authors. We see that data on upper picture correlate well with development of coherent vortical structures at different stages of transition. Hence it may be suggested that controlling vortical coherent structures one can influence the integral and fluctuative characteristics of boundary layer.

Except the idea of structural character of disturbances development at different stages of transition, the idea of influence the frequency characteristics of oredered vortical structures lays in the base of control methods development. As we said before, fluid particle has dual property of its motion: it moves along a definite trajectory and has a spectrum of oscillatios during motion where one can separate the definite energy-carrying frequencies for each stage of transition or for every type of coherent vortical structures.

In accordance with these two approaches the methods of influence the coherent vortical structures have been elaboreted. As the principal factor (third approach or principle of influence), the influence energy must be of the same order as the energy and dimension of disturbing motion at corresponding stage of transition. In table there are having been developed methods consisted of seven groups: mechanical (I), dynamic (II), kinematic (III), electric (IY), acoustical (Y), combined (YI) and active ones with feedback system (YII). Let consider mechanic methods. Oscillating surface has to contribute to ordering or damping the corresponding vortical structures. Oscillated my be the part of the surface, for example forepart.

Transverse projections or indentations are intended to generate transverse vortexes which have the axis of rotation in transverse direction.

Longitudinal projections or indentations are intended for generation of longitudinal vortices. The most studied for those purposes are riblets of different type.

Longitidinal stationare vortex-generators differ from riblets by discreteness of longitudinal size and variety of forms.

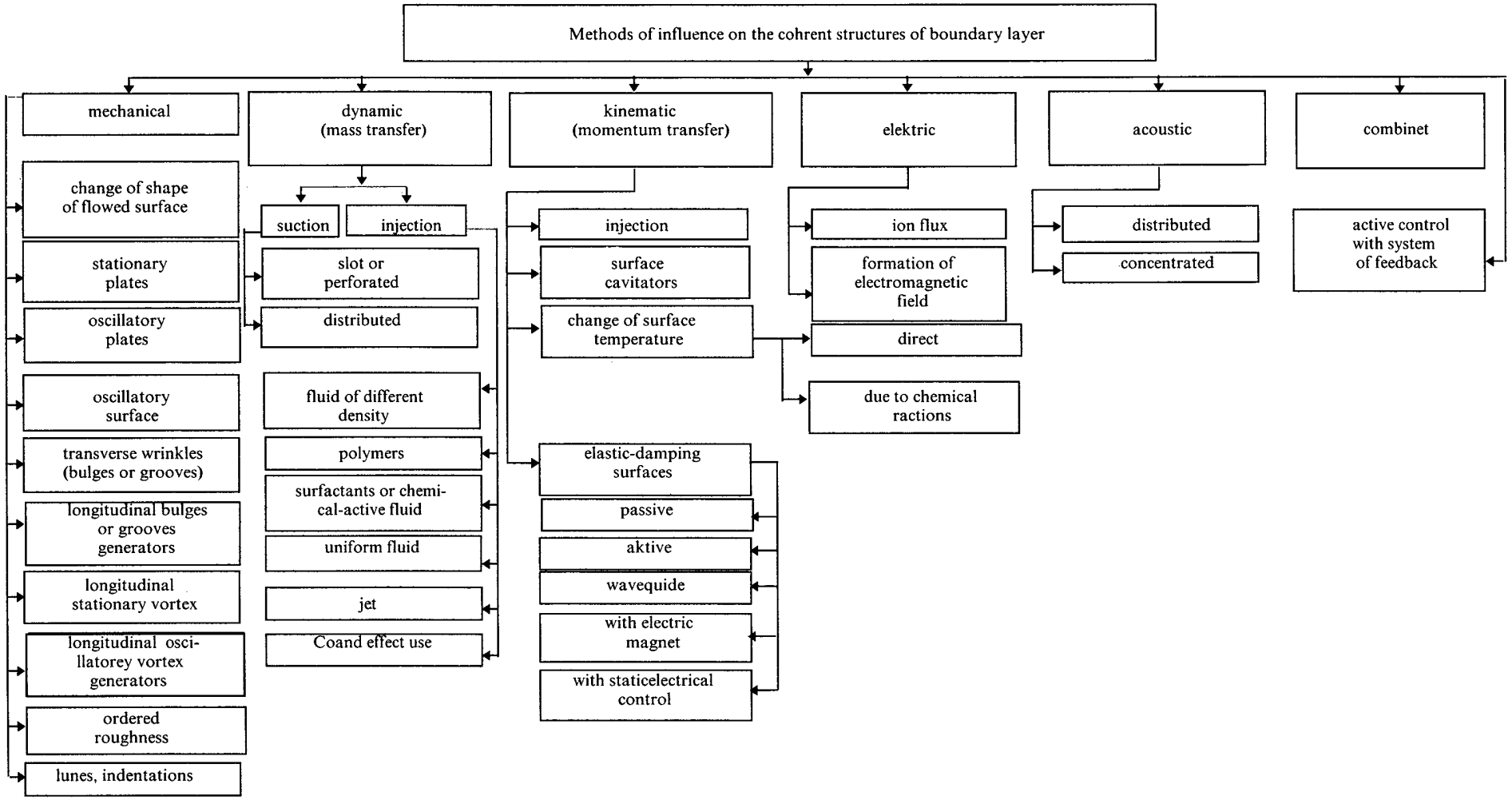
Methods of influence on the cohrent structures of boundary layer
mechanical
dynamic (mass transfer)
kinematic (momentum transfer)
elektric
acoustic
combinet
change of shape of flowed surface
stationary plates
oscillatory plates
oscillatory surface
transverse wrinkles (bulges or grooves)
longitudinal bulges or grooves generators
longitudinal stationary vortex
longitudinal osci-llatorey vortex generators
ordered roughness
lunes, indentations
suction
injection
slot or perforated
distributed
fluid of different density
polymers
surfactants or chemi-cal-active fluid
uniform fluid
jet
Coand effect use
injection
surface cavitators
change of surface temperature
elastic-damping surfaces
passive
aktive
wavequide
with electric magnet
with staticelectrical control
ion flux
formation of electromagnetic field
direct
due to chemical ractions
distributed
concentrated
active control with system of feedback

Longitudinal oscillatory vortex-generators differ from previons ones by ability of dynamic influence the boundary layer.

Ordered roughness serves for the same goals: organization of longitudinal and transverse vortices.

Lunes are new little-studied method of influence the vortical structure of biundary layer. Depending on task setted, the lunes may be arranged in longitudinal or transverse order.

Change of shape of surface flowed around may be either cyclic or stationary. Stationary plates may be put into the boundary layer in order to destroy the large-scale vortices. As an example of such plates, there are LEBU that is rings mounted equidistantly from flowed cylindric surface.

Oscillatory paltes are the oscillatory LEBU. Dynamic methods are based on principle of mass transfer and differ from known ones by that that influence is fulfilled on the part of flowed surface. Concerned to those methods is slot, perforate or distributed suction of boundary layer.

Injection or blow in to the boundary layer are made on discrete parts too. Injection may be done by means of blowing the stratified or uniform fluids as well as water solution of polymer, surfactants and chemically active fluid. Method of injection may differ from each other in particular jet-method or using Coanda effect.

Kinematic methods are based on principle of momentum transfer. They consists of injection as in previous case, mounting discrete surface cavitators, regulation of temperature of flowed surface by heating or resulting from chemical reactions with free stream fluid. Separate class is elastic-damping surfaces: one-layer o multi-layer, isotropic or not, passive or active.

Related to electric methods are setting ion flux in boundary layer and generation of electro-magnetic field around the flowed body in case of small conductivity of free stream fluid. Acoustical methods may be distributed or concentrated. These methods are based on principle of generation of additional pulsative specially directed field of pressure.

The most perspective are combined methods which use simultaneously the combination of different considered methods and/or combination with active methods of control.

Some of methods considered have been studied experimentally.

MEASURING METHODS OF BOUNDARY LAYER PARAMETERS

Boundary layer velocity field is visualized with tellurium method [3] and with coloured streaks. Velocity measurements are carried out with the laser Doppler anemometer (LDA) and DISA thermoanemometer [2].

The hydrodynamic bench, equipment and devices are described in Fig. 2.

A low-turbulence hydrodynamic test bench comprises special equipment and devices. The following are the basic technical data of the test bench: length of test bench 7 m, length of test section 3 m, cross-section of test section 0.09×0.25 m, range of operating speeds 0.05÷1.5 m/sec, effuser contraction factor equal to 10. Mounted on the test bench are the following main devices: a duplex bottom of the test section, a removable cover of the test section. The test bench is equipped with a boundary-layer bleed in the corners of the test section. The cover of the test section can be tilted to various angles and rails are laid out along the test section, over which the car with special apparatus, LDA and DISA moves.

Small oscillations of various types were introduced into the boundary layer with the help of specially designed oscillators for measuring neutral oscillations. Supports were arranged further downstream, making it possible to obtain small tellurium jets. The oscillator vibrational frequency changes in the course of the experiment, the amplitude of the tellurium jet oscillations being recorded.

The method of investigation of natural transition at nonlinear stages consists in the following. First of all a boundary layer is examined in different aspects with the tellurium method along the test section.

Simultaneus photography of velocity profiles in vertical and transverse directions and also of longitudinal tellurim small jets gives the possibility to construct the spatial-temporary picture of exciting motion and velocity field during different stages of transition.

Analysis of profiles U(z) gives the possibility for determining the characteristic points along y and z axes where the boundary layer kinematic parameters are measured with LDA and DISA. All these measurements are made under a low turbulence level ($\varepsilon \leq 0{,}05\%$).

PHYSICAL PATTERN OF STAGES OF LAMINAR-TURBULENT BOUNDARY LAYER TRANSITION

We have the large enough amount of experimental data in order to conclude that at the low turbulence level the transition process is characterised by the succesive change of disturbing motion types. The model of this succession was developed (Fig. 3) on the basis of the study of the natural boundary layer transition and the well-known results of Knapp and Roach, Klebanoff and oth., Tani, Morkovin, Kline and many others. The wave transformation process during transition to turbulence can be devided into the following stages (Fig. 3):

- plane disturbances amplification;
- wave modulation in phase - three-dimensional effect emergency;
- generation of the longitudinal rows of Λ-shaped vortices;
- arrangement of the longitudinal vortex system;
- transformation of votices in form and intensity, indulation of vortices;
- breakdown of peripherical parts of undulating vortices;

generation of turbulent spots, their growth confluence and turbulent boundary layer development.

At present there are two concepts explaining the successive development of the transition process:

- it is defined by modes development and interaction in a boundary layer;
- it is defined by the vortex filaments behaviour.

Both concepts are reasonable - the conditions and mechanism of their interaction are discussed in detail in my book.

Small particle of liquid contains double information concerning its movement:

- as the vibrating element it is characterized by frequency-wave and other parameters;
- as the moving element it is characterized by vorticity, i.e. by the trajectory of its movement.

In any case it is necessary also to analyse the structure of disturbances: for example, the form of linear and nonlinear waves, the form and direction of vortices and, besides, the disturbing motion intensity.

FORMATION OF THREE-DIMENSION DISTURBANCES IN A BOUNDARY LAYER OF FLAT PLATES WITH VARIOUS PROPERTIES

According to results shown in [2], it is obvious, that the allocated way of longitudinal vortical systems formation in a boundary layer (BL) will be effective at concurrence of sizes and intensity of generated and natural disturbances. The longitudinal wire and the stripes covering them still created additional roughness in [2], and to some extent, their influence on BL was similar to action of riblets.

It is expediently to increase intensity of influence of these stripes on the BL, not increasing at that their hydraulic roughness. Results of numerous experience with riblets of the various form are widely known. Two other ways, different from riblet, raising intensity of influence on the BL are offered below.

One of them consists in weak heating of longitudinal wires. The other one consists in using of a composite elastic plate, an outside layer of which made in form of longitudinal alternating strips with the various modules of elasticity.

Before estimation of a boundary layer reaction on periodic on z structure of plates, influence to a flow of a similar plate 10 made from the similar material as outside layers of plates 7 was investigated with the help of visualization. The simultaneous visualization of three jets in a plane xz has shown extremely stable it's behavior along the whole plate. The jets parallelism of a streamline surface was not practically broken even at passage them through a lattice of vortex generators Bl (d). A small jets closing among themselves is visible in a plane xz on x=0,4 m, that is displayed irrespective of presence or absence of vortex generators.

The visualization of natural distribution of U(z) has also reflected the specific character of disturbances development. If a undulation of a structure U(z) is fully displayed on a rigid surface at $Re \approx 1 \cdot 10^5$, here it is poorly planned only at distance from a wall. The maximum bend of a tellurium cloud is observed at $y=0{,}01$ m $\approx \delta/2$; the further influence of a wall becomes weaker together with reduction of intensity of a disturbing movement. It is necessary to note small speeds of three-dimension disturbances

increasing, that is expressed in an extremely weak stretching of tellurium clouds at moving them downwards on a flow. The opposite effect was observed at a flow over the membrane surface not having a damping properties. The reduction of speeds of flat disturbances increasing in a boundary layer of damping surfaces [2] was found out at research of linear stability.

It is possible to conclude from here, that the elastic surfaces with large factor of damping interfere with the fast changes of the kinematics characteristics of a flow bypassed them. This effect is similar to one found out at a rigid ribbed surface allocated influence on a boundary layer.

The similar results are received for a plate 7, a with a cross regularity of properties: the dark longitudinal strips correspond to edges of rigidity of about $2 \cdot 10^{-4}$ m height on fig. 4 (d-h). The first three photos (a-c) characterize a field of current before an elastic insert ($Re=1,1 \cdot 10^5$), the other - over it ($Re=1,4 \cdot 10^5$). It is visible, that even at greater Reynolds number the distortion of a current fields less over the insert. At the tellurium cloud movement in direct affinity from a plate a small-scale toothed is not displayed in it, that was observed at visualization in a case of a rigid ribbed surface. Apparently, the distinction in mechanical properties of longitudinal strips in aggregate with microroughness or ribbing of a surface appears the insufficient reason for creation of vortical system type disturbances in a boundary layer at the specified values of Re and λ_z.

At the analysis of received results it is necessary to mean the fact concerning to specificity of measurements. Oscillatory movements in a plane of xz characteristic for a stage of nonlinear disturbances development, result in fact that the statistically average parameters are registered in vertical planes of structures u'(y) and U(y) measurement. The visualization of U(z) frequently shows the wavy lines displacement on z with compelled length of a wave. At accepted geometry of ribbed plates with rather narrow longitudinal paths, the change of kinematics parameters over them can be fixed both by strengthening of distinction between properties of strips, or, probably, by increasing their width.

In this connection the heating of rigid edges of a plate 7, a was undertaken with the help of an electrical current. It is necessary to note, that the rubbery materials in the best way correspond to the purpose of experiment owing to their high heat-insulating qualities: the preservation of a positive difference of temperatures between edges and elastomer will create the regular on z change of kinematics parameters of a boundary layer, connected to occurrence of convection flows along edges (change of δ, u', U, speeds values of distribution and increase of disturbances). Besides, it was specified, that the absorbing ability of soft rubbers decreases with growth of temperature, that should also stimulate formation of three-dimensional disturbances with set parameters. However, at a movement of a tellurium cloud over a plate, peculiarities of current are accumulated in it and a waviness with $\lambda_z=0,012$ m is displayed at absence of fluctuations or it's moving on z. The influence of an elastic plate is expressed above usually in an alignment of a structure U(z). The further heating forms such powerful field of disturbances that there is the erosion of clouds in irregular longitudinal bunches at once behind a tellurium wire.

Thus, experiments have shown the longitudinal reinforcement of a streamline surface with a small step $\lambda_z<\delta$ reduces non-uniformity of kinematics parameters of a boundary layer in трансверсальном direction at the expense of primary orientation of a disturbances field lengthways x. It follows from increase of u' in aggregate with results of current on z visualization: the absence of a small-scale regularity of tellurium lines speaks about reduction of v', that is naturally caused by damping properties of a streamline surface; the termination of an oscillatory movement on z - about reduction of w'. Heating of reinforced elements creates conditions for formation and maintenance of longitudinal vorteces system, which, however, differs from smaller intensity similar to one on a rigid surface: the compelled periodicity on z of a tellurium line is displayed at moving it downwards a flow, at least, on twice greater distance than on a rigid ribbed surface.

Further on it is necessary to continue study of proposed mechanism of influence the coherent vortical structures.

REFERENCES

1. Babenko V. V. "On interection of flow with elastic surface," Mechanisms of turbulent flow, Moskow: Nauka. 1980, p. 292-301.
2. Babenko V. V., Kanarsky M. V., Korobov V.V. "Boundary layer on elastic plates," Kiev, Naukova dumka, 1993 - 264 p.
3. Wortmann F. X. Eine Methode zur Beobachtung und Messung von Wasserstromung mit Tellur. -Z. Fur Angew. Phys., 1953, 5, №6, -s. 200-206.

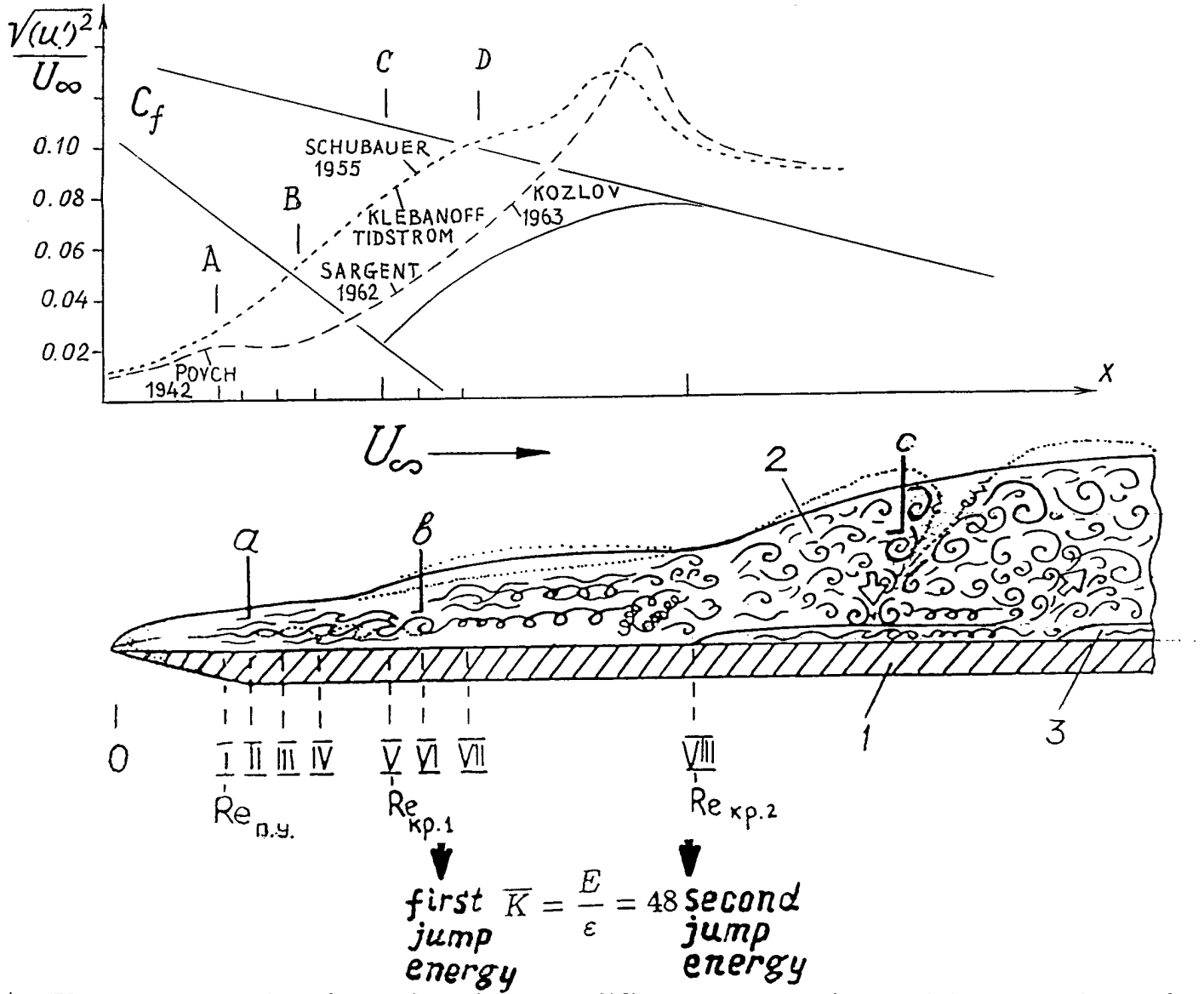

Fig. 1. Flow structure in a boundary layer at different stages of transition: 1 - alongwise flowed flat plate; 2 - boundary layer; 3 - viscous sublayer; - VIII - stages of transition; a,b,c, -places of sensors location.

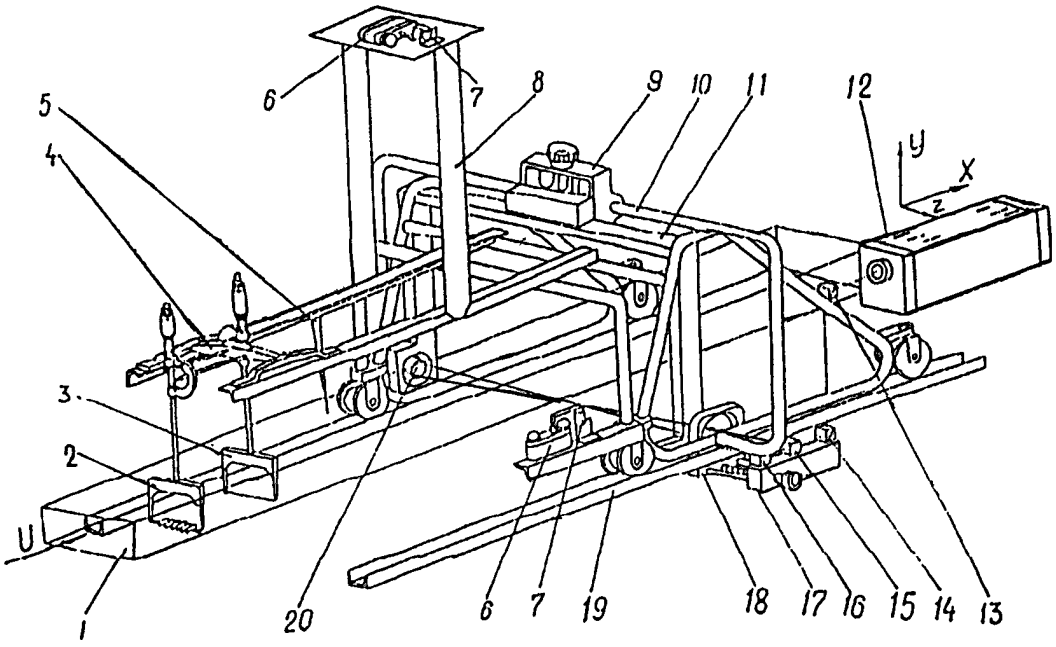

Figure 2. The sketch of the hydrodynamic channel test section with devices

1 - the test section; 2 - vortex generators; 3,4 - tellurium wire with a holder, 5 - anode (visualization system), 6,7 - photoregistration system, 8-11 - moving truck with devices, 12-19 - system of laser anemometry.

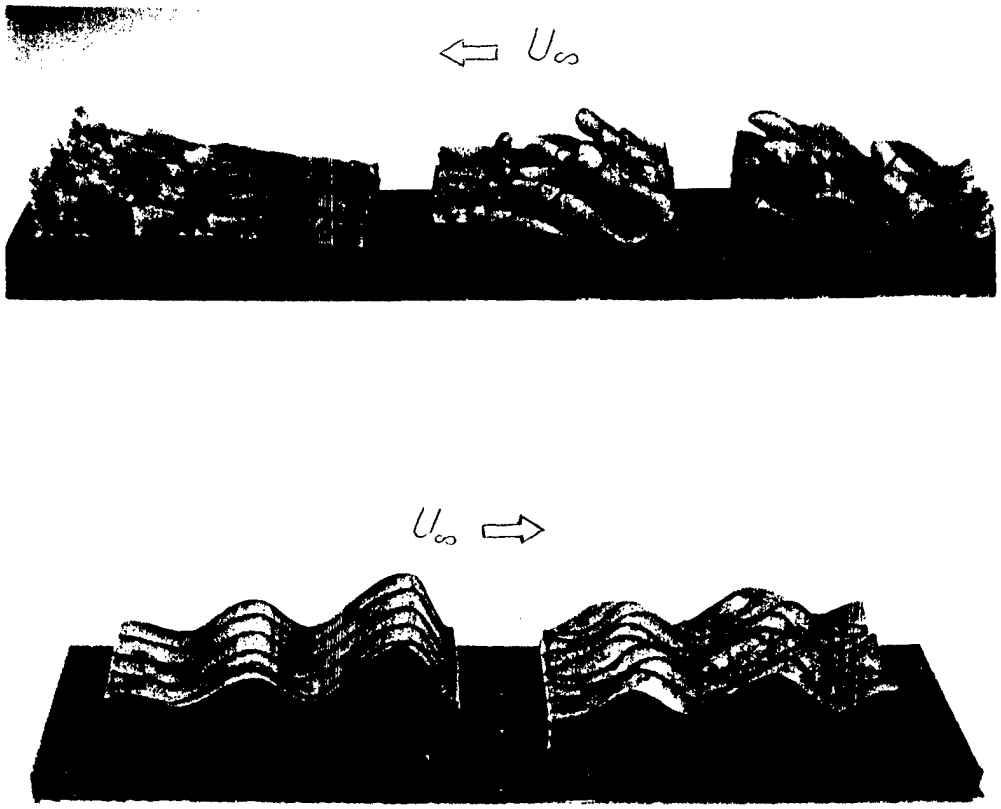

Fig. 3 The physical model of the disturbances type successive transformation during the transition to turbulence: a — amplification of plane disturbances; b — phase modulation of the wave, three-dimensional effects appearance; c — amplitude modulation of the wave, "peaks" and "valleys" forming; formation of longitudinal rows of Λ — shaped vortices; d — organization of the longitudinal vorteces system, e — vorteces form and intensity changes in space and time; transition to a zigzag trajectory of the vorteces movement; breakdown of peripherical parts of the meandering vortices. Active formation of turbulent spots, their growth, amalgamation and turbulent boundary layer development.

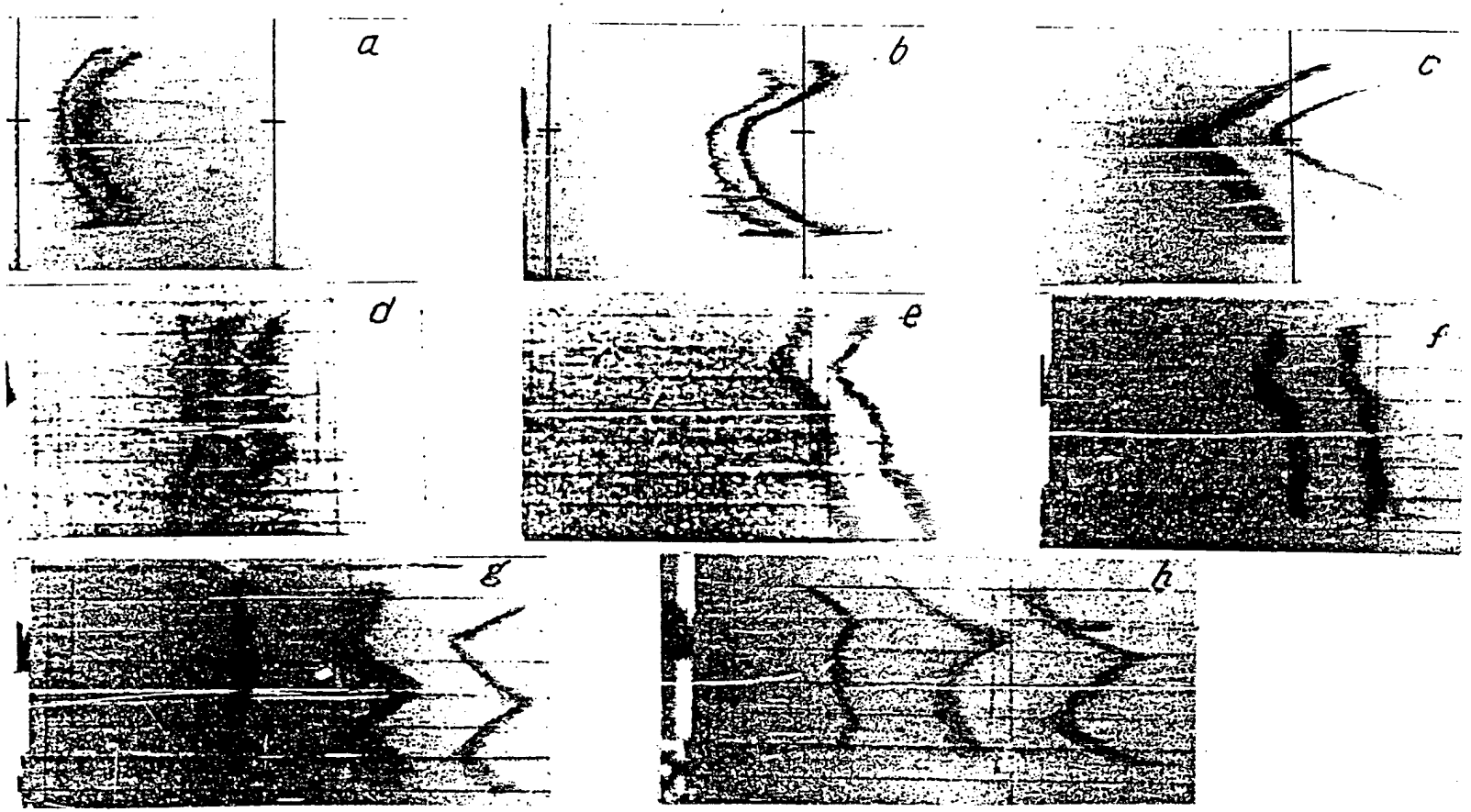

Fig. 4. Visualization of U(z) at U_∞=0.05 m/s before a plate 7a: x=1.6 m; y=0.002 m (a), 0.004 m (b), 0.008 m (c); and over it: x=2.18 m; y=0.002 m (d), 0.004 m (e), 0.006 m (f), 0.008 m (g), 0.01 m (h).

DRAG REDUCTION WITH SUBMERGED RIBS AND ITS MECHANISM IN A TURBULENT BOUNDARY LAYER OVER D-TYPE ROUGHNESS

Shinsuke MOCHIZUKI and Hideo OSAKA
Faculty of Engineering, Yamaguchi University
Tokiwadai 2557, Ube 755-8611, Japan
shinsuke@po.cc.yamaguchi-u.ac.jp

A turbulence management device, submerged ribs inside transverse grooves, for a d-type rough wall is proposed based on observations of coherent motions, and tested experimentally in a turbulent boundary layer under zero pressure gradient. The skin friction measurements with a direct drag balance clearly show that the present device is effective with a maximum drag reduction rate of 10% of the original d-type roughness. Moreover, the present method provides for even less skin friction over a rough wall with a maximum reduction rate of just 3% compared with smooth surface. The turbulent intensities and Reynolds shear stress measurements prove that the submerged ribs suppress the turbulent production and dissipation process, and our proposed model for momentum exchange near the rough wall is reasonable. A conditional averaged analysis shows that strength of ejection associated with a pair of streamwise vortices is reduced and as is bursting frequency by the submerged ribs in a drag reduction case.

1. INTRODUCTION

Management of fluid flows, governed by the nonlinear partial differential equation, is a major subject in fluids engineering, and for wall turbulence we have seen remarkable advancement in drag reduction techniques [1]. New ideas classified as active methods, which need a certain amount of extra energy, such as spanwise wall oscillation and selective suction programmed by sophisticated control schemes have been proposed and tested in DNS and experimental studies [2]. Furthermore, by a number of tests involving practical aircraft flight the array of micro streamwise grooves or "riblets" were shown to substantially reduce of the skin friction by 8-10% [3,4].

Experimental and numerical approaches to elucidating the mechanisms of the drag reduction phenomenon over riblets over the last decade [5,6] have been unable to establish a consensus as to the sense of the dynamics of turbulence. Since the early days of research into the turbulence field over riblets, coherent structures such as bursting phenomenon, streamwise vortical structure, and hairpin eddy have been investigated based on flow structures of dynamical significance which often depend on the investigator. There are two major problems preventing agreement on the mechanisms: (1) in most of the experiments the wall shear stress was determined with indirect methods assuming similarity in mean quantities or estimated from results provided by other studies, (2) up to now kinematics of coherent structure has been viewed as relatively easy to perform and described in detail [7], whereas dynamics of the quasi-periodic three-dimensional vortical motions can be hardly discussed with well-defined mathematical expressions.

By regarding riblets as a kind of roughness, one may conclude that roughness can alter the structure in the wall layer and reduce drag. In fact, by recalculating Nikuradse's pipe flow data, Tani [8] pointed out that with sand grain roughness submerged in the viscous sublayer, skin friction becomes smaller compared with that of a smooth wall pipe. Recently, management with wall protrusions chosen to excite the appropriate propagating mode for the sublayer waves was led by numerical simulations, and in an experimental test in a two-dimensional turbulent channel flow, random array of the protrusions achieved about 10% drag reduction [9]. That three-dimensional roughness gives less skin friction compared with smooth surface, has practical applications in engineering, and requires that alternative formulations be made to represent the roughness effect on the mean velocity profile for small values of roughness Reynolds number.

In the present study, based on experimental observations on coherent structure, we propose a drag reduction control device submerged into transverse grooves of d-type roughness, and test its effectiveness by direct drag balance measurement in a zero-pressure gradient turbulent boundary layer. Then, we investigate the turbulent structure altered by the wall modification using conventional time averages and a conditional sampling analysis.

2.EXPERIMENTAL APPRATUS AND TECHNIQUES

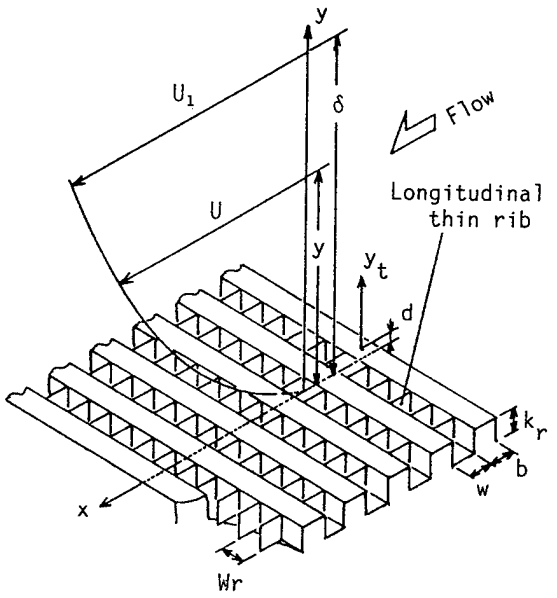

Figure 1: Schematic of flow field, nomenclature and coordinate system.

2.1 Experimental Set-up and Measurement

Experiments were performed in a low turbulence wind tunnel 0.5m wide, 0.3m high, and 4m long in Yamaguchi University. Free stream turbulence was kept below 0.3% and static pressure in the free stream was adjusted to be constant along the wind tunnel (pressure coefficient C_p was within 0.5%). Figure 1 shows overall flow field, nomenclature and the coordinate system. A d-type rough wall is of a two-dimensional roughness which consists of rectangular bars closely arrayed with the same streamwise space as the element width, namely, the pitch ratio $(b+w)/k_r$ of 2. The roughness height k_r, element width b, and groove width w are all 3mm and the rough wall was made by machining transverse grooves out on a 18mm-thickness bakelite plate.

The wall shear stress was measured with a direct drag balance which provides an excellent skin friction data set for a smooth wall turbulent boundary layer under zero pressure gradient [10]. The floating element of the balance has a 60mm diameter surface containing 10 pitches of a roughness element. Velocity measurement was carried out with constant temperature anemometers and single and crossed hot-wire probes. A 5 μm diameter and 1mm length tungsten filament was employed as a sensor and a pair of filaments were welded on prongs of the crossed hot-wire probe with 0.5mm separation at about a 90° cross angle. The velocity signal from the anemometers was recorded on optical disks as sets of digital data by a 12 bit AD converter and a PC, and then mean velocity and Reynolds stresses were obtained by taking the average of 100,000 data sampled at a rate chosen for the frequency band of the fluctuating velocity signals (typically, 10kHz at the highest Reynolds number, and 4kHz at the lowest).

2.2 Drag Reduction Device Proposed by Observations of the Coherent Eddy

A cross-stream view of a model for momentum exchange between a boundary layer and a groove is sketched in Fig.2 with arrangement of submerged thin ribs to prevent the induced spanwise fluid movement. By using the conditional sampling technique [11], a pair of streamwise vortices, often referred to as a typical coherent eddy in the near wall region over a smooth surface, can be detected over d-type roughness on which a so-called quasi-smooth flow is established. A pair of streamwise vortices, probably being two legs of a hairpin vortex, associated with the bursting phenomenon play a significant role in turbulence production as well as momentum transport in the wall layer. Therefore, the strength of the streamwise vortices is supposed to be proportional to the amount of turbulence production during a busting. Over d-type roughness, plausibly, flow induced inside the grooves makes the bursting stronger with the aid of low momentum fluid pumped out of the grooves. By preventing induced spanwise momentum transport inside the grooves with the submerged longitudinal thin ribs, the strength of the vortices is reduced and the turbulence production and dissipation rate decrease. The spanwise spacing of arrangement of thin ribs should be of the same order of magnitude of the spanwise scale of the streamwise vortices, λ_z , which is usually characterized with the viscous wall unit ($\lambda_z^+ \approx 100$). The spanwise spacing W_r was chosen to be 3mm corresponding to a rib Reynolds number W_r^+ ($\equiv W_r u_\tau/\nu$) in the range 35-150 in the present experiment. Experimental uncertainties in the present measurement procedure are given in Table 1.

Table 1 Experimental uncertainties

	U	$\overline{u^2}$	$\overline{v^2}$	$\overline{w^2}$	$\overline{uv}$	C_f
Uncertainty (%)	1.5	1.7	11	9.5	5.0	5.0

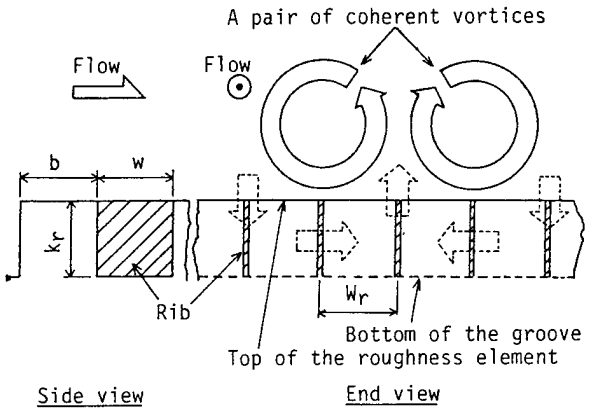

Figure 2: A model for momentum exchange over a d-type rough wall and turbulence control with the submerged ribs inside transverse grooves.

3. RESULTS AND DISCUSSION

3.1 Skin-Friction Measurement

The local skin friction coefficient C_f is plotted as a function of the Reynolds number based on momentum thickness $R_\theta \equiv U_1\theta/\nu$ in Fig.3. The solid line represents Kármán-Schoenherr's semi-empirical formula for a zero pressure gradient, smooth wall, turbulent boundary layer. Over a transitionally rough Reynolds number range, R_θ<2000 [12], evidently the skin friction coefficient is reduced by the ribs submerged into the grooves. Moreover, note that for R_θ=750-1200, the coefficient lies below the curve for a smooth wall boundary layer, indicating a realization of smaller wall friction over non-smooth surface. As the Reynolds number decreases, at around R_θ=800, the skin friction coefficient C_f of the d-type rough wall flows coincides with the corresponding value predicted by the semi-empirical formula for smooth wall surface. Whereas, as $R_\theta \to \infty$ the ribs cease to reduce the skin friction and drag increases caused by roughness for R_θ>2000. Over such a high Reynolds number range, the spanwise spacing W_r is too

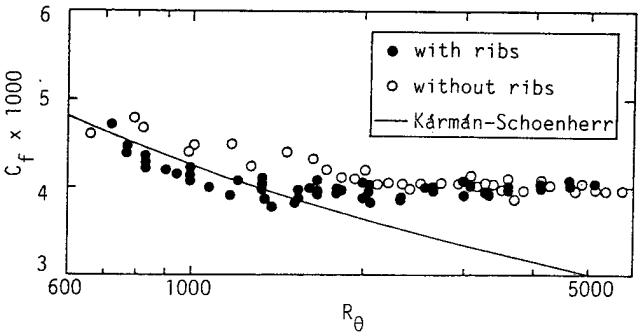

Figure 3: Local skin friction coefficient obtained by direct drag balance measurement.

large to manage the streamwise coherent vortices: for example, the rib Reynolds number W_r^+ is 150 at R_θ=5000.

The drag reduction rates are defined as

$$\Delta C_{fd} = (C_{fR} - C_{fd}) / C_{fd} \times 100 \quad (\%),$$
$$\Delta C_{fs} = (C_{fR} - C_{fs}) / C_{fs} \times 100 \quad (\%), \qquad (1)$$

for the original d-type roughness and the smooth surface, respectively, and are plotted against the relevant Reynolds numbers in Figs.4, 5 and 6. Here, C_{fR}, C_{fd}, and C_{fs} are the local skin friction coefficients of the managed and the original d-type roughness and the smooth surface. The dotted area covers uncertainties of the ratio mostly due to data scattering in skin friction measurement. Figure 5 contains results for the same value of the rib Reynolds number W_r^+, which is the most relevant parameter to describe the present management, but at two different streamwise locations, that is, under different bulk Reynolds numbers. In Fig.4 the maximum reduction rate reaches about 10% at around R_θ=1000, and the skin friction is reduced over a wide Reynolds number range, R_θ=750-5000. In Fig.5 where the reduction rate is plotted against the rib Reynolds number W_r^+, drag reduction is achieved for approximately W_r^+<100; this evidently shows our model for momentum exchange to be reasonable. However, the reduction rate depends on the bulk Reynolds number, because the turbulent boundary layer is in a transitionally rough regime for R_θ<2000. Figure 6 confirms less skin friction; the maximum reduction rate ΔC_{fs} is 3% over the d-type roughness modified with submerged ribs compared with the smooth surface.

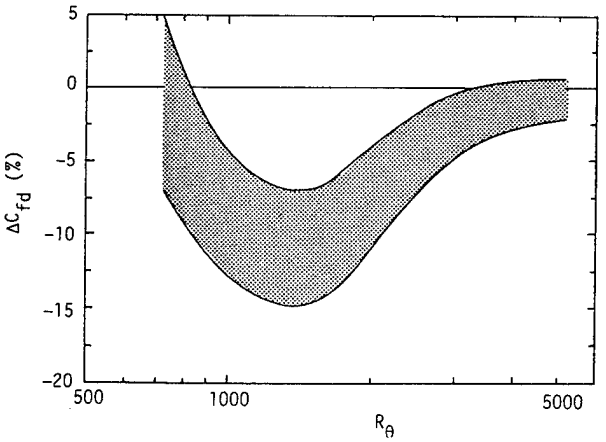

Figure 4: Reduction rate in local skin friction coefficient compared with the original d-type roughness.

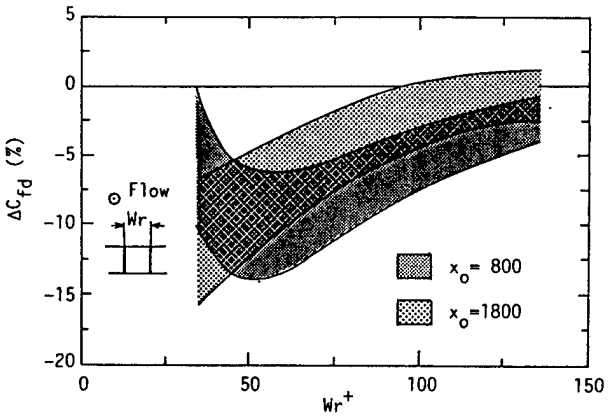

Figure 5: Reduction rate in local skin friction coefficient compared with the original d-type roughness as a function of rib Reynolds number.

3.2 Mean Velocity and Reynolds Stresses

Figure 7 shows logarithmic mean velocity profiles which were measured over a groove and mid-span of two ribs at 225mm downstream corresponding to 2000 viscous wall length units of the beginning of the wall modification. The virtual origin of the transverse coordinate $y = y_l + \varepsilon$ in the velocity plot is placed at a downward location shifted from the top of the surface by error in origin ε, which is properly determined with the friction velocity obtained in the direct drag balance measurement by assuming the similarity of velocity profile is valid. The solid lines represent the standard log law for a smooth wall turbulent boundary layer given at the Stanford Conference in 1968. The logarithmic profile in mean velocity distribution in the wall layer is fairly reasonable even over the modified d-type rough surface, if the virtual origin is properly considered. At R_θ=750 and 1210 where the

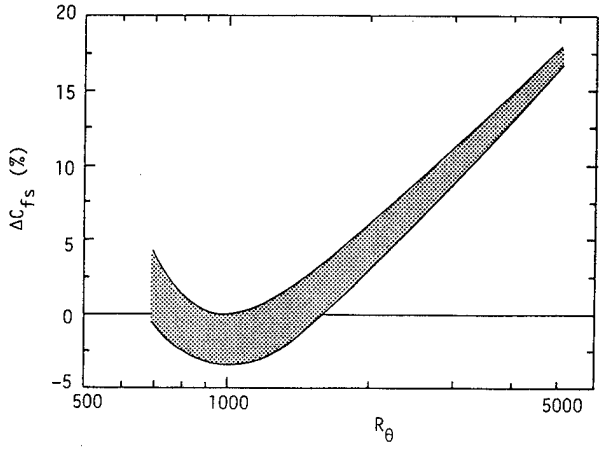

Figure 6: Reduction rate in local skin friction coefficient compared with the smooth wall turbulent boundary layer under zero-pressure-gradient.

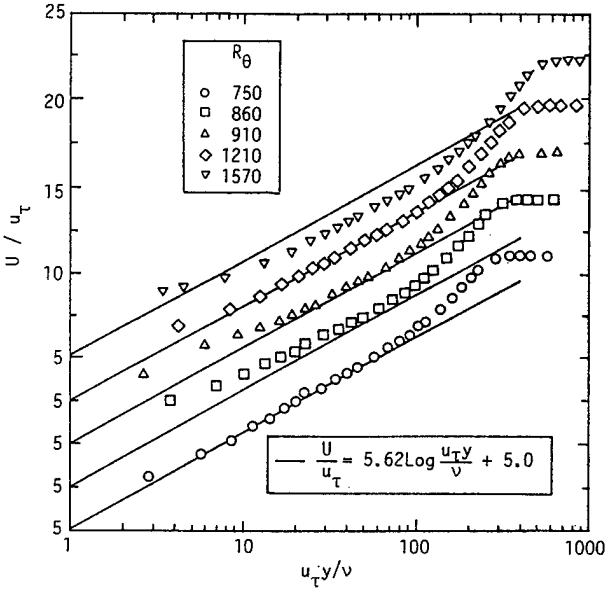

Figure 7: Logarithmic velocity profile in the flow field altered by the submerged ribs.

smooth and the modified d-type rough wall flows take the same value of the skin friction coefficient, the velocity data both of the modified and the original d-type roughness lie on the standard log law for smooth surface. Whereas, at R_θ=860 and 910 where the skin friction coefficient takes a smaller value compared with smooth surface, the logarithmic velocity profiles are slightly shifted upward, as often observed in drag reduction over riblets [5]. Otherwise, at R_θ=1570 where the drag increases due to roughness (see Fig.3), the logarithmic profile is shifted downward by the roughness function which is normally a positive value.

The roughness function $\Delta U/u_\tau$, ordinarily indicating drag increase over rough surfaces, is plotted against the Reynolds number based on error in origin ε, which is the representative length scale for d-type roughness. By assuming the *Kármán* constant κ in the logarithmic profile to be 0.41, the roughness function was measured as a downward shifting value from the standard log law. The results in a transitionally rough regime $u_\tau\varepsilon/\nu$ <5 significantly deviate from the empirical formula for a fully rough Reynolds number range $u_\tau\varepsilon/\nu$>5. Interestingly, in the case of drag reduction by the submerged ribs, the roughness function and the Reynolds number $u_\tau\varepsilon/\nu$ take negative values simultaneously. When requiring a continuous representation going through the origin for dependence of the roughness function on the Reynolds number from drag increase through drag reduction, we need an alternative form, for example, a simple linear function.

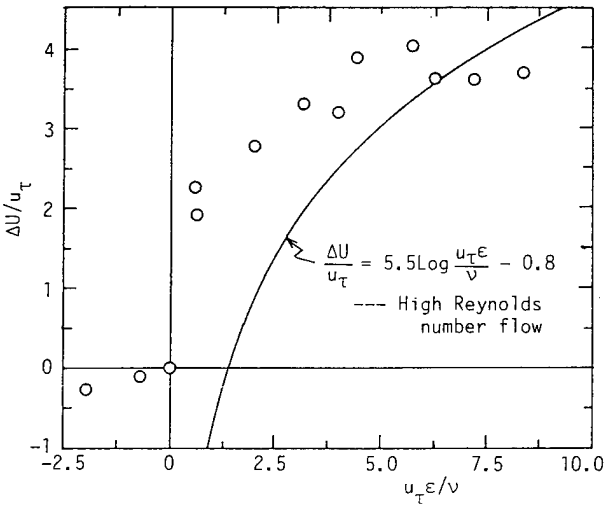

Figure 8: Roughness function plotted against the Reynolds number based on the error in origin.

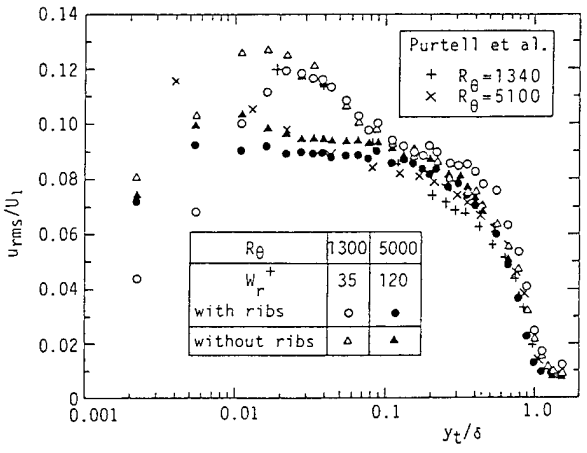

Figure 9: Turbulent intensity profiles of streamwise fluctuating velocity component.

Turbulent intensities, u_{rms}, v_{rms}, and w_{rms}, and Reynolds shear stress profiles are given in Figs.8, 9, 10, and 11, respectively. To see the influence of the ribs on the activity of the energy-containing turbulent eddies, these profiles are normalized with the outer scales, boundary layer thickness δ and the free stream velocity U_1. Here, we shall look at typical two results for a drag reduction case at R_θ=1300 corresponding to W_r^+=35 and for a no drag reduction case at R_θ=5000 corresponding to W_r^+=120. Evidently, the streamwise turbulent intensity u_{rms}/U_1 is reduced in the wall layer in the drag reduction case at R_θ=1300, and the maximum reduction rate is about 45%, although all the flows over the d-type rough wall and the smooth wall [13] take the maximum value of u_{rms}/U_1 at the same distance from the wall y^+ ($\equiv yu_\tau/\nu$) $\approx$ 15. Otherwise, at around the edge of the inner layer y_t/δ=0.2, the turbulent intensity is slightly enlarged by the turbulence management. This suggests that the influence of the wall modification spreads into the outer layer and alters the amount of momentum or energy entrainment from the free stream. In spite of no reduction in the skin friction coefficient at R_θ=5000, the turbulent intensity is slightly reduced by the wall modification. When comparing the present profiles to those of the smooth wall flow at R_θ=1300, the turbulent intensity takes larger values throughout the outer layer both over the modified and the original d-type rough surfaces.

In the v_{rms}/U_1 profiles (Fig.8), this turbulent intensity component is reduced by 12% in the modified d-type rough wall flow. A much larger reduction in this component was observed in drag reduction phenomenon by polymer adding turbulent flow (Tom's effect) [14]. Probably, the injected polymer solution filled into a whole flow field directly alters the large scale energy containing eddies, on the other hand, the submerged ribs in the present method indirectly influence the large scale eddies through the turbulence production and diffusion process. This difference in mechanisms of turbulence management appears in the reduction rate for the transverse turbulent intensity component. In the profiles of the w_{rms}/U_1 component (Fig.10), the magnitude of the turbulent intensity is slightly reduced in the wall layer at R_θ=1300. In Fig.11, obviously the Reynolds shear stress is reduced by approximately 25% in the drag reduction case at R_θ=1300. It follows that the ribs submerged into transverse grooves suppress

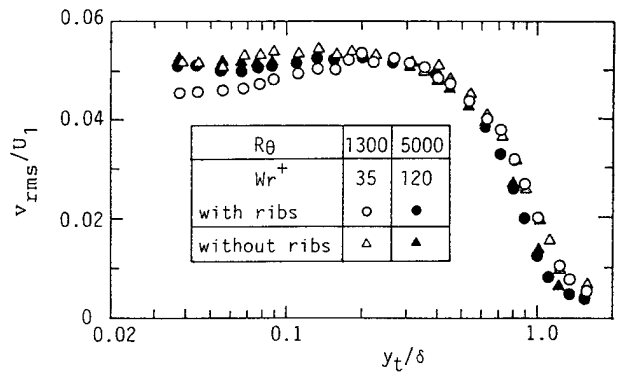

Figure 10: Turbulent intensity profiles of the fluctuating velocity component normal to the wall.

momentum transport near the rough wall. However, the constant stress layer [15], in which turbulence scales with the friction velocity and the assumption of logarithmic velocity profile are supported, can be reasonably recognized in the wall layer even when the ribs alter the structure of the turbulence near the wall.

3.3 Conditional Analysis

Using a conditional sampling analysis we next investigated the coherent structure which is a basis for proposing the present turbulence management technique. Here, the VITA technique [16] was employed to detect bursting events producing most of the turbulent energy near the wall. When the turbulent kinetic energy averaged over a certain time interval T exceeds the threshold level, it is considered that the energetic turbulence producing process has taken place. A preliminary experiment gives the best parameter to specify the detection scheme: averaging time interval T was adjusted to be 20 times the viscous wall time scale ν/u_τ^2 and threshold level is 0.8 times the local streamwise turbulent energy $\overline{u^2}$ obtained from conventional time averaging.

Figure 12 shows ensemble averaged signals of, $\tilde{u}, \tilde{v}$, and $\widetilde{uv}$ components obtained at $y^+(\equiv yu_\tau/\nu)$=17 in the drag reduction case of R_θ=1300. The averaged signals are calculated from about 300 samples selected with an additional condition of acceleration at detection time t=0. In cases of both modified and original d-type roughness, we can see typical patterns of bursting; the ejection of low momentum fluid ($\tilde{u}<0$ and $\tilde{v}>0$) followed by a high speed sweep ($\tilde{u}>0$ and $\tilde{v}<0$), in the ensemble averaged signals. However, the strength (peak value) of the ejection becomes smaller in the drag reduction case. Whereas, in the sweep process no influence can be seen in the ensemble averaged signals. These results reveal that as we expected when designing the present management device, momentum transport induced by a pair of streamwise vortices associated with the submerged ribs inside the transverse grooves suppress the ejection process. Figure 13 shows the results in the case where the submerged ribs have no influence on alternation of skin friction coefficient at R_θ=5000 corresponding to W_r^+=150. In this case, we also find suppression of the peaks in the ejection process, therefore, the submerged ribs apparently manage momentum transport in the ejection process. Low-Reynolds-number effect on the turbulent structure near the d-type rough wall was reported [17]; dominant motions for turbulent transport near the d-type rough wall are ejection at a transitionally rough Reynolds number (R_θ<2000), but are replaced by sweeps at a fully rough Reynolds number (R_θ>2000). The sweep process is supposed to be closely associated with large-scale vortical motion scaling with the boundary layer thickness, and the submerged ribs with spanwise spacing of the order of intermediate length scale of turbulence, $\approx 100\nu/u_\tau$ can not alter such large scale eddies.

We should describe bursting frequency that is another parameter indicating activity of turbulence production. In the drag reduction case at R_θ=1300, the normalized bursting frequency $f_b\delta/U_1$ is reduced from 0.136 to 0.117 (by 14%) under management with the submerged ribs. Otherwise, at R_θ=5000 the normalized frequency $f_b\delta/U_1$ is increased from 0.097 to 0.120 (by 24%) due to the wall modification. In spite of reduction in the strength of each event corresponding to the ejection process, increase of bursting frequency results in the skin friction coefficient remaining at the same value over the modified d-type rough wall at R_θ=5000.

4. CONCLUSIONS

It is clear that the management device, submerged ribs into the transverse grooves with suitable spanwise spacing, is effective for reducing the drag of d-type rough wall boundary layer over a certain Reynolds number range. At the optimal Reynolds numbers, the skin friction coefficient is reduced by 10% compared to the original d-type roughness. We should note that with the present device, even less skin friction, a 3% drag reduction rate compared with smooth surface, is possible. The turbulent intensity and Reynolds shear stress measurements reveal that the submerged ribs suppress the turbulent production and dissipation rate near the rough wall. These experimental results prove that the proposed model for momentum exchange based on observations of coherent motions near the roughness is suitable.

Based on the mean velocity analysis with the direct drag balance measurement of the wall shear stress, a logarithmic profile with a standard value of *Kármán* constant κ=0.41 can be assumed even when

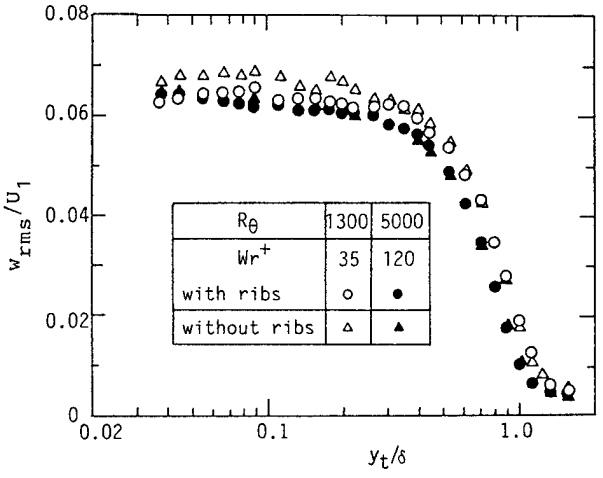

Figure 11: Turbulent intensity profiles of the spanwise fluctuating velocity component.

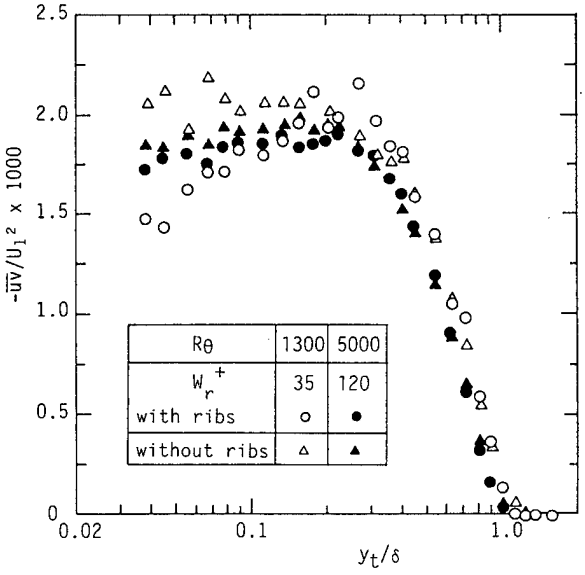

Figure 12: Reynolds shear stress profiles.

the submerged ribs alter the turbulent structure in the wall layer over d-type roughness. In the drag reduction case the logarithmic profile is shifted downward of the log law for smooth surface, and the roughness function and the representative Reynolds number based on the error in the origin take negative values simultaneously.

In conditional sampling analysis-giving evidence of direct influence of the present management system on ensemble averages associated with coherent motions, it is seen that the submerged ribs suppress the ejection process during a bursting both in drag reduction and in no drag reduction cases. The normalized bursting frequency $f_b\delta/U_1$ is reduced by 14% in a drag reduction case at R_θ=1300, but increased by 24% in a no drag reduction case at R_θ=5000.

AKNOWLEGEMENTS

The authors acknowledge the financial support given by the Assistance of the Mazda Foundation for Research in Science and Technology.

REFERENCES

1. M.Gad-el-Hak,"Flow control",*Appl.Mech.Rev.*,Vol.42,261-293, 1989.
2. M.Gad-el-Hak, "Modern developments in flow control", *Appl.Mech.Rev.*, Vol.49, 365-379, 1996.
3. M.J.Walsh, "Riblets", *Viscous drag reduction boundary layers*, (Eds. D.M.Bushnell and J.N.Heffner), Progress in Astronautics and Aeronautics, Vol.123, 203-254, 1990.
4. M.J.Walsh, "Turbulent boundary layer drag reduction using riblets", *AIAA Paper* 82-0169, 1982.
5. K.-S.Choi, "Near-wall structure of a turbulent boundary layer with riblets", *J.Fluid Mech.*, Vol.213, 419-442, 1989.
6. H.Choi, P.Moin and J.Kim, "Direct numerical simulation of turbulent flow over riblets", *J.Fluid Mech.*, Vol.255, 503-53, 1993.
7. S.K.Robinson, "Coherent motions in the turbulent boundary layer", *Annu. Rev. Fluid Mech.*, Vol.23, 601-639, 1991.
8. I.Tani, "Drag reduction by riblet viewed as roughness problem", *Proc. Japan Acad.*, B64, 21-24, 1988.
9. L.Sirovich and S.Karlsson, "Turbulent drag reduction by passive mechanisms", *Nature*, Vol.388, 753-755, 1997.
10. H.Osaka, T.Kameda, and S.Mochizuki, "Re-examination of the Reynolds-number-effect on the mean flow quantities in a smooth wall turbulent boundary layer", *JSME Int.J., Ser.B*, Vol.41, No.1, 123-129, 1998.
11. H.Osaka and S.Mochizuki, "Streamwise vortical structure associated with the bursting phenomenon in a d-type rough wall boundary layer at a low Reynolds number", *Proc.the 6th Symposium on Turbulent Shear Flows*, Toulouse, 16.7.1-16.7.6, 1987.
12. H.Osaka and S.Mochizuki, "Turbulent structure of a d-type rough wall boundary layer in a transitionally rough regime", *Proc. the 1st KSME-JSME Thermal and Fluids Conference*, Seoul, 2.88-2.93, 1988.
13. L.P.Purtell, P.S.Klebanoff and F.T.Buckley, "Turbulent boundary layer at low Reynolds number", *Phys.Fluids*, Vol.24, 802-811, 1971.
14. H.Usui and Y.Sano, "Effect of injected polymer thread on turbulence in a pipe flow", *Transport Phenomena in Turbulent Flow* (Eds. M.Hirata and N.Kasagi), 299-309, Hemisphere, 1988.
15. A.A.Townsend, "The structure of turbulent shear flow", *Cambridge university press*, 1976.
16. R.F.Blackwelder and R.E.Kaplan, "On the structure of the turbulent boundary layer", *J.Fluid Mech.*, Vol.76, 89-112, 1984.
17. H.Osaka and S.Mochizuki, "Statistical quantities of a d-type rough wall boundary layer in a transitionally rough regime", *Proc. the 2nd KSME-JSME Fluids Engineering Conference*, Seoul, Vol.2, 202-207, 1990.

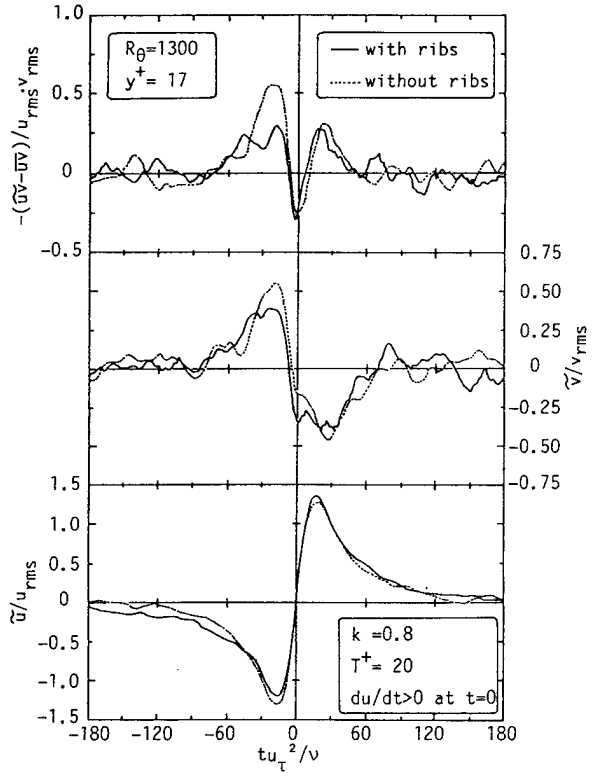

(a) R_θ=1300 (W_r^+=35)

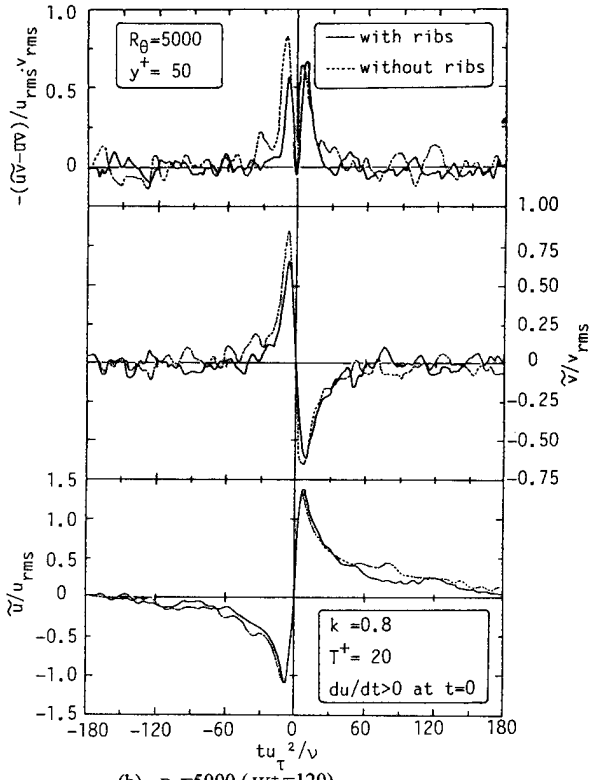

(b) R_θ=5000 (W_r^+=120)

Figure 13: Ensemble averaged signals in the VITA analysis.

A NEW APPROACH TO DRAG REDUCTION

Aline J. Cotel
Department of Mechanical Engineering
University of Manitoba
Winnipeg, MB, CA R3T 5V6
acotel@mail.cc.umanitoba.ca

Robert E. Breidenthal
Department of Aeronautics and Astronautics
University of Washington
Seattle, WA 98195-2400
breident@aa.washington.edu

Abstract - A novel method is proposed for the reduction of turbulent skin friction. It is based on a recent model of vortex persistence on surface fluxes in stratified flows. When a vortex is near an interface, such as a solid wall, the fluxes of mass, momentum, and energy at the wall depend on the stationarity, or persistence, of the vortex with respect to the wall. For a stationary vortex, the theory predicts that the surface fluxes will be independent of the small scale turbulence. If streamwise vortices are introduced into a turbulent boundary layer, the theory implies that the skin friction can be dramatically reduced, provided that the streamwise vortices can be held sufficiently stationary. Any net drag reduction also requires that the energy invested in the streamwise vortices is largely recovered at the trailing edge.

I. INTRODUCTION

Conventional approaches to reducing skin friction usually involve reducing the velocity gradient at the surface, such as by displacing the vorticity through electromagnetic torques or by the inhibition of transition to turbulence. Riblets are a notable exception, where surface grooves are intentionally introduced.

A new approach for the potential reduction of skin friction has been deduced from observations on stratified entrainment. Before applying the concept to skin friction, it is instructive to consider the physics of stratified entrainment.

In experiments on entrainment across a thin, stratified interface subjected to impinging turbulence, it was found that the entrainment rate normalized by the impingement velocity could have widely different values, even when conventional parameters such as Reynolds and Schmidt numbers were held constant. For example, a vertical jet impinging on the interface yielded an entrainment rate proportional to the Richardson number to the - 1/2 power, whereas tilting that same jet only 15 degrees from vertical and precessing it yielded an exponent of - 3/2 [1]. At a Richardson number of 10, the entrainment rates differ by a factor of two orders of magnitude. The Reynolds and Schmidt numbers were essentially identical in the two experiments. The differing results could not be explained by conventional parameters.

A fundamental difference between these two flows is the stationarity of the impinging turbulence. The vertical jet generated a quasi-stationary impingement dome, at the sides of which fluid was entrained across the interface. In contrast, the precessing jet impinged on the interface in a moving, nonstationary way, such that entrainment appeared to be achieved by the rebound of the impingement dome, following the suggestion of Linden [2] for impinging vortex rings.

II. PERSISTENCE THEORY

If stationarity accounts for the markedly different results, then the transition between the two regimes must depend on some quantitative measure of the stationarity. We have defined the vortex persistence T to be the number of rotations a vortex makes during the time it moves a distance equal to its own diameter with respect to the interface [3]. Thus the persistence is π times the eddy velocity ratio of rotational to translational speeds (see Figure 1). Note that T can only be defined in the presence of an interface of some sort in the problem, since otherwise the translational speed is arbitrary.

Persistence may also be important in the limit of large Richardson number, where the stratification is so strong that the interface remains flat for all eddies, even the smallest. Closely related to this question is the issue of surface fluxes at flat, solid walls under boundary layers in unstratified flow, such as heat transfer.

According to surface renewal theory [4], the heat flux is proportional to the square root of the ratio of the thermal diffusivity and the rotation period of the appropriate eddy. In high Reynolds number turbulence, there is a wide spectrum of possible eddy sizes, ranging from the largest to the smallest, the latter being the Kolmogorov microscale. Which eddy is the correct choice?

In the absence of compressibility or stratification, there are only are two special eddy sizes in high Reynolds number turbulence: the smallest and the largest. In any given flow, the wall fluxes can depend on only one of them. There are also two asymptotic limits of the persistence parameter. The theory asserts that the surface fluxes are controlled by the smallest eddies for $T<T^*$, and by the largest eddies for $T>T^*$ (see Figure 2). The critical value T^* is presumably of order unity.

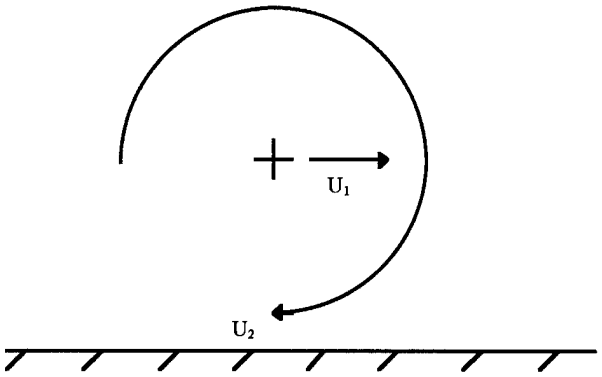

Figure 1. Persistence parameter $T=\pi U_2/U_1$

If the large vortex is not stationary, then the statistics are likewise not stationary, so that the scalar transport is not limited by the large scale eddies. The smallest scale eddies control the flux. Only when the boundary layer itself becomes turbulent does the skin friction depend on the fine scale eddies, since the strongest, large vortices are now moving rapidly with respect to the wall.
Said another way, the surface flux of heat can be switched from its turbulent value to its laminar value if large eddies are sufficiently strong and stationary. The criterion for sufficient strength is that the eddy in question possess the largest induced velocity. The criterion for sufficient stationarity is that $T>T^*$.

The theory developed from these stratified flow experiments is in accord with the wall heat transfer literature. The heat transfer under a forced, laminar boundary layer was measured as a function of the level of freestream turbulence [5]. It had been supposed that the heat transfer rate would increase smoothly with increasing freestream turbulence in a wind tunnel. However, the surprising result is that heat transfer is completely independent of freestream turbulence, at least up to very high values of turbulence. Of course, it is well known that once the boundary layer itself became turbulent, the heat transfer coefficient would increase markedly. Thus heat transfer increases for some kinds of turbulence, but not for others. What is different about the two types of turbulence?

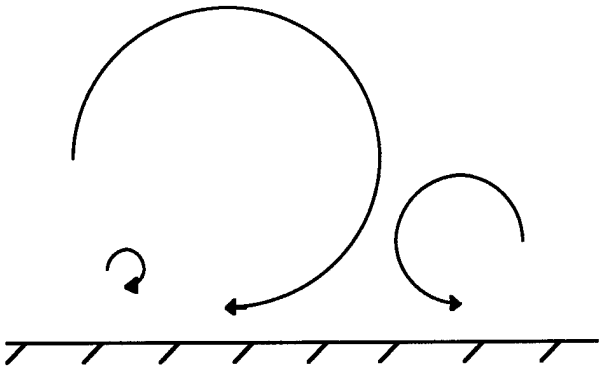

Figure 2. Persistence of the large vortex determines which eddy size controls the surface fluxes

In the heat transfer experiments, the fine scale turbulence in the freestream had no effect on heat transfer because the mean flow was sufficiently steady, corresponding to a stationary virtual large scale vortex. However, when the boundary layer itself became turbulent, the large eddies within it moved rapidly downstream, at a celerity of about 80% of the freestream speed, so that their persistence was small. The small scale turbulence thus controlled the surface flux.

This can also be viewed from a statistical viewpoint. Suppose the large vortex is stationary. Even if the transport by the smallest eddies across their own diameter was instantaneous, the heat transfer would still be rate-limited by the relatively slow rotation rate of the large vortex. It is the bottleneck. The problem is statistically stationary.

III. SKIN FRICTION

According to Reynolds' analogy, heat transfer is proportional to skin friction. Consequently, it is anticipated that with sufficient vortex stationarity, the skin friction will also be reduced, as its dependence suddenly switches from the smallest to the largest eddies, corresponding to the change from turbulent to laminar values. Thus at ship Reynolds numbers, the skin friction would decrease by more than an order of magnitude. This hypothesis has not yet been tested by skin friction experiments.

A vortex must be sufficiently stationary for the surface flux to decrease. Consider an array of counter-rotating, streamwise vortices near a flat wall. If the vortex core diameter is comparable to the vortex height above the wall and to the vortex spacing, the instability time scale is comparable to the vortex rotational period. This implies that the persistence parameter is low, of order unity. If seems likely that this is below or near the ($T=T^*$) transition. Thus the vortices probably require some means of artificial stabilization to hold them in place, through either passive or active control, to raise T above its critical value. Ironically, while the momentum transfer at the wall would be reduced by the addition of strong vortices in the boundary layer, the momentum transport throughout the rest of the boundary layer would be enhanced, as is known for conventional vortex generators. So any tendency for boundary layer separation would be inhibited.

If these streamwise vortices are sufficiently strong in comparison to the eddies in the turbulent boundary layer, the value of their persistence will determine the skin friction. A plausible estimate for the required strength is that their induced velocity is comparable to the freestream speed.

Sufficiently strong vortices may be able to resist the deformations of the background turbulence for an appreciable time. However, in order to achieve the necessary stationarity, the natural self-induced inherent in the streamwise vortices themselves must somehow be inhibited.

Balle [6] has suggested that the quasi-stability of the vortices in the Karman vortex street may be exploited to inhibit two-dimensional instabilities. Suppose that the streamwise vortices are all co-rotating, and the wall surface is corrugated, with the axis of the corrugations nominally in the streamwise direction. Suppose further that the surface undulations are designed such that they correspond to the dividing streamline in the ideal flow model of a Karman street. Such vortices are stable to two-dimensional, phase-coherent perturbations.

The question of three-dimensional instability remains. From dimensional considerations, the characteristic growth time τ for a Crow-type instability is

$$\tau = \delta^2/\Gamma \qquad (1)$$

where Γ is the circulation of one streamwise vortex and δ is its characteristic height from the wall, comparable to the boundary layer thickness. Because of the relatively large magnitude of circulation required to dominate the background turbulent vortices of the boundary layer, the characteristic 3-D instability time scale is relatively short. Consequently, the inhibition of 3-D instabilities is probably the most challenging task to achieving the necessary vortex persistence.

IV. ENERGY RECOVERY

Assuming that the theory is correct and that the streamwise vortices can be controlled, the third requirement for drag reduction is that the energy invested in the vortices is largely recovered at the trailing edge of the body. Otherwise it is only a Pyrrhic victory, since the reduction in skin friction is not enough to compensate for the unrecovered energy lost in the vortices.

Anti-swirl vanes at the trailing edge should be able to extract most of the rotational energy in the vortices, especially since the latter are to be held stationary (see Figure 3). The vanes would have their own parasitic drag, largely from laminar skin friction, so the overall system performance must account for this cost in the overall drag budget.

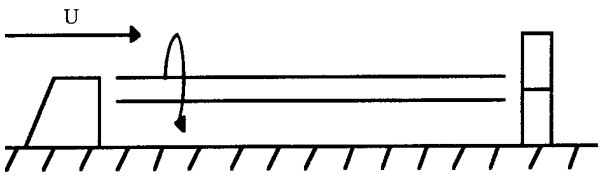

Figure 3. Schematic of the approach. Streamwise vortices are first introduced with vortex generators, held stationary with active control, and finally extracted downstream with anti-swirl vanes

V. CONCLUSIONS

A new approach to drag reduction exploits a persistence theory for surface fluxes near vortices. If the nearby vortex is sufficiently stationary, the surface fluxes are independent of the small scale turbulence. Applying the theory to the problem of skin friction, it is proposed that streamwise vortices, introduced near the leading edge and held stationary by active or passive control, would yield reduced skin friction underneath them. The net drag reduction depends on the ability to recover the rotational energy of the vortices, as well as any energy expended in vortex control. The next step is a laboratory test of the underlying theory in combination with passive or active control of streamwise vortices to test the concept. Heat transfer would be measured, as it is much easier to measure than skin friction.

VI. REFERENCES

1. A.J. Cotel, J.A. Gjestvang, N.N. Ramkhelawan and R.E. Breidenthal "Laboratory Experiments of a Jet Impinging on a Stratified Interface", *Experiments in Fluids*, **23**, 155-160, 1997.

2. P.F. Linden "The Interaction of a Vortex Ring with a Sharp Density Interface: A Model for Turbulent Entrainment", *Journal of Fluid Mechanics*, **60**, 467-480, 1973.

3. A.J. Cotel and R. E. Breidenthal "Persistence Effects on Stratified Entrainment", *Applied Scientific Research*, **57**, 349-366, 1997.

4. M.A. Leveque "Les Lois de la Transmission de Chaleur par Convection", *Ann. Mines*, **13**, 201-239, 1928.

5. A. Edwards and B.N. Furber "The Influence of Free Stream Turbulence on Heat Transfer by Convection from an Isolated Region of a Plane Surface in Parallel Flow", *Proceedings of the Institute of Mechanical Engineering*, **170**, 941, 1956.

6. G. Balle, private communication, 1998.

DIRECT NUMERICAL SIMULATIONS OF DRAG MODIFICATION USING RANDOMIZED FORCE FIELDS

R. B. Dahlburg
Laboratory for Computational Physics and Fluid Dynamics
Naval Research Laboratory
Washington, DC 20375-5344

R. A. Handler
Remote Sensing Division
Naval Research Laboratory
Washington, DC 20375

W. C. Sandberg
Laboratory for Computational Physics and Fluid Dynamics
Naval Research Laboratory
Washington, DC 20375-5344

L. Sirovich
Department of Mathematics
Brown University
Providence, RI 02912

Abstract- Recent numerical[1] and physical[2] experiments of channel flow have clearly shown that large reductions in drag can be achieved by forcing the turbulence at appropriate length and time scales. In this paper we present new results from direct numerical simulations of turbulent channel flow in which we apply internal body forces, intended to model Lorentz forces, to the turbulence, using a random phasing. In all cases where the drag is modified we observe an increase, suggesting that random phasing alone is insufficient to achieve drag reduction. Some future directions for the research are discussed.

I. INTRODUCTION

Recent numerical[1] and physical[2] experiments have clearly shown that significant reductions in drag can be achieved by forcing the turbulence at appropriate length and time scales. In fact, the above cited numerical experiments show that a reduction on the order of 58% can be achieved. These dramatic reductions in drag have been achieved by a novel forcing in which the phases of the energy containing wave-like modes of turbulence are periodically randomized. It is further noted that the reduction achieved in this way rivals that pro-induced drag reduction. A remarkable result is that the drag reduced turbulence achieved in this way is almost indistinguishable in every way from that achieved using polymers. This work also hints at a fundamentally new view of turbulent boundary layer dynamics[3]. The physical experiments[2] noted above were designed to mimic this forcing by employing a randomized array of surface roughness and were also successful in reducing drag by more than 10%. These investigations point out that forcing the turbulence at the appropriate length and time scales is the key to the successful control of wall bounded turbulence. It is also clear that the use of direct numerical simulations can be an extremely cost effective tool in exploring not only the fundamental physics of turbulence, but also in testing novel ideas and rapidly sorting out what works, what does not, and why.

In this paper we present new results from direct numerical simulations of turbulent channel flow in which we apply internal body forces to the turbulence, using a random phasing. The forcing models that which can be achieved using Lorentz forces. Since a real force is applied to the flow, in this case work is being done. In this respect the present calculations differ from the earlier phase randomization simulations in which no work was done on the fluid[1].

II. SETTING UP THE PROBLEM

We have performed direct numerical simulations of turbulence in a periodic channel with rigid no-slip walls. Following earlier treatments[4, 5] a fully spectral code is used, in which the velocity field is approximated by Fourier modes in the streamwise (x) and spanwise (z) directions and Chebyshev polynomials in the wall-normal (y) direction. In the present instance the turbulent flow is driven by a constant streamwise pressure gradient. For all simulations reported here we have used 65 x 64 x 68 grid points in the y, z, and x directions, respectively. The channel dimensions are $L_y = 2h$, $L_z = 5h$, and $L_x = 10h$ where h is the channel half width. Our starting point is the Navier-Stokes equations, written here in a dimensionless rotation form:

$$\frac{\partial \mathbf{v}}{\partial t} = \mathbf{v} \times \boldsymbol{\omega} - \nabla \Pi + \frac{1}{R}\nabla^2 \mathbf{v} + A\mathbf{F}, \tag{1}$$

$$\nabla \cdot \mathbf{v} = 0, \tag{2}$$

where $\mathbf{v}(\mathbf{x}, t)$ = flow velocity, $\boldsymbol{\omega}(\mathbf{x}, t) = \nabla \times \mathbf{v}$ = vorticity, $\Pi(\mathbf{x}, t)$ = mechanical pressure + kinetic energy density, $R = U_o L_o/\nu$ = Reynolds number (with the viscosity assumed to be constant and uniform). Furthermore, $\mathbf{F}(\mathbf{x}, z)$ is the applied Lorentz force, and $A(t)$ is the amplitude of this force. In this representation, U is measured in units of the velocity field at $y = 0$. The time is measured in units of characteristic flow time, L_o/U_o, where the characteristic distance, L_o, is defined by the half-width of the channel.

The force field corresponding to the wave-like modes is given by:

$$\mathbf{F}(x, z) = Re\{\exp[i(\mathbf{k} \cdot \mathbf{x} + \phi)]\} \tag{3}$$

where ϕ_{nm} is a random phase. This gives

$$F_x = \sum_{n,m} [\cos(k_n x + k_m z + \phi_{nm}) + \cos(k_n x - k_m z - \phi_{nm})] \tag{4}$$

and

$$F_z = \sum_{n,m} [\cos(k_n x + k_m z + \phi_{nm}) - \cos(k_n x - k_m z - \phi_{nm})] \tag{5}$$

The time dependence is a square wave function given by:

$$A(t) = \begin{cases} \xi, \text{ if mod } (its)=100 \text{ and } it\text{-}its < 10; \\ 0, \text{ otherwise;} \end{cases} \tag{6}$$

where it is the iteration level and its is basically every hundredth iteration. The parameter ξ is the amplitude of the forcing function.

Before applying random forcing with the Lorentz force we integrated forward in time until a steady state was established. This was shown to satisfy the averaged form of the streamwise momentum equation for statistically steady turbulence. In this flow we have chosen a pressure gradient such that $R^* = u^* h/\nu = 125$ in the steady state. Once we have established a steady state turbulence in this way the fluctuating force field is turned on.

III. LOW WAVENUMBER LORENTZ FORCING

The particular cases that we have chosen rely on the phase randomization calculations for fixing the wavenumber space. For the forcing functions defined in equations 4 and 5 we have $0 \le n \le 11$ and $1 \le m \le 6$. The forcing function is turned on every one hundred time steps for a duration of ten time steps, as indicated in equation 6. Some results of the numerical simulations are shown in Figures 1 and 2. Figure 1 shows the mass flux Reynolds number, R_b, as a function of t^*. The quantity t^* is related to the viscous time by $t^* = (u^*)^2 t/\nu$. The calculations shown in Figures 1 and 2 are run for approximately 40 viscous time periods.

We define the mass flux Reynolds number as $R_b = U_b h/\nu$, where $U_b = 1/2 \int_0^{2h} \bar{U}(y)\, dy$. A decrease in drag would appear in Figure 1 as an increase in R_b. It is apparent that in no case does drag reduction occur. Rather, above a threshold value of $\xi \approx 0.1$ R_b is seen to decrease strongly, indicating an increase in drag. For $\xi \approx 0.25$ the decrease in R_b is about 3%, while for $\xi \approx 1.$, R_b decreases by about 19%. Figure 2 shows the friction Reynolds number $R^*(= u^*/h\nu)$ as a function of it.

Here the friction velocity $u^* = (\tau_\omega \rho)^{1/2}$, with τ_ω being the wall shear stress and ρ is the mass density of the fluid. As noted above, R^* must return to its equilibrium value of 125 since the driving pressure was held constant throughout the simulations. In all cases we see that R^* returns to a value close to its initial value, indicating that the system has settled down to a new turbulent state.

IV. CONCLUSIONS

The numerical calculations reported in this paper represent a first attempt to reduce drag in turbulent flows by the application of spatially random Lorentz forces. Unfortunately, in no case was drag reduction achieved. Hence random phasing of the Lorentz force is apparently insufficient for producing drag reduction. In fact, we observed significant drag increases for several cases. To achieve this increase in drag a rather large force had to applied. This force was on the order of 1000 times the driving pressure gradient. A key difference between these simulations and earlier ones[1] is that here we are doing work on the flow. In the earlier phase randomization calculations no work was done. It is intriguing that force amplitudes of 10 to 100 times the driving pressure gradient did not change the drag significantly.

Our present results point the way to future directions for this research. As was performed for the phase randomization calculations different wavenumber bands should be investigated. Different phases and forcing frequencies and durations also should be tried. Vertical tapering of the force would confine its effect to the buffer layer, and hence this feature should be included. Finally, the present simulations utilize a spatially random but temporally constant Lorentz force profile. The effect of temporal randomness might be significant. It would also be of interest to determine the relationship between the applied force and the turbulent dynamics that underlie the apparent insensitivity to a range of external force amplitudes.

V. ACKNOWLEDGMENTS

This work was supported by ONR. The numerical simulations were performed on the Cray C90 at WPAFB under a grant of time from the DoD HPC program.

VI. REFERENCES

1. Handler, R. A., E. Levich and L. Sirovich, *Drag reduction in turbulent channel flow by phase randomization,* Phys. Fluids A, 5 686, (1993).

2. L. Sirovich and S. Karlsson *Turbulent drag reduction by passive means*, Nature, August, 753, (1997).

3. P. Carpenter, *The right sort of roughness*, Nature, August, 13, (1997).

4. J. Kim, P. Moin, and R. Moser, *Turbulence statistics in fully developed channel flow*, J. Fluid Mech., 177, 133, (1987).

5. R.A. Handler, E.W. Hendricks, and R.I. Leighton, *Low Reynolds number calculation of turbulent channel flow: a general discussion,* Naval Research Laboratory Memorandum Report 6410, (1989).

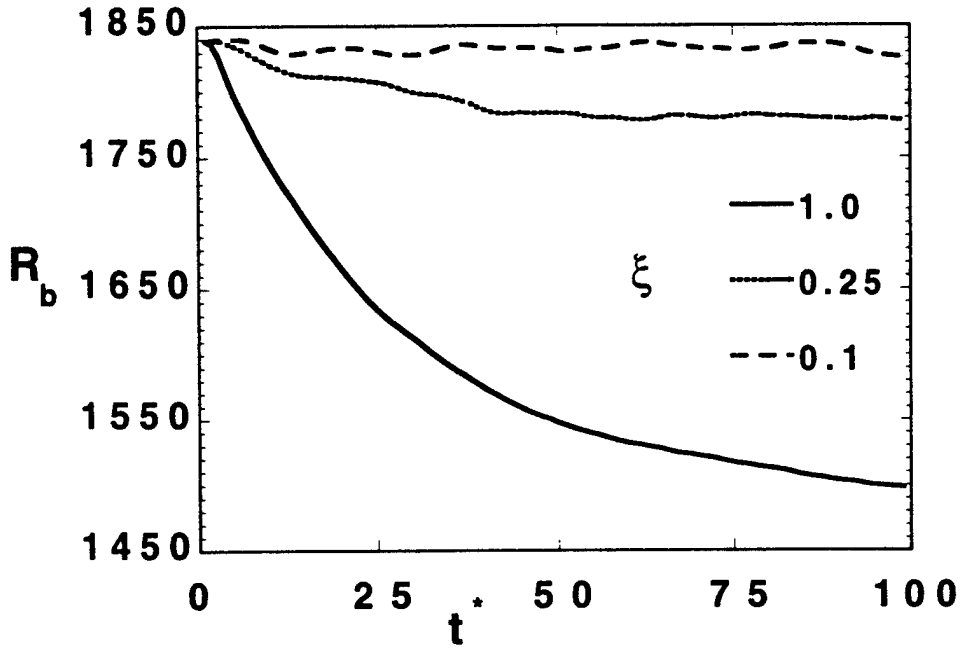

Figure 1: Mass flux Reynolds numbers versus time.

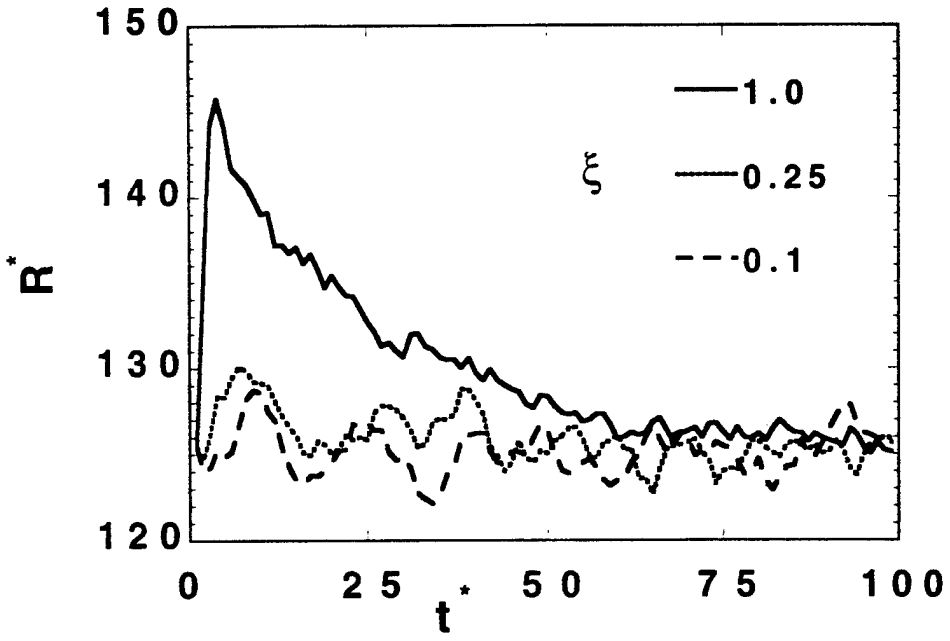

Figure 2: Friction Reynolds numbers versus time.

ADAPTIVE FEED-FORWARD CONTROL OF TURBULENT BOUNDARY LAYERS

K.S. Breuer, R. Rathnasingham*, K. Amonlirdviman
Department of Aeronautics and Astronautics
Massachusetts Institute of Technology
Cambridge, MA 02139
breuer@mit.edu

We discuss recent progress in active control of the near-wall region of a turbulent boundary layer using a linear adaptive feed-forward control. A wall-based detection scheme is described which effectively detects coherent structures and predicts downstream flow behavior. The detection scheme is based on correlation function measured experimentally between adjacent input sensors and defined control points. By saving only the portion of the signal that is correlated over some small spanwise distance, large-scale coherent structures can be effectively identified in real time. The conditioned input signals are used to compute optimal linear transfer functions between the sensors and the control locations and these transfer functions are then used in an adaptive feed-forward control system to minimize turbulent fluctuations at the control points. The algorithm is demonstrated to work surprisingly well, reducing turbulent velocity fluctuations in the near wall region by over 30% and reducing wall pressure fluctuations by 17%.

1 INTRODUCTION

Recent advances in the understanding of near-wall turbulent shear flow structure have resulted in several suggestions for active control including schemes based on qualitative physical arguments [5], formal optimal control [3], neural networks [9] and reduced-order dynamical representations of the near-wall region [7] (A review of the main approaches was recently presented by Moin and Bewley [15]). Several problems, both theoretical and practical face the successful implementation of a real-time turbulence control scheme. From the theoretical side, the complexity of the turbulent boundary layer and its dynamics make the choice of a control algorithm far from intuitive. From the practical side, the spatial and temporal scales at which the control must be executed make the design of sensors, actuators and control hardware very challenging.

This paper describes some of the recent results demonstrated in our group in which a conceptually simple control algorithm has been developed for near wall turbulence control [19, 16]. The algorithm is based on the short-time linear dynamics of the coherent structures and an adaptive feed-forward algorithm to predict and inhibit the development of turbulence-producing events. The experiments have shown a uniform 31% reduction in turbulent u'-fluctuations in the near-wall region as well as a 17% reduction in turbulent wall-pressure fluctuations.

2 OVERVIEW OF CONTROL STRATEGY

The control approach is based on two key assumptions, namely: (i) that the majority of the turbulence-producing events in the near-wall region of the flow are associated with the large-scale "coherent structures" and (ii) that these coherent structures may be modeled (for short times) by dynamical equations which are linear with respect to the mean flow. The first assertion is supported by a large body of research on coherent structures over the past twenty years, and is well-illustrated by Johansson, Alfredsson & Kim's analysis of numerically-generated turbulence [10] in which they report that the coherent structures, while only occupying 25% of the volume in the near-wall region, are responsible for 50% of the total turbulence production. The assumption of linearity is based on the observation that the strong mean shear of the near-wall turbulent flow will dominate the short-time evolution of small perturbations. This is consistent with the framework provided by the Rapid Distortion Theory of turbulence [8] and other models for near-wall turbulence [12]. In addition, experiments by Johansson, Her & Haritonidis [11] found that conditionally-sampled u, v and p signals scaled linearly with threshold amplitude, again suggesting an amplitude-invariant behavior for these coherent structures. For the purposes of control, this linearity assumption need only hold for the short time it takes a structure to advect from an upstream sensor to an actuator and does not imply that turbulence production as a whole is governed by a linear mechanism.

Given these working assumptions, the control strategy pursued in these experiments is shown schematically in figure 1. A multiple-input, multiple output (MIMO) linear filter [2] is constructed as an estimate of the transfer function between signals from a spanwise array of upstream wall-based sensors (in this case from three sensors: $s_1(t), s_2(t)$ and $s_3(t)$) and the signals from sensors located at downstream control points (again, in this case, three sensors: c_1, c_2 and c_3). The estimated transfer function is represented in figure 1 as $\hat{H}_1$, while the physical (true) relationship between the upstream

*Present Address, Schlumbeger Research Center. Ridgefield CT

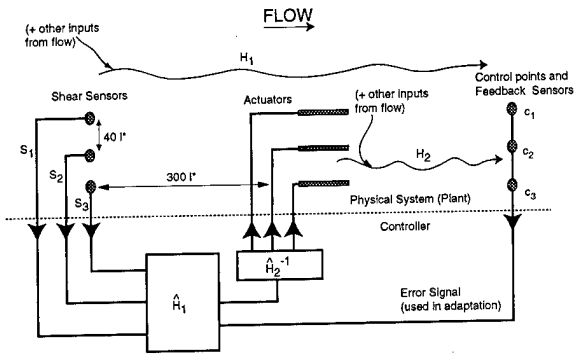

Figure 1: Schematic diagram showing the plant - the turbulent boundary layer - together with detection sensors (s_1, s_2, s_3), actuators (a_1, a_2, s_3) and downstream control points (c_1, c_2 and c_3). The block diagram below the dotted line represents the controller including the adaptive feedback path. H_1 and H_2 are actual transfer functions, while $\hat{H}_1$ and $\hat{H}_2$ are their linear estimates, derived from cross-correlation measurements.

and downstream sensors is indicated by H_1. in general H_1 will not be equal to $\hat{H}_1$, the difference resulting from both nonlinear relationship between the two arrays of sensor signals and the fact that the signals at the downstream sensor array will also be affected by other inputs not sensed by the upstream sensor array (for example, outer-flow effects, etc).

In a similar manner, we construct a linear transfer function between the actuators and the downstream control points (in this case, a 3×3 matrix of transfer functions). This is represented by $\hat{H}_2$ and, as before, the "true" relationship between the actuators and c_i is nonlinear and includes additional inputs, not captured by this representation.

With these two transfer functions (or, more correctly, systems of transfer functions), we construct a feed-forward control system such that if $\hat{H}_1$ and $\hat{H}_2$ were completely accurate descriptions of the full system, the fluctuating signal at each control point, c_i would be zero. In reality, small variations, slow changes and more-importantly, nonlinearities and non-observed inputs will result in an error at the control points such that the fluctuations will not be identically zero. However, the error can be further minimized by perturbing the filter coefficients, either randomly or by some proscribed adaptive optimization scheme. In this manner, the overall control performance can be optimized or adapted to suit changing freestream conditions.

This control approach is quite general and may be applied to an arbitrary number of upstream sensors, actuators and downstream sensors (control points). It has several appealing features, namely:

1. The filters are pre-computed, and only require low-bandwidth adaptation to maximize their performance. This architecture greatly simplifies the implementation when compared, for example, with neural network or "bang-bang" control schemes which typically require large computational resources for real-time operation and extensive training periods.
2. In the current implementation, the filters are linear FIR filters which could even be implemented using analog technology for high speed and low cost. More complex filter implementations (IIR) can be implemented with a moderate increase in complexity for even more efficient hardware implementation.
3. The template of transfer functions is finite and independent of what goes on in the rest of the flow. This is self-determined by the fact that the correlation between the sensors systems will naturally approach zero as their separation increases and thus no additional contribution to the transfer function is achieved. This means that control is local and can be implemented as an overlapping network of local controllers with only moderate "supervisory" attention to optimize and update filter coefficients.
4. This local nature of the control allows for complete scalability to larger areas of control authority. The local processing power need not become more powerful, only more dense.

2.1 SENSOR PRE-CONDITIONING

Central to the success of this scheme is the ability to accurately predict the flow state at the downstream sensors, c_i, using the upstream wall sensors, s_i. For the turbulent boundary layer, the dominant contribution over such large distances is by the large-scale coherent structures, and thus the problem of prediction becomes one of (i) identification of the large scale structures and (ii) prediction of their evolution. If we assume that we can define large scale structures statistically, i.e. any signal that retains finite correlation over some spanwise distance, then the identification can be efficiently achieved using a conditioned spectral analysis [2] which isolates the correlated portion of (any) two signals. This is best expressed in the frequency domain:

$$C_{ij}(\omega) = \frac{G_{ij}(\omega)}{G_{jj}(\omega)} S_j(\omega) \qquad (1)$$

where C_{ij} is the correlated part of the two signals S_i and S_j ($s_i(t)$ and $s_2(j)$ expressed in the frequency domain), G_{ij} and G_{jj} are the cross-spectra and auto-spectra respectively. Note that for a spatially homogeneous field (such as the spanwise direction in a turbulent boundary layer), C_{ij} is identical to C_{ji}.

The conditioning filter, G_{ij}/G_{ii}, is nothing more than a linear filter which pre-conditions the input signals weighting them to favor a frequency band determined to be most highly correlated. In this sense, it is a rather simple pre-conditioning and many more complex pre-conditioning schemes can be envisaged, particularly if a dynamic model of the near-wall region of the boundary layer were available, in which case a Kalman filter could be constructed. This would give a real-time identification of large-scale structures and, presumably, a superior performance over the simple case presented here.

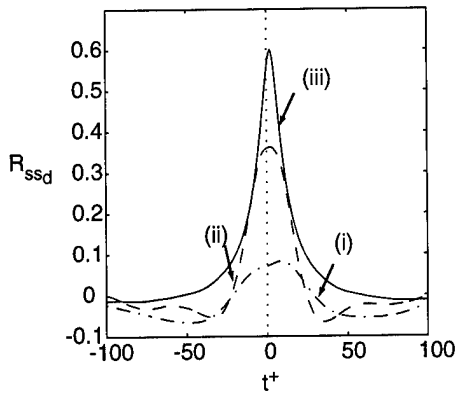

Figure 2: Cross-correlations between the upstream wall-shear sensors and the downstream velocity sensor, c_2 (located $300l^*$ downstream and at $y^+ = 10$). The three curves represent (i) s_2 aligned in the cross-stream direction (sensitive to streamwise shear), (ii) s_2 aligned in the streamwise direction (more sensitive to spanwise shear) and (iii) The correlated portion of s_1 and s_2 (c_{12}), both aligned to be sensitive to spanwise shear.

The effectiveness of the conditioned spectral analysis is illustrated in figure 2 which shows the measured cross-correlation between the shear measured by the upstream sensor (s_1) and a velocity sensor placed at c_2, $300l^*$ downstream of the middle sensor (s_2). All of the experiments reported here were conducted in a fully-developed, zero-pressure-gradient turbulent boundary layer with $Re_\theta = 1960$. For reference, the friction velocity, u_τ, was 0.31 m/s, the viscous length scale, l^*, was 55 μm and the viscous time scale, t^*, was 270 μs. Each wall sensor consisted of a flush-mounted constant-temperature hot wire, sensitive to wall shear. When the wires are aligned normal to the flow direction, they are most sensitive to streamwise shear. However, figure 2 indicates that in this orientation the correlation between the wall shear and the downstream velocity sensor is relatively poor. However, when the surface wires were aligned in the flow direction (making them more sensitive to spanwise shear), a marked improvement in the cross-correlation is observed. Furthermore, after adopting the signal conditioning technique (equation 1), the maximum cross-correlation (now between C_{12} and c_2) improves by an additional 50% to 0.6. The time delay of the maximum corresponds to the transit time of the large-scale structures from one sensor to the other and represents a lag in the control scheme.

The alignment of the hot wire with the flow is somewhat counter-intuitive and care must be taken in interpreting its results. A conventional hot-wire shear sensor (one aligned perpendicular to the primary flow direction) is predominantly sensitive to the streamwise shear stress, $\partial u/\partial y$ and only slightly sensitive to the magnitude of the spanwise shear stress, $|\partial w/\partial y|$. By rotating the wire, the mean signal of the sensor remains dominated by the streamwise shear (since it is so large). However, the fluctuating part of the signal (which is the only part of interest to the linear controller) is now dominated by the magnitude of the spanwise shear fluctuations and only slightly sensitive to fluctuations in streamwise shear. The improved performance of spanwise shear as a control input has also been noted in numerical experiments for active flow control [13].

A second practical aspect of the sensor configuration is also worth noting: the alignment of the wire gives the sensor extremely good spatial resolution in the spanwise direction (limited by the thickness of the sensing wire which for these experiments was 2.5 μm - less than $l^*/20$). The streamwise resolution of the sensor (dictated by the length of the sensing wire) is somewhat worse (in our case about $10l^*$). However, this preferential sensitivity matches the shape of the coherent structures we are trying to detect which are typically greatly elongated in the streamwise direction. This geometric factor might be one reason for the observed improvement in control performance.

2.2 FORWARD PREDICTION AND THE WIENER FILTER

With the pre-conditioned input signals, we now need to predict the evolution of the large-scale structures so that we can schedule the actuators to minimize the error signal at the downstream control points. Again, assuming a statistically linear transfer function, we derive a Wiener filter to optimally predict the downstream flow quantity, c_i, from the conditioned input data. The Wiener filter is the linear filter which minimizes the mean-square error between the flow field predicted by the sensor inputs and the actual flow properties at a remote location. The filter is expressed as a set of weighting constants which multiply the input signal (collected at different points in both space and time) and thus maps the input signal onto a predicted value for the desired flow parameter. The weighting constants are determined by solving a set of simultaneous equations which relate the auto- and cross-correlations of the sensor inputs and the correlations with the desired output. These equations may be expressed as a series of linear equations:

$$\begin{bmatrix} \Phi_{11} & \Phi_{12} & \cdots & \Phi_{1N} \\ \Phi_{21} & \ddots & & \\ \vdots & & \ddots & \\ \Phi_{N1} & & & \Phi_{NN} \end{bmatrix} \begin{bmatrix} H_1 \\ H_2 \\ \vdots \\ H_N \end{bmatrix} = \begin{bmatrix} \Phi_{1y} \\ \Phi_{2y} \\ \vdots \\ \Phi_{Ny} \end{bmatrix} \quad (2)$$

where Φ_{ij} is the auto-correlation of the input signals taken from different time/space slices, and Φ_{iy} is the cross-correlation between the input and output signals. Solving for $H_1, H_2, \ldots H_N$ results in the linear filter to estimate the output from the N inputs. The inputs can be located anywhere in space and time and can even be comprised of multiple flow quantities, so long as the cross correlations between each of the sensors are known. As described here, the filter is derived as a Finite Impulse Response (FIR) filter. This can, if so desired, be approximated as a Infinite Impulse Response (IIR) filter for more compact representation in a real-time control

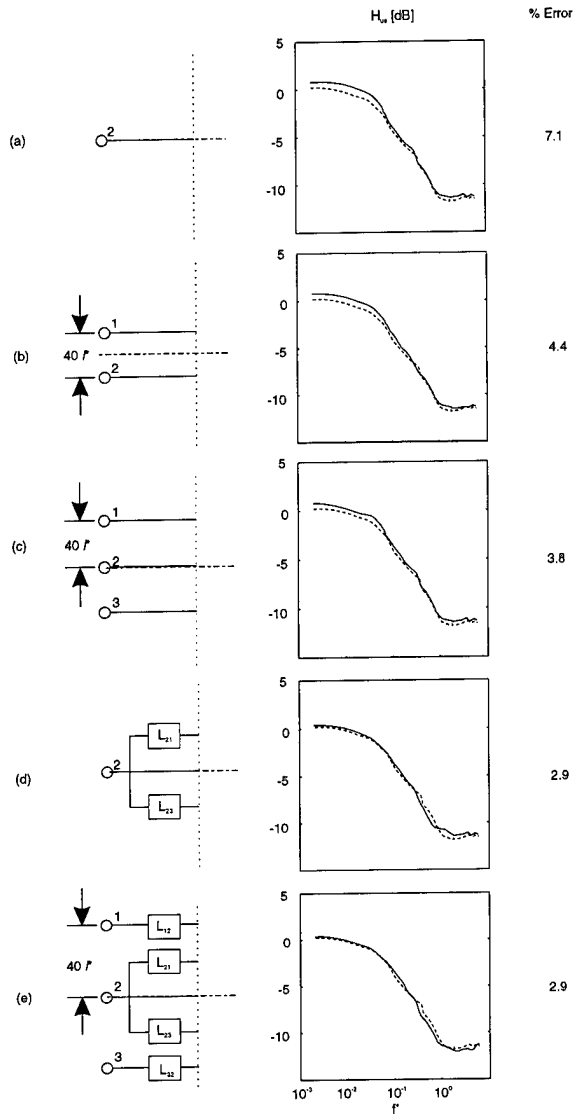

Figure 3: Cross-spectra between the detection sensors and the streamwise velocity $300l^*$ downstream; (a) with a single sensor, (b) with a pair of sensors separated by $40l^*$ in the spanwise direction, (c) with three sensors separated by $40l^*$, (d) with a single sensor whose signal is filtered to emphasize the most coherent structures in the flow and (e) three sensors centered about the downstream measurement point and all filtered to emphasize the large scale motion. The solid and dashed lines represent the predicted and measured spectra, respectively. The dashed-dotted line represents the line that passes through the downstream measurement point.

system. However, this must be done with care to avoid filter instabilities and causality problems in the control system.

2.3 ADDITIONAL INPUT WEIGHTING SCHEMES

In its most basic form, the Wiener filter uses the raw input signals or perhaps the pre-conditioned signals, as described earlier. However, by combining the input signals in different ways, different Wiener filters can be derived, each with different forward prediction performance. This is illustrated in figure 3 which shows a variety of different combinations and their different predictive performance. Here, the predictive performance is measured as the rms difference between the predicted signal and the signal actually measured (in this case the streamwise fluctuating velocity 300 l^*downstream of the input sensors). Figure 3a shows that a single in-line sensor predicted u_{rms} with an error of 7.1%. Using a pair of sensors (figure 3b) made a marked improvement, reducing this error to 4.4%. The increased performance of the second configuration suggests that the flow structures that contribute to the linear relationship between the upstream and downstream signals possess some degree of spanwise spatial coherence. An addition of a third sensor, shown in figure 3c, further reduces the prediction error to 3.8%, indicating that the coherence of the large scale flow structures extend up to $80l^*$ in the spanwise direction (agreeing with the typically quoted value of $100l^*$)

Figures 3d and e represent configurations with filters incorporated to emphasize the coherent scales. Each FIR filter, L_{ij}, has 32 poles and was constructed from the cross-spectra between adjacent sensors, as described earlier. The configuration shown in figure 3d uses a filtered signal from the middle sensor alone to estimate the signals from all three sensors. This was done by combining the signal from the middle sensor with the filters L_{21} and L_{23} which correspond to the part of the adjacent sensor signals that are correlated with the middle sensor signal. The prediction error for this configuration was 2.9% and corresponded to the lowest value obtained. The effect of the filters can be readily observed from the plots of the cross-spectra. The low frequencies were more accurately reproduced than in the unfiltered cases shown in Figures 3a. This improvement was attributed to the preferential weighting of these lower frequencies imposed by the conditioned analysis. Finally, an attempt to combine all sensors to produce an optimal configuration is shown in figure 3e. It combines the highly effective prediction of the middle sensor with the filtered signals of the adjacent sensors to extract the most coherent parts from all signals. The prediction error of 2.9% was identical to that with just the middle sensor. This seems to suggest the addition of adjacent sensors will have no effect on the prediction of u. However, on closer examination of the cross-spectra, the lower frequencies is seen to be more accurately predicted, so that although the overall error is unchanged (over the entire frequency range), the improved prediction of the larger scales may improve controllability of the flow.

The phase diagrams, which were not shown in the figures, exhibited a constant slope (always true for a FIR filter), which corresponded to a lag that matched the average convection speed of the large scale structures ($u_c^+ = 10.7$, where the convection speed u_c has been normalized by the friction velocity, u_τ). This lag was seen to be constant for all cross-spectra between the upstream and downstream sensors.

3 CONTROL PERFORMANCE

With the shear sensors aligned with the flow direction, the forward prediction, $\hat{H}_1$, was thus computed from the conditioned signals C_{12} and C_{23} and then approximated by a linear 32-pole FIR filter. This low-order approximation is necessary for efficient implementation in our real-time digital controller. The final form of the filter was able to predict u' measured at c_2 from shear stress measured at s_1, s_2 and s_3, (300 l^*apart) with a maximum rms-error of less than 3%. $\hat{H}_1$ was then combined (as shown in figure 1) with $\hat{H}_2$ - the transfer function between each actuator control voltage and c_i - to provide the appropriate input to the actuator array so that the resultant signal at the downstream sensors would be (ideally) zero. For the current experiments, the adaptation algorithm simply minimized the rms of the error signal, c_2, by varying the gain and lag of the forward predictive filter. More sophisticated forms of adaptation are possible and will be explored in the future.

For the current results, only three sensors and three actuators were used in a proof-of-concept experiment. The actuators chosen were resonant membrane "zero-net-mass-flux" devices, similar in nature to those described by Coe *et al.* [6], although modified so that the control jet discharges from a streamwise-aligned slit measuring 10 l^* by 150 l^*. The physical parameters of the actuators were chosen so as to optimize the actuator's performance [17]. The resultant devices operated at a resonant frequency of 2 kHz and were capable of producing exit velocities up to .4 m/s (1.3 u_τ). The oscillatory flow through the streamwise slit was measured [14] and found to produce a pair of counter-rotating streamwise vortices, very similar to that observed (in a laminar boundary layer) by Jacobson & Reynolds [9] who used similar devices and who also successfully demonstrated control of streamwise vortical structures in a laminar boundary layer.

As discussed above, all of the experiments were carried out in a fully developed, zero-pressure-gradient turbulent boundary layer at a Reynolds number based on momentum thickness of 1960. The viscous length and time scales at this Reynolds number are 55μm and 270μs, respectively. To ensure the statistical convergence of the measured data, record lengths were based on a 95% confidence level with a 0.2% uncertainty in the root-mean-squared value. This resulted in data records consisting of 2×10^6 independent sample points.

The control loop was implemented using a 60 MHz DSP-based real-time signal-processing board and operated at 35 kHZ ($9.5f^*$) - much faster than was actually required. For the current experiments, the downstream sensor was a traversable hot wire, located downstream of the actuator array and the control objective was thus to minimize u' fluctuations at the location of this sensor. A more technologically relevant objective might be to use a wall-mounted shear or pressure sensor, with corresponding objectives of minimizing turbulent wall shear or pressure fluctuations. The convenience of a movable sensor for diagnostics and optimization dictated the choice of u' for most of the experiments, although we also report on some limited experiments aimed at the control of p_{rms}.

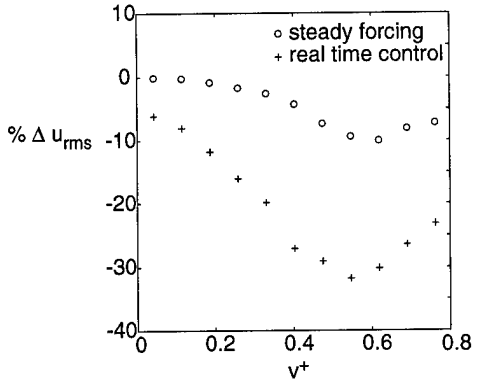

Figure 4: Percentage change in u_{rms} above the middle actuator (a_2) slit as a function of the (rms) forcing amplitude.

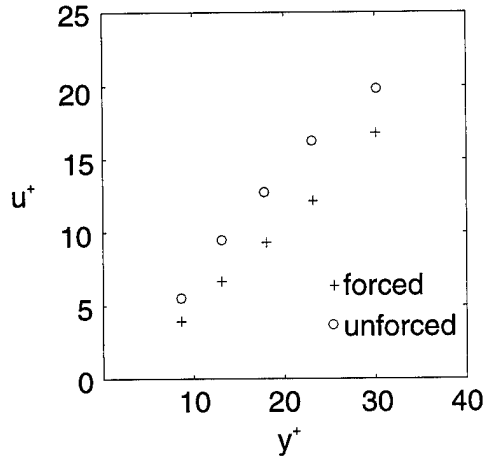

Figure 5: Near-wall velocity distribution with and without active control, showing the reduction in velocity gradient near the wall resulting in a 7% reduction in wall shear stress.

Figure 4 shows the performance of the controller as functions of the filter gain (i.e. actuator amplitude) and plots the percentage reduction in u_{rms} at the location of the downstream sensor which, in this case was positioned at the downstream end of middle actuator exit slit and at $y^+ = 10$. Although the identification stage predicted that the control jet amplitude of $\bar{v}_{control} = 0.45u_\tau$ should be optimal, the adaptation indicates that a higher amplitude of $\bar{v}_{control} = 0.55u_\tau$ yields slightly better performance, with a maximum reduction in u_{rms} of approximately 31%. Data from open-loop forcing (i.e. constant amplitude forcing, with the upstream sensors disconnected) is indicated by circles and also indicate some reduction in u_{rms} although the net result is only about one third as effective as the active control, for the same energy input. As the actuator gain is increased beyond the optimal, the energy injected by the actuators overwhelms the control benefits and the rms signal returns to its undisturbed value.

The reduction in u_{rms} is also accompanied by a reduction in the local *mean* velocity at the control location. This is

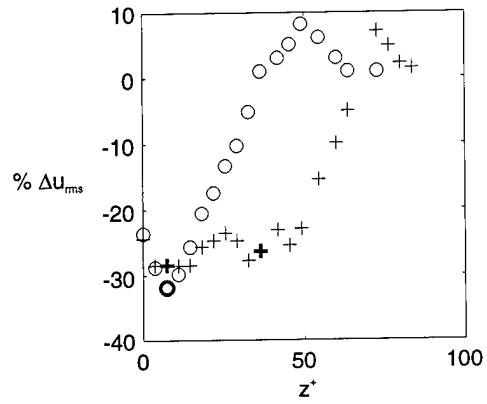

Figure 6: Percentage change in u_{rms} above the actuator array as a function of the spanwise coordinate z^+. Circles indicate results using one actuator while plusses indicate results obtained using three actuators. The actuators are located at z^+= 0 and 40. The bold symbols represent control optimization points.

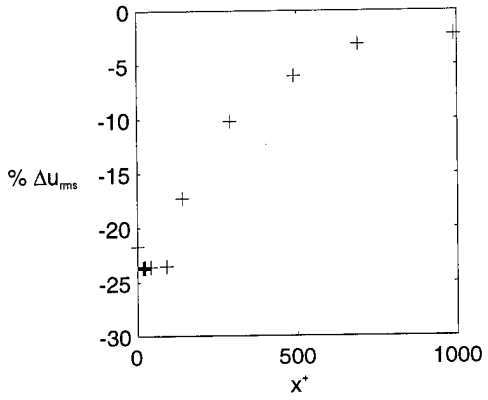

Figure 7: Percentage change in u_{rms} above the actuator array as a function of the streamwise coordinate x^+.

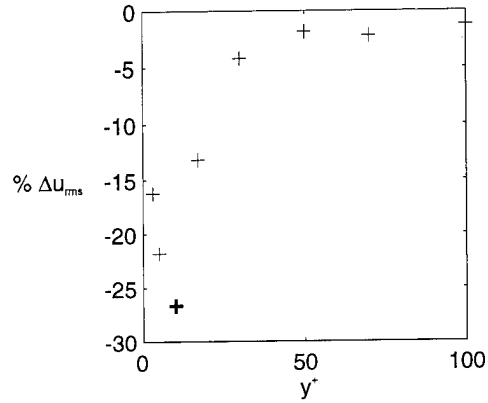

Figure 8: Percentage change in u_{rms} above the actuator array as a function of the wall-normal coordinate y^+.

shown in figure 5 which shows the near-wall velocity profile. The controlled and non-controlled mean velocities at each y-location were obtained by switching the actuators on and off, without moving the hot wire probe. By this means a 7% reduction in the near-wall mean velocity gradient was measured. Although the inference of wall shear from a measured mean velocity profile is often problematic and subject to errors, the comparative measurement indicated by figure 5 clearly shows a reduction in wall shear.

The spanwise extent of the controlled flow is illustrated in figure 6 which shows the reduction in u_{rms} at $y^+$of 12 and plotted versus z^+at a station immediately behind the actuator array (and at the same streamwise station as the control points). Since the measurements are symmetric with respect to z^+= 0, only one side of the actuator array is shown. Two series of data are plotted here, control achieved using one actuator and control achieved using all three actuators. The single actuator result indicates that the maximum reduction is achieved slightly off-center from the axis of the actuator, and the controlled region relaxes to its undisturbed state approximately 50 z^+on either side of the actuator. A slight overshoot is also observed at the spanwise edge of the controlled region. The use of all three actuators extends the spanwise range of the controlled field and slightly decreases the overshoot.

The variation in the streamwise direction, x, and the wall-normal direction, y, are shown in figures 7 and 8 respectively. Here we see that the relaxation of the controlled flow takes place over a streamwise distance of approximately 1000 l^* before returning to the uncontrolled fluctuation level. With all three actuators in operation, more extensive measurements [18] reveal that a wedge of controlled flow is created directly downstream of the actuator array which relaxes back to the natural boundary layer structure with a half angle of approximately 15°as fully turbulent fluid mixes back in with the controlled fluid at the edges of the control patch. The vertical extent of the controlled flow, indicated by figure 8, shows maximal control is achieved at $y^+ = 12$ - the point at which the transfer functions were optimized (indicated by the bold plus symbol) and that the region of control is limited to the near wall region ($y^+ < 50$) - perhaps not surprising when one realizes that the coherent structures are confined to the near wall region and so one the control of these near wall structures should only have limited spatial influence.

The extensibility of the control region by using additional spanwise actuators suggests that a larger spanwise array will enable both larger spanwise regions of controlled flow as well as more extensive regions in the streamwise direction (due to reduced edge contamination). This concept is currently being tested.

Figure 9 shows the velocity power spectrum of the uncontrolled and controlled flows (both open- and closed-loop conditions). The frequency at which the actuator operates is clearly seen as the small peak at high frequency representing the energy injected by the actuator. Note that, for the open-loop condition, this peak is sharp, while for the closed-loop condition, the peak is broadened due to the amplitude modulation of the actuator signal. However, this energy injection is negligible when compared to the broad reduction in energy in the frequency band associated with the coherent structures which occurs at lower frequencies. In this manner we clearly

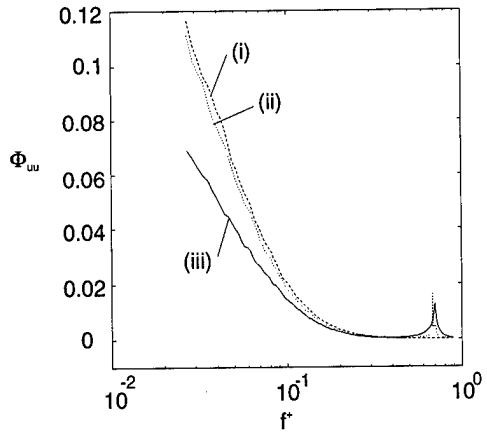

Figure 9: Spectrum of streamwise velocity fluctuations for the uncontrolled (i) , open-loop (ii) and closed-loop (iii) cases. The peak at high frequency is the actuator resonant frequency.

see how the actuator input is rectified by the flow and results in reduced fluctuation energy.

Although these results are shown for the control of u_{rms}, the control scheme is equally applicable to the control of any flow quantity. One particularly important control objective is the reduction of the wall-pressure fluctuations. By replacing the downstream velocity sensor with a wall-mounted pressure sensor, the described procedure (generation of the linear predictive filter and subsequent linear control) was repeated and we were able to achieve 17% reduction in p_{rms}. The decreased efficiency of the system is primarily due to the increased distance between the actuator and the control point (the wall pressure sensor, c_2, was 200 l^*downstream of the actuator, while, in the case of the control of u', the hot-wire was directly downstream of the actuator). This increased separation resulted in a reduced accuracy of both the forward prediction filter, $\hat{H}_1$, and the actuator transfer function, $\hat{H}_2$.

4 DISCUSSION AND CONCLUSIONS

The experimental results clearly indicate that the feed-forward control algorithm described works and is successful in moderating the turbulence intensity in the near-wall region of a fully turbulent boundary layer. The performance of the system is enhanced by the use of pre-conditioned input signals which emphasize the lower frequencies that are associated with large-scale structures. In the current experiments, the detection of large-scale structures is achieved using a conditioned spectral analysis which essentially band-passes the input signals with a filter that is derived by maximizing the coherence between two adjacent wall sensors. Although we see that this works surprisingly well, there is no doubt that improvements in the detection of the large-scale structures can be achieved if one could implement a dynamic recognition algorithm so that large-scale structures can be recognized and isolated in real time (at present they are only recognized in a statistical sense). This improvement requires some understanding of the dynamics of the coherent structures in the near wall region and, if this were available, then an adaptive (Kalman) filter could be implemented which should improve the large-scale detection further. Possible candidates for near wall models include the low-order system proposed by Waleffe [20] or possibly those based on Karhunen-Loève eigenmodes [1]. Waleffe's approach seems at present more appealing since it includes streamwise dependencies which are clearly essential for this application.

Using this technique, we find that we can predict the flow using a *purely linear system* with surprisingly good accuracy over 300 l^*downstream. The accuracy of the forward prediction supports the original hypothesis that the near wall dynamics are, for short times, dominated by linear interactions with the mean shear. Given the success of the forward prediction, the overall success of the scheme, which currently realizes over 30% reduction in turbulent fluctuation intensity, is perhaps not surprising.

This paper represents a summary of research results some of which as been published in Physics of Fluids [19] and presented at 1997 and 1998 AIAA Conferences [18, 4]. The work was supported by the Office of Naval Research, grant N00014-92-J-1918 monitored by Dr. L. Patrick Purtell.

References

1. N. Aubry, P. Holmes, J. L. Lumley, and E. Stone. The dynamics of coherent structures in the wall region of a turbulent boundary layer. *J. Fluid Mech.*, 192:115–173, 1988.

2. J. S. Bendat and A. G. Piersol. *Random Data.* Wiley, 1986.

3. T. R. Bewley and P. Moin. Optimal control of turbulent channel flows. In K. W. Wang, A. H. Von Flotow, R. Shoureshi, E. W. Hendricks, and T. M. Farrabee, editors, *Active Control of Vibration and Noise*, volume DE Vol. 75. ASME, 1994.

4. K. S. Breuer, K. Amonlirdviman, and R. Rathnasingham. Adaptive free-forward control of turbulent boundary layers. AIAA Paper 98-1025, 1998.

5. H. Choi, P. Moin, and J. Kim. Active turbulence control for drag reduction in wall-bounded flows. *J. Fluid Mech.*, 262:75–110, 1994.

6. D. J. Coe, M. G. Allen, M. A. Trautman, and A. Glezer. Micromachined jets for manipulation of macro flows. In *Proceedings of the Solid-State Sensor and Actuator Workshop*, Hilton Head, SC, June 1994.

7. B. D. Coller, P. Holmes, and J. L. Lumley. Control of bursting in boundary layer modes. *Applied Mech. Rev.*, 47(6, Part 2):139–149, June 1994.

8. J. C. R. Hunt and D. J. Carruthers. Rapid distortion theory and the "problems" of turbulence. *J. Fluid Mech.*, 212:497–532, 1990.

9. S. Jacobson and W. C. Reynolds. An experimental investigation towards the active control of turbulent boundary layers. Technical Report TF-64, Stanford University, Department of Mechanical Engineering, 1995.

10. A. V. Johansson, P. H. Alfredsson, and J. Kim. Evolution and dynamics of shear layer structure in near wall turbulence. *J. Fluid Mech.*, 224:579–599, 1991.

11. A. V. Johansson, J. Her, and J. H. Haritonidis. On the generation of high amplitude wall-pressure peaks in turbulent boundary layers and spots. *J. Fluid Mech.*, 175:119–142, 1987.

12. M. T. Landahl. On sublayer streaks. *J. Fluid Mech.*, 212:593 – 614, 1990.

13. C. Lee, J. Kim, D. Babcock, and R. Goodman. Application of neural networks to turbulence control for drag reduction. *Phys. Fluids*, 9(6):1740 –1747, 1997.

14. T. Lorkowkski. Small-scale forcing of a turbulent boundary layer, 1996. Fluid Dynamics Research Laboratory Report 97-1.

15. P. Moin and T. Bewley. Feedback control of turbulence. *Appl. Mech. Rev.*, 47(6):S3 – S5, June 1994. (Part of Mechnaics USA 1994, edited by A.S. Kobayashi).

16. R. Rathnasingham. *System Identification and Active Control of a Turbulent Boundary Layer*. PhD thesis, MIT, Department of Aeronautics and Astronautics, 1997. (MIT FDRL TR 97-6).

17. R. Rathnasingham and K. S. Breuer. Coupled fluid-structural characteristics of actuators for flow control. *AIAA J.*, 35:832–837, 1997.

18. R. Rathnasingham and K. S. Breuer. System identification and active control of a turbulent boundary layer. AIAA Paper 97-1793, 1997.

19. R. Rathnasingham and K. S. Breuer. System identification and control of turbulent flows. *Phys. Fluids*, 9(7):1867–1869, 1997.

20. F. Waleffe. On a self-sustaining process in shear flows. *Phys. Fluids*, 9(4):883–900, 1997.

FLOW MANAGEMENT
USING INHERENT TRANSITION AND RECEPTIVITY FEATURES

Yurchenko, N.F.
Institute of Hydromechanics
National Academy of Sciences, Kiev, Ukraine

Rivir, R.B.
Propulsion Directorate, AFRL/PRTT
Wright-Patterson Air Force Base, Dayton, OH, USA

Abstract - It is shown that the effectiveness of the motion connected with a flow structure in a near-wall region can be naturally improved by manipulation with streamwise vortices. These vorticies represent inherent structural elements of boundary layer, which are strongly affected by body forces. The scales of vortices in boundary layer were analytically obtained under the influence of buoyancy/centrifugal forces. These scales and their location were used for the analysis of the vortex dynamics around a turbine blade. The numerical calculations revealed non-similarity between the shear stress and heat flux and suggested recommendations for the generation and maintenance of vortical boundary layer structures, which will enhance attached flow on the suction surface.

I. INTRODUCTION

Low-pressure turbine blades for both air, and seawater applications usually represent a compromise between a desire to highly load the aft section, to reduce the number of components, and highly loading the aft section resulting in increased sensitivity to separation and the associated efficiency penalties. Low Reynolds number operation at off design conditions or for very small blade dimensions results in enhanced separation on the suction surface which is not accurately predicted. Separation and transition typically might occur at a nominal 60% of axial chord (Ref. 1, 2). Low Reynolds number effects become especially important for the separation problem at chord Reynolds numbers, Re_{ch}<100,000. The low-pressure designs currently employed therefore are far from being optimal for the range of flow conditions encountered.

Optimization of the turbine performance and work should be based on insight into the dynamics of the mechanisms of vortex flows which takes into account the blade geometry (curvature effects) and the operational regimes (flow temperature stratification affected by body forces and Reynolds numbers (centrifugal forces and buoyancy). Possibilities to favorably modify the near-wall vortical structure for given flow parameters are formulated in the frame of the receptivity problem, i.e. The boundary layer's response to controlled excitation may be studied in terms of its receptivity to the possibility of favorably modifing the near wall vortical structures. The receptivity formulation provides the specification of the appropriate boundary layer control techniques.

The inherent feature of flows effected by body forces is the development of secondary flows in a form of the large-scale boundary layer structure, or streamwise counter-rotating pairs of vortices. The vortex dynamics of these flows can therefore be used naturally for manipulation and optimization of the attachment of separated flows.

The general objective of the present work consisted of fundamental studies of the development and control of boundary layers under body forces, as well as the application of these results to control flows on the suction surface of turbine blading at low Reynolds numbers. The objective was to examine the boundary layer structure over a turbine blade taking into account centrifugal effects and then application of this information to develop recommendations related to the generation and maintenance of a stable vortical flow structure that is optimal from the viewpoint of hydraulic losses.

Generally, these recommendations should concern both the suction, and pressure sides of the blade. They should include the possibilities to modify both the blade shape and its surface using special techniques (e.g. riblets or organized surface roughness). These techniques should stimulate and maintain a favorable boundary layer vortical structure to delay flow separation on the suction surface.

II. THEORETICAL BACKGROUND

The flow geometry over a turbine blade surface involves both signs of curvature, which are varying with axial chord location. The computation needs to address boundary layers as they are effected by centrifugal forces or, for the more general case, by body forces (centrifugal forces and buoyancy). Gõertler stability of boundary layers over concave surfaces (e.g., Ref. 4, 5) along with the stability of thermally stratified flows represents the state of the art of the problem for the turbine blade application using traditional approaches.

E. Nikiforovich, Ref. 7, in a more general approach, which is different from the known stability theories, naturally accounts for the combined effect of all body forces in a flow (Ref. 6, 7). Theoretically this approach is based on the asymptotic analysis of the full Navier-Stokes equations using a small parameter explicitly depending on body forces. In case of centrifugal forces only this small parameter is

$$\varepsilon = Re_R^{-1} \tag{1}$$

where Re_R is the Reynolds number ($U_\infty R/\nu$) based on the radius of curvature, R.

Estimates for spatial-temporal vortical scales in a boundary layer are given from this analysis in terms of the basic flow parameters. The analysis has shown that the longitudinal vortices, as an essential flow structural feature, originate from the interaction of two vorticity sources (one due to viscous and one due to centrifugal forces) when their intensities become comparable at a certain downstream distance

$$X_0 = A\, R\, Re_R^{-1/3} \tag{2}$$

where A is a constant. The minimum spatial scale in normal and spanwise directions for these longitudinal vorticies is,

$$L_0 = R\, Re_R^{-2/3} \tag{3}$$

A similar analysis was carried out for the case of buoyancy, with the small parameter, $\varepsilon=\beta(T_s-T_o)$, where β is a coefficient of volumetric thermal expansion, T_s and T_o are correspondingly surface and mean flow temperatures. The normal spatial scales of these buoyancy driven vortices and the downstream location of their formation are again expressed in terms of the basic flow parameters.

Experimental results have been obtained for a transitional boundary layer over a concave surface (Ref. 4) which matches both of the theoretical approaches and the physical mechanisms as interpreted by the theoretically deduced values of scale (Ref. 6, 7).

III. RESULTS

Preliminary experiments (Ref. 2) on riblets applied to a blade in a turbine cascade with turbulence levels to 8% showed a 6-8% decrease in average blade heat transfer from riblets which were scaled for the maximum curvature location. Although skin friction was not measured directly, it was assumed to follow heat transfer. The turbulence scale was much larger than the riblet spacing. It would normally be expected that this level of turbulence would dominate any effect the riblets might have. However the micro surface effects of riblets appear to alter macro free-stream flows and offer the possibility of passive boundary layer control due to the induced longitudinal vortices. Therefore the problem obviously needs more physically deep and mathematically rigorous investigation.

The two-dimensional equations of a stratified boundary layer together with continuity and thermal conductivity equations were solved numerically using a finite-difference method. The calculations showed the important role of body forces in affecting the laminar-turbulent transition process and the boundary layer characteristics, in particular, the effects on the velocity and temperature profiles. It was found that buoyancy

essentially influences downstream distributions of heat flux, Q(x), and shear stress, F(x). Figure 1, where T_s and T_e are correspondingly the surface and the free-stream temperature, shows the non-similarity between these distributions. This observation can be used for heat transfer optimization. The inherent flow structure which develops under body forces appears to be advantageous from the viewpoint of heat transfer enhancement: heat flux grows faster downstream than does the shear stress as streamwise vortices appear in a boundary layer.

However, to apply this basic result to the case of turbine blade flow optimization, the spatial scales of naturally developing streamwise vortices over the turbine blade should be measured and compared against the theoretical model. Comparison of the boundary layer's experimentally observed receptivity to the artificially generated disturbances of this type also needs to be documented.

Liquid crystal visualization made it possible to observe longitudinal vorticies on the pressure surface of a Langston 2D cascade that is described in Ref 8. The blade shape defines the geometry for the flow. The pressure surface had a radius of curvature varying from the leading edge of R= 1.59mm - 6.35mm, increasing through R~25.4mm. The aft section increased to R=305mm. The chord Reynolds numbers ranged from Re_C=50,000 to 300,000. The experimentally observed structure had a spatial scale of λ_z=0.8 mm at Re_C=67500. These structures were initiated at the location $x_0/c \approx 0.2$-0.7 (chord, c=178mm).

These experimental results were processed and analyzed using the relationships of equation (2) and (3). The x_0/c calculated value of the non-dimensional downstream distance where the streamwise vortices should appear, under given experimental conditions, was checked for 3 values of curvature radius, R=17.8mm, 127mm and 305mm, for Re_C = 100,000 and 67500. The calculated value showed good agreement between the observed experimental values (x_0/c=0.2). According to the theory (Ref. 7), $\lambda_z = 8L_0$ where L_0 is a vortex spatial scale normal to the velocity vector. The scales, L_0, of the streamwise vortical structure expressed in terms of the basic flow parameters were calculated and found to be L_0=0.1mm for R=127mm, Re_C=67,500; L_0=0.09 mm for R=127mm, Re_C=100,000; L_0=0.12 mm for R=254mm, Re_C=67,500. These calculations of L_O all show good agreement (calculated λ_z =8mm, 7.2mm, 9.6mm,) with the experimentally observed value of λ_z=0.8 mm.

Gõertler theory was used to interpret the experimental data and to establish its correlation with the above theoretical approach. The well-known centrifugal stability diagram is useful to interpret the amplification rates of streamwise vortices with various scales which evolve in boundary layers as a function of the Gõertler number $G = U_0 \delta_2^{3/2} \nu^{-1} R^{-1/2}$. Vortices described by the non-dimensional wavelength, $\Lambda = \lambda_z^{3/2} U_0 / \nu R^{1/2} \approx 39$, are neutral, i.e. have a zero amplification rate for a wide range of Gõertler numbers. Larger scale vortices are described in the Gõertler diagram by the straight lines of Λ = constant > 39. It is interesting to check where the experimentally observed vortices are located on the diagram. This estimation was made for the 8 mm scale vortices from the expression $\Lambda = \lambda_z^{3/2} Re_C / c R^{1/2}$, for R=127mm, Re_C=67,500 it was found that Λ = 24, and for R=127mm, Re_C=100,000, Λ = 36.

This means that the streamwise vortical structure which appears in the boundary layer of a low pressure turbine blade cascade is of a neutral type, i.e. neither amplifying, nor decaying in a downstream direction. This flow structural feature can be used to keep a thermodynamic balance in the boundary layer using different methods of boundary layer control. In the controlled case, it is essential to maintain the favorable vortical structure as long as possible. This mechanism can be observed and exploited in the receptivity problem.

The receptivity investigation of a boundary layer effected by body forces was carried out by the generation of regular systems of longitudinal vortices using special vortex-generator arrays mounted transversely on the test surface. The boundary layer response was analyzed as a function of the spatial scale of vortices, λ_z, and the Reynolds number of the flow.

Flows with buoyancy were also investigated in a closed wind tunnel with a test section of 2.85x0.30x0.30m (Ref. 9) at a free-stream velocity, U_0=10 m/s or 20 m/s. The test section plate consisted of conducting foil surface which was heated electrically to maintain a temperature difference with the free-stream of T_s-T_e=20°. The foil was insulated on the backside to provide a constant heat flux surface to the flow. The local surface temperature distribution was measured using flush mounted thermocouples.

The detailed description of these experiments in boundary layers effected by centrifugal forces is given in (Ref. 4). Figures 2 and 3 illustrate the boundary layers reaction to the longitudinal vortices induced with different λ_z scales at different downstream x_0 locations. The preferable values of both parameters to enhance heat transfer may be obtained from these figures. The general idea of utilization of natural flow dynamics and boundary layer control based on the generation of inherent vortical structure is seen to be possible and the validity of the (Ref. 6, 7) theory has been demonstrated in a flow under the influence of body forces.

Simple calculations of the scale of longitudinal vortices and a downstream position of their natural formation can be made for given flow conditions. An appropriate tool for boundary layer control (vortex generators, riblets, roughness elements, etc.) may then be employed to generate vortices of the estimated scale and location. Figure 4 illustrates experimental evidence of the favorable role of longitudinal vortices to delay boundary layer separation under the adverse streamwise pressure gradients.

IV. CONCLUSIONS

Calculated spatial scales of the vortical flow structure over a turbine blade for the given test conditions using the theoretical relationships of (Ref. 9) are in a good agreement with the observed experimental data. Gõertler stability analysis showed a neutral character of regular vortices in a turbine blade boundary layer. The non-similarity between heat and momentum fluxes in boundary layers effected by buoyancy was numerically shown. This mechanism gives the basis to optimize heat transfer using streamwise vortices as naturally occurring flow structures. The effectiveness of boundary layer control, in a form of heat transfer enhancement, depends on the receptivity of a boundary layer to streamwise vortices, that its selective response to the spatial scale of the generated vortices and the downstream location of their formation. Stimulation and maintenance of streamwise vortices corresponding to the requirements of flow optimization can result in the delay of the flow separation on a suction surface of a turbine blade.

V. REFERENCES

1. J. W. Baughn, R. J. Butler, A. R. Byerley, R. B. Rivir "An Experimental Investigation of Heat Transfer, Transition and Separation on Turbine Blades at Low Reynolds Number and High Turbulence Intensity", ASME International Engineering Congress And Exposition, San Francisco, CA, Nov 1995.

2. R. B. Rivir, P. A. Maciejewski "The Effects of Free Stream Turbulence and Surface Riblets on Heat Transfer in a Linear Cascade", International Gas Turbine Institute, Hague, Netherlands, ASME 94-GT-245, June 1994.

3. E. I. Nikiforovich, N. F. Yurchenko "Vortical Flows - Properties and Analogues" (in Russian), Hydromechanics, Kiev, Ukraine, *70*, pp. 131-154, 1996.

4. N. F. Yurchenko, V. V. Babenko, L. F. Kozlov "Development of Three-Dimensional Disturbances in Transitional Boundary Layers", Proceedings of the IUTAM Symposium on Laminar-Turbulent Transition, Novosibirsk, pp. 329-335, 1984.

5. W. S. Saric "Goertler Vortices", Annual Review of Fluid Mechanics, *26*, pp. 379-409, 1994.

6. E. I. Nikiforovich, R. B. Rivir, N. F. Yurchenko "Kinematic Similarity of Flows Developing Under Body Forces", 8th Taylor-Couette Workshop, Boulder, Colorado, 1995.

7. E. I. Nikiforovich, N. F. Yurchenko "Boundary-Layer Flows with Centrifugal Forces", ERCOFTAC Bulletin, *32*, pp. 61-65, March 1997.

8. S. T. Walsh, D. N. Barlow, R. J. Butler, K. W. VanTreuren, A. R. Byerley, J. W. Baughn, R. B. Rivir, "Effect of Passive and Active Air Jet Turbulence on Turbine Blade Heat Transfer," International Gas Turbine Institute, Orlando, Florida, ASME 97-GT-131, June 1997.

9. N. F. Yurchenko, A. A. Pedishius, G. P. Zygmantas "Boundary Layer Receptivity and Heat Transfer Enhancement" (in Russian, abstract in English), Engineering-Physical J., 56, pp 916-924, 1989.

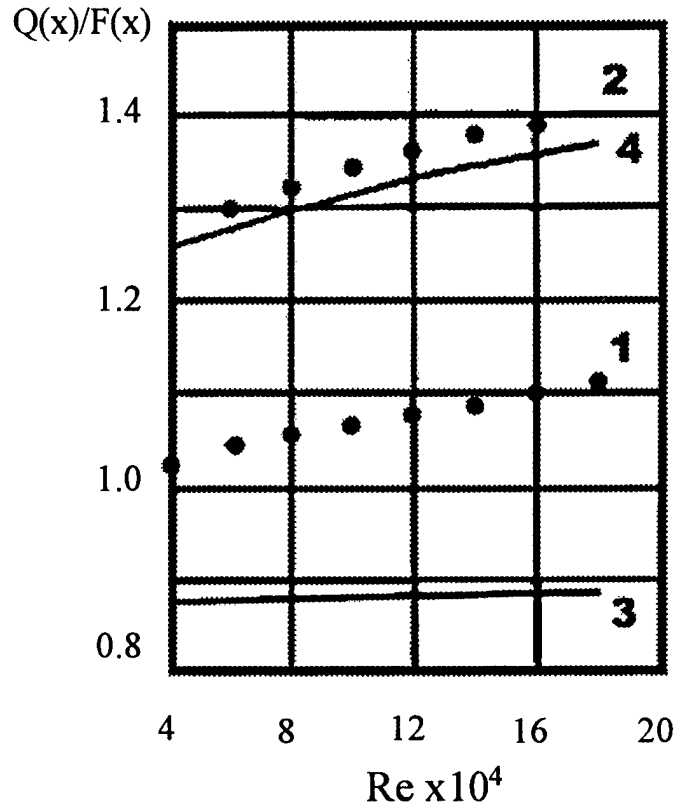

Fig. 1. Downstream variations of a heat flux related to the shear stress Q(x)/F(x) in flows with buoyancy for Ts>T0, Pr=0.7 (1), Pr=7.0 (2) and without buoyancy for Pr=0.7 (3), Pr=7.0 (4).

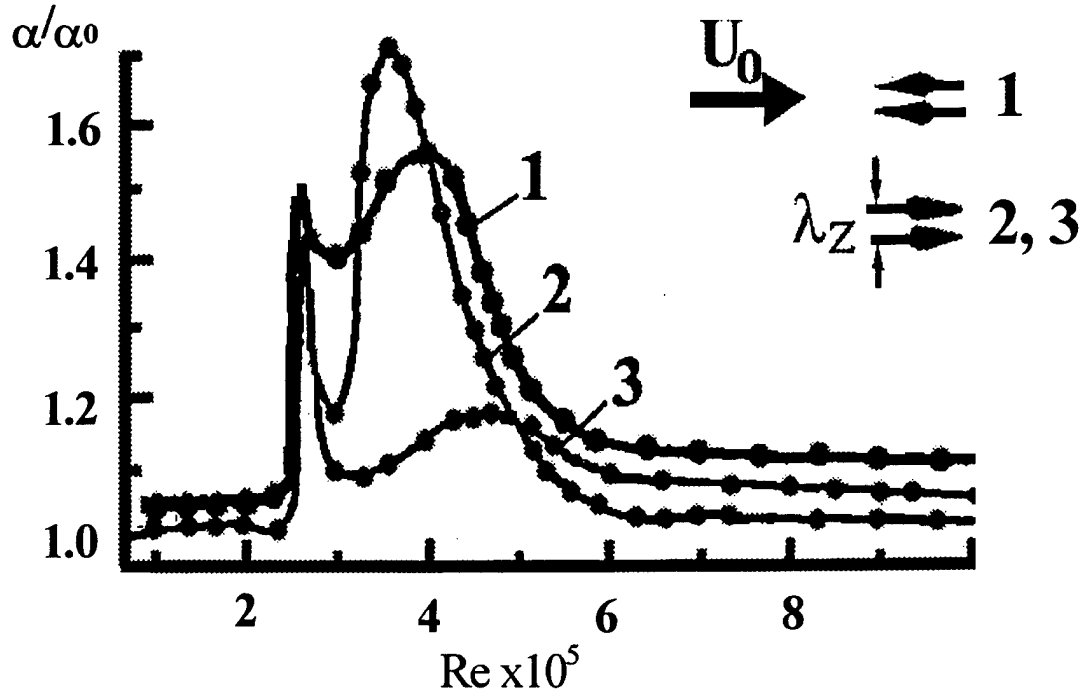

Fig. 2. Heat transfer variation vs Re in a boundary layer disturbed by the vortex generators of different shape: 1 - λ_z=1.5 cm, 2 - λ_z=1.5 cm, 3 - λ_z=1.8 cm.

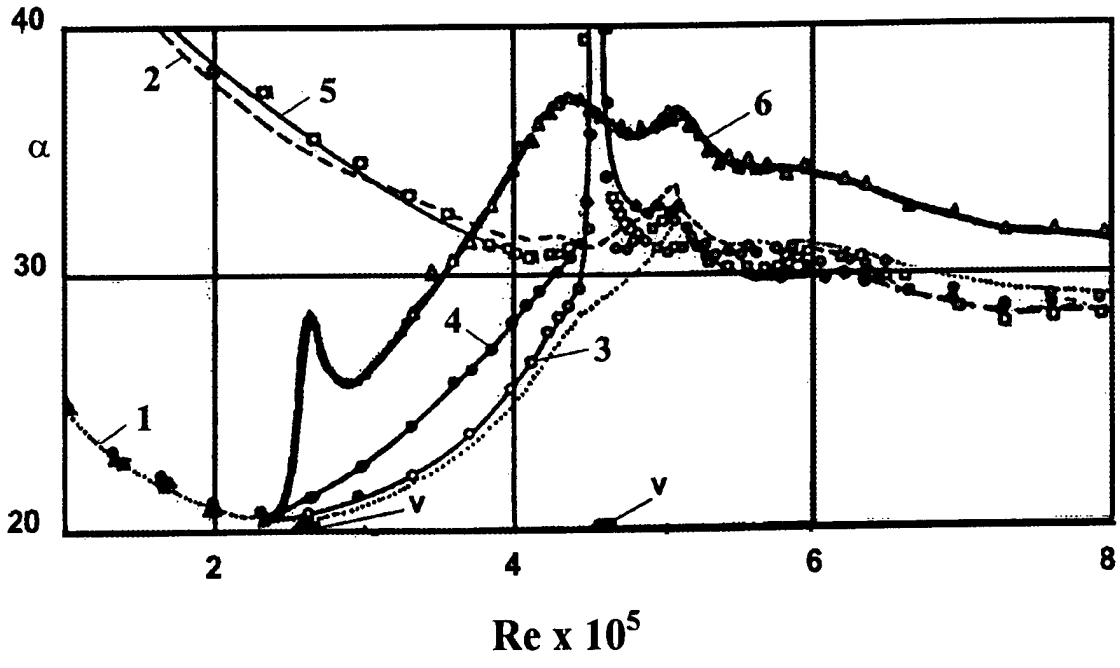

Fig. 3. Heat transfer variations along a heated flat plate depending on a streamwise position x_0 of vortex generators
1, 2 - reference measurements for the natural laminar-turbulent transition and for the tripped boundary layer;
3 - a single vortex generator; 4, 5, 6 - vortex generation with λz=1.5 cm; 2, 5 - tripped boundary layer;
V - position of vortex generators

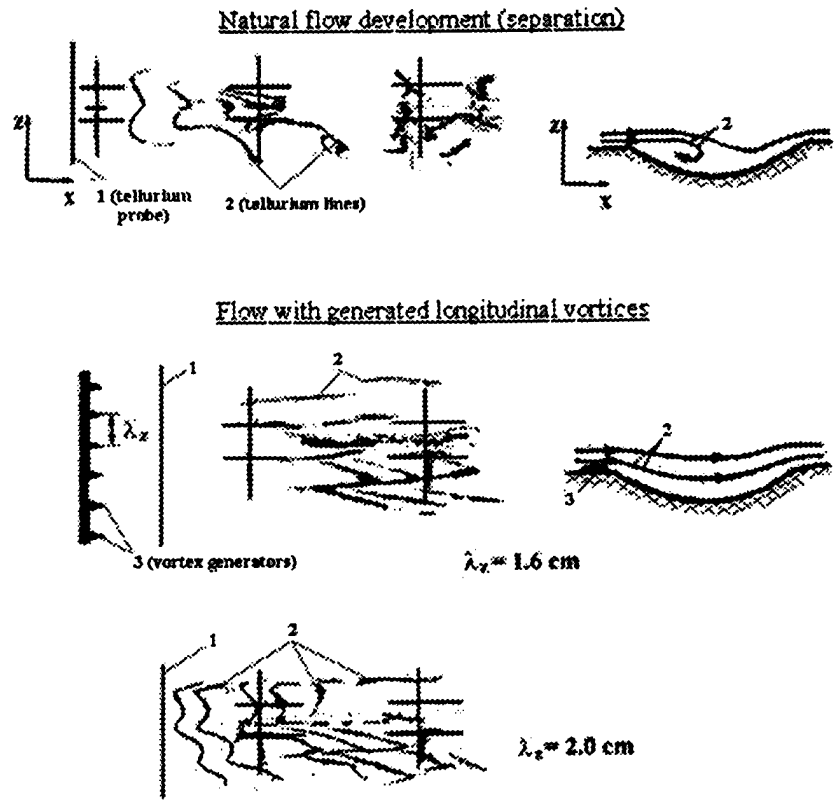

Fig. 4. Influence of longitudinal vortices on a water flow with unfavorable streamwise pressure gradient
(over the surface with a concave section: R=1m, U_0=4 cm/s, x=0.6 m)

Seawater Physics

IN-SITU ESTIMATION OF THE ABUNDANCE AND SIZES OF PARTICULATES IN THE SEA

D.V. Holliday
Tracor Aerospace
4669 Murphy Canyon Road, #102
San Diego, CA 92123-4333
holliday@galileo.tracor.com

Abstract - The speed threshold at which turbulent flow near a boundary is initiated can be modified by the presence of particulates in the fluid. In sea water, much of the particulate mass is due to either living organisms or detritus with a biotic origin. Advances in acoustical technology have resulted in the availability of new information on the abundance, size spectra, patchiness and temporal variability of distributions of zooplankton and micronekton in the open sea and in the littoral zones of the world's oceans. This contribution includes an overview of this measurement technology, the instrumentation, and descriptions of several modes in which such sensors have been deployed to estimate particulate abundances by size. A brief description is provided of the mathematical method used to transform acoustical scattering measurements at multiple, high, acoustical frequencies, i.e., frequencies spanning a range from one hundred kilohertz to ten megahertz, to estimates of particulate abundances, their sizes and their physical characteristics. Recent advances in applying inverse theory to this problem allows separation of particulates into different types. Data illustrating the spatial and temporal distributions of zooplankton abundance and its variability are presented for a variety of geographic locations.

I. INTRODUCTION

A transition from laminar to turbulent flow near a boundary can be triggered by a near-encounter of volume inhomogeneities in the fluid with the boundary. In specific situations, very fine airborne particles with a terrestrial origin (dust and sand) sometimes contribute to the abiotic part of the marine particle field, as do resuspended sediments in very shallow water, turbidity flows across the shelf, sediment-laden fresh water outflows from rivers and such nearshore phenomena as rip tides. However, in general, most particulates in the marine environment have a local biotic origin. Living plants (phytoplankton) and animals (zooplankton and micronekton) are major contributors to a highly variable size-abundance spectrum of particulates in the ocean. Detritus (dead or decaying plants, whole animals, animal parts, and fecal pellets) also contribute to the total spectrum of volume inhomogeneities in the marine water column.

The spatial distribution of particulates in the marine environment is heterogeneous (patchy and layered) in both horizontal and vertical dimensions. In the horizontal, scales of patchiness range from less than a meter to hundreds of kilometers. In the vertical dimension, scales of heterogeneity range from centimeters to hundreds of meters (Figure 1).

Particulates in the ocean are also characterized by a widely variable temporal spectrum, with changes in local abundances and spatial pattern ranging from minutes, through daily, seasonal and annual cycles, to decadal or longer. The correlations and coherences between these temporal variations and possible "driving" phenomena in ocean physics, such as the depth of the pycnocline, fine-structure in temperature and salinity, mixing, turbulence, fronts, gyres and internal waves have been the subject of numerous studies during the last decade.

The abundance of particulates in the sea also varies with the sizes of the particles. Even in the least productive parts of the "blue water" ocean, millimeter size particulates often number in tens to hundreds per cubic meter. Densities can reach tens of millions per cubic meter, or more, in layers and patches. There is often a trend towards higher abundances in the biologically productive littoral or coastal zone.

II. PREDICTION, REMOTE AND *IN SITU* ESTIMATES OF PARTICLE ABUNDANCE

Measurements of the spatial and temporal distribution of phytoplankton from satellites with ocean color capabilities (e.g., SeaWifs) are now common for the upper tens of meters, but much of the phytoplankton biomass is subsurface and is often distributed in a complex of layers near or below the thermocline. Further, the standing stock of phytoplankton (measured by satellites) is not necessarily a good analog for the standing stock of zooplankton, micronekton, or larger animals. At depths of 50 or 100 m, depending on the local optical extinction depth, particularly in the littoral zone, satellite estimates of phytoplankton abundance can often be problematic.

Attempts to model and predict the distribution and dynamics of marine life at levels in the food web above the primary producers (phytoplankton) will, at best, currently provide only strategic (long term, large scale) information about the particulate field in the sea.

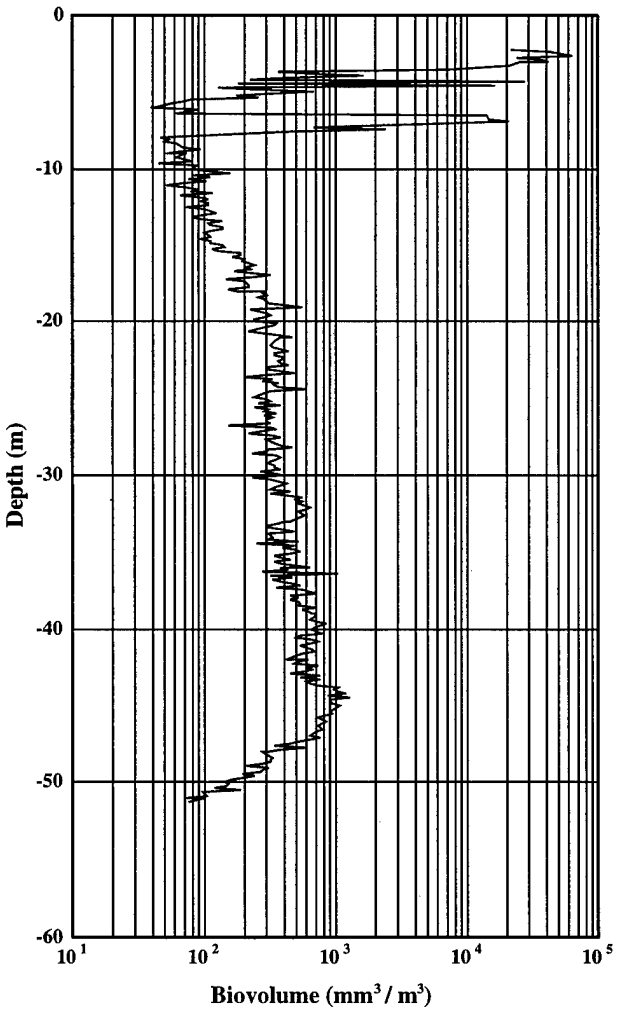

Figure 1: Vertical distribution of zooplankton at a station 15 km off southern California in June 1996. Seventy eight percent of the biomass was in a complex of thin layers above 9 m. *Calanus pacificus* adults were the dominant zooplankters in the upper 10 m.

Existing models, whether based on first principles (e.g., upwelling, nutrients, phytoplankton blooms, zooplankton growth and reproduction) or on correlations or coherences with readily observed parameters, such as sea surface temperature or ocean color, do not yet provide reliable information at tactical (short term, local area) scales. There has been progress during the last decade in the prediction of changes in vertical distribution and in overall abundance on seasonal time scales at larger spatial scales. However, in a wide sense, small scale and short term prediction of pattern and change at secondary and higher levels in the food web are not yet ready for application at tactically useful scales of time or space. Because animals, from sub-millimeter size zooplankton to large nekton, have the option to make choices in response to their physical and food environment, one can not count on much small-to-medium scale coherence between phytoplankton distributions and the spatial or temporal pattern of the higher trophic levels. Plankton actively react to their local environment, changing their locations in the water column to optimize growth and reproductive strategies in response to a variety of stimuli and conditions, many of which have not yet been identified. The word "plankton", derived from the Greek word for "drifter", should be taken rather lightly, at least in the vertical dimension. Even millimeter-sized zooplankton often migrate vertically tens of meters in response to light or food cues. Larger "plankton", a few centimeters in length, which we sometimes categorize as micronekton (e.g., euphausiids) routinely migrate hundreds of meters in the vertical.

We presently have no reliable means to measure or infer the distribution of zooplankton or micronekton with remote satellite sensing. If one wishes to know the sizes, abundances and distributions of particles in the marine environment on small scales, at a specific time and place, there are currently only two viable approaches. Both involve direct measurement. One is optical, the other is acoustical. Optical particle counting (OPC) is a field in transition from experimental to routine application. Holography, another optical method, remains experimental, but holds promise for examining small (cm scale) fields in great detail. In the epipelagic zone, many animals are transparent, giving them a significant advantage in survival in an environment that provides few places to hide. While this does not eliminate optical methods, this transparency does often limit their effectiveness. Acoustical methods are based on the contrasts between the density and compressibility of the animal's bodies and the surrounding sea water. Even nearly neutrally buoyant organisms, such as chaetognaths and jellies (e.g., doliolids, medusae) have sufficient compressibility contrast with the water around them to allow their detection. In addition, many such "soft bodied" animals eat crustaceans, which can be acoustically detected as gut contents. At this particular point in the development of sensing methods, an acoustical methodology seems to have some advantage over optical methods, especially for remote sensing at distances of several meters. Therefore, the following discussion focuses on the relevant acoustical methods.

III. ACOUSTICAL DETECTION AND CHARACTERIZATION OF PARTICLES

During the last decade there have been substantial technology-based advances related to acoustical observations of millimeter-sized marine particulates, especially for zooplankton. Laboratory and *in situ* measurements of scattering from a variety of marine taxa (Greenlaw, 1977; Pieper and Holliday, 1980; Holliday and Pieper, 1984; Medwin and Clay, 1998, pp. 391-402; Stanton, *et al* 1998) have led to the development of a variety of mathematical models for acoustical scattering with frequency, particle size and shape as parameters (Greenlaw, 1977; Pieper and Holliday, 1984; Holliday, 1987; Holliday, 1992; Stanton *et al*, 1998a; Stanton *et al*, 1998b; Stanton *et al*, 1998c). Both measurement and modeling reveal a consistent, non-monotonic dependence of acoustical scattering on both particle size and the frequency of ensonification.

This complexity in scattering from small marine zooplankton has major implications in the quantitative acoustical assessment of their size-abundance spectra as well as of the total biomass. Measurements of acoustical scattering at a single, discrete frequency can lead to major errors in estimation of the abundance and size of particles. An increase in scattering can occur under reasonably common circumstances as a result of lower numbers of smaller particles. Likewise, a decrease in scattering can result from the presence of larger numbers of larger particles. Thus, *spatial distributions and temporal changes in acoustical scattering at a single, discrete frequency can* ***not*** *be reliably interpreted in terms of parallel changes in abundance or sizes of small zooplankton or micronekton.* Similar models, and conclusions, apply to detrital particles with biotic origins and to abiotic scatterers such as sand or resuspended sediments. On the other hand, the same characteristics that prevent us from easily interpreting volume scattering at single frequencies allow us to extract both size and abundance estimates from multi-frequency scattering measurements.

IV. MULTI-FREQUENCY METHODS

Though it is more complex in practice, for reasons discussed in Holliday (1977), the successful transformation of acoustical volume scattering strength measurements to estimates of the size-abundance spectra or biomass spectra for marine particulates is in principle very straightforward. There are several basic assumptions (Holliday and Pieper, 1995), which must be met, the most important of which are that the frequencies used must span the transition from Rayleigh to geometric scattering for all of the sizes of particles that are contributing to the scattering and that we be able to quantitatively describe the dependence of the backscattered sound on the acoustical frequencies used and on the morphology (size, shape and physical characteristics, such as the density and compressibility contrasts between the water and the particles that cause the scattering.

While one can easily generalize to several kinds of scatterers, e.g., bubbles, small crustaceans, elastic particles such as sand grains, or zooplankton with shells or exoskeletons (e.g., some gastropods and pteropods), elongate scatterers such as euphausiids or shrimps, and perhaps even larval fish, for simplicity, we will restrict our discussion in this overview to just two kinds of particles, say small crustaceans and resuspended sand. Models that, at least to first order, describe the reflectivity (target strengths) from each of these kinds of particles can be found in the literature (Holliday, 1992; Holliday 1987). While more complex models are available for some taxa, in the absence of good *a priori* information on their presence, small crustaceans (e.g., copepods) tend to dominate high frequency sound scattering in most locations and are generically relatively well described by the truncated fluid sphere model (Pieper and Holliday, 1984; Holliday, 1992). If *a priori* information is available regarding the taxa which are present, and if more precise or better models are available for those taxa, then those can and should be used. It should be stressed that one must consider all of the species or taxa that contribute to the scattering, not just the ones of specific interest in the study being undertaken.

The acoustical volume scattering strengths (S_{V_i}) at each frequency, indexed by i, from a mix of two kinds of particles can be written as:

$$S_{V_i} = \sum \sigma_{ij}' n'_j + \sum \sigma_{ip}'' n''_p, . \qquad (1)$$

where j and p are size indices for each scatterer type. The first sum is over j and the second over p. The terms n'_j and n''_p are the respective particle abundances for the two scatterer types at each size. The terms σ_{ij}' and σ_{ip}'' represent the mathematical models that describe and quantify the acoustical backscattering dependence on frequency and size for each type of scatterer.

Equation 1 represents a set of linear equations whose solution is:

$$[n' n'']^T = [\alpha^T \alpha]^{-1} \alpha^T [S_V], \qquad (2)$$

where $\alpha = [\sigma' \sigma'']$. $[S_V]$ represents a column vector whose elements are the volume scattering strengths at each frequency.

In practice, because one cannot make completely noise free estimates of volume scattering strengths, one must constrain the individual elements of the abundance vector to non-negative values. Application of these constraints and additional examples of the use of multi-frequency acoustical methods in bioacoustics, along with a discussion of many of the assumptions employed, can be found in Holliday and Pieper (1995) and in Medwin and Clay (1998), Figures 4a and 4b, and pp. 462-465. An overview of the inverse method used to transform acoustical volume scattering strengths at multiple

frequencies to estimates of zooplankton biomass size spectra is also described in Medwin and Clay (1998), pp. 461-462. Additional details can be found in Holliday (1977) and in Greenlaw (1979).

V. INSTRUMENTATION AND MODES OF DEPLOYMENT

In plankton bioacoustics, the 1990's have been characterized by a transition from experimental, prototype zooplankton acoustics sensors such as the Multi-frequency Acoustical Profiling System (MAPS™) to the less complex, more "user-friendly" Tracor Acoustic Profiling System (TAPS™). The twenty one frequency MAPS™ was designed for research into the details and character of acoustical scattering at high frequencies (100 kHz to 10 MHz) and allowed description of the scattering in sufficient detail to quantify the processes which define scattering from many kinds of small zooplankton at high frequencies. The TAPS™ series of instruments was evolved from this detailed understanding of the multi-frequency scattering process for small zooplankton. Although the smallest sizes are not as well quantified and less size resolution is available than was the case with 21 frequencies, the current generation of TAPS™ systems are more affordable and much more easily deployed and operated by the interested user community. As a consequence, they are much more widely used than the technically more capable, much more complex MAPS™ could have ever been.

With the introduction of the TAPS™, which operate in a band extending from 265 kHz to 3 MHz at four, six or eight frequencies, depending on the size resolution desired, the available modes of deployment have been greatly expanded from the original "cast mode only" methods used widely in the 1980's (e.g., along with a CTD from a ship). Additional operating modes now include towing on various net frames (e.g., MOCNESS and large trawls); underway to-yo profiling (e.g., the SeaSoar™ data of Figures 2 and 3), use as a downlooking multi-frequency echo sounder; deployment in an inverted echo sounder mode at a fixed location on the bottom (Barans, *et al*, 1997); and long term use at discrete depths on a mooring, with telemetry to shore or internal data recording, depending on the location. In some bottom mooring, profiling modes, vertical resolutions of the water column can be as fine as ca 12.5 cm in depth, with complete multi-frequency profiles every two minutes (Greenlaw, *et al*, 1998). The data rate is largely limited by communication bandwidths and could be substantially increased (e.g., to a few seconds).

Advances have also been made in both the mechanics and the methodology used to transform acoustical scattering data to estimates of crustacean biomass and elastic scatterers. These calculations are usually termed "inverse" calculations, to distinguish them from the "forward" calculations in which volume scattering is calculated from

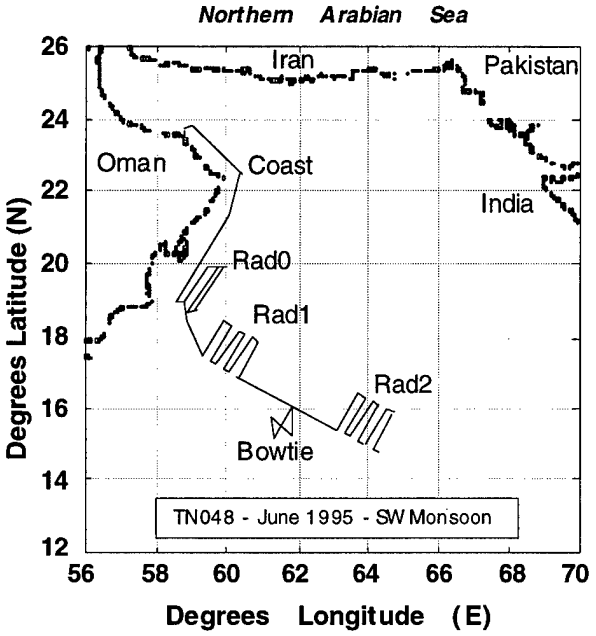

Figure 2: Cruise track for the TAPS™ SeaSoar™ deployment during the ONR ARI on Upper Ocean Atmospheric Forcing (TN-048) in the Arabian Sea during the southwest monsoon in July 1995.

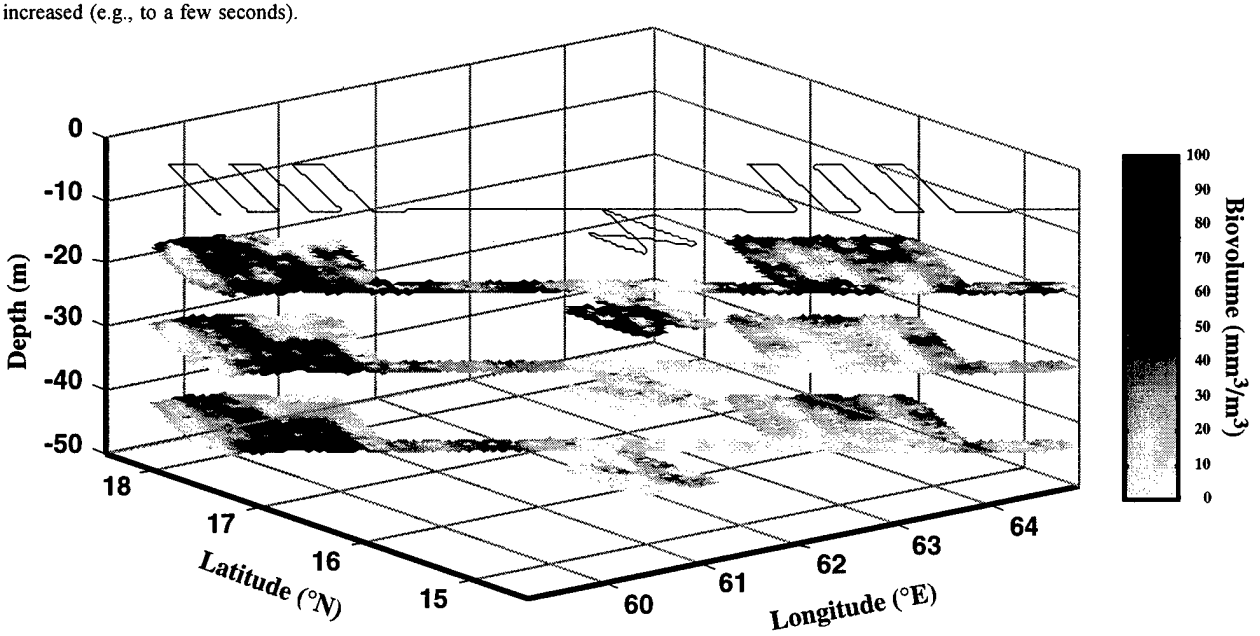

Figure 3: Horizontal distributions at several discrete depth strata (12.5 m, 25 m and 37.5 m) for zooplankton biomass of animals with sizes between 0.50 and 0.75 mm Equivalent Spherical Radii (ESR). The ESR is the radius of the sphere which would contain the actual volume of the individual zooplankters. The size range displayed here includes several species of adult copepods, e.g., *Eucalanus, Rhincalanus, Euclirella and Euchaeta.* The data were derived from volume backscattering at six frequencies (265, 420, 700, 1100, 1850 and 3000 kHz). Numerical abundance was estimated, by size, for the volumes ensonified by the TAPS™ and biovolumes were computed. The gray scale represents biovolume (mm^3/m^3), an analog of displacement volume, and is directly related to the zooplankton biomass in the indicated size range.

estimates of the sizes and abundances of animals present. MATLAB™ m-file code is available to make the inverse transformations and to display the results. This code can be executed on a number of widely available computers.

VI. DATA AND EXAMPLES

Large scale measurements with TAPS™ on a SeaSoar™

As a part of the ONR ARI on Upper Ocean Atmospheric Forcing, a TAPS-6™ was deployed on several SeaSoar™ cruises in the Arabian Sea, including one during the southwest monsoon (TN-048) in July 1995. This program was a part of a coordinated effort to study the effects of monsoons on the biological productivity of the northern Indian Ocean and involved scientists working within the context of the ONR study, US JGOFS and US GLOBEC. The cruise track involved several transects and "radiator grid" patterns as illustrated in Figure 2. The TAPS™ was to-yo'ed repetitively to depths of several hundred meters at intervals of about 10 minutes. Volume scattering measurements at six frequencies were binned into 12.5 m bins in the vertical. The transformation of these measurements to zooplankton biovolume revealed a complex horizontal and vertical distribution of biomass (Figure 3). For clarity of presentation, data from only three depth bins are illustrated. In some, but not all locations, there were correlations of varying strengths at larger scales with the local physical oceanography, as observed with satellite and shipboard sensors.

Small scale measurements in a cast mode

Six frequency TAPS™ data were collected at the BITS pilot mooring site about 15 km off the southern California coast in June 1996. A close examination of the total biomass profile (Figure 1) reveals the presence of at least four thin layers above the seasonal thermocline. The thermocline at this station was between about 18 and 20 m. Fluorescence, an indication of chlorophyll A in phytoplankton, exhibited a broad peak starting near 18 m and extending to about 50 m. The chlorophyll maximum was near 30 m. These data were originally processed with one quarter meter depth resolution. Additional data from this profile, including the detailed temperature and fluorescence profiles can be examined in Holliday, *et al* (in press, 1998). The shallowest layer, which peaked at ca 3.25 m, contained 63.5% of the total water column biomass above 50 m. Two very thin layers, which were not resolved and appeared to be a single layer with 0.25 m depth resolution, occurred near 4.5 m and encompassed 6.5% of the biomass at this location. A fourth layer, between 6.5 and 7.5 m contained another 8.4% of the biomass. Together, these four structures accounted for over 78% of the zooplankton biomass at this station. Direct, conventional net sampling, with a MOCNESS, revealed that various stages of a small copepod, *Calanus pacificus*, were the dominant scatterers in these layers. The size-abundance spectrum for each of these layers differed. An assemblage of small copepods (0.050 to 0.500 mm ESR) were distributed over a wider range of sizes at 2.6 m than in the layer near 7 m, where a single size dominated in the small size classes. Animals with sizes between 3.019 and 3.653 mm ESR occurred in the 7 m layer, but did not appear in the 2.6 m layer (Figure 4). While there were similarities in size structure, differences were also evident in the size-abundance compositions of the two thin layers near 4.5 m (Figure 5) and at depths near the top and bottom of the chlorophyll maximum layer (Figure 6).

Separating multiple scattering types into size-abundance spectra

In November 1995, TAPS™ data were collected at five frequencies near the crest of Georges Bank, where the water is about 40 m deep. Nearby, underwater sand dunes contribute sand to the water column during periods of high tidal currents. The size-abundance spectra at 5.5 m were extracted from the volume scattering data at this location for small crustacea (left panel, Figure 7) and elastic scatterers (middle panel, Figure 7). The acoustical scattering spectrum for each of these two scattering types and the dashed line in the rightmost panel illustrates the contribution of the sand to the acoustical scattering spectrum.

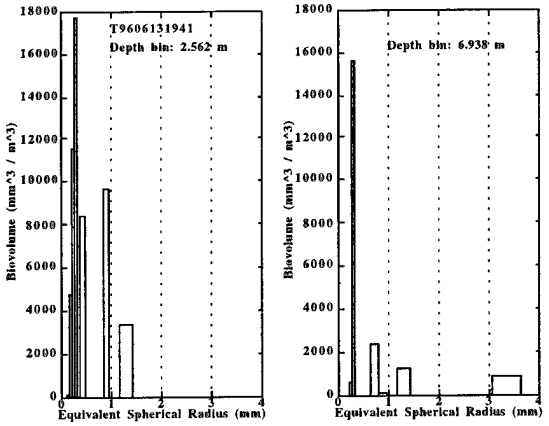

Figure 4: Acoustically estimated size-abundance spectra for two thin layers detected with the TAPS™ off southern California in June 1996. The station was located just inshore of the shelf-slope break about 15 km SSE of the Los Angeles - Long Beach harbor entrance.

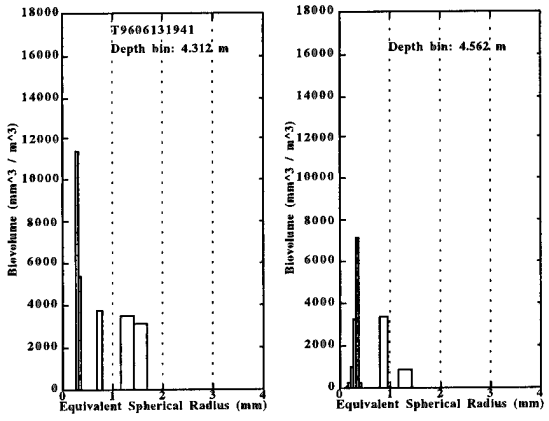

Figure 5: Size-abundance spectra for zooplankters in two very thin layers separated by only 0.25 m, near 4.5 m depth.

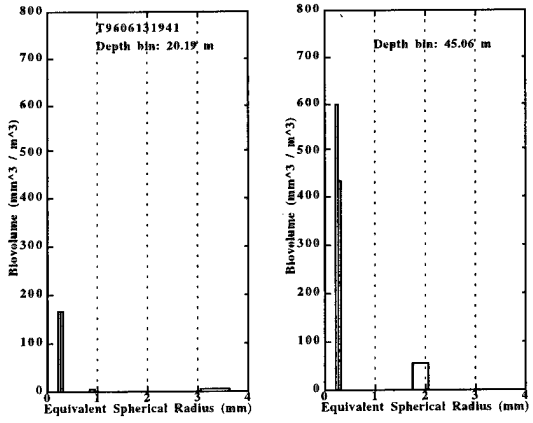

Figure 6: Size-abundance spectra from two locations in a relatively broad layer centered on the chlorophyll (fluorescence) maximum. The data in the left panel is from a depth near the top of the layer of phytoplankton, while the right panel illustrates the size-abundance spectrum from a depth near the bottom of this layer.

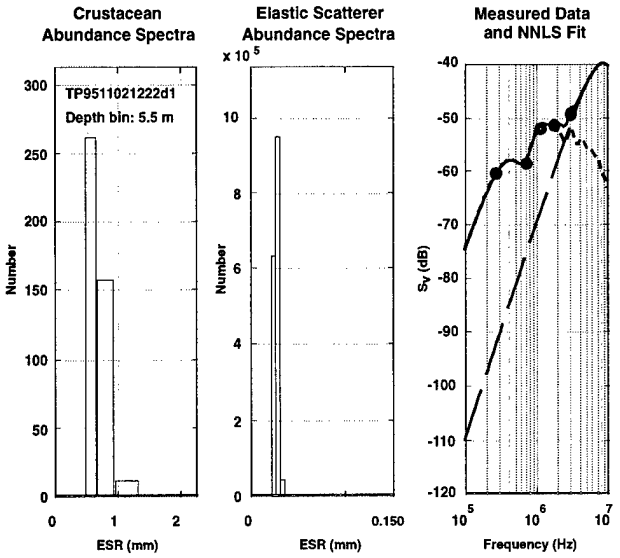

Figure 7: Abundance spectra vs size, expressed as the equivalent spherical radius (ESR), for crustaceans and elastic scatterers (sand) at 5.5 m near the crest of Georges Bank. Total scattering was computed from the results of a Non-Negative Least Squares (NNLS) inverse calculation and are displayed, along with the measured data in the rightmost panel.

VII. DISCUSSION AND CONCLUSIONS

In most marine environments, including the littoral zone, particulate fields often occur in vertically layered, horizontally patchy structures. Within these layers particulate densities can be thousands of times those just below and just above the structure. Differences in the size-abundance spectra within different layers often reflects the presence of different assemblages of zooplankters in those layers. While the physical environment may dynamically modulate these layers in depth (e.g., by mechanisms such as internal waves), it is worth considering whether or not one might take advantage of an *in situ* measurement of the particle size-abundance spectrum to adjust the operating depth of high speed underwater vehicles, avoiding depths at which particulates are most abundant, thereby minimizing encounter rates with particles which are likely to trigger the onset of turbulent flow on or near the vehicle's surface. At times, adjustment of vehicle depth by as little as a meter could lower the encounter rate with zooplankton by several orders of magnitude.

If we wish to know, and perhaps adaptively respond to, the local abundance of particles in the sea, we are presently left with no alternative but to measure those distributions *in situ*. During the last decade there have been major advances in acoustical methods for studying the distribution of small particulates in aquatic environments. During the next decade, it is likely that technology would allow direct *in situ*, real-time measurements of the size-abundance spectrum of particles several meters ahead of a high speed vehicle. The principal barrier to doing this today is simply the speed with which the necessary acoustical measurements can be transformed to size-abundance spectra. This barrier is unlikely to persist for more than a few years and is, even today, more a question of cost than of available technology.

VIII. ACKNOWLEDGMENTS

The basic research underlying the multi-frequency acoustical technology discussed in this contribution was sponsored by ONR's Biological Oceanography Program, with contributions from Tracor, the Ocean Technology and Biological Oceanography programs at the National Science Foundation, NOAA/AOML and NOAA/NMFS. The assistance of K. Brink's team (WHOI) in collecting the SeaSoar™ data from the northern Indian Ocean is gratefully acknowledged. We are also indebted to Richard Pieper and John Dawson (both USC), Anne Lebourges (ORSTOM), R.S. Player and Paul Jarrett for their assistance in collecting the TAPS™ data at the BITS site off Los Angeles. The development of the TAPS™ was funded by Tracor. Charles Greenlaw's long and short term contributions to the development of this technology have been invaluable. I also thank Duncan McGehee for processing the Arabian Sea data and for a critical reading of the manuscript.

IX. REFERENCES

D.V. Holliday, "Extracting Bio-Physical Information from the Acoustic Signatures of Marine Organisms", in Ocean Sound Scattering Prediction, pp. 619-624, (1977).

C.F. Greenlaw, "Acoustical estimation of zooplankton populations", Limnol. Oceanogr. 24: 226-242 (1979).

D.V. Holliday and R.E. Pieper, "Volume scattering strengths and zooplankton distributions at acoustic frequencies between 0.5 and 3 MHz, J. Acoust. Soc. Am. 67: 135 -1 46 (1980).

R.E. Pieper and D.V. Holliday, "Acoustic measurements of zooplankton distributions in the sea", J. Cons. Int. Explor. Mer 41: 226-238 (1984).

D.V. Holliday, "Acoustic determination of suspended particle size" in "Coastal Sediments '87", M.C. Kraus, ed., American Society of Civil Engineers, New Orleans, LA, May 12-14, 1987, ASCE, New York, NY, pp. 260-272 (1987).

J.H. Costello, R.E. Pieper, and D.V. Holliday, "Comparison of acoustic and pump sampling techniques for the analysis of zooplankton distributions", J. Plankton Res. 11(4): 703-709 (1989).

D.V. Holliday, "Zooplankton acoustics" in Oceanography of the Indian Ocean, B.N. Desai, ed., pp. 733 - 740 (1992).

D.V. Holliday and R.E. Pieper, "Bioacoustical oceanography at high frequencies", ICES J. mar Sci. 52: 279-296 (1995).

D.V. Holliday, R.E. Pieper, C.F. Greenlaw and J.K. Dawson, "Acoustical sensing of small-scale vertical structures in zooplankton", Oceanography [in press, 1998].

C.A. Barans, B.W. Stender, D.V. Holliday and C.F. Greenlaw, Variations in the vertical distribution of zooplankton and fine particles in an estuarine inlet in South Carolina", Estuaries 20(3): 467-482 (1997).

M.S. Berman, J.R. Green, D.V. Holliday and C.F. Greenlaw, "Acoustic determination of the fine-scale distribution of zooplankton on Georges Bank", Mar. Ecol. Prog. Ser. (submitted).

H. Medwin and C.S. Clay, Fundamentals of Acoustical Oceanography, Academic Press, NY, 709 pp. (1998).

T.K. Stanton, D. Chu, P.H. Wiebe, L.V. Martin and R.L. Eastwood, "Sound scattering by several zooplankton groups. I. Experimental determination of dominant scattering mechanisms", J. Acoust. Soc. Am. 103: 225-235 (1998a).

T.K. Stanton, D. Chu and P.H. Wiebe, "Sound scattering by several zooplankton groups. II. Scattering models", J. Acoust. Soc. Am. 103: 236-253 (1998b).

T.K. Stanton, P.H. Wiebe and D. Chu, "Differences between sound scattering by weakly scattering spheres and finite-length cylinders with applications to sound scattering by zooplankton", J. Acoust. Soc. Am. 103: 254-264 (1998c).

C.F. Greenlaw, D.V. Holliday, C.A. Barans and B.W. Stender, "Long-term, high-resolution acoustical monitoring of plankton in an estuary", Eos, Transactions of the American Geophysical Union, 79: OS31A-15 (1998).

D.V. Holliday and C.F. Greenlaw, "Resolving zooplankton on sub-meter scales at intervals of minutes", Eos, Transactions of the American Geophysical Union, 79: OS51H-8 (1998).

BIOFOULING CONTROL: A CRITICAL COMPONENT OF DRAG REDUCTION

Dr. Geoffrey Swain
Ocean Engineering
Florida Institute of Technology
Melbourne, FL 32901
Tel 407 674 7129, Fax 407 984 8461
Email: swain@fit.edu

Abstract – Biofouling control is a critical component of drag reduction in marine environments. The most effective antifouling coatings are the self-polishing copolymer organotin (SPC/TBT) based paints. However, due to adverse environmental impacts of the organotin biocides, regulations are in place to restrict their use. There is now a requirement to develop environmentally friendly alternatives. What are the antifouling and hydrodynamic characteristics that made the SPC coatings so successful, and what new technologies are being explored to provide a viable alternative? This paper provides a baseline of performance characteristics necessary for biofouling control and then presents alternative technologies that have been tried or proposed as antifouling methods. At present, the most promising environmentally friendly systems are based on non-toxic silicone foul-release technology. These surfaces will become fouled, however, the organisms are easily removed. The goal is to engineer surfaces that are durable, have a five plus year working life, and self-clean by hydrodynamic forces generated when a ship is underway.

I. INTRODUCTON

Biofouling control is a prerequisite for drag reduction in marine environments. Modern day antifouling (AF) paints are extremely effective at preventing the accumulation and growth of fouling organisms. Environmental issues and regulations are, however, requiring the development of systems that are based on non-toxic or non-polluting antifouling strategies.

The most effective systems are the self-polishing organotin (TBT/SPC) paints (See Figure 1). These are able to provide in excess of five years protection, a roughness not exceeding 100 microns average hull roughness (AHR), and complete protection against biofouling [1]. A cost benefit analyses made by Milne and Abel [2] comparing the TBT/SPC to the next best non-tin alternative (1980s) estimated that these coatings saved the world commercial fleet some $2.4 billion dollars in direct fuel savings, extended drydocking, improved ship availability and capital savings. The problem with the TBT/SPC systems is that the tributyl tin (TBT) has been shown to adversely affect the environment. TBT has become one of the most studied anthropogenic inputs into the marine environment. It was shown that extremely low concentrations will cause defective shell growth in the oyster, *Crassostrea gigas* (20ng l^{-1}) [3] and imposex in the dog-welk, *Nucella sp.* (1ng l^{-1}) [4]. These findings led to regulations that prohibit the use of TBT, in most industrial nations, on boats less than 25m in length [5]. In December 1985, the US Congress passed the Fiscal Year 1986 Appropriation Bill with the rider that prohibited the US Navy from the purchase or application of any organotin AF coatings until certain conditions were met. Although this ban was lifted in 1989, the US Navy has chosen not to implement their use [6]. Further-more the Office of the Chief of Naval Operations has formulated a vision for the environmentally sound ship of the 21st century, which will ensure compliance with environmental requirements while maintaining fleet effectiveness and readiness [7]. More recently TBT has been implicated in the deaths of bottle nosed dolphins (*Tursiops truncatus*) [8], and the International Maritime Organization (IMO) are looking at how to further reduce harmful effects of organotin by more restrictions or a total ban [9].

Ships, boats and structures coated with AF paints act as a point source input of the biocide used to control fouling. For example, a 65,000 Gross Registered Tons container ship (260m long) has an approximate wetted surface area of 13,000m^2. If it is coated with a TBT/SPC based system with a biocide output of 4$\mu g/cm^2$/day then the TBT input into the environment would be about 190 kg/year. If a copper based AF system was used with a minimum biocide output of 20$\mu g/cm^2$/day then the copper input into the environment would be about 950 kg/year. The environmental impacts of such outputs are being questioned, and it is apparent that non-toxic technologies are required to control biofouling while maintaining the drag reduction performance achieved by the biocide based systems. This paper will discuss the hydrodynamic penalties associated with biofouling, identify the characteristics that make TBT/SPC systems so effective and investigate alternative technologies that may provide an environmentally acceptable solution.

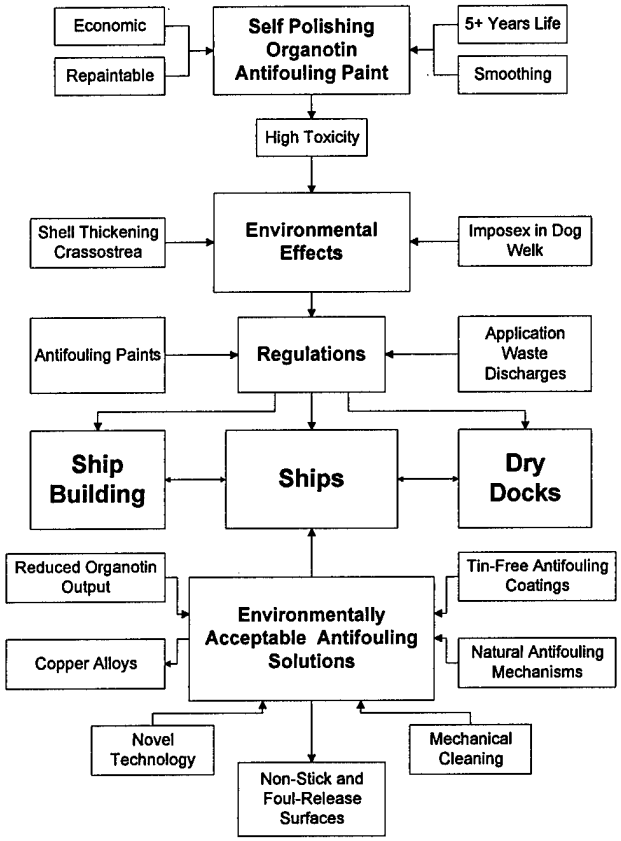

Figure 1. Performance and environmental criteria of the TBT/SPC systems and the development of environmentally friendly antifouling technology

II. BIOFOULING AND DRAG

The effects of biofouling on drag are hard to predict due to the complexity and variability of fouling community structure [10]. Marine growth accumulations vary according to geographical area, season, operating schedule, hull zonation, and the effectiveness of the antifouling system. An example of biofouling community structure for a ship moored in Honolulu, Hawaii for three months is shown in Figure 2 [11]. This vertical profile demonstrates differences in the fouling community structure with depth. Horizontal variations in the fouling communities were also observed.

One of the earliest scientific investigations of the effect of biofouling on drag was by McEntee in 1915 [12]. He exposed 3.0m x 0.6m coated steel plates to fouling in the Chesapeake Bay for twelve months and conducted monthly towing tank resistance measurements at velocities between 1.0 to 4.5 m/s. The fouling layer consisted of slimes and small barnacles and was found to cause about a four-fold increase in

resistance. A summary of the early research related to the effects of marine fouling on ship resistance is documented in *Marine Fouling and Its Prevention* [13]. Power trials on the US destroyer Putnam and the US battleship Tennessee and towing trials on the Japanese ex-destroyer Yudachi demonstrated that coating breakdown and biofouling could double the ship resistance within one year.

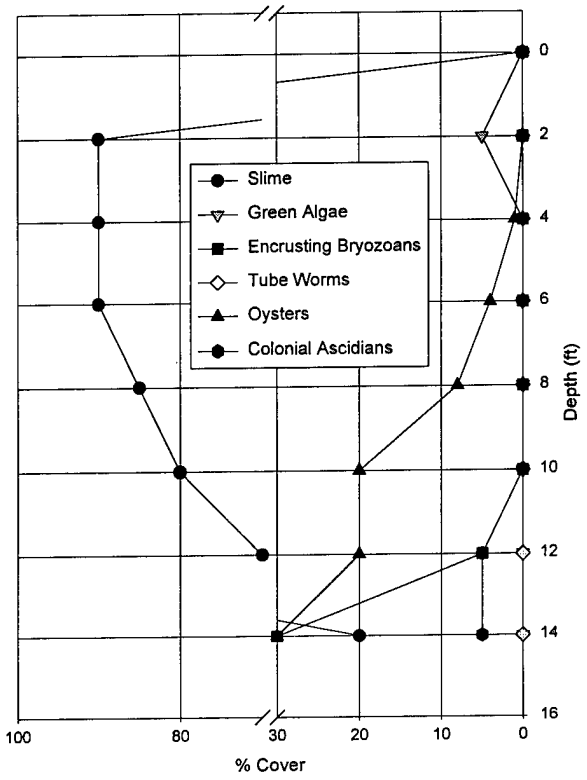

Figure 2. Vertical profile of biofouling on a ship hull moored at Honolulu HI

Modern day AF coatings prevent the type of fouling and increase in drag observed above. However, it is well known that biological slimes are able to colonize toxic surfaces and under certain operating conditions may grow on AF coatings [14]. The contribution of these films to ship hull drag should not be overlooked. One demonstration of this effect is described in ship trials of the Knox class frigate, USS Brewton [15, 16]. The ship was coated with an ablative antifouling paint containing both cuprous oxide and tributyltin oxide. She had been subject to fouling in Pearl Harbor, Hawaii for 22 months. An initial hull inspection by divers indicated the presence of a microbial biofilm but little hard fouling. Hull roughness measurements gave a mode, median and mean of 180,190 and 272 microns respectively. The ship was instrumented to measure shaft horsepower and speed and power trials were made over a mile course. The ship then returned to port to undergo hull cleaning before running a second ship power trial. Post hull cleaning roughness measurements showed only a slight decrease in roughness, the mode, median and mean being 160, 182 and 264 respectively. It was found, however, that there was as much as an 18% decrease in the required shaft horsepower to propel the ship at same speed after cleaning. This was associated with the removal of the microbial biofilm.

Lewthwaite et al. [17] used a small pitot type tube to make detailed boundary layer velocity distribution measurements on a 23m Admiralty fleet tender. Over a two year period they measured an increase in skin friction of about 80% which was associated with a dense slime estimated to be about 1mm thick, but virtually free of weed and shell growth. In a more detailed study, which included identification of the fouling organisms present in the slime film, Schultz [18] used a water tunnel and laser Doppler velocimeter to measure the effects of biofilms (74 to 319μm thick) on boundary layer structure at momentum thickness Reynolds numbers from 5,500 to 19,000. He measured increases in wall shear stress on fouled plates of 33 to 187% compared to the smooth plate conditions.

Several other studies [19,20,21] have also demonstrated the significance of low form and slime fouling on hydrodynamic drag. These findings show that even modern day antifouling systems may become colonized by bacteria, diatoms and algal communities. Control is typically achieved by the use of co-biocides. However, these are also coming under scrutiny for environmental effects.

III. ANTIFOULING METHODS

There are an abundance of patents and ideas relating to biofouling control, although, few are practical, economic or effective [22,23,24,25]. Most present day systems still rely on a coating with active biocides to protect a surface. However, environmental concerns over the effects these compounds may have on non-target species, has led to the call for "environmentally friendly antifouling" systems. The term "environmentally friendly antifouling" remains to be fully defined. In its purest sense, it can be interpreted as meaning a system that has no toxic components. In its broadest sense it may be defined as lessening the impact of the TBT/SPC coatings (Figure 1).

Tributyltin Self-Polishing Copolymer Systems

The introduction of the TBT/SPC coatings in the early seventies revolutionized biofouling control on ships [26,27,28]. An understanding of the mechanisms that made these coatings so successful helps to identify the properties that are required of replacement technology. TBT is an extremely active biocide with chronic effects being observed on many common invertebrates at levels below 1 $\mu g\ l^{-1}$ [29]. It is bonded to the acrylic polymer backbone as the TBT ester of methacrylic acid, tributlytin methacrylate. This is then copolymerized with methyl methacrylate to form a copolymer [30]. On immersion to seawater, the coploymer at the paint surface reacts to release the TBT. This causes the copolymer to become brittle and hydrophilic which removes the copolymer chain providing both self-polishing action and a new supply of biocide. The coating remains stable because the reaction is confined to an extremely narrow surface layer due to the hydrophobic properties of the unreacted paint film.

TBT/SPC paints are usually formulated with cuprous oxide pigments and other organic co-biocides. These combinations enable paint manufacturers to formulate coatings that comply with the maximum release rate of $4\mu g/cm^2$/day TBT, provide in excess of five years fouling-free performance and maintain excellent hull roughness properties (about 100 microns). They are considered the benchmark from which to judge new systems.

Tin-free Antifouling Coatings

The most common alternative biocide to organotin is copper. It is about ten times less toxic than TBT [31], and therefore on its own it is less effective. For this reason there is much interest in co-biocides which act synergistically to enhance the performance of copper based coatings. The most commonly found additions are; diuron, triazine, isothiazolin and zinc omidine. Diuron and triazine have been shown to be persistent in the environment [32, 33, 34]. Isothiazolin shows less accumulation. These biocides may be included in conventional matrix paints (soluble matrix, continuous contact, diffusion) or in ablative type systems (self-polishing polymers, saponifying polymers) [27]. The conventional matrix paints typically provide a 12 to 18 month active life and the ablative saponifying types up to 3 years. More recently self-polishing tin free coatings have been developed [35,36,37] with claims of five years protection. However, these compounds are already under scrutiny. Triazine has been detected at excessively high levels close to marinas and high boating activity [34] and even copper has come under scrutiny [38,39]. Such findings, the high cost of biocide registration, and the history of regulation, increases the need to find a non-toxic alternative.

Copper Alloys

It is well known that the 90:10 copper-nickel alloys provide excellent mechanical, corrosion and AF properties [40]. They have been successfully used as the hull plate material on several boats [41] and more recently as cladding material. With the use of modern adhesives and polymers, copper alloys can be applied to steel hulls and structures without creating bimetallic corrosion problems. In unpolluted seawater this alloy exhibits relatively low homogeneous corrosion rates, which

prevent fouling, and yet maintains a relatively smooth surface. It is interesting to note that a 1mm thick copper foil homogeneously corroding at 20μg/cm²/day would theoretically last for about 120 years. In some ways it is surprising that these materials have not received wider use, however, higher capital cost compared to AF paints, the possibility of galvanic interactions with other metal components and cathodic protection systems, and unpredictable performance in polluted waters has prevented their widespread adoption.

Natural Antifouling Mechanisms

One possible source of new technology is from the understanding of natural antifouling processes. In recent years there has been an explosion of research in this area, mainly focused on chemical inhibition. It has long been known that the settling phases of marine organisms respond to a diversity of chemical cues [42, 43]. This has generated interest in identifying compounds that might repel or inhibit fouling organisms [23,44]. For a compound to be considered effective, it must satisfy certain conditions. These include:

- Non-toxic mode of action.
- Active at low concentrations.
- Rapid breakdown to non-polluting substances.
- Effective over a broad spectrum of biofouling organisms.
- Compatible with coating systems.

Much of the research has investigated substances derived from organisms that are known to remain free from fouling. For example, extracts from bacteria [45,46], algae [47,48,], sea grasses [49], corals [50], sponges [51,52] and even terrestrial plants [53] have been identified as active antifouling agents. The identification of active compounds is just one of the steps required before they transition to become active ingredients of AF coatings. A mechanism must be found from which they can be incorporated into the coating matrix and be supplied to the surface at a rate sufficient to prevent fouling and yet not wasteful of the compound [54]. Natural sources or synthetic analogues must be identified to ensure supply at reasonable cost. The compounds must also pass rigorous scrutiny from environmental regulation agencies [55]. For these reasons no natural products have been commercialized for antifouling. However, researchers are still hopeful that they may identify compounds that can deter fouling without compromising the environment.

Physiological responses that lead to a reduction in biofouling are also known. All arthropods undergo periodic moults, which will inevitably shed old fouled surfaces [56]. Tissue sloughing in the sponge *Halichondria panicea* has also been associated with antifouling activity [57]. A deep layer sloughing in the coralline algae, *Spongites yendoi*, however, was shown not to have any antifouling function [58]. Antifouling systems comprising a multi-layered surface from which the top layer could periodically be peeled have been proposed, but, to date, no practical system has successfully been engineered.

There have been several studies that have investigated the surface properties of marine organisms with respect to biofouling control. Dogfish egg cases [59] and the epidermis of sea urchins [60] were investigated under funding from MAST II Project [61]. These studies identified a variety of interesting mechanisms, but none, as yet, have been transferred to practical solutions. From a hydrodynamic standpoint, the three groups that are of greatest interest are the cetaceans (whales and porpoises), teleosts (bony fish) and elasmobranchs (cartilaginous fish). The no-foul condition of porpoise and killer whale skin has been attributed to the outermost aspect being composed of a glycoproteinaceous material with low surface free energy [62,63].

The application of natural control in terms of disease [64] and predation [65] has also been suggested. For many reasons, the introduction of disease into marine ecosystems is unacceptable and unlikely to work. The use of predation has been tried on offshore oil platforms where starfish were introduced to control mussels. The experiment failed due to wave action removing the starfish and for simple reasons relating to the dynamics of ecosystems.

Finally, it should be remembered that behavioral activities frequently associated with biofouling control include spending extended periods of time out of the water (seals, sea lions, sea otters etc.), migrating into fresh water, or attending cleaning stations (shrimp on coral reefs). Similar behaviors are often used to control biofouling on ships and boats.

Novel Technology

There are several review papers that discuss novel ideas for the prevention of biofouling [22,23,24,25]. As yet none of these methods have surpassed the performance of the conventional AF coatings. For this reason, only a brief summary is provided for completeness.

A classification of novel antifouling technology is shown in Figure 3. There have been several ideas to provide chemical control via air bubble curtains [66,67] or chemical production at the surface [68,69]. The most obvious problem with these sorts of treatments is that they act as point source inputs of unwanted chemicals into the environment. One possible exception maybe found in the control of pH. Mor [70] demonstrated that if the pH could be maintained below 4 or above 10 then fouling was prevented. A high pH surface, with biocidal properties, was recently created by formulating paints that contain lime [71]. To date, however, none have been made to work in a marine environment.

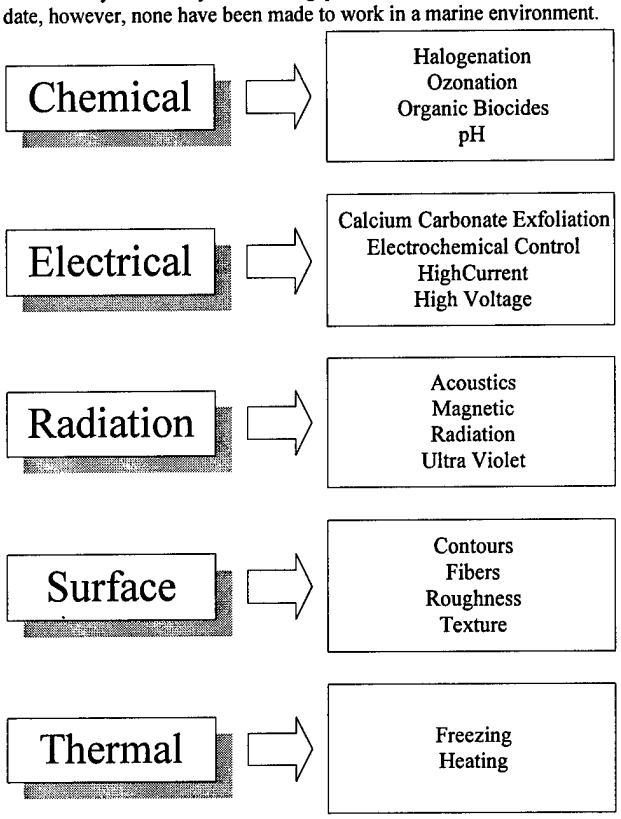

Figure 3. Novel Antifouling Technology

The use of high voltage or current has also been tried [72,73]. These do not work due to low seawater resistance, cathodic chalk formation, and possible corrosion related problems [74].

Several forms of radiation have been investigated. Ultraviolet radiation is routinely used to sterilize seawater in pipe systems [75] but is not considered practical for external surfaces due to rapid attenuation. Radioactive surfaces using thallium 204 have been shown to be extremely effective against fouling at intensities of 20 rad/hr, but not at all at 2 rad/hr [76,77]. Such levels are considered too high for safe handling and therefore such methods are considered unacceptable. Magnetic fields have been shown to have temporary effects on some organisms [78], however, there are no published demonstrations of any antifouling effect. The most commonly tried form of radiation for biofouling control is acoustics. This has been tried using external vibration sources and by the use of piezoelectric coatings. There have been several reports of success [79,80,81]. The power requirements, however, are relatively high, and the effect may be restricted to one fouling type [81]. Furthermore, the presence of bulkheads and other material properties impacts the distribution of energy.

It is well known that the physical condition of a surface will affect the settlement of biofouling [83]. Smooth surfaces generally foul less than rough surfaces, however, no topographical surface condition has been identified that will prevent biofouling. One recent idea has been the use of microfibers [84], but this has yet to be verified by long term field-testing.

Thermal control of biofouling is well known and practiced at some power utilities [85]. However, heat or cryogenic treatment of ship hulls and structures are impractical.

Mechanical Cleaning

The mechanical removal of biofouling must be one of the oldest methods of control and is still routinely applied to modern day ships [86]. Cleaning is often accomplished in water by large rotating brushes and it is generally used to supplement failed antifouling coatings. Underwater ship hull cleaning extends the operational period of a ship by cleaning the hull and activating what remains of an antifouling coating. Such practice has recently come under critism due to the large release of antifouling coating and associated biocides. This further emphasizes the need to develop non-toxic coating systems.

Non-Stick and Foul-Release Surfaces

From an environmental perspective the non-stick and foul-release technologies offer the most attractive option for biofouling control. Unfortunately, the present coating formulations are still not as effective as the existing SPC/TBT systems, and further development, perhaps in combination with a change in ship hull husbandry, is required.

Interest in the use of non-stick surfaces for biofouling control was stimulated by the synthesis of the polytetrafluoroethylene and other hydrophobic plastics. In 1958, Bruner [87] issued a patent claiming that such surfaces prevent adhesion and growth of barnacles, however, we now know this claim to have been erroneous. It took the scientific studies of Baier [88, 89] and Dexter [90] to explain the mechanism for the non-stick phenomena. They demonstrated that settlement and attachment by microorganisms could be related to the surface free energy of the substrate. They further identified a surface free energy of between 22-24 dynes/cm that produced a minimum in biological adhesive strength. These observations increased interest in the development of non-stick surfaces and a number of fluorinated coatings were developed with superior non-stick characteristics [91,92]. They were, however, unable to provide sufficient non-stick characteristics to prevent attachment by macrofouling organisms, and they exhibit disappointing foul-release properties. The only alternative to fluorinated compounds identified as having non-stick and foul-release properties are the silicones. In addition to having low surface energies and low micro-roughness for non-stick, these materials posses other properties that confer foul-release. Silicones possess low glass transition temperatures, T_g, and it is suggested that these minimize mechanical locking of biological glues and increases slippage and foul-release [93,94]. Furthermore, most commercial poly(dimethylsiloxane) based coatings contain fluid additives and it is suggested that these create weak surface layers and macromosaic surfaces that further promote foul-release [95].

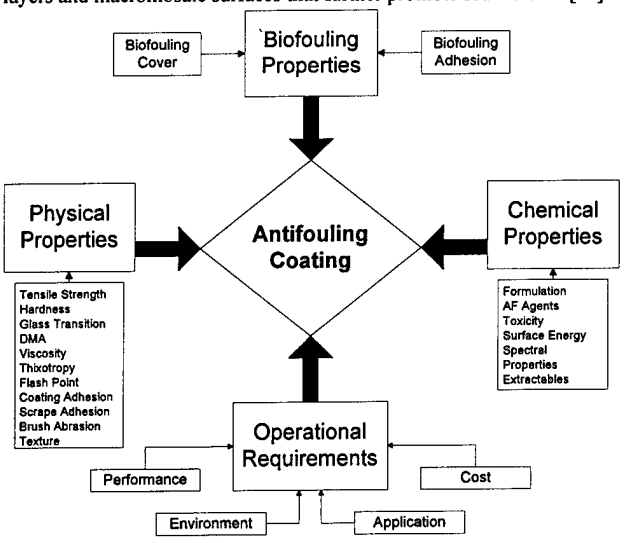

Figure 3 Requirements for a Non-Toxic Foul-Release Coating

Silicone was first reported as a foul release coating in 1972 in a patent registered to the Battelle Institution [96]. During the seventies and eighties there was only limited interest in these coatings, partly due to the success of the TBT/SPC systems and also due to some of the practical limitations of existing silicone formulations [97,98]. It was only when the biocide containing coatings came under pressure from environmental regulations that a concerted effort was made to better understand the mechanisms by which silicone formulations function and to improve their performance.

The Office of Naval Research (ONR) has funded research that has made significant contributions to the understanding and development of silicone foul-release coatings. During the 1994 ONR Biofouling Contractors Workshop, a list of criteria considered important for the evaluation and understanding of such coatings was developed [99] (See Figure 3). These were categorized under four main headings: biofouling properties, operational requirements, physical properties, and chemical properties.

The biofouling properties that determines the effectiveness of these coatings is different from traditional AF systems. Traditional antifouling coatings use a biocide to prevent settlement and to poison the organisms. Therefore an active surface will remain totally free of fouling (See Figure 4). A non-toxic surface, however, may become totally covered by fouling organisms. Its effectiveness is determined by the ease with which the organisms become detached.

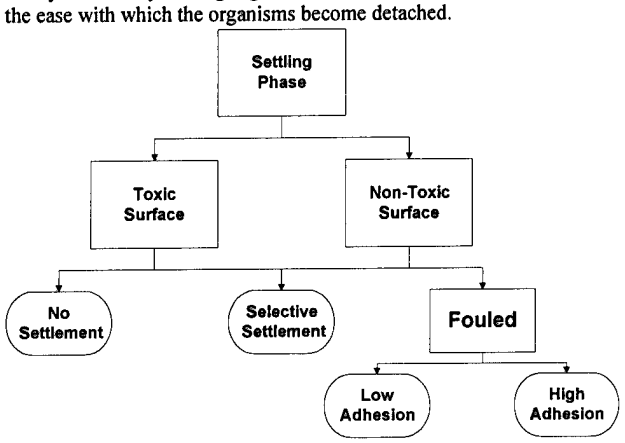

Figure 4 Settlement matrix for toxic and non-toxic surfaces.

A variety of techniques have been used to measure the adhesion strengths of organisms (diatoms [100], *Enteromorpha sp.* [97], mussels, [101,102], limpets [103], tubeworms [104], and barnacles [104,105,106,107,108,109,110,]) to different substrates. The ONR Biofouling Control Program has adopted an ASTM standard for the measurement of barnacle adhesion strength in sheer [109]. There is now a significant database of barnacle adhesion strength measurements for different species and for different substrates. Some examples of barnacle adhesion strength (*Balanus eburneus*) on different materials exposed to biofouling at the Florida Institute of Technology static immersion site are shown in Figure 5.

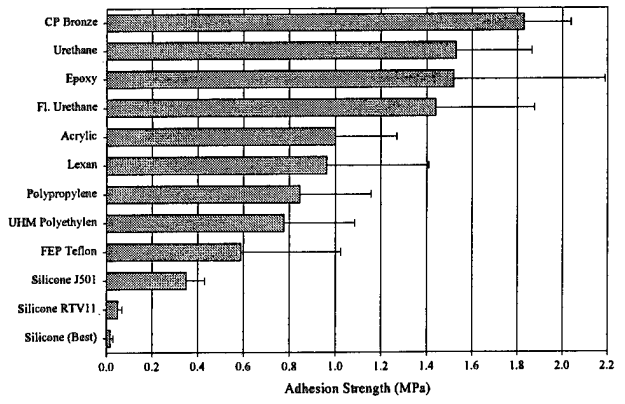

Figure 5 Barnacle Adhesion Strength in Shear

The differences between non-stick surfaces such as FEP Teflon (0.59 MPa) and the best foul-release silicone (0.02 Mpa) can be seen.

The operational requirements for a foul-release coating are that it self-cleans when the vessel is underway. It is possible to predict the velocity for foul release by relating barnacle adhesion strength to

hydrodynamic drag forces (Figure 6). Theoretical drag and lift forces may be calculated from the basic equations:

$$F_D = \frac{1}{2} C_D \rho V^2 A_f$$

$$F_L = \frac{1}{2} C_L \rho V^2 A_p$$

where: F_D = Drag Force, N; F_L = Lift Force, N; C = Coefficient of Drag; C_L = Coefficient of Lift; V = Average Velocity, m/s; A_f= Frontal Area, m, A_p= Projected Area, m; ρ = Density, kg/m^3.

The drag and lift coefficients for typical acorn barnacles have been measured at about 0.5 and 0.45 respectively [104, 112] and remain reasonably constant at high Reynolds number. It has also been shown that the shear adhesion strength of a barnacle is between 2.5 to 3.0 times as great as the tensile strength [105,109]. Assuming free stream velocity and no boundary layer, we would predict that barnacles on the best performing silicone shown in Figure 5 would self-clean at about 10 knots. The validity of such a prediction was confirmed during speed trials on a 41' US Coast Guard utility boat that was coated with a silicone formulation under the Environmental Security Certification Program. It was found that the boat velocity required for barnacle foul-release in the bow section closely corresponded to the velocity predicted using barnacle adhesion data obtained for the coating and the assumptions made above [113]. In contrast, we would predict that a ship would have to travel in excess of 50 knots to cause foul-release from an FEP Teflon surface.

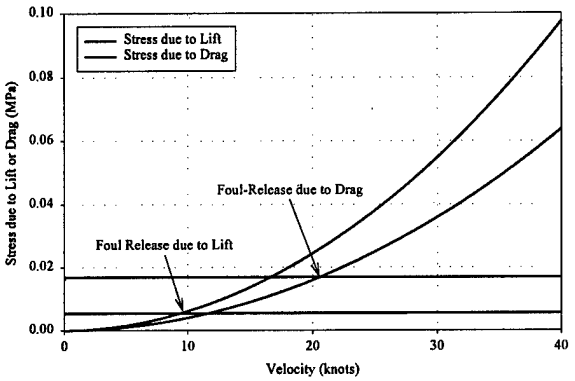

Figure 6. Theoretical Foul-Release Velocities for the Barnacle *Balanus eburneus* from the Best Silicone

Although the theoretical hydrodynamic forces experienced by individual barnacles are easily calculated, there are several factors that complicate the real life situation. Barnacles are gregarious and tend to live in clusters surrounded by other fouling organisms. This will complicate the flow patterns and the resulting force vectors experienced by individual organisms. It has also been shown that barnacle adhesion strength differ among species [109]. There are also variations in the adhesion strengths and drag and lift coefficients of fouling types [103]. These factors, in conjunction with the variable hydrodynamic characteristics of boundary layer thickness and flow patterns along a ship hull make it difficult to predict foul-release with any certainty. It is conceivable that the hydrodynamic lift and drag forces on certain low form soft and hard foulers will never be sufficient to cause foul-release. In this case, some sort of in-water hull cleaning would be required [114].

The foul-release performance of the silicone coatings is getting close to satisfying the requirements for successful biofouling control. Their surfaces also appear to perform as hydrodynamically smooth surfaces. This would provide a drag reduction advantage over the best average hull roughness obtained with the SPC/TBT coatings.

The current disadvantages with the silicones are their poor mechanical properties, difficulties with adhesion to tie coats, and their relatively high costs. Further investment in advancing the technology is required before they can be considered a replacement for the SPC/TBT systems.

IV. SUMMARY

Biofouling control must be considered a part of any drag reduction program. The challenge is to find an environmentally acceptable method that will provide equal or better performance to the SPC/TBT systems. The tin-free ablative type paints will provide an interim solution, however, their reliance on copper and other biocides make them a target for future environmental regulations. It is possible that new ideas may be found from studying natural AF mechanisms, and from a better understanding of the cues that determine the settlement of the dispersal phases. The idea of discovering a non-toxic compound that deters settlement is indeed attractive.

Many novel ideas have been proposed for biofouling control. Several are not considered environmentally acceptable, others are not feasible with present technology, and many do not work. However, it is important that new ideas continue to be promoted and evaluated through peer review and trial and error.

The technology that shows the greatest promise is non-stick foul-release surfaces. Over the last few years significant improvements in coating performance have been achieved. Non-toxic hydrodynamically self-cleaning coatings are now a reality. The remaining challenge is to improve application and durability issues. One solution may be to combine foul-release coatings with frequent hull cleaning programs.

The final note is to remember that the development of new AF technology requires a multidisciplinary approach. Knowledge of the biological, chemical, and physical properties are required as well as an understanding of operational requirements of the system.

V. ACKNOWLEDGEMENTS

The information and ideas presented in this paper are the result of meetings, discussions and collaboration with a large number of persons involved in marine operations and biofouling control. I am particularly indebted to the Office of Naval Research (Grant No. N00014-91-J-1465) the Environmental Security Certification Program, the Defense Advanced Research Project Agency, and to other organizations (Conoco, Dow Corning, DuPont, General Electric) who have funded our research program. I would also like to acknowledge all my students and colleagues who have, and continue to work towards a solution.

VI. REFERENCES

1. A. Milne "Roughness and Drag from a Marine Paint Chemist's Viewpoint", Int. Workshop on Marine Roughness and Drag, The Royal Institution of Naval Architects, London, Paper 12, March 1990.
2. A. Milne and P.D. Able "Cost Benefit Analyses of Remediation of TBX Contamination", Environmental Impact of Tributyl Tin (TBT) and Development of Methods for the Treatment of Contaminants by Biotechnological Means, MEDSAP 91-1/UK/002/INT06, 1995.
3. C. Alzieu "TBT Detrimental Effects on Oyster Culture in France – Evolution Since Antifouling Paint Regulation. Proceedings Oceans' 86 Organotin Symposium. Marine Technology Society. Washington, DC. V.4:1130-1134, 1986.
4. P.E. Gibbs and G.W. Bryan "Reproductive Failure in Populations of Dog-Whelk *Nucella lapillus*, Caused by Imposex Induced by Tributyltin from Antifouling Paints", J. Mar. Biol. Ass. U.K. V.67:507-523, 1986.
5. Anon "The Legislative Position of TBT-Containing Antifoulings", Propeller, V1 Issue 1, Courtaulds Coatings, Jly/Aug 1994.
6. R. Alberte et al. "Biofouling Research Needs for the United States Navy: Program History and Goals", Biofouling, Vol.6, pp. 91-95, 1992.
7. A.D. Nickens, J.F. Pizzino and C.H. Crane, "Environmental Compliance: Requirements and Technology Opportunities for Future Ships", Naval Engineers Journal, pp. 349-371, May 1997.
8. K. Kannan et al. "Elevated Accumulation of Tributyltin and Its Breakdown Products in Bottlenose Dolphins (*Tursiops truncatus*) Found Stranded along the U.S. Atlantic and Gulf Coasts", Environ. Sci. Technol., 31, 296-301, 1997.
9. Anon. "Harmful Effects of the Use of Antifouling Paint with TBT Discussed", Marine Environment Protection Committee Session, International Maritime Organization, 40th Session, September 1997.
10. J.B. Ricketts "Naval Ship Self-Assessment of Hull Powering Performance Using Propulsion Shaft Torsionmeters and GPS", Naval Engineers Journal, pp. 181- 193, May 1997.
11. G.W. Swain and M. Schultz "SLICE Inspection Report", Environmental Security Certification Program, August 1997.
12. W. McEntee "Variation of Frictional Rsesistance of Ships with Condition of Wetted Surface", Trans. Soc. Nav. Arch. And Mar. Eng., 24, p 85, 1915.

13. L.W Redfield and A.C. Hutchins, "Ship Resistance" in *Marine Fouling and Its Prevention*, Ch. 2, U.S. Naval Institute Press, Annapolis, MD, 1952.
14. R.L. Townsin "Ship Design for Fuel Economy - Bottom Condition and Fuel Conservation", West European Graduate Education in Marine technology, 8th School, Gothenburg, 1983.
15. E.G. Haslbeck and G. Bohlander Microbial Biofilm Effects on Drag - Lab and Field", *Proceedings 1992 S.N.A.M.E. Ship Production Symposium*, 1992.
16. E.G. Haslbeck and G. Bohlander "Hydrodynamic Drag Evakuation of Antifouling Coatings – Laboratory and Field", Proceedings of Emerging Nonmetallic Materials for the Marine Environment, Honolulu, HI, 18 – 20 March, 1997.
17. J.C. Lewthwaite, A.F. Molland, and K.W. Thomas "An Investigation into the Variation of Ship Skin Frictional Resistance with Fouling", *Transactions Royal Institute of Naval Architects*, Vol. 127, 1985 pp. 269-284.
18. M. P. Schultz "The Effect of Biofilms on Turbulent Boundary Layer Structure"' PhD Dissertation, Ocean Engineering, Florida Institute of Technology, Melbourne, FL, 1998.
19. G.I. Loeb, D. Laster, and T. Gracik "The Influence of Microbial Fouling Films on Hydrodynamic Drag of Rotating Discs", in *Marine Biodeterioration, An Interdisciplinary Study*, edited by Costlow, J.D. and Tipper, R., Naval Institute Press, Annapolis, MD, 1984, pp. 88-94.
20. B.F. Picologlou, N. Zelver, and W.G. Characklis "Biofilm Growth and Hydraulic Performance", *A.S.C.E. Journal of the Hydraulics Division*, HY5, 1980, pp. 733-746.
21. A.K. Lewkowicz and D.K. Das "Turbulent Boundary Layers on Rough Surfaces With and Without a Pliable Overlayer: A Simulation of Marine Fouling", *Proceedings of the A.S.M.E/A.S.C.E. Bioengineering, Fluid Engineering, and Applied Mechanics Conference*, 1981, pp. 174-186.
22. "Marine Fouling and Its Prevention", Woods Hole Oceanographic Institution, 1952.
23. E.C. Fischer et al. "Technology for Control of Marine Biofouling – A Review", Marine Biodeterioration: An Interdisciplinary Study, Naval Institute Press, 1981.
24. R Mitchell and P Benson "Micro- and Macrofouling in the OTEC Program: An Overview", US Department of Energy, ANL/OTEC-BCM-011.
25. G. Swain, "Antifouling Practice: The Present and the Future, A European Perspective", Technical Report to the Office of Naval Research, February 1996.
26. A. Milne and G. Hails, Patent GB 1 457 590, International Paint Plc, 3 April 1974.
27. A. Milne "Ablation and After: the Law and the Profits", Polymers in a Marine Environment, Paper 17, 23-24 October 1991.
28. R.L. Townsin et al. "Speed, Power and Roughness: The Economics of Outer Bottom Maintenance" In: Trans. RINA. 123, 1981.
29. M. Rexrode "Ecotoxicology of tributyltin", Oceans 87 Proceedings, Volume 4, International Organotin Symposium pp 1443-1455, 1987.
30. C.D. Anderson "Tin vs. Tin-Free Antifoulings", Conference Proceedings, Protecting the Ship While Safeguarding the Environment, London, 5-6 April 1995.
31. D. Anderson and R. Dalley, "Use of Organotins in Antifouling Paints", Proceedings Oceans 86, V. 4, Washington DC, September 1986.
32. Anon "Review of Current and Future Marine Anti-Fouling Coatings", Marine Safety Agency, UK, Report 93/TIPEE/4787, 1993
33. M. Callow and G. L. Willingham, "Degredation of Antifouling Biocides", Biofouling, V.10, pp 239 – 249, 1996.
34. F. Pearce "Alternative Antifouling Widespread in Europe" New Scientist, p 7, 14 January 1995.
35. Yoshihiro Honda "Quantum Leap Technology After Ban of TBT in Japan", Proceedings of Emerging Nonmetallic Materials for the Marine Environment, Honolulu, HI, 18 – 20 March, 1997.
36. Ping-Lin Kuo et al. "Interface-Crashed Self-Polishing Type of Tin-Free Antifouling Coating", Proceedings of Emerging Nonmetallic Materials for the Marine Environment, Honolulu, HI, March, 1997.
37. Anon. "Five-year Japanese TBT-free SPC system – but at a price!", Ship Repair and Corrosion Technology, 1st Quarter, pp 24-31, 1997.
38. Claisse and C. Alzieu "Copper Contamination as a Result of Antifouling Paint Regulation?", Mar. Pollut. Bull., V 26, No. 7, pp 395-397, 1993.
39. J.J. Molnar "Copper Storage in the Liver of the Wild Mute Swan (Cygnus olor). Its Possible Relation to Pollution of Harbor Waters by Antifouling Paints", Arch. Pathol. Lab. Med. V.107, No.12, pp.629-632, 1983.
40. "Marine Engineering with Copper-Nickel", The Institute of Metals, London, 19-20 April 1988.
41. D.W. Czimmek and L.W. Saundor, "Economic and Technical Feasibility of Copper-Nickel Sheathing of Ship Hulls", Marine Technology, Vol. 22, No. 2, pp. 142-154, April 1995.
42. J.R. Pawlik "Chemical Ecology of the Settlement of Benthic Marine Invertebrates", Oceanogr Mar Biol Annu Rev 30: 273-335, 1992.
43. M.G. Hadfield "Research on Settlement and Metamorphosis of Marine Invertebrate Larvae: Past, Present and Future", Biofouling Vol. 12, Vol. 1-3, pp 9-30, 1998.
44. A.S. Clare "Marine Natural Product Antifoulants: Status and Potential", Biofouling Vol. 9, pp 211-229, 1996.
45. Holmstrom et al.. "Regulation of Activity and Settlement of Marine Organisms by Bacterial Extracellular Components", Proceedings of Emerging Nonmetallic Materials for the Marine Environment, Honolulu, HI, 18 – 20 March, 1997.
46. S. James et al. "Marine Bacteria Immobilized in Hydrogel Prevent Settlement of Larvae" 3rd International Marine Biotechnolgy Conference, Tromsoe, Norway, 1994.
47. N.G.M. Nadal "Process for producing antibiotic, antifungal and antifoulant substances by solvent extraction of *Sargassum natane*, *Chondria littoralis* and *Cympolis barbata* and the resulting products", US Patent No. 3,415,928, 10 Dec 1968.
48. P.D. Steinberg, R. de Nys, S. Kjelleberg "Chemical Inhibition of Epibiota by Australian Seaweeds", Biofouling, Vol. 12(1-3), pp227-244, 1998.
49. J.S. Todd et al. "The antifouling activity of natural and synthetic phenolic acid sulfate esters", Phytochemistry, Vol. 34, No. 2, pp 401-404, 1993.
50. Rittschoff et al. "Barnacle In Vitro Assays for biologically Active Substances: Toxicity and Settlement Inhibition Assays using Mass Cultured *Balanus amphitrite amphitrite* Darwin", Biofouling, Vol. 6 (2), pp115-123, 1992.
51. C. Unabia and M. Hadfield "Bioactive Marine Isonitrile Compounds form Hawaiia Sponges as Models for Synthetic Nontoxic Antifoulant and Antibiotic Agents", Proceedings of Emerging Nonmetallic Materials for the Marine Environment, Honolulu, HI, 18 – 20 March, 1997.
52. P.R. Willemsen "The screening of Sponge Extracts for Antifouling Activity using a Bioassay with Laboratory Reared Cyprid Larvae of the Barnacle *Balanus amphitrite*" Int Biodeterior Biodegrad *-9: 361-373, 1995.
53. S.S Sawant and A. Wagh " Terrestrial Plants: A Potential Source for Isolation of Eco-Friendly Antifouling Compounds", Proceedings of Emerging Nonmetallic Materials for the Marine Environment, Honolulu, HI, 18 – 20 March, 1997.
54. G.R. Weisman et al. "Controlled Release Antifouling Coatings. 1. Approaches for Controlled Release of 2,4-Dinitrophenolate and Benzoate into Seawater", Biofouling Vol. 6 (2) pp123-147. 1992.
55. Environmental Protection Agency, USA.
56. K. Becker and M. Whal "Behaviour Patterns as Natural Antifouling Mechanisms of Tropical Marine Crabs", J.Exp. Mar. Biol. Ecol. Vol. 203, No. 2, pp 245-258.
57. D. Barthel and B. Wolfrath "Tissue Sloughing in the Sponge *Halichondria panicea*: A Fouling Organism Prevents Being Fouled", Oecologia Vol. 78 No. 3, pp. 357-360, 1989.
58. D.W. Keats, P. Wilton, G. Maneveldt "Ecological Significance of Deep-Layer Sloughing in the Eulittoral Zone Coralline Alga, *Spongites yendoi* (Foslie) Chamberlain (Corallinaceae, Rhodophyta) in South Africa", J. Exp. Mar. Biol. Ecol. Vol. 175, No.2, pp145-154, 1994.
59. J.C. Thompson et al. "Antifouling Performance of the Embryo and Eggcase of the Dogfish *Scyliorhinus canicula*", J. mar. biol. Assoc. U.K., Vol. 74, pp 823-836, 1994.
60. J.D. McKenzie and I.V. Grigolava "How do Marine Invertebrates Keep their Surfaces Free from Microfouling", 9 International Congress on Marine Corrosion and Fouling, Portsmouth, U.K., 17-21 July 1995.

61. M.J. Cowling and T. Hodgkiess "High Technology Antifouling Coatings for Submarine Sensors Based on Modelling and Synthesis of Natural Antifouling Processes" Contract No: MAS2-CT91-0009, European Commision, 1991.
62. R. Baier et al. "Porpoise and Killer Whale Skin as Natural Examples of Low-Drag, Low Adhesion Biomaterial Surfaces", Transactions of the 2nd World Congress on Biomaterials, 10th Annual Meeting for the Society for Biomaterials, Minneapolis, MN, p.190, 1984.
63. H. Gucinski and R. Baier "Surface Properties of Poroise and Killer Whale Skin In Vivo", Amer. Zoologist, Vol. 23, No.4, p506, 1983.
64. W.D.P. Stewart "Preventing Formation of Marine Growth by the Use of Predatory Bacteria", BSRA Report
65. Anon "Report of the Marine Fouling Working Party for the Director of Petroleum Engineering", Department of Energy, UK, OT-R-8001, Feb. 1980.
66. F.G.W. Smith "Mechanical Control of Ship-Bottom Fouling by Means of Air Bubbles", Fla. Acad. Sci. Quarterly Journal, Vol. 9 pp. 153-161, 1946.
67. G.W. Swain "The Use of Ozone Air Bubble Curtains for the Protection of Fixed Structures from Marine Fouling", Internal Report. Dept. of Mech. Eng., University of Southampton ME/80/3.
68. T. Matsunaga "Electrochemical Prevention of Biofouling", Proceedings of Emerging Nonmetallic Materials for the Marine Environment, Honolulu, HI, 18 – 20 March, 1997.
69. J. Shibata et al. "Ship Hull Anti-Fouling System Utilizing Electrolyzed Sea Water"' Proc 3rd International Congress on Marine Corrosion and Fouling, 1972.
70. E. Mor, " Influence du pH du Substratum sur la Fixation des Organismes du Fouling",
71. Anon, "Development of Lime Paint Offers New Weapon in Antimicrobial Arsenal", Paint & Coatings Industry, pp 216-217, October 1997.
72. E.S. Castle "Electrochemical Control of Marine Fouling", Ind. Eng. Chem. Vol. 43 No. 4, pp.901-904, 1951.
73. R.K. Nazirov et al. "Fouling of Structures in Marine Oil Fieldsand its Prevention", In Protection Against Marine Growth, Trans, of the Oceanographic Committee, ACSIL transl. #1560, pp. 21-27, USSR Academy of Sciences, 1960.
74. P. Czerski "Experimental Models for the Evaluation of Microwave Biological Effects", Proc IEEE Vol 63, No. 11, PP. 1540-1544, 1975.
75. R. Plotner "Sensor Fouling on Deep Submergence Vehicles", In: Marine Sciences Instrumentation, Proc. 4th National ISA Marine Sciences Symposium, Vol. 4, pp. 267-295, 1968.
76. Morley et al. "The Use of Radioactivity Against Marine Fouling", J. Oil. Col. Chem. Assoc., Vol. 41, pp. 445-452, 1958.
77. C.B. Wootten "Method for Prevention of Fouling and Corrosion Utilizing Technecium-99", U.S. Patent No. 4,123,338, 31 Oct 1978.
78. V.F. Gerencser et al. "Inhibition of Bacterial Growth by Magnetic Fields", Nature, 196 (4854), pp. 539-541, 1962.
79. A.M. Aksel'band "Ultrasonic Protection of Ships from Fouling", In Transactions of the Oceanographic Commision, The Academy of Sciences, U.S.S.R., Vol. 13, 1960.
80. R. Giordano et al. "Effects of Ultrasound on Unicellular Algae", J. Acoust. Soc. Am. Vol 60, No. 1, pp. 275-278, 1976.
81. P.V. Murphy and M.J. Latour "Preventing Marine Fouling", U.S. Patent No 4,170,185, 9 Oct. 1997.
82. D. Rittschof et al "Cues and Context: Larval Responses to Physical and Chemical Cues", Biofouling, Vol. 12, Nos. 1-3, PP. 31-44, 1998.
83. J.M. Hills and J.C, Thomason."The Effect of Scales of Surface Roughness on the Settlement of Barnacle (*Semibalanus balanoides*) Cyprids. Biofouling, Vol. 12, No. 1-3, PP. 57-70, 1996.
84. G. Forsberg "Fiberflock – A Biomimicking Nonfouling Concept". Proceedings of an International Workshop, Biofouling: Problems and Solutions, University of New South Wales, Eds. S Kjelleberg and P. Steinberg, p77, April 1994.
85. D.C. Sommerville "Heat Treatment Optimization Studies at the Diablo Canyon Power Plant", Proceedings: Condenser Biofouling Control - State-of-the-Art Symposium, EPRO CS-4339, Nov. 1985.
86. NAVSEA "Waterborne Underwater Hull Cleaning of Navy Ships", Naval Ships' Technical Manual S9086-CQ-STM-010, Chapter 081, Oct. 1989.
87. W.M. Bruner "Method for Preventing Adhesion and Growth of Barnacles", U.S. Patent 2,865,702, 23 Dec. 1958.
88. R.E. Baier "Surface Properties Influencing Biological Adhesion", in R.S. Manly, Ed. Adhesion in Biological Systems, Academic, New York, 1970.
89. R.E. Baier "Influence of the Initial Surface Condition of Materials on Bioadhesion" Proceedings of the 3rd International Congress on Marine Corrosion and Fouling, pp 633-639, October 1972.
90. S.C. Dexter "Influence of Substrate Wetability on the Formation of Bacterial Slime Films on Solid Surfaces Immersed in Natural Sea Water", Proceedings of the 4th International Congress on Marine Corrosion and Fouling, pp 137-144, June 1976.
91. J.R. Griffith and J.D. Bultman "Fouling Release Coatings", Naval Engineers Journal, pp.129-132, April 1980.
92. R.F. Brady et al. "Nontoxic Alternatives to Antifouling Paints", J. Coatings Technology Vol 59, pp 113-119, 1987.
93. B.Z. Newby, M.K. Chaudhury, H.R. Brown "Macroscopic Evidence of the Effect of Interfacial Slippage on Adhesion", Science Vol. 269, pp1407-1409, 8 Sept. 1995.
94. A.E. Mera et al "Toward Minimally Adhesive Surfaces Utilizing Siloxanes", Naval Resrach Reviews, Vol XLIX, pp. 4-8, 1997.
95. W.A. Finzel and H.L. Vincent "Silicones in Coatings", Federation Series on Coating Technology, March 1996.
96. K. Kroyer, Great Britain Patent 1,397,001, 1973.
97. A. Milne and M. Callow, "Non-Biocidal Antifouling Processes", Trans I MarE, Conf. 2, Paper 37, 1984.
98. A. Milne, M. Callow and R. Pitchers, "The Control of Marine Fouling by Non-Biocidal Systems", Stud. Environmental Scxiences, 28 (Algal Biofouling), 145, 1986.
99. G.W. Swain Field Evaluation of Non-Toxic Antifouling Coatings: New Field Technologies and Performance Criteria", Naval Resrach Reviews, Vol XLIX, pp. 46-50, 1997.
100. M.A. Harper and J.F. Harper "Measurements of Diatom Adhesion and their Relationship with Movement", Br. Phycol. Bull. Vol. 3 No. 2, pp195-207, 1967.
101. H.A. Price "Seasonal Variation in the Strength of Byssal Attachment of the Common Mussel, *Mytilus edulis*L.", J. Mar. Biol. Assoc. U.K., Vol 60, pp. 1035-1037.
102. J.H. Waite "Nature's Underwater Adhesive Specialist", Int. J. Adhesion and Adhesives, Vol. 7, no. 1, pp 9-14, 1987.
103. M.W. Denny "Biology and the Mechanics of the Wave-Swept Environment", Princeton University Press, 1988.
104. K. Becker "Attachment Strength and Colonization Patterns of Two Macrofouling Species on Substrata with Different Surface Tension (in situ studies)", Marine Biology, Vol.117, pp301-309, 1993.
105. G.W. Swain and M.P. Schultz "The Testing and Evaluation of Non-Toxic Antifouling Coatings", Biofouling Vol. 10, p 187-197, 1996.
106. A. Becka and G. Loeb "Ease of removal of barnacles from various polymeric materials", Biotechnology and Bioengineering, XXVI, pp. 1245-1251, 1984.
107. J.D. Bultman, J.R. Griffith and D.E. Field "Fluoropolymer Coatings for the Marine Environment", In Proc. Symp. on Marine Biodeterioration, eds. J.D. Costlow and R.C. Tipper, pp 237-249, Naval Institute Press, Annapolis, MD, 1981.
108. J.F. Grenon, J.Elias, J.Moorcroft, D.J. Crisp. "A New Apparatus for Force Measurement in Marine Bioadhesion". Marine Biology, 53, 381-388, 1979
109. G.W. Swain, J.R. Griffith, J.D. Bultman, H.L. Vincent, "The Use of Barnacle Adhesion Measurements for the Field Evaluation of Non-Toxic Foul Release Surfaces" BiofoulingVol. 6, pp.105-114. 1992.
110. A.B. Yule, G. Walker, "The Adhesion of the Barnacle, *Balanus balanoides*, to Slate Surfaces", J.mar.biol.Ass. U.K., 64, 147-156, 1984.
111. ASTM D5618 "Standard Test Method for Measurement of Barnacle Adhesion Strength in Shear", American Standard for Testing and Materials, 1994.
112. M. Schultz "The Measurement of Hydrodynamic Forces on Fouling Organisms", MS Thesis, Ocean Engineering, Florida Institute of Technology, Melbourne, FL., August 1992.
113. G. Swain and M. Schultz "Advanced Non-Toxic Antifouling Coatings Technology Demonstration, NRL / GE Duplex Coating Systems, 41' Utility Boat. U.S. Coast Guard Reserve Training Center, Yorktown, VA."' Environmental Security Technology Certification Program. Second Inspection Report. October 1996.
114. K. Schumacher "An Instrumented Rotating Brush Device to Evaluate the Removal of Biofouling from Non-Toxic Antifouling Coatings. MS Thesis, Florida Institute of Technology, 1996.

ENVIRONMENTAL FACTORS FOR OCEAN BUBBLES

Jeffrey L. Hanson
The Johns Hopkins University
Applied Physics Laboratory
Laurel, Maryland 20723-6099
jeffrey.hanson@jhuapl.edu

Abstract - Acoustic reverberation experiments conducted during the extensive Critical Sea Test (CST) Program led to the conclusion that near-surface microbubble clouds are the primary source of low frequency (0-1000 Hz) acoustic surface backscatter during elevated winds. Crucial issues remaining from CST, however, were (1) explanation of large site-to-site differences, at similar wind speeds, in surface scattering strength; and (2) understanding how to extend the CST deep water results to coastal areas. It is demonstrated here that the CST observation disparities can mostly be attributed to physical and biological processes related to the supply, mixing, and removal of bubbles in the upper ocean. Using the extensive CST environmental and acoustic observation set, as well as satellite remote sensing products available over the World Wide Web, it is empirically shown that site-to-site differences in acoustic bubble scatter are related to the mean ocean temperature, biological productivity, and wave conditions at each site. As these are all readily available environmental parameters from satellites and operational models, they may ultimately be employed to routinely estimate the temporal and geographic variability in near-surface bubble characteristics.

1. Introduction

As an important element of underwater sonar performance, low-frequency (0-1000 Hz) acoustic surface scattering strength (SSS) measurements have been made in a variety of oceanographic conditions by numerous investigators. The recent series of Critical Sea Test (CST) experiments (1988-1992) has provided a rich set of observations, obtained with a consistent technique, in the six different environments shown in Figure 1 [1]. The calibrated CST results can be readily compared with earlier measurements such as those of Chapman and Harris obtained north of Bermuda in 1962 [2].

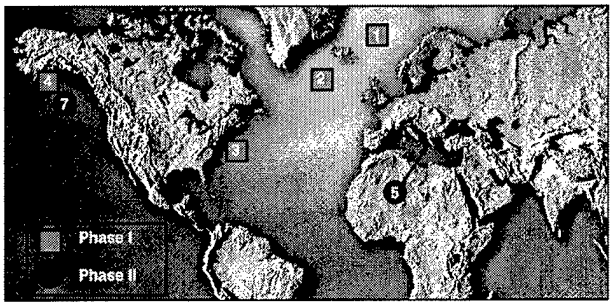

Figure 1 CST Surface Scatter Measurement Locations

Surface scattering results from the CST program have been reviewed in a series of reports [1], [3] - [6]. The CST results most relevant to our study are listed here:

- SSS is strongly linked to short-term (~ 1 h) wind history.
- Supporting environmental data suggest that SSS is more closely associated with tenuous bubble clouds than with breaking wave events.
- Acoustic model comparisons with CST results indicate that near-surface (~ 1-3 m) microbubbles, entrained by wave orbital motions, contribute most to SSS.
- Significant differences (6-7 dB) are noted between CST-4 and CST-7 SSS results at similar wind-forcing conditions. Unexplained differences also exist between other CST data sets and with Chapman-Harris.
- CST 1, 2, 3, 4, 5, and 7 results used to construct NRL Ogden-Nicholas-Erskine (ONE) empirical SSS model. Environmental input is the 1-hr backaveraged wind speed [1].

A crucial issue remaining from the CST program is explanation of the large site-to-site differences in SSS from bubbles. The extended analysis of CST observations reported here has led to a possible explanation for these differences.

2. Research Objective

Our hypothesis is that site-to-site variations in SSS are a result of physical and biological factors related to the supply, mixing, and removal of bubbles in the upper ocean. As the wind speed input of SSS models appears to adequately prescribe the local, short-term forcing of the upper ocean, the missing environmental factors must relate to the background setting of each site (swell, mixing, temperatures, dissolved gasses, surfactants, etc.). Hence, our primary research objective was to examine the influence of bubble-related environmental factors on SSS with particular emphasis on parameters linked to seasonal and geographic variations in near-surface bubble populations. The need to identify the 'missing link' for explaining site-to-site differences in SSS is recognized.

3. Site-to-Site SSS Variability: Environmental Factors

3.1 SSS Prediction Errors

The NRL ONE model predicts SSS as a multiparameter function of frequency, grazing angle, and wind speed. Observation departures from ONE predictions, aside from measurement errors, result from environmental influences not well represented by wind speed alone. Here we isolate these departures by calculating the SSS prediction error

$$SSSe = SSS_{ONE} - SSS_{obs} \quad (1)$$

with the 'ONE' and 'obs' subscripts referring to model predictions and observations, respectively.

The mean *SSSe* at 500 Hz for each of the CST and Chapman-Harris sites appears in Figure 2. The mean levels were calculated by averaging the prediction errors for each experiment over all wind speeds, all grazing angles > 10°, and over the frequency band 400-600 Hz. Error bars depict one standard deviation about the means. It is observed that CST-2 and CST-5 are over-predicted and that CST-1, CST-3, CST-4, and Chapman-Harris are under-predicted. The CST-7 values are close to zero; this is expected as CST-7 has contributed by far the most observations used for the ONE model fits. The differences between CST-4 and CST-7 levels have been particularly frustrating to the research community as both experiments occurred in the Gulf of Alaska under similar wind and wave conditions. Note that much larger differences exist between the remaining CST experiments, such as extreme differences between CST-3 and CST-5 of nearly 15 dB.

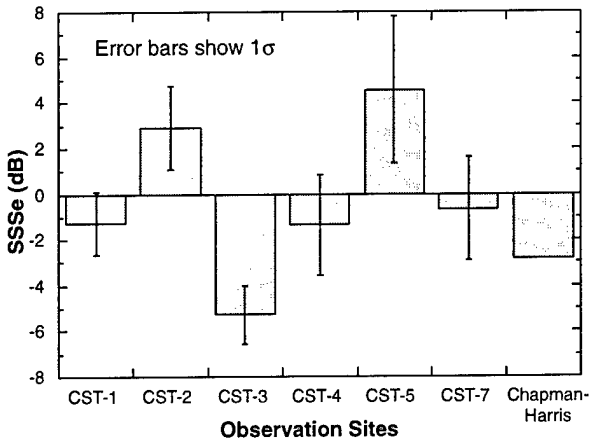

One standard deviation error bars are depicted.

Figure 2 Mean Surface Scatter Strength Prediction Error ($SSS_{ONE} - SSS_{obs}$) at 500 Hz

Our approach is to empirically relate *SSSe*, averaged over various frequency, grazing angle, and wind speed regimes, with the bubble-related environmental descriptors described in Section 3.2.

3.2 Environmental Descriptors

The ONE model wind speed input represents those environmental processes that influence surface scatter on short (hourly) time scales including surface wave development and the supply of bubbles by breaking waves. Missing from this model, however, are environmental descriptors for the background setting of each site, such as swell activity, mixed-layer temperature and depth, gas saturation, and surfactants. Both laboratory experiments and theoretical calculations have shown the importance of these background conditions on processes that supply, entrain, and remove bubbles from the upper ocean [7] - [9]. The full complement of supporting environmental data collected during CST, combined with remote sensing products, has allowed a reasonable test of their importance to SSS.

The environmental descriptors found to be most important for site-to-site SSS variability appear in Table I. Four factors are employed to describe bubble supply, entrainment, and removal processes in the ocean: wind speed (U_{10}), ocean temperature (*sst*), significant wave height (h_s), and chlorophyll concentration (*chl*). The importance of wind speed has already been demonstrated by its success in the various SSS model formulations (for example, Chapman-Harris and ONE).

Bubble Issue	Process	Descriptor
Supply	Wave breaking	Wind speed Ocean temperature
Entrainment	Wave mixing	Wave height* Ocean temperature
Removal	Gas dissolution	Chlorophyll concentration

* Mean over entire test duration.

Table I
Environmental Descriptors for Surface Scatter by Bubbles

Significant wave height, averaged over the entire test duration, is employed here to represent the test site background energy setting and helps account for the effects of swell on wave breaking and mixing. It is expected that high-energy environments will support denser and deeper bubble populations.

Sea surface temperature (*sst*) significantly influences both the supply and removal of bubbles in the upper ocean. Both surface tension and viscosity are highest in cold water; this fact offers a preliminary explanation for reduced whitecap coverage in high latitudes [10]. Water temperature also controls gas solubility. As less air can dissolve in warmer water, we expect longer bubble lifetimes and hence, denser bubble populations with water temperature increases. CST surface temperatures were collected from 0.5-1.5 m depth and represent the typical ocean temperature within the near-surface bubble layer.

Phytoplankton biomass, characterized by remotely sensed chlorophyll concentrations, will also influence bubble lifetimes through two complementary mechanisms [11]. First, surfactants secreted by biological communities are known to provide a stabilizing coating to seawater bubbles. Second, phytoplankton blooms can supersaturate the water with respect to oxygen and other atmospheric gases. Both of these effects will decrease the rate of bubble dissolution and promote larger bubble populations in biologically productive areas. This effect will be most important in nearshore and coastal waters where biological productivity is greatest.

Monthly mean phytoplankton pigment (chlorophyll) concentrations for the CST and Chapman-Harris sites were obtained from the Coastal Zone Color Scanner (CZCS) mission results. This observation set covers 7.5 yr from October 1978 through June 1986. Global color maps of mean monthly pigment concentrations from CZCS can be viewed on the World Wide Web [http://seawifs.gsfc.nasa.gov/SEAWIFS.html]. These maps depict a dramatic seasonal and geographic variability in ocean chlorophyll production by marine phytoplankton. Driven by light and nutrient availability, global phytoplankton blooms occur at high latitudes between early spring and late summer. Furthermore, plankton blooms are observed throughout the year in coastal environments as a result of increased nutrient availability from coastal runoff. As the CST program did not begin until 1988, the CZCS pigment concentrations can only be used to represent typical conditions at each site.

3.3 A Simple Check of Hypothesis

The dependence of gross site-to-site differences in surface scattering on the bubble-related environmental descriptors (Table I) can be demonstrated with a few simple empirical tests. *SSSe* values from CST and the Chapman-Harris model were first averaged over three distinct frequency bands: 0-150 Hz, 400-600 Hz, and 800-1000 Hz. The data from all runs (individual observation sets) within each CST experiment were included in the averages as well as observations at all grazing angles > 10°. This gross averaging process was performed to minimize uncertainty due to random measurement errors, environmental patchiness, short-term variability, etc. Each experiment is now conveniently described by the set of mean prediction errors, with corresponding baseline environmental descriptors, listed in Table II. Note that wind speed values do not appear in Table II. The objective is to identify additional environmental factors, beyond local wind effects, that contribute to SSS variability. It is assumed that wind speed contributions are adequately represented by the ONE model and are hence already 'accounted for' in the *SSSe* values.

The combined *SSSe* values depend on the three environmental descriptors in a manner that agrees with physical intuition. To facilitate display of these multidimensional results, we will first normalize the data with respect to the h_s dependence. Note that CST-2 and CST-4 are both cold water experiments with close *chl* values, and that CST-5 and CST-3 are both warm water experiments with close *chl* values. The *SSSe* differences between these experiment pairs should be dominated by h_s effects. This is verified by the *SSSe* vs. h_s plot of Figure 3. The differences between *SSSe* values of each experiment pair, and at each frequency range, are represented by a series of linear regressions. Note that all of the regressions are of similar slope with higher observed scattering strengths (relative to ONE predictions) as mean wave height increases. The regression slopes were averaged within frequency bands

Source	h_s m	*sst* °C	*chl* mg/m^3	Mean *SSSe* (dB) 0 - 150 Hz	400 - 600 Hz	800 - 1000 Hz
CST 1	1.8	10.7	1.140	1.1	-1.3	- no data -
CST 2	2.5	8.3	0.516	4.8	2.9	3.2
CST 3	1.4	28.1	0.045	-2.3	-5.3	-0.1
CST 4	3.2	3.3	0.320	2.1	-1.4	0.8
CST 5	0.6	23.0	0.088	2.6	2.9	5.0
CST 7	3.3	5.5	0.176	1.0	-0.7	0.3
Chapman-Harris *	2.7	18.0	0.263	-1.5	-3.2	-2.6

* Chapman-Harris h_s and *sst* estimates obtained from *U.S. Navy Marine Climatic Atlas* CD-ROM.

Table II
Mean Quantities Used for Investigation of Site-to-Site Differences

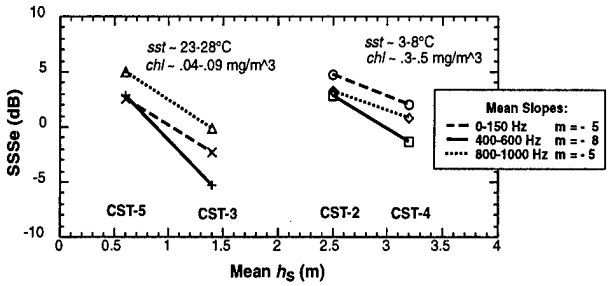

Mean regression slopes for each frequency band were used to normalize the *SSSe* averages in Table II for surface wave effects.

Figure 3 Influence of Background Wave Energy on Surface Scatter Strength for Sites with Similar Temperature and Chlorophyll Characteristics

and used to produce wave-height normalized prediction errors (*SSSn*) for each of the observations in Table 2. The normalization is given by

$$SSSn = m(h_{sREF} - h_s) + SSSe \qquad (2)$$

where m is the average regression slope for each frequency band indicated on Figure 3 and a reference wave height of $h_{sREF} = 2.0\ m$ was chosen.

There are now two remaining variables on which *SSSn* depends: phytoplankton pigment concentration and ocean temperature. Inspection of the site environmental data in Table 2 suggests that data can be sorted into two groups: (1) a set of cold-water observations (*sst* < 11 °C) that includes CST-1, CST-2, CST-4, and CST-7; and (2) a set of low-productivity observations (*chl* < 0.3 mg/m^3) that includes CST-3, CST-5, CST-7, and Chapman-Harris. Note that only CST-7 falls into both groups.

The dependence of *SSSn* on pigment concentration for the cold-water observation set appears in Figure 4. The results imply an important role of biological activity in surface scatter. This trend is strongest at mid-frequencies (400-600 Hz). Scattering level increases (represented by decreasing *SSSn*) with biological production are probably due to higher dissolved gas levels from biological productivity and the presence of biological surfactants, both of which will extend the life of ambient bubbles.

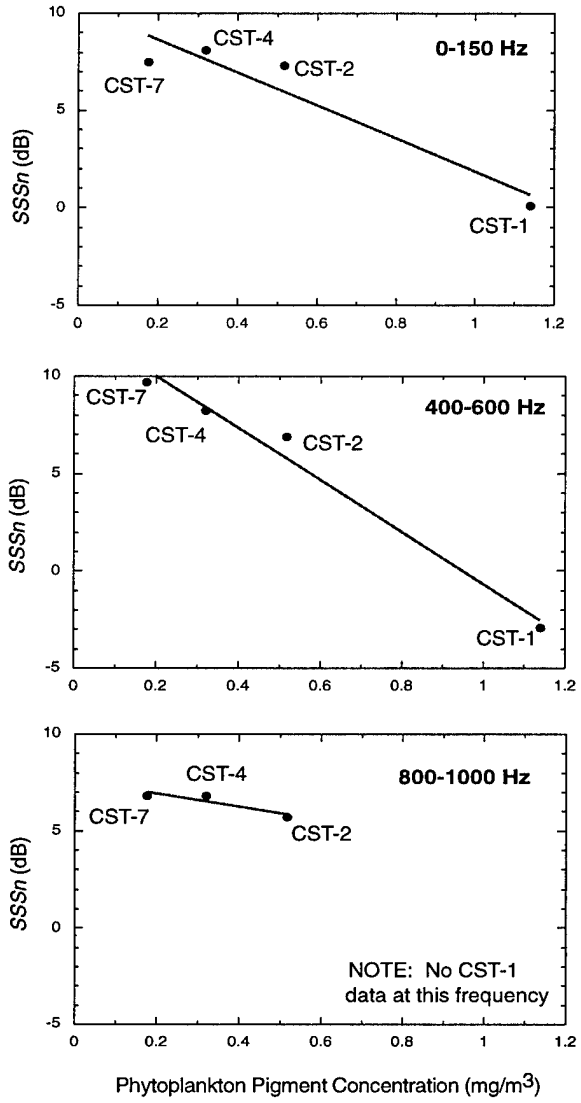

Figure 4 Influence of Biological Productivity on h_S-Normalized Surface Scatter Strength Prediction Error for the Cold Water (≤ 11°C) Observation Sites

The dependence of *SSSn* on *sst* for the low pigment observations appears in Figure 5. A definitive trend of increasing scatter (represented by decreasing *SSSn*) with increasing temperature is observed at all frequencies. These results indicate an important role of ambient ocean temperature in modulating surface scatter levels. The influence of temperature on bubble entrainment and gas dissolution results in high levels of ambient bubbles in warm water. Furthermore, near-surface stratification in warmer regions may effectively trap bubbles near the surface where the scattering effect is most important.

The results shown in Figures 3 through 5 suggest that a linear model for the dependence of *SSSe* on h_s, *sst*, and *chl* might explain a significant fraction of the site-to-site variance in SSS. The method of least-squares multiple regression was employed to test the performance of a linear model for the surface scatter prediction error

$$SSSe = \alpha h_s + \beta sst + \gamma chl + b, \qquad (3)$$

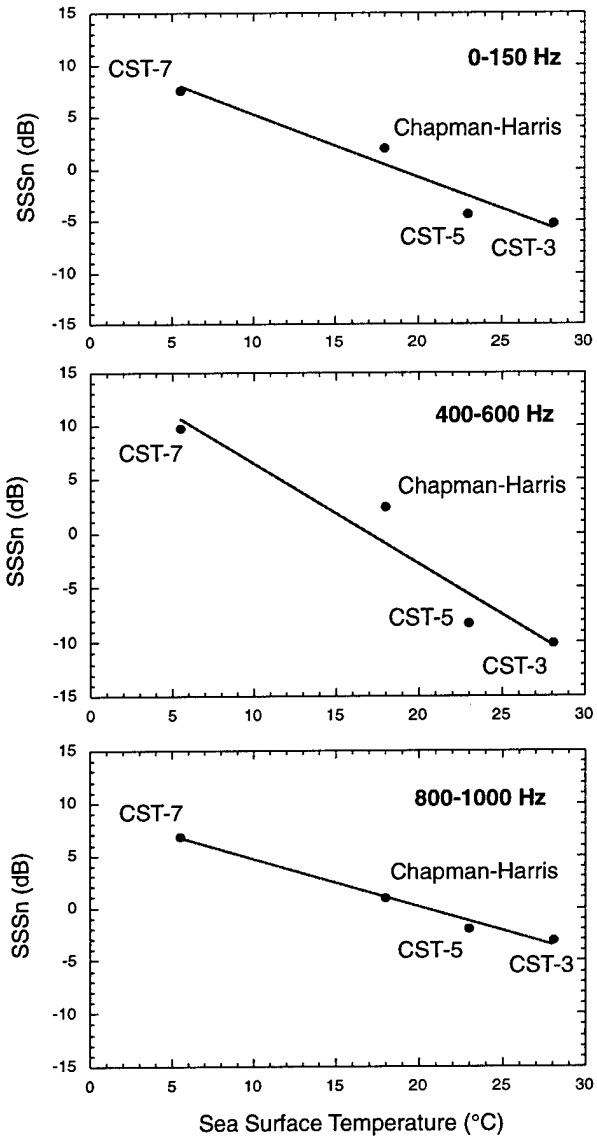

Figure 5 Influence of Ocean Temperature on h_S-Normalized Surface Scatter Strength Prediction Error for the Low Productivity ($chl \leq 0.3$ mg/m) Observation Sites

with fit coefficients α, β, and γ for wave height, ocean temperature, and chlorophyll concentration, respectively. For the model calculations, the *SSSe* averaging was restricted to narrow wind speed, frequency, and grazing angle bands so that the results represent a specific set of environmental and acoustic conditions.

This preliminary model is quite successful in describing gross site-to-site differences in SSS. Typical results appear in Figure 6. Here the regression coefficient and the three model fit coefficients are plotted as a function of acoustic frequency at 15-25° grazing angle for the case of 8-10 m/s winds. Note that a high regression coefficient is obtained at all frequencies indicating that the model explains a large percentage of the total variance. There is a linear transition of all model parameters across frequency with the h_s and *sst* fit coefficients essentially constants.

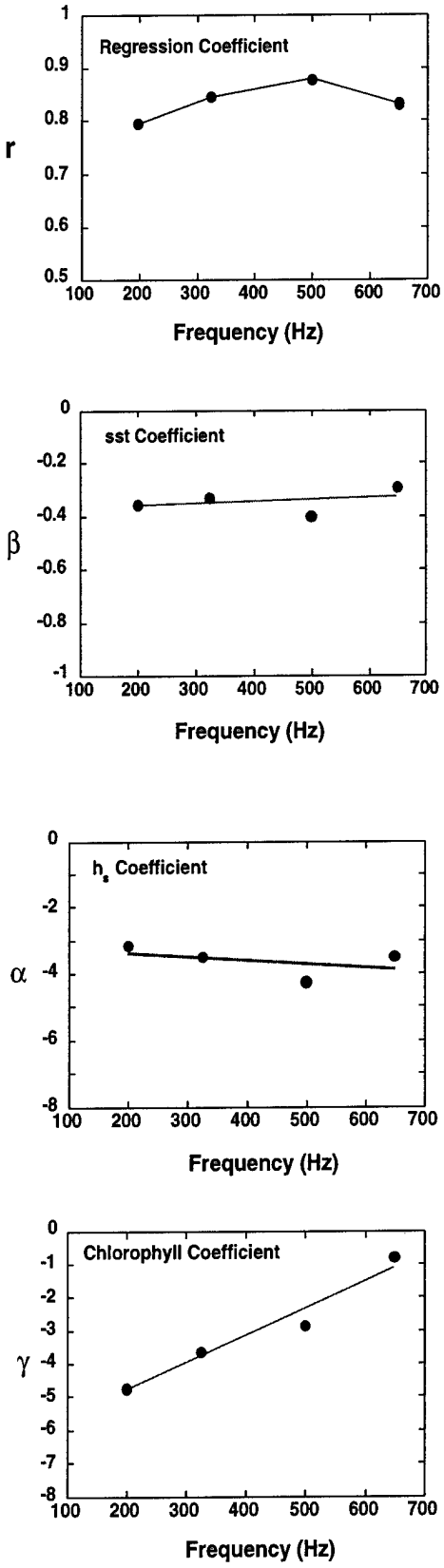

Figure 6 Multiple Linear Regression Results for the Case of U_{10} = 8-10 m/s and 15-25° Acoustic Grazing Angle

Using α and β to normalize the data for both wave height and ocean temperature effects, as demonstrated earlier, allows a direct comparison of prediction error with phytoplankton pigment concentration. This normalization is given by

$$SSS_n = \alpha\left(h_{s_{REF}} - h_s\right) + \beta(sst_{REF} - sst) + SSSe\,, \qquad (4)$$

where the reference values $h_{s_{REF}} = 2.0\ m$ and $sst_{REF} = 15°C$ were chosen. The normalized 500 Hz SSS prediction errors (*SSSn*) at each site for winds of ~10 m/s appear in Figure 7. A logarithmic fit to the data is given by

$$SSSn = -[4.8 + 3.6\log(chl)]\,, \qquad (5)$$

with regression coefficient $r = 0.91$. The CST-2 results are slightly farther than two standard deviations from the mean and are not included in the regression. This is perhaps due to inaccuracy of the monthly mean CZCS *chl* value in representing CST-2 conditions; inspection of the CZCS data for this site suggests extreme spatial variability in *chl* at that location and time. The remaining data of Figure 7 indicate that phytoplankton blooms contributed up to 5 dB in average SSS site-to-site differences during CST. Extrapolating these results to nearshore phytoplankton pigment concentrations of 50 to 100 mg/m^3 indicates that SSS values can be 10 to 12 dB higher than ONE model predictions in shallow water environments.

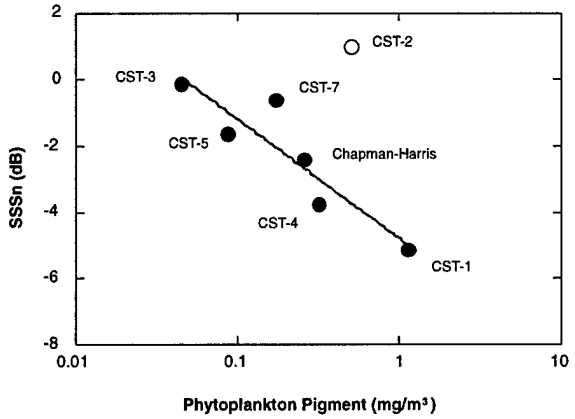

Figure 7 Dependence of Normalized SSS Prediction Error on Phytoplankton Pigment Concentration for an Acoustic Frequency of 500 Hz at 10 m/s winds, 20° Grazing Angle and with $h_S = 2.0$ m and $sst = 15°C$

4. Conclusions and Recommendations

4.1 Conclusions

- Gross site-to-site differences in low-frequency acoustic bubble scatter are explained by seasonal and geographic environmental factors.
- Biological productivity increases acoustic bubble scatter in the open ocean. This is likely due to increased dissolved gas levels and the presence of biochemical surfactants, both of which will extend bubble lifetimes. This effect will be amplified in shallow water environments.
- Acoustic bubble scatter is higher in warm water. This is likely a result of greater bubble supply due to viscosity and surface tension effects and decreased gas solubility which acts to extend bubble lifetimes. Increased temperature variability will greatly influence scattering strength statistics in shallow water environments.
- Acoustic bubble scatter, in similar wind conditions, increases in higher-energy environments. Here the background ocean energy level was characterized by significant wave height averaged over several days.

4.2 Recommendations for Continued Research

- Determine the relevance of these results to other near-surface bubble observation sets
- Develop a near-surface bubble model with physical and biological parameters for site-to-site variability

5. Acknowledgments

Valuable discussions with Alan Brandt, Fred Erskine, David Farmer, Scott Hayek, Frank Henyey, John Sweeney, Eric Thorsos, and Svein Vagle helped shape the hypotheses leading to these results. Environmental and acoustic data were provided by Rick Marsden, Mike Nicholas, Pete Ogden, and Larry White. Mike Mandelberg contributed to the data assimilation, organization, and preliminary analyses. Financial support provided by the Office of Naval Research (code 32OA).

6. References

1. M. Nicholas, P. M. Ogden, and F. T. Erskine, "Improved Empirical Descriptions for Acoustic Surface Backscatter in the Ocean," accepted for publication in *IEEE J. of Ocean Engr.*, 1998.

2. R. P. Chapman and J. H. Harris, "Surface Backscattering Strengths Measured with Explosive Sound Sources," *J. Acoust. Soc. Am.* **34**, 1592-1597, 1962.

3. J. L. Hanson, "Winds, Waves, and Bubbles at the Air-Sea Boundary," *Johns Hopkins APL Tech Dig.*, **14**, pp. 200-208, 1993.

4. P. M. Ogden and F.T. Erskine, "Surface Scattering Measurements Using Broadband Explosive Charges in the Critical Sea Test Experiments," *J. Acoust. Soc. Am.*, **95**, pp. 746-761, 1994.

5. P. M. Ogden and F. T. Erskine, "Surface and Volume Scattering Measurements Using Broadband Explosive Charges in the Critical Sea Test 7 Experiment," *J. Acoust. Soc. Am.*, **96**, pp. 2908-2919, 1994.

6. E. I. Thorsos, R. C. Gauss, R. J. Soukup, and J. M. Fialkowski, "Measurements and Modeling of the Spectral Character of Low Frequency, Low Grazing Angle Surface Reverberation," *J. Acoust. Soc. Am.*, **95**, pp. 2828, 1994.

7 S. A. Thorpe, P. Bowyer, and D. K. Woolf, "Some Factors Affecting the Size Distributions of Oceanic Bubbles," *J. Phys. Oceanogr.*, **22**, pp. 382-389, 1992.

8. J. Wu, "Variation of Whitecap Coverage with Wind Stress and Water Temperature," *J. Phys. Oceanogr.*, **18**, pp. 1448-1453, 1988.

9. P. A. Huang, Y-K Poon, and J. Wu, "Temperature Effects on Generation and Entrainment of Bubbles Induced by a Water Jet," *J. Phys. Oceanogr.*, **21**, pp. 1602-1605, 1991.

10. J. Wu, "Individual Characteristics of Whitecaps and Volumetric Description of Bubbles," *IEEE J. Oce. Engineering*, **17**(1), pp. 150-158, 1992.

11. P.S. Liss and R.A. Duce, eds., *The Sea Surface and Global Change*, Cambridge University Press, 1997.

A BOAT-MOUNTED FOIL TO MEASURE THE DRAG PROPERTIES OF ANTIFOULING COATINGS APPLIED TO STATIC IMMERSION PANELS

Brett S. Kovach
Ocean Engineering
Florida Institute of Technology
Melbourne, FL 32901
Tel 407 674 8005, Fax 407 984 8461
Email: bkovach@fit.edu

Dr. Geoffrey Swain
Ocean Engineering
Florida Institute of Technology
Melbourne, FL 32901
Tel 407 674 7129, Fax 407 984 8461
Email: swain@fit.edu

Abstract – Legislation restricting the use of biocides in antifouling paints has directed attention towards the development of nontoxic silicone foul-release coatings. It has been shown that these coatings will become fouled, but when subjected to an external flow, the fouling can be removed by hydrodynamic forces generated at the surface. It was decided to investigate the drag forces experienced by fouling communities and determine the free stream velocities required for foul-release from coatings with known barnacle adhesion strengths.

Two identical instrumented foils were built to accept standard (0.254m x 0.305m) static immersion antifouling panels and to be towed alongside a 7m powerboat. The flow characteristics of the foils were determined by wind tunnel testing. Fully fouled test panels are attached to the foil which is dragged through seawater at predetermined speeds. During testing the shear force, flow velocity, and video of the foul-release are recorded simultaneously. The foul-release properties are then correlated with barnacle adhesion shear strength according to ASTM 5618. Preliminary testing of two silicone panels demonstrates the relationship between barnacle adhesion strength, foul-release, and drag.

I. INTRODUCTON

Biofouling of ships, boats and other marine vehicles is controlled by the use of antifouling (AF) paints that contain biocides. Marine organisms increase the roughness of the vehicle's surface, which causes an increase in skin friction drag. It has been estimated that the U.S. Navy spends an extra $100 million annually in added fuel costs due to the effects of biofouling on their ships [1]. This does not include the money and time spent for biofouling control (AF coatings, dry dockings, and hull cleanings).

The self-polishing copolymer organotin systems (SPC/TBT) provide the best present day AF coating. These have in excess of 5 years operating life and have the advantage that they smooth with time, hence reducing skin friction drag [2]. They are also extremely toxic and have been shown to adversely affect the environment [3]. This had precipitated environmental regulations restricting their use [4] and the requirement to develop environmentally friendly alternatives [1].

At present the most promising alternatives to the use of biocides are the non-toxic, silicone, and foul-release coatings. The concept is not new. Oils, greases, fluorinated polymers and silicones have all been tried as a means to prevent the permanent attachment of fouling organisms [5, 6, 7]. To date, the silicones have provided the best performance, and they are now accepted as a viable alternative to traditional antifouling treatments in situations where there are restrictions with regard to the use of biocides. Unfortunately their performance, in terms of cost, durability, longevity and antifouling, still does not meet that of the self-polishing organotin systems. Therefore, further research and development are required to better understand how they function and to improve their performance.

Foul-release coatings work by reducing the adhesion strength of organisms to the surface. They will become fouled but the adhesive strength are sufficiently low that the hydrodynamic forces generated under flow will detach organisms. Thus, the two determining factors controlling foul-release are the hydrodynamic forces acting on the fouling and the adhesion of the fouling to the surface.

The purpose of this investigation was to develop a system to evaluate the performance of foul-release coatings by measuring biofouling adhesion strengths and the hydrodynamic forces required for removal.

Biofouling Adhesion

Biofouling adhesion is an important measure of the effectiveness of foul-release coatings. The lower the adhesion strength, the lower the velocity needed for foul-release. Barnacles are good candidates to quantify adhesion on surfaces. A method to measure their adhesion strength in shear is now included as an ASTM standard to evaluate the foul-release properties of coatings [8]. Barnacle adhesion strength has been measured on both natural and artificial surfaces [7, 9, 10, 11, 12, 13]. Furthermore, it has been shown that the tensile adhesion strength of barnacles is about 3 times less than the shear adhesion strength [7, 14]. This is important when considering the lift and drag forces imparted to an organism by hydrodynamic flow.

Biofouling Hydrodynamics

Fouling organisms subjected to an external flow experience lift and drag forces [15, 16]. The magnitude of the forces depends on the size of the organism and the thickness of the boundary layer. Organisms extending through the boundary layer will experience greater form drag as compared to an organism within the boundary layer. They act to increase the roughness of the surface.

There have been limited studies that have examined the hydrodynamic forces on fouling organisms. Denny used strain gage force transducers to measure the lift and drag on sessile marine organisms exposed to wave swept environments. He found lift and drag coefficients of the acorn barnacle to be 0.5 at Re_x of 10^5 [9, 15]. Schultz, who measured the lift and drag of barnacles attached to a foil towed through the water, found similar coefficients (C_L=0.45, C_D=0.5, at $Re=10^5$)[16]. These data indicate that the total hydrodynamic forces acting on a barnacle to be almost 90% lift. This means that the total hydrodynamic force acting to remove a barnacle is pulling at 64 degrees from the surface [17].

The above analysis, however, only considers solitary barnacles. Barnacles often grow in clusters, which resemble that of a mound with taller barnacles in the center [18]. This grouping, along with the presence of other fouling organisms makes it difficult to estimate the forces acting on individual barnacles. In general, the lift and drag forces acting on macrofouling have yet to be defined due to the complexity of the flow over the heterogeneous communities.

II. INSTRUMENTED FOIL

Two instrumented foils were designed and built to hold standard static immersion test panels (0.254m x 0.305m) (See Figure 1). One foil acts as a control using test panels with known surface properties, and the other foil accommodates the fouled panels. The foil sections are NACA 0012 symmetric airfoils, 0.305m high and 1.03 m long. They are mounted to 32mm diameter stainless steel rods which are attached to either side of an aluminum frame mounted on the rear of a 7m power boat. The tops of the foils are set 0.5m below the surface of the water and each is trimmed to be normal to the flow by an electromechanical actuator.

The test panels are mounted on a portal-type floating-element force balance which is built into the foil [19]. There is a 3mm gap around the test panel. The force gage uses four strain gages connected in a full bridge circuit which creates a linear voltage response force gage that is insensitive to moments. The advantage of using this type of gage is that it can be optimized for a specific range of forces thus increasing sensitivity. Inside the foil the dead space around the force gage is filled with high-density foam to minimize the inertial effects of seawater circulation on the measurements.

A pitot-static probe extends above the test section to measure the dynamic pressure that can be used to determine the freestream flow velocity, U, using Bernoulli's equation.

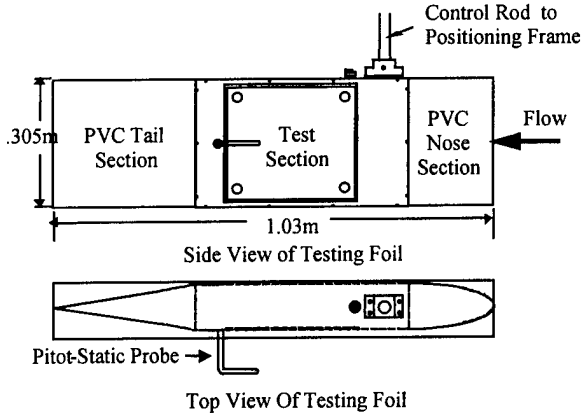

Figure 1. Instrumented Foil Drawing

The foil used to test the foul-release coatings has a video camera mounted adjacent to the test section. This enables real time foul-release to be observed.

The foils are dragged through the seawater creating a flow around the test section (See Figure 2). The force gage measures the shear force due to the flow over the test surface at different velocities. Each foil is adjusted to keep the foil into the flow of the seawater as the boat's trim angle changes with increasing speed. Instrumentation on the boat includes a datalogger to record the drag forces on the panels and the free stream velocity (See Figure 3). A HI-8 video recorder provides real time images of foul-release. The video is digitized and a real-time movie is recorded with the force and velocity data displayed as the fouling is released from the coating.

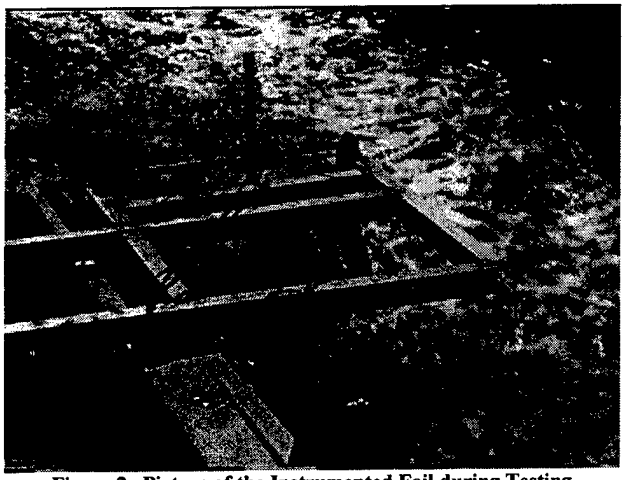

Figure 2. Picture of the Instrumented Foil during Testing

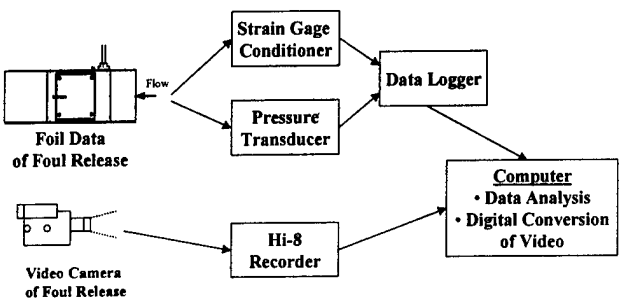

Figure 3. Foil Testing System

Wind Tunnel Calibration

Several tests were run in a low speed wind tunnel to characterize the flow around the foil. This enabled errors to be minimized in the floating-element region. Floating-element force balances are subject to errors associated with the gap around the test section [20, 21, 22, 23]. These include: flow through the gap and circulation around the test section, misalignment errors of the test section height, pressure effects caused by a normal pressure distribution acting nonuniformly across the test section, and nonuniform flow patterns across the test section.

The wind tunnel tests included: flow visualization tests using tufts of yarn and titanium dioxide streaks, pressure profiles measured with the gaps sealed and unsealed, and boundary layer profiles using hot wires located before and after the test section to examine the consistency of the flow.

The flow visualization tests revealed that there was no extraneous flow around the gaps and no separation anywhere on the foil. Static pressure taps were used to investigate the flow in the region of the test section with the gaps sealed and unsealed (See Figure 4). The pressure distribution shows that the gaps had no effect on the flow and the curves are almost identical. Notice the pressure distribution over the test section is nearly constant. This indicated that there is no significant pressure gradient over the test section.

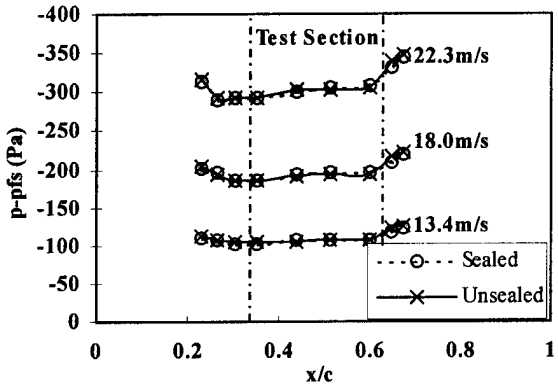

Figure 4. Pressure Distribution Across the Foil Test Section with the Gap Sealed and Unsealed (p is the static pressure, p_{fs} is the freestream pressure, x is the distance from the leading edge of the foil, c is the chord length of the foil)

The boundary layer profiles were obtained using a hotwire anemometer at four locations before and over the test section (See Figure 5). Because of the error associated with the determination of boundary layer thickness, the data were nondimensionalized using the displacement thickness, δ^*. The boundary layer profiles are similar over the test section, and are typical of turbulent boundary layer profiles [24, 25]. The boundary layer thickness was approximately 18mm over the middle of the test section at a Re_X of 8.3×10^5.

These tests suggest that if the misalignment of the test section is kept to a minimum, the instrumented foil's systematic errors should be small.

III. TEST PROCEDURE

The roughness of the coating is first measured using the British Marine Technology hull roughness analyzer. The coatings are then immersed in seawater at the Florida Institute of Technology Static Immersion site. The panels are caged to prevent disturbance by fish and other grazing organisms that have been shown to remove fouling from the test panels [26]. The coatings are visually inspected for physical condition and fouling according to ASTM D3623 Testing Antifouling Panels in Shallow Submergence [27]. When sufficient fouling has become established the panels are removed from the water and one side is evaluated for fouling adhesion.

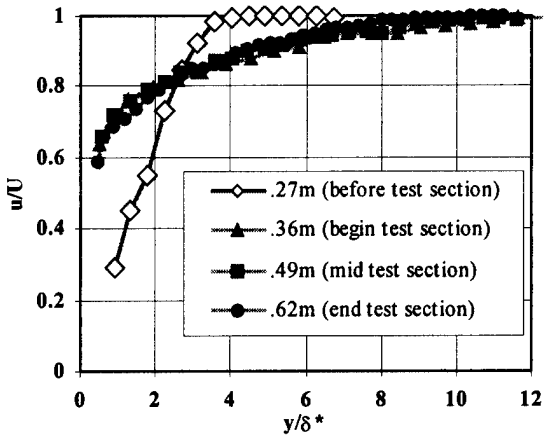

Figure 5. Mean Velocity Distribution for Free Transition Over the Length of the Instrumented Foil (U_{AIR} = 22.3 m/s, u is the local velocity, y is the distance normal to the surface, δ* is the displacement thickness)

On the backside of the test panel barnacle, shear adhesion measurements are performed according to ASTM 5618 [8]. This method uses a force gage to apply steadily increasing shear force to the base of a barnacle. The force for detachment is recorded and the base diameter, d, of the barnacle measured in four directions. The adhesion strength in shear, τ_B, is calculated by dividing the force for removal by the base area of the barnacle.

$$\tau_B = \frac{F_s}{\frac{\pi}{4}\left(\frac{d_1 + d_2 + d_3 + d_4}{4}\right)^2} \quad (1)$$

The panel is then attached to the instrumented foil. Care is taken to ensure that the panel is flush with the foil surface. The instrumentation is then zeroed with the external devices off and repeated with the devices on. This step is a check to confirm that all the devices are working properly. The water temperature is recorded and a water sample taken to determine density and kinematic viscosity. The foil is then run at 4, 8, 12, 16, and 20 knots for a period of one minute at each velocity. During the speed runs, velocity, shear force and video readings are taken continuously. At the end of the 20 knot run the panel is cleaned back and the runs at the 5 speeds repeated to obtain the skin friction drag in the clean condition.

Testing is dependent on weather conditions permit (a flat sea surface , <0.3m chop, and wind <5knots).

IV. RESULTS

Preliminary data is presented for two silicone-based foul-release coatings with known barnacle adhesion characteristics (silicone A and silicone B). Each coating was applied using a draw down process which leaves a very smooth (< 20 micron roughness) and uniform surface. The coatings were allowed to foul for three months (See Figures 8, 12). Each coating had a thick (15mm) accumulation of fouling consisting mainly of encrusting bryozoans, barnacles, silts, slimes and some tubeworms.

Barnacle adhesion data was collected for *Balanus eburneus* on the backsides of the test panels (See Figure 6). Each shear strength value was the average of at least 20 measurements. Silicone A had the highest barnacle shear strength ($7.5x10^4$Pa), and silicone B had a lower adhesive strength ($2.5x10^4$Pa).

Hydrodynamic tests were run on the front side of each panel. After each run was complete, the last frame from the video footage was used as the after photograph for foul release (See Figures 8-15). It can be seen that no foul-release occurred on silicone A. Foul-release on silicone B, however, started to occur at 4 knots. This was mainly encrusting bryozoans. At 12 knots barnacles started to be removed.

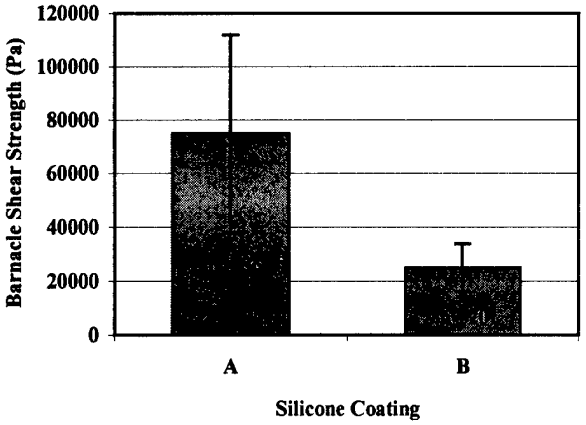

Figure 6. Barnacle Adhesion Data

The force data of each test is plotted in Figure 7. A moving average of ten data points was used to reduce noise.

V. DISCUSSION

The barnacle shear adhesion strength for the silicones was much less than that found on other surfaces. For example, it has been reported that typical barnacle adhesion strength (*Balanus eburneus*) on epoxy is $1.5x10^6$Pa and Teflon, the lowest reported non-silicone coating, is $5.9x10^5$Pa [28]. The silicones are an order of magnitude lower, clearly outperforming all other coatings.

No foul-release occurred on silicone A. Foul-release, however, did occur on silicone B and it is interesting to compare the observed foul-release velocities for barnacles to those predicted by theory. A simple analysis was made to relate the velocity for foul-release to the measured barnacle adhesion strength. This was made for a solitary acorn barnacle using the following assumptions: the barnacle was subjected to freestream velocity; the drag and lift coefficients were C_L=0.45 and C_D=0.5 [9, 15, 16]; the barnacle base diameter, base height, and top diameter ratios were 6:4:3 (See Figure 16). It can be seen that lift forces are greater than drag forces. It has also been shown that the tensile adhesion strengths are about 3 times less than the shear adhesion strengths [7, 14]. Using this information, theory would predict that the minimum velocity to remove barnacles on silicone A is about 20 knots. On silicone B, however, foul-release should occur at 12 knots. Observations of the video showed that barnacles were removed from silicone B at 12 knots but no barnacles were removed from silicone A. It is apparent that silicone based systems are close to providing a hydrodynamically self-cleaning surface for barnacles.

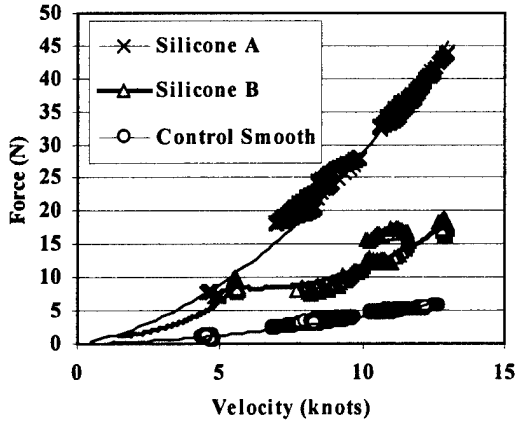

Figure 7. Drag Force Data Comparison

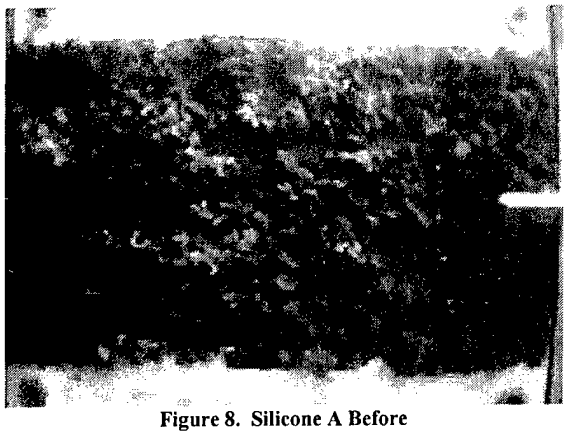

Figure 8. Silicone A Before

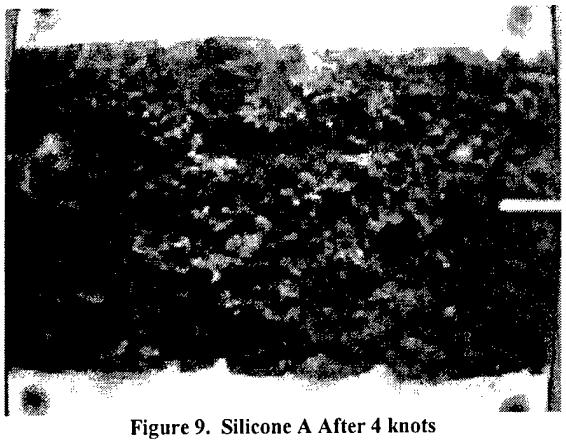

Figure 9. Silicone A After 4 knots

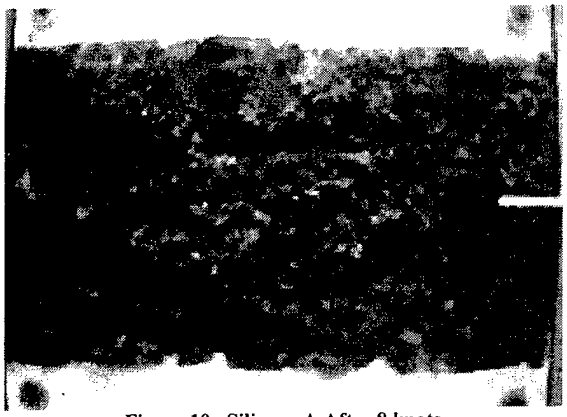

Figure 10. Silicone A After 8 knots

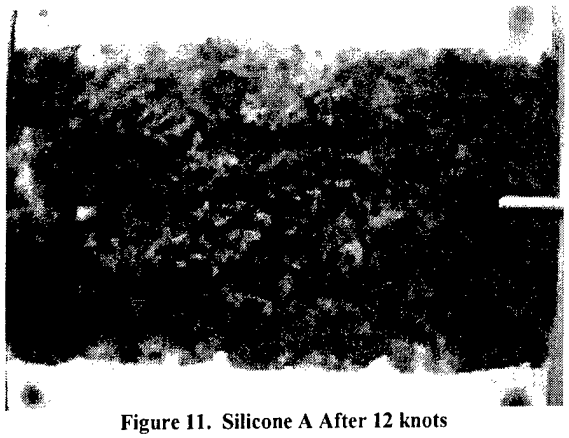

Figure 11. Silicone A After 12 knots

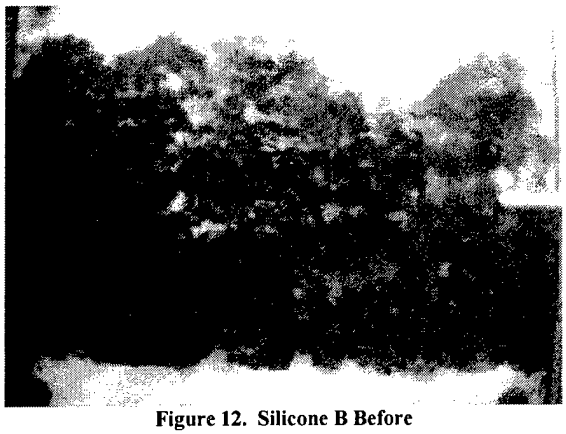

Figure 12. Silicone B Before

Figure 13. Silicone B After 4 knots

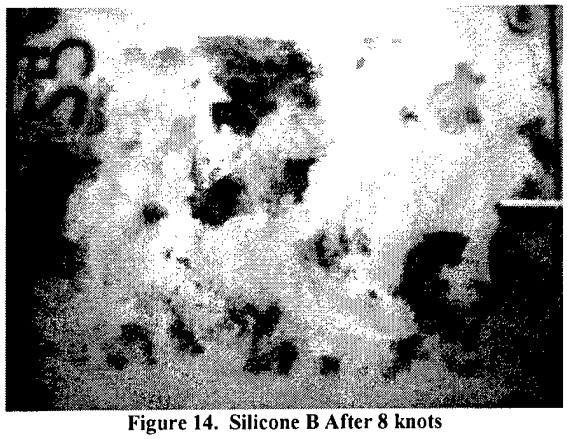

Figure 14. Silicone B After 8 knots

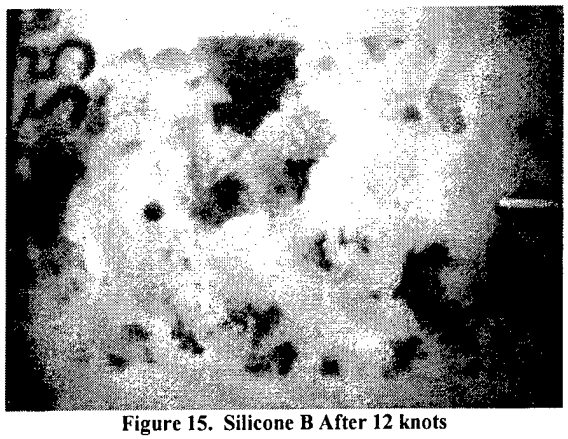

Figure 15. Silicone B After 12 knots

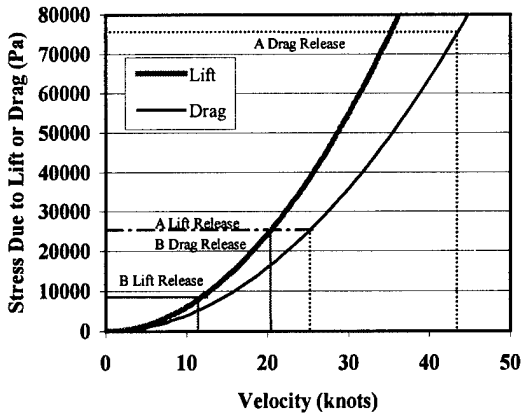

Figure 16. Prediction of Foul Removal for a Single Acorn Barnacle

The drag force measurements allow skin friction to be compared to foul-release. The increase in drag force associated with velocity increases measured on silicone A were representative of a panel with constant roughness (See Figure 7). This was expected, since only small parts of the overlying fouling was seen to release. The drag force data for silicone B, however, shows a reduction in skin friction which corresponded to foul release. At 10 knots, the force data started at the higher point, and as the fouling was released, the measured force decreased at the higher velocities. The force at the same velocities was then reduced. This verified quantitatively that the coating was releasing fouling. For the preliminary data presented here, the foil was only run to a maximum velocity of 12 knots. This was due to strengthening requirements on the cross frame.

The instrumented foil has given us the opportunity to observe the interaction between hydrodynamic forces and foul-release from silicone-based coatings. It is gratifying to see that performance characteristics of fouling organisms with well defined morphology and adhesion characteristics parallel theoretical predictions. Future work will investigate the adhesion strength and foul release of other hard fouling organisms (oysters/ tubeworms/ limpets) and the more complex issues involved with fouling communities. This should enable predictive models to be created that can forecast foul-release from ship hulls.

VI. CONCLUSIONS

The instrumented foil provides a method for evaluating the foul-release properties of coatings. Preliminary data has demonstrated that silicone foul-release coatings with low barnacle adhesion strengths will hydrodynamically self-clean. For the barnacle, *Balanus eburneus*, there is also a good correlation between predicted and observed foul-release velocities. Future testing and analysis will further improve our understanding of the interaction between fouling adhesion, hydrodynamic forces, and foul-release.

VII. ACKNOWLEDGEMENTS

This work was supported by the Office of Naval Research (N00014-91-J-1465), the Defense Advanced Research Project Agency, and General Electric. Also, much appreciation goes to Judith Stein and Jim Cella for their continued assistance. We would also like to acknowledge everyone at the Center for Corrosion and Biofouling Control at F.I.T. who have contributed to this project.

VIII. REFERENCES

1. R. S. Alberte, S. Snyder, B. J. Zahuranec, and M. Whetston. "Biofouling Research Needs for the United States Navy: Program History and Goals", *Biofouling*. 6 (2), 1994, 91-95.
2. R. L. Townsin, D. Byrne, A. Milne and T. Svensen. "Speed, Power and Roughness: The Economics of Outer Bottom Maintenance", Trans. RINA 123, 1981: 459-483.
3. M. A. Champ and W. C. Pugh. "Tributyltin Antifouling Paints: Introduction and Overview", Oceans 97 Proc., 1987: 1296-1308.
4. Senate of the United States. "Organotin Antifouling Paint Control Act of 1988", April 18, 1988.
5. J. D. Bultman, J. R. Griffith and D. E. Field. Fluoropolymer Coatings for the Marine Environment", *In Proc. Symp. on Marine Biodeterioration*, eds. J.D. Costlow and R.C. Tipper, Naval Institute Press, Annapolis, MD., 1981, 237-249.
6. W. A. Finzel and H. L. Vincent. "Silicones in Coatings", *Federation Series on Coatings Technology*, March 1996, Federation of Societies for Coatings Technology.
7. G. W. Swain, J. R. Griffith, J. D. Bultman and H. L. Vincent. "The Use of Barnacle Adhesion Measurements for the Field Evaluation of Non-toxic Foul Release Surfaces", *Biofouling*. 6 (2), 1992, 105-114.
8. ASTM D5618 Standard Test Method for Measurement of Barnacle Adhesion Strength in Shear. American Standard for Testing and Materials, Paint-Tests for Formulated Products and Applied Coatings. 6.01, 1994.
9. M. W. Denny, T. L. Daniel, and M. A. R. Koehl. "Mechanical Limits to Size in Wave-Swept Organisms", *Ecological Monographs* 55, 1985: 69-102.
10. G Walker. "The Adhesion of Barnacles", *J. Adhesion*, 12, 1981: 51-58.
11. A. B. Yule and G. Walker. "The Adhesion of the Barnacles, *Balanus Balanoides*, to Slate Surfaces", *J. Marine Biology*, 1984: 147-156.
12. A. B. Yule and D. J. Crisp. "Adhesion of Cypris Larvae of the Barnacle, *Balanus balanoides*, to Clean and Arthropodin Treated Surface", *J.Mar.Biol.Ass.* U.K., 63, 1983, 261-271.
13. A. Becka and G. Loeb. "Ease of Removal of Barnacles from Various Polymeric Materials", *Biotechnology and Bioengineering*, XXVI, 1984, 1245-1251.
14. K. Becker. "Attachment Strength and Colonization Patterns of Two Macrofouling Species on Substrata with Different Surface Tension (in situ studies)", *Marine Biology* 117, 1993: 301-309.
15. M. W. Denny. "Forces on Intertidal Organisms due to Breaking Ocean Waves: Design and Application of a Telemetry System", *Limnology and Oceanography* Vol. 27, 1982: 178-183.
16. M. Schultz. *The Measurement of Hydrodynamic Forces on Fouling Organisms.* Florida Institute of Technology, Master's Thesis, 1992.
17. M. W. Denny. " A Limpet Shell Shape that Reduces Drag: Laboratory Demonstration of a Hydrodynamic Mechanism and an Exploration of its Effectiveness in Nature", *Can. J. Zool.* 67, 1989: 2098-2106.
18. S. Vogel. *Life in Moving Fluids.* Princeton: Princeton University Press, 1983.
19. R. G. Dean and R. A. Dalrymple. *Water Wave Mechanics for Engineers and Scientists.* Prentice-Hall, Englewood Cliffs, NJ., 1984.
20. J. M. Allen. "Experimental Study of Error Sources in Skin-Friction Balance Measurements", *J. Fluids Eng.* March 1977, 197-204.
21. J. G. Winter. "An Outline of the Techniques Available for the Measurement of Skin Friction in Turbulent Boundary Layers", *Prog. Aerospace Sci.* Vol. 18, 1977: 1-57.
22. S. Dhawan. *Direct Measurement of Skin Friction.* California Institute of Technology, Ph.D Dissertation, 1951.
23. F. B. O'Connell and J. C. Westkaemper. "Measurement of Errors Caused by Misalignment of Floating Element Skin Friction Balances:, AIAA Journal, January 1965: 163-165.
24. P. S. Klebanoff, P. S. "Characteristics of Turbulence in a Boundary Layer with Zero Pressure Gradient", NACA Rep. 1247, 1955.
25. H. Schlichting. *Boundary Layer Theory.* New York: McGraw-Hill, 1979.
26. G. W. Swain, W. G. Nelson, and S. Preedeekanit. "The Influence of Biofouling Adhesion and Biotic Disturbance on the Development of Fouling Communities on Non-Toxic Surfaces", Biofouling 12, 1998: 257-269.
27. ASTM D3623. Standard Test Method for Testing Antifouling Panels in Shallow Submergence. American Standard for Testing and Materials, Paint Products and Applications. 6.02, 1994.
28. G. W. Swain, M. P. Schultz and H. L. Vincent. "Shear Force Measurements of Barnacle Adhesion for Field Evaluation of Nontoxic Foul-Release Surfaces", *Recent Developments in Biofouling Control.* Oxford and IBH Publishing Co., New Delhi, 1994.

THE EFFECT OF BIOFILMS ON TURBULENT BOUNDARY LAYER STRUCTURE

Michael Schultz
Division of Marine and Environmental Systems
Ocean Engineering Program
Florida Institute of Technology
150 West University Blvd.
Melbourne, FL 32901
schultzm@winnie.fit.edu

Geoffrey Swain
Division of Marine and Environmental Systems
Ocean Engineering Program
Florida Institute of Technology
150 West University Blvd.
Melbourne, FL 32901
swain@fit.edu

Abstract – Practical application of drag reduction techniques on marine vehicles requires that the effects of biofouling be addressed. Materials exposed in the marine environment, even those protected by antifouling (AF) paints, are rapidly colonized by microfouling. In order to gain a better understanding of its effects, this study compares the mean and turbulent boundary layer velocity characteristics of surfaces covered with a marine biofilm with those of a smooth surface. Measurements were made in a nominally zero pressure gradient, boundary layer flow with a two-component laser Doppler velocimeter (LDV) at momentum thickness Reynolds numbers of 5,500 to 19,000 in a recirculating water tunnel. Profiles of the mean and fluctuating velocity components, including the longitudinal-plane turbulent shear stress, were measured. An average increase in the skin friction coefficient of 33% to 187% was measured on the fouled specimens. The skin friction coefficient was found to be dependent on not only biofilm thickness but also its morphology. Relative increases in the longitudinal-plane shear stress as well as the longitudinal and wall-normal turbulence intensities were also noted for the fouled specimens.

I. INTRODUCTION

Any attempt to make seawater drag reduction a reality must contend with marine biofouling. While modern antifouling (AF) systems are effective in controlling most macrofouling (e.g. barnacles, tubeworms, macroalgae, etc.), they do become colonized by microfouling organisms that produce a slime film. In some cases, the growth of this film is stimulated on copper and organo-tin AF paints [1]. The effect of biofilms on frictional resistance and turbulent boundary structure is, therefore, of great interest in predicting the hydrodynamic performance of marine vehicles.

A significant body of research has been devoted to studying the effects of marine fouling on frictional resistance. Much of the early work is documented in *Marine Fouling and Its Prevention* [2]. Most of this research addressed the effects of macrofouling. However, studies by Sir Archibald Denny and researchers at Langley Field both demonstrated that slime films can significantly increase skin friction resistance.

An extensive investigation into the effects of microbial slime layers on pipe flow was carried out by Picologlou et al. [3]. They noted that the thickness and morphology of the slime film is effected by the hydrodynamic conditions to which it is exposed. It was also observed that the viscoelastic character of the biofilm combined with its filamentous nature seemed to cause additional energy dissipation mechanisms that led to higher frictional resistance.

Lewkowicz and Das [4] used uniformly distributed nylon tufts attached to a rough flat plate in order to model a marine slime growth. Detailed profiles of both mean and turbulent flow velocities were measured. They found that the local shear stress coefficient, c_f, in a zero pressure gradient flow was an average of 18% higher for the model slime film with a background roughness than for the background roughness alone.

Loeb et al. [1] measured the influence of microbial biofims on the hydrodynamic drag of rotating discs Their data showed an increase in frictional resistance of 10 to 20% due to slime films. Pre-roughened discs were also tested both before and after exposure to biofilm formation, since it was hypothesized that a thin slime film might reduce the drag of rough surfaces by effectively smoothing them. This was not the case, as an increase in frictional drag of 10% was measured for the fouled, rough disc.

Lewthwaite et al. [5] conducted an experiment in which velocity profiles were taken on a vessel at sea over a two year period. In this study, a 23 m fleet tender was operated in temperate waters and was subjected to marine biofouling buildup. A pitot-static tube traverse system was outfitted on the ship through several sea tubes located along the length of the hull. From the velocity profiles, the local skin friction coefficient, c_f, was found. They measured an increase in c_f from 0.0023 to 0.0042 over the exposure period. A corresponding 15% reduction in ship speed was observed. There were no quantitative measurements made on the fouling settlement on the hull. However, it was noted that when the vessel was pulled, it was virtually free of hard fouling and macroalgae. It was covered with a dense slime film estimated to be 1 mm thick. When the hull was cleaned and returned to the water, measurements confirmed that c_f returned approximately to its clean hull value.

Haslbeck and Bohlander [6] conducted a full-scale ship trial in order to better quantify the effect of microbial biofilms on ship drag. In their investigation, the USS BREWTON, a Knox class frigate, was instrumented to measure shaft horsepower and ship speed over a mile course. The ship, which was coated with an ablative antifouling paint containing both cuprous oxide and tributyltin oxide, had been subjected to fouling in Pearl Harbor, Hawaii for 22 months. An initial hull inspection by divers indicated the presence of a microbial biofilm but little hard fouling. Ship power trials over a mile course were made. The USS BREWTON then returned to port to undergo hull cleaning. Another ship power trial was then conducted. It was found that there was as much as an 18% decrease in the required shaft horsepower to propel the ship at same speed after the microbial biofilm was removed.

While it can be concluded that biofilms have the potential to markedly increase ship drag, the authors are unaware of any study in which the mean and turbulence structure of boundary layer flows over natural marine biofilms were measured. This information is vital in the understanding and prediction of flows over fouled hulls. The goal of the present research is to address these issues.

II. EXPERIMENTAL FACILITIES AND METHOD

The experimental work was carried out at the Harbor Branch Oceanographic Institution (HBOI) water tunnel [7]. The tunnel is 2.44 m in height, 8.53 m in length, and 1.22 m in width and is constructed of mild steel coated with marine polyamide epoxy. The test section is 0.61 m by 0.61 m and is 2.54 m in length. The contraction ratio in the tunnel is 4 to 1. Flow management devices include turning vanes placed in the tunnel corners and a polycarbonate honeycomb flow straightener in the entrance to the contraction section. The resulting free-stream turbulence intensity in the test section ranged from 2.5 % to 3.5 % in the velocity range that was used in the present experiment. The tunnel is powered by a 7.5L, V8 internal combustion engine that turns a 0.81 m diameter, three bladed, brass propeller. The engine is rated at 167 kW at 4400 rpm and 484 N-m of torque at 2800 rpm. The free-stream velocities in the test section can be adjusted from 1.2 m/s to 4.0 m/s. The velocity can be maintained to within 0.05 m/s throughout the range. A hinged glass window, 1.22 m in length located in the tunnel's test section, allows viewing of experiments as well as access to the test section.

The test matrix consisted of five specimens. Two smooth, unfouled surfaces were used as controls. The remaining three specimens were subjected to biofilm build up for 6, 14, and 17 days. In order to look at boundary layer development and the effect of varying Reynolds number, velocity profiles were taken at three downstream positions. The profiles were taken at 1.13 m, 1.43 m, and 1.73 m from the leading edge and at three free-stream velocities (nominally 1.5 m/s, 2.25 m/s, and 3.0 m/s). Velocity profiles consisted of about 50 logarithmically spaced sampling locations across the boundary layer.

The test specimens were mounted in a splitter plate type fixture that was inserted into the tunnel and generated a fully developed, turbulent boundary layer. The plate was 0.58 m in width, 2.06 m in length, and 54 mm thick. It was constructed of polyvinylchloride (PVC) and stainless steel and was mounted horizontally in the tunnel's test section. The leading edge of the test plate was shaped to mimic the forward portion of a NACA 0012-64 air foil. The forward most 280 mm

of plate was covered with #36 grit sandpaper to hasten development of a turbulent boundary layer and to artificially thicken it.

The top of the boundary layer plate was mounted 370 mm from the top tunnel wall and was held in place with four, 38 mm diameter, stainless steel rods that allowed slight adjustments to the free-stream pressure gradient. The plate had a removable section to facilitate interchanging of test specimens. The test specimens were fabricated from cast acrylic sheet. Each specimen measured 558 mm in width, 1168 mm in length, and 12.7 mm in thickness. The forward edge of the specimen was located 710 mm from the leading edge of the plate.

Mean velocity, turbulence intensities, and Reynolds shear stress measurements were made using a two-component, fiber-optic laser Doppler velocimeter (LDV) system. A 5W Coherent Innova Model 70A Argon-ion laser served as the light source. The remainder of the integrated system was manufactured by TSI. This included a Model 9201 ColorBurst® beam separator, Model 9271 fiber-optic couplers, a Model 9832 fiber-optic probe, a Model 9230 multi-color receiver, and an IFA 655 digital burst correlator signal processor. All components were controlled by a personal computer using TSI's FIND-Windows® software. The probe was fitted with a TSI Model 9253 lens. The focal length of the lens was 349.8 mm. The resulting probe volume diameter was 90 μm, and its length was 1.3 mm. The probe was mounted on an AMPRO System 1618, three-axis traverse unit. The traverse allowed the position of the probe to be maintained to ± 1 μm in all directions.

In order to facilitate two-component, near wall measurements, the probe was tilted downwards at an angle of 4^0 with the horizontal and was rotated 45^0 about its axis. This minimized bias error due to introduction of the w' fluctuations into the v' measurements. Using this setup, measurements as close as 40 μm to the wall were made. Velocity measurements were conducted in coincidence mode with 10,000 random samples per location. Doppler bursts for the two channels were required to fall within a set coincidence window or the sample was rejected. This coincidence window was set at 50 μs, 30 μs, and 20 μs for the 1.5 m/s, 2.25 m/s, and 3.0 m/s flows, respectively.

The biofilms on the fouled test specimens were grown at the HBOI Aquaculture facility. Water from the Indian River Lagoon was continuously pumped through a sand filtration system and into three grow-out tanks. The tanks were 2.3 m in length, 0.9 m in width, and 0.55 m in height. A valve at one end of the tank allowed seawater to flow in. Each tank was fitted with a stand-pipe that maintained the water depth at 130 mm and allowed water to drain. One test specimen was placed face up on the bottom of each tank and allowed to foul over a period of days. During these experiments, the salinity of the water in the tanks ranged from 20 ppt to 36 ppt. The water temperature ranged from 25^0 C to 35^0 C. The thickness of the biofilm on the test specimens was determined using a Gardco comb-type wet film paint thickness (WFT) gauge. It had a thickness measurement range of 25 μm to 2032 μm with a resolution of 25 μm in the 25 μm to 305 μm range. Sixty thickness measurements were made both before and after subjecting each biofilm to hydrodynamic testing in the water tunnel. These were made on the damp biofilm in air. After hydrodynamic testing, a sample of the biofilm was taken and examined under a compound microscope to identify the organisms present. For a more detailed description of the experimental setup, the reader may refer to [8].

The mean and turbulence statistics for each measurement location were found using the basic statistical package in the aforementioned FIND-Windows® software. These results were then used to calculate the boundary layer parameters. In the present investigation, three methods were used to determine the local skin friction coefficient, c_f, for the smooth walls and two methods were used for the fouled walls.

For the smooth specimens, c_f was found using Bradshaw's method, the sublayer slope method, and the Reynolds stress method. The details of Bradshaw's method, which is based on inner layer similarity, are given in references [9,10]. Log-law reference values of y^+=100 and U^+=16.24 were used in the present study. The sublayer slope method simply involves finding the velocity gradient in the linear sublayer to obtain the wall shear stress. The final method that was used to find c_f on the smooth specimens was the Reynolds stress method, which is detailed in [11]. For the fouled plates, the analysis was a bit more complex. First, before c_f could be found, the location of the virtual origin ($y+\varepsilon=0$) had to be determined. An adaptation of the method proposed by Perry and Joubert [12] for the determination of the virtual origin on rough surfaces was used. The log-law slope method, which is detailed in [5], and the Reynolds stress method were then used to find c_f.

III. RESULTS AND DISCUSSION

In order to reference each of the test samples, an alpha-numeric code is used. The first letter represents the test specimen type. "S" is a smooth plate. "F" is fouled plate. The first number indicates the replicate number. To further facilitate the reference of individual velocity profiles, an additional letter and number are added to the previous designation. To indicate the downstream distance from the leading edge, x, the letters A-C are used. "A" represents the 1.13 m profiling station, "B" the 1.43 m station, and "C" the 1.73 m station. The nominal free-stream velocity is indicated with the numbers 1-3. The number "1" represents 1.5 m/s, "2" represents 2.25 m/s, and "3" represents 3.0 m/s. For example, "S2B3" refers to a profile made on smooth specimen replicate 2 at x =1.43 m and U_e = 3.0 m/s.

The biofilm on each of the three fouled plates was characterized by visual assessment both before and after hydrodynamic testing. The results of this evaluation are shown in table I. Examination of the biofilm with the aid of a microscope showed that the film on F1 was composed mainly of extracellular polymer substances (EPS), blue-green algae (*Anabaina oscillarioides*), and marine diatoms (dominated by *Melosira spp.*). F2 was fouled with EPS, green algae (*Enteromorpha spp.*), and marine diatoms (dominated by *Melosira spp* and *Thallasiothrix spp.*). The biofilm on F3 was almost entirely composed of filamentous green algae (*Enteromorpha spp.*). The overall mean thickness (± SD) of the biofilms based on 60 individual measurements was found. Before hydrodynamic testing, the thicknesses of F1, F2, and F3 were 347 μm ± 69 μm, 163 μm ± 41 μm, and 310 μm ± 100 μm, respectively. After hydrodynamic testing, the thicknesses of F1, F2, and F3 were 74 μm ± 46 μm, 126 μm ± 27 μm, and 344 μm ± 145 μm, respectively.

The mean boundary layer velocity profiles for the three fouled specimens were affected to varying degrees (See Figure 1). The profiles for F3, the biofilm dominated by filamentous green algae, were generally shifted the most from the smooth curve. Biofilms F1 and F2, which consisted of a slime film, had less effect on the profile. Figure 2 shows the law of the wall profiles of S1 and the fouled specimens as they develop down the plate. The downward velocity shift, ΔU^+, can be noted on all the fouled plate profiles. The magnitude of the shift varied greatly with specimen as well as the downstream position. The large variation in ΔU^+ with x may have been due, in large degree, to the heterogeneity of the biofilm over the specimen surface. One can note that the smooth specimen wakes are lower than is typical for a zero pressure gradient, fully developed boundary layer. This was due to the relatively high background turbulence levels (2.5% – 3.5%) in the test section. Hancock and Bradshaw [13] have shown that free-stream turbulence of this magnitude can alter outer layer structure and depress the wake. Also of note is the variability in the wake on the fouled specimens. There was, however, no statistically significant trend of increase or decrease in Π for the fouled specimens.

The basic boundary layer parameters calculated for the smooth and fouled test plates are shown in table II. To determine if the differences seen were significant within the experimental uncertainty, statistical tests were conducted. These consisted of two-way analyses of variance (ANOVAs) with specimen and Re_x as factors. In cases where the ANOVA indicated significant differences for one of the factors, multiple pairwise comparisons were run using Tukey's test. The significance level for all the tests was set at $\alpha = 0.05$ (95% confidence).

The ANOVA carried out on the boundary layer thickness results showed that neither specimen nor Re_x had a significant effect. This may have been due to the high degree of variability in δ. For example, the absolute deviation of δ between the smooth plate replicates ranged from 2.0% to 13.2% of the mean for the 9 profiles and averaged 7.1%. This was due in part to the inability to control U_e more precisely in the water tunnel. Thole and Boggart [14] have also observed that high free-stream turbulence levels increase the uncertainty in finding δ. Results from Lewkowicz and Das [4], on a simulated biofilm roughness, showed that biofilms had a thickening effect on the boundary layer of 25% to 30% above that of a background roughness.

The presence of the biofilm did have a significant effect on the boundary layer displacement thickness, δ^*. The ANOVA indicated an effect of specimen as well as Re_x. Multiple pairwise comparisons

indicated a significant increase in δ^* over that of the smooth specimens as a result of the biofilm for all the fouled specimens tested. Differences between all specimens were found with the exception of S1 versus S2 (the controls) and F1 versus F2. The biofilm also had an effect on the momentum thickness of the boundary layer, θ. The ANOVA again showed significant differences with specimen as well as Re_x. Pairwise comparisons indicated a significant increase in θ, resulted from the fouling. The only exception was F2, which was not significantly different than S1. Differences were also found between all the remaining specimens except S1 versus S2 and F1 versus F2.

The shape factor, H, was significantly increased by the presence of the biofilm as well. This suggests that the mass flux is altered to a higher degree than the momentum flux for these flows. The ANOVA indicated differences due to both specimen and Re_x. Multiple pairwise comparisons showed differences for all the specimens with the exception of S1 versus S2 and F1 versus F2. The average increase in H with fouling was 7.0% for F1, 4.8% for F2, and 12.6% for F3 compared to the smooth plates. The increase in H with the presence of fouling was also seen by Lewkowicz and Das [4] in flow over a model biofilm and is a typical surface roughness effect. The Clauser length, Δ, was not significantly affected by the presence of the biofilm. There was a higher degree of variability for the fouled specimens, however. It seems that the variability was related to the fouling extent, as F3, the most heavily fouled specimen, had the largest variability.

The wall shear stress results for the smooth and fouled specimen profiles are shown in tables III and IV. The c_f results for the two replicate smooth plates were compared using paired t-tests. No significant differences between the replicates were found for the three c_f determination methods. The c_f results obtained for each of the smooth profiles were then pooled by c_f method and a two-way ANOVA was carried out. In order to compare the present results to previous results, c_f's predicted by Falkner's fit of c_f versus Re_θ were also included [15]. It is given by the following [1]:

$$c_f = \frac{0.013}{Re_\theta^{\frac{1}{6}}} \qquad (1)$$

The two factors for the ANOVA were c_f method and Re_x. Since the data were not normally distributed and attempts to transform to obtain normality failed, Friedman's test, a non-parametric two-way ANOVA, was carried out. This indicated that there was statistical agreement between all the c_f methods and Falkner's formula. The c_f values obtained using Bradshaw's method were chosen to serve as a baseline with which to compare the fouled plate results. This was because of the lack of sufficient sublayer points in two smooth plate profiles and because of the larger scatter in the results obtained using the Reynolds stress method.

Of particular interest from a practical perspective was the effect of the biofilms on the wall shear stress coefficient. Both the log-law slope method and the Reynolds stress method showed increases in c_f for the fouled plates. The increase varied widely, however. The c_f values for the fouled plates found using the Reynolds stress method ranged from 57% less than to 65% greater than the values obtained by the log-law slope method. In order to statistically compare the results from the two methods, a signed rank test (α=0.05) was used. No statistically significant difference between the methods was found. It was decided to use the log-law slope method for comparison with the smooth plate results.

In order to observe the change in c_f for the fouled specimen results, comparison with the smooth plate results at the same Re_θ was carried out. Since Re_θ was increased significantly for the fouled specimens, a profile by profile comparison with the controls was not feasible. For this reason, the c_f's for the fouled plates were compared to the following equation that was fit to the present smooth plate results found using Bradshaw's method [2]:

$$c_f = \frac{0.0105}{Re_\theta^{0.14}} \qquad (2)$$

All the fouled plates had increased c_f values compared to the smooth condition. Fouled specimens F1, F2, and F3 showed increases in c_f of 8% to 133%, 3% to 70%, and 11% to 369%, respectively. The average increase was 68% for F1, 33% for F2, and 187% for F3. It has been postulated that thin biofilms may reduce drag by acting as a compliant surface. This effect was not observed in the present study, however.

The variation in c_f was greatly increased for the fouled plates. To put this in better perspective, S1 had a mean c_f ($x10^3$) ($\pm$ SD) of 2.91 $\pm$ 0.13, and S2 had a mean c_f ($x10^3$) of 2.92 $\pm$ 0.16. Fouled plates F1, F2, and F3 had mean c_f ($x10^3$) values of 4.83 $\pm$ 1.59, 3.85 $\pm$ 0.78, and 8.12 $\pm$ 4.15, respectively. A Kruskal-Wallis ANOVA on ranks and Student-Newman-Keuls pairwise comparisons indicated a significant difference between all of the smooth panels and the fouled panels with the exception of S1 versus S2 (the controls) and F1 versus F2. The c_f results for the fouled specimens show that not only biofilm thickness but also composition and morphology are important in determining the wall shear stress. The average increase in c_f for slime films with a mean thickness before testing of 163 μm and 347 μm was 33% and 68%, respectively. The increase in c_f for a surface dominated by filamentous green algae (*Enteromorpha spp.*) with a mean thickness of 310 μm averaged 187%. It seems that the flapping motions of filamentous algae can remove larger amounts of momentum from the mean flow than non-filamentous films of the same thickness.

Much of the variability within c_f results on the same specimen can be attributed to the complex and dynamic nature of the biofilm. First, it is not homogenous and uniform, but is splotchy. This was especially true for F3. Biofilms may be thought of as a constantly varying streamwise roughness, not only in height but also in morphology. This brings the underlying assumption of boundary layer equilibrium, which is inherent to wall similarity methods, into question. A study by Andreopoulos and Wood [16], in flows subjected to a short length of surface roughness, has found that boundary layers do not fully recover to a self-preserving state for large downstream distances (>55δ). Work by Antonia and Luxton [17] has shown, that on k-type surface roughness, the boundary layer adjusts rather slowly to a step change from rough to smooth surface condition. Antonia and Luxton [18] have also observed that flows moving from smooth to rough surfaces adjust much more rapidly (~ 10δ). Further complicating the present situation was removal of the biofilm from the surface due to shear stress over the duration of the experiment.

Some of the variation in the c_f results for the fouled plates may also be attributed to the method itself. Using Bradshaw's method for smooth plate flows, there is only a single free parameter, c_f. Additional parameters, ΔU^+ and ε, enter the analysis for rough wall flows. While the extra two degrees of freedom can produce a "better" log-law fit in a statistical sense, they can also lead to increased error in c_f. Natural scatter in the inner region data due to the influence of roughness elements may be masked in producing a least-squares fit of the log-law. Archarya and Escudier [19] report that the use of rough wall analyses with ΔU^+ and ε not identically set to zero on smooth wall data produced c_f's with an average error of 12%.

Research by Perry et al. [20], Bandyopadhyay [21], Ligrani and Moffat [22] and others has furthered the understanding of boundary layer flows over k-type and d-type roughnesses. Even in these "regular" roughness arrangements, the determination of c_f can be problematic. In general, an independent method for finding c_f is desirable. But, the common methods used on "regular" roughnesses, such as a floating element force balance or pressure taps, are not generally feasible on biofilms and could not be used in the present investigation.

Granville's method [23] of finding the velocity shift, ΔU^+, at the same value of Re_{δ^*} resulted in ΔU^+ ranging from 2.18 to 9.60, 0.54 to 6.19, and 1.81 to 14.98 for F1, F2, and F3, respectively. Plots of ΔU^+ versus k^+ for the three fouled specimens did not show a good collapse to a Colebrook or Nikuradse type roughness function (see Figure 3). There was a high degree of scatter in these plots, although there was a significant trend of increasing ΔU^+ with increasing k^+. This may be due to the use of an inappropriate roughness length scale. The scale used was the mean biofilm height before testing. Attempts to incorporate other scaling lengths including the mean biofilm height after testing, the r.m.s. biofilm roughness, the boundary layer thickness, and the origin offset did not lead to any better collapse than the mean roughness alone. The equivalent sand roughness, k_s, was calculated for each fouled profile. It was of interest to see if a relationship existed between the measured mean roughness height, k, and k_s. However, the two parameters were poorly correlated. It can be concluded that the mean roughness height of the biofilm measured with a paint wet film thickness

gauge, by itself, does not provide an appropriate roughness scaling factor. Picologlou et al. [3] indicated a better correlation between k_s and the mean biofilm height in their pipe flow experiments. They also had difficulty in finding a functional dependency between the two, however.

The inability to scale the roughness effects using a single length scale parameter is not surprising, especially for a surface as complex as a marine biofilm. Patel and Yoon [24] note that at present there is no theoretical way to predict the roughness function based on roughness configuration alone, and a single length parameter is usually not sufficient to characterize the surface. A profile of the surface might allow a more meaningful parameter to be obtained. Since the biofilm is compliant, changes in the profile would occur with time and flow conditions. Surface topography obtained using a laser interferometer, as was used by Lee et al. [11] on compliant surfaces, might make a more meaningful surface characterization possible.

The turbulence intensities across the boundary layer for S1 and the fouled specimens are shown in Figures 4 and 5, respectively. Both the u' and v' turbulence intensities were greatly increased in the presence of the biofilm. The effect was noted not only in the near wall region but also out to the edge of the boundary layer in some cases. This seems to indicate an increase in large scale motions over these biofilms. The largest percent increase in the longitudinal turbulence was observed for $0.2<y/\delta<0.5$ for all the profiles. For F1, the increase in the average u' and v' turbulence intensities in this region were 29% and 25%, respectively. There was an average increase of 23% and 19% for F2 and an increase of 52% and 45% for F3. The effect is, therefore, dependent on the extent and morphology of the fouling. F3, a biofilm dominated by filamentous green algae, showed the largest increase in turbulence intensity. It can also be seen from Figure 5 that the turbulence intensity profiles for F1 and F2 remain nearly constant down the surface indicating a near equilibrium boundary layer condition. The profiles for F3 do not collapse well to a single curve, and therefore, have not reached equilibrium. This may have been due to the splotchy nature of F3. Another possibility could be an insufficient development length after the step change in roughness, as the profiling stations were located between ~15δ to ~40δ from the start of the fouling. Bandyopadhyay [21] has shown that sand roughnesses require much greater length to reach a state of equilibrium.

Figure 6 shows the Reynolds shear stress profiles for S1 and the fouled specimens. The fouled specimens not only show an increase in the peak Reynolds stress in the inner region but also exhibit higher values well into the outer region. The profiles followed trends similar to the turbulence intensities with respect to boundary layer equilibrium. Again, the profiles for F3 do not collapse to a single curve. Fair collapse of the data is seen for F1 and F2 with the exception of profile F1B1, which exhibited a peak that was atypical of the other profiles for this specimen. The peaked nature of the profiles for F2, F3, and F1B1 indicate a smaller equilibrium or constant stress region than for the smooth plate flows.

The eddy diffusivity across the boundary layer for S1 and the fouled plates are shown in Figure 7. The peak in the smooth profile occurs at about $y/\delta = 0.3$, where $\nu_T/(u_*\delta)$ reaches 0.068. Hinze [25] has calculated a similar profile using data from Klebanoff and Townsend. Not only the shape of this profile, but also the value and location of the peak agrees well the present results. One notable feature of both the smooth and fouled profiles is the almost linear variation in the eddy diffusivity in the inner region.

The task of accurately scaling laboratory c_f's to ship scale frictional resistance coefficients (C_F) is a complex one. Even if reliable lab results for a given biofilm are available, fouling on an actual ship hull is likely to be much more heterogeneous. Differences in fouling over a hull can occur for various reasons including light shading effects, larval zonation in the water column, and differences in the flow patterns and stresses along the hull. The complexities in boundary layer flows over biofilms such as surface compliance, deformation, and removal may also increase the error in the prediction of ship scale effects. Given the inability to obtain a suitable length scale parameter to express the roughness function for these biofilms and the aforementioned difficulties, predictions of C_F at ship-scale are not offered here. It seems, however, that there is the potential for significant performance penalties as a result of low-form fouling on marine vehicles, and this should not be ignored when assessing the viability of seawater drag reduction methods.

IV. CONCLUSION

The results of the present study have demonstrated the importance of low form fouling on hydrodynamic drag. Seawater drag reduction methods must address their effects in order to be practical. This study has also shown that the increase in skin friction in flows over biofilms is not only dependent on the their thickness but also their composition and morphology. For example, the average increase in the skin friction coefficient (c_f) for slime films with a mean thickness of 163 μm and 347 μm was 33% and 68%, respectively. The average increase in c_f for a surface dominated by filamentous green algae (*Enteromorpha spp.*) with a mean thickness of 310 μm was 187%. Waving algae filaments seem to draw a greater amount of momentum from the mean flow than do slime films alone. A statistically significant increase in the displacement thickness (δ*), momentum thickness (θ), and shape factor (H) was found for flows over the biofilms. The roughness functions indicate that relatively thin biofilms (mean biofilm thickness < 350 μm) can produce fully rough flow conditions. Standard Colebrook-type and Nikuradse sand roughness functions do not sufficiently collapse the biofilm results to a universal curve using the mean roughness height as a characteristic length scale. A method of characterizing these complex surfaces under flow may lead to a more appropriate scaling parameter. The present study showed that biofilms can increase turbulence intensities across a large part of the boundary layer. Average increases in the longitudinal and wall-normal intensities of 23% to 52% and 19% to 45%, respectively, were measured for $0.2<y/\delta<0.5$ on the fouled specimens. Reynolds shear stress was also increased significantly.

Acknowledgements

We would like to thank the Office of Naval Research, the Defense Advanced Research Projects Agency, the Environmental Security and Technology Certification Program, and the General Electric Corporation for their support of this research and their commitment to the advancement of biofouling control. Thanks go to Dr. Andrew Clark and the engineering staff at Harbor Branch Oceanographic Institution for their assistance and use of their facilities. We are also grateful to Professor C.S. Subramanian for helpful comments about this manuscript.

V. REFERENCES

1. G.I. Loeb, D. Laster, and T. Gracik "The Influence of Microbial Fouling Films on Hydrodynamic Drag of Rotating Discs", in *Marine Biodeterioration, An Interdisciplinary Study*, edited by J.D. Costlow and R. Tipper, Naval Institute Press, Annapolis, MD, 1984, pp. 88-94.
2. *Marine Fouling and Its Prevention*, U.S. Naval Institute Press, Annapolis, MD, 1952.
3. B.F. Picologlou, N. Zelver, and W.G. Characklis "Biofilm Growth and Hydraulic Performance", *A.S.C.E. Journal of the Hydraulics Division*, HY5, 1980, pp. 733-746.
4. A.K. Lewkowicz and D.K. Das "Turbulent Boundary Layers on Rough Surfaces With and Without a Pliable Overlayer: A Simulation of Marine Fouling", *Proceedings of the A.S.M.E/A.S.C.E. Bioengineering, Fluid Engineering, and Applied Mechanics Conference*, 1981, pp. 174-186.
5. J.C. Lewthwaite, A.F. Molland, and K.W. Thomas "An Investigation into the Variation of Ship Skin Frictional Resistance with Fouling", *Transactions Royal Institute of Naval Architects*, Vol. 127, 1985, pp. 269-284.
6. E.G. Haslbeck and G. Bohlander "Microbial Biofilm Effects on Drag - Lab and Field", *Proceedings 1992 S.N.A.M.E. Ship Production Symposium*, 1992.
7. S. Gangadharan, C.R. Wimberly, A. Clark, and B. Collino "Design, Construction and Operation of a Cost Effective Water Tunnel at Harbor Branch Oceanographic Institution", Paper presented at S.N.A.M.E. Southeast Section Meeting, October 11, 1996, Fort Pierce, FL.
8. M.P. Schultz "The Effect of Biofilms on Turbulent Boundary Layer Structure", Florida Institute of Technology, Ph.D. dissertation, May, 1998.
9. P. Bradshaw "A Simple Method for Determining Turbulent Skin Friction from Velocity Profiles", *Journal of Aeronautical Science*, Vol. 26, 1959, p. 841.
10. K.G. Winter "An Outline of the Techniques Available for the Measurement of Skin Friction in Turbulent Boundary Layers", *Progress in the Aerospace Sciences*, Vol. 18, 1977, pp. 1-57.

11. T. Lee, M. Fisher, and W.H. Schwarz "Investigation of the Stable Interaction of a Passive Compliant Surface with a Turbulent Boundary Layer", *Journal of Fluid Mechanics*, Vol. 257, 1993, pp. 373-401.
12. A.E. Perry and P.N. Joubert "Rough-Wall Turbulent Boundary Layers", *Journal of Fluid Mechanics*, Vol. 37, 1963, pp. 383-413.
13. P.E. Hancock and P. Bradshaw "The Effect of Free-Stream Turbulence on Turbulent Boundary Layers", *Journal of Fluids Engineering*, Vol. 105, 1983, pp. 284-289.
14. K.A. Thole and D.G. Bogard "High Freestream Turbulence Effect on Turbulent Boundary Layers", *Journal of Fluids Engineering*, Vol. 118, 1996, pp. 276-284.
15. R.J. Garde *Turbulent Flows*, John Wiley and Sons, New York, 1994.
16. J. Andreopoulos and D.H. Wood "The Response of a Turbulent Boundary Layer to a Short Length of Surface Roughness", *Journal of Fluid Mechanics*, Vol. 118, 1982, pp. 143-164.
17. R.A. Antonia and R.E. Luxton "The Response of a Turbulent Boundary Layer to a Step Change in Surface Roughness Part 2. Rough to Smooth", *Journal of Fluid Mechanics*, Vol. 53, Pt. 4, 1972, pp. 737-757.
18. R.A. Antonia and R.E. Luxton "The Response of a Turbulent Boundary Layer to a Step Change in Surface Roughness Part 1. Smooth to Rough", *Journal of Fluid Mechanics*, Vol. 48, Pt. 4, 1971, pp. 721-761.
19. M. Acharya and M.P. Escudier "Measurements of the Wall Shear Stress in Boundary Layers", *Proceedings of the 4th International Symposium on Turbulent Shear Flows*, Karlsruhe, Germany, 1983, pp. 277-286.
20. A.E. Perry, W.H. Schofield, and P.N. Joubert "Rough Wall Turbulent Boundary Layers", *Journal of Fluid Mechanics*, Vol. 37, Pt. 2, 1969, pp. 383-413.
21. P.R. Bandyopadhyay "Rough-Wall Turbulent Boundary Layers in the Transition Regime", *Journal of Fluid Mechanics*, Vol. 180, 1987, pp. 231-266.
22. P.M. Ligrani and R.J. Moffat "Structure of Transitionally Rough and Fully Rough Turbulent Boundary Layers", *Journal of Fluid Mechanics*, Vol. 162, 1986, pp. 69-98.
23. P.S. Granville "Three Indirect Methods for the Drag Characterization of Arbitrarily Rough Surfaces on Flat Plates", *Journal of Ship Research*, Vol. 31, No. 1, 1987, pp. 70-77.
24. V.C. Patel and J.Y. Yoon "Application of Turbulence Models to Separated Flow over Rough Surfaces", *Journal of Fluids Engineering*, Vol. 117, June, 1995, pp. 234-241.
25. O. Hinze *Turbulence*, John Wiley and Sons, New York, 1975.

VI. LIST OF NOMENCLATURE

C_F frictional resistance coefficient = $(2F_D)/(\rho U_e^2 S)$
c_f wall shear stress or skin friction coefficient = $(2\tau_o)/(\rho U_e^2)$
F_D drag force
k some measure of roughness height
k^+ roughness Reynolds number = ku_*/ν
k_s sand roughness height or equivalent sand roughness height
Re_x Reynolds number based on x = xU_e/ν
Re_{δ^*} displacement thickness Reynolds number = $\delta^* U_e/\nu$
Re_θ momentum thickness Reynolds number = $\theta U_e/\nu$
S wetted surface area
x streamwise distance from plate leading edge
U, V mean velocity in the x and y
U_e freestream velocity
U^+ inner layer non-dimensional velocity = U/u_*
ΔU^+ roughness or velocity loss function
u, v instantaneous velocity in the x and y direction
u', v' fluctuating velocity component in the x and y direction
u_* shear velocity = $\sqrt{\tau_o/\rho}$
y normal distance from the boundary
y^+ inner layer non-dimensional distance = yu_*/ν
α statistical significance level
Δ Clauser length scale = $\delta^* U_e/u_*$
δ boundary layer thickness
δ^* displacement thickness
ε wall datum error
κ von Karman constant (= 0.41)
ν kinematic viscosity of the fluid
ν_T eddy diffusivity = $-\overline{u'v'}/(\partial U/\partial y)$
Π wake parameter
θ momentum thickness
ρ density of the fluid
τ_o wall shear stress

Table I. Visual assessment of fouled test specimens.

Specimen	Total % Fouling Cover	Constituents and Their % Cover
F1 before	97	Slime 97% (light to medium density film)
F1 after	70	Slime 70% (very light density film)
F2 before	98	Slime 94% (medium density film) Filamentous green algae 4%
F2 after	91	Slime 90% (medium density film) Filamentous green algae 1%
F3 before	95	Slime 70% (medium density film) Filamentous green algae 25%
F3 after	82	Slime 70% (medium density film) Filamentous green algae 12%

Table II. Boundary layer parameters.

Profile	Re_θ	δ (mm)	δ^* (mm)	θ (mm)	Δ (mm)	H
S1A1	6537	33.1	4.33	3.36	109.8	1.29
S1B1	6499	33.3	4.40	3.36	112.4	1.31
S1C1	8106	42.6	5.40	4.22	139.7	1.28
S1A2	8539	33.1	3.84	2.98	100.7	1.29
S1B2	12510	37.9	4.59	3.62	120.4	1.27
S1C2	10380	35.6	4.56	3.56	120.1	1.28
S1A3	10560	31.7	3.76	2.89	101.5	1.30
S1B3	11480	32.5	3.90	3.12	103.7	1.25
S1C3	14410	43.2	4.99	3.99	134.1	1.25
S2A1	5575	29.9	3.87	3.00	97.4	1.29
S2B1	6332	35.3	4.31	3.37	109.1	1.28
S2C1	6973	37.4	4.71	3.57	121.5	1.32
S2A2	8517	27.7	3.84	2.98	102.4	1.29
S2B2	9973	35.3	4.42	3.48	116.3	1.27
S2C2	9101	36.6	4.26	3.38	109.6	1.26
S2A3	11980	30.0	3.91	3.03	105.8	1.29
S2B3	12650	35.9	4.41	3.53	119.4	1.25
S2C3	15170	35.8	4.29	3.43	114.5	1.25
F1A1	6457	29.3	5.01	3.56	86.1	1.41
F1B1	7563	37.3	5.97	4.16	125.7	1.44
F1C1	9208	38.4	6.87	5.02	164.5	1.37
F1A2	9730	29.7	4.81	3.47	81.6	1.39
F1B2	10100	34.8	5.07	3.60	87.6	1.41
F1C2	12090	37.2	5.99	4.23	123.6	1.42
F1A3	13930	38.7	4.86	3.81	106.6	1.28
F1B3	12290	32.0	4.43	3.41	109.8	1.30
F1C3	14920	36.6	5.39	4.13	140.9	1.31
F2A1	5672	27.2	4.30	3.07	94.9	1.40
F2B1	7455	35.4	5.49	4.03	108.3	1.36
F2C1	8222	39.9	5.95	4.48	130.2	1.33
F2A2	9545	29.5	4.67	3.49	111.1	1.34
F2B2	11020	33.6	5.45	4.05	140.7	1.35
F2C2	12200	39.3	5.86	4.48	154.7	1.31
F2A3	9753	26.0	3.68	2.69	82.5	1.37
F2B3	15370	35.9	5.53	4.25	139.7	1.30
F2C3	12990	35.4	4.85	3.69	100.0	1.31
F3A1	6680	28.3	5.59	3.76	80.4	1.49
F3B1	7713	35.1	6.45	4.37	157.0	1.48
F3C1	9380	37.8	8.09	5.41	108.7	1.49
F3A2	10190	34.3	5.63	3.90	68.6	1.44
F3B2	11760	34.9	6.31	4.47	159.6	1.41
F3C2	13640	42.7	7.61	5.13	95.0	1.48
F3A3	13840	32.6	5.40	3.88	76.3	1.39
F3B3	18630	38.1	7.01	5.14	166.1	1.36
F3C3	19100	37.8	7.55	5.33	138.0	1.42

Table III. Wall shear stress coefficients for the smooth specimens.

Profile	Re_θ	c_f (x10^3) Bradshaw Cross Plot	c_f (x10^3) Sublayer Slope	c_f (x10^3) Reynolds Stress
S1A1	6537	3.12	2.99	2.81
S1B1	6499	3.07	2.84	2.90
S1C1	8106	2.99	2.76	2.61
S1A2	8539	2.92	2.85	2.78
S1B2	12510	2.92	2.81	2.50
S1C2	10380	2.88	2.70	2.50
S1A3	10560	2.74	2.70	2.97
S1B3	11480	2.83	-	2.93
S1C3	14410	2.77	2.82	2.63
S2A1	5575	3.16	3.19	2.81
S2B1	6332	3.13	3.06	2.90
S2C1	6973	3.01	3.07	2.67
S2A2	8517	2.82	2.83	2.89
S2B2	9973	2.89	2.71	2.72
S2C2	9101	3.02	3.03	2.65
S2A3	11980	2.73	2.71	2.93
S2B3	12650	2.73	2.61	2.90
S2C3	15170	2.80	-	2.91

- missing data

Table IV. Wall shear stress coefficients for the fouled specimens.

Profile	Re_θ	c_f (x10^3) Log-law Slope	c_f (x10^3) Reynolds Stress
F1A1	6457	6.77	4.65
F1B1	7563	4.51	6.40
F1C1	9208	3.49	4.30
F1A2	9730	6.97	4.42
F1B2	10100	6.70	4.42
F1C2	12090	4.69	4.22
F1A3	13930	4.16	3.95
F1B3	12290	3.27	3.45
F1C3	14920	2.92	3.75
F2A1	5672	4.10	4.25
F2B1	7455	5.15	4.50
F2C1	8222	4.18	3.60
F2A2	9545	3.54	4.75
F2B2	11020	3.00	4.75
F2C2	12200	2.87	3.50
F2A3	9753	3.98	4.60
F2B3	15370	3.14	3.95
F2C3	12990	4.71	4.35
F3A1	6680	9.67	7.95
F3B1	7713	3.38	5.16
F3C1	9380	11.07	10.38
F3A2	10190	13.45	5.80
F3B2	11760	3.12	5.15
F3C2	13640	12.81	8.60
F3A3	13840	10.04	5.75
F3B3	18630	3.57	5.50
F3C3	19100	5.99	7.75

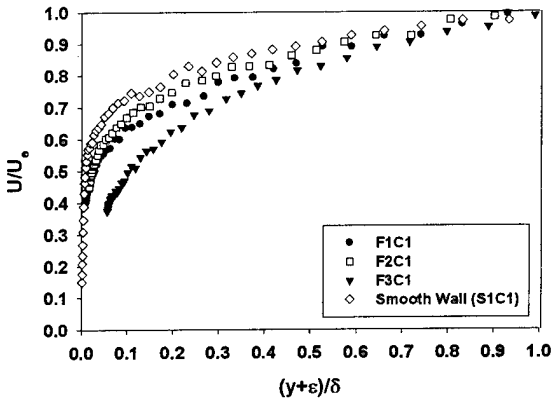

Figure 1. Plot of U/U_e vs. y/δ showing the effect of fouling extent.

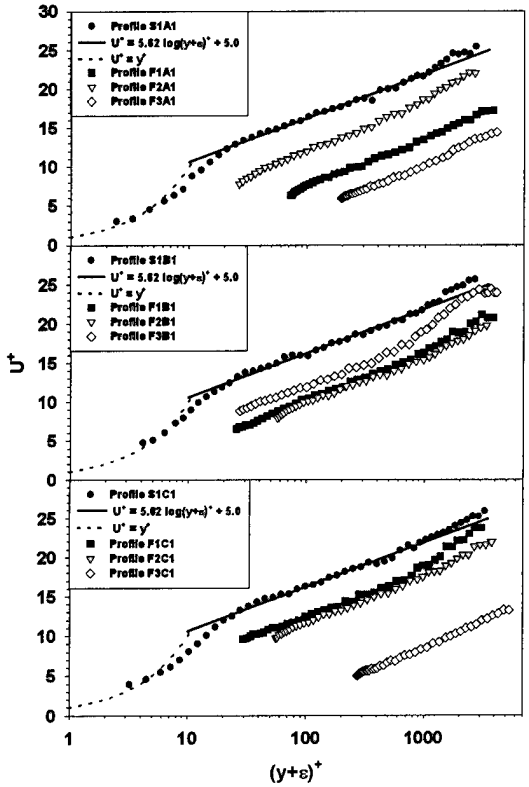

Figure 2. Law of the wall plots for smooth and fouled specimens.

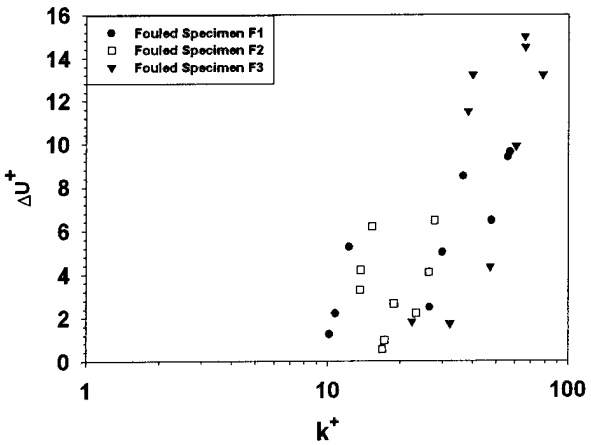

Figure 3. Roughness functions for the fouled specimens.

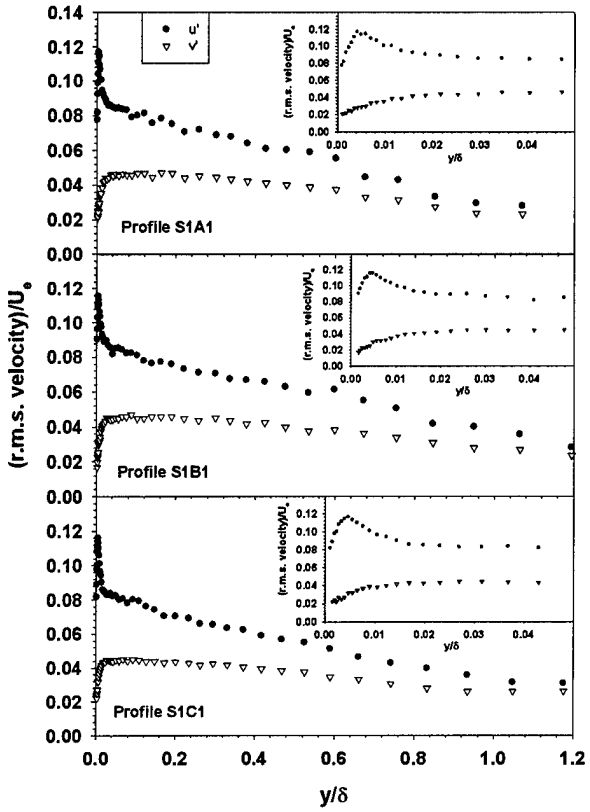

Figure 4. Turbulence intensity plots smooth specimen, S1.

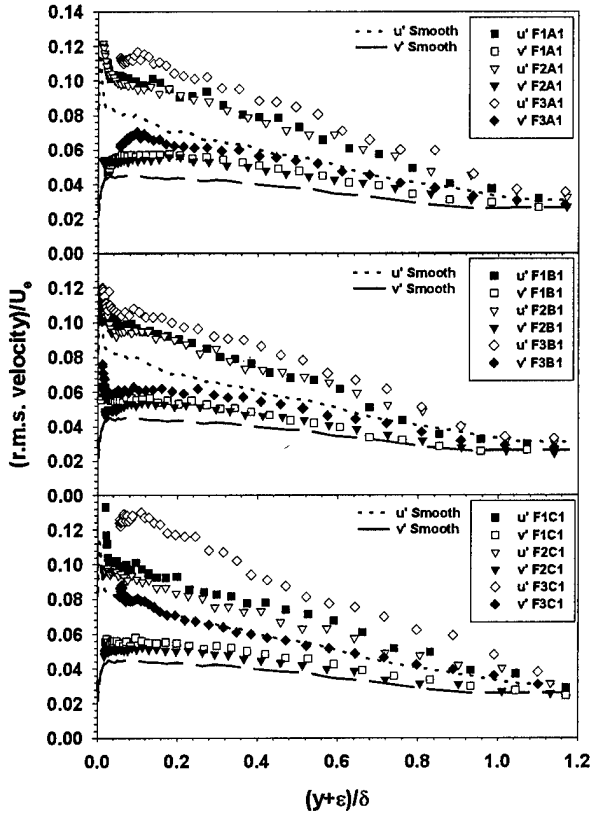

Figure 5. Turbulence intensity plots for the fouled specimens.

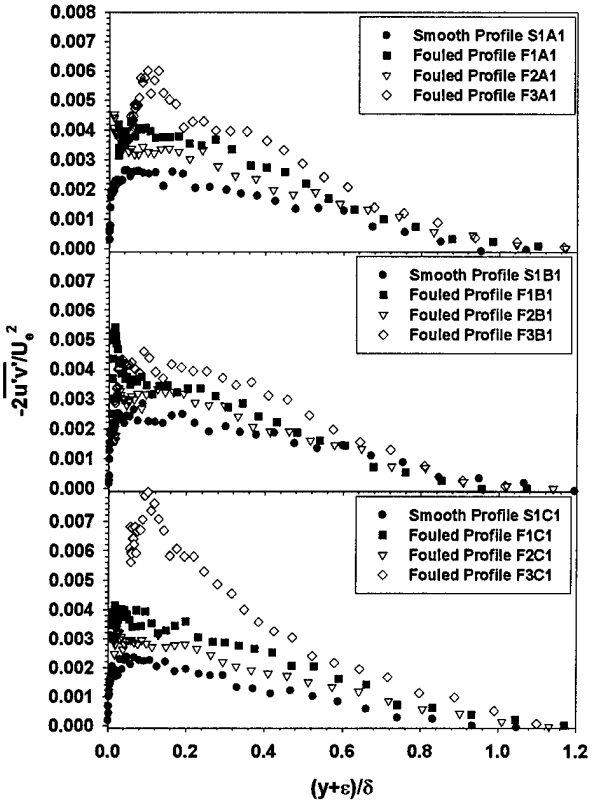

Figure 6. Reynolds shear stress plots for the smooth and fouled specimens.

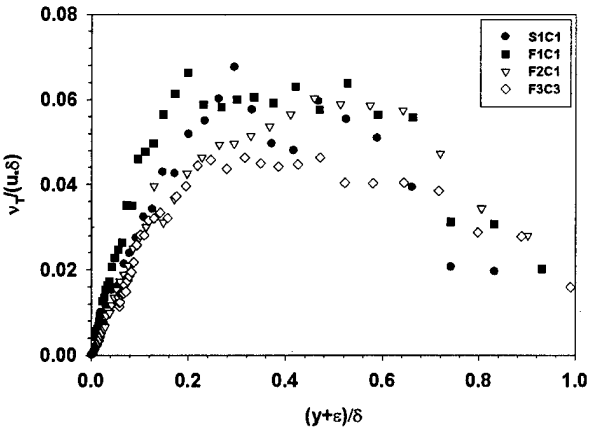

Figure 7. Eddy diffusivity plots for the smooth and fouled specimens.

Turbulent Drag Reduction Methods: Compliant Coatings

RECENT ADVANCES IN THE USE OF COMPLIANT WALLS FOR DRAG REDUCTION

Peter W. Carpenter
University of Warwick
Coventry, CV4 7AL, England
pwc@eng.warwick.ac.uk

Abstract - Recent work on the use of compliant walls for laminar flow control in low-disturbance marine environments is reviewed. The key role of hydroelastic instability is explained and discussed. It now appears that it may well be possible to maintain laminar flow at indefinitely high Reynolds numbers by the use of multiple-panel compliant walls with properties tailored to the local flow conditions. The recent theoretical and experimental work on transition in the three-dimensional boundary layer over rotating compliant disks is also reviewed. Wall compliance has a stabilizing effect on the crossflow vortices and an even more marked stabilizing effect on the absolute instability recently discovered by Lingwood. Finally the effects of wall compliance on fully turbulent boundary layers are briefly discussed.

I. INTRODUCTION

More than forty years have elapsed since Kramer [1] first reported his pioneering experiments on the use of compliant coating for drag reduction in sea water. The general acceptance of the validity of his findings has waxed and waned several times since then. Kramer, himself, believed that his coatings reduced drag by postponing the onset of laminar-turbulent transition. There is certainly supporting theoretical and experimental evidence for this view [2,3,4,5]. An alternative explanation for the drag reduction could be that wall compliance favourably affects the fully turbulent boundary layer. Here the evidence is less clear and certainly a convincing theoretical explanation is lacking. However, there have been carefully conducted experiments in water where a drag reduction is clearly observed. Such a study was described recently by Choi *et al.* [6].

In this paper the recent work on the use of wall compliance for laminar flow control will be reviewed in Section II. Most of the work on compliant walls, both experimental and theoretical, has involved the flat-plate boundary layer. However, the effect of wall compliance on the three-dimensional boundary layer over a rotating disc has also been studied experimentally [7-9] in the past. The problem with these earlier studies was that only the torque was measured, so when it fell or increased for a compliant disc compared with a rigid one, the underlying physical cause was not revealed. Recently, at Warwick, we have undertaken a combined theoretical [10], computer simulation [11] and experimental [12] study of transition in the rotating-disc boundary layer. The results will be briefly presented in Section III. The effects of wall compliance on fully turbulent boundary layers will be briefly considered in Section IV.

Since there have been several reviews on these and related topics in recent years [13-15], I will mainly discuss recent work at Warwick.

II LAMINAR FLOW CONTROL

Little is currently known about the effects of wall compliance on laminar-turbulent transition in high-disturbance environments where by-pass transition comes into play. On the other hand a great deal is now known about the effects of wall compliance on transition in the low-disturbance environments typical of many aeronautical and marine applications. Accordingly the present review will focus on transition in low-disturbance environments. In such cases, when the boundary layers are similar to that found over a flat plate, the route to transition begins with the amplification of quasi-two-dimensional Tollmien-Schlichting waves as they propagate along the boundary layer. In the great majority of experimental studies such waves are produced artificially as monochromatic wavetrains using a vibrating ribbon or some other driver. Likewise most theoretical studies implicitly address this artificial situation. It is important to appreciate, however, that T/S waves have been observed many times in natural transition (see, for example, [16,17]). But, as first demonstrated by Schubauer and Skramstadt [16], the use of a driver to excite the boundary layer artificially produces much cleaner signals.

In natural transition the boundary layer is excited via freestream turbulence, acoustic radiation, vibration, roughness or some other agency. The process whereby T/S waves are generated through such sources of natural excitation is known as receptivity. The effect of wall compliance on receptivity may well be important, but it has been little studied to date. Some relevant information is given in [18]. For the rigid wall T/S waves grow as they propagate downstream and eventually reach sufficiently large amplitudes for nonlinear effects to become significant. At this point the disturbances become three-dimensional and the several stages of transition proper rapidly ensue. The actual transition zone itself is characterized by turbulent spots and there is no direct evidence by this stage of the original T/S waves. Nevertheless the final stage of transition would not have occurred without the intial amplification of the T/S waves. In the sort of low-disturbance environment often found in aeronautical and marine applications the initial amplification of T/S waves (the so-called linear regime of transition) typically extends over 70 to 80 percent of the total transition process. The aim of using compliant walls for laminar flow control is greatly to extend this linear regime or even to suppress the growth of T/S waves entirely.

It has been known since the seminal theoretical studies of Benjamin and Landahl [19,20] (see [2] also) that the more compliant the wall the greater is the stabilizing effect on T/S waves. Indeed if the wall is made sufficiently compliant T/S waves can be completely suppressed. The problem is that highly compliant wall are vulnerable to hydroelastic instabilities. Accordingly, the key to the successful use of wall compliance for laminar flow control is to make the wall as compliant as possible without making it hydroelastically unstable. There appear to be two main classes of hydroelastic instability, namely *travelling-wave flutter* which is convective, and *divergence* which is absolute in nature [3]. Although this simple picture is broadly correct, it is further complicated by the fact that it is now known that for compliant walls with good transition-delaying properties divergence tends to be replaced by another absolute instability which forms through a coalescence of the T/S waves and travelling-wave flutter [2,13,21].

The theory explaining the effect of wall compliance on T/S waves has been corroborated by the careful experiments in water by Gaster [4] and his co-workers. The compliant panels used in these experiments comprised a relatively thick and soft silicone-rubber substrate covered with a thin, much stiffer, latex-rubber sheet. As well as Gaster and his co-workers, other authors [22,23] have investigated the stability of boundary layers over such surfaces. Since the theoretical model is essentially the same in all these cases, Gaster's study can be regarded as confirmation of the essential validity of the theoretical approach. In brief, he measured the growth of artificially generated monochromatic T/S waves as they propagated along the boundary layer over various compliant walls. In all cases, including the rigid control, good agreement was found between the predicted and measured growth. A more recent account of Gaster's experimental study is given by Lucey and Carpenter [5]. Their work is based on a slightly modified theory which accounts for the tension applied to the outer sheet, leading to slightly improved predictions of T/S amplitudes when compared with the experimental data.

The Gaster study confirmed that the growth of T/S waves could be reduced by wall compliance. A 30 percent increase in the transitional Reynolds number was also obtained. The transition delay was limited by the experimentsl set-up rather than the compliant wall. It should be appreciated, however, that obtaining a transition delay

was not the aim of the study; in fact, it was undertaken in order to confirm that the evolution of T/S waves over compliant walls could be theoretically predicted with confidence. Another very significant outcome of the study was the observation that over most of the compliant panels transition did not occur because of the amplification of T/S waves. What was observed instead was a very sudden breakdown when the flow speed exceeded a certain critical flow speed. It has been shown in [5] that this sudden breakdown can be fully explained and predicted using the linear theory for travelling-wave flutter [3,24]. The discovery of this new route to transition shows how vital an understanding of hydroelastic instability is for designing compliant walls for laminar flow control.

The mechanism for the other hydroelastic instability, divergence, is easy to understand. When a small disturbance induces a small displacement to a compliant surface a pressure force is generated. The magnitude of this force is proportional to the dynamic pressure of the freestream. Consequently, when a sufficiently high flow speed is reached the pressure force will outweigh the restorative structural forces in the wall and divergence waves will form in the wall. These waves would act much like roughness and trigger transition. Thus divergence must be avoided if laminar flow control is to be achieved. Divergence has been observed many times for compliant walls [3,13,14]. The most detailed experimental study was carried out by Gad-el-Hak and his co-workers [25,26]. They found that divergence waves travelled very slowly, typically a few percent of the freestream flow speed. Divergence was only observed over highly damped walls in turbulent flow. Travelling-wave flutter supplanted divergence when the compliant walls were lightly damped. Theoretical studies of divergence [3,13] suggested that divergence is an absolute instability. This has been confirmed more recently by numerical simulation [27] and a rigorous theoretical study [28].

The requirement of a turbulent flow for the existence of divergence has only recently been fully appreciated in the theoretical work. It has been known for some time [29] that the presence of the boundary layer alters the phase and magnitude of the wall pressure compared with the pressure in the potential flow just outside of the boundary layer. Indeed, for the laminar boundary layer there are accurate approximate expressions for estimating the pressure at the wall [24]. What our recent numerical simulations [30] have shown is that the amplitude in pressure is reduced to a much greater extent in laminar-boundary layers than in turbulent ones. Accordingly, the critical flow speed for divergence is much greater for a laminar boundary layer. Actually, it now appears that theoretically in the case of a laminar boundary layer, divergence is replaced by another absolute instability formed by the coalescence of a Tollmien-Schlichting wave and travelling-wave flutter. This has been demonstrated analytically in the case of the plane channel flow[21]. It has been long suspected that this instability is absolute [3,13]. Recent numerical simulations [10] have established this for certain. Experimentally it would probably be difficult to distinguish this new absolute instability from divergence.

Previously [3,13,23] the divergence onset speed was estimated using potential flow theory. From the recent work on divergence and the other absolute instability it is now known that this is a very conservative estimate and that the walls can be made substantially more compliant without incurring the danger of absolute instability. In fact, it is possible to suppress T/S waves completely over a streamwise length of the surface [18]. The compliant-wall properties can be tailored to suppress the T/S waves for a range of Reynolds number based on boundary layer thickness. In this way multiple-panel surfaces [31] could be used in order to suppress the T/S waves for the entire surface. The practical question then becomes: How short can a compliant panel be without losing its capability of suppressing T/S waves? This question was addressed in [18] for plane channel flow. The simulations have been repeated [11] for the boundary layer with much the same results. It turns out that, although the response of a finite compliant panel can be very complex, those with appropriate properties continue to suppress T/S waves even when as short as a single T/S wave. This implies, that in the absence of an, as yet undiscovered, receptivity mechanism, T/S waves can be completely suppressed at indefinitely high Reynolds numbers and laminar flow maintained by the use of multiple-panel compliant walls composed of relatively short panels. Small compliant panels have the further advantage of being less vulnerable to hydroelastic instability.

Even using the very conservative, previous estimates of the critical flow speed for divergence, very substantial postponement of transition is possible (up to a six-fold increase in transitional Reynolds number) according to the theory [23,31]. Moreover, the mechanical properties of the compliant wall required to maintain laminar flow could be readily realized in practice in a marine environment. In fact, in most respects, the properties required at relatively high speeds are probably less demanding than those corresponding to the flow speeds typical of the Gaster experiments. The maximum flow speed in Kramer's tests was 18 m/s. These tests were carried out in the sea and the compliant coatings were made from natural rubber. At similar flow speeds the theoretical optimum wall properties for maintaining laminar flow are quite similar to those of the Kramer coatings. Accordingly it should not be too difficult in practice to make such optimum coatings.

III. TRANSITION OVER ROTATING COMPLIANT DISKS

Transition in the three-dimensional boundary layer over a rotating disk has been widely studied because it is a simple model exhibiting many of the features exhibited by the three-dimensional flows found in practical aeronautical and marine applications. There have been several experimental studies of the rotating compliant disk, e.g. [7-9]. In these experiments the only quantitative measurements were of the torque required to drive the disk. A change in the torque required to drive a compliant disk compared with a rigid one at the same rotational speed was regarded as evidence of a drag increase or reduction. Torque reduction was observed in some cases [9]. Visual observations could also be made of hydroelastic instabilites forming on the disk surface. In that way torque increases could sometimes be explained [7,8]. But, until our recent research programme, it was not known how boundary-layer stability or transition would be affected by wall compliance for the rotating disc.

The transition process in the boundary layer over a rigid rotating disk is quite different from and possibly more complex than that for the flat-plate boundary layer. Wall compliance brings additional complexity. Three different instabilities have been identified. The most widely studied is the so-called Type I instability or crossflow vortex. This is found in many other three-dimensional flows. The instability mechanism is essentially inviscid and is associated with the presence of an inflexion point in the velocity profile. This instability is much more powerful than Tollmien-Schlichting waves for which the instability mechanism is essentially viscous. It was shown recently that, nevertheless, wall compliance has a strong stabilizing effect on these more powerful inflexion-point instabilities [32]. Both stationary (with respect to the disk) and travelling cross-flow vortices can exist. The former are by far the most commonly studied experimentally, but the latter are the most rapidly growing. Our recent theoretical [10] and numerical simulation [11] studies show that wall compliance has a strong stabilizing effect on both travelling and stationary cross-flow vortices. The experimental study [12] is less clear. It appears to corroborate the theory in that there is an apparent rise in the critical Reynolds number for the cross-flow vortices for the compliant disk as compared with a rigid one. Transition occurs earlier for the compliant disk, however.

The second instability found in the rotating-disk boundary layer is the so-called Type II. The instability mechanism is viscous and involves Coriolis acceleration. The effect of wall compliance appears to be more complex in this case in that small levels of compliance lead to a substantial drop in the critical Reynolds number for this instability whereas larger levels of compliance appear to be stabilizing. Under certain circumstances the Type I and Type II instability coalesce, giving rise to local algebraic growth even when the instability is convectively stable. This seems to be of little practical consequence for rigid walls [11]. In contrast wall compliance seems to lead to this algebraic growth occurring at considerably lower Reynolds numbers than for the rigid wall. It is possible that this mechanism is responsible for the earlier transition seen in the experiments on a rotating compliant disk.

An absolute instability is also found in the rotating-disk boundary layer. [33,34] This also comes about due to the coalescence of two eigenmodes, namely the Type I and Type III -- a hitherto rather obscure eigenmode. It appears that this absolute instability is a common route to transition. According to our theoretical [10] and numerical simulation [11] studies even a low level of compliance has a strongly stabilizing effect on the absolute instability. This may well be the most practically significant effect of wall compliance on the rotating disc because it appears that the absolute instability occurs in several other flows some of which are of practical interest [25].

IV. EFFECT OF WALL COMPLIANCE ON TURBULENCE

Much of the experimental evidence of the effects of wall compliance on turbulent boundary layers is rather inconclusive. Direct numerical simulations [36] suggest that compliant walls with properties selected to be effective in the linear regime of transition remain highly effective well into the nonlinear regime where the flow structures have become highly three-dimensional. One might expect, therefore, that such relatively highly compliant surfaces would be effective in reducing turbulence levels in the fully turbulent boundary layer. On the other hand, the scale and form of the near-wall structures in a turbulent boundary layer are completely different from those found in the linear and weakly nonlinear transition regimes.

Recently Choi *et al.* [6] have reported small reductions in drag (up to 7 percent) and in skin friction and wall-pressure fluctuations in boundary layers over compliant walls in the form of a single viscoelastic layer. These results confirm earlier results obtained in Russia with the same compliant coatings. What is particularly noteworthy in these experiments is that the degree of wall compliance is very low (the walls are about 100 stiffer than the Kramer coatings when allowance is made for the differences in flow speed. This suggests a quite different mechanism is involved than for the walls used for transition delay. It is also worth noting that the compliant rotating disks used in our experimental study [12] were also much stiffer relative to the Kramer coatings. In this case also, although wall compliance brought earlier transition, it also led to markedly lower levels of turbulence intensity in the full turbulent boundary layer.

What physical mechanism could come into play for fairly stiff compliant walls? Our theoretical analysis shows that when the wall compliance is small, the main effect is the pseudo-random wall displacements due to the effect of the turbulent pressure fluctuations driving the wall. It appears that the effect of these wall displacements on the near-wall structures is much larger than the direct interaction between the near-wall structures and the compliant wall. It is known from the work of Sirovich and his co-workers, e.g. see [37], that random phase changes to the near-wall structures can interfere with bursting process thereby lead to substantial drag reduction. This effect was realized in experiments by using randomized chevron-shaped roughness elements. It may be that the pseudo-random displacements created in the compliant wall by the fluctuating turbulent pressure field has much the same effect.

V. CONCLUSIONS

Recent work on the use of wall compliance to maintain laminar flow in a low-disturbance marine environment has been reviewed. All the evidence suggests that appropriately designed multiple-panel compliant walls could maintain laminar flow at indefinitely high Reynolds numbers. The material properties required for these panels should be practically achievable. Further work is required on the effects of wall compliance on receptivity mechanisms. Also further experimental study is desirable, including proof-of-concepts tests at the flow speeds of practical interest in a marine environment.

The recent work on the rotating-disk boundary layer was also reported. It appears that wall compliance also has a strong effect on transition in this highly three-dimensional boundary layer. In particular, even low levels of wall compliance have a strongly stabilizing effect on the absolute instability which provides the route to transition in some practical flows.

Recent work on the effects of wall compliance on fully turbulent flows is briefly reviewed. It appears that using fairly stiff compliant walls leads to reductions in drag and turbulence intensity. A possible physical mechanism which could account for this is outlined.

ACKNOWLEDGEMENTS

The work at the University of Warwick reported here was supported by the UK Engineering and Physical Sciences Research Council.

VI. REFERENCES

1. M.O. Kramer "Boundary-layer stabilization by distributed damping", *J. Aero. Sci.* **24**, 459, 1957; *J. Amer. Soc. Naval Engrs.* **72**, 25-33, 1960.

2. P.W. Carpenter and A.D. Garrad "The hydrodynamic stability of flow over Kramer-type compliant surfaces. Part 1. Tollmien-Schlichting instabilities", *J. Fluid Mech.* **155**, 465-510, 1985.

3. P.W. Carpenter and A.D. Garrad "The hydrodynamic stability of flow over Kramer-type compliant surfaces. Part 2. Flow-induced surface instabilities", *J. Fluid Mech.* **170**, 199-232, 1986.

4. M. Gaster "Is the dolphin a red herring?", *Proc. IUTAM Symp. on Turbulence Management and Relaminarisation, Bangalore, India* (edited by H.W. Liepmann and R. Narasimha), Springer, New York, 285-304, 1987.

5. A.D. Lucey and P.W. Carpenter "Boundary layer instability over compliant walls: comparison between theory and experiment", *Phys. of Fluids* **7**, 2355-2363, 1995.

6. K.-S. Choi, X. Yang, B.R. Clayton, E.J. Glover, M. Atlar, B.N. Semenov and V.M. Kulik "Turbulent drag reduction using compliant surfaces", *Proc. Roy. Soc. London* A **453**, 2229-2240, 1997.

7. R.I Hansen and D.L. Hunston "An experimental study of turbulent flows over compliant surfaces", *J. Sound & Vib.* **46**, 297-308, 1974.

8. R.I. Hansen and D.L. Hunston "Fluid-property effects on flow-generated surface waves in compliant surfaces", *J. Fluid Mech.* **133**, 161-177, 1983.

9. K. Chung "Composite compliant coatings for drag reduction utilising low modulus high damping silicone rubber", PhD dissertation, MIT, 1985.

10. A.J. Cooper and P.W. Carpenter "The stability of rotating-disc boundary-layer flow over a compliant wall. *J. Fluid Mech.* ***350***, 231-270, 1997.

11. C. Davies and P.W. Carpenter "Non-parabolic disturbance behaviour in incompressible boundary layers", *Bull. Amer. Phys. Soc.* ***42***, 2138, 1997.

12. A.J. Colley, P.J. Thomas and P.W. Carpenter "An experimental investigation of the stability of the boundary layer over a rotating disk covered with a compliant coating", *3rd Euro. Fluid Mech. Conf, Göttingen, Germany*, Sept. 1997.

13. P.W. Carpenter "Status of transition delay using compliant walls", *Viscous Drag Reduction, Prog. in Astro. and Aero.* **123** (edited by D.M. Bushnell and J.N. Hefner) AIAA, 79-113, 1990.

14. M. Gad-el-Hak "Compliant coatings: The simpler alternative", *Experimental Thermal and Fluid Science* (to appear), 1998.

15. P.W. Carpenter "Current status of the use of wall compliance for laminar flow control", *Experimental Thermal and Fluid Science* (to appear), 1998.

16. G.B. Schubauer and H.K. Skramstadt "Laminar boundary layer oscillations and transition on a flat plate", *NACA Rep. 909*, 1948.

17. H. Schlichting *Boundary Layer Theory.* 7th Ed., McGraw Hill, 1979.

18. C. Davies and P.W. Carpenter "Numerical simulation of the evolution of Tollmien-Schlichting waves over finite compliant panels", *J. Fluid Mech.* **335**, 361-392, 1997.

19. T.B. Benjamin "Effects of a flexible boundary on hydrodynamic stability", *J. Fluid Mech.* **9**, 513-532, 1960.

20. M.T. Landahl "On the stability of a laminar incompressible boundary layer over a flexible surface", *J. Fluid Mech.* **13**, 609-632, 1962.

21. C. Davies and P.W. Carpenter "Instabilities in a plane channel flow between compliant walls", *J. Fluid Mech.* **352**, 205-243.

22. K.S. Yeo "The stability of boundary layer flow over single- and multi-layer viscoelastic walls", *J. Fluid Mech.* **196**, 359-408, 1988.

23. A.E. Dixon, A.D. Lucey and P.W. Carpenter "Optimization of viscoelastic compliant walls for transition delay", *AIAA J.* **32**, 256-267, 1994.

24. P.W. Carpenter and J.S.B. Gajjar "A general theory for two- and three-dimensional wall-mode instabilities over isotropic and anisotropic compliant walls", *Theor. Comp. Fluid Dynamics* **1**, 349-378, 1990.

25. M. Gad-el-Hak, R.F. Blackwelder and J.J. Riley "On the interaction of compliant coatings with boundary layer flows", *J. Fluid Mech.* **140**, 257-280, 1984.

26. M. Gad-el-Hak "The response of elastic and viscoelastic surfaces to a turbulent boundary layer", *J. Applied Mech* **53**, 206-212, 1986.

27. A.D. Lucey and P.W. Carpenter "A numerical simulation of the interaction of a compliant wall and inviscid flow", *J. Fluid Mech.* **234**, 121-146, 1992.

28. K.S. Yeo, B.C. Khoo and H.Z. Zhao "The absolute instability of boundary-layer flow over viscoelastic walls", *Theor. Comp. Fluid Dynamics* **8**, 237-**252**, 1996.

29. J.H. Duncan, A.M. Waxman and M.P. Tulin. "The dynamics of waves at the interface between a visco-elastic coating and a fluid flow", *J. Fluid Mech.* **158**, 177-197, 1984.

30. A.D. Lucey, G.J. Cafolla and P.W. Carpenter "Numerical simulation of a boundary-layer flow interacting with a passive compliant boundary", *Lecture Notes in Physics* **490**, 406-411, 1997.

31. P.W. Carpenter "The optimization of multiple-panel compliant walls for delay of laminar-turbulent transition", *AIAA J* **31**, 1187-1188, 1993.

32. A.J. Cooper and P.W. Carpenter "The effect of wall compliance on inflexion point instability in boundary layers", *Phys. of Fluids* **9**, 468-470, 1997.

33. R.J. Lingwood "Absolute instability of the boundary layer on a rotating disk",*J. Fluid Mech.* **299**, 373-405, 1995.

34. R.J. Lingwood "An experimental study of absolute instability of the rotating-disk boundary-layer flow ", *J. Fluid Mech.* **314**, 373-405, 1996.

35. R.J. Lingwood "Absolute instability of the Ekman layer and related rotating flows", *J. Fluid Mech.* **331**, 405-428, 1997.

36. R.W. Metcalfe, F. Battistoni, J. Ekeroot and S. A. Orszag "Evolution of boundary layer flow over a compliant wall during transition to turbulence", *Boundary Layer Transition and Control,* Cambridge, UK, Royal Aero. Soc., 36.1-36.14, 1991.

37. L. Sirovich and S. Karlsson "Turbulent drag reduction by passive mechanisms", *Nature* **388**, 753-755, 1997.

RECENT DEVELOPMENTS IN INTERFERENCE ANALYSIS OF COMPLIANT BOUNDARY ACTION ON NEAR – WALL TURBULENCE

Boris.N. Semenov & Alena.V. Semenova
Institute of Thermophysics, Siberian Branch of Russian Academy of Sciences,
Prospekt Ac. Lavrentyev, 1, Novosibirsk, 630090, Russia
irena@hydro.nsc.ru

Abstract - The interference form of the compliant boundary action is analysed on the base of linear harmonic solution for viscous sublayer of turbulent near-wall flow. This action can lead to decrease or to increase of turbulence production (accordingly, of turbulent friction and noise), depending on the vibrational characteristics of flowed surface. The phase-frequency region of positive action - PFRPA (the turbulence production decrease) of compliant boundary is determined. The main result of these calculations is the prognostication of the necessary vibrational characteristics of compliant surface. PFRPA was calculated for boundary layer on smooth and rough flat plate. Reynolds number increase from 1 million till 200 millions leads to PFRPA decrease. Calculations show the decrease and degeneration of PFRPA for increased roughness. Calculations lead to the conclusion that small polymer additives in a flow extend PFRPA and, accordingly, the drag reduction possibilities of compliant coatings. The same prognosis follows from PFRPA calculations for compliant coating with drag reducing riblets on its surface.

1. INTRODUCTION

Two forms of wave action of the viscoelastic boundary on near-wall turbulence caused by specific properties of compliant coating are considered for the modelling of a phenomenon. Firstly, it is absorbtion, dissipation (inside viscoelastic coating) of the energy of pressure fluctuations deforming a wall. This hypothesis was offered by Kramer [1-3] for the laminar flow stabilization. That was used by Semenov [4], Voropaev and Babenko [5], Korobov and Babenko [6] for modelling the near-wall turbulence transformation. But a priori it is clear that the Kramer hypothesis of the energy absorption can't explain a cause of many facts of the turbulent friction increase. And that compromised the idea of drag reduction using compliant coatings. Kulik [7] analysed our experimental data[8] for turbulent drag decrease and increase using one-layer coatings and determined that the production and dissipation of turbulent energy in turbulent boundary layer is greater by many times than the absorbtion and dissipation of fluctuation energy by viscoelastic coating. That is why, this (dissipative) factor can't be essential. Moreover, there are experimental data contradicting the hypothesis of "distributed damping". The coatings lose the ability to reduce turbulent friction and even increase it with the increase of energy absorbtion by coating.

Another form of the compliant boundary action was analysed by Semenov [9, 4, 10] on the base of linear harmonic solution of problem on its kinematic-dynamic interaction with viscous sublayer of turbulent near-wall flow. He used the near-wall turbulence model of Sternberg[11]. This simplified linear model allowed him to obtain the solution in the analytical form. This is important for the analysis of phenomenon (and for estimations of new numerical solutions too). The field of velocity fluctuations as well as the Reynolds stresses are formed as a result of superposition of two waves: 1) going out of turbulent core, being powerful stable generator of long-wave perturbations, and 2) reflexed from a wall. Addition of compliance to boundary properties leads to variation of amplitude and phase of the induced wave and respectively to a change of interference picture of turbulence production. Its action can lead to decrease or increase of turbulent stresses in dependence upon the wave properties of flowed surface. The comparison with the experimental data testified to the validity of the interference approach [7]. That is why, the term "interference compliant coatings" should be used unstead of the term "damping coatings".

The next solutions (in interference theory) were obtained by Skripatchev [12, 13] for the near-wall turbulence model of Schubert & Corcos [14], by Trifonov [15, 16] and Kereyko [7] for monoharmonic model of Goldshtik & Shtern [18]. Voropaev & Popkov [19] used the model of Sternberg [11] for consideration of near-wall turbulence for coatings deformed in all directions.

Alas! Some scientists continue wasting their time on calculations of dissipative action of compliant coatings in turbulent flows still. And unfortunately, even the last review (Gad-el-Hak [20]) contains an information about these investigations without a criticism.. So here it is necessary to consider the main difference in possibilities of two forms of compliant surface action again in spite of repeated former publications [21-23].

Real isotropic compliant coatings can change mainly the normal (to a wall) velocity component υ. Longitudinal (u) and transversal (w) components can be changed by compliant surface a little. So the possible direct variation of turbulent energy balance is very small: $\Delta\langle\upsilon^2\rangle / \left(\langle u^2\rangle + \langle\upsilon^2\rangle + \langle w^2\rangle\right) <<< 1$, because $\langle\upsilon^2\rangle << \left(\langle u^2\rangle + \langle w^2\rangle\right)$. The interference action leads to the variation of the Reynolds stress production $\Delta\left(-\rho\langle u\upsilon\rangle\right) = \Delta\left(-\rho\langle u^2\rangle^{1/2}\cdot\langle\upsilon^2\rangle^{1/2}\cdot R_{u\upsilon}\right)$, where ρ is the density of fluid. Here both υ and correlation coefficient $R_{u\upsilon}$ can be changed by compliant surface. So the possible variation can be enough great: $\dfrac{\Delta\langle u\upsilon\rangle}{\langle u\upsilon\rangle} \approx \dfrac{\Delta\langle\upsilon^2\rangle^{1/2}}{\langle\upsilon^2\rangle^{1/2}} + \dfrac{\Delta R_{u\upsilon}}{R_{u\upsilon}}$.

The analogous conclusion follows from estimations for anisotropic coatings. In this case longitudinal and normal components of velocity fluctuation of surface can have identical levels. And so $2\,\Delta\langle\upsilon^2\rangle / \left(\langle u^2\rangle + \langle\upsilon^2\rangle + \langle w^2\rangle\right) <<< 1$, but $\dfrac{\Delta\langle u\upsilon\rangle}{\langle u\upsilon\rangle} = \dfrac{\Delta\langle u^2\rangle^{1/2}}{\langle u^2\rangle} + \dfrac{\Delta\langle\upsilon^2\rangle^{1/2}}{\langle\upsilon^2\rangle^{1/2}} + \dfrac{\Delta R_{u\upsilon}}{R_{u\upsilon}}$, i.e. the possible variation of Reynolds stress can be larger for small as before variation of turbulent energy balance.

Thus the main factor of compliant surface action on near-wall turbulence isn't an absorption of turbulent energy by viscoelastic coating but it is the change of Reynolds stress production determined from the interference theory.

II.TURBULENCE MANAGEMENT FOR DRAG REDUCTION

Turbulence management is a total problem of investigations of well-known methods of drag reduction using polymeric additives, gas microbubbles, compliant coatings, riblets. And here it is important to determine the main aim of this management.

It is known from the analysis of energy balances for turbulent flows on smooth plate and in pipes [24] that turbulence production is the greatest part of friction work. It is possible to suppose that it is an universal property of all near-wall turbulent flows and that it is right for turbulent drag reduction.

Calculations of ratio (E) of turbulence production to friction work were carried out for a check-up of this hypothesis according to:

$$E = \frac{1}{\tau_w U_0}\int_0^y \left(-\rho\langle u\upsilon\rangle\right)\frac{dU}{dy}\cdot dy \qquad (1)$$

Where U_0 is the main-stream velocity or the velocity on the axis, $U(y)$ -the mean velocity profile, τ_w - the friction stress on a

wall. It is known [24] that the total shear stress is constant for flows in pipes and in near-wall region of turbulent boundary layer, i.e. $-\rho\langle uv\rangle+\rho\nu\frac{dU}{dy}=\tau_w$. So it is possible to write (1) in universal coordinates ($y^+=yv_d/\nu$, $U^+=U/v_d$, where the friction velocity $v_d=(\tau_w/\rho)^{1/2}$ and the viscous scale ν/v_d are used in order to obtain non-dimensional values, ρ and ν - density and kinematic viscosity of fluid) [24]:

$$E(y^+)=\frac{1}{U_0^+}\int_0^{y^+}\left(1-\frac{dU^+}{dy^+}\right)\frac{dU^+}{dy^+}dy^+ \qquad (2)$$

Calculations were carried out for different efficiency of drag reduction $\Psi=1-\tau/\tau_w$ to Ψ=0.6. These values are observed in tests for flows with polymeric additives. Velocity profiles are described below - in part VI. Here the pipe flow with R^+=5000 for Ψ=0 is considered as an example ($2R$ is the pipe diameter, $R^+=Rv_d/\nu$ and R^+= 5000 $(1-\Psi)^{1/2}$ for drag reduction). The results are shown in Table I and in Figures 1, 2.

Ψ	0	0.1	0.2	0.3	0.4	0.5	0.6
$E(R^+)$	0.70	0.68	0.66	0.64	0.62	0.60	0.58

Table I. The ratio of total turbulent energy production to friction work for different efficiencies of drag reduction.

And so the quota of turbulence production in spended energy (or friction work) decreases for drag reduction efficiency increase as $E(R)=0.70-0.2\Psi$.

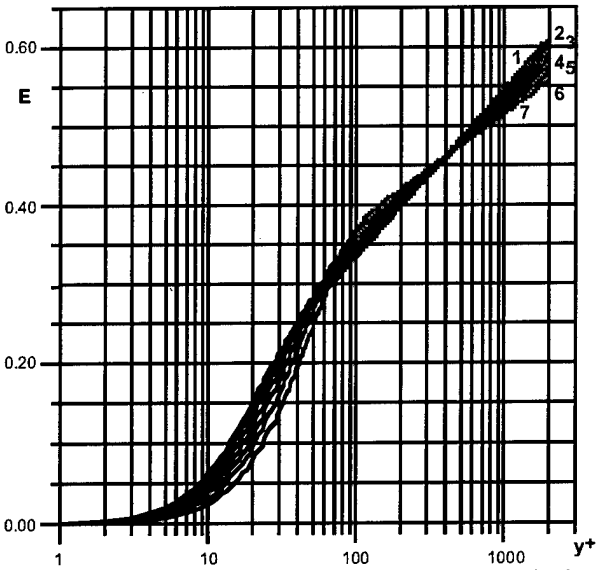

Figure 1. Calculated dependence (2) of turbulent energy production on the distance from a wall: (1) Ψ = 0, (2) Ψ = 0.1, (3) Ψ = 0.2, (4) Ψ = 0.3, (5) Ψ = 0.4, (6) Ψ = 0.5, (7) Ψ = 0.6

Here (in Figure 1) all lines have the crossing point about y^+ = 400 and E = 0.465. So it is possible to use the region preceding this point for estimations of drag reduction depending on turbulence production decrease.

According to data in Figure 2, the quota of region between a wall and y^+ = 400 in total turbulent energy production increases for drag reduction efficiency increase from $E/E(R)$ = 0.66 at Ψ=0 to $E/E(R)$ = 0.79 at Ψ=0.6.

Conclusions:

– Directly proportional cross-correlation between the wall friction and the turbulence production exists.

– It is right for drag reduction $0<\Psi\le 0.6$ that the turbulence production is the main and stable quota in spended energy.

– The main aim of turbulence management for achievement of drag reduction is the decrease of turbulence production.

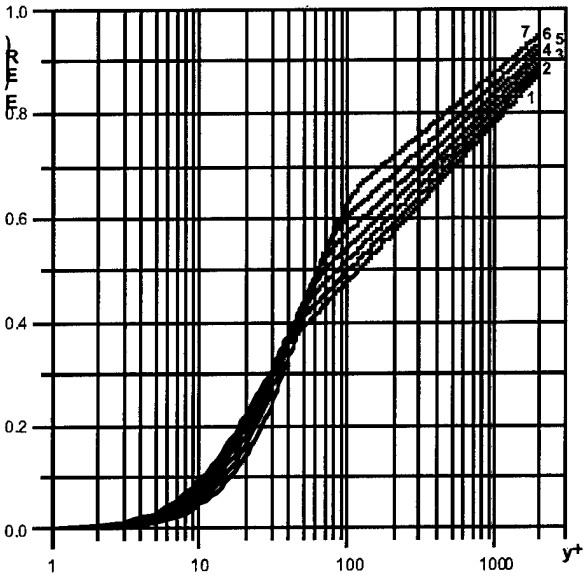

Figure 2. The quota of region between a wall and y^+ in the total turbulent energy production (from a wall to R^+)

III. INTERFERENCE ANALYSIS

The existing analysis was elaborated on the base of theoretical solutions determining 1) the interference effect of compliant boundary on near-wall turbulence [9] and 2) the correlation of oscillation characteristics of compliant boundary with viscoelastic properties of materials for some scheme of real * isotropic coatings [10, 25]. Here the first problem is considered mainly.

According to the interference theory [9, 10, 21, 26] the main modelling parameter is the dimensionless complex compliance of boundary $\Pi\exp(i\theta)$ where the module is $\Pi=\rho v_d^3/(\nu C_d)$, the argument θ is the phase of the boundary displacement relative to the turbulent pressure fluctuation. Here $C_d=C_0/K_d$; C_0 is the equilibrium stiffness and K_d is the dynamic coefficient of coating oscillation, i.e. the ratio of amplitude of forced oscillations at frequency $\omega=2\pi f$ to the displacement for static loading ($\omega=0$), where ω is the angular frequency of pressure fluctuation acting on the boundary. In practice it is more convenient to consider an opposite dimensionless parameter, called the complex dynamic stiffness $\overline{C}_d\cdot\exp(i\theta)$, where $\overline{C}_d=1/\Pi$.

For correct theoretical consideration of this problem two conditions in the modelling and selection of oscillation characteristics of compliant boundary for drag reduction are required. The aperiodicity of turbulent fluctuations and their wide spectrum lead to the first condition, that the coatings should not have any free vibrations. Only this approach permits to obtain a single-valued solution of this problem. In practice, one can assume a sufficiently rapid damping of the free vibrations.

The second logical condition imposes restriction on the compliance module following from the requirement of hydraulic smoothness of an oscillating surface. This restriction results in a necessary condition for the considered problem of interaction between compliant boundary and viscous sublayer since the viscous sublayer exists only over a smooth wall. The analysis of experimental data [4] has shown that this condition determines the limiting compliance values, so the required stiffness is given by

$$C_d \ge 0.007\rho U_0^3 \mathrm{Re}_0^{-0.3}/\nu \qquad (3)$$

The Reynolds number Re_0 is based on the distance from the nosing edge to the compliant coating beginning x_0. For large Reynolds numbers the above condition will become

$$C_d \ge 0.003\rho U_0^3 \mathrm{Re}_0^{-0.21}/\nu \qquad (3a)$$

The obtained solution [9] shows that variation of Reynolds stress in near-wall region by compliant surface depends on

* Now some researchers try to prepare anisotropic coatings. But here technological difficulties are very great. And they were not overcome still.

complex compliance and distance y from a wall. So it was necessary to determine an integral characteristic of compliant surface action in the full near-wall region. According to considerations described in section II, the turbulence production was selected as a criterion of compliant wall action. However it is possible to calculate Reynolds stresses only for y less then limited ordinate y_{lim}, determined according to the restrictions of the theoretical model of Sternberg [11]. The wall influence is observed only for short distance from a wall: for $y < l$, but the main problem of these investigations is exactly the study of wall action. There l is called the dynamic viscous sublayer thickness [11], determined as:

$$l \approx 5/(\pi f/\nu)^{1/2} \qquad (4)$$

And so everything an be OK if the solved problem is restricted:

- The turbulence production for different frequencies must be integrated for $0 \le y \le l(f) \le y_{lim}$. This idea can be realized by a restriction of low frequency considered in this analysis.
- Only the change of turbulence production by compliant surface action (but not the turbulence production itself) is considered here.
- The analysis is carried out at abscissa x_0 of the compliant coating beginning since used parameters (the mean velocity profile $U(y)$, the ratio of transversal and longitudinal wave numbers k_z/k_x, the convection velocity U_c) can be determined from well-known experiments on a rigid surface.
- The calculations are carried out separately for every frequency without a generalization in all frequency region, that permits to except the inherent (in Sternberg model [11]) mistake in frequency spectrum determination.

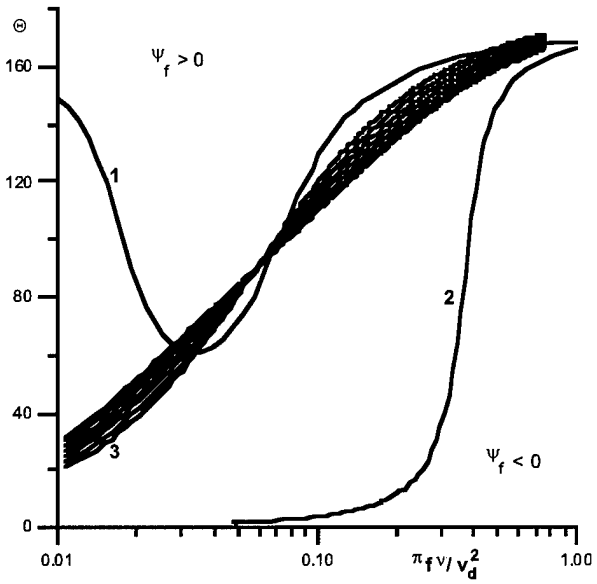

Figure 3. Phase-frequency diagram. Calculations [21]: $k_x = k_z$, $U_c^+ = 21.6$; (1) $U^+ = 16\left(1 - \exp(-y^+/16)\right)$; (2) $U^+ = y^+$.

(3) Phase characteristic of tested coating [25]: Ψ = 42%, Re = (1.5-5.3)10^6, $U_0 = 5.1$ *m/s*, $\omega_0 = 3500$ *1/s*, $n/\omega_0 = 1.3 \pm 0.3$.

The positive effect of compliant surface on turbulent friction and noise (i.e. their decrease) is connected with the decrease of turbulence production that was considered above – in Section II. So for the fixed frequency f the turbulence production change should be:

$$-\int_0^l \left[\langle u_f v_f \rangle \left(\frac{dU}{dy}\right) - \langle u_f v_f \rangle_c \left(\frac{dU}{dy}\right)_c \right] dy \ge 0 \qquad (5)$$

Here, index "f" shows the belonging only to the considered frequency, index "c "corresponds to the compliant surface action. The interference action for the fixed frequency f is neutral ($\psi_f = 0$) if this integral is equal to zero. In this (neutral) case the dependence of phase delay θ on frequency is independent on the compliance module. Two examples of the neutral line are shown in Figure 3 (lines 1, 2). The region above the neutral line corresponds to turbulence production decrease ($\psi_f > 0$, i.e. positive action of compliance) below – to an increase ($\psi_f < 0$, i.e. negative action of compliance).

One calculated variant corresponds to the linear profile of mean velocity, other variant – to velocity profile written by Schubert & Corcos [14] with good accuracy for turbulent flow near smooth hard wall at $y^+ \le 50$. These examples demonstrate the importance of accurate description of velocity profile. They show also that the profile linearization increases the phase-frequency region of positive action (PFRPA). So the second calculated variant shows a possible way of searches of new conditions for drag reduction.

The first calculated variant was used for the choice of phase-frequency conditions on the compliant boundary for drag reduction. It is shown that in the region $10^{-2} < \pi f\nu/U_d^2 < 0.2$ a tongue-like extension of positive action region is observed. It is important to note that this is the region of the main production of Reynolds stresses according to experimental investigations of near-wall turbulence [24]. Therefore, in order to obtain the turbulent drag reduction, it is necessary to find the phase-frequency characteristics of compliant coatings within this zone above the neutral line. This is the third condition for turbulent drag reduction. It was written for the choice of the natural frequency f_0 [25]:

$$0.02 < \pi f_0 \nu / U_d^2 < 0.06 \qquad (6)$$

This condition was approved [25] with the use of experimental data of Kramer [2], Blick et al. [27] and Semenov [25]. One example from [25] is shown in Figure 3.

Both this comparison and the prognostication and searches of necessary viscoelastic materials required to elaborate some methods of calculation of correlation between oscillation characteristics of compliant surface and viscoelastic properties of materials [21, 25, 28], to create the necessary equipment and the experimental methodology for investigations of viscoelastic properties of materials [29, 30, 31].

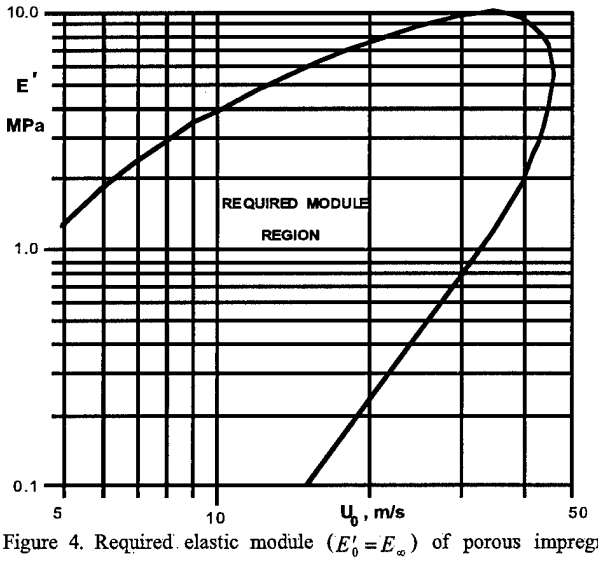

Figure 4. Required elastic module ($E_0' = E_\infty$) of porous impregnated coating for drag reduction in water, $x_0 = 0.2$ *m*, $\nu = 10^{-6}$ m^2/s

Taking into account these additional remarks, it is possible to use the design and manufacturing process of compliant coating for turbulent drag reduction suggested by Semenov [26, 32]. Figures 4 and 5 show the predicted results for drag reduction in water (details were described in [28]). The density of porous impregnated material must be similar to that of the flow (since open pores of material are connected with flow) i.e. $\rho_0 = \rho = 10^3$ kg/m^3 . Poisson's ratio for elastic porous materials $\mu_0 \approx 0.5$. The value of n/ω_0 depends on

size of pores (n is the damping factor of free vibrations, ω_0 is the natural angular frequency of the first harmonic) but it is taken as $n/\omega_0 =$ 1 for the present analysis. Figure 4 shows the dependence of the required elastic modulus E_0 on the flow velocity, where a suitable material must have the elastic module within the noted region.

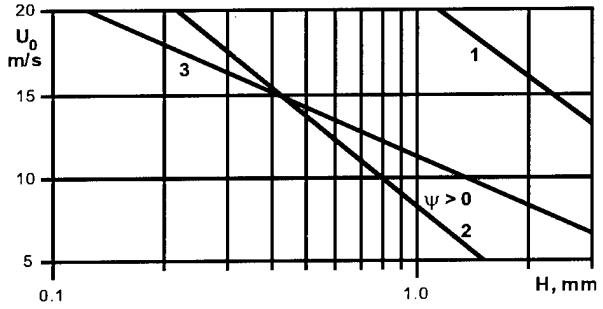

Figure 5. Predicted region of turbulent drag reduction in water for one-layer smooth coating made from a porous viscoelastic material with ventilated pores, $E_0 = E' = 10^5\ N/m^2$, $\mu_0 = 0.5$, $\rho_0 = 10^3\ kg/m^3$, $n/\omega_0 = 1$, $x_0 = 0.2\ m$, $\nu = 10^{-6}\ m^2/s$

In Figure 5 the required coating thickness H is plotted against the flow velocity. As it is shown here only a narrow "wedge' formed from the condition (3) (indicated by the bold line 3) and the condition (6) (indicated by the usual lines 1, 2) will provide a region of turbulent drag reduction. The above mentioned methodology of the choice of compliant coatings and conditions of their test was used in investigations of one-layer coatings [8, 23, 33, 34].

IY. IMPROVEMENTS OF INTERFERENCE THEORY

Recently the interference theory (elaborated in 70th-80th [9, 10, 21, 26]) satisfied the needs of researchers and engineers since it gave a possibility to find compliant coatings and flow conditions for drag reduction. But there was some dissatisfaction too since the existing theory didn't permit to find the optimum. And formerly many questions (about the influence of Reynolds number, roughness, pressure gradient, background turbulence and other) had not both a theoretical and experimental answers. Now new problems arise while using coatings jointly with other drag reducing means.

The attempts of improvements of interference theory were made for a long time. New models of the near-wall turbulence were considered. But the use of Schubert & Corcos model [14] considering the full system of linearized equations of Navier-Stokes didn't improve the possibilities of interference theory [12, 13]. The monoharmonic model of Goldshtik & Shtern [18] can't give the right conclusions and recommendations for compliant boundary since this theory considers unreal structure of velocity fluctuation. (k_z/k_x =1/12 – see further Figure 8). Now the hope of the development of interference theory is connected with the new wave model of Semenov [35] considering Cauchy problem for linearized equations of Navier-Stokes. But the work was only began. The described here improvements of interference theory are connected with more accurate definition of turbulent flow parameters used for calculations.

Mean velocity profile.

Formerly the exponential profile supposed by Schubert & Corcos [14] was used for calculations. But this profile is correct only for $y^+ < 50$ according to estimations made by these authors while comparing it with experimental data of Coles. Now it is necessary to extend the region of calculations to $y^+ \approx 400$ and to have a possibility to take into account the friction increase and decrease .

The new profile was obtained by growing together the modified exponential profile for near-wall region with the logarithmic profile for turbulent core. This operation was carried out by continuity of (dU/dy^+) and $U^+(y^+)$. And so the new profile was written as:

$$U^+ = 16A\left[1 - \exp\left(-y^+/(16A)\right)\right] \quad \text{at} \quad 0 < y^+ \le y^+_{\delta l},$$
$$U^+ = 2.5\ln(y^+) + B + S^+ \quad \text{at} \quad y^+ \ge y^+_{\delta l}, \qquad (7)$$

where B = 5.526657; S^+ and A depend on a friction increase by surface roughness or a friction decrease by drag reducing means.

$S^+ = 0$, $A = 1$, $y^+_{\delta l} = 46.9116$ are the parameters for a smooth surface without drag reducing means. The comparison (in Figure 6) of this profile with experimental data shows their good concordance.

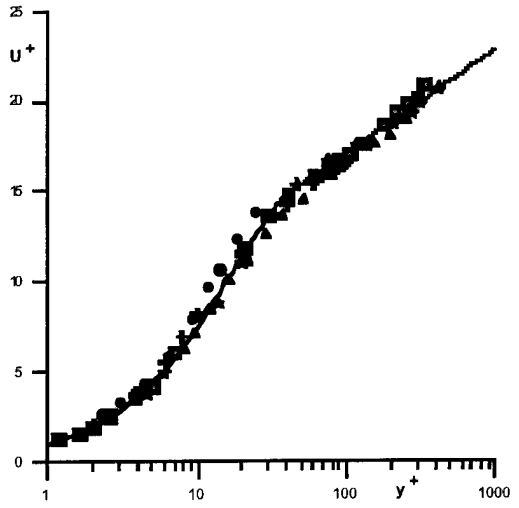

Figure 6. Comparison of velocity profile, calculated according to (7) for near-wall region of turbulent flow ($S^+ = 0$, $A = 1$), with experimental data: ✚ Coles [14], ■ Kchabakhpasheva & Perepelitza [36], ▲ Poznajaja [37], ● Kchabakhpasheva & Mikhailova [38], ★ T.Mizushina & H.Usui [39]

Convection velocity

All former calculations of PFRPA were carried out for the constant convection velocity $U_c = 0.8\ U_0$. Our calculations show the strong dependence of PFRPA on variation of this parameter. So this parameter must be written with more accurate definition.

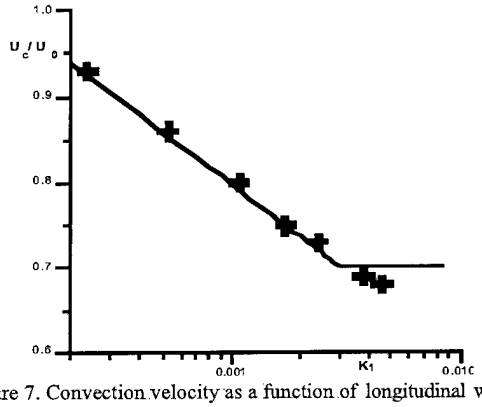

Figure 7. Convection velocity as a function of longitudinal wave number. Line: the calculation according to (8).
✚ Experimental data of Blake [41]

According to Bernard [40] the convection velocity determines the turbulence structure in near-wall region of turbulent flows. It depends on wave number k_x and doesn't depend on frequency of fluctuations. And, may be, the convection velocity is equal to the velocity of eddy centre disposed in turbulent core.

And now the convection velocity is calculated as

$$U_c/U_0 = \left[2.5\ln(1/k_1) + B\right]\cdot\left(c_f/2\right)^{0.5} \qquad (8)$$

with the restriction following from experimental data of different authors: $U_c \le 0.7\ U_0$. Here c_f is the friction coefficient,

$c_f = 2\tau_w/\rho U_0^2$, $k_1 = k_x\nu/v_d$. According to formula (8) the upper limit is $U_c = U_0$ but in real calculations (in the considered region of wave numbers) $U_c < 0.9\,U_0$. The comparison (in Fig. 7) of this calculation with experimental data of Blake [41] shows a suitability of formula (8).

Velocity fluctuation structure.

The former analysis [10] of compliant boundary action on near-wall turbulence has already showed the importance of the correct taking into account the velocity fluctuation structure, namely the ratio of transversal and longitudinal components of velocity fluctuation. Now this parameter is discussed again.

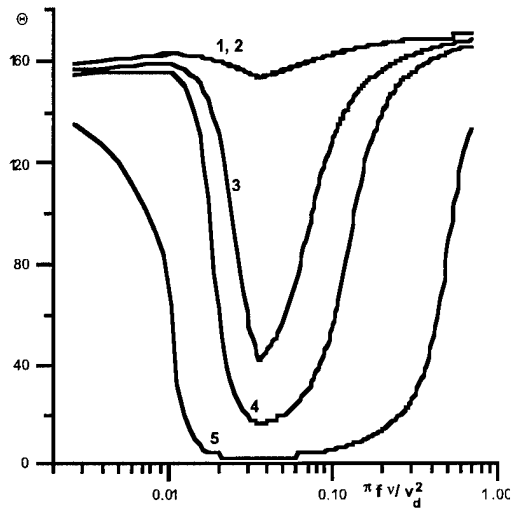

Figure 8. Dependence of PFRPA of smooth compliant surface on the velocity fluctuation structure (k_z/k_x): (1) $k_z/k_x = 0$, (2) $k_z/k_x = 1/12$, (3) $k_z/k_x = 0.8$, (4) $k_z/k_x = 1.0$, (5) $k_z/k_x = 1.6$; $\mathrm{Re}_0 = 10^7$

According to Sternberg model [11], $w_f/u_f = k_z/k_x$. It is known from tests of Laufer [42] at $y^+ = 650$ that this ratio depends on the dimensionless wave number k_1 and varies from ~ 0.65 for $k_1 = 5\times10^{-5}$ to ~ 2.2 for $k_1 \geq 0.04$. The results of PFRPA calculations for different values of this ratio are shown in Figure 8. They demonstrate very strong dependence of PFRPA on k_z/k_x. It turns out that compliant boundary can't manage with two-dimensional wave fluctuations propagating in the main flow direction ($k_z/k_x \approx 0$). But this fact can't worry since these fluctuations are absent in near-wall turbulent flows. And it shows that any theory considering these fluctuations (for example, $k_z/k_x = 1/12$ in monoharmonic theory [18]) gives unacceptable solution for compliant boundary. In all calculations authors consider $k_z/k_x = 1$ as the most dangerous but real variant.

Y. ON INFLUENCE OF REYNOLDS NUMBER AND SURFACE ROUGHNESS

The problem on influence of Reynolds number on drag reducing possibility of compliant coatings was considered formerly [28, 32]. Here the solution is defined more precisely. The results are shown in Figure 9 for smooth surface.

Reynolds number increase leads to PFRPA decrease. Here it is necessary to remind that Re_0 is determined for the beginning x_0 of compliant surface. And these results show the requirement to minimize x_0. And, please, note: the experimental data are still absent for a check-up of this prognosis, but they are very necessary.

All experimental attempts of drag reduction using rough compliant coatings were unsuccessfull (but systematic investigations of roughness influence are still absent). And all researchers try to minimize the compliant surface roughness in spite of many technological difficulties. So it is important to estimate the roughness limit. The interference theory permits to consider the influence of surface roughness for the transition zone of its values (smooth→rough). In this case the viscous sublayer becomes more thin, the logarithmic profile of mean velocity is displaced down [24].So in (7): $S^+ < 0$, $A < 1$. The results of numerical investigations of the dependence of PFRPA on compliant surface roughness (see Table II and Figure 10) lead to the conclusion that the reasonable limit of sand roughness is $k_s^+ \sim 15$. A higher roughness liquidates a possibility of compliant surface use for drag reduction.

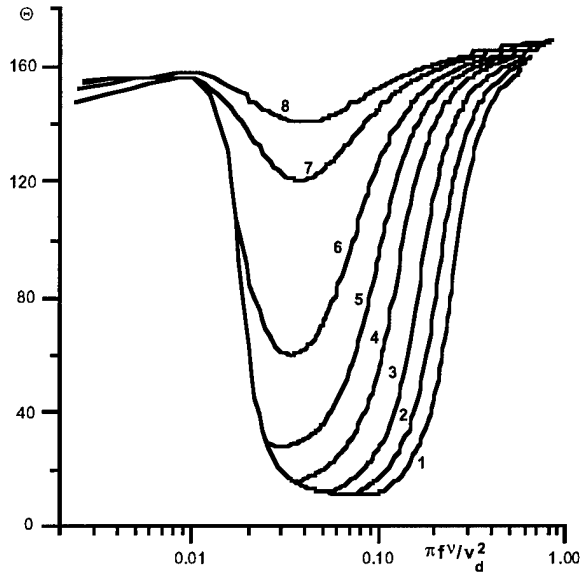

Figure 9. Dependence of PFRPA of smooth compliant surface on Reynolds'number: (1) $\mathrm{Re}_0=10^6$, (2) $\mathrm{Re}_0=2\times10^6$, (3) $\mathrm{Re}_0=4.2\times10^6$ (4) $\mathrm{Re}_0=10^7$, (5) $\mathrm{Re}_0=2\times10^7$, (6) $\mathrm{Re}_0=4\times10^7$, (7) $\mathrm{Re}_0=10^8$, (8) $\mathrm{Re}_0=2\times10^8$; $k_z/k_x=1.0$

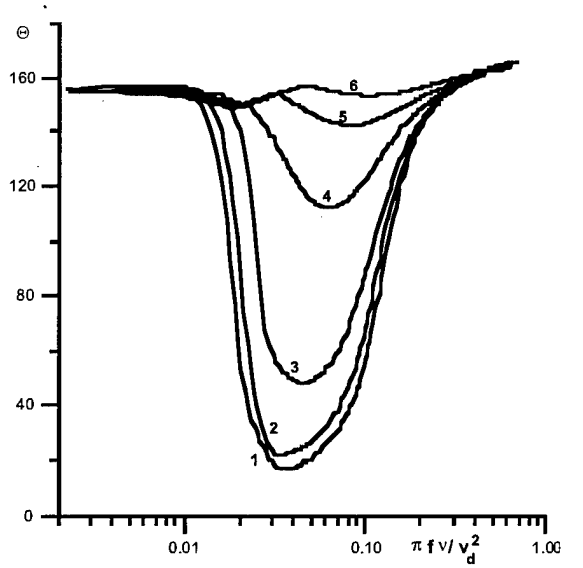

Figure 10. Dependence of PFRPA of compliant surface on its sand roughness: (1) $k_s^+ < 3$, (2) $k_s^+ = 5$, (3) $k_s^+ = 10$, (4) $k_s^+ = 15$, (5) $k_s^+ = 20$, (6) $k_s^+ = 25$; $\mathrm{Re}_0=10^7$; $k_z/k_x=1.0$

k_s^+	S^+	A	y_{gl}^+
5	-0.55	0.956	43.5
10	-1.733	0.860	37.0
15	-2.75	0.773	31.1
20	-3.6	0.697	26.2
25	-4.35	0.626	21.5

Table II. Parameters for calculation of mean velocity profile on rough surface. $\mathrm{Re}_0 = 10^7$.

YI. JOINT USE OF COMPLIANT SURFACE WITH OTHER DRAG REDUCING MEANS

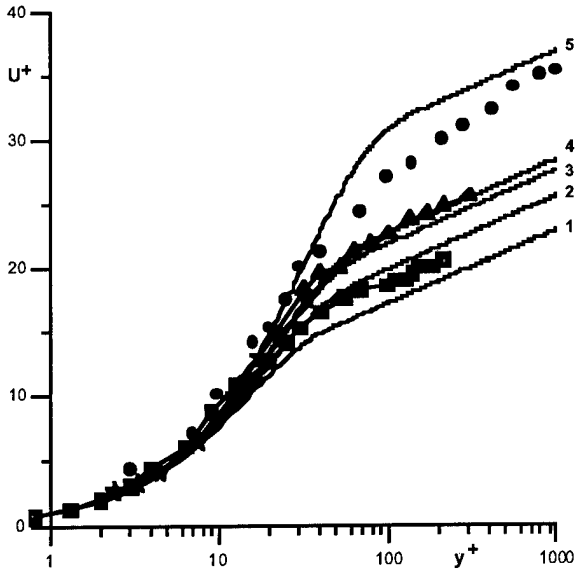

Figure 11. Comparison of mean velocity profile calculated according to (7) for near-wall region of turbulent flow containing drag-reducing polymeric additives with experimental data

Sign	Refer	Ψ_R^+	S^+	A	y_{gr}^+	Line N
–	here	0	0	1.	46.9	1
■	[37]	0.309	2.8	1.20	61	2
★	[46]	0.393	4.8	1.36	72.5	3
▲	[45]	0.443	5.6	1.42	79	4
●	[37]	0.686	14.1	2.01	126	5

Table III. Data for figure 11.

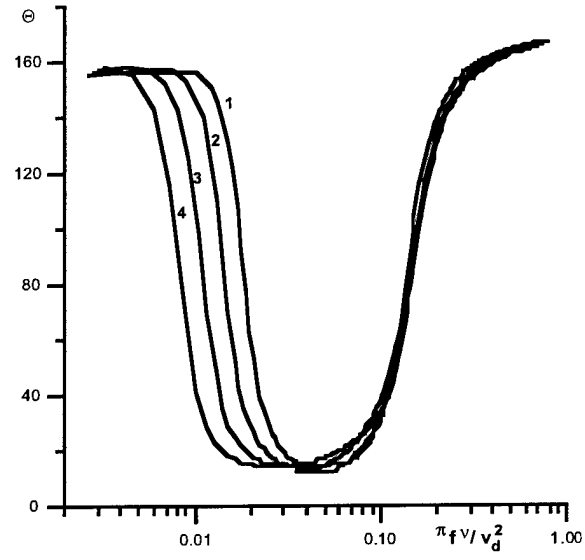

Figure 12. Dependence of PFRPA of smooth compliant surface on drag reduction using polymer additives: (1) Ψ= 0, (2) Ψ=0.1, (3) Ψ=0.2, (4) Ψ=0.3; $Re_0 = 6.2\times10^6$

Ψ	S^+	A	y_{gr}^+
0.1	1.462	1.114	55.13
0.2	3.190	1.244	64.83
0.3	5.277	1.399	76.59

Table IY. Parameters for calculation of mean velocity profile on smooth surface in flow with drag reducing polymeric additives. $Re_0 = 6.2\times10^6$

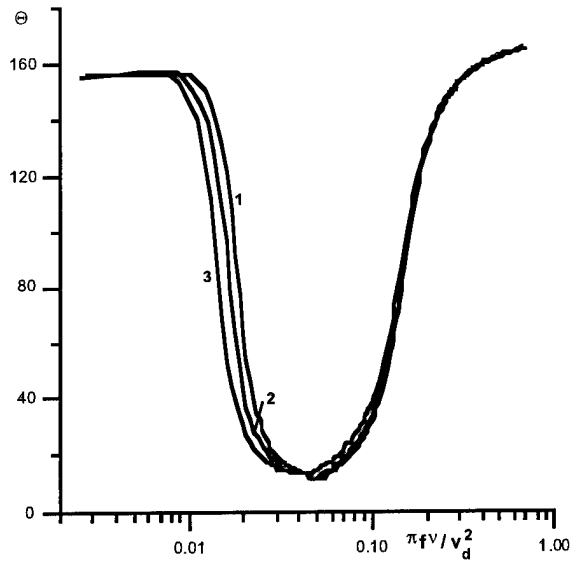

Figure 13. Phase-frequency diagram for compliant surface with drag reducing riblets: (1) Ψ= 0, (2) Ψ=0.05, (3) Ψ=0.1, $Re_0 = 6.2\times10^6$

Ψ	S^+	A	y_{gr}^+
0.05	0.702	1.0547	50.86
0.1	1.462	1.114	55.13

Table Y. Parameters for calculation of mean velocity profile on surface with drag reducing riblets. $Re_0 = 6.2\times10^6$

The results of the first analysis of interference model [10] predicted an increase of PFRPA for the mean velocity profile linearization and induced to search for some means for its realization. Apparently all means of turbulent drag reduction enjoy this action. Two means – polymer additives and riblets are particularly interesting since they suppress only microeddy structures which are not subject to compliant surface managing long-wave disturbances.* So here it is necessary to take into account only a change of the mean velocity profiles for interference analysis.

According to Virk et al. [44] drag reducing polymeric additives lead to "slip" S^+ (the logarithmic profile of mean velocity displaces up) calculated as: $S^+ = \sqrt{2}\left(c_f^{-0.5} - c_{f_0}^{-0.5}\right)$ for R^+. So the viscous sublayer becomes more thick, in (7): $S^+ > 0$, $A > 1$. The comparison (in Figure 11) of experimental data for mean velocity profiles and the results of calculation made according to (7) for these variants (described in Table III) shows their good concordance for $\Psi_{R^+} < 0.5$.

Results of PFRPA calculations shown in Figure 12 (parameters are shown in Table IY) lead to the conclusion that small polymer additives in a flow extend PFRPA and accordingly the drag reduction possibilities of compliant coatings.

The same prognosis follows from PFRPA calculations for compliant coating with drag reducing riblets on its surface (see Figure 13 with Table Y). And, please, note that a combination of compliant surface and riblets must be the fine variant of passive methods of turbulence management realized without additional energy expenditure.

ACKNOWLEDGEMENTS

The work was supported by the INTAS Research Grant N 94 –3737.

* The first experimental results of drag reduction using compliant coatings and polymeric additives jointly showed fine outlooks of this study [43].

REFERENCES

1. M.O. Kramer "Boundary Layer Stabilization by Distributed Damping", *J. Aeron. Sci.*, 1957, **24**, N6, 459-460.
2. M.O. Kramer "Boundary Layer Stabilization by Distributed Damping", *J.Amer. Soc.* Nav. Eng., 1960, **72**, N1, 25-33.
3. M.O. Kramer "Boundary Layer Stabilization by Distributed Damping", *Nav. Eng. J.*, 1962, **74**, N2,341-348.
4. B.N. Semenov "The Effect of Elastic Covers on a Turbulent Boundary Layer", *Investigations of Boundary Layer Control*, 1976, IT AN SSSR, Novosibirsk, 92-101.
5. G.A. Voropaev & V.V. Babenko "The Turbulent Boundary Layer on Elastic Surface", *Hydromechanics*, 1978, Naukova Dumka, Kiev, N38, 71-77.
6. V.I. Korobov & V.V. Babenko "On a Mechanism of Interaction of Elastic Wall with Flow", *J. Eng. Phys.*, 1983, **44**, N5, 730-733.
7. V.M. Kulik "The Analysis of Interaction of One-Layer Monolithic Damping Covers with Turbulent Flow", *J. Eng. Phys.*, 1986, **51**, N6, 959-965.
8. V.M. Kulik, I.S. Poguda & B.N. Semenov "Experimental Study of the Effect of One-Layer Viscoelastic Coatings on the Turbulent Friction and Pressure Pulsations at the Wall", *J. Eng. Phys.*, 1984, **47**, N2, 189-196.
9. B.N. Semenov "Interaction of an Elastic Boundary with the Viscous Sublayer of a Turbulent Boundary Layer", *Zh. Prikl. Mekh. Tekh. Fiz.*, 1971, N3, 58-62.
10. B.N. Semenov "On Interferent Form of the Influence of Viscoelastic Boundary on Wall Turbulence", *The Influence of Polymer Additives and Surface Elasticity on Wall Turbulence*, 1978, IT AN SSSR, Novosibirsk, 57-74.
11. J. Sternberg "A Theory for Viscous Sublayer of a Turbulent Flow", *J. Fluid Mech.*, 1962, **13**, N2, 241-271.
12. V.V. Skripatchev "The Theoretical Analysis of Viscoelastic Boundary Action on Near-Wall Turbulence", *Proc. Conf. on Drag Reduction*, 1978, Moscow.
13. V.V. Skripatchev & A.P. Teslo "The Drag of Plates and Tubes with Elastic Walls", *Hidravlika I Hidrotekhnika*, 1983, Naukova Dumka, Kiev, N37, 52-57.
14. G. Schubert & G.M. Corcos "The Dynamics of Turbulence Near a Wall According to a Linear Model", *J. Fluid Mech.*, 1967, **29**, N1, 113-135.
15. G.F. Trifonov "Theoretical Investigation of the Influence of Elastic Boundary Characteristics on Turbulent Flow", *The Influence of Polymer Additives and Surface Elasticity on Wall Turbulence*, 1978, IT AN SSSR, Novosibirsk, 75-85.
16. G.F. Trifonov "Self-Consistent Model of Interaction between Turbulent Flow and Deformable Wall", *Thermodynamics of Turbulent Flows*, 1986, IT AN SSSR, Novosibirsk, 5-16.
17. G.V. Kereyko "On an Interaction of Near-Wall Turbulence with Compliant Surface", *Izv. AN SSSR MJG*, 1990, N4, 67-72.
18. M.A. Goldshtik & V.N. Shtern "The Monoharmonic Theory of Near-Wall Turbulence", *Turbulent Flows*, 1977, Nauka, Moscow, 102-110.
19. G.A. Voropaev & V.I. Popkov "On an Interaction of Compliant Surface with Viscous Sublayer of Turbulent Boundary Layer", *Hydromechanics*, 1988, Naukova Dumka, Kiev, N57, 32-36.
20. M. Gad-el-Hak "Compliant Coatings: One Last Chance?" *Manuscript for the Workshop on Flow Control: Fundamentals and Practices*, 1-5 July 1996, Corsica.
21. B.N. Semenov "On Interference Action of Viscoelastic Boundary on Near-Wall Turbulence", *Proceedings of 6th Nat. Congress on Theor. and Appl Mech.*, 1989, Varna, **3**, 330-333.
22. B.N. Semenov "On Two Forms of Action of Viscoelastic Boundary on Near-Wall Turbulence", *Abstracts of 3rd European Turbulence Conference*, July 1990, Stockholm, 4.2.
23. V.M. Kulik, I.S. Poguda & B.N. Semenov "Experimental Investigation of One-Layer Viscoelastic Coating Action on Turbulent Friction and Wall Pressure Pulsations", *Recent Developments in Turbulence Management*, 1991, Kluwer, 236-289.
24. J.O. Hinze "Turbulence", 1959, Mc Graw-Hill.
25. B.N. Semenov "Analysis of Deformation Characteristics of Viscoelastic Coatings", *Hydrodynamics and Acoustics of Near-Wall and Free Flows*, 1981, Nauka, Novosibirsk, 57-76.
26. B.N. Semenov "On Conditions of Modelling and Choice of Viscoelastic Coatings for Drag Reduction", *Recent Developments in Turbulence Management*, 1991, Kluwer, 241-262.
27. E.F. Blick, R.R. Walters, R. Smith & H.Chu "Compliant Coating Skin Friction Experiments", *AIAA Paper*, 1969, N69-165.
28. B.N. Semenov "Analysis of Four Types of Viscoelastic Coating for Turbulent Drag Reduction", *Emerging Techniques in Drag Reduction*, 1996, MEP, London and Bury St. Edmunds, 187-206.
29. V.M. Kulik & B.N. Semenov "On the Certification of Wave Properties of Viscoelastic Coatings Affecting Wall Turbulence", *Hydrodynamic Flows and Wave Processes*, 1983, IT AN SSSR, Novosibirsk, 117-129.
30. V.M. Kulik & B.N. Semenov "Two-Parametric Technique of Measuring of the Viscoelastic Properties of Polymer Materials", *Metrologiya*, 1986, N4, 32-38.
31. V.M. Kulik & B.N. Semenov "The Measurement of Dynamic Properties of Viscoelastic Materials for Turbulent Drag Reduction", *Emerging Techniques in Drag Reduction*, 1996, MEP, London and Bury St. Edmunds, 207-218.
32. B.N. Semenov "On the Properties of Viscoelastic Boundary for Turbulent Friction Reduction", *Sib. Fiz. Tech. Zn.*, 1993, N1, 63-73.
33. K.-S. Choi, X.Yang, B.R. Clayton, T. Glover, M. Atlar, B.N. Semenov & V.M. Kulik "Experiments on Turbulent Drag Reduction Using Compliant Surface", *Proceedings of 1st Int. Conference on Flow Interaction*, 1994, Hong Kong, 543-546.
34. K.-S. Choi, X.Yang, B.R. Clayton, T. Glover, M. Atlar, B.N. Semenov & V.M. Kulik "Turbulent Drag Reduction Using Compliant Surfaces", *Proceedings of Royal Society*, A, 1997, **453**, 2229-2240.
35. B.N. Semenov "Joint Use of Laser Anemometry in a Flow and Measurements on Compliant Wall", *Proceedings of 7th Int. Conference: Laser Anemometry, Advances and Applications*, 1997, Karlsruhe, 141-148.
36. E.M. Khabakhpasheva & B.V. Perepelitza "On Peculiarities of Near-Wall Turbulence in Water Flows with Polymeric Additives", *J. Eng. Phys.*, 1970, **18**, N6, 1094-1097.
37. N.G. Poznjaja "A Model of Near-Wall Turbulent Flow of Polymeric Solutions of Small Concentrations", *Turbulent Flows*, 1974, Nauka, Moscow, 158-165.
38. E.M. Khabakhpasheva & E.S. Mikhailova "The Turbulence Investigation in a Flat Water Channel Flow", *Experimental Investigation of the Near-Wall Turbulence and Viscous Sublayer Structure*, 1976, IT AN SSSR, Novosibirsk, 33-57.
39. T. Mizushina & H. Usui "Reduction of Eddy Diffusion for Momentum and Heat in Viscoelastic Fluid Flow in a Circular Tube", *The Physics of Fluids*, 1977, **20**, N10, pt II, S100-S108.
40. P. Bernard "Etude Tridimensionelle de la Sous-Couche Visque Use Dans une Veine Rectangulaire par des Mesures de Transfert de Matiere in Paroi", *Int. J. Heat and Mass Transfer*, 1973, **16**, N1 129-144.
41. W.K. Blake "Turbulent Boundary-Layer Wall-Pressure Fluctuations on Smooth and Rough Walls", *J. Fluid Mech.*, 1970, **44**, N4, 637-660.
42. J. Laufer "The Structure of Turbulence in Fully Developed Pipe Flow", 1954, NASA Rep. 1174.
43. B.N. Semenov, V.M. Kulik, V.A. Lopyrev, B.P. Mironov, I.S. Poguda & T.I. Yushmanova "The Combined Effect of Small Quantities of Polymeric Additives and Pliability of the Wall on Friction in Turbulent Flow", *Fluid Mech. – Soviet Res.*, 1985,**14**, N1, 143-145.
44. P.S. Virk, E.W. Merrill, H.S. Miskley, K.A. Smith & E.L. Mollo-Christensen "The Toms Phenomenon: Turbulent Pipe Flow of Dilute Polymeric Solutions", *J. Fluid Mech.*, 1967, **30**, N2, 305-328.
45. E.M. Khabakhpasheva & B.V. Perepelitza "Fields of Velocities and Turbulent Fluctuations for Small High-Molecular Additives to Water", *J. Eng. Phys.*, 1968, **14**, N4, 598-601.
46. E.S. Mikhailova & E.M. Khabakhpasheva "Near-Wall Turbulence for Flow of PAA Dilute Solution", *Experimental Investigation of the Near-Wall Turbulence and Viscous Sublayer Structure*, 1976, IT AN SSSR, Novosibirsk, 58-68.

COMPLIANT COATINGS: THE SIMPLER ALTERNATIVE

Mohamed Gad-el-Hak
Department of Aerospace & Mechanical Engineering
University of Notre Dame
Notre Dame, IN 46556
Mohamed.Gad-el-Hak.1@nd.edu

Abstract

Boundary layer manipulation via reactive control strategies is now in vogue. The payoffs are handsome but the difficulties involved are daunting. There are however much simpler alternatives to this kind of sophisticated flow alteration devices and the present article discusses one such alternative: passive compliant walls. Much of the details, even the list of cited references, are omitted here because of space limitations and the reader is referred to the paper in *Applied Mechanics Reviews*, vol. 49, no. 10, part 2, pp. S147–S157, 1996.

1 Introduction

A compliant wall, as opposed to a rigid one, offers the potential for favorable interference with a wall-bounded flow. Laminar-to-turbulence transition may be delayed or advanced, boundary layer separation may be prevented or triggered, flow-induced noise may be modulated, and skin-friction drag in both laminar and turbulent flows may be altered. The challenge is of course to find a coating with the right physical properties to achieve a desired goal.

Passive compliant coatings have been around long before reactive flow control was even contemplated. For better or worse, hydrodynamically speaking, the epidermis of most nekton is pliable at their typical swimming speeds. For close to half a century the science and technology of compliant coatings has fascinated, frustrated and occasionally gratified Homo sapiens searching for methods to delay laminar-to-turbulence transition, to reduce skin-friction drag in turbulent wall-bounded flows, to quell vibrations, and to suppress flow-induced noise. Compliant coatings offer a rather simple method to delay laminar-to-turbulence transition as well as to interact favorably with a turbulent wall-bounded flow. In its simplest form, the technique is passive, relatively easy to apply to an existing vehicle or device, and perhaps not too expensive. Unlike other drag reducing techniques such as suction, injection, polymer or particle additives, passive compliant coatings do not require slots, ducts or internal equipment of any kind. Aside from reducing drag, other reasons for the perennial interest in studying compliant coatings are their many other useful applications, for example as sound absorbent materials in noisy flow-carrying ducts in aero-engines, and as flexible surfaces to coat naval vessels for the purposes of shielding their sonar arrays from the sound generated by the boundary-layer pressure fluctuations and of reducing the efficiency of their vibrating metal hulls as sound radiators.

The original interest in the field was spurred by the experiments of Kramer (1957) who demonstrated a compliant coating design based on dolphin's epidermis and claimed substantial transition delay and drag reduction in hydrodynamic flows. Those experiments were conducted in the seemingly less-than-ideal environment of Long Beach Harbor, California. Subsequent laboratory attempts to substantiate Kramer's results failed, and the initial interest in the idea fizzled. A similar bout of excitement and frustration that dealt mostly with the reduction of skin-friction drag in turbulent flows for aeronautical applications followed. Those results were summarized in the comprehensive review by Bushnell et al. (1977). During the early 1980s, interest in the subject was rejuvenated mostly due to modest investment in resources by the Office of Naval Research in the United States and the Procurement Executive of the Ministry of Defence in Great Britain. Significant advances were made during this period in numerical and analytical methods to solve the coupled fluid-structure problem. New experimental tools were developed to measure the minute yet important surface deformation caused by the unsteady fluid forces. Coherent structures in turbulent wall-bounded flows were routinely identified, and their modulation by the surface compliance could readily be quantified.

Careful analyses by Carpenter and Garrad (1985) and Willis (1986) as well as the well-controlled experiments reported by Daniel et al. (1987) and Gaster (1988) have, for the first time, provided direct confirmation of the transition-delaying potential of compliant coatings, convincingly made a case for the validity of Kramer's original claims, and offered a plausible explanation for the failure of the subsequent laboratory experiments. There is little doubt now that compliant coatings can be *rationally* designed to delay transition and to suppress noise on marine vehicles and other practical hydrodynamic devices. Transition Reynolds numbers that exceed by an order of magnitude those on rigid-surface boundary layers can be readily achieved. Although the number of active researchers in the field continues to dwindle, new promising results are being produced. Recent theoretical work by Davies and Carpenter (1997a) and Carpenter (1998) indicates that transition to turbulence can be delayed indefinitely, at least in principle, provided that optimized multiple-panel compliant walls are used and that the freestream is a low-disturbance environment. There is also recent evidence of favorable interactions of compliant coatings even for air flows (Lee et al., 1995) and even for turbulent boundary layers (Lee et al., 1993a; Choi et al., 1997).

The present article emphasizes the significant compliant coating research that took place during the last 10–15 years and suggests avenues for future research. The reader is referred to prior reviews for more classical work on the subject, for example those by Bushnell et al. (1977), Gad-el-Hak (1986a; 1987; 1996), Riley et al. (1988), Carpenter (1990), and Metcalfe (1994). Following these introductory remarks, a somewhat sketchy history of the subject, particularly prior to 1985, is recalled. This will help place more recent developments in proper perspective.

2 Subject Prior to 1985

Before embarking on describing the recent accomplishments in the field of compliant coatings, we first elaborate on its history prior to 1985. This seemingly arbitrary date is chosen because it demarks the time after which tools for rationally designing a compliant coating to delay transition became more readily available. The victories and defeats of the subject matter will become clear through the discussion that follows. The idea of using compliant coatings for drag reduction motivated much of the earlier work in this area and was first introduced by Kramer (1957) based on his earlier observation, while crossing the Atlantic ocean in 1946, of dolphins swimming in water. He advanced the concept that the stability and transition characteristics of a boundary layer may be influenced by coupling it hydroelastically to a compliant coating. In

his pioneering paper and several subsequent publications, Kramer (1960a; 1960b; 1960c; 1961; 1962; 1965; 1969) reported substantial drag reduction for towed underwater bodies covered with compliant coating modeled after the dolphin skin. He hypothesized that by tuning the elastic wall damping to a frequency near that of the most unstable Tollmien-Schlichting wave, it would be possible to dissipate partially the instability waves, thus delaying the transition to turbulence. Kramer's tests were performed by towing a test model behind a motor boat in Long Beach Harbor. Unfortunately, many attempts by other investigators to repeat Kramer's experiments under more controlled conditions failed to yield similar conclusions (e.g., Puryear's, 1962, experiment in a towing tank). This so-called Kramer controversy will be revisited in Section 4.

Theoretical work by Benjamin (1960), Betchov (1960), Landahl (1962), and Kaplan (1964) indicated that drag reduction by delaying transition is possible. However, the theoretically predicted successful coatings had specific characteristics that would be extremely difficult to match in practice. It is important to stress that almost all this early work addressed the delay of transition and ignored the potential for reducing turbulence skin friction with compliant coatings.

During the mid-1960s, Benjamin (1966) explored the possibility that a compliant coating may affect the skin-friction drag in a fully-developed turbulent boundary layer without necessarily delaying transition. Dinkelacker (1966) conducted careful tests of a compliant surface in a water pipe flow. He systematically attempted to determine the repeatability of rigid-tube data, the influence of small steps in the tube wall, and the possible occurrence of organ pipe acoustic modes. Dinkelacker's results seemed to indicate a modest reduction in drag by using a compliant wall.

Blick and his co-workers at the University of Oklahoma experimentally demonstrated significant reductions in turbulence skin friction for compliant surfaces in air (Fisher and Blick, 1966; Looney and Blick, 1966; Smith and Blick, 1966; Blick and Walters, 1968; Chu and Blick, 1969). Subsequent tests by Lissaman and Harris (1969), who attempted to substantiate Blick's conclusions, yielded only extremely modest gains. In another study, McMichael et al. (1980) demonstrated that the apparent reduction in turbulence skin friction in the University of Oklahoma's experiments could be a consequence of experimental deficiencies coupled with the improper interpretation of data. McMichael et al. concluded that drag reduction via compliant coating in gaseous flows would not be as successful as in liquids.

During the 1970s various compliant materials were tested in water at the Naval Ocean Systems Center, the Naval Research Laboratory, the Naval Undersea Systems Center, and the Advanced Technology Center of the LTV Corporation, all in the United States. In no case was a statistically significant reduction in drag measured. Fischer and Ash (1974) presented a general review of concepts for reducing skin friction, including the use of compliant coatings. Bushnell et al. (1977), in summarizing the work conducted at the NASA Langley Research Center and the general status of compliant surface drag reduction, stated that, while it was possible to increase the transition Reynolds number by perhaps a factor of 2, there was no definitive reduction of drag for *turbulent* flows in air. They also stated that drag reduction in turbulent flows in water is potentially feasible and can be accomplished using surfaces that can be practically built. It is of particular interest to note that much of the research on compliant coatings has been based on materials that attempt to replicate dolphin skin. Yet, in the Russian book *Nekton* (Aleyev, 1977) it is indicated that the "wrinkling" of the dolphin skin has no hydrodynamic-drag advantage. Other characteristics of the dolphin's skin may, however, be beneficial. This subject will be revisited in Section 5.4.

Bushnell et al. (1977) put forward the possibility of a feedback mechanism in turbulent wall-bounded flows through which the quasi-periodic, coherent structures termed bursts regenerate. Older bursts grow, migrate away from the wall, and interact to produce a pressure field which contains pulses of sufficient duration and amplitude to induce new bursts in the near-wall region. This model is supported by the measurements of Burton (1974), who reported a strong correlation between the occurrence of a burst and the imposition on the wall flow of a large moving adverse-pressure gradient followed by a favorable pressure-gradient. Bushnell et al. hypothesized that a successful compliant coating would modulate the preburst flow in the turbulent boundary layer by providing a pressure field that would tend to block the feedback mechanism and, thus, inhibit burst formation. This would result in a reduction in the number of bursts occurring per unit time and also in the skin-friction drag. Orszag (1979) assumed this conceptual model and performed numerical calculations of wall boundary layer instability to explore the effects of complaint surfaces. His results, although preliminary, indicated that turbulence drag reduction may be possible for certain classes of materials. He concluded that compliant walls which support only short wavelengths may have an appreciable effect in inhibiting further bursts in a turbulent boundary layer.

During the U.S. Navy-sponsored research program conducted over the period 1980–1985, the subject of boundary layer interaction with compliant coatings has been re-examined to answer the question: can compliant coatings delay transition and/or significantly reduce turbulence skin friction on bodies at high Reynolds numbers? Several significant developments have been achieved by the many investigators participating in this research program. Although unrefutable experimental evidence of compliant coating drag reduction was still lacking by 1985, our understanding of boundary layer flow over a compliant surface has increased dramatically over this period. That understanding proved crucial to the subsequent successes in the field, a subject which will be emphasized throughout the rest of this paper.

3 System Instabilities

From a fundamental viewpoint, a rich variety of fluid-structure interactions exists when a fluid flows over a surface that can comply with the flow. Not surprisingly, instability modes proliferate when two wave-bearing media are coupled. Some waves are flow-based, some are wall-based, and some are a result of the coalescence of both kind of waves. What is most appealing about compliant coatings is their potential to inhibit, or to foster, the dynamic instabilities that characterize both transitional and turbulent boundary layer flows, and in turn to modify the mass, heat and momentum fluxes and change the drag and the acoustic properties. While it is relatively easy to suppress a particular instability mode, the challenge is of course to prevent other modes from growing if the aim is, say, to delay laminar-to-turbulence transition. From a practical point of view, it is obvious that an in-depth understanding of the coupled system instabilities is a prerequisite to rationally designing a coating that meets a given objective.

There are at least three classification schemes for the fluid-structure waves, each with its own advantages and disadvantages. The original scheme is due to Benjamin (1963) and divides the waves into three classes according to their response to irreversible energy transfer to and from the compliant wall. Both class **A** and class **B** disturbances are essentially oscillations involving conservative energy exchanges between the fluid and solid, but their stability is determined by the net effect of irreversible processes such as dissipation in the coating or energy transfer to the solid by non-conservative hydrodynamic forces. Class **A** oscillations are Tollmien-Schlichting waves in the boundary layer modified by the wall compliance, in other words by the motion of the solid in response to the pressure and shear-stress fluctuations in the flow. T-S waves are stabilized by the irreversible energy transfer from the fluid to the coating, but destabilized by dissipation in the wall. Class **B** waves reside in the wall and result from a resonance effect much the same as wind-induced waves over a body of water. Their behavior is the reverse of that for class **A** waves, stabilized by wall damping but destabilized by the non-conservative hydrodynamic forces. Essentially class **B** waves are amplified when the flow supplies sufficient energy to counterbalance the coating internal dissipation. Finally, class **C** waves are akin to the inviscid Kelvin-Helmholtz instability and occur when conservative hydrodynamic forces cause a unidirectional transfer of energy to the solid. The pressure distribution

in an inviscid flow over a wavy wall is in exact antiphase with the elevation. In that case, class **C** waves can grow on the solid surface only if the pressure amplitude is so large as to outweigh the coating stiffness. Irreversible processes in both the fluid and solid have negligible effect on class **C** instabilities.

If one considers the total disturbance energy of the coupled fluid-solid system, a decrease in that energy leads to an increase in the amplitude of class **A** instabilities, class **B** is associated with an energy increase, and virtually no change in total energy accompanies class **C** waves. In other words, any non-conservative flow of activation energy from/to the system must be accompanied by disturbance growth of class **A/B** waves, while the irreversible energy transfer for class **C** instability is nearly zero.

The second classification scheme is due to Carpenter and Garrad (1985; 1986). It simply divides the waves into fluid-based (Tollmien-Schlichting instabilities, TSI) and solid-based (flow-induced surface instabilities, FISI). FISI are closely analogous to the instabilities studied in hydro- and aeroelasticity, and include both the traveling-wave flutter that moves at speeds close to the solid free-wave-speed (class **B**) and the essentially static, and more dangerous, divergence waves (class **C**). The main drawback of this classification scheme is that under certain circumstances the fluid-based T-S waves and the solid-based flutter can coalesce to form a powerful new instability termed transitional mode by Sen and Arora (1988). According to the energy criterion advanced by Landahl (1962), this latest instability is a second kind of class **C** waves. In a physical experiment, however, it is rather difficult to distinguish between the static-divergence waves and the transitional ones.

The third scheme to classify the instability waves considers whether they are convective or absolute (Huerre and Monkewitz, 1990). An instability mode is considered to be absolute if its group velocity is zero. On the other hand, the unstable development of a disturbance is said to be convective when none of its constituent modes posses zero group velocity. Both classes **A** and **B** are convective, while class **C** divergence and transitional modes are absolute. As Carpenter (1990) points out, the occurrence of absolute instabilities would lead to profound changes in the laminar-to-turbulence transition process. It is therefore pointless to consider reducing their growth rate or postponing their appearance to higher Reynolds number; nothing short of complete suppression would work. Figure 1 combines and summarizes all three classification schemes.

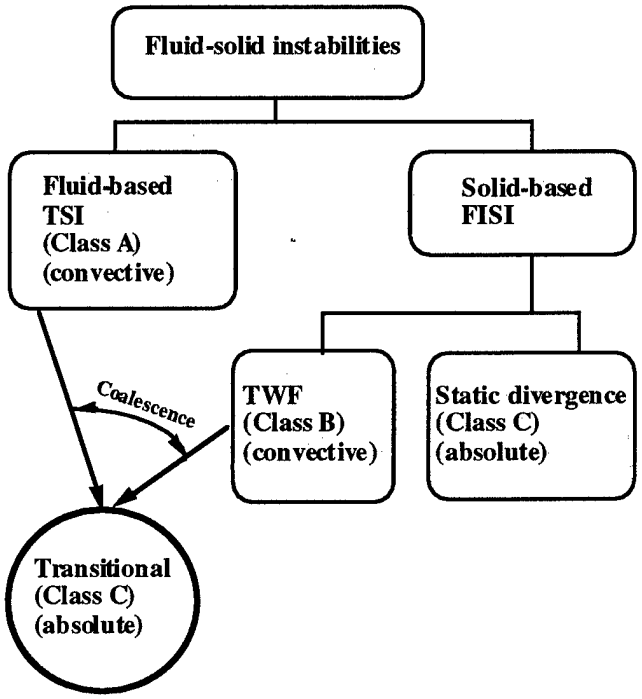

Figure 1: Summary of all three classification schemes

4 The Kramer Controversy

It may be worth recalling in more details the pioneering work of Max O. Kramer and the controversy surrounding it. The entire field of compliant coatings became the *Rodney Dangerfield* of fluid mechanics research, getting no respect from a skeptical community, largely because of the loss of credibility of Kramer's original experiments. However as will be seen below the most recent evidence resurrects the good name of this ingenious German-American and with it renewed confidence in this waning and waxing field.

As already mentioned, Kramer (1957; 1960a; 1960b; 1960c; 1961; 1962; 1965; 1969) conducted his original experiments by towing a model behind an outboard motor boat in Long Beach Harbor, California. His early tests showed a drag reduction of more than 50% when a dolphin-like skin was used. A typical successful coating used by Kramer consisted of a flexible inner skin, an outer diaphragm, and stubs, all made of soft natural rubber. The cavity between the outer diaphragm and the inner skin was usually filled with a highly viscous damping fluid, such as silicone oil, which in Kramer's view damped out the Tollmien-Schlichting waves.

Subsequent experiments to confirm Kramer's findings were conducted in a towing tank, a lake, or a water tunnel (Puryear, 1962; Nisewanger, 1964; Ritter and Messum, 1964; Ritter and Porteous, 1964). No significant drag reduction was observed in any of these investigations. Since then, many researchers have assumed that Kramer's results were in error and that his observed drag reduction could have come about as a result of favorable changes to the form drag or the accidental excretion of the silicone oil used as the damping fluid during the tests. Surface discontinuities could have favorably altered the pressure drag, and the released oil could have acted as a drag-reducing polymer when released into the boundary layer and the ambient fluid.

Carpenter and Garrad (1985) stated that: "It is probably no exaggeration to suggest that the credibility of Kramer's coatings is now rather low." Acceptance of his results was not granted by the scientific community because the rigorous standards of scientific investigation were not met and the gradual improvements by Kramer to meet these standards were not adequate (Johnson, 1980). It did not help his cause any that Kramer's explanations of his own empirical results, though intuitively appealing, were proven physically incorrect. For example, we now know that damping in the solid *destabilizes* TSI.

Almost 30 years after Kramer's original investigation, Carpenter and Garrad (1985) presented a very careful analysis of his experiments (e.g., Kramer, 1957) and the subsequent tests (Puryear, 1962; Nisewanger, 1964; Ritter and Messum, 1964; Ritter and Porteous, 1964) that attempted to provide independent evidence of the drag-reducing capabilities of Kramer's coatings. Based on their own rigorous analysis of the hydrodynamic stability of flows over Kramer-type compliant surfaces, Carpenter and Garrad argue that Kramer's coatings were only marginally capable of delaying transition. Any unfavorable factor, such as an adverse pressure gradient, a step where the compliant surface is joined to a rigid surface or an unusually high freestream turbulence level, could badly affect the performance of the coating. Also, a particular coating was designed for a restricted range of Reynolds number and was therefore unlikely to delay transition outside that range.

Carpenter and Garrad (1985) contend that one or more of the above adverse factors may have existed in the experiments conducted by Puryear (1962), Nisewanger (1964), Ritter and Messum (1964), and Ritter and Porteous (1964). Puryear's (1962) experiments were conducted using a prolate spheroid in a towing tank. He did not use Kramer's coating with the best performance, and serious problems were encountered in making a smooth joint between the rigid and compliant surfaces. Nisewanger's (1964) tests were conducted by releasing a lighter-than-water body of revolution from the bottom of a lake. His Kramer-like coating contained a fluid with a viscosity below that of the optimum fluid as determined from Kramer's results. Ritter and Messum (1964), and Ritter and Por-

teous (1964) conducted their experiments in a water tunnel using either a flat plate or a cylindrical model with an elliptic nose. The conventional flume had a relatively high freestream turbulence level, which may render the facility unsuited for transition experiments.

In addition to these adverse effects, some evidence existed in the tests conducted to confirm Kramer's results for the onset of a hydroelastic instability in the coating. Such large-amplitude waves would certainly lead to drag increase, and their presence may indicate that the boundary layer was already turbulent. Based on these experiments, Carpenter and Garrad (1985) concluded that the results presented in these tests should not be taken as conclusive evidence that the Kramer coatings are not capable of delaying transition and that "the case against Kramer's coating may not be so strong as popularly supposed."

Carpenter's (1988) optimization procedure described in Section 5.2, results in a compliant coating that is capable of delaying transition by a factor of 4–6 in Reynolds number. It is therefore quite conceivable to design a Kramer-type coating that may lead to a drag reduction of the order reported by the original inventor himself. The above analysis of Kramer's tests illustrates the importance of carefully selecting the flow facility to conduct compliant coating experiments. The background turbulence in the facility should particularly be monitored if transition delay is sought. This is precisely what was done in the successful experiments conducted by Gaster (1988) to confirm the theoretical prediction of Carpenter and Garrad (1985), both described in more details in the following section.

5 Transitional Flows

5.1 Linear Stability Theory

Both the hydrodynamic and the hydroelastic stability theories have reached an impressive level of maturity during the last two decades. The linear theories can be handled, for the most part, analytically, while the nonlinear stability theories are more computer intensive. Perhaps no one has contributed more to the recent application of the stability theory to compliant coatings than Peter W. Carpenter, originally with the University of Exeter and presently with the University of Warwick. His list of relevant publications includes 65 papers and growing; obviously only a selected few will be cited in the present short article.

Within the framework of the linear stability theory, two-dimensional small disturbances are assumed to be superimposed upon a steady, unidirectional mean flow. The nonlinear, partial Navier-Stokes equations are then reduced to the well-known Orr-Sommerfeld equation which is a fourth-order, linear, ordinary differential equation. The order of this equation increases when additional complexities are included in the problem. For rotating-disk flows, for example, Coriolis and streamline-curvature terms are incorporated leading to a sixth-order stability equation. The major difficulty in integrating the Orr-Sommerfeld equation is that it is highly stiff and unstable, which makes it virtually impossible to apply conventional numerical schemes. Explicit codes with step size that is commensurate with the global behavior of the solution lead to numerical instabilities, and alternative routines have been developed to handle this stiff eigenvalue problem.

An added difficulty when the walls are compliant is the interfacial conditions which require continuity of velocity and stress. Those boundary conditions can also be linearized, but special care should still be exercised in handling them. Appropriate equations must be used for the compliant walls to be able to fully couple the fluid and solid dynamics. Many types of compliant surfaces exist, so that there are numerous models for the solid. Those models can be either surface-based or volume-based. The former model reduces the spatial dimensions by one, and is therefore less computationally demanding. An example is the thin plate-spring model used by Garrad and Carpenter (1982), Carpenter and Garrad (1985; 1986), Domaradzki and Metcalfe (1987), Metcalfe et al. (1991), and Davies and Carpenter (1997a; 1997b), among others, to simulate Kramer-type coatings. This model is relatively simple yet contains characteristics representative of a broad range of surfaces. If a coordinate system is chosen with the x-axis lying along the undisturbed free surface and the y-axis normal to this surface, then the equation for the y-component of the momentum of the compliant coating reads

$$\frac{\partial^2\eta}{\partial t^2} = \frac{T_\ell}{m}\frac{\partial^2\eta}{\partial x^2} - D\frac{\partial\eta}{\partial t} - \frac{\mathcal{F}}{m}\frac{\partial^4\eta}{\partial x^4} - \frac{k}{m}\eta + F \qquad (1)$$

where $\eta(x,t)$ is the y-displacement of the surface from its equilibrium state at time t and position x, T_ℓ is the longitudinal tension and $\mathcal{F}$ the flexural rigidity of the thin plate, m is the mass per unit area, D is the damping coefficient, k is the spring constant, and F is an external forcing term.

The volume-based models are based on the Navier equation and include single and multi-layer coatings (Duncan et al., 1985; Fraser and Carpenter, 1985; Buckingham et al., 1985; Yeo, 1988) as well as isotropic and anisotropic materials (Yeo, 1992; 1990; Duncan, 1988). The equations describing the stability of the coupled system form a numerical eigenvalue problem for the complex wavenumber of the disturbance. Duncan (1987) offers a useful comparison between the results obtained from a surface-based model and a corresponding volume-based one.

Compliant walls do suppress the Tollmien-Schlichting waves due to the irreversible energy transfer from the fluid to the solid, but solid-based instabilities proliferate if the coating becomes too soft. For the class **A** T-S waves, the wall compliance reduces the rate of production (via Reynolds stress) of the disturbance kinetic energy. Simultaneously, the viscous dissipation is increased and thus the balance between the energy production and removal mechanisms is altered in favor of wave suppression.

Experimental validation of the stability calculations is rather difficult and requires well-controlled tests in a quiet water or wind tunnel. Several careful experiments to test the flow stability to two-dimensional as well as three-dimensional controlled disturbances have been reported in the past few years (Daniel et al., 1987; Gaster, 1988; Lee et al., 1995; 1997). A simple compliant model predicts a dramatic decrease in the instability of the flow, and this prediction agrees well with the experimental observations when a thick, soft coating is covered with a thin, stiff layer.

The papers by Lee et al. (1995; 1997) report the results of wind tunnel experiments and actually demonstrate the stabilizing potential of compliant coatings in aerodynamic flows; a remarkable achievement that has been deemed impractical in the past (Bushnell et al., 1977; Carpenter, 1990). Excellent agreements are reported between the results of the stability theory and the hydrodynamic experiments (Willis, 1986; Daniel et al., 1987; Gaster, 1988; Riley et al., 1988; Carpenter, 1990; Lucey and Carpenter, 1995). The paper by Lucy and Carpenter, in particular, applies the linear stability theory to predict the experimentally observed evolution of both Tollmien-Schlichting waves and traveling-wave flutter in water flows. For the wind tunnel experiments, Carpenter (1998) has conducted the corresponding calculations, but his preliminary results thus far are negative: the density of an effective coating must be comparable to the fluid density otherwise no transition delaying benefits are observed. This theoretical result leaves open the question of explaining the positive experimental findings of Lee et al. (1995). Reductions in the maximum rms-amplitude of as much as 40% are observed for the softer coating, which may lead to delayed transition.

5.2 Coating Optimization

If a compliant coating is to be designed for use on an actual vehicle, a relevant question may be: what are the optimum wall properties to give the greatest transition delay? The large number of available parameters makes it imperative that a rational (i.e., one derived from first principles) selection process be conducted. For obvious reasons, the trial-and-error empirical approach used in the past *(if it is soft, let us try it!)* should not even be contemplated. This should be particularly true now that rational optimization procedures are becoming readily available as described below. A wall that is too compliant (i.e., too soft) can substantially delay transition via TSI by shrinking its unstable region in the frequency-

Reynolds number plane, but rapid breakdown can occur through the amplification of wall-based instabilities (Lucey and Carpenter, 1995). Both kinds of FISI are potentially harmful. The divergence instabilities are absolute, nearly static, and yield to wholesale deformations of the surface which are likely to trigger premature transition due to a roughness-like effect. Flutter instabilities, though convective, are also dangerous. Their narrow band of unstable frequencies extends indefinitely as Reynolds number increases downstream. Thus, once these instabilities are encountered at some downstream location, sustained growth follows. This is unlike the broad-band Tollmien-Schlichting instabilities which grow then decay as the different waves travel downstream and pass through the lower and upper branches of their neutral-stability curve.

A workable strategy for coating optimization suggested by Carpenter (1988) is to choose a restricted set of wall properties such that the coating is marginally stable with respect to FISI (both flutter and divergence). The remaining disposable wall parameters can then be varied to obtain the greatest possible transition (via TSI) delay. For the plate-spring, surface-based model, for example, there are two disposable parameters: the wall damping and the critical wavenumber for divergence. The downstream location of the transition region is estimated from an e^n-criterion, where n is typically chosen in the range of 7–10. The lower exponent represents the approximate limit of validity of the linear stability theory for a low-disturbance environment, and provides a rather conservative calculation.

Although wall dissipation destabilizes Tollmien-Schlichting waves, a viscoelastic coating with moderate level of damping leads to greater delay in transition as compared with purely elastic surfaces. Apparently the stabilizing effects of wall damping on traveling-wave flutter allow a softer wall to be used, and thus more than offset the adverse effects of coating dissipation on TSI.

Coating optimization with respect to TSI growth rate is performed at a rather narrow range of Reynolds numbers. On a growing boundary layer, the Reynolds number increases monotonically, and a compliant coating will not be optimum over the whole length of a vehicle. Carpenter (1993) suggests that a multiple-panel wall, placed in series, with each panel optimized for a particular range of Reynolds numbers, is likely to produce larger transition delays than a single-panel wall. His calculations for a two-panel, plate-spring-type compliant wall indicate an additional performance improvement of over 30% over an optimized single-panel wall.

It seems reasonable that a large number of panels, say 10, in series would lead to superior performance, but of course the calculations involved become prohibitive very quickly. An additional benefit from using multi-panels is that shorter panels are more resistant to both static-divergence waves and traveling-wave flutter (Carpenter, 1993; Lucey and Carpenter, 1993; Dixon et al., 1994), thus allowing softer panels to be used which further suppress TSI and improve the coating performance.

In the flat-plate and similar boundary layers in low-disturbance environments, the quasi-two-dimensional Tollmien-Schlichting waves dominate the laminar-to-turbulence transition. Various receptivity processes are responsible for generating 2-D instabilities which are probably initially three-dimensional and randomly distributed. Low-disturbance environments could be realized, for example, in free flight and marine vehicles. Very recently, Davies and Carpenter (1997a) and Carpenter (1998) have shown that in such environment, complete suppression of the Tollmien-Schlichting waves is possible provided that optimized multiple-panel compliant walls are used with each panel tailored to suit its local surrounding. Assured by the experimental observations that static-divergence waves are only observed when the wall-bounded flow is turbulent, Carpenter's (1998) new assumptions are somewhat less conservative than those used in earlier theories (Carpenter, 1993; Dixon et al., 1994). The new finding raises the possibility of maintaining laminar flow, in situations where the T-S instabilities are the primary cause of transition, to indefinitely high Reynolds numbers, a very profound prospect indeed.

Work on nonlinear stability theory has recently been in the forefront and confirms that transition-delaying coatings, optimized using the linear theory, maintain their beneficial effects into the latter stages of transition to turbulence (Metcalfe et al., 1991; Joslin et al., 1992; Thomas; 1992a; 1992b). Lee et al. (1997) studied experimentally the effects of a compliant surface on the growth rates of both the subharmonic and three-dimensional fluid-based instabilities of a laminar boundary layer in air. Their results suggest that a delay of the excitement of the secondary instability can be achieved by suppressing the growth of the primary waves using surface compliance.

5.3 Practical Examples

Most of the theoretical as well as experimental compliant coating research has been concerned with canonical boundary layers. Nevertheless, an attempt is made in here to estimate the potential benefit of applying the technique for field applications where strong three-dimensional and pressure-gradient effects and, for aeronautical applications, compressibility effects may be present. The typical Reynolds numbers, based on vehicle speed and overall length, for a hydrofoil, a torpedo and a nuclear submarine are, respectively, of the order of 10 million, 50 million and 1 billion. Applying an e^n-type calculations (with the exponent chosen conservatively to be $n = 7$) to an optimum two-panel, plate-spring-type compliant wall, Carpenter (1993) computes a transition Reynolds number of 13.62×10^6, as compared with 2.25×10^6 for a rigid wall. This means that the laminar region that would normally extend over 23%, 5% and 0.2% of the respective vehicle lengths would, with the use of an optimum coating, extend over a larger length of 100%, 27% and 1%. Computing the corresponding overall drag coefficients using standard methods for a mixed laminar-turbulent boundary layer over a flat plate, the potential reduction in skin-friction drag using the optimum two-panel compliant wall can be as much as 83%, 19% and 0% for the three respective vehicles. Obviously the large submarine does not benefit, as far as drag reduction is concerned, from the use of transition-delaying compliant coating but the smaller vehicles do. However, extending the laminar region on a submarine even by 1 m can be significant for sonar applications requiring longer quiet regions of the boundary layer.

For aeronautical applications, a cruising commercial jet aircraft has a fuselage Reynolds number of the order of 0.5 billion and a wing Reynolds number of the order of 50 million. Again, increasing the transition Reynolds number by a factor of 5 or so is significant for the wing but not for the fuselage. Skin-friction reduction of the order of 20% is achievable for the wings (whose skin-friction drag accounts for about 50% of the skin friction of the entire aircraft and 25% of the total drag). Finding a compliant coating that would reduce the turbulent skin-friction drag would of course be very beneficial for both the typical fuselage and long submarine.

The estimates above were made for a simple plate-spring model. Using more than two panels can provide further transition delay. More complex compliant surfaces, particularly anisotropic ones designed specifically to suppress the Reynolds stress fluctuations, can conceivably offer more spectacular savings. Such custom-designed coatings can also favorably interact with fully-turbulent flows. Even for laminar flows, the calculations involved when complex, wall-based models are used, though straightforward in principle, are quite demanding in practice.

5.4 The Dolphin's Secret

The ability to swim or to fly with minimum skin-friction and pressure drag is of extreme importance to the Darwinian survival of certain nektonic and avian species. *Homo sapiens* interested in building the fastest submarine or the most fuel-efficient aircraft have much to learn about alternative drag-reduction approaches from their humble earthlings. As Max O. Kramer has remarked close to half a century ago, a school of porpoises, including the young and the old, the weak and the strong, showing off its seemingly effortless glide along a fast ocean-liner is a sight to behold.

Cetaceans appear to possess unusually low overall drag coefficients. This is the basic for the so-called Gray's (1936) paradox, in which a steady-state energy balance based on the anticipated mus-

cle power of various nekton, including the dolphin, failed to explain their unusually fast swimming speeds. Gray clocked bottlenose dolphins, *Tursiops trucatus*, swimming at speeds exceeding 10 m/s for a period of 7 s. If one assumes that cetaceans power output is equal to that of other mammals ($\sim$ 35 W/kg of body weight), then such speeds are reached under turbulent flow conditions only if dolphins can expend several times more power than their muscles can generate. Lang (1963) concluded that based on energy considerations, dolphins could not exceed a speed of 6 m/s for periods greater than 2 hours.

Transition delay is of course an obvious albeit arduous technique for achieving about an order of magnitude lower skin-friction drag, but does the dolphin posses an exotic means by which such difficult flow control goal can be accomplished? Obviously the dolphin is not sharing its secrets with other fellow mammals. Kramer's (1957; 1961) invention of a compliant coating tried to mimic the dolphin's epidermis and claimed drag reduction of as much as 60%. His explanation for the dolphin's secret is that their skin, like his successful compliant coating, is capable of substantially delaying laminar-to-turbulence transition. Kramer's work was discredited for a while but now seems to be back in vogue as remarked in Section 4. The calculations presented in Section 5.3 indicate that it is quite conceivable to design a Kramer-type coating that delay transition by a factor of 4–6 in Reynolds number and that drag reduction of the order reported by Kramer is also quite possible. Does the dolphin or other similar fast swimmers posses such a coating?

In a recent article, Bushnell and Moore (1991) quote the relevant energetic and controlled swimming studies, but conclude by supporting the explanation offered by Au and Weihs (1980) that dolphins, which must periodically breath air, achieve high-speed swimming by simply *porpoising*, i.e., momentarily leaping out of the water thereby reducing their drag force by a factor of 800 (density ratio of air and water). This more than pays for the additional interfacial or wave drag and accounts for the abnormally low apparent drag-coefficients inferred from the assumption of fully-submerged travel.

The present author, however, does not concur with the above *final solution* to the Gray's paradox. Dolphins have been clocked at sustained and burst speeds of close to 10 and 20 m/s, respectively. *Delphinus delphis* has a typical length of 2 m. This leads to sustained and burst Reynolds numbers based on the overall length of the order of 20 million and 40 million, respectively. Carpenter (1993) reports the results of optimizing a rather simple plate-spring coating. Using a single panel, as compared with a rigid surface a 4.6-fold increase in transition Reynolds number is estimated, which leads to a drag reduction of 36% at the typical dolphin's sustained speed and 20% at burst speed. Using a mere two-panel coating, the transition Reynolds number becomes 6.1 times the value for a rigid surface, and the potential drag reductions for the sustained and burst speeds are now 52% and 30%, respectively.

These lower levels of skin friction are compatible with the available muscle power for a dolphin of the size used above. Admittedly, the above estimates were made for a flat-plate boundary layer and may not hold when pressure-gradient and other shape effects are taken into account. Additionally, the dolphin has also pressure drag on top of the (much larger) skin friction. On the other hand, cetaceans have had millions of years of evolutionary adaptations to hone their coatings for maximum speed and efficiency, and it is quite conceivable that their epidermis is quite more complex, and hydrodynamically beneficial, than the simple ones computed in the examples above. Moreover, each portion of the skin could have been optimized for the appropriate range of local Reynolds numbers. Therefore, the dolphin's apparent success is not incompatible with having optimum compliant coatings to substantially delay laminar-to-turbulence transition, and therefore to attain inordinately low coefficients of drag.

Other fascinating questions related to the amazing swimming abilities of the dolphin include the possibility that its excreted mucin is a drag-reducing additive. Is there a hydrodynamic advantage to the warm-blooded cetaceans because their epidermis temperature is higher than the ambient one (in which case the near-wall water viscosity is lowered and the turbulent boundary layer may be relaminarized)? Does the dolphin's particular body shape during coasting (with no attendant overall body deformation) or actual swimming (accompanied by appropriate body oscillations) offer additional drag-reducing advantages? Also, what are the potential benefits to the porpoise when it uses ship-generated bow waves for body surfing? These subjects, though related to the above discussion, are outside the scope of the present brief and are therefore left for another circumstance.

6 Turbulent Wall-Bounded Flows

Unlike the laminar and transitional flows investigated in Section 5, compliant coating effects on turbulent boundary layers are rather difficult to study theoretically. In fact *any* turbulent flow is largely unapproachable analytically. For a turbulent flow, the dependent variables are random functions of space and time, and no straightforward method exists for analytically obtaining stochastic solutions to the governing nonlinear, partial differential equations. The statistical approach to solving the Navier-Stokes equations always leads to more unknowns than equations (the closure problem), and solutions based on first principles are again not possible. Direct numerical simulations (DNS) of the canonical turbulent boundary layer have thus far been carried out up to a very modest momentum-thickness Reynolds number of 1410 (Spalart, 1988).

How would one go about rationally choosing a coating to achieve a particular control goal for a turbulent boundary layer? Analytical optimization procedures such as those used to delay transition (Section 5.2) would not work for fully-turbulent flows. In order to analyze the full problem, direct numerical simulations of the turbulent boundary layer should be coupled to a finite-element model of the compliant coating, a task that is extremely time consuming, expensive and taxes the fastest supercomputer around. Modeling the turbulence by an eddy-viscosity or even a more sophisticated closure scheme is less computationally demanding, but there is no guarantee that turbulence models developed primarily for rigid surfaces would work for a compliant surface. In fact, it is not difficult to argue that closure models based on mean quantities miss completely the all important spectral contents of a fluid-solid interaction, and will therefore never work.

A turbulent boundary layer is characterized by a hierarchy of coherent structures. Near the wall, the dynamics are dominated by the quasi-periodic bursting events (Robinson, 1991). A crude albeit resourceful attempt to model a turbulent boundary layer interaction with a single-layer, isotropic, viscoelastic coating has been advanced by Duncan (1986). He approximates the turbulent flow over the coating by a potential flow with a superimposed pressure pulse, convecting downstream, that mimics the pressure footprint of a single bursting event. In order to relate the problem to a real turbulent flow, the pressure pulse characteristics are taken from actual boundary layer measurements and the potential flow is modified to incorporate the reduced magnitudes and phase shifts found experimentally in boundary layer flows over moving wavy walls. At low flow speeds (relative to the transverse-wave speed in the solid), the coating response to the pressure pulse is stable and primarily localized under it. At intermediate speeds, the response is still stable but includes a discernible wave pattern tagging along behind the pressure pulse. At the highest speed studied, large-amplitude, unstable waves develop on the compliant surface, much the same as the FISI observed experimentally. Duncan and Sirkis (1992) have recently extended the above model to anisotropic compliant coatings. They report that certain anisotropic surfaces provide more effective control over the amplitude and angular extent of the generated stable response pattern. Larger amplitudes are generated as compared with isotropic surfaces, thus providing for greater potential for modifying the turbulence.

Whenever the flow speed in a turbulent boundary layer becomes sufficiently large compared with the transverse free-wave speed in the solid, flow-induced surface instabilities proliferate. The pressure fluctuations within the flow are an order of magnitude larger than the normal and tangential viscous stresses, and drive the coating response. In laminar wall-bounded flows it is difficult to observe

the hydroelastic waves in their unstable state. As soon as flutter or divergence waves grow, rapid breakdown to turbulence takes place in the boundary layer and the flow is no longer laminar.

Most of the experimental studies concerning compliant coating effects on turbulent boundary layers focused on documenting the unstable flow-induced surface instabilities. When divergence waves or flutter are unstable, the effects, though adverse, are pronounced and are somewhat easier to document. Only recently few hardy souls have attempted to investigate the wall-bounded flows when these FISI are stable or neutrally stable. Obviously the latter kind of studies have to await the development of refined techniques to measure the minuscule surface deformation and the associated coherent structure modulation when the FISI are neutrally stable.

Both Gad-el-Hak (1986) and Hess et al. (1993) introduce non-intrusive methods for the point measurement of the instantaneous vertical surface-displacement of a compliant coating, while Lee et al. (1993b) offer an optical holographic interferometer, in connection with an interactive fringe-processing system, to capture whole-field random topographic features. The latter technique is more expensive to set up but offers higher spatial resolution, of the order of 1 micron, and yield simultaneous surface displacement information on a large section of the compliant coating. Both the local and global methods were initially employed to document the unstable surface response to the pressure fluctuations in turbulent boundary layers. The holographic interferometer was recently used to record the surface topography in the presence of *stable* flow-induced deformations (Lee et al., 1993a).

The onset speed and wave characteristics of the solid-based class **B** and **C** instabilities were systematically documented in a series of towing-tank experiments (Gad-el-Hak, 1986). Divergence waves were observed on a single-layer viscoelastic coating made from a PVC plastisol. The flutter appeared on an elastic coating made from common household gelatin, but, in the absence of damping, its threshold speed was consistently lower than that for divergence. The damping in the PVC coating stabilized the traveling-wave flutter and hence only divergence was observed there. For the elastic coating, flutter appeared first and dominated the observed surface deformation. For both kind of waves, the threshold speed decreases with coating thickness, in other words thin surfaces (relative to the displacement thickness of the boundary layer) are less susceptible to hydroelastic instabilities than thick ones.

Typical profiles of unstable class **B** and **C** waves were also recorded in the same hydrodynamic experiments using a laser displacement gauge. The vertical displacement at a point associated with the slow moving, asymmetric, large-amplitude divergence waves contrasts the faster, more-or-less symmetric, smaller-amplitude flutter. Both waves cause roughness-like effect, but the static divergence is the more dangerous instability. The phase speed of the static-divergence waves is of the order of 1% of the freestream speed, and their wavelength is about 5–10 times the coating thickness. The corresponding quantities for the flutter are 40% and 1.5–3, respectively.

Hess (1990) and Lee et al. (1993a) also investigated compliant coating effects on turbulent boundary layers. Both experiments were conducted in the same water tunnel, but the second paper focused on the stable interaction between the fluid and a single-layer, homogeneous, viscoelastic coating made of a mixture of silicone rubber and silicone oil. Lee et al.'s coating was chosen based on the criterion established by Duncan (1986). In the presence of a stable wave pattern on the compliant surface, the flow visualization experiments indicated low-speed streaks with increased spanwise spacing (by as much as 80%) and elongated spatial coherence compared with those obtained on a rigid surface. More significantly, for the particular compliant coating investigated an intermittent relaminarization-like phenomenon was observed at low Reynolds numbers. Lee et al. (1993a) also report a slight thickening of the buffer region and viscous sublayer and an upward vertical shift in the compliant law-of-the-wall. The streamwise turbulence intensity, the local skin-friction coefficient and the Reynolds stress across the boundary layer were all reduced, indicating a possible interruption of the feedback loop which allows the turbulence to be self-sustaining. Thus, potentially favorable interaction between a compliant coating and a turbulent boundary layer has been demonstrated for the first time. The more recent hydrodynamic experiments by Choi et al. (1997) provide additional evidence for favorable interaction and indicate a total drag reduction for a long, slender body of revolution of the order of 7%.

7 The Future

The diminishing pool of researchers remaining active in the field of compliant coatings includes teams from the University of Warwick, University of Nottingham, Johns Hopkins University, University of Houston, University of Maryland, and the Institute of Thermophysics in Novosibirsk. A larger pool was involved during the early 1980s, but the realities of research funding combined with the checkered past of the field led to the present decline.

Few suggestions for future research are given in here. The optimization procedures discussed in Section 5.2 have not been validated experimentally. Gaster-type experiments should be repeated using optimized coatings, including multi-panel ones. The recent claims by Davies and Carpenter (1997a) and Carpenter (1998) regarding the possibility of maintaining laminar flow to indefinitely high Reynolds numbers are very profound. Experiments, particularly field ones in low-disturbance environments, specifically designed to test those claims would be extremely useful.

The results of the transitional-boundary-layer, wind-tunnel experiments reported by Lee et al. (1995; 1997) are intriguing and fly in the face of the conventional wisdom. They indicate that compliant coatings are capable of delaying transition even for air flows. Past calculations using a plate-spring model and considering the extremely large density of typical walls compared with the density of air indicated that very flimsy coatings would be required to achieve transition delay and that the situation gets worse as the air speed increases. This led Carpenter (1990) among others to conclude that the use of wall compliance is impractical for aeronautical applications. But the plate-spring results do not apply in any straightforward way to the homogeneous, single-layer walls studied by Lee et al. (1995). Validating the recent favorable results using both independent experiments and numerical simulations would open the door for aerodynamic applications, something that was seriously considered but later abandoned by NASA and the aerospace industry. The optimization procedures developed by Carpenter (1988) for transitional hydrodynamic flows should be extended to air flows. Experiments should be conducted using the resulting optimized coatings.

More complex coatings could potentially yield superior performance as compared with the relatively simple walls studied thus far. Multi-panels, multi-layers, anisotropic coatings and combinations thereof should be investigated. In any such research program, experiments has to be guided with theoretical results. As already mentioned, trying to pick a compliant coating by trial and error is a very inefficient use of limited resources and will perhaps never work.

Favorably modulating a fully-turbulent flow, in contrast to merely delaying transition, is also of great practical importance. The experimental results reported by Lee et al. (1993a) are very encouraging, but the coating used was chosen based on a rather simplistic model of the turbulence pressure fluctuations. In order to custom-design compliant coatings to achieve particular control goals for turbulent wall-bounded flows, direct numerical simulations of the coupled fluid-structure system have to be performed. Turbulence modeling via classical closure schemes, while sufficient for some simple flows over rigid surfaces, will perhaps not yield reliable results for compliant walls. DNS, on the other hand, requires extensive computer resources and is quite expensive to carry out. The bottom line is that relatively large investment in resources are required for this task, but the enormous potential payoffs could easily justify the expenditure.

Most of the research thus far has considered incompressible, zero-pressure-gradient, flat-plate boundary layers. Effects of compressibility, pressure gradient and three-dimensionality on the performance of compliant coatings are largely unknown. Such studies

will yield invaluable information for field application of the control technique for both air and water flows. Most practical aerodynamic flows are in the moderate-to-high Mach number regime, and compressibility effects must therefore be investigated before compliant coatings are used on actual aircraft. Related to the pressure-gradient effects is the question of separated flows: does compliant coating affect separation favorably or adversely? Other stability modifiers, such as favorable pressure-gradient, suction or heating/cooling, do delay transition as well as prevent separation. It is not known whether compliant coatings also have this dual benefit, and it may be beneficial to research the possibility. Finally, real flows are three-dimensional and involve complex geometries. A model problem for three-dimensional flows is the rotating disk. Few experiments were conducted using a rotating disk with a compliant face (Hansen and Hunston, 1974). More recently, Cooper and Carpenter (1995; 1997a; 1997b; 1997c) analyzed the cross-flow (type **I**; inviscid) as well as the viscous (type **II**) fluid-based instabilities which develop in the same three-dimensional flow. The preliminary results are encouraging and indicate that compliant coatings can suppress the more dangerous type **I** instabilities.

Active compliant coatings, though bringing us back to the complexity of reactive control systems, is an emerging area deserving of further research. Energy expenditure is required to drive the wall, but the potential for significant net drag reduction is higher than that for passive coatings. The feasibility of the concept for stabilizing laminar boundary layers has been shown through numerical experiments (Metcalfe et al., 1986). Active coatings could also be used to suppress the Reynolds stress and reduce the skin-friction drag in turbulent wall-bounded flows, but any realistic field application of the technique has to await further development of reasonably-priced and rugged microfabricated sensors and actuators (Gad-el-Hak, 1994; 1996b).

Using the subject of compliant coatings to make a point, I would like to end this section with a personal commentary. There is a growing impatience among our fellow citizens with the glacial pace of transferring knowledge from the laboratories to the factories, getting back the invested research dollars of yesterday in the form of stronger industrial competitiveness tomorrow. In his closing remarks on the occasion of the presentation of the 1990 American Physical Society Fluid Dynamics Prize, Lumley (1992) lamented that the United States is a curiously unsympathetic environment for a theoretician, or any scientist interested in fundamental work. Through all its ups and downs, compliant coating research provides a good case study. Although in the general scheme of things this basic research is but a drop in the ocean, its triumphs and debacles are not untypical. The usual five-year cycle for academic research is just enough to get off the ground.

When the compliant coating research program was re-ignited in the early 1980s, few veterans from the 1960s and 1970s were around to share their valuable experiences, and the newcomers have had to climb the learning curve from its bottom. Nevertheless, we now know how to carry out stability calculations, solve fully coupled fluid-solid problems, numerically simulate turbulent flows, conduct well-controlled experiments for both transitional and turbulent flows, reliably measure surface deformation, identify as well as quantify coherent structures, optimize a coating for a particular task using first principles, ... In other words, the compliant coating research community has now most of the tools it needs for significant further progress. Unfortunately, this community has recently been forced into an early retirement.

As amply illustrated in this paper, compliant coating research, despite its checkered history, offers the potential for substantial transition delay and favorable interactions with turbulent boundary layers. It requires modest commitment of resources, but the payoff is extraordinary. It might be worth recalling that a mere 10% reduction in the total drag of an aircraft translates into a saving of $1 billion in annual fuel cost for the commercial fleet in the United States alone. Contrast this benefit to the annual cost of less than $2 million for the 5-year compliant coating research program that was sponsored by the U.S. Office of Naval Research in 1980. Private capital will not and cannot step in place of the government to support leading-edge research with long-term promise but without short-term return. Do we have the will, desire, patience and resources to continue the journey towards real-life applications? In so many similar circumstances in the past, the answer was no. Scarce resources were spent for five years only to be hastily diverted to newer areas, long before the fruits of our labor have even had a chance of being reaped. But even in these difficult times of trying to reduce the federal budget deficit, one hopes for a different road to prosperity—and I do not mean for the researchers involved—this time around.

And while we are at it, cutting funds for basic research in general may be popular but is certainly unwise. Today's research generates the knowledge from which the future is built, and a responsible government must strike a balance between near-term goals and long-term economic growth and prosperity. Reducing spending on current outlays is one thing, but investing less in the country future is an entirely different matter. Fundamental knowledge provides the foundation for a nation's productivity and economic growth, sustains its high standard of living, improves its quality of health and environment, and ensures its security. The overall detrimental impact of reducing government funding for basic research probably will not be felt for a generation, but it will be felt.

8 Parting Remarks

Passive compliant coatings present a much simpler alternative to reactive flow control strategies aimed at favorably interfering with wall-bounded flows. The last 10–15 years witnessed renewed interest in compliant coatings as a means to achieve beneficial flow control goals. Significant advances were made in numerical and analytical techniques to solve the coupled fluid-structure problem. Novel experimental tools were developed to measure the stable as well as the unstable surface deformations caused by the pressure fluctuations in the boundary layer. In turbulent wall-bounded flows, coherent structures were routinely identified and their modulation by wall compliance could be quantified.

Most significant results in the field thus far were obtained when a strong cooperation existed between theory and experiment. Recent theoretical work indicates that complete suppression of the Tollmien-Schlichting waves may be possible, provided that optimized multiple-panel compliant walls are used. The new finding raises the possibility of maintaining laminar flow to indefinitely high Reynolds numbers, a very profound prospect indeed. Recent experiments indicate favorable compliant coating interactions even for aerodynamic flows and even for turbulent boundary layers. More research is needed, however, to confirm these latest results.

The coupled system instabilities are now well understood, and compliant coatings can therefore be *rationally* designed to achieve substantial, perhaps even indefinite, transition delay in hydrodynamic flows. That recent shift from random to rational search for the right kind of coating is not unlike the great paradigm change in synthetic chemistry that took place near the beginning of the twentieth century. Increased understanding of the molecular geometry of organic compounds changed the scene from a hapless alchemist muddling around hoping to chance the right combination of ingredients, heat, pressure and catalysts to produce something useful to a professional chemist figuring out what she wants and working backward from the shape of a desired molecule for, say, a synthetic hormone. In fact, the present analogy is apt: the fluid dynamist working with the Navier-Stokes equations can tell the chemist the exact properties of the compliant coating to be synthesized to achieve a given goal. If the needed molecular structure is too complicated, futuristic nano-scale machines can assemble the required molecules directly, element by element.

DRAG REDUCTION OF THE OCEAN SURFACE BY THE SURFACE WAVES

Alexander Y. Benilov
Davidson Laboratory, Stevens Institute of Technology
Castle Point on Hudson
Hoboken, New Jersey, 07030, USA
abenilov@stevens-tech.edu

Abstract -The experimental and theoretical study, presented in the paper, demonstrates that the key parameter controlling the aerodynamic resistance of the ocean surface is the wave age. (1) For the "young" waves, the ocean surface behaves as a rough solid surface. The roughness parameter exceeds the thickness of laminar sub-layer and the drag coefficient may be significantly greater than it would be for a smooth surface. The wind looses its energy and momentum and the wave grows. (2) When the wind waves reach the developed state, the ocean surface behavior becomes similar to the smooth solid surface. The fluxes of wind energy and momentum balance the losses which the waves experience by breaking. (3) The ocean surface becomes "oversmoothed" in the case of the "old" waves. The roughness parameter becomes less than the thickness of laminar sub-layer and the drag coefficient becomes less than it would be for a smooth solid surface under the same wind conditions. In this case, the waves transfer their energy and momentum to the atmospheric boundary layer. A comparison shows that the theoretical conclusions have a good correlation with measurements.

I. INTRODUCTION

The transport of momentum, heat, humidity, and salt occurs across the air-sea interface. The character of this transport is regulated by the turbulence of the air-sea interface. Influences of surface waves on surface layers of the atmosphere and ocean have been well noted by many researchers [1-12]. These influences are very complex and still poorly understood, although there have been numerous experimental investigations and analytical studies. There is not sufficient observational data to specify completely the quantitative impact of surface waves on the characteristics of air-sea boundary layers. One of the major difficulties in air-sea interaction problems is the correct description of surface-wave effects. Here, the distinctive feature is the oscillation of the air-water interface, so that the standard methods of description of turbulence are generally inapplicable.

An important factor giving rise to the boundary layer in the atmosphere above the sea surface is the expenditure of momentum and energy of the wind on the generation of waves and currents [13-15].This constitutes a fundamental difference of the atmospheric surface layer not only from the ordinary layer above a smooth wall (solid surface), but also from the boundary layers above stationary rough surfaces. The interval of the atmospheric boundary layer right above the water surface, which is a few tens of meters thick, is called the atmospheric surface layer. A distinctive property of this layer is that within it, the vertical fluxes of momentum, heat, moisture, and various types of passive impurities vary little with height, and they can be taken as constants. This experimentally established fact is important in studying the turbulent boundary layer above the ocean and the interaction of the atmospheric boundary layer with the underlying surface because of the fluxes that completely define the turbulent structure of the layer [16].

II. VERTICAL STRUCTURE

It is known that the turbulent boundary layer of the atmosphere is stratified; turbulent processes within it are influenced by buoyancy, which in turn results from changes in air density owing to fluctuations in temperature and humidity. In particular, the structure of the main interval of the atmospheric surface layer at a distance above sea level greater then a few times the height of the largest waves was described by the Monin-Obukhov theory [4, 7, 10, 11, 16]. This theory gives equations relating the steady-state characteristics of turbulence at various heights to known turbulent fluxes of momentum, heat, and humidity under particular stratification conditions. The important parameter of the theory is the Monin -Obukhov buoyancy scale, which can be used to distinguish two sub-layers within the surface layer. In the lower sub-layer, at heights less than the buoyancy scale, the effect of stratification is small and the laws applying to a turbulent boundary layer in a fluid of uniform density are applied. The mean wind velocity profile, $\overline{U}_a(z)$, has the classical form

$$\overline{U}_a(z) = \frac{u_*}{\kappa} \ln\left(\frac{z}{z_0}\right), \qquad (1)$$

where z is the distance from undisturbed ocean surface, u_* is the friction velocity, κ is the Karman's constant, z_0 is the roughness parameter. In a regular turbulent flow over a rough solid surface, the roughness parameter is associated with the actual roughness of the surface. The situation is totally different from the ocean condition where the roughness parameter is a result of the wind-wave interactions. The so-called logarithmic turbulent boundary layer is similar in many respects to the turbulent boundary layer above stationary smooth or rough surfaces. However, the roughness parameter has tremendous variability and varies from 0.00001 cm to 10 cm. This results in the variability of the drag coefficient of the ocean surface ranging from 0.0005 to 0.01 [2, 11]. These experimental facts clearly demonstrate that the atmospheric surface layer differs fundamentally from both the ordinary boundary layer above a smooth wall (solid surface) and the boundary layer above a stationary rough surface. The upper sub-layer occurs at heights greater than the buoyancy scale, where the effect of stratification is more important than the effect of mean wind shear. In unstable stratification, the equations of turbulent convection are applied in this layer. Conclusions derived from the Monin - Obukhov theory are the principal tool for calculating the characteristics of the turbulent atmospheric surface layer.

Much valuable data on the vertical and local structure of turbulence are published in monographs [2, 3, 5-8, 10]. The primary conclusion to be drawn from this data is that at a sufficient distance above the sea surface (equal to a few times the height of the highest waves) the Monin - Obukhov similarity theory gives a satisfactory description of the characteristics of turbulence. Empirical data on the universal characteristics of turbulence in terms of this theory were presented in full form by Kader and Yaglom [17], who systematized measurements of turbulence in the atmospheric surface layer over land. There are still insufficient measurements in the atmospheric surface layer above water for such a systematization, but the results that Kader and Yaglom present can be used as a substitute when making estimates for marine conditions. The assumption of local equilibrium of turbulence is valid in the turbulent spectra of this part of the surface layer above the ocean.

In the layer of air between the logarithmic sub-layer and the water surface, however, the theory of similarity cannot be applied owing to the strong influence on dynamic conditions exerted by the surface waves. An example of such influence in a mean velocity profile is shown in Figure 1. This deviations can be presented in an universal form (Figure 1b) where $\Delta\overline{U}_a(z_{min})$ corresponds to the lower horizon z_{min}. One can see that the deviation from the "logarithm"-law is not small and may have a magnitude ~0.5 m/s. The wave "age", C_0/u_*, defines the sign of the deviations, C_0 is the phase velocity of the wave which corresponds to the spectral peak of wind wave. The effect of the wave factor is shown up in all characteristics of turbulence. The effective mechanism is redistribution of the vertically invariant flux of momentum between the turbulent and wave components of momentum [1-3, 5, 6, 8, 10, 18-21]. It is known from observations that in the layer of air about ten meters thick, waves make a significant contribution to the mean and fluctuating fields. The waves increase the intensity of the fluctuations [3, 6] and change the nature of the correlation between the fluctuation characteristics [7, 22-25]. The peaks produced by waves are clearly distinguishable in the fluctuation spectra. The waves also make a considerable contribution to the total fluxes of momentum, heat and moisture. The mathematical procedure for filtering stationary random processes can be used to reconstruct the contributions of waves and turbulence [25].

Measurements in the air layer between the crests and troughs of the waves have proven to be difficult. Therefore little is known about the turbulence and the wave induced disturbances within this layer. Few measurements on the laminar sub-layer in the vicinity of the water surface

were done, and a brief description of results is given in [7, 9]. The recent findings [19] used Particle Image Velocimetery (PIV) techniques. Images of the flow using neutrally-buoyant 20-60μm diameter fluorescent micro-beads as tracers provided the detailed fluid velocity information in the viscous sub-layer beneath the waves, within the top 1 mm of the surface. The study discovered that the mean tangential stress was significantly less than wave form drag [18].

III. TURBULENT FLUXES

The theoretical approaches to the structure of turbulence and wave disturbances in the atmospheric surface layer require us to specify the vertical fluxes of momentum, heat and moisture. Thus, the models of the atmospheric surface layer must identify the physical causes of the variability in the fluxes of momentum, energy, heat and moisture, the laws governing this variability, and the mechanisms making the principal contribution to the variability of the fluxes. In the customary terminology, the problem consists of determining the factors causing the drag of the ocean surface and the laws of heat and mass transfer between ocean and atmosphere.

The development of detailed models that could answer the above questions is made difficult by the important fact that the fluxes of momentum and energy between the atmosphere and ocean are expended on the generation and maintenance of waves, currents and turbulence. But the question remains as to how the fluxes are distributed between these three dynamically different components of motion. So far, no definitive answer to this problem has been found. The most popular approach in practical calculations is the simple hypothesis that the dimensionless coefficients of drag, heat transfer, and evaporation are constant and of approximately equal magnitude, roughly 10^{-3}. The numerical estimates of the coefficients are consistent with the mean values obtained by averaging all available measurements. According to measurements taken by numerous researchers [2-5, 7, 8, 10, 11, 27], the coefficients of drag, heat transfer and evaporation range over two orders of magnitude, from 10^{-4} to 10^{-2}. The physical basis for the assumption of constant coefficients is the conclusion, based on an analysis of experimental data, that surface waves exert a strong influence on the aerodynamic characteristics of the sea surface. Since wind waves are rapidly converted to equilibrium waves, the accepted figure for the coefficients corresponds precisely to this case. A correction for variations in the interaction between the boundary layer of the atmosphere with the ocean was made by the researchers noted above. They employ empirical equations to present the interaction coefficients as functions of the wind speed. These equations, as one can see in [11], generally have the same level of error as the hypothesis, as they are constant.

Theoretical models of the interactions between the turbulent boundary layers of the atmosphere and ocean, developed from the simplest models with a constant turbulent viscosity to k - ε turbulent model, can be used to estimate the magnitude of interaction, neglecting the energetic of wind waves. But these calculations do not explain the actual variability of the interaction parameters.

Simple estimates of the interaction between wind and waves indicate that wind waves are very energy-intensive and accumulate a considerable fraction of the total momentum and energy of the atmospheric boundary layer; the flux of momentum to the waves is comparable in magnitude to the total flux of momentum to the sea surface, and the influence of waves is not confined to the dynamic characteristics of the atmospheric boundary layer, but also extends to the rate of heat transfer between the ocean and the atmosphere.

The mutual adaptation of the wind and waves can be studied directly via the integral laws of conservation of momentum and energy in the atmospheric boundary layer and in surface waves [11, 14, 28], using integral methods that are common in the classical boundary layer theory, the main principles of the theory of wind waves [1, 29] and the mechanism of wind wave breaking described by Longuet-Higgins [30].

The equations for the wave momentum and energy, in the case of horizontally uniform waves, finally yield an evolutionary equation for the phase velocity $C_0(t)$,

$$\rho_w \frac{\beta}{g} C_0^2 d_t C_0 = \rho_a u_*^2 - \frac{1}{3}\gamma_1 \rho_w \beta C_0^2 . \qquad (2)$$

where ρ_w is the water density, β is the Phillips' constant, the second term in the right hand side represents the wave breaking , $\gamma_1 \approx 3x10^{-4}$ is the Longuet-Higgins' constant in the wave breaking parameterization. The equations of wind momentum and energy yield the equations on $u_*(t)$ and the boundary layer thickness δ(t),

$$d_t\left[U_{a,\delta}\delta\left(\frac{u_*}{\kappa U_{a,\delta}}\right)\left(1-\frac{z_0}{\delta}\right)\right] = u_*^2, \qquad (3)$$

$$d_t\left\{ U_{a,\delta}^2\delta\left(\frac{u_*}{\kappa U_{a,\delta}}\right)\left[1-\frac{u_*}{\kappa U_{a,\delta}}\left(1-\frac{z_0}{\delta}\right)\right]\right\} = \qquad (4)$$

$$= u_*^2\left(\gamma U_{a,\delta} + C_0\right),$$

$$\frac{z_0}{\kappa} = \exp\left(-\frac{\kappa U_{a,\delta}}{u_*}\right), \qquad (5)$$

where $U_{a,\delta}$ is the known wind velocity at the upper boundary of atmospheric boundary layer $z = \delta(t)$, γ is the dimensionless dissipation constant. For developed waves, the wave equation (2) defines two dimensionless parameters – the root mean square wave elevation $g\sigma_\eta / u_* = a_1$ and the frequency of wave spectral peak $\omega_0 u_*/g = a_2$. Calculated and well known experimental appraisals conform with one another better than one could expect. The asymptotic analysis of (2) - (5) shows that the drag coefficient of sea surface in the fully developed wave case reduces to a value which is about the drag coefficient of smooth flow.

The generation of wind waves consists of the following two main stages: 1) the generation of non-collapsing waves, in which there is little collapse and the evolution of the atmospheric boundary layer and the waves is not affected and 2) the concluding stage, in which effective wave breaking occurs. Calculations indicate that the principal factor governing the dynamic properties of the atmospheric boundary layer above the sea and the state of the underlying surface is the ratio of the phase velocity of the spectral peak of the wind waves to the friction velocity; this finding corresponds well to numerous measurements, and this approach explains the observed variation in the characteristics of the atmospheric boundary layer(Figures 2-5), since the surface waves are able to adapt themselves to particular wind conditions, and it also can be used to derive numerous empirical equations for developed wind waves. Allowing for wave breaking makes it possible to trace the evolution of the wind and waves all the way to the equilibrium steady state. The theory can be used to derive practically all known empirical equations related with the characteristics of the atmospheric surface layer and to find the limiting law of drag of the sea surface, which is qualitatively very similar to the experimental figures obtained in 1960 for Hurricane Donna[4].

Several modified models were developed to incorporate the characteristics of the atmospheric boundary layer and the sea waves (Gumbatov, Mamedov, 1983; Belberov, 1985; Akhmetov et al., 1987); these models were in agreement with measurements.

The full integral model (2) - (5) extends the previous results. The following important result from the full model is worth noting: this theory makes it possible to calculate the flux of momentum to waves, the amount of the momentum flux from the wave breaking that is consumed in the generation of drift currents, the flux of energy to the waves, and the amount of the flux energy from the wave breaking that is used in the generation of turbulence in the upper layer. This model can also be used to construct a theory of heat transfer [11] in the course of the development of wind waves which qualitatively agrees with measurements [24].

Measurements were taken of the dynamic and thermodynamic characteristics of the surface layer above water that govern its vertical and local structure (see for example [6, 22-24, 31]). These studies indicate that these quantities are highly dependent on the degree of development of the waves. Figures 2 shows the empirical dependence, based on these observation, of the roughness length z_0 as a function of the wave age C_0/u_* (where C_0 is typical phase velocity of surface waves customarily associated with the maximum of the wave spectrum, u_* is the friction velocity) . With a certain dispersal, experimental points gather around one, universal dependence, which in a broad scope of parameter C_0/u_* change ($5 \le C_0/u_* \le 90$) can be approximated by the second order polynomial [12]:

$$\frac{1}{\kappa}\ln\left(\frac{z_v}{z_0}\right) = -3.5 + 1.29\left(\frac{C_0}{u_*}\right) - 0.0069\left(\frac{C_0}{u_*}\right)^2 \pm 5, \qquad (6)$$

where $z_v = 0.11\ \nu/ u_*$ is the roughness parameter of the smooth wall, ν is the coefficient of molecular viscosity of the air, $\kappa = 0.4$. The same data were presented in the form of the drag coefficient deviation, $\delta C_u = C_u - C_{u,smooth}$, where $C_{u,smooth}$ is the drag coefficient of "smooth" wall (Figure 3).

The both forms demonstrate strong wave influence on the drug reduction and the roughness of the ocean surface.

The equation (6) was applied for a numerical modeling of influences of ocean waves on turbulence of the air-sea system [32]. The model shows good agreements with measurements of influences of waves on wind and geostrophic drag coefficients. It is also possible to classify the cases of deviation from logarithmic law for the mean wind velocity $U_a(z)$ [6].

IV. DISCUSSION AND CONCLUSION

The wind-wave interaction produces significant impact on the atmospheric boundary layer above the ocean surface. Three fundamental features of this interaction are as follows:

1.For the "young" waves, the ocean surface behaves as a rough solid surface. The roughness parameter exceeds the thickness of laminar sub-layer and the drag coefficient may be significantly greater than it would be for a smooth surface. This regime corresponds to the strong interaction between the wind and the surface waves. The wind looses its energy and momentum and the wave grows. In the presence of developing waves ($C_0/u_* \leq 33$ 5), momentum is transferred from the wind to the waves, which ultimately causes large deviations from smoothness and gives rise to "rough" air flow conditions and agrees very well with the integral model [14] and (2)-(5). One can see that the drag coefficient, observed and predicted, reduces about ten times (Figure 4), and that yields the variability of roughness parameter $gz_0 / \overline{U}_a^2$ ranging from 10^{-1} to 10^{-7} (Figure 5).

2.When the wind waves reach the developed state, the ocean surface behavior becomes similar to the smooth solid surface. The fluxes of wind energy and momentum balance the losses which the waves experience by breaking. In this intermediate situation ($C_0/u_* \approx 33$ 5) and the ocean surface is nearly aerodynamically smooth ($z_0 \approx z_v$), the waves usually may be treated as developed and thus as largely unaffected by the wind (that corresponds an asymptotic state of interaction between wind and waves in the model), so that the entire flux of momentum from the atmosphere ultimately is imparted to currents rather than to the waves as a result of viscous friction with the underlying surface and the wave breaking. In this case, according to the recent measurement [19], the wave breaking mechanism dominates in transmitting the momentum to the drift current. Figure 6 shows, by the asymptotic solution of (2) - (5) and the data of the Marine Hydrophysics Institute wind-wave tank by Leikin and Rosenberg, how the equilibrium state between wind and waves establishes in terms of the ratio $\overline{U}_a / C_0$. One can see that the theoretical prediction with $\gamma = 0.5$ and the deep water data ($\overline{U}_a$ = 3 m/s) meet the same limit value.

3.The "old" waves are not associated with the local wind condition, except propagating in the same direction as the local wind. The ocean surface becomes "oversmoothed". The roughness parameter becomes less than the thickness of laminar sub-layer and the drag coefficient becomes less than it would be for a smooth solid surface under the same wind conditions. In this case, the waves transfer their energy and momentum to the atmospheric boundary layer. When swells are present or in a situation of slackening winds but with already developed waves($C_0/u_* \geq 33$ 5), the atmospheric boundary layer receives additional momentum from the waves and "oversmoothed" conditions of air flow over the sea surface occur. This means that the waves play role of a propulsive force with respect to the air boundary layer.

V. REFERENCES

1. O. M. Phillips, "The Dynamics of the Upper Ocean. Cambridge University Press", 1966.
2. S.A. Kitaygorodskiy "The Physics of Air-Sea Interaction", Israel Programs for Translation, Jerusalem, 1973.
3. A. S. Dubov "Transfer Processes Near an Interface", Gidrometeoizdat, Leningrad, 240 pp.,1974.
4. S.S. Zilitinkevich, A. S. Monin, And D.V. Chalikov "Interaction Between the Ocean and Atmosphere", In: Oceanology. Physics of the Ocean. Vol.1. Hydrophysics of the Ocean. Nauka Press, Moscow, pp. 208-339,1978.
5. E.K. Byutner "Dynamic of the Atmospheric Surface Layer", Gidrometeoizdat, Leningrad, 158 pp., 1978.
6. V.V. Yefimov "Dynamics of Wave Processes in the Atmospheric and Oceanic Boundary Layers", Naukova Dumka Press, Kiev, 256 pp., 1981.
7. G.N. Panin "Heat and Mass Transfer Between a Water Body and the Atmosphere Under Natural Conditions", Nauka Press, Moscow, 206 pp., 1985.
8. R.S. Bortkovskii "Air-Sea Exchange of Heat of Moisture During Storms", D. Reidel Pub.Co. 159 pp., 1987.
9. K.N. Fedorov, A I Ginzburg "The Near-Surface Ocean Layer", Gidrometeoizdat, Leningrad, 1988.
10. G.L Geernaert and W.L. Plant, (Ed.) "Surface Waves and Fluxes, Volume 1 - Current Theory", Kluwer Academic Publishers, 336 pp., 1990.
11. B.A. Kagan "Ocean - Atmosphere Interaction and Climate Modeling", Cambridge University Press, 377 pp. , 1995.
12. A.Y. Benilov "Influence of Surface Waves on the Atmosphere Turbulent Boundary Layer", In: Numerical methods in laminar & turbulent flow, vol. 9, Pineridge Press, Swansea, U.K., pp. 960-971, 1995.
13. B. Benjamin "Shearing Flow Over a Wavy Boundary", J.Fluid Mech., v.66, 1959.
14. A.Y. Benilov, A. I. Gumbatov et al. "Nonsteady - State Model of the Development of the Turbulent Boundary Layer above the Sea with Generation of Surface Waves", Izv.Ac.Sci.USSR,Atm.Ocean.Phys., v. 14, No.11, 1978.
15. A.Y. Benilov "Dynamic Structure of the Upper Ocean Including The Effects of Surface Waves and Breaking", TR-SIT-DL Project No. 5540, Stevens Institute of Technology, Hoboken, NJ, 53 pp., 1997
16.A.S. Monin and A.M. Yaglom "Statistical Fluid Mechanics: Mechanics of Turbulence. Vol.1 -2", MIT Press, 1987.
17. V. Kader and A. M. Yaglom "Mean Fields and Fluctuation Moments in Unstably Stratified Turbulent Boundary Layers", J. Fluid Mech.,v. 212, pp. 637-662,1990.
18. M.L. Banner "The Influence of Wave Breaking on the Surface Pressure Distribution in Wind-Wave Interactions", J.Fluid Mech., v.211, 463-495, 1990.
19. M.L. Banner and W.L. Peirson "Aerodynamic Roughness of the Sea Surface". Johns Hopkins Conference in Environmental Fluid Mechanics, pp. 13-14, 1998.
20. D.V. Chalikov "Numerical Simulation of the Boundary Layer Above Waves", Boundary Layer Meteorology, v. 43, No. 1, pp. 63-98, 1986.
21.D.V. Chalikov "The Parameterization of the Wave Boundary Layer", Journal of Physical Oceanography, v.25, No.6, Part 1, pp. 1333-1349, 1995.
22. Y.A. Volkov "Spectra of Velocity and Temperature Fluctuations of the Air Flow Above a Surface". Izv. Ac. Sci. USSR, Atm. Ocean .Phys., v.5, No.12, pp.1251-1265, 1969.
23.V.I. Makova "Characteristics of the Dynamic Regime of Turbulence in the Atmospheric Surface Layer in Various Stages of Wave Development", Izv. AC. Sci. USSR, Atm. Ocean. Phys., v. 11, No. 3, pp.297-307, 1975.
24. A.S. Aliyev, S. L. Zubkovskiy, and L. R. Tsvang "Universal Functions for Atmospheric Turbulence Above the Sea", In: Atmospheric Physics and the Problem of Climate, Nauka Press, Moscow, pp.194-215, 1980.
25. A.Y. Benilov, O.A. Kuznetsov, and G.N. Panin "On the Analysis of Wind Wave-Induced Disturbances in the Atmospheric Turbulent Surface Layer", Boundary Layer Meteorology, v. 6, No. 1-2, pp. 269-285, 1974.
26.M.A. Donelan "The dependence of aerodynamic drag coefficient on wave parameters", In: Proceedings of the First International Conference on Meteorology and Coast Zone, Boston, MA, Amer.Meteorol.Soc. 381-387, 1982.
27.G.L. Geernaert, G L, K Katsaros, and K Richer "Variation of the drag coefficient and its dependence on sea state", J.Gephys.Res., v.91, 7667-7679, 1986.
28.A.Y. Benilov "On the Interaction of the Wind Field with Waves on a Shallow Sea", In: Interaction of the Atmosphere, Hydrosphere and Lithosphere in the Coastal Zone of the Sea. The Kamchiya -79 Experiment, Sofia, Bulgarian Academy of Sciences, pp. 175-184, 1983.
29.V.E. Zaharov and M. M. Zaslavskii "Kinetic Equation and Kolmogorov Spectra in the Weakly Turbulent Theory of Wind Waves", Izv. Ac. Sci. USSR, Atm. Ocean. Phys., v. 18, No. 9, pp.970-979, 1982.
30.M.S. Longuet-Higgins " On Wave Breaking and the Equilibrium Spectrum of Wind-Generated Waves. Proc. Roy. Soc., A 310, No. 1501, pp. 151-159, 1969.
31. A.Y. Benilov, A. I. Gumbatov et al. "Interpretation of Measurements of the Mean Wind Speed in the Atmospheric Surface Layer", Izv. Ac. Sci. USSR., Atm. Ocean. Phys., v. 12, No 10, pp. 1011-1019, 1976.
32.L.N. Ly and P. Luong "A mathmatical coastal ocean circulation system with breaking waves and numerical grid generation", Applied Mathematical Modeling, v. 10, No. 10, 633-641, 1998.

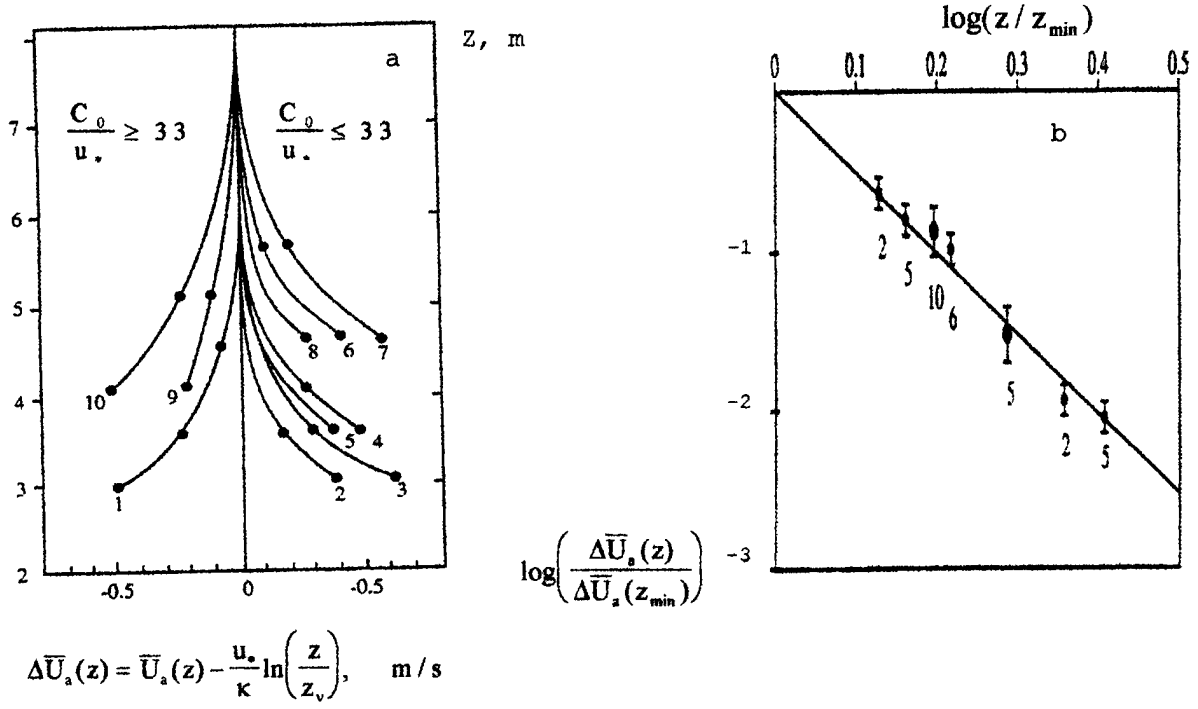

Figure 1. Deviation of mean velocity profiles from the "logarithm"-law in the interaction sub-layer.

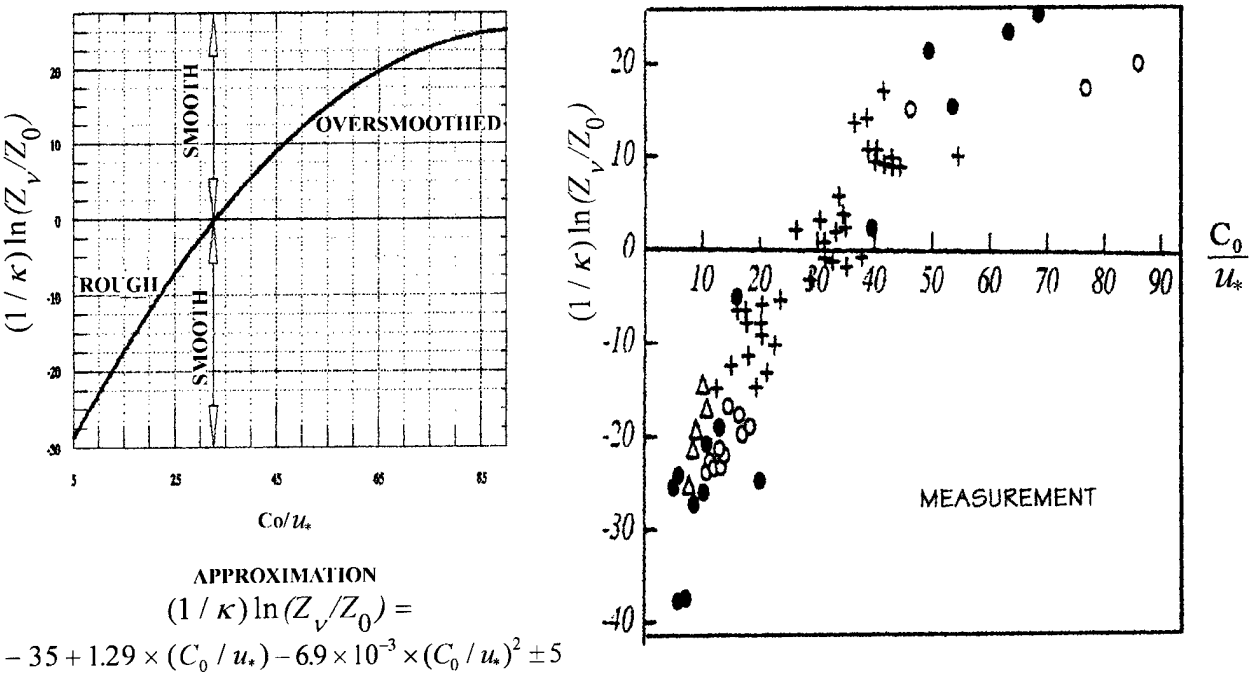

APPROXIMATION

$$(1/\kappa)\ln(Z_v/Z_0) = -35 + 1.29 \times (C_0/u_*) - 6.9 \times 10^{-3} \times (C_0/u_*)^2 \pm 5$$

Figure 2. Aerodinamical features of the ocean surface

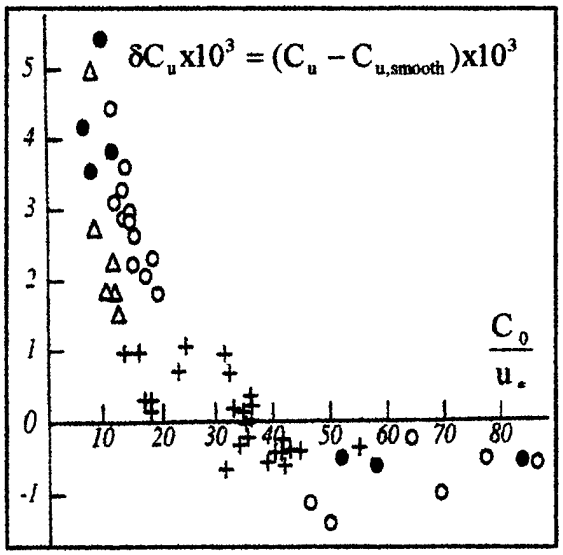

Figure 3. Sea surface drag reduction in terms of the drag coefficient deviation, $\delta C_u = C_u - C_{u,\,smooth}$, as a function of the wave age, C_0/u_*.

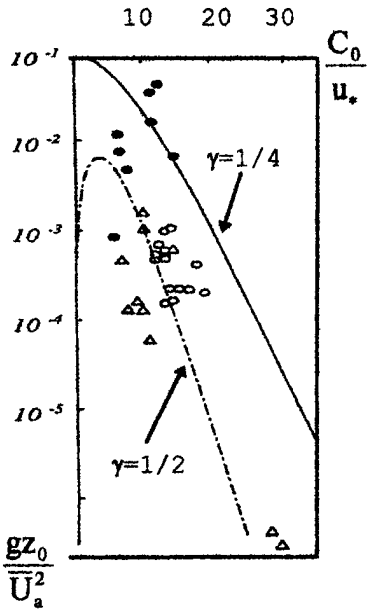

Figure 5. Roughness of the ocean surface, theory and observation.

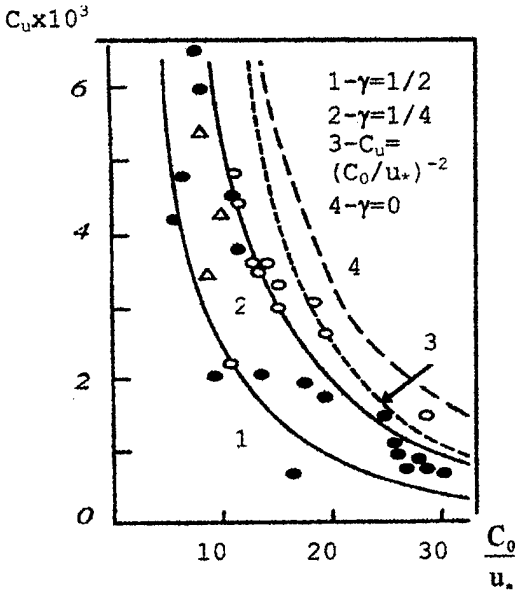

Figure 4. Drag reduction of the ocean surface -- theory and observation.

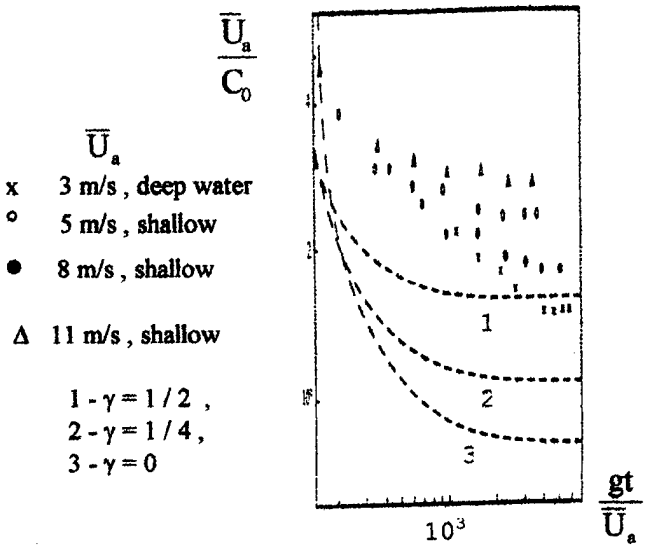

Figure 6. Phase velocity of the surface wave spectral peak in the generation regime, theory and measurement (the data of the Marine Hydrophysics Institute wind-wave tank by Leykin and Rosenberg)

BLUBBER AND COMPLIANT COATINGS FOR DRAG REDUCTION IN FLUIDS: V. DRIVING POINT SHEAR IMPEDANCE MEASUREMENTS ON COMPLIANT SURFACES

Edwin R. Fitzgerald
Johns Hopkins University
3400 N. Charles St.
Baltimore, MD 21218

James W. Fitzgerald
Kildare Corporation
1 Spar Yard St.
New London, CT 06320

Abstract - An automated dynamic mechanical measurement system for complex shear compliance, $J^* = J' - iJ''$, and shear modulus, $G^* = G' + iG'' = 1/J^*$, from 2 to 10,000 Hz has been used to obtain these viscoelastic parameters for excised samples of dolphin blubber and skin at 21°C from 2 to 1000 Hz as previously described. This measurement system has been modified to allow determinations of complex driving point shear impedance (force/velocity) on compliant surfaces, including living animal tissues. Shear impedance measurements are reported for compliant polymer gel-foam composite coatings with viscoelastic properties close to those of dolphin blubber for small wafer-shaped samples with vibrational shearing forces across their entire faces, and for extended sheets where the shear force vibrator acts on only a portion of the sheet surface. This later type of in situ shear impedance measurement has been made on compliant coatings of several discs used for rotating disc drag measurements which show a drag reduction and a delay in the onset of turbulence compared to drag measurements of an uncoated, rigid disc of the same dimensions. These results are in accord with the matched shear impedance explanation of low dolphin drag, and suggest the possibility of in situ surface shear impedance measurements on live dolphins to get improved values of their viscoelastic properties and increased drag reduction.

I. INTRODUCTION

The matched shear impedance explanation of low dolphin drag requires viscoelastic properties of the skin and blubber so that they act as a compliant layer load of shear impedance, Z_L, which matches the effective shear impedance, Z_O, of incipient boundary layer turbulence acting as an equivalent shear force generator. With matched impedances, maximum power transfer and energy absorption in the blubber dampens the incipient turbulence, maintains laminar flow, and provides drag reduction [1, 2]. Measurements from 2 to 1000 Hz of complex shear compliance and modulus, $J^* = J' - iJ''$ and $G^* = G' + iG''$, on excised blubber samples vs. time after death allow extrapolation to 0 hours to get "live" values as illustrated in Fig. 1 for blubber and skin from a stranded harbor seal for which rescue efforts failed [3]; similar measurements on excised samples of blubber from a stranded dolphin gave the frequency dependences of the elastic, J', G', and viscous, J'', G'', components of compliance and modulus for "live" dolphin blubber as shown in Fig. 2. Also shown in Fig. 2 are the corresponding elastic and viscous compliance and modulus components for two polymer gel-foam composites that match closely the dolphin blubber viscoelastic properties [4,5]. An equivalent mechanical circuit representation of turbulent flow over a compliant surface suggests that the dolphin load impedance depends chiefly on the blubber, but also on a parallel terminal impedance from the dolphin muscle and skeleton [2]. In order to get direct measurements of driving point shear impedance on live dolphins, a mobile automated measurement system has been designed. The present system for small, wafer- shaped samples has been modified also to make driving point shear impedance measurements on extended surfaces such as the compliant coatings on large discs used for rotating drag measurement, and to allow in situ surface impedance measurements on live animal tissues.

II. MEASUREMENT METHOD

An automated dynamic mechanical measurement system for the elastic and viscous components of complex shear compliance, modulus, loss tangent, $J''/J' = G''/G'$, and shear wave velocity and attenuation was used to get the frequency dependence of compliance and modulus for the dolphin blubber and the compliant coating composites shown in Fig. 2. In this system a rigid plate, with fine wire embedded flat coils suspended transversely to permanent magnetic fields, B_1, B_2, is used to vibrate the surfaces of a pair of small wafer-shaped samples clamped between the plate and fixed outer blocks. An oscillating electric current, I^*_1 through one of the coils of length, ℓ_1, produces a vibrating force, $F^*_1 = B_1\ell_1 I^*_1$, which moves the plate and a second coil of length, ℓ_2, with velocity, v^*, so that a motional emf, $E^*_2 = B_2\ell_2 v^*$ is generated in tne second coil. The impedance

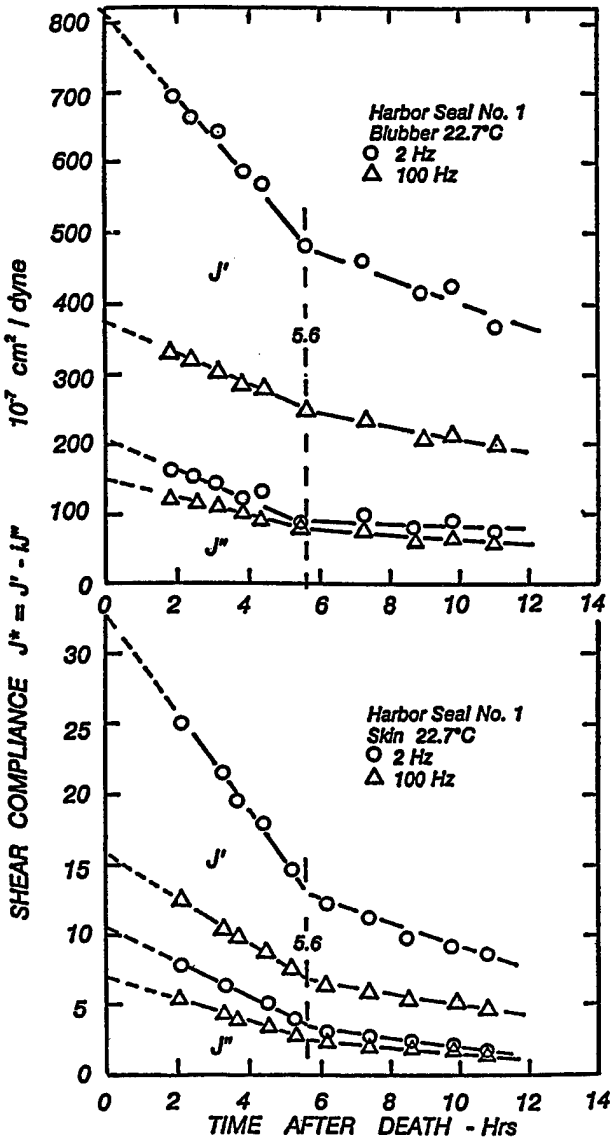

Figure 1. Time after death variation of shear compliance elastic (J') and viscous (J'') components for harbor seal blubber and skin; extrapolations to 0 hours give "live" tissue values.

(force/velocity) of the plate, without samples, is,

$$Z_{MP}^* = F_1^* / v_2^* = B_1 \ell_1 B_2 \ell_2 I_1^* / E_2^* \quad (1)$$

With a pair of samples clamped against the plate the impedance is,

$$Z_{MT}^* = B_1 \ell_1 B_2 \ell_2 I_1'^* / E_2'^* , \quad (2)$$

and the sample impedance is $Z_{MS}^* = Z_{MT}^* - Z_{MP}^*$. For samples of cross sectional area, 2A, and thickness, h, the shear compliance for sinusoidal current and force at frequency, f, is,

$$J^* = (-i Y_{MS}^* 2A/h) / 2\pi f , \quad (3)$$

where $Y_{MS}^* = 1 / Z_{MS}^*$. The mechanical parameters are thus found in terms of an electrical transfer admittance, $Y_{12}^* = I_1^* / E_2^*$. The system has a range from 2 to 10,000 Hz at temperatures from -50 to 150°C. A complete description is given in several publications [6,7].

Sample pairs of dimensions 1.25 in. x 1.25 in. x .125 in. thick, or smaller and thinner, have been measured in the standard electromagnetic transducer shown in schematic cross section in Fig. 3A, but a small, offset extension at the end of the drive plate is needed for the driving point shear impedance determinations as depicted in Fig. 3B. The area in contact with the surfaces measured is 0.7 x 0.6 in. giving an area of 0.42 in^2, (2.71 cm^2). In order to make certain that slipping is not present, measurements are made at current/force values varied by a factor of two; if measured impedance values are unchanged, slipping is absent, and the force-deformation response can be considered as linear.

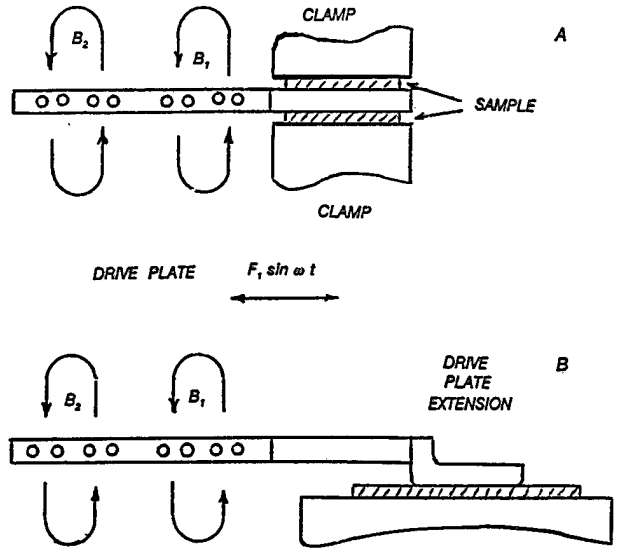

Figure 3. A. Schematic cross section of transducer drive plate with force coil 1 in magnetic field B_1 and velocity coil 2 in field B_2. The entire inner faces of the sample pair are subject to the vibrating shear force. B. Modifided drive plate with an extension to measure driving point shear impedance of a portion of a surface.

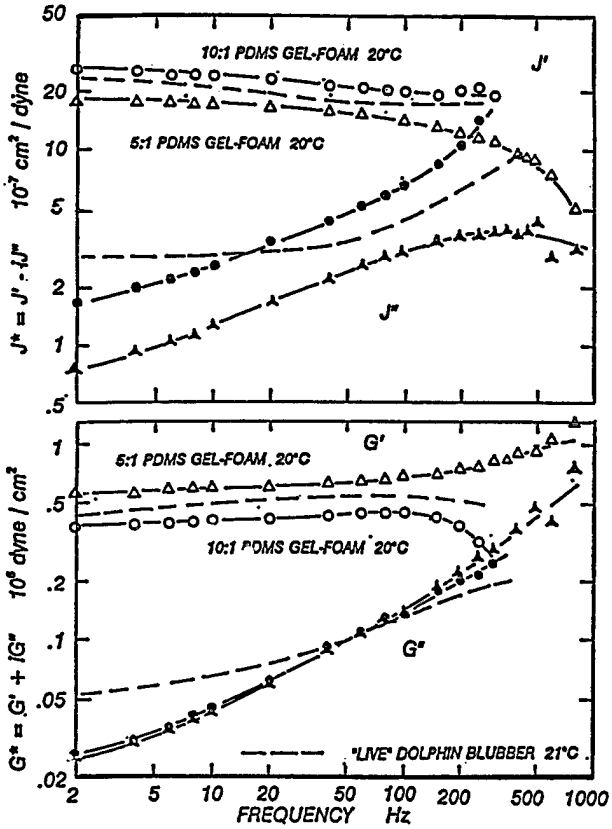

Figure 2. Frequency variation of shear compliance and modulus, J*, G*, for "live" dolphin blubber (dashed lines) matched by 10:1 (circles) and 5:1 (triangles) polymer:curing agent polydimethyl siloxane (PDMS) gel-foam composites.

III. DRIVING POINT SHEAR IMPEDANCE OF COATED DISCS

Surface shear impedance measurements were made at eight equally spaced locations around each face of 20-cm diameter discs coated with 0.5 and 1.0 cm thick layers of polymethyl siloxane gel-polyurethane foam composites as shown in Fig. 4. Mean values of the 8 complex impedance components ($Z_{MD}^* = R_{MD} - iX_{MD}$) measured for each side of the disc were found, and are displayed in the logarithmic plot of Fig. 5. From this figure it is evident that the impedance is essentially the same for the disc with 1.0 cm thick coating and the disc with the 0.5 cm thick coating.

The disc coatings were built up from 0.125 in. thick gel-foam layers cemented together and cured at 120°C for 1 hour under moderate pressure. After completion of the in situ impedance measurements, several layers of gel-foam were removed and cut into sheets 2 in. x 3 in., 2 in. x 2 in., and 1 in. x 2 in. and thicknesses of .115 in. and .205 in. Driving point shear impedances were again found to be independent of thickness, but increased some as the sheet size increased.

Samples of the gel-foam coating of the same size as the 0.7 in. x 0.6 in. contact face of the drive plate extension gave values of complex compliance from 2 to 400 Hz calculated by Equation 3 that closely matched the values of sample pairs measured in the unmodified transducer. The shear impedance in this case, measured for two different sample thicknesses, was inversely proportional to thickness for the same sample area as expected from Equation 3. The dynamic mechanical measurements of samples where the entire sample face is subject to the shear force give absolute compliance values, J, that vary from J = 10.5 to 8 MPa^{-1} at 20°C compared to "live" dolphin values of 23 to 19 MPa^{-1} (10^{-7} cm^2 / dyne) at frequencies from 2 to 1000 Hz at 21°C. The compliant coatings on these discs, therefore did not match the "live" dolphin blubber viscoelastic properties as well as the polymer gel-foam composites of Fig. 2. However, the match was close enough to reduce drag, and to delay the onset of turbulencce from 210 rpm to 260 rpm compared to a rigid, uncoated disc as shown in Fig. 6. This corresponds to a Reynold's No. transition delay from Re =2.2 x 10^5 to 2.7 x 10^5.

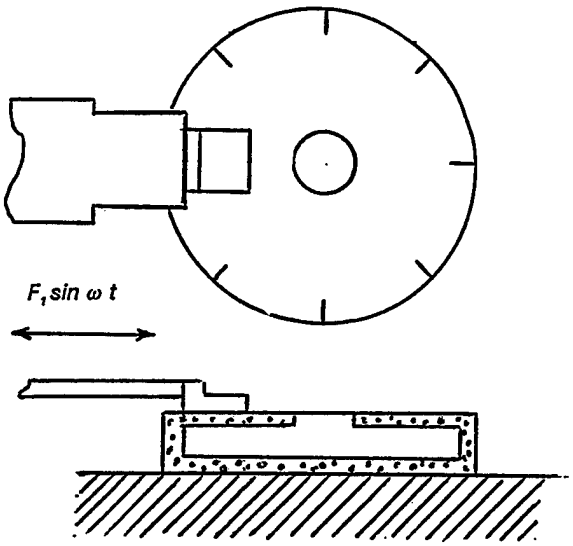

Figure 4. Schematic top and side views of the modified drive plate of Fig. 3B in position to measure driving point shear impedance at 1 of 8 places along the edge surfaces (top and bottom) of compliant coatings on discs used for rotating disc drag measurements.

IV. DRIVING POINT SHEAR IMPEDANCE OF THIN SHEETS

The modified driving plate with a 0.6 in. x 0.7 in. vibrator surface was used to get some preliminary information on the effect of sheet size and thickness; the sheets were taken from the compliant coatings on the discs used for rotating drag measurements.

Table I. Size effects on 20°C driving point shear impedance of polymer gel-foam sheets .115 and .205 in. thick .

Sheet Size LxW	Thickness in.	Vibration Direction	Area Ratio*	Shear Impedance Magnitude Z_M 10^4 dyne -sec/cm 2 Hz to 300 Hz	
2.2x2.2	.110	2.2	11.5	140	3.30
2.2x3.0	.110	3.0	15.7	170	4.13
2.2x2.2	.205	2.2	11.5	151	2.90
2.2x3.0	.205	3.0	15.7	165	3.44
2.2x2.2	.205	2.2	11.5	151	2.90
3.0x2.2	.205	2.2	15.7	168	3.09

*Sheet /vibrator

From Table I some very tentative conclusions can be stated: (1) Impedance increases with size of the sheet relative to the area acted on by the force vibrator; (2) the impedance is independent of thickness for sheet/vibrator area ratios greater than 10; (3) If the vibrating force acts over the entire sample area, impedance depends directly on sample area, and inversely on thickness.

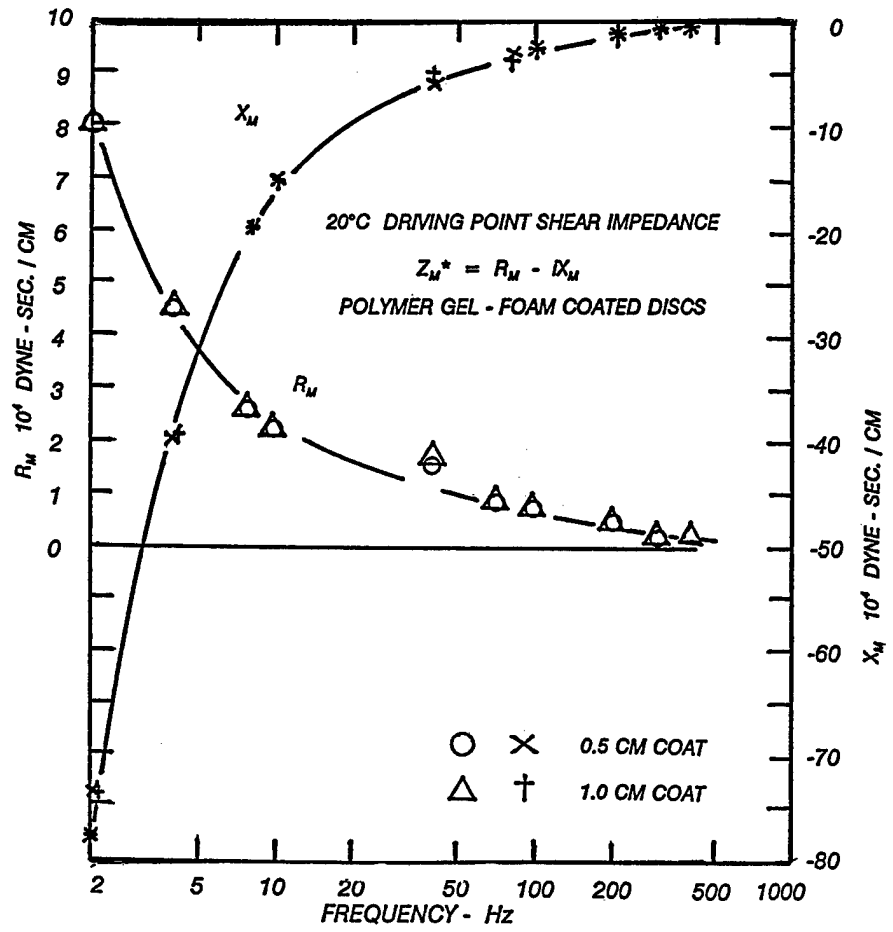

FIGURE 5. Frequency variation at 20°C of resistive (R_M) and reactive (X_M) components of driving point shear impedance of 0.5 cm (circles, crosses), and 1.0 cm thick (triangles, daggers) polymethyl siloxane gel-polyurethane foam coatings measured in place on 20-cam diameter discs used for rotating disc drag measurements of Figure 6.

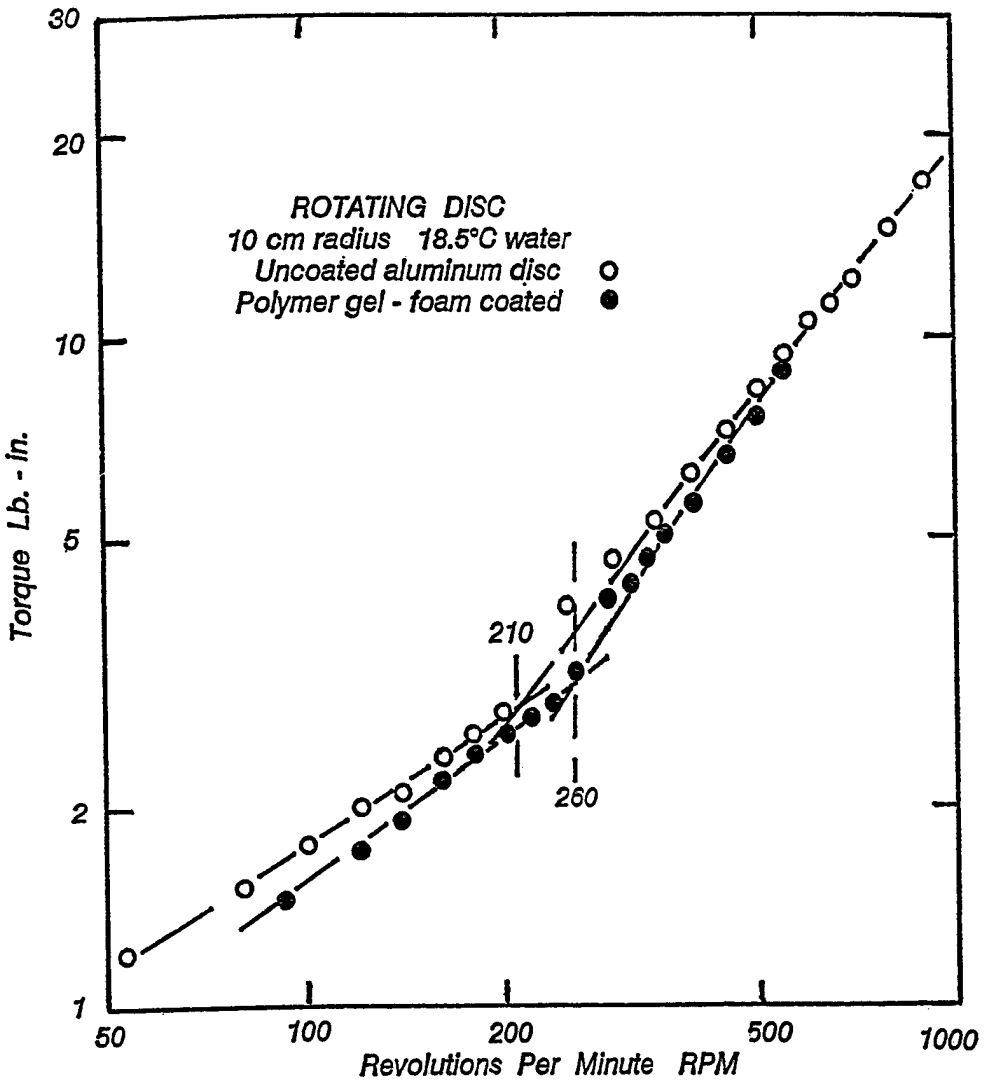

Figure 6. Drag torque vs revolutions per minute (rpm) for a rigid reference disc (open circles), and for a coated disc with a .485 cm thick polymethyl siloxane gel-polyurethane foam and a smooth .015 cm thick natural rubber latex cover (filled circles). The rigid disc has a laminar to turbulent flow transition at 210 rpm, but the 0.5 cm thick polymer gel-foam-latex coated disc transition is delayed to 260 rpm. This corresponds to a Reynold's No. transition delay from 2.2×10^5 to 2.7×10^5. Results for a 1.0 cm thick coating are similar with a 260 rpm transition.

V. CONCLUSIONS

Drag reduction and delayed laminar to turbulent flow in water have been found for 10 cm radius, 4.5 cm thick, rotating discs coated with a polymer gel-foam composite with viscoelastic properties close to those measured for "live" dolphin blubber. Preliminary measurements are reported of driving point shear impedance on portions of surfaces on polymer gel-foam coated drag discs, and on small sheets of the same composites. These measurements were made with a modification of the present automated system for dynamic mechanical measurements on small, wafer-shaped samples where the entire sample surfaces are subject to a vibrational shear force. Prior measurements were made on excised blubber from a stranded dolphin for which rescue efforts failed; extrapolation to 0 hours of shear compliance vs time after death was needed to get "live" tissue values. Surface shear impedance measurements made, in situ, on live dolphins will give more information on their viscoelastic properties that could lead to improved drag reduction in sea water.

VI. REFERENCES

1. E.R. Fitzgerald and J.W. Fitzgerald " Blubber and Compliant Coatings for Drag Reduction in Fluids I. " *Proc. 2nd Int'l. Conf. Intel. Mt'ls.* 510-522, 1994; *Mtls. Sci. & Engr.* **2** 209-214, 1995

2. J.W. Fitzgerald, E.R. Fitzgerald, W.M. Carey, and W.A. Von Winkle "Blubber and Compliant Coatings for Drag Reduction in Fluids II." *Proc. 2nd Int'l. Conf. Intel. Mt'ls.* 523-533, 1994; *Mtls. Sci. & Engr. C* **2** 215-220, 1995

3. E.R. Fitzgerald "Dynamic Mechanical Measurements of Marine Mammal Tissues" *J. Acoust. Soc. Am.* **101** 2163, 1997

4. E.R. Fitzgerald and J.W. Fitzgerald "Blubber and Compliant Coatings for Drag Reduction in Fluids III." *3rd ICIM/ECSS'96 SPIE* vol **2779** 83-88, 1996

5. J.W. Fitzgerald, E.R. Fitzgerald and J.E. Martin "Blubber and Compliant Coatings for Drag Reduction in Fluids IV." *4th ECSS'98* (Proc. to be published)

6. E.R Fitzgerald "Automated Measurement System For Dynamic Mechanical Properties" *Proc. Am. Chem. Soc. Div. Polymeric Mater. Sci.* **60** 573-578, 1989; *7. U.S. Patent* No. 5,081,872, 1992

BLUBBER AND COMPLIANT COATINGS FOR DRAG REDUCTION IN FLUIDS: VI. ROTATING DISC APPARATUS FOR DRAG MEASUREMENT ON COMPLIANT LAYERS

James W. Fitzgerald, James E. Martin, and Eugene F. Modert
The Kildare Corporation; One Spar Yard Street, New London, CT 06320

Abstract - The "Matched Shear Impedance Hypothesis for Compliant Layer Control of Boundary Layer Turbulence" requires that the shear impedance of the compliant layer match that of the turbulent boundary layer, which is viewed as a fluctuating shear-force generator. Under matched conditions, energy is transferred from the incipient turbulence into the compliant layer and absorbed by viscous losses . . .thus delaying the onset of turbulence. The dolphins thick blubber, not it's thin skin, is viewed as such a matched load. Previous efforts in these continuing studies have developed candidate compliant materials that have complex dynamic shear compliances (J* = J' - iJ") close to those of blubber. The rotating disc apparatus of this study was developed to measure the torque (drag) of these materials. Initial measurements reported herein indicate that blubber-like compliant materials do, indeed, delay the onset of turbulence. Harder materials appear to have no effect, whereas softer materials develop surface "ripplings" that increases drag. These preliminary results appear to confirm the matched impedance hypothesis.

I. INTRODUCTION

After some 40 years of extensive investigations, the issue of whether or not compliant surfaces can reduce hydrodynamic drag remains unresolved [1]. Based on Kramer's [2, 3] initial identification of the dolphin's skin as the basic mechanism, most of the past work has concentrated on thin (~0.3cm) compliant coatings. The various proposed hydrodynamic models [4, 5, 6] suggest that the compliant surface deflects in some preferred manner and interacts with the boundary layer Tollmein-Schlicting waves so as to reduce their stability, therby delaying the transition from laminar to turbulent flow. Surprisingly, in spite of the extensive past work by many investigators, in most cases the compliant surface being studied has not been adequately characterized by measurement of its dynamic complex viscoelastic properties .

The "Matched Shear Impedance Hypothesis for Compliant Layer Control of Boundary Layer Turbulence" takes a completely different approach to the problem, more akin to "acoustics" then "hydrodynamics" (Figure 1). This model's [7, 8, 9, 10] basic postulates are:

> The turbulent boundary layer (TBL) is viewed as a fluctuating "shear stress generator" coupled to the "compliant-layer load" through the viscous "inner boundary layer".
>
> To transfer appreciable "fluctuating" energy (power) from the TBL shear-stress generator to the compliant-layer load, the shear impedance of the load must be "matched" to the shear impedance of the TBL generator.
>
> Under matched load conditions, the build-up of the fluctuating energy of incipient turbulence is reduced by energy flow into the compliant layer where it is dissipated by losses in the viscoelastic compliant layer material, thus delaying the onset of turbulence.
>
> Dolphin blubber represents just such a matched-load with the required high loss tangent.

Figure 2 shows an equivalent circuit representation of the Matched Shear Impedance Hypothesis.

II. ROTATING DISC APPARATUS

Most of the preceding investigations of hydrodynamic flow over compliant surfaces have been deficient in one or more of the following areas:

> Concentration on the thin skin of the dolphin rather than the thick blubber.
>
> Not characterizing the compliance of the surface by measurements of the dynamic complex shear compliance (J* = J' - iJ") and, hence, the driving-point shear impedance.
>
> Lack of a convenient laboratory method of measuring the drag, with sufficient precision and under controlled conditions.

The rotating disc apparatus of this paper addresses the last of these deficiencies.

Pioneering work utilizing rotating disc apparatus for studying flow over compliant surfaces was done by Hansen & Hunston [11,12]. Their apparatus used thin discs ~0.98 cm thick by ~20.9 cm diameter, and covered the range of $Re \approx 10^4$ to $Re \approx 5 \times 10^5$. The compliant coatings were thin (~0.34 cm) soft plastisols ($|J^*| \approx 3 \times 10^{-4}$ cm^2 / dyne) that developed surface instabilities, accompanied by a marked increase in torque (drag) in the vicinity of ~ $Re \approx 5 \times 10^4$. Another set of rotating disc experiments were made by Chung & Merrill [13] on thin coatings of a soft silicone rubber with a diluent silicone oil. Again, a pronounced rippling of the surface was accompanied by a marked increase in drag as turbulence developed in the vicinity of $Re \approx 10^4$.

The isometric sketch of Figure 3 shows the rotating disc apparatus of this study. It consists of a variable speed motor connected, by means of a pulley-belt drive, to a shaft-mounted disc, rotating in a water bath. The drive-shaft has an in-line torque/rpm sensor whose outputs are read by digital meters. The equipment measures both torque (0-100lb-in) and rotational speed (0-10,000 rpm). Both analogue (± 5 volt) and digital (RS-252-C) outputs are available, in addition to the panel meters.

Figure 4 shows the design of the rotating discs. The basic rigid (aluminum) reference disc is 20 cm in diameter and 4.5 cm thick, with edges having a radius of ~0.16 cm. The molded compliant layered discs have the same outside dimensions and surface-smoothness as the rigid-reference discs; but, three different thicknesses of compliant layers: viz. 0.5 cm, 1.0 cm, and 2.0 cm. The effect of the surface compliance (i.e., the driving point impedance), if any, will be the difference between the torque of the rigid-reference disc and that of the compliant-layered disc. Significant differences in drag (torque) as small as a few percent can be determined.

In summary, the rotating disc apparatus has the following measurement capabilities:

- Rotating speed range; 60 rpm to 2250 rpm
- Torque range; 0-100 lb-in
- Compliant layer thickness; 0.5, 1.0, & 2.0 cm
- Rotating discs, 4.5 cm thick x 20 cm diameter
- Reynold's number range; 5×10^4 to 2.25×10^6
- Drag (torque) measurement precision; ~ ±0.5%
- Measurements at room temperature, only

III. APPARATUS CALIBRATION

One of the problems resulting from the required thickness of the rotating discs, particularly at the higher rotational speeds, is that the rotating disc "stirs" the bath (30" D x 24" H) into a general rotating water mass. As a result of the rotating water mass, the relative velocity of rotating disc through the water is reduced, accompanied by a reduction in torque (drag). The Himmelstein Precision Torque Meter Readout (Model 66042) and In Line Torque Sensor (Model MCRT 2901T) has an A - D conversion time of only 30 microseconds. Stability is achieved after one second, the same time base upon which the instrument output is gated. Sampling occurs as an integration of the output over each second. Measurements of torque vs time indicated that even at the highest rotational speeds, the torque remained substantially constant in a 2-4 second window and then begins to decay as the water mass rotation sets in. In effect, the disc, driven by the 2 hp electric motor, reaches its terminal rotating speed in ~1 second. Measurements made in the 2-4 second period following, represents the true

rotational speed and torque through quiescent water. We, therefore, adopted the "2nd-second" measurement method throughout our studies.

Table-I shows a series of torque measurements made on the rigid-reference disc, using the "2nd-second" method. It should be noted that these are completely independent measurements starting with a non-rotating disc in quiescent water. The mean of the 10 runs was T = 19.33 lb-in, with a standard deviation of σ =0.068. The maximum spread was only 0.20 lb-in, or ~± 0.5%. This represents a measurement precision not often encountered in hydrodynamic drag measurements.

TABLE-I: REPEATABILITY

RPM	TORQUE (lb.-in)	STATS
1000	19.3	19.33 Mean
1000	19.2	0.0675 Std Dev
1000	19.3	19.4 Max
1000	19.3	19.2 Min
1000	19.4	0.200 Spread
1000	19.3	
1000	19.4	
1000	19.4	
1000	19.3	
1000	19.4	

The customary dimensionless torque coefficient is:

$$C_T = \frac{T}{(\rho/2)\ \omega^2 R^5} \qquad (1)$$

and Reyonold's number for the rotating disc is:

$$Re = \frac{(R\ 2)(\omega)}{\upsilon} \qquad (2)$$

Where: C_T = torque coefficient; T = measured torque; ρ = density of water; ω = rotational speed; R= disc radius; Re= Reynold's number and υ = kinematic viscosity of water.

Figure 5 shows the torque vs. rpm calibration of the rigid disc. Transition from laminar to turbulent flow occurs at $\omega \approx$ 210 rpm, which corresponds to a peripheral speed of v ≈ 4.3 knots. Figure 6 shows a corresponding rigid disc drag coefficient vs. Reynolds No., with laminar-to-turbulent flow at Re≈ 2.2×10^5.

IV. REPRESENTATIVE MEASUREMENTS

Figure 7 shows the shear compliance | J* | vs frequency for some representative compliant materials from a companion study [14]. The materials are identified as follows:

PDMS - 10:1 polymer:curing agent polydimethyl siloxane gel
BLB - dolphin blubber
PMS - polymethyl siloxane gel / polyurethane foam composite
15SILR - Shore A 15 durometer silicone rubber
35NEOR - Shore A 35 durometer Neoprene rubber
55NEOR - Shore A 55 durometer Neoprene rubber

Rotating discs measurements on the Neopreme rubbers showed no perceptible drag differences from the drag measurements on the reference rigid discs. The molded 15-durometer silicone rubber discs also showed no perceptible delay of turbulence, but surface flaws may have masked any effect, and this sample will have to be remolded and rerun. No rotating disc samples have yet been made with the PDMS (polydimethyl silicone gel), but with a complex shear module of | J* | ≈ 2×10^{-5} cm / dyne, surface deflections can be expected to increase the drag.

Figure 8 shows the comparison of the transition from laminar to turbulent regimes for the rigid reference disc and the PMS (polymer gel-foam) coated disc. The transition takes place at $\omega \approx$ 210 rpm, corresponding to Re ≈ 2.2×10^5, for the rigid disc. The transition is delayed to $\omega \approx$ 260 rpm, corresponding to Re ≈ 2.7×10^5, for the PMS disc. These preliminary measurements were made with a gel-foam compliant layer not fully matched to blubber. . . | J* | ≈ 10×10^{-7} cm² / dyne for PMS as compared to | J* | ≈ 20×10^{-7} cm² / se for BLB. Moreover, the surface roughness of the gel-foam was excessive and sample preparation techniques will have to be improved.

V. CLOSING REMARKS

The gel-foam sample transition from the laminar to the turbulent regime at $\omega \approx$260 rpm corresponds to a peripheral velocity of v ≈5.8 knots. A fully matched, smooth sample could be expected to extend this delay of the onset of turbulence even further. Operational dolphins typically cruise at ~10 knots [15]. If we assume that this represents an "energy conserving" speed corresponding to the laminar-turbulent transition, a smooth fully matched compliant coated disc might be expected to extend the transition to $\omega \sim$ 448 rpm, or Re ≈ 4.7×10^5.

These preliminary rotating disc measurements appear to support the "Matched Shear Impedance Hypothesis for Compliant Boundary Layer Control of Boundary Layer Turbulence"

VI. REFERENCES

1. Gad-el-Hak,M., *Applied Mechanics Review* (1986) 39, 511-523
2. Kramer, M., *Journal of Aeronautical Science* (1957) 24, 459-460
3. Kramer, M., *Advances in Hydroscience* (1965) 2, 111-130
4. Purhouse, M., *Cambridge Unversity Ph.D. Thesis*, (1977)
5. Schlichting, H., *Boundary Layer Theory*, McGraw-Hill (1979)
6. Carpenter, D. & Garrad, A., *Journal of Fluid Mechanics* (1985), 155
7. Fitzgerald, J., *Laminar & Turbulent Boundary Layers* (1984) ASME, 91
8. Fitzgerald, J., et al, *American Chemical Soc. Mtg. Chichago, IL* (1985)
9. Fitzgerald, J., *Final Technical Report, SBIR Contr.* H66604-87-C-1742 (1988)
10. Fitzgerald, J., et al, *2nd Int. Conf. on Intelligent Materials* (1994)
11. Hansen, R. & Hunston, D., *Journal of Sound & Vibration*,(1974) 34
12. Hansen, R. & Hunston, D., *Journal of Sound & Vibration*, (1976) 46
13. Chung, K. & Merrill, E., *Compliant Coating Drag Reduction Rev. ONR* (1984)
14. Fitzgerald, J., et al, *4th ECSS* (1998) - to be published
15. Fitzgerald, J. *Naval Institute Proceedings*, p. 12-13 (Dec. 1997)

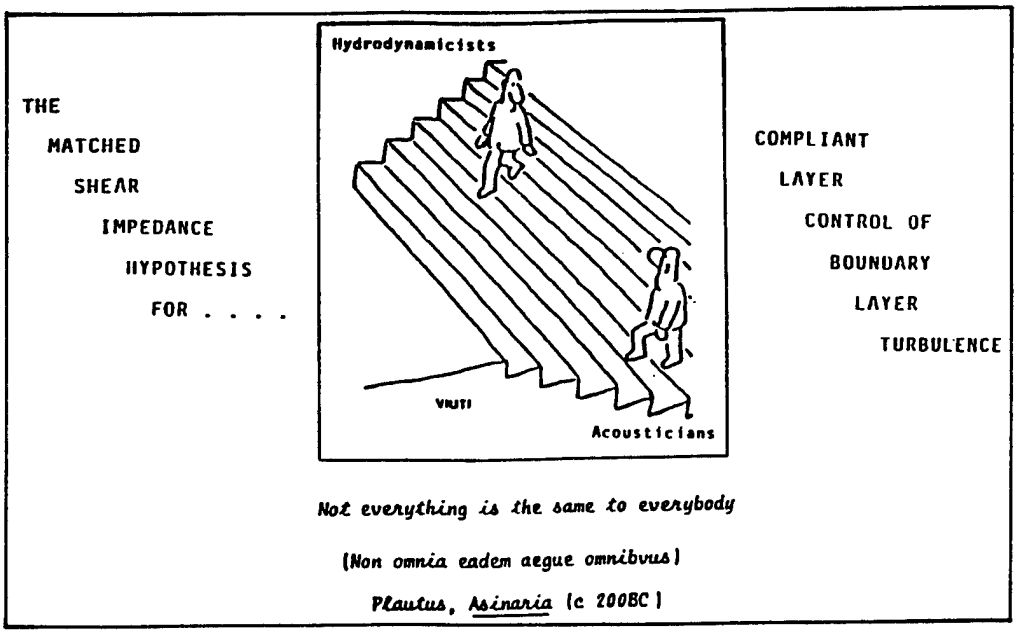

Figure 1: Hydrodynamics vs. Acoustics

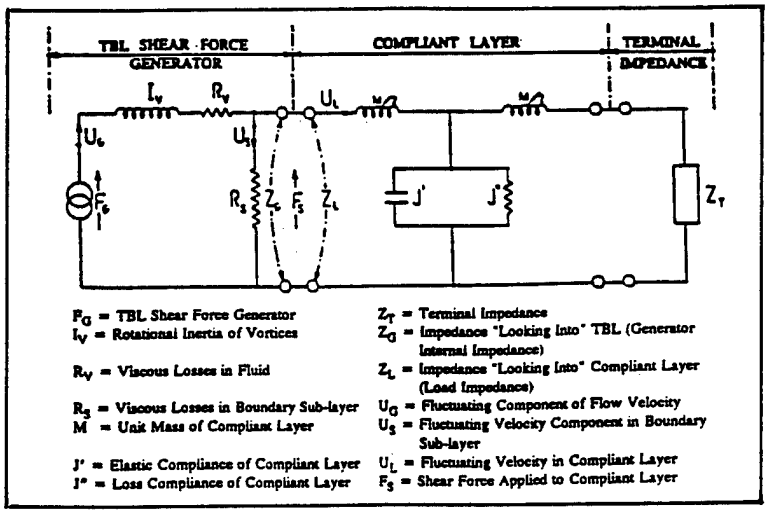

Figure 2: Equivalent Circuit

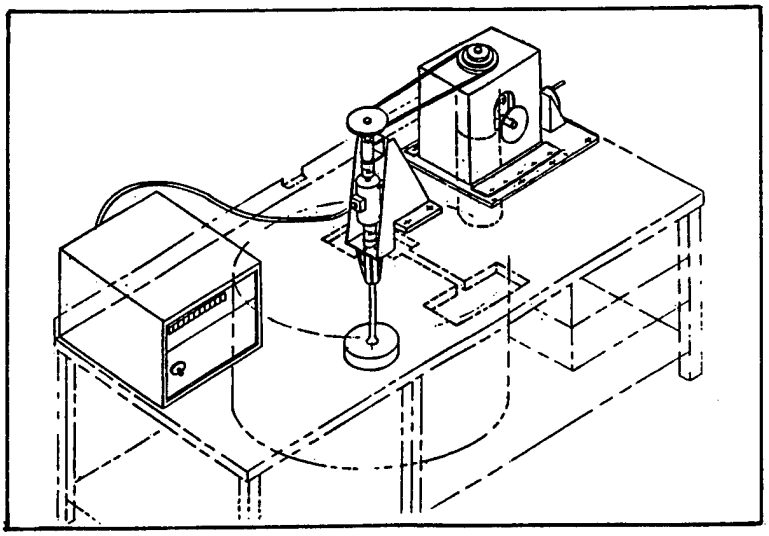

Figure 3: Rotating Disc Apparatus

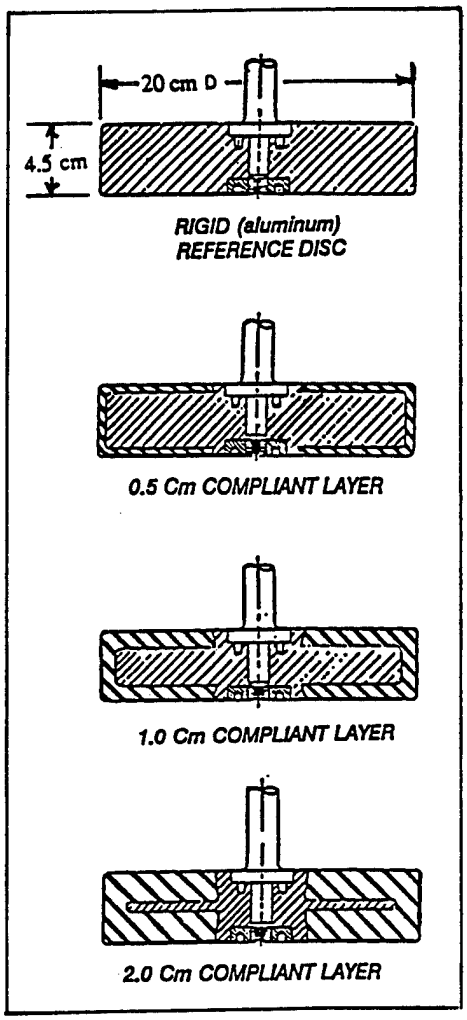

Figure 4: Rotating Discs

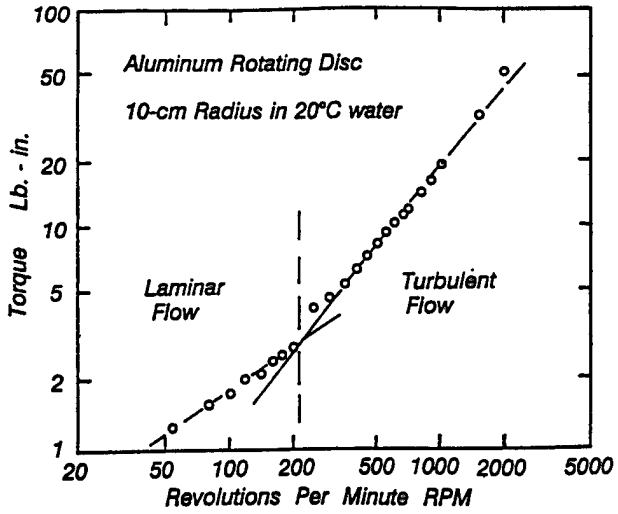

Figure 5: Rigid Disc Torque vs. rpm

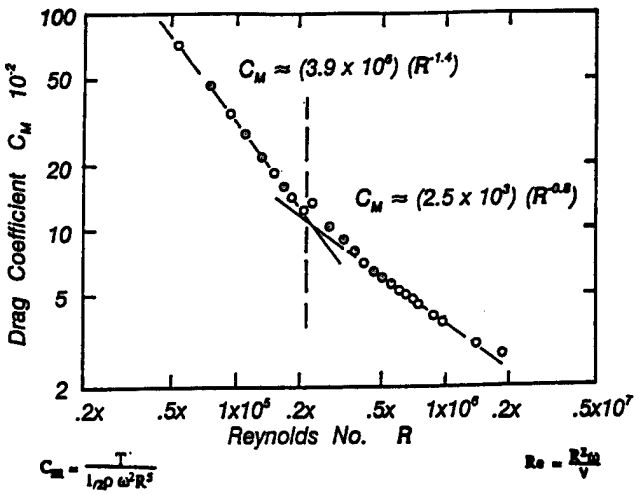

Figure 6: Rigid Disc Drag Coefficient vs. Reynolds No.

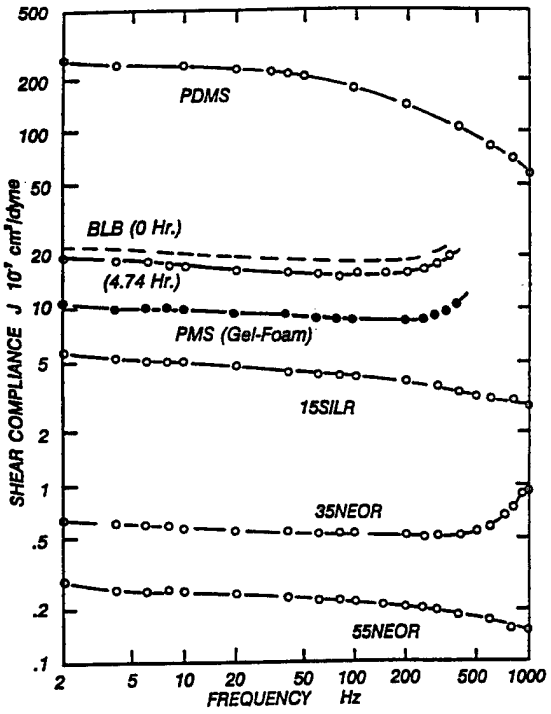

Figure 7: Shear Compliance of Representative Compliant Materials (see text)

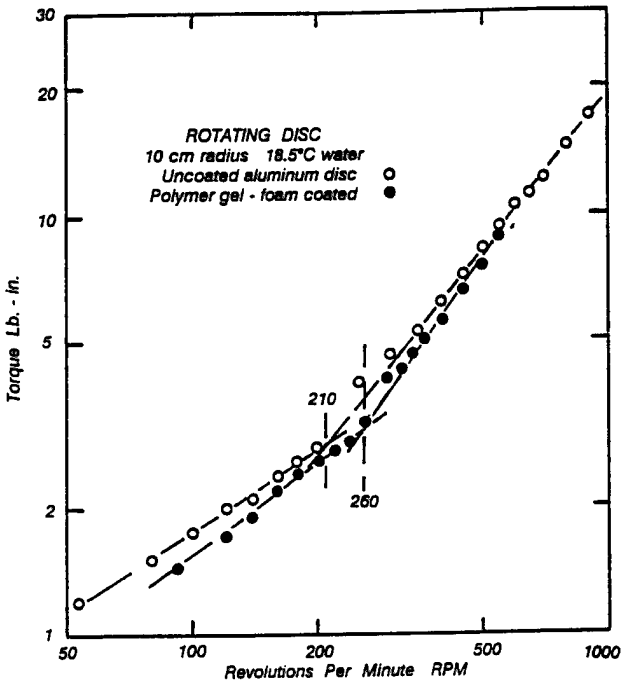

Figure 8: Comparison of the transition from laminar to turbulent regimes for the Rigid Reference Rotating and a Polymer Gel-Foam Coated Disc

INTERFACE WAVES ON A COMPLIANT COATING BOUNDED BY A FLUID FLOW AND THEIR EXCITATION BY ACOUSTIC RESONANCE

Herbert Überall
Department of Physics
Catholic University of America
Washington, DC 20064

Walter Madigosky
Vector Research Division
A & T, Inc.
Rockville, MD 20852

Abstract - The stability of interface waves on a compliant coating, attached to a rigid substrate and exposed to a laminar or turbulent fluid flow, has been the subject of several theoretical studies, and of experimental investigations in which the onset and growth of instability waves was determined. In the original experiments of Krämer, he attempted to retard the onset of the flow instability, for increasing values of flow speed, on a flow boundary that imitated a dolphin skin. Of the large number of subsequent experiments, some could, or could partly confirm Krämer's results which had indicated a substantial instability retardation and drag reduction by such a surface; other experiments could not. Exhaustive surveys of the experimental and theoretical literature on the subject can be found in two British PhD theses by Willis and by Yeo, and we shall give an overview of this literature. Solutions of the characteristic equation of the problem have been obtained by us, which furnish dispersion curves and stability information for the interface waves. It is shown that the excitation of these interface waves by incident inhomogeneous acoustic signals can occur in a resonant fashion, thus permitting an experimental determination of the dispersion curves, of the onset of instability, and of the growth properties of interface waves.

I. INTRODUCTION

Seawater drag arises from the onset of flow instabilities above a limiting value of flow velocity along a surface, for both rigid and compliant surfaces but in a different fashion for each. Drag reduction then consists in retarding the onset of the instability by a suitable choice of the surface parameters. After presenting an overview of the experimental situation and its analysis, we note that the onset of instabilities arises in a resonant fashion by a coincidence of the flow velocity with the speed of the boundary waves which is governed by the dispersion of the latter. We propose a method of experimental determination of the boundary wave dispersion curves by acoustic resonance experiments using inhomogeneous incident sound waves. Knowledge of the dispersion curves in their dependence on the surface wave properties thus allows the control of the onset of instability, and of the grow of the interface waves.

The problem of flow instabilities along compliant surfaces goes back to the experiments of Krämer [1]. In these, he attempted to retard the onset of the flow instability for increasing values of flow speed by coating a rigid flow boundary with a compliant layer bonded to the rigid surface with stubs, the space between the stubs containing a viscous liquid. This surface was supposed to model the skins of dolphins which had been thought to possess instability-retarding, and hence drag-reducing qualities [2,3]. Of the large number of subsequent experiments, some could, or could partly confirm Krämer's results which had indicated a substantial instability retardation and drag reduction by such a surface; other experiments could not. In spite of considerable existing literature, there still seems to reign a certain amount of confusion due to the dependence of the problem on a large number of variables. Exhaustive surveys of the experimental and theoretical literature on the subject can be found in two comprehensive British PhD theses by Willis [4] and by Yeo [5].

The following variables enter the problem and can be independently altered:

A. For the fluid flow: (1) the fluid can be viscous or inviscid; the flow velocity can be constant, or depend on the distance y away from the boundary (thus forming a boundary layer); (3) the flow can be a laminar or potential flow (flow speed everywhere parallel to the surface), in particular a Blasius boundary layer flow; or it can be a turbulent flow.

B. For the wall: (1) the boundary may be rigid; or else the walls may be compliant, i.e. the wall material may be elastic or viscoelastic; (2) the wall may be a half-space, a single (visco) elastic layer bonded to a rigid boundary, or it may consist of multiple layers; (3) these layers may be homogeneous or inhomogeneous (in particular, be given by the Krämer model); (4) the layers may be isotropic or anisotropic (e.g., consist of a fiber-reinforced material).

With such an enormous amount of possibilities to choose from, it is clear that it will be quite hard to systematize the subject matter to be studied. In the literature, individual investigations have thus always chosen selected cases; their results still need to be reviewed and categorized in a systematic fashion.

II. THE FLOW STABILITY PROBLEM

With a boundary layer, the flow velocity is measured by its asymptotic value U_∞ (at transverse distances $y \to \infty$). At any U_∞ disturbance waves may develop along the wall boundary, having the form

$$u = \phi(y)\exp[i(\alpha x+\beta z)-i\omega t] \qquad (1)$$

where x is the flow direction, and y the direction normal to the wall. This disturbance is referred to as three-dimensional [5]; however, most studies were made for two -dimensional disturbances where $\beta \equiv 0$, and $\omega = \alpha c_p$ where c_p is the phase velocity of the disturbance wave. If $\mathrm{Im}\alpha>0$ the disturbance wave decays and the flow is one of "spatial stability", ω being taken as real. Alternately, one may look for real α and complex ω; in that case, $\mathrm{Im}\omega<0$ leads to "temporal stability" (the two cases can be related to each other). If the opposite is true, the disturbance will grow either spatially or temporally, and instability will take place with undesirable consequences (turbulent flow, hydrodynamical drag being generated). Instability will set in if U_∞ exceeds a certain value termed "onset flow velocity", or "critical velocity".

If a boundary layer exists, one has $\phi(y)\neq$ const and $\phi(y)$ can be obtained by solving the "Orr-Sommerfeld" equation. Satisfying the boundary condition at the wall leads to an eigenvalue equation and to corresponding normal-mode solutions for $\phi(y)$.

The way how to formulate the boundary conditions on a flexible moving wall was, incidentally, shown by Benjamin [6-8], see also [9].

The complex eigenvalues ω determine the temporal stability; an instability region is defined by positive values of Imω. This is typically presented as in Fig. 1 [4], e.g. for a rigid wall, R being the Reynolds number, proportional to the flow velocity; —— is the Imω = 0 (or neutral stability) contour, and --- are contours of instability corresponding to Imω = 0.002, 0.004,... . Similar diagrams of (real) ω vs. R, at constant values of Im α, can be drawn for spatial instability. The curves depend, of course, on all other parameters of the problem (e.g., elastic modulus E of the wall, viscoelastic parameters of fluid and wall material, etc.), as well as on the geometry.

The idea is, of course, to "retard" the onset of instability by finding a combination of geometrical and material parameters such that the region of instability becomes as small as possible, or moves into a region of the (α,R) plane where it can do the least harm. The mentioned studies [4,5] claim significant progress in the direction of delaying the onset of instabilities, and hence of drag reduction.

In the history of the problem, several mainly theoretical studies stand out. These are the work of Benjamin [6-8] who discovered and classified three basic types of instabilities; the work of Landahl [10] and Kaplan [11] who introduced a physical explanation (in terms of energies of flow and wall) for stabilization dependence on material parameters (although their numerical results are invalid); and the work of Carpenter and Garrard [12,13] who studied the stability problem of Krämer-type compliant surfaces in great detail by solving the Orr-Sommerfeld equation. Similar extensive studies are those of Willis [4] and of Yeo [5] which extended the Orr-Sommerfeld solution to walls containing isotropic and anisotropic multiple layers, and even included three-dimensional disturbances [5]. However, other studies showed [9,14] that useful results (e.g., the classification of instabilities [13]) can already be obtained with quite simple models of flow and wall.

Benjamin's classification of unstable disturbances [8] resulted in three basic types of instabilities, to which Carpenter and Garrad [13] have added a fourth, as follows:

1) Tollmien-Schlichting instabilities. These correspond to unstable disturbance waves on a rigid wall (see Fig. 1) where they can exist for a viscous flow. If the wall is made compliant (and the flow may then be inviscid), these disturbance waves continue existing in modified form, and were designated "Class A" by Benjamin [8], or TSI elsewhere. They are found to be stabilized by changing the wall from rigid to compliant, and increasing its compliance (i.e. the instability region of Fig. 1 shrinking), but to be destabilized (i.e., the instability region becoming larger again) if wall damping is introduced and increased.

2) Compliance-induced flow instabilities, termed "Class B" by Benjamin. They appear in addition to the TSI if the wall is made compliant, and can occur even with inviscid fluid flow. The terminology of Yeo [5], "compliance-induced flow instabilities" (CIFI), is preferable for these instabilities rather than Carpenter and Garrad's [13] term "flow-induced surface instabilities" (FISI). This instability is essentially a resonance instability; it occurs when the flow speed is close to the natural speed of surface waves in the wall [4].

Diagrams such as Fig. 1 can be drawn for compliant walls, indicating both TSI and CIFI. Typically, they look as shown in Fig. 2. Changes in compliance and wall damping are found to have the opposite effect on CIFI as they do on TSI: the CIFI instability region grows if the wall becomes more compliant, and it shrinks if wall damping is increased. This can be understood from energy considerations [10], or simply from the fact that the disturbance waves that cause TSI reside mainly in the fluid, while those that cause CIFI reside mainly in the wall. An optimal instability-retarding wall will thus be one that minimizes the combined TSI and CIFI instability regions; minimizing just one of these leads to an increase in the other.

3) Kelvin-Helmholtz instability, termed "Class C" by Benjamin [8]. This instability arises out of a coalescence of Class A and Class B waves, as will be discussed below.

4) Static Divergence (SD), the fourth instability classified by Carpenter and Garrad [13]. It has been observed [15] in the form of very slow-moving (speed ~ some % of U_∞), large amplitude waves causing a dramatic increase in drag.

All these modes can lead to (traveling wave or standing wave) "flutter" [13] if the group velocity of the instability waves falls to zero, this being an absolute instability that is not convected away. As to their excitation, it is observed [15] that no significant interactions between a boundary layer flow and a compliant surface will occur for flow speeds below the transverse wave speed of the solid.

Theoretical studies considered the types of instability and their onset in a qualitative fashion. Duncan et al [14] assumed an elastic or viscoelastic layer bonded to a rigid half-space, and a potential flow using, like Ref. [9], Benjamin's pressure boundary condition on a moving surface. They extended the approach to include turbulent or laminar boundary-layer flow by modifying the pressure boundary condition to allow for a reduced magnitude and a phase change, taking these data from experiments on turbulent flow [16], or from calculations. Dispersion curves of disturbance waves were obtained from the characteristic equation which resulted from satisfying the boundary conditions [9]. These dispersion curves contain downstream and upstream branches, which will be continued here to be called that way even though a sufficient increase in U_∞ converts the upstream-traveling waves of the upstream branch into downstream-traveling waves.

Reference [14] found a static response (SD) for a viscoelastic wall due to the inclusion of a reduced magnitude and a pressure phase change. As to the other types of instabilities, we here present two examples of dispersion curves obtained in Ref. [14] (Fig. 3 for an elastic, and Fig. 4 for a viscoelastic wall) where three instabilities (Class A, Class B and Kelvin-Helmholtz, C) are visible. Recall that

$$\alpha = \omega/c_p, \tag{2}$$

and a complex wavenumber $\alpha = \alpha_r + i\alpha_i$ may be expressed by a complex phase velocity $c_p = c_r + ic_i$; instability corresponds to $\alpha_i<0$ and hence to $c_i>0$.

From Landahl's energy analysis of the instability classes [10], the upstream (downstream)-propagating waves on the upstream (downstream) branches of the dispersion curves are Class B. However, the downstream-propagating portion of the upstream branch is Class A, as indicated. For larger wavenumbers α, there is a coalescence of dispersion curves with the simultaneous appearance of $c_i \equiv$ Im c_p in the form of a complex conjugate phase velocity pair $c_p = c_r \pm ic_i$, classified as a type C (Kelvin-Helmholtz) instability. The effect of wall damping (Fig. 4) shows that the B-type waves have changed from neutrally stable to decaying ($c_i<0$), while the A-wave has become destabilized ($c_i>0$). The Kelvin-Helmholtz instability has become even more unstable (the positive branch of c_i has increased in magnitude). With this simple model (not requiring solution of the Orr-Sommerfeld equation), Duncan et al. [14] have been able to explain in a rather quantitative fashion the experimental values of the onset velocities of instabilities with laminar and turbulent flows

obtained by Hansen et al. [17] and by Gad-el-Hak et al. [18].

III. ACOUSTIC EXCITATION OF INTERFACE WAVES

This topic has been investigated by us in a theoretical study [19], with the result that the dispersion curves of the interface waves on a wall bounded by a fluid flow can be determined by experiments resonantly exciting these waves with an incident inhomogeneous signal. Obtaining these dispersion curves gives us access to a control of the flow instabilities, and hence to drag reduction. (Earlier experiments achieved excitation with a mechanical shaker).

We consider a viscoelastic layer of thickness d with rigid backing, bounded by an inviscid compressible fluid, extending the approach of Pierucci [20] (which considered an elastic layer and outgoing sonic disturbances exp ikx+imy only) to also include incident signals. Using the Navier-Stokes equations for the flow, and the proper boundary conditions at both the surfaces of the elastic layer and its backing, taking $\beta = 0$ in Eq. (1), a characteristic equation is obtained. Its solutions, Fig. 5 for a nonviscous rubber layer, show real and imaginary parts of c_p for the lowest interface wave mode at kd = 10, with both downstream and upstream branches. The Im $c_p>0$ causes an instability due to exponential growth of the interface wave, and the merger of the two c_p branches denotes the onset of this CIFI instability. For a viscous rubber layer, Fig. 6, changes of the dispersion curves due to viscosity are evident.

With an incident acoustic signal expi(kx-my) added, the outgoing disturbance has amplitude A of the form

$$A = (E + iF)/(E - iF) \tag{3}$$

where E - iF = 0 is the former characteristic equation, and the normal displacement u_z on the interface is

$$u_z = |2mF/(E-iF)|, \tag{4}$$

giving rise to resonant behavior when c_p approaches an eigenvalue. In Fig. 7 is shown u_z at $U_\infty/c_T = 1.79$ (left, just before the merger of downstream and upstream branches), and at $U_\infty/c_T = 1.80$ (right, just after the merger), indicating the observable resonant behavior which leads to a possible experimental determination of interface wave dispersion curves and flow instabilities.

IV. RECOMMENDATIONS FOR FURTHER WORK

Advanced British theories (involving solutions of the Orr-Sommerfeld equation) compare favorably with experiments [4,5,12,13] while more straightforward US models [9,14] also compare semiquantitatively with experiments [15-18]. A first investigation should be carried out in order to reconcile the two theoretical approaches, and to understand why the simpler picture also leads to reasonable results, in order to justify its use for the predictions of further experiments. If found accurate, it could be employed to cases of more complicated advanced coatings (e.g. multilayer) where it might more readily lead to useful results. Other, more specific recommendations can be listed as follows:

A. General topics: (1) parametric studies for multiple-layer walls; (2) replacing rigid wall backing by an air-backed metal layer; (3) suppression of certain instabilities by restricting wall motion via placement of inextensible sheets.

B. Resonance formalism: to be developed for the excitation of CIFI waves which occurs when the flow speed approaches the natural speed of surface waves in the wall [4].

C. Wall design: (1) Investigation of the effects of periodicity of multilayer walls, and its possible generation of stop bands that may retard transitions; (2) effects of wall anisotropy, e.g. continuously changing parameters, or fiber-reinforced walls.

REFERENCES

1. M. O. Krämer, "Boundary layer stabilization by distributed damping," *J. Aero. Sci.* 24, 459 (1957); *J. Am. Soc. Naval Engrs.* 72, 25 (1960); 74, 341 (1962).
2. J. Gray, "Studies in animal locomotion VI: The propulsive powers of the dolphin," *J. Expt. Biol.* 13, 192 (1936); "How fish swim," *Scientific American* 197, 48 (1957).
3. M. O. Krämer, "The dolphins' secret," *New Scientist* 7, 1118 (1960).
4. G. J. K. Willis, "Hydrodynamic stability of boundary layers over compliant surfaces," *PhD thesis, University of Exeter, England*, 1986.
5. K. S. Yeo, "The stability of flow over flexible surfaces," *PhD thesis, Cambridge University, Cambridge, England*, 1986.
6. T. B. Benjamin, "Shearing flow over a wavy boundary," *J. Fluid Mech.* 6, 161 (1959).
7. T. B. Benjamin, "Effects of a flexible boundary on hydrodynamic stability," *J. Fluid Mech.* 9, 513 (1960).
8. T. B. Benjamin, "The threefold classification of unstable disturbances in flexible surfaces bounding inviscid flows," *J. Fluid Mech.* 16, 436 (1963).
9. C. A. Evrensel and A. Kalnins, "Response of a compliant slab to inviscid incompressible fluid flow," *J. Acoust. Soc. Am.* 78, 2034 (1985).
10. M. T. Landahl, "On the stability of a laminar incompressible boundary layer over a flexible surface," *J. Fluid Mech.* 13, 609 (1962).
11. M. T. Landahl and R. E. Kaplan, "Effect of compliant walls on boundary layer stability and transition," *Agardograph* 97, 363 (1965).
12. P. W. Carpenter and A. D. Garrad, "The hydrodynamic stability of flow over Krämer-type compliant surfaces. Part 1. Tollmien-Schlichting instabilities," *J. Fluid Mech.* 155, 465 (1985).
13. P. W. Carpenter and A. D. Garrad, "The hydrodynamic stability of flow over Krämer-type compliant surfaces. Part 2. Flow-induced surface instabilities," *J. Fluid Mech.* 170, 199 (1986).
14. J. H. Duncan, A. M. Waxman and M. P. Tulin, "The dynamics of waves at the interface between a viscoelastic coating and a fluid flow," *J. Fluid Mech.* 158, 177 (1985).
15. See, e.g., M. Gad-el-Hak, "Compliant coatings research: A guide to the experimentalist," *J. Fluid Struct.* 1, 55 (1987).
16. J. M. Kendall, "The turbulent boundary layer over a wall with progressive waves," *J. Fluid Mech.* 14, 259 (1970).
17. R. J. Hansen et al., "Hydrodynamic drag and surface deformations generated by liquid flows over flexible surfaces," in *Viscous Flow Drag Reduction*, Prog. Astro. Aero. 72, 439 (1979).
18. M. Gad-el-Hak, R. F. Blackwelder, and J. J. Riley, "On the interaction of compliant coatings with boundary layer flows," *J. Fluid Mech.* 140, 257 (1984).
19. M. Talmant, H. Überall and W. Madigosky, "Interface waves on a compliant coating bounded by a fluid flow, and their excitation by acoustic resonance," *J. Acoust. Soc. Am.* 94, 2793 (1993).
20. M. Pierucci, "Surface waves on an elastic medium in the presence of an inviscid flow field," *J. Acoust. Soc. Am.* 60, 965 (1977).

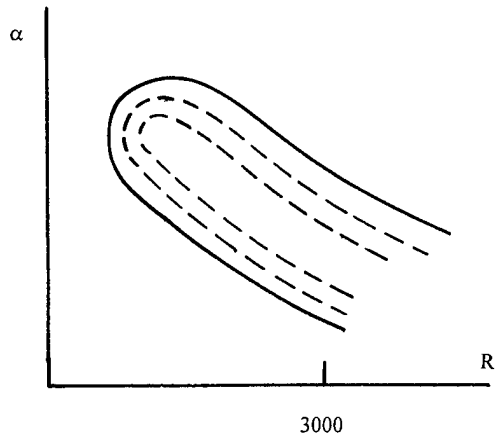

Fig. 1. Temporal instability region for flow over a rigid wall.

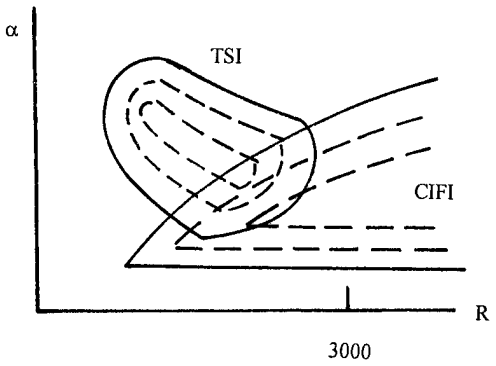

Fig. 2. Instability regions for flow over a compliant wall.

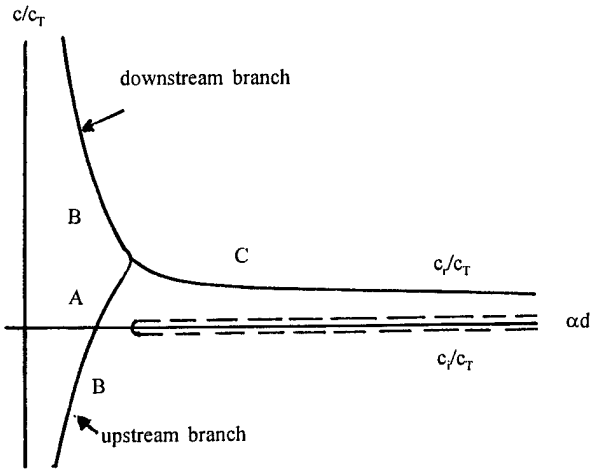

Fig. 3. Dispersion curves of disturbance waves for an elastic wall [14] (phase velocity normalized by shear speed c_T; d = wall thickness; flow speed = 1.85 c_T), indicating the location of instabilities A - C.

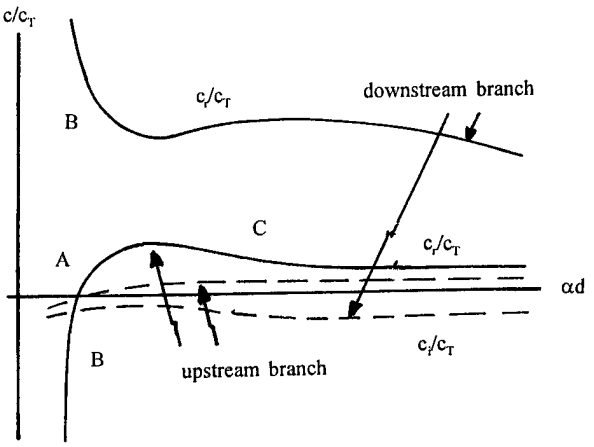

Fig. 4. Dispersion curves of disturbance waves for a viscoelastic wall [14] (phase velocity normalized by shear speed c_T; d = wall thickness; flow speed = 1.85 c_T), indicating instabilities A - C.

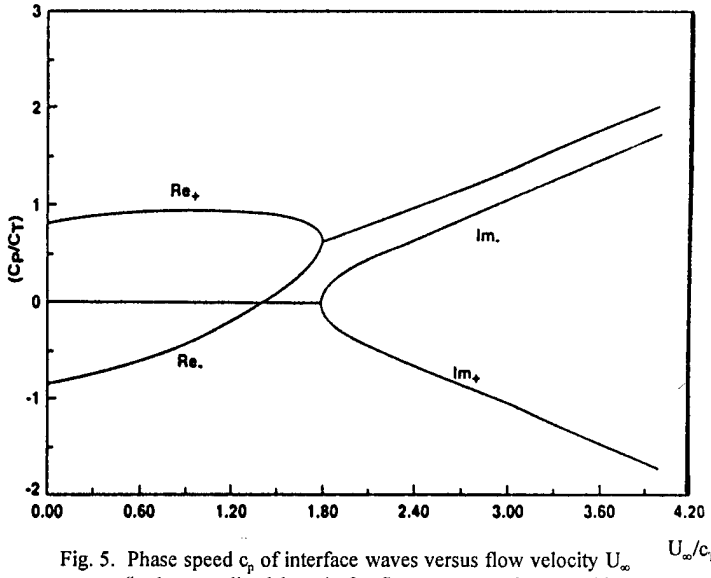

Fig. 5. Phase speed c_p of interface waves versus flow velocity U_∞ (both normalized by c_T), for flow over nonviscous rubber layer: real and imaginary parts of the lowest mode at kd = 10.

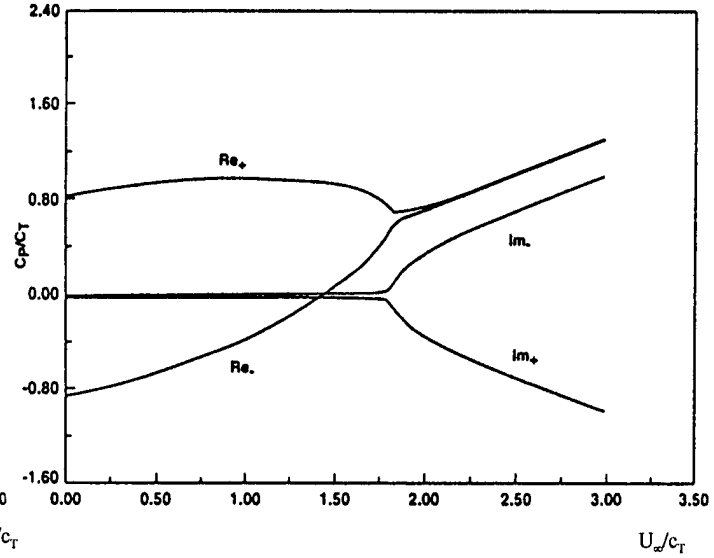

Fig. 6. Same as Fig. 5 but for a viscous rubber layer and kd = 5.

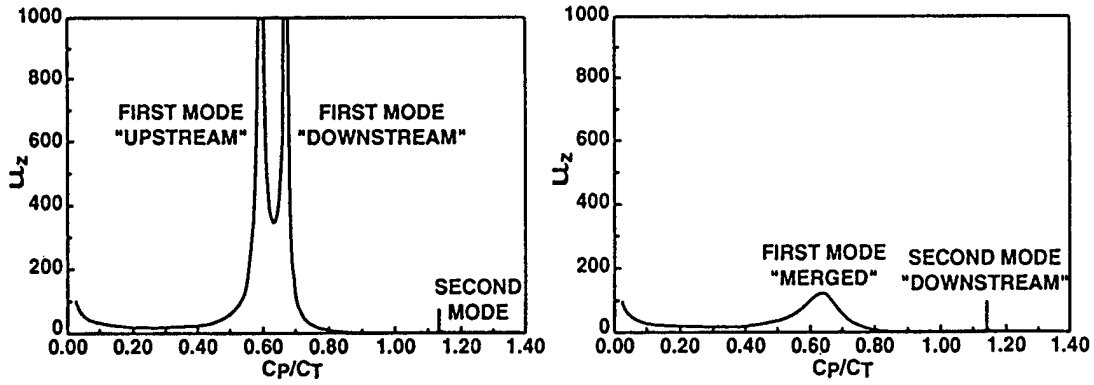

Fig. 7. Normal displacement u_z at the interface of a nonviscous rubber layer, indicating acoustic resonant excitation of modes at kd = 10; (left) Excitation of the branches of the first and second mode at $U_\infty/c_T = 1.79$; (right) at $U_\infty/c_T = 1.80$.

ANALYSIS OF EVOLUTION OF DISTURBANCES IN CHANNEL FLOW OVER A WAVY WALL

D.N. Riahi
Department of Theoretical and Applied Mechanics
216 Talbot Laboratory, University of Illinois at Urbana-Champaign
104 S. Wright Street, Urbana, Illinois 61801 U.S.A.
d-riahi@uiuc.edu

Abstract Perturbation and scaling analyses at high Reynolds number are applied to study evolution of finite amplitude disturbances in channel flow over a wavy wall. Using the governing flow system for the incompressible fluid, fundamental evolution equations are derived which provide an initial value problem for the basic flow composed of a mean flow plus a quasi-modal harmonic structure. The solution to this basic flow system is slightly perturbed by disturbances in the form of vortices which have spanwise structure but vary weakly with respect to both streamwise and time variables. These disturbances can strongly destabilize the flow in the case of channel flow bounded by flat and smooth walls. However, in the case of channel flows over wavy walls, certain wavy boundaries can modify the basic flow and superimpose longitudinal vortices whose structures and scales are due to the wavy walls.

I INTRODUCTION

For shear flows bounded by smooth and flat walls, Benney [1] developed a so-called meanflow-first harmonic interaction theory which concerns about three-dimensional instability of parallel shear flows with respect to disturbances in the forms of longitudinal roll vortices and involved interactions between first harmonics of waves and the mean shear flows. At high values of Reynolds numbers such interactions were nonlinear and took place on a fast time scale. Instability to spanwise disturbance rolls was then detected in several cases. Benney speculated that such instability may explain the well-known experimental observations of Klebanoff et al. [2]. These experiments showed clearly the evidence for spanwise-periodic streamwise vortices maintained by the wave motion and provided proof that three-dimensional waves can dominate the nonlinear shear flow regime. In the present study wavy wall formulation developed by Riahi [3] and the Benney theory [1] are employed to analyze shear flow in a channel flow over a wavy wall. We found some interesting results. In particular, we found that certain wavy walls can lead to birth of longitudinal vortices whose structures are imposed by the wavy wall structure. This result indicates possible procedure for shear flow control and, in particular, application to seawater drag reduction.

II ANALYSIS AND RESULTS

We consider problem of an incompressible fluid flow in a channel of average depth d bounded above by a flat and smooth boundary and bounded below by a wavy surface which varies with respect to both time and space variables. We use a cartesian system of coordinates with origin on the average location of the wavy wall. Our model is based on the non-dimensional forms of the Navier-Stokes and continuity equations. The boundary conditions for the velocity vector $\mathbf{u}$ of the flow are

$$\mathbf{u} = -\sum_{m=1} \frac{(\delta \mathrm{h})^m}{m!} \frac{\partial^m \mathbf{u}}{\partial y^m} \quad \text{at} \quad y = 0, \tag{1}$$

$$\mathbf{u} = 0 \quad \text{at} \quad y = 1, \tag{2}$$

where y is the transverse variable, δ is the magnitude of the amplitude of the wavy wall, which is assumed to be small (δ<<1), $\mathrm{h}(x,z,t)$ is the wavy wall shape function, x is the streamwise variable, z is the spanwise variable and t is the time variable. The terms in the right-hand-side of (1) arise simply by the contributions of the higher order terms in a Taylor-series expansion about y=0 of $\mathbf{u}(x, \delta h, z, t)$.

Next, we consider the following expansions for the dependent variables

$$(u, \upsilon, w, p) = (u_0, 0, 0, 0) + \delta(\tilde{u}_1, \upsilon_0 + \tilde{\upsilon}_1, w_0 + \tilde{w}_1, \tilde{p}_1) + c.c. + \ldots, \tag{3}$$

where u is the streamwise velocity, υ is the transverse velocity, w is the spanwise velocity, p is the pressure, and all the coefficients are assumed to be functions of x_s, y, z and t_s, where x_s and t_s are slow variables defined by

$$x_s = \delta x, t_s = \delta t. \tag{4}$$

In addition, c.c. in (3) indicates complex conjugate. The wavy wall shape function h is assumed to have the following simple form

$$h = A(x_s, z, t_s)\exp[i(\alpha x_s - \omega t_s)/\delta] + \delta' A' \cos(\beta z).\exp(i\alpha' x_s - \omega' t_s) + c.c., \tag{5}$$

where $i = \sqrt{-1}$, α and α' are streamwise wave numbers of the wavy wall, β is spanwise wave number of the wavy wall, ω and ω' are frequencies of the wavy wall, A' is a constant and δ' is another small parameter (δ<<δ'<<1).

To zeroth order in δ', (5) leads to dependence for the first harmonics $(\tilde{u}_1, \tilde{\upsilon}_1, \tilde{w}_1, \tilde{p}_1)$ on x and t of the form

$$(\tilde{u}_1, \tilde{\upsilon}_1, \tilde{w}_1, \tilde{p}_1) = (u_1, \upsilon_1, w_1, p_1)\exp(i\alpha x - i\omega t), \tag{6}$$

where $(u_1, \upsilon_1, w_1, p_1)$ are functions of x_s, y, z and t_s. Using (3)-(6) for the order δ in the governing fluid flow system lead to base flow system for the combined mean flow variables $(u_0, \upsilon_0, w_0, p_0)$ and the first harmonic coefficients $(u_1, \upsilon_1, w_1, p_1)$. The only non-zero boundary condition for this system is that due to u_1 where

$$u_1 = -A \frac{\partial u_0}{\partial y} \text{ at } y = 0. \tag{7}$$

Due to δ' term in (5), the solution found for the above system is then perturbed by disturbance rolls whose x_s, z and t_s dependence is of the form given by the second term in the right-hand-side of (5). This leads to preference of particular flow which contains longitudinal vortices whose flow characteristics and structure are closely linked to those of the wavy wall. We extended these results to the case where the δ' term in (5) is represented by a continuous spectrum of rolls modes [4], and we found essentially the same results as those described above. Presently we are investigating stability of three-dimensional basic flow which is essentially superposition of the above two-dimensional basic flow and the longitudinal vortex flow, and the results will be reported elsewhere. We plan to extend the present model to turbulence regime, using Reynolds and Hussain [5] approach, and then apply to seawater drag reduction research. Some level of numerics plus some use of basic flow data will be expected to carry out stability investigation of the flow adjacent to wavy walls, and the subsequent drag calculation and optimization procedure versus different types of wavy walls will then follows.

REFERENCES

[1] D.J. Benney "The evolution of disturbances in shear flows at high Reynolds numbers", *Stud. Appl. Math* **70**, 1-19 (1984).

[2] P.S. Klebanoff, K.D. Tidstrom and L.M. Sargent "The three-dimensional nature of boundary-layer instability", *J. Fluid Mech* **12**, 1-34 (1962).

[3] D.N. Riahi "Effects of roughness on nonlinear stationary vortices in rotating disk flows", *Mathl. and Comput. Modelling* **25**, 71-82 (1997).

[4] D.N. Riahi "Modal package convection in a porous layer with boundary imperfections", *J. Fluid Mech.* **318**, 107-128 (1996).

[5] W.C. Reynolds and A.K.M.F. Hussain "The mechanics of an organized wave in turbulent shear flow. part 3. Theoretical models and comparison with experiments, *J. Fluid Mech.* **54**, 263-288(1972).

Turbulent Drag Reduction Methods: Spanwise Fluid Motion & Wall Motion

THE MECHANISM OF TURBULENT DRAG REDUCTION WITH WALL OSCILLATION

Kwing-So Choi and Brian R. Clayton
Department of Mechanical Engineering
The University of Nottingham
Nottingham NG7 2RD, United Kingdom
kwing-so.choi@nottingham.ac.uk

Abstract - An extensive study of the turbulence structure in the near-wall region of the boundary layer with spanwise-wall oscillation was conducted in a wind tunnel by hot-wire measurement and flow visualisation. This is to experimentally confirm the results of recent studies and to understand the mechanisms involved in the drag reduction of turbulent boundary layer when the wall is oscillated in a spanwise direction. Measurement of the streamwise development of skin-friction coefficient over the oscillating wall surface shows that there are as much as 45% reductions in skin-friction drag. The logarithmic velocity profiles are shifted upwards, the turbulence intensities reduced, the velocity skewness and kurtosis increased in the near-wall region, suggesting that the viscous sublayer is thickened as a result of drag reduction with wall oscillation. The flow visualised pictures suggest that the streamwise vorticity of alternate signs generated by the periodic Stokes layer over the oscillating wall is tilted into the spanwise direction, creating a net spanwise component of the vorticity. This seems to have reduced the velocity gradient near the wall as observed in the previous study. It is also found that the realignment of the longitudinal vortices in the near-wall region into spanwise direction weakens the near-wall burst activity, leading to a reduction in turbulent skin-friction.

1. INTRODUCTION

Akhavan and her colleagues [1] at the University of Michigan recently conducted a direct numerical simulation (DNS) study of turbulent channel flow, demonstrating for the first time that the skin-friction drag of a channel flow can be reduced by oscillating one of the walls in a spanwise direction. Their results show that a 40% reduction in turbulent skin-friction drag can be obtained by a spanwise-wall oscillation only after five periods of oscillation with the non-dimensional period set at 100. The logarithmic velocity profile of the boundary layer is shifted upwards, suggesting that the viscous sublayer is thickened as a result of the spanwise-wall oscillation. It is also shown that the intensities of velocity fluctuations are reduced by up to 30%. The basic findings of this investigation were later confirmed by Baron and Quadrio [2] in their DNS study.

These numerical simulations were followed by an experimental investigation by Laadhari *et al.* [3], who demonstrated that the mean velocity gradient of the boundary layer is reduced near the oscillating wall. The reductions in the turbulence intensities across the boundary layer were also demonstrated, suggesting that the skin-friction drag of the turbulent boundary layer may be reduced by the spanwise-wall oscillation. Choi [4] suggested a possible mechanism of turbulent drag reduction by spanwise-wall oscillation, arguing that the sequence of turbulence events can be disturbed if the wall moves quickly by more than the spanwise correlation distance of near-wall turbulence, leading to a reduction in the energy production of the boundary layer. In other words, the spatial coherence between the longitudinal vortices and low-speed streaks may be disrupted by oscillating a wall in a spanwise direction [2].

The objective of the present investigation is firstly to confirm the results of these studies, particularly the amount of turbulent drag reduction by a spanwise-wall oscillation. This was achieved by measuring the streamwise development of skin-friction coefficient over the oscillating wall surface. The probability density functions and the higher-moment turbulence statistics of velocity fluctuations were documented over an oscillating wall and they were compared with those without wall oscillation. In order to understand the mechanism of turbulent drag reduction by spanwise-wall oscillation, an extensive study of near-wall structure of the boundary layer modified by the wall oscillation was carried out using the hot-wire anemometry and flow visualisation technique. The phase averaged velocity profiles were then obtained over a period of wall oscillation, and the conditional averaged burst signatures were studied in order to investigate the effect of spanwise-wall oscillation on the near-wall turbulence activities.

II. EXPERIMENTS

The experiments [5] were performed in an open-return, low-speed wind tunnel at the University of Nottingham (Fig. 1). The boundary layer was tripped at the inlet of the working-section to ensure a fully-developed turbulent boundary layer over the test surface. The freestream velocity of the present investigation was U_∞ = 2.5m/s with a corresponding Reynolds number of R_θ = 1190 based on the momentum thickness. The pressure gradient along the length of the working section was nearly zero, with the shape factor of the boundary layer H = 1.44 at the trailing edge of the oscillating plate. The sinusoidal oscillation was produced by a crank-shaft system, with oscillation frequencies up to 7 Hz and peak-to-peak amplitudes of up to 70mm.

The streamwise velocity measurements were made with Dantec 56C CTA system using a single, miniature, hot-wire probe (Dantec 55P15). This sensor has a 5μm-diameter sensing element, 1.2mm long, which is operated at a constant temperature mode with an over-heat ratio of 1.8. Measurements of spanwise velocities were made with a subminiature X-wire probe specially made by Dantec, which has a 2.5μm-diameter sensing element, 0.5mm long. The total length of the gold plated wires is 1.5mm with a space of 0.5mm between the two wires. The X-wire probe was operated at an overheat ration of 1.5 to reduce the noise due to thermal cross talk, but with a sufficient sensitivity to the velocity. The data from the anemometer were sampled at a rate of 2kHz through IOTech ADC 488/8S analogue-to-digital converter. The Preston tubes used for the skin-friction measurements were connected to a differential pressure transducer (Furness Control FC0510) with 0.001 Pa resolution, accurate to 0.25% of reading. Flow visualisation was performed at a freestream velocity of 1.5 m/s using a smoke-wire technique [6]. A pulsed copper-vapour laser with a power output of 15W at a pulse rate of 10kHz was used as a light source, which was fanned out with a cylindrical lens to produce a light sheet at 7.5 wall units from the wall. Still photographs with a smoke wire placed at $y^+ = 4$ were taken using a Nikon F-801 camera with a simultaneous video recording by a Sony CCD-V800E Hi8-colour camcorder. The high-speed video recording was also made with a Kodak Ektapro Motion Analyzer, with a shutter speed of 1/500 sec at 500 fps.

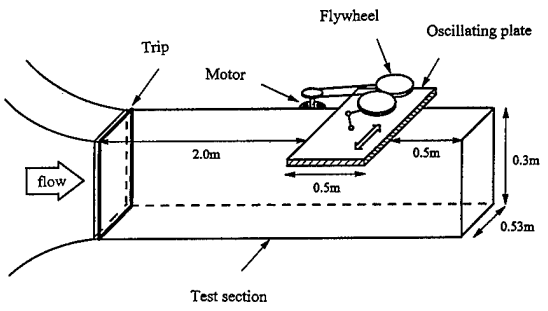

Figure 1. Experimental facility.

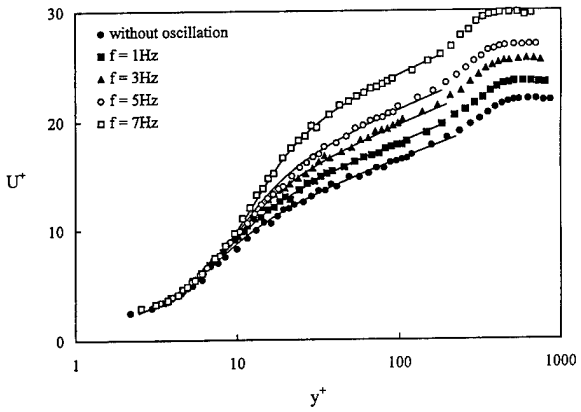

Figure 2. Logarithmic velocity profiles of the boundary layer 10mm downstream from the trailing edge of the oscillating plate, for different frequencies of wall oscillation (Δz = 70mm).

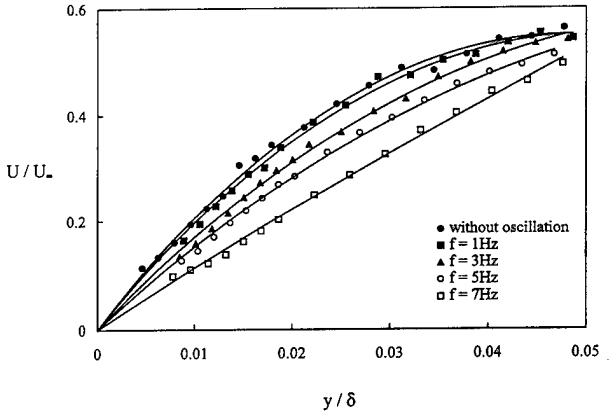

Figure 3. Outer-scaled velocity profiles in the near-wall region of the boundary layer 10mm downstream from the trailing edge of the oscillating plate, for different frequencies of wall oscillation (Δz = 70mm).

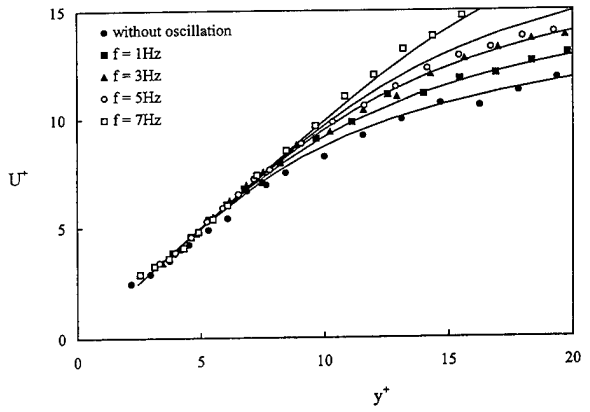

Figure 4. Inner-scaled velocity profiles in the near-wall region of the boundary layer 10mm downstream from the trailing edge of the oscillating plate, for different frequencies of wall oscillation (Δz = 70mm).

III. RESULTS AND DISCUSSIONS

The mean-velocity profiles from the present study are shown in Fig. 2 in a log-law plot, where all the profiles were non-dimensionalised using the friction velocity for each oscillating condition. The curves drawn through the data [7] cover the entire region of the boundary layer including the viscous sublayer, which seem to fit all the profiles very well. The logarithmic velocity profiles are shifted upwards with an increase in oscillation frequency, suggesting that the skin-friction drag is reduced by the spanwise-wall oscillation. When the outer-scaled velocity profiles are plotted in linear coordinates (Fig. 3), it is clear that the mean velocity gradient in the near-wall region is significantly reduced with wall oscillation. This reduction in the mean velocity gradient, which is also seen in the experimental results of Laadhari *et al.* [3], clearly demonstrates that the wall-shear stress of the turbulent boundary layer is reduced by the spanwise-wall oscillation. The inner-scaled velocity profiles (Fig. 4) show, on the other hand, that the extent of linear region of the viscous sublayer is increased from $y^+ \approx 2.5$ [8] to $y^+ \approx 10$ at the maximum oscillation frequency (7Hz) of the present experiment.

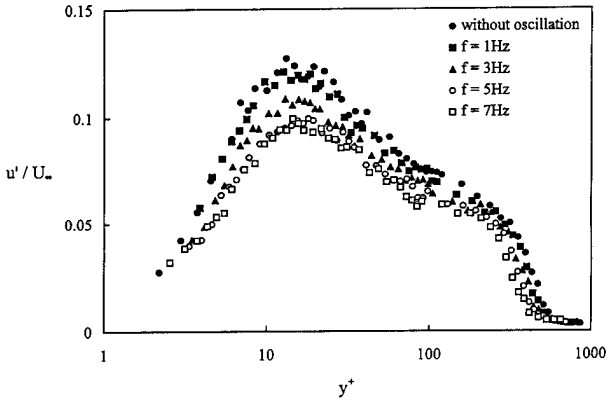

Figure 5. Turbulent intensity profiles of the boundary layer 10mm downstream from the trailing edge of the oscillating plate, for different frequencies of wall oscillation (Δz = 70mm).

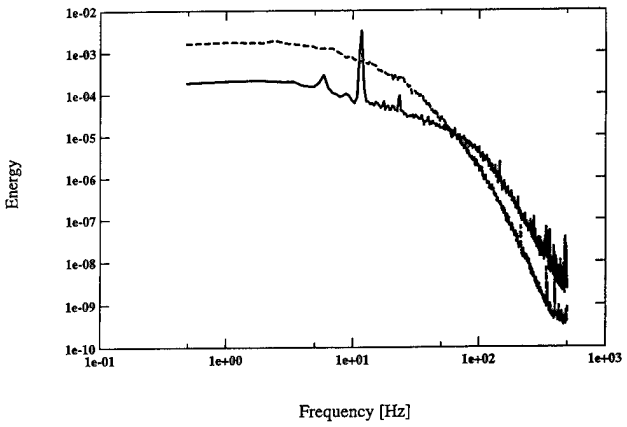

Figure 6a. Energy spectra of velocity fluctuations at $y^+ = 1.5$: — with wall oscillation, --- without wall oscillation.

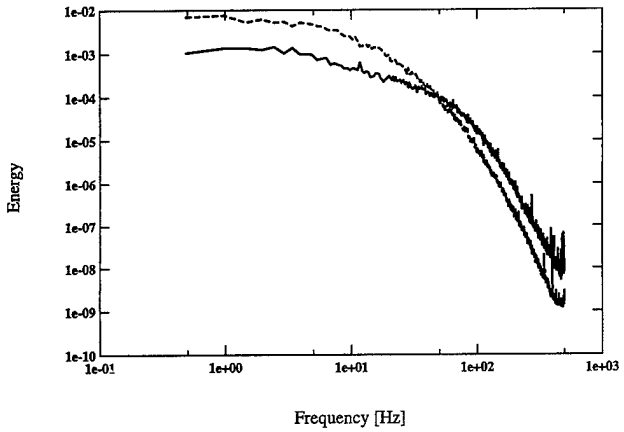

Figure 6b. Energy spectra of velocity fluctuations at $y^+ = 4$:
— with wall oscillation, --- without wall oscillation.

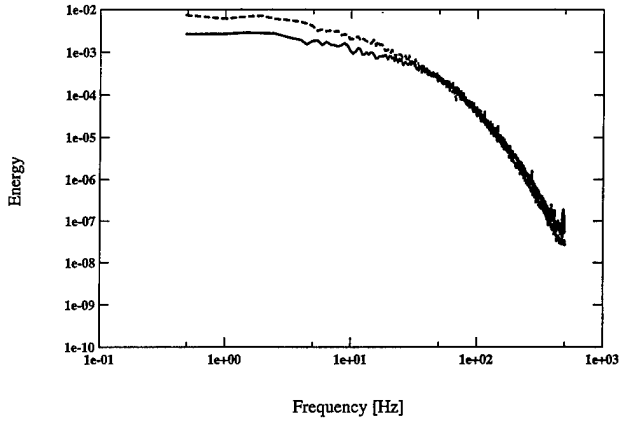

Figure 6c. Energy spectra of velocity fluctuations at $y^+ = 20$:
— with wall oscillation, --- without wall oscillation.

The turbulence intensities of the boundary layer are plotted in Fig. 5 against the non-dimensional distance y^+ from the wall, where large reductions in the intensity values are evident within the inner region when the wall is oscillated in a spanwise direction. The experimental results by Laadhari *et al.* [3] as well as numerical data by Jung *et al.* [1] and Baron and Quadrio [2] exhibit a similar behaviour. The reductions in turbulence intensities are also demonstrated in the energy spectra taken at $y^+ = 1.5$, 4 and 20 (Figs. 6a, 6b and 6c, respectively). It seems that the turbulence energy is dramatically reduced at low frequencies, say below 50Hz while the energy at higher frequencies is increased. This suggests that there is a transfer of energy from the large-scale turbulence eddies to small-scale ones by the periodic Stokes layer developed over an oscillating wall.

The skewness and kurtosis of the velocity fluctuations (Figs. 7 and 8, respectively) are increased with wall oscillation within the near-wall region, agreeing very well with the DNS results by Baron and Quadrio [2]. These increases in higher moments can be interpreted as a manifestation of the increase in the viscous sublayer thickness by the spanwise-wall oscillation [6, 9], which have been observed in several drag-reducing flows. The probability density functions of velocity fluctuations at $y^+ = 1.5$ (Fig. 9a) and at $y^+ = 4$ (Fig. 9b) over an oscillating wall exhibit long tails of positive probability, reflecting the increases in the skewness and kurtosis within the viscous sublayer. They also show that the velocity signal has predominantly positive, spiky excursions in this region of the boundary layer. The probability density function at $y^+ = 20$ (Fig. 9c) still show a sign of increase in skewness and kurtosis with a long tail of positive probability, but the difference is not as great at this location of the boundary layer as within the viscous sublayer (Figs. 9a and 9b).

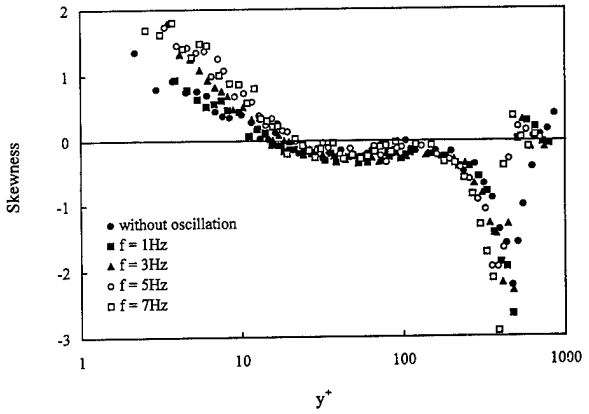

Figure 7. Skewness profile of the boundary layer 10mm downstream from the trailing edge of the oscillating plate, for different frequencies of wall oscillation ($\Delta z = 70$mm).

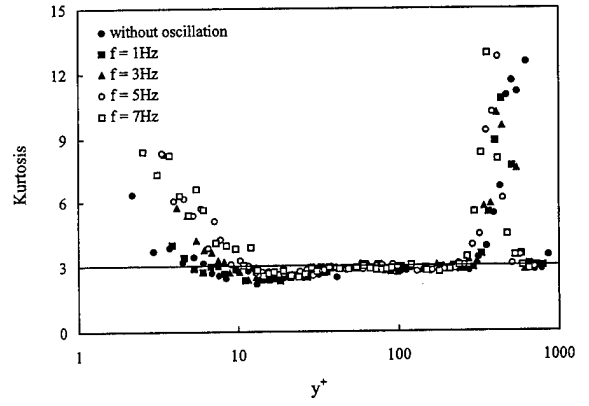

Figure 8. Kurtosis profile of the boundary layer 10mm downstream from the trailing edge of the oscillating plate, for different frequencies of wall oscillation ($\Delta z = 70$mm).

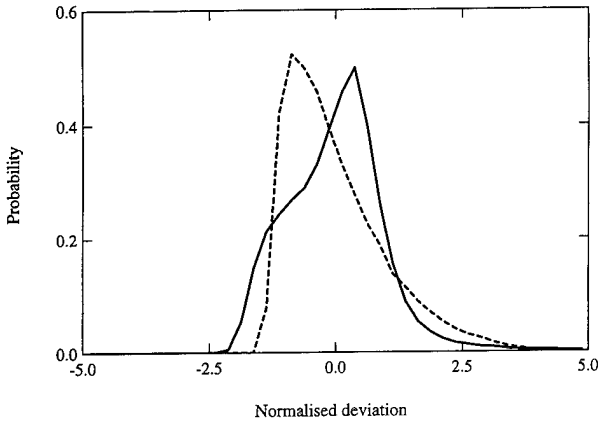

Figure 9a. Probability density functions of velocity fluctuations at $y^+ = 1.5$: — with wall oscillation, --- without wall oscillation.

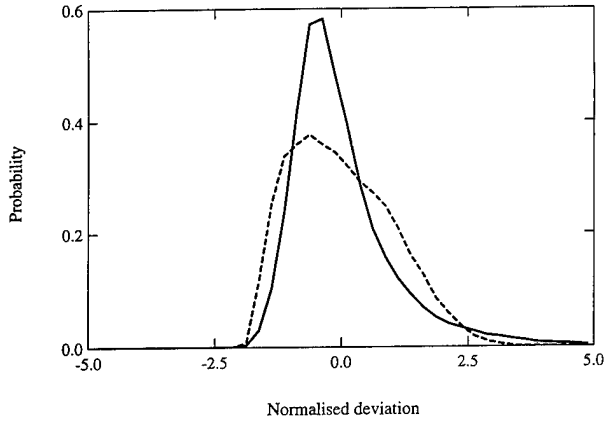

Figure 9b. Probability density functions of velocity fluctuations at $y^+ = 4$: — with wall oscillation, --- without wall oscillation.

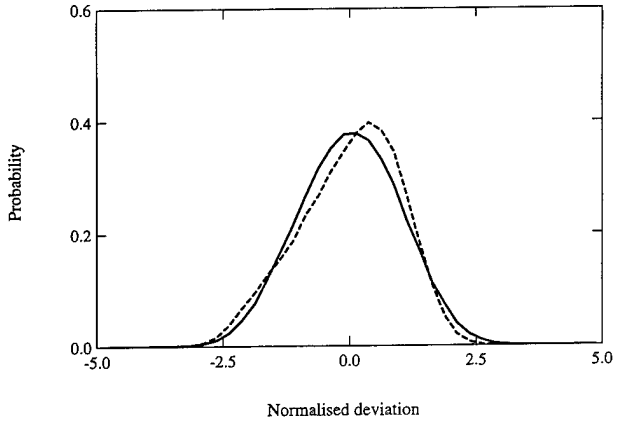

Figure 9c. Probability density functions of velocity fluctuations at $y^+ = 20$: — with wall oscillation, --- without wall oscillation.

The streamwise variation of skin-friction coefficient of the boundary layer is given in Fig. 10, showing that the skin-friction coefficient over the oscillating wall begins to reduce just upstream (about two boundary layer thicknesses) of the leading edge to reach a maximum level of drag reduction somewhere near the middle of the plate. The present data clearly indicate that there are as much as 45% reductions in the skin-friction coefficient compared with that without wall oscillation, which is in close agreement with the results of direct numerical simulations [1, 2]. The skin-friction coefficient then seems to revert back gradually towards the level corresponding to the condition without wall oscillations in the downstream of the oscillating plate. Nearly 20% reduction in C_f is still evident after more than two boundary layer thicknesses from the trailing edge of the oscillating plate, indicating that the relaxation process is rather slow.

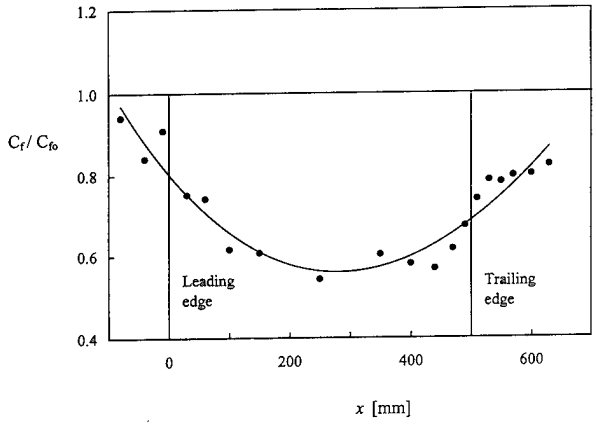

Figure 10. Downstream variation of skin-friction coefficient C_f with a spanwise-wall oscillation (f = 5Hz, Δz = 50mm), as a ratio to the skin-friction coefficient C_{fo} without oscillation. The leading edge of the 500mm long oscillating plate is located at $x = 0$.

When a flat plate is oscillated tangentially in still fluid, a thin layer of periodic shear flow called the Stokes layer is formed over the plate as a result of viscous diffusion from its surface. In other words, the Stokes layer over an oscillating wall is a constant source of vorticity of alternate signs as the wall moves back and forth [10] in a spanwise direction. If there is a stream of uniform flow across an oscillating wall surface, the vortex sheets produced by the periodic Stokes layer will be convected by the boundary layer. Figure 11 shows the theoretical, laminar velocity profiles of the Stokes layer over the oscillating wall in still fluid (i.e. without boundary layer flow) at different phase of wall oscillation. The experimental data obtained with an X-wire probe are phase averaged over a period of wall oscillation, and are also shown in this figure. It is observed that the measured velocity profiles are very similar to the theoretical profiles of laminar Stokes layer in both their shape and phase relationship, although their magnitude seems to be slightly less than that of theoretical values. It should be noted here that the thickness of the Stokes layer over an oscillating wall is similar to that of the viscous sublayer under the experimental conditions where the turbulent drag reductions are observed. Also, the Reynolds number of the Stokes layer is well below the critical value, so that the Stokes layer remains laminar [11-13]. These are considered to be important conditions in obtaining the turbulent drag reduction with spanwise-wall oscillation, since the modification of the near-wall structure seems to result from an interaction of the Stokes layer with the viscous sublayer of the turbulent boundary layer where the majority of the energy production takes place.

The streamwise velocity profiles are also phase averaged over a period of wall oscillation, and are shown in Fig. 11. There are no noticeable changes in these profiles at different phase of wall oscillation outside the viscous sublayer. Examining the phase averaged velocities within the viscous sublayer closely, however, it is observed that the streamwise velocity profiles exhibit a cyclic change with the change in wall velocity during the oscillation. In other words, the velocity signal is modulated by the periodic Stokes layer at a frequency twice that of the wall oscillation, which can be seen in the phase-averaged velocity signal over one period of wall oscillation (Fig. 12). From this figure, the streamwise velocity profile at $y^+ = 1.5$ seems to be nearly in phase with the spanwise wall velocity but with perhaps a slight phase lag. At $y^+ = 4$, the streamwise velocity is lagged nearly $\pi/2$ behind the wall velocity. No clear phase relationship between the streamwise velocity and the wall velocity is observed at $y^+ = 20$.

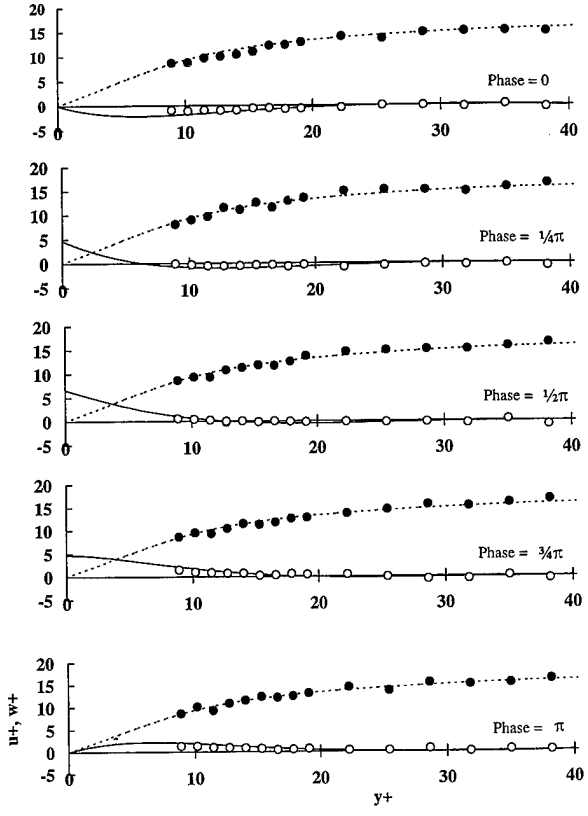

Figure 11. Velocity profiles in the Stokes layer: — theory (spanwise velocity profiles), o phase averaged experimental data (w^+), --- Dean's formula (streamwise velocity profiles), • phase averaged experimental data (u^+).

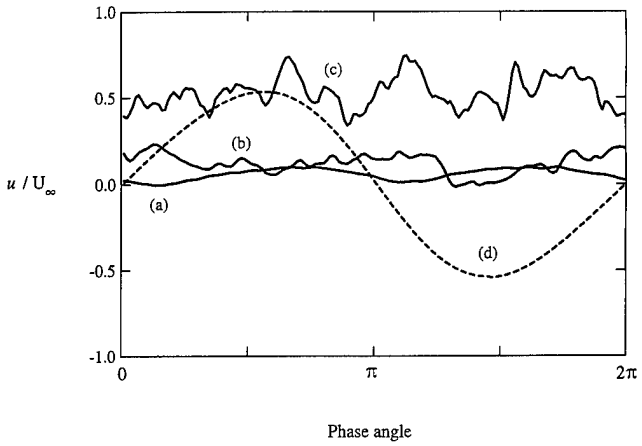

Figure 12. Phase averaged wall velocity --- and streamwise velocity profiles: a) at $y^+ = 1.5$, b) at $y^+ = 4$ and c) at $y^+ = 20$.

Figures 13a and 13b are the flow-visualised pictures of the turbulent boundary layer showing the modified near-wall structure when a wall is oscillated in a spanwise direction. As the oscillating wall moves upwards (Fig. 13a) the streamwise vorticity of the vortex sheet generated by the periodic Stokes layer is titled upwards as shown by an arrow indicating the vorticity vector Ω. As a result, a positive spanwise component of the vorticity is created in the near-wall region of the boundary layer. When the oscillating wall moves downwards (Fig. 13b), on the other hand, the vorticity vector Ω is titled downwards as shown by an arrow in the figure. Here, the vortex sheet produced by the downward movement of the oscillating wall has a negative vorticity as compared with the positive vorticity during the upward motion. Therefore, the downward motion of the oscillating wall again creates a positive spanwise component of vorticity. This means that a net spanwise vorticity is created in a turbulent boundary layer during upward as well as downward motion of the oscillating wall. The numerical study carried out by Baron and Quadrio [2] indeed shows the existence of the local intensity maximum of the spanwise vorticity fluctuations at $y^+ = 15$, which can be considered as the location of the net spanwise vorticity created by the Stokes layer over the oscillating plate.

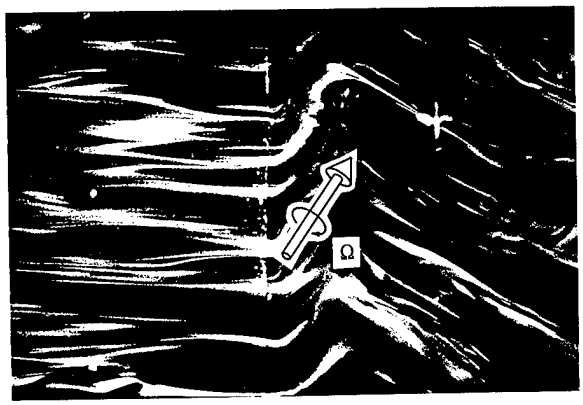

Leading edge of oscillating plate

Figure 13a. Flow visualisation of the near-wall region of the boundary layer with wall oscillation (f = 5Hz, Δz = 50mm). The leading edge of the oscillating plate is visible near the centre of the picture. The flow is from left to right and the oscillating plate on the right is moving upwards.

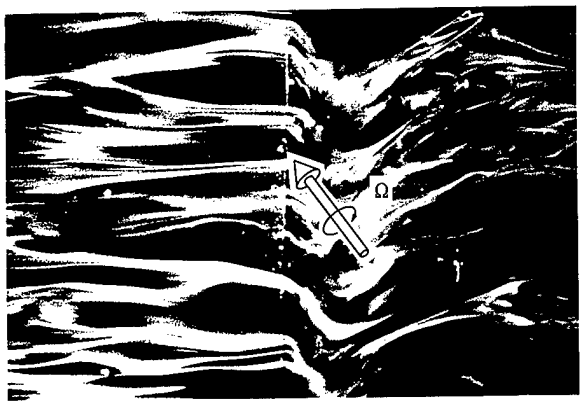

Figure 13b. Flow visualisation of the near-wall region of the boundary layer with wall oscillation (f = 5Hz, Δz = 50mm). The leading edge of the oscillating plate is visible near the centre of the picture. The flow is from left to right and the oscillating plate on the right is moving downwards.

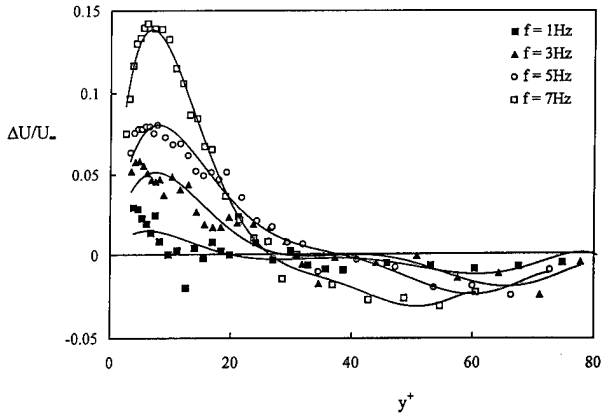

Figure 15. Velocity reductions Δu in the boundary-layer profiles 10mm downstream from the trailing edge of the oscillating plate, for different frequencies of wall oscillation (Δz = 70mm).

A conceptual model for the turbulent boundary layer over an oscillating wall is shown in Fig. 14 to demonstrate the effects of the net spanwise vorticity Ω_z created by the wall oscillation at the edge of the viscous sublayer. Using this model, it can be expected that the mean velocity gradient in the near-wall region ($y^+ < 15$) will be reduced by the induction of the spanwise vorticity. The mean velocity will be increased outside the viscous sublayer ($y^+ > 15$), on the other hand, shifting the logarithmic velocity profile upwards. These behaviours affecting the boundary layer profiles are clearly demonstrated in the present experimental results given in Fig. 3 and Fig. 2, respectively. Indeed, the measured changes in the boundary layer profiles due to wall oscillation (Fig. 15) agree very well with the prediction using the conceptual model (Fig. 14). The crossover point of the measured velocity profiles is located at $y^+ \approx 25$, which is quite consistent with the present conceptual model. It must be emphasised here that the net spanwise vorticity Ω_z does not seem to induce any inflection points in the boundary layer profile as shown in Fig. 4. Therefore, no increases in the level of the burst activity are expected as a result of the velocity induction by the spanwise vorticity.

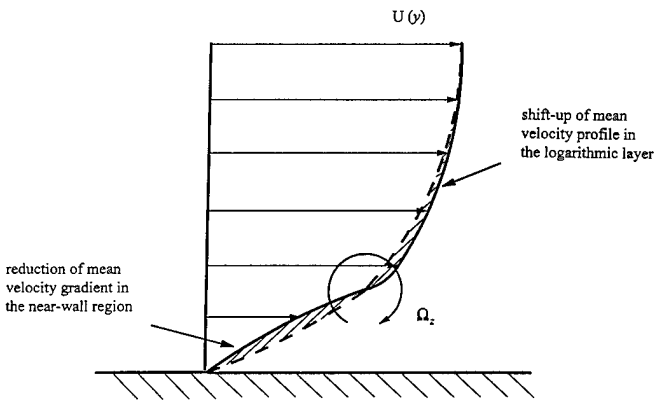

Figure 14. Conceptual model for a turbulent boundary layer over an oscillating wall, showing a spanwise vorticity Ω_z created by the periodic Stokes layer.

The results of flow visualisation in the near-wall region of the boundary layer also show that the pairs of longitudinal vortices move downstream in a sinuous form as the test plate oscillates in a spanwise direction. Figure 13a shows the near-wall boundary layer structure over the oscillating plate as it moves upwards, where the longitudinal vortices in the viscous sublayer are twisted by the Stokes layer realigning themselves into the direction of an arrow shown in the figure. When the oscillating plate moves downwards, the longitudinal vortices are twisted into the opposite direction as shown by an arrow in Fig. 13b. As a result, the streamwise vorticity associated with the longitudinal vortices is reduced in the near-wall region of the boundary layer. Indeed, it is found in the DNS results [2] that the intensity of streamwise vorticity fluctuations is nearly halved across the entire thickness of the boundary layer as the wall oscillates in a spanwise direction. As a consequence, the *near-wall burst* [6] activity is weakened leading to a reduction in turbulent skin-friction drag as observed in the present experiment. Here, the near-wall bursts are associated with the downwash of high-momentum fluid towards the wall as a result of induction by the pairs of longitudinal vortices as they stretch into the streamwise direction. Therefore, the strength of the downwash during the near-wall burst is reduced as the vorticity of the pairs of longitudinal vortices is reduced. It should be noted that the tilting of the longitudinal vortices will only affect the streamwise component of vorticity, since the spanwise realignment of the vortices takes place in alternate directions with the wall oscillation.

Figure 16a shows the conditionally sampled signature of the near-wall burst using the VITA technique at $y^+ = 1.5$ over the oscillating wall. The change in the burst signature is remarkable in the near-wall region of the boundary layer, where the duration of the burst is reduced to nearly one third of that without wall oscillation. A similar reduction in burst duration is observed at $y^+ = 4$ (Fig. 16b). Even outside the viscous sublayer at $y^+ = 20$ (Fig. 16c) the effect of wall oscillation on the burst signature is still significant, with the burst duration nearly a half of that without wall oscillation. Note that the vertical scale of the burst signatures (Figs. 16a, 16b and 16c) is normalised to allow a comparison of the behaviour of the velocity fluctuations be made. It has been observed that the turbulence intensity of the boundary layer is reduced with wall oscillation (Fig. 5), reducing the intensity of the near-wall bursts.

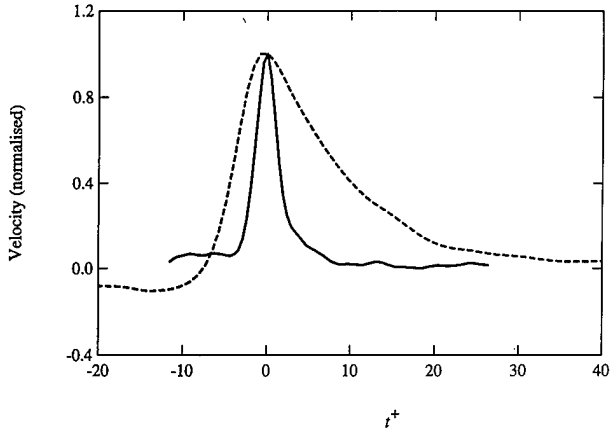

Figure 16a. Conditionally sampled near-wall burst signatures at $y^+ = 1.5$: — with wall oscillation, --- without wall oscillation.

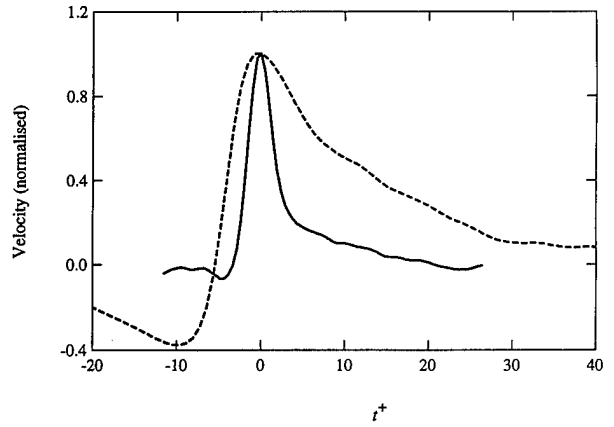

Figure 16b. Conditionally sampled near-wall burst signatures at $y^+ = 4$: — with wall oscillation, --- without wall oscillation.

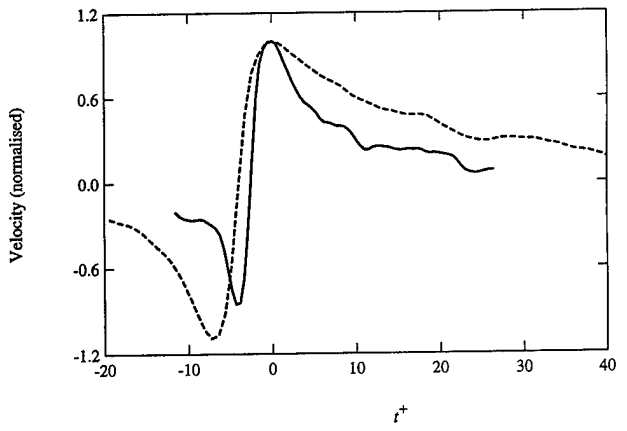

Figure 16c. Conditionally sampled near-wall burst signatures at $y^+ = 20$: — with wall oscillation, --- without wall oscillation.

IV. CONCLUSIONS

A wind tunnel study of the turbulent boundary layer with a spanwise-wall oscillation was carried out, where the skin-friction reductions as much as 45% were observed when the oscillation frequency and amplitude were adjusted to give an optimum speed of wall oscillation. With the logarithmic velocity profiles of the boundary layer shifted upwards and the turbulence intensities reduced by the spanwise-wall oscillation, the present results convincingly confirmed the basic conclusions of the recent direct numerical simulations. It was also shown that the skewness and kurtosis of the velocity fluctuations within the near-wall region are increased with a wall oscillation, agreeing very well with the boundary layer profiles of the DNS results.

It is believed that the mechanism of drag reduction by a spanwise-wall oscillation strongly relates to the net spanwise vorticity generated by the periodic Stokes layer, which reduces the mean velocity gradient of the boundary layer within the viscous sublayer. At the same time, the longitudinal vortices are realigned into the spanwise direction by the Stokes layer over the oscillating wall, reducing the streamwise vorticity in the near-wall region of the boundary layer. As a result, the *near-wall burst* activity, which is associated with the downwash of high-momentum fluid near the wall, is weakened leading to a reduction in turbulent skin-friction drag.

Although the present study was carried out in a wind tunnel, the basic findings from this research are applicable to fresh water as well as seawater environment. Indeed the author has recently carried out an experiment study of a turbulent pipe flow using water where a section of the pipe was oscillated in a circumferential direction [14]. The results indicated that the skin-friction factor of the pipe is reduced by as much as 25% as a result of active manipulation of near-wall turbulence structure by circular-wall oscillation.

The work was supported by EPSRC Research Grants, GR/J06917 and GR/K27780. The subminiature X-wire probes used in this investigation were made available from Rolls-Royce.

V. REFERENCES

1. Jung, W.J., Mangiavacchi, N., and Akhavan, R., "Suppression of Turbulence in Wall-bounded Flows by High Frequency Spanwise Oscillations," *Phys. Fluids*, Vol. A4, No. 8, 1992, pp. 1605-1607.

2. Baron, A., and Quadrio, M., "Turbulent Drag Reduction by Spanwise Wall Oscillations," *Appl. Sci. Res.*, Vol. 55, 1996, pp. 311-326.

3. Laadhari, F., Skandaji, L., and Morel, R., "Turbulence Reduction in a Boundary Layer by a Local Spanwise Oscillating Surface," *Phys. Fluids*, Vol. A6, No. 10, 1994, pp. 3218-3220.

4. Choi, K.-S., "Turbulent Drag Reduction Strategies," in *Emerging Techniques in Drag Reduction*, edited by K.-S. Choi, K.K. Prasad, and Truong, MEP, London, 1996, pp. 77-98.

5. Choi, K.-S., DeBisschop, J.-R., and Clayton, B.R., "Turbulent Boundary-Layer Control by Means of Spanwise-Wall Oscillation", to appear in *AIAA J.*, 1998.

6. Choi, K.-S., "Near-wall Structure of Turbulent Boundary Layer with Riblets," *J. Fluid Mech.*, Vol. 208, 1989, pp. 417-458.

7. Dean, R.B., "A Single Formula for the Complete Velocity Profile in a Turbulent Boundary Layer," *Trans. ASME J. Fluids Engineering*, Vol. 98, No. 4, 1976, pp. 723-727.

8. Durst, F., *et al.*, "LDA Measurements in the Near-wall Region of a Turbulent Pipe Flow," *J. Fluid Mech.*, Vol. 295, 1995, pp. 305-335.

9. Pal, S., Deutsch, S., and Merkle, C.L., "A Comparison of Shear Stress Fluctuation Statistics Between Microbubble Modified and Polymer Modified Turbulent Boundary Layers," *Phys. Fluids*, Vol. A1, No. 8, 1989, pp. 1360-1362.

10. Sherman, F.S., *Viscous Flow*, McGraw-Hill, New York, 1990.

11. Sarpkaya, T., "Coherent Structures in Oscillatory Boundary Layers," *J. Fluid Mech.*, Vol. 253, 1993, pp. 105-140.

12. Akhavan, R., Kamm, R.D., and Shapiro, A.H., "An Investigation of Transition to Turbulence in Bounded Oscillatory Stokes Flows, Part 1. Experiments," *J. Fluid Mech.*, Vol. 225, 1991, pp. 395-422.

13. Akhavan, R., Kamm, R.D., and Shapiro, A.H., "An Investigation of Transition to Turbulence in Bounded Oscillatory Stokes Flows, Part 2. Numerical Simulations," *J. Fluid Mech.*, Vol. 225, 1991, pp. 423-444.

14. Choi, K.-S. and Graham, M., "Drag Reduction of Turbulent Pipe Flows by Circular-wall Oscillation," *Phys. Fluids*, Vol. 10(1), 1998, pp. 7-9.

ON THE PHYSICS OF SKIN FRICTION REDUCTION THROUGH WALL OSCILLATION

M R DHANAK AND C SI
FLORIDA ATLANTIC UNIVERSITY
BOCA RATON, FL 33431
E-MAIL: dhanak@oe.fau.edu

Abstract – The interactions between streamwise vortices near a wall and a modified Stokes layer, induced by spanwise oscillations of the wall beneath, is described using an exact numerical solution of the Navier Stokes equations. The model flow characterizes the interactions between quasi–streamwise vortices in the inner layer of a turbulent boundary layer and an oscillating wall. In the absence of wall oscillations, as shown by Orlandi and Jimenez, the model flow involving wall–vortex interactions leads to formation of low speed streaks and an increase in skin friction at the wall surface. The wall oscillation is shown to induce annihilation of the low speed streaks, resulting in a reduction in the skin friction, the Reynolds stress and the rate of production of kinetic energy. These effects are consistent with observations in experimental and DNS studies of turbulent boundary layers and channel flows.

I. INTRODUCTION

There is significant experimental and numerical evidence that coherent structures in the inner layer of a turbulent boundary layer play an important role in the generation of Reynolds stress. These coherent structures are typically in the form of long quasi–streamwise vortices[4] which act to redistribute the longitudinal velocity field into alternating high and low speed regions while maintaining the convection of momentum normal to the wall (see for example, Kim et al[1], Spalart[2], Jimenez and Moin[3]). Based on these observations, Orlandi and Jimenez[5] have suggested a cross–plane model for the interaction between these flow structures and the rigid surface. They show that the model captures the crucial aspects of the interactions between the coherent structures and the wall and predicts fairly well the formation of low speed streaks and pertinent characteristics of turbulent skin friction. Recent experimental and direct numerical simulation studies (Laadhari et. al[6], Jung et al.[7] and Moin et al.[8]) also show that imposition of an oscillatory spanwise pressure gradient or spanwise oscillation of the wall beneath the boundary layer temporarily inhibits production of turbulence in the flow, leading to transient reductions in all turbulent quantities, including the Reynolds stress and the turbulent kinetic energy. It seems evident that these changes are related to the modification of the coherent flow structures and their distribution in the inner wall region. In this paper, we investigate the implication of the wall oscillation on the interaction between the quasi–streamwise coherent structures in the inner layer and the wall using the Orlandi–Jimenez model. Thus we numerically study the cross–plane evolution of a streamwise vortex pair and its interaction with the surface beneath, when the latter is subjected to spanwise oscillation. Hence, we show how the oscillation modifies the interaction, leading to annihilation of the low speed streaks and a reduction in the skin friction, the Reynolds stress and the rate of production of kinetic energy, consistent with observations in experimental and DNS studies of turbulent boundary layers and channel flows.

II. FORMULATION

We consider the flow in a Cartesian co–ordinate system $Oxyz$ with Ox along the streamwise direction, so that y–z is the cross–plane of interest (figure 1). The vortices in the inner layer experience axial stretching associated with straining induced by, for example, other structures; if the quasi–streamwise vortices arise from developing hair–pin eddies, it can be shown that the flow induced by the "head" of the hairpin can give rise to such straining. We, therefor, consider the velocity in our model flow to be of the form,

$$\boldsymbol{u} = [q_0(y,z,t) + x(\phi(y)' + q_1(y,z,t)),\ -\phi(y) + v_1(y,z,t),\ w_1(y,z,t)]$$

where $[x\phi(y)', -\phi(y), 0]$ is the Hiemenz flow[9] representing the straining flow; the associated straining rate is here denoted as a. All of the flow variables are non–dimensionalized with respect to the wall units. The velocity field is an exact solution of the Navier–Stokes equations with the x component of vorticity, ω_x, satisfying,

$$(\frac{D}{Dt} - \nabla^2)\omega_x = \omega_x(q_1 + \phi')$$

where $D/Dt = \partial/\partial t + (v - \phi)\partial/\partial y + w\partial/\partial z$ and $\nabla^2 = \partial^2/\partial y^2 + \partial^2/\partial z^2$. The contribution q_0 to the streamwise component satisfies

$$(\frac{D}{Dt} - \nabla^2)q_0 = -q_0(\phi' + q_1) - C_1$$

where C_1 is a constant to be determined by initial conditions. The contribution q_1 is a measure of the change in $\partial u_x/\partial x$ from that given by the Hiemenz flow and satisfies,

$$(\frac{D}{Dt} - \nabla^2)q_1 = -q_1(2\phi' + q_1) - v_1\phi''.$$

The cross–stream components of velocity are obtained by solving a Poisson equation. The flow is considered to be periodic in the z–direction with a wavelength Z. At the upper boundary of the computational domain the flow is assumed to be undisturbed and along the wall no–slip boundary condition is enforced. Thus, the boundary condition at the wall is given by $\boldsymbol{u}(x,0,z,t) = [0, 0, W_0\cos(2\pi(t + \chi T/T)]$, where W_0 is the amplitude, χ is the phase and T is the period of oscillation. Fot $t < 0$, the flow consists of a shear layer in the streamwise direction and a Stokes layer in the cross–plane, in the presence of the straining flow; an exact solution of the Navier–Stokes equations[10] is utilized for this consideration. At $t = 0$, a vortex pair, in the form of unsymmetrical vortex sheet sections (see figure 2a), of the type used by Orlandi and Jimenez[5], is introduced into the flow. The ensuing interaction is studied for different values of χ, corresponding to the phase of the oscillation when the vortices are introduced in the flow, and for different values of the period T. Time marching is performed using a third–order Runge–Kutta scheme in time.

III. RESULTS

We choose $a = 0.15$ and the vortex strength $\Gamma = \pm 300$ as typical values[4] to illustrate the interaction. The introduction of the coherent structures in the vicinity of the wall causes the average streamwise skin friction to increase due to the convection of the momentum normal to the wall. Figure 2(a, b) show the vorticity contours in the cross–stream plane at two times during the evolution of a vortex pair in the absence of wall oscillation. The vortex sheets roll up into coherent structures which convect towards each other. This in turn enhances the self induced motion of the pair away from the wall. However, the wallward motion induced by the straining flow acts to attenuate this convection, thereby enhancing the interaction of the pair with the wall. Layers of vorticity of opposite sign to that of the primary vortices are generated on the wall beneath the vortices and interact destructively with the latter. Further, the oppositely signed coherent vortices also undergo mutual cancellation. The contours of the streamwise velocity contribution q_0, corresponding to times shown in figure 2 (a, b) are depicted in figures 3(a, b) respectively and illustrate the development of a low speed streak in the manner described by Orlandi and Jimenez[5]. The streak is most intense around $t^+ = O(7.5)$, but eventually disappears as the vorticity in the pair undergoes cancellation. The cycle of the "event", comprising the appearance of the coherent vortices in the wall region, their interaction with the wall, and subsequent decay, lasts for a period of $t^+ = O(30)$. However, on the basis of a dimensional argument, Orlandi and Jimenez[5] suggest that in turbulent boundary layers, for $t^+ > O(20)$, the three–dimensional effects not accounted for in the model, including the processes which give rise to the coherent vortices, would become important so that inferences based on the model for times beyond this may not be reliable.

The effect of the oscillation was considered for a range of values of T and χ for a fixed value of $W_0 = 12$, this being the value considered in the DNS study of Jung et al[7]. The case corresponding to $T = 100$ and $\chi = 3/8$ is illustrated in figures 2 and 3. The developing vorticity contours at $t^+ = 7.5$ are shown in figure 2c. During the depicted phase, the wall is moving from right to left and the Stokes layer acts to sweep the right vortex beneath the left vortex, thereby destroying the approximately symmetrical development of the pair, apparent in figure 2(b), in the absence of oscillation. The orientation of the vortex pair is such that the straining flow brings it closer to the wall, leading to an accentuated interaction with the Stokes layer and rapid annihilation of the coherent structures. By $t^+ = 18$, the coherent structures are no longer apparent, compared to the corresponding time $t^+ = 30$ in the absence of oscillation. The associated effect on the low speed streak is shown in figure 3c. The streak, so well developed at $t^+ = 7.5$ in the absence of oscillation, is barely apparent. The oscillatory motion acts to severely distort the streak, mixing low speed and high speed momentum, thereby reducing

the region over which the Reynolds stress contribution $-u'v'$ is positive. For the phase corresponding to $\chi = 0$ (not shown), the wall is moving from left to right when the vortices are introduced, so that the left vortex is swept underneath the right vortex. For other phases, either of the vortices may be swept beneath the other. In all cases, the Reynolds stress contribution is reduced during the interaction. The comparison between the skin friction coefficient, c_f, in the presence of oscillation, averaged over the different values of χ and its value, c_{f0}, in the absence of oscillation, is shown in figure 4 for various periods of wall oscillation. A reduction of around 10% is achieved in all cases, the maximum value being for a period of $T^+ = 75$. This reduction is consistent with the results, for small times, of the DNS study[7] of turbulent flow in a channel. For large times, well beyond the validity of the present model and presumably involving many interactions of the type described here, Jung et al[7] obtained over 40% reduction in skin friction, the maximum reduction corresponding to $T^+ = 100$.

For a fixed value of a, the reduction in skin friction in our model increase with increase in Γ. The oscillation also acts to attenuate the other attributes of turbulent flow, such as the Reynolds stress and the rate of production of turbulent energy, as shown in figures 5 and 6, consistent with the results of the DNS study of Jung et al[7].

IV. DISCUSSION

As shown by Orlandi and Jimenez[7], the crucial aspects of the dominant feature of the inner layer of a turbulent boundary layer, viz. the formation and maintenance of long streamwise streaks with low streamwise–speed momentum ejection in the middle and high streamwise–speed down–wash at each side, are well captured by the cross plane model described here. The model helps to elucidate the influence of wall oscillation on the interactions in the wall region. It illustrates that when a periodic spanwise cross flow associated with the oscillatory motion of the surface, is present, the coherent structures are deformed in a way which promotes their interaction with the rigid surface beneath, leading to their rapid annihilation. The low speed streaks are significantly distorted due to mixing of momentum associated with the low–speed ejection regions and that associated with the high–speed 'sweep' regions, resulting in a reduction in the rate of momentum convection normal to the wall. This in turn has a direct impact on the Reynolds stress. The severity of the impact of the oscillation depends on the phase of the oscillation relative to the time when the vortices appear in the vicinity of the wall. Besides the effect on the Reynolds stress, the wall oscillations also have important attenuating effects on the rate of production of kinetic energy. It is likely that these effects, in turn, have important implications for the mechanism, not accounted for in the model, which gives rise to the coherent structures and consequently on the number density of the structures in the vicinity of the wall.

ACKNOWLEDGEMENT

This work was partially supported by the Office of Naval Research under grant N00014–94–1–0453 and by the National Science Foundation under grant BCS–9211 847.

REFERENCES

1. J. Kim, P. Moin, and R. Moser, *J. Fluid Mech.*, **177**, 133, 1987.
2. P. R. Spalart, *J. Fluid Mech.*, **187**, 61, 1988.
3. J. Jimenez, and P. Moin, *J. Fluid Mech.*, **225**, 221, 1991.
4. S. K. Robinson, *Ann. Rev. Fluid Mech.*, **23**, 601, 1991.
5. P. Orlandi, and J. Jimenez, *Phys. Fluids.* **6**, 634–641, 1994.
6. F. Laadhari, L. Skandaji, and R. Morel. Phys. Fluids. **6**, 3218–3220. (1994).
7. W. Jung, N. Mangiavacchi, and R. Akhavan, *Phys. Fluids*, **A4**, 1605, 1992.
8. P. Moin, T. Shih, D. Driver, and N. Mansour, *Phys. Fluids* A2, 1846, 1990.
9. H. Schlichting, *Boundary–Layer Theory*, 6th ed. McGraw–Hill, NY, 1968.
10. J. T. Stuart, In *Laminar Boundary Layers*, Ed. L Rosenhead. Dover. 1963.

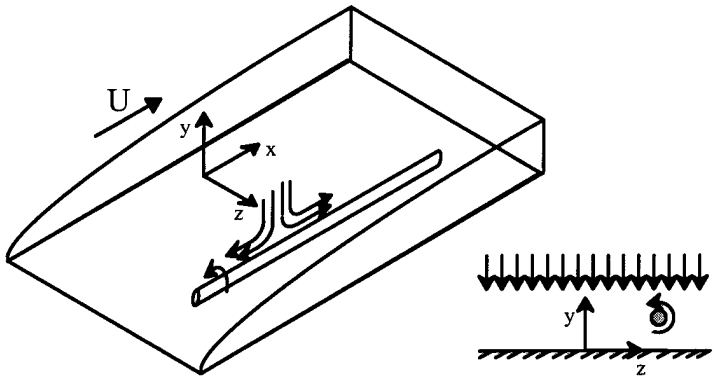

Figure 1. Schematics of the model flow.

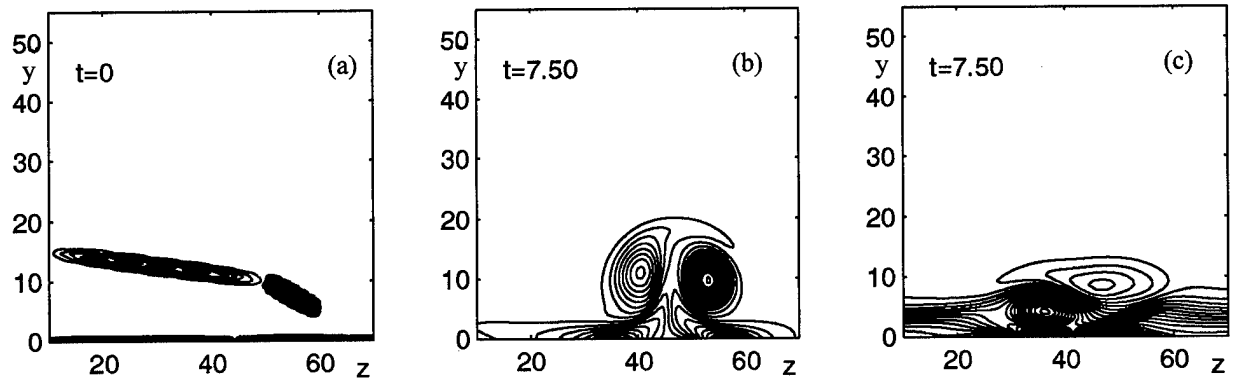

Figure 2. Evolution of a pair of streamwise vortex sheets of equal but opposite strength, at (a) $t^+ = 0$, and at $t^+ = 7.5$ in (b) the absence of oscillation, and (c) the presence of spanwise wall oscillations with $W_0 = 12$, T = 100. The figures show vorticity contours. $\Gamma = 300$, $a = 0.15$. $\Delta\omega_x = 0.9$ in (a) and 0.3 in (b) and (c).

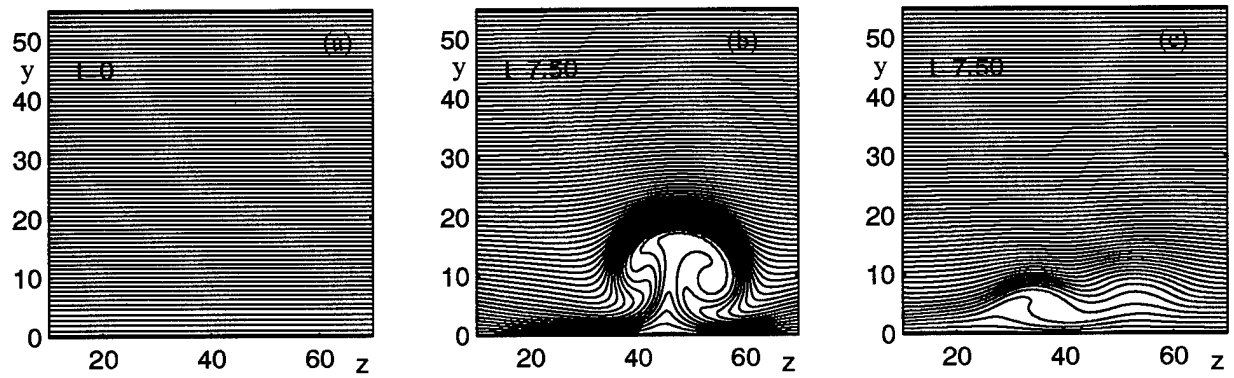

Figure 3. Streamwise velocity contours corresponding to the cases shown in figure 2. The influence of spanwise wall oscillation on the streamwise velocity streaks is apparent in the figure. 3(a) in the absence of and 3(b) in the presence of wall oscillation $\Delta q_0 = 0.75$.

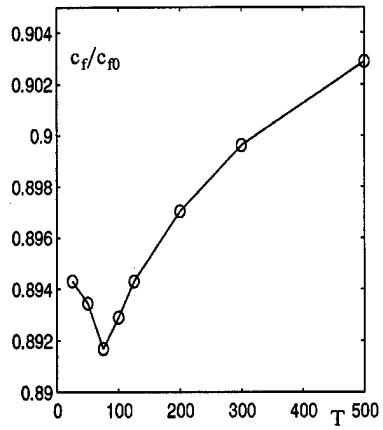

Figure 4. Ratio of averaged (with respect to z, t and χ) skin friction, c_f and c_{f0} as a function of oscillation period T.

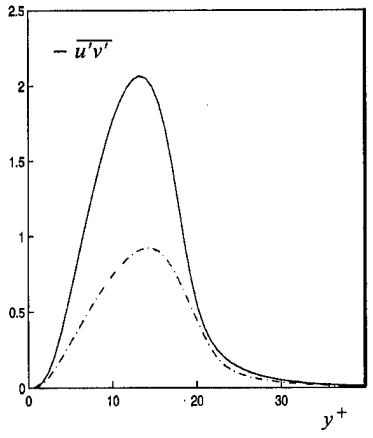

Figure 5. Comparison of the Reynolds stress in the absence of oscillation (——) with the corresponding stress, averaged over eight equally spaced phases χ, in the oscillatory case (– – –).

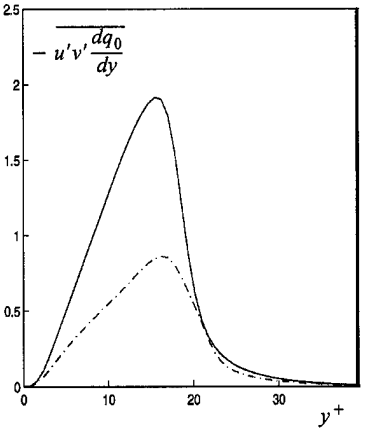

Figure 6. Comparison of the rate of production of kinetic energy in the absence of oscillation (——) with the corresponding rate, averaged over eight equally spaced phases χ, in the oscillatory case (– – –).

LOCAL OSCILLATING BLOWING IN A TURBULENT BOUNDARY LAYER

Sedat Tardu
Laboratoire des Ecoulements Géophysiques et Industriels
Grenoble - France ; Sedat.Tardu@hmg.inpg.fr

Abstract- The effect of time periodical blowing through a slot on the spatio-temporal characteristics of the wall shear stress and the turbulence in the buffer layer is experimentally investigated. It is shown that the local imposed unsteadiness affects considerably the fine structure of the near wall turbulence. The drag is reduced by steady blowing, essentially because of a different redistribution of the quadrant events. The unsteady blowing affects the vorticity generation mechanism, without appreciably interacting with this redistribution. At high imposed frequency and just downstream of the slit the near wall flow is relaminarized during the acceleration phase while it is unstable during deceleration. Spanwise vorticity of the same sign as the mean flow is accumulated and reinforced during this phase. This patch of vorticity rolls up into a coherent structure which convects downstream and increases the drag in a predictable way. These results may have important applications in the controle of separation.

I. INTRODUCTION

Aim of the research

Intensive research carried on the passive means of managing the near wall turbulence with the main goal of reducing the skin-friction has given somewhat deceptive results. Indeed, surface mounted longitudinal grooves, although being most successful, cannot achieve skin-friction reduction larger than 10% and their capacity of reducing drag is constrained to within a small range of the riblets spacing and heights being therefore quite sensitive to the changements of external flow conditions or the Reynolds number. The large eddy break up devices, on the other hand, do not result in a net reduction of the skin friction according to a consensus largely established by now.

The active and passive management of the turbulent wall shear stress is ultimately related to the interaction of the coherent structures present in the inner layer with the near wall flow. The ad-hoc out of phase active control scheme reported by Choi and al. (1994) may easily be replaced in this context. The wall shear stress τ is instantaneously enhanced in the regions wherein the spanwise vorticity $\omega_{z,0}$ is stretched due to the stagnation flow induced by the quasi-streamwise vortices - QSV (Tardu,1995, p. 378). A simple analysis conducted by Orlandi and Jiménez (1994) establishes the close relationship between τ and the characteristics of the QSW through $\tau^+ \propto \sqrt{R_{vqs}}\,\frac{u^+(2\,y_v^+)}{y_v^+}$. In this relationship, R_{vqs} and y_v^+ are respectively the mean Reynolds number and the distance to the wall of the QS vortical structures. According to this relationship, the drag reduction may be achieved either by decreasing the intensity of the QSV's or by pushing them away from the wall. The objective of this study is to explore the capacity of time and space periodical suction and blowing to increase y_v^+ and achieve drag reduction. The reasons of using such a scheme are summarized hereafter.

Control strategy

The model suggested here is essentially based on the results reported recently by Acton and Dhanak (1993) although it differs basicaly in the methodology. We consider a distribution of sources and sinks which are uniformly periodical in space and whose intensities $C_n(t)$ (related to the suction and blowing velocities) are sinusoidal in time (Fig. 1). One has therefore N sources and sinks by wave length Λ with $C_n(t) = C_{n+N}(t)$. We deal with the periodicity in the streamwise direction at the present moment , but the same scheme will be applied to the periodical suction-blowing in the spanwise direction too (Fig. 2) . The temporal variation is choosen as $C_n(t) = (-1)^n C_0\left[1 - \cos\left(2\pi f_e t - 2\pi\frac{n}{N} + \Phi_n\right)\right]$. In this expression f_e stands for the ejection frequency in the inner layer, C_0 and Φ_n are respectively the amplitude and phase of the suction and blowing. This distribution represents an injection i followed by an aspiration i+1 with a phase shift of $\frac{-2\pi}{N} + \Phi_{i+1} - \Phi_i$. An inviscid computation of the effect of this management on the distance of a "street" of vortical structures shows that the former varies in time with:

$$K\,y_v = \ln\left[\alpha - \frac{1}{2}K^2 C_0\, t \sum_{n=0}^{n=N-1}(-1)^n \cos\Phi_n\right] + \tilde{F}(t/T)$$

where F(t/T) is a periodical function with periodicity $T=1/f_e$. This relationship is similar to that given by Acton et Dhanak (1993, p. 245). It is clearly seen that if the phases are manipulated according to $\sum_{n=0}^{n=N-1}(-1)^n \cos\Phi_n < 0$, the distance y_v of the vortical structures will presumably increased once these structures interact intermittently with the pulsed surface. The expected consequence of this intervention is a reduction of drag according to the discussion made in the first section. It is without saying that the reaction of the near wall turbulence to this intervention may not be predicted by such a simple analysis and a detailed study is undoubtly necessary.

The present steady deals with the effect of a local unsteady forcing on the wall turbulence. The main aim is to investigate the time-space relaxation of the near wall flow manipulated by a time varying blowing through a localized spanwise slit. The control strategy deals clearly with first forcing the near wall turbulence, determining subsequently its frequency response and introducing finaly local suboptimal control with a *feasible distribution of MEMS* depending upon the reaction of the near wall flow.

II. DEFINITIONS, EXPERIMENTAL SET-UP and DATA REDUCTION

An experimental model has been developed in the low-speed wind tunnel of our laboratory (Fig.2a) . The blowing and suction at the wall are done through spanwise slots of dimensions 0.6*100 mm which correspond to 10*1667 in wall units. There are one blowing and one suction slot by wavelength $\Lambda = 45$ mm. ($\Lambda^+ = 750$) and the pulsed surface recovers a total length of 3Λ i.e 2250 in wall units (Fig. 2,see Tardu, 1997 for further details) . Hereafter (+) denotes values nondimensionalized with the inner variables, i.e the shear velocity $u_\tau = \sqrt{\frac{\tau}{\rho}}$ and the kinematic viscosity ν .

A special pulsating device has been designed for the present purpose. Quite satisfactory sinusoidal waveforms of the suction/blowing wall normal velocities have been obtained this way for the amplitude of the imposed velocities up to $A_{v\text{-}y^+=0} = \hat{A} = 1.5$ m/s ($\hat{A}^+ = 6$) and the imposed frequency 10Hz < f < 50 Hz ($2.5*10^{-3} < f^+ < 12.5*10^{-3}$) (see Fig. 2b).

The wall shear stress measurements have been performed by means of a Cousteix-Houdeville wall hot-wire gauge (HWG) to avoid problems caused by the conduction into the substrate . Nice results have been obtained up to the statistics of order 4 and the details may be found in Tardu (1998). The length of the sensing element is 200 μm which corresponds to a spanwise extend of $\Delta_z^+ \approx 5$ at X=1 m. from the transition point with $\overline{U}_\infty = 6$ m/s . The total duration of each record is $T_{tot} \approx 5000\,T_\infty$ where $T_\infty = \frac{\delta}{U_\infty}$ is the outer time scale. This is enough to ensure the convergence of the statistics up to 4-th order moments including those of the time derivative of the fluctuating signals.

One should be carefull in the interpretation of data in the presence of an organized motion as is the case with unsteady blowing in this study. In order to extract the deterministic and deduce the undeterministic part of the flow quantities the classical triple decomposition is used. A flow quantity $q(\vec{x}, t; T)$ is decomposed into a time mean $\bar{q}$ an oscillating $\tilde{q}$ and a fluctuating q' part :

$$q(\vec{x}, t; T) = \bar{q}(\vec{x}) + \tilde{q}(\vec{x}, t/T) + q'(\vec{x}, t)$$

where T stands for the period of the oscillating blowing. The ensemble or the phase average is performed in order to determine the amplitude $A_{\tilde{q}}$ and phase $\Phi_{\tilde{q}}$ of the oscillating part $\tilde{q}$ from which the instantaneous fluctuating part q' is adequately determined. The beginning of each cycle was provided by a pulse from a photoelectric cell triggered by the pulsator, and the trigger signal was also recorded. The modulation characteristics have been determined through a least square Fourier analysis. The procedure is the same as in Tardu et al. (1994) wherein further details are provided.

Blowing severity

In flows with uniformly distributed continuous blowing/suction (transpired layers through porous surface), the parameter which

characterizes the intervention at the wall is given by $B_f = \frac{\overline{v}_0 \overline{U}_\infty}{\overline{u}_\tau^2} = \overline{v}_0^+ \overline{U}_\infty^+$ where $\overline{v}_0$ stands for the injection/suction velocity at the wall. This is expected, since B_f appears directly in the momentum integral equation of the transpired boundary layer and plays a role similar to the Clauser pressure-gradient parameter. However, the characterization of the severity of local blowing/suction by strips is not straightforward and B_f is not suitable for describing the flow characteristics past the local intervention, as clearly shown by Sano and Hirayama (1985) and Sokolov and Antonia (1993) . Indeed, the local suction/blowing involves phenomena related to the relaxation of near wall turbulence downstream of the intervention zone. When $\overline{v}_0^+$ is high, but the injection is done over large areas, the flow has enough time to relaxe and reach its equilibrium state rapidly. On the other hand, in case of large injection velocities $\overline{v}_0^+$ over short distances, the near wall turbulence can hardly maintain its equilibrium state and its structure is expected to be strongly affected . The ratio of the injection or suction flow to the *incoming* flow rate, i.e $\Theta = v_0 L_x / \int_0^\infty \overline{U}\, dy$ is therefore introduced and proved to be adequate to measure the blowing/suction severity.

We proceeded with particularly small slot widths compared with previous studies quoted above. For instance, the experiments reported by Sano and Hirayama have been conducted with two different configurations wherein L_x was respectively 50 and 25 mm corresponding to $L_x^+ \approx 2000$ and $L_x^+ \approx 1000$ under their experimental conditions. Recall that the slit width is only $L_x^+ = 7$ here. As a consequence, the severity parameter is low. The injection velocity in steady blowing experiments investigated here is $\overline{v}_0$= 1m/s and the severity parameter is only Θ = 0.006 . The shape parameter just downstream of the slit at x/δ=0.1 is H=1.4 under these circumstances. In unsteady blowing experiments, the injection velocity $\langle v_0 \rangle$ changes in a cyclic manner between 0 and 2 m/s. The maximum value of the severity parameter in the oscillation cycle is therefore Θ = 0.012 . The shape parameter measured at the same station increased to H= 1.7 at $\overline{v}_0$ = 2 m/s but still remained below the critical value corresponding to flows prone to separate.

III. RESULTS

One of the main aims of this study is to determine whether a periodic time-varying blowing of the form $\widetilde{v}_0^+ = \widehat{A}^+ (1-\cos 2\pi f^+ t^+)$ affects the near wall turbulence characteristics when compared with a steady injection by slot with the same time-mean blowing velocity $\overline{v_0^+} = \overline{\widetilde{v}_0^+} = \widehat{A}$ resulting in the same time mean severity parameter $\Theta = \langle \Theta \rangle$. In other words, the question is whether the near wall flow interacts with the imposed unsteadiness or not. Therefore, we will systematically compare the mean flow characteristics obtained with unsteady and steady blowing hereafter. Before discussing the results, the notation needs to be clarified. Here, an asterisk (*) refers to quantities measured in the manipulated boundary layer, while the subscript S indicates steady blowing. Thus $\frac{\overline{\tau}_S^*}{\overline{\tau}}$ is the ratio of the time-mean wall shear stress in the presence of local steady blowing to the wall shear stress of standard boundary layer (SBL), and $\frac{\overline{f_e}_S^*}{f_e}$ is the ratio of the frequency of the energetic events, etc. In a similar manner, the subindex U corresponds to unsteady blowing, i.e $\overline{\tau}_U^*$ and $\overline{\tau'\tau'}_U^*$ represent respectively the wall shear stress and the wall shear stress intensity in the boundary layer manipulated by time periodical local injection.

Main mechanism of local suction/blowing. Equivalence between steady-unsteady blowing

The management of the near wall turbulence by suction/blowing is closely related to the flux of vorticity induced locally at the wall. Consider indeed the phase averaged streamwise equation of momentum *over* the slit::

$$\langle v_0 \rangle \frac{\partial_0 \langle u \rangle}{\partial y} = = -\frac{1}{\rho}\frac{\partial \langle p_0 \rangle}{\partial x} + \nu \frac{\partial_0^2 \langle u \rangle}{\partial y^2}$$

since $\langle u'v' \rangle \propto y^2$ near the wall. The subindex "0" in this equation (and hereafter) refers to quantities computed at the wall. Noting that the phase averaged spanwise vorticity at the wall is $\langle \omega_{z0} \rangle = \frac{\partial_0 \langle v \rangle}{\partial x} - \frac{\partial_0 \langle u \rangle}{\partial y} \approx -\frac{\partial_0 \langle u \rangle}{\partial y}$ because $\frac{\partial_0 \langle v \rangle}{\partial x}$ can be neglected except at the ends of the slit one has:

$$\langle v_0 \rangle \langle \omega_{z0} \rangle = \frac{1}{\rho}\frac{\partial \langle p_0 \rangle}{\partial x} + \nu \frac{\partial_0 \langle \omega_z \rangle}{\partial y}$$

which expresses the simple fact that there is equilibrium between the advection of vorticity through the slit and flux of vorticity at the wall. In the case of *suction* there is real physical removal of spanwise vorticity from the wall and the flux of vorticity is positive (since $\langle v_0 \rangle < 0$ and $\langle \omega_{z0} \rangle < 0$) as in a boundary layer with favorable pressure gradient. The withdrawn vorticity is rapidly replaced at the wall to keep the non slip condition at force so that there is a rapid generation of vorticity $\delta \langle \omega_{z0} \rangle$ *of the same sign* as in the incoming flow. As a consequence the flow accelerates by an amount which is approximately $\frac{\delta \langle u \rangle}{\delta x} \propto -\frac{\delta \langle \omega_{z0} \rangle}{\delta x} y > 0$ resulting in a local *increase* of the wall shear stress by $-\frac{\delta \langle \omega_{z0} \rangle}{\delta x} > 0$. Although it is well known that suction is qualitatively similar to flows with $\frac{\partial \langle p \rangle}{\partial x} < 0$ the former is fundamentally different in turbulent boundary layers because it involves also the removal of both streamwise and wall normal vorticity . In the case of blowing there is no removal or addition of vorticity but one still may argue that there is a flux of vorticity which is now negative as in adverse pressure gradient case. The spanwise vorticity, together with vortical intensive energetic structures are displaced and pushed away from the wall by say $\delta \langle y_v \rangle \propto \langle v_0 \rangle \delta \langle t_c \rangle$ where $\delta \langle t_c \rangle$ is the effective convection time of the structures as they are advected over the slit. This induces a *deficit* of $\delta \langle u_w \rangle \propto \langle \omega_{z0} \rangle \delta \langle y_v \rangle < 0$ in the non slip velocity at the wall. This is subsequently corrected by the formation of a thin vortex sheet in front of the wall (and of its image) with vorticity of opposite sign to that existing in the flow. The strength of this sheet may be estimated as $\frac{\delta \langle \Gamma_0 \rangle}{\delta x} \propto -\delta \langle u_w \rangle \approx -\langle \omega_{z0} \rangle \delta \langle y_v \rangle$ which subsequently dilutes through diffusion. Consequently the flow decelerates near the wall i.e $\frac{\delta \langle u \rangle}{\delta x} < 0$ and the wall shear stress decreases. This phenomena involves directly upstream of the local blowing/suction. The zone downstream of the slit is concerned with the relaxation of the turbulence structure modified by the discontinuous intervention.Note that the arguments presented here are not new : they are based solely on the spanwise vorticity and does not include the effect on the quasi-streamwise energy producing eddies. The analysis is therefore not complete yet it may provide a first schematic model to go insight more complexe phenomena.

We will now discuss the equivalence between the unsteady and steady blowing with the same time mean blowing severity parameter in terms of boundary conditions i.e flux of vorticity. First note that the pressure gradient term $\frac{\partial \langle p_0 \rangle}{\partial x}$ is retained in the streamwise momentum equation. In Falkner-Skan type flows the boundary layer approximation is often used and a specific distribution of suction/blowing velocity is required to obtain similarity solutions. In other sample computations dealing with steady discontinuous viscous suction the pressure gradient is ignored at a first glance (Sherman, 1990 p. 372). The importance of this term needs detailed full computation but it is logical to neglect it in an approximate qualitative analysis. Furthermore, in the case of unsteady blowing there is an additional complexity because the wall normal velocity induces an oscillating pressure gradient without any flux of vorticity according to $\frac{\partial \langle v_0 \rangle}{\partial t} = -\frac{1}{\rho}\frac{\partial \langle p_0 \rangle}{\partial y}$. This fact may question the boundary layer approximation near the slit. However, the main mechanism is still the flux of vorticity under the present working conditions. With a sinusoidal blowing velocity $\widetilde{v}_0^+ = \widehat{A}^+ (1-\cos\omega^+ t^+)$ expressed in wall units , it is clear that $\frac{\partial \langle p_0^+ \rangle}{\partial y^+} \sim \widehat{A}^+ \omega^+$ while the flux of vorticity is $\frac{\partial \langle \omega_z^+ \rangle}{\partial y^+} \sim \widehat{A}^+$. The maximum imposed frequency in this study is $\omega^+ = 0.1$ which shows that

the wall normal oscillating pressure gradient is an order of magnitude smaller.

According to these remarks the time mean streamwise momentum equation reduces to:

$$\bar{v}_0\,\bar{\omega}_{z0} + \left[\widetilde{\tilde{v}_0\,\tilde{\omega}_{z0}}\right] = \frac{1}{\rho}\frac{\partial \bar{p}_0}{\partial x} + \nu\frac{\partial_0 <\bar{\omega}_{z0}>}{\partial y}$$

when the blowing is unsteady. The time mean severity parameter is fixed constant in this study between steady and periodical blowing. That does not insure the same flux of vorticity for all that mainly because of the "streaming" quantity $\widetilde{\tilde{v}_0\,\tilde{\omega}_{z0}}$ in the brackets of the preceeding equation and since the mean streamwise vorticity can be different under steady and unsteady blowing conditions immediately on the injection slot. It turns out that, in the high frequency regime $\omega^+ = 0.1$ detailed in this paper, the time mean wall shear stress is not affected near the slit (until $x^+ = 40$ downstream) and that the modulation $\tilde{\omega}_{z0}$ is approximately in quadrature with the injection velocity $\tilde{v}_0$. This behaviour may be explained by the fact that the diffusing vorticity is in quadrature with the flux of vorticity in the high frequency regime to the first order (as in Stokes flow over an oscillating flat plate). This may be rigourously shown through a method given by Schlichting (1979, p. 428) but the details will be omitted here. As a consequence, $\widetilde{\tilde{v}_0\,\tilde{\omega}_{z0}}$ is 6 times smaller than $\bar{v}_0\,\bar{\omega}_{z0}$ and the "streaming" appearing in the boundary conditions may be neglected. The high frequency case therefore respects both the equivalence between time mean injection velocities and time mean vorticity fluxes.

Wall shear stress characteristics

Fig. 3 shows the profiles of the ratios $\frac{\bar{\tau}^*}{\bar{\tau}}$ and $\frac{\sqrt{\overline{\tau'\tau'}^*}}{\sqrt{\overline{\tau'\tau'}}}$ and illustrates the effect of steady and unsteady manipulations on the wall shear stress and wall shear stress intensity. The open symbols correspond to time-periodic blowing. It is seen that both steady and unsteady local blowing decreases the drag appreciably . This decrease is persistent up to $X^+ = 500$ downstream of the slot. The average drag reduction is approximately 20% . The imposed unsteadiness is slightly less efficient, but the differences between $\bar{\tau}_U^*$ and $\bar{\tau}_S^*$ are always less than 9%.

The first significant difference between time-periodic and steady local injection is in the reaction of the wall shear stress intensity (Fig. 3b). The wall shear stress intensity is significantly less reduced by unsteady blowing, compared with steady blowing. A similar reaction has been observed in the measurements of the streamwise turbulence intensity performed at $y^+ = 10$ and $X^+ = 30$. These measurements will be discussed in the next section.

The decrease of the wall shear stress intensity by steady blowing appears surprising at a first glance, since one expects an increase of the turbulent intensities in the presence of local injection . However, the effect of blowing on the turbulent intensities is most significant beyond the viscous layer ($y^+ > 50$) according to Sano and Hirayama. These authors have shown that the profiles of $\bar{u}^+{}_S^*$ and $\frac{\sqrt{\overline{u'u'}}^*_S}{U_{\infty S}}$ collapse fairly well with those of SBL when plotted against $y^{+*} = y\frac{\bar{u}_\tau^*}{\nu}$ near the wall (their fig. 5 and 9) . It is easy to show, that under these circumstances $\frac{\sqrt{\overline{u'u'}}^*_S / \bar{u}^*_S}{\sqrt{\overline{u'u'}}/\bar{u}} = \frac{u_\tau}{u_\tau^*}$. Since, $\frac{\sqrt{\overline{\tau'\tau'}}}{\bar{\tau}} \approx \frac{\sqrt{\overline{u'u'}}}{\bar{u}}$ as $y^+ \to 0$ the last relationship results in $\frac{\sqrt{\overline{\tau'\tau'}}^*_S}{\sqrt{\overline{\tau'\tau'}}} \approx \sqrt{\frac{\bar{\tau}_S^*}{\bar{\tau}}}$. The measurements reported here are in good quantitative agreement with this estimation when the blowing is unsteady, but this correspondance is only qualitative in the case of steady injection. It has to be noted that detailed measurements very close to the wall are needed in order to confirm the analysis above, and the closest point to the wall in the data of Sano and Hirayama is only $y^+ \approx 5$.

The effect of the unsteadiness is more pronounced with respect to the fine structure of τ'. Fig. 4a shows that the skewness of the wall shear stress is increased by a factor 1.8 near the slot when the blowing is steady. In contrast, when the injection is unsteady the skewness of τ' is only slightly affected. The mechanism of drag reduction is therefore certainly different in both manipulations. The increase of $S_{\tau'}^*$s may be interpreted either as the strengthening of the quadrant 4 events with $\tau' > 0$ (sweeps), or equivalently the inhibition of the quadrant 2 events with $\tau' < 0$ (ejections) . We therefore suspect that the steady blowing decreases the drag by modifying the inner structure of the flow through the distribution of the quadrant contributions. This is only speculative at the present moment and in order to give a clear answer to this question more detailed measurements have to be performed. The imposed unsteadiness presumably does not affect the quadrant distribution, although measurements of conditional Reynolds stresses may provide a definitive answer to this speculation. It will be shown in the next section that the unsteadiness interacts strongly with the vorticity generation mechanism near the wall.

The flatness of the fluctuating wall shear stress reacts in a manner similar to $S_{\tau'}^*$ (Fig. 4b). $F_{\tau'}^*$s increases significantly near $x \approx 0$ while the unsteady blowing does not affect appreciably the spotty character of the fluctuating wall shear stress.

The skewness $S_{u'}^*$ and flatness $F_{u'}^*$ measured at $y^{+*} = 10$ and shown by squares in Fig. 4 behave in the same manner as $S_{\tau'}^*$ and $F_{\tau'}^*$. The comments are therefore similar . The increase of $S_{u'}^*$s may be interpreted as the enhancement of the convective diffusion by turbulence, i.e. the term $-\frac{\partial}{\partial x}\overline{u'\frac{q^2}{2}} = -\frac{1}{2}\frac{\partial}{\partial x}\left\{\overline{u'^3} + \overline{u'v'^2} + \overline{u'w'^2}\right\}$ of the turbulence energy, $\overline{q^2}$, equation. This term is an order of magnitude smaller in the canonical boundary layer compared with $-\frac{\partial}{\partial y}\overline{v'\frac{q^2}{2}}$, but it is certainly important near the slot in the presence of injection. The integration of the equation $\frac{D}{Dt}\frac{\overline{q^2}}{2}$ between two planes $x/\delta \approx 0$ at the injection point, and at $x/\delta \approx 2$ downstream where the flow reaches its equilibrium state, shows that there is a net contribution to the flux of energy of the order of $\left(\frac{1}{2}\overline{u'^3}\right)_{x/\delta=0} = \frac{1}{2}\overline{u'^2}^{3/2} S_{u'}$ due to the transfer from regions of large intensity to regions of smaller intensity as imposed by the local injection at the wall. The results presented here show that in the case of steady injection there is an increase of the convective flux and this is in agreement with Sano and Hirayama (1983) who reported that the (steady) blowing increases the values of each term in the turbulent energy equation . There are two additional terms in the equation governing the mean turbulent kinetic energy $\overline{q^2}^*$ for unsteady blowing. These are respectively in the advective and the production terms and they result from the interactions between deterministic parts of the corresponding components . The turbulent diffusion term is however of the same form as in $\frac{D}{Dt}\overline{q^2_S}^*/2$. Since the skewness factors are only slightly affected by unsteady blowing, one may conclude that the imposed unsteadiness inhibits considerably the streamwise convective flux of energy. The effect of the imposed unsteadiness is strongly frequency dependent : at larger imposed frequencies ($f^+ > 0.015$) , the flow is "relaminarized "during half of the oscillation cycle near the slot and the flatness and the skewness increase during these periods showing the presence of highly intermittent hardly active sweep type events. As a consequence the time mean of these quantities increase also near the wall. These points will further be discussed in the last part of this section.

Modulation characteristics

Fig. 5a shows the phase average of $<u'u'>/\overline{u'u'}$ measured at $y^{+*} = 10$ and $x^{+*} = 44$, for $f^+ = 0.017$. It is found that the streamwise velocity is modulated but that $a_{\tilde{u}}$ does not exceed 0.20 . The response of <u> is nonlinear and harmonics larger than one are of importance in the high imposed frequency regime.

The first streaking feature of $<u'u'>/\overline{u'u'}$ shown in Fig. 5a is the occurrence of unexpectably large modulations of the turbulence intensities which lead to relative amplitudes as high as $a_{\widetilde{u'u'}} \approx 0.8$. It is quite surprising to note such severe effects on the turbulence when one recalls that the unsteady <v> forcing is only local. These large modulations point at the existence of a *relaminarization* phase during the cyclic oscillations.

The strong modification of the wall turbulence structure is better captured in Fig. 5b which shows the phase average of the skewness of du'/dt and of the ejection frequency $<f_e^{+*}>$ identified by modified u'-level technique at $f^+ = 0.017$ by using the phase averaged thresholds. Recall that $S_{du'/dt}$ is related to the vorticity stretching and the non linearity in the inner layer. Fig. 5b shows that both the vorticity generation and production

mechanisms are altered at high blowing frequency during almost the half of the oscillation cycle.

The effect of the imposed unsteadiness on the vorticity stretching mechanism was further investigated by examining the behaviour of $S^*_{du'/dt\ U}$ at $y^+=10$ versus the imposed frequency (Fig. 6). It is found that the steady blowing does not affect the skewness of du'/dt. The changes of $S^*_{du'/dt\ U}$ indicate therefore a direct effect of the imposed unsteadiness. Fig. 6 shows that in the low imposed frequency regime there is no effect of the oscillations on $S^*_{du'/dt\ U}$ and $S^*_{du'/dt\ U}$ which is close to the value in SBL. The skewness $S^*_{du'/dt\ U}$ decreases steadily once $f^+ > 0.005$ and this constitutes one of the most interesting results inferred from this study. The vorticity stretching mechanism and therefore the nonlinearity are weakened by oscillating blowing by a factor of 3 in the high imposed frequency regime (Fig. 6). This effect is saturated once $f^+ > 0.007$. Note also that there does appear to be a slight kink in the data near $f^+ \approx f^+_{cr} = 0.01$.

Detailed analysis of the wall turbulence near the injection slot in the high frequency regime

It has been clearly conjectured that the most interesting features of unsteady local blowing are perceptible in the high frequency regime. Detailed analysis in the region x+50 downstream of the slit will now be given at the highest frequency that we could reach in this study i. e $f^+=0.017$.

Time mean flow

Fig. 7 shows the time mean streamwise velocity profiles in the standard boundary layer and in the presence of steady or unsteady blowing at $x^+=31$ downstream of the slit. The velocity $\bar{u}$ and the wall normal coordinate y are scaled with the local inner variables i.e by $\bar{u}_\tau$ in the SBL and $\vec{u}_{\tau S}$ or $\vec{u}_{\tau U}$ in the manipulated boundary layer. The first streaking feature of the results summarized in Fig. 7 is the insensitivity of the time mean streamwise velocity profiles to the imposed unsteadiness. It is indeed seen that both $\vec{u}_S^{\,+}$ and $\vec{u}_U^{\,+} = \overrightarrow{\langle u \rangle}^+$ corresponding respectively to steady and unsteady blowing collapse fairly well in the entire boundary layer. It is recalled that the wall shear stress is also unaffected at the mean by oscillating blowing at this particular station and that $\frac{\bar{\tau}^*_S}{\bar{\tau}} = 0.67$ while $\frac{\bar{\tau}^*_U}{\bar{\tau}} = 0.67$.

One distinguishes easily in Fig. 7 between the viscous sublayer, the buffer layer and the log-layer in the MBL in the same way as in the canonical boundary layer. The viscous sublayer is considerably thickened in the presence of blowing and one has $\vec{u}_S^{\,+} \approx \vec{u}_U^{\,+} = y^+$ at $y^+ < 12$. Note also that the velocity profiles collapse well with $\bar{u}^+ = 2.5 \ln y^+ + 10.5$ for $y^+ > 40$ pointing at the existence of a constant shear layer with time mean equilibrium. The buffer layer, on the other hand, is somewhat thinned and extends from only $y^+ = 12$ to $y^+ = 40$.

The upward shift observed in the log region in the manipulated boundary layer is in agreement with the direct numerical simulations conducted by Choi and all. (1997) who investigated the effects of blowing and suction from a spanwise slot. This is a common feature of drag reduced flows and we will now show that it may be quantitatively explained by Rotta's theory (1950, see also Hinze, 1975; p. 619). Rotta used the Prandtl mixing-length hypothesis and modelled the shear stress as :

$$\frac{\partial \bar{u}^+}{\partial y^+} - \overline{u'v'}^+ = \left[1 + l_m^{+2} \frac{\partial \bar{u}^+}{\partial y^+} \right] \frac{\partial \bar{u}^+}{\partial y^+} = 1$$

where, contrarily to the classical theory, the mixing length is taken as $l_m^+ = \chi \left(y^+ - \delta_v^+ \right)$ with δ_v^+ standing for the thickness of the viscous sublayer in wall units and χ the von Karman's universal constant. The virtual origin of the mixing length is therefore shifted by δ_v^+ and the flow within $y^+ < \delta_v^+$ is supposed to be completely viscous. The streamwise velocity distribution resulting from this closure reads for large values of y^+ $\bar{u}^+ = A \ln y^+ + B$, with $A = \frac{1}{\chi}$ and $B = \frac{1}{\chi}(\ln 4\chi - 1) + \delta_v^+$ (Hinze, 1975; p. 627). It is seen that B is directly related to the viscous sublayer thickness. Taking $\chi = 0.4$ and $\bar{\delta}^+_{v\,S} \approx \bar{\delta}^+_{v\,U} = 12$ in the manipulated boundary layer, leads to B=10.6 which is in close agreement with the results summarized in Fig. 7. Consequently, and according to the Rotta's model, one may easily argue that the increase of the constant B in the log-layer encountered in flows with drag reduction is a direct consequence of the thickening of the viscous sublayer and vice versa.

The turbulence intensity $u'^+ = \sqrt{\overline{u'u'}} / \bar{u}_\tau$ distributions expressed in local inner variables (i.e, $u'^{*+}_S = \sqrt{\overline{u'u'}^*_S} / \vec{u}_{\tau S}$, $u'^{*+}_U = \sqrt{\overline{u'u'}^*_U} / \vec{u}_{\tau S}$) and obtained at $x^+=40$ are shown in Fig. u'. The turbulence intensity in the manipulated buffer layer exceeds the standard boundary layer profile by roughly 15% . There are noticeable qualitative and quantitative differences in the reaction of u' to steady and unsteady blowing. It is seen in Fig. u' that, in the presence of unsteady blowing u'^{*+}_U reaches its maximum at $y^+=10$ somewhat earlier than u'^{*+}_S. It keeps its maximum furthermore in the whole buffer layer $10<y^+<30$. This unexpected reaction shows that the imposed unsteadiness increases mixing in the inner layer and this peculiarity may also have some applications. A detailed analysis of the fine structure (i.e the skewness and flatness of u' and the skewness of du'/dt) has revealed that the turbulence has an isotropic character in the whole buffer layer, indicating that the imposed unsteadiness acts as a "whitening filter". The steady blowing, on the other hand, does not affect the qualitative behaviour of the u'^{*+}_S profiles which presents a well defined maximum near $y^+ \approx 13.5$ as in the canonical boundary layer.

Phase averages

Wall shear stress

Fig. 9 a shows the cyclic modulation of the wall shear stress at $x^+=20$ and 40 downstream of the slit. The phase average $\langle \tau \rangle$ is scaled with the time mean wall shear stress $\bar{\tau}_{SBL}$ of the unmanipulated standard boundary layer. The waveform of the injection velocity (to not scale) is also shown in this Fig. It is clearly seen that $\langle \tau \rangle$ is strongly modulated during the oscillation cycle and that its response becomes strongly non linear with increasing downstream distance. The striking feature of the reaction of $\langle \tau \rangle$ takes place during the acceleration phase of the injection velocity. The wall shear stress decreases rapidly during this phase until it reaches the laminar limit defined as the value that a laminar Blasius boundary layer would have at the same Reynolds number. The corresponding phase averages of the wall shear stress intensity $\frac{\langle \tau'\tau' \rangle}{\bar{\tau}'\bar{\tau}'_{SBL}}$ are shown in Fig. 9b. The near wall turbulence activity is totally suppressed at $x^+=20$ during half of the oscillation cycle coinciding once more with the acceleration phase of $\langle v_0 \rangle$. At $x^+=40$ there is a slight increase in $\langle \tau'\tau' \rangle$ at t/T= 0.6. The close inspection of the data has shown that this corresponds to a transitional spot resulting from the set-up of a time space localized instability. The velocity profiles near t/T=0.8 (i.e in the middle of the deceleration phase) are indeed found strongly inflectional (not shown here) indicating that the flow is first relaminarized and that it subsequently enters into a retransition phase.

Streamwise velocity and streamwise turbulence intensity

The phase averages of the streamwise velocity $\langle u \rangle$ measured at $x^+=40$ are normalized with the time mean velocity $\bar{u}^*_U$ in Fig. 10. They express therefore the relative modulation of $\langle u \rangle$. The modulation of $\langle u \rangle$ is large in the low buffer layer $y^+<10$ ($y^{+*}<8$) and decreases very rapidly in the low log layer. The penetration depth of the perturbation induced by oscillatory blowing is about $\delta y^+= 20$ at this particular x^+ position. The streamwise turbulence intensity, in return decreases rapidly during the acceleration phase in the low buffer layer (Fig. 11) and the modulation penetrates further until the low log layer.

IV. DISCUSSION

The ensemble of ingredients characteristic of relaminarization are present near the slot at $x^+< 40$ and during half of the cycle namely:

*The wall shear stress decreases considerably until reaching the value that a laminar boundary layer would have at the same Reynolds number.

*Dissipation dominates the near wall flow which is stabilized.

*The velocity fluctuations in the inner layer are not zero but their contribution to the dynamics of the flow becomes inconsequential

*The frequency of active Reynolds stress producing events decrease considerably and a thin region near the wall extending to approximately 2-3 wall units grows from the wall being free of fluctuating streamwise vorticity. The thickness of this zone reaches almost 5 wall units during half of the oscillation cycle.

* The stretching of quasi-streamwise vorticity decreases strongly as indicated by even negative value of the skewness of the streamwise velocity fluctuations. This part of the oscillation cycle coincides also with large increases of the Taylor time scale.

The space time evolution of the near wall flow at further downstream locations is also quite interesting altough it could not be discussed here and

will be presented at the symposium. First the velocity profiles become strongly inflectional at x^+=40 and the flow enters into retransition further downstream following the scheme strickly similar to that reported by Narasimha and Sreenivasan (1973). This gives place to the accumulation and enhencement of a patch of spanwise vorticity of the same sign as the mean vorticity during the decelaration phase. This patch rolls up into a coherent structure near the wall. The birth of this structure (shown by an arrow in Fig. 9a) and its subsequent development are perfectly well localized both in time and space . This structure is convected downstream with a convection velocity roughly equal to 10 in wall units. Consequently the wall shear stress increases almost in a Dirac function fashion at times and locatios which are perfectly predictible. The whole phenomena relaxes further downstream. It is emhasized here that the phase averaged velocity profiles did show anywhere points with local gradients equal to zero and therefore the observed behaviour is not due to an unsteady separation according to Moore-Sears criteria.

V. CONCLUSION

*The unsteady blowing decreases the wall shear stress without affecting the skewness. In other words and presumably, it does not affect the distributions in the quadrants. This conclusion has to be checked further by detailed <u'v'> measurements.

* There is a clear effect of the imposed unsteadiness on the the time mean flow and therefore a clear coupling between the imposed oscillating blowing and the near wall turbulence.

* The modulation of the shear is confined in a layer of thickness $\delta^+_{uns} \propto 1/\sqrt{f^+}$ and the amplitude of the shear increases with imposed frequency. There is subsequently an oscillating pressure gradient resulting from continuity. This imposed nonhomogeneous and time varying pressure gradient affects locally the time-space development of the coherent structures. On the other hand, if it is argued that the suction essentially removes vorticity near the wall, the unsteady suction may allow us to control the thickness of the boundary layer to manipulate. The unsteady suction deserves in this sens a detailed study.

* The high sensitivity of <u'u'> to the imposed frequency (Fig. 5a) suggests the possibility of management of the near wall turbulence in an interesting way. The unsteady blowing through spanwise slits separated by x^+=50 and through which the blowing at one slot is in opposition of phase with the other, may result in important reduction of the near wall turbulence activity.

* Finally, the investigation of the same technique by making use of streamwise slits to affect the quasi-streamwise structures may reveal interesting features.

VI. REFERENCES

1. Acton E., Dhanak, M.-R. " The motion and stability of a vortex array above a pulsed surface" J. Fluid Mech. 247, pp. 231-245; 1993
2. Bewley T., Choi H., Temam R., Moin P. " Optimal feedback control of turbulent channel flow" Annual Research Briefs, CTR; pp. 3-14 ; 1993
3. Choi H., Moin P., Kim J. "Active control for drag reduction in wall-bounded flows" J. Fluid Mech., 262, pp. 75-110; 1994
4. Kim J., Moin P., Moser R., 1987 " Turbulence statistics in fully developed channel flow at low Reynolds number" J. Fluid Mech., 177, 133
5. Narasimha R., Sreenivasan K.R., 1973 "Relaminarization in highly accelerated boundary layers" J. Fluid Mech. ,61, pp. 417-447.
6. Orlandi P., Jiménez J., 1994 " On the generation of turbulent wall friction" Phys. Fluids, 6, pp. 634-641
7. Sano M., Hirayama N., 1985 " Turbulent boundary layers with injection and suction through a slit" Bulletin of JSME, vol.28,pp.807-814
8. Schlichting H., 1979 "Boundary-Layer Theory" Seventh Edition ;McGraw Hill .
9. Sherman F. , 1990 "Viscous Flow" ; McGraw Hill
10. Sokolov M., Antonia R.-A. " Response of a turbulent boundary layer to intensive suction through a porous strip" Ninth Symp. on Turbulent Shear Flows, Kyoto, pp. 5-3-1 to 5-3-6, 1993.
11. Tardu, S., Binder G., Blackwelder R. "Turbulent channel flow with large amplitude velocity oscillations" J. Fluid Mech., 267, pp. 109-151
12. Tardu, S., 1995 "Coherent structures and riblets" Appl. Sc. Research. , 54, pp. 349-385
13. Tardu ,S., 1998 "Near wall turbulence control by local time-periodical blowing" To appear in Exp. Th. Fluid Science. 14 pages.

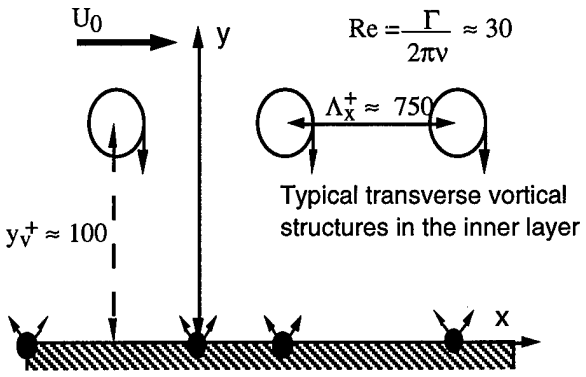

nth source:

$$C_n(t) = (-1)^n C_0\left[1 - \cos\left(2\pi f_e t - 2\pi\frac{n}{N} + \Phi_n\right)\right]$$

Figure 1 Control strategy

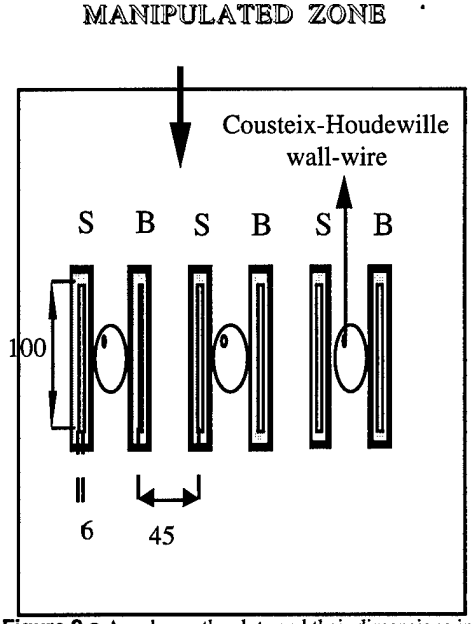

Figure 2 a Are shown the slots and their dimensions in mm . S and B refers respectively to suction and blowing.

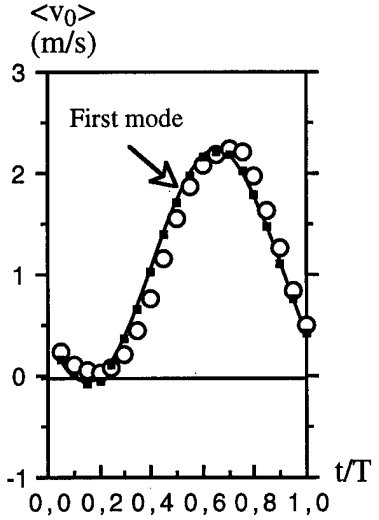

Figure 2b- Example of phase average of the injection velocity; the imposed frequency in wall units is f^+= 0.017.

a-

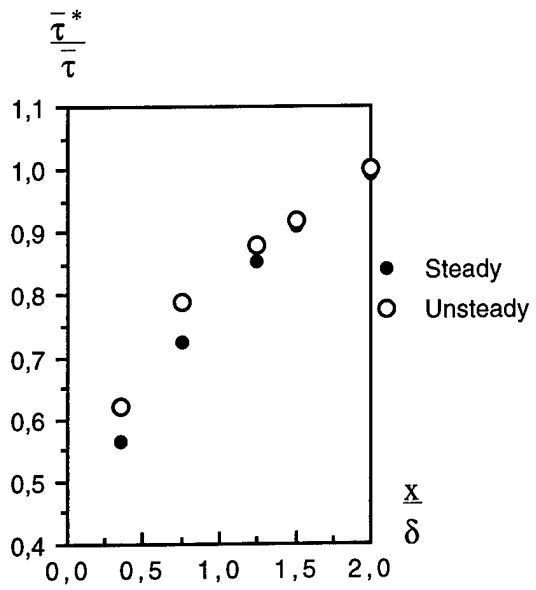

b-

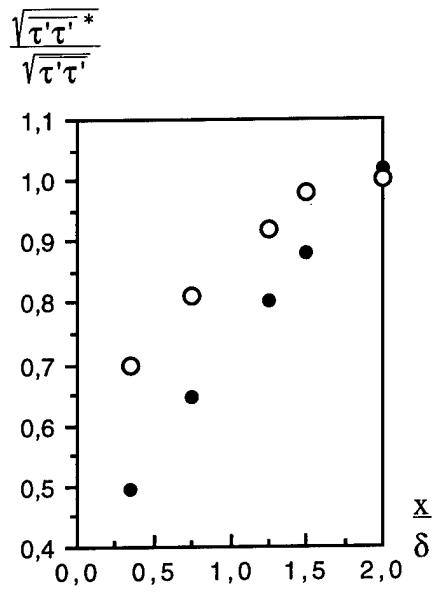

Figure 3 Ratio of (a) the time mean wall shear stress and (b) the wall shear stress intensity (b) in the manipulated versus standard boundary layers. Comparison of steady and unsteady blowing; $f^+ = 0.0072$ and $\hat{A}^+ = 5.4$ for different x stations downstream of the slot; δ is the local boundary layer thickness.

a-

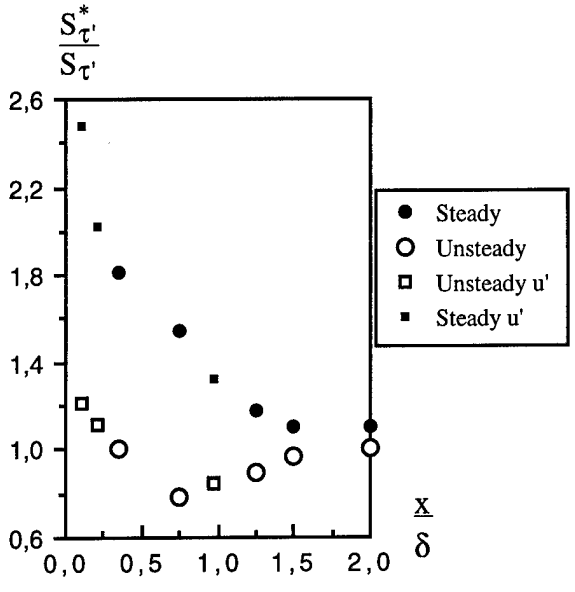

b-

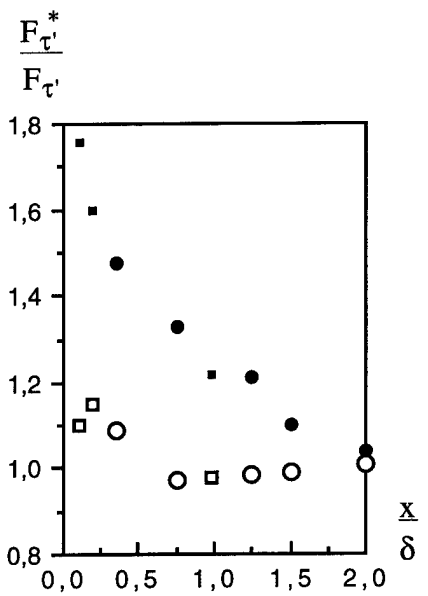

Figure 4 -Ratio of (a) the skewness and (b) flatness of the instanteneous wall shear stress in the manipulated and unmanipulated boundary layer. Comparison of steady and unsteady blowing; $f^+ = 0.0072$ and $\hat{A}^+ = 5.4$. Also shown the corresponding statistics of u' measured at $y^+=10$. See (a) for captions.

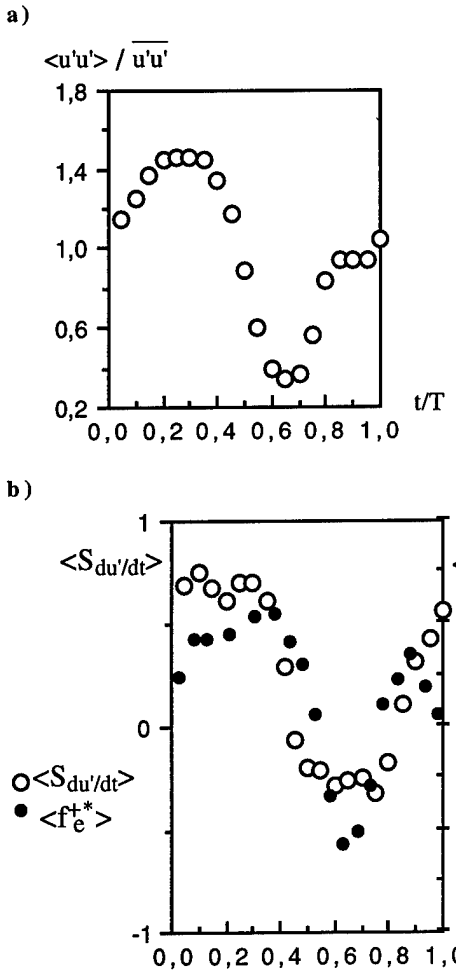

Figure 5 Phase averages at y^+=14 and x+= 44: a- Turbulence intensity at f^+=0.017 ; b- Skewness of time derivative of u' and the ejection frequency determined by mu'-l technique; the imposed frequency for (b) is f^+=0.017

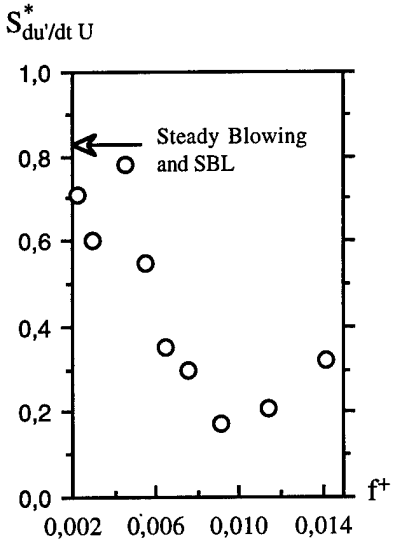

Figure 6 Skewness of the streamwise velocity time derivative at y^+=14 under unsteady blowing vs. the imposed frequency. $\widehat{A}^+$ = 5.4; U_∞ =4 m/s.

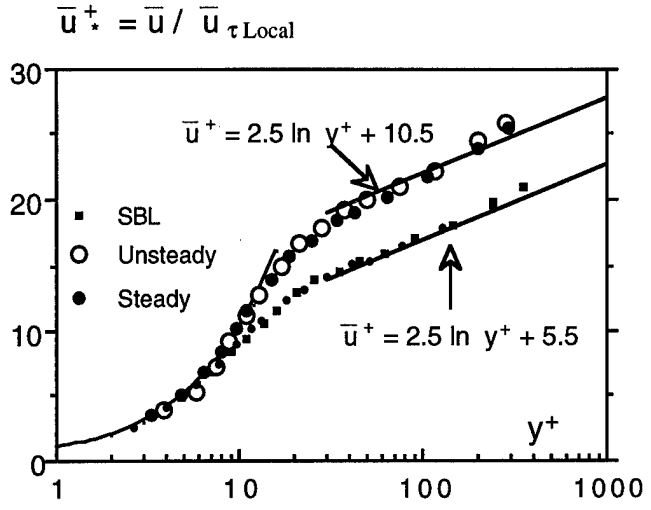

Figure 7 Time mean velocity profiles at x^+=40. Comparison steady-unsteady blowing. The imposed frequency is f^+=0.017 .

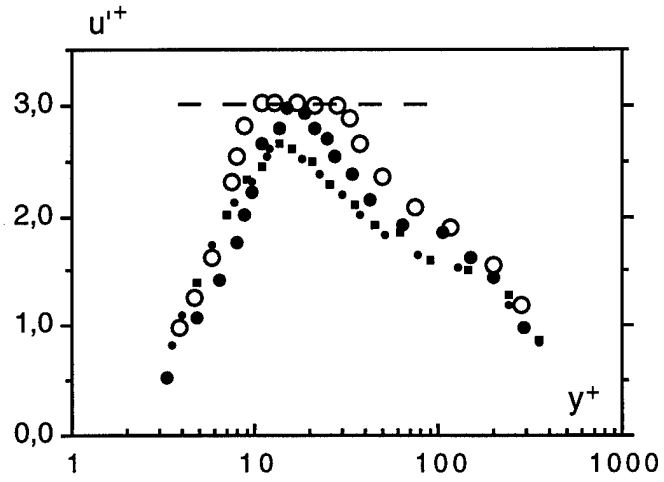

Figure 8 Time mean streamwise turbulence intensity at x^+=40. Comparison steady-unsteady blowing. The imposed frequency is f^+=0.017 . For caption see Fig. 7

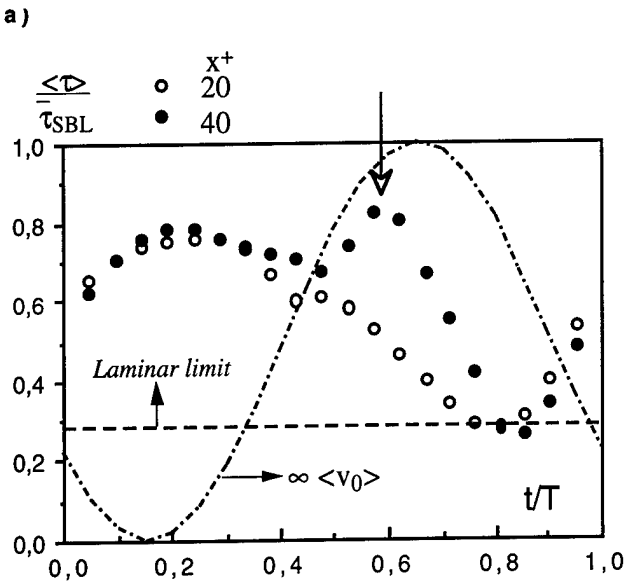

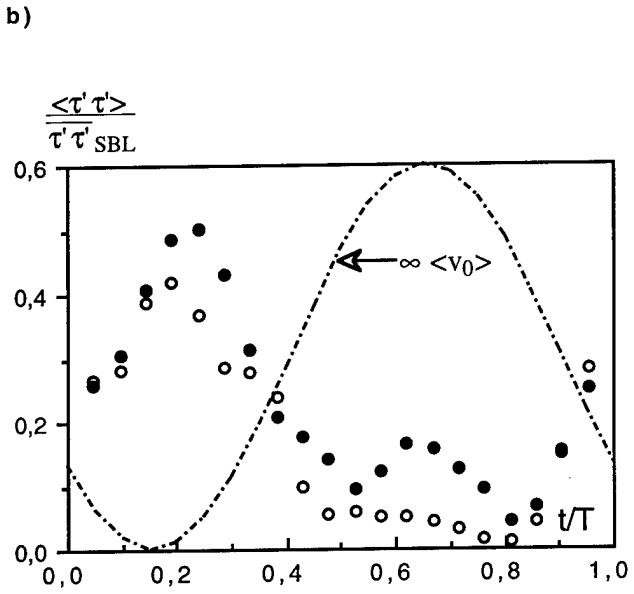

Figure 9 Phase averages of the wall shear stress (a) and wall shear stress intensity (b) at x^+=20 and 40 downstream of the injection slit. The imposed frequency is f^+=0.017.

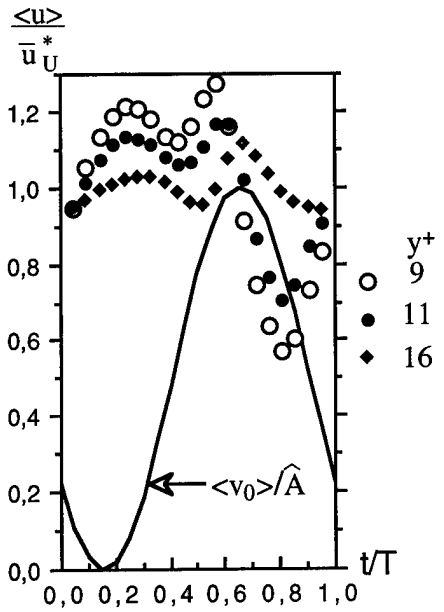

Figure 10 Phase average of the streamwise velocity at different epochs of the oscillation cycle.

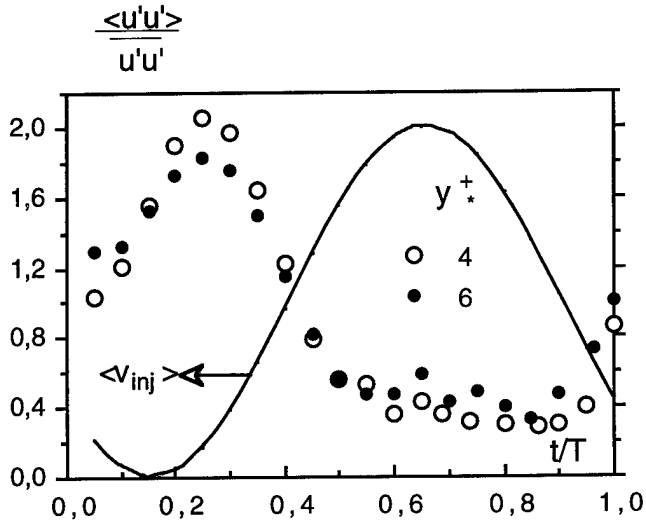

Figure 11 Modulation of the turbulence intensity in the viscous sublayer.

DRAG REDUCTION THROUGH THE NEAR WALL VORTEX SYSTEM MANAGEMENT
INTERNATIONAL SYMPOSIUM ON SEAWATER DRAG REDUCTION

Yu. N. Savchenko
Institute of Hydromechanics of Ukrainian National Academy of Sciences
8 / 4, Zhelyabov str., Kyiv, 252057, Ukraine
Fax (044) 446 42 29, e-mail: sav@ihm.kiev.ua

The systems of surface vortices were observed on a skin of quickly swimming dolphins, penguins, fishes and on the boundary between the two streams in form of Kelvin - Helmgoltz flow. Results of experimental and theoretical investigation on the skin friction drag reduction by means of artificial vortex systems generation near the wall on the two-dimensional surfaces of bodies of revolution are presented in this paper. The two-dimensional potential model of the vortex system near the solid wall is considered as a basic theoretical model. It was shown that we can choose the vortex chain parameters so that the fluid velocity on the wall becomes a periodic function with zero mean value. The boundary layer is not developed in such flow, and the mean value of the friction force is equal to 0. These theoretical investigations help to choose optimal parameters of the vortex system for drag reduction. The experiments of the secondary vortex flow registration in the hollows of the traveling waves along the surface are demonstrated. It was shown that such flow arises when the velocity of spreading the traveling waves is equal to 0.5 of the free stream velocity. Results of the experiments on generation of the vortex spiral systems on bodies of revolution with help of the special rotating turbines. It was noted that besides the positive effect for the drag reduction, such generators of the spiral vortices having turbine shape can produce some additional energy.

I. INTRODUCTION

In 1955 Assapian and Cramer have discovered the phenomenon of traveling wave formation on a skin of quickly swimming dolphins and fishes and delivered the question about their roles in reaching the high speeds in water [1].

In 1967 Merculov theoretically has shown that the traveling waves can form a secondary vortical system in fluid and for the first time has connected the friction drag reduction with vortical system existence near the surface [2]. This fundamental conclusion has been confirmed experimentally [3]. It was found that

(1) the vortex system formed by traveling waves is a main cause of reduction of the surface friction;

(2) the created vortex system is relatively steady;

(3) the vortex system begins to form when the phase speed of traveling wave C reaches the half of the mainstream velocity V_∞ ;

(4) at $C/V_\infty > 0.6$ the surface drag coefficient ceases to depend on Reynolds number, that is evidence of secondary flow periodicity.

Kalugin and Panchuk have demonstrated the process of secondary flow formation by traveling wave by means of the numerical solution of Navier-Stokes equation [4]. The total formation of vortices has proved to cease after passing by flow approximately of twenty wave lengths λ .

We used the vortex analogy with roller of radius R for estimation of energy for the vortical system maintenance in a traveling wave [5] (Fig. 1). In accordance with this analogy the vortex moves relatively to surface with velocity $0.5V_\infty$ and rotates with angular velocity $\omega = V_\infty / 2R$. The necessary energy along the length L and surface width unit is approximately presented in form of sum of three parts:

1) the kinetic energy of rotary roller motion $E_\omega = \rho\pi R^2 V_\infty^3 / 32\lambda$, where ρ is fluid density;

2) the kinetic energy belonging to vortex-roller from V_∞ to $0.5V_\infty$ $E_k = 3\rho\pi R^2 V_\infty^3 / 16\lambda$ for fluid deceleration;

3) the viscous dissipation energy $E_\nu = 4\pi\nu\rho\omega^2 R^2 L/\lambda$, where ν is kinetic viscosity coefficient.

The sum has the form:

$$E = E_\omega + R_k + E_\nu = \frac{\pi\rho L V_\infty^2}{\lambda}\left[1 + \frac{7}{32}\left(\frac{R}{L}\right)^2 \mathrm{Re}_L\right]. \qquad (1)$$

In the case of large $\mathrm{Re}_L = V_\infty L/\nu$, a ratio of the energy E to the turbulent boundary layer energy of the flat plate [6] $E_F = 0.0307 L\rho V_\infty^2 0.5\mathrm{Re}_L^{-\frac{1}{7}}$ is equal to:

$$\frac{E}{E_F} \approx 44.7 \frac{R^2}{\lambda L}\mathrm{Re}_L^{\frac{1}{7}}. \qquad (2)$$

It is clear that the possible advantage increases at increase of L and can reach the values considerably more than $0.1E_F$.

As far as the surface with traveling waves is a difficult problem for technical realization, it is appropriate to create directly a similar vortical system by special generators of vortices [9].

We give the theoretical explanation of concepts of the friction drag reduction in the fluid flow by means of a vortex chain creation near the body surface. We use the two-dimensional potential flow, which is parallel to the flat wall, from infinite chain of point vortices as a basic theoretical model.

It is shown that we can chose the vortical chain parameters so that the fluid velocity on the wall becomes a periodic function with mean value *0*. The boundary layer is not developed in such flow, and the mean value of the friction force is equal to *0*. The estimations of real vortex parameters are given and we can expect advantage in spent power.

II. THE TWO-DIMENSIONAL POTENTIAL MODEL

We consider the vortex system near the solid surface representing part of an infinite chain of point vortices located on the wall parallel to the flat wall (Fig. 2). We assume that the flow is two-dimensional and potential. The source of coordinates is located on the wall, axis *Ox* is directed to the free stream, axis *Oy* is directed vertically upwards. We designate that h is the vortex distance from the wall, l is the distance between the vortices, Γ is the circulation of vortices. If the rotation occurs counter-clockwise, the circulation is considered as positive. We can easily obtain the such flow complex potential by the reflection method [7]:

$$W(z) = V_\infty z + \frac{\Gamma}{2\pi i}\sum_{k=-\infty}^{\infty} \ln\frac{z - z_k}{z - z_k'} + const = \\ = V_\infty z + \frac{\Gamma}{2\pi i}\left[\ln\sin\frac{\pi(z - ih)}{l} - \ln\sin\frac{\pi(z + ih)}{l}\right] + const, \qquad (3)$$

where $z_k = kl + ih$, $z_k' = kl - ih$, $k = 0, \pm 1, \pm 2, \ldots$.

Differentiating (3) with respect to z, we obtain the flow complex velocity:

$$\bar{V}(z) = u(x, y) - i\upsilon(x, y) = V_\infty + \frac{\Gamma}{2il}\left[\cot\frac{\pi(z - ih)}{l} - \cot\frac{\pi(z - ih)}{l}\right]. \qquad (4)$$

In this case on wall the boundary condition of zero normal velocity $\upsilon(x, 0) = 0$ is executed. It is known [7] that the point vortices move together with fluid. Assuming in (4) $x = 0$, $y = h$, we obtain that in equal intervals the vortices move relatively to the wall with velocity:

$$\frac{d x_0}{d t} = V_1 = V_\infty + \frac{\Gamma}{2l}\coth\frac{2\pi h}{l}. \qquad (5)$$

Thus, in ratio (3), (4) instead of z we should substitute $z - V_1 t$ for arbitrary moment t. However, to consider the flow instant state at $t = 0$ is enough for our purposes.

The vortical street model consisting of two vortical chains was used by Karman for drag estimation of bad-streamlined bodies in fluid [7]. He has shown that the vortical street with parallel location of vortices (3) is unsteady. Therefore, in experiment we observe the chess location of vortices in the street. We shall not here take into account the possible motion of vortices in the chain relatively each other, as far as:

(1) we interest the comparatively short chain section in streamlined surface limits;

(2) the vortical chains near the surfaces are observed in the experiment [3].

Assuming in (4) $y = 0$, we obtain the fluid velocity distribution on the wall (when $t = 0$):

$$u_\omega(x) = V_\infty + \frac{\Gamma}{l}\frac{\sinh(2\pi h/l)}{\cosh(2\pi h/l) - \cos(2\pi x/l)}. \qquad (6)$$

III. CHOOSING THE VORTICAL CHAIN PARAMETERS

The fluid speed on wall (6) is periodic function in x with period l. We calculate its mean value in period:

$$\overline{u}_\omega = \frac{1}{l}\int_0^l u_\omega(x)\,dx = V_\infty + \frac{\Gamma}{l}. \qquad (7)$$

We require that the mean velocity on the wall $\overline{u}_\omega$ is equal to 0, then from (7) we obtain the condition connecting the vortical chain parameters:

$$\frac{\Gamma}{V_\infty l} = -1. \qquad (8)$$

In this case the speed of motion of vortices relatively to the wall is equal to:

$$V_1 = V_\infty\left(1 - \frac{1}{2}\coth\frac{2\pi h}{l}\right). \qquad (9)$$

The function $u_w(x)$ twice changes the sign and reaches the values maximal to modulo within the one period range $0 < x < l$:

$$u_\omega(0) = V_\infty\left(1 - \frac{\sinh(2\pi h/l)}{\cosh(2\pi h/l) - 1}\right) < 0,$$
$$u_\omega(0.5l) = V_\infty\left(1 - \frac{\sinh(2\pi h/l)}{\cosh(2\pi h/l) + 1}\right) > 0. \qquad (10)$$

Thus, in arbitrary point of the wall the fluid speed may be presented in the form:

$$u_\omega(t) = V_\infty b\left(\frac{h}{l}\right)\sin\left(\frac{2\pi V_1}{l}\right), \quad b \ll 1. \qquad (11)$$

Methods of the boundary layer calculation on the stationary wall are given in [6] at periodic free stream in form of (11). It is possible to show that in this case the friction force on the wall is also periodic function of time, and its mean value is equal to 0.

IV. THE ESTIMATION OF RAREFACTION IN VORTICES

In potential model of vortical chain near the wall (3) the points of location of vortices are singular, since in them the fluid speed is equal to $+\infty$, and pressure is equal to $-\infty$. To estimate the real rarefaction in the centers of vortices we replace the point vortices by vortices of finite dimensions [7]. In this model a separate vortex has a core with radius a, inside of which the fluid has constant vorticity, i.e. rotates with constant angular velocity ω. Outside of the core the flow is considered potential. We compare linear velocity value on the core boundary and obtain $\Gamma = 2\pi\omega a^2$. If we write below the Euler equation in cylindrical coordinates, then on the core surface we obtain:

$$p(a) = p_\infty - \int_a^\infty \rho\frac{V^2}{r}\,dr = p_\infty - \frac{\rho\Gamma^2}{8\pi^2 a^2}.$$

And inside of the core:

$$p(r) = p(a) - \int_r^a \rho\frac{V^2}{r}\,dr = p_\infty - \frac{\rho\omega^2}{2}\left(2a^2 - r^2\right).$$

The pressure minimum is reached in the core center:

$$p_{\min} = p_\infty - \rho(\omega a)^2 = p_\infty - \frac{\rho\Gamma}{(2\pi a)^2}.$$

As is known the cavities arise in cores of vortices at great rarefaction. The powerful vortices are destroyed quickly in water [8]. Therefore, to subordinate the flow parameters to the cavitation absence conditions in vortices is expedient with account (8):

$$p_{min} = P_\infty - \rho\left(\frac{V_\infty l}{2\pi a}\right)^2 > p_\upsilon, \quad \frac{a}{l} > \frac{1}{\pi\sqrt{2\sigma}}, \quad P_{\min} > p_\upsilon, \qquad (12)$$

where p_υ is saturated water vapor pressure($p_\upsilon = 2350Pa$ at temperature 20° C), $\sigma = 2(p_\infty - p_\upsilon)/\rho V_\infty^2$ is cavitation number. The condition (12) sets the restriction for circulation and dimension of generated vortices. It slackens with motion depth increase (i.e. with increase p_∞). At motion in air the cavitation in vortices does not arise, the condition (12) becomes unnecessary.

V. THE ESTIMATION OF POWER NECESSARY FOR VORTICAL SYSTEM GENERATION

The friction force acts on one side of a plate with length L and single width in the uniform flow with velocity V_∞ at full developed turbulent boundary layer [6]:

$$F = \frac{1}{2}\rho V_\infty^2 L c_F, \quad c_F = \frac{0.075}{(\log \mathrm{Re}_L - 2)^2}, \qquad (13)$$

where $\mathrm{Re}_L = V_\infty L/\nu$ is Reynolds number. The power necessary to overcome this force is equal to $N_F = F V_\infty$. Obviously, that the vortical system creation to reduce the friction drag on the plate makes sense, if the power spent for creation of vortices N_υ and the power necessary to overcome residual friction force is less than N_F. We evaluate the power necessary to generate vortices by two different ways.

(1) *By theorem about changing the motion quantity.* The single point vortex induces the complex velocity in fluid near the wall [7]:

$$u(x,y) - i\upsilon(x,y) = \frac{\Gamma}{2\pi i}\left(\frac{1}{z - ih} - \frac{1}{z + ih}\right).$$

We calculate the quantity of motion per one second transmitted by one fluid vortex:

$$K_x = \rho \int_{-\infty}^{\infty} \left(\int_0^{\infty} u(x, y) dy \right) dx = \frac{4\rho\Gamma h}{3\pi}, \quad K_y = 0.$$

We obtain the necessary power, if we multiply K_x by number of generated vortices per one second V_1 / l and by free stream velocity V_∞:

$$N_K = \frac{4\rho\Gamma h}{3h} \frac{V_1}{l} V_\infty. \qquad (14)$$

We can treat the formula (14) so that the drag force $F_v = K_x V_1 / l$ acts on the mean on the generator of vortices (and hence on the body). This drag force is analogous to Karman drag force.

(2) *For vortices of finite dimensions.* We assume that generator creates the vortex core with radius a. Then it induces the necessary velocity field. We can evaluate the energy E spent for vortex generation as a sum of fluid rotary motion kinetic energy in the core:

$$E_1 = \frac{\pi\rho\omega^2 a^2}{4} = \frac{\rho\Gamma^2}{16\pi}$$

and the kinetic energy spent for fluid volume deceleration in the core from V_∞ to V_1:

$$E_2 = \frac{\rho\pi a^2}{2}(V_\infty^2 - V_1^2).$$

Then the power necessary for generation of vortices V_1 / l for one second is equal to:

$$N_a = (E_1 + E_2)\frac{V_1}{l}. \qquad (15)$$

We have obtained two various expressions for required power. At that N_a as one of parameters includes the vortex core radius a, and N_K does not depend on a. We calculate the value a, when both expressions give the equal power value. We put in (13), (14) $\Gamma = -V_\infty l, V_1 = 0.5V_\infty$, then the equality $N_K = N_a$ gives:

$$\frac{a}{l} = \frac{1}{3\pi}\sqrt{32\frac{h}{l} - \frac{3}{2}}. \qquad (16)$$

Obviously, the inequalities $a < h$ and $a < 0.5\ l$ should be fulfilled. The range $0.25 < h / l < 0.75$ has practical interest. The combination of parameters $a = h = 0.25\ l$ corresponds to the analogy "vortices - rollers" described in Introduction [5]. The approximate values of parameters l, h, a were observed also in experiments with traveling wave [3].

We shall think that the mean residual friction force is equal to 0 on the plate. Then with account of (8) and when $V_1 = 0.5V_\infty$, the vortex system generation gives the advantage in power in case of the condition being satisfied:

$$M = \frac{N_F}{N_v} = \frac{16\pi n c_F}{1 + 6\pi^2 (a/l)^2} > 1 \quad or \quad \frac{a}{l} < \frac{1}{\pi}\sqrt{\frac{8}{3}\pi n c_F - \frac{1}{6}} \qquad (17)$$

where $n = L / l$ is a number of vortices along the plate length.

VI. SPIRAL SYSTEM OF TRAVELLING VORTICES

The spiral system of traveling vortices can be formed by a rotating turbine fixed on the head part of moving body. In this case we will obtain the helicoidal system of vortices running from turbine blades. It has initial circulation Γ according to the trailing edge theory by Jukovsky (Fig. 3):

$$\Gamma = -P / \rho V L.$$

It is significant to note the influence of the disposition of the angular vortex axis on the drag reduction with respect to a three-dimensional traveling vortex system. There are three main cases:

1. The axis of vortices coincides with the vector of the external flow velocity (Gortler vortex system). In this case the velocity at the vortex boundary cannot coincide with the vector of flow at the wall. Therefore, it is useless for the drag reduction.

2. The vortex axis is normal to the external flow vector. In this case a full coincidence of vortex velocities with the flow and wall is possible according to the 2D traveling vortex flow model.

3. Intermediate angular disposition of the vortex line. In this case the velocity coincidence is possible only with a component of the external flow vector. This vortex system can be produced by turbine having the power:

$$N = \eta k \rho V_\infty^3 S_t,$$

where S_t is working area [m^2], $\eta = 0.59$ is the maximum efficiency of the turbine. The spiral vortex system on the body is shown in Fig. 4.

VII. EXPERIMENTAL INVESTIGATIONS

Bionics conception for direct vortex system creation is based on a structure of sawfish and swordfish bodies.

Other examples exist in hydromechanics where a similar vortex system really appears -- as Kalvin-Helmholts vortices (Fig. 5) on the joint boundary of two opposite flows [10].

In the experiments a few types of devices were used as vortex system generators: an oscillating disk or a cone, and a turbine (Fig. 6) The vortex generator is fixed on the conical head of the circular cylinder part of the model. The photos of the vortex street are taken by a moving camera. Visualization of vortical structures used a semisubmerged model of revolution, aluminum particle additions in a water flow. Experiments indicated the possibility of producing a vortex system up to 50 vortex diameters along the length. When we tested a model with turbine on the conical head, the drag was measured on the cylindrical part and on the conical head part separately. The spiral vortex generator (turbine) is fixed on the conical head, and has possibility to do useful work (electric power). In this case, the total effect consists of the power, N_d, which includes the drag reduction , ΔX , and the useful turbine power, N_t

$$N = N_d + N_t = \Delta X V_\infty + N_t.$$

The maximum of drag reduction attained on the cylindrical part was 18 %. The total maximal effect of the drag reduction by vortex system and combined turbine power was 33 % (Fig. 7). The turbine power was estimated at assumption that the efficiency was maximal ($\eta_{t\max} = 0.59$, $N_{t\max} = 0.28\rho V_\infty^3 S_t$, where S_t is working section of the turbine).

These experiments was carried out with hydrofoil boat in undisturbed flow conditions.

Another method of drag measurement is based on free immersion of body in water. For stable immersion regime the model weight M in water is equal to the drag force $F = \xi \cdot \frac{\rho V^2}{2} \cdot S$

$$M = F \Big/ _{\frac{dV}{dt} = 0}$$

Scheme of the experiment is shown in Fig 8. Wire supported model was used in these experiments (Fig. 9).

The drag coefficient may be calculated according to the formula

$$\xi = \frac{M}{\rho\frac{V^2}{2} \cdot S},$$

where: V is velocity of stable motion ($V = \frac{0.7}{t_l}$ m/s); S is area of wetted surface; $M = F$ is model weight in water.

The maximal direct effect of drag reduction obtained by using special turbine was about 13%. This result was obtained from comparison of the model tests with turbine and without turbine.

It is necessary to note the total drag reduction result in this case will be more high because of useful turbine work has not considered.

It is anticipated that total advantage of drag reduction with the optimization will reach 25 - 30%. The observation and photo-registration of the vortex systems on body of model was made through caissons windows. Visualization of spiral vortex systems was made due to air bubbles presence in the vortex cores on initial part of underwater trajectory near free surface (Fig. 4).

VIII. CONCLUSIONS

* The analysis of two-dimensional potential model of vortical chain parallel flat wall has shown, that such vortex system can create the periodic flow with mean speed equal to *0* on wall. It is assumed, that the size of vortices is much more than boundary layer thickness on wall. Therefore, this flow is external on relation to boundary layer. In real fluid in such boundary layer the flow also will be periodic, and we can expect the abrupt reduction of mean value of friction drag on wall. Thus, he advantage will be reached in such case, if the power spent for creation of vortices will less of power for overcoming the friction drag, at uniform flow around a plate.

* The simple estimations of power N_a necessary to create vortical system and rarefaction in vortices p_∞ permit the parameters of generator of vortices giving the power advantage to choose.

* The obtained results for two-dimensional modeling flow was possible to be applied for calculation of real feasible flows. In this case the turbine taking away the energy from mainstream and returning it to moving body can be as a generator of vortices.

* The experimental results have shown the real possibility for the friction drag reduction on a body of revolution about 13% without additional useful power on a turbine. The experiments on secondary flow visualization have proved that the drag reduction effect occurs due to the spiral vortex system generation.

IX. REFERENCES

1. *Hydrobionics in shipbuilding*. L.: TsNII TEI, 1970.-272 p. (In Russian)

2. Merkulov V.I. "The flow of viscous fluid along the traveling wave", *News of SD AS USSR in series of Techn. Sciences*, 1967, 2th ed., #8, pp. 3-9. (In Russian)

3. Savchenko Yu.N. and Merculov V.I. "The experimental studies of the flow along the traveling wave", *Bionics*, 1970, 4th ed., pp. 116-120. (In Russian)

4. Kalugin V.I. and Panchuk V.I. "The flow of viscous incompressible fluid along the traveling wave", *Bionics*, 1970, N4, pp. 104-110. (In Russian)

5. Savchenko Yu.N. "Hydrodynamic effects of traveling wave", *Bionics*, 1979, 13th ed., pp. 19-24. (In Russian)

6. Schlichting H. "Boundary Layer Theory", 6th ed. - *New York: McGraw--Hill Book Co.*, 1968.

7. Kochin N.Ye., Kibel I.A., Poze N.V. "The theoretical hydromechanics", 1,2 parts,M., *GRPhML*, 1963.(In Russian)

8. Knapp R.T., Daily I.W. Hammitt F.G. "Cavitation". *McGraw--Hill Book Co.*, 1970.

9. Savchenko Yu.N., Korennaya L.I., Savchenko V.T. Skin friction drag with special vortex systems in boundary layers. *Proceeding of Conference. "Evromech 372"*, Kiev, 1994.

10. Milton Van Dyke "An Album of Fluid Motion", *The Parabolic Press, Stanford*, California, 1982.

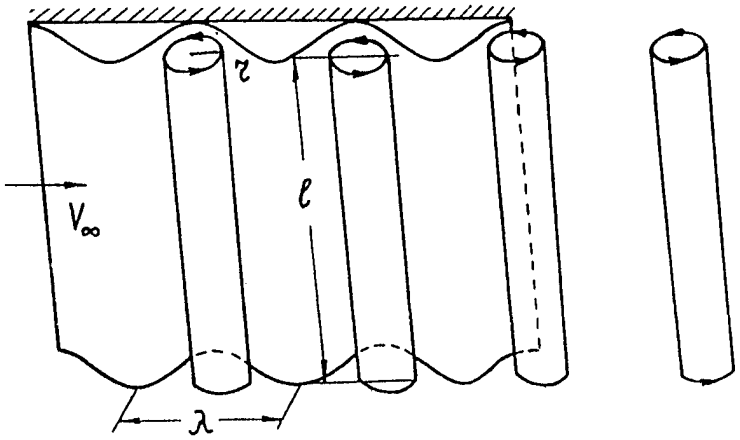

Figure 1. Scheme of travelling waves generating by vortex system

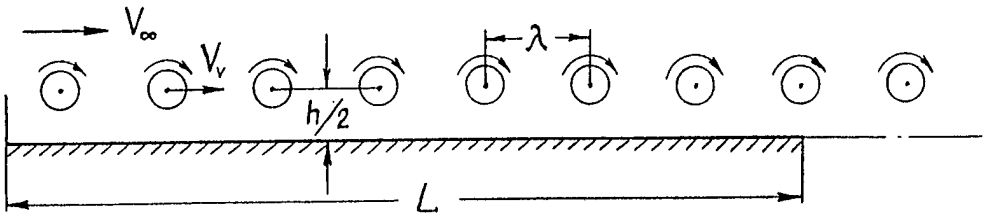

Figure 2. Scheme of vortex chain

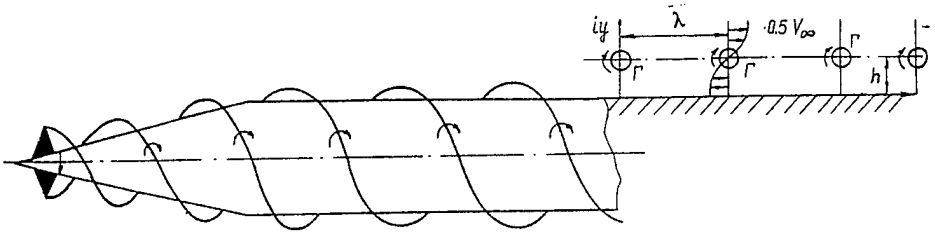

Figure 3. Scheme of spiral system of vortices

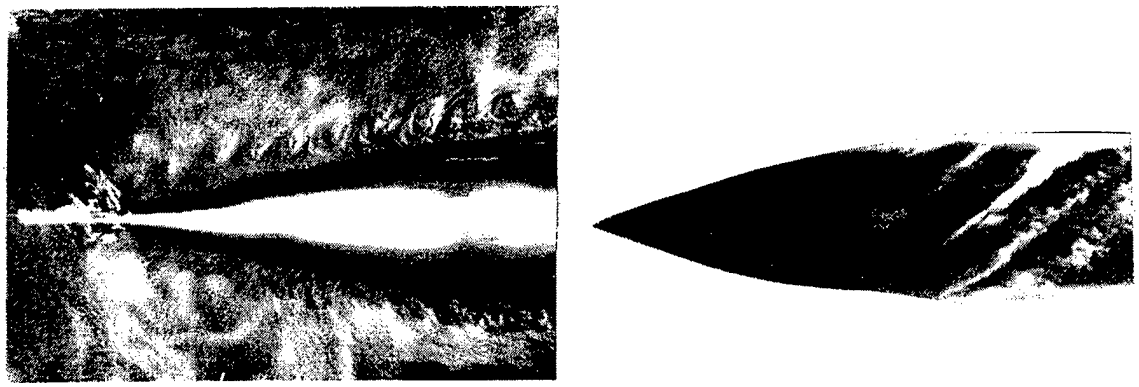

Figure 4. Spiral vortex systems

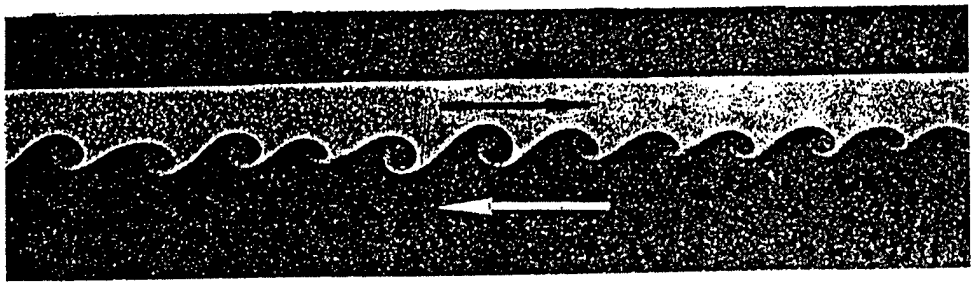

Figure 5. Kalvin-Helmgolts vortex system

Figure 6. Vortex generators

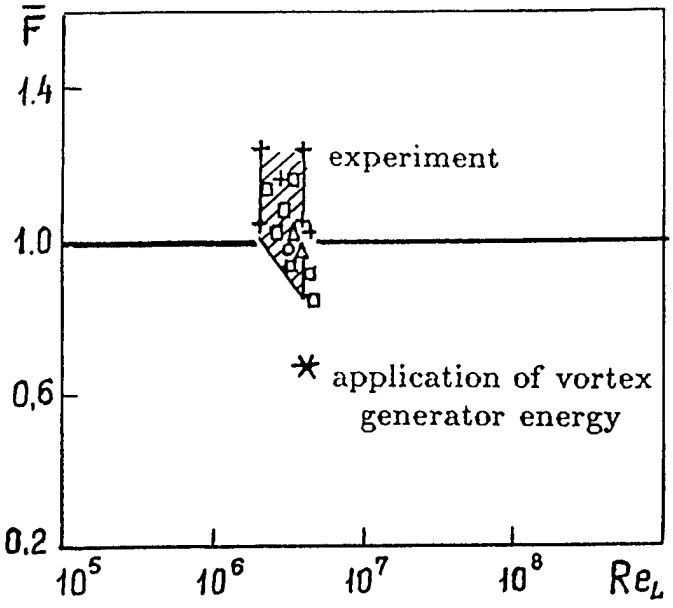

Figure 7. Drag of models in experiment

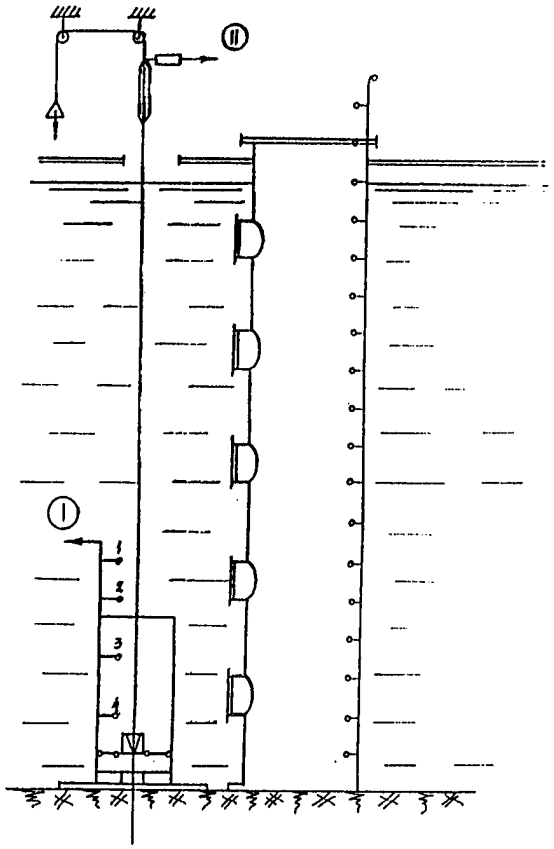

Figure 8. Scheme of experiment.

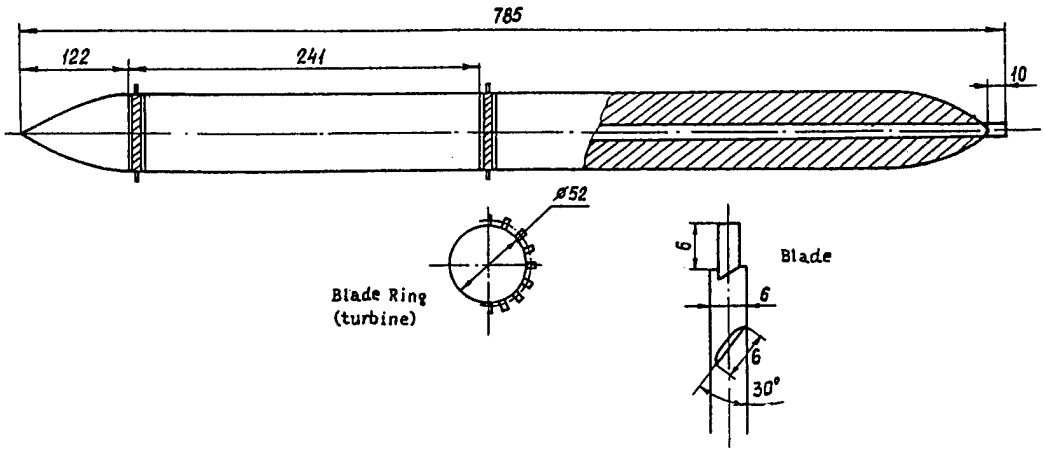

Figure 9. Scheme of model with turbine type of vortex generator

BOUNDARY LAYER CONTROL AT WAVE-LIKE SWIMMING

Lyudmyla Koryenna
National Academy of Sciences of Ukraine - Institute of Hydromechanics
8 / 4, Zhelyabov str., Kyev, 252057, Ukraine
Fax (044) 446 42 29, e-mail: sav@ihm.kiev.ua

Boundary layer formation on the wave-like deformable body are here considered. Concepts similar to Prandtl's about boundary layer control by means of the moving surface of the body has existed in nature at wave-like swimming. This is fish and dolphins motion with running waves. The delay of transition from the laminar to turbulent boundary layer takes place at greater critical Reynolds numbers. And the reduction of the surface friction takes place at Reynolds numbers which are less than critical ones. The correlation between parameters of the wave is a main thing here for engineering. The wave-like deformable body can be used not only as the mechanism for creation of a thrust force but also as the mechanism influencing on the boundary layer in control systems for decrease of the resistance forces.

I. INTRODUCTION

In the present research there are used two big experimental works: the measurements of the thrust force of the wave-like deformable plate in three-dimensional flow on specially constructed equipment, Figure 1, carried out by author and the data for water animal kinematics taken from earlier reports of the Institute of Hydromechanics. Actually the wave plate is a mechanical model of wave propulsion having prescribed kinematic parameters. The range of these parameters is wider in comparison with the range for water animals (fish and dolphins). The surface friction on the working elements of the wave propulsion is internal losses in the propulsion. There is an example of struggle for reduction of the surface friction in nature, by the correlation between the wave parameters with regard to Reynolds numbers.

II. KINEMATICS

The coordinate system $oxyz$ connected with the body moves uniformly and with the velocity V relative to the stationary fluid, Figure 2. The running wave

$$y = A(x)\sin(\omega t + \beta x + \varphi_0) \qquad (1)$$

propagates along the body in the direction from the leading edge to the trailing edge with the constant relative velocity $C = \lambda f$. Here, $A(x)$ is the amplitude function, $\omega = 2\pi f$ is the circular frequency, $\beta = 2\pi / \lambda$ is the wave number, λ is the wavelength, f is the frequency, φ_0 is the phase angle.

The wave was generated the following way. Seven links were fixed to the plate, Figure 1. They produced phase-shifted sine oscillations so that the running wave was created.

It is possible to imagine the running wave as follows. We take a rigid "infinite" sinusoid enclosed in a piece of a flexible sleeve. This sleeve plays the role of the wave-like deformable body. When the sinusoid is moved inside the sleeve, all elements of the sleeve are subjected to transverse oscillations. The sleeve represents a transversely deformable body according to the wave propagation. The velocity of the sinusoid inside the sleeve is the wave velocity, C. The body begins its motion opposite to the direction of the running wave with velocity V, and always $V < C$ in the propulsion regime.

We see this is a body having the form of a sinusoid in the flow. In each following moment of time the very same element of the sinusoid takes the new element of the plate. Thus the surface (or boundary) of this sinusoid is moving along the sinusoid.

Each element of the wave-like deformable body "n" in Figure 2 moves along the sinusoid and on the other hand it makes a transverse oscillatory motion. There is a velocity of moving surface W_L; an external flow velocity, W^*; a tangential component of the external flow velocity, W_l^*. The values of the instantaneous flow velocity and the instantaneous velocity of the moving surface of each element change continuously.

III. SOME EXPERIMENTAL RESULTS

The thrust force of the plate was measured experimentally for successively modified parameters V, f, $A(x)$, L/λ (L is the streamwise length of the plate). The velocities V and C were held constant for each experiment.

The Reynolds numbers $R_L = VL / \nu$, where ν is the kinematic viscosity of fluid, and the Strouhal number $S_L = fL/V$ were changed respectively in limits from 1.25 to 4.6×10^5 and from 0.6 to 6. The ratio of velocities $C / V = S_\lambda$ was limited from 0.64 to 21.

It is necessary to draw attention to the regimes of plate deformations on which the thrust of the plate is equal zero. These regimes are analogous to those of fish motion as the thrust force created by the fish body is equal on value and is directed oppositely to the resistance force of the fish body. For the plate on these regimes Strouhal numbers calculated with the wavelength $S_\lambda = f\lambda/V = C/V$ were within the limits 1.18 to 1.44. For fish and dolphins Strouhal numbers $S_\lambda = f\lambda/V = C/V$ range from 1.05 to 1.59 in experiments done earlier by other authors in the water tunnel of the Institute of Hydromechanics. Thus the range of Strouhal numbers for our plate is within the range of Strouhal numbers for water animals. This fact shows the reliability of data obtained in experiments with the plate and in experiments with fish and dolphins. But it must be discussed further in the following way.

For complete identity of the conditions for formation of the hydrodynamic forces on the wave-like deformable plate and at active motion of water animals there are missing mucus of fish and compliant skin of dolphins in experiments with plate. That is why the Strouhal number scale for plate is inside the one for fish and dolphins, Figure 3. It should be noted that scale for plate is exactly in the center of the one for fish and dolphins, i.e. our experimental results agrees with the kinematic data of the water animals very well. We have full simulation on the hydrodynamic forces due to kinematics and effect of the moving surface.

IV. FRICTION FORCES

Effects of moving surface (by L.Prandtl and H.Cherny): An idea of L.Prandtl was to reduce the velocities in the boundary layer by means of moving surface of the body in the flow direction. It is possible to remove completely the boundary layer if the surface of the body has the velocity that is equal to the external flow velocity.

The theoretical and experimental researches of moving surfaces were undertaken more than once including the question of boundary layer control. The parameter of the moving surface p was introduced into the theoretical research [1] for the plate in the form of the half-plane as the ratio of the velocity of the moving surface to the mainstream velocity. The following conclusions were derived which reveal the effects of moving surfaces.

When the velocity of the moving surface equals the value and direction of the mainstream velocity, $p = 1$, the hydrodynamic forces do not act on the plate. The flow around the plate is potential.

When the velocity of the moving surface is more than the mainstream velocity, $p > 1$, the plate has no resistance force, it has thrust force.

When the velocity of the moving surface and the mainstream velocity are directed opposite to each other, $p < 0$, the plate has a resistance force less than on stationary surface at $p = 0$.

The effects of the moving surfaces in applications in engineering could be very useful. But complexity of design and increase of cost block the way to the technical applications of the

effects of the moving surfaces. At the same time nature makes wide use of the effects of moving surfaces as will be shown below.

Parameter of the moving surface of the running wave: Let us enter the parameter p, similar by structure to the parameter for the half-plane. This is the ratio of the velocity of the moving surface W_L to tangential component of the external flow velocity W_t^* on the plate element "n", Figure 2. Naturally this parameter has another value for each element of the wave-like deformable plate and in each following moment of time on the individual plate element.

$$p = \frac{W_L}{W_t^*} \tag{2}$$

For the regime of propulsion under consideration the surface moving in flow direction takes place necessarily in the extreme points of our sinusoid, $y = y_{max}$, as the velocities $W_L = -C$ and $W_t^* = U_\infty^* = -(C - V)$ are directed to one side, Figure 2. Bearing in mind that $S_\lambda = f\lambda/V = C/V$ we have

$$p_{y_{max}} = \frac{C}{C - V} = \frac{S_\lambda}{S_\lambda - 1} \tag{3}$$

The parameter $p_{y_{max}}$ at the extreme points of the sinusoid depends only on Strouhal number. The regimes $L/\lambda = 1$ and the thrust $T = 0$ for experiments with the plate are the closest to the regimes of the water animal's motion. The range of parameter $p_{y_{max}}$, 3.28–6.55, for the plate in this regimes is within the range of parameter $p_{y_{max}}$, 2.7–21, in experiments with live water animals.

Going over to the general case, not the extreme points of the sinusoid, we must take into account the velocity of oscillatory motion of the considered plate element $V_y = dy/dt$, Figure 2b. The angle α formed by the neutral axis of the running wave and the considered element of the plate, $\alpha = tan^{-1} dy/dx$, indicates the position of the considered plate element.

In general case

$$p = \frac{C + V_y dy/dx}{C - V - V_y dy/dx} \tag{4}$$

We see, from (4), the surface moving in the flow direction is realized if

$$C - V > V_y dy/dx \tag{5}$$

And the surface moving oppositely to the flow direction take place if

$$C - V < V_y dy/dx \tag{6}$$

The kinematic data of the water animals were used for calculations. The following results were obtained.

The ratio (5) is fulfilled on all points of the dolphin body. The scheme of the moving surface in the flow direction is fully realized here.

The ratio (6) is fulfilled for fish on a significant part of their body. Consequently $p < 0$ and the scheme of the moving surface oppositely to the direction of the flow takes place here.

It is necessary to note, that p for the different fish species has close values, in the range from –2.54 to –2.68 for the caudal flipper at $y = 0$. It is considerably different from $p = 389$ for the dolphin, see the table, Figure 4.

So, the scheme of the moving surface in the flow direction, $p > 0$, is realized for the entire length of the dolphin body moving at $R > R_{cr}$, and the scheme of the moving surface oppositely to the flow direction, $p < 0$, is realized on a significant part of the fish body moving at $R < R_{cr}$.

From structure of (3) follows that when $V = 0$ and $y = y_{max}$, then $p_{y_{max}} = 1$. Hence, friction forces at extreme points of the sinusoid are absent, and in other points of the sinusoid are less than they were at regimes when V is not equal to 0. Therefore, in order to reduce the influence of the friction forces (internal losses in propulsion), the regimes $V = 0$ must use in the analysis of experimental results.

Physical processes of boundary layer control with running wave: The knowledge of the physical processes taking place in the boundary layer of the wave-like deformable body is necessary for successful use of the effects of the running wave and the moving surface in engineering. The method of geometrical summation of the velocity profiles in the boundary layer of the wave-like deformable body is here offered for the case of the moving surface in the flow direction and for the case of a moving surface oppositely to the flow direction, Figure 5. This is the first step to uncovering the physical processes and for qualitative comparisons. The two regimes below, which were close to the regimes of the live moving water animals and to the regimes in both [2] and the author's experiments, were chosen for accuracy and clearness.

Regime **A**: $p = 4.33$; $V = 0.5$ m/s; $C = 0.65$ m/s; $C/V = 1.3$

Regime **B**: $p = -2.33$; $V = 0.5$ m/s; $C = 0.35$ m/s; $C/V = 0.7$

All velocity profiles are constructed in the same scale, Figure 5. The theoretical Blasius profile for the laminar boundary layer was used for construction of the velocity profiles a for W_t^* and b for W_L. It was taken into consideration that the velocities W_t^* and W_L complete the total cycle of changes for the distance that equals 1/2 wavelength. The velocity profile c is obtained by geometrical summation of the profiles a and b. The resulting profile c is constructed in coordinate system connected with the element of the "sinusoid". It is necessary to take up the coordinate system connected with the moving surface (with the plate). There were given velocities equal in magnitude W_L and directed oppositely to W_L for the plate element and for the environmental fluid, profile d. The velocity of the external flow in the resulting profile e is equal in magnitude of the velocity V and in the opposite direction.

The theoretical Blasius profile for the laminar boundary layer on the flat plate is the dot-and-dash curve in the profile e.

Comparing the calculated velocity profiles for wave-like deformable plate at $p > 0$ and $p < 0$ we will note the following important properties of these profiles.

Regime **A:** The resulting profile e at $p > 0$ is similar in form to the experimental velocity profile in the boundary layer of the wave-like deformable plate [2]. This velocity profile is more convex in comparison with the one on the flat plate and is similar to the profiles of the stable type. Transition from laminar to turbulent boundary layer is delayed in this case [3].

The scheme of the moving surface in the flow direction is realized on the entire body length of the dolphin moving at Reynolds numbers which are larger than critical ones. Hence the velocity profile in the boundary layer of the dolphin body should be the profile of the stable type, and transition in the boundary layer is delayed.

Really, there are interesting results in [4]. The amplitude of the pressure pulsation in the boundary layer depends on the type of the dolphin motion at $R > R_{cr}$. The level of the pressure pulsation in the boundary layer corresponds to the developed turbulent flow for passive motion (inertial). But for active motion the level of the pressure pulsation is considerably less (1.5 – 2 times) and corresponds to insufficiently advanced turbulent flow.

Regime **B**: In case of $p < 0$ (the scheme of the moving surface oppositely to the flow direction) the value of the velocity gradient (du/dy_1) at $y_1 = 0$ is less in comparison to the velocity gradient (du/dy_1) at $y_1 = 0$ on the flat plate. As the local viscous shear on the body surface is directly proportional (du/dy_1) at $y_1 = 0$, then the surface friction should be slightly smaller than on the flat plate. This agrees with the conclusions in [1].

The scheme of the moving surface against the flow direction is realized for a significant part of the fish body moving at Reynolds numbers which are lower than critical. Hence the local viscous shear for fish should be smaller than on the flat plate.

V. CONCLUSION

The nature suggests the detailed perfect boundary layer control method. The surface friction at wave-lake swimming is decided by Reynolds number and correlation of the running wave kinematic parameters corresponding to Reynolds number. There is a principal result:

$$\text{if} \quad R > R_{cr}, \quad \text{then} \quad C - V > V_y dy / dx,$$

$$\text{if} \quad R < R_{cr}, \quad \text{then} \quad C - V < V_y dy / dx$$

which should come in useful for designers of boundary layer control systems. It is important to remember that in addition to effects of the moving surface the devices like that can simultaneously create the thrust force which is useful force.

VI. REFERENCES

1. H.H. Cherny "Boundary Layer on a Plate with Moving Surface", *Reports Akademii Nauk SSSR*, 213, 4, pp 802–803.
2. S. Taneda, Y. Tomonari "An Experiment on the Flow around a Waving Plate ", *J.Physical Society of Japan*, 36, 5, May 1974, pp 1683–1689.
3. H. Schlihting " Theory of Boundary Layer ", *Moscow, Russia, Nauka*, 1974, pp 197–205.
4. Ye.V. Romanenko "Foundations of Statistical Biohydrodynamics", *Moscow, Russia, Nauka*, 1976.

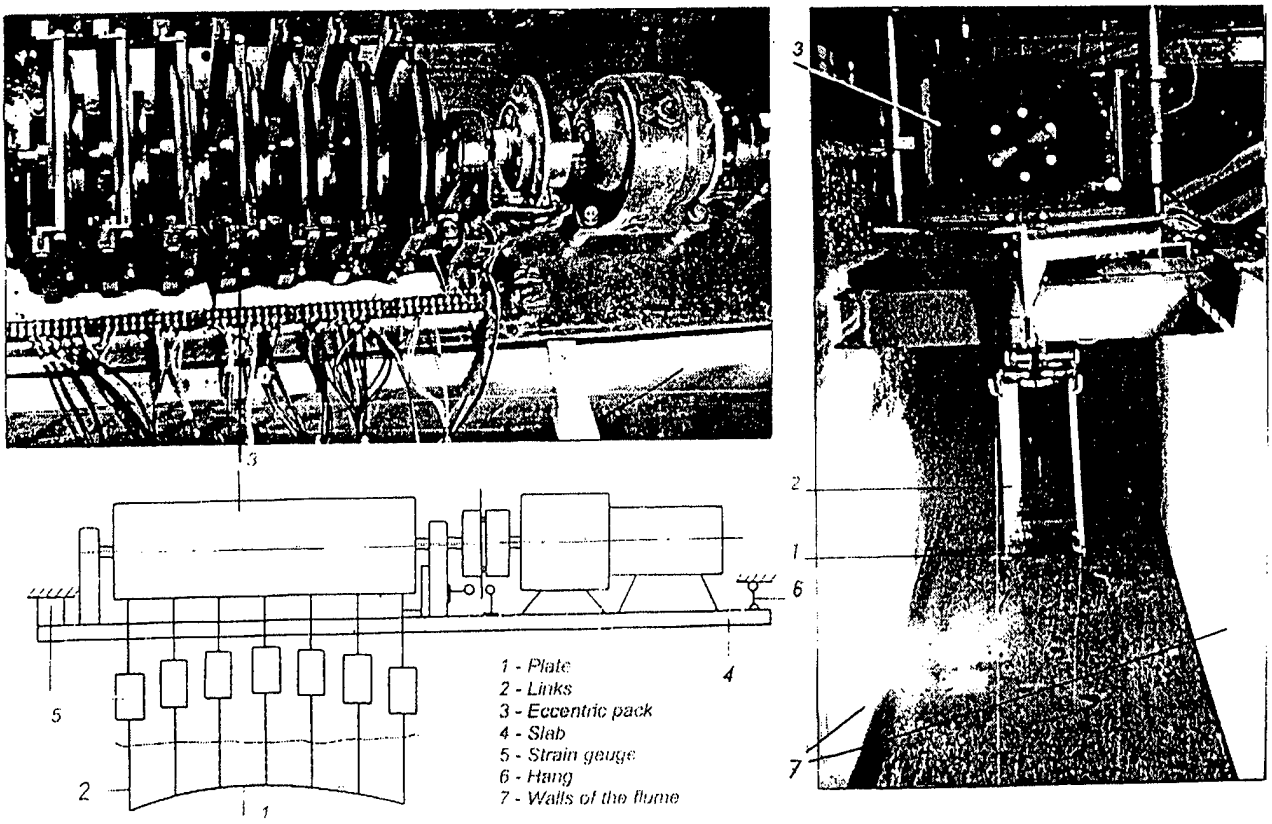

Figure 1. Experimental installation.

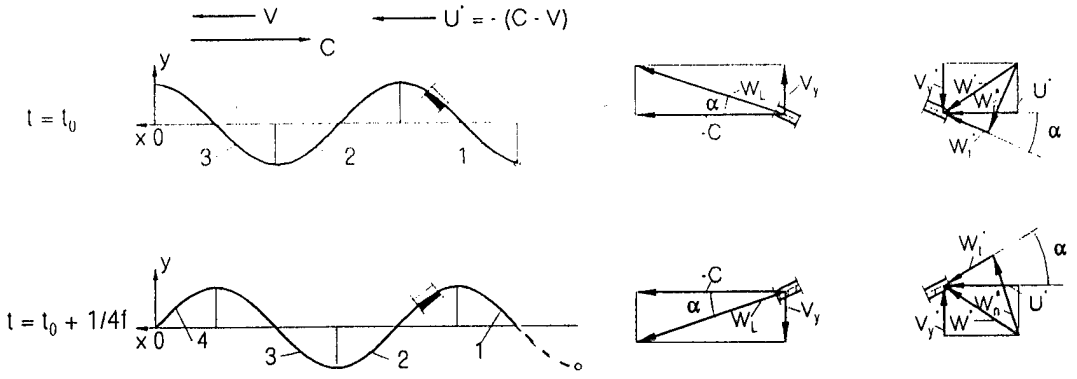

Figure 2. Kinematics of a wave body.

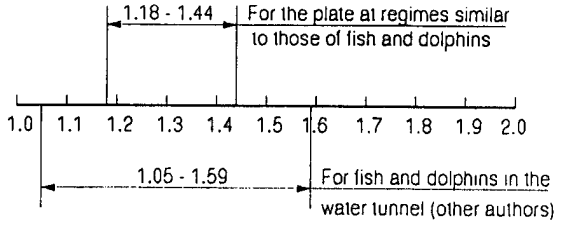

Figure 3. Scale for Strouhal numbers $S_\lambda = C / V$.

Water animal varieties (Latin)	L [m]	V [m/s]	$Re = \frac{VL}{\nu}$	C [m/s]	$C-V$ [m/s]	λ [m]	A [m]	f [Hz]	$\left(V_y \frac{dy}{dx}\right)_{y=0}$ [m/s]	$\frac{\left(V_y \frac{dy}{dx}\right)_{y=0}}{C-V}$	P
Tursiops truneadus	2.60	2.34	$6 \cdot 10^6$	3.12	0.78	1.90	0.15	1.64	0.77	0.99	389
Belone	0.48	1.05	$4.5 \cdot 10^5$	1.21	0.16	0.22	0.03	5.58	1.04	6.53	-2.55
Pomatomus saltatrix	0.42	1.72	$6.5 \cdot 10^5$	1.95	0.23	0.37	0.05	5.27	1.61	7.00	-2.58
Sarda sarda	0.16	1.12	$1.6 \cdot 10^5$	1.25	0.13	0.13	0.02	9.58	0.94	7.53	-2.68
Cristivomer namaycush	0.21	1.33	$2.5 \cdot 10^5$	1.48	0.15	0.15	0.02	9.74	1.21	8.10	-2.54

Figure 4. Parameter of the moving surface p for the caudal flipper of the dolphin (first line of the Table) and of four fish species (other lines of the Table).

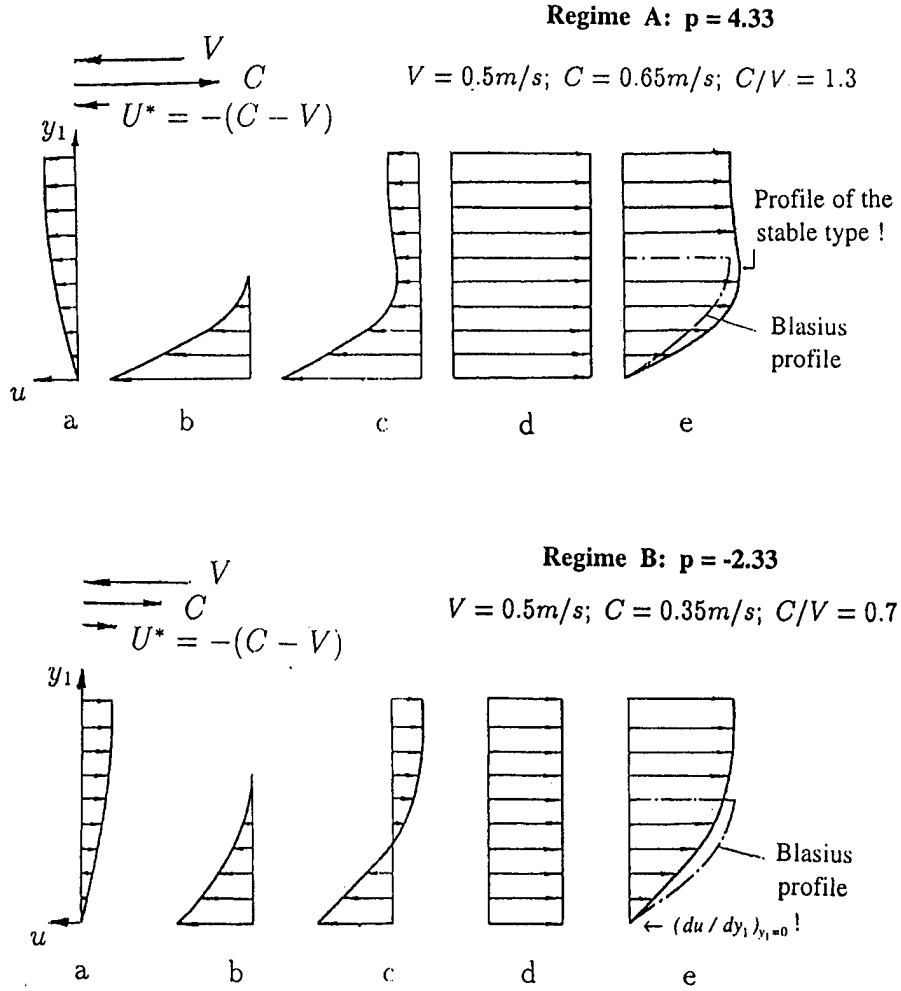

Figure 5. Velocity profiles in a boundary layer of the wave-like deformable body.

SUBSTITUTION OF ROLLING FOR SLIPPING AS AN EFFECTIVE MECHANISM OF DECREASING HYDRODYNAMIC DRAG

Vladimir I. Merkulov
Institute of Theoretical and Applied Mechanic
SB of the Russian Academy of Sciences, Novosibirsk, 630090, Russia
merkulov@itam.nsc.ru

Abstract- As is shown by theoretical and experimental researches, the general mechanism of crucial reduction of hydrodynamic drag consists in substituting rolling friction for slipping fricti on (1).This mechanism is realized at a boundary layer reconstruction with formation of periodic transverse vortices that are r olling wit hout slipping over the body surface. A small velocity gradient characterizing such a motion conditions low energy dissipation. A travelling wave on elastic body surfaceworks as a mechanism of formation of a periodic vortex structure for s ome water animals,such as dolphins. At appropriate elastic parameters of the surface, the wave is excited in a regime of hyd roelastic flutter. The surface roughness, as it takes place with sharks, expands the range of velocities at which travelling w aves are excited, though it decreases their energy efficiency. Another vortex formation mechanism abundant in nature employs the specifics of the flow along a slender rough body. Analytical calculations validated by direct experiments showed that hel ical vortices with a high amplitude growth increment are generated on a slender rough body. Arriving at the fish body, well-d eveloped helical vortices reconstruct the boundary layer in such a way that the normal flow with slipping of fluid layers wit ha high velocity gradient is replaced by a motion with rolling of vortices with a small velocity gradient and, as a consequence , with low hydrodynamic drag.

I. INTRODUCTION

The rostrum of a sword-fish is a slender body covered by small-scale roughness. Nearly parallel flow is formed at a small distance from the leading edge, which changes weakly downstream due to both viscosity and slight thickening of the rostrum. One can try to approximate this flow by fluid motion along an infinite thin rough needle.

The needle surface roughness generates continuously small disturbances in the flow. The stability of initial laminar flow guarantees the absence of other disturbances except for those diffusing from the cylinder surface. For one-scale roughness, we will have one-scale turbulence with a known mixing path length.

The presence of turbulent oscillations causes the appearance of turbulent viscosity that exceeds multiply the molecular viscosity in the gradient flow region. The flow which is of interest to us can be described by the Reynolds equations with a certain turbulent viscosity which can be determined using the Prandtl technique in terms of known, in the present case constant mixing path length. The solution obtained can be analyzed for stability. Inviscid solutions depend on turbulent viscosity only via the averaged velocity profile.

II.MATHEMATICAL FORMULATION OF THE PROBLEM.

The equation of the average momentum in the boundary layer model in the cylindrical coordinate system r, z is written as

$$\rho(U\frac{\partial U}{\partial z}+V\frac{\partial U}{\partial r})=-\frac{1}{r}\frac{\partial}{\partial r}(r\rho\overline{uv})$$

Here, U and V are components of the averaged velocity profile, u, v are components of the fluctuating velocity.

According to the Prandtl model [1], the Reynolds stress can be expressed in terms of the averaged velocity gradient $(\partial U/\partial r)$ and mixing path l as follows:

$$\overline{uv}=-l^2(\partial U/\partial r)^2.$$

Thus, the averaged momentum equation is reduced to the equation

$$U\frac{\partial U}{\partial z}+V\frac{\partial U}{\partial r}=\frac{l^2}{r}\frac{\partial}{\partial r}[r(\frac{\partial U}{\partial r})^2]. \quad (1)$$

The continuity equation has a usual form.

$$\frac{\partial(Ur)}{\partial z}+\frac{\partial(Vr)}{\partial r}=0 \quad (2)$$

Assuming the needle diameter to be equal to zero, we obtain the following boundary conditions for unknown functions U and V.

$U=V=0$ for $r=0, z>0$

$U=1, V\to 0$ for $r\to\infty$

One can conclude from the form of equation (1) that it is independent of velocity scale but depends on the roughness scale. Assuming the coordinates r, z be normalized to a certain size L, the quantity l will be a measure of relative roughness.

III. SOLUTION OF THE PROBLEM

From the analysis of dimensionality of equation (1), it follows the existence of a self-similar solution of the form $U=U(\eta)$ where $\eta=r/(l^2z)^{1/3}$. Let us represent the function $U(\eta)$ in terms of the second derivative of some other unknown function $\phi(\eta)$

$$.U=\phi''(\eta)$$

and determine the second component of velocity from the continuity equation (2).

For this purpose, let us pass to new variables $..z=\xi;\quad \eta=r/(l^2z)^{1/3}$.

Then we will need the relations $\partial\eta/\partial r=\eta/r=1/(l^2\xi)^{1/3}$

$\partial\eta/\partial z=-\eta/3z$

$\partial\xi/\partial r=0;\quad \partial\xi/\partial z=1.$

Let us substitute in equation (2) the relation for the function U.

$$.\frac{\partial(Ur)}{\partial r}=-r\frac{\partial U}{\partial z}=r\phi'''\frac{\eta}{3\xi}.$$

whence we can obtain

$$..\frac{\partial}{\partial\eta}(Vr)/(l^2\xi)^{1/3}=\frac{\eta^2(l^2\xi)^{1/3}}{3\xi}\phi'''.$$

$$V=\frac{(l^2\xi)^{1/3}}{3\xi\eta}\int\phi'''\eta^2d\eta=\frac{(l^2\xi)^{1/3}}{3\xi\eta}[\eta^2\phi''-2\eta\phi'+2\phi]. \quad (3)$$

Now we will turn to the momentum equation (1).

After substituting the above formulas for U and V, the left-hand side is converted to the following form

$$.\frac{\phi'''}{3\xi\eta}(-2\eta\phi'+2\phi)$$

Let us now transform the right-hand side of this equation.

$$\frac{l^2}{r}\frac{\partial}{\partial r}[r(\frac{\partial U}{\partial r})^2]=\partial\phi'''\xi\eta(\phi'''+2\eta\phi'''')$$

Finally, we obtain an equation for $\phi(\eta)$

$$\phi'''(2\eta\phi'''' + \phi''' + \frac{2}{3}\eta\phi' - \frac{2}{3}\phi) = 0 \qquad (4)$$

with the boundary conditions

$\phi'' = 0$ for $\eta = 0$

$lim(\phi/\eta - \phi') = 0$ при $\eta \to 0$

$lim(\phi''\eta - 2\phi' + 2\phi/\eta) = 0$ при $\eta \to \infty$

IV. ANALYSIS OF EQUATION (4).

For small values of argument η in equation (4), the main terms are the highest derivatives that describe viscous forces

$$2\eta\phi'''' + \phi''' = 0,$$

which has the following solution

$$\phi'' = \sqrt{\eta}.$$

For large values of η the main terms are the convective terms

$$\phi'' = \sqrt{\eta}$$

which vanish at $\phi = \eta^2$.

V. ANALYSIS OF STABILITY OF THE SOLUTION.

Let us designate by the letters u, v, w, p the small perturbations of components of velocity vector and pressure, which will be sought in the form

$$u, v, w, p = Reel[Fr, iGr, Hr, \rho Pr]\exp(in\phi + i\alpha(x - ct)).$$

Here, α is the wave number and c is the phase velocity. For unknown functions $F(r), G(r), H(r)$ after eliminating $P(r)$, we obtain the following system of ordinary differential equations

$$n(U - c)G + \frac{d}{dr}[(U - c)rH] = 0$$

$$\alpha(U - c)(nF - \alpha rH) + nU'G = 0$$

$$\alpha rF + r\frac{d}{dr}G + G + nH = 0$$

, that must be solved with uniform boundary conditions $F, G, H, P \to 0$ at $r \to 0$ and $r \to \infty$.

The second equation of this system is an algebraic one and makes it possible to exclude the function F.

As a result, one can obtain a system of two equations of the first order for two unknowns H, G.

$$n(U - c)G + \frac{d}{dr}[(U - c)rH] = 0 \qquad (5)$$

$$n(U - c)(r\frac{dG}{dr} + G) - nrU'G + (n^2 + \alpha^2 r^2)(U - c)H = 0 \quad (6)$$

Excluding H from this system, we obtain one second-order equation with one unknown.

$$(U - c)\frac{d}{dr}[\frac{r}{n^2 + \alpha^2 r^2}\frac{d}{dr}(rG)] - \qquad (7)$$

$$(U - c)G - G\frac{d}{dr}(\frac{rU'}{n^2 + \alpha^2 r^2}) = 0$$

The system of equations (5)-(6) or equation (7) equivalent to it with uniform boundary conditions can have a solution only for certain values of c and α that are called eigenvalues.

Stability of various axisymmetric flows is studied in detail in a well-known paper of Batchelor and Gill [4]. In particular, they showed that the flow can lose stability with respect to inviscid form of perturbations if the following condition is satisfied at some internal point:

$$\frac{d}{dr}(\frac{rU'}{n^2 + \alpha^2 r^2}) = 0.$$

Here, as usually, n is the number of the azimuthal mode, and α is the wave number of the longitudinal travelling wave.

This condition is a generalization of the known condition on an inflection point in the profile of a parallel-plane flow to an axisymmetric flow.

It is easy to see that this condition is not valid for the Poiseuille flow with a logarithmic profile and for any profile if we confine ourselves to axisymmetric disturbances ($n = 0$).

At the same time, for a profile on a rough cylinder obtained by us, this condition is always valid at point $r_k = n/\sqrt{3}\alpha$.

Batchelor and Gill showed that most unstable are disturbances with the number $n = 1$.

Concerning the conditions of physical realization, we are interested in the case when the product $\alpha c = \omega$ is a real number, hence, α is a complex number conjugated with c. In this case, the real part of the wave number α_r determines the wave length λ in accordance with the relation $\alpha_r = 2\pi/\lambda$, and the imaginary part α_i determines the downstream change of disturbance amplitude according to the law $\exp(-\alpha_i z$.

The reference length in the problem under consideration can be only the wave length, which will be accepted as a unit of measurement. With such normalization, $\alpha_r = 2\pi$, and

$$r_k = Reel\frac{1}{\sqrt{3}\alpha} = \frac{\alpha_r}{\alpha_r^2 + \alpha_i^2} = \frac{1}{2\pi\sqrt{3}[1 + (\alpha_i/\alpha_r)^2]}$$

Since $\alpha_i < \alpha_r$, then the dimensionless distance to the critical layer will be determined by a small number 0.092.

Let us rewrite equation (7) in the following way:

$$r\frac{d}{dr}[\frac{r}{n^2 + \alpha^2 r^2}\frac{d}{dr}(rG)] - rG = \qquad (8)$$

$$\frac{r^2 G}{U - c}\frac{d}{dr}(\frac{rU'}{n^2 + \alpha^2 r^2})$$

Let us represent an approximate solution to this equation, which satisfies uniform boundary conditions, in the following form:

$rG = 0$ for $r < r_k$

$rG = rK_l'(r\alpha)$ for $r > r_k$

Here K_l is the Hankel function of the lth order.

The condition of continuity of this function at point $r = r_k$

$$K_1'(r_k\alpha) = 0 \qquad (9)$$

can be provided by choosing an arbitrary value of the wave number α.

Using direct substitution, one can verify that the chosen function satisfies equation (8) for velocity profile

$$U = \sqrt{r} atr < r_k$$

$$U = constatr > r_k$$

and is an approximate solution for all profiles similar to this one.

The first root of equation (9) has the following complex value: $0.90 - i0.58$. The negative imaginary part ensures a rapid growth of disturbance amplitude.

VI. CONCLUSION.

The conducted qualitative analysis of solution properties and the estimate of some of its parameters allows one to prepare an experimental verification of the hypothesis according to which a thin rough rostrum of a sword-fish performs a function of vortex generator.

Firstly, we found out that dimensionless parameters of the flow along a rough cylinder are independent of velocity scale. This makes it possible to carry out experiments with an arbitrary velocity convenient for the experimentor.

Secondly, we found out that the velocity profile formed by the rough cylinder is stable with respect to axisymmetric disturbances. At the same time, helical disturbances of the travelling wave shape

$f(r)exp[i\alpha(z - ct) + in\theta]$

are unstable with a continuous spectrum of frequencies. This means that forced generation of such disturbances with

a small initial amplitude ensures an onset of increasing disturbances which, having achieved a certain amplitude, as we suppose, form a steady periodic flow. The most unstable form is a helical vortex filament corresponding to the value $n = \pm 1$. Superposition of two such forms provides an intersecting vortex geometry that will then evolve into inclined circular vortices embracing the cylinder. Such waves can be generated by transverse oscillations of the cylinder in one plane, two disturbance waves being excited during one period of oscillations.

VII. REFERENCES

1. Merkulov V.I. Fluid Flow Control, Nauka, Novosibirsk, 1981, 180 p.

2. Schlichting H. Grenzschicht-Theorie, Verlag G.Braun, Karlsruhe, 1951.

3. Betchov R., Criminale W.O., Jr. Stability of Parallel Flows, Academic Press, New York, London, 1967.

4. Batchelor F.K., Gill A.E. Analysis of the axisymmetric jets, J.Fluid Mech., 14, pp.529-551, 1962.

Turbulent Drag Reduction Methods: Polymer

THE OF COMBINATION POLYMER, COMPLIANT WALL AND MICROBUBBLE DRAG REDUCTION SCHEMES

Boris.N. Semenov
Institute of Thermophysics, Siberian Branch of Russian Academy of Sciences,
Prospekt Ac. Lavrentyev, 1, Novosibirsk, 630090, Russia irena@hydro.nsc.ru

Abstract -The promising study of turbulence management by joint use of compliant coatings with other drag reduction means is proposed. Its outlooks are conditioned by different considered factors and confirmed by the first experimental and theoretical results.

1. INTRODUCTION

The combined use of different means is one of the main principles of nature development. The study of hydrodynamic problems of bionics (Aleyev [1], Bushnell & Moore [2]) also convinces us of correctness of this statement. Bionics is the way from observations and astonishment at making the first estimations (the conclusion about the paradox existence) to the explanation for the phenomenon.

The characteristic "nature" example of the study of bodies with low drag is the investigation of dolphins, the search of reasons of well known paradox of Gray [3]. These investigations showed that in consequence of long evolution dolphins possess different variants of adaptation to the different, rapidly changing conditions of their inhabitation in sea (Woodcock [4], Focke [5], Semenov [6], Alekseeva & Semenov [7], Wu & Chwang [8]). Here the excellent variants of economical swimming of dolphins were discovered and described. For example, Woodcock [4] described the "motionless" swimming of dolphins near the ship nosing. Focke [5] investigated this fact. He showed by calculations that dolphins (using pressure distribution near the ship nosing) can swim with any ship velocity and without essential energy losses (as "external passengers of ship–travellers without tickets"). The other example: Wu and Chwang [8] show by theoretical calculations that dolphins can obtain an energy for their swimming from a wavy stream. So they can swim in sea waves with minimum energy losses (quoted work permit to explain the physical essence of surf boards too). Above–mentioned results requested to introduce new, additional conditions for a selection of dolphin speed observations (used for analysis of Gray's paradox). But note: they can't explain Gray's paradox for observations of high speed swimming of dolphins under conditions of the absolute calm, far from ships. And here the other conclusion is important. As the result of long evolution dolphins enjoyed different variants of an adaption to very different and often changed residing conditions in sea. So our problem is a search and a study of many "secrets"of dolphins. Here the analysis of the dolphin body shape (Young [9], Hertel [10]) was the important step to explain the observed low drag. The other important step was made by Kramer [11-13], who simulated the dolphin skin compliance in delaying the transition to turbulence. Now Semenov [14] has given the additional explanation for low drag (of dolphin *Tursiops Tursio Ponticus*) taking into account also the possibilities of joint use of compliant dolphin skin, water-soluble secretions decreasing drag and gas microbubbles observed in experiments.

Technical progress is connected with this main principle of nature development (the combined use of different means) too. There are a lot of possible variants of the combined use of different (and numerous) methods of drag reduction for different hydrodynamic conditions. Two passive means (compliant coatings and riblets) and two active means (polymeric additives and gas microbubbles) are considered here in order to estimate outlooks for their joint action investigations.

II. SOME NOTES ON INVESTIGATION OUTLOOKS

These notes can be interesting to both researches of near-wall turbulence and representatives of industry using scientific successes. So first of all it is important to note that all considered methods of turbulence management (compliant coatings, riblets, air microbubbles, PEO additives) satisfy the requirements of the ecology.

The motivations of fine outlook on joint use of the considered methods of drag reduction can be divided into four groups:

Initial approach.

The initial approach to joint use of different drag reducing means took into account only the simplified dependence of possible drag reduction efficiency Ψ for their joint action on their individual efficiencies Ψ_i:

$$\Psi = 1 - (1 - \Psi_1)(1 - \Psi_2)\ldots(1 - \Psi_n) \qquad (1)$$

This expression is correct if all considered drag reducing means act independently and don't change the action conditions for the others.*

In this case the possible drag reduction efficiency for joint action of different drag reducing means must be less then the sum of their individual drag reducing possibilities

$$\Psi < \sum_{i=0}^{n} \Psi_i \quad \text{for} \quad \Psi_i > 0 \qquad (2)$$

The prognosticated negative deviation from the sum of individual efficiencies $dev\,\Psi \equiv \Psi - \sum_{i=0}^{n} \Psi_i$ depends on their values and number n of means used jointly for turbulence management.

These dependences can be analysed at ease for the variant of equal individual efficiencies: $\Psi_1 = \Psi_2 = \ldots = \Psi_n$. So the deviation from the sum of individual efficiencies is calculated as

$$dev\,\Psi = 1 - \sum_{i=0}^{n} \Psi_i - \left(1 - \sum_{i=0}^{n} \Psi_i \Big/ n\right)^n \qquad (3)$$

This deviation increases for increasing n.

And for $n >> 1$ it has the limit:

$$\lim\left(dev\,\Psi\right) = 1 - \sum_{i=0}^{n} \Psi_i - \exp\left(\sum_{i=0}^{n} \Psi_i\right) \qquad (4)$$

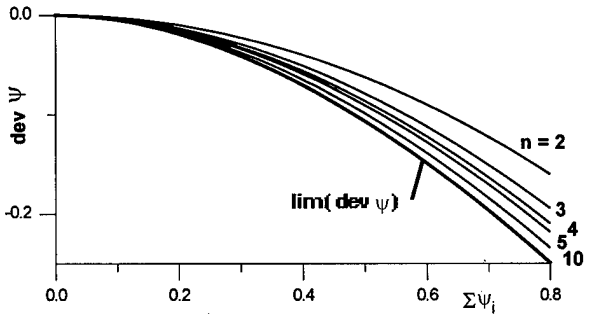

Figure 1. The deviation of drag reduction for joint use of different drag reducing means from the sum of their individual efficiency values: prognosis according to (3) and (4).

Results of this prognosis are shown in Fifure 1. The prognosticated negative deviations are small when the sum of individual efficiencies is less then 20%. But they are very considerable for 80% sum: for example, $dev\,\Psi = -0.16$ for two combined drag reducing means and $dev\,\Psi = -0.25$ for $n >> 1$.

*Here and further drag reduction efficiency is considered concerning turbulent friction coefficient c_{f0} for smooth hard surface: $\Psi = 1 - c_f / c_{f0}$.

This approach was used for our initial estimations. Viscoelastic coatings, riblets, gas bubbles and polymer additives are four well known means for the action on near-wall turbulence. Their actions for the decrease of the turbulence production are very different.

Compliant surface reacts on the long-wave disturbances. According to the estimation of the interference theory of Semenov [15] and experimental data of Kulik et al.[16] the real viscoelastic coating is deformed by the pressure wave with length more than one thousand viscous scales. Viscous scale is ν/υ_d, where friction velocity is $\upsilon_d = \left(\tau_w/\rho\right)^{0.5}$, ρ and ν are density and viscosity of flow, τ_w is friction stress on a wall (Hinze [17]). The small additives in a flow put out the microeddy turbulence for the turbulence linear scales less than one hundred viscous scales (Greshilov et al.[18]). Riblets manage microeddy structures too (Choi [19]). The flowing screen of gas bubbles can destroy the long-wave powerful fluctuations going to the wall from the turbulent core and background flow (Bogdevich et al.[20]).

It is known (Hinze [17], Cantwell [21]) that in the main both microeddies of viscous sublayer and long waves of turbulent core generate a new turbulence. So the joint use of considered methods of drag reduction gives possibility to wait for new qualities of turbulence production decrease. Therefore the combined use of these four methods permits to obtain the best results in turbulent drag reduction as compared with above described prognosis.

Association of useful qualities.

A study of joint use of different methods of drag reduction is promising because of a number of other reasons too. It is attractive already as the base for a possible association of other (in addition to drag reduction possibility) useful properties which are inherent in separate methods.

For example, drag reducing compliant coatings can have the high anti-corrosion properties. One-layer coatings created in Institute of Thermophysics of Russian Academy of Sciences (Kulik et al.[22]) have the excellent immunity to a damage by acids and alkalis.

An other example: the tests carried out by Russian and Bulgarian scientists (Malyuga et al.[23]) show that the creation of an air-bubble layer in near-wall region is a sufficiently effective method for reducing the amplitudes of the propelled - induced pressures and the plate vibrations for ships.

And thirdly, for joint use of compliant coatings, air microbubbles and polymeric additives it is possible to suppress the turbulent wall-pressure fluctuations in the very wide frequency band, that is impossible for any method used separately. So it is possible to believe that these combinations will lead to the strong decrease of the hydrodynamic noise in the very wide frequency band too.

Here it is important into take to account the economic factor.

The turbulence management by compliant coatings and riblets is particularly useful due to their passive nature. As a result additional energy is not required for the turbulence control. The injection of gas microbubbles and polymer additives is connected with the consumption of some energy and materials. Although drag reduction by the high-molecular polymer additive use is realized for its very small concentration in a flow, the expenses for its use may be higher than the economy (for example) of expenses for fuel. Therefore Berman [24] suggested to estimate the specific efficiency Ψ_p/c_p, determining the expediency of drag reduction. He had shown that for a flow in pipe Ψ_p/c_p was decreased as the concentration c_p was increased (for a flow with constant concentration of polymer additives) and was significantly less at the friction minimization than specific efficiency at moderate values of drag reduction Ψ_p. It is connected with nonlinear form of dependence of Ψ_p on c_p and asymptotic achievement of maximum value of drag reduction. Semenov [25, 26] has carried out analogous analysis for a flow with variable concentration of polymer additives in a flow (for turbulent boundary layer on a plate) and showed that from the point of view of profit it is worth while not to tend to the drag minimization but to restrict drag reduction nearly twice (Ψ_p < 50%). So the combined investigations must be carried out for variants of small consumptions of PEO too. And only the joint use of the considered methods can permit to achieve maximum and profitable efficiency of drag reduction.

The similar situation is realized for drag reduction using gas-bubbles. However in this case it is possible even to achieve drag reduction "free of charge" by the use of engine exhaust.

"Mutual aid" of different drag reducing means.

And after all here it is necessary to enumerate to some other factors of an interaction between jointly used methods of turbulence management. They are subject to a study as proposed factors of "a mutual aid" promoting to an appearance of new qualities.

The flowing screen of gas bubbles destroyes the powerful fluctuations going to a wall from the turbulent core and background flow. So the bubble screen defends polymer additives acting with high efficiency just in near-wall region. It decreases their ousting from this region.

The drag reducing polymers (polyethylene oxide, polyacril amide etc.) are the surface-active substances which decrease the surface tension and so the separation diameter of a bubble at its generation on the porous injecting insert. Besides polymer additives in flow prevent the bubble coalescence and also impede bubble rising. Note that it is very important for drag reduction to have microbubbles with diameter less than 0.2 mm. The decrease of microbubble diameter leads to an improvement of screening properties of bubble layer, to a displacement of the peak concentration of gas bubbles in water flow to a wall and to a decrease of the bubble buoyancy velocity. Hence, one can expect that the flow of high-polymer solutions aerated by gas bubbles will result in mutual increase of the effects of drag reduction on a streamlined surface (Malyuga et al.[27, 28]).

Waves and eddies are responsible for the near-wall turbulence production near smooth surface. The wave action role is decreased as a result of the surface roughness increase. Compliant coatings respond to the pressure fluctuation waves. So the viscoelastic boundary action losses a physical sense as a result of high roughness of surface (Semenov & Semenova [29, 30]). The increase of the viscous sublayer thickness by polymer additives increases the permissible roughness of compliant surface that simplifies and cheapens the coatings preparation technology.

Semenov & Semenova [29, 30, 31] have carried out the first calculations for joint action of compliant boundary and polymer additives in the turbulent boundary layer in order to explain the obtained experimental results (Semenov et al.[32, 33], Kulik et al.[34, 35]). One of possible factors of an interaction between two considered methods of turbulence management is the action of compliant boundary on mass transfer in near-wall region. Carried out calculations showed that the mass transfer decrease (increase) by the use of viscoelastic coating decreases (increases) the polymer consumption a little. The other factor is the influence of polymer additives in a flow on the interference action of viscoelastic boundary on near-wall turbulence. The calculations show that injected polymer additives extend the phase-frequency region of positive action of compliant boundary, i.e. they extend possibilities of drag (and noise) reduction by compliant coatings. These two problems are described in Section IV in details.

Semenov & Semenova [29, 30] considered the action of drag reducing riblets for joint use with compliant coating and concluded that its extend the phase-frequency region of positive action of compliant boundary too.

The viscoelastic coating for drag reduction is the mechanical vibrational system with amplitude-phase-frequency characteristic chosen for action on near-wall turbulence spectrum band responsible for the main production of new turbulence. And, of course, this choice must take into account the existence of the natural turbulence background conditions. However, both for different usual experimental hydrodynamic installations and for practical objects (ships, pipe-lines) the existence of additional strong pressure fluctuations in flow is quite possible. These additional pressure fluctuations can swing the compliant coating in the frequency region of its negative action very essentially. So the total production of new turbulence (for all frequency region) can be even increased. The important factor of an action of gas bubble layer is the defence of near-wall region of the turbulent boundary layer. So the injection of gas bubbles into near-wall flow will ensure stable drag reduction action of viscoelastic coating for different exploitation conditions.

Further the following indexes are used for meaning: compliant surface – C, polymer additives – P, air-microbubbles – A, riblets – r and joint use – their combinations.

III. EXPERIMENTAL INVESTIGATIONS

Quantity of experimental investigations is the little still. Only some variants of joint use of different drag reducing means were considered.

Already the first experiments (carried out at the Institute of Thermophysics RAS) for joint use of compliant coatings and polymer additives (Semenov et al.[32, 33]) showed fine outlooks of this study. There was obtained that the total effectiveness of turbulent drag reduction is equal to the algebraic sum of the individual small effectivenesses of these methods of turbulence management. These successes initiated new investigations.

Experimental conditions.

The experiments were carried out in the saline lake Issyk-Kool where $2.1m$ - long, $0.175m$ - diameter streamline body of revolution was towed by the tow boat with speed $U_0 = 6 - 15 m/s$.

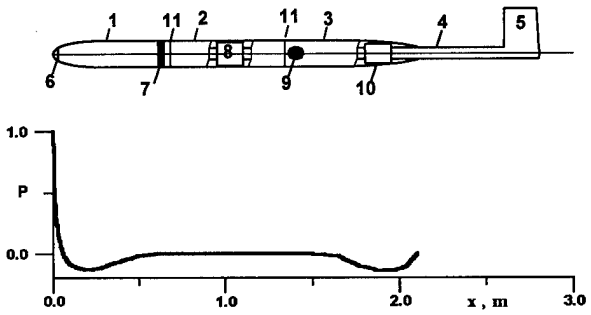

Figure 2. Scheme of the model with the dimensionless hydrodynamic pressure distribution. 1 – nosing, 2 – floating cylindrical element, 3 – stern part, 4 – thrust tube, 5 – knife strut, 6 – ringed slot, 7 – porous insert, 8 – floating-drag balance, 9 – piezoresistive pressure transducer, 10 – three-component balance, 11 – ringed slit.

This model (see Fig. 2) was described in details formerly by Kulik et al.[16, 36]. It was equiped (in the middle of its length) with $0.66m$ - long "floating" surface element for measuring of the skin-friction drag. There were tested different variants of these cylindrical elements. One had a solid smooth surface and the others were mounted with compliant coatings. Careful measurement of friction coefficient for the case of hard polished surface in water flow c_{f_0} was used for comparison as a standard.

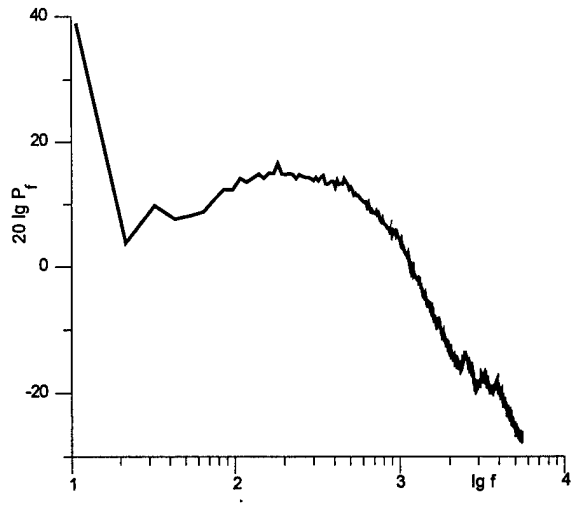

Figure 3. The dimensionless spectra of wall-pressure fluctuations measured behind floating element with hard surface. $U_0 = 9$ m/s.

The model nosing had a ring slot for polymeric solution injection. The model was equiped with the 35-mm long insert made from porous metal for air injection. Sizes of injected microbubbles are varied from 0.07 mm to 0.2 mm.

All experiments were carried out for low background turbulence conditions. The spectrum analysis of measured wall-pressure fluctuations (see the example in Figure 3) in frequency band from 10 Hz to 10 kHz revealed strong peaked deviation from smooth distribution in frequency only for low frequencies (below 20 Hz), that is inessential for these investigations.

All experimental conditions were described in details by Semenov et al. [37].

Joint action of compliant coatings and polymer additives.

New results of these investigations were described by Kulik et al.[34, 35], Semenov et al.[37]. There was varied the mass consumption q of polyethylene oxide (PEO of different molecular mass M). The corresponding dimensionless parameter is $q_\delta = q / (\rho_P \pi D \delta U_0)$, where D is diameter of the measured "floating" element, ρ_P – density of PEO, δ – thickness of turbulent boundary layer calculated for water flow (with temperature T) without polymer additives for the middle abscissa of the "floating" element (with solid smooth surface). According to Kutateladze & Leontyev [38] the thicknesses of diffusion and dynamic turbulent layers near this "floating" element are approximately equal. So q_δ is like to the near-wall concentration of PEO for the middle abscissa of the "floating" element.

The first experimental results of Semenov et al.[32, 33] showed that $\Psi_{CP}(q_\delta)$ is shifted concerning $\Psi_P(q_\delta)$ so as: $\Psi_{CP}(q_\delta) \approx \Psi_C + \Psi_P(q_\delta)$, i.e. the summarizing property was discovered for the joint of compliant coating and polymer additives that confirmed our initial prognosis for small individual effectivenesses. However contrary to initial estimations it was noted that for the case of increase of separate effects the magnitude of combined drag reduction exceeded their sum. So further it is considered the deviation of the drag reduction efficiency for joint action from the sum of the drag reduction efficiencies for separate actions in order to investigate this summarizing property.

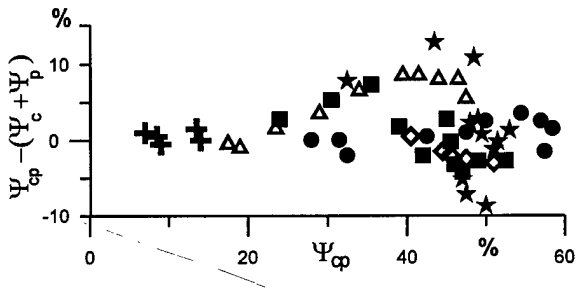

Figure 4. Deviation of friction reduction for joint use of compliant coating and polymer additives from the sum of their individual efficiencies as a function of efficiency of joint action.

For U_0=9 *m/s*:

△ coating N6 (from compound N1, H=2 *mm*), T = 16...17 °C $\psi_C = -11.5\%$, M(PEO) = 3.5 mln., $2.1 \cdot 10^{-6} \le q_\delta \le 1.2 \cdot 10^{-5}$;

✚ coating A, T = 8.5...10.5 °C, $\psi_C = +2.6\%$, M(PEO)=4.5 mln., $6.0 \cdot 10^{-8} \le q_\delta \le 5 \cdot 10^{-7}$;

● coating N10 (from compound N2, H = 7 *mm*), T = 17°C, $\psi_C = +6\%$, M(PEO) = 3.5 mln, $1.6 \cdot 10^{-6} \le q_\delta \le 1 \cdot 10^{-5}$;

◇ coating N 10, T =10.5 °C, $\psi_C = +12\%$, M(PEO)=3.5 mln., $3.5 \cdot 10^{-6} \le q_\delta \le 5.5 \cdot 10^{-6}$;

For U_0=7 *m/s*: T = 6.5...8.5 °C, M(PEO) = 4.7 mln,

■ coating N10, $\psi_C = +5\%$, $4 \cdot 10^{-7} \le q_\delta \le 3.5 \cdot 10^{-6}$;

★ coating N7 (from compound N2, H = 2.5 *mm*), $\psi_C = +9\%$, $4 \cdot 10^{-7} \le q_\delta \le 3.5 \cdot 10^{-6}$.

In Figure 4 are shown data (from Semenov et al.[37]) for the joint use of different compliant coatings (both decreasing and increasing the turbulent friction) and polymer additives (for the great variation of polymer consumption and, accordingly Ψ_P). These results witness the existence of three zones:

1) zone of the exact sum of individual efficiencies ($\Psi_{CP}(q_\delta) \approx \Psi_C + \Psi_P(q_\delta)$);

2) zone of positive deviation ($\Psi_{CP}(q_\delta) > \Psi_C + \Psi_P(q_\delta)$);

3) zone of negative deviation ($\Psi_{CP}(q_\delta) < \Psi_C + \Psi_P(q_\delta)$).

Here the zone of the exact sum is observed for all tested variants till $\Psi_{CP} < 20\%$. Zones of positive and negative deviations follow the zone of the exact sum when polymer consumption increases. But here we see considerable differences for different tested variants.

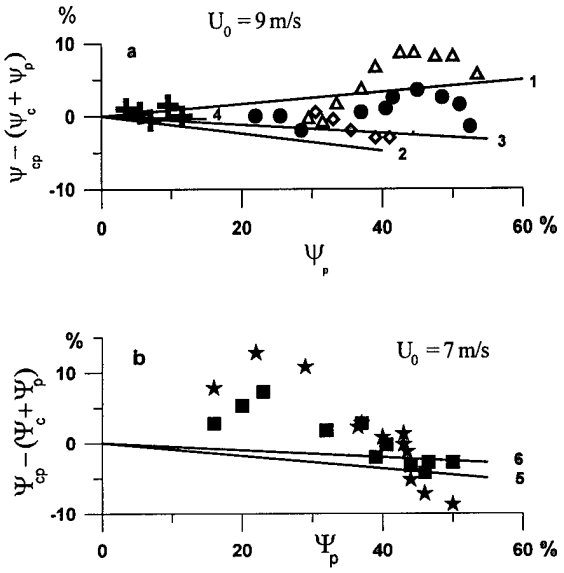

Figure 5. The comparison of drag reduction deviations calculated according to (5) (lines) with measured deviations (signs)

△ $\psi_C = -115\%$, line 1; ◇ $\psi_C = +12\%$, line 2;

● $\psi_C = +6\%$, line 3; ✚ $\psi_C = +2.6\%$, line 4;

★ $\psi_C = +9\%$, line 5; ■ $\psi_C = +5\%$, line 6.

Experimental results from Figure 4 are shown in Figure5 again for their comparison with initial prognosis. Here these results are considered in dependence on drag reduction of hard surface by polymer additives i.e. on individual efficiency of polymer additives Ψ_P.

According to (1): $\Psi_{CP} = 1 - (1 - \Psi_C)(1 - \Psi_P)$. The prognosticated deviation must be

$$dev\,\Psi \equiv \Psi_{CP} - (\Psi_C + \Psi_P) = -\Psi_C \Psi_P \qquad (5)$$

So in this case the deviation must be negative for "positive coating" ($\Psi_C > 0$) and positive for "negative coating"($\Psi_C < 0$).

The deviations prognosticated according to (5) (shown in Figure 5 by lines) are contrary to experimental data for the second and third zones. Thus these results show the presence of an interaction of compliant coating and polymeric additives. So above mentioned zones can be termed as:

2) zone of positive interaction of two considered methods of drag reduction (with $\Psi_{CP}(q_\delta) > \Psi_C + \Psi_P(q_\delta)$);

3) zone of negative interaction of two considered methods of drag reduction (with $\Psi_{CP}(q_\delta) < \Psi_C + \Psi_P(q_\delta)$).

Joint action of air-microbubbles and polymer additives.

Malyuga et al. [27, 28] carried out the first experiments on drag reduction using the injection of PEO (WSR-301) – solutions aerated by air bubbles. They measured the friction in 3 points of the hard flat plate from distance 0.25*m* (N1), 0.99*m* (N2) and 2.23*m* (N3) behind the slot for U_0 = 5 – 10*m/s*. They determined that an aeration of injected PEO solutions can lead to an increase of their efficiency of drag reduction. The maximum additional increase of their efficiency was measured: 36% in point N2 and 16% in point N3. But in point N2 were measured both an increase and a decrease of drag reduction efficiency. And here the results were worse for an increase of PEO consumption. It is important to note, that used highly large consumptions of injected air and polymer were in this experiment. The corresponding dimensionless parameters were

$$1.3 \cdot 10^{-3} \le C_A = Q/(U_0 \cdot S) \le 1.7 \cdot 10^{-3};$$

$$1.05 \cdot 10^{-6} \le q_\delta \le 7.8 \cdot 10^{-6}.$$

Here S is the surface of studied plate part, Q is the volumetric consumption of injected air.

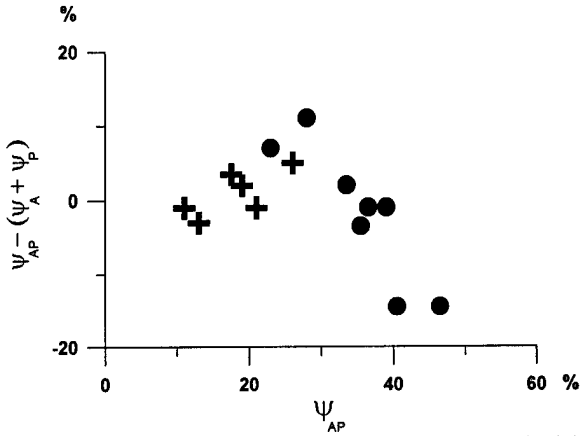

Figure 6. Deviation of friction reduction on hard surface for joint use of polymer additives and air microbubbles from the sum of their individual efficiencies as a function of efficiency of joint action.

✚ U_0 = 9 *m/s*, *M*(PEO)=4.5 mln., $1.0 \cdot 10^{-7} \le q_\delta \le 4.6 \cdot 10^{-7}$, $2.3 \cdot 10^{-4} \le C_A \le 3.2 \cdot 10^{-4}$;

● U_0 = 7 *m/s*, WSR-301, $1.0 \cdot 10^{-6} \le q_\delta \le 2.7 \cdot 10^{-6}$, $1.36 \cdot 10^{-3} \le C_A \le 1.73 \cdot 10^{-3}$.

Some above mentioned results and new data (Semenov et al.[37]) obtained in experiments (described in Section "Experimental conditions") for very small consumptions of air and polymer are shown in Figure 6. Here we can see the same three zones: the zone of exact sum, zones of positive and negative interaction.

Note, that the negative interaction zone corresponds to very high consumptions of PEO and air.

Joint action of compliant coating and air-microbubbles.

The first experiment is described by Semenov et al. [37]. One compliant coating was tested for very small consumption of injected air: $2.1 \cdot 10^{-4} \le C_A \le 3.7 \cdot 10^{-4}$. $U_0 = 9$ *m/s*, $T = 8.5...10.5$ °C. Drag reduction of hard surface by air-microbubbles Ψ_A was varied from 7% to 14%. There was obtained that the total efficiency of turbulent drag reduction is equal to the sum of individual efficiencies: $\Psi_{CA} = \Psi_C + \Psi_A$.

Joint action of riblets and surface compliance.

According to theoretical estimations of Semenov & Semenova [29] this combination must be the fine variant of passive (without energy expenditure) methods of turbulent drag reduction.

But experimental data are still absent.

Joint action of riblets and polymer additives.

The first experimental results were described by Reidy & Anderson [39] and Choi et al. [40]. They have found that the individual effectivenesses of two methods of drag reduction are sumed up for their joint use. Note: they considered very small consumptions of polymers.

Koury & Virk [41] and Virk & Koury [42] investigated this problem in detail: for two polyethyleneoxides ($M = 5.3 \cdot 10^6$ and $M = 7.9 \cdot 10^6$) and one polyacrylamide ($M = 7.4 \cdot 10^6$), in two hydraulically smooth pipes of 7.82*mm* and 10.2*mm* i.d. and in four

riblets pipes formed by respectively lining each of the smooth pipes with 0.11*mm* and 0.15*mm* V – groove riblets of equal height and spacing. Within the polymeric regime, at moderate drag reductions of order 50%, drag reduction in the riblet walled pipe significantly exceeded that in the smooth pipe, by as much as 15%. But the greatest drag reduction by riblets in water was measured ~ 10%. So the positive deviation from the exact sum of individual effectivenesses is observed here. At conditions of asymptotic maximum drag reduction, of order 80%, friction factors in the present riblet-walled pipe were identical to smooth for $h^+ < 10$, but departed off the smooth asymptote in the direction of lesser drag reduction for $h^+ > 10$. And here the negative interaction is observed.

Joint action of riblets and air-microbubbles.

The opinion about the promising study of this combination is based on an expectation that riblets and air-microbubbles manage with very differed structures of turbulence. But both experimental and theoretical investigations were not carried out still.

Joint action of compliant coating, air-microbubbles and polymeric additives.

The first experiment is described by Semenov et al. [37]. Russian scientists measured the friction of floating cylindrical element (see "Experimental conditions" here). They carried out tests for very small consumptions of air and PEO. They used the one-layer compliant coating tested also by Choi et al. [43] after this experiment. Results are shown in Figure 7. Here the positive deviation increases monotonously with increasing consumptions of air and PEO. It showes the presence of an interaction of compliant coating, air-microbubbles and polymer additives in whole region of this investigation.

Note: the effectiveness of drag reduction for joint use of compliant coating, air-microbubbles and PEO-additives exceeded the sum of individual effectivenesses by as much as 11% (for Ψ_{CAP} =35%).

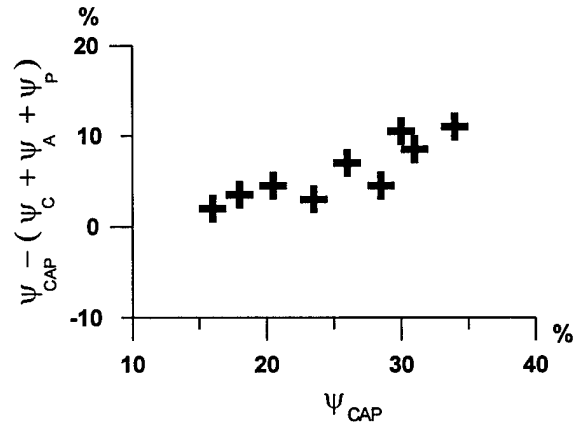

Figure 7. Deviation of friction reduction for joint use of compliant coating A, air microbubbles and polymer additives from the sum of their individual efficiencies as a function of efficiency of joint action. T = 8.5...10.5 °C, U_0 = 9 *m/s*, *M*(PEO)=4.5 mln, $1.5 \cdot 10^{-7} \le q_\delta \le 4.5 \cdot 10^{-7}$, $2.0 \cdot 10^{-4} \le C_A \le 3.7 \cdot 10^{-4}$.

IV. THEORETICAL ANALYSIS OF INTERACTION BETWEEN COMPLIANT BOUNDARY AND POLYMER ADDITIVES

The discovered peculiarities of drag reduction using a complex of different methods of turbulence management require theoretical explanations.

Compliant coatings and polymer additives manage with very differed structures of near-wall turbulence. So both methods of drag reduction are independent according to this point of view.

But other factor of an interaction between compliant boundary and polymer additives is a possible reason of observed contradictions between experimental data and initial prognosis: a change of action conditions of one method by other method of drag reduction.

The considered influence of the viscoelastic boundary on the turbulent diffusion of polymer additives.

One possible factor of an interaction between two considered methods of turbulence management is the action of compliant boundary on mass transfer in near-wall region. Here the integral approach was used. The calculation analysis was carried out on the base of approximate model [26] for a flat plate analogous to the construction scheme tested in quoted experiments [32-35] described here in Section "Experimental conditions".

It is supposed that the slot injection of PEO-solutions at x_i satisfies the conditions of pulseless injection of polymeric additives into near-wall flow [25]. Here the constant efficiency of drag variation using compliant coating Ψ_C (independent on polymer additives in flow) is considered from $x_1 = 0.35L$ to $x_2 = 0.65L$. L is the body length. For this part of the body it was calculated:

$$\Psi_{CP} = \int_{x_1}^{x_2} (\Psi_C + \Psi_\tau - \Psi_C \Psi_\tau) c_{f0} dx \Big/ \int_{x_1}^{x_2} c_{f0} dx \qquad (6)$$

The local friction reduction by PEO additives is determined according to the formula grounded in [26]:

$$\Psi_\tau = 0.51 arctg\left(3 c_W M^{0.85}\right) \qquad (7)$$

The near-wall concentration of PEO may be determined according to the experimental data of Fabula & Burns [44] as:

$$c_W = 2\bar{q} L / \delta_\Psi \qquad (8)$$

The thickness of turbulent boundary layer δ_Ψ is determined as

$$\delta_\Psi = 9.441 x_i / \sqrt{Re_i} + \int_{x_i}^{x} \frac{(1-\Psi_\tau)(1-\Psi_c)}{0.141} c_{f0} dx \qquad (9)$$

where $Re_i = U_0 x_i / \nu$, ν is the kinematic coefficient of water viscosity, $\Psi_c = 0$ for $x < x_1$ and $x > x_2$. Here the existence of laminar boundary layer from x = 0 to x_i is proposed. In the point of transition from laminar form a flow to a turbulent one (at $x = x_i$) the condition of continuity of momentum thickness is written. On its base the initial thickness of turbulent boundary layer at $x = x_i$ is determined. Here the power form of the velocity profile with index 1/11 was taken.

So the friction coefficient (without polymer injection) is calculated according to the Falkner's formula [45]:

$$c_{f0} = 0.0256 \left(x U_0 / \nu\right)^{-1/7} \qquad (10)$$

The system of equations (7), (8), (9) is solved for given molecular *M*, dimensionless coefficient of PEO consumption $\bar{q} = q / \rho U_0 S$, Reynolds number $\mathrm{Re} = U_0 L / \nu$. After its solution the drag variation Ψ_{CP} (for $\Psi_C \neq 0$) and drag reduction Ψ_P (for $\Psi_C = 0$) are calculated according to (6). On the base of these calculations the deviation of drag reduction for joint use of compliant surface and polymer additives from the sum of efficiencies for separate actions is determined.

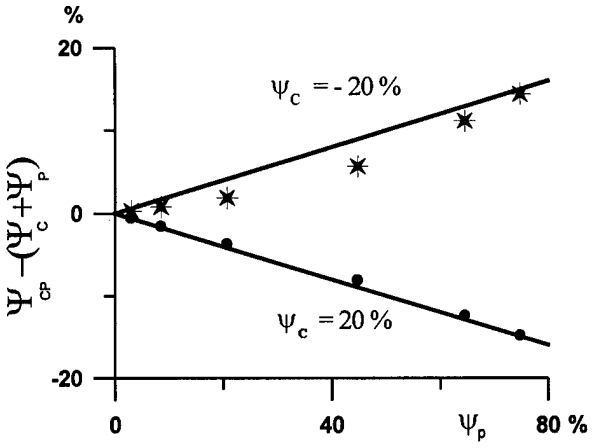

Figure 8. The estimation of the mass transfer change influence by the viscoelastic boundary on drag reduction deviation (points). Lines correspond to the initial prognosis according to (5).

The carried out calculations show that the mass transfer decrease (increase) by use of viscoelastic coating decreases

(increases) the polymer consumption a little. So it is unlikely that is the main factor of the interaction between these two methods of turbulence management. However this approach can and must be taken into account for future investigations and accurate analysis.

One example is shown in Fig.8. We see that in both considered cases (Ψ_C = 20% and Ψ_C = –20%) the calculated deviations (points) differ from the initial prognosis (lines) inessentially.

The interference action of viscoelastic boundary on near-wall turbulence in flow with polymer additives.

Here the other factor of interaction between two methods of drag reduction (the influence of polymer additives in a flow on the interference action of viscoelastic boundary on near-wall turbulence) is considered.

Formerly the interference form of compliant boundary action was analysed by Semenov [46,15] for turbulent near-wall flow of Newtonian fluids. He used the near-wall turbulence model of Sternberg [47]. The main modelling parameter (written by Semenov for solution of problem [46]) is the complex dimensionless compliance of boundary. He determined the region of this parameter values for drag reduction [48-50]. This theoretical model was used for modelling and choice of one-layer compliant drag reducing coatings. These coatings provided up to 20% drag reduction in experiments [16, 36]. They were used in above - written experimental combined investigations of different methods of turbulence management too.

Here the interference approach is used for a compliant boundary of a water flow with PEO additives. In this case is suitable the former solution [46] of the problem on an interaction between a viscoelastic boundary and the viscous sublayer of a turbulent boundary layer. Here we take into account that PEO additives in a flow don't change the long-wave structures, the ratio of wave-numbers for transverse (k_z) and main (k_x) directions.

Drag reduction by polymer additives, a change of velocity profile $U(y)$, viscosity and wave-velocity are taken into account in calculations. It is important to note that the increase of the viscous sublayer thickness by polymer additives increases the region of permissible use of the linear theory near a wall.

The complex compliance of the boundary (the modelling parameter) is characterised by amplitude and phase of the boundary displacement relative to the turbulent pressure fluctuation. This parameter must be determined for the frequency band of the main production of turbulence. In connection with increase of thickness of viscous sublayer, permissible amplitudes of oscillations of viscoelastic boundary increase.

The obtained solution [46] shows the restriction of the phase region $\Theta(\omega)$ for positive action of viscoelastic boundary (for drag reduction). This positive action is connected with decrease of near-wall turbulence production. For fixed frequency ω ($\omega = 2\pi f$, where f is cyclic frequency) the production change of the turbulence energy should be

$$-\int_0^l \left[\langle uv\rangle (dU/dy) - \langle uv\rangle_C (dU/dy)_C\right] dy \geq 0 \qquad (11)$$

Index "c" corresponds to compliant boundary. The interference action of compliant boundary for fixed frequency ω is neutral if this integral is equal to zero. According to the near-wall turbulence model of Sternberg [47] the calculated viscous sublayer thickness l is connected with the fluctuation frequency as $l \approx 5/(\omega/2\nu)^{1/2}$.

For the neutral action variant, the mean velocity profile $U(y)$ is written according to the experimental data for a hard wall.

The improved interference theory (presented by Semenov & Semenova [29] at this Symposium) was used for the first calculations of joint action of compliant boundary and polymer additives.

Neutral phase-frequency lines (calculated according to the condition (11)) restrict (from below) a region of Θ for positive action of compliant boundary ($\Psi_C > 0$). One example for $\mathrm{Re}_0 = 6.2 \cdot 10^6$ is shown in Figure 9 (for two variants of the abscissa). The phase shift Θ of the compliant boundary displacement relative to acting fluctuating pressure is on the ordinate. The dimensionless frequency is on the abscissa. In the upper Figure it is made dimensionless by the use of real flow viscosity ν near a wall and real friction velocity v_d. In the lower Figure it is made dimensionless by the use of kinematic viscosity of water ν_w and friction velocity without drag reduction v_{dw} in order to compare the different influences of drag reducing polymer additives for identical conditions of a water flow.

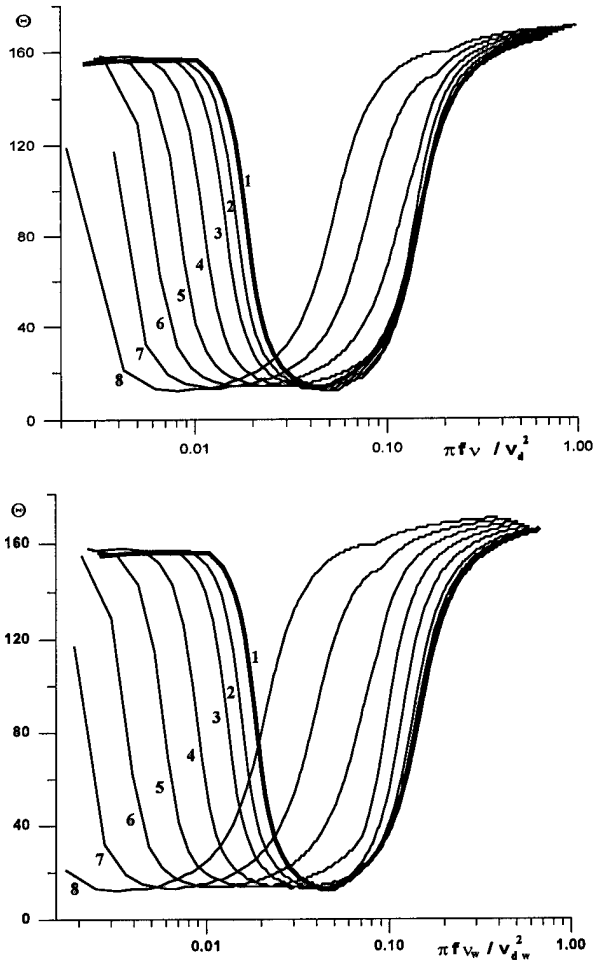

Figure 9. Dependence of PFRPA of smooth compliant surface on drag reduction using polymer additives: (1) $\Psi_P = 0$, (2) Ψ_P = 5%, (3) Ψ_P = 10%, (4) Ψ_P = 20%, (5) Ψ_P = 30%, (6) Ψ_P = 40%, (7) Ψ_P = 50%, (8) Ψ_P = 60%; $\mathrm{Re}_0 = 6.2\times10^6$; k_z/k_x =1.0.

We see that injected polymer additives extend the phase-frequency region of positive action (PFRPA) of compliant boundary. This extension of PFRPA is maximum at $\Psi_P \approx 40\%$.

The injection of drag reducing polymeric additives into a flow leads to a displacement of PFRPA to the left that can lead even to the change of the action sign of compliant boundary (from "+" to "-" and on the contrary).

We see, that from $\Psi_P \approx 30\%$ the right branch of the neutral line is displaced distinctly to the left. So minimum velocity of possible drag reduction using compliant coating must increase with increasing individual efficiency of drag reducing polymeric additives. For example, it must increase to two times at $\Psi_P \approx 50\%$.

It leads to explanation of reasons of drag reduction peculiarities discovered in experiments [32-35, 37] on joint use of compliant coating and polymer additives.

The used theoretical approach doesn't permit still to carry out a quantitative comparison. It is a problem for future investigations.

ACKNOWLEDGEMENTS

The work was supported by the INTAS Research Grant N 94–3737.

REFERENCES

1. Y.G. Aleyev "Nekton",1977, Dr.W.Junk b.v. Publ., the Hague.
2. D.M. Bushnell & K.J Moore "Drag Reduction in Nature", *Annu. Rev. Fluid Mech.*, 1991, **23**, 65-79.
3. J. Gray "Studies in Animal Locomotion. The Propulsive Powers of the Dolphin", *J. Exp. Biol.*, 1936, **13**, 192-199.
4. A.H. Woodcock "The Swimming of Dolphins", *Nature*, 1948, **161**, 602.
5. H. Focke "Ueber die Ursachen der Hohen Schwimmgeschwin-digkeiten der Delphine", *Z. Flugwiss.*, 1965, **13**, N2, 54-61.
6. B.N Semenov "On the Existence of the Hydrodynamic Phenomenon of Dolphins (*Tursiops Tursio Ponticus*)", *Bionika*, 1969, Naukova Dumka, Kiev, N3, 54-61.
7. T.E. Alekseeva & B.N. Semenov "On the Determination of the Hydrodynamic Drag of Dolphins", *Zh. Prikl. Mech. Tekhn. Fiz.*, 1971, N2, 160-164.
8. T.Y. Wu, & A.T. Chwang "Extraction of Flow Energy by Fish and Birds in a Wavy Stream", *Swimming and Flying in Nature*, 1975, Plenum Press–New-York, 687-702.
9. A.D. Young "The Calculation of the Total and Skin Friction Drags of Bodies of Revolution at 0^0 Incidence",1939, *ARC RM 1947.*
10. H. Hertel "Structur–Form–Bewegung", 1963, Krauskopf Verlag–Mainz.
11. M.O. Kramer "The Dolphin's Secret", *New scientist*, 1960, **7**, 1118-1120.
12. M.O. Kramer "Boundary Layer Stabilization by Distributed Damping", *J.Amer. Soc.* Nav. Eng., 1960, **72**, N1, 25-33.
13. M.O. Kramer "Boundary Layer Stabilization by Distributed Damping", *Nav. Eng. J.*, 1962, **74**, N2,341-348.
14. B.N. Semenov "The Study of Dolphins as Low-Drag Bodies (e.g. Tursiops Tursio Ponticus)", *Proc. 4th Int. Congress Soc. Techn. Biology and Bionics*, 1998, Munich.
15. B.N. Semenov "On Conditions of Modelling and Choice of Viscoelastic Coatings for Drag Reduction", *Recent Developments in Turbulence Management*, 1991, Kluwer, 241-262.
16. V.M. Kulik, I.S. Poguda & B.N. Semenov "Experimental Investigation of One-Layer Viscoelastic Coating Action on Turbulent Friction and Wall Pressure Pulsations", *Recent Developments in Turbulence Management*, 1991,Kluwer, 236-289.
17. J.O. Hinze "Turbulence", 1959, Mc Graw-Hill.
18. E.M. Greshilov, A.M. Evtushenko, L.M. Lyamshev & N.L. Shirokova "Some Peculiarities of an Action of Polymeric on Near-Wall Turbulence", *J. Eng. Physics*, 1973, **25**, 999-1004.
19. K.-S. Choi "Turbulent Drag Reduction Strategies", *Emerging Techniques in Drag Reduction*, 1996, MEP, London and Bury St. Edmunds, 77-98.
20. V.G. Bogdevich, N.V. Malykh, A.G. Malyuga & I.A. Ogorodnikov "Acoustic Properties of Wall Bubble Layer in Water of Great Void Fraction", *Hydrodynamics and Acoustics of Near-Wall and Free Flows*, 1981, IT AN SSSR, Novosibirsk, 77-107.
21. B.J. Cantwell "Organized Motion in Turbulent Flow", *Annu. Rev. Fluid Mech.*, 1981, **13**, 457-515.
22. V.M. Kulik, I.S. Poguda & B.N. Semenov "The Action of Viscoelastic Coatings on the Friction Reduction for Flows of Water and Polymeric Solutions", *Proc. 12th Short Course for Pipe-Line Problems*, 1989, Upha, 42-43.
23. A.G. Malyuga, V.I. Mikuta, & G. Gerchev "The Influence of Near-Wall Bubble Layer on Screw Propeller-Induced Effects on the Wall", *Proc. 17th Session of BSHC*, 1988, Varna, **2**, 42/1-42/12.
24. N.S. Berman "Drag Reduction by Polymers", *Annu. Rev. Fluid Mech.*, 1978, **10**, 47-64.
25. B.N. Semenov "The Polymeric Solution Injection into Flow for Drag Reduction", *Siberian Phys. Techn. J.*, 1991, N4, 99-108.
26. B.N. Semenov "The Pulseless Injection of Polymeric Additives into Near-Wall Flow and Perspectives of Drag Reduction", *Recent Developments in Turbulence Management*,1991, Kluwer, 293-308.
27. A.G. Malyuga, V.I. Mikuta & O.I. Stoyanovsky "Turbulent Drag Reduction at Flow of Polymer Solutions Aerated by Air Bubbles", *Near-Wall and Free Turbulent Flows*, 1988, IT AN SSSR, Novosibirsk, 121-130.
28. A.Malyuga, V.Mikuta, A.Nenashev, S.Kravchenko & O.Stoyanovsky "Local Drag Reduction at Flow of Polymer Solutions Aerated by Air Bubbles", *Proc. 6th Nat. Congress*, 1989, Varna, 74/1-74/6.
29. B.N. Semenov & A.V. Semenova "Recent Developments in Interference Analysis of Compliant Boundary Action on Near-Wall Turbulence", *Proc. Int. Symposium on Sea Water Drag Reduction*, 1998, Newport.
30. B.N. Semenov & A.V. Semenova "The Interference Action of Compliant Boundary on Near-Wall Turbulence", *Zh. Prikl. Mekh. Tekh. Fiz.* (to be publish).
31. B.N. Semenov & A.V. Semenova "Joint Influence of Compliant Boundary and Polymer Additives on Near-Wall Turbulent Flow", *Thermophysics and Aeromechanics* (to be publish).
32. B.N. Semenov, V.M. Kulik, V.A. Lopyrev, B.P. Mironov, I.S. Poguda & T.I. Yushmanova "The Combined Effect of Small Quantities of Polymeric Additives and Pliability of the Wall on Friction in Turbulent Flow", *Fluid Mech. Soviet Research*, 1985, **14**, N1, 143-149.
33. B.N.Semenov, V.M.Kulik, V.A.Lopyrev, B.P.Mironov, I.S.Poguda & T.I. Yushmanova "Towards the Influence of Flow Polymer Additives and Surface Compliance on Wall-Turbulence", *Proc. 5th Nat. Congress Theor. Appl. Mech.*, 1985, Varna-Sofia **2**, 371-376.
34. V.M. Kulik, I.S. Poguda, B.N. Semenov & T.I. Yushmanova "The Influence of Flow Velocity for Combined Effect of Compliant Surface and Polymer Additives on Turbulent Friction", *Izvestiya SO AN SSSR, Ser.Techn. Nauk*, 1987, N15, 42-46.
35. V.M. Kulik, I.S. Poguda, B.N. Semenov & T.I. Yushmanova "Effect of Flow Velocity on the Synergistic Decrease of Turbulent Friction by a Compliant Wall and a Polymeric Additive", *Soviet J. Appl. Phys.*, 1988, **2**, N1, 49-54.
36. V.M. Kulik, I.S. Poguda & B.N. Semenov "Experimental Study of the Effect of One-Layer Viscoelastic Coatings on the Turbulent Friction and Pressure Pulsations at the Wall", *J. Eng. Phys.*, 1984, **47**, N2, 189-196.
37. B.N. Semenov, A.I. Amirov, V.M. Kulik, A.G. Malyuga & I.S. Poguda "The Experiment on Turbulent Drag Reduction by Joint Use of Compliant Coating, Gas Microbubbles and Polymer Additives", *Thermophysics and Aeromechanics* (to be publish).
38. S.S. Kutateladze & A.I. Leontyev "Heat and Mass Transfer and Friction in Turbulent Boundary Layers", 1972, Moscow, Energiya.
39. L.W. Reidy & G.W. Anderson "Drag Reduction for External and Internal Boundary Layer Using Riblets and Polymers", *AIAA Paper*, 1988, N138.
40. K.-S. Choi, G.E. Gadd, H.H. Pearcey, A.M. Savill & S. Svensson "Tests of Drag-Reducing Polymer Coated on a Riblet Surface", *Appl. Sci. Res.*, 1989, **46**, 209-216.
41. E. Koury & P.S. Virk "Drag Reduction by Polymer Solutions in Riblet-Lined Pipes", *Abstracts 8th European Drag Reduction Working Meeting*, 1993, Lausanne.
42. P.S. Virk & E. Koury "Maximum Drag Reduction by Polymer Solutions in Riblet-Lined Pipes", *Abstracts 9th European Drag Reduction Meeting*, 1995, Ravello-Napoly.
43. K.-S. Choi, X.Yang, B.R. Clayton, T. Glover, M. Atlar, B.N. Semenov & V.M. Kulik "Turbulent Drag Reduction Using Compliant Surfaces", *Proceedings of Royal Society*, A, 1997, **453**, 2229-2240.
44. A.G. Fabula & T.G. Burns "Dilution in a Turbulent Boundary Layer with Polymeric Friction Reduction", 1970, Pasadena-California: Naval Undersea Res. & Development Center, TP171.
45. Ya. I. Voitkunsky, R.Ya. Pershitz & I.A. Titov "Handbook on Theory of a Ship", 1960, Sudpromgiz, Leningrad.
46. B.N. Semenov "Interaction of an Elastic Boundary with the Viscous Sublayer of a Turbulent Boundary Layer", *Zh. Prikl. Mekh. Tekh. Fiz.*, 1971, N3, 58-62.
47. J. Sternberg "A Theory for Viscous Sublayer of a Turbulent Flow", *J. Fluid Mech.*, 1962, **13**, N2, 241-271.
48. B.N. Semenov "Analysis of Deformation Characteristics of Viscoelastic Coatings", *Hydrodynamics and Acoustics of Near-Wall and Free Flows*, 1981, Nauka, Novosibirsk, 57-76.
49. B.N. Semenov "On the Properties of Viscoelastic Boundary for Turbulent Friction Reduction", *Sib.Fiz.Tech. Zn.*, 1993, N1, 63-73.
50. B.N. Semenov "Analysis of Four Types of Viscoelastic Coating for Turbulent Drag Reduction", *Emerging Techniques in Drag Reduction*, 1996, MEP, London and Bury St. Edmunds, 187-206.

SIMILARITIES AND DIFFERENCES IN DRAG REDUCTION BEHAVIOR OF HIGH POLYMER AND SURFACTANT SOLUTIONS

Jacques L. Zakin
Department of Chemical Engineering
The Ohio State University
Columbus, OH 43210
zakin.1@osu.edu

Jiri Myska
Institute of Hydrodynamiccs
Czech Academy of Sciences
Prague, Czech Republic

Zhiqing Lin
Department of Chmical Engineering
The Ohio State University
Columbus, OH 43210
lin.379@osu.edu

Abstract - The two most widely studied types of drag reducing additives are high polymers and surfactants. Their turbulent flow behaviors have many similarities but significant differences exist in their maximum drag reducing asymptotes, the limiting slopes of their mean velocity profiles for maximum drag reducing solutions as well as the magnitudes of peak values of v'/u^* and the peak locations. Stress deficits due to small values of Reynolds stresses have been observed for both types of additives but zero Reynolds stress profiles have been reported only for surfactant solutions. These differences indicate that the mechanisms of drag reduction for the two types of additives are different. The fact that mechanical degradation of surfactant systems is reversible while for high polymers it is irreversible make the former more versatile for applications.

I. INTRODUCTION

Drag reduction in turbulent flow was first recognized by Mysels, et al some fifty years ago [1,2,3]. They found the pressure drop in pipe flow for gasoline thickened by aluminum disoaps was less than that of gasoline at the same flow rate. Soon after, Toms [4,5] reported similar results with dilute solutions of high molecular weight polymethylmethacrylate in monochlorobenzene. Because of wartime security considerations, Mysels results were published after Toms'. In the past five decades turbulent drag reduction has been an active research field with over 4900 references [6], most of them dealing with high polymer drag reduction.

High polymers are very effective in reducing friction losses and have proven valuable in increasing flow rates in crude oil and other hydrocarbon pipelines most spectacularly in the 48-inch, 800-mile long Alyeska Pipeline from the North Slope in Alaska to Valdez. With currently available polymers, concentrations of 1 ppm in crude oil can give significant drag reduction [7].

Polymer additives are, however, susceptible to mechanical degradation and chemical bonds are broken irreversibly and the highest molecular weight, most effective molecules are the ones most sensitive to scission. Thus polymers lose their effectiveness when passing through a pump and additional polymer must be injected downstream of a pumping station to reduce friction losses in the next pipeline section. Polymers are therefore only useful in once-through applications. Fortunately polymer injection at only a few "bottleneck" sections of the Alyeska Pipeline was needed to increase throughput when North Slope production exceeded pipeline capacity [7].

Surfactant additives in water generally require higher concentrations than high polymers but their microstructures do reform quickly after mechanical degradation in pumps or in other regions of high shear. Surfactants have low molecular weights, of the order of hundreds, but can form long worm-like micelles which are believed to form 3-D network structures. While these structures are easily broken, they reform rapidly so that the surfactant solutions regain their effectiveness rapidly. Thus surfactants can be used in recirculation systems such as district heating or district cooling systems and research activity on surfactant drag reduction has grown appreciably in the past ten to fifteen years.

Catonic, nonionic, anionic and zwitterionic surfactants have all been shown to be effective drag reducing additives. Often a counterion is required to obtain good drag reduction.

This paper will discuss similarities and differences in drag reduction behavior between high polymer and surfactant systems. Significant differences in their behaviors indicate that the nature of their interactions with the turbulent flow field may be different. Since most studies have been done with cationic surfactants, this type of additive will be compared with high polymer additives.

II. COMPARISONS OF HIGH POLYMER AND SURFACTANT DRAG REDUCERS AND OF THEIR TURBULENT BEHAVIORS

A. Microstructure

The microstructures of polymers and surfactant drag reducing additives are quite different. Uncharged, flexible polymers form random coils in solution which may uncoil and elongate under shear or elongational forces. Polymers which contain charged groups are elongated even at rest. It is generally believed that surfactants that are effective drag reducers have worm-like or thread-like micelle structures. These systems may form three-dimensional networks which fully pervade the solution at rest or they may require shear to form networks.

B. Onset of Drag Reduction

Figure 1, in which friction factor is plotted against generalized Reynolds number, illustrates the types of onset behavior observed in high polymer systems [8]. The solution is a 200 ppm polyethylene oxide (400,000 molecular weight) in benzene. Onset for polymer drag reduction occurs when a critical shear rate is reached. This shear rate decreases with molecular weight, concentration, goodness of the solvent and, for coiled polymers, the flexibility of the polymer solution chain [9]. If the critical shear rate occurs in the laminar flow region, no sharp onset is observed but only a gradual departure from the laminar line as Reynolds number increases (see Fig 1, 0.833mm ID tube). Liaw et al [9] called this "concentrated" polymer solution drag reducing behavior. For the larger tubes, onset is observed as departures from the Von Karman turbulent friction factor curve at higher Reynolds numbers when a critical shear rate is exceeded. Decrease of polymer concentration in a single tube yields similar changes in onset behavior, ie increase in the critical Reynolds number. "Concentrated" and "dilute" drag reducing behavior correspond to Type B and Type A behavior noted by Virk [10].

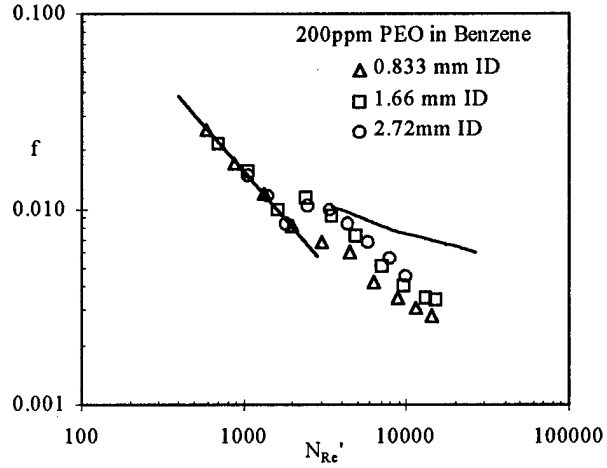

Figure 1. Effect of tube diameter on onset of polymer drag reduction

Almost all surfactant drag reduction friction factor data reported show gradual departure from the laminar friction factor line. There are a small number of reports of onset in the turbulent region. For example Gyr and Bewersdorff [11] show an example of a dilute surfactant solution (2mM of tetradecyl trimethyl ammonium bromide and sodium salicylate with 2mM sodium bromide added) giving onset in the turbulent regime.

C. Mechanical Degradation

As noted earlier, the high molecular weight polymers which are the most effective drag reducers, are also the most susceptible to chain scission in shear fields [12]. Extensional flows are even more effective than shear flows in causing degradation. Many investigators have reported on shear degradation of high polymers and some on the effects of predominantly extensional flows. Once a primary chemical bond has been broken, there is almost no chance that it will reform so polymer degradation is irreversible. Thus polymers can only be effective in once-through operations.

Surfactant micellar structures, on the other hand, rapidly self-assemble after mechanical degradation. The easily broken up microstructures reassemble in times of the order of seconds. Thus these additives have been successfully field tested in district heating and district cooling recirculation systems providing energy savings of 30 percent or more[13-16].

D. Maximum Drag Reduction Asymptotes

Virk demonstrated that for high polymers, a maximum drag reduction asymptote exists [17]. However, a number of experimenters, using surfactant and aluminum disoap drag reducing additives, have reported friction factor data lying significantly below Virk's limiting drag reducing asymptote. Zakin et al [18] examined these data as well as their own and proposed a new limiting asymptote for surfactant and aluminum disoap systems. The two asymptotes are shown in Figure 2. Virk's equation for the high polymer asymptote is [17]:

$$1/\sqrt{f} = 19.0 \log_{10}(N_{Re}\sqrt{f}) - 32.4 \quad (1)$$

or

$$f = 0.58 N_{Re}^{-0.58} \text{ (for } N_{Re} = 4{,}000 \text{ to } 40{,}000) \quad (2)$$

where f = friction factor and N_{Re} = Reynolds number.

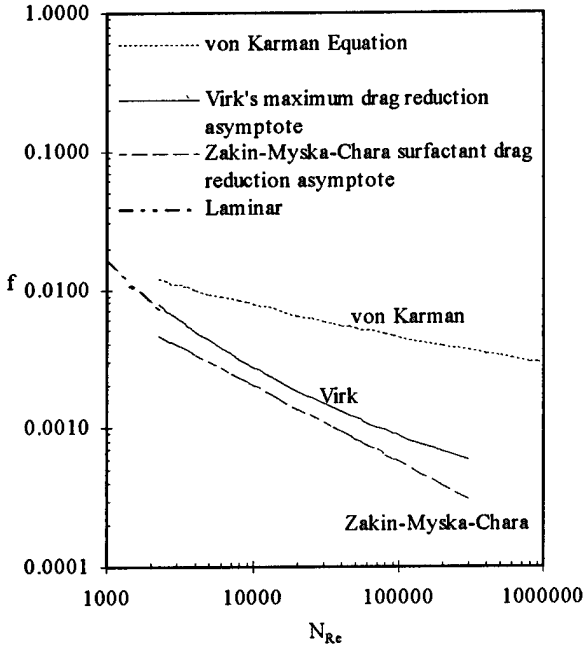

Figure 2. Friction factor vs Reynolds number

The limiting asymptote equation for surfactant and aluminum disoap solutions is [18]:

$$f = 0.32 N_{Re}^{-0.55} \quad (3)$$

This equation predicts friction factors more than 40% lower than Eq. 2 in some regions.

E. Mean Velocity Profile

For high polymer drag reducing systems, Virk proposed an elastic sublayer model with a limiting mean velocity profile equation:

$$u^+ = 26.9 \log_{10} y^+ - 17 \quad (4)$$

This limiting velocity profile is consistent with the maximum drag reduction asymptote for high polymers (Eq. 1).

Recently, Zakin et al [18] offered another limiting profile equation reflecting the steeper slope they observed in the intermediate region for surfactant solutions approaching the maximum drag reducing asymptote for surfactants (Eq. 3) and also for aluminum disoaps in hydrocarbons:

$$u^+ = 53.9 \log_{10} y^+ - 65 \quad (5)$$

where $u^+ = u/u^*$, u = local mean velocity, u^* = friction velocity, $y^+ = yu^*/\nu$, y = distance from the wall and ν = kinematic viscosity. This limiting slope for surfactant and aluminium disoap solutions is twice that for high polymers. The lower limiting drag reducing friction factor asympotote for surfactants, Eq. 3, is a consequence of this steeper slope.

A schematic illustrating the two limiting equations is shown in Figure 3. Eq. 5 indicates a mixing length constant half of that of Eq. 4.

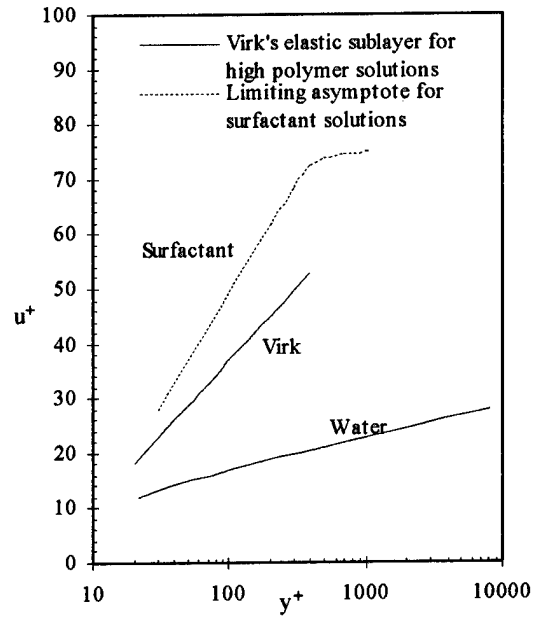

Figure 3. Mean velocity profiles (u^+ vs y^+)

F. Turbulence Measurements

1. *Axial Intensity Measurements*

A number of investigators have measured axial turbulence intensities of drag reducing fluids in channels and in pipes. Unfortunately, direct comparisons of the two types of additives in the same test systems are not available but some comparisons can be made.

Root mean square axial turbulence intensities at the center of the channel or the pipe for drag reducing polymer and surfactant solutions are about equal to or lower than for Newtonian solvents at the same Reynolds

number [19]. Peak values of u'/u* near the wall of about 2 to 4 were observed for most drag reducing systems compared with 2.5 to 3.0 for the solvents. However, a peak value of 8 was reported by Rudd [20] for a polymer solution in a channel and by Bewersdorff and Ohlendorf [21] for a surfactant solution in a pipe at very high Reynolds number. Peak values increase with Reynolds numbers, as clearly shown in the data for a drag reducing surfactant solution of Schmidt [22], T.J. Hanratty's student. In contrast, his peak water intensities decreased slightly with Reynolds number.

In the data shown by Gampert and Rensch [19] and others, the u'/u* peak occurred at higher y^+ values for drag reducing systems than the $y^+ \approx$ 10-15 location typical of solvent data. Peak location is relatively insensitive to Reynolds number for solvents and for drag reducing systems.

2. *Transverse or Radial Intensity Measurements*

Radial intensities in the core region are lower for drag reducing solutions than for Newtonian solvents, both in absolute intensities, v', and in normalized intensities, v'/u* [22-24]. While maximum intensities occur at $y^+ \approx 100$ for Newtonian solvents, for drag reducing polymer solutions Gampert and Rensch [19] show a shift of the maximum intensity of v'/u* to somewhat higher values of y^+ with modest decrease in peak intensities. Schmidt [22], on the other hand, shows peak intensities reduced by 65% to 90% compared to water for a surfactant drag reducing system. Peak values for this system were shifted to lower y^+ values than those for water.

3. *Reynolds Stresses*

Wei and Willmarth [25] found 'large' negative Reynolds stresses in the near wall region of their channel into which concentrated PEO solutions were injected and small Reynolds stresses across the profile. Earlier, Durst et al [26] had also observed negative Reynolds stresses close to the wall. Schummer and Thielen [27], Willmarth et al [28] and Bewersdorff [29] had earlier noted stress deficit profiles based on their measurements of Reynolds stresses and mean velocity profiles. A stress deficit can also be seen near the wall in the earlier data of Patterson et al [30] for a high molecular weight polyisobutylene in mineral oil drag reducing solution.

Schmidt's [22] Reynolds stress measurements in a cationic surfactant drag reducing solution (Ethoquad T/13-50 — Sodium Salicylate) in a channel showed nearly zero Reynolds stress profiles at Reynolds numbers of 19,060, 29,750 and 49,130. This result, like those mentioned above, requires postulation of an additional (viscoelastic) stress term of significant magnitude. Kawaguchi et al [31, 32] obtained similar zero Reynolds stress profile results with a different cationic surfactant solution in a channel. The zero values are probably caused by a combination of low v' values of these surfactant solutions and phase differences between the u' and the v' intensities. Conditioned sampling of Reynolds stress data for these surfactant systems is needed to determine the magnitudes of the four possible combinations of u' and v' values. This would clarify how and why they sum to zero Reynolds stress and also the behaviors of turbulent sweeps and ejections in these systems.

III. CONCLUSIONS

While there are similarities in the drag reducing behavior of high polymer and surfactant systems, there are significant differences, most notably the limiting asymptotes for maximum drag reduction and the ultimate slopes of the mean velocity profiles. Other differences are the larger reductions in peak v'/u* values for surfactant drag reducing solutions and a shift in the location of the peak value to lower y^+ compared to Newtonian solvents while the polymer solution peaks shifted to higher y^+.

Both types of additives have demonstrated a stress deficit, but near zero Reynold stress profiles have been observed in surfactant solutions, but not in polymer solutions. These differences indicate that there is some difference in the mechanism(s) for drag reduction for the two types of additives most probably because of differences in the interactions between turbulent eddies and elongated polymer molecules and their interactions with surfactant networks.

Finally, the ability of surfactant solutions to recover after mechanical degradation while high polymers are irreversibly degraded, allows the former to be used in a wider variety of applications including recirculation systems.

Acknowledgments

This research was supported in part under Grant 12.074E, Program in Science and Technology Cooperation, Office of Science Advisor, U.S. Agency for International Development. Financial support by the Czech Agency of the Czech Republic, Praha, is also gratefully acknowledged.

IV. REFERENCES

1. K.J. Mysels, US Patent 2,492,173 (1949).
2. G.A. Agoston, W.H. Harte, H.C. Hottel, W.A. Hottel, W.A. Klemm, K.J. Mysels, H.H. Pomeroy and J.M. Thompson, Ind. Eng. Chem., 46, 1017-1019 (1954).
3. K.J. Mysels, Chem. Eng. Prog. Symp. Series, 67, 45-49 (1971).
4. B.A. Toms, "Some Observations on the Flow of Linear Polymer Solutions Through Straight Tubes at Large Reynolds Numbers," in *Proc. 1st Int'l Rheological Congress*, II, Part 2, North Holland Publishing Co., Netherlands, 1949.
5. B.A. Toms, Phys. Fluids, 20, 53-55 (1977).
6. R.H. Nadolink and W.W. Haigh, Appl. Mech. Rev., 48, 351-460 (1995).
7. J.F. Motier, L.-C. Chou and N. Kommareddi, "Commercial Drag Reduction, Past, Present and Future," in *Turbulence Modification and Drag Reductions*, ASME Pub, FED - vol, 237(2), 229-234 (1996).
8. G.C. Liaw, PhD Dissertation, Univ of Missouri-Rolla, 1968.
9. G.C. Liaw, J.L. Zakin and G.K. Patterson, AIChE J., 17, 391-397 (1971).
10. P.S. Virk, Nature, 253, 109 (1975).
11. A. Gyr and H.-W. Bewersdorff, *Drag Reduction of Turbulent Flows by Additives*, Kluwer Academic Publishers, Dordrecht, The Netherlands, 1995, page 161.
12. G.K. Patterson, H.C. Hershey, C.D. Green and J.L. Zakin, Trans. Soc. Rheol., 10, 489-500 (1966).
13. F. Hammer, "Demonstration of Smooth Water in the District Heating System of Herning, Denmark," in *Proc. Int'l Symp. on Fluids for District Heating*, Copenhagen, pp. 139-150 (1991).
14. H.H. Kleuker, W. Althaus, A. Steiff and P.M. Weinspack, "Results of the Eco-Demonstration-Project in Volklingen (Germany)," in *Proc. Int'l Symp. on Fluids for District Heating*, Copenhagen, pp.123-137 (1991).
15. J. Pollert, J.L. Zakin, J. Myska and P. Kratochivel, "Use of Friction Reducing Additives in District Heating Systems at Kladno-Krocehlavy, Czech Republic," in *Proc. 85th Int'l District Heating and Cooling Assoc.*, Seattle, pp.141-156 (1994).
16. K. Gasljevic and E.F. Matthys, "Field Test of a Drag Reducing Surfactant Additive in a Hydraulic Cooling System," in *Turbulence Modification and Drag Reduction*, ASME Pub, FED-vol 237(2), 249-260 (1996).
17. P.S. Virk, AIChE J., 21, 625 (1975).
18. J.L. Zakin, J. Myska and Z. Chara, AIChE J., 42, 3544-3546 (1996).

19. Gampert and A. Rensch, "Polymer Concentration and Near Wall Turbulence Structure of Chemical Flow of Polymer Solutions," in *Turbulence Modification and Drag Reduction*, ASME Pub, FED-vol 237(2), 129-136 (1996).

20. M.J. Rudd, J. Fluid Mech., 51, 673-685 (1972).

21. H.-W., Bewersdorff and D. Ohlendorf, Colloid Poly. Sci., 266, 941-953 (1988).

22. G.M. Schmidt, "Surfactant Induced Drag Reduction in a Channel Flow Facility," B.S. Thesis, Univ. of Illinois, Urbana-Champaign, 1997, Prof. T.J. Hanratty, Advisor.

23. B. Gampert and C.K. Yang, "The Influence of Polymer Additives on the Coherent Structure of Turbulent Channel Flow," in *Structure of Turbulence and Drag Reduction*, A. Gyr. Editor, Springer-Verlag, Berlin, 1990.

24. J. Myska, Z. Chara and J.L. Zakin, J. Hydrol. Hydromech, 45, 151-172 (1997).

25. T. Wei and W.W. Willworth, J. Fluid Mech., 245, 619-641 (1992).

26. F. Durst, T. Keck and R. Kleine, "Turbulence Quantities and Reynolds Stress in Pipe Flows of Polymer Solution," in *Proc. 1st Int'l Conf. on Laser Anemometry Advances and Applications*, BHRA, 1985.

27. P. Schummer and W. Thielen, Chem Eng Comm., 4, 593-606 (1980).

28. W.W. Willmarth, T. Wei and C.O. Lee, Phys. Fluids, 30, 933 (1987).

29. H.-W. Bewersdorff, Rheol. Acta, 23, 527 (1984).

30. G.K. Patterson, J. Chosnek and J.L. Zakin, Phys. Fluids, 20, S89 - S99 (1977)

31. Y. Kawaguchi, Y. Tawaraya, A. Yobe, K. Hishida and M. Maeda," Turbulent Transport Mechanism in a Drag Reducing Flow with Surfactant Additive Investigated by Two Component LDV," in *Proc. 8th Int'l Symp. on Application of Laser Techniques to Fluid Mechanics*, Lisbon, July 8-11, 1996

32. Y. Kawaguchi, Y. Tawaraya, A. Yabe, K. Hishida and M. Maeda, "Active Control of Turbulent Drag Reduction in Surfactant Solutions by Wall Heating," in *Turbulence Modification and Drag Reduction*, ASME Pub, FED-vol.237(2), 47-52 (1996).

DRAG-REDUCING ADDITIVES FOR RECIRCULATING HYDRONIC SYSTEMS : FULL-SCALE SYSTEM ENGINEERING ANALYSIS AND FIELD TEST

K. Gasljevic, K. Hoyer, and E.F. Matthys
Department of Mechanical and Environmental Engineering
University of California, Santa Barbara
Santa Barbara, CA 93106, USA

Abstract - In addition to several laboratory studies, we have conducted engineering system analyses and a full-scale field test to investigate the suitability of surfactant drag-reducing additives for recirculating fluid transport and hydronic thermal distribution systems. The objective of using such additives can be energy conservation, a decrease in pipe and pump size, an increase in flow rate or heat transfer, an increase in system length, or even a combination thereof. Many such systems involve numerous pipe loops, fittings, valves, pumps, filters, and heat exchangers; which may all affect the fluid or be affected by it in various ways. Accordingly, we chose a relatively complex cooling system in a building as a representative system in which to conduct a large-scale engineering field test of the additive technology. This system was extensively analyzed and instrumented. It was then found during the field test that it is indeed possible to achieve significant reductions in pumping power while keeping the system fully-operational, controllable, and able to deliver nominal performance, yet without requiring special maintenance or new hardware. For this to be possible, however, we found that it was necessary to overcome critical reductions in the heat exchangers performance. We were indeed able to do so, and the field test was judged to be very successful, clearly proving the technical viability of the drag-reducing additive technology for this type of system, and providing also a wealth of new information essential to the implementation of this technology in industrial, commercial, or military applications.

1. INTRODUCTION

In our work we have focused on the application of drag-reducing additives in recirculating internal flow applications such as those involving heating or cooling of space and equipment, for example. In such applications, the objective of the technology may be a decrease in energy consumption, a decrease in pipe and pump size, an increase in flow rate and heat transfer, an increase in system length, or a combination thereof. For recirculating applications, surfactant additives are much better-suited than polymeric ones, although much less studied until recently. We conducted therefore a wide variety of laboratory tests ranging from very fundamental issues of turbulence / fluid interactions to more applied issues such as pump or heat exchanger performance studies for these fluids. Drag-reducing additives have long been studied with the hope to implement them in practical engineering situations. Often, however, the practical implementation of the technology has proven much more complicated than anticipated and in some cases fraught with apparently insurmountable difficulties, often resulting from complex interactions between components at the system-wide level. This has been the case in particular for applications aiming at energy savings in recirculating systems. We believed therefore that a large-scale field test in an operational system would be essential for both viability assessment and technology optimization.

In order to conduct a large-scale test that would cover all the main technological issues that are common to recirculating systems, we chose as representative system a relatively complex hydronic space cooling system in a building, with our main objective being a reduction in energy usage for the system. This particular objective is, of course, in itself of great interest for many applications, but all the finding of the test are also readily translatable in terms of hardware size reduction, or an increase in flow rate, heat transfer, or system length, as desired. Similarly, our findings can also be readily extended to other types of internal recirculating systems such as equipment cooling or heating, power generation, chemical processes, etc. For conciseness, we will focus in the remainder of this article on energy savings in hydronic systems, but the reader is urged to keep the broader applicability of the results in mind.

Although polymers are very effective drag-reducing additives, it has been generally recognized by now that polymeric drag-reducing additives are not well-suited for recirculating flow applications because of their susceptibility to permanent mechanical degradation, but that surfactant additives -on the contrary- are very promising fluids for those applications, because they do not suffer from permanent mechanical degradation. These surfactants are the additives we have been studying for hydronic heating and cooling systems applications. Such systems in large buildings or groups of buildings appear to be promising potential energy conservation applications for surfactant drag-reducing additives. About 15% or 20% of the chiller full-load power consumption in a large cooling system may be spent to drive the circulating pumps. Savings of, say, 50% of this energy, (which our preliminary analyses suggest is possible), would indeed be substantial. In some cases, like flow in long straight pipes, the implementation of drag-reducing additives is straightforward. Cooling and heating systems are complex, however, and typically include many fittings, valves, heat exchangers, pumps, etc. The flow conditions within these systems may also change significantly depending on load. An appropriate drag-reducing additive should then provide satisfactory drag-reduction efficiency over the full range of changing system conditions, while not impairing system performance. In addition to system control and performance, one must also consider corrosion, fouling, and general maintenance issues. This type of application is therefore significantly more complex than large primary distribution loops which involve mostly long straight pipes.

In a previous feasibility study [1] we have analyzed the general characteristics of hydronic cooling and heating systems on the one hand, additive properties on the other, and interactions between the two. A number of potential problems and proposed solutions were identified. Various interaction issues between drag-reducing surfactant additives and typical components of hydronic systems were also tested in our laboratory : pumps [2], heat exchangers [3], flow development and entry effects [4], fittings, etc.

Some field tests on drag-reducing additives in hydronic cooling and heating systems have been conducted in the past. Earlier tests were conducted with polymer solutions (e.g. [5,6]), but the basic shortcoming of polymer additives is the rapid permanent degradation they experience in recirculating systems. Recognition that surfactants are also good drag-reducing additives, but without the sensitivity to permanent degradation provided an incentive for more tests with surfactant solutions. Not surprisingly, early efforts were focused on large primary distribution loops in district heating systems. These are very favorable applications for drag-reducing additives because the system involves primarily long straight pipes, with few fittings and few heat exchangers. In such conditions, the overall drag reduction is expected to come close to the 80% or 85% that can be readily achieved in fully-developed flow in straight pipes. Much of this work was conducted in Europe where large district systems are much more common than in the US. Extensive large-scale tests in Germany [7], for example, in a district heating system showed indeed 80% total pressure drop reduction. The total heat transfer capacity of the plate heat exchanger was reduced by only up to 15% A similar test in Denmark [8] with the same additive showed 75% total drag reduction.

The system we conducted our field test in is a smaller yet more complex HVAC system in a building. We chose this system as a test bed because it includes all the main features of other types of recirculating systems. Some tests in building systems were conducted previously, but because of the complexity of such systems the apparent savings in

pumping power were lower than in district heating systems, and the results also more difficult to interpret. Rose et al. [9], for example, tested surfactant-drag reducers in a building heating system. They observed the expected level of drag reduction in straight portions of the pipes, but noted that the overall drag reduction was smaller. Young [10] reported results of his test in a system consisting of a short chilled water loop with a large air coil. After introduction of a surfactant additive, the flow rate increased by a factor corresponding to a total drag reduction level of 34%, but it is likely that because of the short pipe length this drag reduction resulted largely from the reductions in friction in the two heat exchangers themselves. The heat transfer coefficient of the chiller was reduced by up to 55%, and that of air coils by up to 35%. Pollert et al. [11] tested the surfactant Habon, used in previous tests in Germany, in a secondary distribution loop of a district heating system in the Czech Republic. The distribution side of that district system is similar to a single building system, with many fittings and branching, and a large number of heat exchangers. They observed an increase in flow rate corresponding to about 30% total drag reduction and about 20% of heat transfer reduction in the tube-in-tube heat exchanger.

It is important to note the significant difference in results achieved in the district systems, characterized by long runs of straight pipes, on the one hand, and the building systems where many valves and fittings may interfere with drag reduction, on the other. Unfortunately, whereas a good empirical knowledge of the drag reduction phenomenon has been achieved for fully-developed conditions in straight pipe, we have much less information about flow in the more complex components of a typical hydronic circulation systems (e.g. fittings, pumps, valves, heat exchangers etc). We have therefore endeavored to obtain such information, and in particular in a manner that is general enough in scope and fundamental enough in nature to be applicable to other processes involving fluid transportation and heat exchange for drag-reducing surfactant solutions. In this article, however, we limit ourselves to a description of some of the results obtained in our field tests.

2. COOLING SYSTEM OVERVIEW

Our feasibility study suggested that larger relative (and of course absolute) savings would be achieved in larger buildings (because most of the total pressure drop corresponds then to straight pipes where high drag reduction can be achieved), but it is more convenient to conduct tests first in a smaller system, that one can keep better control of, and where the hardware is of smaller size and the fluid quantities to handle are more limited. Typically, a smaller system will nevertheless involve all the issues that will also be encountered in large systems. If the effects on all the components are thoroughly analyzed, the results can then be extrapolated readily to larger systems. The building chosen for our test (the Engineering 2 building at UCSB) has three floors, each with two cooled wings. A layout of the chilled water loop is shown in Figure 1. There are typically about 5 or 6 rooms cooled in each wing, with one cooling coil per room, for a total of 34 cooled rooms, all laboratories. The total area of the cooled space is about 2800 m^2 (30,000 ft^2), far less than the size of buildings thought to be best-suited for the use of drag-reducing additives. The chilled water is cooled in a 200 tons (700 kW thermal power) chiller and circulated by one of two pumps in constant flow rate mode. The pumps, chiller, cooling towers, fans, are all located on the penthouse floor. (More detailed technical specifications for the main pieces of equipment and the piping can be found in [12]. An individual room air temperature is controlled by a thermostat located in the room. The thermostat operates two valves, one on the hot water coil (there is also a hot water distribution system similar to the chilled water system described here), and one on the cold water coil. The main control valves in the chilled water system are three-way valves, which control the water flow through the coil depending on the cooling demand, while maintaining the total flow through the valve approximately constant through diversion of cold water in a bypass line in parallel with the coil and including also a balancing valve.

For balancing purposes, there is also one circuit-setter valve in the return line of each coil assembly. In addition, there are also 2 butterfly valves (1 normally fully open) in each of the 6 main flow branches (2 wings, 3 floors each) for balancing between branches (Fig. 1). (Our analysis of the system showed cases of poor balancing and general overthrottling, however.) Finally, there is also one main throttling valve downstream of each pump that is provided for final adjustment of the water flow rate. These valves are also partially closed in the case of our system, but provide relatively small throttling.

3. FIELD TEST STRATEGY AND IMPLEMENTATION

The field test was divided in two phases, each having a different main objective. In the first test we used an asymptotic fluid, i.e. a fluid which provided maximum drag-reducing effect in all components of the system. This fluid, however, provided also maximum heat transfer reductions in all heat exchangers. In many cases (e.g. systems where good heat transfer is needed in the types of heat exchangers which are affected by drag-reducing additives) this may not be acceptable. This is the case for this particular cooling system, but it was necessary to quantify in this test the maximum overall drag reduction achievable.

In the second phase of the test, a different fluid was used in order to eliminate the unwanted heat transfer reduction in heat exchangers by intentional degradation, i.e. temporary elimination of the drag-reducing ability of the fluid. Under these conditions, the total drag reduction and pumping power savings achieved were necessarily smaller than in the first phase.

In addition to drag and heat transfer reductions, several other aspects of additive use were addressed in both tests, such as operability, maintenance, compatibility with the materials in the system, chemical stability of the additive, safety, etc.

3.1 Drag reduction and pumping power savings

At a given flow rate, the reduction in pressure drop is proportional to the reduction in pumping power. For better analysis of the results, it is preferable to maintain the same flow rate in the system after introduction of surfactant additive as it was with water. (This is also needed to achieve actual savings in pumping power.) As this system was designed as a constant flow rate system, we had to install a variable-speed drive on the chilled water circulation pump so that a reduced speed can be used to maintain the nominal flow rate when the pressure drop in the system decreases. The comparison between pump heads in operation for surfactant solution and water at the same flow rate should therefore give us total drag reduction and pumping power savings. It is important, however, to keep all valves in the system at the same degree of opening, for a meaningful comparison to be achieved. (In this case, the pressure drop on all control valves will remain the same as for water, at the given -nominal- flow rate through the heat exchangers. It is indeed necessary for good control and balancing that a certain amount of the total pump head be used for pressure drop on valves). Some valves, such as the balancing valves, are maintained in a fixed position to provide proper distribution of chilled liquid in the system. There are, however, also control valves, one for each room or coil unit. In order to keep all the control valves in the same position, we allowed the chilled water temperature to rise to the ambient temperature (with the chiller compressor turned off) and let the control system open all valves fully in a (futile) attempt to cool the rooms to the preset temperature. No heat transfer measurement is possible, of course, under such conditions, however. (Theoretically, this approach would not be necessary for three-way control valves such as those used in this building, which should provide a constant total flow rate through the heat exchanger and the by-pass at all positions, but this was not the case, as our measurements have shown).

Besides the pump head measurement, we also measured the electrical power used by the electric motor driving the pump as another quantification of the total drag reduction, but this power depends on additional parameters such as efficiency of the motor and pump which can vary with load and speed. In addition to the total drag (or pumping power) reduction in the whole system, we also measured local drag reduction in many locations in the system. The parts of the system in which drag reduction was measured vary in size from a whole wing to a very short section of piping. The pressure drop as a function of the flow rate was also measured for all the typical valves in the system (i.e. balancing valves, circuit setters, and bypass valve through the coils) as well as for the

evaporator and some typical coils. We also calculated the total drag reduction in the system from the measured local drag reduction in typical components and sections by integration over the whole system, in order to see if the calculation matched the total drag reduction measured. A good match between the total drag reduction obtained in these two ways would indeed be a strong indication that measurements are appropriate and that no unknown or unanticipated effect significantly affected the results.

Another issue of interest was the level of drag reduction that can be achieved in large size fittings. There was indeed very little information available about this issue, and we wanted to make some measurements to investigate this question. We had seen earlier in the laboratory that a 1/2" threaded elbow exhibited no drag reduction and even some increase in pressure drop at low Reynolds numbers, but our analysis at that time suggested the possibility that there may well be some drag reduction present in elbows of larger size, and especially so for smoother welded elbows. Accordingly, we chose a section of the 6" pipe at the outlet of the evaporator which contains 3 elbows and some sections of straight pipe for our measurements in these elbows. Pressure taps of a special design that allow averaging of 3 pressure measurements at each connection were used to minimize the effect of viscoelastic pressure hole error, since these may be significant because of the very low pressure differences measured.

3.2 Heat transfer capacity of the heat exchangers

There are two types of heat exchangers in this cooling system. One is a large shell-and-tube exchanger which serves as the chiller's evaporator, in which the refrigerant evaporates on the shell side and the circulating chilled water or solution is cooled on the tube side. There are also 34 coils, one for each cooled room, in which the chilled water cools incoming air. The coils are in parallel arrangement with the evaporator, so that the chilled water passes once through the evaporator and only once through one of the coils, for each cycle around the loop. The coils are made of finned copper tubes, with the air flowing on the outer side of the pipes, and the chilled water solution inside the tubes. The coil tubes go through several passes across the air flow, each pass starting with a 180° elbow.

Reduced heat transfer on the surfactant side would result in an increase in the temperature difference needed to transfer a given amount of heat, which in turn would reduce the overall system thermodynamic efficiency. There is some difference between the two types of heat exchangers, however. The secondary fluid in the coils is air, which has poor heat transfer properties compared to water. As a consequence, the dominant resistance to heat transfer is usually on the air side for these coils (even considering the fins), which means that any reduction in heat transfer on the surfactant side will affect the total heat transfer to a smaller extent, as our tests in the laboratory had already shown. For the evaporator, the corresponding situation was much less clear, because the heat transfer to the evaporating refrigerant depends considerably on the design of the heat exchanger.

A major difficulty we encountered in our measurements of the heat transfer capacity of the evaporator was that the chiller was operating most of the time in unsteady mode, which would introduce large errors in the measurements. We had therefore to increase artificially the cooling load in order to overcome this problem and to achieve a steady operation with high thermal loads. This was accomplished by running the hot water boiler simultaneously with the chiller. For a number of cooling coils, the control valves were disconnected from the thermostatic control and blocked manually in the fully-open-to-the-coil position. This ensured full cooling load on those coils. The air supplied to the rooms was then maintained at the desired temperature by the normal thermostatic control action on the heating coils. We could measure in this fashion the heat transfer capacity of the evaporator in steady conditions at any load. This technique was a major improvement in the measurement procedure. Not only were results more accurate at high thermal loads, but this approach enabled us to run and test the cooling system at any load, even during the winter time. The temperature measurements for water were achieved by direct immersion of thermoresistors, whereas the refrigerant saturation temperature was calculated from measured saturation pressure in the evaporator shell. (The effects of superheat and subcooling can be neglected for purpose of comparison between water and surfactant solution operation, at the same load and the same operating conditions.)

The extent of a possible reduction in heat transfer will likely be greater in the coils with longer straight tubes, because the flow will have a greater opportunity to develop downstream of the entrance and of the 180° bends. Accordingly, to quantify the worst possible case, we have identified the largest coil with the longest straight exchanger tubes and instrumented it with all the necessary sensors for water and air temperature measurements. The heat flux was measured on the water side, because water flow rate measurements are more accurate. This flow rate was obtained from an orifice meter in the branch with all the other coils shut off. The air flow rate is kept essentially constant in this system, which simplifies the measurements. The air velocity was measured in the center of the duct with a Pitot tube. This measurement alone can not be used for air flow calculations, but can be used for comparison purposes since it should remain constant for a given flow rate. The air flow rate was then calculated from the heat balance. Reliable measurements could be obtained only under steady conditions, and achieving these was done in a fashion similar to that used for the evaporator measurements.

3.3 Measurement techniques and accuracy

Variable reluctance pressure transducers were used for pressure measurements at various locations in the system. These feature interchangeable diaphragms to cover wide measurement ranges with good accuracy. With appropriate calibration, they are capable of 1% accuracy for pressure difference measurements in the upper 1/4 of any diaphragm range. The instrumentation of the main 6" distribution pipe was challenging, however, because of the very low level of measured pressure differences. This is because of the large diameter and the short sections of pipe over which the pressure differences are measured. The problem is compounded for the flow of surfactant solution, for which the errors due to viscoelastic effects (also known sometimes as hole pressure errors) may become relatively large. This may be so even for differential pressure measurements if there are imperfections in the holes such as burrs or deviations in shape. To alleviate the problem, several pressure taps were installed at each of a couple of axial locations in the longest straight run of pipe. The use of several taps and averaging at a given axial location increases greatly the accuracy of these small pressure difference measurements.

A total flow measuring device was installed at the pump discharge. It is a non-magnetic impeller-based sensor which provides a frequency signal proportional to the flow rate. The manufacturer lists the sensor as having a 1% accuracy. There may, however, be a greater error when measuring the flow rate of our surfactant solutions because of the viscoelastic nature of the fluid. Our laboratory experience with similar flow measuring devices suggested that the deviations in flow rate measurements relative to water are mostly due to viscosity, and less so due to differences in velocity profile. However, as will be discussed later, the surfactant solution prepared from the particular batch used for this test did not show any increase in viscosity relative to water. This reduced the problem of flow measurement error due to the different fluid properties for water and the surfactant solution. Accordingly, we can consider the total flow rate measurement, both for water and surfactant solution to be comparatively repeatable within about 3% (and underestimated for the surfactant solution, meaning that the power savings estimates will also be underestimated).

In addition to this total flow sensor, each of the six branches has also an orifice-type flow sensor installed. Calibration data have been obtained that enable us to convert the measured pressure drop to a flow rate. These orifice meters are rated at 1% accuracy with water, but the same considerations regarding the measurement of flow rate of a surfactant solution mentioned for the impeller flow meter apply here as well. Paddle wheel flowmeters were also used for some local drag reduction measurements. Their accuracy is about 4% after calibration, which is less than the installed impeller and orifice flowmeters. This reduced accuracy is of lesser importance, because these flowmeters are used only for local drag reduction measurements, and not for the total energy savings measurements.

Analyzing the uncertainty of the pressure drop measurements, one

should consider that a meaningful comparison of pressure drops for runs with water and drag-reducing solution must be conducted at the same flow rate. Consequently, a major uncertainty factor is that of the flow rate measurements, not only because this uncertainty is higher than the uncertainty in pressure drop measurements, but also because the pressure drop is function of the velocity squared. Overall, for water runs, the uncertainty of pressure drop measurements is +3%/-3% of the actual quantity measured; and for surfactant solution +3%/-7%, taking into account the uncertainty in underlying flow rate measurements.

Fluid temperature measurements were obtained from 1/8" sheathed thermoresistor sensors. An exception is the refrigerant temperature in the evaporator which is calculated from saturation pressure measurements. All temperature measurements were interfaced to a computerized data acquisition system. The nominal accuracy of the thermoresistors used for the temperature measurements is 0.1°C, but careful calibration gave us a proven accuracy of better than 0.05°C, including a negligible error in resistance measurement. The uncertainty in the heat transfer capacity calculation for the heat exchangers is mostly due to the uncertainty in the temperature difference measurements (and to a lesser degree due to the flow rate measurements). The uncertainty in the heat transfer capacity of the air cooling coil is +5%/-5% for the water runs, and +5%/-7% for the surfactant solution runs. For the evaporator, the uncertainty in heat transfer capacity is somewhat higher than for the air coil (because the saturation temperature is calculated from saturation pressure measurement), namely about +7%, -7% of the measurement, for both water and surfactant runs. Those uncertainty limits refer to the nominal (maximum) thermal loads (in contrast to pressure drop measurements), and remain the same in absolute values at lower thermal loads.

4. RESULTS AND DISCUSSION

We will present separately the results for the first and the second phases of the test, because very different objectives were aimed at and significantly different fluids were used. In the presentation of results for the first phase the focus will be on drag reduction measurements, whereas for the second phase we will emphasize the heat transfer results. The reader should keep in mind that one can not achieve maximum drag reduction (as in the first phase) and an unimpaired heat transfer (as in the second phase) at the same time. An optimum should be found for any particular system, and a fluid with appropriate degradation characteristics should be used.

4.1 First Phase of the field test: Maximum Drag Reduction

The measurements were first conducted with water and then repeated with the surfactant solution. The drag-reducing surfactant additive used in the test was Ethoquad T13-50 by AKZO Chemicals. The surfactant is tris (2-hydroxyethyl) tallowalkyl ammonium acetate (tallowalkyl-$N(C_2H_4)OH)_3Ac$). We used as counterion 2-hydroxyl benzoate (sodium salicylate) from Aceto, Inc. in a 1 : 2.5 molar ratio of surfactant to counterion salt. The solvent used for the surfactant solution was tap water. The numbers used hereafter for solution concentration refer to the surfactant, with an assumed constant 2.5 molar ratio of NaSal to surfactant. Drag reduction was continuously measured during the whole test period at a flow velocity of 1.5 to 2 m/s in a 15 mm pipe we installed for that purpose on the second floor. This is the average chilled water velocity in pipes throughout the system. At that velocity, the drag reduction level in that pipe was about 75% (i.e. about asymptotic) for a concentration of 1000 ppm to 1200 ppm, which suggested that asymptotic drag reduction is likely in all straight pipes in the system for fully-developed conditions. (We know from laboratory tests that drag reduction measured in pipes of different diameters for this type of fluid scales with bulk velocity within 5%, for pipes with diameters larger than 10 mm [13] which allows us to evaluate the drag reduction level in bigger pipes.) However, this particular solution showed problems of chemical instability, particularly at low concentrations, and we increased the concentration further to about 2300 ppm of surfactant, maintaining the same molar ratio of counterion to surfactant of 2.5. In this manner we achieved maximum drag reduction effects for this system, but had to leave the heat transfer control test for the second phase, when another, more chemically stable surfactant was used.

4.1.1 Drag reduction and pumping power savings

We have measured the pump head for water and surfactant solutions, while keeping all control valves in the fully open to the coils position and varying the flow rate by adjustment of the variable speed drive. Some results are shown in Fig. 2. The hydraulic pumping power can be calculated from the flow rate and pump head for both water and surfactant solution. The comparison of the pump heads at the same flow rate gives then a direct measure of pumping power savings. We see that the pump head and therefore the hydraulic pumping power was reduced by about 30% over the entire range of measurements.

We also measured the electrical power used by the pump motor. The reduction in electrical power used by the pump motor was about 25%, or slightly less than the reduction in hydraulic pumping power. Interestingly, both numbers are very close to the original pre-test estimates (25%) generated by assuming asymptotic drag reduction in straight pipes, and no drag reduction in fittings and valves.

In addition to overall pressure drop reduction, we also measured the drag reduction level in many singular components of the system, as well as in one entire wing. These data were then used to calculate the overall drag reduction by summing contributions of each sub-system. In this cooling system, about 20% to 30% of the total pump head results from the pressure drop in the fittings, and we were therefore particularly interested in measuring the pressure drop in some large fittings which could not be tested readily in our laboratory. Although the fittings are of various types, elbows and tees are the most common in the system and may be looked at as "representative" fittings. We have therefore measured the pressure drop for a series of three 6" elbows for water and surfactant solution. Over velocities ranging from 0.5 m/s to 2 m/s, the pressure drop coefficient for the series of 3 elbows was found to be reduced by about 40% relative to water. More details on the results and experimental configuration can be found in [12]. Considering that a significant portion of the pressure drop in the system may be due to the pressure drop in fittings, the drag reduction in large fittings may then contribute significantly to the overall drag reduction for the whole system.

The drag reduction level was also measured in the return line of one of the six horizontal chilled water distribution loops, namely the north wing of the second floor. This wing plus the other five constitute most of the chilled water pipe system (besides a short section of 6" pipe supplying the chiller and the vertical distribution lines). A more complete analysis of these measurements can be found elsewhere [12] as well. The drag reduction levels measured in this line at the nominal flow rate were 55%, 37% and 34%, depending on flow distribution in the coils. We can then use these results of local drag reduction to predict the overall drag reduction for the whole system. The 37% corresponds to a flow configuration which is a good approximation for the pressure drops in the return loops of all coils. (The circuit setters may be on average slightly more closed in the coils closer to the vertical main to compensate for less pressure drop in the horizontal main.) The supply lines are very similar to the return lines and the same drag reduction level is to be expected there. The other components in the horizontal distribution lines of the 6 wings that are still not accounted for are the coil control valves, the coils themselves, and the butterfly balancing valves (one in each wing). There is no drag reduction in the valves and only little drag reduction in the coils (see below). Since about one third of the total pressure drop in horizontal distribution corresponds to the pressure drop in these components, our average drag reduction gets reduced to about 26%. However, to complete the picture we still have to consider the vertical portion of the distribution system, and the evaporator. About 50% drag reduction was measured in the evaporator (see below) and similar drag reduction is expected in the vertical pipes (which actually contribute very little to the total pressure drop). About 80% of the total pressure drop in the system ($2.6\ 10^5$ Pa with water) is due to the horizontal distribution lines and only 20% to the vertical distribution lines and evaporator. Our estimate of the total drag reduction becomes then about 30%, which is about the reduction in pump head actually measured, a confirmation of the general validity of our analysis.

4.1.2 Heat transfer reduction

The heat transfer capacities (U) of the evaporator and coil were calculated from measurements, as described below, for water and for the surfactant solution. They are defined as the amount of heat transferred from one fluid to another, for a unit logarithmic temperature difference. For the evaporator, the logarithmic temperature difference is calculated from the measured inlet and outlet chilled water (or solution) temperature and the saturation temperature of the refrigerant. The temperatures of the chilled liquid were measured directly, whereas the refrigerant temperature was taken to be the saturation temperature corresponding to the refrigerant pressure measured in the evaporator (with supercooling of the refrigerant assumed negligible). The results for the chiller thermal capacity per unit logarithmic mean temperature difference across the evaporator are shown in Fig. 3. As can be seen, the reduction in thermal capacity of the evaporator is about 30% for the range of thermal load covered (from about 120 kW to 310 kW). The lower limit is the lowest load achievable with the current chiller control setup. (The chiller can not safely operate below this limit, because hot gas bypass which would allow operation at very low load is not provided in this unit). On the other hand, we could not run the chiller beyond 310 kW of thermal load, because the overcurrent protection for the compressor motor shuts the system off at that point (even though this is less than the nominal thermal load, mainly because of the relatively poor condition of the cooling tower). The pressure drop of the chilled liquid (water or surfactant solution) in the evaporator was also measured at various flow rates. About 60% drag reduction was achieved with the surfactant solution over the whole range of flow rates. The evaporator tubes are about 15.5 mm in diameter and 4 m long, but the drag reduction measured under fully-developed conditions in a custom 1/2" pipe (15.7 mm) loop added immediately downstream of the evaporator showed 75%, however. The difference can be attributed to undeveloped flow conditions in the upstream part of the evaporator tubes and to entry effects. The fact that the measured total heat transfer reduction in the evaporator is only 30% can be explained by a larger heat transfer resistance on the refrigerant side than on the chilled liquid side. This is an important point, because it illustrates that the anticipated large heat transfer reduction on the surfactant side of the heat exchangers may not necessarily translate into correspondingly large decreases in overall heat exchanger performance -- which would likely render the systems inoperable without further intervention.

The largest coil heat exchanger was also instrumented for heat capacity reduction measurements. The overall heat transfer capacity of this coil was measured in two regimes: with constant water flow (varying the air flow) and with constant air flow (varying the water flow). Figure 4 shows the heat transfer capacity of the coil per unit logarithmic temperature difference (calculated in the same way as for the evaporator) for various liquid flow rates, but with constant air flow rate. The air flow rate is maintained as high as possible (about 3 times higher than normal) to make the effect of heat transfer reduction on the liquid side more apparent. At the maximum liquid flow rate, the reduction in thermal capacity of the coil, when running the surfactant solution instead of water, is 20%. When the liquid flow rate is reduced the reduction becomes slightly larger, up to 30%. These results are similar to those obtained during our tests of a similar air coil in the laboratory [3].

Pressure drop measurements for the same coil, for both water and the surfactant solution showed drag reduction ranging from 0% to 35%, depending on the solution flow rate. This is significantly less than the 60% drag reduction measured in the evaporator and the 75% measured in fully-developed flow conditions. The likely reason for this low drag reduction level is that the flow could not develop fully in the short sections of straight coil tubes between the 180° elbows.

4.2 Second phase of the field test: Heat transfer control

The primary objective for the second phase of the field test was to prove that the heat transfer in all heat exchangers can be maintained at the same level as for water by proper choice of the surfactant solution and by relying on intentional temporary degradation. An extensive investigation of the nature and phenomenology of the temporary degradation and recovery of surfactant solutions was first undertaken in the laboratory. Various surfactant solutions were tested to determine the chemical characteristics of the phenomena. As a result of those tests we decided to use a new nonionic surfactant solution (SPE95285), developed for us by Dr. M. Hellsten of Akzo Nobel Chemicals, in a concentration of around 2500 ppm. This solution was thought to provide good control of heat transfer in both heat exchangers and also high enough drag reduction in the rest of the system to provide satisfactory pumping power savings.

In addition to the measurements used in the first phase of the field test, we developed for the second phase some portable devices that enabled us to measure the fluid characteristics at practically any location in the system, which in turn allowed us to ascertain the average drag reduction and heat transfer reduction in every section. To achieve this, we measured drag reduction in customized 2 mm and 5 mm inner diameter portable characterization test pipes. The corresponding fluid was diverted from the system though the test pipes by special fittings which provided a smooth cone-shaped entry so that the fluid entered the pipe 'as is' and was not temporarily degraded by the entry. The drag reduction ability of the fluid was calculated by measuring the pressure drop and flow rate in the characterization pipe, which gave us information on the drag reduction in the system at that location. To facilitate this comparison, the fluid velocity in the characterization pipe was kept equal to the fluid velocity in the main system, in order to eliminate diameter effects. From the drag reduction ability of the fluid we can then estimate the heat transfer reduction using the DR / HTR relationships we developed. We were therefore able to generate a map of the local drag reduction in the whole building, and then to integrate these measurements to obtain the total drag reduction and pumping power savings. We can also calculate the heat transfer on the surfactant solution (water) side, and consequently the overall heat transfer in the heat exchangers knowing the relationship between the heat transfer resistances on both sides of the heat exchanger. This approach is not only more accurate than the integral measurements of the overall heat transfer capacity, but also more general, and the results can be readily applied to other systems of different size and heat exchangers characteristics.

4.2.1 Drag reduction and pumping power savings

At the nominal flow rate the pump head in the system was reduced by about 12% (Figure 2). The reduction in electrical power used by the pump motor was also measured at about 12%. The difference with the 30% reduction in total head measured in the first phase is due to the loss of drag reduction in the heat exchangers and in the pipes downstream of the heat exchangers.

In addition to the overall pressure drop reduction, we also measured the drag reduction level in many singular components of the system, as well as in one entire wing. These data were then used to calculate the overall drag reduction by summing contributions of each sub-system, as was done in the first phase. We calculated the expected overall level of drag reduction for the system and obtained a good match with the total drag reduction measurements. Both the direct measurements and the integration of local measurements showed an overall pressure drop--i.e. power-- reduction of about 10 to 15%, with a slightly greater reduction at high thermal loads because of the effect of temperature on the drag-reducing ability of the solution. A full report on local drag reduction measurements will be published elsewhere. Figure 5 shows a distribution of drag-reducing effects in the whole system.

4.2.2 Heat transfer control

The heat transfer control used in this field test works on the principle of temporary fluid degradation and subsequent recovery. The recovery as a function of time, as well as the level of degradation caused by a given pressure drop on the degrading device, depends on the temperature. In our case, the temperature difference between the supply and return was about 3°C at full thermal load, but in other systems it could be 5°C, which is a common design practice value. For the fluid temporary degradation upstream of the evaporator, the fluid has to be degraded at the higher temperature level, which means higher

degradation is needed. Fortunately, high degradation is taking place in the pump itself. If the pump hydraulic efficiency is 70%, it means that 30% of the total pumping power --or 42% of the effective pumping power-- is dissipated in the pump itself. This translates to an equivalent pressure drop of 42% of the actual pump head, or in our case about 17 psi worth of degradation, which is much more than any other discrete degrading component in the system. In the case of the coil, the situation is different. The fluid must be degraded at lower temperature, which means a lower pressure drop is needed. The recovery in the case of the cold fluid is also slower, and the distance between the degrading valve and the coil is therefore less critical.

Degradation devices with large discrete pressure drop are available at proper locations to be used for our heat transfer control purposes, but on the other hand --given proper choice of the fluid--there is no other location in the system with discrete pressure drops that is high enough to cause undesired temporary degradation of the fluid. In principle, it is possible to tailor the degradation and recovery characteristics of a surfactant system by varying one or more of the influential parameters. A 12% of drag reduction capability was measured with the 5 mm pipe at the evaporator exit . The overall drag reduction in the evaporator at nominal flow rate is measured at between 4 and 6%, with increasing drag reduction at higher average temperatures. From the 6% drag reduction in the evaporator we would expect about 10% heat transfer reduction on the fluid side based on the fixed heat transfer/drag reduction ratios we identified. Indeed, the actual heat transfer measurements (Fig. 3) show that the overall heat transfer reduction in the evaporator is essentially zero within the experimental uncertainty which is estimated to be ±4% maximum, because there is about 4 times higher heat transfer resistance on the refrigerant (Freon) side than on the solution (water) side.

In the building tested, the control valves as well as the balancing valves are located downstream of the coils. For our purposes it is better to have the control valve upstream of the coil to provide temporary fluid degradation and to eliminate the possible heat transfer reduction. Since these valves exhibit a pressure drop of about 5 psi at nominal flow rate to the coil --which is normally enough for degradation-- heat transfer control on the coil can then be achieved without additional throttling. To provide and investigate fluid degradation at the coil entry, we used an existing shut-off valve upstream of the coil for flow control, with similar effects. This valve was manually throttled to generate a pressure drop of approximately 5 psi. The overall drag reduction in the coil for the relevant temperature range was then between 5% and 12% depending on the mean temperature. Local measurements of solution properties conducted with the 5 mm pipe indicated that the drag reduction ability was about 5% to 35% (depending on temperature) at the coil exit, and no drag-reducing ability or total degradation at the coil inlet. The measured overall heat transfer reduction when the fluid was degraded by the upstream valve is negligible (Figure 4). In fact, looking at the overall drag reduction we would indeed expect an overall heat transfer reduction of only about 2% in the coil. This estimate is based on the known drag/heat transfer reductions ratio and the ratio between air and water side heat transfer resistances, which ranges from about 5 to 10 depending on the conditions (as can be seen from the data corresponding to changing air velocities for water during phases 1 and 2 in Figure 4).

5. SUMMARY AND CONCLUSIONS

We conducted a field test of surfactant additives in a complex recirculating hydronic system in a building that includes all the main components likely to be found in other hydronic systems that could benefit from the drag reduction technology. In addition to an improved understanding of the fluid / flow and fluid / hardware interactions, specific objectives could be energy savings, pump and pipe size reduction, an increase in flow rate or heat transfer, or an increase in system length. One could also combine some of these features. In this case, we focused on energy savings, and paid particular attention to the connection between local and system wide engineering issues and analyses. The test was divided in two phases.

In the first one, we measured the overall decrease in pressure drop across the system using a fluid giving maximum drag reduction. The pump head (and therefore the pumping power) was found to decrease by about 30%. This number is relatively low because of the presence of many valves and fittings in this relatively small yet complex system. Much higher savings could be obtained in bigger or simpler systems. The system was found to remain operational, but the heat exchangers suffered from significant decreases in thermal capacity.

In the second phase of the test, we focused therefore on the issue of elimination of these heat transfer reductions, and we were indeed able to eliminate completely the undesirable heat transfer limitations through appropriate choice of the fluid and temporary fluid degradation at necessary locations. This elimination has to be accompanied by lower drag reduction in the heat exchangers, however, and the net overall pressure drop reduction was smaller. Again, proportionally greater savings would be achieved in a bigger / simpler system or with a more optimized fluid. Alternatively, one could also achieve hardware size reduction, increased flow rate and heat transfer, or increased system length. As in the first phase of the test, the implementation of the technology was simple, and no maintenance, corrosion, operability, performance, nor control difficulties were found.

This large-scale field study was very successful and shows conclusively that it is indeed possible in practice to use surfactant drag-reducing additives in complex recirculating systems, even those involving heat exchangers. The new results and understanding generated should bring us much closer to the stage of widespread implementation of the drag reduction technology in many types of recirculating industrial, commercial, and military fluid systems.

ACKNOWLEDGEMENTS

The authors gratefully acknowledge financial support by the California Institute for Energy Efficiency (contract No. 4902610 to EFM) the California Energy Commission (contract No. 500-94-022 to EFM), and the University of California; the assistance provided by the Facilities Management personnel at UCSB; laboratory work by Mr. G. Aguilar; and the additives samples and chemistry information kindly provided by Drs. S. Shapiro and M. Hellsten (AKZO Nobel Chemicals).

REFERENCES

1. Gasljevic K. and E.F. Matthys, 1993, "On saving pumping power in hydronic thermal distribution systems through the use of drag-reducing additives", Energy and Buildings, Vol. 20, pp. 45-56.
2. Gasljevic K. and E.F. Matthys, 1992, "Effect of drag-reducing surfactant solutions on centrifugal pumps performance", In Recent advances in non-Newtonian flows, AMD-Vol.153, ASME Pub., pp. 49-56.
3. Gasljevic K. and E.F. Matthys ,1993, "Effect of drag-reducing additives on heat exchangers", In Developments in non-Newtonian flows, AMD-Vol. 175, ASME Pub., pp. 101-108.
4. Gasljevic K. and E.F. Matthys. 1997. Experimental investigation of thermal and hydrodynamic development regions for drag-reducing surfactant solutions. Journal of Heat Transfer vol. 119, No. 1, pp. 80-88.
5. Leca A. and M. Leca, 1984, "Drag Reduction and Heat Transfer Measurements with Polyacrylamides on a Model of a District Heating System," *In* Drag Reduction (Proc. of the 3rd International Conference on Drag Reduction, R. Sellin and R. Moses eds), IAHR Pub., paper D8.
6. Martischius F.D. and W. Heide, 1984, "Drag Reduction in Heating Systems: Stabilization of Polyacrylamide Solutions up to Temperatures of 150°C," *In* Drag Reduction (Proc. of the 3rd International Conference on Drag Reduction, R. Sellin and R. Moses eds), IAHR Pub., paper D9.
7. Steiff A., W. Althaus, M. Weber and P. Weinspach; 1989. "Application of drag-reducing additives in district heating systems", In Drag Reduction in Fluid Flow: Techniques for friction control (eds: R.H. Sellin and R.T. Moses), Ellis Horwood Pub., Chichester, pp. 247-254.
8. Hammer F., 1993, "Smooth water in district heating", Fernwarme International, Vol. 22 (4), pp. 142-150.

9. Rose G.D., K.L. Foster, V.L. Slocum, and J.G. Lenhart; 1984. "Drag Reduction and Heat Transfer Characteristics of Viscoelastic Surfactant Formations." *In* Drag Reduction (Proc. of the 3rd International Conference on Drag Reduction, R. Sellin and R. Moses eds), IAHR Pub., paper D6.
10. Young C.O'C. J., 1994, "Drag reduction in chilled water distribution system of a 200-ton absorption chiller", Proc. of the 85th International District Heating and Cooling Association Conf., IDHCA Pub., Vol. 85, pp. 301-317.
11. Pollert J., J. Zakin, J. Myska, and P. Kratochvil, 1994, "Use of friction reducing additives in district heating system field test at Kladno - Krocehlavy, Czech Republic", Proc. 85th International District Heating and Cooling Association Conf.", IDHCA Pub.. Vol. 85, pp. 141-156.
12. Gasljevic K. and E.F. Matthys. 1996. "Field test of a drag-reducing surfactant additive in a hydronic cooling system", *In* Drag Reduction and Turbulence Modification, vol. FED-237; vol. 2, pp. 249-260; ASME, NY.
13. Gasljevic K. and E.F. Matthys. 1995. "On the Diameter Effect for Turbulent Flow of Drag-Reducing Surfactant Solutions." In Development and Applications of Non-Newtonian Flows III, Vol. FED-231, pp. 237-243, ASME Pub, Washington D.C.

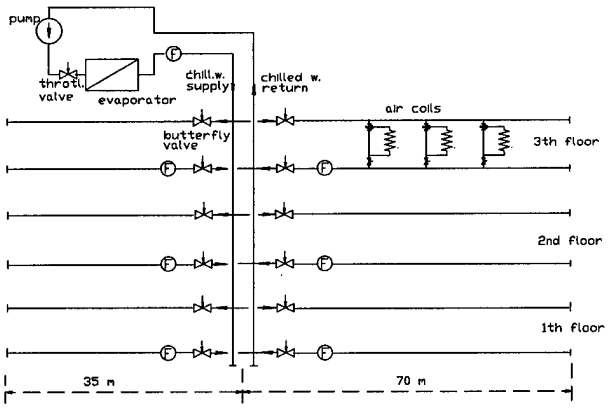

Fig. 1 Schematic of the chilled water system. The chilled water is distributed to 3 floors of the building, with two cooled wings at each floor. There are on average 4 to 5 cooling coils in each wing (some shown here only on the third floor north wing for clarity). Butterfly valves are used to balance the water flow rate between the wings. F stands for flow rate sensor.

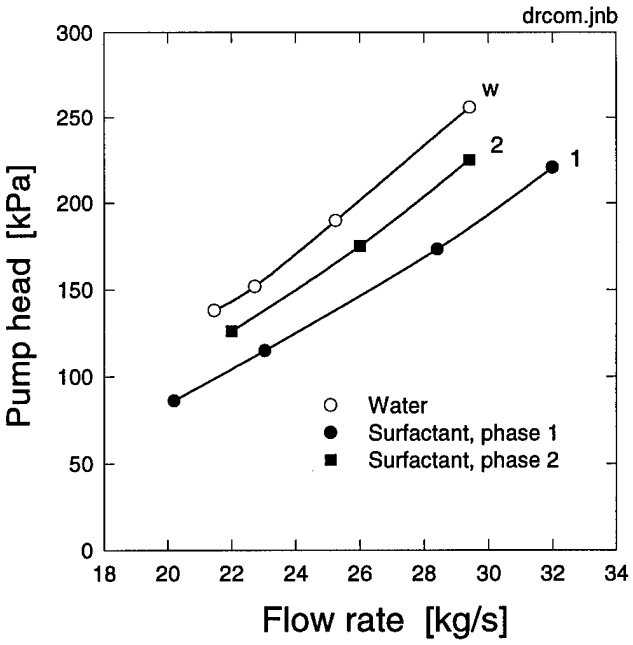

Fig. 2 Pump head for water and for the 2 surfactant solutions.

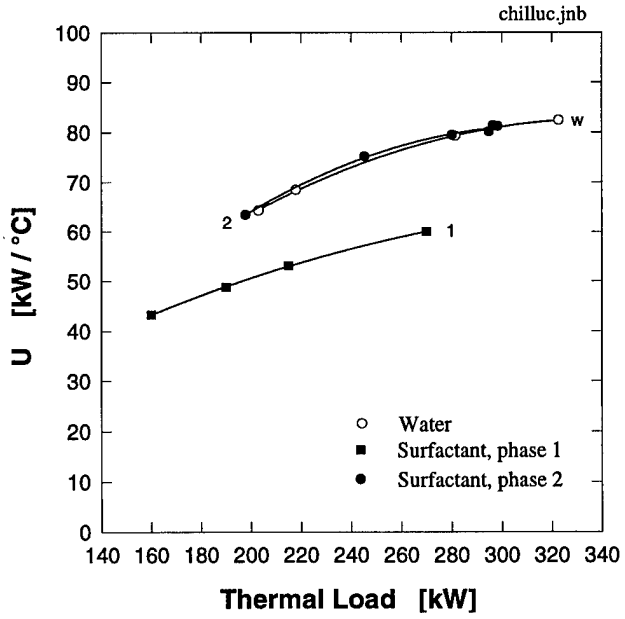

Figure 3 : Overall heat transfer capacity of the evaporator as a function of thermal load at a nominal fluid flow rate of 28.5 l/s, for both water and the 2 surfactant solutions.

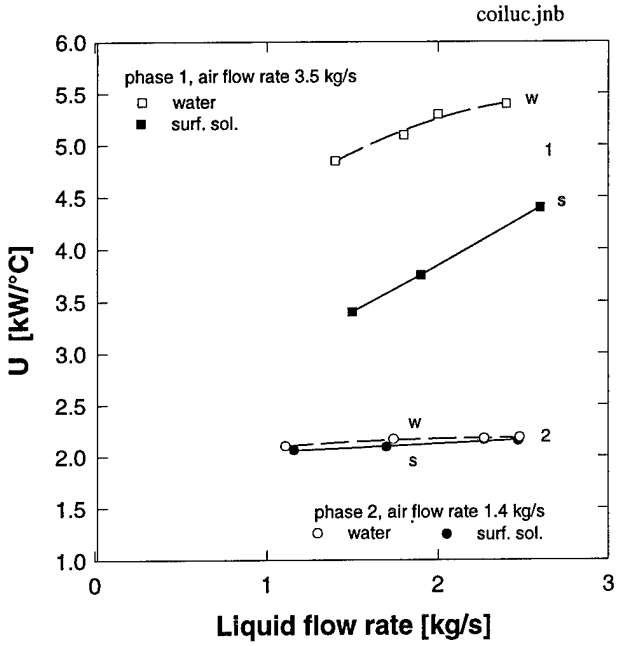

Figure 4 : Heat transfer capacity of the cooling coil for water and the 2 surfactant solutions.

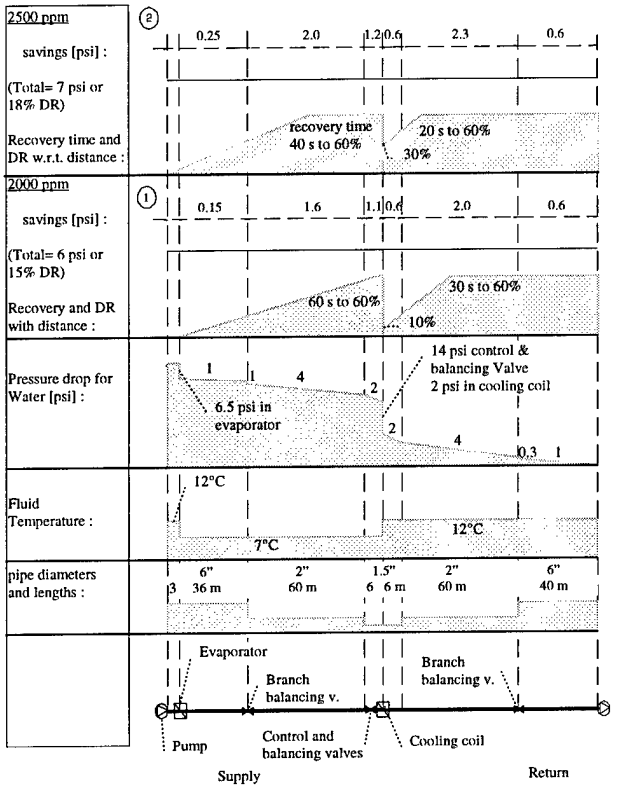

Figure 5 : System temperature and pressure distribution as a function of distance downstream of the pump.

PRACTICAL APPLICATIONS OF DILUTE POLYMER ADDITIVES FOR WATER CRAFT

Tadeusz Kowalski ,Ph.D. Professor Emeritus,
Department of Ocean Engineering,
University of Rhode Island.

Abstract - Effect of long chain polymers on drag of bodies moving through water or water moving inside pipes is well established. In the 1960's and 1970's there was a substantial research conducted in many countries. The interest in the use of polymer additives decreased in subsequent years due to technical difficulties of injection and due to the costs associated with continuous injection. Research of the effect of polymer additives on turbulent drag is described leading to a number of significant findings and possible explanation of the mechanism of drag reduction. Tests of the turbulence characteristics in the boundary layer with and without the polymer injection were conducted and marked changes in the structure of the turbulent eddies were measured. Suppression of small scale eddies and shift of the turbulence spectrum towards the larger eddy sizes were observed. Injection methods were tested by varying the angle of the injection slots to the flow in the boundary layer. The optimum injection was with the slots at five degrees inclination to the flow, producing almost tangential stream of polymer entering the boundary layer. Discovery of the polymer persistence effect in the boundary layer during drag reduction tests substantially reduced the expenditure of polymer additives. It was found that a pulsed injection of one second duration followed by fifteen second pause retained its drag reduction effect at a substantial decrease of the amount of polymer. Examples of some practical drag reduction applications of polymer additives in external flows are given together with suggestions for future research.

I. INTRODUCTION

The objectives of the investigation were to explore the phenomenon of drag reduction due to the presence of polymer additives in the boundary layer and to obtain an insight into the mechanism of the drag reduction.

The scope of the research was to:

i) investigate the turbulence changes in the boundary layer caused by the injection of polymer additives

ii) develop a probable mechanism of the drag reduction including a molecular entanglement hypothesis

iii) investigate persistence effect of additives in the boundary layer leading to the polymer pulsing injection method

iv) test the effect of polymer on propeller

v) test the effect of polymer additives on sound propagation in water

vi) suggest possible applications of the drag reduction phenomena

II. EXPERIMENTAL RESULTS AND DISCUSSION

A dramatic change in the character of the turbulence was observed in the boundary layer each time dilute solution of the polymer additive was injected. The small amplitude (high frequency) turbulent velocity fluctuations disappeared and the large amplitude (low frequency) fluctuations were enhanced. The change in the distribution of eddy sizes was confirmed by observation using two methods.

First, using strip chart records of the velocity fluctuations. Figure 1 shows a typical record. Stretching the record's time base shows the effect quite clearly. Curve (a) represents the turbulent fluctuations in water and curve (b) with polymer additives. These records allowed the calculations of microscale of turbulence by the zero crossing technique. When polymer was injected the size of the eddies increased up to 100 % near the solid boundary. The top part of Fig.1 shows an unexpected phenomenon of the persistence effect of polymer. Injection was pulsed for 1sec. followed by a 15 sec pause and the effect on the microscale of the turbulent eddies decreased slowly. Later,experiments with a flat plate confirmed this persistence effect.

Second, using measured energy density spectra and energy dissipation spectra. Figure 2 shows typical curves of both spectra. The figure shown refers to 20 ppm injection of Polyox WSR 301 of average molecular weight of $4x10^6$. The hot film probe was located 3 feet downstream from the injection slot and 0.05 inches above the bottom of a flume. F refers to the energy density and n^2F to the energy dissipation. The dissipation curves give a clear picture of the effect of the polymer additive since the areas under them represent part of the viscous dissipation in the flow (confined to the u-component of the turbulent velocities in these tests). The curves indicate the change of scale of the microeddies by the shift of the peak of the curve for the flow with polymer towards the lower frequency end of the spectrum. Since the viscous dissipation for one-dimensional spectra is proportional to the areas under the dissipation curves integration was performed to show the effect of polymer additives on energy losses. The areas under the dissipation spectra curves, at two locations downstream and a number of heights inside the boundary layer, are shown in Fig. 3. The substantial reduction in the dissipation of energy across the boundary layer is evident. Although the measurements could not be taken close to the viscous sublayer (the size of the hot film probe did not allow this) it can be observed from the trends of the curves that the maximum dissipation area has been substantially affected by the presence of polymer additives. The peak of the curve that existed in the case of water has disappeared. The polymer curve is also a flatter one. This indicates that the additive is most effective near the position of maximum turbulence production in the boundary layer. The largest relative increase in microscale occurred close to the boundary. For optimum practical application the polymer should, therefore, be injected and retained close to the boundary. Associating eddy sizes with the geometry of the boundary layer an increase in microscale close to the boundary will increase the thickness of the sublayer. A thicker boundary sublayer reduces the velocity profile gradient at and near the wall. Since the wall shear stress is proportional to the velocity gradient at the wall the frictional drag at the surface will also decrease.

Another turbulence characteristic investigated was the uv (x and y direction velocity fluctuations) component of the Reynolds shear stress tensor. The presence of polymer in the boundary layer drastically decreased the shear stress component. The curves of turbulent shear correlation coefficient versus frequency, Fig. 4, show that the turbulent shear, which together with the velocity gradient is responsible for the production of turbulence is considerably lower when polymer is injected. This indicates that the transfer of momentum from the mean flow to the turbulence is reduced by the action of the polymer and, thus, conserves energy of the mean motion. This occurs over the whole range of frequencies and not only at the higher range as in the energy density spectrum. The polymer molecules seem to act as barriers restricting communication across the boundary layer and forcing the liquid to flow in a semi-laminar manner. The resistance in such a flow would be expected to be lower. It is suggested that the polymer molecules entangle and form macromolecular networks which become stretched and oriented in the direction of the main flow under the action of shear stresses. Such a physical model could explain the reduced momentum transfer across the boundary layer. Figure 5 gives the distribution of the turbulent shear correlation coefficient with the distance from the wall. The results for water and for polymer show opposite correlation trends. The correlation for the polymer is much reduced close to the wall indicative of velocity profiles near separation and of reduced wall shear stresses. It thus appears that the action of the polymer suppresses the turbulence energy within the boundary layer and reduces the wall shear stresses, Kowalski (1)

A possible model of the interaction between polymer molecules and the fine structure of turbulence, the so-called dissipative eddies, can be suggested. Physically only like-size material objects can produce sufficient interaction to cause substantial transfers of momentum between them. It is therefore to be expected that the interference of polymer additives with the turbulent eddies will be noticeable when the molecular sizes of the additives are of the same order of magnitude as the dissipative eddies. The sizes of the dissipative eddies in water, in these experiments, can be estimated from Kolmogorov's hypothesis about the eddy scales, Hinze (2). The calculations gave the maximum dissipation eddy scale as 0.01 in.

The size of the polymer molecule in a randomly coiled configuration is given by:

Length of a monomer times square root of number of monomers in a chain.

For the Polyox WSR 301 Diameter of coiled molecule =

0.00004 in. Length of uncoiled molecule = 0.004 in.
The diameter of the polymer molecule is of the most common molecule in the solution. Since the polymer consists of a distribution of molecular weights, sizes of molecules are distributed around the predominant or most common size. It is therefore unlikely that the polymers of presently available molecular weights can theoretically have any direct effect on the drag or the turbulence characteristics of the flow. The experimental evidence however indicates that there is an effect.

The eddy structure in the boundary layer is constantly changing with large eddies being continuously created by the interaction of shear stress tensor and the mean velocity gradient. These then decompose into smaller and smaller eddies until they reach the size of the dissipative ones that turn into thermal energy. At any time, at any place there are eddies of all sizes present in the flow.

A given polymer additive of a certain molecular weight and chemical composition can be characterized by the size of its molecule, the chain arrangement, the energy of the chain entanglement, and possibly by the chemical or hydrogen bonding between the chains. Under the influence of turbulent motions, which can be characterized by the intensity of the turbulence and the sizes of the dissipative eddies, there is a level of mixing in the flow to produce certain sizes of macromolecular networks. The drag reduction will then begin at a specific range of values for those parameters. A functional statement for this threshold of polymer action can be expressed by combining the following parameters:

Diameter of coiled molecule of polymer or its radius of gyration.
Concentration of polymer in the flow
Hydrodynamic and flow perturbation properties of molecule
Internal friction coefficient of a molecule
Viscosity of solvent
Kinematic viscosity
Wave number of dissipative eddies
Intensity of turbulence

The result is a function that describes the effects of the polymer additive on the threshold of polymer action in defining the onset of drag reduction. This function can be split into two parts; the first part depends on the polymer additive, the second part on the characteristics of the turbulent flow. For detailed discussion of the polymer entanglement hypothesis see Kowalski (3).

Velocity Profiles

Very marked differences in the velocity profiles were observed when polymer was injected. The typical blunt profile of the turbulent flow became a sharp laminar-type with a hint of inflection suggesting approach to a separation type profile. Figure 6 shows the velocity profiles at two different positions downstream from the injection point. The shapes of the profiles indicate that they are still developing and have not reached the equilibrium stage. The change in the velocity profiles shows that the polymer slows down the velocity near the boundary, producing a smaller velocity gradient at the wall, and speeds it up away from the boundary. A smaller velocity gradient at the wall implies a thicker viscous sublayer confirming the results of the turbulence characteristics measurements. Calculations of velocity profile parameters gave additional indication of the large changes caused by the polymer in the boundary layer. The shape factor for water or air has a theoretical value of 1.4 (experimental results gave the value of 1.5 and remained reasonably constant) the H values for the flow with the polymer additives varied from 2.6 to 3.7. These are well into the conventional separation velocity profile range. The larger value of H occurred 1 ft and the smaller 3 ft downstream from the injection point. This can be the result of dilution of the additive as it flows downstream.

Flat Plate Drag Reduction

Experiments with a flat plate in a flume gave significant results regarding the optimization of the injection techniques in external flows. The results are shown in Figs. 7 and 8 . They show the drag reduction effect of dilute polymer solutions of different concentrations. Each concentration produced a different degree of drag reduction. Starting with very dilute solution of 20 ppm the drag reduction increases for 30, 50 and 100 ppm. The peak of the drag reduction is progressively higher but requires an increased expenditure of polymer additives. There seems to be a limit to the solution concentration effect as the curves of Fig. 8 show a leveling trend of drag reduction for concentrations of 200, 300 and 500 ppm. This may indicate a saturation of the near boundary region and pushing of the excess of the additive into the outer region of the boundary layer or even into the main flow. In addition, at high polymer concentrations the injected additive may not have time to properly dissolve in the near boundary region before it is diffused away from the boundary.The curves indicate that it is better to use smaller injection rates of higher concentration solutions. The 5 degree inclination of the injection slots used in these test is considered to be a practical manufacturing limit. Therefore the only way to keep the additive closer to the boundary is to operate at low injection rates and as the flow velocity increases to have an increasing number of injection slots distributed in the flow direction. In this way sufficient polymer additives will be kept close to the boundary for longer distances along the surface, Kowalski (4)

Effect of polymers on sound propagation in water

Suppression of small scale eddy sizes in the flow due to presence of polymer lead to the question of polymer's influence on the sound propagation. Tests were conducted with a sound transducer immersed in a polymer solution in a dome shaped container which was placed in a flume with water flowing round the dome. Marked effects were observed especially on the white noise spectrum. It is suggested that the suppression of smaller turbulent eddies resulting in drag reduction also suppresses the noisy part of the sound spectrum. This leads to the conclusion that polymer additives could be used to tailor the sound spectrum either by injection on the outside the sonar dome or by filling the dome with polymer solution.

III. POSSIBLE APPLICATIONS FOR POLYMER ADDITIVES

Full scale tests

Drag reduction due to the injection of long chain polymer additives has been well established on the laboratory scale. There is not yet a lot of information on full scale tests. The author conducted some comparative tests on sailing yawls in Chesapeake Bay. Two yawls were used running on parallel course matching their speeds. Polymer solution was injected through a 1/2 inch plastic tubing wrapped around the under-water part of the bow 1/10 boat length aft of the waterline at the bow. Noticeable increase in speed was observed (not measured) over the companion sailboat. While this was not a proper instrumented test a satisfactory confirmation of full scale effect of polymer additives in salt water was obtained.

An instrumented test was carried out by the A.E.W.Haslar on a coastal minesweeper in the English Channel. Drag reduction was measured but of smaller percentage then the laboratory tests would indicate. This is explained by the fact that polymer was injected through external piping wrapped outside the hull at one station close to the bow. The polymer additive missed the viscous sublayer where the maximum drag reduction takes place and aft parts of the wetted surface of the hull must have been missed altogether. Tests of the author's pulsed injection method, although scheduled at the end of the trials, could not be carried out because of inclement weather and some delays in the main part of the test, cut the trials short.

Hydrofoil boat application.

Hydrofoil boats exhibit a characteristic curve of Drag versus Speed. The drag increases with the speed to a maximum at the take-off speed and then drops down to fully foil-borne values. Temporary injection of polymer additives while hull-borne will reduce the drag and eliminate the hump in the drag curve. Tests with hydrofoil boat model in a towing tank at the U.S.Naval Academy, Annapolis performed by the author confirmed this effect. The tests were performed with uniformly dissolved polymer in the towing tank water giving a 20 ppm concentration . The drag reduction on the hull was not as high as was expected. At that time it was not realized that polymer affects detrimentally the lift force of the lifting surfaces.

Application to torpedoes

Another short duration use of the polymer additives could be to increase the speed or the running distance of torpedoes. However, this will not apply to torpedoes with laminar boundary layer flows

Effect of polymer on the propeller performance

Tests were conducted on a model propeller in a flume and a decreased efficiency was measured. This was thought to be caused by the effect of the polymer on the thrust and torque of the propeller. The

model propeller must have been operating in laminar flow regime where the polymer increases the drag, hence higher torque; and the lift of the propeller could also be adversely affected by the polymer, hence lower thrust. Full scale propeller trials should be run to confirm this explanation. This is an important issue since some of the injected polymer will eventually reach the propeller.

IV. SUGGESTIONS FOR FUTURE RESEARCH

Full scale trials are essential to prove different applications of polymer drag reduction.

1. Optimization of injection methods which should include the injection nozzle design, distribution of nozzles along the wetted surface, concentration of polymer additive and the pulsing method of injection. These tests should be performed on surface ships, catamarans, SWATH ships, torpedoes and submarines

2. Large scale, high Reynolds numbers, tests of propeller operating in a dilute polymer solution.

3. Tests with underwater transducers to determine the possibility of enhancing the operation of sonars. The injection of polymer on the outside of the hull of submarines could possibly alter their acoustic signature or alter it at will during combat situation.

V. REFERENCES

1. T. Kowalski "Ph.D. Dissertation" Department of Mechanical Engineering, University of Waterloo, Canada, 1969
2. J.O.Hinze "Turbulence" McGraw-Hill
3. T.Kowalski "Macromolecular Entanglement Hypothesis in Drag Reduction Flows" Cambridge University, International Conference on Drag Reduction, September 1974
4. T.Kowalski "Turbulence Suppression and Viscous Drag Reduction by Non-Newtonian Additives" Transaction of the Royal Institution of Naval Architects, 1968

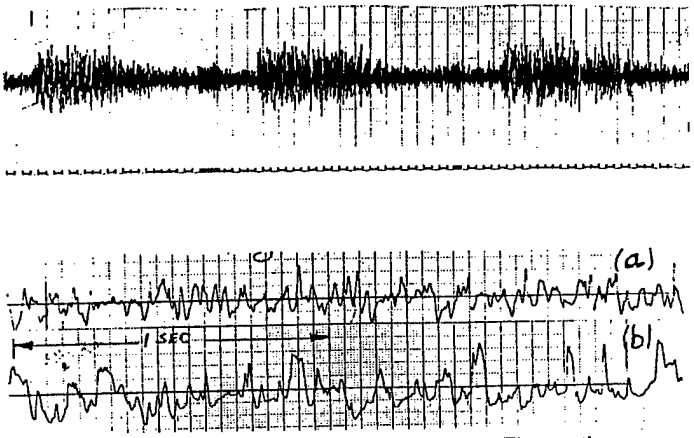

Figure 1. Record of Turbulent Velocity Fluctuations

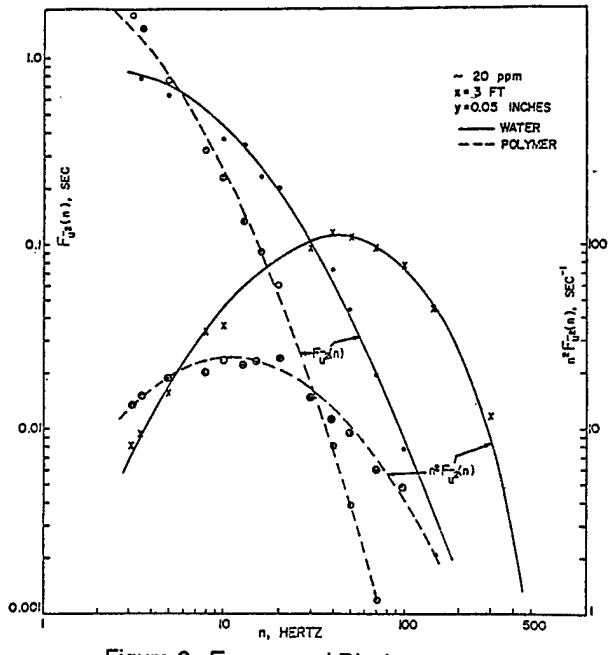

Figure 2. Energy and Dissipation Spectra

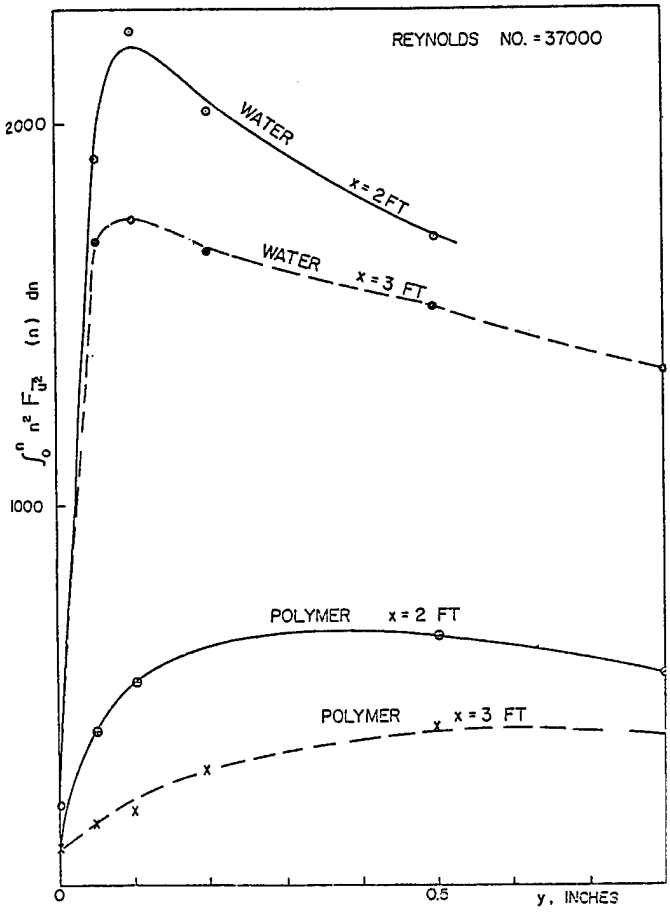

Figure 3. Energy Dissipation Function

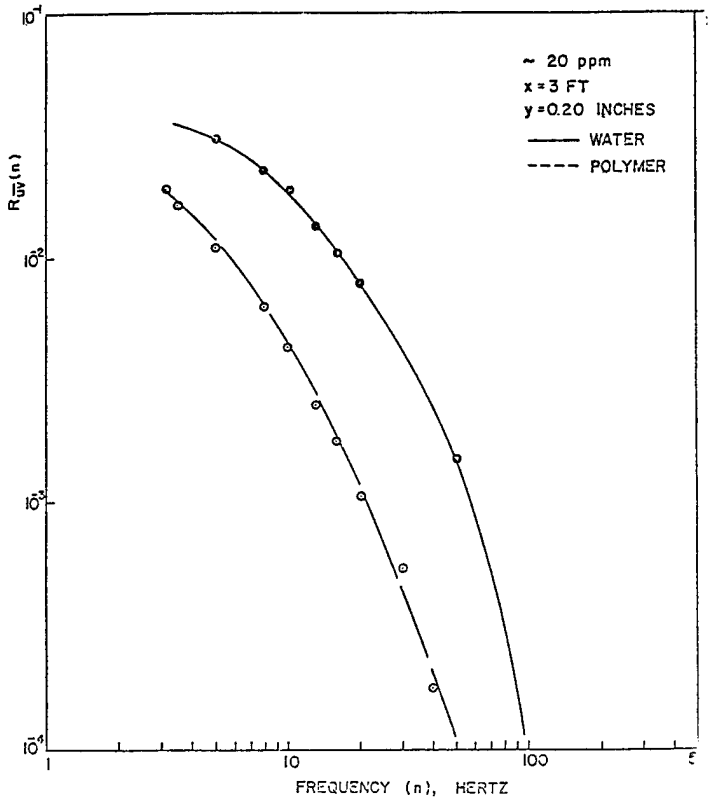

Figure 4. Turbulent Shear Correlation Spectra

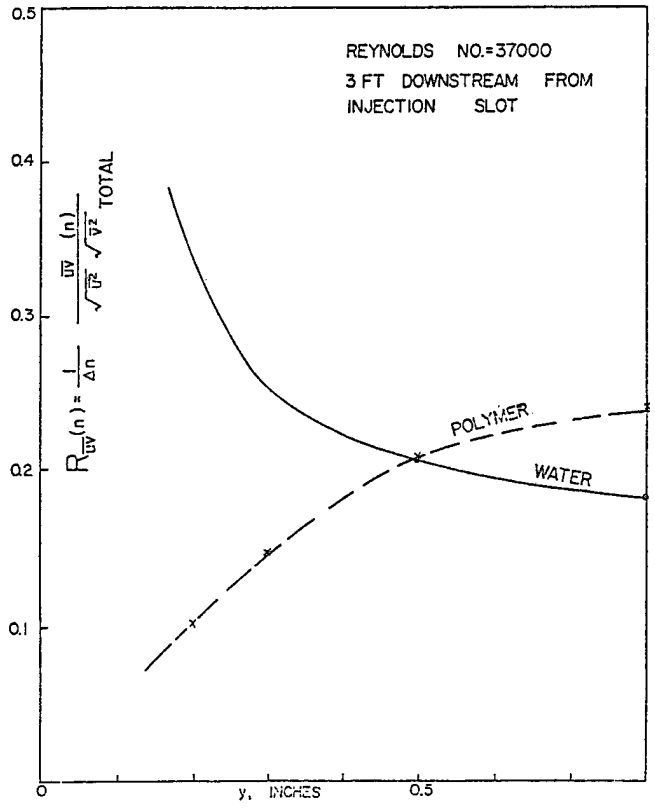

Figure 5. Turbulent Shear Correlation

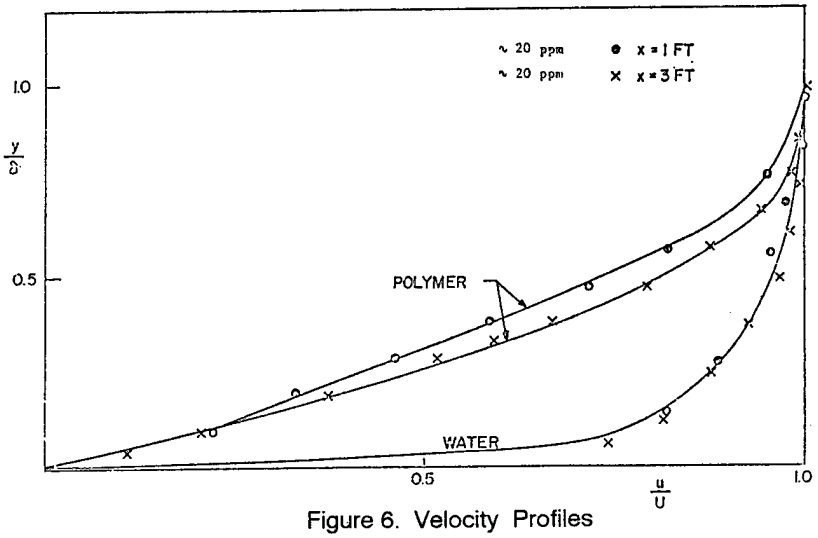

Figure 6. Velocity Profiles

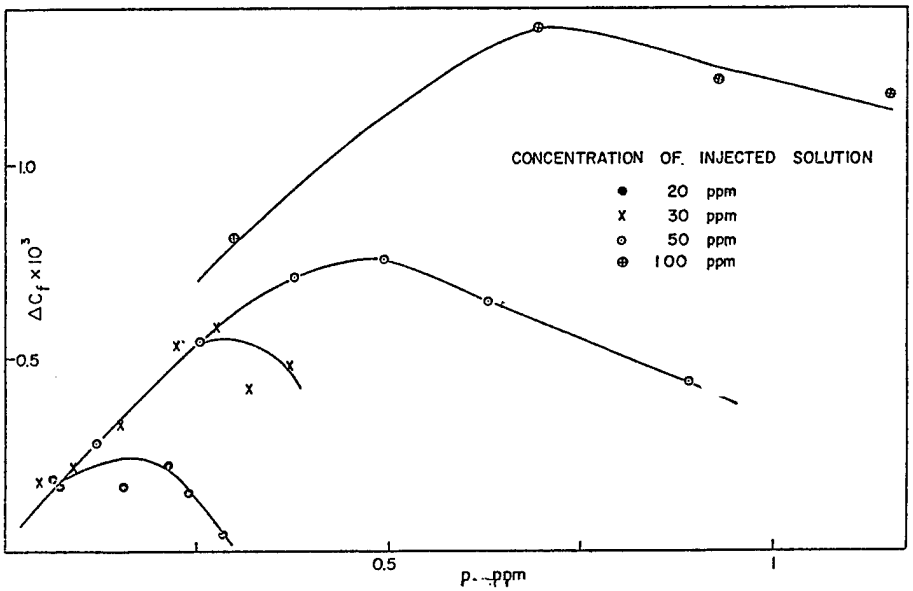

Figure 7. Flat Plate Drag Reduction - Low Concentration

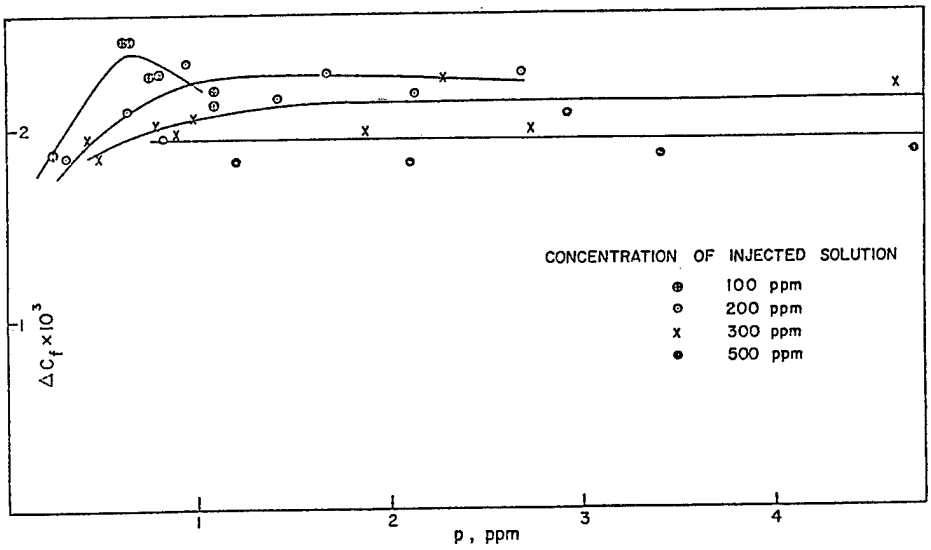

Figure 8. Flat Plate Drag Reduction - High Concentration

EXPERIMENTAL RESEARCH OF THE INFLUENCE OF CONDITIONS OF POLYMER ADMISSION TO THE BOUNDARY LAYER ON A DROP OF TURBULENT FRICTION

Vladimir G. Pogrebnyak
Ecological Center of scientific and applied researches 31, Shorsa Street, Donetsk, 340050, Ukraine Fax-(0622)-92-83-16
bvn@dgci.donetsk.ua

Yuri F. Ivanyuta
A.N. Krylov Central research Institute
44, Moskovskoye Shosse,
Saint-Petersburg, 196158, Russia

Abstract - Results on injection using under-slot chambers with changing angle of entrance into the slit, attest that when the polymer solution is supplied to the body surface, angles of entrance into the slit being small, the reduction of tangential stresses of friction shows itself practically immediately following the area of introducing polymer into the flow. If the polymer solution is supplied into the boundary layer through the slit with a big entrance angle, there takes place a delayed manifestation of hydrodynamic activity of polymer molecules. It has been shown that polymer solutions flow through the under-slot chamber in the supercritical mode, with generation of dynamic structures having relatively big time of structure relaxation in them. The formation of supermolecular structures is connected with deformation action of hydrodynamic field on macromolecules which causes the change of their thermodynamic state, promoting supermolecular structure-formation in semi-diluted and moderately concentrated polymer solutions. The consequence of this is the appearance of an area with reduced hydrodynamic activity of the polymer on the body surface following the place of introducing the polymer solution into the boundary layer.

INTRODUCTION

Among known methods of the artificial effect on a boundary layer (BL) of objects of shipbuilding with the purpose of decreasing hydrodynamic resistance of friction, the method of supplying solutions of polymers is almost unique, in the field of development of which certain practical progress has been reached. The research, conducted in this direction, concerned improvement of hydrodynamics of external flow of bodies by a polymeric solution as well as problems of perfecting mixing devices. To problems of hydrodynamics of polymeric solutions in elements of systems of input of polymers in a boundary layer of a streamline body was not given due attention.

It is considered, that in case of current of solutions of polymers through slots and other elements of systems of input, essential "anomalies", which could considerably affect Toms effect, cannot be observed. Such a conclusion follows from the analysis of the data, obtained when researching shift laminar currents, for which the effects of elastic deformations are insignificant. In the systems of input, as a rule, complex current, consisting of a superposition of shift current and mainly longitudinal one (with stretching) is realized. In case of a complex current the effects of elastic deformations become so great, that neglecting them should in most cases result in the fact that the potential capabilities of the polymeric components are used not completely, especially this should be noticeable at large speeds of motion of objects of a ship-building profile.

In the given paper regularities and manifestations of elastic deformations were investigated in case of a current of solutions of polymers in conditions, characteristic of internal and external problems with reference to objects of shipbuilding.

EXPERIMERNTAL

We have used a special hydrodynamic bench, permitting to realize the exhaust velocities of water flow through a channel up to 35m/s; the channel had length of 8,5 m. Orifices for measuring pressure and the sensors of force of friction were placed on the lower wall of the channel. The system of injection consisted of a dosator, underslot chamber with varying conditions of deforming the polymeric solution in the input area of the slot. The angle of declination of the injected polymeric jet in relation to a wall did not vary. In the experiments there varied: angle of opening the slot, concentration of injected polymeric solution, speed of injection, molecular mass and kind of polymer as well as the speed of a filling flow (water).

RESULTS AND DISCUSSION

On Fig.1 the experimental data describing features of current of water solutions polyethylene oxide (PEO) in the underslot camera are indicated.

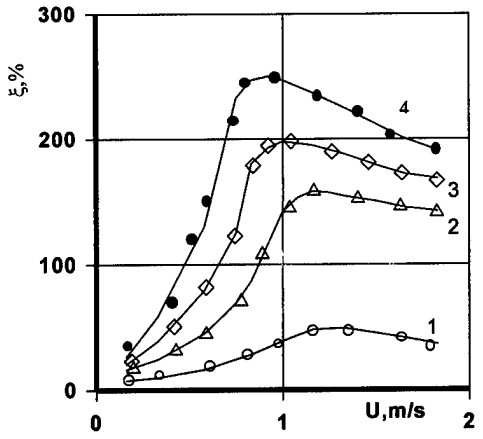

Fig.1. Influence of U and angle of entrance into a slot onthe relative pressure differential:1-9°, 2-13°, 3-22°, 4-34°. C_{PEO}=0.1%, M_{PEO}=4·10^6

It can be seen, that the phenomena, unusual for purely viscous mediums are characteristic of such currents. At certain critical (threshold) values of average exhaust velocity U the relative pressure differential begins sharply to increase, and it is the sharper the more is the concentration of polymer in a solution. The marked character of dependence $\xi = f(U)$ testifies about high dissipation of energy during the course of

solutions of polymers through an injector i.e. the increased hydrodynamic resistance on supercritical flow rates is observed.

The considered experimental data agree with the results obtained when researching currents of polymeric solutions in model conditions of elements of systems of input (through short capillary tubes and a slot). Such currents are in detail investigated by us in papers [1 - 5]. Here we shall mark the most important moments of manifestation of effects of elastic strains in case of a current with expansion of solutions of polymers. Transition to a mode of current with an increased dissipation of energy is accompanied by formation of the source flooded jet as "cord" or "filiet" enclosed by secondary currents in the shape of a ring-shaped vortex. In case of supercritical mode of current for area of the concentration lying between very diluted and moderately concentrated solutions of polymers, there happens rather strong deformation effect of a hydrodynamic field on molecular chains. The deployment degree of a polymeric chain reaches 60%. In half-diluted and moderately concentrated solutions of polymers, the relaxation times of the developed circuits and weakly-deformed individual chains differ more, than by 2 orders.

The reason for so large time of swerving is supermolecular structures generated under an operation of a hydrodynamic field in a polymeric solution. The last circumstance should be essentially reflected in decrease of turbulent friction, if the time of life of supermolecular formations originating in a polymeric of supplying solution in a moment it in boundary layer, is comparable to the tine of stay at a surface of a streamline body.

The results on injection onto the lower wall of the channel with application of underslot chambers with a varying angle of entrance in a slot testify (Fig.2),

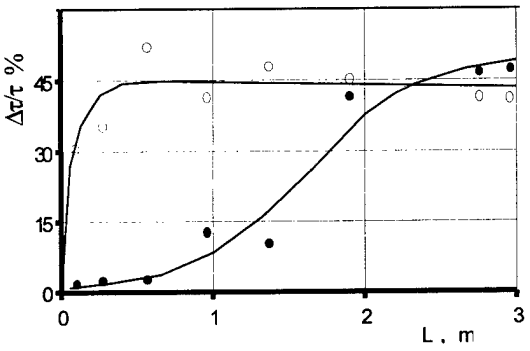

Fig2. Influence of an angle of entrance on the distribution of decrease of tangent voltages along the lower wall of the channel for injections of solution PEO mass $2\cdot10^6$, V_0=16.5m/s, Q=50sm^3/s, C_{PEO}=0.3%; β°: 1-7.8°, 2-165°.

that when the polymeric solution is supplied to the surface of a streamline body at small angles of an entrance in a slot, the drop of tangent stresses of friction is exhibited practically at once behind the place of introduction of a polymer in the flow.

If the polymeric solution is introduced into a boundary layer through the chamber with a large angle of an entrance, delay of development of hydrodynamic activity of polymer molecules takes place.

It should be mentioned that the distribution of tangent voltages and relative pressure losses along the length of the channel correlate among themselves. From Fig.2 it follows, that the modification of a mode of a course of a polymeric solution through the underslot camera from poorly dissipative one up to hardly dissipative one at the expense of modifications of conditions of entrance results in lowering general effect of friction resistance decrease(reduction) (on a three-meter long plot of a streamline surface) almost by 2 times.

There has been (Fig.3) registered a considerably greater separation of curves of dependence of a drop of resistance from $\gamma=Q\cdot C_{PEO}/\Omega\cdot V_0$ (where Q -is speed of injection, C_{peo} - concentration of injected polymeric solution, Ω -moistened surface, V_0 -is speed of a filling flow) on concentration of polymer C_{PEO} in case of admitting the polymer onto the surface of a streamline body in conditions of strong deformation effect of the hydrodynamic field on the injected solution, than in conditions of weak gradient effect.

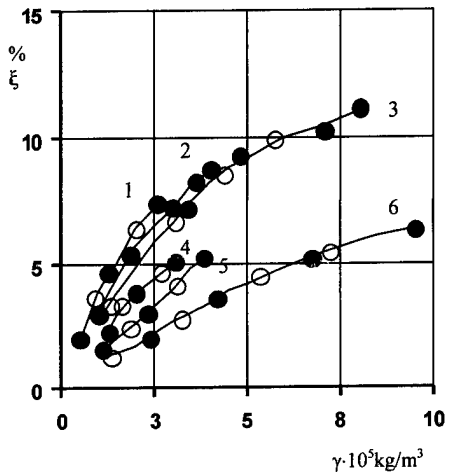

Fig.3. Dependence of general pressure losses in the channel from the indicated concentration of PEO mass $2\cdot10^6$, V_o: ● =16.5m/s, O =25m/s; β°=7.8°(1,2,3), β°=165°(4,5,6); C_{PEO} : 1and 4-0.05% , 2 and 5 - 0.1% , 3 and 6 – 0.3%.

The visualization of currents of a polymeric solution in an underslot chamber testifies, that the conditions of entrance render influence on the drop of hydrodynamic resistance only in case, when there is loss of stability of current, stipulated, as was shown by us earlier[1-3], by the formation of dynamic supermolecular structures, causing sharp increase of current dissipativities. The reduction of efficiency of a polymeric solution at the expense of the deformation effect on it, in the input system reached 25 % and above at V_0>15m/s. Increase of filling flow speed results in the extension of the area with reduced hydrodynamic activity of a polymer. The role of the area with reduced hydrodynamic activity of polymer introduced into the boundary layer is the more significant, the less is the length of a streamlined body. It is easy to explain this if you remember, that time of life of derivated structures in conditions of stretching current are of the order of 0,1-0,2 s and more than [4]. This is the time, during which polymer, which has left a slot, has reduced activity stipulated by its memory. Obviously, the more there will be the velocity of the main stream, the larger is the area behind a slot filled in with a polymeric solution in this condition, and its sizes will be evaluated as $l_\lambda=\theta_{sw}\cdot V_o$, where θ_{sw} - by the time of structural relaxation of supermolecular formations. Then, for example, for velocity of filling stream of 25 m/s this area should be distributed

downwards along a stream up to 2,5 m, if θ_{sw} = 0,1s. The estimated sizes of area of reduced hydrodynamic activity of polymer will quite agree with experimentally obtained results.

From comparison of results of experiments for injections of polymeric solutions of various concentration through the underslot camera with a changed angle of entrance (Fig.3 $\gamma = Q \cdot C_{peo}/\Omega \cdot V_o$, where Q is speed of injection, C_{peo} - concentration of injected polymeric solution, Ω - moistened surfaces ,V_o –speed of a filling flow) follows, that for want specific average concentration of polymer in the boundary layer the efficiency of a diminution of resistance is reduced with growth of concentration of the injected polymeric solution and it is the stronger the higher is the angle of entrance. In [6] there was put forward a hypothesis that viscoelastic effects (swelling of a jet) near a slot strengthen a dagging of a solution of polymer by the external boundary layer and result in a faster decrease(reduction) of concentration of polymer on the a surface of a streamline body. The results of papers [7,8] force to reconsider this hypothesis, as visualization of current behind a slot [7] and measurement of concentration of polymer in the boundary layer [8] have not shown amplifications of a diffusion of polymer. Most acceptable is the explanation based on the influence of effective viscosity (if you understand it in a broad sense) which does not contradict the results describing dependence of hydrodynamic activity of polymer from conditions of supplying of a polymeric solution to the surface of a streamline body. The dynamic structures formed under an operation of a hydrodynamic field in a polymeric solution call its densening [1,3], and this, naturally, should diminution of a diffusion of polymer in the boundary layer.

The detected regularities of the manifestation of elastic deformations when admitting polymer solution onto the surface of a streamline body allows to offer a way to evaluate resistance of bodies of revolution. Resistance of streamline bodies of revolution when admitting polymeric solution to the boundary layer accounting for the effects of elastic deformations thus arising can be determined as:

$$X = \int_0^{l_\lambda} \chi(x)\tau_{wo}\,dx + \int_{l_\lambda}^{L-l_\lambda} \chi(x)\tau_{wl}\,dx ,$$

where χ is perimeter of object, τ_{w0} and τ_{wl} - tangential stresses with supply and with no supply of polymer to a boundary layer, L- length of object, $l_\lambda = \theta_{sw} \cdot V_0$ (θ_{sw}- time of structural relaxation of super-molecular formations, V_0 –speed of the body).

CONCLUSION

The data obtained in this paper testify, that when solving problem on drop of resistance to the motion of a body by means of injecting polymeric solutions in a boundary layer in a part of development of optimum versions of systems of admission, it is necessary to take into account the possible development of effects of elastic deformations in them.
The drop of effect of reduction of resistance to motion when supplying polymeric solution into a boundary layer of the object results from the combination of deformation effect of a longitudinal hydrodynamic field, realized in the system of supply and of the molecular -concentration characteristics of a polymeric solution.

REFERENCES

1.Pogrebnyak V.G.,Ivanyuta Y.F.,Frenkel S.Y." The Structure of the Hydrodynamic Field and Distorsions of the Molecular Shape of Flexible Polymers under Free-Converging Flow Conditions" Polymer Science USSR ,1992, vol.34, No.3. p.270-273.

2. Pogrebnyak V.G.,Ivanyuta Y.F.,Naymchuk N.V., and Tverdokhleb S.V "Experimental investigation of solutions of polymers under near-the-wall turbulence simulated conditions" Interfacial Layers under Complex Conditions, Ed. By Mironov B.P., Novosibirsk,USSR, 1984, p.120-127.

3. Pogrebnyak V.G.,Ivanyuta Y.F.,Naymchuk N.V., Tverdokhleb S.V., and Frenkel S.Y. "Flow structure of polyethylene oxide solutions in the input zone of a short capillary" Inzh.-Fiz. Zh., 1985, vol.49, No.4, p.614-621.

4. .Pogrebnyak V.G. "Deformation relaxation time of polymers' solutions" Hydro and gasdynamics of flows with heat and mass transfer, Ed. By Nikulin V.A., Izhevsk, USSR, 1989,Issue 3, p.143-149.

5. Pogrebnyak V.G., Naymchuk N.V., and Tverdokhleb S.V, "Dynamic structureformation in the solutions of hydrodynamically active polymers" Inzh.-Fiz. Zh., 1992, vol.63, No.2. p.147-150.

6. Wu. J., Fruman D.H., Tulin M.P. " Drag reduction by polymer diffusion at high Reynolds numbers " J. of Hydronautics., 1978, vol. 12, Juli, p.134-136.

7.Fruman D.H. and Galivel P. "Anomalous effects connected with ejection of polymer, reducing resistance, in turbulent boundary layers of pure water" Technical papers from the Symposium on Viscous Drag Reduction ,Ed. By Gary R. Hough, Vought Advanced Technology Center, Dallas, Texas, vol.72, November 1979.

8. Vdovin A.V. and Smolyakov A.V. "Diffusion of solutions in a turbulent boundary layer" Zh. Prikl. meh. i teh. Fiz.1978, No2,p.66-73.

Drag reduction dynamics

V.M.Kulik
Institute of Thermophysics, Russian Academy of Sciences,
Novosibirsk, 630090, Russia

It was experimentally shown that solution of PEO changes its drag reduction (DR) efficiency during the process of flow in tube or between coaxial cylinders. DR initially increases, then reaches its maximum value and then decreases. It is explained by change of solution properties during the process of turbulent flow. The maximum DR corresponds to the Virk ultimate value. To describe this universal dependence the simple formula is suggested. It was shown that solution of PEO can work very effectively in conditions of high shear stresses.

The method of DR determination by pressure drop was analysed and corrected. It was noted that neglect of a flow kinetic energy change can lead to considerable error in DR value. Neglect of DR dynamics lowers real possibilities of PEO-solution. The method of action on DR dynamics decreasing the growth stage and prolonging the zone of maximum efficiency is suggested.

The resumption of DR growth when flow restarted after short stop was obtained. The explanation of DR decrease in tubes of large diameter is suggested.

In the earliest work on DR by polymer solution (Fabula, 1963) it was obtained that DR differs on the tube length. But the author analysed only the results for the second half of the test tube and approximated the pressure distribution along the tube by a straight line. After this work all authors began to ascribe some certain DR value to each hydrodynamics regime of polymer solution flow. There are a lot of works on the DR dependence on different parameters: sort of polymer, its molecular weight, concentration, temperature, pH-factor of medium, shear stresses, flow velosity, tube diameter, etc: see reviews of Hoit (1972), Virk (1975), Berman (1978), Sellin (1982).

It is well known that in a turbulent flow the polymer solution properties change (Balakrishnan & Gordon, 1975; Berman, 1980; Kalashnikov & Tsiklauri, 1990). Globule-like supermolecular structures consisted of many linked macromolecules are destroyed. The number of binding and linking is reduced. Macromolecules are aligned and elongated. Macromolecules, which are close enough, begin to crystallize and give insoluble dust. It means that drag reduction is not constant value but depends on interaction time of macromolecules with shift, elongation shears and pulsation stresses.

In our investigation two setups were used. The first one with rotating coaxial cylinders has an advantage that it directly shows time dependence of DR change of fluid volume between the cylinders (Kulik & Semenov, 1991). The experimental points (fig.1) obtained for concentration of PEO from 4 to 100 ppm lay on one curve, if the ratio of the interaction time to concentration is used as an abscissa. This fact is in a good agreement with Belokon & Kalashnikov (1977) and confirms the hypothesis of the concentration-time analogy. But unlike preceding investigation, where the authors had observed in detail only monotonous decrease of DR, in given case the initial time interval with the DR growth is found, and the maximum DR is fixed. It must be specially noted the DR decrease is sharper as the solution concentration increases further c>200 ppm, and the concentration- time analogy is infringed.

As it is well-known, high-molecular polymers are able to form supermolecular structures in a static concentrated solution, which are the colloid particles. The process of association leads to a significant decrease of concentration of effectively working macromolecules. As energy of the Van-der-Vaals interaction is, at least, by the factor of 10-20 less then energy of chemical polymerization bonds, the process of the supermolecular formation disintegration must predominate over the process of the breaking up of molecules at first, if one considers the number of dissociations. That's why on the certain stage the degradation of macromolecules accompanying by the process of the breaking up of the colloid particles has the least action on the DR change then the dissociation of supermolecular structures.

For studying DR dynamics when c<100 ppm the second setup (fig.2) was made. The duration of a single pass of the fixed liquid volume trough the smooth tubes of different length and inner diameter D=2.0 mm were measured. The length of the longest tube L=4 m corresponds to L/D=4 000. Every next tube was twice as long as previous one. The minimum length of the tube was equal to 0.25 m (L/D=125) in the first series of experiments and 0.125 m (L/D=62.5) in the second one. To attain a turbulent flow with large Re the tank can operate under a high pressure of 16 MPa. It makes possible to pass water trough the longest tube at velocity U=40 m/s (Re =$8\cdot10^4$). Compressed air enters trough a solenoid valve into the tank and dissipates by a set of screens to reduce a disturbance of horizontal liquid surface. The platinum electrodes of diameter 0.5 mm react on medium conductance between them and the body of tank. The top gauge controls by start of the timer, the lower gauge controls by stop of the timer and a valve closing. Liquid volume between electrodes V_0=642 sm^3, volume of tank - 1l . An effluence of liquid situated upon the top electrode (volume 0.25 l) ensures the stability regime of flow before a start of the timer.

All tubes and the tank were thermostated with constant temperature 25^0 C. The basic solution of 2% -concentration was prepared a week before the measurements. The dilute solutions were prepared a day before its testing. The water distillate was used for the solutions preparation. Just before the measurements 1 ml of 0.5% NaCl solution was added to 1l of tested solution in order to guarantee the sufficient electric conductivity of medium.

The measurements were carried out in range of Reynolds number from $6\cdot10^3$ to $8\cdot10^4$ (fig.3). It is easy to see that drag reduction varies along the tube, therefore efficiency of a solution action can't be determined correctly by only one number - it is a function of time and intensity of interaction between polymer macromolecules and a turbulent flow. There are three regions with different behavior of drag reduction. The first one is characterized by a drag reduction increase along the tube. This region at small velocities and large concentrations occupies the largest part of the tube. So, at U=3 m/s and c=100 ppm the drag reduction growth is observed along the all length of the tube. The second zone is determined by maximum drag reduction. This region, as the first one, is observed here for some but not all regimes. The increase of a flow velocity moves the place of maximum drag reduction appearance to the beginning of the tube, and the solution concentration growth moves it to the tube end. For example, when c=20 ppm maximum drag reduction at U=5 m/s appears within the range 1-2 m, but at U = 13 m/s - within the range 0.5-1 m. And, at last, on the third region the efficiency of drag reduction decreases. This behavior of Toms phenomenon is typical for weak concentration and high velocity of a flow.

The ultimate possible drag reduction (according by Virk) are shown in fig.4 and in fig.3 by dash lines. We can see the good agreement between the measured data of maximum drag reduction and calculated ones. The dependence of ultimate drag reduction on Re can be described by following formula:

$$\Psi_{ul} = 0.554\ arctg\ (0.024\sqrt{\mathrm{Re}}\ ). \qquad (1)$$

Size of the tubes and possibility of setup allowed to determine maximum drag reduction for not all solution concentration and flow velocities. So, when U = 3 m/s the tube is too short to find maximum drag reduction for solution with c = 100 ppm. For solutions with c = 1 ppm and c = 2 ppm maximum drag reduction can't be measured correctly for some velocity because a place of them appearance is on the initial part of their tube (0 ÷ 125) D.

Sedov et al. (1979) drew the conclusion about a drag reduction decrease when $\tau > 80$ N/m^2. But when the overall picture of drag reduction change is shown this conclusion is not confirmed (see fig.5). A decrease in drag-reducing efficiency was not found even for very high shear stresses $\tau_p = \tau_0 (1 - \Psi) = 800$ N/m^2 as it is shown in fig.3(d). Growth of shear stressed increases a rate of drag reduction change and shifts a place of maximum drag reduction appearance to a tube beginning. It seems likely that it is the main reason of the slope of the efficiency obtained them.

In the second series of experiments DR dynamics was studied for 4 samples of PEO with different molecular weights: $0.3 \cdot 10^6$ ($[\eta] = 2.2$ dl/g), $0.8 \cdot 10^6$ (5 dl/g), $1.93 \cdot 10^6$ (10 dl/g) and $3.25 \cdot 10^6$ (15 dl/g). The results of measurement are shown in fig.6. Here, as before, there are three regions with different behaviour of drag reduction: a growth, maximum value and a slope down. The region of growth is especially noticeable at low velocity (see figs.6(a),(b)) and becomes more considerable with increase of molecular weight.

The region of maximum drag reduction is removed to the tube beginning with increase of velocity or decrease of M_w. So at U=3m/s and M_w>0.8 mln [see fig.6(a)] the growth of drag-reducing efficiency is observed along all the tube, i.e. the tube is too short to show maximum drag reduction. But at U =5 m/s maximum drag reduction is reached on the distance 0.5 ÷ 1 m for solution with M_w=0.8 mln [fig.6(b)], on 1 ÷ 2 m for M_w=1.93 mln and for M_w=3.25 mln beyond the tube limit. At 10 m/s [see fig.6(c)] maximum drag reduction is reached on distance 0.25 ÷ 0.5 m for solution with M_w=0.8 mln and so on. Maximum values of drag reduction are near the ultimate drag reduction determined by formula (1).

From these figures it can immediately be seen that maximum drag reduction does not depend on molecular weight if weight is more then certain value. So solution with M_w=0.3 mln can not reach the ultimate drag reduction. However, at the large Reynolds numbers the measured values of maximum drag reduction are more then ultimate ones [see figs.6(d),(e)].

With the aim of determination the reason of Virk's maximum drag reduction law violation let's analyse the method of hydrodynamic friction calculation from pressure drop measuring. According to Bernoulli equation, pressure drop is required to work against friction and to change kinetic energy of a flow

$$\Delta = \frac{2l}{R}\tau + 0.5\rho U^2(\alpha_2 - \alpha_1). \qquad (2)$$

Here α - coefficient of kinetic energy which takes into account the distribution of velocity u at tube cross-section area S:

$$\alpha = \frac{\oint_S u^3 dS}{SU^3} = \frac{2\pi \int_0^R u^3 (R - y) dy}{\pi R^2 \left[2 \int_0^R u (1 - y/R) d(y/R) \right]} \qquad (3)$$

For usual turbulent flow, when velocity profile does not change, respectively kinetic energy doesn't change and usual formula holds:

$$\Delta = \frac{2l}{R}\tau.$$

A situation may be significantly changed when liquid is non-Newtonian fluid.

For determining the relationship between Δ and τ it is necessary first to know the dependence of α on Re and Ψ. For this task a velocity profile for fixed Re and Ψ was found using the condition for equality of a volume velocities for water and a polymer solution

$$\int_0^{R_0^+} v_o^* u_o^+ (1 - y_o^+/R_o^+) d(y_o^+/R_o^+) = \int_0^{R^+} v^* u^+ (1 - y^+/R^+) d(y^+/R^+)$$

the usual two - layer profile of velocity for water

$$u_o^+ = y_o^+ \qquad y_o^+ \le 11.6 \qquad (5)$$

$$u_o^+ = 2.5 \lg y_o^+ + 5.5 \qquad 11,6 \le y_o^+ \le R_o^+,$$

and Virk' velocity profile

$$u^+ = y^+ \qquad y^+ \le 15$$

$$u^+ = 11.7 \lg y^+ - 17 \qquad 15 \le y^+ \le y^+ \qquad (6)$$

$$u^+ = 2.5 \lg y^+ + B \qquad y^+ \le y^+ \le R^+,$$

where $u^+ = u/v^*$, $R^+ = Rv^*/v$, v^*- shear velocity, v-kinematic viscosity, y- radial distance from pipe wall, $y^+ = y v^*/v$.

Determined velocity profile was substituted in Eq.(3) and next formula was used

$$\int x^n \ln^m x dx = \frac{x^{n+1}}{m+1} \sum_{k=0}^{m} (-1)^k (m+1) m (m-1) \ldots (m-k+1) \frac{(\ln x)^{m-k}}{(n+1)^{k+1}}.$$

The calculated results are shown in fig.7. Coefficient of kinetic energy flow α is changed greatly at small Re and large Ψ. It is worth noting that coefficient α for laminar flow (Poiseulle velocity profile) is equal to 2, but with growth of Re and Ψ coefficient α tends to 1, not to 2, as one may suggest because of laminarization action of polymer additions.

Let's consider our typical case for the first measuring part:
$D = 2R = 2 \cdot 10^{-3}$ m, $U = 20$ m/s,
$x/D = 62.5 \div 125$, $\Psi_1 = 0.7$, $\Psi_2 = 0.6$, $\Psi = 0.5(\Psi_1 + \Psi_2) = 0.65$.
From Fig.8 we have $\alpha_1 = \alpha_{(\psi=0.7)} = 1.27$, $\alpha_2 = \alpha_{(\psi=0,6)} = 1.16$.
Using Blasius formula for water

$$\tau_0 = \frac{0.316}{8} (Re)^{-1/4} \rho U^2,$$

Eq.(2) is transformed into:

$$\Delta = \frac{2l}{R} \tau_0 \left[(1 - \Psi) + \frac{2 \cdot R}{0.3164 l} (Re)^{1/4} (\alpha_2 - \alpha_1) \right] \qquad (7)$$

After substitution our data in Eq.(7)

$$\Delta \cong \frac{2l}{R} \tau_0 (0.35 - 0.08).$$

We have that the contribution from a kinetic energy change to pressure drop is equal to 22.5% of friction one. Without this contribution drag reduction is 8% above the true value. If a decrease in hydrodynamic efficiency takes a place on a measuring part of a tube (in a cases of weak solution concentration or high flow velocity) the contribution from a kinetic energy change has opposite sign.

As we can see from an analysis Eq.(7), the influence of a kinetic energy flow change becomes significant in two cases:

- large drag reduction ($\Psi > 0.5$) when the first term in square brackets is decreased;

- velocity profile is strongly changed. Because velocity profile depends on local drag reduction, this influence is pronounced at the beginning tube part (Kulik, 1992).

Generally for correct measurement of friction stress it is necessary to measure not only pressure drop but the velocity profiles on the limits of the measuring tube part. In fig.6 corrected value of drag reduction is shown by the dark sings. Correction was made only for the first measuring tube part, because its value on the second section is significantly smaller. As indicated by these figures the correction reduces the slope angles for growth and loss of drag reduction. Finally the most interesting fact: the corrected drag reduction never exceed the ultimate value. This result widens the region of application of Virk' ultimate drag reduction low.

Neglect of a change of flow kinetic energy may be the reason why drag reduction exceeds the ultimate value (Beversdorff, 1993; Zakin et al.,1996). Unfortunately, in those papers drag reduction dynamics were not studied but from dependence of Ψ on Re it may be safely suggested that Ψ was strongly varied along a tube, consequently, a contribution not taken into account may be important. Ramu & Tullis (1976) obtained the pronounced change of drag-reducing efficiency on the initial part of canal was obtained. It is the fine illustration of necessity to correct obtained here extremely high value of drag reduction ($\Psi = 0.95$) and to reduce it.

In Toms' phenomenon papers the dependencies of hydrodynamics efficiency on different parameters (concentration, molecular weight, temperature, wall shear stress and so on) usually were given. For correct understanding of the obtained results it is necessary to take into account drag reduction change during the process of a flow, i.e. the strong dependence of results on location of a measuring tube part and on a method of measurement. On small diameter tubes the duration of pass of fixed liquid volume is measured. This method gives a mean value of drag reduction on the whole tube length

$$\psi_{measure} = \frac{1}{L}\int_0^L \psi(l)dl. \qquad (8)$$

It is clear that drag reduction defined by this method is less than maximum drag reduction and real dependencies of efficiency upon polymer properties and turbulent flow parameters will be connected in complicated manner.

Using tubes with bigger diameter one can measure local pressure drops on several distances from the tube inlet. However, to determine a drag reduction dynamics one must have very long tube with $L/D>10^3$ which involves reasonable difficulties. For example, if D = 5 sm a tube must be as long as 50 m. Usually experiments are carried out using shorter tubes and tested solution must be passed through a tube several times. Yet this method is not enough correct. At the first, a neglected dissipation of kinetic energy of the flow by small-scale addies takes a place after passing through a tube. It leads to additional destruction. At the second, in time intervals between the passes the supermolecular structures are formed in solution because of partial reversibility of drag reduction growth (Semenov et al.,1990). Fisher & Rodriguez (1971) confirmed nonequivalence of action of several passes to one pass through a tube with length divisible to number of passes was shown. If a setup has a closed circuit there are the same drawbacks: additional destruction of solution happens in a pump and a partially relaxation - in expanded sections of a tube.

Besides, the next important fact must be taken into account. The value of drag reduction is defined as

$$\Psi = (\tau_o - \tau_p)/\tau_o,$$

where τ_p and τ_o - the shear stresses for solution and water at the same Re value, in other words, at the same volume velocity of flow in constant diameter tube. However, drag reduction in pipe flow is customarily quantified by comparing friction coefficient values and the next formula is really use

$$\Psi = (\Delta P_o - \Delta P_p)/\Delta P_o,$$

where ΔP_p and ΔP_o - are pressure drops on the measuring part of a tube with and without polymer respectively.

Consequently for correct comparison of experimental results it is necessary to define the correct relationship between ΔP and τ.

Obtained results of drag-reducing efficiency during a flowing of polymer solutions somewhat modify the traditional understanding about Toms phenomenon action. Local drag reduction is changed along a tube and it is necessary to see the three stages of this process: growth, maximum and slope down, in other words to study the drag reduction dynamics. This dynamics should be taken into account for determination of various parameters influence (temperature, concentration, molecular weight, conditions of preparation and so on). It can add significant corrections to existing dependence.

In particular, it may be deduced that some part of tube exists where drag reduction is near the ultimate value for wide region of concentration and molecular weight of polymer. This ultimate drag reduction depends only on Re. Consequently, the concept of a "optimum" concentration should be only used in a narrow sense.

The problem of test of different polymer samples should be transformed too. Different marks may be described by angles of slope up, by persistence of maximum drag reduction and by intensity of slope down. A study of action methods on Toms phenomenon dynamics which make faster a drag reduction growth and prolong time of its maximum value is perspective.

Addition of low-molecular substance is one of methods of action on drag reduction dynamics. Initial stage is resumed again when flow restarts after stop. However if the solution is subjected to stress for a extended time, which includes the destruction, a resumption of growth stage is not shown practically. In our experiments near-ideal resumption of growth stage was obtained after one minute of rest. It seems likely that this time of recreation must be considerably shorter and be determined by time of conformation realignment of stretched macromolecules into the state of minimum potential energy.

Existence of growth stage explains the reason why polymer solutions in tube of large diameter have low efficiency. In tube with small diameter (D<5sm) all molecules are in zone of intensive turbulent interaction, because elastic sublayer may cover all sectional area of tube. With increase of tube diameter this sublayer takes up only small part of section. The convection mass transfer brings a "fresh" polymer additives into the zone responsible for drag reduction. These macromolecules have no time to pass through the growth stage and diffuse in the core of a flow. When these macromolecules will be again in near-wall area the drag reduction will increase beginning from low initial value. Almost the same takes place when polymer solution is injected into a boundary layer over moving body. But in this case macromolecules diffused out from boundary layer waste without results.

References

A.G. Fabula, "The Toms phenomenon in the turbulent flow of very dilute polymer solutions," Proc. 4th Internat. Congr. Rheol. 1963.

J.W. Hoyt, "The effect of additives on fluid friction," ASME J. Basic Eng. **94**, 258 (1972).

P.S. Virk, "Drag reduction fundamentals," AIChE J. **21**, 625 (1975).

N.S. Berman, "Drag reduction by polymers," An. Rev. Fluid Mech. **10**, 47 (1978).

R.H.J. Sellin, J.W. Hoyt and O. Scrivener," The effect of drag-reducing additives on fluid flows and their industrial applications," J. Hydraulic Research **20**, 29 (1982).

C. Balakrishnan and R.J. Gordon, "Influence of molecular conformation and intermolecular interactions on turbulent drag reduction," J. App. Polymer Science **19**, 909 (1975).

N.S. Berman, "Evidence for molecular interactions in drag reductions in turbulent pipe flow," Polymer Eng. and Science **20**, 451 (1980).

V.N. Kalashnikov and M.G. Tsiklauri, "Above-molecular structure of dilute solutions of high-molecular polymers exhibing decreased turbulent friction," J. Engineering Physics **58**, 49 (1990).

in *Recent Developments in Turbulence Management,* edited by K.-S. Choi (Kluwer Academic Publishers, 1991), pp. 309-321.

V.S. Belokon and V.N. Kalashnikov, "Hydrodynamics drag and degradation of dilute polymer solutions in turbulent rotating flow between the coaxial cylinders", *Preprint 91, Institute for Problems in Mechanics,* Moscow, 1977.

L.I. Sedov, V.A. Ioselevich, V.N. Pilipenko and N.G. Vasetskaya, "Turbulent diffusion and degradation of polymer molecules in a pipe and boundary layer," J. Fluid Mech. **94,** 561 (1979).

V.M. Kulik, "Dynamics of the Toms phenomenon effect in polyethylene oxide solution tube flow," J. of Engineering Physics **62**, 228 (1992).

H.-W. Beversdorff, "Turbulence structure of dilute polymer and surfactant solution in artificially roughness pipes," Appl. Sci. Research **50**, 347 (1993).

J.L. Zakin, J. Myska and Z. Chara, "New limiting drag reduction and velocity profile asymptotes for Nonpolymeric additives systems," AIChE J. **42**, 3544 (1996). K.L.V. Ramu and J.P. Tullis, "Drag reduction and velocity distribution in developing pipe flow," J. Hydronautics **10**, 55 (1976).

B.N. Semenov, A.I. Amirov, V.M. Kulik and O.N. Marennikova, "Effect of supermolecular structures in PEO-solutions on drag reduction," Archiv Mech. **42**, 639 (1990).

D.H. Fisher and F. Rodriguez, "Degradation of drag-reducing polymers," J. Appl. Polym. Sci. **15**, 2975 (1971).

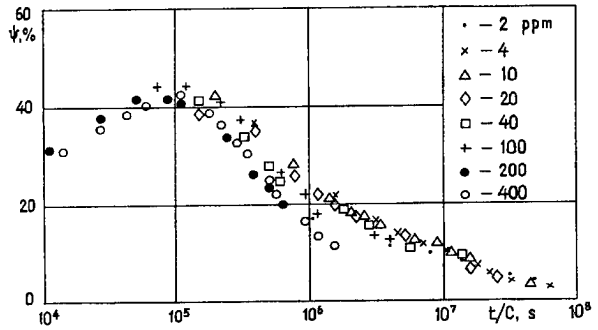

Fig.1. Drag reduction by WSR-301 versus of the interaction time.

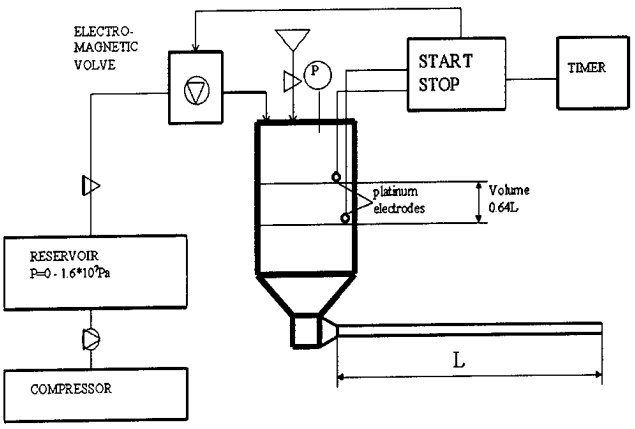

Fig.2. Scheme of setup.

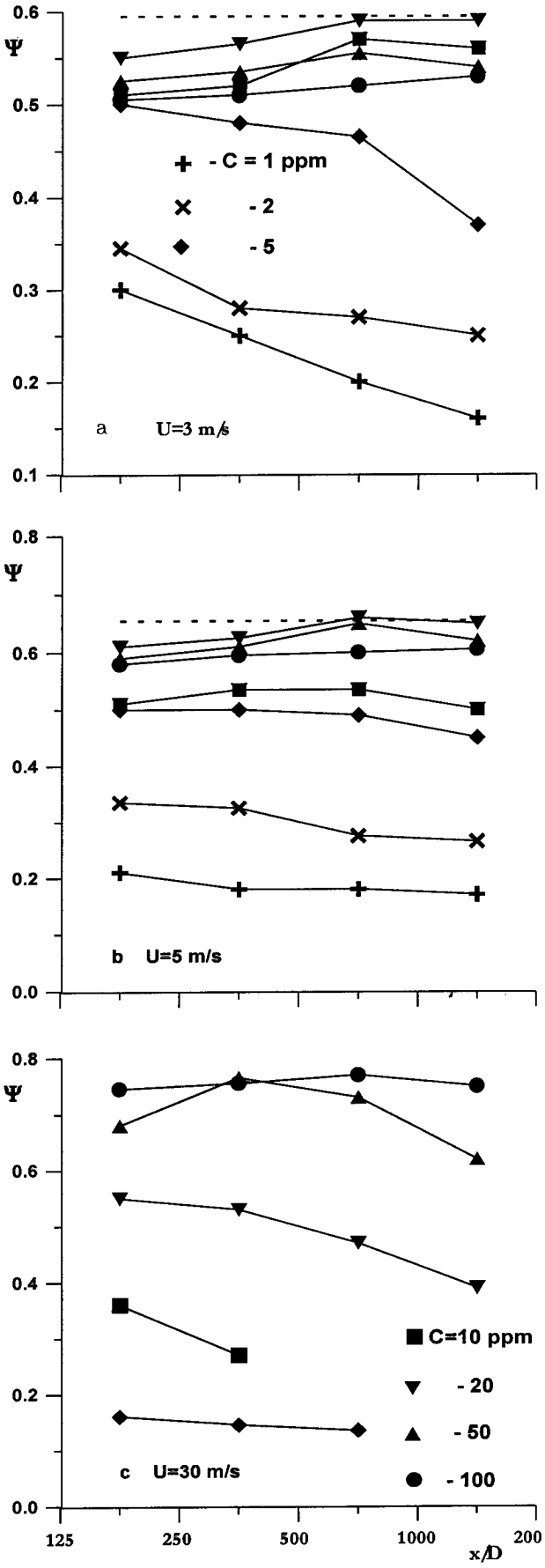

Fig.3. Drag reduction change along the tube.

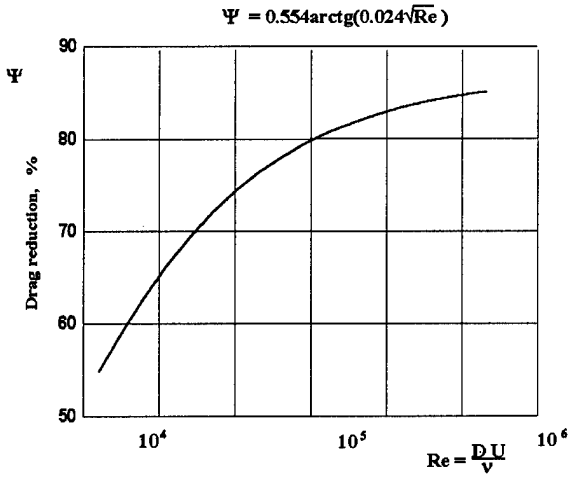

Fig. 4. Dependence of ultimate DR on Reynolds number

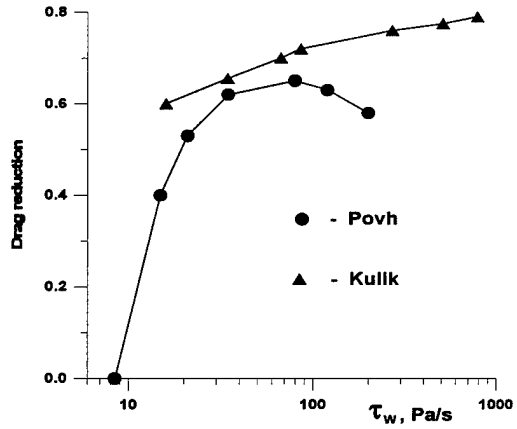

Fig.6. Dependence of ultimate DR on shear stress

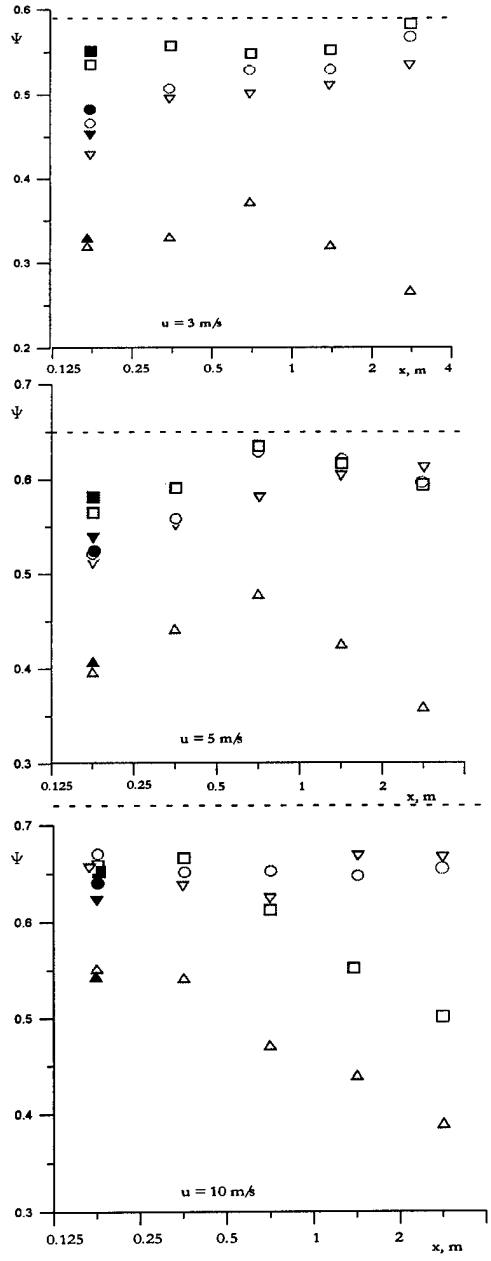

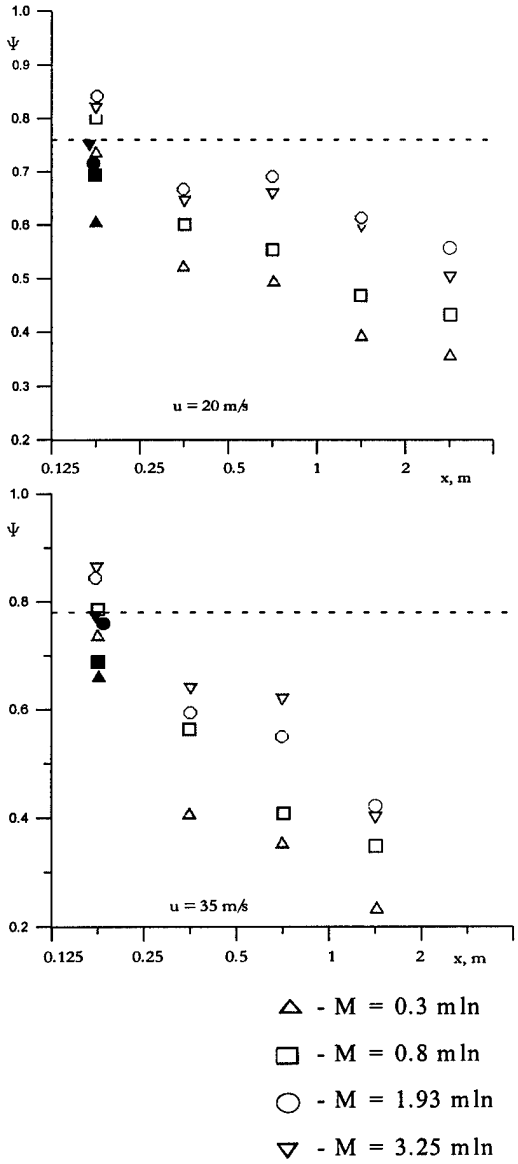

Fig.6. Drag reduction change along the tube

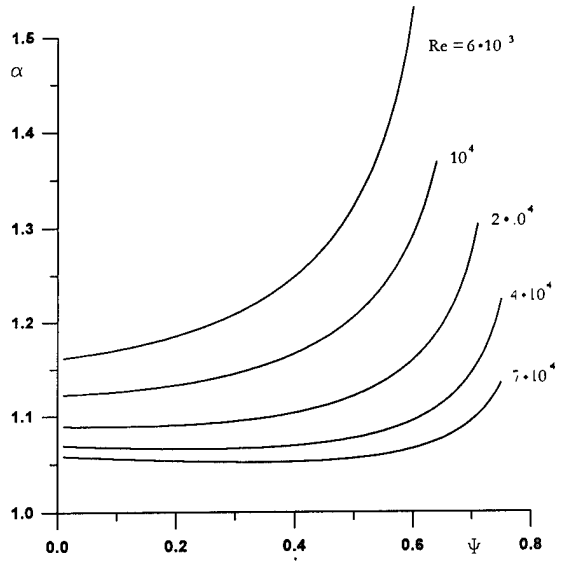

Fig.7. Dependence of kinetic energy coefficient on drag reduction

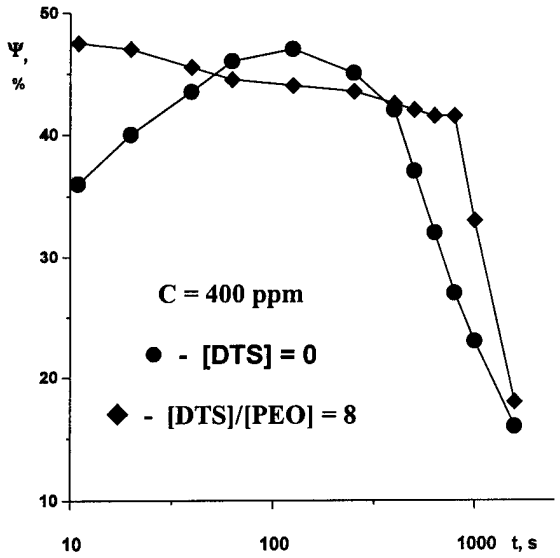

Fig.8. Drag reduction dynamics with addition of low-molecular substance

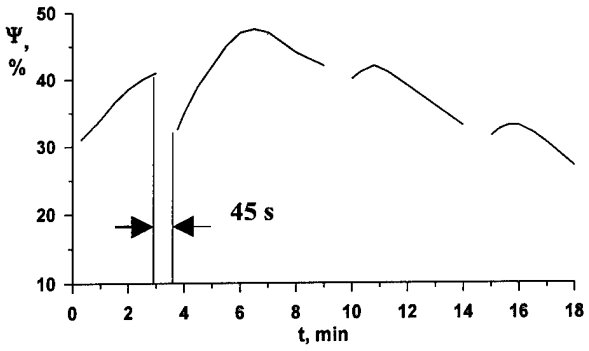

Fig.9. Resumed again of initial stage when flow restart after stop

ON THE HYDRODYNAMICAL SMOOTHNESS IN POLYMER SOLUTIONS

Walter B. Amfilokhiev
Saint-Petersburg State Marine Technical University
Department of Hydromechanics
190008 Lotsmanskaya street, 3,
Saint-Petersburg, Russia

Kirill M. Mazaev
Saint-Petersburg State Marine Technical University
Department of Hydromechanics
190008 Lotsmanskaya street, 3,
Saint-Petersburg, Russia

Abstract - As it is known, at small heights of hills of rough surface it appears hydrodynamically smooth because hills are wholly shipped in viscous sublayer and do not render any influence on to friction resistance. In dilute polymer solutions viscous sublayer and the buffer zone is significant thicker than in pure solvent. Thus, surfaces, which were rough in water, in a polymer solution can appear hydrodynamically smooth. On the basis of a developed numerical research of an internal and external problem about hydrodynamic smoothness of a rough surface it is shown that hydrodynamic smothness depends on a type of polymer, concentration of solution, kind of roughness and its size and Reynolds number.

One of active (i.e. connected with expenses of energy or substance) ways of viscous drag reduction is use of the polymer additives. It is established at present that the additives of many natural and synthetic polymers have property to reduce friction resistance of turbulent flows essentially (up to five times) at extremely low concentrations, thousandths or even ten-thousandths of percent. In this method the question on interaction of polymer with a rough surface is especially important for practice. The importance grows if one takes into consideration that the majority of experiments with rough surfaces (including classical experiments by Nikuradse with rough pipes) were carried out with artificial ("grainy" or "sandy") roughness, the influence of which to a flow differs from influence of technical one strongly.

I. ACCOUNT OF POLYMERS INFLUENCE

The fact is experimentally established, that on some distance from a wet surface the undimensional near-wall average velocity profile in a polymer solution can be expressed with the universal logarithmic law of a wall:

$$\varphi = \frac{1}{\kappa} ln\,\eta + B, \qquad (1)$$

where $\varphi=u/u_\tau$, $u=u(y)$ - dimensional longitudinal velocity, $u_\tau=\sqrt{\tau_w/\rho}$ - shear velocity, τ_w - shear stress on a wall, κ=0,4 - the first constant of a turbulence, $\eta=u_\tau y/\nu$ - normal to a wall undimensional dynamic coordinate, y - appropriate dimensional coordinate, ρ and ν - density and kinematic viscosity of a liquid, B - function of polymer influence, which must pass in the second constant of a turbulence (for a smooth surface) in case of a Newtonian liquid flow,i.e. in the flow of pure solvent - water. The formula that was offered in [1] is in accordance with

$$B = B_0 + \sqrt{2}\left[40\,lg\left(\frac{A}{A_0}+4\right) - 28\right], \qquad (2)$$

where B_0=5,2 - second constant of a turbulence, A_0=26 - constant by Van-Drist (the numerical meanings of A_0 and B_0 are not independed, they correspond each other [2]), $A=A_0/\alpha$ - parameter, similar to a constant, but taking into account polymer effect. It gives the appropriate meaning of B for (1). Taking into account the connection between A and A_0, it is possible to present formula (2) as

$$B = 24.6\,ln\left(\frac{1}{\alpha}+4\right) - 34.4\,. \qquad (3)$$

The quantity α can be connected with the turbulent relaxation time Θ [3,4]:

$$\alpha = \frac{1}{A_0}\sqrt{\sqrt{A_0^4 + 4\beta_\Theta^2} - 2\beta_\Theta}\,, \qquad (4)$$

$$\alpha_{min} \le \alpha \le 1,\ \beta_\Theta = \frac{u_\tau^2 \Theta}{\nu}, \qquad (5)$$

where Θ depends on properties of polymer and concentration of solution.

The function of polymer influence B (3) is formally similar to well known roughness function [2] with that difference, that, being included in the universal logarithmic law (1), it lifts the line $\varphi(\eta)$ concerning the law for a Newtonian liquid at a smooth wall

$$\varphi = \frac{1}{\kappa} ln\,\eta + B_0, \qquad (6)$$

while the influence of a roughness lowers the line (1) comparative to (6). Then the roughness function can be present in the form, similar (3):

$$B = 24{,}6\,ln\left(\alpha_r + 4\right) - 34{,}4, \qquad (7)$$

where $\alpha_r \le 1$ - parameter, taking into account influence of a roughness. The function of joint roughness and polymers influence takes the form

$$B = 24{,}6\,ln\left(\frac{\alpha_r}{\alpha}+4\right) - 34{,}4, \qquad (8)$$

where α looks like (4), and α_r can be obtained by comparison (7) with any known roughness function.

II. ACCOUNT OF ROUGHNESS INFLUENCE

The roughness function [5] that corresponds to the half-empirical theory of turbulence by Millionshchikov [6] is used in the numerical method. This theory is one of few ones in which the roughness is characterized with not one but two geometrical parameters: average hills height of roughness (mathematical expectation) k and root-mean-square deviation (root square of dispersion):σ -

$$k = \frac{1}{l}\int_0^l y_k\,dx, \quad \sigma^2 = \frac{1}{l}\int_0^l (y_k - k)^2\,dx, \qquad (9)$$

where $y_k(x)$ - curve of surface profilogram, l - length of a profilogram. Such description of a roughness allows to calculated (without using an additional empirical data) rather wide class of rough surfaces. So, the small value of the ratio σ/k corresponds to a uniform roughness (in [6] it is shown, that at $\sigma/k \approx 0{,}2$ ...0,3 Nikuradse experiments are well described), the growth of $\sigma/k \approx$ correspondsto increase of roughness ununiformity (for ship surfaces $\sigma/k \approx 1{,}1 \ldots 1{,}4$).

In the Millionshchikov's theory the principle of a superposition of three parts of total viscosity is postulated for near-wall layer with constant shear stress near a rough surface. This parts are molecular and two turbulent ones. The first of the callers, as usual, is connected with distance from a wall, and the second depends on a size of hills of roughness, leaning out of a viscous sublayer:

$$\nu_{\Sigma} = \nu + \kappa u_{\tau}(y - \delta_0) + \kappa u_{\tau}(k^* - \delta_0), \tag{10}$$

where δ_0 - thickness of a sublayer, outside of which turbulence has place, k^* - meanprobabilitstic height of hills, leaning out of a this sublayer. The equation

$$\tau = \rho \nu_{\Sigma} \frac{du}{dy} = const = \tau_w \tag{11}$$

after integration gives

$$\varphi = \frac{u}{u_{\tau}} = \begin{cases} \eta, \quad 0 \le \eta \le \beta_0 = \delta_0 u_{\tau} / \nu, \\ \dfrac{1}{\kappa} ln \dfrac{1 + \kappa(\eta - \beta_0) + \kappa(\eta_k^* - \beta_0)}{1 + \kappa(\eta_k^* - \beta_0)} + \beta_0, \quad \eta > \beta_0, \end{cases} \tag{12}$$

where $\eta_k^* = k^* u_{\tau}/\nu$, and at $\eta_k^* \le \beta_0$ a hydrodynamical smooth regime takes place ($\eta_k^* - \beta_0 = 0$) and

$$\varphi = \frac{1}{\kappa} ln[1 + \kappa(\eta - \beta_0)] + \beta_0. \tag{13}$$

The last formula allows to find numerical meaning β_0, since at large η it passes in the universal logarithmic law of a wall

$$\varphi = \frac{1}{\kappa} ln\eta + \frac{1}{\kappa} ln\kappa + \beta_0 \tag{14}$$

Since $B_0 = 5{,}2$ and $\kappa = 0{,}4$, it is obvious that $\beta_0 = B_0 - \frac{1}{\kappa} ln\kappa = 7{,}5$.

At rather large η it is possible to obtain [5] from (12):

$$\varphi = \frac{1}{\kappa} ln\,\eta + \frac{1}{\kappa} ln\,\kappa + \beta_0 - \frac{1}{\kappa} ln[1 + \kappa(\eta_k^* - \beta_0)], \tag{15}$$

i.e. the profile in the form (1), where

$$\left.\begin{aligned} B &= B_0 + \Delta B, \quad B_0 = \frac{1}{\kappa} ln\,\kappa + \beta_0 = 5{,}2, \\ \Delta B &= -\frac{1}{\kappa} ln[1 + \kappa(\eta_k^* - \beta_0)] \end{aligned}\right\} \tag{16}$$

Meanprobabilistic height of hills, leaning out of a sublayer δ_0, is found with help of a probability density p:

$$k^* = \frac{\int_{\delta_0}^{\infty} p y_k dy_k}{\int_{\delta_0}^{\infty} p dy_k}, \tag{17}$$

If to consider, that the distribution of hills heights y_k submits to the normal law, then

$$k^* = k\left(1 + \frac{\sigma}{k}\sqrt{\frac{2}{\pi}q}\right), \tag{18}$$

where

$$\left.\begin{aligned} q &= [(1 - \mathrm{erf}h)\exp(h^2)]^{-1}, \\ h &= \frac{\delta_0 - k}{\sigma\sqrt{2}} = \frac{\beta_0 - \eta_k}{\frac{\sigma}{k}\eta_k\sqrt{2}}, \quad \eta_k = \frac{u_{\tau} k}{\nu} \\ \eta_k^* &= \eta_k\left(1 + \frac{\sigma}{k}\sqrt{\frac{2}{\pi}q}\right). \end{aligned}\right\} \tag{19}$$

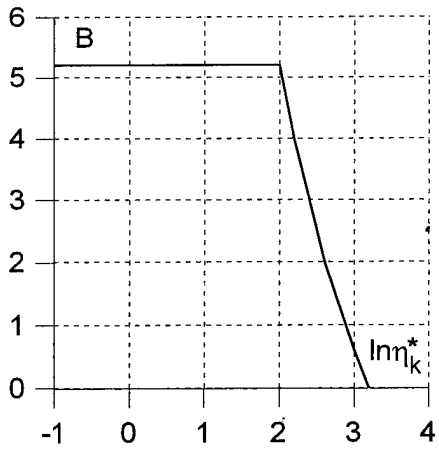

Fig. 1. The universal roughness function.

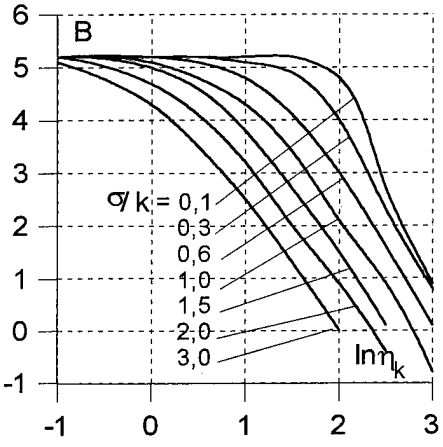

Fig. 2. The family of roughness functions.

In result the universal form of the expression of roughness function $B(\eta_k^*)$, that is in accordance with eq. (16) (fig. 1), can be developped into the family of functions $B(\eta_k)$ (fig. 2), and curves of this family will be different depend on value of parameter of non-uniformity σ/k:

$$B = B_0 - \frac{1}{\kappa} ln[1 + \kappa[\eta_k \left(1 + \frac{\sigma}{k}\sqrt{\frac{2}{\pi}q}\right) - \beta_0]]. \qquad (20)$$

For the proof of admissibility of roughness function (16) boundary layers of plates with a regular roughness [5] and rotating disks with a technological roughness [7] were calculated. In both cases it occurs that the calculated results were in good accordance with the experimental ones.

III. JOINT INFLUENCE OF POLYMERS AND ROUGHNESS

In the case of polymer solution flow at a rough surface it is necessary to replace the roughness function (7) by function of joint polymers and roughness influence (8). Firstly it is necessar to obtain a formula for α_r. It is possible by comparing of roughness functions in the forms (7) and (16):

$$\alpha_r = exp\left(1.61 + \frac{\Delta B_r}{24.6}\right) - 4, \qquad (21)$$

secondly, one has to take into account a thickening of a viscous sublayer according to polymer effect for that to present function ΔB, appearing in (16), as

$$\Delta B_r = \begin{cases} -\kappa^{-1} ln[1 + \kappa(\eta_k^* - \beta)], & \eta_k^* > \beta \\ 0, & \eta_k^* \le \beta. \end{cases} \qquad (22)$$

Here β - undimensional sublayer thickness in a flow of a solution. For its definition it is possible to take into account that the formulas (16) and (22) have the same form, but with β instead of β_0. In result instead of (15) it is received:

$$\varphi = \frac{1}{\kappa} ln\,\eta + \frac{1}{\kappa} ln\,\kappa + \beta - \frac{1}{\kappa} ln[1 + \kappa(\eta_k^* - \beta)]. . \qquad (23)$$

In the case of a smooth surface the last formula turns in

$$\varphi = \frac{1}{\kappa} ln\,\eta + \frac{1}{\kappa} ln\,\kappa + \beta \qquad (24)$$

and it has to coincide with an expression (1) provided that B is the function of polymer influence on a smooth surface, i.e. is determined by expression (3):

$$24{,}6 ln(\frac{1}{\alpha} + 4) - 34{,}4 = \frac{1}{\kappa} ln\kappa + \beta. \qquad (25)$$

In result

$$\beta = 24{,}6\, ln\left(\frac{1}{\alpha} + 4\right) - 32{,}1, \qquad (26)$$

that gives $\beta \approx 7{,}5 = \beta_0$ when $\alpha = 1$.

The second limit for β can be obtained from an asymptote [8], which corresponds to the maximum drag reduction at $Ru_\tau/\nu > 100$ [3], where R - radius of a pipe or boundary layer thickness, -

$$\varphi = \frac{1}{\kappa} ln\,\eta + 32. \qquad (27)$$

Comparison (27) with (24) gives $\beta_{max} = 41{,}3$, then from (26) one can get $\alpha_{min} = 0{,}092$.

The shape of of universal functions of joint polymers and roughness influence $B(\eta_k^*)$ (the formula (8) with the account (4), (21) and (22) and with a simplify hypothesis $\beta = \beta_0/\alpha$) at several meanings $\alpha = const$ is shown in fig. 3. At transition to usual coordinates $B(\eta_k)$ each of these curves gives family of functions differed one from the other by meaning of σ/k, as it was visible in fig. 1 and fig. 2 for usual roughness in water. The minimum meaning $\alpha \approx 0{,}1$ corresponds to a case of limiting drag reduction, meaning $\alpha = 1$ - to a case of water flow. In fig. 3. it is visible, that the formally constructed curves $B(\eta_k^*)$ at $\alpha < 1$ cross usual roughness function $B_r = B(\eta_k^*)\big|_{\alpha=1}$, leaving in area of smaller numerical meanings. However, resistance in a solution should be less, than in water, or - in an extreme case of a square-law regime - the same. Therefore the functions of joint influence (8) should use only so long as their meanings are more, than meaning B_r at the same η_k^*. The coordinates of crossing points $B(\eta_k^*)$ and B_r correspond to approximate dependence

$$\eta_{k0}^* = exp\left(3.39 + \frac{0{,}147}{\alpha}\right). \qquad (28)$$

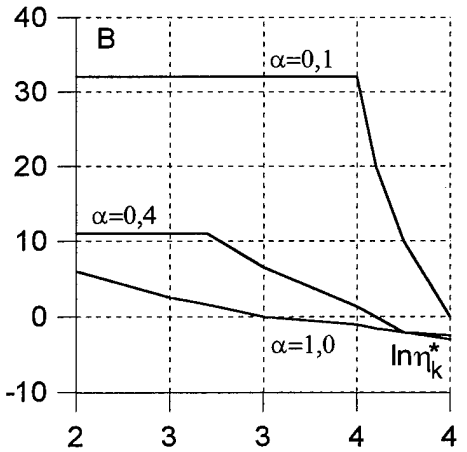

Fig. 3. Functions of joint polymers and roughness influence.

IV. HYDRODYNAMIC SMOOTHNESS IN WATER.

As it was shown above, the roughness function B for water can be represented as (16). Thus the condition of a hydrodynamic smoothness can be written down so:

$$\eta_k^* \le \beta_0 = 7{,}5, \tag{29}$$

where η_k^* is defined with the formulas (19). Reynolds number on roughness hills height can be presented as η_k

$$\eta_k = \sqrt{\frac{\lambda}{8}} \cdot \bar{k} \cdot Re, \tag{30}$$

where λ - hydraulic factor of friction, $\bar{k} = k / d$, $Re=Vd/\nu$, V - mean (bulk) velocity, $d=2R$ - pipe diameter. Thus, the meaning of permissible roughness hills height $\bar{k}_{pos}$ depends on Re and parameter of non-uniformity σ/k. Using the Coles profile for a smooth pipe with $\Pi=0{,}1$

$$\frac{u}{u_\tau} = \frac{1}{\kappa} ln \frac{u_\tau y}{\nu} + B_0 + \frac{\Pi}{\kappa}(6\bar{y}^2 - 4\bar{y}^3). \tag{31}$$

and integrating it pie cross section, it is possible to find the resistance law as

$$\frac{V}{u_\tau} = \frac{1}{\kappa} ln\left(\frac{u_\tau}{V}\frac{2RV}{2\nu}\right) + B_0 - \frac{3}{2\kappa} + 0{,}15 \tag{32}$$

or, in an undimensional form, -

$$\sqrt{\frac{8}{\lambda}} = \frac{1}{\kappa} ln\left(\frac{Re}{2}\sqrt{\frac{8}{\lambda}}\right) + 1{,}6. \tag{33}$$

Then from (29), (19) and (30) follows

$$\sqrt{\frac{\lambda}{8}} \cdot \bar{k}_{pos} \cdot Re\left(1 + \frac{\sigma}{k}\sqrt{\frac{2}{\pi}} \cdot q(h)\right) = 7{,}5. \tag{34}$$

From the equations (33) and (34) connection $\bar{k}_{pos}$ with Re can be found. Results of accounts for pipes (the internal problem) are shown in fig. 4.

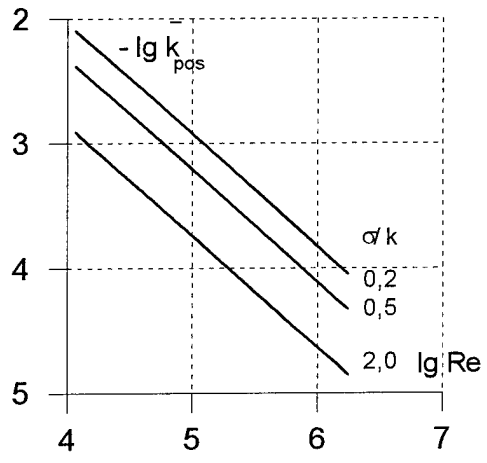

Fig. 4. Dependence of permissible roughness from Reynolds number for water in pipes

Dependences of permissible roughness hills height from Re in logarithmic scale represent practically parallel straight lines. Influence of a parameter of roughness non-uniformity σ/k can be seen clearly: with increase of this parameter with 0,2 ("grain" roughness) up to 2,0 (the technical roughness) permissible roughness hills height decreases.

An external problem can be solved analogously. For this purpose a boundary layer should be predicted, the size $d/2=R$ is replaced with boundary layer thickness δ; instead of V it is possible to use velocity u_0 on outer border of a boundary layer, and $\sqrt{\lambda / 8}$ can be replaced with $\sqrt{c_f / 2}$, where

$$c_f = 2\tau_w / (\rho u_0^2)$$

is local friction factor. Then the formulas similar to (33) and (34) will define a local hydrodynamic smoothness. However, in practice a general hydrodynamic smoothness has the greater interest. It connects with full friction resistance coefficient

$$C_F = \int_0^1 c_f d\bar{x},$$

where $\bar{x} = x/L$, x - longitudinal coordinate in a boundary layer, L - length of a body. In this case the hydrodynamic smoothness has not so much physical, how many quantitative sense, as along a wetted surface, on different parts of it, in accordance with growth of a boundary layer, there will be all three regimes of roughness display (square-law, transitive and hydrodynamically smooth). By setting acceptable accuracy of account (e.g. 0,5 %), the regime of a general hydrodynamic smoothness can be found for definite σ/k and $\bar{k} = k / L$ in result of calculation of a curve $C_F(Re)$ via a point of its deviation from the curve C_F for a smooth surface. Such calculations were produced in [9] for flat plates. In result connection between $\bar{k}_{pos}$ and Re was determined and it can be seen in fig. 5. It is interesting (but natural), that at σ/k=0,2 the line $\bar{k}_{pos}$ (Re) does not practically differ from one in [10], where it was obtained with the help of recalculation of results of Nikuradse experiments in pipes to flat plates (i.e. the line in [10] is in connection with uniform sand-grain roughness).

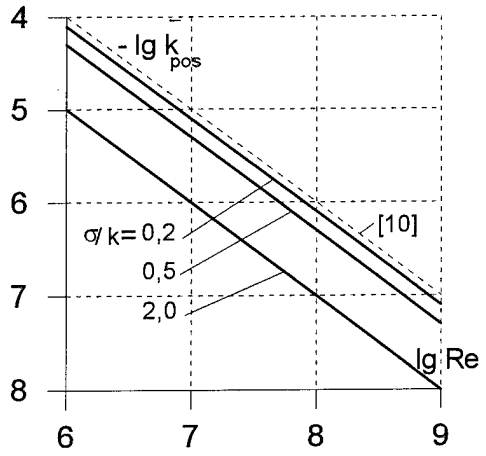

Fig. 5. Dependence of flat plate permissible roughness from Re for water.

V. HYDRODYNAMIC SMOOTHNESS IN POLYMER SOLUTION

The polymer solution flow near a rough wall is determined by a condition as (29) with replacement β_0 on β in accordance with the formula (26):

$$\eta_k^* \le \beta = 24.6\, ln\left(\frac{1}{\alpha} + 4\right) - 32.1 \qquad (35)$$

where η_k^* is defined as (19).

In result the equation placed below will be an analogue of the formula (30)

$$\sqrt{\frac{\lambda}{8}} \cdot \bar{k}_{pos} \cdot Re\left(1 + \frac{\sigma}{k}\sqrt{\frac{2}{\pi}} \cdot q(h)\right) = 24{,}6\, ln\left(\frac{1}{\alpha} + 4\right) - 32{,}1. \qquad (36)$$

From here it is visible, that the function $\bar{k}_{pos}(Re)$ turns out different for different α. The resistance law (in a pipe) still corresponds to Coles profile (31) with B instead B_0 and can be written down as

$$\frac{V}{u_\tau} = \sqrt{\frac{\lambda}{8}} = \frac{1}{\kappa} ln\left(\frac{Re}{2}\sqrt{\frac{\lambda}{8}}\right) + B - \frac{3}{2\kappa} + 0{,}15 \qquad (37)$$

where B - function of polymer influence for a smooth surface, i.e. (3).

Using (36) and (37) one can get dependence $\bar{k}_{pos}(Re)$ for any given meanings α and σ/k. Such results are obtained for pipes (fig. 6) and can be compared with a similar picture, found earlier (fig. 4) for a pure solvent.

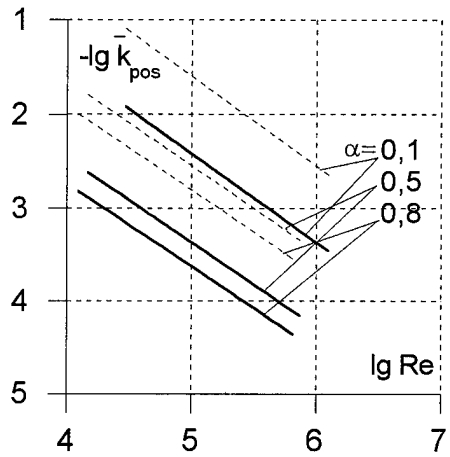

Fig. 6. Dependence of permissible roughness from *Re* for polymer solution in pipes (----σ/k=0,2, —σ/k=2,0).

CONCLUSION

The convenient characteristic of a hydrodynamic smoothness is dependences $\bar{k}_{pos}(Re)$. They turn out different depending on meanings σ/k (characteristics of the roughness form) and α (characteristics of polymer efficiency dependent from its kind and molecular weight and from concentration of a solution [4,7]). As all dependences in logarithmic coordinates are close to linear, it is possible to establish influence of parameter α on meaning $\bar{k}_{pos}$ at any *Re*:

$$lg\,\bar{k}_{pos}\big|_{\alpha\neq 0} \Big/ lg\,\bar{k}_{pos}\big|_{\alpha=0} = -0{,}592\alpha^2 + 1{,}113\alpha + 0{,}452 \qquad (38)$$

This relation depends on σ/k also.

REFERENCES

1. Амфилохиев В.Б., Дробленков В.В. Использование математических моделей полимерного эффекта при расчете пограничного слоя интегральным и конечно-разностным методами, *Труды ЛКИ, 1986, вып. "Математическое моделирование и автоматизированные системы в судостроении"*, с.53-60.
2. Федяевский К.К., Гиневский А.С., Колесников А.В. Расчет турбулентного пограничного слоя несжимаемой жидкости, - *Л.: Судостроение,* 1973, 256 с.
3. Mizushina T., Usui H., Yoshida T. Tyrbulent pipe flow of dilute polymer solutions, *J.Chem.Eng. of Japan*, 1974, v.7, No.3, p.162-167.
4. Ходорковский Я.С. Турбулентное пристенное движение упруговязкой жидкости, *Инженерно-физический журнал*, 1976, т.30, №1, с.110-114.
5. Амфилохиев В.Б., Мазаева Н.П. Двухпараметрическая схема учета шероховатости в расчетах пограничного слоя, *Труды ЛКИ, вып."Ходкость и мореходные качества судов"*, 1982, с.3-12.
6. Миллионщиков М.Д. Турбулентные течения в пристеночном слое и в трубах, *Атомная энергия,* 1970, т.28, вып.3, с.207-220.
7. Амфилохиев В.Б., Мазаева Н.П. Вращение шероховатого диска в неньютоновской жидкости, *Труды ЛКИ, 1987, вып."Мореходность и стабилизация технических средств освоения океана"*, с.30-36.
8. Seyer F.A., Metzner A.B. Turbulence phenomena un drag reducing systems, *AIChE Journal*, 1969, v.15, No.3, p.426-434.
9. Амфилохиев В.Б., Мазаева Н.П. Расчет гидродинамического трения поверхностей с реальной шероховатостью, *Материалы по обмену опытом НТО им. акад. А.Н.Крылова, вып. 400 "Совершенствование ходовых, мореходных и маневренных качеств судов"*, с.4-15.
10. Шлихтинг Г. Теория пограничного слоя, *М.: Наука,* 1974, 712 с.

Turbulent Drag Reduction Methods: Microbubble

EXPERIMENTAL EVIDENCE FOR A LINK BETWEEN MICROBUBBLE DRAG REDUCTION PHENOMENA AND PERIODICALLY EXCITED WALL-BOUNDED TURBULENT FLOW

Madan Mohan Guin
Department of Mechanical Engineering
The Johns Hopkins University
122 Latrobe Hall / 3400 N. Charles St.
Baltimore, Maryland 21218, USA
guin@titan.me.jhu.edu

Hiroharu Kato
Department of Naval Architecture & Ocean Engineering
The University of Tokyo
7-3-1 Hongo, Bunkyo-ku
Tokyo 113 JAPAN
kato@fluidlab.naoe.t.u-tokyo.ac.jp

Yoshiaki Takahashi
Technology Development Department
Shipbuilding and Offshore
IHI Ltd.
1-1, Toyosu 2-chome, Koto-ku
Tokyo 135, JAPAN
yoshiaki_takahashi_1@ihi.co.jp

[1]*Abstract* - Better collapse of microbubble drag reduction data is obtained against the near-wall bubble concentration α_w than against the cross-section average value α_m in a turbulent channel flow. This is primarily because, α_w includes most of the bubbles participating in the drag reduction process, compatible with a general view that the phenomena are inner-region-dependent. When combined with bubble diameter and flow velocity, the near-wall concentration yields a bubble passing frequency ω_b. Accordingly, bubbles are pictured as discrete bodies passing by a fixed point at the wall at the local velocity. The channel results show good scaling with this frequency normalized by the inner variables ω_b^+. Under some reasonable assumptions, similar scaling is shown to hold good with the well known hot-film results of Madavan, Deutsch, and Merkle [J. Fluid Mech. **156**, 237 (1985)]. In either case, poor collapse occurs with ω_b normalized by the outer variables. Based on the new scaling, it is proposed that the basic physical mechanism of microbubble drag reduction may possibly be a special case of wall-bounded turbulent flow where the near-wall region is subjected to periodic high frequency excitations by the passing bubbles at an idealized frequency ω_b.

I. INTRODUCTION

Skin friction reduction in a turbulent boundary layer by the introduction of small gas bubbles into the flow has been the subject of several recent investigations. Laboratory studies in various test configurations, injection methods and flow conditions have confirmed this phenomenon (e.g. 1-18). The skin friction in a microbubble-modified boundary layer is found to be even 80 % less than the undisturbed value under suitable conditions. An excellent review on the subject including many references can be found in Merkle and Deutsch (11). Considering the possibility of such high magnitude, attempts are currently being made in applying this method in reducing the viscous drag of ships and underwater vehicles. However, to the best of the authors' knowledge, sufficient progress has not yet been made in this direction.

A clear understanding of the physical mechanism of this drag reduction method is necessary in order that the method can be effectively applied to practical ship boundary layers. Although, the process is argued to be due to increase of effective viscosity in the wall region due to the presence of small bubbles (5,19-21), other possibilities cannot be entirely ruled out. A main purpose of this paper is to provide evidence for a possible mechanism in which skin friction reduction might occur due to excitation of the near-wall region by the passing bubbles. This is based on a new scaling parameter involving bubble passing frequency ω_b normalized by the inner variables. These results are an outcome of experiments carried out in a two-dimensional water channel reported in detail in Ref. 16 and 17.

II. DEPENDENCE ON NEAR-WALL BUBBLE CONCENTRATION α_w

The experiments referred to above were conducted in a horizontal water channel specially built for this purpose at the University of Tokyo. The channel had a width 2δ of 10 mm and span b of 100 mm with the smaller dimension in the vertical direction (Fig. 1). The Reynolds number based on channel height and mean velocity varied from 50 to 90 x 10^3 at nominal temperature of 25^0C. A pair of sintered plastic porous plates mounted flush with the top and bottom walls could create small air bubbles when dry compressed air was blown through them. The location of these plates was 61 channel heights downstream of a smoothly matching inlet after a settling chamber and contraction. The wall friction was measured with a floating-element transducer with a 5 mm circular sensing disk mounted on the top wall located 67 channel heights downstream of the injection plates. Bubble diameter was determined by still photographs taken through the transparent acrylic top wall. The resolution was sufficient to measure the mean bubble diameter to a reasonable accuracy by projecting the photographic negative against a film analyzer equipped with digital cross-wire position indicators.

The ratio between the skin friction coefficients C_f with air and C_{fo} without air based on pure-water density was found at comparable bulk velocity U_m. Use of pure-water density in the definition of C_f is justified by the existence of a bubble-free region, albeit of the order of the viscous sublayer thickness next to the wall (6,10,11) with the liquid as the medium of momentum exchange with the wall. Absence of bubble impingement against the wall has been verified with the hot-film signals used for shear measurements in Madavan, Deutsch and Merkle (MDM2, Ref. 4) and Ref. 11.

Bubble concentration profiles at the shear measurement location were obtained using a sampling probe with a flattened mouth facing the flow traversing in the wall-normal direction (Fig. 2). Typical profiles are given in Fig. 3 showing the ratio of local concentration α to the cross-sectional average value $\alpha_m = Q_a/(Q_a+2U_{mw}b\delta)$, where Q_a is the volumetric injection rate of air and U_{mw} is the bulk velocity of water. These profiles clearly show a dependence on the flow velocity, injection orientation with respect to gravity, and air quantity. A near-wall bubble concentration α_w was obtained from such profiles by averaging within a wall-normal distance of 1 mm from the top wall.

The C_f/C_{fo} values are plotted in Fig. 4(a) against the cross-sectional average bubble concentration α_m. As in water-tunnel boundary layers (e.g. MDM2), the skin friction reduction is found to generally increase with α_m within the range of these experiments. However, the data points do not collapse well, notably the points corresponding to the cases with air-injection from the porous plate located at the bottom wall are quite apart from those corresponding to the opposite cases. This behavior may initially appear to be due to α_m lacking the information of detailed bubble distribution patterns in the flow. At the same time, however, in Fig. 4(b), the C_f/C_{fo} values collapse reasonably well against the near-wall concentration α_w which also seems to bear no systematic relation with the detailed distribution

[1] This work was carried out during the first author MMG's graduate studies at the University of Tokyo, Japan

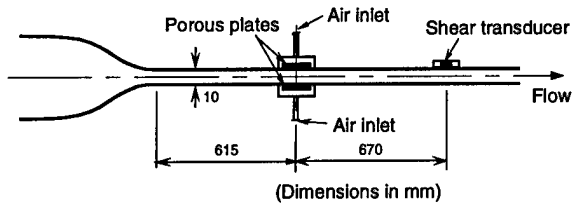

Figure 1. Schematic diagram of the channel in elevation

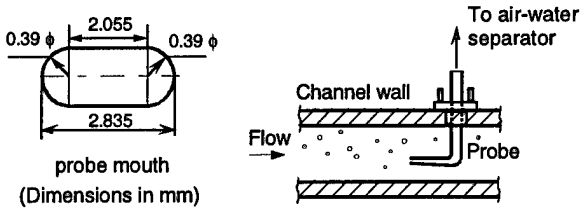

Figure 2. The sampling-type probe for measurement of local bubble concentration.

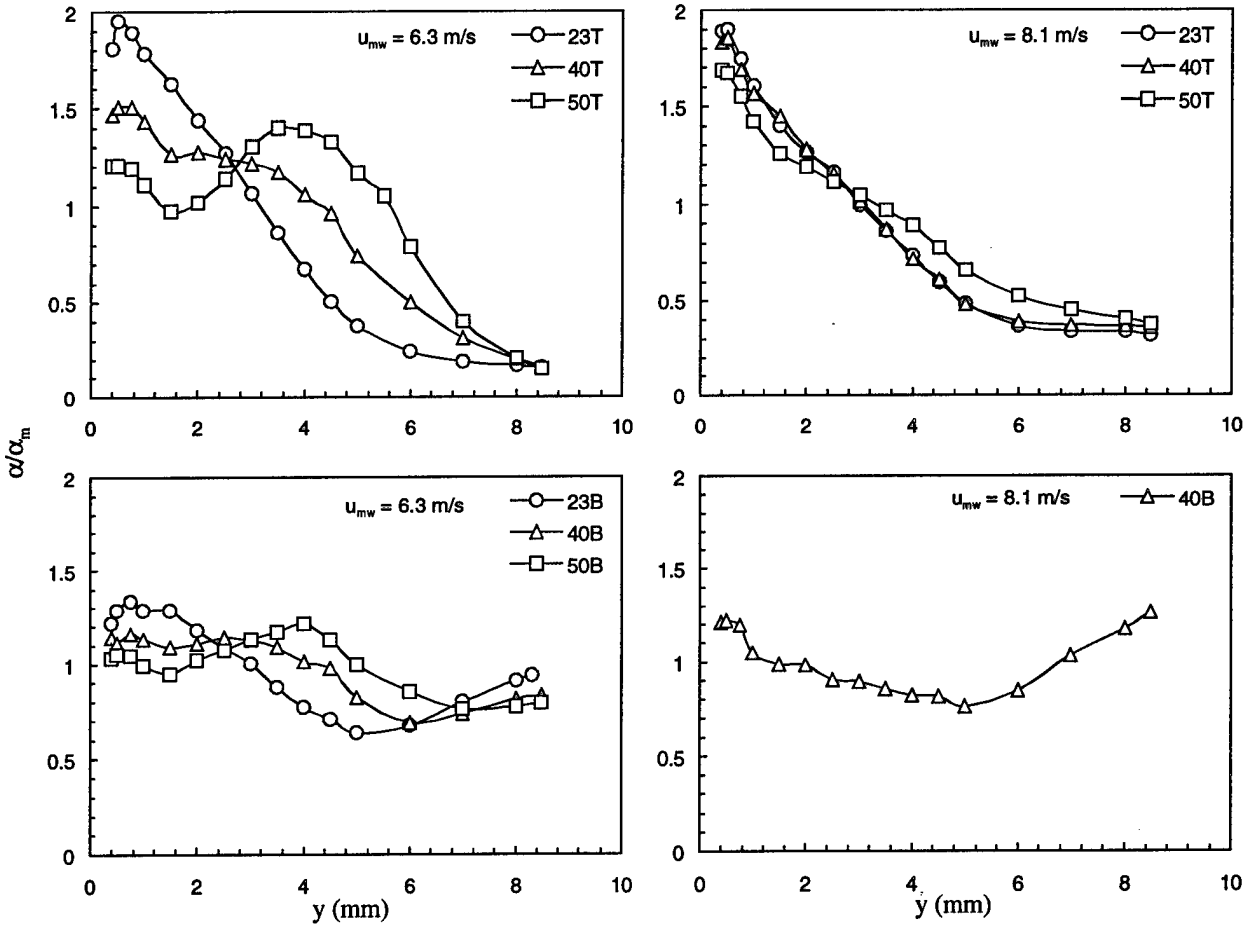

Figure 3. Bubble concentration profiles in the channel measured by the sampling probe. The numbers in the legend refer to Q_a in l/min. 'T' and 'B' represent the location of the porous plate on the top and bottom channel walls respectively. y = 0 corresponds to the top wall.

of bubbles in the bulk of the flow (Fig. 3). Therefore, it is logical to say that wall friction is not influenced by the presence or absense of bubbles far away from the wall and their distribution patterns. The main strength of α_w is that it comprises most of the bubbles contributing to the drag reduction, irrespective of the details away from the wall. Similarly, the weakness of α_m is not that it is devoid of any information of the profile variation, but that it comprises a large number of bubbles not participating in the drag reduction process. These observations are additional confirmation of the well-known concentration profile results of Pal, Merkle and Deutsch (PMD, Ref. 10) showing that bubbles have to be present within about 150 viscous units to be effective in the drag reduction process. Close examination of previously obtained results supports these points (e.g. 2,6,11). These are also in agreement with the generally accepted view that microbubble drag reduction is inner-region dependent (see also Ref. 5).

Although somewhat arbitrary, the region of definition of wall-concentration used above, viz. 1 mm from the wall, corresponds to a y^+ value of 200 to 400, well within the logarithmic region including the buffer zone. (Here, y^+ is the wall coordinate yu_τ/ν, where, y is the dimensional wall-normal distance, u_τ is the friction velocity under drag reducing conditions, and ν is the kinematic viscosity of pure water.) This region is of the order of the y-dimension of the sampling probe mouth. Although the nearest position of the probe-center from the wall was of the order of 100 viscous units, it is difficult to assign too much confidence on the local values in this rather narrow region

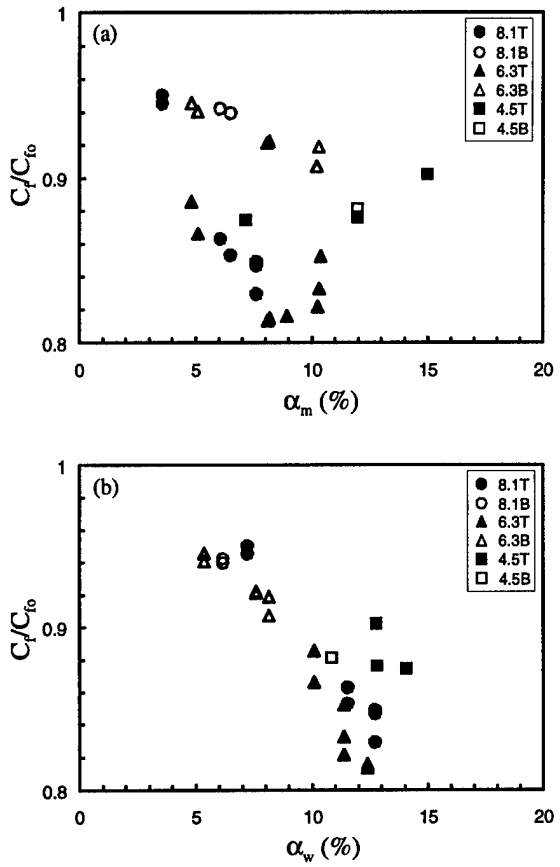

Figure 4. Dependence of skin friction ratio from direct shear measurements in the channel on (a) mean bubble concentration and (b) wall bubble concentration. The numbers in the legend mean the bulk water velocity in m/s. and the location of the porous plate on the channel walls. 'T' and 'B' represent the location of the porous plate on the top and bottom channel walls respectively.

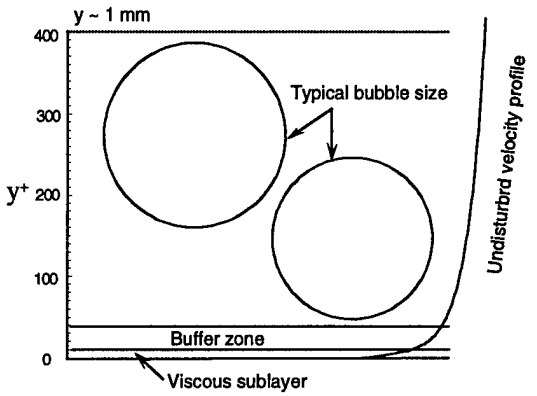

Figure 5. Relative dimensions of the bubbles in inner variables.

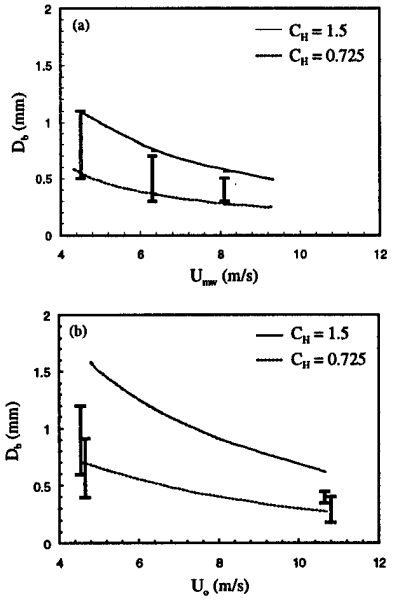

Figure 6. Variation of observed bubble diameter with velocity for porous plate injection methods and comparison with Hinze(22) (a) Channel (b) PMD. The vertical bars denote the observed range of diameters.

from the frontal-area averaging inherent in the sampling method. Moreover, the bubble size itself in viscous units D_b^+ ranged from about 100 to 250 in the entire range of these experiments (Fig. 5 and 6). Thus, in an average, there can be at best one or two bubble layers in the region of interest. Therefore, it is somewhat inappropriate to distinguish much among the y-locations within a resolution smaller than the bubble size. Accordingly, in the range of these experiments, an average within 1 mm is assumed to be the best representative of the near-wall bubble concentration.

III. NEW SCALING OF CHANNEL RESULTS WITH BUBBLE PASSING FREQUENCY ω_b

Since the phenomena are inner-region dependent, an appropriate scaling parameter should consider the fundamental quantities representative of the dynamics near the wall, i.e., the friction velocity u_τ and kinematic viscosity ν. It must be recognized that, unlike clear-water flow, another length scale exists in the form of bubble diameter D_b. As already seen, the local near-wall bubble concentration α_w has an important role. In one sense, this quantity is a passive volume fraction of gas irrespective of the bubble diameter in the mixture as would be measured by a locally averaging device like a sampling probe. Viewed another way, bubble concentration combined with bubble diameter has the connotation of a frequency. Bubbles can be pictured as discrete bodies passing by a fixed point at the wall at the local velocity. This view is strengthened by considering the narrow region of definition of α_w which can include at best one or two layers of bubbles in the present experiments. Bubble passing velocity is assumed to be equal to the local velocity of water which in this region of 200 - 400 viscous units can be approximately the bulk velocity U_m. The local void fraction is then converted into a bubble passing frequency,

$$\omega_b = 2\pi\left(\alpha_w U_m / D_b\right) \tag{1}$$

The physical picture is analogous to the case of a wall-bounded flow with the near-wall region is subjected to periodic velocity perturbations at an idealized frequency given by ω_b. This frequency combined with the inner time scale yields the normalized frequency $\omega_b^+ = \omega_b \nu / u_\tau^2$ or the normalized period $T^+ = 2\pi/\omega_b^+$. In addition, a length parameter characterizing oscillatory viscous flow normalized by the inner variables is the Stokes length defined as, $S^+ = u_\tau(2/\nu\omega_b)^{0.5}$ which is also equal to $(2/\omega_b^+)^{0.5}$. The value of u_τ is taken under drag-reducing conditions and ν is the pure-water kinematic viscosity. This

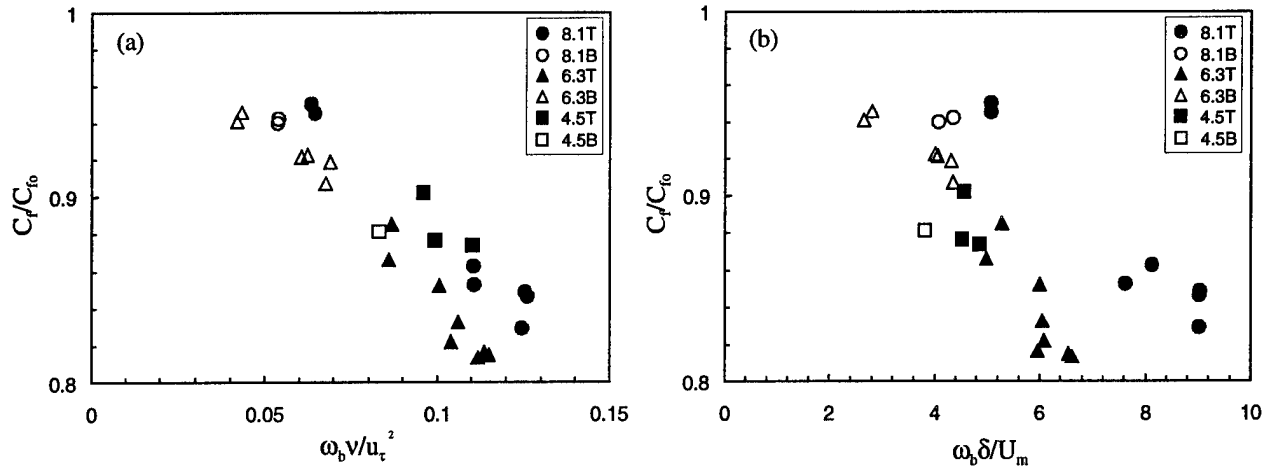

Figure 7. Dependence of local skin friction ratio on bubble passing frequency normalized by (a) inner and (b) outer time scales from direct shear measurements in the channel. The measured wall void fraction α_w is used in determination of the bubble frequency. The legend is same as in Fig. 4.

is justified by the presence of a bubble-free region next to the wall as mentioned before.

The measured wall shear ratios in the channel are plotted in Fig. 7(a) against ω_b^+ evaluated with the measured quantities. Despite some scatter, the data points collapse reasonably well. This is again a confirmation that the phenomena are inner-region-dependent. The poor collapse in the frequency normalized by outer variables $\omega_b\delta/U_m$ in Fig. 7(b) is in agreement with the insensitiveness of the phenomena to the outer region. Thus, combined with the physical picture and arguments in the preceding paragraphs the normalized bubble passing frequency ω_b^+ appears to be a pertinent scaling parameter. In the following section, we examine if similar scaling also holds good in the well documented case of the water tunnel boundary layer with local hot-film measurements by MDM2.

IV. EXTENSION OF ω_b^+ SCALING TO MDM2.

The data examined in this section are taken from figures 8 to 13 of the original reference in which the mean local skin friction ratio was measured by hot-film gauges and plotted against an average bubble concentration. In order to extend the present scaling to these results, information on wall concentration and bubble diameter are necessary.

In the absence of measurements, the determination of a most probable wall bubble concentration in these cases is difficult. For example, there is a possibility of the bubble cloud moving away from the wall in the plate-on-bottom and, to a lesser extent, in the plate-on-top configurations as shown by PMD. This would tend to reduce the near-wall concentration. This is also one reason why, despite gross likeness in shape, the bubble distribution patterns obtained in the channel in terms of α/α_m shown in Fig. 3 may not be quantitatively extended to the case of MDM2 since, in the former, bubbles stay within the thickness of the channel while tending to diffuse out of a boundary layer. For the present purpose, however, a tentative assumption is made equating the local wall concentration α_{wi} to the local average bubble concentration $q_{ai} = Q_a/(Q_a+U_o(\delta_i-\delta_i^*)L)$, which is deduced for each measuring station i using the original boundary layer properties. Here, Q_a is the volumetric air flow rate, U_o the free-stream velocity, δ_i and δ_i^* the local boundary layer thickness and displacement thickness respectively, and L is the spanwise length of the porous plate.

The range of bubble diameter measured in the channel (Fig. 6a) and those reported by PMD (Fig 6b) using also porous plates corresponding to their air-flow I and II are seen to agree with each other by the treatment of Hinze(22) predicting the largest drop size D_{max} stable against break-up

$$D_{\max}\left(\frac{\rho}{\sigma}\right)^{\frac{3}{5}}\varepsilon^{\frac{2}{5}} = C_H \qquad (2)$$

where, ρ and σ are the liquid density and surface tension respectively, and ε is the dissipation. The observed diameters closely fall within the curves corresponding to the values of the empirical constant C_H of 0.725 and 1.5. The first value is the one originally proposed by Hinze. Using these information as guideline, the bubble diameter in the case of MDM2 is determined. This method of extending the diameter variation to an entirely different experiment involves large uncertainty. But it seems justified to some extent, as the main flow velocity and the shear layer thickness are comparable among PMD, MDM2 and present channel. In this way, local ω_b^+ values are calculated using Eqn. 1 and the C_f/C_{fo} ratios are plotted in Fig. 8(a) for the original data set of MDM2. The data indeed correlate very well independent of velocity, air-flow rate and plate orientation. Despite the uncertainties in bubble diameter and the wall concentration involved in the assumptions, this good collapse seems surprising. If the exact values of D_b and α_{wi} were used in calculating ω_b^+, such very good correlation could be weakened. In any case, α_{wi} is expected to be nearly proportional to q_{ai} whose effect would be to change the magnitude of ω_b^+ proportionately rather than to seriously affect the goodness of the data collapse. The plot in Fig. 8(b) in terms of the frequency normalized by the outer variables may be contrasted. As in the channel case (Fig. 7b), this plot again demonstrates that the phenomenon does not scale with outer variables.

Thus, inner variable scaling with the bubble passing frequency is seen to be quite effective also in the case of a water tunnel boundary layer examined above though under several assumptions. The agreement in the values in both channel and the case of MDM2 shown together in Fig. 9 tends to suggest that ω_b^+, or the equivalent parameters S^+ and T^+ shown in the abscissa, may even be universal. In addition to the effective bubble concentration, these parameters establish the importance of bubble diameter and the inner variables. Based on the new scaling, although at present speculative, there seems to be a possibility that skin friction reduction in a microbubble-modified boundary layer could be due to the excitation imparted to the wall region by the passage of the bubbles in close proximity to the wall. Further, there seems to be a threshold frequency around ω^+ value of 0.04 above which drag reduction occurs. Interestingly, this

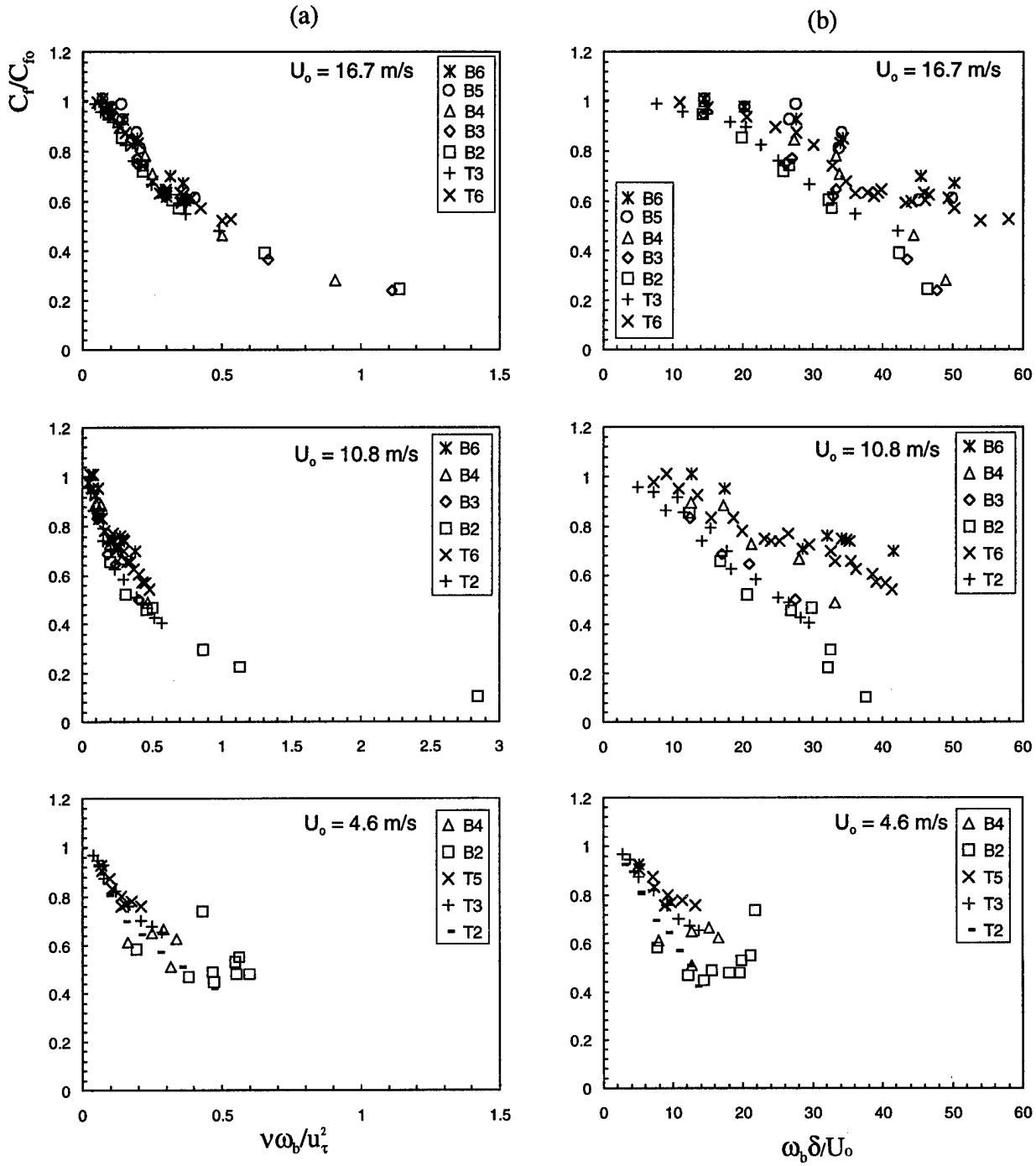

Figure 8. Dependence of local skin friction ratio on bubble passing frequency normalized by (a) inner and (b) outer time scales from the hot-film measurements of MDM2. The first digit in the legend implies plate configuration: plate-on-top denoted by 'T' and plate-on-bottom by 'B'. The second digit is the hot-film probe position in increasing order in the downstream direction.

frequency is close to the sublayer burst frequency found in the literature.

V. CONCLUSIONS

Despite gross uncertainties, it is clear that the bubble passing frequency ω_b^+ normalized by the inner variables is a relevant nondimensional parameter governing microbubble drag reduction phenomena. The bubble concentration near the wall within a wall-normal distance comparable to the bubble dimensions together with the diameter and velocity yields a near-wall bubble passing frequency. Good collapse of skin friction ratios with this quantity is obtained in the experiments in a channel. Similar scaling with quantitative agreements is also found to apply in the boundary layer case of MDM2 under some assumptions. The quantity ω_b^+ can serve as a good design parameter in applying the methods to real ships. More importantly, from a physical point of view, it brings out the possibility that microbubble drag reduction could be the outcome of high frequency excitation of the near-wall region by the passing bubbles.

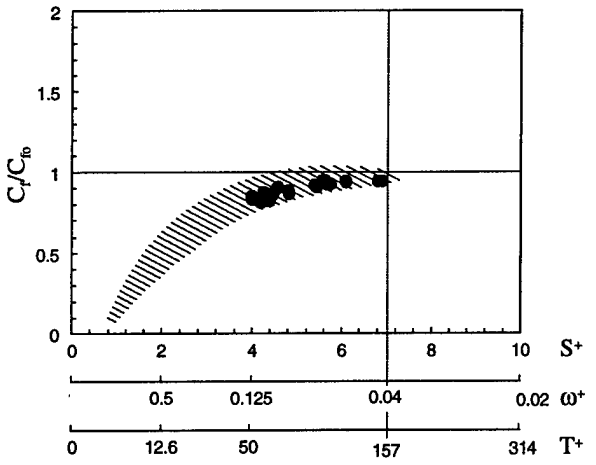

● Present (Direct shear measurements in channel with microbubbles)
※ MDM2 (Hot-film shear measurements on flat-plate with microbubbles)

Figure 9. Comparison of the scaling between MDM2 and channel. The value of $\omega^+ \sim 0.04$ appears to be a threshold value for drag reduction.

There also seems to be a threshold frequency close to the sublayer burst frequency above which drag reduction might occur. Due to considerable difficulties of measurements in the wall region in the presence of bubbles, direct supporting data has not been obtained yet.

ACKNOWLEDGMENTS

We are thankful to Professor H. Yamaguchi for helpful advice, and M. Maeda, M. Miyanaga and T. Matsuzawa for their valuable assistance during the experiments. Encouragement from E. Sugita of IEM Ltd. Y. Yoshida and A. Masuko of IHI Ltd. is thankfully acknowledged. We acknowledge the financial support from the Ministry of Education, Science, Culture and Sports of Japan (the *Monbusho*) in the form of a scholarship to MMG. Useful discussions with Professor Vijay H. Arakeri of the Indian Institute of Science, Bangalore, India during a visit by MMG is gratefully acknowledged.

REFERENCES

1 M. E. McCormick and R. Bhattacharyya "Drag reduction of a submersible hull by electrolysis," Nav. Eng. J. **85**, 11 (1973).

2 V. G. Bogdevich, A. R. Evseev, A. G. Malyuga, and G. S. Migirenko "Gas-Saturation effect on near-wall turbulence characteristics," in *Second Intl. Conference on Drag Reduction, Paper D2* (BHRA Fluid Eng., Cambridge, England), p. 25 (1977).

3 N. K. Madavan, S. Deutsch, and C. L. Merkle "Reduction of turbulent skin friction by microbubbles," Phys. Fluids **27**, 356 (1984).

4 N. K. Madavan, S. Deutsch, and C. L. Merkle "Measurements of local skin friction in a microbubble-modified turbulent boundary layer," J. Fluid Mech. **156**, 237 (1985). [referred to as MDM2]

5 N. K. Madavan, S. Deutsch, and C. L. Merkle "Numerical investigations into the mechanisms of microbubble drag reduction," J. Fluids Eng. **107**, 370 (1985).

6 C. L. Merkle, S. Deutsch, S. Pal, J. Cimbala, and W. Seelig "Microbubble drag reduction," in *Proceedings of the Sixteenth Symposium on Naval Hydrodynamics* (Berkeley, California, USA), p. 199 (1986).

7 K. Tokunaga "Reduction of frictional resistance of a flat plate by microbubbles," Trans. West Japan Soc. of Nav. Arch. **73**, 79 (1986).

8 E. Baba, "Discussion on Merkle et al,[6]" in *Proceedings of the 16th Symposium on Naval Hydrodynamics* (Berkeley, California, USA), p. 214 (1986).

9 S. Deutsch and J. Castano "Microbubble skin friction reduction on an axisymmetric body," Phys. Fluids **29**, 3590 (1986).

10 S. Pal, C. L. Merkle, and S. Deutsch "Bubble characteristics and trajectories in a microbubble boundary layer," Phys Fluids **31**, 744 (1988). [referred to as PMD]

11 C. L. Merkle and S. Deutsch "Microbubble drag reduction," in *Frontiers in Experimental Fluid Mechanics, Lecture notes in Eng.*, edited by M. Gad-el-Hak (Springer-Verlag Berlin), vol 46, p. 291 (1989).

12 S. Deutsch and S. Pal "Local shear stress measurements on an axisymmetric body in a microbubble modified flow field," Phys. Fluids A **2**, 2140 (1990).

13 H. Clark III and S. Deutsch "Microbubble skin friction reduction on an axisymmetric body under the influence of applied axial pressure gradients," Phys. Fluids A **3** 2948 (1991).

14 H. Kato, M. Miyanaga, Y. Haramoto and M. M. Guin "Frictional drag reduction by injecting bubbly water into a turbulent boundary layer," in, *ASME Symposium on Cavitation and Gas-Liquid flow in Fluid Machinery and Devices*, FED-Vol 190, p. 185 (1994).

15 H. Kato, M. Miyanaga, H. Yamaguchi and M. M. Guin "Frictional drag reduction by injecting bubbly water into turbulent boundary layer and the effect of plate orientation," in, *Advances in Multiphase Flow* (ed. A. Serizawa, T. Fukano and J. Bataille (Proc. 2nd Intern. Conf. Multiphase Flow, Kyoto), Elesevier Science B.V., p 85 (1995).

16 M. M. Guin "Studies on frictional drag reduction by microbubbles in turbulent boundary layers," Ph.D. thesis, The University of Tokyo, 1995.

17 M. M. Guin, H. Kato, H. Yamaguchi, M. Maeda and M. Miyanaga "Skin friction reduction by microbubbles and its relation with near-wall bubble concentration in a channel," J. Marine Sc. and Tech. **1**, 241 (1996).

18 M. M. Guin, H. Kato, H. Yamaguchi, M. Miyanaga and M. Maeda "Direct skin friction measurements and observation of drag reduction in a two-phase air-water channel," in, *ASME Symposium on Turbulence Modification and Drag Reduction*, San Diego, CA, USA. FED-vol 237, p. 93 (1996).

19 J. L. Marié "A simple analytical formulation for microbubble drag reduction," J. PhysicoChem Hydrodyn. **13**, 213 (1987).

20 Y. Yoshida, Y. Takahashi, H. Kato, A. Masuko and O. Watanabe "Simple Lagrangian formulation of bubbly flow in a turbulent boundary layer (bubbly boundary layer flow)", J. Marine Science and Technology, **2**, 1 (1997).

21 H. Kato, Y. Fujii, H. Yamaguchi, and M. Miyanaga "Frictional drag reduction by injecting high-viscosity fluid into turbulent boundary layer," J. Fluids Eng. **115**, p. 206 (1993).

22 J. O. Hinze "Fundamentals of the hydrodynamic mechanism of splitting in dispersion processes," AIChE J. **1**, 289 (1955).

ROLE OF BUBBLE INJECTION TECHNIQUE DRAG REDUCTION

Dr. Robert Latorre
University of New Orleans
911 Engineering Building
New Orleans, LA 70148
Tel. (504)-280-7180
e-mail: rglna@uno.edu

Professor Viktor V. Babenko
Institute of Fluid Mechanics
National Academy of Sciences 8/4 Zheliabov Str.
Kiev, Ukraine 252057
e-mail: vb@bionics.Kiev

Abstract - One approach to reducing viscous drag is to introduce air along the wetted surface. This paper begins with a discussion of the boundary layer characteristics and how it is influenced by the gas injection. Then the results of sets of experiments are discussed showing how the surface orientation influences the results of air injection. Overall the results indicate a 20-30% reduction in the value of Cf by air injection.

I. INTRODUCTION

Viscous resistance denoted by the coefficient of friction Cf accounts for a large proportion of surface and submerged craft drag. It represents 50-65% of the surface ship seawater drag and 60-75% seawater drag for submerged craft. It is possible to design optimal hull forms with computer software. This makes the reduction of viscous resistance an important problem.

Hull surface air injection is one approach to reducing this viscous drag. This air injection can be accomplished in several ways:

(1) Bubble injection from electrolysis, nozzles or screens, McCormick [1], Sperrou [2], Yoshida [4], Barnabel [3], Takahashi [4];
(2) Air film from hull slits, Latorre [6];
(3) Air cavity formation, Basin [7];

This paper discusses the first approach – bubble injection from electrolysis, nozzles, and screens. It begins with a discussion of the boundary layer characteristics and how the presence gas bubbles creates a favorable influence to reduce viscous drag. The test results using electrolysis to generate bubbles on a body of revolution are presented. The reduction in the coefficient of friction Cf are compared using the results from tests with bubbles generated by upstream injectors, Yoshida [2] and upstream screens Barnabel [3], Takahashi [4]. The test results show the influence bubble orientation and bubble size on the reducing coefficient of friction Cf. These results are useful to estimate the drag reduction for surface craft as well as submerged craft with bottom and deck air injection.

II. Bubble interaction with boundary layer

A large number of theoretical and experimental researches of the kinematic and integral characteristics of a two-phase boundary layer have been carried out for the case when a film of gas bubbles is supplied into a fluid. Recent experiments are summarized in Table 1.

It is assumed that a solid film forms a border between a liquid and gaseous boundary layer. This film will be generated on a body surface as a result of gas injection. This problem is solved for a flow over a plate. It is shown in this case that the presence of a two-phase boundary layer on a plate results in a significant resistance reduction. The creation and maintenance of a gas solid film requires maintenance of a steady interface where there is the tendency towards film break-up into separate bubbles and the transition to a turbulent mode of motion.

A uniform transition in the fluid properties across the boundary layer is assumed along with the film character of the gas flow in the fluid. The assumption about the uniformity of a gas film front in a transverse direction is used in the theoretical treatment along with a number of other assumptions.

The other approach – diffusion of bubbles in a gas-water mixture moving near a wall – is also used in understanding of the physics of this two-phase flow.

The principle of the boundary layer receptivity to various disturbances is used as the basis of the present experimental research. The essence of this method consists of the following: the exciting motion passes a series of specific formations in form of a coherent vortex structures during the boundary layer development. Tollmien-Schlichting waves or Klien's vortexes are examples of such structures. It is possible to use this method to effect integrally on all types of vortical structures and achieve resistance reduction. Injection or suction of a boundary layer is examples of such a method. However, it is possible to reduce resistance by this method through effects on separate kinds of coherent vortical structures (CVS). This method of receptivity consists in introducing of disturbances comparable to the existing coherent vortex structures in the boundary layer. An example of this approach will be shown below.

Method of Air Injection	Test Section	Flow [m/s]	Void [%]	Cf/Cf0	Ref.
Electro-lysis	Tow Tank 1 m Body	0.33-2.0	0-75 amps	0.70 – 0.95	[1]
Bottom Screen	NA	a)4.36 b)8.55 c)10.9	a)0-0.3 b)0-0.4 c)0.4-0.8	0.7-1.0 0.45-1.0 0.2-0.4	[3]
Top Screen	0.1 m 0.015 m 3 m long	a)5 b)7 c)10	a)0-0.25 b)0-0.2 c)0-0.25	a)0.75-1 b)0.65-1 c)0.7-1.0	[4]
Injectors	0.6x0.6 m Tunnel 150 mm wide slot 20° angle	8.0	a)35 l/m b)100l/m c)200l/m	a)0.95-1 b)0.8-0.9 c)0.2-0.5	[5]

Table 1. Published experimental results of drag reduction by bubble Injection.

III. Measurement of Boundary Layer Characteristics

Research of a boundary layer along a working site of a hydrodynamic bench with low turbulence $\varepsilon \approx 0.05$ % was carried out using the telluric method. The sensitivity of the telluric method allows visualizing the deformation of velocity profiles U(z) (Fig. 1) at $\varepsilon \approx 0.05$ %. Fig 1 shows photos of velocity profiles U(z) at various values of x.

The Reynolds number determined experimentally was $Re = 5.4 \cdot 10^4$.

The photographs show the profile U(z) begins to deform near a critical layer at $Re = 4 \cdot 10^4$ already (Fig.1-a). This is the premises to develop disturbances in a boundary layer up to a point based on Re.

The distribution of U(z) becomes ordered (Fig. 1-b) at increased Reynolds number. At $Re \sim 10^5$, there is a stable regularity in the arrangement of "peaks" and "valleys" at defined values of z with $\lambda_z = (1.5 \div 2)\delta$. The speed of the telluric line distribution downstream is constant and depends on the z-location measurement in each series of experiments.

The width measurements of the boundary layer show the deformation of a profile U (z) is observed in a very narrow area $y/\delta = 0.2 \div 0.3$ for these Reynolds numbers. The deformation appears near to a

critical layer outside of which the flow structures are plane-parallel. For increased x, the maximum width of this non-linear deformation increase from 0.2(y/δ) up to 0.4(y/δ). This is in agreement with the measurements of Klebanov [3,7] where the width of y increased downstream.

This investigation in low turbulence $\varepsilon \approx 0.05$ % shows that although the transition phases maintain their characteristic features and a undergo a sequence of alternation, their development is significantly delayed by the low turbulence. The non-linear effects are initiated at a phase of a linear plane wave. They develop in a narrow conical layer symmetrical to the xz plane as a critical layer extending as a cone downstream (Fig. 2). The observed peaks and valleys are generated under influence of a non-linear deformation of a plane wave induced by a curvature of a flow line and by change of a primary vorticity. The longitudinal vortex systems are not yet formed.

The development of the temporal and spatial disturbances within a boundary layer at Re~0.7, 0.8 and $1.1 \cdot 10^5$ was also investigated by telluric method.

The maximum amplitude of U(z) at Re~0.7×10^5 was observed at y = $3 \cdot 10^{-3}$m and at Re ~ 0.8 $\times 10^5$ it was observed at y = $5 \cdot 10^{-3}$ m. However at Re~ $1.1 \cdot 10^5$ two maximum amplitudes were observed at y = $2 \cdot 10^{-3}$ m and $4 \cdot 10^{-3}$m. The presence of these two maximums indicates the more complex structure of exciting motion. Photos of velocity profiles U(z) at Re~ $0.8 \cdot 10^5$ are presented in Fig.3. The results of this flow visualization enabled the development of a flow pattern scheme for the initial phases of non-linear deformation of a plane wave at large turbulence ε (Fig. 4). Additional vortex pairs resulted in the characteristic small-scale deformation of profile speeds U(z) (Fig.3) being formed near the surface. From this un-stationary flow character detected in the experiments, it is possible to consider that the whole system of longitudinal vortices is changeable. They are able to change their form, size, the number of vortex pairs, as well as their ratios and their temporal and spatial trajectories of motion. This is reflected on kinematic characteristics. Small differences in the a and b system of vortexes (Fig. 4) essentially changes the resulting velocity profile U(z).

IV. Influence of Surface on Boundary Layer

The various mechanical devices intended for formation of long and transverse vortexes in a boundary layer are developed and applied in engineering designs. Examples of such design solutions can be found in the scientific articles and patents. Despite of their efficiency they have one disadvantage: the creation of additional friction resistance. One design solution to this problem of added drag is adopting a ribbed surface. Tests were made with five strips of $6 \cdot 10^{-5}$ m x 0.003 m x 0.23 m of standard scotch tape pasted at 0.012-m intervals along the bottom of the test section. Site. The rib effect was created by setting lengths (0.2 m) of $0.12 \cdot 10^{-3}$ m diameter wire under these strips.

The operation of this system with reduced strip (0.02 m length) was checked at Re= $7 \cdot 10^4$. The results in Fig. 5-a show the velocity distribution U(z) does not differ from the smooth surface velocity distribution. The visualization of U(z) of the boundary layer flow over a surface with a ribbed surface is shown in Fig. 5 (b-g). The ribbing of the surface begins at x = 0.9 m from the bottom leading edge of the test section. It is clearly visible from these figures that the serration of a telluric cloud appears near to a surface above the strips in a range Re= $(0.7 \div 1.5) \cdot 10^5$. The form the cloud shed from a telluric wire (d, e) is identical with the cloud formed by the telluric wire moving over the strips (f) and at the limits (g). The limit "g" is 5 cm downstream of rear edge of the strip. The speed of disturbance growth defined by the degree of a cloud deformation downstream is less noticeably in a case "f" than in a case "d". The overtaking part of the cloud becomes more plane and the magnitude of velocity change on z is decreased. This can be taken as the result of an optimum interaction of disturbances inserted with λz = 0.012 m and natural disturbances at increased Reynolds number.

V.Tests with Electrolysis Bubbles

The experiments with electrolysis bubbles were also completed. Un-insulated wires were pasted to a plate. They were energized by a constant charge (10 volts) as well as a pulse charge (400 volts, 0.1 ÷ 0.5 s impulse frequency). A hydrogen bubble film was formed on a wire surface as a result of electrolysis and the surface film moves downstream. This longitudinal bubble film increases the intensity of the longitudinal vortex disturbances. This increases hydrodynamic stability and delays the boundary layer transition. Consequently, the drag of this two-phase flow is significantly reduced with longitudinal flow over the wires

A Plexiglas body of revolution model was developed for measuring two-phase surface flow influence on the drag and boundary layer characteristics. The 0.415-m x 0.04 diameter Plexiglas model is shown mounted in the water tunnel in Fig. 6. The metal (brass) nose and tail part of the model were connected to a DC power supply. The voltage was set at 10 ÷ 30 volts during the tests. A film of bubbles moved downstream into the boundary layer from the rear edge of the metal nose. These tests show a 10-15% reduction in the model resistance depending on the current and voltage. This is similar to McCormick's towing tank test results summarized in Table 1[1].

VI.Bubble Injection from Upstream Screens

Table 1 summarizes the results of systematic tests of a plate with bubbles injected through an upstream screen. The tests reported in the monograph of Barbanel [3] were completed using bubbles generated by a bottom screen with round openings. The drag measurements were done in a water tunnel at test speeds of 4 < V< 8 m/s. The bubble and water mixture along the downstream surface is characterized by φ, the void fraction measured by a laser. The total force is measured on a test plate and the results reduced to coefficient of friction Cf' with bubble injection and Cf without bubble injection. The results of the tests are then characterized by the ratio Cf'/Cf. The test results are plotted as Cf'/Cf versus void fraction φ in Fig.7.

Figure 7 also shows the results of Takahashi et al.[4]. Takahashi [4] drag measurements are made with a top mounted plate in the water tunnel. A top mounted screen at the tunnel entrance generates the bubbles.

It is clear in Fig. 7 that bubble injection from the top results in some differences in the drag reduction when compared to the bottom bubble injection. Aside from differences in the bubble size due to differences in the screen size, the comparison in Fig. 7, shows the influence of the bubble buoyancy. In the bottom bubble tests of Barbanel, the bubble injection is limited to an effective contact region. Outside of this region, bubble buoyancy lifts them from the bottom surface. With the top screen, the bubbles tend to collect in the bottom surface and as Takahashi's results in Fig. 7 shows, this can reduce the plate drag reduction. For nominal void fraction φ of 0.5 to 0.1, the presence of bubbles results in a 15-20%. drag reduction. Figure 7 also indicates this drag reduction process is more effective for larger amounts of bubble injection at higher flow speeds. At these higher flow speeds the bubble buoyancy is relatively smaller and has smaller influence on the drag reduction process as shown in Fig. 7.

VII.Bubble Injection from Nozzle Injections

Table 1 also includes the results of Yoshida et. al. [5] tests with upstream bubbles injected through nozzles arranged slightly below the upper wall of the 0.6 x 0.6 test section of the University of Tokyo's propeller cavitation tunnel. The bubble diameter from the injectors was larger than the bubble diameter generated by the screens. The other significant difference was the orientation of the nozzles and test plate. During these tests, the bubbles would enter the flow below the plate and then collect on the upper surface as they moved downstream. The bubble buoyancy assisted the process by insuring contact with the upper plate.

These tests were performed for tunnel speeds of 4 < V < 8 m/s. The total force was measured on a test plate and the results reduced to coefficient of friction Cf' with bubble injection and Cf without bubble injection.

The results of these tests are plotted as the ratio of Cf'/Cf the different bubble-water void fraction φ for different injection rates in Fig.8. The comparison with the results reported by Barbanel [3] indicates the drag reduction with injectors and screens is different This difference is due to three factors:

1. The larger bubble size from the injectors
2. The orientation of the injection angle and downstream flow
3. The injection from the tunnel top

At the same time, the results support the earlier conclusion that the larger amount of bubble injection acts to have a large reduction in the plate drag. The results independently support the conclusion that

frictional drag reduction in the order of 60-70% can be realized by bubble injection.

VIII.Concluding Remarks

This paper has presented the results of systematic tests on the influence from introducing bubbles on a wetted surface. These bubbles were generated by:

a) Electrolysis
b) Upstream screen in the bottom
c) Upstream injectors

Detailed experiments indicate the bubbles favorably interact with the boundary layer structure delaying transition as well as reducing the surface viscous drag.

These results lead to several interesting conclusions

1. The presence of bubbles in the surface boundary layer has a favorable influence on reducing the energy losses given by lower surface drag.
2. The systematic tests show that the ratio of Cf' with bubbles to Cf without bubbles is in the order of $0.20 < Cf'/Cf < 0.85$
3. The systematic tests show that the ratio of Cf'/Cf is sensitive to the amount of bubble injection which is expressed as the void fraction φ
4. Comparison of the drag reduction shows that at low speeds the bubble injection orientation can have a strong influence on the drag reduction.

The utilization of bubble injection has many applications in seawater drag reduction. It is hoped this paper will encourage designers to utilize this approach.

IX.REFERENCES

1. McCormick, M., Bhattacharyya, R., "Drag Reduction of a Submersible Hull by Electrolysis", Naval Engineers Journal, April 1993, PP 11-16.
2. Sperrou E. M., Djonson V. K., Ekkert R.T. "Two-phase Boundary Layer and Drag Reducing Friction on the Plate". – TASME (1962) v. 29, No.2
3. Barbanel B. A., Bogdevich V. G., Maltsev L. I., Malyuga A. G. Some Practical Applications of Boundary Layer Control Theory, Malaxit, St.Petersburg, 1994, 47pp.
4. Takahashi, T., Kakugawa and Kodama, Y., "Streamwise Distribution of the Skin Friction Reduction by Microbubbles", Journal Society of Naval Architects of Japan, Vol. 182, Dec. 1997 pp.1-8
5. Yoshida Y., Takahashi Y., Kato H., Masuko A., Watanabe O. "Simple Lagrangian Formulation of Bubbly Flow in a Turbulent Boundary Layer (bubble boundary layer flow), Journal of Marine Science and Technology, SNAJ Vol. 1, No. 5, 1996, pp. 241-254.
6. Latorre, R., "Ship Hull Drag Reduction Using Bottom Air Injection", Ocean Engineering, vol. 24, no.2, 1997, pp. 161-175.
7. Basin A. M., Krotkin A. I., Kozlov L. F. "Control of Ship Boundary Layer", Sodostreniye, Leningrad, 1968, 492pp.

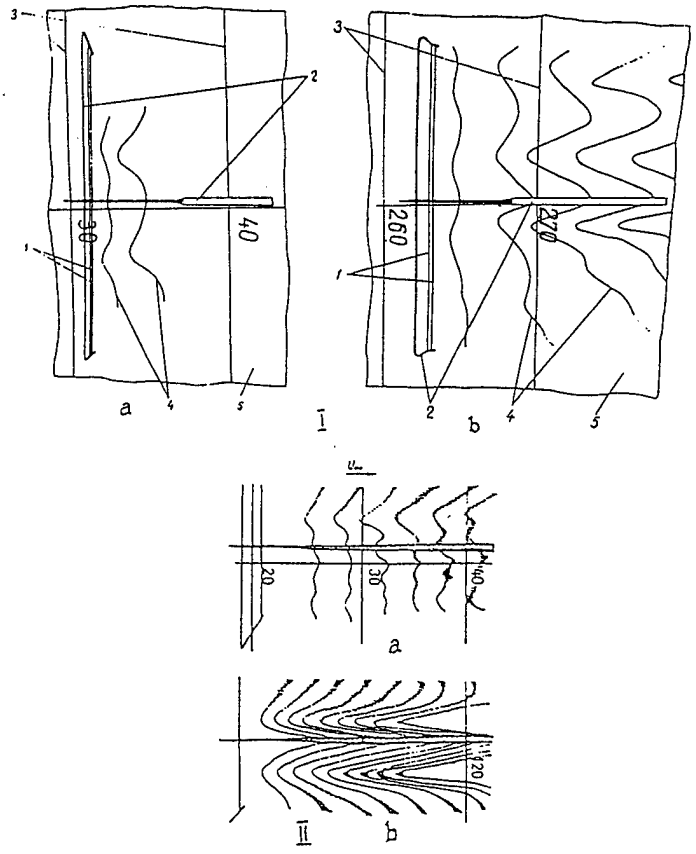

Fig.1 Traces from the photographs of the tellurium lines in the xz plane for U_∞ = 10.5 cm/s, $y/\delta \approx 0.2$ at the beginning (a) and at end (b) of the working section for (I) – Horizontal and (II) – Inclined Plates;

Key: 1 – tellurium wires;
2 – holder;
3 – mark of distance from the beginning of the working section (cm);
4 – velocity profile trace;
5 – second bottom.

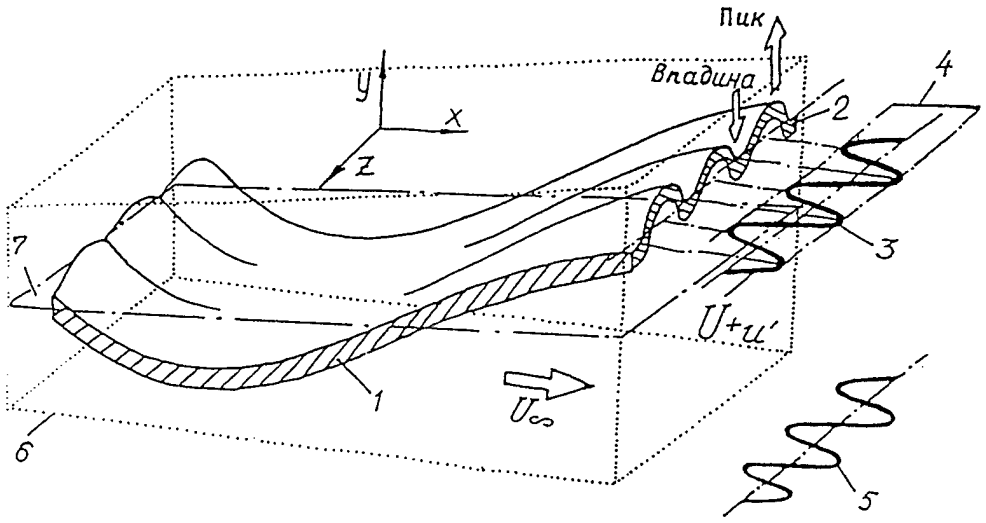

Fig. 2 Evolution of non-linear disturbances in low turbulent flow;
Key: 1 – plane of Tollmien-Schlichting wave;
2 – non-linear secondary disturbances;
3 – velocity profile U(z);
4 – projection of velocity profile U(z) onto plan xy (viewed from one side);
5 – projection onto plane xz (looking from above);
6 – conical layer of non-linear disturbances development;
7 – plane xz of critical layer

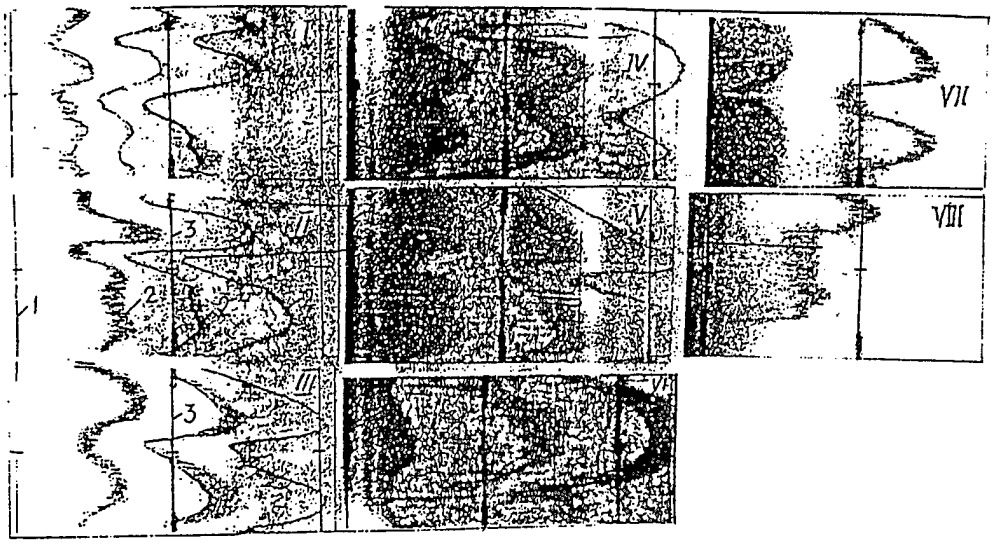

Fig. 3 Photos I-VIII of Velocity Profiles U(z) during natural transition of the boundary layer $U_\infty = 6.7 \cdot 10^{-2}$ m/s; distance between tellurium wire and the beginning of the working section $x_t = 1.1$ m; timing between tellurium clouds = 0.5 s;
I - $y_t = 3 \cdot 10^{-3}$ m ; II - $4 \cdot 10^{-3}$ m; III - $5 \cdot 10^{-3}$ m ; IV - $6 \cdot 10^{-3}$ m;
V - $7 \cdot 10^{-3}$ m; VI - $8 \cdot 10^{-3}$ m ; VII - $9 \cdot 10^{-3}$ m ; VIII – $1.2 \cdot 10^{-2}$ m
Key:
1 – tellurium wire;
2 – tellurium clouds;
3 – distance scale on the bottom distance of tellurium wire from the bottom;

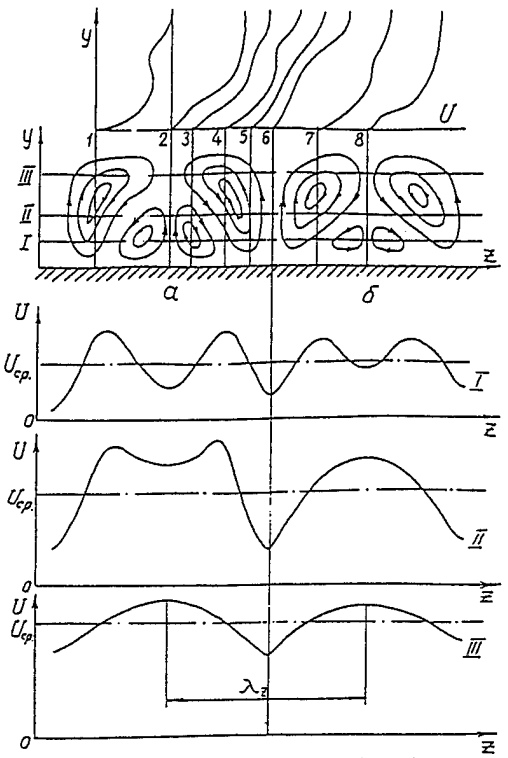

Fig. 4 Flow structure of initial stages of non-linear plane wave deformation for large turbulence ε

Top 1-8 section cuts showing U velocity profile

a, b – Types of longitudinal vortex structures;

Bottom I- II - III xy section cuts showing U velocity variation along z

Ucp= average.

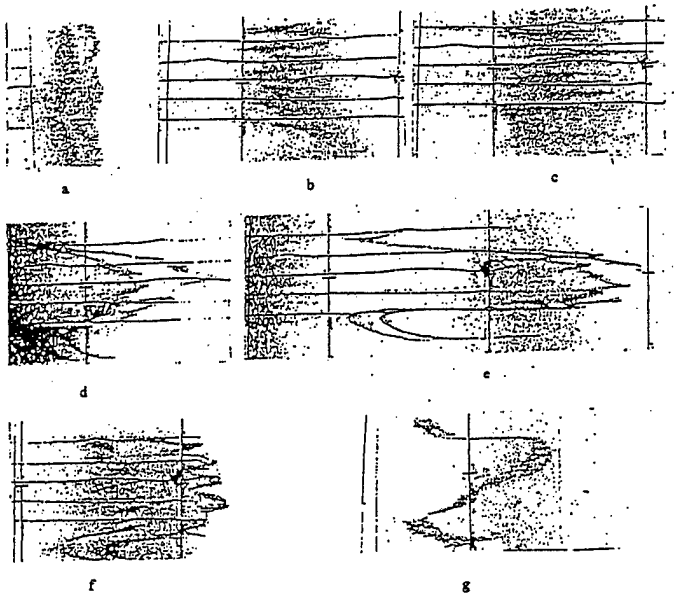

Fig. 5 Traces showing influence of regular ribbed surface on boundary layer flow U(z) ($\lambda_z = 0.012$ m)

a –Re = $7 \cdot 10^4$, y = $1.0 \cdot 10^{-3}$ m (0.02 m length of edges);

b – Re = $5 \cdot 10^4$, y = $1.5 \cdot 10^{-3}$ m; (0.2 m length of edges);

c - Re = 10^5, y = $5 \cdot 10^{-4}$ m, (0.2 m length of edges);

d - Re = 10^5, y = $1.5 \cdot 10^{-3}$ m, (0.2 m length of edges);

e - Re = 10^5, y = $1.0 \cdot 10^{-3}$, (0.2 m length of edges);

f – Re = $1.4 \cdot 10^5$, y = $1.5 \cdot 10^{-3}$ m, (0.2 m length of edges);

g – Re = $1.5 \cdot 10^5$, y = $1.5 \cdot 10^{-3}$ m. (0.2 m length of edges)

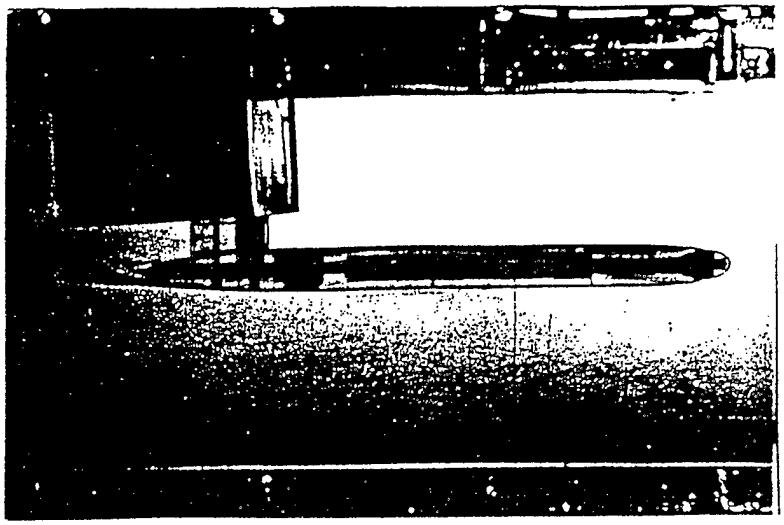

Fig. 6 Photo of Plexiglas body of revolution in water tunnel,
Length = 0.415 m, dia = 0.04 m.

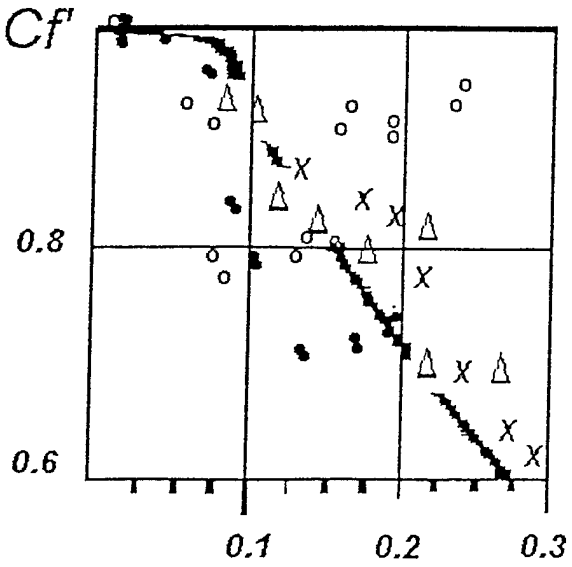

Key:

Bottom Screen Barbanel [3] Flow Speed u[m/s] △ : u = 4.36 m/s X : u = 8.55 m/s

Top Screen Takahashi [4] Flow Speed u[m/s] O : u = 5.0 m/s ● : u = 7.0 m/s

at 500 mm downstream

Fig. 7 Influence on downstream Screen Air Injection on Cf' = Cf with air / Cf without air at Flow Velocity u.

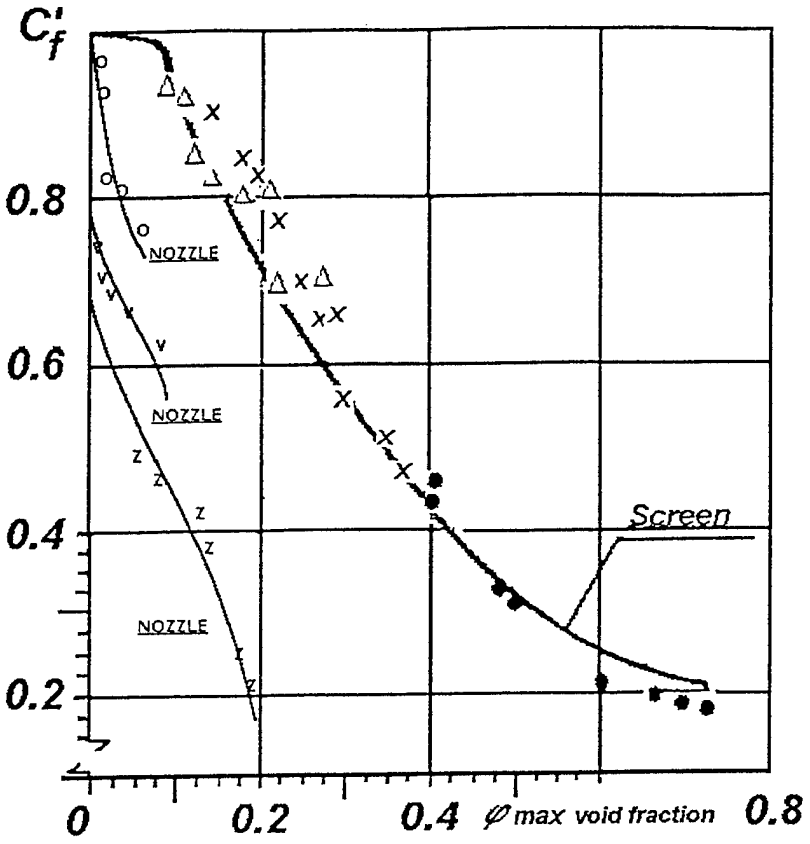

Key:

Nozzle Yoshida [2] Flow Speed u[m/s] o, v, z = 8.00 m/s
Injection Rate Q[l/min] o = 35 l/min v = 100 l/min z = 200 l/min

Bottom Screen Barbanel [3] Flow Speed u[m/s] △ : u = 4.36 m/s X : u = 8.55 m/s ● : u = 10.9 m/s

Fig. 8 Influence on downstream Air Injection on Cf' = Cf with air / Cf without air at Velocity u.

OPTIMIZATION OF THE DISTRIBUTED GAS INJECTION INTO A TURBULENT BOUNDARY LAYER FOR THE DRAG REDUCTION

V.G. Bogdevich, L.I. Maltzev, and A.G. Maluga

Institute of Thermophysics,
Siberian Branch of the Russian Academy of Sciences, RUSSIA

Abstract - The gas-bubble saturation of near-wall liquid flows as an effective method for reduction in the skin friction had passed already the stage of laboratory testing and now can be recommended for practical applications on sea ships.

The key question for engineer accomplishment of this method for drag reduction is the development of the optimal method of boundary water layer saturation with air microbubbles. One of possible methods is the air injection through a porous coating. The purpose of this report is to make the analysis of different parameters of the coating and the recommendations on the optimal air injection into the water boundary layer.

I. INTRODUCTION

The gas bubble saturation of the near-wall liquid flow is a well-known method for drag reduction for water-moving objects.

To the present time many works were performed in this field. The main characteristics of he drag-reducing gas-liquid boundary layer were revealed. It was demonstrated that the gas concentration profile has a maximum for applicable variants of this technique (a considerable drag reduction with a low gas flow rate). This maximum of gas concentration must be high, and the layer with a high gas concentration must be thin. This thin layer has to be close to the solid wall. Most likely that the bubble size in a given transversal cross-section of the boundary layer is not significant for reduction of the local friction. However, to provide a microbubble boundary layer with drag reduction along the whole body, we must provide formation of very small bubbles.

So, the requirements to near-wall gas-liquid layers, producing reduced friction, are known. There are exist some methods for their formation. To the present day three methods for gas injection to the near-wall liquid flow became wide-spread:

- distributive blow-in of gas through a penetrable coating [1–4];
- slot injection of a gas-liquid mixture [5–6];
- slot gas injection under the near-wall water jet [5].

First impressive results on friction reduction due to gas microbubble saturation of water boundary layer were obtained using the first method. The most number of papers in this field also imply the use of the penetrable sheets. However, the possibilities of this method are still not discovered completely and the application to real objects faces with some problems. The matter is that the choice of the parameters of a penetrable sheet and its position on a moving body is a multi-parameter task. The structure of this coating, material properties, the porosity distribution over the gas ejection area – all these features affect the efficiency of the gas bubble saturation for friction reduction.

All these problems, as well as some others, are discussed in this report.

II. EXPERIMENTAL SETUPS

Our experiments were performed in two series. We used an streamlined flat plate (Figure 1) for the first series, and an axisymmetrical model – for another series.

The plate had the following size: 910 mm (length) × 350 mm (width) × 60 mm (thickness). We installed a porous flat sheet (with the size of 350 mm × 100 mm) on the plate's top side at the distance of 300 m from the front edge. There was an air supply chamber inside the body which was covered with a porous coating. It was sectioned into 6 equal parts placed consequently along the stream. The pressure-regulated air flow can be supplied to every of these sections through special pipelines.

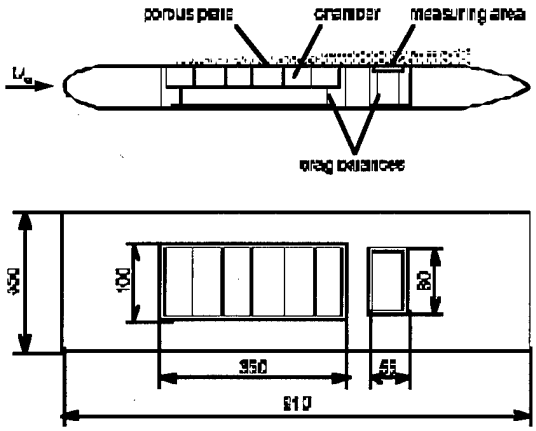

Figure 1. Schematic diagram of a flat plate

In our case a porous covering was a stack of thin sheets with groves on both sides. Actually, this penetrable covering was a perforated element with microchannels directed normally to the streamlined surface. The sheet thickness was 1.2 mm, and the slits between stacked sheets were about 30 microns.

Downstream (50 mm) of this porous area we put an impenetrable measuring plate with the size of 55 mm × 80 mm. Both penetrable and measurong plates were installed on springy elements which allowed us to measure the integral friction forces for every plate. The flat plate was tested in a water tunnel. It was installed in the horizontal plane of the working section with a cross-section 400 mm × 400 mm. All tests were performed at the main flow velocity $v_\infty = 3$ m/s.

The axisymmetrical model had a diameter of 175 mm, its length was 1750 mm with a long cylindrical part which was about

75% of the total length. Downstream the ogival head part (length – 100 mm) we installed 4 removable rings made from penetrable or impenetrable material.

The penetrable coverings were fabricated according the technique, mentioned above. The thickness of stacked sheets was 0.8 mm, and the intersheet clearance was 30 microns. The relative area of every section was 8% of the total wetted area of the studied body. The model was tugged by a special scooter in an open pool with the velocity of 15 m/s.

III. EXPERIMENTAL RESULTS

A. The effect of the relative area of the penetrable coating on the efficiency of the gas bubble saturation

The coefficients of the integrated friction on the measuring plate as functions of the penetrable section length are plotted in Figure 2 (flat plate).

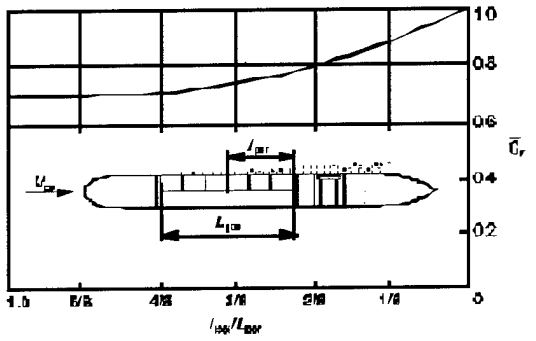

Figure 2. The integrated skin friction ratio on the measuring plate vs. the length of porous plate for $C_Q = 0.0028$

We had a uniform gas injection to the near-wall stream with a flow rate, corresponding to the dimensionless coefficient $C_Q = 0.0028$, through all six sections. The effect of the friction reduction on the measuring plate was 30%. Here $C_Q = Q/(S \cdot v_\infty)$, where Q is the volumetric gas flow rate, S is the area of penetrable coating and v_∞ is the main flow velocity. After we tuned off the gas supply through first three sections, the effect of friction reduction stayed almost the same (keeping the ratio $C_Q = 0.0028$) – see Figure 2. Note that with the same C_Q the twice reduction in area means the twice reduction in the air flow rate.

The following switching off the 4th and 5th sections (with the same $C_Q = 0.0028$ and corresponding decrease in the flow rate Q) caused the linear loss in the initial drag reduction.

The dependency of the total drag coefficient on the gas flow rate is depicted in Figure 3 for our axisymmetrical model. It was four variants of the gas injection into the stream. Here the gas flow rate coefficient is $C_{Q1} = Q/(S_1 \cdot v_\infty)$, where S_1 is the wetted area of the body.

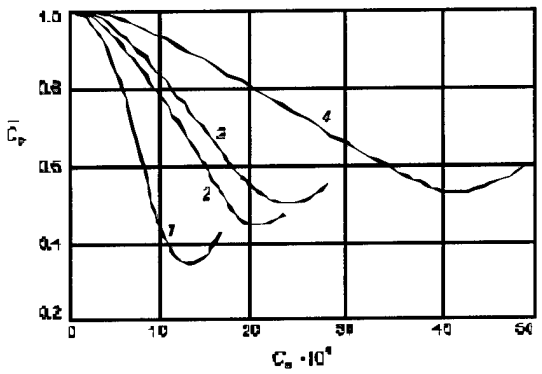

Figure 3. Drag coefficients of axisymmetrical body vs. the coefficient of the air flow rate.
1 – $S_{por} = 0.08S_{tot}$; *2* – $S_{por} = 0.16S_{tot}$; *3* – $S_{por} = 0.24S_{tot}$; *4* – $S_{por} = 0.32S_{tot}$

Curve *1* describes the gas injection through the section one, curve *2* – through first two sections, curve *3* – through first three sections, and curve *4* – through all four sections. One can see that only gas blow-in through the first section yielded a considerable drag reduction with a low volumetric air flow rate (comparative with other variants).

A further decrease in the relative penetrable area to 4% of the total model area diminished the efficiency of the gas bubble saturation as a tool for drag reduction.

From our experiments with a flat plate and an axisymmetrical model we came to the conclusion that there exists an optimal ratio of the penetrable area to the total wetted area, and this ratio is significantly less than 1.

B. The effect of the gas injection intensity

Our comprehension of the mechanism of drag reduction dictates that the bubble saturation of a turbulent boundary reduces the transversal impulse flow of liquid. As a result, these bubbles prevent the intensive development of the boundary layer. Moreover, the fluid density near a solid wall also decreases.

The upper limit of gas content in the mixture may be up to 81% (if bubbles are spheres of different diameters).

Obviously, the increase in the gas content above certain level causes the flow restructuring. Numerous examples demonstrates that being attained some minimum, the drag begin to increase with air flow rate. It is explained by merge of bubbles and resulting loss of the two-phase layer stability.

The second problem of the air injection intensity is the outlet velocity of gas from pores.

There are data on the pressure distribution downstream the porous injection zone at different levels of C_Q (Figure 4). Obviously, at $C_Q < 0.01$ one cannot observe any significant change in the wall pressure. But at $C_Q > 0.01$ there exists a zone of decreased pressure; this may be interpreted as water stream repulsion from the wall due to air blow-in.

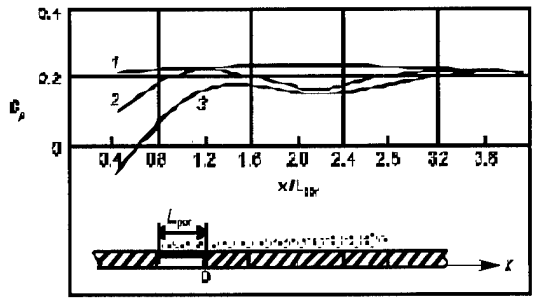

Figure 4. Pressure distribution along the plate after the injection section. *1* – $C_0 = 0.007$; *2* – $C_0 = 0.012$; *3* – $C_0 = 0.022$

The air flow rate $C_Q = Q/\left(S_{\text{por}} \cdot v_\infty\right)$ is a mean-rate relative velocity of air injection through the porous zone (as if air were supplied uniformly through the whole zone of the porous element). We already explained that the penetrable covering is a stack of thin sheets, ant air is fed through the inter sheet clearings. Their thickness was 1.2 mm, ant the slot size was 0.03 mm. Therefore, the actual velocity of air injection is 40 times higher than the calculated mean-rate velocity.

We can see from Figure 4 that the flow restructuring in the near-wall gas-liquid flow and the formation of detachment zone behind the injection zone take place for mean-rate air velocity of $C_Q = 0.01$ (that is, the actual velocity at the slot outlet was $\overline{v_*} = 0.4$).

In our experiments with the axisymmetrical model the most significant drag reduction was achieved for air blow through the only first section. For this $S_{\text{por}} = 0.08 \times S_{\text{tot}}$ at $C_{Q1} = 0.00125$. Here the sheets thickness was 0.8 mm with the clearance size equal to $\Delta h = 0.03$ mm. The best result on drag reduction was obtained for $C_Q = 0.0156$ ($\overline{v_*} = 0.42$).

From all things concerned, we can conclude that in making the bubble-saturated layer for drag reduction (with a porous coat-ing) we have to obtain a uniform (in mathematical sense) air injection with the out-of-pores velocity not higher than 40% of the main stream. Velocity above this level may cause intensive mix-ing in the boundary layer; this would spoil the gas concentration profile and increase the pressure and velocity pulsation in the boundary layer.

C. The effect of air injection distribution along the stream on the efficiency of the air saturation

Experiments with axisymmetrical model demonstrated that the law of the flow rate of injected air along the stream must be decreasing. Experiment with sectioning of the injection zone and different variant of active sections combinations persuaded us that the best results were obtained if the air flow rate decreases from the first section to the next one (counting downstream). There was always a negative pressure gradient on the head part of real objects. Looking from the practical point of view, it will be easy to provide a desired air flow rate distribution along the body using a single air-supply chamber with a uniform porous covering.

D. The wetting effect of the porous coating on the characteristics of a gas-liquid flow

There are three media which participate in formation of a gas-liquid flow: gas, liquid, and solid porous coating. All the results mentioned above were obtained for models fabricated from aluminum alloys (and porous coating as well). That is, they had hydrophilic surfaces.

But our experiments with the flat model discovered that the treating of the porous coating by a special hydrophobic substance change situation dramatically. If the porous material was hydrophobic, we have gaseous torches at the pores outlets. Their interaction with water stream makes an unstable loose gas-liquid flow.

Figure 5 demonstrates the difference in the integral gas-saturation effect between hydrophilic and hydrophobic porous coatings.

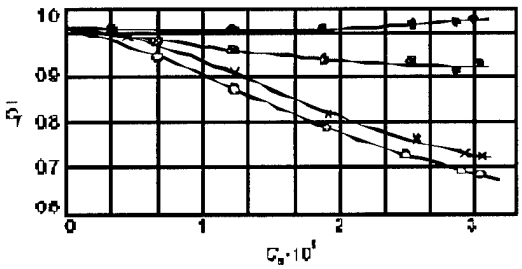

Figure 5. Integrated skin friction on the porous plate (curves *1*, *2*) and on the measuring plate (curves *3*, *4*) as the functions of the air flow rate coefficient *1*, *2* – hydrophobic porous coating; *3*, *4* – hydrophilic porous coating

The gas inflation through the hydrophobic porous coating did not yield any friction reduction on the coating (curve *1*), and made only slight decrease of that on the measuring plate downstream the porous zone (curve *2*).

Under the other equal conditions, the air inflation through a hydrophilic coating allowed us to decrease friction considerably both on the coating (curve *3*), and on the measuring plate downstream it (curve *4*).

IV. CONCLUSION

We made experiments with a streamlined plate and axisym-metrical model aimed to find out the effect of different parame-ters of porous coatings on the efficiency of the gas-bubble-satura-tion method on the friction reduction.

It was discovered that the percentage of the porous zone on an oblong body must be about 8–10% of the total wetted area. This penetrable coating have to be positioned at the head part of the body, where exists a negative pressure gradient. An efficient variant may be obtained if the air injection rate decreases along the body. The material of the porous coating must be hydrophilic.

Naturally, these are only recommendations. The precise knowledge of an injection distribution and parameters depends on the shape and size of the body, etc.

V. ACKNOWLEDGMENT

The research described in this report was partially supported by INTAS, grant number INTAS-94-3737.

VI. NOMENCLATURE

C_f integrated skin friction with gas bubbles;

C_{f0} integrated skin friction without gas bubbles;

$\overline{C_f}$ dimensionless integrated skin friction, $(\overline{C_f} = C_f / C_{f0})$;

C_Q dimensionless air flow rate, $(C_Q = Q/(v_\infty S_{por}))$;

C_{Q1} dimensionless air flow rate, $(C_{Q1} = Q/(v_\infty S_{tot}))$;

v_∞ main-flow velocity, (m/s);

S_{por} area of the porous coating, (m^2);

S_{tot} area of the wetted surface of a body, (m^2);

v_* air velocity through pores, (m/s);

Q volume air flow rate, (m^3/s);

D hydrodynamic drag of axisymmetrical body with gas saturation, (kg);

D_0 hydrodynamic drag of axisymmetrical body without gas microbubbles, (kg);

$\overline{C_D} = D/D_0$.

VII. REFERENCES

1. G.S. Migirenko and A.R. Evseev, "Turbulent boundary layer with gas saturation". *In: Problems in thermal physics and physi-cal hydrodynamics,* Novosibirsk: Nauka Publ. House, 1974. (In Russian).

2. V.G. Bogdevich and A.G. Malyuga, "Distribution of skin fric-tion in turbulent boundary layer of water behind the gas injection point". *In: Study on the boundary layer control.* Novosibirsk, 1976. (In Russian).

3. V.G. Bogdevich and A.R. Evseev, "Effect of gas saturation on wall turbulence". In: C.C.Kutateladze and G.S. Migirenko (ed.), *Investigation of Boundary Layer Control.* Novosibirsk: Thermo-physics Institute Publishing, 1976. (In Russian).

4. G.L. Merkle and S. Deutsch, "Microbubbles Drag Reduction". In: Bushnell and Hefner (eds.) *Viscous Drag Reduction in Boundary Layers. (Progress in astronautics and aeronautics*; vol. 123), 1993.

5. L.I.Maltzev, "Jet Methods of Gas Injection into Fluid Bound-ary Layer for Drag Redution", *Appl. Sci. Res.* v. 54, 1995.

6. H. Kato, M. Miyanaga, and M.M. Guin, "Frictional Drag Re-duction by Injecting Bubble Water into Turbulent Boundary Layer". FED v. 190, *Cavitation and Gas-Liquid Flow in Fluid Machinery and Devices*. ASME, 1994.

EFFECT OF MICROBUBBLE DISTRIBUTION ON SKIN FRICTION REDUCTION

Yoshiaki Kodama
Ship Research Institute
6-38-1, Shinkawa, Mitaka
Tokyo 181-0004, Japan
kodama@srimot.go.jp

Abstract - Microbubble experiments were carried out using a small circulating water tunnel. The skin friction reduction up to 40% was obtained. The local void ratio was measured using two methods, one by inserting a suction tube in the test section, and the other by counting the bubbles from photographs. The results suggest that the local void ratio near the wall is a dominant factor for the skin friction reduction.

I. INTRODUCTION

It is well known that small bubbles called microbubbles injected into the boundary layer on a solid wall reduce the skin friction significantly[1]. But the energy needed for injection is not nominal, and the net drag reduction is difficult to obtain when it is applied to full-scale ships. Therefore, it is necessary to reduce the amount of air and/or increase the drag reduction by studying the drag reduction mechanism. Recently, studies on microbubbles have been carried out in Japan experimentally[2] and numerically[3]. The author's group are studying the mechanism and the scale effect of microbubbles[4], in order to apply the technique to full-scale ships. In this paper, some recent experimental results will be shown.

II. EXPERIMENTS

II.1 Test facility

A small circulating water tunnel specially designed for microbubble study was constructed (Fig.1). The air is injected in the test section to generate microbubbles. At downstream of the test section there is a

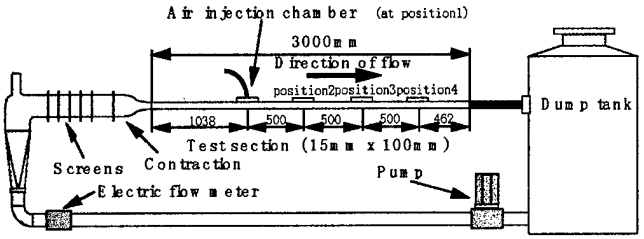

dump tank, in which the injected bubbles are removed by buoyancy, thus making continuous tests possible.

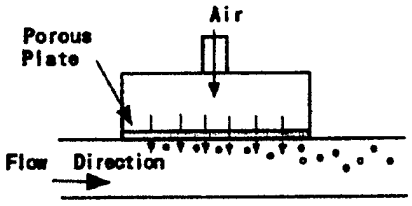

Fig.1 A small circulating water tunnel for testing microbubbles

Fig.2 Bubble generation using a porous plate

The tunnel has a test section of 100mm times 15mm times 3000mm in size. The bubbles are generated by injecting air through a porous plate made of metal with nominal pore radius of 10mum (Fig.2). The plate is located at 1038mm downstream from the upstream end of the test section, where the flow is fully developed. This location will be called Position 1. At three consecutive locations, 500mm apart from each other, various measurements are possible. These locations will be called Positions 2, 3, and 4 in the downstream order.

The amount of injected air is represented by the average void ratio α_a defined as

$$\overline{\alpha}_a \equiv \frac{Q_a}{Q_a + Q_w} \qquad (1)$$

where
Q_a : air flow rate
Q_w : water flow rate

II.2 Bubble photographs

Photographs of the microbubbles were taken using a high-definition CCD camera (Fig.3)[5]. A YAG laser was used as a light source, taking advantage of its short duration. The light sheet was placed 30mm from

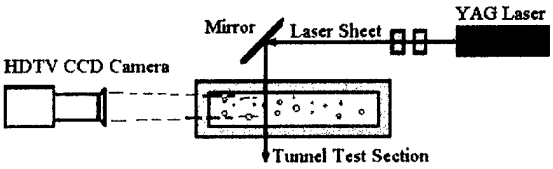

the plane of symmetry toward the camera, in order to get a better image. Fig.4 shows the photos at α_a=0.05 in Positions 2 and 3. The flow is from

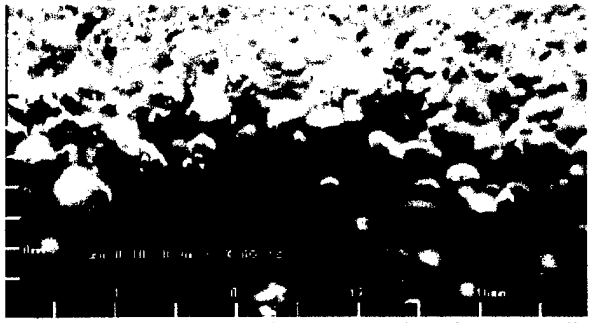

right to left. The top end of each photo corresponds to the upper wall of the test section. The vertical length of the photo corresponds to 10mm. The bubbles are clustered near the top end, where the bubbles were generated. The size of the bubbles are mostly less than 1mm in diameter, although it depends on the flow speed.

Fig.3 Camera and light source layout[5]

(a) U=7m/sec, Position 2

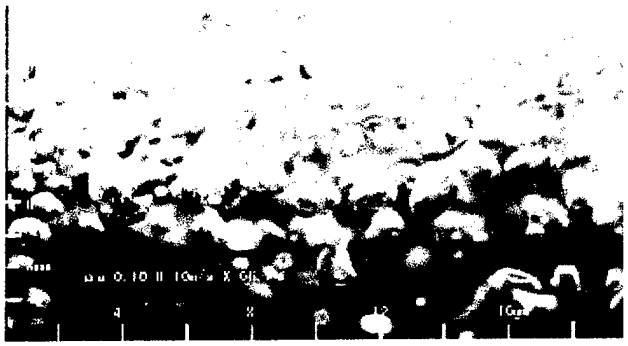

(b) U=10m/sec, Position 2

(c) U=7m/sec, Position 3

(d) U=10m/sec, Position 3

Fig.4 Photographs of microbubbles at α_a =0.053[5]

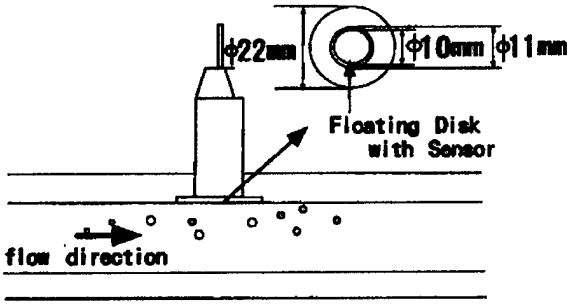

II.3 Skin friction

A skin friction sensor is useful in measuring skin friction directly[6]. A sensor of 2 grams full scale was used for measuring skin friction with or without bubbles (Fig.5). The sensor was placed on the plane of symmetry of the test section.

Fig.5 Skin friction sensor

In Fig.6, the measured Cf values are shown as the ratio to C_{f0}, the Cf value in the non-bubble condition. When the air is injected, the flow speed increases, and therefore, in the bubble condition, the C_{f0} value was corrected as a function of Q_a using the following formulae.

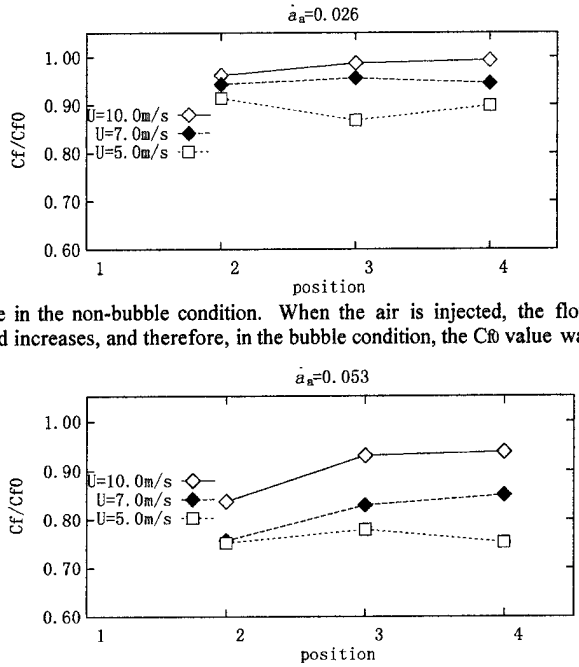

(a) α_a =0.026

(b) α_a =0.053

(c) α_a =0.081

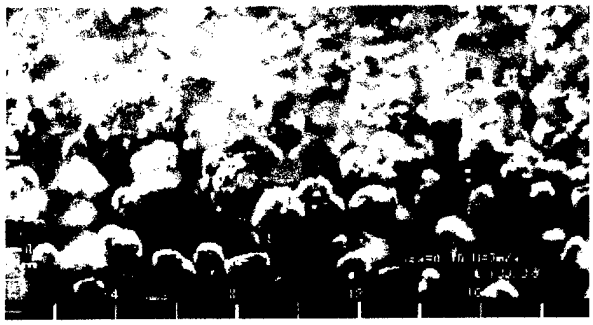

$$C_{f_0}(Q_a) = C_{f_0}(0)\frac{\tau(u)}{\tau(U)} \qquad (2)$$

$$\tau(f) = 0.03325\rho\nu^{1/4}f^{7/4}r^{-1/4} \qquad (3)$$

(d) αa =0.11

Fig.6 Skin friction reduction.

The skin friction was measured at three speeds in three downstream locations, changing the rate of bubble injection. At U=10m/sec, the skin friction reduction increases as αa increases, saturating at αa =0.081 and 0.11 and reducing rapidly in the downstream direction. At U=7m/sec, the overall tendency is similar to that at U=10m/sec, except that the reduction persists longer in the downstream direction. At U=5m/sec, the tendency is different from the other two, i.e., the reduction saturates at small αa values and appears to increase in the downstream direction. In total, the microbubbles are the most effective at U=7m/sec.

What is difficult to understand is that, at αa =0.026 and 0.053, the skin friction reduction is consistently r at smaller U. Generally the bubble size is greater at lower speeds due to the smaller shear stress acting on the porous plate where the bubbles are generated, and, if it is true that

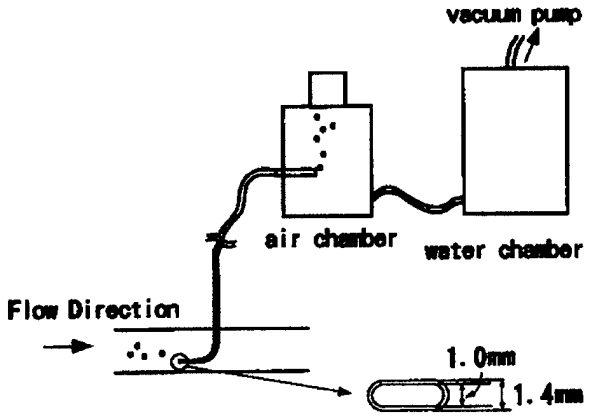

smaller bubbles cause r skin friction reduction, the tendency should be

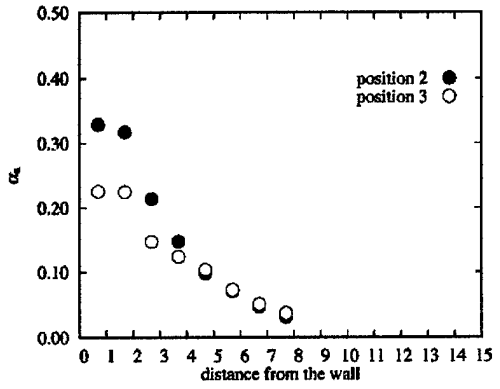

the opposite.

II.4 Local void ratio

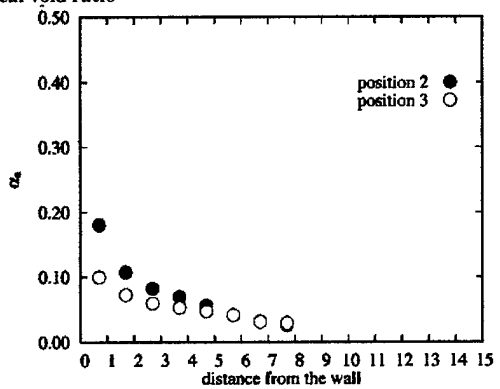

In order to clarify that point, it is necessary to measure local properties. Thus the local void ratio αa was measured using a suction tube system (Fig.7) similar to the one used in ref.6. A small tube with a flat opening was placed in the test section. The tube was connected to a vacuum pump for suction through two chambers to measure air volume and water volume separately.

Fig. 7 Suction tube for measuring local void ratio

(a) U=7m/sec

(b) U=10m/sec

Fig.8 Local void ratio αa at αa =0.053.

The measurements were made at two speeds in two locations at αa =0.053 (Fig.8). At U=7m/sec, αa closest to the wall is greater in Position 2 than in Position 3, which, together with the results shown in Fig.6(b), suggests that the local void ratio near the wall is the dominant factor for skin friction reduction. The αa values closest to the wall at U=7 and 10m/sec and in Positions 2 and 3 correlate well with the Cf / Cf0 values in those conditions. But the integrated αa at U=10m/sec is clearly smaller than that at U=7m/sec. They should be about the same because αa was kept the same. The reason for this is perhaps that the suction pressure was not appropriately controlled, as described in ref.6.

II.5 Measurements using photographs

The distribution of the bubbles was measured at αa =0.053 from the photographs as shown in Fig.4. The measurement volume was 18.75mm times 10mm times 1mm, the size of the photo and the thickness of the laser sheet. At each condition the number and size of the bubbles were obtained by counting in eight photos and averaging. The average number of counted bubbles was 111.9 at U=7m/sec and 144.1 at U=10m/sec.

Fig.9 shows the bubble radius distribution and Table 1 shows the mean bubble radius. The bubble radius is distributed between zero and 0.8mm. There is no significant difference in Positions 2 and 3. The bubble size is slightly smaller at the higher speed.

(a)U=7m/sec.

(b) U=10m/sec.

Fig.9 Bubble radius distribution. αa =0.053.

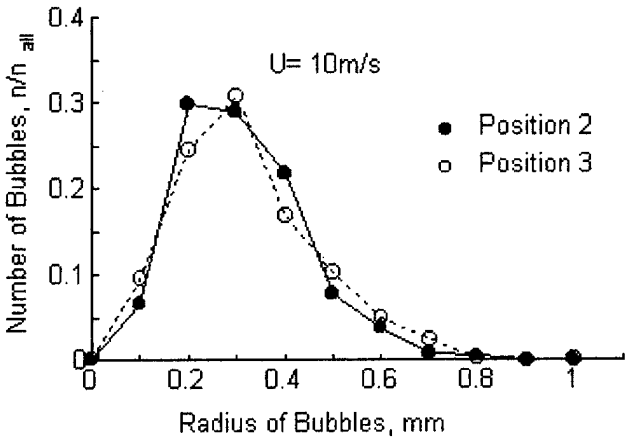

Fig.10 shows the local void ratio. Oscillations in the distribution suggest that the number of photographs used in each condition (i.e. 8) was not enough. At U=7m/sec, the distributions in Positions 2 and 3 are similar,

U \ Position	2	3
7 m/sec	0. 38	0. 34
10 m/sec	0. 31	0. 33

and they are comparable to those in Fig.8(a). At U=10m/sec, Position 3

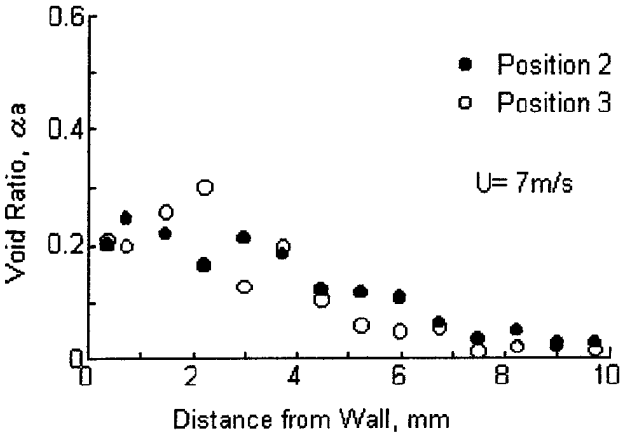

seems to have higher void ratio near the wall, which is in contradiction to that shown in Fig.8(b).

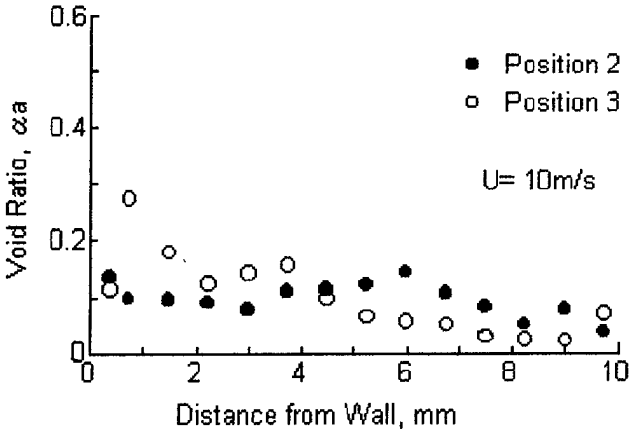

Table 1 Mean bubble radius (mm)

U \ Position	2	3
7 m/sec	0. 118	0. 094
10 m/sec	0. 111	0. 093

(a) U=7m/sec.

(b) U=10m/sec.

Fig. 10 Local void ratio distribution in depthwise direction.

Table 2 Void ratio integrated in half depth. α_a =0.053 & $\alpha_{a\,H/2}$=0.10ms

summing all the bubble volume and dividing by the measurement volume. The corresponding average void ratio termed as $\alpha_{a\,H/2}$ is obtained using eq.(1) where Q_w this time is the flow rate in the upper half of the test section. Thus α_a =0.053 corresponds to $\alpha_{a\,H/2}$=0.10. The integrated void ratios are in good agreement with $\alpha_{a\,H/2}$, suggesting the reliability of this method based on photographs.

This result suggests that the suction tube method whose results are shown in Fig.8 has a problem, especially at U=10m/sec. Further study is needed in this point.

III. CONCLUSIONS

The skin friction was measured in a circulating water tunnel at various flow conditions with or without bubbles. The local void ratio was measured using two methods. They suggest that the local void ratio close to the wall is a dominant factor for skin friction reduction due to microbubbles. Further studies are needed for clarifying the mechanism for skin friction reduction by microbubbles, and for reducing the amount of bubbles needed, in order to put the method into practical use.

IV.REFERENCES

1.Bushnell, D.M. and Hefner, J.N.(ed.):Viscous Drag Reduction in Boundary Layers", Progress in Astronautics and Aeronautics vol.123, AIAA, 1990.

2.Kato, H. et al.:"Frictional Drag Reduction by Injecting Bubbly Water

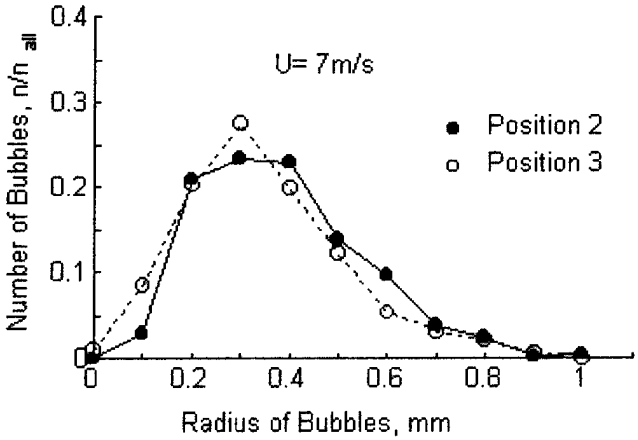

into Turbulent Boundary Layer"; Cavitation and Gas Liquid Flow in Fluid Machinery and Devices, FED-vol.190,ASME, 1994, pp185-194.

3.Kanai,A. et al.:"Direct numerical simulation of multiple bubbles in a boundary layer", Proceedings of the 11th Computational Fluid Dynamics Symposium, pp.221-222, December 1997, Tokyo, Japan.

4.Takahashi,T. et al.:"Streamwise Distribution of the Skin Friction Reduction by Microbubbles", J. of the Society of Naval Architects of Japan, vol.182, November 1997.

5.Kakugawa,A. et al.:"The Effect of Microbubble Distributions on Drag Reduction", 70th General Meeting of Ship Research Institute, December 1997.

6.Guin, M.M. et al.:"Direct Skin Friction Measurements and Observation of Drag Reduction in a Two-Phase Air-Water Channel," ASME Symposium, San Diego, 1996.

7.Schlichting,H.:"Boundary-Layer Theory", 6th edition, McGrawhill, 1968.

COMBINED POLYMER AND MICROBUBBLE DRAG REDUCTION

R.B. Philips, J.M. Castano and J. Stace

Naval Undersea Warfare Center
Division Newport
Newport, Rhode Island 02841

philips@c80.npt.nuwc.navy.mil
castanojm@code80.npw.nuwc.navy.mil

Abstract - Two well known skin friction reducing techniques were combined to examine the possibility of realizing synergistic drag reductions, i.e., a reduction in drag greater than the sum of each reducing technique individually. Polymer (polyethylene Oxide) additive and gas (compressed air in the form of a microbubble sheet) injection into fully developed turbulent boundary layers have separately demonstrated substantial and consistent drag reducing capabilities. These two robust drag reducing techniques were combined in a flat plate, salt water, tandem injection experiment employing a set of floating element drag balances immediately behind the injection locations to measure integrated skin friction. Individually each additive showed expected levels of drag reduction. Combining the two techniques showed drag reduction levels exceeding the individual sum of drag reduction up to 10%. The order of injection was an important factor in obtaining synergy.

I. INTRODUCTION

A number of investigators have noted the similarities between polymer and microbubble drag reduction [1] [2] [3]. The injection of polymers or microbubbles into the boundary layer has been shown [4] [5][6][7] to remove turbulent flow energy and change momentum transport near the wall in a turbulent boundary layer thereby reducing skin friction. For microbubble drag reduction, Pal et al. [6] and, more recently, Guin et al.[8] have demonstrated that bubble concentrations must be maximized between the wall and a y+ of 150 for effective drag reduction ($y+ = y\,u^*/\nu$ where, y is normal distance from the wall, u^* is the friction velocity and ν is the kinematic viscosity). Walker et al. [9] determined the optimal polymer injection rate for polymer drag reduction in a channel to be 5.1 times the volumetric flow rate of the viscous sublayer, demonstrating the importance of maximizing the polymer concentration in or near the buffer layer. This observed similarity in the drag reducing mechanism of each method suggests the possibility of mutually enhancing their respective mechanisms by simultaneously injecting polymers and microbubbles into a turbulent boundary layer. The ability to increase skin friction reduction beyond the sum of the individual components, thereby creating a synergistic effect, implies that bubbles may promote the elongation of polymer molecules and/or that polymers enhance the concentration of small bubbles near the wall. In either case, the size of the smallest turbulent fluctuations would be increased, resulting in a thickening of the buffer layer and an upward shift in the log-region velocity profile.

Indeed, a study performed by Malyuga et. al. [10] in the former Soviet Union suggests synergistic drag reduction takes place when microbubble and polymer injection takes place simultaneously. Malyuga, who performed microbubble drag reduction experiments in the late 1970's, injected aerated polyethylene oxide solution into a turbulent boundary layer and measured skin friction on three 23-mm diameter flush mounted disks downstream of the injection point. Malyuga's team concluded that there was a "... mutual intensification of two methods for drag reduction." They attribute this effect mostly to the greater concentration of small diameter bubbles which they observed when the polymer solution was aerated just prior to injection. Few physical dimensions of the polymer aeration process were provided from which to discern the possible bubble size distribution. The aerated polymer solution was injected through an 8-degree, 1.8 mm wide slot. The Russian authors suggested their polymer (polyethylene oxide - PEO) reduced bubble surface tension thereby generating smaller bubbles than expected. They measured local skin friction reductions up to 80% at the floating element closest to the injection slot, with reductions tapering off further downstream. Malyuga noted that the drag reduction levels attained by aerating the polymer solution would exceed reduced drag levels measured with only air or only polymer injection into the boundary layer.

The possibility of enhancing the intrinsic ability of each polymer molecule, and/or gas microbubble, to reduce skin friction once introduced into a turbulent boundary has significant ramifications. In many applications, both techniques are limited in practice by their friction reducing density, i.e., the amount of drag reduction per unit volume of polymer solution or gas injected into the boundary layer. Microbubble drag reduction on submerged vehicles requires a greater mass of gas to maintain reduced drag as speed and ambient pressure increase. Efficient polymer drag reduction techniques require either highly concentrated polymer slurries be carried by the vehicle then hydrated to lower concentrations prior to injection or the onboard processing of the bulk material into a drag reduction solution. If the combination of polymer and microbubbles can reduce the volume of gas and/or polymer solution required to maintain desired levels of drag, these two robust and well known techniques become much more attractive for undersea applications.

In this study, a flat plate test geometry with two ejectors placed in tandem was employed to determine if synergistic drag reducing effects were possible with simultaneous, but separate, polymer and microbubble injection. Two separate ejectors were employed for the additives to eliminate uncertain plenum mixing attributes from the test variables. The parameter space for this investigation included streamwise injection order (i.e., polymer upstream of microbubbles and vice versa), volumetric flow rates for both additives. The measured quantities were integrated shear stress at multiple downstream locations, and other ambient pressure, temperature and velocity values. Laser anemometry was employed to confirm the baseline boundary layer parameters, in addition to the integrated shear stress measurements. Salt water was used as the base fluid since bubbles produced in salt water are roughly an order of magnitude smaller than those produced similarly in fresh water (Cary et. al. [11], Hrubes et. al. [12] and Monahan et. al [13]), and bubble size may be a factor in microbubble drag reduction and in combination with polymers. In a previous bubble size study, Kuklinski [14] showed that the salt water had a very significant effect upon bubble size versus fresh water. However the combination of polymer with salt water produced little additional effect upon the bubble size distribution.

II. FACILITIES AND PROCEDURE

The experiments were conducted in the closed loop Hydrodynamics Research Water Tunnel at NUWC. It operates with both man-made salt water and fresh water for investigations where the fluid medium is a critical parameter and has a fully integrated water treatment system. This facility includes an on-line air removal or deaeration system. The maximum operating velocity in the test section is 7.6 m/s (25 ft/s), which is driven by a 30 hp motor. The motor drives an axial flow pump, which has four blades with twist designed to give uniform radial velocity profiles. A stainless steel honeycomb with 0.25-inch cells, six inches thick (for an aspect ratio of 24) is located upstream of the nozzle to straighten the flow and control of background turbulence. Finally, the tunnel is equipped with an automated static pressure control system, which maintains the pressure in the test section within ± 1 psi.

The facility has a 3.05 m (10-ft) long test section, with a .305m (1-ft) square cross section, which allows for large arclength Reynolds number investigations. The test section has 16 access panels or windows 25.4 cm (10-in) by 61 cm (24-in), which allow for up to 65% of the test section to be optically accessible. Pressure taps along the test section, and in the window panels, allow for streamwise pressure gradient measurements, which are made with a rotating tap selection valve and pressure sensor.

The flat plate testbed, has an elliptical leading edge and can be positioned in the test section so as to produce a variety of streamwise

pressure gradients. A trailing edge flap is used to make small pressure gradient corrections to be made while running. The plate has three identical 0.508 m long by 0.178 m wide inserts which can be removed,

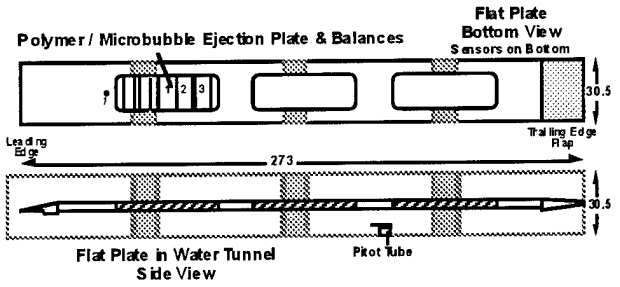

Fig. 1. Schematic of overall flat plate (dimensions in cm)

instrumented and re-inserted at any of three streamwise locations. Side and top views of the plate configuration are provided in figure 1. The orientation of the plate was such that the injection and drag balances were on the bottom surface of the flat plate. This made the fabrication of the drag balances easier.

For this test the first insert was designed to carry a polymer injection module, a microbubble injection module, and three floating element skin friction balance modules. Each module was interchangeable so that their relative streamwise positions could be varied as desired. A schematic of this instrumented injection insert is given in figure 2.

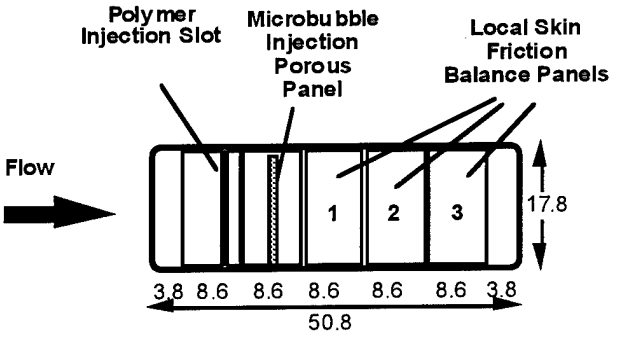

Fig. 2. Schematic of injectors and drag balances - upstream polymer, downstream microbubble shown (dimensions in cm)

In the design of this experiment, flexible injection geometries were considered an important feature since this would allow for injection position and mixing parameters to be analyzed. The five modules shown in figure 2 can be positioned in any order desired, however, the only configurations tested to date consisted of three balance modules downstream of two injection modules. The three floating element balances were designed to be very stiff yet sensitive to ± 3.0 grams over a range of 100 grams (±3% error under static, calibration load conditions). A sample calibration curve is provided in Figure 3. Error bars indicating ±2 standard deviation levels are shown. Drag was measured via a shear web member made of 0.002-inch thick brass shims for each element. Four bending members which only allow motion in the streamwise component support each element and eliminate the possibility of buckling the paper-thin brass shear webs. To further inhibit buckling and promote high bubble concentrations near the wall at lower speeds, the plate-on-top test geometry configuration was used. This required that all the injection and balance test modules face downward, with additives injected beneath the plate in the test section's free stream flow. The center of drag balances 1 and 2 were located 0.679m and 0.766m from the leading edge of the plate respectively.

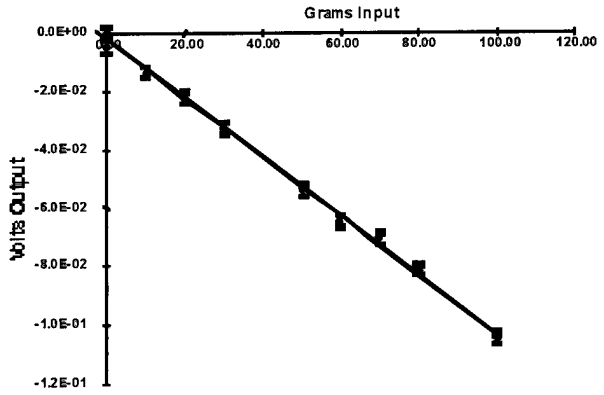

Fig. 3. Plot of drag balance calibration.

Both injection modules (see figure 4) consisted of a small plenum with a row of twelve 1.6 mm (1/16th-in) diameter holes spaced 9.5 mm (3/8-in) apart, through which the additives were introduced. The polymer injection plenum contained a small amount of open-cell foam, and had an 17.8 cm (7-in) wide by 1.6 mm (1/16th-in) slot angled at 15-degrees to the wall. The slot injection angle was designed to minimize boundary layer perturbations during injection. Previous experience with polymer injection hardware has shown that a shallow angle produces a smaller disturbance. This was also the shallowest angle that could be machined while retaining the desired tolerances across the slot. The downstream edge of the slot was fared (rounded) so that the ejected polymer would enter the boundary layer without having to flow over a sharp edge. This provided uniform spanwise distribution of the polymer which was visually confirmed by adding red dye to several preliminary runs of polymer injection.

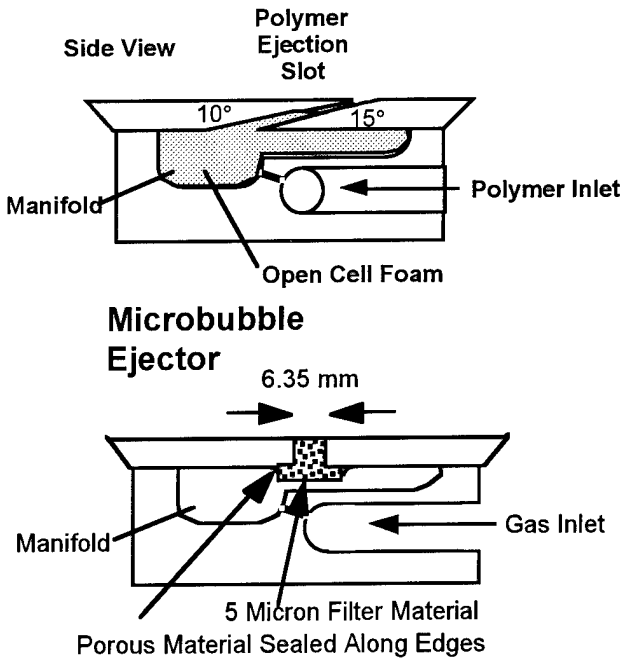

Fig. 4. Schematic of polymer and microbubble ejectors

The air injection module had a 16.5 cm (6.5-in) wide by 6.35 mm (0.25-in) slot into which a 5-μm absolute sintered plastic filter material was fitted. This provided a flush, smooth wetted surface through which a fairly uniform sheet of microbubbles was injected normal to the streamwise flow. There were no quantitative measurements of bubble concentration profiles. Visual observation served to check on the uniformity of the microbubble sheet.

The polymer injection procedure consisted of mixing 18.8 grams of PEO Water Soluble Resin (WSR-301) powder into 18.9 liters of

fresh tap water and allowing the 1000 wppm solution hydrate several hours. Once the 0.1% PEO concentrated solution was sufficiently hydrated, a flexible neoprene tube running through a peristaltic Masterflex L/S pump head was used to pump the polymer solution through the plenum and into the flat plate boundary layer. The Masterflex pump system included a calibrated flow rate readout correlated to the RPM of the three rollers in the pump head providing 600 ml/min ± 3 ml/min at ambient pressure. In-situ calibrations of the polymer pumping system were performed (with the help of graduated cylinders) which provided a correction for test section static pressure conditions. These calibrations demonstrated the polymer flow rate measurements were accurate to within ±5%. The polymer injection flow rate coefficient is defined as,

$$C_{Q_{poly}} = \frac{\{\text{concentration}\} \times \{\text{polymer solution flow rate}\}}{\{\text{baseline boundary layer flow rate}\}} \quad (1)$$

and values ranged from $C_{Q_{poly}} = 2$ to 20 ($x10^{-7}$).

The computer controlled air injection system used a 100 psi proportional in-line regulator designed to maintain a target pressure within ± 2 psi. A simple floating ball flow meter calibrated to a range of 100 ± 20 standard cubic feet of air per hour (SCFH) was positioned just outside the test section. Air flow and temperature (via a J-thermo-couple) were measured and recorded at the entry point of the air flow meter to provide the necessary gas volumetric flow rate correction. A ball valve at the test section air inlet point was used to activate and shut-off the air injection sequence. The gas injection flow rate coefficient is defined as,

$$C_{Q_{gas}} = \frac{\{\text{gas volume flow rate}\}}{\{\text{gas vol flow rate}\} + \{\text{boundary vol layer flow rate}\}} \quad (2)$$

and values ranged from $C_{Q_{gas}} = 75$ to 300 ($x10^{-3}$).

The test variables and all the tunnel operational parameters were continuously monitored and recorded by LabView data acquisition Software. The sampling rate for the tunnel operating parameters was set at 40 Hz and included the bulk velocity, motor RPM, tunnel static and bypass system tank pressures, bulk temperature, and auxiliary system parameters. Data acquisition is performed via a National Instruments SCXI-1000 signal conditioning system and an AT-MIO-16X high-performance multifunction analog, digital and timing I/O board in a 166 MHz Pentium Computer. All the strain gauge data was low pass filtered at 100 Hz, and the sampling rate for all cases was 1 kHz. Drag balances 1 and 2 provided consistent data for most of the runs. Balance 3 failed early on in the experimental program and no results from it will be shown.

The general procedure for the synergy runs consisted of establishing the desired test section velocity (4.27 or 6.10 m/sec) and static pressure (5 to 8 psig) conditions for the run, and then initiating injection sequences while recording time histories for all the test variables. A typical run would include: (1) initiating the data acquisition system to provide a time-history of the event; (2) beginning a velocity 3-step increase up to test velocity giving drag data at different velocities for in-situ balance verification; (3) after reaching steady state at the desired test velocity, a baseline microbubble-only drag reduction injection sequence; (4) after a few minutes to purge gas from the tunnel, a polymer-only injection sequence was begun during which, after several seconds of polymer injection, the same microbubble flow rate previously used was also injected; (5) the polymer and microbubble injection was secured; (6) after purging the tunnel of air, the previous step was repeated at different polymer injection rates; (7) upon completing several dual injection sequences, the flow was reduced to zero velocity in steps to recalibrate the balance drag vs. velocity response. An example of the time history of a data run is shown in figure 5. Post processing of the data consisted of removing observed linear trends (strain gages were not temperature or pressure compensated). Relative drag reduction results were obtained by normalizing drag measurements by the drag with no injection.

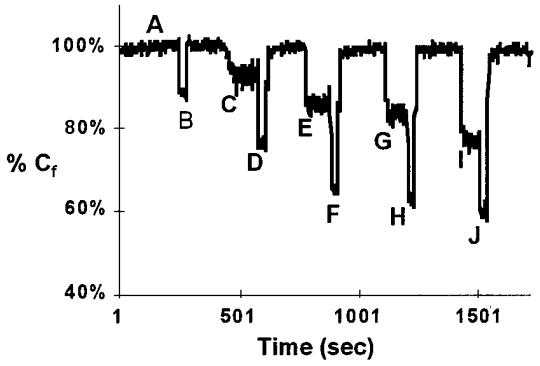

Fig. 5. Time history for drag reduction measurements at 6.1 m/sec, upstream microbubbles, downstream polymer (PEO). A - baseline condition; B - microbubble ejection C_Q=0.098, %C_f=87.9%; C - polymer ejection C_Q=2.7E-07, %C_f=93.3%; D - polymer + microbubbles %C_f=75.2% microbubble C_Q same as B Polymer C_Q same as C; E - polymer ejection C_Q=5.4E-07, %C_f=85.5%; F - polymer + microbubbles %C_f=64.0% microbubble C_Q same as B Polymer C_Q same as E; G - polymer ejection C_Q=6.7E-07, %C_f=82.9%; H - polymer + microbubbles %C_f=61.7% microbubble C_Q same as B Polymer C_Q same as G; I - polymer ejection C_Q=1.0E-06, %C_f=93.3%; J - polymer + microbubbles %C_f=57.8% microbubble C_Q same as B Polymer C_Q same as I.

The baseline boundary layer parameters at the gas and polymer injection location were determined from measurements of velocity profiles by a one-component laser Doppler velocimeter. The profile data were then integrated and curve-fitted to the Law-of-the-Wall to deduce the friction velocity at the surface. Profile sweeps were made as close as possible to the trailing edge of each floating element and at several downstream locations. Several profiles and their corresponding arclength positions are shown in Fig 6 for the 4.27 m/sec (14 ft/sec) case. The profiles are normalized by the displacement thickness and free stream velocity. The fully developed nature of the turbulent boundary layer, corresponding to arclength Reynolds numbers of between 3 and 4 million, is evidenced by the collapsing profile data. Hot film data from probe position 1 (0.4 m from leading edge of plate) indicated turbulent flow at 4.27 m/sec.

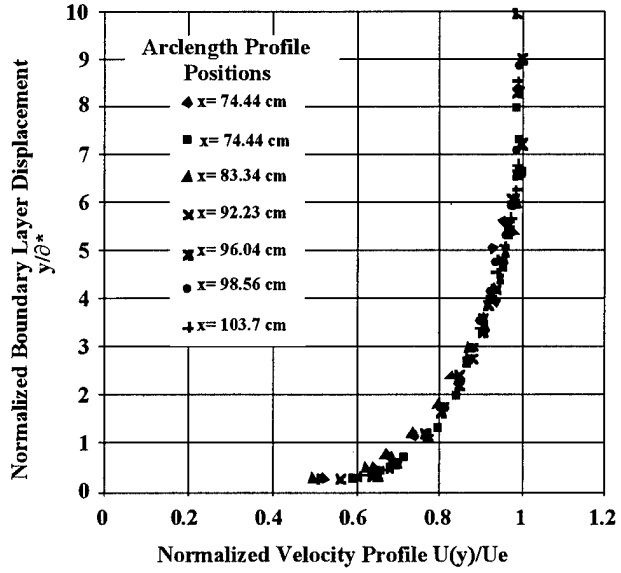

Fig. 6. Normalized velocity profile.

II. RESULTS AND DISCUSSION

For this study, synergistic drag reduction is defined as reductions in drag which are greater than the sum of the drag reductions observed during individual injection (of either gas or polymer). The focus of this effort was to explore the possibility of generating such synergistic drag reduction by employing these two additives in a combined injection into the boundary layer and of mapping regions containing synergy.

During each data run, typified by fig. 5, the response of the drag balances to several flow speeds was examined prior to the start of the drag reduction portion of the run. This provided an in-situ calibration check on all the strain gauges. Also, each additive was injected independently, to provide a gas-only and polymer-only drag reduction response as a function of injected flow rate. The percent drag reduction, defined as

$$DR\% = (C_{f_0} - C_f) \times 100 / C_{f_0} \qquad (3)$$

where C_{f_0} is the baseline or no-injection skin friction coefficient. Sample independent injection data are plotted in Figures 7 and 8. Both additives generated the expected increase in drag reduction with increased additive injection rate.

The first series of combined injection tests were performed with the polymer injection slot located 6.60 cm upstream of the gas injection slot. Figure 9 shows these results. This configuration demonstrated only slight synergistic reductions in drag at best, and more generally, decreased drag reducing capability. In the following figures the experimental combined level is plotted versus the % drag reduction of the two techniques assuming they are only additive. Plotting in this manner clearly shows regions of synergy. The additive drag reduction levels are on the abscissa and the measured levels on the ordinate. The line indicates the reductions are strictly additive. Those values below the line indicate no synergy was present. Results above the line indicate synergy.

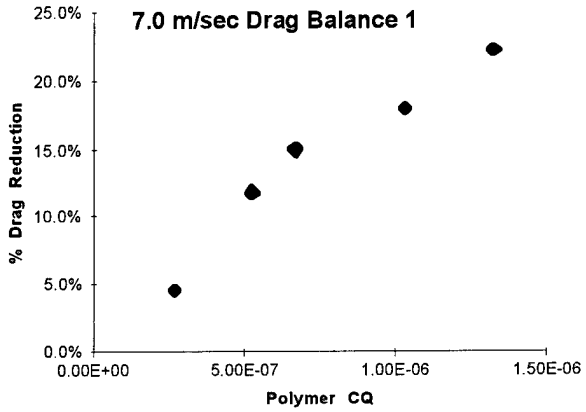

Fig. 7. Plot of typical polymer drag reduction.

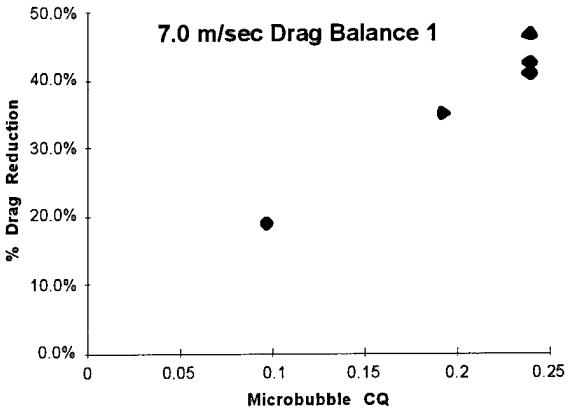

Fig. 8. Plot of typical microbubble drag reduction.

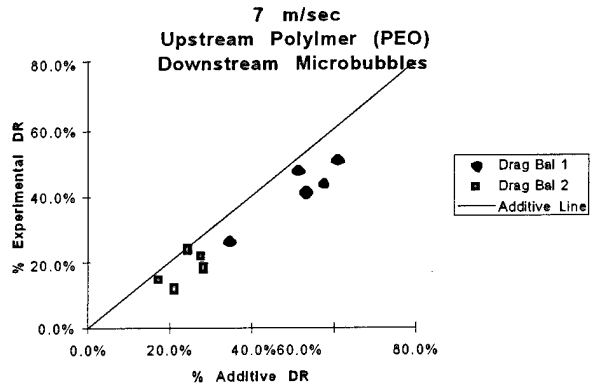

Fig. 9. Plot of experimentally measured combined and additive drag reduction (upstream polymer).

The tandem injection ports were then switched so as to place the polymer injection slot 10.7 cm behind the microbubble injection location. No other changes were made to the balance hardware or instrumentation. Now the polymer solution is being injected between a sheet of microbubbles and the flat plate's surface. The results at 4.27 m/sec show (figure 10) the existence of synergy on drag balances 1 and 2. Figure 11 presents the results on both drag balances for 6.10 m/sec. Both balances clearly show the presence of synergy. Synergy was found for the many cases were microbubble injection.

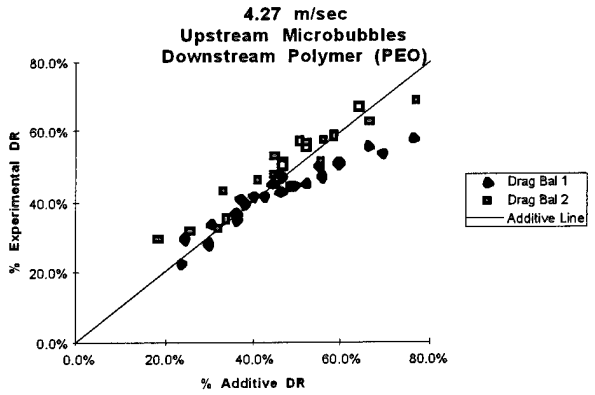

Fig. 10. Plot of experimentally measured combined and additive drag reduction (upstream microbubbles).

was upstream and polymer downstream.

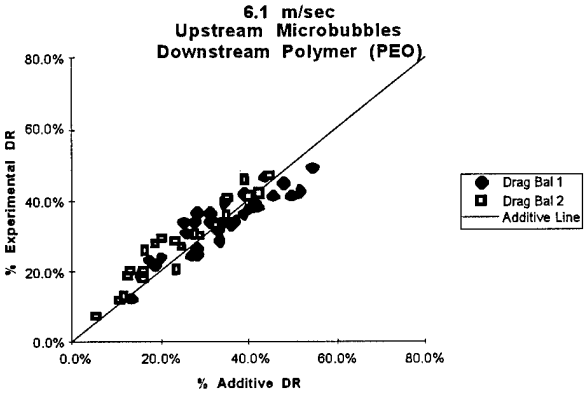

Fig. 11. Plot of experimentally measured combined and additive drag reduction (upstream microbubbles).

Figures 10 and 11 show the existence of synergy however they do not indicate the relative levels of drag reduction between polymer and microbubble drag reduction to achieve this result. The following figure attempts to show the individual magnitude of drag reduction (either polymer or microbubble) required for synergy.

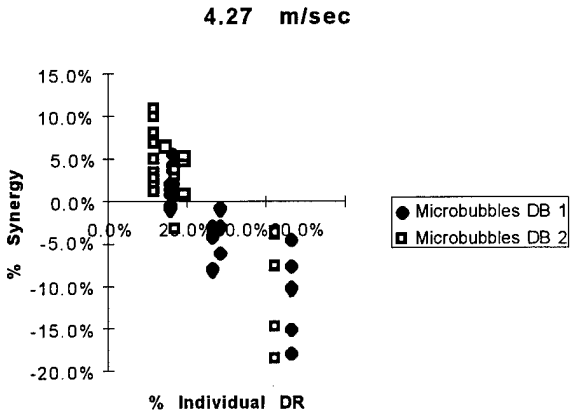

Fig. 12. Effect of % microbubble drag reduction level upon % synergy

Figure 12 is a plot of the individual independent microbubble drag reduction level for both drag balances versus the percent synergy achieved when combined with polymer. From this figure it is clear that microbubble gas ejection levels exceeding 30% drag reduction do not produce synergy, in this configuration at this tunnel speed. At higher speed the trend is the same but higher gas flow rates are required to definitize the result. The effect with polymer shows a trend toward lower synergy with increasing drag reduction, however this trend is not as pronounced as in the microbubble case. Figure 13 shows the relationship between microbubble and polymer injection C_Q versus the amount of synergy achieved. This case is for drag balance 1 at 6.10 m/sec with upstream microbubble, downstream polymer injection. Note the best levels of synergy are achieved for low microbubble injection for nearly all polymer injection rates.

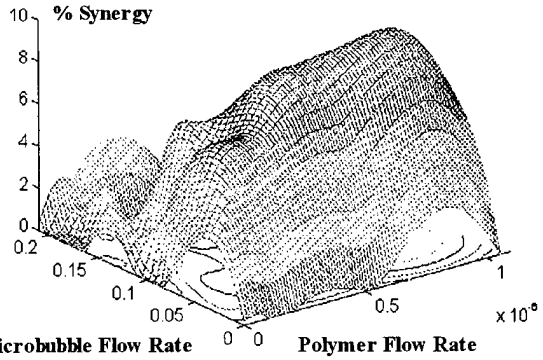

Fig. 13. Contour Plot of synergy vs microbubble and polymer C_Q.

IV. DISCUSSION

Synergy was found for the combined injection of polymers and microbubbles. When the order of injection was microbubbles upstream and polymer downstream there were clear cases of synergy. The reverse order did not demonstrate synergy. The observed synergy implies that the effectiveness of individual additives is enhanced when used in combination. Turbulent mixing at very small scales is assumed to be locally isotropic, making the order of microbubble and polymer mixing irrelevant to their near wall effect on the flow. The lack of synergistic reductions when polymer is introduced upstream of a microbubble injection slot implies that intrinsic interaction, or near wall mixing of the two additives does not have a strong influence on the resulting TBL. In this configuration (polymer upstream , microbubbles downstream) the polymer layer introduced into the boundary layer appears to experience more mixing as it encounters the microbubble ejector. As microbubble injection increases, more mixing occurs, reducing the overall level of polymer drag reduction as the polymer diffuses more rapidly out of the buffer layer where it is effective. The observed synergistic reductions obtained with microbubble injection upstream of a polymer slot demonstrate that when a bubble sheet rides over a confined, polymer solution, larger reductions are possible. Since intrinsic interactions are not important, preferential enhancement of one of the additives' drag reducing mechanisms must be taking place. Knowing that both additives work best when present in the near wall region, we suggested that the microbubble sheet is inhibiting polymer transport or diffusion away from the wall thereby locally increasing the relative polymer concentration at the buffer layer.

Testing aerated polymer injection from the same slot would solidify this hypothesis. If our hypothesis is accurate, then no significant synergistic reductions will be observed, since the aerated polymer mixture will not effectively prevent polymer diffusion. If synergistic reductions are observed, then alternate hypotheses of polymers enhancing the surfactant chemistry of microbubbles should be considered.

One feature of this test it is important to bear in mind. All testing was performed in salt water. From the results of Kuklinski the bubble size does not change with the addition of the polymer solution. Similar experiments conducted in fresh water may show differences in bubble size with the addition of polymer. This could change the character of synergy.

V. ACKNOWLEDGMENTS

R. Philips would like to acknowledge many useful discussions on experimental procedures with Dr. C. Henoch. Drs. P. Bandyopadhyay and P. Hendricks provided helpful critique of the this work. Dr. R. Kuklinski supplied the microbubble sizing information for polymer solutions in salt water. This work was supported under in-house Bid and Proposal funding.

VI. REFERENCES

1. J. L. Lumley, 1977: "Drag reduction in two-phase and polymer flows", *Physics of Fluids*, **20**,(10):S65-S71, Part II .

2. S. Deutsch and J. Castano 1986: Microbubble skin friction reduction on an axisymmetric body. *Physics of Fluids*, **29**, 3590-3597.

3. A. Fontaine and S. Deutsch 1992: The influence of the type of gas on the reduction of skin friction drag by microbubble injection. *Experiments in Fluids*, **13**, 128-136.

4. Hoyt 1991, in Viscous Drag Reduction, edited by D. M. Bushnell, Progress in Astronautics and Aeronautics, vol. 23, 413-432

5. N. Madavan, S. Deutsch, and C. Merkle 1985: Measurements of local skin friction in a microbubble modified turbulent boundary layer. *J. Fluid Mech.*, **156**, 237-256.

6. S. Pal, S. Deutsch, and C. Merkle 1989: A comparison of shear stress fluctuation statistics between microbubble modified and polymer modified turbulent boundary layers. *Physics of Fluids A1*, 1360-1362.

7. J. E Koskie and W.G. Tiederman 1991, "Polymer Drag Reduction of a Zero Pressure Gradient Boundary Layer," Purdue University Report PME-FM-91-1

8. M.M. Guin, K. Hiroharu, H. Yamaguchi, M. Maeda and M. Miyanaga, in publication: "Reduction of skin friction by microbubbles and its relation with near-wall bubble concentration in a channel," . *J. of Marine Science and Technology*.

9. D. Walker and G. Tiederman 1989: "The concentration field in a turbulent channel flow with polymer injection at the wall," . *Experiments in Fluids 8*, 86-94.

10. A. Malyuga, V. Mikuta, and A. Nenashev 1989: Local drag reduction at flow of polymer solutions aerated by air bubbles. *Proceedings of the 18th Scientific & Methodological Seminar on Ship Hydrodynamics* , Varna Bulgaria Sept. 25-30 1989, pp. 74-1 - 74-6. Kuklinski, 1997 Personal Communication

11. W. M. Carey, J. W. Fitzgerald, E. C. Monahan and Q.Wang 1993: "Measurement of Sound Produced by Tipping Trough with Fresh and Salt Water," **JASA 93**, No. 6.

12. J. D. Hrubes , C. W. Henoch, G. C. Pacifico, and W. G. Fennell 1994: "Development of a Gas/Liquid Hydrocyclone Separator for a High Energy Aqueous Battery," NUWC Division, Newport, Technical Report 10,346.

13. E. C. Monahan, Q. Wang, X. Wang , and M. B. Martin, 1994: "Air Entrainment by Breaking Waves: A Laboratory Assessment," FED-Vol. 187, *Aeration Technology, ASME*.

14. R. Kuklinski, 1997, personal communication.

MICROBUBBLE FORMATION AND SPLITTING IN A TURBULENT BOUNDARY LAYER FOR TURBULENCE REDUCTION

James C. S. Meng and James S. Uhlman, Jr.
Naval Undersea Warfare Center
Newport, Rhode Island 02841-1708

Abstract - Bubble formation traditionally has been addressed by chemical engineers for bubbles generated in a stationary liquid. Here the emphasis is on obtaining quantitative relationships of bubble formation in a high-speed turbulent boundary layer (TBL) and on determining whether bubble splitting is a possible mechanism for absorbing turbulence energy and, therefore, turbulence reduction. This study is conducted to address the mechanisms that dominate during a bubble formation in a TBL, and how to establish quantitatively the relationship among Q_{pore}, d_{pore}, and U_0. This study offers some insight into bubble size regimes, bubble size spectrum, bubble splitting, and bubble transport in a TBL. Based on the results, a concept of the possible mechanism for microbubble drag reduction based on bubble splitting energetics is presented. An estimation is made of the total amount of turbulent kinetic energy needed to split bubbles in a TBL and is compared with the total energy available in a TBL. It is suggested that bubble splitting is a plausible basic mechanism for reducing turbulence in a microbubble-laden TBL.

1. BUBBLE FORMATION DYNAMICS

1.1 Hydrodynamics of Bubble Formation. The physics governing the formation or "breakaway" of a microbubble at a pore in a wall beneath a moving liquid are complex. In order to model the physics properly, one must consider effects of low Reynolds number viscous and inertial forces, wall effects, buoyancy, surface tension, and free-surface phenomena, including surface chemistry, all varying with time. To model such a problem analytically would require an immense effort. The goals here are much more modest. By identifying various hydrodynamic forces and performing approximate force balances, both parallel and perpendicular to the wall, one can obtain equations that yield order-of-magnitude estimates of the bubble breakaway size under various assumptions. Therefore, the first step is to identify and quantify the various forces, both tangential and normal to the wall. We will start with the tangential forces.

When a bubble is exuded from a pore in a wall into a liquid flow parallel to the wall, the flow exerts a drag force on the bubble. As a result of the drag force the bubble shape is altered, becoming skewed. The skewed bubble shape introduces a component of surface tension force parallel to the wall, which balances the drag force. The bubble detaches from the wall when some critical skew angle is reached or when either a lift force or the buoyancy overcomes the vertical component of surface tension, whichever occurs first.

The horizontal component of surface tension force was obtained by Al-Hayes and Winterton [1, 2]; they calculated the horizontal component of surface tension force from the following equation:

$F_{st} = -\left\{\frac{58}{\theta_0 + 5} + 0.14\right\} \times \frac{1}{2}\pi R\sigma \sin\theta_0 \times (\cos\theta_r - \cos\theta_a)$, where σ is the surface tension between air and water and θ_0 is the equilibrium contact angle between the bubble and the wall, i.e., $\sin\theta_0 = r/R$, and θ_r and θ_a are the receding and advancing contact angles (figure1), respectively, when the bubble is in a cross flow. Values for the various angles involved were determined experimentally, and the quantity in brackets is a correction factor that Al-Hayes and Winterton applied to their equation to improve the comparison between theory and experiment. Following Al-Hayes and Winterton, we can assume that the angles are

$\theta_0 \doteq 40°, \theta_r \approx 30°$, and $\theta_a \approx 50°$, then $F_{st} = -0.16\pi R\sigma \sin\theta_0$. (1)

If we now assume that the drag force balancing the surface tension is $F_D = \frac{1}{2}\rho C_D U_0^2 \pi R^2$, substituting $C_D = 1.22$ and θ_0, θ_a, and θ_r values we obtain the following drag-surface tension force balance equation: $\rho((U^2R)/\sigma) = 0.17$.

An alternative formulation of the balance between the drag force on the bubble and the horizontal component of surface tension force can be derived by assuming that the contact angle of the bubble has a simple sinusoidal dependence. With this assumption $\theta = \theta_0 + \delta\theta\cos\phi$, where ϕ is the angle about the base of the bubble clockwise from upstream (figure 1). Hence, $\theta_a = \theta_0 + \delta\theta$ and $\theta_r = \theta_0 - \delta\theta$. The horizontal component of the surface tension force is then $F_{st} = r\sigma\int_0^{2\pi}\cos[\theta_0 + \delta\theta\cos\phi]\cos\phi\, d\phi = -2\pi r\sigma \sin\theta_0 J_1(\delta\theta)$, where J_1 is the Bessel function of order 1 (Gradshteyn and Ryzhik [3]). However, $J_1(\delta\theta) \approx 1/2\delta\theta$ for $\delta\theta << 1$, thus we find

$F_{st} = -\pi r\sigma \sin\theta_0\, \delta\theta$. (2)

According to the data of Al-Hayes and Winterton [1, 2] the quantities $|\theta_0 - \theta_a|$ and $|\theta_0 - \theta_r|$ appear to be fairly constant, with a value of approximately 10°. Thus $\delta\theta = 0.17$, so (1) differs from (2) by r/R. If the drag force is now assumed to follow Hadamard's law because the bubble Reynolds number is very low, then the drag force to surface tension force balance becomes $4\pi\mu RU_0 \cong \pi\sigma\,(r^2/R)\delta\theta$.

Proceeding to the normal force balance case, the normal component of surface tension force can be calculated similarly to the tangential case, and we have $F_{sn} = 2\pi\, r\, \sigma \sin\theta_0 J_0(\delta\theta) \cong 2\pi\sigma\, r^2/R$. Another normal force to consider is the low Reynolds number "Saffman" lift force (see Saffman [4, 5]). Its effect is to lift the bubble away from the wall. Strictly speaking, the Saffman lift result applies only to a particle in an unbounded fluid. However, it is applied here to a bubble near a wall for the purpose of an engineering order-of-magnitude estimate. Voloshko et al. [6] identified other normal forces to be the added mass term $\varepsilon_m \frac{\pi\rho r^4 v_0^2}{12R^2}$, the gravity or buoyancy term $(4/3)\,\pi R^3(\rho - \rho')g$, and the gas injection flux term $\rho' v_0^2 \pi r^2$, where ε_m is the added mass coefficient, ρ' is the gas density, and v_0 is the velocity of the gas as it exits a pore. If in addition the Saffman lift term $C_L\,\pi\rho R^2 U_0(\nu k)^{1/2}$ and surface tension terms are also included, following Voloshko et al. [6] a modified Voloshko equation governing bubble normal force balance becomes

$$\varepsilon_m \frac{\pi\rho r^4 v_0^2}{12R^2} + 2\pi\frac{r^2\sigma}{R} = \frac{4}{3}\pi R^3(\rho - \rho')g + C_L\pi\rho R^2 U_0(\nu k)^{1/2} + \rho' v_0^2 \pi r^2, \quad (3)$$

where U_0 is the flow past the wall at the bubble centerline, υ is the kinematic viscosity of the liquid, and k is the effective shear in the liquid at the bubble centerline.

1.2 Bubble Size Regimes. In contrast to the commonly referred to bubble geometry, depicted in figure 1, as much as four bubble regimes can be identified (figure 2). To analyze the bubble size spectrum, which may be a natural consequence of generating bubbles in a TBL, the basic bubble hydrodynamics are extended to include analysis of bubble geometries other than a semisphere. The sheared spherical cap case was attributed to MacIntyre [7], while the other three cases were identified by Silberman [8]. These four regimes can be delimited by comparison of the ratio of the gas pore-exit velocity with the liquid velocity.

For the sheared spherical cap case (figure 2(a)), height $h = R - (R^2 - r_{pore}^2)^{1/2}$, where R is the radius of curvature of the cap, and the cap volume $\pi/6\, h(h^2 + 3r_{pore}^2)$ is assumed to be the bubble volume after it is sheared off the pore. Since the spherical cap cannot be sheared off the pore faster than the fluid flows over the pore, we find that $\frac{\pi}{6}\frac{h(h^2 + 3r_{pore}^2)}{Q} \geq \frac{r_{pore}}{U_0}$, where Q is the volumetric gas flow rate. Replacing h in terms of R and r_{pore} and taking the limit of small r_{pore}/R, the above equation becomes:

$\frac{\pi r_{pore}^3}{4Q}\left(1+\frac{1}{12}\left(\frac{r_{pore}}{R}\right)^2\right) \geq \frac{R}{U_0}$, or $\frac{Q}{\pi r_{pore}^2 U_0} \leq \frac{1}{4}\frac{r_{pore}}{R}$. Judging from the figure, $r_{pore}/R < 0.2$, and replacing Q with $\pi r^2_{pore}\, v_{pore}$, we obtain $v_{pore}/U_0 \leq 0.05$.

In the single bubble regime, figure 2(b), the bubble formation time is longer than the time it takes for the fluid to flow over the pore. Since the bubble in this case has the time to grow to a nearly spherical shape, the bubble volume is $4/3\ \pi R^3$. The time scale for the bubble growth is then $4/3\ \pi R^3/Q$, which is greater than the flow time, i.e., $\frac{4}{3}\frac{\pi R^3}{Q} > \frac{r_{pore}}{U_0}$, or $\frac{Q}{\pi r_{pore}^2 U_0} < \frac{4}{3}\left(\frac{R}{r_{pore}}\right)^3$. Replacing Q with πr^2_{pore} and using the minimum value for the right-hand side, we find that for the single bubble regime $v_{pore}/U_0 \leq 1$ should apply.

In the jet disintegration regime (figure 2(d)), as a result of high gas-injection rate, the jet formation time is shorter than the flow time; it is the instability of the gas jet that determines the final bubble size. Rayleigh [9] studied this problem and found that the wavelength of the maximum amplification of instability is 6.48 times the mean jet diameter J.

Therefore, the jet formation time is $\frac{6.48\ J\frac{\pi J^2}{4}}{Q}$, and it should be shorter than the flow time r_{pore}/U_0. In other words, $\frac{Q}{\pi r_{pore}^2 U_0} > 12.96\left(\frac{J}{d_{pore}}\right)^3$. Replacing Q with $\pi r^2_{pore}\, v_{pore}$ and using the maximum value for the right-hand side, we find $v_{pore}/U_0 \geq 10$ for the jet regime.

The intermediate regime (figure 2(c)) corresponds to a bent jet, and the bubble breakaway mechanism is due more to the liquid dynamics than the dynamics of the jet itself. In this regime, the formation time analysis gives $v_{pore}/U_0 \geq 5$. We have thus completed a description of different bubble regimes. Naturally, different hydrodynamic mechanisms control the bubble formation in different regimes and different dependencies of the bubble size on v_{pore}/U_0, and the surface tension results. It is important to note that one single parameter v_{pore}/U_0 emerges from this analysis as the key parameter demarcating the different regimes. In figure 3 are the approximate values of bubble diameter criteria. The ordinate is the ratio d_{bubble}/d_{pore}, and the abscissa is the "injection coefficient," or more precisely the ratio v_{pore}/U_0 that was identified to be the key parameter in the bubble formation time analysis. As noted in figure 3, two distinct regions are identified: the liquid at rest, which corresponds to the $v_{pore}/U_0 \to \infty$ limit; and the flowing liquid case.

In the liquid at rest case, the bubble sizes are determined by two possible normal force balances (assuming the wall to be normal to the gravity force vector). Notice that in this case, the tangential force balance is not operative. First, at low gas-injection rate, the bubble buoyancy is in equilibrium with the surface tension between the gas bubble and the wall, i.e., $\frac{4}{3}\pi\left(\frac{d_{bubble}}{2}\right)^3 \rho_{liquid}\, g = \pi d_{pore}\sigma$, or $\frac{d_{bubble}}{d_{pore}} = \left(\frac{6\sigma}{\rho g d_{pore}^2}\right)^{1/3}$. Second, at a higher gas-injection rate, Silberman [8] applied three assumptions to obtain the following relationship: $\frac{d_{bubble}}{d_{pore}} = 1.41\left(\frac{Q^2}{g d_{pore}^5}\right)^{1/5}$. The three assumptions are: the unstable wavelength obtained by Rayleigh in a stationary environment is valid in a shearing flow, Bernoulli's equation can relate the jet velocity and jet height against gravity, and the diameter of the bubble is related to the liquid velocity U_0 the same way as the gas jet velocity. The last assumption is probably the weakest.

In the flowing liquid case, the physics governing bubble size can be divided into at least three regimes, which in turn can be further divided into smaller groups. At the high injection limit, i.e., $v_{pore}/U_0 > 10$, the gas jet instability perpendicular to water flow was obtained by Silberman [8]: $\frac{d_{bubble}}{d_{pore}} = 2.4\left(\frac{Q}{U_0 d_{pore}^2}\right)^{1/2}$. Notice the dependence of bubble diameter on the flow rate Q. This result has been verified by Silberman and recently by Reischman and Holzmann [10]. In practice, this high injection rate limit typically applies to an ejection using discrete drilled holes. The physics in the intermediate regime is unknown; an analytic formula for the bubble size cannot be easily obtained. As the injection coefficient reduces, we move into the single bubble regime, i.e., during the bubble formation the gas cavity appears to resemble a bubble geometry. In this regime, two distinct force balances exist: normal and tangential. It is intuitively convincing that in a rapidly flowing liquid, if the gas exit velocity equals approximately that of the liquid tangential velocity, the mechanism of bubble breakaway should be determined by a normal force balance. As the gas exit velocity reduces further, or as the liquid velocity increases while the gas exit velocity holds constant, the dominant force balance switches to the tangential mode.

In the normal force balance mode, at least two possibilities exist. At the high v_{pore}/U_0 end, the Saffman lift force balances the inertial force surrounding an expanding bubble. From (3) we find from the modified Voloshko equation that, for this case $\varepsilon_m\left[\frac{\pi\rho r_{pore}^4 v_{pore}^2}{12R^2}\right] = C_L \pi\rho R^2 U_0 u_\tau$, where u_τ is the local friction velocity and ρ the liquid density.

Rearranging, we find $\frac{d_{bubble}}{d_{pore}} = \left[\frac{\varepsilon_m}{12C_L}\left(\frac{v_{pore}}{U_0}\right)^2 \frac{U_0}{u_\tau}\right]^{1/4}$, which does depend on the injection coefficient to the ½ power. For the lower v_{pore}/U_0 case, Saffman lift will balance the surface tension between the gas bubble and water on the wall, i.e., $2\pi\frac{r_{pore}^2}{R}\sigma = C_L\pi\rho R^2 U_0\, u_\tau$, or $\frac{d_{bubble}}{d_{pore}} = \left(\frac{4\sigma}{\rho U_0^2 C_L d_{pore}}\frac{U_0}{u_\tau}\right)^{1/3}$, where $\frac{U_0}{u_\tau} = \left(\frac{2}{c_f}\right)^{1/2}$, and c_f is the local skin friction coefficient on the wall. Notice that this result does not depend on the injection coefficient. The question of whether there are any other normal force balances could arise can be addressed by examining the modified Voloshko equation (3). Dividing equation (3) by $\rho U^2_0\, r^2_{pore}$, we find

$$\frac{\pi\varepsilon_m}{12}\left(\frac{r_{pore}}{R}\right)^2\left(\frac{v_{pore}}{U_0}\right)^2 + 2\pi\frac{\sigma}{U_0\mu}\frac{\nu}{RU_0} = \frac{4\pi}{3}\frac{g r_{pore}}{U_0^2}\left(\frac{R}{r_{pore}}\right)^3 + \pi C_L\left(\frac{R}{r_{pore}}\right)^2\left(\frac{c_f}{2}\right)^{1/2} + \pi\frac{\rho'}{\rho}\left(\frac{v_{pore}}{U0}\right)^2.$$

Substituting $\varepsilon_m = 32$, $\frac{\sigma}{U_0\mu} \cong 7$, $\frac{\nu}{U_0 R} \cong 10^{-2}$, $c_f \cong 3\times10^{-3}$ $\frac{g r_{pore}}{U_0^2} \cong 10^{-6}$, $\pi C_L = 6.46$, $\frac{\rho'}{\rho} \cong 10^{-3}$, for $U_0 = 10$ m/sec, $r_{pore} = 10\mu$m, we can write the above equation as follows:

$$8.3\left(\frac{r_{pore}}{R}\right)^2\left(\frac{v_{pore}}{U_0}\right)^2 + 0.4 = 10^{-6}\left(\frac{R}{r_{pore}}\right)^3 + 0.25\left(\frac{R}{r_{pore}}\right)^2 + 10^{-3}\left(\frac{v_{pore}^2}{U_0}\right).$$

From this we see that we can neglect the buoyancy term (first term on the right-hand side) compared with the Saffman's lift term (second term on the right-hand side). The balance type of force depends on the magnitude of only two parameters: R/r_{pore} and v_{pore}/U_0. For $v_{pore}/U_0 = 1$, the first term on the left-hand side (i.e., the water inertia surrounding an expanding bubble) balances the Saffman lift and gives a result of $R/r_{pore} \cong 2.4$. For $v_{pore}/U_0 << 0.1$, again the Saffman lift force dominates the right-hand side of the equation, while the dominant term on the left-hand side shifts to the surface tension term (the second term) and gives a lower result of

$R/r_{pore} = 1.2$. No other physically meaningful possibility seems to exist; thus concludes the discussion of the normal force balance.

For the tangential force balance case, only one possible combination exists: the water drag on a gas bubble, or on a gaseous cap, balances the surface tension between the gas bubble and the wall. As indicated in figure 2, two bubble breakaway geometries are possible: a nearly spherical bubble case, and a nearly spherical cap case. In reality, neither occurs. In fact, unstable waves on the bubble surface should be present as a result of both the unsteady forcing of the turbulent flow over them and the liquid local pressure gradient generated by the growing bubble. Whether the bubbles will break away as a result of this unstable wave growth is unknown. A water tunnel experiment on a single bubble formation, visualized at close range, is a plausible approach to address this issue.

For the spherical bubble case, we have $\pi R^2 \tau_w = \pi\sigma \frac{r_{pore}^2}{R}\delta\theta$, where $\delta\theta = 0.17$, as given before, and τ_w is the local wall shear stress. From this we find $\frac{d_{bubble}}{d_{pore}} = \left(\frac{2\sigma\delta\theta}{\tau_w d_{pore}}\right)^{1/3}$. (4)

Alternatively, we can replace τ_w with $(1/2)\rho U_0^2 C_D$, where C_D is the drag coefficient over the bubble. But this also opens questions about the validity of using U_0 as the relative liquid velocity over the bubble, and also that C_D is not known until the bubble Reynolds number is known, which requires *a priori* knowledge of the bubble size. As the injection coefficient reduces, we move into the spherical cap regime. For the tangential force balance, the tangential surface tension force is described by equation (2). The shear force is $2\pi Rh\tau_w$, where

$h = R\left(1-\left(1-\left(\frac{r_{pore}}{R}\right)^2\right)^{1/2}\right)$, or $h \cong \frac{1}{2} r_{pore}\, r_{pore}/R$, where small r_{pore}/R is applied. Equating them, we find $R = \sigma\delta\theta/\tau_w$. Substituting the values of σ, $\delta\theta$, and $\tau_w = \rho u_\tau^2$ at 10 m/sec, we find $R = 74$ μm, which is 7 times greater than the pore size (10 μm), consistent with our assumption that $r_{pore}/R < 1$. The bubble diameter after breakaway, d_{bubble}, is related to the cap height h by $d^3_{bubble} = h^3 + 3r^2_{pore}\, h$. Substituting h and carrying out simplifications, we have $d^3_{bubble} = r^3_{pore}\left(3\frac{r_{pore}}{2R} + \left(\frac{r_{pore}}{2R}\right)^3\right) \cong \frac{3}{2} r^3_{pore}\frac{r_{pore}}{R}$, or $d_{bubble} = \left(\frac{3}{2}\frac{r_{pore}}{R}\right)^{1/3} r_{pore}$, $\frac{d_{bubble}}{d_{pore}} = \frac{1}{2}\left(\frac{3}{4}\frac{\tau_w d_{pore}}{\sigma\delta\Theta}\right)^{1/3}$, an interesting result because the shear stress dependence is the reverse of that for the single bubble regime case. In the spherical cap regime, bubbles are smaller than the pore size and increase in size with τ_w; while in the single bubble regime, bubbles are greater than the pore size and decrease with local τ_w.

1.3 Estimation of Pore Characteristics of a Porous Surface. Porous shells and flat plates have been used extensively for microbubble drag reduction. These surfaces typically are formed by pressing and sintering powdered metal particles. The void space among the powders provide the required porosity. Estimation of the pore characteristics is essential for predicting and controlling the bubble size. In this subsection, we derive the required relationship among the pore size, number of pores per unit area, and percentage of surface porosity. Porous titanium shells and plates traditionally are used in the industry for filtration purposes. The pore size typically is specified in terms the size of the smallest particles filtered out, instead of the pore size per se. In liquid flows, titanium filters made by Gould will normally retain particles approximately one-third of the mean pore size. No generalization to gas flows was made, but the retention size is known to be much finer.

The distribution of pore size is not available, but given the fact that particles three times smaller than the mean pore size are filtered out, there must be a sharp drop-off in the large pore size end of the spectrum. The standard deviation in pore size σ_{pore} must be smaller than the mean pore size $\bar{d}_{pore}$. Therefore, for engineering purposes we can assume that $\sigma_{pore} \cong \frac{1}{2}\bar{d}_{pore}$ and that the pores follow a Gaussian distribution, i.e., $p(d_{pore}) = \frac{1}{\sqrt{2\pi}\sigma_{pore}} e^{-\frac{1}{2}\left(\frac{d_{pore}-\bar{d}_{pore}}{\sigma_{pore}}\right)^2}$. This distribution can be used to make engineering estimates of pore size and bubble sizes.

Grades	Size Range Mean Pore Size (Microns)	Smallest Particle Filtered Out in Liquid (Microns)
Ti-2003	3	1
Ti-2505	5	2
Ti-4010	10	3
Ti-5015	15	5
Ti-6525	25	8

Table I. Gould Titanium Standard Filtration Grades

To calculate the gas flow rate through individual pores, it is necessary to know the surface porosity, i.e., the percentage of area occupied by pores. Typically, a "density" is given that indicates the ratio of the weight of the porous material to that of the solid material of the same nominal volume. Let us denote this density by ξ; then it is seen that $\xi = \frac{\rho_{solid} V_{solid}}{\rho_{total} V_{total}} = \left(\frac{\ell_{solid}}{L}\right)^3$, where ℓ_{solid} and L are lengths characterizing the solid part and the entire porous material, respectively. If $\ell^3_{solid} + \ell^3_{void} = L^3$, where ℓ_{void} is a length characterizing the void portion of the porous material, then $\frac{\ell_{void}}{L} \cong (1-\xi)^{1/3}$, so the surface porosity η can be estimated to be $\eta \cong \left(\frac{\ell_{void}}{L}\right)^2 = (1-\xi)^{2/3}$. Given a 45-percent density we find the surface porosity to be 67 percent.

It is useful to relate the mean powder size d_{powder} to the mean pore size d_{pore}. This is possible if we assume that there are as many pores as there are powder particles. Then we can say $\frac{N_{powder}\frac{1}{6}\pi\bar{d}^3_{powder}}{V_{total}} = \xi$, or $\frac{N_{pore}\frac{1}{6}\pi\bar{d}^3_{pore}}{V_{total}} = 1-\xi$, so that $\frac{\bar{d}_{powder}}{\bar{d}_{pore}} = \left(\frac{\xi}{1-\xi}\right)^{1/3} \cong 0.93$ for $\xi = 0.45$. Once d_{pore} and η are found, the number of pores per unit surface area, N_{pore}/S, can be calculated to be $\frac{N_{pore}}{S} = \frac{(1-\xi)^{2/3}}{\frac{\pi}{4}\bar{d}^2_{pore}}$. For $d_{pore} = 10$ μm and $\xi = 45$ percent, we have $\frac{N_{pore}}{S} = 0.85\times10^6$ pores / cm^2.

2. BUBBLE SIZE DISTRIBUTION IN A TBL

From analysis of the bubble size spectrum it is clear that, given a flow speed U_0, by keeping one of the two parameters Q and r_{pore} constant but varying the other one, bubbles of different sizes will be generated as a result of different physics mechanisms being activated. For the commonly used porous ejectors made of pressed and sintered metal powders, the pore sizes are not uniform, and the gas ejector pore size spectrum will lead to a spectrum of bubble sizes. Furthermore, in a TBL environment, even if both Q and r_{pore} are held constant, the wall shear stress fluctuates. The absolute magnitude of the fluctuating shear stress is greater than twice the mean shear stress, i.e., $\tau_{max} \approx 2\bar{\tau}_w$. Since the local instantaneous τ_w determines nearly all modes of balance, bubbles generated in a TBL should have a bubble size spectrum with a bandwidth equal to at least two times the mean bubble size. In this subsection we discuss the shear stress fluctuations, analyze a bubble size spectrum obtained in the ocean, identify possible physics affecting bubble formation in sea water versus

the physics in fresh water, and identify the possible bubble splitting and coalescence effects on a bubble size spectrum.

2.1 Shear Stress Fluctuation in a TBL. The τ_w in a TBL in terms of the probability density function (PDF) and the ratio (Burton [11]) of the variance $\sigma(\tau_w)$ to the mean, $\bar{\tau}_w$, $\frac{\sigma(\tau_w)}{\bar{\tau}_w} = 0.31$, were given by Sandborn [12], who found that the ratio ranges from 0.2 to 0.4. Kreplin and Ecklemann [13] determined the skewness $S(\tau_w)$ and the flatness $F(\tau_w)$ on the wall. Several sets of PDFs of τ_w do exist but were measured at a small distance away from the wall, i.e., $y^+ \cong 1$ to 5. Brodkey, Wallace, and Ecklemann [14] determined individually the PDFs of u as a result of ejection, sweep, and inward and outward interactions, and they superposed them to obtain the total PDF(u), at $y^+ = 3.4$. Since within $y^+ = 5$ the $P(u) \cong P(\tau_w)$, we can regard this resultant P(u) to be representative of $P(\tau_w)$. Bhatia, Durst, and Jovanovic [15] obtained $P(\tau_w)$ at $y^+ = 3.7$ to 6, while Kreplin and Ecklemann [13] obtained it at $y^+ = 1.6$ to 100. Figure 4 shows Sandborn's PDF (τ_w) data versus the normalized $\tau_w / \bar{\tau}_w$. Inspired by the lognormal distribution suggested by Nakagawa and Nezu [16] for the streak spacing λ^+, and also by the fact that λ^+ and τ_w are both positive variables, we have attempted to fit the $P(\tau_w)$ data by a lognormal distribution, i.e., $P(\tau_w) = \frac{1}{\sqrt{2\pi}\sigma\tau_w} \exp\left(-\frac{(\ell n\tau_w - \mu)^2}{2\sigma^2}\right)$, where $\mu = \overline{\ell n\tau_w}$ and $\sigma^2 = \overline{(\ell n\tau_w - \mu)^2}$. Several possibilities exist; the most obvious is to first obtain μ and σ^2 from the raw data. As shown in figure 4, the curve fit to the data mean and variance is poor. As a comparison, the least square fit is also shown. Sandborn indicated that the high shear end of data was not trustworthy; therefore, we reduced the value of the highest five data points and refitted by the lognormal distribution and the least square, both of which are also shown in figure 4. Due to the reduction of τ_w, using the normalized abscissa variable, the curves are shifted to the right; but as we can see, a much smaller difference exists in the later approach between the lognormal and the least square fits. In fact, τ_w and a variance of τ_w, $V(\tau_w)$ can be calculated from μ, σ^2 by $\bar{\tau}_w = e^{\left(\mu + \frac{\sigma^2}{2}\right)}$, $V(\tau_w) = e^{2\mu}[e^{2\sigma^2} - e^{\sigma^2}]$. From the values given in figure 4 we find $\frac{(V(\tau_w))^{1/2}}{\bar{\tau}_w} = e^{-\frac{\sigma^2}{2}}\left(e^{2\sigma^2} - e^{\sigma^2}\right)^{1/2} = 0.24$, from the raw data fit and, similarly, 0.24 from the modified Sandborn data set; both are close to the value accepted in the turbulence community. Given the equation that determines the bubble breakaway diameter from d_{pore} and τ_w, the knowledge of the PDFs for the pore size and the wall shear stress will enable the determination of a PDF for the bubble diameter.

2.2 Gallagher's Bubble Size Distribution. Gallagher [17] obtained a microbubble size distribution in sea water at typical ship speeds. He used an underwater camera and the Bete-Fog bubble analyzer to obtain bubble size spectrum. He presented one bubble size distribution for a ship speed of 12 knots, using pores of 3/64-inch diameter through a vertical steel pipe of 2 7/8-inch outside diameter and pumping air at the rate of 0.027 liter/sec/pore. The underwater camera was located 2 feet downstream of the vertical pipe. Figure 5 shows Gallagher's data in terms of the number of bubbles (dashed line) and the percentage of occurrence (heavy solid line) versus the bubble diameter in microns. On the same figure, a normalized Rayleigh spectrum is also shown in a thin dotted solid line. As shown, the Rayleigh spectrum seems to fit the bubble size spectrum and is represented by a simple parameter of the bubble diameter at the maximum percentage occurrence at 221 μm. Also illustrated are the bubble sizes, predicted using the different force balances described in the previous subsection: lift = surface tension, and drag = surface tension for the bubble regime and jet instability. Assuming $\tau_w = \frac{1}{2}\rho U_0^2 C_D$ and using $C_D = 0.2$ at $Re_d \cong 4 \times 10^5$ from Schlichting [18], we find $d_{bubble} = 206$ μm from drag (tangential) balance and $d_{bubble}/d_{pore} = 0.17$, while $d_{bubble} = 317$ μm from the lift (normal) balance and $d_{bubble}/d_{pore} = 0.26$. The former balance gives a result that is fairly consistent with the observed maximum percent occurrence value (d_{max}) at 221 μm. The bubble size indicated by the splitting will be addressed in the following subsection; suffice it to say that it seems to occur where the bubble size spectrum data deviate the most from the Rayleigh spectrum. The bubble size due to jet instability was 5000 μm and does not seem to be relevant here.

An attempt to fit Gallagher's data by the lognormal distributions was also carried out. A comparison of the best fits of the Rayleigh and lognormal distributions, shown in figure 6, was motivated by the following consideration. Given that $P(\tau_w)$ follows a lognormal distribution $\Lambda(\mu,\sigma_2)$, and (from the force balances) that $P(d_{bubble}) = P\left(\frac{1}{\tau_w^{1/3}}\right)$, then according to the lognormal distribution (Aitchison and Brown [19], p. 11) $P(d_{bubble})$ should follow a lognormal distribution of $\Lambda\left(-\frac{1}{3\mu}, \frac{\sigma^2}{9}\right)$. As shown in figure 6, the lognormal distribution seems to fit the data better (except for the secondary peak at a small bubble diameter, which could be a result of the bubble splitting phenomenon). By combining the force balance equations with the PDF of fluctuating shear stress results, and assuming that $P(d_{bubble}) = P\left(\left(\frac{\sigma r_{pore}^2 \delta\theta}{\tau_w}\right)^{1/3}\right)$ from drag balance and $P(d_{bubble}) = P\left(\left(\frac{4\sigma\, d_{porc}^2}{\rho U_0^2 C_\ell}\frac{U_0}{u_\tau}\right)^{1/3}\right)$ from lift balance, we can construct simulated bubble size distributions. These results are shown in figure 7 (the solid histograms are for the drag balance case, and the blank histograms are for the lift balance case). Initially, C_D was assumed to be 0.2, and the PDFs were generated. As shown in the figure, the peak values are consistent with the observed d_{max} value, but the size bandwidths are one order of magnitude smaller than the data indicated. Then, since we did not know the exact geometry of the pores relative to the pressure minimum point of flow over a long cylinder, we reduced the C_D by a factor of 20. The resulting pairs of bubble size spectrum are also shown in figure 7. The lift balance gives significantly greater spread in the bubble size, but the peak value moved out of the observed bubble size range. The drag balance case increases the bubble size of maximum population by a factor of 2, but the bandwidth increased very little. This analysis and comparison of data clearly indicated that some physics are lacking in the modeling presented so far. Two more physical phenomena have been identified: the sea water physics and bubble splitting in a TBL; they are discussed below.

2.3 Smaller Microbubbles in Sea Water. As early as 1954, Fox and Herzfeld [20] found that minute bubbles are stabilized by encapsulation in an organic film. Riley [21] found a coincidence between stable microbubble formation and the seasonal occurrence of natural organic particles. Blanchard [22] found that bubble coalescence is much more rapid in tap water than in sea water, and Monahan [23] found much smaller bubbles produced in sea water than in tap water. Scott [24] conducted a rigorous experiment designed to determine the effects of salt versus organic materials. He purified the tap water by distillation from potassium permanganate solution and by filtration through activated carbon. He heated commercial grade salt at red heat sufficient for fusion, driving off any organic material, and then blew nitrogen through a 3-cm-diameter porous glass membrane (with pore sizes in the 5-μm to 15-μm range). He found that a rapid decrease in the bubble size resulted from the addition of the pure salt to the purified water. He also found the bubble distribution in the purified salt water (35g/liter concentration) to be visually identical to that formed in real sea water.

Johnson and Cooke [25] set out to prove the existence of and to visualize the surface organic film on bubbles formed in sea water. They formed bubbles in air-saturated sea water by the shear produced at the surface of a sintered glass frit through which air was blown. After the bubble dissolution, a small transparent particle remained, about 5 μm in diameter and composed of the material originally present on the bubble. It was systematically photographed, and the organic material was identified by Detwiler [26] to be proteinaceous molecules, such as glycoproteins and

protoglycans. To verify the above facts, we equipped an axisymmetric model with air ejectors and towed it in a tow tank in both tap water and salt water; figure 2.8 shows the bubbles that were generated in each by the shearing motion of the water. The salt water was prepared by putting 640 lb. of fine table salt in 3500 gallons of tap water. The salinity was calculated to be 21 percent by weight, which is about 60 percent of the typical sea water salinity. As shown in figure 8, much smaller bubbles and a much denser bubble cloud were formed in salt water. In salt water, bubbles were observed to stay at the depth (17 inches) where they were generated and eventually dissolved into the ambient salt water; in tap water, the bubbles rose and coalesced to form larger bubbles, which rose faster and eventually burst on the surface.

We can identify three major basic physics mechanisms as possible origins of smaller bubbles in sea water: reduced surface tension between the gas bubble and water, organic film, and metalionic film. The most intuitive physics mechanism is the reduction of surface tension between the gas bubble and water. Scott [24] stated that the surface activity of salt increases the surface tension of the solution, consistent with the formula given in Kraus [27], i.e., $\sigma_{\text{sea water}} = 75.63$ (dyne/cm) - 0.144T(°C) + 0.221S. On the other hand, it is well known (Batchelor [28]) that any absorbed contaminant molecules at an air-water interface will orient themselves and exert on each other a repulsive bimolecular force that partially balances the surface tension of the pure water, so the net effect is that the surface tension value is smaller in sea water than it is in purified tap water. The decrement is proportional to the amount of surface contaminant and the gradient of contaminant concentration. Davis and Acrivos [29] analyzed the effect of varying surface tension on a bubble and found that the drag coefficient of a bubble covered with a surface contaminant is consistent with the experimental data if the maximum surface tension reduction is from 10 percent to 45 percent. The only qualitative way to resolve this seemingly complex issue is to directly measure the surface tension value for each sea water experiment.

Effects of the absorbed organic films on gas bubble radial oscillations have been modeled by Fox and Herzfeld [20], Avetisyan [30], and Glazman [31]. Fox and Herzfeld modeled the film as an isotropic elastic shell, so no surface tension dependence was found; Avetisyan represented the absorption film as a non-Newtonian liquid characterized by hypothetical viscoelastic properties; Glazman derived a new term at the bubble-film-water interface to include the nonuniform surface concentration and the resultant surface tension and represented the film as a viscoelastic film. He found that smaller bubbles are formed as a result of the film, and an additional restoring force induced by the film's dilational elasticity increases the bubble resonance frequency. The true physics of the organic film on the bubble are far from being completely resolved, but intuitively we can see the following effects on bubble oscillation: the organic film will create a surface tension gradient that resists bubble oscillation, and the viscoelastic nature of the film will likely damp the high frequency bubble oscillations. In either case, smaller bubble oscillation amplitudes are expected, and the smaller the bubble, the greater the damping effects of the surface film on the bubble oscillation. Another possible effect of the sea water surface contaminant on bubbles is to increase the bubble drag coefficient, making the bubbles less mobile and hence reducing the bubble collision speed, collision frequency, and subsequent coalescence. Finally, the potential for the resinous surface film to be stabilized by metal ion complex was suggested by Degens [32]. This would have the net effect of making the bubbles electrically charged, so that bubbles will repel each other, therefore reducing the occurrence of bubble collision and subsequent coalescence.

3. BUBBLE SPLITTING IN A TURBULENT BOUNDARY LAYER

As shown in figure 6, Gallagher's data show a secondary peak that exists at 50 μm, indicating that some of the bubbles greater than 50 μm might have been broken up into smaller bubbles. Another indication of the existence of bubble splitting can be seen in figure 7, which shows the simulated bubble size spectrum using the shear stress spectrum. By comparing the simulated bubble size spectrum with Gallagher's data, we found that the peak matches but the bandwidth does not, indicating that other mechanisms exist to make bubbles larger and smaller than the predicted mean bubble size. Theoretically, bubble splitting should be considered whenever bubble generation is taking place in a turbulent flow. The reason that in a laminar boundary layer, the maximum shear stress occurs right on the wall and is a steady shear stress, so once the bubbles are generated and transported away from the wall, they do not encounter higher stress. In a TBL, however, the maxima of Reynolds stresses $\cong \tau_w$ and the turbulent kinetic energy $\cong 10\ \tau_w$ both occur away from the wall at about $y^+ = 30$ to 100, so bubbles must encounter greater turbulence intensity and unsteady stresses than the stresses very near the wall, which are responsible for the bubble creation.

In principle, three splitting stresses can be identified: the mean shear stress τ, the turbulent Reynolds stresses $\overline{\rho u_i' u_j'}$, and the turbulent fluctuating pressure $\overline{p'^2}$, which is proportional to the turbulent kinetic energy. There is, however, only one resistance stress: the surface tension σ/d_{bubble}. Depending on the bubble (or droplet) Reynolds number $\frac{d_{\text{bubble}}}{\nu_g}\left(\frac{\tau}{\rho_g}\right)^{1/2}$, (where subscript g represents gas phase), two different force balances can be realized. At the low Reynolds number limit, the mean shear stress and surface tension balance each other. At the high Reynolds number limit, the discrete phase, the bubbles (or droplets) feel the influence of turbulence in the continuous phase. The kinetic energy of the turbulent motion in the continuous phase will bring about the breakup of the discrete phase. This is the case in which we are most interested.

Historically, chemical engineers have shown the greatest interest in this problem, since they are concerned with the problems of dispersion of gas-liquid systems for atomization and froth formation, and with liquid-liquid systems for emulsification. This problem had the attention of the most distinguished scientists during the early part of this century. Taylor [33] developed theories and experiments to study the "globule deformation" in the Couette and plane hyperbolic flows. The globules are stationary, the study corresponds to the $\text{Re}_{\text{globule}} < 1$ limit, and it is valid if the drops are small compared with the local regions of viscous flow. These facts, however, were not explicitly stated. Taylor obtained the results of $\text{We} = \tau d_{\text{globule}}/\sigma$ versus the ratio of μ_d, where d stands for the dispersed phase, to μ_c, where c stands for the continuous phase. His findings—that no breakup will take place either at the low $\mu_d/\mu_c < 3 \times 10^{-4}$ or at the high $\mu_d/\mu_c > 20$ limits— has inspired many subsequent studies, especially those by Acrivos [34] and Rallinson [35]. Unfortunately, none of these results applies to our case of interest.

Hinze [35] laid the foundation of the fundamental physics of droplet breakup in a moving stream. He put Taylor's work ($\text{Re}_{\text{globule}} < 1$) into perspective, relative to a droplet breakup in an air stream and emulsification in a turbulent flow, for the $\text{Re}_{\text{drop}} > 1$ case. For droplet breakup in an air stream, Hinze defined a new Weber number, $\text{We} = \frac{\rho_c U_0^2 d_{\text{droplet}}}{\sigma}$, replacing τ in Taylor's expression with the dynamic pressure of the air stream $\rho_c U_0^2$. He found that the mode of droplet breakup was very different for We greater or less than $\text{We}_{\text{critical}}$. For $\text{We} >> \text{We}_{\text{critical}}$, droplets were stripped off the drops owing to the waves and ripples generated on the drops. This relevant fact could have its counterpart for bubbles. For emulsification in a turbulent flow, Hinze pointed out that the critical Weber number will not be the same for all the globules—some statistical mean value will determine the average size of the largest globules that can withstand the breakup forces. For an isotropic and homogeneous turbulence case, Hinze worked out the maximum droplet diameter from the experimental data obtained by Clay [36]. Clay's data were obtained in an apparatus consisting of two concentric cylinders containing two immiscible fluids. The inner cylinder rotated, and one of the fluids formed discrete drops. By relating his analytic expression and Clay's data, Hinze [37] found that the maximum drop diameter is determined by the following critical Weber number: $\text{We}_{\text{critical}} = \frac{\overline{\rho u'^2} d_{\text{drop}}}{\sigma} \cong 1.17$. From Hinze's analysis of the maximum drop

size in a turbulent flow, i.e., $d_{drop_{max}} \cong 0.725\left(\frac{\sigma}{\rho_c}\right)^{3/5} \varepsilon^{-2/5}$, we can obtain an expression for the corresponding drop size in a TBL if we assume that the isotropic turbulence assumption still applies. From Hinze [37] (p. 64) we find the maximum ε to be $\varepsilon_{max} \cong \frac{30u_\tau^3}{\delta}$, where δ is the local boundary layer thickness. Expressing δ and ρu_τ^2 in terms of Re_x and substituting into the above relationship, we obtain

$d_{drop_{max}} = 1.03\left(\frac{\sigma}{\rho U_0^2}\right)^{3/5} x^{2/5} Re_x^{0.04}$, where x is the downstream distance along a flat plate. Sleicher [39] did turbulent flow experiments using two immiscible liquids in a 48-ft-long Lucite pipe with a 1½-inch inner diameter. He found that the fraction of drops that broke up was very sensitive to flow velocity, and in every case the breakup occurred very close to the pipe wall, which is where the turbulence was the least isotropic and homogeneous. Although Sleicher's data do not deal with bubble breakup, they are very relevant to our concern here because they deal with breakup in a TBL. He gave the following results for the critical Weber number: $\frac{\rho_c U_0^2 d_{drop_{max}}}{\sigma} = 38\eta^{1/2}(1+0.7\eta^{-0.7})$, where $\eta = \sigma/\mu_c U_0$, μ_c is the viscosity of the continuous phase, and U_0 is its velocity.

Sevik and Park [40] conducted a study of air bubbles splitting in a turbulent jet. Their apparatus consisted of a water jet, oriented vertically upward, with an air nozzle located at its center. The water nozzle diameter was 1.5 inch, and the water velocity at the nozzle exit varied from 7 ft/sec to 16 ft/sec. Air was injected into the center of the water jet, and air nozzle diameters varied from 0.071 inch to 0.25 inch. Bubbles with diameters varying from 4 mm to 5.8 mm were generated in the laminar core of the low turbulence jet of water and subsequently were broken up by the jet turbulence downstream. The initial bubble sizes were designed to be greater than the Kolmogorov [41] microscale, which was on the order of 25 μm, so that the bubble breakup would occur and would be characterized by the single parameter of critical Weber number according to Kolmogorov [41]. It was found that the bubbles remained near the center of the water jet and that breakup was substantially completed at an axial distance of 9 to 10 water nozzle diameters. Beyond that, no additional changes in bubble size took place. The bubbles were also progressively broken into smaller and smaller ones as the jet velocity increased. Sevik and Park's [40] most important finding was that if a characteristic frequency of the turbulence is set to the lowest resonant frequency of the bubble oscillation with constant volume, the critical Weber numbers correspond to both Clay's experimental data and their own. Furthermore, they stated that progressively smaller bubbles were generated when the critical Weber number was exceeded and when the higher frequencies of the turbulence excited the higher modes of the bubble oscillation.

Sevik and Park [40] measured $We_{critical}$ of air bubbles generated in a water jet and found that $\frac{\overline{\rho u'^2} d_{bubble}}{\sigma} = 2.6$. By equating bubble and flow frequencies, $\frac{\left(\overline{u'^2}\right)^{1/2}}{d_{bubble}} = f_{bubble} = \frac{1}{2\pi}\left[\frac{(n+1)(n-1)(n+2)\sigma}{\rho r_{bubble}^3}\right]^{1/2}$, at n=2 they found the following theoretical result: $\frac{\overline{\rho u'^2} d_{bubble}}{\sigma} = 2.48$, which is close to the experimental result. Inspired by these results, we consider the balance of the turbulent kinetic energy exerting influence on a bubble to the surface tension energy, which is the only energy resisting the breakup, i.e., $\overline{\rho u'^2}\frac{4}{3}\pi\left(\frac{d_{bubble}}{2}\right)^3 = \frac{\pi}{2}\sigma d_{bubble}^2$. We find $\frac{\overline{\rho u'^2} d_{bubble}}{\sigma} = 3$, which is fairly close to the above experimental result. Summarizing all these results, we show in figure 9 the maximum bubble diameters versus the flow speed. We can see that all three curves of $\frac{\overline{\rho u'^2} d_{bubble}}{\sigma} = C$, with C = 2.48 and 3, are nearly identical. The $y^+ = 25$ and 100 curves are provided to indicate the boundaries of maximum turbulence production.

As the majority of the bubbles become smaller than $y^+ = 100$, we conjecture that more microbubble drag reduction can be expected. Interestingly, we see that at 5 m/sec the splitting just commences, which might be relevant to the observation that drag reduction begins to emerge at this speed. At 20 m/sec, more bubbles are of the size of $y^+ = 25$; further increase in speed should ensure that most of the bubbles are smaller than $y^+ = 25$, therefore increasing the opportunity for bubbles interacting with the turbulence production that would normally take place in a single phase fluid turbulent flow. It is intuitively convincing that the more bubble splitting taking place, the more the turbulence kinetic energy is drained from the TBL; therefore, the more skin-friction reduction. Hinze's isotropic turbulence result for droplets, which is never smaller than $y^+ = 100$, is also shown. The curve for 0.01δ shows that at speeds less than 10 m/sec, bubbles larger than 0.01δ would survive the splitting; at speeds greater than 10 m/sec, bubbles would be much smaller than 0.01δ.

4. BUBBLE TRANSPORT IN A TBL

One of the tools necessary to investigate microbubble drag reduction is a method of determining the motion of microbubbles in a TBL. The model employed here assumes a spherical microbubble in a mean TBL velocity profile. Any effects of the rotation of the bubble are ignored. The forces on the microbubble are calculated as if the bubble were actually a rigid particle. This assumption is based on evidence that surface phenomena encountered in the real world environment make this a better approximation than the usual free surface model (see Batchelor [28]). The fluid is assumed to be Newtonian and incompressible. We assume that the time scale T over which a bubble alters its breakaway size by diffusion, splitting, or coalescence is such that $T >> \nu/u_\tau^2$. We can then assume that the bubble size remains constant during the calculation of its short time trajectory in a TBL. This is equivalent to stating that the bubble size does not change significantly until the bubble has traveled many viscous lengths.

The drag of the microbubble is $D = C_D(Re)\cdot\frac{1}{2}\rho U_{rel}\pi^2 R^2$, where the drag coefficient C_D is a function of the relative velocity bubble-diameter Reynolds number $Re = 2\frac{U_{rel}R}{\nu}$, and U_{rel} is the difference between the bubble velocity and the fluid velocity. The drag coefficient is calculated from a series of functional fits given by Morsi and Alexander [42]. A microbubble in a shear flow also experiences a lift force. For small Reynolds numbers this force is $L = 6.46\,\rho\,U_{rel}\,R^2\,(\nu k)^{1/2}$, where k is the magnitude of the velocity gradient (Saffman [4]).

All pressure gradients are taken into account, including the pressure gradient due to gravity, which causes buoyancy. All inertial effects are also considered: the mass of the microbubble, the added mass of the microbubble, and the so-called Basset's force: $B = 6\rho R(\pi\nu)^{1/2}\int_{-\infty}^{t}\frac{dU_{rel}}{d\tau}\frac{d\tau}{(t-\tau)^{1/2}}$. The basic equations thus take the form:

$$\frac{4}{3}\pi R^3\frac{d}{dt}\left\{\rho' u + C_A\rho(u-\tilde{u})\right\} = -C_D\cdot\frac{1}{2}\rho\left|\tilde{V}\right|(u-\tilde{u})\pi R^2$$
$$-6.46\rho(v-\tilde{v})R^2\nu^{1/2}\left(\frac{\partial\tilde{v}}{\partial x}\right)^{1/2} - \frac{4}{3}\pi R^3\frac{\partial p}{\partial x} \qquad (5)$$
$$-C_H\rho R^2(\pi\nu)^{1/2}\int_{-\infty}^{t}\frac{d}{d\tau}(u-\tilde{u})\frac{d\tau}{(t-\tau)^{1/2}}, \text{ and}$$

$$\frac{4}{3}\pi R^3 \frac{d}{dt}\left\{\rho' v + C_A \rho (v - \tilde{v})\right\} = -C_D \cdot \frac{1}{2}\rho \left|\vec{V}\right| (v - \tilde{v}) \pi R^2$$

$$- 6.46 \rho (u - \tilde{u}) R^2 \nu^{1/2} \left(\frac{\partial \tilde{u}}{\partial y}\right)^{1/2} - \frac{4}{3}\pi R^3 \frac{\partial p}{\partial y} + \rho' \frac{4}{3}\pi R^3 g \qquad (6)$$

$$- C_H \rho R^2 (\pi \nu)^{1/2} \int_{-\infty}^{t} \frac{d}{d\tau}(v - \tilde{v}) \frac{d\tau}{(t-\tau)^{1/2}},$$

where the velocity of the bubble is given by V = u i + v j, and the velocity of the fluid in the absence of the bubble is $\tilde{V} = \tilde{u}i + \tilde{v}j$. The coefficients C_A and C_H are the added mass and history (or Basset's) force coefficients, respectively. These are functions of the "acceleration number"

$$\Lambda c = \frac{\left|\vec{V} - \tilde{\vec{V}}\right|^2}{2R \frac{d}{dt}\left|\vec{V} - \tilde{\vec{V}}\right|}, \text{ as given by Odar and Hamilton [43].}$$

The relative importance of the forces on a microbubble can be determined by forming their ratios and calculating the numerical values of the ratios for any case of interest. To simplify, we can use the drag force as the basis of comparison, since even a cursory examination of the physics involved serves to demonstrate that the drag force must always be significant in any case of interest. Assuming that the relative velocity bubble Reynolds number is small, the form of the drag force used for comparison with other forces is Hadamard's drag, $4 \pi \mu R U_{rel}$, where μ is the fluid viscosity, R is the microbubble radius, and U_{rel} is the relative velocity between the fluid and the microbubble.

Forming ratios of these forces with the drag force, we find

$$\frac{\text{LIFT}}{\text{DRAG}} = 0.51 R^+ (k^+)^{1/2}, \quad \frac{\text{BASSET}}{\text{DRAG}} = \frac{C_H}{4\pi^{1/2}} \frac{R^+}{U^+} \int_{-\infty}^{t^+} \frac{dU^+}{d\tau^+} \frac{d\tau^+}{(t^+ - \tau^+)^{1/2}},$$

$$\frac{\text{BUOYANCY}}{\text{DRAG}} = \frac{1}{3}\frac{R^{+2} G^+}{U^+}, \quad \frac{\text{GRAVITY}}{\text{DRAG}} = \frac{1}{3}\alpha \frac{R^{+2} G^+}{U^+}, \quad \frac{\text{INERTIA}}{\text{DRAG}} =$$

$$\frac{1}{3}\alpha \frac{R^{+2}}{U^+}\frac{dU^+}{dt^+}, \text{ and } \frac{\text{ADDED MASS}}{\text{DRAG}} \frac{1}{3} C_A \frac{R^{+2}}{U^+}\frac{dU^+}{dt^+}, \text{ where } R^+ = \frac{Ru_\tau}{\nu},$$

where $u_\tau = \left(\mu \frac{du}{dy}\Big|_{wall} \rho\right)^{1/2}$, $k^+ = \frac{k_\nu}{u_\tau^2}$, $U^+ = \frac{U_{rel}}{u_\tau}$, $t^+ = \frac{tu_\tau^2}{\nu}$,

$G^+ = \frac{\nu g}{u_\tau^3}$, and $\alpha = \rho'/\rho$.

As an example, let us assume $u_\tau \cong 1.44$ m/s and $\nu = 10^{-6}$ m^2/s, so we find $G^+ \cong 3.3 \times 10^{-6}$. Now assume that for a bubble in ocean water $\alpha \cong 2.2 \times 10^{-2}$. To estimate the nondimensional relative velocity, acceleration, and velocity gradient, it is necessary to consider regions where these quantities are large, that is, regions where the forces will be large. As an order-of-magnitude estimate we can state that $U^+ \cong 10.0$, $k^+ \cong 1.0$, and $dU^+/dt^+ \cong 10.0$. In order to estimate Basset's force, suppose that the bubble has experienced a roughly constant acceleration during the last Δt^+ of time, prior to which it was moving with constant velocity. This supposition yields an order-of-magnitude estimate for most cases because the solutions of the above equations tend to behave exponentially. Hence, the periods of high acceleration occur over short time intervals. With these assumptions we can approximate Basset's force as

$\int_0^{t^+} \frac{dU^+}{d\tau^+}\frac{d\tau^+}{(t^+ - \tau^+)^{1/2}} \cong 2\frac{dU^+}{dt^+}(\Delta t^+)^{1/2}$. In addition, the above arguments show that we can state $\Delta t^+ \cong 1$.

If we now take the added mass coefficient C_A and the history or Basset's force coefficient C_H to make their high acceleration values $C_A = 1/2$, $C_H = 6$, then we can calculate the force ratios. Proceeding with the aforementioned example, with microbubble sizes chosen that are typical of those found in engineering situations, we arrive at the following results:

	Bubble 10μ	Bubble 100μ	Bubble 1000μ
R+	14.4	144.0	1440.0
Lift / Drag	7.3	73.5	735
Inertia / Drag	1.5	152.1	15210.0
Added Mass / Drag	34.5	3450.0	3.5×10^5
Basset / Drag	24.4	243.8	2437.5
Gravity / Drag	5.0×10^{-7}	5.0×10^{-5}	5.0×10^{-3}
Buoyancy / Drag	2.3×10^{-5}	2.3×10^{-3}	2.3×10^{-1}

With the exception of gravity and buoyancy, all other influences on microbubble acceleration are of at least the same order of magnitude as the drag, and they generally dominate the drag during periods of high velocity and acceleration. Of particular interest is the lift force, which can be orders of magnitude greater than the drag force in the high shear flow of a boundary layer. The lift force acts in the direction of increasing relative velocity magnitude, so a microbubble released at the wall experiences a strong lift force that pulls it away from the wall. Initially, the lift force is many times the drag force, and the bubble will move almost perpendicularly away from the wall. As the drag force slowly brings the relative velocity between the microbubble and the fluid to zero and the bubble moves to regions of lower shear, the lift force diminishes rapidly and the bubble eventually moves parallel to the wall (see figures 10 and 11).

Outside the boundary layer, however, the lift force is generally negligible because of the comparatively small values of velocity gradient encountered in the external flow. For example, the maximum velocity gradient that exists in the potential flow about a circular cylinder is on the order of U_∞/a, where U_∞ is the freestream velocity and a is the radius of the cylinder. If we assume that $u_\tau = 1.44$ m/s, and if a = 1 m, then in terms of the nondimensional quantities this velocity gradient is

$\frac{\tilde{U}}{\tilde{a}} = \frac{U_\infty}{u_\tau} \Big/ \frac{au_\tau}{\nu} = 1.7 \times 10^{-5}$, which is very small compared to the value found in the boundary layer where $k^+ \cong 1$. Hence, outside the boundary layer the main forces to be considered are drag force, pressure force, inertial force, and added mass force.

The Advected Particle Trajectory (APT-1) program takes all the relevant forces into consideration and can calculate the trajectories of the bubbles from the time they depart the wall to their long time asymptotic path. Once the microbubble size spectrum has been determined (including bubble splitting and coalescence effects), we know where, in diameter, most of the microbubble population reside. We can employ the microbubble diameter probability density function p(D) to describe the distribution in bubble sizes passing any downstream station. From this PDF we can define the mean bubble diameter μ_D, the variance σ^2_D, and skewness σ_D of the distribution. The bulk of the microbubble population can be estimated to lie between the diameters $\mu_D \pm \sigma_D$. The trajectories, followed by bubbles of these sizes as they pass through the TBL, serve to bound the portion of the boundary layer containing most of the microbubbles. For sufficiently small variance and skewness these trajectories also bound the region of greatest void fraction; hence the magnitude of the local void fraction maximum can be increased by reducing the variance in bubble diameters. Similarly, control of the location of this void fraction maximum can be accomplished by controlling the mean bubble diameter.

In order to examine further the phenomenon of microbubble drag reduction, it became necessary to obtain an estimate of the void fraction variation in the TBL. In the first attempt the APT-1 code was employed to calculate trajectories for bubbles of the diameters μ_D and $\mu_D \pm \sigma_D$ for the cases of three microbubble diameter spectra, for which the means and standard deviations (μ_D, σ_D) in microns were (338,34), (156,16), and 33,5,3.5, respectively. The trajectories for these three cases, shown in figure 12, were calculated with a mean TBL profile produced by the axisymmetric TAPS code. The body shape was that of an axisymmetric body with a length Reynolds number of $U_\infty L/\nu = 8.9 \times 10^7$ and a Froude number of $U_\infty/\sqrt{gL} = 2.55$. Each trajectory was calculated from three different locations, corresponding to x/L = 0.11, 0.53, and 0.82. The trajectories are presented in terms of both y/δ and y^+ versus x/L. For clarity, only the trajectories for the mean bubble size are shown for the case $\mu_D = 33.5$ microns.

The microbubble trajectories can be used to obtain estimates of the void fraction profile. Consider the evolution having downstream distance of bubbles with diameters in the interval (D, D, + ΔD) in proximity to a plane or nearly plane wall. Following typical turbulence modeling practice we consider the flow to consist of a basic steady portion (the mean turbulent flow profile) with a strong spatially varying cross-stream diffusion rate (an eddy viscosity model $\nu_e = \nu_e(y)$). If for the moment we neglect the diffusion, we can easily calculate the trajectories of the bubbles of diameter D and D + ΔD as though the flow were laminar. For ΔD/D << 1, these trajectories are separated by a very small distance; Δ and all the bubbles with diameters in the interval under discussion have trajectories that lie between these two trajectories.

For convenience we assume that all the bubbles in the initial distribution begin their trajectories at one point on the body, with the same initial conditions. Each of the trajectories can be described by a function of the form $y = f_D(x)$; so if $\gamma(D;x,y)\Delta D$ describes the void fraction at (x,y) as a result of bubbles in the interval (D,D + ΔD), then the above initial condition can be written as $\gamma(D; x,y)\,\Delta D = C\,\delta(y - f_D(x))\,p(D)\,\Delta D$, where C is an as yet undetermined constant, and δ is the Dirac delta function. Assuming the diffusion process obeys the linear diffusion equation with diffusion coefficient ν_e, the void fraction γ will then evolve downstream as

$$\gamma(D,x,y)\Delta D = \frac{C\,p(D)\,\Delta D}{2(\pi\nu_e t)^{1/2}} \exp\left\{\frac{-(y - f_D(x))^2}{4\,\nu_e t}\right\},$$ where we have

assumed that $\partial\nu_e/\partial y << u\Delta/L$ in the regions of interest, and that $U_\infty y/\nu_e >> 1$, so wall effects can be neglected. The coordinates of the mean bubble path (x_D, y_D) are related by $y_D = f_D(x_D)$ and can also be expressed parametrically by $x_D = x_D(t)$, $y_D = y_D(t)$. Hence, by the implicit function theorem, we can write $t = t_D(x)$, so that

$$\gamma(D;x,y)\;\Delta D = \frac{Cp(D)\,\Delta D}{2(\pi\nu_e t_D(x))^{1/2}} \exp\left\{\frac{-(y - f_D(x))^2}{4\nu_e t_D(x)}\right\}.$$ Then the local

void fraction can be recalculated by $\alpha(x,y) = \int_0^\infty dD\,\gamma(D;x,y)$. The quantities f_D and t_D in the expression for γ are implicit functions of D. In order to determine the value for C we require that the total void flux past any downstream plane, perpendicular to an axisymmetric body with diameter D_{body}, be conserved so that $Q = \pi D_{body} \int_0^\infty dy\,\alpha(x,y)\;u(x,y)$.

Thus we see that $Q = C\,\pi\,D_{body} \int_0^\infty dy\,u(x,y) \int_0^\infty dD\,p(D)\,g(D;x,y)$, where

$$g(D;x,y) = \frac{1}{2(\pi\,\nu_e t_D(x))^{1/2}} \exp\left\{\frac{-(y - f_D(x))^2}{4\,\nu_e t_D(x)}\right\}.$$ Interchanging

orders of integration, we can write

$Q = C\,\pi\,D_{body} \int_0^\infty dD\,p(D) \int_0^\infty dy\,u(x,y)\,g(D;x,y)$. However, if u(x,y)

varies slowly enough with y, that is, if $\left.\frac{1}{U_\infty}\frac{\partial u}{\partial y}\right|_{y_D} << \left(\frac{U_\infty}{\nu_e L}\right)^{1/2}$, then we

can approximate u(x,y) by some $\tilde{u}$ for the purpose of integration over y to find that $\int_0^\infty dy\,u(x,y)\,g(D;x,y) \cong \tilde{u}$. If we further assume that the initial microbubble distribution is sufficiently narrow that $1/U_\infty\,\partial u/\partial y << 1/\Delta$, then any dependence of $\tilde{u}$ on D can be ignored, and the second integration can be performed to arrive at $Q \cong C\,\pi\,D_{body}\,\tilde{u}$. Therefore the local void fraction can be computed as $\alpha(x,y) \cong$

$$\frac{Q}{\pi D_{body}\,\tilde{u}} \int_0^\infty dD\,p(D)\,g(D,x,y), \text{ or } \cong \frac{Q}{\pi D_{body}\,u(x,y)} \int_0^\infty dD\,p(D)\;g(D,x,y).$$

Examples of void fraction profiles and their evolution with downstream distance on an axisymmetric body are shown in figure 13.

5. MICROBUBBLE DRAG REDUCTION MECHANISM

5.1 Decay of Drag Reduction Downstream. Madavan, Deutsch, and Merkle [44] (abbreviated MDM hereafter) indicated that the ratio $\Delta c_f/c_f$ decays by 50 percent over a distance of 25δ, where δ is the boundary layer thickness. This observation raises a question about why this happens and how it can be prevented or mitigated in practice. Intuitively, we can suggest three basic mechanisms to be the potential origin of the loss of effectiveness of the microbubble drag reduction: growth of TBL thickness reducing the local void fraction; bubble diffusion away from the wall due to the turbulent eddy diffusivity; and bubble coalescence and subsequent rise away from the wall due to the larger buoyancy. The last mechanism is expected to be greatly reduced in sea water, especially for higher speeds. The second mechanism depends upon the magnitude of the turbulent eddy diffusivity $u_\tau\delta$, which also depends on δ, the boundary layer thickness. This fact led us to focus our discussion on the first mechanism: how the growth of δ(x) will degenerate the effectiveness of microbubble drag reduction.

The nominal void fraction, i.e., the average void fraction in a microbubble-laden TBL, was suggested by MDM as $C_V =$

$\frac{Q_{gas}}{Q_{gas} + Q_{boundary\ layer}}$, where $Q_{boundary\ layer} = (1 - \delta^*/\delta)U_0 b\delta$, and b is the

width of the gas ejector. In a single-phase liquid TBL, $1 - \delta^*/\delta = 0.87$. Defining $Q_{gas} = c_q v_0 s = c_q v_0 bL$, where s is the porous surface area, $b = \pi D$, and L is the length of ejection, we have

$$C_V = \frac{1}{1 + \frac{0.87\delta}{C_q L}}. \qquad (7)$$

The rates of change of C_V and δ are then related by $\frac{dC_V}{dx} =$

$-\frac{0.87}{C_q L} C_V^2 \frac{d\delta}{dx}$, so that if dδ/dx is reduced, so is dC_V/dx; hence it is

expected and hoped that the decay of the microbubble drag reduction can be reduced. The following discussion focuses on whether this basic mechanism can be identified as the primary one, how much reduction of dδ/dx is needed to slow the decay of C_V, and how, in practice, such a mitigation can be implemented.

First we compare the decay rate of C_V with the MDM data on the persistence of skin friction reduction over the distance downstream. According to MDM, $\Delta c_f/c_f$ decays by about a factor of 2 over a distance of 30δ. Since the MDM data show that $\Delta c_f/c_f$ is proportional to the C_V, we expect that C_V should be reduced by a factor of 2 over a distance of 30δ. Such an assumption can be compared with equation (7). MDM (in their figure 17) gave the following key parameters: L = 7 inches, $c_q \cong 0.02$ for $\Delta c_f/c_f$ at speed $U_0 = 10$ m/sec, $C_{V0} = 0.48$ at $x_0 = 409$ mm will yield

$a\left.\frac{\Delta c_f}{c_f}\right|_0 = 0.85$, at $x_1 = 575$ mm, $\left.\frac{\Delta c_f}{c_f}\right|_2 = 0.4$ with an equivalent $C_{V1} = 0.20$;

in other words, a nearly 50-percent reduction in $\Delta c_f/c_f$ for a 50-percent reduction in C_V. Using $\delta = 0.37\,x/Re_x^{0.2}$ and $U_0 = 10.8$ m/sec, we find $\delta(x_0) = 0.71$ cm and $\delta(x_1) = 0.93$ cm. Substituting into (7), we find $C_{V1}/C_{V0} \cong 0.8$, certainly not sufficient to explain the 50-percent reduction observed in the MDM data.

From Migirenko and Evseev's [44] void fraction profile data, we see a distinct peak in the void fraction at $y/\delta \cong 0.1$, and if we neglect the

bubble-bubble interactions, then theoretically the local void fraction should follow the diffusion equation. In other words, the void fraction should follow $c(y) \propto e^{-y^2/4\nu_e t}$, where y is the distance from the void fraction peak and $\nu_e \cong 0.04\, u_\tau \delta$ (Hinze [37], p. 645). To find one e-fold time or, equivalently, the distance downstream, for c(y) to reduce by e^{-1}, we set $4\nu_e t = (1/2\ \delta)^2$. Substituting ν_e into the above, we obtain $\Delta x \cong \frac{1}{2} U_0 t \cong 1/1.28\ (2/c_f)^{1/2}\ \delta \cong 35\delta$ for $c_f = 0.001$, where Δx is not very different from the MDM data of 30δ. This indicates that diffusion of bubbles instead of growth of the TBL thickness might be the dominant mechanism for the decay of microbubble drag reduction.

The next relevant question is how much growth there is in $\delta(x)$ over a distance of 30δ, and how much suction is required to reduce its growth. From the expression for $\delta(x)$ we find at the same speed, $\frac{\Delta\delta(x)}{\delta(x)} = 0.8\frac{\Delta x}{x} = 24\frac{\delta(x)}{x} = \frac{8.88}{Re_x^{0.2}}$, so that at $Re_x = 10^7$, $\Delta\delta/\delta \cong 0.3$. The required suction coefficient is then defined as $C_{q_s} = \frac{\pi D\int_0^{0.3}\delta(x)dy}{U_0 A}$, where A is the suction area and D is the diameter of the axisymmetric body. Equivalently, the above equation can be rewritten as $C_{qs} = \frac{\delta}{L}\int_0^{0.3}\left[1-\left(1-\frac{y}{\delta}\right)^{1/7}\right]d\left(\frac{y}{\delta}\right)$, where $A = \pi DL$ and $u/U_0 = 1 - (1 - y/\delta)^{1/7}$ (Hinze [37], p. 632) were applied.

5.2 Bubble Splitting as a Turbulence Reduction Mechanism. From previous discussion about bubble splitting, we can estimate the total amount of turbulent kinetic energy needed to split bubbles in a TBL and compare that with the total energy available in a TBL. From this estimation, we can identify whether the bubble splitting is a plausible basic mechanism for reducing the turbulence. Furthermore, if it is indeed plausible, we could identify what can be done to maximize its effects. From the energy balance point of view, it takes a Reynolds stress $\overline{\rho u'^2} = 3\sigma / d_{bubble}$ to initiate bubble splitting. Assuming that bubbles stay spherical in shape, the work needed to split a bubble from a diameter of d_{bubble} into bubbles of diameter ½ d_{bubble} (abbreviated henceforth as d_b) is $\int_{\frac{d}{2}}^{d}\frac{3}{d_b}4\pi\left(\frac{d_b}{2}\right)^2 dd_b = \frac{9}{8}\pi\sigma d_b^2$, and the energy needed to split N bubbles is $9/8\pi\sigma d_b^2 N$. Assuming the bubble size spectrum follows a Rayleigh spectrum, as shown in figure 5, $n(d_b) = N\frac{d_b}{d_{b0}^2}e^{-1/2\left(\frac{d_b}{d_{b0}}\right)^2}$, the total amount of turbulence energy required to split all N bubbles into bubbles with diameters of half their original sizes can be calculated from $N\int_0^\infty \frac{9}{8}\pi\sigma\frac{d_b^3}{d_{b0}^2}e^{-1/2\left(\frac{d_b}{d_{b0}}\right)^2}dd_b = \frac{9}{4}\Gamma(2)\,\pi\sigma N d_{b0}^2$, where d_{b_0} is the bubble diameter of the maximum population in the Rayleigh spectrum. The power P_s needed to split all N bubbles is then $9/4\ \Gamma(2)\pi\sigma\, \dot{N} d_{b0}^2$. To relate the bubble generation rate $\dot{N}$ to the gas ejection rate Q, we first integrate the Rayleigh spectrum to find the total gas volume and then differentiate it with respect to time in order to obtain the volumetric gas flow rate: total gas volume $= N\int\frac{4}{3}\pi\left(\frac{d_b}{2}\right)^3\frac{d_b}{d_{b0}^2}e^{-1/2\left(\frac{d_b}{d_{b0}}\right)^2}dd_b = \left(\frac{\pi}{2}\right)^{3/2} N d_{b0}^3$. Thus the volumetric gas flow rate Q can be expressed as $Q = \left(\frac{\pi}{2}\right)^{3/2}\dot{N} d_{b0}^3$, where $\dot{N}$ is the number of bubbles generated per time. Expressing $\dot{N}$ in terms of Q, we have the rate of turbulence energy required to split bubbles: $P_s = \frac{9}{4}\pi\sigma d_{b0}^2\left(\frac{2}{\pi}\right)^{3/2}\frac{Q}{d_{b0}^3}$, or $P_s = \frac{9}{(2\pi)^{1/2}}\frac{\sigma}{d_{b0}}Q$. This power should be compared with the total turbulence power available in a TBL over an axisymmetric body, which can be derived as follows.

The power per unit width (from Hinze [37], p. 642, figure 7-20) is $P'_{TBL} = \int_0^\delta \overline{\rho q^2}dy$, where $\overline{q^2} = \overline{u'^2} + \overline{v'^2} + \overline{w'^2}$, and $\sim \overline{q^2} = 8u_\tau^2\left(1-\frac{y}{\delta}\right)$, so that $P'_{TBL} = 4\rho u_\tau^2\delta$, where δ is the boundary layer thickness. Multiplying P'_{TBL} by πDU_0, where D is the diameter of an axisymmetric body and U_0 the body speed, we have $P_{TBL} = 4\pi\rho_\tau^2\delta U_0 D$. The ratio of P_S to P_{TBL} is then

$$\frac{P_S}{P_{TBL}} = \frac{9}{2(2\pi)^{1/2}}\left(\frac{\sigma}{\rho u_\tau^2 d_{b0}}\right)\left(\frac{Q}{\pi D\delta U_0}\right). \quad (8)$$

The first term in parentheses represents the ratio of surface tension stress to turbulent wall shear stress for a bubble with a diameter of d_{b_0}; the second term in parentheses represents the ratio of gas flow rate to that of the TBL axisymmetric body. To estimate the first term in parentheses, we apply the following facts: $\overline{\rho u'^2_{max}} \cong 9\rho u_\tau^2$, $d_{b_{max}} \cong 3d_{b_0}$, so that $\frac{\overline{\rho u'^2_{max}}\, d_{b_{max}}}{\sigma} = 3 = 27\frac{\rho u_\tau^2 d_{b_0}}{\sigma}$, and $\frac{\sigma}{\rho u_\tau^2 d_{b_0}} \cong 10$. Equation (8) represents the fraction of energy expended to split all bubbles from d_b into ½ d_b. In practice, this ratio should be equal to the drag reduction ratio. Although this analysis is preliminary in nature, it does indicate that bubble splitting can be a primary cause of the effectiveness of microbubbles to reduce turbulence. To increase the effectiveness, we can increase the surface tension between the water and the gas; therefore, injecting a certain liquid or using a gas with higher value of σ might be useful. Since d_{b0} decreases with flow speed U_0, by increasing U_0 a higher reduction might also be possible. However, we must also increase the gas flow rate Q proportionally.

6. CONCLUSIONS

Hydrodynamic forces, both tangential and normal to the wall, have been identified. Quantitative relationships with gas-injection-induced bubble formation on a wall are obtained. Fundamental unknowns are the bubble shape, the drag force over it, and the lift force on a bubble in a TBL. Bubble size regimes have been identified to be: spherical cap, single bubble, intermediate, and jet disintegration regimes. The controlling parameter has been found to be the ratio of gas exit velocity to the external flow velocity. At very low injection rate, the tangential force balance mode determines bubble size, i.e., water drag and surface tension balance each other. At higher injection rates, the normal force balance mode takes over, i.e., the lift force balances the surface tension or water inertia surrounding a bubble. At even higher injection rates, jet instability determines the bubble size. There are still unknown regions between the gas jet and bubble regimes. Effects of sea water have been identified but not quantified. Effects of bubble splitting have been found to be very significant and might well be the key origin of microbubble drag reduction mechanisms. Transport of bubbles in a TBL has been simulated. The smaller the bubble, the more likely the bubbles will stay near the wall. The unknowns are the quantitative lift force formulation, bubble coalescence, and splitting effects.

7. REFERENCES

1. Al-Hayes and Winterton, "Bubble Growth in Flowing Liquids," *International Journal of Heat Mass Transfer*, vol. 24, pp. 213-221, 1981.

2. Al-Hayes and Winterton, "Bubble Diameter on Detachment in Flowing Liquids," *International Journal of Heat Mass Transfer*, vol. 24, pp. 223-230, 1981.

3. I. S. Gradshteyn and I.M. Ryzhik, *Table of Integrals, Series, and Products*, A. Jeffrey (ed.), Academic Press, New York, 1980.

4. P. G. Saffman, "The Lift on a Small Sphere in a Slow Water Flow," *Journal of Fluid Mechanics*, vol. 22, p. 385, 1965.

5. P. G. Saffman, "Corrigendum," *Journal of Fluid Mechanics*, vol. 31, p. 625, 1968.

6. Voloshko, et al., *Inzhenerno-Fizicheskii Zhurnal*, vol. 35, no. 6, pp. 1066-1071, 1978.

7. F. MacIntyre, "Bubble Generation on a Heated Body," personal notes, University of Rhode Island, Graduate School of Oceanography, 1981.

8. E. Silberman, "Gas Jets in Liquids, Production of Bubbles By the Disintegration of Gas Jets in Liquids," *5th Midwestern Conference on Fluid Mechanics*, p. 263, 1957.

9. Lord Rayleigh, "On the Stability of Cylindrical Fluid Surfaces," *Phil. Mag. of London*, vol. 34, pp. 177-180, 1892.

10. M. M. Reischman and J.M. Holzmann, "Digital Image Analysis of Two Phase Flow Data," NOSC Technical Report 502, Naval Ocean Systems Center, San Diego, CA, 1980.

11. T. E. Burton, "The Connection Between Intermittent Turbulent Activity Near the Wall of a Turbulent Boundary Layer with Pressure Fluctuations at the Wall," Report No. 70208-10, Acoustics and Vibration Laboratory, MIT, Cambridge, MA, 1974.

12. V. A. Sanborn, "Evaluation of the Time Dependent Surface Shear Stress in Turbulent Flows," ASME Publication 79-WA/FE-17, 1979.

13. H.R. Kreplin and H. Ecklemann, "Bearer of the Three Fluctuating Velocity Components in the Wall Region of a Turbulent Channel Flow," *Physics of Fluids*, vol. 22, no. 7, p. 1233, 1979.

14. R. S. Brodkey, J.M. Wallace, and H. Eckelmann, *Journal of Fluid Mechanics*, vol. 63, p. 209, 1974.

15. J. C. Bhatia, F. Durst, and J. Jovanovic, "Corrections of Hot-Wire Anemometer Measurements Near Walls," *Journal of Fluid Mechanics*, vol. 122, pp. 411-431, 1982.

16. H. Nakagawa and I. Nezu, "Structure of Space-Time Correlations of Bursting Phenomena in an Open-Channeled Flow," *Journal of Fluid Mechanics*, vol.104, p.143, 1981.

17. J. J. Gallagher, "Microbubble Size Distributions Data Collection and Analyses," *OCEAN 1984 Conference*, 1984.

18. H. Schlichting, *Boundary Layer Theory*, McGraw-Hill, New York, 1960.

19. J. Aitchison and J.A.C. Brown, *The Lognormal Distribution*, Cambridge University Press, Cambridge, England, 1957.

20. F. E. Fox and K.F. Herzfeld, *Journal of the Acoustical Society of America*, vol. 26, pp. 984-989, 1954.

21. G. A. Riley, *Limnology Oceanography*, vol. 8, p. 372, 1963.

22. D. C. Blanchard, "The Electrification of the Atmosphere by Particles from Bubbles in the Sea," *Progress in Oceanography*, vol. 1, pp. 72-202, 1963.

23. E. C. Monahan, "Sea Spray and Its Relationship to Low Elevation Wind Speed," Ph.D. Thesis, MIT, Cambridge, MA, 1966.

24. J. C. Scott, "The Role of Salt in Whitecap Persistence," *Deep Sea Research*, vol. 22, pp. 653-657, 1975.

25. B. D. Johnson and R.C. Cooke, "Generation of Stabilized Microbubbles in Sea water," *Science*, vol. 213, p. 209, 1981.

26. A. Detwiler, "Surface-Active Contamination on Air Bubbles in Water," in *Surface Contamination: Genesis, Detection, and Control*, K.L. Hittal, ed., Plenum Press, New York, 1979.

27. E. B. Kraus, *Atmosphere-Ocean Interaction*, Clarendon Press, Oxford, England, 1972.

28. G. K. Batchelor, *An Introduction to Fluid Dynamics*, Cambridge University Press, Cambridge, England, 1967.

29. I. A. Avetisyan, *Soviet Physics of Acoustics*, vol. 23, pp. 285-288, 1977.

30. R. E. Glazman, "Effects of Absorbed Films on Gas Bubble Radial Oscillations," *Journal of the Acoustical Society of America*, vol. 74, p. 980, 1983.

31. E. T. Degens, in *The Global Carbon Cycle: SCOPE Report 13*, B. Bolin et al., eds., pp. 57-77 Wiley, New York, 1979.

32. G. I. Taylor, "The Formation of Emulsion in Definable Field of Flow," *Proceedings of the Royal Society*, London, Series A, vol. 146, p. 501, 1934.

33. A. Acrivos, *The Breakup of Small Drops and Bubbles in Shear Flows*, New York Academy of Sciences, New York, 1983.

34. J. M. Rallison, *Journal of Fluid Mechanics*, vol. 109, p. 456, 1981.

35. J. O. Hinze, "Fundamentals of the Hydrodynamic Mechanism of Splitting in Dispersion Processes," *American Institute of Chemical Engineers Journal*, vol. 1, no. 3, p. 280, 1955.

36. P. H. Clay, *Proceedings of the Royal Academy of Sciences*, vol. 43, pp. 852-979, 1940.

37. J. O. Hinze, *Turbulence*, Second Edition, McGraw-Hill, New York, 1975.

38. C. A. Sleicher, Jr., "Maximum Stable Drop Size in Turbulent Flow," *American Institute of Chemical Engineers Journal*, vol. 8, no. 4, p. 471, 1962.

39. M. Sevik and S.H. Park, "The Splitting of Drops and Bubbles by Turbulent Fluid Flow," *Journal of Fluid Engineering*, p. 53, 1973.

40. A. N. Kolmogorov, "On the Disintegration of Drops in a Turbulent Flow," Doklady Akad., Nauk, SSSR, vol. 66, p. 825, 1949.

41. S. A. Morsi and A. J. Alexander, "An Investigation of Particle Trajectories in Two-Phase Flow Systems," *Journal of Fluid Mechanics*, vol. 55, p. 193, 1972.

42. F. Odar and W.S. Hamilton, "Forces on a Sphere in a Viscous Fluid," *Journal of Fluid Mechanics*, vol. 18, pp. 302, 1964.

43. N. K. Madavan, S. Deutsch, and C.L. Merkle, "Measurements of Local Skin Friction in a Microbubble Modified Turbulent Boundary Layer," Technical Memorandum 84-136, Pennsylvania State University Applied Research Laboratory, 1984.

44. G.S. Migirenko and A.R. Evseev, "Turbulent Boundary Layer with Gas Saturation," *Problems of Thermophysics and Physical Hydrodynamics* (in Russian), Novosibirsk, Nauk, 1974.

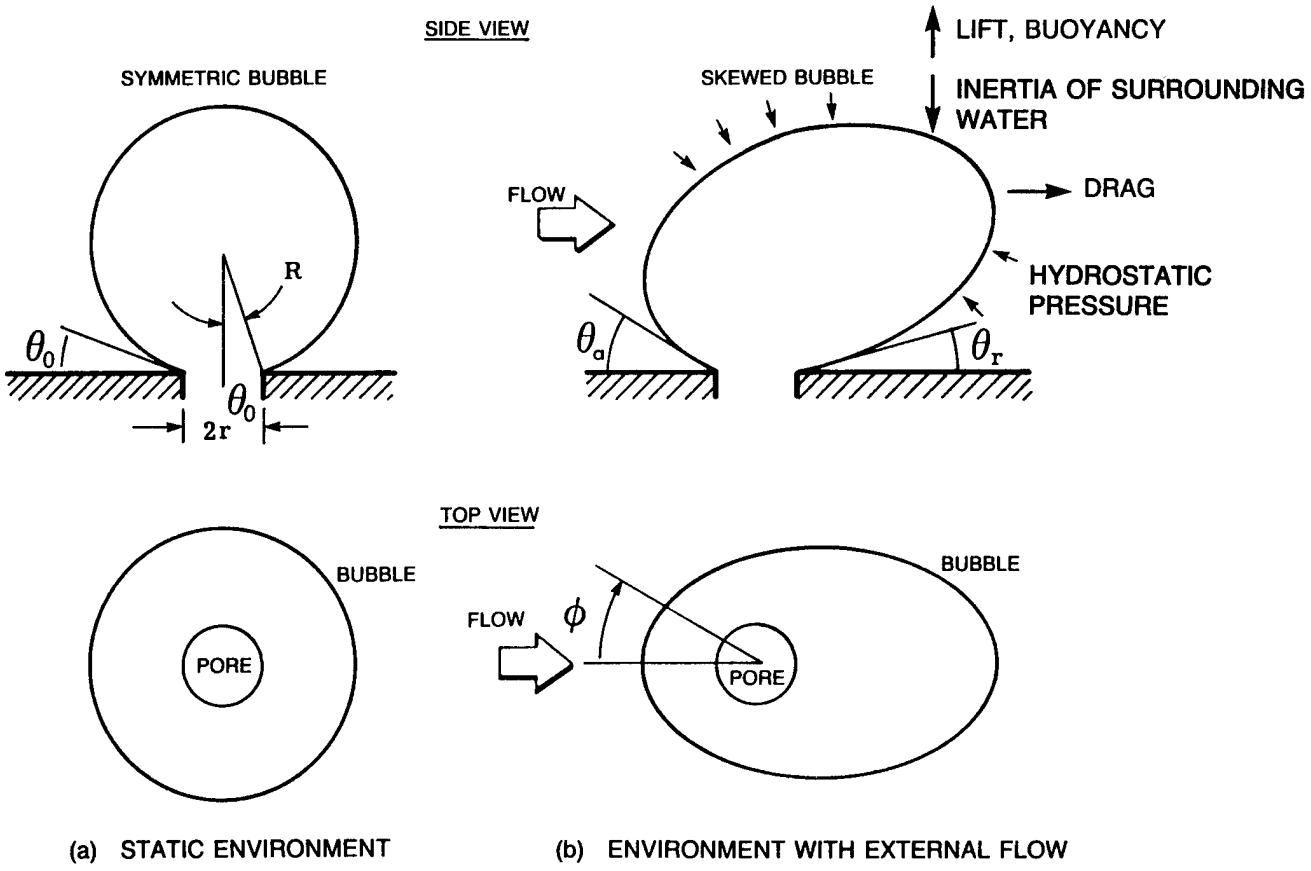

Figure 1. Bubble Formation Geometry and Nomenclature in Static and Flowing Environments

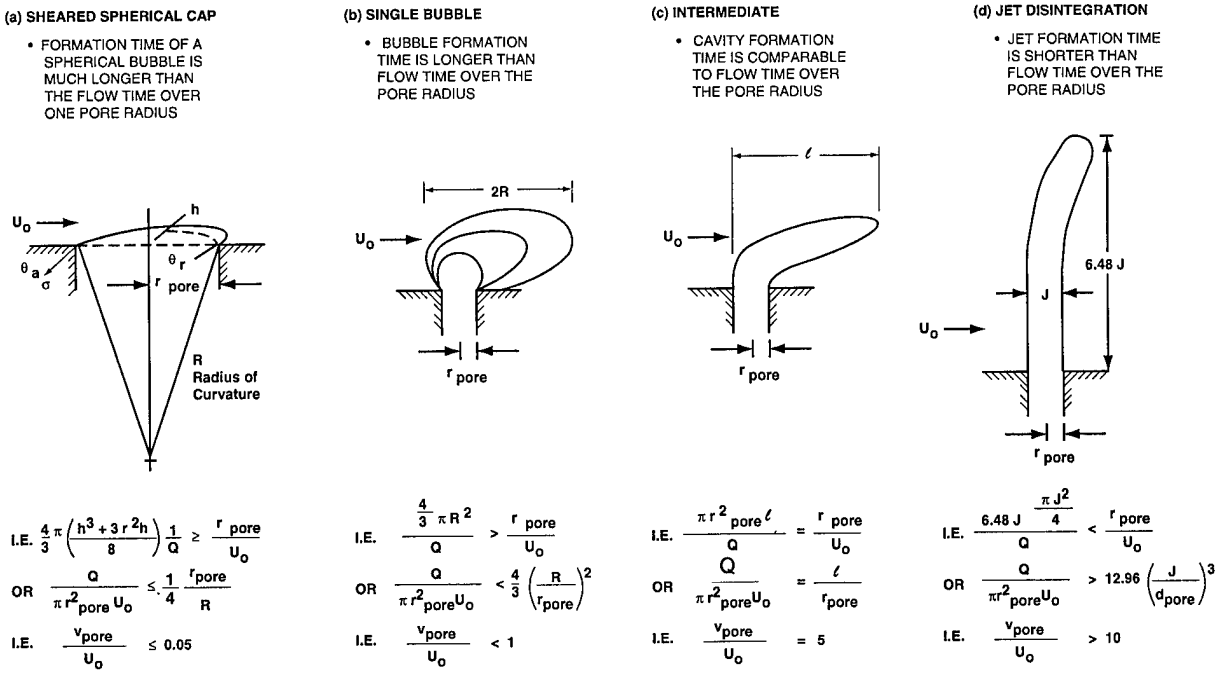

Figure 2. Bubble Formation Time Analysis

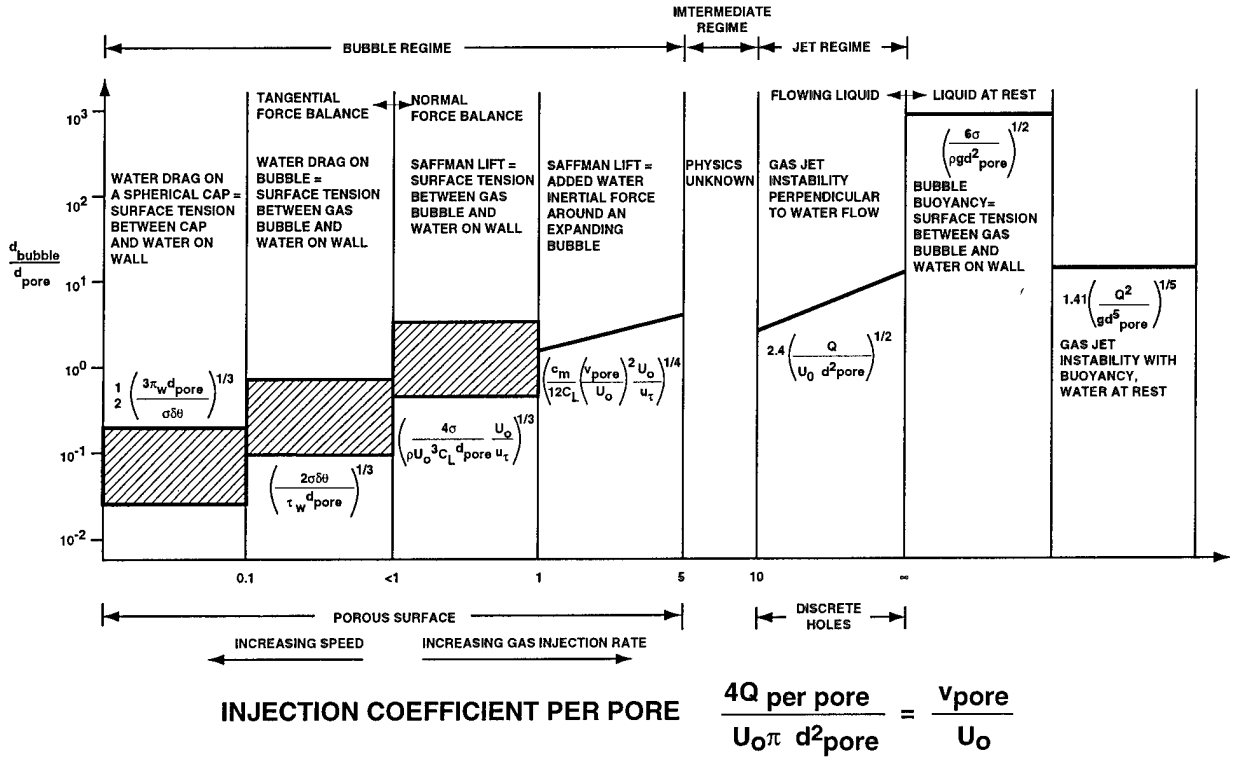

Figure 3. Approximate Realms of Bubble Diameter Criteria

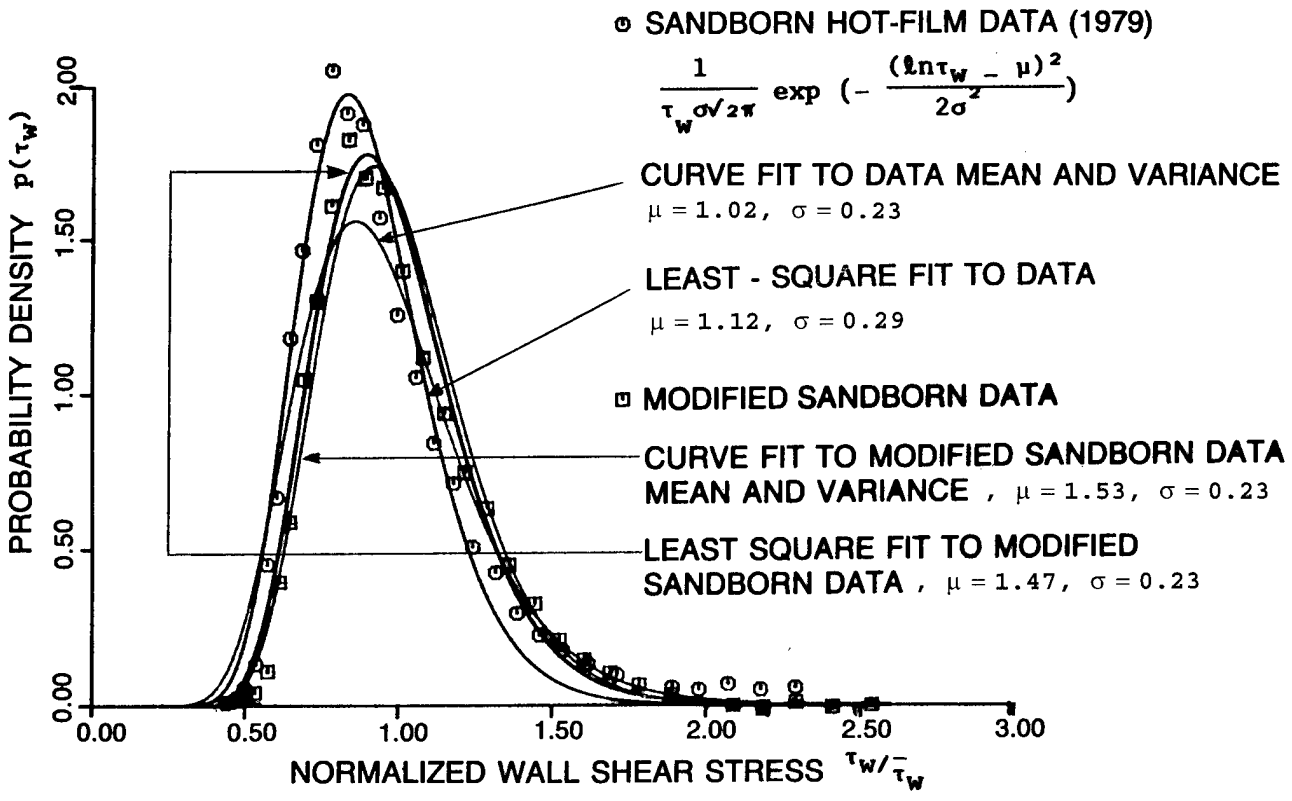

Figure 4. Normalized Probability Density Distribution of Surface Shear Stress over a Flat Plate

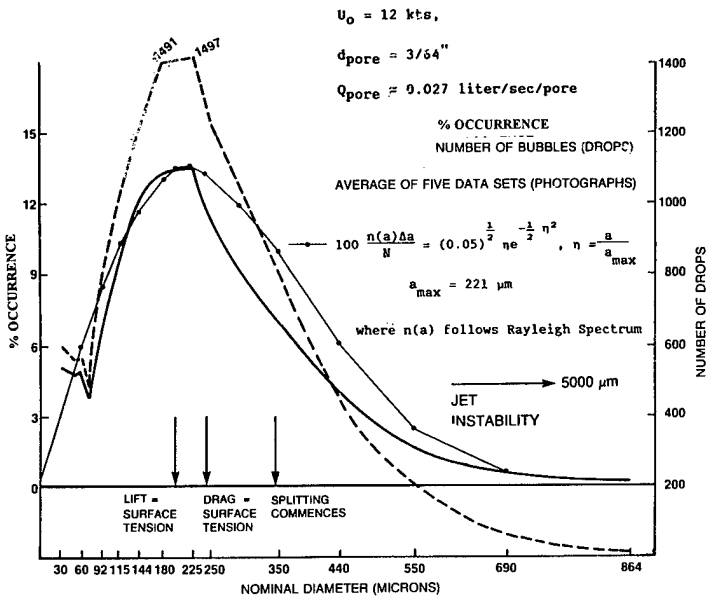

Figure 5. Bubble Size Spectrum Obtained by Gallagher (1984) with an MIT Camera and Bete Fog Analyzer

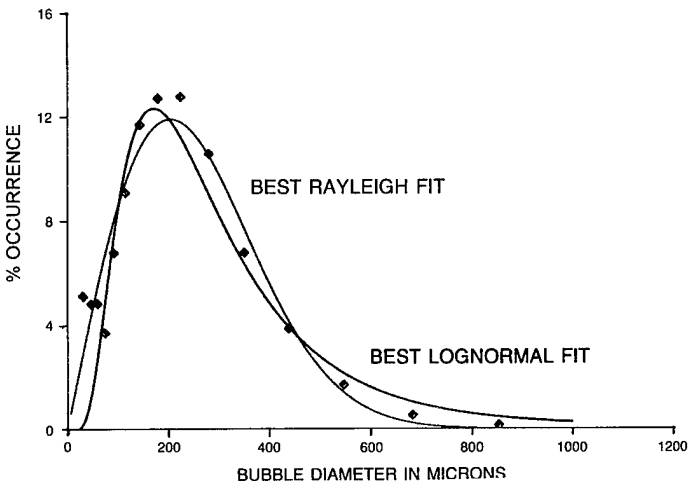

Figure 6. Comparison of Rayleigh and Lognormal Fits to Gallagher's Bubble Size Spectrum

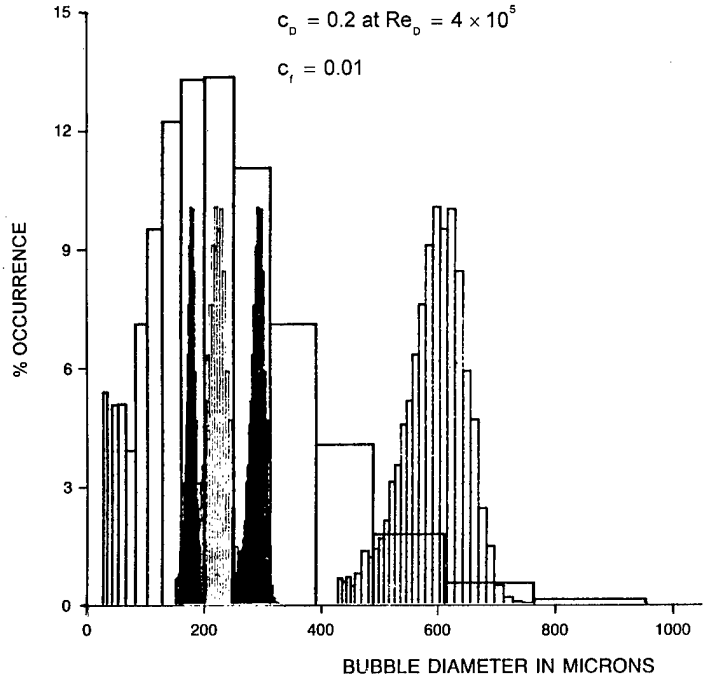

Figure 7. Comparison of Simulated Bubble Size Spectra with Gallagher's Ocean Data

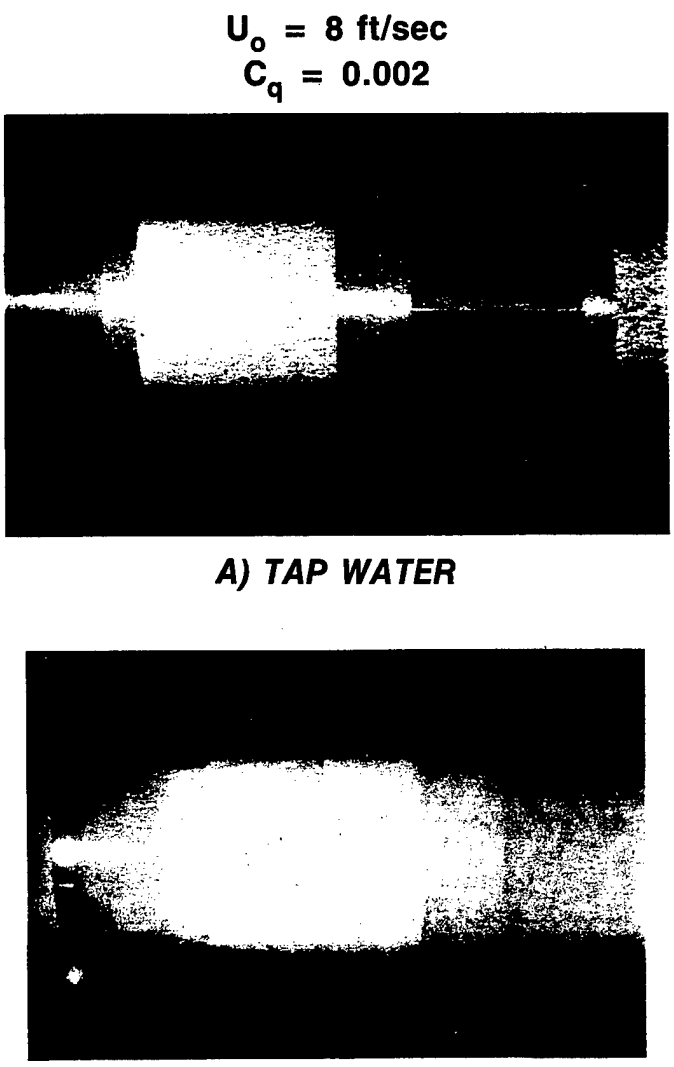

Figure 8. Microbubbles Ejected Through Two Rings

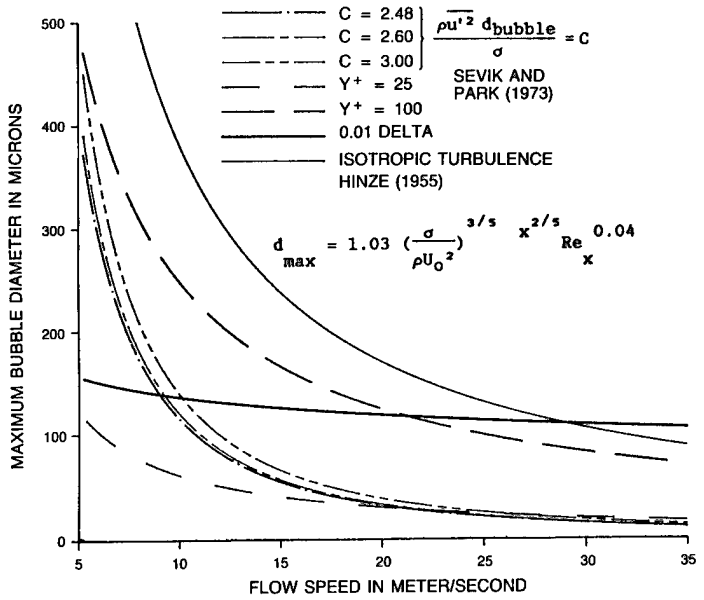

Figure 9. Maximum Bubble Size in a TBL as a Result of Bubble Splitting

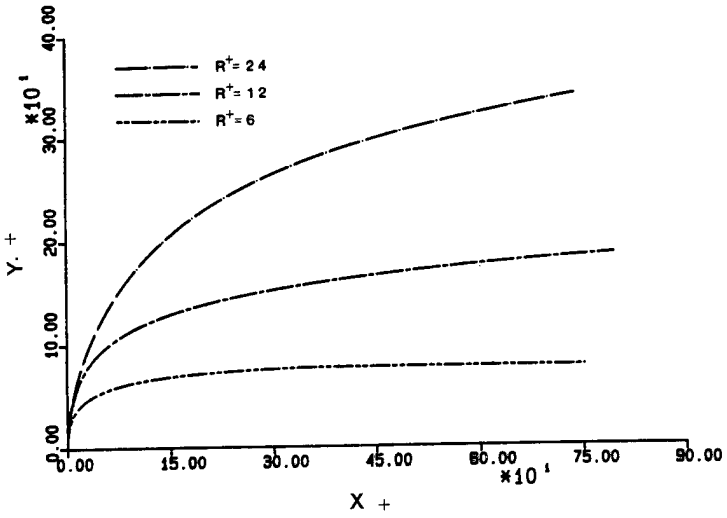

Figure 10. Nondimensional Particle Trajectories

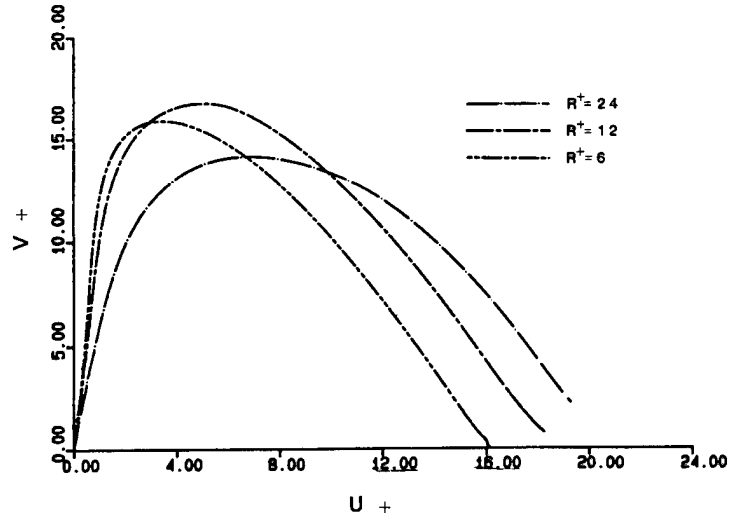

Figure 11. Nondimensional Particle Velocities

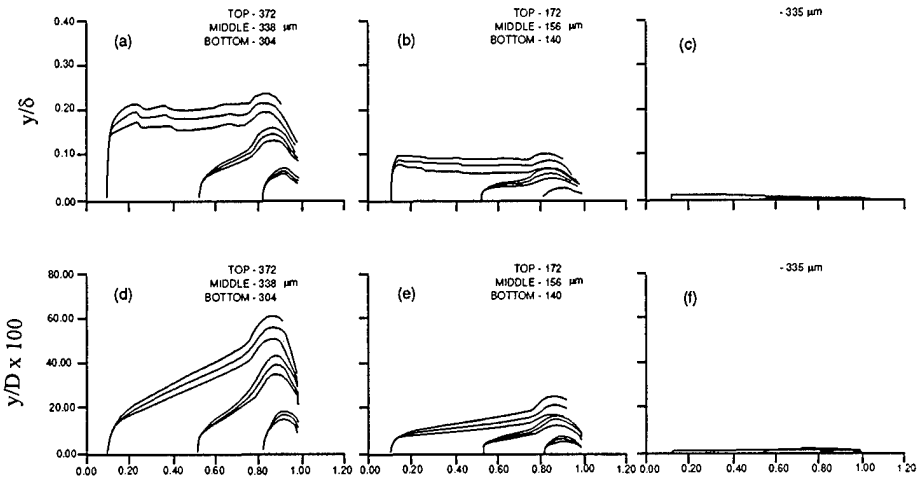

Figure 12. Microbubble Trajectories

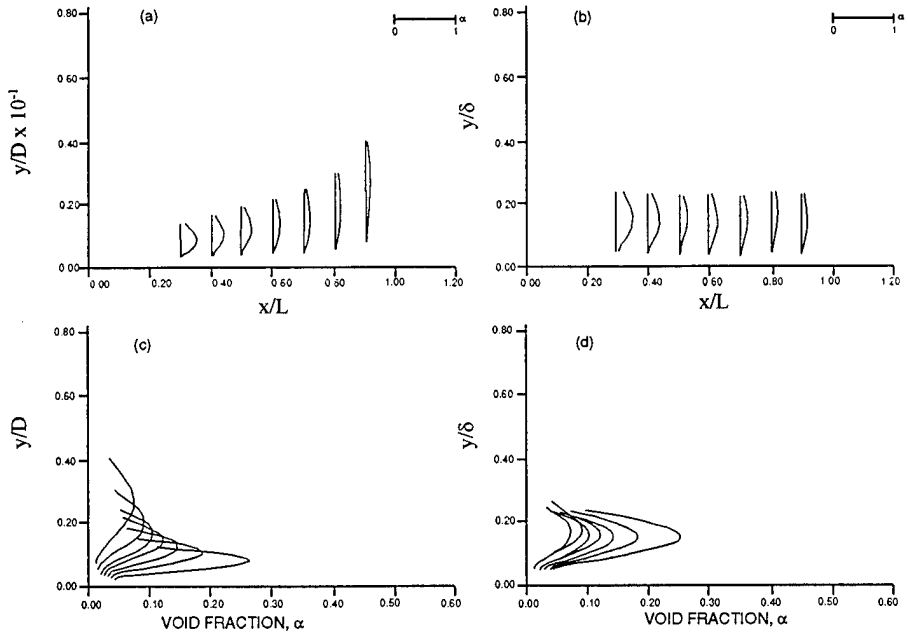

Figure 13. Void Fraction Profiles

Turbulent Drag Reduction Methods: Electromagnetic Drag Reduction

ENGINEERING INSIGHT OF NEAR-WALL MICROTURBULENCE FOR DRAG REDUCTION AND DERIVATION OF A DESIGN MAP FOR SEAWATER ELECTROMAGNETIC TURBULENCE CONTROL

J.C.S. Meng
Naval Undersea Warfare Center
Newport, Rhode Island 02841-1708
mengjc@code80.npt.nuwc.navy.mil

Abstract - The latest findings regarding the dynamics and cause-effect relationships of near-wall microturbulent events are summarized, together with quantification of the sequence of microturbulent events and a description of the geometric pattern of microturbulent events. A historical perspective on microturbulence and drag reduction is given in terms of phenomenological structural models and the effects of drag reduction on near-wall microturbulence events. With this focus, the engineering dynamics of the key microturbulent events are expressed in terms of microturbulent spatial (streamwise, spanwise, normal to wall) and temporal scales versus Reynolds number. From these dynamics, rudimentary estimates of the force and energetics of each event are derived based on known phenomenological turbulence structural models. The electromagnetic turbulence control (EMTC) and drag reduction concepts are related. The spatial distribution of the control elements relative to the microturbulence patterns, the electrical field actuation frequency versus microturbulence occurrence, and the Lorentz pressure gradient power and EMTC efficiency in terms of the magnetohydrodynamic interaction parameter and load factor map are described. The conclusion is that any methodology for control of turbulence can be effective only if it is built on a robust foundation of the near-wall turbulence phenomenology.

Emerging techniques in drag reduction invite a fundamental question, i.e., based on the known dynamics and cause-effect relationships of microturbulent events, where should the turbulence production chain be disrupted? Any effective drag reduction strategy must eventually be traced to the root-cause of turbulence production. To address this question, some of the currently known cause-effect relationships of microturbulent, near-wall events, the turbulence production cycle, and related drag reduction strategies are summarized. The insights gained should be very useful for practical engineering applications of drag reduction.

1. CAUSE-EFFECT RELATIONSHIPS OF MICRO-TURBULENT EVENTS AND TURBULENCE PRODUCTION CYCLE

Smith [1] described how to advance from descriptive and empirical results to a synthesis of cause-effect relationships implied by microturbulent events. He illustrated that, because of the high shear flow near the wall, the spanwise line vortex is distorted, followed by the narrowing of the streamwise parts and broadening of the bent spanwise parts of the hairpin vortices as the distortion progresses, leading to a universal spanwise spacing in viscous units of about 100. Multiple vortex lines interact with each other, resulting in migration of both vortices and vorticity away from the wall—a mechanism by which smaller initial vortices evolve into larger and more visible vortex structures. The well observed low-speed streaks can be explained in terms of the trailing part of the interacting hairpin vortices. The bursting of the vortices is simulated as a result of the interaction between the essentially inviscid vortex and the viscous, erupting, near-wall fluid and in response to the passage of wall-region vortices. The response is made visible in terms of the sudden increase in the displacement thickness due to the interaction. If the vortex is strong enough, it leads to a burst; if not, streaks may form. Impingement of vortices on the streaks creates the appearance of a waviness and swaying. Regeneration of the vortices is simulated as a result of the similar three-dimensional unsteady interaction creating an adverse streamwise pressure gradient in the region between the trailing vortex lines. As the vortex moves progressively closer to the wall, the adverse pressure gradient intensifies and local flow separates, leading to ejection. Subsequent displacement of the ejected fluid is counteracted by an inflow of higher momentum fluid from immediately upstream, which appears as the sweep event, thus completing the streak, ejection, burst, and sweep cycle. Numerical simulations carried out by Robinson [2] also supported Smith's cause-effect relationships and showed that less than 50% of lifted streaks roll up to form a new vortex; the others dissipate and disappear. Those that roll up and erupt penetrate to distances on the order of $y^+ \approx 100$.

Choi [3] provided another cause-effect near-wall turbulence model, starting from his observation of "near-wall bursts," an event similar to sweep but occurring very near to the wall at about $y^+ \leq 15$. These near-wall bursts appear in a staggered pattern.

In search of a unified framework to unite several seemingly disjointed concepts, a process of hairpin vortex growth and the formation of coherent hairpin packets in wall turbulence was proposed by Zhou et al. [4]. Using a combination of particle image velocimetry and numerical simulations $Re_\theta = 930$, they found that the hairpin vortex dynamics can unify several earlier models and quantify the dynamic conditions under which they can occur. Drawing insights from both the experiments and numerical simulations, they showed that the shear layer, the ejections, the low-speed streaks, liftup, oscillation, and burst all evolve from the hairpin vortex packets. The hairpin packet forms low-speed regions extending several hundred y^+ above the wall and several thousand viscous lengths downstream. Above a critical layer, the hairpin vortex grows and multiplies, while below a critical layer the vortex gradually dissipates. With sufficient strength, a single hairpin can grow and create both new quasi-streamwise vortices and new hairpin vortices. The vortices in the packet advect downstream with little dispersion.

The simulation of Zhou et al. [4] provided a detailed account of the sequence of the dynamic events leading to the formation of an Ω-shaped vortex and sorted out the causes and effects of the generation mechanism. By subtracting the convection velocity and using the imaginary part of the eigenvalue of the velocity gradient tensor, they visualized the vortical structure with great clarity. The hairpin vortex packet creates a region of low-momentum flow between itself and the wall. This low-momentum region impinges on the upstream high-momentum fluid to form an upstream shear layer. Beneath this low-momentum region and within the horizontal part of the vortices is the low-speed streak between the wall and $y^+ \approx 20$. Beneath each primary hairpin vortex is a flow induced by the vortex induction away from the wall and upstream; this is the ejection. Multiple ejection events form the burst. The hairpin vortices have a diameter of approximately 25-50 viscous units. The average distance from wall is about $y^+ = 78$. The spanwise spacing of the vortices is about 100 viscous units near the buffer region and decreases to about 40 away from the wall toward the head of the vortex. The streamwise separation between the hairpin vortices is about 100-150 viscous units. There is also a stagger of about 25-50 spanwise spacing units, leading to a 12° pattern. The envelope of the hairpin vortex packet makes an angle of 15° to 17° with the wall. It takes about $t^+ \approx 25$ for the hairpin vortex to evolve into a shear layer. It takes another $t^+ \approx 25$ for the ejection flow to evolve at a height of about $y^+ \approx 85$. Overall, it takes about $t^+ \approx 120$ to complete the cycle of the creation of a new hairpin vortex. This populates the entire boundary layer with hairpin vortices and streamwise vortices.

One may argue that all of these results have been derived from relatively low Reynolds number flow visualizations and numerical simulations, and that extrapolation to higher Reynolds numbers needs to be validated. In a very innovative experiment conducted over a flat plate over the Great Salt Lake Desert, Klewicki et al. [5] showed that at

$Re_\theta \approx 1.5 \times 10^6$ the mean spanwise spacing of low-speed streaks was approximately 100. In addition, they also found that the crescent-shaped pocket pattern width is ≈ 127, which follows a scaling law of $Re_\theta^{0.12}$, and that the mean time between pocket events is $t^+ \approx 36$. Ferguson et al. [6] presented a Markov state-transition analysis of turbulence structure above a gravel bed. The Markov states were interpreted as the four quadrants defined by Lu and Willmarth [7] of the fluctuating streamwise and normal velocity components. Ferguson et al.'s measurements of transition probabilities illustrated a Markov probability methodology for characterizing the sequence of the wall layer turbulence phenomenology. They showed that a statistically significant preference for the wall layer undergoes acceleration, declination, deceleration, and then inclination, i.e., through quadrants 1 ,2, 3, 4, 1. This sequence suggests the coherent structure of streak, ejection, burst, sweep, and back to streak. Gyr and Muller [8] showed that bedforms reflect the interaction of coherent flow structures with the size of the grains and the bedform height. Depending on the size and height in viscous units, smooth bed, ripple, bedform, and dunes are characterized. Consistent with intuition, sweeps are shown to be the mechanism for sediment transport and are responsible for grain motion. Grain height patterns are then considered to be a visualization of the ejection-sweep events. Gyr and Muller showed that, using the convective velocity, the sweep frequency can be translated into a length scale to form a rhomboidal pattern, with periodic streamwise length in viscous units of about 500, and spanwise spacing viscous scale of about 100, again producing a pattern of 12°. This pattern also inspires the hypothesis that the sweeps are synchronized in the statistical sense.

Figure 1 combines the above information and extends the conceptual schematic of near-wall phenomenology (Meng.[9]).

2. NEAR-WALL EVENTS AND DRAG REDUCTION STRATEGIES

All of these findings are very illustrative, but how do we make them useful for engineering applications? Since we concluded earlier that any practical drag reduction approach must focus on affecting near-wall structures, and since we know the complete cycle of near-wall events and their relevance to turbulence production, the question is which event should be inhibited to achieve maximum drag reduction.

One approach can be derived by observing that the fundamental fluid dynamic cause of high drag or momentum loss is the sweep, which results from ejection and burst, which in turn results from an adverse pressure gradient in the near-wall region caused by viscous/inviscid interaction. Therefore, to control the turbulence or to achieve drag reduction, one would rely on controlling (at the microscale level) creation of the adverse pressure gradient. This may lead to the concept of microcells of a streamwise favorable pressure gradient to determine where and when it detects a strong enough microflow separation. Before proceeding to the drag reduction strategy, let us first examine the empirical facts of the drag reduction effects on near-wall events.

2.1 Drag Reduction Effects on Microturbulent Events. Tiederman and Luchik [10] injected polymer into the sublayer and found increases in λ^+ and in the time between bursts T^+_B. Using wall pressure measurements, they also established that the increase in λ^+ and T^+_B corresponds to drag reduction. The upward shift in the log-law velocity profile has been well observed in polymer flows. Sirmalis [11] observed dyed turbulent boundary layers with low concentrations of polymer and found that the fine-scale turbulence was eliminated, leaving only coarse turbulence, and that the boundary layer thickness was thinned.

For passive control, Choi [3] examined, as an example, the relevance of the near-wall turbulence structures over the drag-reducing riblets. He found that the mean velocity profile shifted away from the wall, and he found an increase of viscous sublayer thickness similar to that produced by drag-reducing polymer. The duration of the near-wall burst was reduced by a factor of two, whereas the frequency was increased. The average spanwise spacing between the vortex pairs over a riblet surface was two times larger than that over a smooth surface. Choi et al. [12] applied direct numerical simulations of turbulent flows over riblet surfaces and showed that riblets mitigate the Reynolds shear stress-producing events by restricting the location of the streamwise vortices above the wetted surface, so that only a limited area of the riblets is exposed to the sweeps, and by impeding the spanwise cross-stream flows necessary to replace the near-wall fluid ejected away from wall during ejection. Effects on the mean velocity and turbulence statistics are limited to the inner region of the boundary layer. The observed global effects are an upward shift in the log-law velocity profile, increased sublayer thickness, displaced virtual origin of the wall, reduced momentum thickness, and an increase in mean streak spacing. Through simulations, Kim et al. [13] found that the center of the streamwise vortex is located on average at $y^+ \approx 20$, with a diameter about $d^+ \approx 30$, so that the optimal spacing of the riblets is $s^+ \approx 20$, with an included angle of 60°. This is probably the most direct example of how basic near-wall turbulence understanding was used to design a drag reduction scheme. Recently, Tang and Clark [14] showed that the peak value u'_{rms} is lower by 10%, the peak in the u'_{rms} profile shifts from $y^+ \approx 15$ for the plain surface to $y^+ \approx 25$ for the riblets and, correspondingly, the peak location of turbulence production, defined as the Reynolds stress multiplied by mean flow gradient, is also pushed toward $y^+ \approx 25$. The probability density functions show a dramatic reduction in the occurrence of ejections and sweeps as compared with a smooth surface.

For the active control case, Kim [15] described a numerical experiment of active turbulence control by suppressing the sweep and ejection events associated with the streamwise vortices using out-of-phase blowing and suction. The results showed that the out-of-phase blowing prevents the formation of high vorticity regions on the surface. These regions are located away from the surface, and the strength of the vorticity is reduced, resulting in a reduction of the surface viscous drag. The structure of the wall layer streaks has also been changed, with their strength reduced considerably and increased physical spacing, while mean spacing in wall units stays approximately the same. Using well-established numerical simulations, Choi et al. [16] showed that significant drag reduction is achieved when the surface boundary condition is modified to suppress the dynamically significant coherent structures present in the wall region. They identified two key drag-reduction mechanisms: first, deterring the sweep motion without modifying the primary streamwise vortices above the wall, so that the high shear rate regions on the wall are moved to the interior of the flow; and, second, stabilizing and preventing lifting of the spanwise vorticity near the wall, thereby suppressing a source of new streamwise vortices above the wall. The apparent outward shift of turbulence statistics in the controlled flows indicates a displaced virtual origin of the boundary layer and a thickened sublayer. It was found in numerical simulations with active control that there is an upward shift in the log-law; namely, the intercept of the log-law with $u^+ = y^+$ is increased from $y^+ \approx 10$ in the natural state to $y^+ \approx 15$. Peak locations of all turbulence intensities, production, and dissipation are shifted away from the wall by the same amount. The viscous sublayer is thickened and the displacement thickness increased, while the momentum thickness is decreased, which is related to the skin-friction. The streaky structures below $y^+ \approx 5$ are clearly diminished, and the streak spacing above $y^+ \approx 5$ is increased by the control. The local maximum of the streamwise vorticity fluctuations in the controlled flows is farther away from the wall compared with that in the natural flows, suggesting that the sweeps are attenuated.

2.2 Strategies for Near-Wall Turbulence Modification for Drag Reduction. Jimenez and Moin [17] carried out numerical experiments by reducing the spanwise spacing of the computational domain below $100\nu/u_\tau$ and found that the flow does not remain turbulent unless the spanwise domain is increased. Jimenez and Moin suggested that without streaks there would not be turbulence. Kim [15] suggested that reducing the streaks, or the longitudinal vortices that create the streaks due to interaction with the wall, is the best strategy for turbulence control. Choi [3] concluded that given the strategy of restricting the spanwise movement, the effectiveness can be maximized by choosing the optimal spacing of the riblets so that it is nearly equal to the gap between the longitudinal vortices during the near-wall bursts.

A useful observation by Choi et al. [12] is that sweep dominates Reynolds stress production near the wall, while ejection dominates away from wall. This finding raises a possibility for efficient wall skin-friction reduction methodologies; i.e., should the focus be solely on reducing sweeps rather than on both primary microturbulent events. Choi et al. [16] stated that drag is reduced mainly by deterring the sweep motion without modifying the primary streamwise vortices above the wall, so that the high-shear-rate regions on the wall are moved to the interior of the flow $y^+ \geq 5$. Active control changed the evolution of the wall vorticity layer by stabilizing and preventing lifting of the spanwise vorticity near the wall, thus weakening a source of new streamwise vortices above the wall. It was also observed that active control schemes do not alter the structure of the outer wall turbulence, but simply attenuate its strength and move the effective origin outward.

Kim [15] suggested an active scheme that detects sweeps or ejections and that disturbs their sequence of energy-producing activities each time the sweeps or ejections are seen to affect the turbulent events, it is possible—based on numerical simulations—to achieve 20% and 40% drag reductions, respectively, for suction/blowing at the wall surface and for spanwise wall oscillation. Choi et al. [16] compared their results from active blowing and suction with those of Narasimha [18] from unsteady blowing and suction and showed that the former has a significant effect on turbulence statistics away from the wall, while the latter has only marginal effects in the interior of the flow. The difference appears to be due to the use of a feedback control. Even in cases where the mass input at the wall is applied passively at the bursting frequency, useful interaction may not take place between control inputs and flow structure because of the spatial and temporal randomness of turbulence structure (Bushnell and McGinley [19]).

Choi et al. [16] also investigated a variety of strategies for active control of dynamically significant coherent structures to achieve skin friction reduction. It was found that wall pressure alone is not an adequate detector of the flow toward the wall or away from it. Surface shear stress correlates better with the normal velocity, although the best indicator is the spanwise derivative on the wall of the normal gradient of spanwise velocity, which has little practical application potential. Handler et al. [20] investigated use of phase randomization. By selectively randomizing the largest length scales of the turbulence, they found a 50% drag reduction, a phenomenon similar to that of polymer injection. Figure 2 summarizes the foregoing observations.

Reasoning that the spatial dimensions and time periods of the near-wall events are not identical in each occurrence but rather they evolve, grow, and dissipate as a function of time and they do not advect in a frozen pattern (as Taylor's hypothesis holds) but can be statistically determined, Meng [21] invoked a strategy to capture the events in probabilistic sense and advocated utilizing a Markov process in the active control of turbulence. He reasoned that, given the short duration of the events, simply detecting them will not be effective and a predictive methodology is necessary. In other words, given the present state, a prediction of what will be the most likely events to be taking place over a fairly large area of repeatable patterns is required so that counteractions can be remotely applied. He illustrated this strategy by applying it to the electromagnetic control of turbulence.

3. CONCEPTS OF ELECTROMAGNETIC CONTROL OF TURBULENCE IN TERMS OF NEAR-WALL TURBULENCE.

3.1 Laminar MHD Stability. MHD stability of an incompressible, electrically conducting fluid, boundary layer flow along a flat plate in the presence of a transverse magnetic field without imposed electric field was analyzed by Watanabe [22] and later by Watanabe [23] with uniform suction or injection. The neutral stability curves of Tollmien-Schlichting waves and the critical Reynolds numbers were calculated for various values of the MHD interaction parameter and the suction or injection parameter. He concluded that stability increases with increasing MHD interaction and increasing suction parameters, and that the friction coefficient decreases with increasing MHD and increasing injection parameters, while displacement thickness increases with increasing MHD and increasing injection parameters.

3.2 Streamwise Vorticity Inhibit Theory Based on Wall Layer Conductance by Electrolyte Injection and Counter Vorticity Generated by Wallward Lorentz Pressure. Nosenchuck and Brown [24] were the first to introduce the concept of populating the boundary layer with discrete, independent, electromagnetically controlled regions. Their hypothesis was based on direct control of the coherent motions responsible for turbulence production—the normal velocity fluctuations and the Reynolds stresses in the near-wall region—and they postulated that a relaxation time after the removal of the Lorentz force would exceed the time to respond to it. Their theoretical basis was that the counter-vorticity generated by the Lorentz force would inhibit coupling between the inner and outer regions in the boundary and suppress the amplification of the streamwise vorticity. The details were provided in Nosenchuck and Brown's patent [25] for the single-tile concept. Their experiment was conducted in a fresh-water channel on a flat plate turbulent boundary layer, $Re_\theta \approx 1100$; the conductance σ of the boundary layer was enhanced by supplying a small flux of dilute NaOH electrolyte with the optimal conductivity-enhancing layer thickness to be $10 < y^+ < 30$. For the single-tile experiment, the magnetic flux was $B_z \approx 0.05$ tesla, steady-state electrical current density $j \leq 20$ mA/cm^2 over a dimension on the order of $x^+ \approx 1000$, $z^+ \approx 500$, and the laser sheet illumination was at a height of $y^+ \approx 1$. The flow visualization results indicated complete lack of vertical transport from the near-wall region with the electric field turned on, thereby substantiating the observation of the reduction of the time-series axial velocity fluctuations. It was expected that the relaxation time after the electric field is turned off would also be long compared with the time for the flow to respond to the Lorentz force and the EMTC on time would be short compared with the relaxation time. Conversely, Nosenchuck and Brown [25] stated that by reversing the Lorentz pressure away from the wall one can destabilize the flow in the boundary layer and induce turbulence.

For the three-tile experiment, the electrodes were sequentially activated at 10 Hz, 1/3 duty cycle, flow speed at 0.15 m/s, $Re_\theta \approx 1350$ in a test tank 1.5 m wide, 0.5 m high, and 6 m long. The magnetic flux was $B_z \approx 0.016$ tesla, and the maximum electrical current density $j \leq 10$ mA/cm^2. Three tiles cover a total dimension of 0.24 m streamwise by 0.18 m spanwise, or in terms of viscous units $x^+ \approx 1500$ by $z^+ \approx 1150$, and the individual tile dimension is on the order of $x^+ \approx 500$, $z^+ \approx 1150$. The laser sheet illumination was at a height of $y^+ \approx 20$. When the tiles were activated, little dye was seen in the laser sheet, indicating a decrease of vertical transport, with an expected attenuation of near-wall turbulent motions. A turbulent spot was also artificially generated upstream of the EMTC region, and the turbulence disappeared once it entered the EMTC region. The injection of conductivity-enhancing electrolyte was still believed to be necessary.

3.3 Spanwise Rolling Vortices Resonance Theory. Nosenchuck and Brown [26] presented another patent using a multiple, sequentially activated EMTC tile concept. The ability of generating a Lorentz pressure gradient normal to the wall by the injection of a wall layer of electrolyte was eliminated and replaced by the pulsing phase control of the EMTC cells. Conceptually, pulse phasing creates a series of rotational-flow regions in the boundary layer, and these rotational flow regions continually reinforce the small amount of vorticity created by the gradients of the Lorentz pressure vector. It was conceptualized that a "critical" velocity profile could be maintained that would reduce the drag to that between the laminar flow and the uninhibited turbulent flows. The spacing of the EMTC cells was described to be 10 times the height of the maximum field strength based on the Maxwell equations. The optimal frequency of the equal-phase tiles was determined experimentally. It was found that there is a critical frequency at which a condition analogous to resonance is attained, and it is expressed as: $f_{critical} \propto U_\infty / d_{cell}$, where U_∞ is the free-stream velocity and d_{cell} is the cell spacing. In experiments without electrolyte injection over a different eight-cell array 0.3 m in length streamwise by 0.4 m spanwise with magnetic flux of 0.6 tesla, $j \approx 100$ mA/cm2, each equal-phase tile was actuated for 0.75 s at 1/4 duty cycle and the flow velocity was 0.3 m/s so that $f_{critical} \approx 3$ Hz, the measured drag was reduced 90% from 0.1 N/m^2 to about 0.01 N/m^2.

Nosenchuck [27] later conducted more experiments without electrolyte injection in a small water tunnel with NaOH solution of electrical conductivity $\sigma \approx 2.5$ S/m. The 8 x 8 array EMTC plate was 8 in. x 15 in. in size, with center-to-center spacing of 0.7 in. between stainless electrodes and neodymium boron iron magnets. Altogether there were 64 electrodes arranged with 8 electrodes per spanwise row and 8 rows streamwise. At speeds from 0.075 to 0.3 m/s, $Re_x \approx 5 \sim 7.5 \times 10^5$, the flows ranged from the laminar to the transitional flow regimes. By injecting dye from the leading edge and laser-induced fluorescence of disodium fluorescein, Nosenchuck clearly visualized the ability of the Lorentz pressure gradient to create wavelike rotational flows near the wall. With the maximum magnetic induction of 0.7 tesla and applying 4 to 7 volts (0.5 to 2 amps) for laminar flow, 7 to 15 volts (2 to 4 amps) for transitional flows, and 15 to 38 volts (4 to 12 amps) for turbulent flows, they determined empirically the critical frequencies from 4 Hz (0.075 m/s) to 900 Hz (4 m/s). When EMTC was activated, hot-film probe output traces were shown to indicate 80% reduction at 0.525 m/s and 25% to 55% reduction at 4 m/s. The basic premise was that vorticity rotating counter to that naturally generated on the wall would push the maximum vorticity away from the wall. The maximum effect occurs when the vorticity source on wall generates a wave pattern that resonates with the natural vorticity source and therefore reduces the skin friction. It was also shown that the "critical frequency" (above which no bubbles were generated) was about 300 Hz at 1 m/s

Subsequently, Nosenchuck [28] showed refined experimental results using surface hot-film probes to measure the spanwise variation of streamwise shear stress, cylindrical hot-film probes traversing normal to the wall to measure streamwise velocity, and a pitot tube for free-stream characteristics. At low speed, 0.07 m/s, $Re_x \approx 6 \times 10^4$, with streamwise magnets and cross-stream electrodes operated at 3 volts (0.2 amps) and from 2 to 3.5 Hz, results of streamwise velocity profiles revealed the expected near-wall jet-like feature. Coefficients of friction versus Reynolds number showed that results were substantially lower than the well-established laminar flow lines, which raised questions about the tunnel flow ambient pressure gradient. By showing the drag reduction ratio versus the power ratio defined as the ratio of EMTC power to that naturally occurring, Nosenchuck expected that the maximum drag reduction ratio would be obtained at the point where the power ratio equals 1. In laminar flows at speeds of 0.1 and 0.3 m/s, the drag ratio is larger than 1, meaning a drag increase, while in turbulent flows at speeds of 1.0 and 3.0 m/s, the drag ratio is less than 1, meaning a drag reduction even as the power ratio increases beyond 1.

Nosenchuck [29] presented some other tests results for a novel axisymmetric model. A roughly 10-in.-diameter, 3-foot-long model with a teardrop tail cone and numerous tiles was released for buoyant rise in a 15- to 20-foot-tall pipe filled with salt water. The model breaks over the water surface and drops back into the water. Using magnets affixed to the buoyant model and tracking the time history of the trajectory as the model lifts, acceleration due to the activation of EMTC was interpreted as a 50% net drag reduction.

Kral [30] modeled turbulence over an EMTC flat plate. Her results show regions of significant MHD interaction parameter where drag reduction vanishes, with 50% drag reduction levels over the region in between. Crawford and Karniadakis [31] conducted direct Navier-Stokes equations simulation in a fully developed turbulent channel flow to simulate Nosenchuck's experiment on inclined waves and pulsed powering. Crawford & Karniadakis's calculations show a drag reduction on the order of 5%. These channel flow numerical simulation results are progressively more realistic and therefore significant, as a fine resolution EMTC experimental drag measurement is practically very challenging.

Note that all EMTC experiments conducted so far have been based on open-loop control; in other words, all experimental investigators are basically exploring trial-and-error matrices without a quantitative theoretical means to optimize. Bandyopadhyay and Castano [32] explored the possibility of a higher payoff in a more rational and feedback closed-loop control. They proposed that the Lorentz pressure over the tile will generate a Stokes layer of vorticity with a height on the order of $\sqrt{(2\nu/f)}$, which is equal to a thin wall layer with a height of 1 mm. From this a resonance frequency was derived to be 70 Hz, which is in reasonable agreement with their 5 x 5 array of microtiles. This observation can actually be further extended to a more general relationship between the Stokes layer and the ideal height of the microturbulent events, or the height $y^+ \approx 10$, where maximum turbulence production takes place. In other words, $\sqrt{(2\nu/\omega)} \approx 10\ \nu/u_\tau$ or, $f \approx u_\tau^2/(100\pi\upsilon)$, so that a quadratic dependence of the resonance frequency on the speed is expected.

3.4 Theoretical Spanwise Resonance Theory. A convincing "resonance mechanism" for a natural turbulent boundary layer without MHD effects was derived by Jang et al. [33]. Benney and Gustavsson [34] first introduced the "direct resonance concept" that a three-dimensional disturbance with certain wave numbers can grow to a relatively large amplitude. This theory draws from the empirical observation by Morrison et al. [35] of wavelike streamwise fluctuations so that a weakly nonlinear perturbation around the mean velocity might be applicable to the turbulent boundary layer bursting process and from the observation by Blackwelder [36] of the similarity between bursting and the laminar-turbulent transition phenomenon. Guided by this, Jang et al. [33] replaced the Blasius profile with the mean turbulent profile including the sublayer, law of the wall, and logarithmic law of wake profiles, and examined the Orr-Sommerfeld and vertical vorticity equations. The linearized vertical vorticity equation contains a forcing term related to the vertical velocity that provides the physical link. Wherever eigenvalues of both equations in wave number space are identical, resonant growth occurs at the streamwise wave number $\alpha^+ \approx 0.0093$, spanwise wave number $\beta^+ \approx 0.035$, and frequency $\omega^+ \approx 0.09$. Note that $\tan^{-1}(\beta^+/\alpha^+) \approx 15°$ for the wedge pattern well known in the transition regime. These theoretical results agree well with experimental data obtained by Morrison et al. [35]. Further, by applying a nonlinear perturbation method, Jang et. al. [33] showed that this resonance mechanism produced a mean flow of counterrotating streamwise vortices in a turbulent boundary layer.

Relating this well-established theoretical foundation to the near-wall microturbulence phenomenology, there appears to be a physics-based validity to the theory that if the naturally occurring frequency and the wave pattern are detected and countered by the applied EMTC force 90° out of phase, a significant reduction of turbulence and drag reduction can conceivably be achieved. The question then is: How can a design map be derived by relating EMTC to the near-wall turbulence.

4. ESTIMATION OF DYNAMIC SCALING LAWS

The heuristic kinematics and dynamics of microturbulent events and EMTC can be related. In principle, once the dominating physics of a microtubulent event is understood, an imposed Lorentz pressure gradient can be tailored spatially and temporally to relate the imposed EMTC Lorentz pressure in a Eulerian control volume on an evolving Lagrangian microturbulent fluid element subject to all naturally occurring fluctuating forces.

4.1 Natural Microturbulent Ejection Power Scaling. Let us derive dynamic scaling law relationships for all microturbulent events, especially the power scaling for ejection and sweep events for practical application. The power required for a microvortex ejection can be derived from basic dynamics principles. One starts with the definition of power:

$$\vec{F} \cdot \vec{u} = \frac{\Delta(m\vec{u})}{\Delta t} \cdot \vec{u} = \rho \frac{\Delta x \Delta y \Delta z}{\Delta t} (\Delta u + \Delta v) \cdot \vec{u}$$

$$= \rho \frac{(100)^2 \cdot 50}{25 \frac{\nu}{u_\tau^2}} \left(\frac{\nu}{u_\tau}\right)^3 \left[\left(2 \cdot 15 u_\tau^2\right) + u_\tau^2\right] \cong 6.2 \times 10^5 \rho u_\tau \nu^2,$$

where it is assumed that $\Delta x^+ = 100$, $\Delta y^+ = 50$, $\Delta z^+ = 100$, $\Delta t^+ = 25$, $\Delta u = u(y^+ = 80) - u(y^+ = 30) = 2u_\tau$, $\Delta v = u_\tau$, and the local velocity vector is assumed to be $u = 15u_\tau$, $v = u_\tau$. From this relationship, one can easily calculate the energy per ejection by multiplying the above expression of power per ejection by $25\nu/u_\tau^2$ to obtain $1.5\times10^7\rho\frac{\nu^3}{u_\tau}$. The ejection power per unit area in a natural burst cycle is then equal to energy/ejection × number of bursts/span/second/burst separation:

$= 1.5\times10^7\rho\frac{\nu^3}{u_\tau}1.5\times10^{-4}\frac{u_\tau^3}{\nu^2}\frac{1}{T_B 15u_\tau} = 230Re_\theta^{-0.73}\rho u_\tau^3$, or in terms of length Reynolds number $\cong 2.6\times10^3 Re_x^{-0.584}\rho u_\tau^3$. From these relationships, the natural microturbulent ejection scaling for $5\times10^5 < Re_x < 10^7$ can be summarized:

Dynamics:
Vortex liftup force per ejection ≅ $6.2\times10^5\rho\nu^2$
Vortex liftup power per ejection ≅ $6.2\times10^5\rho u_\tau\nu^2$
Vortex liftup energy per ejection ≅ $1.5\times10^7\rho\nu^3/u_\tau$
Power:
Natural microejection power required per unit area
≅ $230Re_\theta^{-0.73}\rho u_\tau^3$.

It is, however, important to point out that ejections contribute significantly to Reynolds stress but account for only a small fraction of the dynamics, as would be expected. This fact can be demonstrated by comparing ejection power per unit area with $1/2\rho U^3 c_f$ and examining the ratio, which can be expressed as $\approx 29Re_\theta^{-0.855} \cong 0.08$ and $\cong 0.01$ for $Re_\theta \cong 10^3$ and 10^4, respectively.

4.2 Natural Microturbulent Sweep Power Scaling. Assuming the frequency-per-span information for sweeps is identical to that of the ejection, the power scaling for sweep events can also be carried out. The power required for a single sweep can be derived from basic dynamics principles. One starts again with the definition of power:

$$\vec{F}\cdot\vec{u} = \rho\frac{(200)^2\cdot100}{100\frac{\nu}{u_\tau^2}}\left(\frac{\nu}{u_\tau}\right)^3\left[\left(4.6\cdot15u_\tau^2\right)+u_\tau^2\right] \cong 2.8\times10^6\rho u_\tau\nu^2,$$

where it is assumed that $\Delta x^+ = 200$, $\Delta y^+ = 200$, $\Delta z^+ = 100$, $\Delta t^+ = 100$, $\Delta u = u(y^+ = 200) - u(y^+ = 30) = 4.6u_\tau$, $\Delta v = u_\tau$, and the local velocity vector is assumed to be $u = 15u_\tau$, $v = u_\tau$. The energy per sweep is then $\cong 2.8\times10^8\rho\frac{\nu^3}{u_\tau}$. The sweep power per unit area in a natural burst cycle is $= 2.8\times10^8\rho\frac{\nu^3}{u_\tau}1.5\times10^{-4}\frac{u_\tau^3}{\nu^2}\frac{1}{T_B 15u_\tau} = 4\times10^3 Re_\theta^{-0.73}\rho u_\tau^3$.

From these relationships, the natural microturbulent sweep scaling for $5\times10^5 < Re_x < 10^7$ can be summarized:

Dynamics:
Force per sweep ≅ $2.8\times10^6\rho\nu^2$
Power per sweep ≅ $2.8\times10^6\rho u_\tau\nu^2$
Energy per sweep ≅ $2.8\times10^8\rho\nu^3/u_\tau$
Power:
Natural microturbulent sweep power required per unit area
≅ $4\times10^3 Re_\theta^{-0.73}\rho u_\tau^3$ or $4.5\times10^4 Re_x^{-0.58473}\rho u_\tau^3$

It is interesting to see that sweeps not only contribute significantly to Reynolds stress and but also account for a major fraction of the dynamics. Comparing sweep power per unit area with $1/2\rho U^3 c_f$ and examining the ratio $504Re_\theta^{-0.855}$, we find it is ≈1.39 and ≈0.17 for $Re_\theta \cong 10^3$ and 10^4, respectively.

4.3 Threshold Lorentz Pressure Power for Electro-magnetic Turbulence Control. The threshold Lorentz pressure required for EMTC can be derived by comparing the Lorentz pressure power per unit area with the power per unit area in natural microturbulent burst cycles. Conceptually, the threshold is where this ratio equals 1. Before one can proceed to derive this ratio, one must establish the length and time scale assumptions, which are summarized below:

EMTC Length Scales:
Spanwise spacing of Lorentz pressure: $100\nu/u_\tau$
Distance normal to wall of Lorentz pressure: $30\nu/u_\tau$

EMTC Time Scales (if pulsed or ac):
Lorentz pressure frequency: $1/T_s$
Lorentz pressure pulse duration: $20\nu/u_\tau^2$.

Since it is not clear *a priori* that thresholds would be identical for the cases of Lorentz pressure in the streamwise direction and normal to the solid wall, calculations will be carried out for both cases. For the normal Lorentz pressure, the Lorentz pressure power/area = $\Delta p\cdot\vec{u}$:

$$\Delta p\cdot\vec{u} = \int_0^{40\frac{\nu}{u_\tau}}\vec{J}\times\vec{B}\cdot\vec{u}\,dy = J_0B_0\int_0^{40\frac{\nu}{u_\tau}}e^{-\frac{2y}{a}}\vec{e}_y\cdot\vec{u}\,dy,$$

where $\vec{J}$ and $\vec{B}$ are the externally applied electrical current density and magnetic flux density vectors, respectively.

In a turbulent boundary layer without an axial pressure gradient, the local vertical velocity has zero mean. The vertical velocity is away from the wall during ejection and bursting, and it is toward the wall during sweep. Unless the Lorentz pressure is sustained long enough to give rise to a velocity along the Lorentz pressure gradient vector, no net work would be done to the flow. In practice, this implies that the EMTC pulse duration should be longer than the duration of bursting. Assuming that a velocity normal to the wall on the order of the natural turbulence, $v \cong u_\tau$ in the active MHD region, then $\Delta p\cdot\vec{u} = \frac{J_0B_0au_\tau}{2}\left(1-e^{-\frac{80\nu}{u_\tau}}\right)$, which is an idealized order-of-magnitude estimation. The threshold Lorentz power normal to the wall must then be equal to or greater than the power required in the natural ejection cycle. In other words, the MHD interaction parameter must satisfy

$$\frac{J_0B_0a}{1/2\rho u_\tau^2}\left(1-e^{-\frac{80\nu}{u_\tau a}}\right) \geq \frac{1\times10^4}{Re_x^{0.584}}.$$

For the streamwise Lorentz pressure gradient case, the local velocity is $u \cong 14\,u_\tau$:

$$\Delta p\cdot\vec{u} = \int_0^{40\frac{\nu}{u_\tau}}J_0B_0e^{-\frac{2y}{a}}u(y)dy, \qquad u(y) = u_\tau\frac{yu_\tau}{\nu}$$

up to $10\frac{\nu}{u_\tau}$, and beyond that $u(y) = u_\tau\left(2.38\ln y^+ + 5.2\right)$, so that

$$\Delta p\bullet\vec{u} = J_0B_0u_\tau a\left[\begin{array}{l}\frac{u_\tau a}{4\nu}\left(1-e^{-\frac{20\nu}{u_\tau a}}\right)-5e^{-\frac{20\nu}{u_\tau a}}+2.6\left(e^{-\frac{20\nu}{u_\tau a}}-e^{-\frac{80\nu}{u_\tau a}}\right)\\ \quad+1.19\ln\left(\frac{u_\tau a}{2\nu}\right)\left(e^{-\frac{20\nu}{u_\tau a}}-e^{-\frac{80\nu}{u_\tau a}}\right)\\ \quad+1.19\left(\frac{u_\tau a}{80\nu}\left[e^{-\frac{80\nu}{u_\tau a}}-4e^{-\frac{20\nu}{u_\tau a}}\right]+E_1\left(\frac{20\nu}{u_\tau a}\right)-E_1\left(\frac{80\nu}{u_\tau a}\right)\right)\end{array}\right]$$

$$\cong J_0B_0u_\tau a\left(15+1.19\left[E_1\left(\frac{20\nu}{u_\tau a}\right)-E_1\left(\frac{80\nu}{u_\tau a}\right)\right]\right),$$

where E_1 is the exponential integral function. Given the power/area in the natural sweep cycle $\cong 4.52\times10^4 Re_x^{-0.584}\rho u_\tau^3$, the threshold streamwise Lorentz power would then follow:

$$\frac{J_0B_0a}{1/2\rho u_\tau^2}\{\cdot\} \geq \frac{9\times10^4}{Re_x^{0.584}},$$

where $\{\cdot\}$ represents the long expression of the geometric factor in terms of the EMTC cell spacing parameter $u_\tau a/\nu$. It is interesting to note that the threshold Lorentz pressure, in terms of the MHD interaction parameter, is higher for the Lorentz pressure gradient normal to the wall than for the streamwise case along the flow.

One way to illustrate this threshold condition is by displaying the ratio of the left-hand side and the right-hand side as a function of the MHD interaction parameter $JBa/\rho u_\tau^2$, and the spacing Reynolds number $u_\tau a/\nu$ as a function of the length Reynolds number. When this ratio is close to or greater than 1, the turbulence control is expected to be effective; a ratio below 1 implies less effectiveness, and a ratio much above 1 may mean over-exertion of control, implying less efficiency. Figure 3 presents the case of free-stream Reynolds number = 10^5. Similarly, figure 4 shows the case where Reynolds number = 10^7 over the same domain of cell spacing Reynolds number and MHD interaction parameter. By comparing the two graphs, one can see that as the free-stream Reynolds number increases, the ratio increases for the same cell spacing Reynolds number and MHD interaction parameter. It is interesting to note that the ratio is the highest for small spacing of electrodes and magnets and an MHD interaction parameter value greater than 1. The ratio decreases as spacing increases and the MHD interaction parameter decreases. Both trends are consistent with a rudimentary understanding of EMTC in a conducting medium. As the free-stream Reynolds number increases, the ratio increases, implying that for the same EM cells and MHD interaction parameter the turbulence control effectiveness increases.

By setting the ratio to be unity, one can relate the EM cell spacing to the MHD interaction parameter as a function of free-stream Reynolds number, thereby defining the threshold condition as a function of Reynolds number. Specifically, this can be expressed as $Re_\tau = -415.9 Re_\tau^{0.1}/\ln(1 - 3124 N_{im} Re_x^{0.584})$ or $Re_{u_\tau a} \cong -80/\ln\left(1 - \frac{1\times10^4}{N_{im} Re_x^{-0.584}}\right)$ for the anti-ejection normal Lorentz pressure gradient (figure 5), and $N_{im} \cong 6.02 \times 10^3\, Re_x^{-0.584}$ for the anti-sweep streamwise Lorentz pressure, and can be considered to be the design map.

4.4 EMTC Efficiency. One seeks an analytic expression that will relate some basic design parameters expressed in terms of nondimensional parameters to the flow's nondimensional parameters, such as the Reynolds number, MHD interaction parameter, load factor, and electrode parasitic voltage losses. This expression can be used to guide the point design as more practical approaches are introduced. First, the ideal efficiency is defined as $\eta_i = \dfrac{\text{Power Saved by EMTC}}{\text{Input Power to Electrodes}}$.

The power saved by EMTC per unit area = $1/2\rho U^3 \Delta c_f$, where c_f is the friction coefficient, and the power input to the electrodes per unit area = IV, where I is the electrical current and V is the voltage, so that $\eta_i = \dfrac{\frac{1}{2}\rho U^3 \Delta c_f}{IV}$. This ratio can be decomposed into products of efficiencies of several dominant physical processes; namely, η_i = (power saved by EMTC per unit area / power expended due to natural turbulence production per unit area) * (power expended due to natural turbulence production per unit area / Lorentz pressure power per unit area) * (Lorentz pressure power per unit area / electrical power delivered in seawater per unit area) * (electrical power delivered in seawater per unit area / input electrode power per unit area).

In other words, the above expression can be interpreted as the product of several intermediate efficiencies: η_i = (turbulent drag reduction efficiency) * (drag / Lorentz power ratio) * (electromagnetohydrodynamic efficiency) * (seawater electrode efficiency)

$$= \frac{\text{Turbulent Drag Reduction}}{\text{Natural Turbulent Drag}} * \frac{\text{Natural Turbulent Drag}}{\text{Lorentz Presure Power}}$$

$$* \frac{\text{Lorentz Pressure Power}}{\text{Electrical Power in Water}} * \frac{\text{Electrical Power in Water}}{\text{Input Electrode Power}}.$$

$$\eta \cong \frac{\Delta c_f}{c_f} \bullet \frac{\frac{1}{2}\rho U^3 c_f}{J_0 B_0 a\left(1 - e^{\frac{-80\nu}{u_\tau a}}\right)10u_\tau} \bullet \frac{J_0 B_0 a\left(1 - e^{\frac{-80\nu}{u_\tau a}}\right)10u_\tau}{I(V - V_0)}$$

$$\bullet \frac{I(V - V_0)}{IV} = \frac{\Delta c_f}{c_f} \bullet \sqrt{\frac{2}{c_f}} \bullet \frac{\rho u_\tau^2}{J_0 B_0 a} \bullet \frac{u_\tau B}{E}.$$

It is interesting to note that the major physical dimensionless parameters — imposed MHD interaction parameter $N_{im} \equiv (J_0 B_0 a)/\rho u_\tau^2$, electrical load factor $L \equiv E/(u_\tau B)$, and potential ratio V/V_0 — emerge in these expressions. The same results can also be obtained by a rigorous application of the pi-theorem. Examining these expressions, one can see that $\eta_i \propto \dfrac{\Delta c_f}{c_f}\dfrac{1}{N_{im}}\sqrt{\dfrac{2}{c_f}}\cdot\dfrac{1}{L}$, so that as $N_{im} \to 0$ and $L \to 0$, η_i would approach infinity. This simplistic argument neglects the fact that as N_{im} and $L \to 0$, meaning that no EMTC is applied, $\Delta c_f / c_f \to 0$; therefore, $\eta_i \to 0$. The real behavior of $\eta_i \to 0$ as N_{im}, and $L \to 0$ must await more detailed experimental observation; however, an asymptotic theoretical analysis of small N_{im} and L parameters is described below.

Note that $\Delta c_f/c_f$ is a function of N_{im}, c_f, and L. Since c_f is a function of Re_θ, $\Delta c_f/c_f$ is a function of Re_θ, N_{im}, and L, and can be obtained only via systematic experimental measurements. The dependence of $\Delta c_f/c_f$ on N_{im} and L must be consistent with its behavior near the origin of the N_{im}, L coordinates. In other words, $\Delta c_f/c_f$ should be $\dfrac{\Delta c_f}{c_f} = N_{im}^{1+a} L^{1+b} f(Re_\theta, N_{im}, L)$, so that $\eta_i = N_{im}^a L^b f(Re_\theta, N_{im}, L)$, where a and b are any positive values. To satisfy the large N_{im}, L value limit behaviors, i.e., $\partial\eta_i/\partial N_{im} < 0$ with $N_{im} >> 0$, $L >> 0$, one expects that $\partial \ln f / \partial \ln N_{im} < a$ and $\partial \ln f / \partial \ln L < b$. Based on experience with seawater MHD propulsion tests and the above observations, one can conjecture η_i to be of the form $\eta_i \propto N_{im}^a L^b e^{-N_{im}} e^{-L}$, which has a single peak at $(N_{im}, L) = (a, b)$. These conditions can guide experimenters in analyzing measurement data.

5. REFERENCES

[1] C.R. Smith, "Coherent Flow Structures in Smooth-Wall Turbulent Boundary Layers: Facts, Mechanisms, and Speculation," in *Coherent Flow Structures in Open Channels*, K.S. Choi, K.K. Prasad, and T.V. Truong (eds.), John Wiley & Sons Ltd., Chichester, England, 1996.

[2] S.K. Robinson, "The Kinematics of Turbulent Boundary Layer Structure," NASA Technical Memorandum 103859, National Aeronautics and Space Administration, Washington, DC, 1991.

[3] K.S. Choi, "Near-Wall Structure of a Turbulent Boundary Layer with Riblets," *Journal of Fluid Mechanics*, vol. 208, 1989.

[4] Zhou, Meinhart, Balachandar, and Adrian, "Formation of Coherent Hairpin Packets in Wall Turbulence," in Chapter 6 of *Self-Sustaining Mechanisms of Wall Turbulence*, R.L. Panton (ed.), *Advances in Fluid Mechanics*, Volume 15, Computational Mechanics Publications, Southampton, UK, and Boston, 1997.

[5] J.C. Klewicki, M.M. Metzger, E. Kelner, and E.M. Thurlow, "Viscous Sublayer Flow Visualizations at R_θ = 1 500 000," *Physics of Fluids*, vol. 7, no. 4, April 1995.

[6] R.I. Ferguson, A.D. Kirkbride, and A.G. Roy, "Markov Analysis of Velocity Fluctuations in Gravel-Bed Rivers," in *Coherent Flow Structures in Open Channels*, P.J. Ashworth, S.J. Bennett, J.L. Best, and S.J. Mclelland (eds.), John Wiley & Sons Ltd., Chichester, England, 1996.

[7] S.S. Lu and W. . Willmarth, "Measurements of the Structure of the Reynolds Stress in a Turbulent Boundary Layer," *Journal of Fluid Mechanics*, vol. 101, 1973.

[8] A. Gyr and A. Muller, "The Role of Coherent Structures in Developing Bedforms During Sediment Transport," in *Coherent Flow Structures in Open Channels*, P.J. Ashworth, S.J. Bennett, J.L. Best, and S.J. Mclelland (eds.), John Wiley & Sons, Ltd., Chichester, 1996.

[9] J. Meng, "Experimental Study of the Spanwise Vortex Resonance Hypothesis for Turbulent Drag Reduction Over a Flat Plate in Salt Water," NUWC-NPT Technical Report, Naval Undersea Warfare Center Division, Newport, RI, 1997.

[10] W.G. Tiederman and T.S. Luchik, "Wall Structure and Drag Reduction," Report PME-FM-82-2, School of Mechanical Engineering, Purdue University, Lafayette, IN, 1982.

[11] J.E. Sirmalis, "A Study of the Drag Characteristics and Polymer Diffusion in the Boundary Layer of an Axisymmetric Body," NUSC Technical Report 4860, Naval Underwater Systems Center, Newport, RI, 1976.

[12] H. Choi, J.P. Moin, and J. Kim, "Direct Numerical Simulation of Turbulent Flow Over Riblets," *Journal of Fluid Mechanics*, vol. 255, 1993.

[13] J. Kim, J.P. Moin, and R. Moser, "Turbulent Statistics in Fully Developed Channel Flow at Low Reynolds Number," *Journal of Fluid Mechanics*, vol. 177, 1987.

[14] Tang and Clark (1996) "Near-Wall Flow Structure in a Low Reynolds Number Turbulent Boundary Layer Over Misaligned Riblets," in *Emerging Techniques in Drag Reduction*, K.S. Choi, K.K. Prasad, and T.V. Truong (eds.), Mechanical Engineering Publications Ltd, Edmunds, England, 1996.

[15] J.J. Kim, "Study of Turbulence Structure Through Numerical Simulations: The Perspective of Drag and Reduction," *Advisory Group for Aerospace Research & Development (AGARD) Report 786, Special Course on Skin Friction Drag Reduction*, 2-6 March 1992, VKI, Brussels, Belgium.

[16] H. Choi, J. Moin, and J. Kim, "Active Turbulence Control for Drag Reduction in Wall-Bounded Flows," *Journal of Fluid Mechanics*, vol. 262, 1994.

[17] J. Jimenez and P. Moin, "The Minimum Flow Unit in Near-Wall Turbulence," *Journal of Fluid Mechanics*, vol. 225, 1991.

[18] R. Narasimha, "The Turbulence Problem: A Survey," *Journal of the Indian Institute of Science*, vol. 64(A), no. 1, 1983.

[19] D.M. Bushnell and C.B. McGinley, "Turbulence Control in Wall Flows," *Annual Reviews in Fluid Mechanics*, vol. 21, 1989, pp. 1-20.

[20] R.A. Handler, E. Levich, and L. Sirovich, "Drag Reduction in Turbulent Channel Flow by Phase Randomization," *Physics of Fluids A*, vol. 5, 1993.

[21] J.C.S. Meng, "Wall Layer Microturbulence Phenomenological Model and a Semi-Markov Probability Predictive Model for Active Control of Turbulent Boundary Layers," in *Self-Sustaining Mechanisms of Wall Turbulence*, R. L. Panton (ed.), Computational Mechanics Publications, Southampton, England, and Boston, 1997 (also in NUWC-NPT Technical Report 10434, Naval Undersea Warfare Center Division, Newport, RI, 1995).

[22] T. Watanabe, "Magnetohydrodynamic Stability of Boundary Layers Along a Flat Plate in the Presence of a Transverse Magnetic Field," *Z. Angew. Math. Mech.*, 58, 1978.

[23] T. Watanabe, "Magnetohydrodynamic Stability of Boundary Layer Flow with Suction or Injection Along a Flat Plate," *Z. Angew. Math. Mech.*, vol. 67, no. 1, 1987, pp. 27-30.

[24] D.M. Nosenchuck and G.L. Brown, "Discrete Spatial Control of Wall Shear Stress in a Turbulent Boundary Layer," *Proceedings of International Conference on Near-Wall Turbulent Flows*, C.G. Speziale and B.E. Lauder, eds., Arizona State University, 1993.

[25] D. Nosenchuck and Garry L. Brown , "Electromagnetic Device and Method for Boundary Layer Control," U.S. Patent 5,320,309, 1994.

[26] D. Nosenchuck and Garry L. Brown, "Multiple Electromagnetic Tiles for Boundary Layer Control," U.S. Patent 5,437,421, 1995.

[27] D.M. Nosenchuck, Technical Discussion at Princeton University, Princeton, NJ, 24 March 1995.

[28] D.M. Nosenchuck, Technical Discussion at San Diego, CA, 27 July 1995.

[29] D.M. Nosenchuck, "Boundary Layer Control Using the Lorentz Force on an Axisymmetric Body," Abstract of paper presented at the *ASME Fluids Engineering Meeting, Active Control Section*, Ithaca, NY, 1996.

[30] L. Kral, "Numerical Simulations of Electromagnetic Control of Turbulence," Abstract of a paper presented at the *ASME Fluids Engineering Meeting, Active Control Section*, Ithaca, NY, 1996.

[31] C. Crawford and G. Karniadakis, "Reynolds Stress Analysis of EMHD-Controlled Wall Turbulence, Part I: Streamwise Forcing," Center for Fluid Mechanics, Turbulence and Computation #96-8, Brown University, Providence, RI, 1966.

[32] P.R. Bandyopadhyay and J.M. Castano, "Micro-Tiles for Electromagnetic Turbulence Control in Saltwater, Preliminary Investigations," *Symposium on Turbulence Modification and Drag Reduction*, ASME Summer Meeting, San Diego, CA, FED vol. 237(2), 7-11 July 1996, pp. 415-421.

[33] P. Jang, D.J. Benney, and R.L. Gran, "On the Origin of Streamwise Vortices in a Turbulent Boundary Layer," *Journal of Fluid Mechanics*, vol. 169, 1986.

[34] D.J. Benney and L.H. Gustavsson, "Direct Resonance in Turbulent Boundary Layers," *Studies in Applied Mathematics*, vol. 64, 1981.

[35] W.R.B. Morrison, K.J. Bullock, and R.E. Kronauer, "Experimental Evidence of Waves in the Sublayer," *Journal of Fluid Mechanics*, vol. 47, pt. 4, 1971.

[36] R. F. Blackwelder, "Similarity Between the Laminar Turbulent Transition and Turbulent Boundary Layer Bursting," *Physics of Fluids*, 26, 1983.

6. BIBLIOGRAPHY

Akhavan, R., R.D. Kamm, and A.H. Shapiro, "An Investigation of Transition to Turbulence in Bounded Oscillatory Stokes Flows, Parts 1 and 2," *Journal of Fluid Mechanics*, vol. 225, 1991.

Alfredsson, P. Henrik, and Arne V. Johansson, "Time Scales in Turbulent Channel Flow," *Physics of Fluids*, vol. 27, no. 8, August 1984.

Astolfi, J.A., and B.E. Forestier, "Study of the Influence of External Manipulations on the Near-Wall Turbulence Structure Using Wall Pressure Fluctuations," 1996.

Bandyopadhyay, P.R., "Turbulence Spot-Like Features," *4th International Conference on Physicochemical Hydrodynamics*, Reprinted from *Annals of the New York Academy of Sciences*,

Blackwelder, R.F., and H. Ecklemann , "Streamwise Vortices Associated with the Bursting Phenomenon," *Journal of Fluid Mechanics*, vol. 94, pt. 3, 1979.

Cantwell, Brian, "Future Directions in Turbulence Research and the Role of Organized Motion," Stanford University, Stanford, CA.

Choi, Kwing-So, "Turbulent Drag Reduction Strategies" in *Emerging Techniques in Drag Reduction*, by K-S Choi, K.K. Prasad, and T.V. Truong, Mechanical Engineering Publications Ltd., London, 1996.

Falco, R.E., "Coherent Motions in the Outer Region of Turbulent Boundary Layers," *Physics of Fluids*, vol. 20, no. 10, pt. II, October 1977.

Head, M.R., and P. Bandyopadhyay, "New Aspects of Turbulent Boundary-Layer Structure," Journal of Fluid Mechanics, vol. 107, 1981.

Hijikata, Kunio, Yuji Sizuki, and Kenji Iwana, "Flow Visualization by Velocity-Pressure Cross-Correlation," *Transactions of the ASME*, vol. 118, September 1996.

Hinze, J.O., *Turbulence*, 2nd Edition, McGraw-Hill, New York, 1975.

Kim, H.T.S., S.J. Kline, and W.C. Reynolds, "The Production of Turbulence Near a Smooth Wall in a Turbulent Boundary Layer," *Journal of Fluid Mechanics*, vol. 50, pt. 1, 1971.

Kirkbride, Alistair D., and Rob Ferguson, "Turbulent Flow Structure in a Gravel-Bed River: Markov Chain Analysis of the Fluctuating Velocity Profile," *Earth Surface Processes and Landforms*, vol. 20, 1995.

Kline,S., W. Reynolds, F. Schraub, and P. Runstadler, "The Structure of Turbulent Boundary Layers," *Journal of Fluid Mechanics*, vol. 30, pt. 4, 1967.

Morrison, W.R.B, K.J. Bullock, and R.E. Kronauer, "Experimental Evidence of Waves in the Sublayer," *Journal of Fluid Mechanics*, vol. 47, pt. 4, 1971.

Nakagawa, Hiroji, and Iehisa Nezu, "Structure of Space-Time Correlations of Bursting Phenomena in an Open-Channel Flow," *Journal of Fluid Mechanics*, vol. 104, 1981.

Offen, G.R., and S.J. Kline, "Combined Dye-Streak and Hydrogen-Bubble Visual Observations of a Turbulent Boundary Layer," *Journal of Fluid Mechanics*, vol. 62, 1974.

Praturi, Ananda K., and Robert S. Brodkey, "A Stereoscopic Visual Study of Coherent Structures in Turbulent Shear Flow," *Journal of Fluid Mechanics*, vol. 89, pt. 2, 1978.

Wark, C., and H. Nagib, "Experimental Investigation of Coherent Structures in Turbulent Boundary Layers," *Journal of Fluid Mechanics*, vol. 230, 1991.

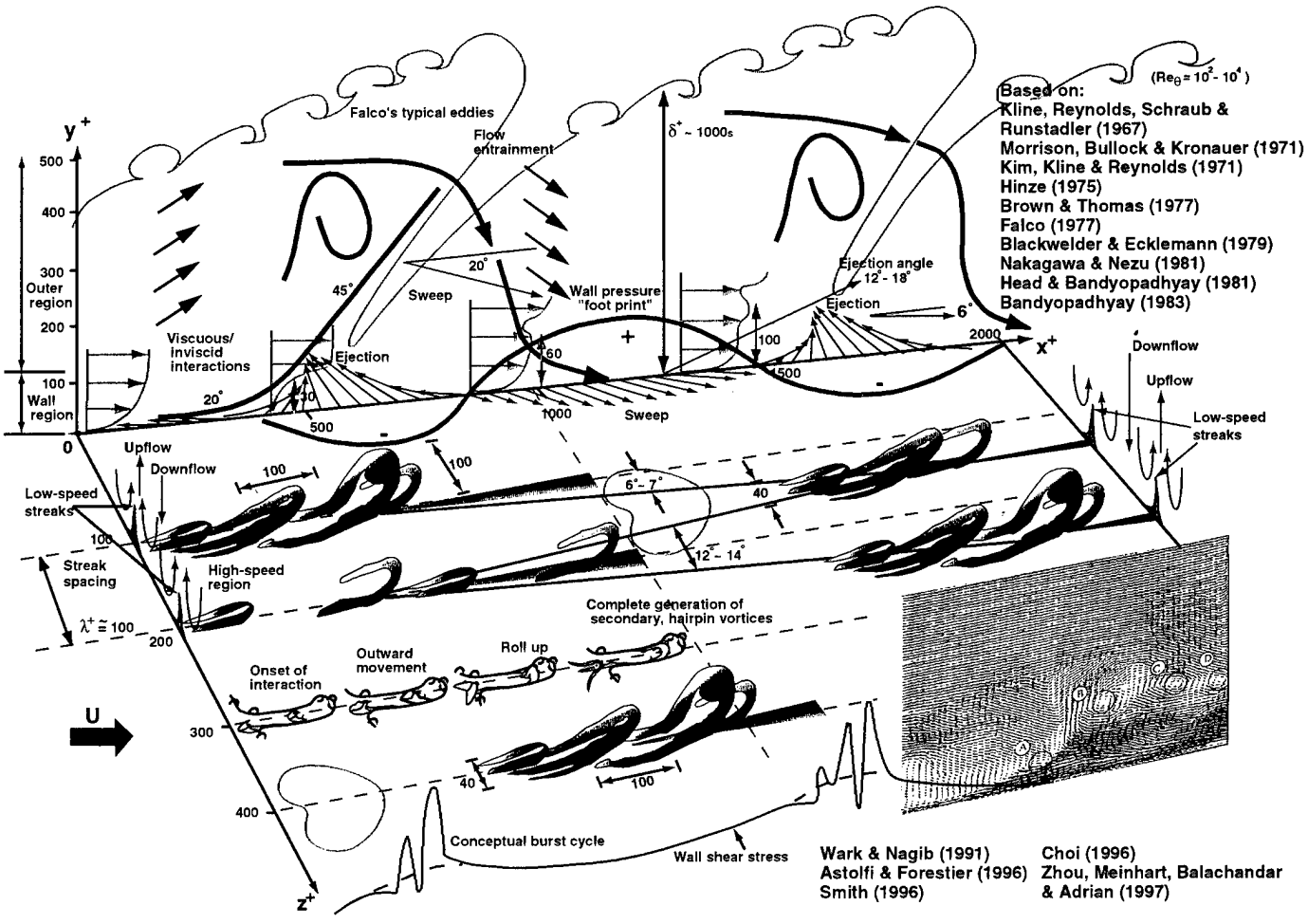

Figure 1. Conceptual Turbulent Boundary Layer Near-Wall Phenomenology

Observed Phenomena	Microturbulent Activities	Fluid Dynamic Mechanisms	Drag Reduction Strategies
Burst ↓	Near-wall burst deforms a spanwise vortex element		
Streaks ↓	Legs of counterrotating, streamwise vortices form low-speed streaks between the legs	Nonlinear self-interaction	Riblets impede spanwise movement of longitudinal vortices, reduce momentum flux within riblet valley, impede energy redistribution from u' to w', and reduce near-wall burst duration and intensity (Choi, 1996). Spanwise movement of $\Delta z^+ \cong 50$ disrupts formation of longitudinal vortices and reduces turbulence production (Akhavan et al., 1991)
Liftup ↓	Stretched vortex evolves into a hairpin vortex loop		Lorentz pressure gradient suppresses amplification of streamwise vorticity (Nosenchuck and Brown, 1993)
Ejections ↓	Ejection of low-momentum fluid away from wall	Nonlinear vortex mutual induction	Polymer injection damps vortical motions, increases spacing of streaks, and reduces ejection and sweep frequencies and intensities (Tiederman and Luchik, 1982). Suction-blowing out of phase with sweep and ejection inhibits longitudinal vortex interaction with wall (Kim et al., 1990)
Breakup ↓		$U(y,z)$ inflectional profile leads to instability	Microbubble splitting in turbulence provides an additional energy dissipation in small scale activities (Meng, 1985)
Sweeps ↓	Sweep of high-momentum fluid toward wall	Large-scale outer structure and advection of mean shear	Compliant coating motion counters local fluid motion and interrupts the turbulence production cycle (Choi, 1996). Deferring the sweep without modifying the streamwise vortices (Choi et al., 1994)
Renewals	Near-wall bursts renew under the vortices, forming a staggered pattern relative to the previous near-wall burst and completing the cycle	Viscous-inviscid interaction	Randomization of largest length scale (Handler et al., 1993)

Figure 2. Near-Wall Turbulence Activities and Drag Reduction Strategies

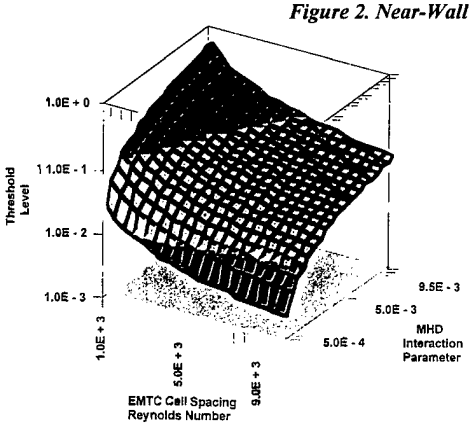

Figure 3. Threshold of EM Control of Microturbulent Ejection vs. Interaction Parameter and EMTC Cell Spacing at Free-Stream Reynolds Number = 10^5

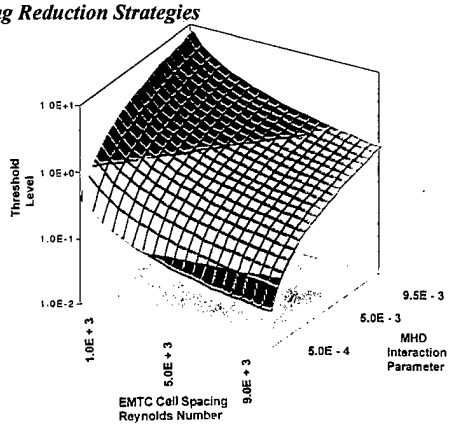

Figure 4. Threshold of EM Control of Microturbulent Ejection vs. Interaction Parameter and EMTC Cell Spacing at Free-Stream Reynolds Number = 10^7

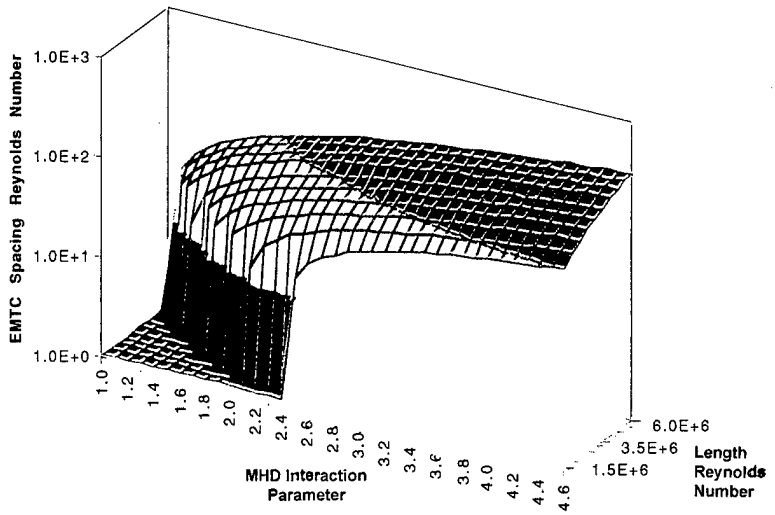

Figure 5. Anti-Ejection EMTC Cell Spacing Reynolds Number Based on u_τ at Threshold Condition vs. MHD Interaction Parameter and Length Reynolds Number

Experiments on Turbulent Channel Flow with Electromagnetic Turbulence Control

Xuejun Fan and Garry L. Brown
Department of mechanical and Aerospace engineering
Princeton University
Princeton, New Jersey 08540
xfan@princeton.edu

I. INTRODUCTION

The possibility of controlling the wall shear stress in a turbulent boundary layer, by applying a Lorentz force J x B perpendicular to the wall, was demonstrated in the paper by Nosenchuck and Brown (1). A large reduction in the Reynolds stress was found. While the measurements and flow visualization showed a substantial effect, the results were from an early experiment and raised a number of questions. Two particularly important issues to be resolved were: firstly, the role that 3-dimensionality had played due to the arrangement of electrodes and magnetic poles; and secondly, the non-dimensional scaling to much larger free stream velocities and to boundary layers of different thickness. The aim of the present experiments is to avoid some of the complexity of the earlier experiments and, as a result, to more clearly illuminate the underlying physics of a body force acting on near wall turbulence, to impose an organized structure on the near wall flow and to explore the effects of scaling. A special purpose water tunnel has been built and arranged to produce a two-dimensional channel flow both with and without wall injection of an electrolyte or a fluid of different density from water. The flow structure near the wall of a channel flow is known to be very similar to that of a boundary layer having the same shear stress. The particular advantages of a fully developed channel flow are that the shear stress is a linear function of the distance from the wall and can be readily measured from the pressure drop along the channel; measurements of the velocity profile and pressure drop along the channel can be used, in principle, to infer the eddy viscosity. Thus the direct effects of a Lorentz force acting on the flow can be measured. A channel flow also has the advantage that a wide range of maximum flow velocities and Reynolds numbers can be achieved. In the present experiments reported here, we have made measurements of the effect of a buoyancy force on the mean flow velocity profile. Nosenchuck and Brown called electromagnetic turbulence control in which the effect is produced by a gradient in conductivity "type I" and the case of uniform conductivity "type II". In the type I case, the action of the Lorentz force is analogous to a buoyancy force with a corresponding density gradient. We anticipate presenting the corresponding results for a Lorentz force as well as the present results for a buoyancy force at the meeting. Measurements for "type II" electromagnetic turbulence control, in which the conductivity is uniform but the Lorentz force has a spatial and temporal variation, will also be made shortly. The concept of an electromagnetic riblet is introduced in this paper.

In common with the effects of buoyancy on a turbulent boundary layer, an important parameter for type I electromagnetic turbulence control is the ratio of Lorentz force production of turbulent kinetic energy to the Reynolds stress production of turbulent energy. This parameter is

$$Ri_L = -\overline{L'v'} / \rho\overline{u'v'}\frac{\partial u}{\partial y}$$

As these correlations are not easily measured directly, a gradient Richardson number is frequently used, i.e. these two definitions for a Richardson number are only equivalent if the turbulent correlations are assumed to be approximated by eddy viscosity relationships and the eddy viscosities for the correlations are all equal. Thus,

$$Ri_B = -g\frac{\partial \rho}{\partial z} / \rho(\frac{\partial u}{\partial z})^2 \quad \text{for the buoyancy case and}$$

$$Ri_L = -\frac{\partial L}{\partial z} / \rho(\frac{\partial u}{\partial z})^2 \quad \text{for the electromagnetic case.}$$

Previously Fan & Brown (2) drew attention to the limitation of the analogy, particularly in a turbulent flow, between the buoyant case and the electromagnetic case due to the further requirement that $\nabla \cdot J = 0$ for the electromagnetic case.

For the experiments for the type I case a novel probe has been developed and used to measured the conductivity profile and the corresponding density profile. Measurements of the Richardson number and the corresponding effect on the mean velocity profile are reported.

II. APPARATUS AND MEASURING TECHNIQUES

A. Water tunnel

A sketch of the water tunnel constructed for this experiment is shown in figure 1. The test section (5 ft. long) is constructed from ¾ - inch-thick acrylic plates. The channel height is 0.50inches and width 8.0 inches. The flow uniformity and quality is controlled by a honeycomb (1 inch long, 1/8 inch in diameter) and a fiberglass screen (16 mesh/inch), followed by a 16:1 contraction. At the downstream end of the test section a ten-degree divergent nozzle was used as a diffuser.

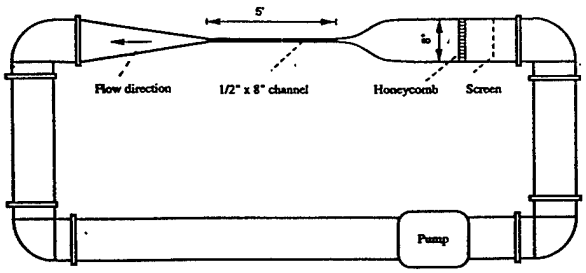

Figure 1. Sketch of two-dimensional water tunnel.

An injection slot is located approximately 30 inches downstream from the entrance to the test section. This carefully designed slot spans the test section and has a 0.055-inch wide outlet.

The tunnel is driven by a 3-horsepower centrifugal pump. The Reynolds number (based on the height of the channel and the maximum mean velocity) can be varied typically from 4,000 to 20,000. Transition has been found at a Reynolds number of approximately 6,000-7,000.

B. Flow Measurements

All velocity measurements reported here have been made with a Pitot tube and the wall shear inferred from Preston tubes calibrated against the static pressure drop in the channel. All tubes were of 0.042 inches outer diameter. Measurements were at locations of 4 inches downstream of the injection slot. A programmable traverse gear was used to move the Pitot tube across the channel.

C. Concentration/density probe

To measure solution concentration, a bipolar pulse technique has been developed by Johnson an Enke (3) which eliminated many of the classical problems encountered with other A. C. bridge methods. It was capable of measuring very rapid changes in conductivity. It has been improved for the measurement of small solution resistance (high concentration) by Daum and Nelson (4). This method involves the sequential application of two successive constant current pulses of equal magnitude but of opposite sign across a conductance cell. The resulting voltage can be electronically rectified and integrated to determine the area under the curve. Under some assumptions, the solution resistance is

directly proportional to the area for a given pulse magnitude and duration.

Though the system worked extremely well for a uniform conductivity cell, the application of the technique to the measurement of concentration profiles in the present channel flow was not straightforward. The difficulty arises from the fact that the solution resistance of a conductance cell is an integral quantity which makes it impossible to localize the measurements.

To resolve this problem, a novel probe has been developed. Two 0.005-inch-diameter platinum wires are inserted ½ inch apart into a plastic tubing of 0.04 inch OD. A pressure drop in this tubing is established and a Poiseuille flow with a maximum velocity of approximately 1m/sec then enables the concentration of the stream tube to be continuously sampled.

A pulse duration of 20 μs was chosen. The system was calibrated using standard NaCl solutions of known concentration. The results are shown in figure 2 where the concentration has been converted to the density. The probe gave highly repeatable results.

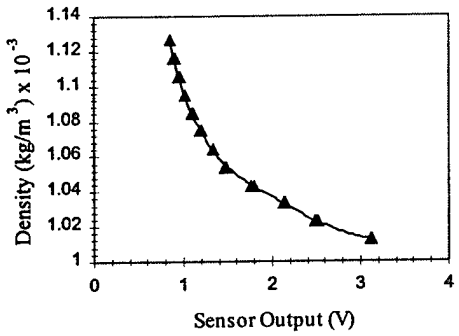

Figure 2. Calibration of the concentration probe for NaCl solution.

III. EFFECTS OF DENSITY GRADIENT

In the first set of experiments, the effect of buoyancy (density gradient) in the channel flow was investigated. The density gradient was established by injecting of 4.0M NaCl solution through the injection slot. Measurements were also made with fresh water injection. Injection rates were carefully measured using an accurate flow meter calibrated for fluids of different density and viscosity.

Mean velocity profiles were measured at Re ~11,000 as shown in figure3-4. Due to the size of the Pitot tube, measurements closer to the wall were not made. The velocity u is calculated from the Pitot pressure and the local fluid density measured with the concentration probe. At the same time, the upstream flow velocity was recorded. It was found that this velocity was unchanged with or without injection. The average velocity based on the total volume flux has then been used to non-dimensionalize the velocity profile measurements.

The density probe was traversed with the Pitot tube. The output during the traverse of the probe is shown in figures 5 and 6 for two different injection rates. In these plots the voltage output has been converted to a density by means of the calibration obtained from figure 2. It can be seen that the fluctuations of density are large. The mean densities are nevertheless significantly less than that of the injected fluid

(i.e. $\frac{\rho_i - \rho_0}{\rho_0} = 0.115$) due to turbulent diffusion into the bulk fluid.

Two polynomials were fitted to the data to determine the mean density profiles from the distributions of instantaneous values.

With the corresponding velocity and density profiles, the near wall gradient Richardson numbers were calculated and are shown in figure 7-8.

At an injection volume flow rate of 1.4% of that of the upstream volume flow rate, the change in symmetry of the velocity profile was quite small. Figure 7 shows that the local Richardson number in this case has a maximum of approximately 1.1 at y/h = 0.27. At the higher injection rate, as shown in figure 5, a significant change in symmetry of

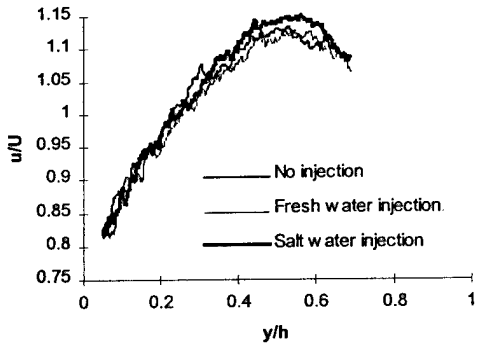

Figure 3. Velocity profiles for flow with injection rate of 1.4%

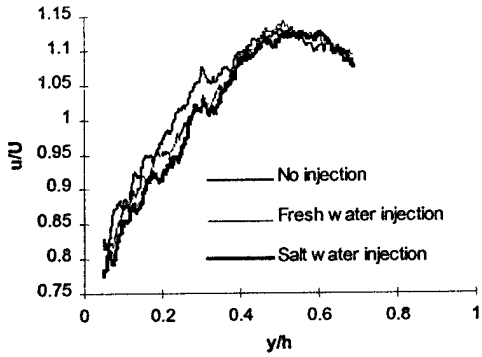

Figure 4. Velocity profiles for flow with injection rate of 2.2%

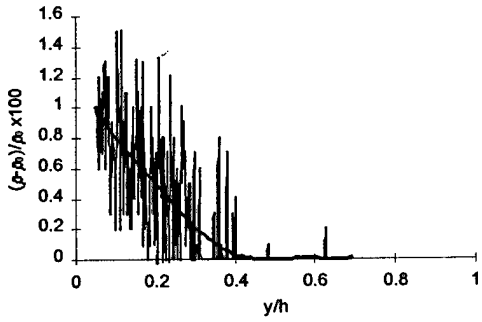

Figure 5. Normalized relative density profile for injection rate 1.4%.

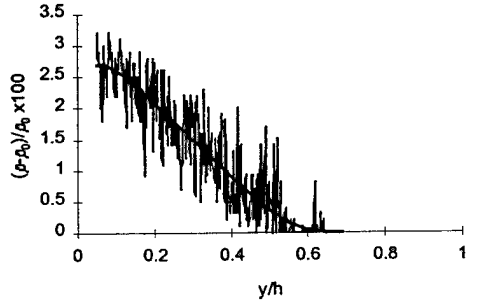

Figure 6. Normalized relative density profile for injection rate 2.2%.

velocity profile can be seen. In this case the gradient Richardson number is well above 1.0 as shown in figure 8. There is a local maximum of approximately 2.2 at y/h = 0.22. The large Richardson numbers for y/h > 0.4 are a result of the small velocity gradient. These results will now be compared with the corresponding effect of a normal Lorentz force, for

which the mean conductivity profile is expected to be approximately similar to the density profile for the corresponding buoyancy case.

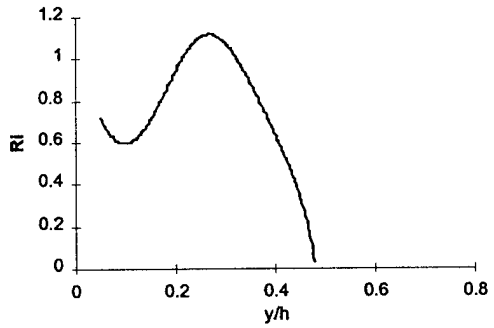

Figure 7. Gradient Richardson number distribution near the wall at 1.4% injection rate.

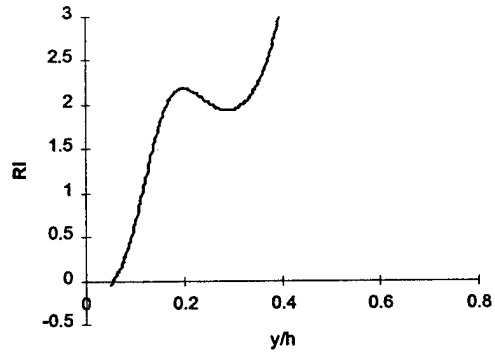

Figure 8. Gradient Richardson number distribution near the wall at 2.2% injection rate.

IV. PROPOSED EXPERIMENTS USING ELECTRO-MAGNETIC RIBLETS

It is well known that longitudinal vortical motion is a principal mechanism for maintaining the Reynolds stress near the wall. Measurements indicate a span-wise scale of approximately 80-100 wall units. The principal effect of a dilute polymer in reducing the wall shear stress (Thoms effect), has been attributed to a change in this near wall structure and a correspondingly larger span-wise scale. Similarly longitudinal riblets have been found to reduce the wall shear stress for a particular span-wise scale and riblet geometry. The proposed experiments are intended to directly control this near wall structure by the application of a span-wise periodic Lorentz force, whose span-wise scale, in wall units, can be varied.

To generate such a structure, a stream-wise magnetic field and an electric field due to surface electrodes mounted on the top and bottom surfaces of the channel are applied. Figure 9 shows the directions of these fields and the resulting flow field that is expected as a result of the Lorentz force near the surface that is not opposed by the pressure field. In the two-dimensional case (electrodes infinitely long in the stream-wise direction), the current field will be perpendicular to the magnetic field, and if the curl of **J** x **B** does not vanish it acts as a source of stream-wise vorticity. How best to achieve this source of vorticity is the subject of present research. To the extent that it can be achieved, the fields might therefore be thought of as electromagnetic "riblets".

In the proposed experiment the electromagnet shown in figure 10 will provide a large periodic axial magnetic field. Similarly the electrodes will be provided with an A. C. voltage. Thus, theLorentz (**J** x **B**) at each electrode remains in the same direction as each field reverses. The alternating current at each electrode will ensure that the electrode impedance will be small, due to the large interfacial capacitance, and bubble formation will be suppressed. Both the magnitude of each field and the phase relationship between them can be varied. The electromagnet has been built by the Sandia National laboratory and a maximum field of 0.7T has been measured.

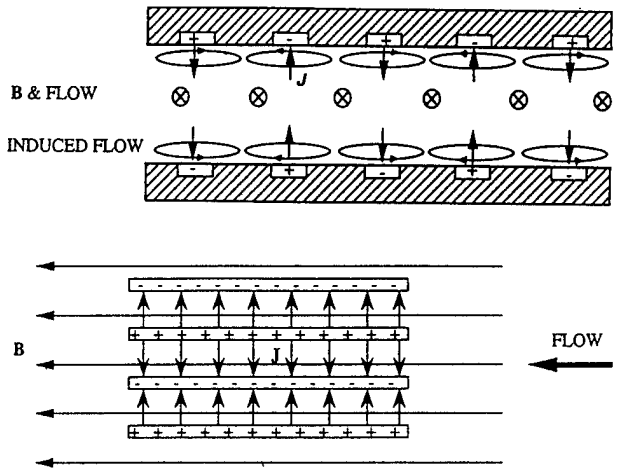

Figure 9. A schematic of electromagnetic riblets. Top: cross-section, bottom: top view.

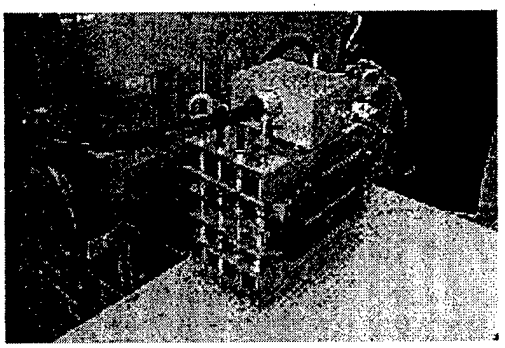

Figure 10. An oblique view of the AC magnet with the associated power factor correction capacitor bank.

V. CONCLUSIONS

A channel flow facility with an electromagnetic control system has been built. The channel flow has enabled some of the issues raised by the early experiment of Nosenchuck and Brown to be studied. Studies of both type I and type II electromagnetic control are being pursued. In the type I case comparisons between the Lorentz force and the buoyancy force as sinks for turbulent energy can be made. Measurements in the buoyancy case confirm that a Richardson number of order one is required to affect the symmetry of the velocity profile. For the type II case, an electromagnetic riblet concept is being explored along with an array of electromagnetic tiles as originally proposed byNosenchuck and Brown.

References:

1. D. M. Nosenchuck and G. L. Brown, Discrete Spatial Control of Wall Shear Stress in a Turbulent Boundary Layer, Near-Wall Turbulent Flows, R. M. C. So, C. G. Speziale and B. E. Launder (Editors), Elsevier Science Publishers, 689-698,1993

2. X. Fan and G. L. Brown, Experiments on the Electromagnetic Control of Turbulence, AIAA 97-2123, June 1997.

3. D. E. Johnson and C. G. Enke, Bipolar Pulse Technique for Fast Conductance Measurements, Analytic Chemistry, Vol. 42, No.3, March 1970.

4. P. H. Daum and D. F. Nelson, Bipolar Current Method for Determination of Solution Resistance, Analytic Chemistry, Vol. 45, No.3, March 1973.

DRAG REDUCTION EXPERIMENTS ON A SMALL AXISYMMETRIC BODY IN SALTWATER USING ELECTROMAGNETIC MICROTILES

Promode R. Bandyopadhyay
John M. Castano,
Daniel Thivierge and
William Nedderman

Naval Undersea Warfare Center
Newport, RI 02841
bandyopadhyay@c80.npt.nuwc.navy.mil

ABSTRACT

Experiments are being carried out on the drag reduction of a small axisymmetric body in salt water using Lorentz forces produced by electromagnetic microtiles. Scaling and measurement issues are considered from the early stage of the work. The experiments are aimed at higher Reynolds number turbulent boundary layer flows with a freestream developing on an axisymmetric body, right from the preliminary stage of planning. A wall-layer scaling of the phenomena is assumed. The main variable of interest is large area time-averaged viscous drag. A small diameter (d) axisymmetric body is constructed that has a long (5d) floating section for measurement of viscous drag. This floating section is filled with numerous electromagnetic microtiles. The recent progress on drag measurements and modeling of the mechanism is reported.

1. INTRODUCTION

Over the last few decades, an important progress has been made in our understanding of turbulence production in a turbulent boundary layer. It is now known that such processes are not entirely random. There are quasi-periodic processes in play which are masked in noise. The discovery of this orderliness has opened the possibility of a rational control of the turbulence production process and eventually of viscous drag. In 1832, Ritchie (1832) experimentally demonstrated that, a conducting liquid can be pumped when electric and magnetic fields are crossed within its bulk. Due to high salinity, seawater is reasonably electrically conducting. In principle, by crossing magnetic fields with electrical fields within a boundary layer, Lorentz force can be produced to pump such a liquid locally whose amplitude, phase, length and time scales can be digitally varied. These developments open up the possibility of controlling the turbulence production process and viscous drag in an ocean going vehicle.

Several years ago, NUWC undertook research on this subject although not much was reported. Drag reduction remained elusive although fluid pumping was demonstrated via flow visualization. Later, Princeton researchers made claims of large drag reduction which generated a considerable interest (Nosenchuck & Brown 1993). These drag reductions were primarily based on local hot film sensor response. Low Reynolds number transitional flat plate results were scaled to high Reynolds number axisymmetric bodies. The mechanism was based on outer layer scaling. Flow visualization revealed the formation of large roller eddies. NUWC efforts at reproducing these results were not encouraging (Meng et al. 1997). In any case, the NUWC and Princeton efforts are at least note worthy for a novel approach to a difficult problem.

The Princeton efforts are now directed towards understanding the mechanism (Fan & Brown 1997). A novel single infinite tile is produced on one wall of a channel flow, the other being a reference wall. The edge effects are less than that in a flat plate boundary layer. Experiments in a channel flow marks a departure in the Princeton thinking of the pursuant mechanism from outer layer to inner layer dominated. Preston tube and pressure drop are used to compute drag reduction on the electromagnetic wall. However, pressure drop can be used to compute wall shear stress only if the flow across the entire channel is fully developed. The electromagnetic perturbation on one wall violates this condition, raising questions on accuracy of pressure drop in shear stress diagnosis. In spite of this innate ambiguity, it is intriguing that a 'Preston tube' registers a clear drop in response when the electromagnetic field is turned on.

A clear evidence of, whether the technique of electromagnetic drag reduction in saltwater does indeed lead to a reduction of surface-integrated viscous drag or not, is lacking so far. The goal of the present experiment is to come up with such an evidence. The first progress report was given in Bandyopadhyay & Castano (1996) and this is a follow-up.

During the planning stage, the present work has been influenced by past negative experience. Past Navy and NASA drag reduction efforts indicate that scaling from low to high Reynolds numbers, and transitioning from laboratory curiosities to field tests can sometimes be problematic. Understanding of the non-linear turbulence mechanism tends to be a controversial and slow process. Techniques that work well in a turbulent flow, viz., polymer and microbubble injection, are probably not that relevant because they involve large changes in fluid properties.

Because the flat plate experiments indicated a strong convergent-divergent edge effect, the present experiment concentrated on an axisymmetric model. This eliminates at least one scaling issue and results in a better flow quality. Because power consumption is bound to be an issue, there is a need to resort to Lorentz forces that focused near the wall where turbulence production is a maximum. As described in the previous report, the turbulence production statistical scales were examined in large and small underwater bodies and in the NUWC quiet water tunnel based on wall layer scaling. Fabrication limits then led to slightly higher dimensions. The wall layer scaling is an approximate guideline, and a mixed layer scaling effect is allowed in the boundary layer nature of the experiments.

There appears to be few general traits of drag reduction. However, there is one that is assumed to be relevant. The riblet work of Wilkinson & Lazos (1987) showed that drag reduction is not uniquely related to the suppression of streamwise component of turbulence (u). Crawford & Karniadakis (1998) have shown via the DNS of riblet flow that, drag reduction is uniquely related to the suppression of the surface-normal component of turbulence (v) near the wall. We assume that this is a universal property of drag reduction. A structural modeling of a vortex in a unit flow domain have shown that vertical Lorentz pressure can lead to a suppression of wall pressure rms levels (Bandyopadhyay & Balasubramanian 1996). It then follows that Lorentz pressure should be directed towards the suppression of the v-component. This results in an orthogonal array of magnets of electrodes. The reality however is far more complicated - the Lorentz pressure is only nominally surface normal in such an arrangement, it is in fact highly three-dimensional. A recent comparison of our work with that of Kral (1998) suggests that the induced flowfield of micro and macrotiles can be basically different. The attempt to control the v-component of turbulence is hoped to further reduce the necessary Lorentz pressure levels. The present wall-layer based arrangement of the magnets and electrodes has been called microtiling here as opposed to the larger length scale based original Princeton or NUWC approach. In this manner we attempt to build the present work on our understanding of the organized nature of turbulence production in a turbulent boundary layer.

The measurement problems in an electrically charged saltwater medium are formidable. Because saltwater is extremely corrosive, the longevity of electrodes and sensors is a problem. Many of the conventional diagnostics do not work. Because saltwater is being electrically charged, ground looping can be a serious issue. Electrolysis can contaminate the response of hot films and LDAs and PIV methods of diagnostics. Because the wall-shear distribution produced by each microtile is three-dimensional, one would like to focus on the surface and time integrated viscous drag to clearly evaluate the drag reduction behavior. To be able to measure changes in drag due to the application Lorentz forcing, the ratio of the tiled to the total surface area of the floating segment for drag measurement should be close to one. Recently, improvements have been made over past drag sensors and the longevity of the electrodes. Even then, the present results should be treated with caution and further verification and detailed measurements are imperative before the present results can be deemed established.

2. MODELING OF MECHANISM

A model of the microtile flow mechanism is given. The mechanism may not be universal and applicable to other tile designs.

2.1 Vorticity Perturbations Due to Microtiles

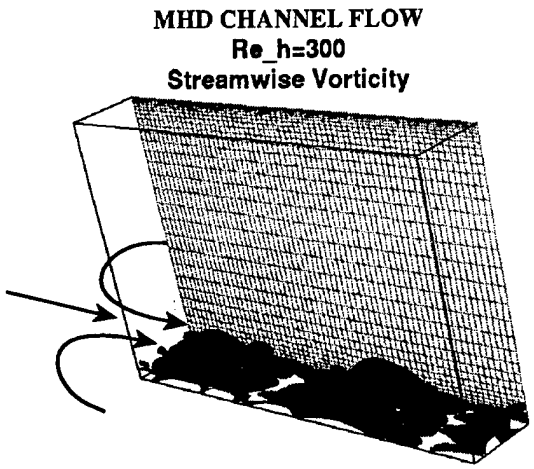

Figure 1. DNS Simulation of streamwise vorticity perturbation induced by the microtiles, after Hatay et al. (1997). The induced flow between the streamwise vorticity pairs is wall ward.

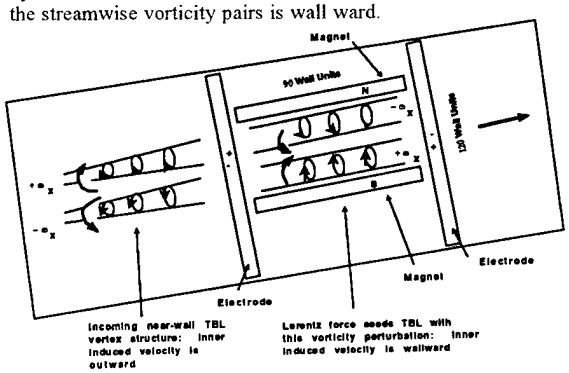

Figure 2. Conceptual sketch showing how an incoming regular near wall vortex pair in a turbulent boundary layer will encounter an opposing pair near wall over a microtile.

In the previous report, a 5x5 array of microtile fabricated on a printed circuit board was described. Dye visualization in a low Reynolds number subcritical channel flow of saltwater was carried out. It showed that that the microtiles, although small, were indeed able to perturb the flow locally. A Stokes' layer resonance model was proposed which suggested that "pillows" of vorticity are formed over the microtiles when the applied electric field is pulsed. Subsequently, DNS simulation was carried out on the same configuration. It showed that the "pillows" of vorticity were in fact ring vortices, the induced flow in the middle being wall ward. The axial vorticity perturbation due to the microtile is shown in Fig. 1. The basic qualitative nature of the vorticity distribution is the same in quiescent, laminar and low Reynolds number turbulent flows and with several different kinds of pulsing, although the entire parameter space is not yet fully explored.

At a freestream speed of 5 m/s, the spanwise scale of the normal and microtile perturbed vorticity pairs will match (Fig. 2). The suggestion is that the microtiled turbulent boundary layer provides a layer of pillows of vorticity whose sense of rotation is opposite to what normally occurs in a turbulent boundary layer. It remains to be seen whether this translates to any near-wall vorticity cancellation or drag reduction.

2.2 Volume of Influence of One Microtile

The distribution of Lorentz force over the present microtile is given in the first report. Figure 3 shows the distribution of boundary layer integral quantities on the floating section of the 75 mm diameter model of the present work (Castano 1997). (They are from a similar sized model carried out in a similar water tunnel). The volume of influence of one microtile is shown in Fig. 4. It encompasses one near-wall vortex pair and the location of maximum turbulence production around 5 m/s. The depth also covers the region of overlap between the outer and inner layer (Fig. 3a).

(a)

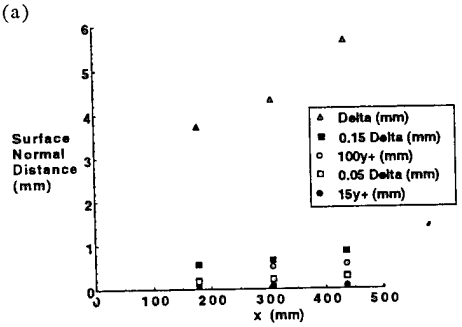

(b)

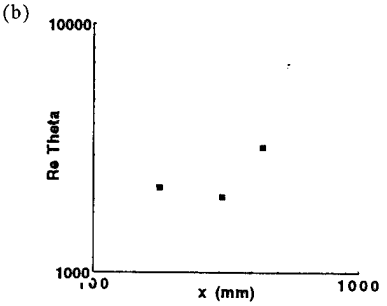

(c)

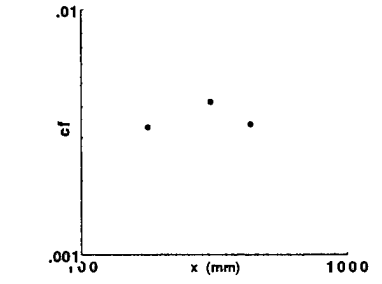

(d)

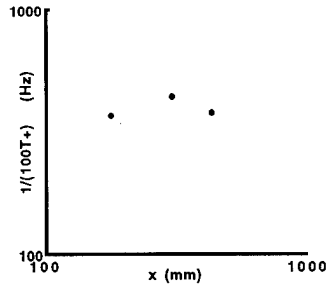

Figure 3. Boundary layer integral quantities over the floating section of the 75 mm diameter model (Castano 1997).

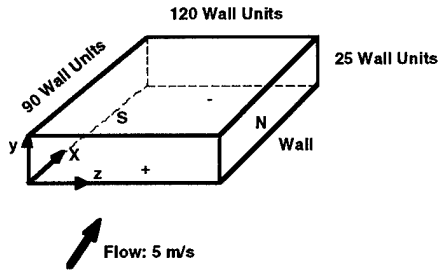

Figure 4. Volume of one microtile in wall units at 5 m/s, over which the Lorentz force field is being applied.

2.3 Stokes' Layer Resonance Model

Assume that pulsed Lorentz pressure is analogues to oscillating the wall giving rise to a Stokes' layer. Turbulence production peaks at:

$$10 \le \frac{yU_\tau}{\upsilon} \le 15 \qquad (1)$$

Propose that Stokes' layer viscous wave length should match waves responsible for turbulence production:

$$\frac{10\upsilon}{U_\tau} \le \sqrt{\frac{2\upsilon}{\varpi}} \le \frac{15\upsilon}{U_\tau} \qquad (2)$$

If $\varpi = 2\pi f_B$, where f_B is pulsing frequency, then

$$314 \le \frac{(U\tau)^2}{f_B \upsilon} \le 707 \qquad (3)$$

Condition (3) is calibrated against turbulence production structure statistics. The drag reduction consequence is not clear and is treated in the next section.

At a freestream speed of 8 m/s, in the middle of the floating section, $U_\tau = 0.33 m/s$, and $\upsilon = 11.4x10^{-7} m^2/s$, the pulsing frequency should be:

$$135Hz \le f_B \le 304Hz \qquad (4)$$

2.4 Condition for Electromagnetic Drag Reduction

Assume that pulsing of the electromagnetic microtiles is analogous to the spanwise wall or fluid oscillation of Akhavan (Jueng et al. 1992), Laadhari et al. and Choi et al. (1998). Their low Reynolds number drag reduction result is reproduced in Fig. 5.

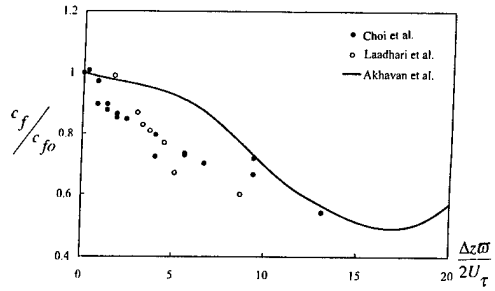

Figure 5. Drag reduction due to spanwise oscillation. DNS of Akhavan: line; measurements of Laadhari et al. and Choi et al. (1998): symbols.

Similarly, propose that near-wall vorticity breakdown will be interrupted if spanwise wall or spanwise fluid displacement follows the relationship in (5) where the spanwise dimension is given in Fig. 6.

$$b^+ \ge 100 \qquad (5)$$

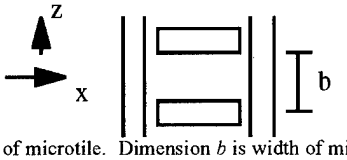

Figure 6. Sketch of microtile. Dimension b is width of microtiles.

Strouhal number for maximum drag reduction (45%) is given by:

$$10 \le \frac{\Delta z \varpi}{2U_\tau} \le 15 \qquad (6)$$

$$10 \le \frac{b 2\pi f_b}{2U_\tau} \le 15 \qquad (7)$$

$$3.2 \le St_b \le 4.8 \qquad (8)$$

Here, St_b is a Strouhal number and f_b is the pulsing frequency. Note that turbulence reproduction physics, namely viscosity and information about structure organization are already accounted for in (8). In the current 75 mm diameter model, in the middle of the floating section, where $U_\tau = 0.33 m/s$, pulsing frequency is:

$$210Hz \le f_b \le 315Hz \qquad (9)$$

The range of f_b in (9) is roughly the same as that of f_B in (4). This suggests that the original Stokes' layer resonance hypothesis in the first report (Bandyopadhyay & Castano 1996) is calibrated against the large drag reduction due to spanwise wall oscillation. The microtile should be able to generate a spanwise fluid oscillation given by (8) for a drag reduction of 45% to occur.

3. EXPERIMENT

The 5x5 microtiles developed on a printed circuit board and described in the first report was taken as the model for building an axisymmetric model sketched in Fig. 7. Figure 8 shows the model in the NUWC Saltwater Tunnel. The floating section is microtiled. The front and back parts of the model rest rigidly on a hollow stainless steel rod through which all coiled wires pass. The electrodes are placed in a cross-stream direction while the three-dimensional permanent magnets (1280) are aligned axially. All microtiles are pulsed in-phase. At a speed of 5.5 m/s, the interaction parameter defined as the ratio of applied Lorentz force times viscous force divided by square of inertia force, $N = \frac{\sigma V_o B_o}{\rho U_\tau^2}$ is 0.6. Here, σ is electrical conductivity of the fluid, V is scalar electric potential, B is magnetic flux, ρ is fluid density, and U_τ is friction velocity, and the subscript o denotes conditions at the wall.

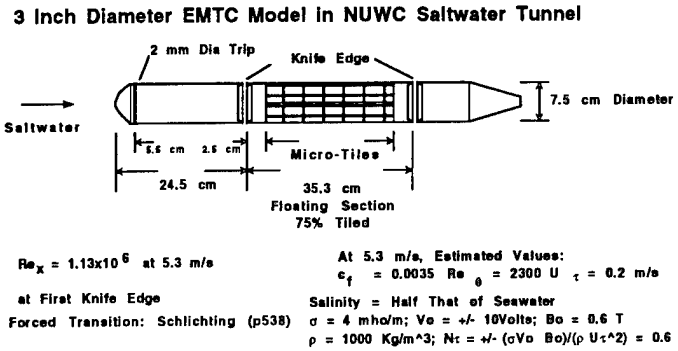

Figure 7. Schematic of the model and the experiment.

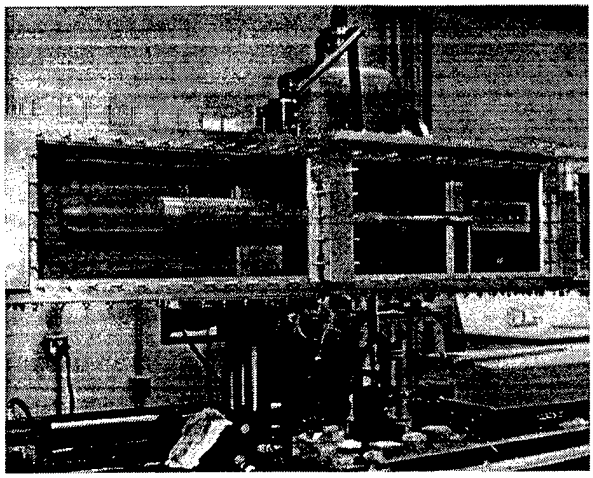

Figure 8. Photograph of the 75 mm (3") diameter 1m long model in the water tunnel. The electromagnetic floating section is visible in the middle.

3.1 Quality of Surface Smoothness:

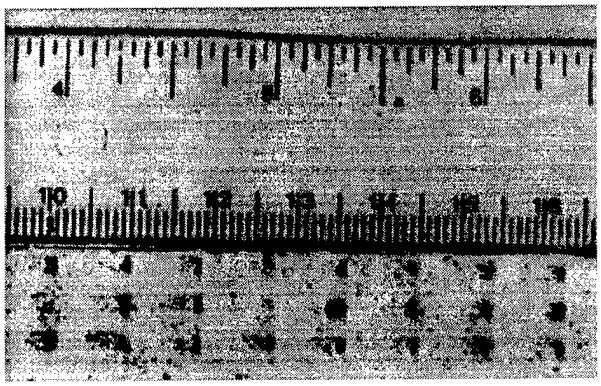

Figure 9. Impression of accumulation of rust roughness over the magnets. Top ruler numerals are in inches and the bottom are in cm. The dark areas below the ruler are from the rust deposition. The flow is from left to right, the rust forming a ramp to the flow.

In the water tunnel, the model is mounted on a sting attached to a cruciform. Due to sting mounting, at high tunnel speeds (7 m/s), the model nose vibrates, whose effect is not known. The test section is 30 cm x 30 cm in cross-section and causes an area blockage of 5%. The boundary layer was tripped with a 2 mm diameter o-sealing ring. These trips do not last long in the saltwater. The estimated boundary layer integral quantities over the floating section at 5 m/s are given in Fig. 3. Although not visible to the naked eye, the seemingly filtered water contains fine rust, which is smooth to the touch. In course of about one hour of run, they accumulate over the magnets in a the shape of a ramp. Figure 9 shows an impression of the rust deposition. These magnets should bring the Lorentz force well into the boundary layer. This rust deposit which slightly varies with filtering, raises question about the validity of smooth wall assumption in all current direct numerical simulations of the flow field. In the present work, the magnets lie below a thin kapton layer on which the electrodes are electroplated. Over time, these electrodes may form microscopic cracks but they do not form a gouging or roughness. In the present work, rust is the only source of roughness which can be minimized after intensive filtering. On the other hand, in many other experiments, where tile fabrication did not follow the electronic fabrication procedure as here, due to corrosion, the plates are far from being hydrodynamically smooth.

3.2 Drag Balance:

In the first set of experiments on the axisymmetric model, an in-house built drag sensor was used. Later on, this was replaced by a commercial balance, further developed for saltwater application, was used. Accurate drag balance measurements in saltwater, that is also charged, is difficult. Not much expertise is available on this subject. These two drag sensors are briefly discussed.

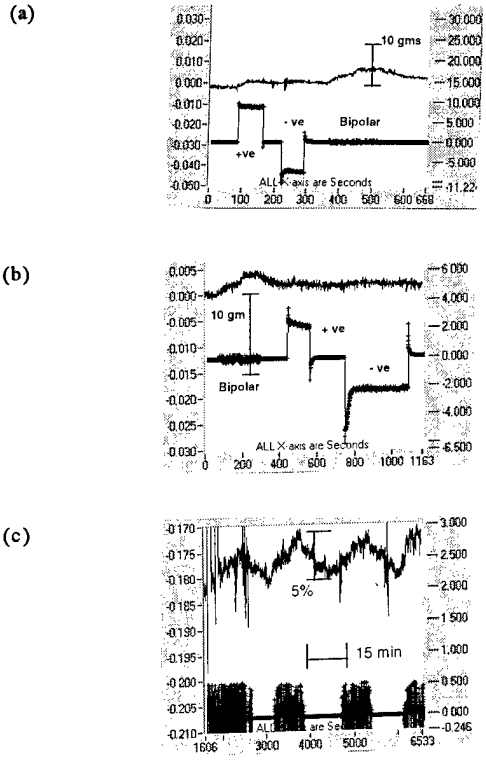

Figure 10. Time trace showing uncertainty in response of ATI Nano coated sensor. Left axis: drag; right: electric field. (a) No weight drag, 10V; (b) No weight drag 5V; (c) 100 gm weight axial force, 10V bipolar pulsing. 30-31 mSi/m; 17-18 gm/l of salt; 18-19 deg c. Model in a sink.

Drag reduction at low levels of drag can not be measured accurately if there is balance stiction. The cables from the electrodes and the strain gages can cause friction inhibiting the freedom of the floating element particularly at low speeds. This problem was eliminated in an in-house sensor where four parallel flexures were used to stiffen and support the floating cylinder. Two thin plates were placed in a plane orthogonal to the flexures, at the center of which two strain gages were placed to measure drag. Internal cables were coiled. The balance followed a linear response over the entire drag (that is, speed) range and displayed no stiction. A similar linear response is also achieved when the calibration is carried out while the

model is immersed in water after being installed in the tunnel using the cruciform. Measurements are presented here with this in-house drag sensor.

In spite of the seeming improvements due to the in-house sensors, it was discovered later, that they were fragile and buckled frequently, did not always have a hysteresis-free linear response and needed temperature compensation. The floating section was still not adequately stiff opening the potential for buckling the strain gage sensor. Questions about sensor insulation, ground looping and spurious body forces giving rise to anomalous balance response, were raised. Due to these reasons, runs were made with two sensors. Those runs where they were in qualitative disagreement were discarded. The measurements reported here are for those runs where the two sensors simultaneously displayed a similar consistent behavior.

The in-house sensor has recently been replaced by an ATI, Inc. Nano sensor. This is a six-component balance of integral construction. The gain has a temperature compensation, but the intercept does not. The sensor and the cables are coated for electrical insulation and use in saltwater. The sensor was installed in the model and dipped for days in a saltwater bath (30 mSi/m, 16.9 gm/l of salt, 18 deg c). The model was stiff and showed no visible movement when drag loads were applied. The calibration was linear in both air and saltwater over periods of hours during which the electrodes were powered on or off. Figure 10 shows the long time trace of the sensor output for 5V and 10V, 70 Hz, positive and negative unipolar and bipolar pulsing of electrode power (Fig. 11) under zero axial loading and a loading of 100 gms. There is a maximum uncertainty of 5 gms at 10V 26A total bipolar pulsing in the no load case. When there is a loading of 100 gms, bipolar pulsing may appear as a 5% drag reduction after 15 minutes of powering. These are the minimum levels of uncertainty achieved so far and seem acceptable. Drag measurements with these Nano sensors in a water tunnel have not yet been carried out.

3.3 Electrode Pulsing:

The present experiments are being carried out with three kinds of pulse shapes shown in Fig. 11. They are unipolar positive and negative, and also bipolar. The present experiment was designed to keep voltage levels as close to 3V as possible. The electrodes are made of pure copper, and nickel and gold plating are given to reduce corrosion. The electrodes were electroplated on kapton layers whereby the surface discontinuities were of electronic industry resolution rather than of mechanical or electrical engineering resolution. This fineness of surface finish, plus choice of frequencies and pulse shapes helped to minimize or eliminate electrolysis. The magnets remain under the kapton layer and are not exposed to saltwater. The bus bars inside the cylinder are insulated. The control circuit was software programmed to vary the pulse form and frequency. The voltages were varied between ± 10V, or 0 to 10V or 0 to -10V, or 0 to 5V, or 0 to -5V. The current level over the entire floating section was a maximum of 24A. Measurements in flat plates in a saltwater aquarium in our laboratory indicate that heating of water does not bring a sufficient change in viscosity to cause a drag reduction. Electrolysis is also not a source of drag reduction or possible noise. The model and the ATI sensors have been dipped in an aquarium of saltwater for several days. The calibration has been checked with electrode power turned on and off. A floating cylinder was also fabricated that did not have the magnets and had only the electrodes.

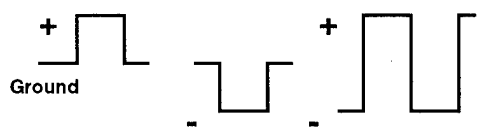

Figure 11. Voltage wave forms of power to electrodes: positive unipolar, negative unipolar and bipolar.

4. TENTATIVE DRAG BALANCE MEASUREMENTS:

The drag results using the in-house sensors are presented. Only those results where both sensors validated each other and trends were reproduced are presented. All other drag response is treated as anomalous. The results presented here are being repeated with the newly developed Nano sensor. Until then, the present results are deemed tentative. The response of the in-house sensor to on / off electrode power cycles is shown in Figs. 12 - 14. The data has scatter, but some trends can be observed. The electrode power is represented as the product of voltage and current. The drag sensor zero is not at zero grams. In Fig. 12, a positive unipolar pulsing increases drag balance output. The effect of negative unipolar is weak, but so is the power level. The negative unipolar effect is supported in Fig. 13 to be the opposite. The powering sequence is reversed in Fig. 13. The positive unipolar behavior shown in Fig. 12 is recovered. The sensor output is lower in negative pulsing. The suggestion is that, a positive unipolar pulsing increases drag, whereas a negative unipolar pulsing decreases drag, and there may be threshold levels of powering. This result should be treated with caution until verified by the planned Nano sensor measurements.

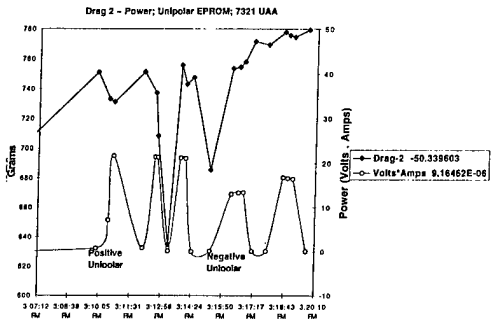

Figure 12. Effect of unipolar pulsing on drag. Flow speed = 5.2 m/s.

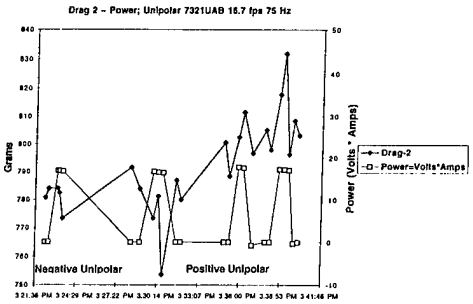

Figure 13. Reproduction of results in Figure 12.

Figure 14 shows the effect of bipolar pulsing. The electrode powering is now represented by the absolute value of the peak value current. The output from both the front and back strain gages are shown. Both gages have generally similar behavior, although not absolutely identical. The balance response is similar to the negative unipolar pulsing case - reduced output when the electrodes are powered.

(a)

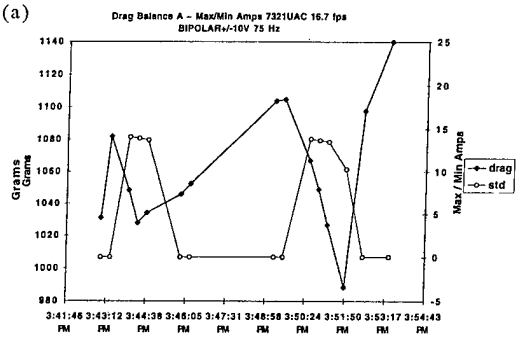

(b)

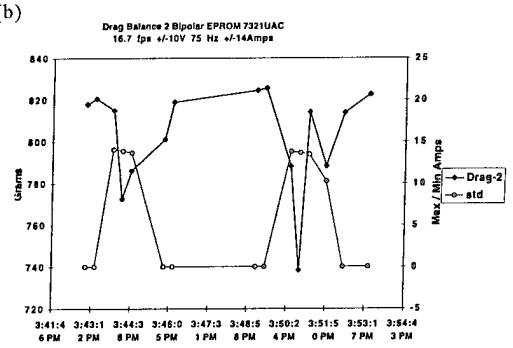

Figure 14. Effect of bipolar pulsing and sensor independence: (a) drag balance 'A', (b) drag balance 2. Symbols: open (power); filled (drag).

4.1 Sans-Magnet Experiment:

(a)

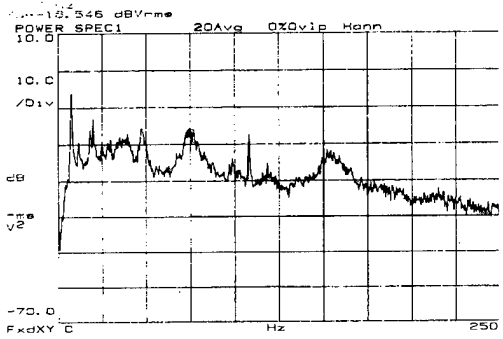

(b)

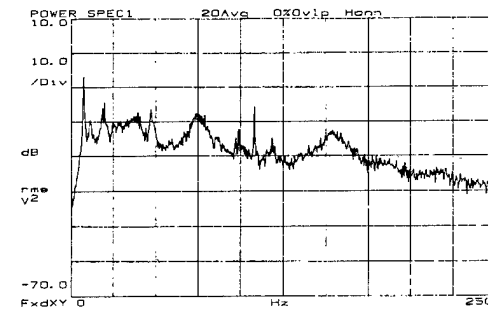

Figure 15. Wall pressure spectrum downstream of the electrodes in the sans-magnets experiment. Freestream speed: 5.3 m/s; (a) electrode power: off; (b) electrode power: on, ± 8V; 20A bipolar at 75 Hz.

A question was raised whether thermal heating due to the electrodes contributes to a drag reduction, or a gage response, that is similar. Hypothetically, thermal plumes could trap recirculating bubbles which could then generate a thrust. An axisymmetric model was fabricated that had electrodes but not the magnets. In addition to the in-house strain gage balance as used before, a commercial balance was also used (Nano balance from ATI, Inc.) which had a temperature compensation for gain (not an intercept compensation). No change in drag was observed in absence of the magnets.

Measurements of wall pressure spectra in the sans-magnets case are shown in Fig. 15. The wall pressure sensor was located at the downstream end of the floating section containing the rows of electrodes. There is question whether hot film is reliable in the present flow field. Due to its inherent construction and working principle, the wall pressure sensor has performed well so far and will be used more extensively in the near future. In an average of 20 spectra, a 2.4 dB reduction is observed at 75 Hz, the frequency of pulsation. There is no other significant reduction over the entire frequency range. It is intriguing to see that even at such a reasonably high Reynolds number turbulent boundary layer, a spanwise array pulsation could be picked up downstream although in a narrow frequency range, and only near the frequency of pulsation (Singh & Bandyopadhyay 1997).

5. CONCLUSIONS:

Laboratory experiments on drag reduction are being carried out in saltwater on a small axisymmetric body at a reasonably high speed and Reynolds number. The variable of interest is surface integrated long time averaged viscous drag. Emphasis has been laid on scaling issues, measurement accuracy and reproducibility. Internally consistent measurements and a flow mechanism have been obtained. These experiments tentatively indicate that a positive unipolar pulsed Lorentz field increases the drag balance output while a negative and a bipolar pulsing reduces the drag balance output. Attempt is being made to verify the measurements with a more robust drag sensor and microtiled surface.

ACKNOWLEDGMENTS

This work was funded by ONR (Program Manager: Dr. L. P. Purtell) and NUWC IR (Program Manager: Dr. S. Dickinson). Their support is gratefully acknowledged.

REFERENCES:

Bandyopadhyay, P. R. & Castano, J. M. "Micro-Tiles for Electromagnetic Turbulence Control in Saltwater - Preliminary Investigations", , *Symposium on Turbulence Modification and Drag Reduction*, ASME Summer Meeting, July 7-11, 1996, San Diego, CA, FED Vol. 237, Vol. 2, 53-60.

Bandyopadhyay, P. R. & Balasubramanian, R. 1996 "Structural Modeling of the Wall Effects of Lorentz Force," *ASME Jou. Fluids Engrg.*, V. 118, 412-414, June 1996.

Castano. J. M. 1997 Private Communication.

Choi, K-S., DeBisschop, J-R. & Clayton, B. R. 1997 "Turbulent Boundary-Layer Control by Means of Spanwise-Wall Oscillation," *AIAA Jou.* (due to appear).

Crawford, C. & Karniadakis, G. 1998 "Shear-stress Modification and Vorticity Dynamics in Near-Wall Turbulence," *Jou. Fluid Mech.* (due to appear).

Fan, X. & Brown, G. L. 1997 "Experiments on the Electromagnetic Control of Turbulence," Paper No. AIAA 97-2123.

Hatay, F., O' Sullivan, P. L., Biringen, S. & Bandyopadhyay, P. R. 1997 "Numerical Simulation of Secondary Flows in Channels Driven by Applied Lorentz Forces," *AIAA Jou. Thermophysics & Heat Transf.* Vol. 11, No. 3, 446-453.

Jueng, W. J., Mangiavacchi, N. & Akhavan, R. 1992 "Suppression of Turbulence in Wall-bounded Flows by High Frequency Spanwise Oscillations," *Phys. Fluids*, vol. A4, No. 8, 1605-1607.

Kral, L. 1998 Private Communication.

Meng, J. C. S., Huyer, S. A., Castano, J. M., Thivierge, D. P. & Hendricks, P. J. 1997 "Experimental Study of the Spanwise Vortex Resonance Hypothesis for Turbulent Drag Reduction Over a Flat Plate in Salt Water," *NUWC-NPT Technical Report 10,680.*

Nosenchuck, N. & Brown, G. L. 1993 "Discrete Spatial Control of Wall Shear Stress in a Turbulent Boundary Layer," in *Near-Wall Turbulent Flows*, (eds. So, R. M. C. & Speziale, C. & Launder, B. E.) 689-698, Elsevir.

Ritchie, W. 1832 "Experimental Researches in Voltaic and Electromagnetism," *Phil. Trans. Roy. Soc. (London)*, vol. 122, 279-298.

Singh, S. N. & Bandyopadhyay, P. R. 1997 "Linear Feedback Control of Boundary Layer Using Electromagnetic Microtiles," *Jou. Fluids Engrg.*, vol. 119, 852-858.

Wilkinson, S. & Lazos, B. S. 1987 "Direct Drag and Hot-Wire Measurements on Thin-Element Riblet Arrays," IUTAM Sympo. on Turbulence Management and Relaminarization, Bangalore, India, Jan. 19-23, 1987.

MHD TURBULENCE EXPERIMENTS, DRAG REDUCTION AND APPLICATION TO NON-MHD FLOW

A. Eidelman, H. Branover, E. Golbraikh and S. Moiseev*

Center for MHD Studies, Ben-Gurion University, P.O.B.653, Beer-Sheva 84105, Israel
eidel@bgumail.bgu.ac.il
*Space Research Institute, Profsoyuznaya st., 84/32, 117810 Moscow, Russia
moiseev@mx.iki.rssi.ru

Abstract – Experimental data on drag reduction in turbulent magneto-hydrodynamic flows and those with polymer additives are compared. A similar behavior of drag reduction, velocity profiles and spectra, Reynolds stresses, turbulent intensity is an argument in favor of a universal turbulence mode independent of the physical nature of the acting factor. We examine properties of such turbulence defined by helicity and possessing a number of features favorable for the formation of a drag-reduced flow, such as regularization, reduced turbulent viscosity, inverse energy transfer, low dissipation. Application of this approach to problems of seawater drag reduction under various conditions will be fruitful.

1. Introduction

After the paper of Toms [1] revealing a considerable (more than twice) reduction of hydrodynamic drag due to the addition of < 10 ppm of polymers, quantitative incompatibility of these two characteristics aroused interest in this effect having a certain economic potential. The problem including basic studies of turbulence proved to be difficult. Although a lot of experimental data has been accumulated and theoretical studies carried out during 50 years, there is no adequate understanding and no respective model of this phenomenon. We believe this is the reason of the failure of all attempts to apply drag reducing surface modifications and boundary layer devices, although they seem attractive for external overflow conditions, particularly, for seawater drag reduction.

Drag reduction can be achieved by different means, both by such additives as polymers, surfactants, asbestos fibers, etc., and by applying a magnetic field in magnetohydrodynamic (MHD) flows, i.e. by essentially different ways of the interaction between the acting factor and the flow. A significant and approximately equal effect achieved suggests that it exists due to a universal turbulence mode in drag-reduced flows that can be achieved by various means. We believe that just this basic approach is fruitful. It involves the study of the conditions of such turbulence mode generation and its properties, and then – their application under specified conditions.

Recent studies of a MHD flow [2] have revealed a turbulence mode with properties closely connected with drag reduction. The appearance of turbulence possessing a certain order and such properties as turbulent viscosity reduction [3], redistribution of kinetic energy [4], are connected with turbulence generated under the conditions of non-zero helicity. Turbulence of such a type arises under the action of constraint by various forces: electromagnetic, Coriolis, buoyancy, and also under the conditions of shear flow. The properties of this turbulence are determined by another (along with energy) non-viscous invariant – helicity, characterizing its topology [5].

The properties of such helical turbulence allow us to have a new insight into experimental studies of MHD flows, where under the action of the magnetic field so called laminarization is observed. The latter term is, in the first place, due the observed drag reduction that was attributed to turbulence suppression up to its total disappearance, as expected according to some theories of MHD flow stability. In fact, this mode remains turbulent, and we suppose that turbulence mode is close to that observed at the reduction of hydrodynamic drag at the expense of additives, such as polymers, etc.

Principal features of turbulent flow parameters with a reduced drag are the following. Their friction drag is bounded between a usual value and the maximum drag reduction asymptote. Mean velocity profile involves a thicker viscous sublayer than usual. Longitudinal velocity fluctuations grow, whereas transverse ones and Reynolds stresses greatly decrease. A similar behavior of a number of main characteristics of MHD turbulent flow obtained in experiments is an argument in favor of a universal key mechanism of significant drag reduction caused by various factors.

2. Integral characteristics of channel flows with drag reduction

The principal manifestation of the flows under study is the decrease in hydrodynamic drag coefficient $\lambda = 8\tau_w/\rho U_o^2 = 8(U^*/U_o)^2$ by $\Delta\lambda$. Here ρ is density, τ_w is wall shear stress, U^* and U_o are dynamic and mean flow velocities, respectively. Drag reduction (DR) is expressed as $DR = \Delta\lambda/\lambda$. Hydrodynamic drag in a turbulent flow in channels, specifically, in smooth pipes of circular cross-section (see Fig. 1, curve 7) can be well approximated by Blasius formula

$$\lambda_B = 0.3164\ Re^{-0.25} \qquad (1)$$

from the critical Reynolds number $Re = U_o d/\nu \geq 2300$ to $Re = 1.5 \times 10^5$. The relation (1) and laminar flow range characterized by the dependence $\lambda = 64/Re$ are shown in Fig. 1. The remaining data presented in Fig. 1 have been obtained in MHD flows [6, 7, 8]. These experiments were carried out in circular pipes of various diameters in uniform magnetic fields, the direction of the field coinciding with mean velocity direction.

The amount of experiments carried out in such a configuration is rather small, but they are of specific interest. Such a flow does not exhibit the coupling between the magnetic field and mean flow, which is of such great importance when the field is transverse. A longitudinal field has no effect on the fully developed laminar pipe flow because the field and the flow are parallel. Therefore, the field should influence the flow only when the flow becomes turbulent, or when small disturbances exist in an otherwise laminar flow. Since the longitudinal field cannot exert longitudinal forces on the flow, it does not affect the mean velocity profile directly. However, it does affect the mean velocity through modification of the turbulent structure of the flow. Consequently, flows of this type reveal directly the influence of the fields on the turbulent structures.

A longitudinal magnetic field was generated by a solenoid with the axis parallel to the test section. Test section diameter varied from 5 mm [6] to 32 mm [7], and the magnetic field reached 1.8 T [8]. Various liquid metals were used as working fluid: NaK eutectic mixture, mercury [6, 8]. To describe MHD experiments, the following dimensionless parameters are used: Hartmann number

$$Ha = Bd(\sigma/\rho\nu)^{1/2} \qquad (2)$$

and interaction parameter

$$N = \sigma B^2 d/\rho U_o \qquad (3)$$

where B is the applied field, σ is the electrical conductivity, Ha^2 and N are the ratios of magnetic forces to viscous forces and to inertial forces, respectively. Due to low viscosity and high electrical conductivity of liquid metals, comparatively high Re and Ha values are reached (3.4×10^5 and 1350) [7].

The dependence of drag coefficient on Re at a constant Ha has a characteristic shape (see Fig. 1). With increasing Re, drag reduction is first decreased more rapidly than in a usual turbulent flow (1). Above a certain Re value depending on Ha number, the magnitude of λ is 2-3-fold smaller than λ_B. Drag reduction reaches its maximum value at a certain critical Ha/Re parameter amounting, according to experimental data, to 0.025-0.035. With further Re increase, drag coefficient grows abruptly at first, and then more smoothly, tending to the dependence (1). Curves 1-4 in Fig. 1 show maximum drag reduction dependencies obtained in MHD experiments [6-8]. For the sake of comparison, in the same figure, Virk's asymptote [9] is plotted according to experimental data obtained with polymer additives. It is approximated by the expression

$$\lambda = 2.32\ Re^{-0.58} \qquad (4)$$

within the range of Reynolds numbers Re = (4 ÷ 40) x 10^3. We have approximated the maximum drag reduction obtained in the experiment [7] by the curve 6 in Fig. 1 and by the expression

$$\lambda = 2.39\ Re^{-0.56} \qquad (5)$$

very close to Virk's asymptote.

Note that in a transverse magnetic field drag reduction is observed just as in a longitudinal one. In [11] plots of relative drag coefficient $\lambda/\lambda_B = f(Re)$ and $\lambda/\lambda_B = f(Ha)$ are shown (see Figs. 6-18, 7-23 [11]). The qualitative character of the dependencies is as in Fig. 1; maximum drag reduction is 50-70% at (Ha/Re) x 10^3 ~ 6.6, and its dependence is close to (5).

The mentioned similarity of the data on drag reduction in MHD case and in case of additives is also observed in the mean velocity U distribution across the channel cross-section. Figs. 2 and 3 show mean velocity profiles formed at the decrease in hydrodynamic drag due to polymer additives [10] and in MHD flows [6]. Here we observe a number of common properties of profiles in both cases. The profiles are presented in near-wall coordinates

$$u^+ = U/U^*,\ y^+ = y\ U^*/\nu \qquad (6)$$

where y is the distance from the wall. The profiles $u^+ = f(y^+)$ measured in the case of drag reduction by a polymer additive of 5 wppm at Re = 3.5 x 10^4 were obtained at various distances downstream of the polymer injection site x/d = 8 ÷ 214 [10]. The principal feature of the profiles at DR < 60% is a nearly parallel shift ΔB of their logarithmic portion

$$u^+ = 5.75 \log y^+ + 5.5 + \Delta B \qquad (7)$$

The larger drag reduction (curves 1-4, Fig. 2), the larger this shift. At ΔB = 0 logarithmic profile (7) fits its linear portion $u^+ = y^+$; then, with growing ΔB, another range, similar to logarithmic one, appears between them. It has a slope increasing with growing drag reduction. This portion of the profile tends to a limiting asymptote [9]

$$u^+ = 26.9\ y^+ - 17 \qquad (8)$$

shown by curve 7 in Fig. 2.

Mean velocity profiles shown in Fig. 3 have been obtained in MHD mercury flow for different Ha numbers up to 614 at various Re numbers. Logarithmic portion of the profile can be approximated by the relation (7) shown by curve 6 (Fig. 3). With increasing Ha/Re ratio, ΔB grows (7) and reaches 10 at 10^3 Ha/Re = 32. Just as in profiles of flows with drag reduction induced by polymer additive, a range with the slope close to the limiting asymptote (8) appears in the profile; it is shown by curve 7 in Fig. 3a. It is noteworthy that here velocity u^+ values remain much below those corresponding to a parabolic profile of a laminar flow shown by curve 8 in Fig. 3a.

Having emphasized a marked analogy in the behavior of drag coefficient and mean velocity profiles of flows with drag reduction caused by additives and MHD flows, we pass to structural properties of MHD turbulence resulting in drag reduction.

3. Helical turbulence of a drag-reduced MHD flow

MHD turbulence has a specific nature that results from the interaction with a magnetic field. Since we are interested in turbulence properties, field orientation is not very important, and longitudinal field has no preference with respect to a transverse one. Therefore, we make use of data on MHD turbulence in a transverse magnetic field, which provide for a more complete insight.

Our experiments were conducted in a mercury flow. The experimental facility involves a test channel, a pump, an overflow constant level tank with a number of dense meshes for damping the entering flow disturbances and a constant level tank. The test channel made of stainless steel has a rectangular 2.8 x 5.6 sq. cm cross-section. Uniform magnetic field was directed normal to the longer side of the channel cross-section. The electromagnetic pole length was 90 cm, and magnetic field B could vary up to 1.2 T. A fine honeycomb was placed into the flow upstream of the test section in order to eliminate penetration of any turbulence from upstream into the test section. We examined the behavior of turbulence generated streamdown of the honeycomb. Local velocity measurements have been performed by means of a conduction anemometer. Turbulence intensity and spectra of velocity fluctuations were defined. A more detailed description of the experimental facility and methods is given in [12].

Experiments have been mainly performed at mean velocity U_o = 0.16 m/s corresponding to Reynolds number Re of 52 x 10^3, and some of the experiments - at U_o = 0.08 m/s. Ha number varied in the range of 60-1200, and interaction parameter N - in the range of 0.1-30, the magnetic Reynolds number being $Re_m = \mu_o \sigma U_o L << 1$; here L is the length scale, and μ_o is magnetic permeability.

Our experiments have confirmed that turbulence intensity decreases under a comparatively weak magnetic field if the parameter 10^3Ha/Re increases up to 2.5. Then the turbulence intensity reveals an abrupt 2-3-fold growth in the intermediate range of 2.5 <10^3 Ha/Re < 5. After that it changes slightly in the range of 5 < 10^3Ha/Re < 10. We have obtained one more specific range of a significant turbulence amplification - that of the parameter increase in the range of 13 < 10^3Ha/Re < 25.

Velocity spectra measured have shown that a qualitative change in the dependence of turbulence intensity on Ha/Re is accompanied by a change in spectral index. Fig. 4 shows velocity spectra measured at N ~ 0.2 and 0.7; here E_u is spectral energy density, and f – frequency. Turbulence velocity spectra obtained under a weak magnetic field (Fig. 4A) are characterized by the spectral slope close to a well-known Kolmogorov's index –5/3 inherent to turbulence in the inertial range. Significant changes in spectral index become evident when the parameter Ha/Re is increased. The respective spectrum shown in Fig. 4B differs from those obtained in the previous mode. Particularly, their spectral index close to –7/3 in the high frequency range [12].

Turbulence velocity spectra obtained in the range of the interaction parameter N >1.4 are shown in Fig. 5. Three spectra (series A) with very close values were obtained in the range of 1.6 < N < 9. The spectrum C corresponds to N =15.6, whereas the spectrum B - to intermediate conditions. Their high frequency ranges are described by spectral indices close to -11/3 or -4. A significant amplification of spectral density is observed at low-frequency scales if N >10.

4. Discussion of the results

We have revealed four modes of turbulent motions based on turbulence intensity versus Ha/Re and on the values of spectral indices, as well. They correspond to the following Ha/Re and interaction parameter values, as shown in the Table.

Modes:	1	2	3	4
10^3Ha/Re	<2.5	2.5-5	5-13	13-25
N=Ha^2/Re	<0.3	0.3-1.4	1.4-10	10-30

MHD Turbulence Modes

The first mode represents a transformation of Kolmogorov's turbulence with spectral index –5/3 noted at rather low values of the parameters Ha/Re ~ 10^{-3} ; N ~ 0.1. It manifests itself in turbulent intensity decrease with growing parameters. The second mode represents helical turbulence generation accompanied by an abrupt transition from the spectral index of –5/3 to that close to –7/3. This transition is an important fact pointing to a qualitative change in turbulence mode. In Kolmogorov's turbulence, the only and the main mechanism of the generation of velocity field and, hence, of the spectral index –5/3 in the inertial scale range is energy transfer. The crucial parameter is, respectively, energy transfer rate $\varepsilon = du^2/dt$ [13]. In the third mode helical turbulence qualitatively changes becoming intermittent. Then, in the fourth mode, the intermittency is developing, and turbulence localization regions grow in number.

In helical turbulence having spectral slope of –7/3, the crucial parameter is helicity transfer rate $\eta = dH/dt$, where $H = \langle u\ \mathrm{rot}\ u \rangle$ is helicity. In this case, a respective inertial spectral range is generated under the action of helicity transfer. This drastically changes motion characteristics, particularly, leads to a decrease and maybe even to a negative value of turbulent viscosity [14]. In case of helical turbulence characteristic features of velocity behavior can be described by the model equation [15]

$$\partial \langle U \rangle / \partial t = \alpha\ \mathrm{rot} \langle U \rangle + \nu \Delta \langle U \rangle \qquad (9)$$

where $\alpha = H\tau$, τ being the correlation time. A new remarkable quality of the equation (10) is the dissipative "antiviscous" force resulting from the term α rot $\mathbf{U} \sim L^{-1}$ providing for the feedback between motions along different axes. This force decreases more slowly than the viscous force ($\sim L^{-2}$) with increasing characteristic scale L.

Direct computation of turbulent viscosity shows that mean helicity and its fluctuations decrease its value. Indeed, using the representation of the helicity parameter $\alpha = \langle\alpha\rangle + \alpha'$, where $\langle\alpha'\rangle = 0$, and letting $\langle\alpha'(t)\,\alpha'(t')\rangle = 2D\delta(t - t')$, we average the equation (9) over the helicity fluctuations and obtain the same equation with the substitutions $\alpha \rightarrow \langle\alpha\rangle$ and $\nu \rightarrow \nu - D$ showing the turbulent viscosity decrease. Turbulent viscosity can essentially decrease [3] in helical turbulence with finite correlation time and non-zero mean helicity. This is important under real ocean conditions, where there is neither homogeneity, nor isotropy. Moreover, even under isotropic and homogeneous conditions, but with the account of sufficiently high correlation times of turbulence and intense helicity fluctuations, turbulent viscosity may reverse its sign. The condition of sign reversal in this case is $\tau_1 > \tau$, where τ_1 is the characteristic time of helicity fluctuations, and τ is the characteristic correlation time of small-scale turbulence, supposing that the amplitude of helicity fluctuations is close to the average level.

Negative viscosity observed in the experiments on the analysis of MHD flows [16] is well explained by helical turbulence model. Turbulent viscosity decrease described by helical turbulence model is observed in experimental studies of drag-reduced flows. Irrelevant of the nature of a factor causing drag reduction, both in MHD flows and in case of polymer additives a decorrelation between u' and v' components of velocity fluctuations takes place, resulting in a decrease in Reynolds stresses. A decrease in one-point correlations $\langle u'\,v'\rangle$ making the principal contribution to Reynolds stresses is presented in Fig. 6 for a MHD flow [17] and in Fig. 7 – for drag reduction by polymer additives [18]. This fact testifies to a profound similarity of turbulence modes at drag reduction under various factors and is one of arguments in favor of our approach.

It is established [19] that in MHD shear flows helicity generation occurs depending on the interaction parameter N value. Helicity increase makes the motion more regular than in Kolmogorov's turbulence. The principal properties of energy transfer are essentially changed in helical turbulence mode. In contrast to Kolmogorov's turbulence, where energy losses occur at the expense of energy transfer from the source scale to the sink small-scale regions with high dissipation, at sufficiently high mean helicity the usual transfer of turbulent energy into the viscous sink is interrupted. In fact, the more oscillations are excited in the system, the better chaotization conditions. Under the conditions of a direct energy transfer, the number of vortical harmonics grows due to vortex splitting, and the chaotization process is accelerated. However, under the conditions of an inverse energy transfer along the spectrum, the number of vortical harmonics decreases due to vortex merging, the chaotization process is slowed down, and quasi-laminarization arises.

Drag coefficient for helical turbulent motions in channels and at the overflow of bodies under the mentioned conditions should decrease. Indeed, drag reduction observed in MHD turbulent flows and interpreted as laminarization has been obtained in flows with turbulent fluctuations. We have revealed in our experiment that helical turbulence mode with the spectral index –7/3 is generated at the parameter Ha/Re value where drag reduction range begins. Fig. 7a shows drag coefficient dependence on Ha/Re parameter obtained in [20] for a broad range of Re numbers in a mercury flow in a smooth channel under a transverse magnetic field. Fig. 7b presents a dependence of spectral index n on Ha/Re parameter obtained in [12]. Apparently, at n values close to –7/3 corresponding to the appearance of helical turbulent mode drag coefficient becomes close to its laminar value shown in Fig. 7a as Hartmann's solution.

It is well-known (see [21] and references therein), a motion of helical nature is generated near the wall, such as, say, streamwise vortical structures. Their evolution is the key point in boundary layer formation and in drag reduction problem. The approach to the problem using helical turbulence model is physically grounded and allows us to interpret data obtained at drag reduction by various means from a single point of view.

5. Conclusion

A significant drag reduction in turbulent flows is achieved by means of additives, such as dilute polymer and surfactants solutions and also observed in magnetohydrodynamic (MHD) flows. Despite different physical nature of the action on the flow, this phenomenon is characterized by similar turbulence properties. A similar behavior of such characteristics of turbulent flows as drag coefficients, mean velocity profiles, Reynolds stresses fall-down obtained in above experiments is an argument in favor of a universal key mechanism of a significant drag reduction due to a specific turbulence mode.

Our studies of MHD turbulence have shown that its mode changes with increasing MHD interaction parameter. The spectral index varies from –5/3 value inherent to Kolmogorov's turbulence to –7/3, when the interaction parameter becomes higher than a certain value. Our studies have shown that a spectrum with the index –7/3 is formed due to the transfer of helicity generated in a shear flow under the action of a magnetic field. The comparison with experimental data on drag reduction in MHD flows shows that it is achieved at the values of the interaction parameter close to the appearance of helical turbulence.

We have shown that helical turbulence possesses a number of features favorable for the formation of a drag-reduced flow, such as a reduced effective viscosity, low dissipation, inverse energy transfer from small scales to large ones. It is known that in turbulent flows near walls helical vortices are developed. These vortices lose their stability and break down leading to kinetic energy production and dissipation near a wall. Helical movement stabilization represents an adequate universal mechanism of the influence of both body forces and additives on the motion near walls leading to drag reduction. The application of this approach to seawater drag reduction under various conditions will be fruitful.

Acknowledgment

The authors are grateful to Mrs. N. Goldbaum for her inestimable assistance in the paper preparation.

References

1. Toms, B.A. 1949. Some observations on the flow of linear polymer solutions through straight tubes at large Reynolds numbers. Proc. of the 1st Internat. Rheology Congress, II, Part 2 (North-Holland, Netherlands), 135-142.

2. Branover, H., Moiseev, S., Eidelman, A. and Nagorny, M. 1994. Quasi-two-dimensional helical turbulence in MHD and geophysical flows. Proc. 2nd Intern. Conf. on Energy Transfer in MHD Flows, Sept. 26-30, 1994, Aussois, France, v. 2, 777-785.

3. Belyan, A.V., Moiseev, S.S. and Chkhetiani, O.G. 1994. On eddy viscosity in helical turbulence. Physics – Dokl., v. 39, No.1, 13-15.

4. Golbraikh, E., Chkhetiani, O., Moiseev, S., Eidelman, A. and Branover, H. 1998. On the character of turbulent energy redistribution in helical flows. Ann. Geophys., v. 16, II.

5. Moffatt, H.K. 1969. The degree of knottedness of tangled vortex lines. J. Fluid Mech., v. 35, p. 1, 117-129.

6. Genin, L.G., Zhilin, V.G. and Petukhov, B.S. 1967. Experimental investigation of turbulent flow of mercury in a circular tube in a longitudinal magnetic field. High-Temperature Sci.-Res. Inst., v. 5, No. 2, 266-271.

7. Klebanoff, P.S. and McMichael, J.M. 1976. On MHD pipe flow. Proc. Bat-Sheva Internat. Seminar on MHD-Flows and Turbulence, Beer-Sheva. J. Wiley, N.Y., p. 73.

7a. Levin, B.V. and Chinenkov, I.A. 1966. Experimental study of turbulent flow of a conducting fluid in a pipe in the presence of a longitudinal magnetic field. Magnetohydrodynamics, No. 4, 147.

7b. Kovner, D.S. and Krasil'nikov, E.Yu. 1965. Experimental study of turbulent pipe flow of an electrically conducting fluid in a parallel magnetic field. Dokl. Akad. Nauk SSSR, No. 5, 1096.

8. Fraim, F.W. and Heiser, W.H. 1968. The effect of a strong longitudinal magnetic field on the flow of mercury in a circular tube. J. Fluid Mech., v. 33, part 2, 397-413.

9. Virk, P.S. 1975. Drag reduction fundamentals. AIChE J., v. 21, No. 4, 625-656.

10. McComb, W.D. and Rabie, L.H. 1982. Local drag reduction due to injection of polymer solutions into turbulent flow in a pipe. AIChE J., v. 28, 547-565.

11. Branover, H. 1978. Magnetohydrodynamic flow in ducts. Wiley & Sons, N.Y., 290 p.

12. Branover, H., Eidelman, A., Nagorny, M. and Kireev, M. 1994. MHD simulation of quasi-two-dimensional geophysical turbulence. In: Progress in Turbulence Res., Eds. H. Branover and Y. Unger., v. 162, 64-79.

13. Monin, A.S., Yaglom, A.M. 1975. Statistical Fluid Mechanics. Ed.Lumley, J. MIT Press, Cambridge, Mass.

14. S. Moiseev, H. Branover, O. Chkhetiani, A. Eidelman and E. Golbraikh. 1998. Role of helicity and chirality in drag reduction in turbulent flows. Proc. Intern. Symp. Seawater Drag Reduction.
15. Moiseev, S.S. 1990. Helical mechanism of large-scale structure generation in continuous media. Plasma Physics, v. 16, No 8, 951-958.
16. Henoch, C., Hoffert, M., Branover, H. and Sukoriansky, S. 1993. Anisotropic turbulence: analogies between geophysical and hydromagnetic flows. In: Current Trends in Turbulent Research. Progr. in Astron. and Aeron., AIAA, v. 149, 190-209.
17. Reed, C.B. and Lykoudis, P.S. 1978. The effect of a transverse magnetic field on shear turbulence. J. Fluid Mechanics, v. 89, No. 1, 147-171.
18. Gampert, B. and Yong, C.K. 1990. The influence of polymer additives on the coherent structure of turbulent channel flow. In: Structure of Turbulence and Drag Reduction, Ed. A. Gyr, Springer-Verlag, Berlin, 223-232.
19. Chkhetiani, O., Moiseev, S., Golbraikh, E. and Eidelman, A. 1997. On the helicity generation in shear flows in the external magnetic field. Ann. Geophys., v. 15, II, C607.
20. Brouillette, E.C. and Lykoudis, P.S. 1967. Magneto-fluid-mechanic channel flow. Phys. Fluids, v. 10, No. 5, 995-1001.
21. Kline, S.J. and Robinson, S.K. 1990. Turbulent boundary layer structure: Progress, status, and challenge. In: Structure of Turbulence and Drag Reduction, IUTAM Symp., Zurich, Switzerland, 1989; Ed. A. Gyr, Springer-Verlag, 3-22.

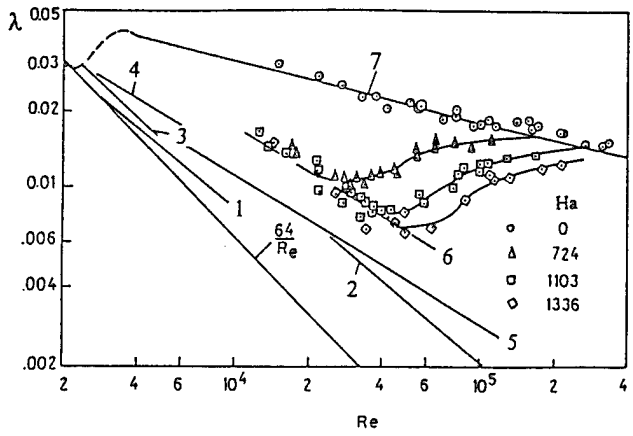

Fig. 1. Dependence of drag coefficient on Reynolds number and Hartmann number (Klebanoff & McMichael, 1976). Comparison with other sources: 1) Fraim & Heiser, 1968; 2) Levin & Chinenkov, 1970; 3) Genin et al., 1967; 4) Kovner & Krasil'nikov, 1966; 5) Virk's asymptote: $\lambda = 2.32\ Re^{-0.58}$; 6) our approximation: $\lambda = 2.39\ Re^{-0.56}$; 7) Blasius formula: $\lambda = 0.3146\ Re^{-0.25}$.

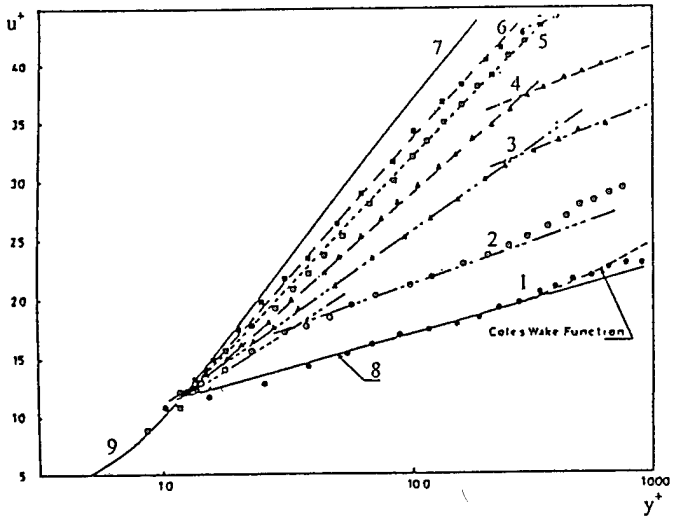

Fig. 2. Mean velocity profiles streamdown of polymer (5 wppm) injection (McComb & Rabie, 1982): 1) x/d = 8; DR,% = -2.5; 2) 40; 26.5; 3) 76; 46; 4) 100; 57; 5) 190; 65; 6) 214; 67; 7) Virk's asymptote: $u^+ = 26.9 \log y^+ - 17$; 8) $u^+ = 5.75 \log y^+ + 5.5$; 9) $u^+ = y^+$.

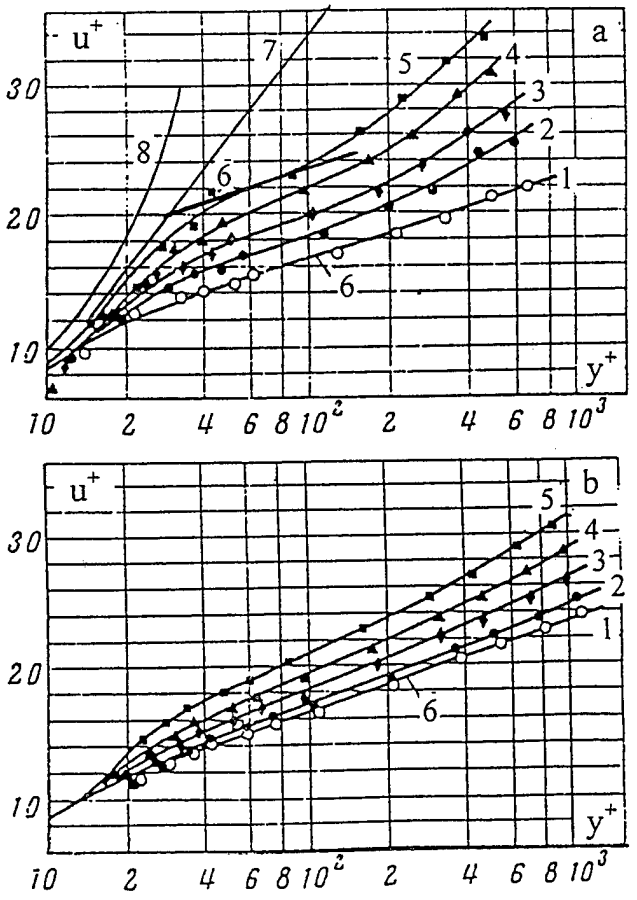

Fig. 3. Mean velocity profiles in MHD flow. Re x 10^4: a) 2.39; b) 4.25; Ha: 1) 0; 2) 279; 3) 390; 4) 502; 5) 614; 6) $u^+ = 5.75 \log y^+ + 5.5$; 7) Virk's asymptote: $u^+ = 26.9 \log y^+ - 17$; 8) parabolic profile.

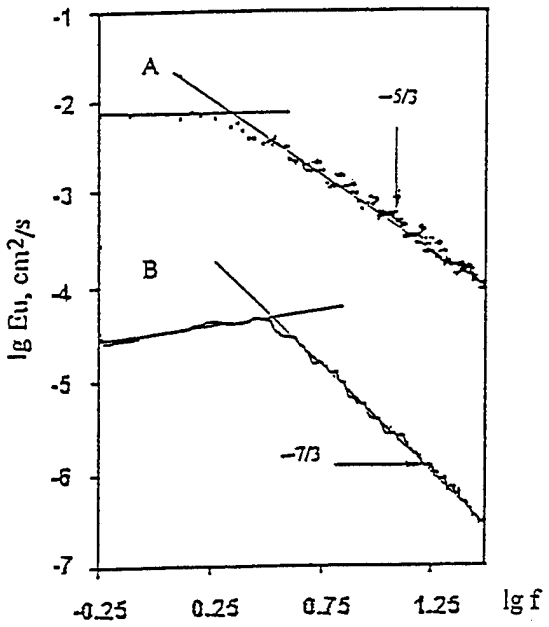

Fig. 4. Velocity spectra transformation under a magnetic field: A: N = 0.2; B: N = 0.7. The spectrum B is shifted downwards by two orders.

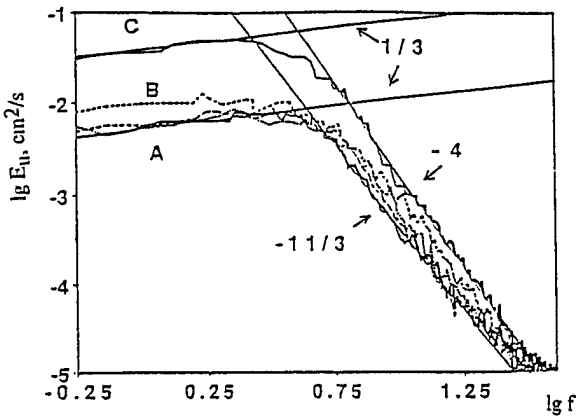

Fig. 5. Velocity spectra evolution with growing interaction parameter N. A: N = 1.6; B: 9.06; C: 15.6.

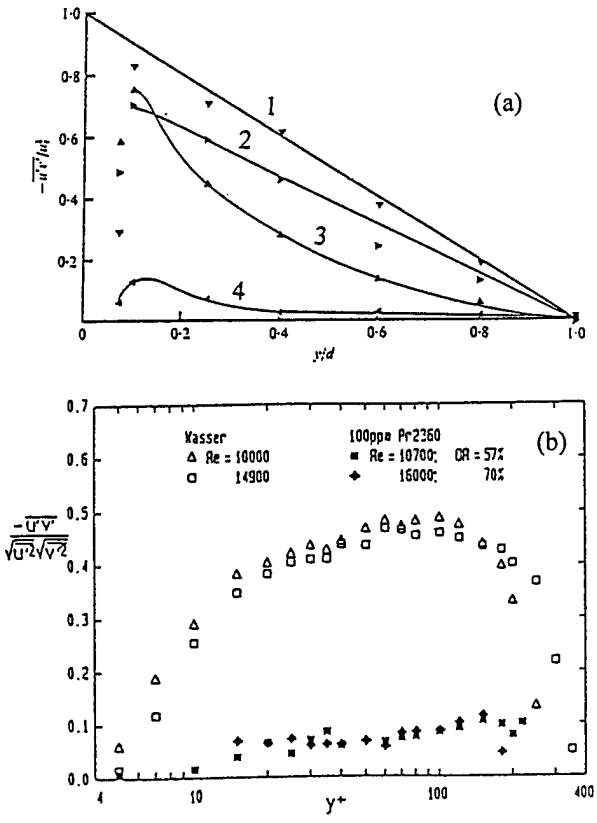

Fig. 6. Reynolds stress profiles transformation in flows with drag reduction: a) MHD flow, Re – 25000; 10^3 Ha/Re: 1) 0; 2) 1.08; 3) 2.07; 4) 3.63 (Reed & Lykoudis, 1978); b) polymer solution flow (Gampert & Yong, 1990).

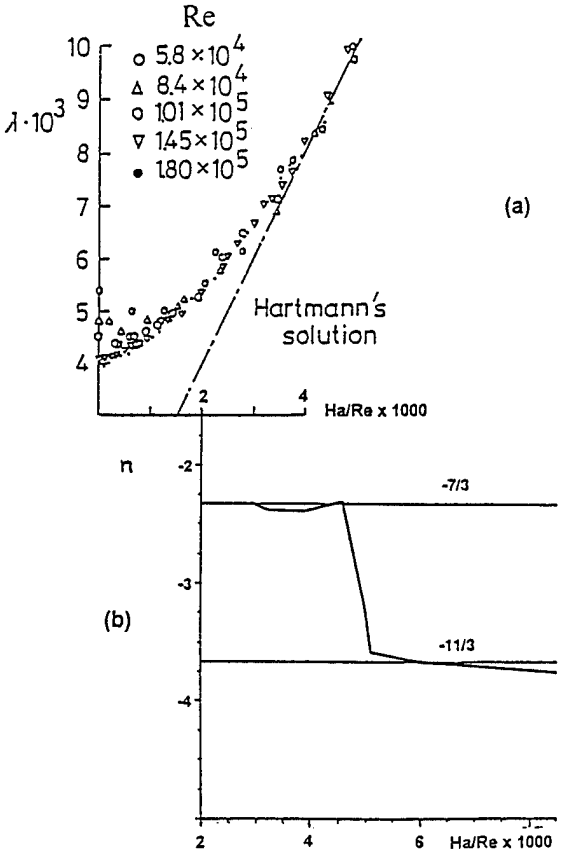

Fig. 7. Drag coefficient λ for MHD turbulent flow as compared with Hartmann's solution for laminar flow (Brouillette & Lykoudis, 1967) (a) and turbulent spectral index *n* (Branover et al., 1994) (b) versus the parameter Ha/Re.

DRAG REDUCTION BY ELECTRO-MAGNETIC FORCES

Vladimir I. Merkulov
Institute of Theoretical and Applied Mechanic
SB of the Russian Academy of Sciences, Novosibirsk, 630090, Russia
merkulov@itam.nsc.ru

Abstract- We present a newphysical and mathematical formulation of a problem on the external flow of an electroconducting fluid (sea water) under the action of the body motion and certain bulk control force (Lorentz force). For the slender axisymmetric bodies we find within the framework of an inviscid model the boundary values of electromagnetic fields depending on the body shape, which ensure the absence of the pressure distur bance in the overall flow field and,in particular,ensure a waveless motion of a half-submersed body. The second example concerns the problem of friction drag decrea se in a viscous liquidby way of displacement of the flow of sliding for the flow with roll ing.In the conclusion the electromagnet ic providing continuous flowingaround sphere for the large numbers of Reynolds is calculated.

I. INTRODUCTION

A strong magnetic field combined with a weak electric field in the case when they occupy a large volume enable one to create a force being sufficient for a practical goal in such a widespread medium as the sea water. The Japanese researchers from the Kobe University of Mercantile Marine have made use of this possibility [1]. However, it is preferable to use such a fine and flexible form of the effect on the fluid, which is represented by the electromagnetic field, not so much for the thrust production as for the control of external fluid flow. For the planar flow the proposed problem formulation has been considered in the author's work [2].

II. FORMULATION OF THE PROBLEM

Let us consider a fluid flow caused by the longitudinal motion of a slender axisymmetric body. We will be interested in the flow character outside the boundary layer the presence of which can be taken into account by increasing the body width. Assuming the inviscid fluid model we arrive at the following equation system [3].

$$\nabla H + \omega \times \mathbf{u} = \mathbf{F} \tag{1}$$

$$\omega = \nabla \times \mathbf{u}; \quad \nabla \mathbf{u} = 0$$

with the boundary conditions

$$u_n = 0 \tag{2}$$

on the boundary,

$$\lim \mathbf{u} = \mathbf{U}$$

at the infinity. Here H is the total energy of the fluid particles including its potential part, $\mathbf{F}$ is the non-potential part of the bulk forces. Let us introduce the stream function of the axisymmetric flow, the Stokes function, by the relationships $\mathbf{u} = U\nabla \times (\alpha^0 \Psi / r)$. Here α^0 is ort the cylindrical coordinate system r, α, z. We express the vector$\mathbf{F}$ also in terms of a scalar function A: $\mathbf{F} = U^2 \nabla \times (\alpha^0 \mathbf{A}/\mathbf{r})$. The operation ∇ applied to equation (1) enables us to eliminate the function H and to obtain for the axisymmetric flow

$$u_z \partial\omega/\partial z + u_r \partial\omega/\partial r = (\nabla \times F)_\alpha \tag{3}$$

Here ω–is azimuthal nonzero component of the vorticity.

For slender bodies the control objectives are attainable with the aid small control forces, then with the accuracy up to the quantities of the second order of smallness we can obtain from [3] a linear equation with constant coefficients

$$[(\partial/\partial z)\nabla \times \nabla \times (\alpha^0 \Psi/r)]_\alpha = [\nabla \times \nabla \times (\alpha^0 A/r)]_\alpha \tag{4}$$

[1]The material presented here was first reported at the International Conference on Marine Electromagnetics (MARELEC 97) on 23-26 June 1997, London, UK.

The integration of this equation leads to the formula

$$\Psi = r^2/2 + \psi + \int_{-\infty}^{z} A(r, z)dz, \tag{5}$$

where ψ– is the Stokes function [3], representing the stream function of the potential flow in the absolute coordinate system, in which the fluid is at rest a the infinity, and the body moves at the speed $-U$ in the direction of the z axis.

Denote by $r = \zeta(z)$ the equation of the surface of the body flowed around. For slender bodies the following formulas are valid: $u_n = u_r = U\zeta'(z) = -(1/r)(\partial\Psi/\partial z)$ at $r = \zeta(z)$. Substituting here the representation (5), we obtain

$$\partial\psi/\partial z = -\zeta'\zeta - A$$

at $r = \zeta(z)$. Now we add to this the condition at the infinity $\lim \partial\psi/\partial z = 0$.

To complete the problem formulation let us write down the Bernoulli integral. For the case of a slender body and a small force we can write with the accuracy up to the second order quantities the following expression for the Bernoulli integral on the surfaces $\Psi = const$:

$$H = H_\infty + \int_{-\infty}^{z} F_z(z)dz \tag{6}$$

III. DETERMINATION OF LORENTZ FORCES

Taking into account a small electric conductivity σ of the water and consequently a small current density one can determine the force $\mathbf{F}$ within the framework of a non-induction approximation. This enables us to introduce the potentials of the electric field ϕ_e and of the magnetic field ϕ_b in such a way that $\mathbf{E} = \nabla\phi_e, \quad \mathbf{B} = \nabla\phi_b$. The Lorentz force related to the density is equal to the product $\mathbf{F} = \mathbf{j} \times \mathbf{B}/\rho$. And since the Ohm,s law for the electroconducting medium moving at a speed $\mathbf{u}$ has the form [4]

$$\mathbf{j} = \sigma(\nabla\phi_e + \mathbf{u} \times \nabla\phi_b).$$

The potentials of the electric and of the magnetic field should be solved under the boundary conditions

$\partial\phi_e/\partial n = e, \quad \partial\phi_b/\partial n = b$ on the boundary,

$\lim \nabla\phi_e = \lim \nabla\phi_b = 0$ at the ∞.

All the arbitrariness in the choice of the control function will finally reduce to the choice of the boundary values for the electric and magnetic fields.For our purposes it is search for the boundary conditions of the form

$e = e_0(z) \sin N\alpha, \quad b = b_0(z) \sin N\alpha$.

Here $e_0(z), b_0(z)$ are slowly varying functions, N is the number of pairs of the poles of electromagnetic fields. For slender bodies the velocity field, the electromagnetic field and the forces created by the latter field can be determined in each section $z = const$. under the assumption of their independence of z. A weak dependence of z is taken into account here by a

weak alteration of the radius and the amplitude values of the field as functions of a parameter, whereas the relative values ζ/r will not depend on z. With regard for the above circumstances the approximate of potentials is [5]

$\phi_e = [e_0(z)\zeta(z)/N](\zeta/r)^N \sin N\alpha$

$\phi_b = [b_0(z)\zeta(z)/N](\zeta/r)^N \sin N\alpha$,

which approximate well the arbitrary boundary conditions. The necessary computations enable us to obtain the formula

$$\mathbf{F} = \mathbf{z}^0 e_0(z) b_0(z)(\zeta/r)^{2(N+1)}(\sigma/\rho)(1 - Ub_0/e_0) \qquad (7)$$

We can see that the boundary values chose by us engender electric and magnetic fields, which are orthogonal to each other and which produce the force oriented along the z axis and this field does not depend on the azimuthal coordinate. The formula last we have that

$$A = -\frac{e_0(z)b_0(z)\sigma(\zeta/r)^2(\zeta/r)^{2N}}{2NU^2\rho}(1 - Ub_0/e_0) \qquad (8)$$

IV. NON-DISTURBANCE MOTION

Let us turn the representation (5) for the stream function Ψ. The first item corresponds to the nondisturbed flow. The second item describes the disturbances caused by the moving body. The third item describes the perturbations from the control force. Let us choose the value of the control force in such a way that its nonzero α component of the vector-potential $\alpha^0 A$ has the following boundary value:

$$A = -\zeta'\zeta \qquad (9)$$

at $r = \zeta(z)$ In this case

$$\Psi = r^2/2 + \int_{-\infty}^{z} A dz$$

. The longitudinal component of velocity for such the function of current will be determined by formula

$$u_z = 1 + (1/r)\int_{-\infty}^{z} (\partial A/\partial r)dz = 1 + \int_{-\infty}^{z} F_z dz.$$

Let us now turn to the Bernoulli equation.

$$u_z^2/2 + u_r^2/2 + p/\rho + \Pi = (p/\rho + \Pi)_\infty + \int_{-\infty}^{z} F_z dz$$

The substitution of expression for the velocity into this equation allows on to get, with the accuracy assumed above, $p = const$ on the equipotentials of the gravitational force. Such the movement called by us non-disturbance near the surface is not accompanied by the formation of gravitational waves, the body does not undergo the wave drag. The parameters of boundary values of the electric and magnetic fields providing non-disturbed movement may be determined by the body geometry. The α component of the vector-potential $\alpha^0 A$ represented by formula (8) will satisfy the boundary condition (9), if the electromagnetic parameters $e_0(z), b_0(z)$ will be chosen from the condition

$$\sigma e_0(z), b_0(z)\zeta^2(z)(1 - Ub_0/e_0) = 2NU^2\rho\zeta'\zeta.$$

Furthermore, the condition for the symmetry of electromagnetic fields and for the axial symmetry of the flow allow the application of the of the obtained results also for the case of a half-submersed body at which the body axis lies in the free surface plane. Not that the control force is present only in those parts of the hull in which $\zeta' \neq 0$, that is in the nose part and in the stern part, and it is absent in the middle cylindrical part. It is easy to understand that it is possible to impose on the control force an additional function of developing the thrust, whereas the existing MHD-propulsion units, which are mounted in the middle part of a ship, cannot realize the control function.

In concluding this section we wish to show that the total work of the control force is equal to zero.

$$N = \int_\tau \mathbf{u}\mathbf{F}d\tau = \int_\tau \mathbf{u}\nabla H d\tau + \int_\tau \mathbf{u}(\omega \times \mathbf{u})d\tau.$$

Here τ is the disturbed volume of the fluid. Since $\mathbf{u}(\omega \times \mathbf{u}) = 0$, we have that

$$N = \int_\tau \mathbf{u}\nabla H d\tau = \oint_{S_1} H u_n dS + \oint_{S_2} H u_n dS = 0.$$

Here $u_n = 0$ on the hull boundary body S_1 and $H = const$ on the control surface S_2 which lies outside the disturbance zone. Thus the electromagnetic system works in the nose part $(\zeta' > 0, Ub_0 < e_0)$ in the regime of pump and requires the power supply, whereas in the stern part $(\zeta' < 0, Ub_0 > e_0)$ the similar system should work in the regime of an MHD-generator. Their powers are equal.

V. PERIODIC FLOW IN UPPER HALF-PLAN

As is known, the equations governing in the viscous flow admit in the upper half-plane only the solution corresponding to the fluid at rest. However, the incorporation of a control force removes this restriction. Let us choose the spatial and temporal change of the control force in accordance with the progressive wave law $\mathbf{F}(x' - Ct, y)$, where C is the phase speed of the progressive wave. In the co-moving coordinate system, which moves at the speed C,the control force takes a stationary for x, which is periodic in $\mathbf{F}(x, y)$. This will enable us to construct an x- periodic flow of a viscous fluid in the upper half-plane. By using the stream function the equations may be written as follows:

$$Re\frac{D(\psi,\omega)}{D(x,y)} = \Delta\omega + \Delta A, \qquad \Delta\psi = -\omega. \qquad (10)$$

Here $\mathbf{z}^0 A$ is vector-potential of the force $\mathbf{F}$, which is defined as follows:$\mathbf{F} = \nabla \times (\mathbf{z}^0 A)/Re$. The system (10) should be solved under the boundary conditions

$$\psi = 0, \quad \partial\psi/\partial y = -C \qquad (11)$$

at $y = 0$,

$$\partial\psi/\partial y = 1 - C \qquad (12)$$

at $y \to \infty$.

Let us represent the solution of the problem (10) in the form

$\psi = \Psi(y) + \psi_1(y), \qquad A = A_1(y) + A_2(y),$,

where $\Psi(y)$ is the stream function of the plane-parallel flow, which may be found by solving the equation

$$\frac{d^4\Psi}{dy^4} = \frac{d^2 A_1}{dy^2}. \qquad (13)$$

under boundary conditions (11),(12). The small function ψ_1 satisfies with the accuracy up to the quantities of the second order of smallness the inhomogeneous equation

$$Re[\frac{d^3\Psi}{dy^3}\frac{\partial\psi_1}{\partial x} - \frac{d\Psi}{dy}\frac{\partial\Delta\psi_1}{\partial x}] = \Delta^2\psi_1 + \Delta A_2, \qquad (14)$$

with the zero boundary conditions

$$\psi_1 = \partial\psi/\partial y = 0$$

at $y = 0$ and $y \to \infty$.

Let us introduce the Orr-Sommerfeld equation of the hydrodynamic stability theory [6]:

$$Re_0[\frac{\partial\Delta\psi_0}{\partial t} + \frac{d^3\Psi}{dy^3}\frac{\partial\psi_0}{\partial x} - \frac{d\Psi}{dy}\frac{\partial\Delta\psi_0}{\partial x} = \Delta^2\psi_0], \qquad (15)$$

Denote by ψ_0 the eigenfunction at the critical point. The eigenvales of the same problem will be denoted by $\alpha_0, Re_0, C_r, C_i = 0$. We will search for the stationary solution of the inhomogeneous problem in the form $\psi_1 = q\psi_0$, where q is a constant

to be determined. Let us substitute this representation into equation (14) and take into account (15). As a result we obtain the relationship

$q(Re/Re_0 - 1)\Delta^2\psi_0 = \Delta A_2$.

Since $Re < Re_0$ and the solution ψ_0 is stable for all disturbances, it proves to be possible to satisfy the relationship last in the energy measure.

$$q(1 - Re/Re_0)\int_\sigma (\Delta\psi_0)^2 d\sigma = \int_\sigma \nabla\psi_0 \nabla A_2 d\sigma$$

This equation relates the amplitude value of the control function to the amplitude of the eigenform.

Further computations require the specification of the control function form. The physical realization of the control function may ensure the following laws:

$A_1 = A_1(0)\exp(-\beta y)$.

$A_2 = A_2(0)\exp(-\beta y)\cos\alpha x$

An order to obtain these dependences on may pay attention to chapter (4). The limit transition $r \to \infty, \quad N \to \infty$ allows one to consider axis-symmetrical flow instead of the plane one.

Let us turn equation (13) , which determines the main flow:

$$U = d\Psi/dy = [A_1(0)/\beta]\exp(-\beta y) + C_1.$$

By virtue of the condition at the infinity. $C_1 = 1 - C$, where C is the phase speed at which the coordinate system chosen by us moves. Consequently

$U = 1 - C - \exp(-\beta y.)$

The coefficient β is related to the displacement width δ via an obvious relationship. If the displacement width is chosen as a reference length, then $\beta = 1$ and $Re = U\delta/\nu$. The exponential profile arising in the process of the suction of the boundary layer studied in detail by Schlichting [6]. It is, in particular, known that the critical Reynolds number for the stationary flow equals to 710^4.

Thus if the control force along the total length of the body sustains the Reynolds number at the level being less than 710^4 , then the boundary layer will preserve the laminar regime as in the case of the suction. As is known, the section through big orifices only destabilized the boundary layer, and the small orifices rapidly become dirty. The control with the aid of a force does not have such a shortcoming. For the periodic flows the drag coefficient is equaled to zero. It is achieved by the work of control force F which has the order $O(1/Re)$. The work of this force has the same order. The addition of a periodic component to the control force appears to ensure a stable periodic flow for larger Reynolds numbers than 710^4.

Let us now turn to the neutral curve for the exponential profile [6].The disturbances with the wave numbers $\alpha > 0.1$ decay at any Reynolds numbers. The subharmonic wave number, for which the periodic flow in the consideration without viscosity is unstable, equals to $\alpha/2 = 0.05$ [7]. However, the viscous force ensure the stability of this disturbance for the Reynolds numbers $< 710^5$.

Note that for the periodic flows the Reynolds number characterizes the local properties of the flow. The number of the periods along the body length may be arbitrary.

VI. NON-SEPARATED FLOW

One can formulate for the control forces an objective of ensuring a non-separation flow around a body of small elongation. It is easy to see that for the prevention of a separation of the dynamic boundary layer it will be required from the control force to have a large energy density sufficient for the compensation of the momentum loss in the dynamic boundary layer. A small electric conductivity of the sea water and the limitations for the magnetic field induction do not enable one to reach such energy densities. Therefore, it is reasonable to aim at the restoration of the pressure in the stern at the expense of forming an external flow by withholding the separated boundary layer near the body and the flow axis. In this case the electromagnetic forces can comprise a large volume as in the previous problems, and no big density will be required from them, and the flow itself will be weakly vortical and be described by the inviscid fluid model. It is known that the flow equations admit both separated and attached solutions. The stability condition performs a physical choice. Since the question of the global stability defies all attempts of the theoretical investigation, we have carried out the physical experiment aimed at answering the above question [2]. A self-motion of a sphere in the fluid was investigated, which was ensured by the supply of the axial momentum in a narrow ring in the middle section by the mechanical means. An almost complete restoration of the pressure was registered in the stern half-sphere, so that the pressure on the wind-side half-sphere exceeded the pressure on the lee side by the amount of the order $O(1/\sqrt{Re})$. Since the fluid dynamics does not depend on the origin of the forces, it is to be expected that the realization of the bulk control forces by electromagnetic means might also ensure a non-separated flow regime and maintain the body motion. The scale for the control force is determined from the condition that its work compensates for all the losses related to the motion, including the viscous losses.

Denote by $\mathbf{P}$ the hydrodynamic drag force. Then the work of this force will be equal to $\mathbf{PU}$. The condition for the body self-motion requires the satisfaction of the equation

$$\mathbf{PU} = \int_\tau \mathbf{F}\mathbf{u_0} d\tau,$$

where τ is the volume occupied by the fluid, $\mathbf{u}^0$ is the fluid velocity in a fixed coordinate system. Since we consider the regimes with a small control effect, then we can assume with an accuracy up to second order of smallness that the flow is potential outside the boundary layer and consequently the velocity is representable in the form $\mathbf{u}^0 = \nabla\phi^0$.

The bulk force $\mathbf{F}$ may be presented by the expression

$$\mathbf{F} = \sigma[\nabla\phi_e + \nabla\phi \times \nabla\phi_b].$$

Here ϕ is the velocity potential of the fluid flow in a moving coordinate system related to the body. The potentials which appear in this formula may be written down for different body shapes coinciding with the coordinate surface of the curvilinear coordinate system [5]. Let us consider, for example, the case of a flow around the sphere of a radius a. In the spherical coordinate system ρ, θ, α we have that

$$\begin{aligned} \phi_0 &= U\rho\cos\theta[1 - (a^3/2\rho^3)], \\ \phi_e &= [-ea/(N+1)]\Phi(\rho\theta)\sin(N\alpha), \\ \phi_b &= [-ba/(N+1)]\Phi(\rho\theta)\cos(N\alpha). \end{aligned} \tag{16}$$

Here $\Phi(\rho\theta) = (a/\rho)^{N+1}\sin(N\theta)$. This representation corresponds to a special choice of the boundary conditions

$\partial\phi_e/\partial n = e\sin^N\theta\sin(N\alpha)$,

$\partial\phi_b/\partial n = b\sin^N\theta\cos(N\alpha) \quad at \quad \rho = a.$

Here, as above, N is the number of the pairs of the poles located along the azimuthal coordinate α. The superposition this function enables us to approximate the boundary conditions of a more general form, however, the biggest energetic contribution is provided by the first item written down by us above.

Using this representations we obtain after some calculations the mechanical work performed by the Lorentz forces:

$$W_m = \int_\tau \mathbf{F}\nabla\phi_0 d\tau = \frac{\sigma\pi a^3 N 2N!!}{(N+1)^2(2N+1)} \times \tag{17}$$

$$Me^2[1 - 3M\frac{4N^3 + 15N^2 + 8N + 3}{2N(2N+3)(2N+7)}].$$

Here $M = Ub/e$ is the loading coefficient. In the particular cases $N = 1, M < 1$

$$W_m = 0.167e^2\sigma\pi a^3 M(1 - M).$$

For $N >> 1, M < 2/3$

$$W_m = \frac{2N!!}{N(2N+1)!!} e^2 \sigma \pi a^3 M(1 - 3M/2).$$

To choose an optimal value of the loading coefficient it is required to determine the electric capacity at the expense of which the needed mechanical work is performed.

$$W_e = \sigma \int_\tau (\mathbf{E} + \mathbf{U} \times \mathbf{B})\mathbf{j} d\tau = \tag{18}$$

$$\sigma \int_\tau [\nabla \phi_e - \nabla(U\rho \cos\theta) \times \nabla \phi_b](\nabla \phi_e + \nabla \phi \times \nabla \phi_b) d\tau.$$

Carrying out the necessary calculations similar to those which have been required for the determination of the electric capacity we find that

$$W_e = \sigma \pi a^3 e^2 \frac{2N!!}{(N+1)^2(2N+3)!!} \times \tag{19}$$

$$[2(2N^2 + 5N + 3) - 5N(2N+3)M + (6N^2 + 6N + 4.5)M^2].$$

The efficiency is determined by the relationship $\eta = W_m / W_e$. In the particular cas $N = 1, M < 1$we have that

$$\eta = \frac{M(1-M)}{4(1 - 5M/4 + 33M^2/40)}. \tag{20}$$

The maximal value of the efficiency is equal to $\eta = 0.11$ and is achieved at $M = 0.55$. For $N >> 1, M < 2/3$ $\eta = M/2(1-M)$.

The maximal value $\eta \to 1$ is achieved at $M \to 2/3$.

VII.SUMMARY

The perspectives of using the electromagnetic forces in ship building are determined by the degree of energetic efficiency. The problems of control for a flow require less density of energy and, hence, they are performed for higher electric efficiency. Arising with this possibility of increasing the velocity of movement decreases to a larger degree the part of Ohms' losses.

VIII. REFERENCES

1. A. Jwata, E. Tada and Y. Saji, "Experimental and theoretical study of superconducting electromagnetic ship propulsion". In Proc. 5th Lips Propeller Symposium Drunen, The Netherlands, p.2,3,1983.

2. V.I. Merkulov, *Fluid Flow Control* Novosibirsk: Nauka 1981 p.180.

3. G.K. Batchelor, *An Introduction to Fluid Dynamics.* Cambridge at the University Press,1970.

4. W. F. Hughes and F. J. Young, *Electromagnetodynamics of Fluids,* New York:J. Wiley,1966.

5. G. A. Korn and T. M. Korn, *Mathematical Handbook for Scientists and Engineers,*New York: McGrow-Hill Book Company, 1968.

6. H. Schlichting, *Grecuzschicht-Teorie* Karlsruhe: Verlag G. Braun, 1950, p. 500.

7. R. T. Pierrehumbert and S. E. Widnall "The two- and three-dimensional instabilities of a spatially periodic shear layer," JFM, v.29, part 3,1967, pp.417-440.

ELECTROMAGNETIC EFFECTS ON LOW SPEED COHERENT STRUCTURES EMBEDDED IN A WALL LAYER

Jean-Paul Thibault, Valéry Botton & Lionel Rossi
PAMIR Team, LEGI,
BP 53 X, 38041 GRENOBLE Cedex, France
Jean-Paul.Thibault@hmg.inpg.fr
Valery.Botton@hmg.inpg.fr

Abstract - This work deals with ElectroMagnetic Flow Control (EMFC) and the basic mechanisms involved in turbulence intensity or skin friction reduction by the use of EMFC. Due to the strong complexity of the problem, our analysis is based on an idealised and simplified approach of the wall normal configuration. The first part of our work is an analytical study of the EM forces and EM vorticity imposed to the boundary layer. Due to the 3D configuration, the analytical computation is very interesting but limited to some specific regions of the EM actuator. Consequently we also present a numerical approach to the electromagnetic problem. Our results clearly demonstrate that the EM vorticity field presents a maximum spanwise vorticity above the magnet poles at a fixed distance from the wall, a maximum streamwise vorticity above the electrodes and a null vorticity at the centre of the EM tile. The comparison of our results with the scales (in wall units) of a canonical boundary layer demonstrates that the imposed EM vorticity is capable of completely redistributing the vorticity in the boundary layer. The second part of our work deals with an experimental approach of the concept using our seawater tunnel. Our contribution is based on an idealised situation : "a synthetic turbulent boundary layer". In fact we use a laminar boundary layer in which coherent structures are produced by a wall hemisphere protuberance and maintained within the boundary layer. Presently we demonstrate that we are able to produce and visualise the coherent structures. An EM actuator is constructed and inserted in the tunnel. We plan to visualise soon the behaviour of the structures when submitted to the EM action.

1 INTRODUCTION

MagnetoHydroDynamics (MHD) makes it possible to apply Laplace-Lorentz forces directly in selected domains of a seawater flow. In particular, one can act directly within a boundary layer by the use of well designed permanent magnets and wall electrodes [1]. Recent experiments ([2], [3], [4]) demonstrate significant drag reduction, turbulence intensity reduction and boundary layer separation prevention. Basically two configurations (resp. wall normal and axial) can be identified whether the direction of the mean Lorentz force is orthogonal or parallel to the wall.

The main feature of the axial configuration, as it seems to us, is the local creation of a favourable pressure gradient likely to prevent separation. Though it can also lower skin friction by the mean of turbulence intensity reduction (see Henoch & Stace [4]), this configuration doesn't seem very promising as far as energetic efficiency is concerned. Significant drag reduction has however been obtained using the wall normal configuration (see [2], [3]) in which the Lorentz force field can be highly rotational and may be seen as an artificial injection of vorticity within the boundary layer.

The mechanism which effectively allows a local (in space and time) EM (electromagnetic) force and EM vorticity to strongly change the behaviour of a turbulent boundary layer is not clearly understood. Our theoretical contribution is devoted to the analysis of idealised and/or asymptotic situations, which intends to select scales and non dimensional parameters in order to pertinently describe the EM flow control. Our experimental contribution is devoted to produce well known coherent structures and to make them interact with EM forces and EM vorticity, which intends to identify the dominant mechanisms implied in turbulence modification. The present paper is restricted to uniform conductivity flows.

In the wall normal configuration, Electromagnetic flow control (EMFC) makes use of wall-flush actuators which can be organised in arrays [5]. Our approach is first to get a better understanding of the action of a single so called "tile" on the flow and then to study the interactions between several tiles within an array.

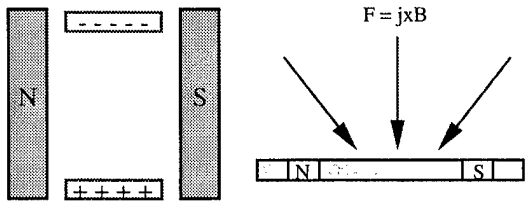

Figure 1: wall normal EM actuator

2 SHAPE OF THE IMPOSED VORTICITY ABOVE AN EMFC ACTUATOR

Let us focus on the wall normal control in a steady state case. Figure 1 shows a typical basic element of EMFC array. It is comprised of a pair of sub-surface magnet poles and of a pair of wall-flush electrodes. The electric currents density, **j** (A/m^2), and the magnetic field, **B** (T), thus created in the flow result in an EM volumic force field (Laplace-Lorentz force).

2.1 GOVERNING EQUATIONS

Regarding hydrodynamics equations, the Navier-Stokes equation includes a (**jxB**) term and the vorticity (**w**=curl **u**) equation includes a (curl (**jxB**)) term:

$$\rho\frac{d\mathbf{u}}{dt}+\nabla P+\rho\,\mathbf{g}=\mu\,\nabla^2\mathbf{u}+\underbrace{\mathbf{j}\mathrm{x}\mathbf{B}}_{\substack{MHD\\Forces}}$$

$$\rho\frac{d\mathbf{w}}{dt}=\rho\,\mathbf{w}\cdot\nabla\mathbf{u}+\mu\,\nabla^2\mathbf{w}+\underbrace{\nabla\mathrm{x}(\mathbf{j}\mathrm{x}\mathbf{B})}_{\substack{MHD\ vorticity\\Source}}$$

When dealing with permanent magnets and low conductivity electrolytes (like sea-water), the (**jxB**) term in the momentum equation is weak compared to the others. However, the EM force field can be highly rotational and can't be neglected when calculating the curl of this equation to derive the vorticity equation. This EM vorticity field appears to be of particular interest in the wall-normal configuration.

Regarding Electromagnetics equations, we are in the case of a weak MHD coupling (Rm<<1) and negligible induced currents (**E**/(**uxB**) >> 1). Consequently the EM unknowns (magnetic induction, electric field, electric potential, etc.) are obviously independent of the flow. The induction equation and the Ohm's law reduces then to:

$$\nabla^2\mathbf{B}=0 \quad \text{and} \quad \mathbf{j}=\sigma\,\mathbf{E}$$

with σ (S/m) the apparent electrical conductivity of the fluid and **E** the imposed electric field (V/m).

In addition, conservation equations of mass, induction and current are also involved in the following development. Notice that, as σ is considered uniform, one has (div **j** = 0) $\Rightarrow$ (div **E** = 0).

The characteristic scales of each EM unknown, and thus of the Lorentz force distribution, are closely linked with the tile's dimensions. Moreover these are the scales to be compared to that of the flow (location of the action) together with that of turbulence (phenomenological point of view). A simple analytical approach together with 3D numerical simulation of the fields are able to provide such information.

2.2 ANALYTICAL APPRAOCH OF THE EM VORTICITY FIELD

As the electric and magnetic fields are independent of the flow, the MHD terms of the hydrodynamics equations can be assess after some simplification. Let us consider a 2D distribution for the magnetic induction **B**, which is fully justified in the case of very long magnets, as in the Nosenchuck experiment's array [5]. Due to the necessarily finite extension of the electrodes, the electric currents field is 3D. Notice that the mean flow can have some direction or an other.

One can then express the EM force and vorticity fields as functions of the electric and magnetic fields:

$$\mathbf{B}\begin{vmatrix} B_x(x,y) \\ B_y(x,y) \\ 0 \end{vmatrix} \qquad \mathbf{E}\begin{vmatrix} E_x(x,y,z) \\ E_y(x,y,z) \\ E_z(x,y,z) \end{vmatrix}$$

$$\mathbf{JxB} = \sigma \begin{vmatrix} -B_y E_z \\ B_x E_z \\ B_y E_x - B_x E_y \end{vmatrix}$$

$$\nabla x(\mathbf{jxB}) = \sigma \begin{vmatrix} \frac{\partial}{\partial y}\left(B_y E_x - B_x E_y\right) - B_x \frac{\partial E_z}{\partial z} \\ -\frac{\partial}{\partial x}\left(B_y E_x - B_x E_y\right) - B_y \frac{\partial E_z}{\partial z} \\ B_x \frac{\partial E_z}{\partial x} + B_y \frac{\partial E_z}{\partial y} \end{vmatrix}$$

in which the electric field conservativity, div**E**=0, allowed some simplifications.

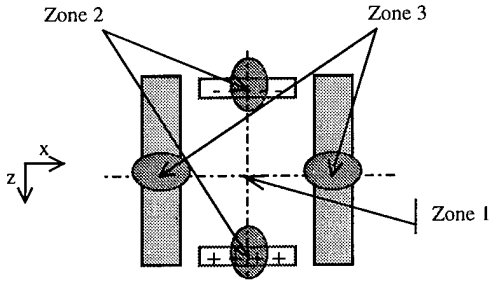

Figure 2: Schematics of the simplification domains

Obviously, the EM force field is dominantly directed towards the wall (rather than wall normal). Moreover, it is interesting to analyse the imposed vorticity distribution in some specific regions above the EM actuator. Using simplifications based on the conservation equations in a uniformly conducting medium, Thibault & Rossi [6] obtained the following expressions of the imposed vorticity. The results are expressed in three particular zones, as shown in figure 2.

zone 1 is the central region of the tile (intersection of the 2 median plans); the curl of the EM force is negligible in this zone :

$$\nabla x(\mathbf{jxB}) = \sigma \begin{vmatrix} 0 \\ 0 \\ B_x \frac{\partial E_z}{\partial x} = 0 \end{vmatrix}$$

zone 2 is the region near by the magnet poles median plan, above the electrodes:

$$\nabla x(\mathbf{jxB}) = \sigma \begin{vmatrix} -E_y \frac{\partial B_x}{\partial y} \\ 0 \\ 0 \end{vmatrix}$$

only the x-component of the EM vorticity is non-zero, and it exhibits a maximum at the wall, since both E_y and $\partial B_x/\partial y$ are maxi at the wall and decrease with y, to zero at infinity.

zone 3 is the region near by the electrodes median plan, above the magnets;

$$\nabla x(\mathbf{jxB}) = \sigma \begin{vmatrix} 0 \\ 0 \\ B_y \frac{\partial E_z}{\partial y} \end{vmatrix}$$

only the z-component is non-zero and exhibits a maximum at a distance δ_a from the wall. Indeed, as the electric field derives from a potential, it is curl-free, thus $\partial E_z/\partial y = \partial E_y/\partial z$. Moreover, as no electrical current can, of course, be provided by the magnets, one has, at their surface, $E_y=0$ and $\partial E_y/\partial z=0$. Now, as this quantity, $\partial E_z/\partial y$, is continuous, null both at the wall and at infinity and obviously not zero everywhere, it reaches a maximum at some distance from the wall. On the other hand B_y is maximum at the magnet surface and decreases with y. Subsequently, the EM vorticity is maximum at some distance δ_a from the wall. This distance entirely depends on the distribution of **E** and **B**, which corroborates the impact of the tile's geometry on the EM action: fringe effects on the electric field thus monitor the 3D EM vorticity distribution.

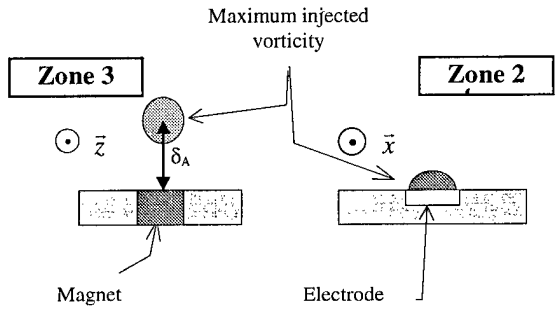

Figure 3: Local spanwise (left) and streamwise (right) EM vorticity maxima

Finally, the topological support of the imposed vorticity can be visualised as a ring standing above the actuator. As the flow can be aligned optionally with the x or the z direction, let's illustrate these expressions in the case of a streamwise direction along the x-axis. The vorticity imposed to the flow is then streamwise in the neighbouring of the electrodes and spanwise above the magnet poles, at a distance δ_a depending on the tile's geometry (see fig. 3). An evaluation of the EM vorticity in terms of wall units (see §3.2), concerning the Nosenchuck experiment, lead Thibault and Rossi [6] to the conclusion that the imposed vorticity is likely to dominate the dynamic of the buffer layer. The vorticity injected into this region of the flow is indeed much stronger than that of a canonical wall layer, and the excitation streamwise wavelength can be adjusted to the typical ejection frequency.

2.3 NUMERICAL APPROACH OF THE EM VORTICITY FIELD

The analytical approach presented above is strictly limited to the two median plans of the EM tile. Anywhere else analytical computation is no more possible and numerical modelling is needed. Let us first of all describe the problem and its governing equations. Both electric and magnetic unknowns are independent of the flow, moreover the magnetic field is produced by permanent magnets and magnetic permeability as well as electrical conductivity of the flow are uniform. Consequently both fields are irrotational and conservative which means they can be formulated as deriving of potentials : ϕ the electric potential and φ the magnetic potential, which both obey a Laplace equation :

$$\Delta\phi = 0 \text{ and } \Delta\varphi = 0$$

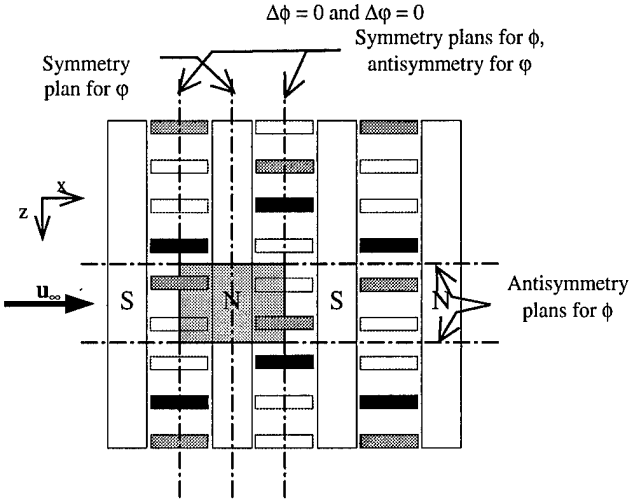

Figure 4: EM array seen from above, symmetries and computational domain

The problem settled in the present paper is focused on the wall normal configuration described by D. Nosenchuck. Figure 4, drawn in the (x,z) plan, gives a top view of the array of electromagnetic tiles which is almost of infinite extend. Our computation is based on a steady state excitation condition which is not strictly proper to a pulsed current excitation mode. From the previous analysis it is clear that the imposed vorticity is strongly non uniform which mainly depends on the geometrical dimensions of EM tiles. An energetic and dynamic optimisation of the concept requires the knowledge of forces and vorticity distributions in a domain of very large extend. The full computation would have a huge size or would have to be based on a very broad meshing of the domain which would not describe properly the imposed vorticity structures. But one can point out that an EM tiles array presents some periodical arrangement regarding magnetic field and currents distribution. The following analysis of the problem aims at identifying the smallest sub-domain on which detailed computation can be done and then extrapolated to the entire array using observed symmetries and anti-symmetries. Finally this method allows in the same time a detailed computation and a very large simulated domain.

On figure 4, the electrodes which are powered at the time considered are coloured in black and dark grey (i.e. + & -) and magnetic poles (i.e. N & S) are permanently active. The electric problem is essentially 3D but one can identify (x,y) plans parting in the middle each pair of active electrodes (see figure 4) which are anti-symmetry plans for the electric potential in the mean time (y,z) plans parting in the middle electrodes (see figure 4) are symmetry plans. The magnetic problem is almost 2D (i.e. independent on z) one can identify (y,z) plans parting in the middle each magnetic pole (see figure 4), as symmetry plans regarding the magnetic potential. The plans (y,z) parting in the middle each electrode are anti-symmetry plans for magnetic potential. Consequently the smallest computational domain identified corresponds to the grey coloured zone (see figure 4), the rest of the array can be extrapolated using the symmetries and anti-symmetries.

Formulation of the boundary conditions on the electric potential is shown on figure 5. The 3D computational domain comprises a bottom plan corresponding to the wall (y = 0) where the potential is fixed on the electrode surface (ϕ = cste), the rest of this plan as well as the two vertical (y,z) plans are of Neumann type ($\partial\phi/\partial n = 0$). The topping plan as well as the two vertical (x,y) plans have a null electric potential ($\phi = 0$).

Formulation of the boundary conditions for the magnetic

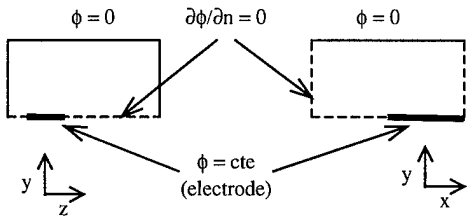

Figure 5: Boundary conditions on the electric potential

potential which is almost a 2D problem (i.e. any (x,y) plan in Neumann type) are shown on figure 6. The bottoming plan corresponds to the upper surface of the iron plate, placed here to drive the magnetic flux directly from a magnet to the next one. Both this plan and lateral faces of the magnets are of Neumann type ($\partial\varphi/\partial n = 0$). The magnetic pole is at constant magnetic potential (φ = cste) and the rest of the boundary have a null magnetic potential ($\varphi = 0$).

The solver used is a standard 3D finite elements using an hexaedric meshing . At present the computation are on progress and are going to be completed soon. After computation of both potential in the 3D domain described previously, we have to calculate the forces and imposed vorticity distributions. And finally to extend the solution to an entire array of EM tiles.

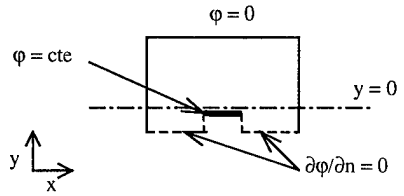

Figure 6: Boundary conditions on the magnetic potential

The perspective of our computation is more interesting because it concerns flow simulation. The problem posed is the behaviour of a turbulent boundary layer submitted to the EM forces distribution computed with the EM model previously described. Hopefully this distribution is independent of the flow itself but on the contrary the proper description of the flow seems more ambitious in the sense that the forces are strongly non uniform and acting very close to the wall. At present we are not completely fixed on the model adapted but it seems that a DNS simulation has to be envisaged seriously. We want to emphasise the fact that this simulation has no physical sense if the first step electromagnetic computation is not properly done.

3 PRELIMINARY EXPERIMENTAL INVESTIGATION OF ELECTROMAGNETIC FLOW CONTROL (EMFC)

The great complexity of a fully turbulent Boundary Layer makes proper experimental investigation of local phenomenon somewhat tricky. In the case of interest here, a deep analysis would be all the more difficult as a complex 3D EM vorticity field should be superimposed to the already very complex structure of the boundary layer. The idea is then to focus on the simpler case of artificial coherent vortical structures conveyed by a laminar boundary layer: this case allows easier (statistical) quantification through the reproductibility of periodic events.

So the first stage is to produce well known discrete coherent structures – hairpin vortices – in a laminar boundary layer in order to create a well organised "synthetic turbulent boundary layer". An extensive description of this type of flow has been found in Acalar & Smith [7]: the process involves a hemispheric protuberance (half-sphere flush-mounted to the wall) entirely contained in an initially

laminar boundary layer (see fig. 7). The standing vortex forms a stationary horseshoe-shaped structure near the leading edge of the hemisphere, which finally develops hairpin vortices created by the separation of the flow over the hemisphere.

The present experiment is carried out in the PAMIR team sea-water tunnel [8], shown in fig. 8. The test section (4 cm x 4 cm x 1 m) is made with Perspex, thus allowing Laser Anemometry and flow visualisation. The flow velocity is adjustable from 0 up to 10 m/s. A tranquillisation chamber, placed upflow the channel, renders the flow laminar and uniform. The electrolyte usually in use is a Sodium-chloride solution of apparent electrical conductivity about 4 S/m. Several sizes of protuberance are also available: till now, 3 radius of hemi-sphere have been tested at the same location in the duct. A compromise has to be found between a fair visualisation (big R) and the range of velocities allowing the sphere to be totally sunk within the boundary layer.

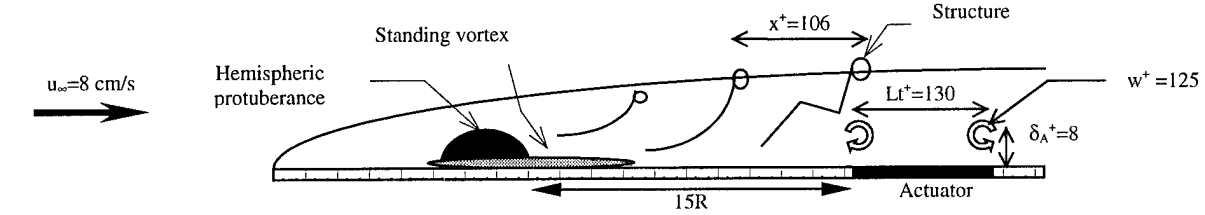

Figure 7: Hairpin vortices production, typical values of the experiment

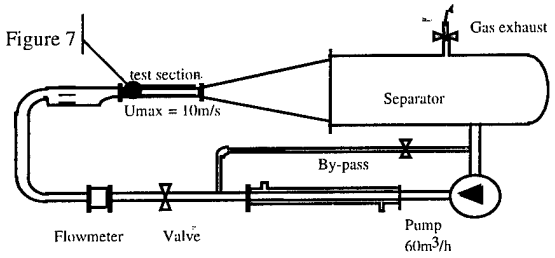

Figure 8: PAMIR-Team Sea-Water tunnel

3.1 PRODUCTION AND VISUALISATION OF HAIRPIN VORTICIES

Thibault & Rossi [6] performed a preliminary experiment with the aim of validating the possible production and visualisation of Hairpin vortices in that facility. Hydrogen-bubbles visualisation gave them access to the structure emission frequency and velocity. Results in good agreement with that of Acalar & Smith [7] have been obtained: figure 9 gives the evolution of the structure emission reduced frequency, $f^+ = f.\nu/u^{*2}$, versus the Reynolds number, Rer, based on the hemisphere radius, R. The first plateau (Rer<700) corresponds to a frequency that linearly increases with the flow velocity. The right hand part of the curve (Rer>700) corresponds to a constant frequency, which is probably due to a transition to turbulence in the vicinity of the protuberance.

Adding, as in the present investigation, an EM actuator forbids hydrogen-bubbles visualisation techniques, for it involves electrolysis of the flowing fluid. Thus the electrodes meant for producing visualisation bubbles may interact with that designed to act on the flow. However, "classical" flow visualisation techniques permit a qualitative approach of the structures feedback to the action of a flush-mounted EM tile.

3.2 PRESENT ELECTROMAGNETIC ACTUATOR

A single EM actuator has been designed and dwelled about 15R downflow the hemisphere. This experiment being preliminary, the tile width (see fig. 10) has been fitted to that of the test duct. Moreover a square shape has been chosen for reasons of simplicity and for purpose of comparison with former experiments. The streamwise electrodes are made with Titanium and their upper side is Platinum-coated. The spanwise permanent rare-earth magnet is equipped with a steel magnetic flux backing plate in order to concentrate the magnetic flux lines. The whole magnet is embedded into the Perspex body, 2 mm deep under the surface of the plate. The induction at the wall is about 0.3 T above the magnet poles.

As proposed by S. Tardu [10], though the magnetic and electric fields are independent of the flow, it is certainly meaningful to evaluate dimensions, and other quantities in relation to the EM tile, in terms of wall units. The late are indeed representative of the typical length scale of interest from an hydrodynamics point of view. The tile can be seen as a square of side $Lt=32.10^{-3}$ m, thus, assuming from a numerical simulation presented by Nosenchuck [5] that $\delta_a \approx 0.06$ Lt, the height of action is $\delta_a \approx 2.10^{-3}$ m. The friction velocity at the location of the tile is, say, 4.10^{-3} m/s (equals $u_\infty/20$ with u_∞=8 cm/s, typical velocity of our experiment). Consequently the undimensionnal scales of the tile are:

- a distance, Lt^+, of 128 wall units between the two vorticity maxima, above the magnet poles,
- the eight of these maxima: δ_a^+=8 wall units, which corresponds to the lower part of the buffer layer.

Notice that the length $Lt^+ \approx 130$ is comparable with the size of the streaky patterns of wall layer turbulence. In the hypothesis of section 2.2, the spanwise EM vorticity intensity can be assess by $w_z \approx \sigma.B_y.\partial E_z/\partial y$. Assuming an electric field gradient of 1000 V/m^2 (i.e. 25 V/m, which corresponds to 100A/m^2 currents, over 15 mm), the undimensionnal vorticity strength $w^+ = w.\nu/u^{*2}$ is about 125, which is much stronger than the natural vorticity generated by shear stress within the wall layer (of the order of 1 wall unit [1]).

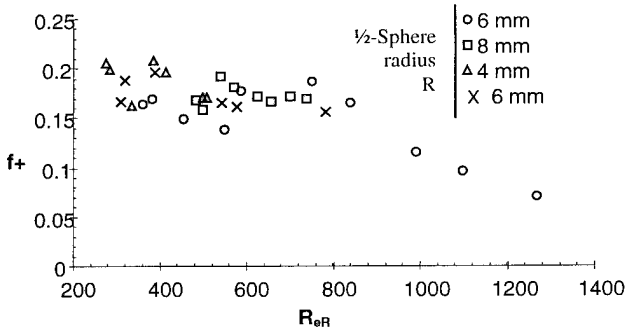

Figure 9: Structure emission reduced frequency versus hemisphere Reynolds number

Furthermore, the convective speed at the location of the maximal injected vorticity ($u^+=y^+=8$) is about 3.2 cm/s, namely 40% of the outer velocity. Consequently, the transit time of a fluid particle over the tile is 1 second at that height, whereas it is 0.4 seconds in the outer flow. This can be compared to the structure emission frequency, 3Hz at 8 cm/s from [6], which corresponds to a 2.7 cm long gap between two successive hairpin vortices, i.e. 106 wall units, see fig. 7.

Every result above is expressed in the case u_∞=8 cm/s; to get the tendencies as functions of the outer velocity, one can assume the Blasius profile: the friction velocity is then given by $(u^*/u_\infty)^2 = 0.332.Re_x^{-1/2}$. Thus, for a given location, one gets:

- $u^* \propto u_\infty^{3/4}$
- δ_a^+ (resp. L_t^+) $= \delta_a.u^*/\nu \propto u_\infty^{3/4}$

- $w^+ = w.\nu/u^{*2} \propto u_\infty^{-3/2}$, since the (dimensionnal) EM vorticity, w, is independent from the outer velocity, u_∞ ,(weak coupling).
- $f^+ = f.\nu/u^{*2} \sim u_\infty^{-1/2}$, assuming for f, emission frequency, a linear dependence to the outer velocity, u_∞, (from [7] and as long as $Re_\tau \leq 700$).

A better quantification of the mechanism is to be provided by a current finite elements simulation of the EM force field. This intends not only to provide such quantitative information in the single tile case, but also to study the electrical coupling between several active tiles of the same array.

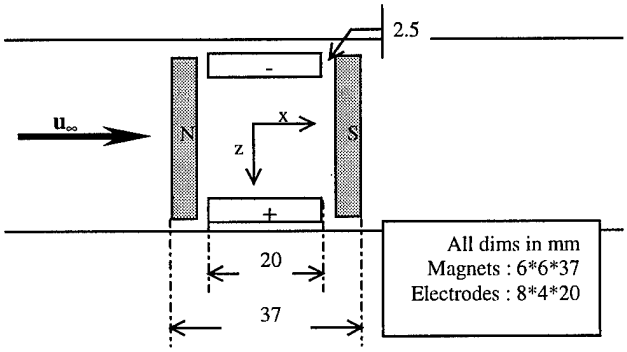

Figure 10: Dimensions of the EM actuator

4 CONCLUSION

Attention is driven on wall normal EM seawater flow control. A simplified analytical approach gives access to the shape of the 3D vorticity ring imposed by an EM actuator within the boundary layer. This analysis, based on a 2D magnetic induction and 3D electric field model, corroborates the description previously provided by Nosenchuck [9]: the imposed vorticity tends to zero in the central region of the tile, is spanwise above the spanwise magnet poles and streamwise above the streamwise electrodes. The maximum spanwise vorticity is at a distance from the wall which is fixed by the geometry, partly through end-effects of the electric field.

Comparison between the scales of this EM "vorticity ring", expressed in wall units, and that of a turbulent flow leads to the conclusion that it strongly acts on the buffer layer. This electromagnetically imposed vorticity is obviously able to reorganise the flow inner structure, since it is much stronger than the natural vorticity of the wall boundary layer.

In order to validate this conceptual basic understanding, both experimental investigation and numerical force-field simulation are currently carried out. Their issue is the understanding of the action of a single tile together with that of interactions between several active tiles of a staggered array.

The experimental approach implies the visualisation of discrete coherent hairpin vortices embedded in a laminar wall layer and locally submitted to the action of an EM actuator. The idea is to accede to the mechanism of action of an EM actuator on single vortical structures. These are indeed, in this case, well-known, isolated and reproductible which allows proper investigation whereas the complexity of a real turbulent flow would forbid it.

The 3D numerical approach is devoted to investigating the EM vorticity field imposed by a staggered array of EM actuators. The model uses symmetries and anti-symmetries of the fields to restrict the computational domain to the smallest: a "cheap" potential-type formulation is derived, which allows detailed simulation of the EM vorticity field by the use of a standard finite elements code. Still on progress, this calculation is presented as the compulsory first step of (further) proper flow calculation.

Further work may be devoted to the choice of pertinent scales and parameters likely to describe the mechanisms implied in drag reduction by electromagnetic means: both deeper experimental study and proper flow simulation are foreseen. Axial EM control is also to be investigated, as devoted to the prevention of boundary layer separation and turbulence intensity reduction.

References

1. J.C.S. Meng, "Wall Layer Microturbulence Phenomenology and a Markov Probability Model for Active Electromagnetic Control of Turbulent Boundary Layers in an Electrically Conducting Medium", *NUWC Division- Newport Technical Digest*, June 1995
2. D.M. Nosenchuck and G.L. Brown, "The Direct Control of Wall Shear-Stress in a Turbulent Boundary Layer", *Proceedings of the International Conference on Near-Wall Turbulent Flows*, Elsevier, pp. 689-698, 1993
3. James C. S. Meng et al., "Experimental Study of the Spanwise Vortex Resonance Hypothesis for Turbulent Drag Reduction over a Flat Plate in Salt Water", *NUWC Division- Newport Technical Digest*, March 1997
4. C. Henoch and J. Stace, "Experimental Investigation of a Salt Water Turbulent Boundary Layer Modified by an Applied Streamwise Magnetohydrodynamic Body Force", *Phys. Fluids 7*,(6) , pp. 1371-1383, June 1995
5. Daniel,M. Nosenchuck, "Boundary Layer Control Using the Lorentz Force", *ASME Fluids Engineering Meeting*, San Diego, July 1996
6. J.-P. Thibault and L. Rossi, "Seawater MHD: Electromagnetic Flow Control", *Third International Conference on Transfer Phenomena in Magneto Hydro Dynamic and Electroconducting Flows*, vol. 1, pp. 243-248, Aussois, France, 1997
7. M.S. Acalar and C.R. Smith, "A Study of Hairpin Vortices in a Laminar Boundary Layer. Part 1. Hairpin Vortices Generated by a Hemisphere Protuberance", *J. Fluid Mech.* Vol. 175, pp.1-41, 1987
8. P. Boissonneau, "Propulsion MHD en Eau de Mer: Etude des Couplages Hydrodynamique-Electrochimie-Electromagnétisme", *Thèse de Doctorat*, UJF Grenoble, May 1997
9. Daniel M. Nosenchuck, "Electromagnetic Turbulence Control", *EBLC Workshop, Dresden, Germany*, July 1997
10. S. Tardu, *Personal communication, 1997*

SOME RESULTS ON ELECTROMAGNETIC CONTROL OF FLOW AROUND BODIES

Tom Weier, Gunter Gerbeth,
Gerd Mutschke, Uwe Fey
MHD Dept., Forschungszentrum
Rossendorf
P.O.Box 510119, D-01314
Dresden
T.Weier@fz-rossendorf.de

Oliver Posdziech
Inst. Aerospace Eng.,
TU Dresden
D-01062 Dresden
posdzie@tfd.mw.tu-dresden.de

Olgerts Lielausis, Ernest Platacis
Institute of Physics Riga
Salaspils-1, LV-2169, Latvia
mbroka@tesla.sal.lv

Abstract - The flow around bodies (cylinder, plate) can be controlled by applying electromagnetic forces originating from electrodes and permanent magnets suitably placed on the surface of the body. There is a large variety for applying those forces with respect to the geometrical arrangement and the electrical current feeding the electrodes. The goals of this approach are flow stabilization, drag reduction or manoeuvrability of the body in an electrically low-conducting fluid like seawater. We present experimental and numerical results for a low Reynolds-number range of $200 < Re < 4000$. Experiments were performed using a copper sulphate electrolytic solution and a sodium hydroxide loop. Flows are considered around a cylinder and over a plate, with Lorentz forces being parallel to the body surface. Experimental results will be presented for the body drag and the wake flow structures depending on different regimes of electromagnetic forcing. In particular, we distinguish between the regimes of direct, frequency-variable sinusoidal or pulsed electric currents. Numerical results confirm the physical tendencies at least for lower Reynolds numbers. Parameter ranges will be given for an optimal electromagnetic flow control in terms of drag reduction and flow laminarization. The energetic balance will be discussed.

I. INTRODUCTION

Drag reduction is a main design issue in engineering because drag estimates to a large amount the running costs of transport of or in fluids. If the fluid is electrically conducting, like seawater, apart from conventional methods there is an additional possibility of control by electromagnetic body forces, i.e. Lorentz forces. In low-conducting liquids, these forces may be generated by the application of suitably chosen magnetic and electric fields. This idea was first published by Gailitis and Lielausis in 1961 [1]. The main advantage of the Lorentz force is that it acts on a volume of the flow and is not confined to the edges of the fluid stream. Therefore, electromagnetic flow control has recently attracted the attention of several research groups [2,3]. Main issues are control of turbulent boundary layers by different strategies, transition delay as proposed in [1], separation control and manoeuvrability.

1.1 Turbulent Boundary Layer Control

Most flows relevant for practical applications are turbulent, simply due to the large length-scales involved. Turbulent skin friction is one of the main sources for drag on airplanes and ships. However, the mechanism leading to the orders of magnitude higher skin friction of turbulent compared to laminar boundary layers, is still largely unrevealed. The kinematics of turbulent boundary layers has been intensively studied in the past (e.g. Klebanoff [4]). The region of highest turbulence production is the buffer layer near the wall. This region controls the magnitude of the wall shear stress τ. Typical flow structures of the buffer layer are low- and high-speed streaks, i.e. spanwise modulations of the streamwise velocity, and streamwise vortices. There is general belief that controlling these structures would lead to considerable reduction of skin friction.

Wall-normal Lorentz forces were applied by Nosenchuck and co-workers [5] in two different configurations. First, a gradient of the conductivity σ produced by injecting an extra electrolyte together with uniform current density and magnetic field was used to suppress lift-off of near wall vortices and therefore Reynolds-stresses. The near-wall fluid has a higher conductivity then the outer flow, between both is a sharp interface with respect to σ. If a flow structure deforms this interface, a Lorentz force counteracting this deformation is generated. Experiments in a turbulent boundary layer with $1100<Re_\theta<1700$ showed a reduction of the friction drag of about 90%. A drawback of this method is, the need to inject additional electrolyte into the boundary layer in order to achieve the desired Lorentz force. This implies additional manufacturing and running costs and makes the design more complicated.

In a second series of experiments, Nosenchuck and co-workers designed special arrangements of single actuators ("Tiles") to checkerboard patterns [6]. These tiles where driven in a certain way to obtain a global modification of the near wall flow characteristics, i.e. a travelling wave structure was generated in the boundary layer, hereby completely replacing the natural flow.

Experiments in a laminar boundary layer with resonant operating tiles, i.e. downstream tiles are amplifying the structures created by upstream tiles, showed peak reductions of the friction drag up to 90% and 50% in the average. It should be noted, that the actuator introduces locally spanwise and streamwise vorticity, but the total amount of these components integrated over the wall is zero. The modified laminar boundary layer is thicker than the Blasius boundary layer, the vorticity distribution is changed, and the average skin friction is finally smaller.

In a turbulent boundary layer with $0.5\cdot10^5 < Re_x < 3.6\cdot10^5$, a reduction of the skin friction by 55% was measured. The reason is argued to be the same as in the laminar case, i.e. a restructuring of the near wall flow with a changed vorticity distribution. In another paper [7], Nosenchuck gave a coefficient of performance $c_\eta=0.71$ which is defined as the fraction of work saved due to a lower drag and the total input energy. Experiments performed at other groups to confirm these results quantitatively were not yet successful.

A first experiment to control a turbulent boundary layer by **streamwise forcing** was performed by Henoch and Stace [8]. The Lorentz force is generated by the simple strip-like geometry (SSG, see Fig. 1) of alternating electric and magnetic poles [1]. The Reynolds numbers in their experiments were in the range of $5\cdot10^5 < Re < 3\cdot10^6$. At very high (7) interaction parameters, an increase in wall-shear and in turbulence due to the Lorentz force was observed. However, the increase in friction drag is compensated by the thrust due to the force. At moderate interaction parameters, the fluctuating shear stress and streamwise velocity components where reduced by approximately 30%, while the mean quantities left unchanged. Henoch and Stace explain this effect by the pumping action of the Lorentz force. By the acceleration of the near-wall fluid, the lift-up of shear-generated wall vortices is disrupted. If this is the case, the force would act similar to the re-laminarizing effect of a favorable pressure gradient [9]. The inner layer is stabilized by the addition of high momentum fluid, thereby the process of turbulence production and dissipation is disrupted. However, in the case of strong interaction parameter, distinct wall jets at the boundaries of electrode and permanent magnet stripes occur due to a spatially inhomogeneous Lorentz force.

The same geometry was numerically studied by Crawford and Karniadakis [10]. By means of a spectral-element method a channel flow was simulated where the Lorentz force was applied at one side. Although details of the force modelling are different from the experiment, major features of the spanwise inhomogeneous distribution are covered. The simulations were done for $Re_{\tau\tau}=200$ and two interaction parameters N=0.1 and N=0.4. The authors report a friction drag increase at the controlled wall for both cases. In detail, while the streamwise intensities decrease, as measured by Henoch and Stace, spanwise and normal fluctuations increase with the interaction parameter. Also, Reynolds stress increases when wall shear stress increases. This is due to the fact, that the Lorentz force distribution acts as a source of spanwise and normal vorticity. So the turbulent motion is influenced, but not necessarily towards lower drag. In the opposite, the streamwise structures in the boundary layer seem to be amplified (see Fig. 33 in [10]).

Widely accepted, streamwise vortices are the main reason for the high turbulent wall drag. A weakening of these vortices should therefore

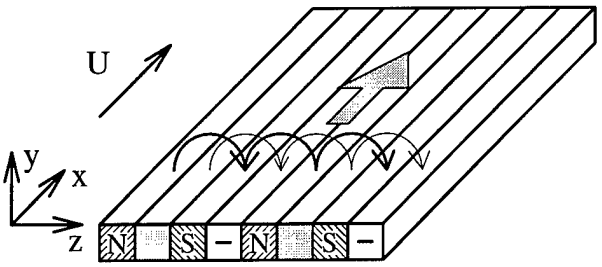

Figure 1: Simple Strip-Like Geometry (SSG)

also reduce turbulent skin friction. Several successful attempts have been done to shear the streamwise vortices with oscillating walls. Choi found a maximum reduction of skin friction by 50% [11]. It should be noted that the reduction takes place at that point, where the shear due to oscillation is acting. Jimenez, while discussing the physical effect of spanwise wall oscillations in comparison with his numerical simulations, pointed out that "...an obvious improvement should be observed by using, e.g. electromagnetic oscillating forces, to induce the same effect over volumes of the order of the wall distance given above (y^+=30)" [12]. Kim undertook a DNS of a channel flow and found by imposing oscillating Lorentz forces in spanwise direction a skin friction drag reduction of 30%. These calculations were done for a Reynolds number corresponding to a boundary layer $Re_x=10^5$. At this Reynolds number, the efficiency is far below 100%, but the energy which has to be spent for the Lorentz force should decrease proportional to Re^2 [13], therefore an efficient operation of this control could be possible for higher Reynolds numbers. An experimental verification of these findings is not yet known to the authors, but appears to be very attractive.

1.2. Transition Delay

The optimum way of controlling turbulence is to prevent its arising because laminar skin friction is orders of magnitude smaller than turbulent one. Therefore, the idea is to achieve transition delay which might be of practical importance at least for flows around smaller objects (e.g. hydrofoils).

The beginning of electromagnetic boundary layer control (EBLC) dates back to the sixties when in Riga it was firstly formulated the idea of achieving transition delay by introducing an appropriate electromagnetic force to the boundary layer [1]. The motivation was to create a spanwise-homogeneous and in wall-normal direction exponentially-decreasing Lorentz force [14] which, under certain conditions, asymptotically leads to an exponential velocity distribution in the boundary layer. The key point is that such exponential velocity profiles are proven to have much better stability properties than ordinary Blasius profiles as it was intensively investigated in suction experiments in the past [15].

To benefit from the better stability properties of an exponential velocity profile, one has to find an appropriate setup of electrodes and magnets in order to create that body force. A first proposal was made in the sixties in Riga, hereafter referred to as simple strip-like geometry (SSG) and shown in Fig. 1. However, already at that time Grinberg [16] showed by an analytical modelling of the field distribution that the resulting force is strongly inhomogeneous in spanwise direction, especially in regions close to the surface. The mathematical reasons behind are simply singularities of the electric and magnetic field at the corners of the electrode planes and the rectangular magnets, respectively. This leads to periodic maxima of the Lorentz force at those places.

Any variation of the Lorentz force in spanwise direction is likely to cause 3-D instabilites in the boundary layer which certainly will diminish or might even completely destroy the desired stabilizing influence of the streamwise forcing. Although this has not yet been checked quantitatively, one goal is certainly to design a geometry of electrodes and magnets which creates a perfectly homogeneous force. This is subject of current work.

1.3. Separation Prevention and Manoeuvrability

Separation prevention reduces form drag and allows higher lift at larger angles of attack. This might be of importance for flows around hydrofoils and rudders where the energetic balance is not the main goal. First experiments were done by Nosenchuck, directly manoeuvering the Buoyant Test Vehicle by a Lorentz force applied only at one side [7].

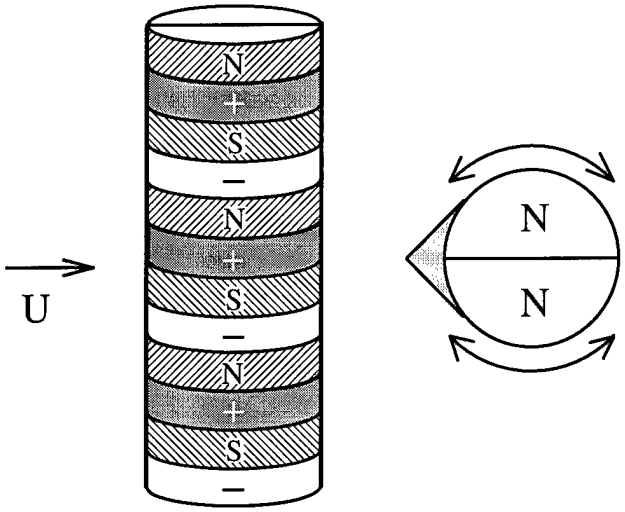

Figure 2: Sketch of the Cylindrical Body

II. MODEL EXPERIMENTS ON BLUFF BODIES AND PLATES

First experiments in a simple **rotating annular tank** (details are described in [17]) were performed to validate the force effects and to visualize flow regimes in order to get qualitative results on the spectrum of possible phenomena. A cylindrical test body covered with electrodes and magnets to create a wall-parallel Lorentz force was assembled. Both half sides of the cylinder might be powered separately (see Fig. 2). The main focus in these experiments was not on turbulent boundary layers, but on separation control, drag reduction and modification of the wake structure. The test fluid was not sea water, but a solution of 10% copper sulphate and 5% sulphuric acid in water. The density is 1120 kg/m^3, the electric conductivity is 16 S/m, and the kinematic viscosity is almost that of water. Compared to sea water, besides it's four times higher conductivity the solution has the advantage that provided a critical current density is not exceeded, no electrolytic bubbles are produced. Instead, anode material is degraded and galvanic copper deposition takes place at the cathode. Growth rates are only in the order of micrometers per hour. The range of Reynolds numbers covered in the experiments is 500<Re<2000. Static forcing as well as sinusoidal time-periodic forcing was investigated in detail. The results were obtained by flow visualization with colour-streaks and particles.

To extend these mainly qualitative results and to investigate certain phenomena in detail, new facilities were built and new measurement technique was installed at Forschungszentrum Rossendorf (FZR). .An **open electrolytic channel** was designed to perform low-speed mid-scale experiments. The covered velocity range is $0.05 < U_0 < 0.22$ m/s in a test section of 0.2 x 0.2 x 1.2 m. The maximum volume flow rate is about 32m^3/h. Honey combs and screens upstream the test section together with a 2-D contraction of 3:1 ensure at 0.22 m/s only 0.5% mean velocity variations and a turbulence level of 1.5%. The device is mainly made of plastics and can be used for seawater as well as for e.g. NaOH or NaCl based electrolytes without corrosion problems. More details will be presented at the workshop.

To cover larger velocities and to allow for "real-size" experiments, a **closed electrolytic tunnel** is currently being assembled at FZR. The velocity range covered is $0.5<U_0<5$ m/s with a contraction ratio of 4:1 ahead a test section of 0.3 x 0.4 x 1.2 m. The pump engine has a power of 15 kW. The material used is mainly stainless steel, as electrolyte NaOH is planned. Furthermore, **joint experiments** at the Hamburg Ship Model Basin HSVA are scheduled to be performed this spring.

In all these facilities experiments are currently underway. **Test bodies** are a cylindrical body on one hand as described above but equipped with stronger magnets (0.28 T) and a SSG plate of 1.5 x 50 x 51 cm size where both sides can be driven separately. Main aims are time-dependent forcing effects for the cylinder wake and manoeuvrability experiments for the plate. First results will be presented in the following. More results of currently ongoing experiments will be included in the oral presentation.

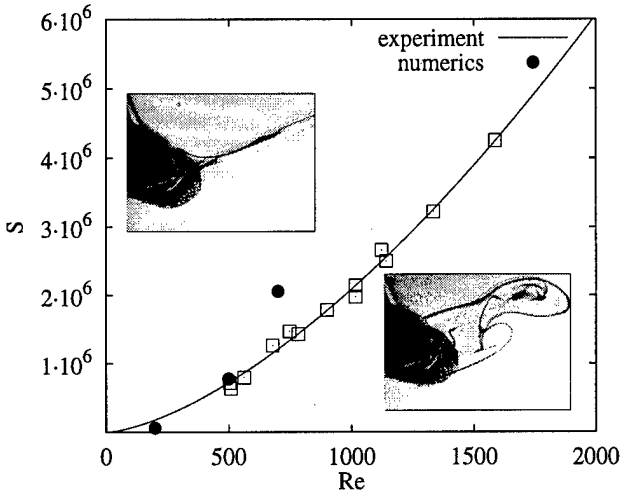

Figure 3: Stability diagram for steady forcing

III. RESULTS

The flow around bluff bodies includes phenomena, which can not be found in the canonical case of flat plate boundary layer under constant pressure. A main feature here is the occurrence of separation, resulting in an complete restructuring of the flow field. Although the boundary layer remains laminar in the cases considered here, the wake of the body is turbulent even for small Reynolds numbers.

With increasing Reynolds number, the flow changes from a creeping flow at Re < 1 to an asymmetric flow for Re < 5, this flow separates for larger Re and the wake becomes unstable at Re≈45. Further increase of the Reynolds number leads to evolving three-dimensional structures at Re≈180 and a transition of the wake flow into turbulence. From Re≈1000 on the separating shear layers are subjected to Kelvin-Helmholtz instabilities, The flow picture doesn't change very much up to $Re\approx 2\cdot 10^5$, where transition of the boundary layer occurs. The now turbulent boundary layer intensifies the momentum transport between boundary layer and the outer flow. Thereby high momentum fluid from the outer flow increases the energy of the boundary layer, and boundary layer separation is shifted towards the rear stagnation point.

Corresponding to these changes in the flow pattern, the total drag c_d on the cylinder changes with the Reynolds number. The friction drag c_f could be obtained from integration of the wall shear stress along the cylinder surface, the pressure drag c_p results from the separated flow at the rear side of the cylinder. Due to this separation, pressure at the rear stagnation point is lower than at the front stagnation point. The friction drag dominates for low Reynolds numbers, while for Re>100 the pressure drag alone determines the total drag.

3.1. Static forcing - Drag reduction

Separation occurs downstream a critical point where the normal derivative of the streamwise velocity vanishes (2-D, steady flow). Applying a streamwise Lorentz force adds momentum to the near-wall flow and therefore leads in general to a delay of separation. Sufficiently strong forces might be able to suppress it completely in certain flow configurations.

The straightforward application of the SSG (Fig. 1) to the circular cylinder is sketched in Fig. 2. The Lorentz force is directed parallel to the cylinder surface. (One could imagine two plates as shown in Fig. 1 each wrapped around a half cylinder, so that the Lorentz forces on both sides of the cylinder have the same direction. For separation suppression they should of cause point downstream.) The stability diagram of the flow, obtained from flow visualization, is shown in Fig. 3. The Reynolds number Re is defined with the cylinder diameter D as the characteristic length. As the interaction parameter $N=(j_0B_0D)/(\rho U_0^2)$ is defined with the imposed magnetic field B_0 and the current density j_0, beside the fluid density ρ the square of the freestream velocity U_0 appears in the denominator. Therefore, an parameter $S=N\cdot Re^2$ is introduced as a nondimensional measure of the applied force which is independent of the flow velocity. Above the drawn critical curve in fig. 3, vortex-shedding is suppressed. The two inserts show flow snapshots at Re=760.

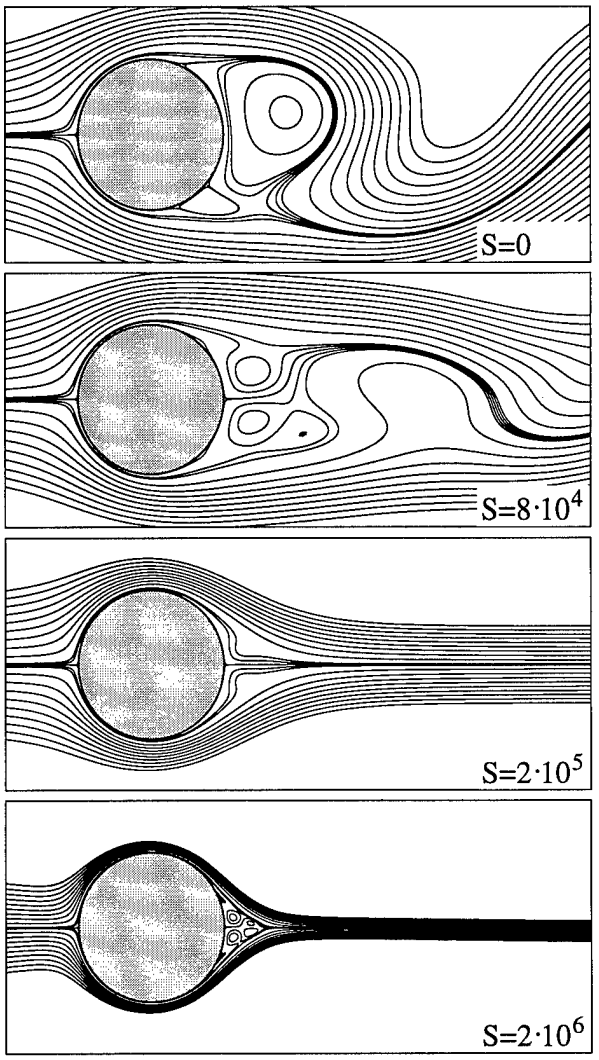

Figure 4: Streamlines for steady forcing at Re=200

No Lorentz force is acting in the right insert, whereas on the left side the flow was stabilized due to a Lorentz force of $S = 1.47\cdot 10^6$.

A strong enough downstream forcing results in a jet originating at the rear stagnation point. This jet exerts a net force on the cylinder in upstream direction, and obviously, the total drag becomes negative. On the other hand, a force directed upstream shifts the separation towards the front stagnation point, and a vortex street with larger vortices than in the unforced case forms. In this situation, an increased drag has to be expected.

These experimental observations are in line with numerical simulations of the flow. They were done using a finite difference algorithm in a vorticity streamfunction formulation, for details of the numerics see [18]. The code solves the two-dimensional Navier-Stokes equation of an incompressible flow

$$\frac{\partial \mathbf{v}}{\partial t} + (\mathbf{v}\cdot\nabla)\mathbf{v} = -\nabla p + \frac{1}{\mathrm{Re}}\Delta\mathbf{v} + N\mathbf{f}, \qquad (1)$$

$$\nabla\cdot\mathbf{v} = 0. \qquad (2)$$

The problem is formulated in cylindrical coordinates, the mesh extends over 121 points in radial and 121 points in azimuthal direction. The grid is equidistant in azimuthal direction and exponentially spaced ($r_i \sim e^{i\gamma}$) in radial direction, where i is the index and γ denotes a scaling factor. The grid is extended to 50 cylinder radii. Due to the exponential spacing in radial direction a sufficient resolution of the boundary layer for the chosen Reynolds number of 200 is obtained. The Lorentz force in Eq. (1) is modeled by the simple relation

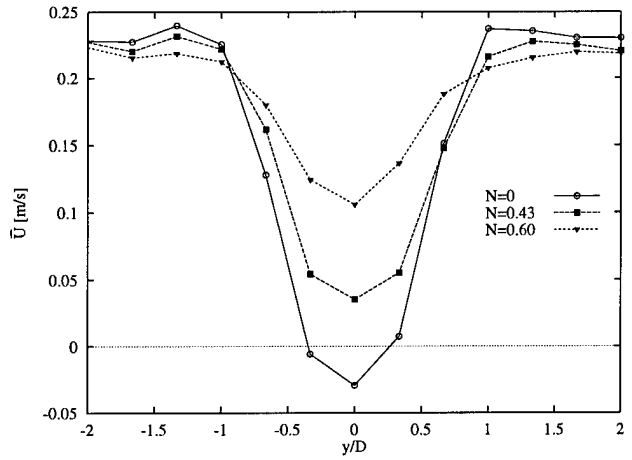

Figure 5: LDA measurements of the streamwise velocity at Re=4400 and x/d=3

$$\mathbf{f} = e^{-\alpha(r-1)} g(\theta) \mathbf{e}_\theta \text{ with } g = \begin{cases} 1 & 5° \le \theta \le 175° \\ -1 & 185° \le \theta \le 355° \\ 0 & \text{elsewhere,} \end{cases} \quad (3)$$

accounting for regions at the front and rear stagnation point where no electrodes are present. The neglect of any radial force component and the constant radial dependence for each angle θ represents, obviously, a simplification of the real experimental situation. The parameter α describes the electromagnetic penetration into the liquid which is mainly defined by the electrode spacing, modeled in correspondence to the experimental situation by $\alpha=5\pi/4$.

Figs. 4 shows calculations of the flow field for different values of the force amplitude S. The isolines of the streamfunction have equal levels in all subfigures. Only a small part of the region covered by the mesh is shown, the flow is from left to right. In the top part of Fig 4 the Kármán vortex street at Re=200 without the action of the Lorentz force is shown. For a force of $S = 8 \cdot 10^4$, corresponding to an interaction parameter of N=2, one can observe that although the wake is still unsteady, separation directly at the wall vanishes. This can be confirmed by looking at the vorticity distribution at the cylinder surface. Flow separation is instead shifted into the near-wall region, like in the case of a moving wall. Behind the cylinder a region with two relatively stable recirculation bubbles forms, wherein the fluid motion is rather slow. From this region vortices are shed with approximately the Strouhal frequency but considerably smaller extension compared to the unforced case. Further increase of S leads to complete stabilization of the flow. For $S= 2 \cdot 10^5$, i.e. N=5, the fluid is already accelerated by the force as can be seen by the narrowing of the streamlines even upstream of the cylinder. At a very high force of $S= 2 \cdot 10^6$ (N=50) a strong jet is produced. Already at the front side of the cylinder, an immense acceleration of the fluid takes place. The fluid leaves the cylinder surface at an angle of approximately 135° measured from the front stagnation point. The two jets merge at 0.5 cylinder diameter downstream the rear stagnation point, enclosing a recirculation region with several small vortices.

LDA measurements of the mean streamwise velocity in the near wake at Re=4400 and small values of the interaction parameter are shown in Fig 5. With increasing interaction parameter, the backflow vanishes and the wake depth decreases. These measurements were done in the open channel with a mild NaOH solution with a conductivity of 4 S/m, e.g. nearly that of typical sea water.

Fig. 6 shows the behavior of the sum of both friction and pressure drag versus the interaction parameter at two different values of the Reynolds number. Both curves have a minimum at an interaction parameter of around 10 (Re=200) respectively 5 (Re=500). As can be seen from Fig 7, pressure drag decreases with increasing interaction parameter because of separation suppression. For sufficiently strong forcing, the pressure drag reaches even negative values. On the other hand, friction drag increases with stronger forcing. Since the boundary layer is laminar and the force accelerates the near-wall fluid, the velocity gradient at the wall and so wall shear stress is increased with growing interaction parameter. This effect dominates the gain in pressure drag at large values of the interaction parameter. However, one has to take into account the momentum added to the flow by means of the Lorentz force. So even at low interaction parameter, the cylinder experiences a net thrust.

3.2. Time periodic forcing

Due to the instantaneous action of the electromagnetic field, a time dependent Lorentz force can be easily implemented by feeding the electrodes in an appropriate manner.

Using time dependent currents offers the possibility to avoid the production of electrolytic bubbles. If the frequency of the applied electric field is high enough, a specific current density could be established by charging and de-charging the electrolytic double layer around the electrodes. This would inhibit electrode reactions and thus chlorine production in sea water environments. Above all, corrosion at the anodes should be reduced dramatically, thereby considerably simplifying the selection of electrode materials. Besides, no over-voltage of the electrode reactions has to be overcome.

From fluid-dynamics point of view, usage of time periodic forces allows to interact with the wake structure in order to establish flow regimes with desired properties as, e.g., low drag. Examples for the control of flows around circular cylinders have been given by Taneda [19] who established a flow regime without a vortex street at Re=300 by oscillatory rotating the cylinder. The same technique was used by Tokumaru and Dimotakis [20] to reduce the drag of a cylinder up to 80% at $Re=1.5 \cdot 10^4$. The reason of the dramatic drag reduction is the reorganization of the vortex street which becomes narrow under the applied control. The momentum defect in the wake is therefore smaller

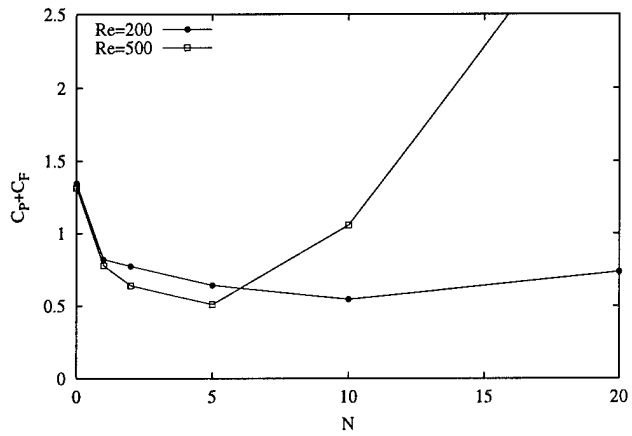

Figure 6: Numerical results for the sum of c_f and c_p versus N for different Re

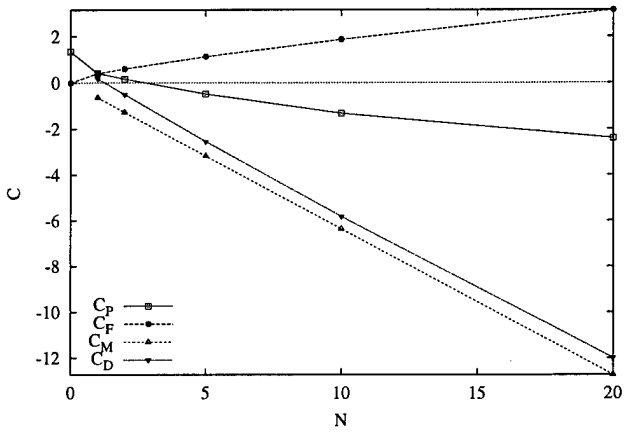

Figure 7: Numerical results for c_p, c_f, c_M and c_d versus N at Re=200

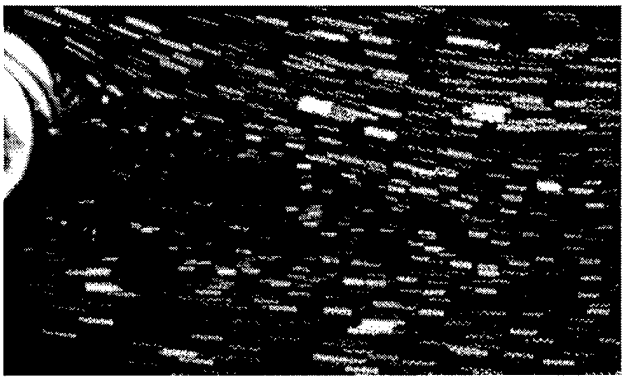

Figure 8: Suppression of the vortex street by antisymmetric forcing, Re=540, Se=1.5, N=27

and so the drag. These result were recently confirmed by Shiels, Leonard and Stagg [21] who applied a vortex method to investigate numerically the flow at Re=300 and Re=$1.5 \cdot 10^4$. An efficiency of the control was computed defined as fraction of the power saved by drag reduction and the power spent on rotating the cylinder. Although the method was found to be not efficient at low Reynolds numbers, it was argued to reach break even at higher Reynolds numbers.

Pack and Joslin [22] reported, that for high Reynolds number flow around an airfoil with a flap, oscillatory blowing is two orders of magnitude more efficient than steady blowing. The effect used here is to enhance mixing of the lower momentum fluid at the wall with higher momentum fluid from the outer flow, thereby increasing the near wall fluids momentum and making the boundary layer more resistant to separation.

Up to now, in our experiments two different types of forcing have been investigated: (i) antisymmetric forcing, where at every instant the force at both sides of the cylinder has the same angular direction, and (ii) symmetric forcing, where the force direction is the same at both sides, i.e. upstream or downstream depending on time.

For sinusoidal forcing with an excitation frequency f_e a dimensionless control parameter Se = $D f_e / U_0$ can be introduced, in the following referred to as excitation Strouhal number. The time-periodic force in (1) is then given as

$$\mathbf{f} = \cos(\omega_e t) e^{-\alpha(r-1)} g(\theta) \mathbf{e}_\theta \qquad (4)$$

with $\omega_e = 2\pi f_e$ and t denoting time. Interaction parameter N and force amplitude S are computed with the effective current density.

For **anti-symmetric** forcing, depending on forcing frequency and interaction parameter, flow regimes can be observed which are similar to the ones of a flow around an oscillatory-rotating cylinder [20]. For forcing frequencies near the Strouhal frequency a lock-in of the flow occurs even for small interaction parameters, i.e. the frequency of the

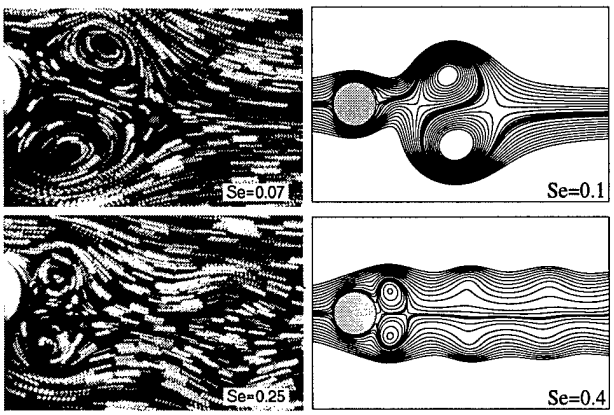

Figure 10: Experimental (left, Re=1100, N=3.3) and numerical (right, Re=200, N=5) results for symmetric forcing at different excitation frequencies

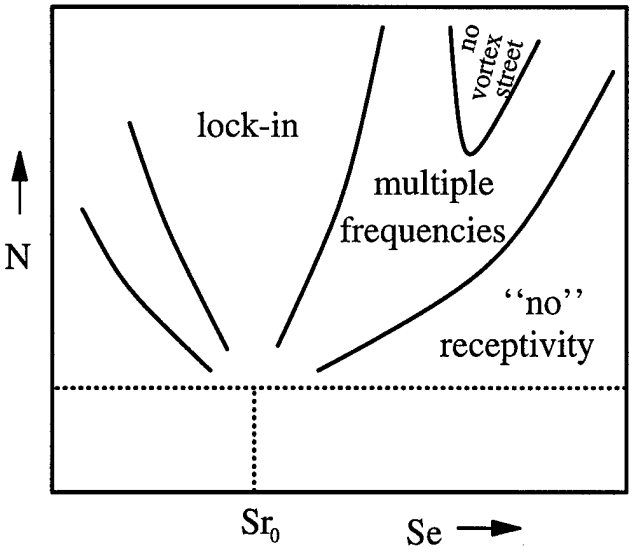

Figure 9: Schematic mode selection diagram for antisymmetric forcing

flow is determined by the Lorentz force frequency. If the forcing frequency is higher than the Strouhal frequency and the interaction parameter is properly chosen, a vortex street with smaller width than in the unforced case forms. Consequently, a smaller drag than in the unforced case is expected. Excitation frequencies smaller than the Strouhal frequency at strong interaction parameter lead to vortex streets with larger vortices and broader wakes than for the natural flow, here drag should be increased. At large values of the interaction parameter and relatively large values of Se, the wake can even be stabilized by the unsteady force (similar effects were observed by Taneda for an rotating cylinder [19].). A corresponding flow visualization is shown in Fig. 8. However, the interaction parameter necessary to reach this flow regime, is approximately ten times larger than the interaction parameter necessary to stabilize the flow by steady forcing.

The flow visualizations can be summarized in a mode selection diagram shown in Fig. 9. This diagram is consistent with the results of Karniadakis and Triantafyllou [23] who investigated the globally-forced flow around a circular cylinder numerically. In both cases, the flow is most sensitive to forcing at frequencies close to the Strouhal frequency.

For the limiting case of Se→0 flow structures similar to the ones of a flow around a stationary-rotating cylinder are expected, i.e. there should also exist flow regimes without vortex shedding but non-vanishing lift due to the Magnus effect.

The flow around a **symmetrically** forced cylinder is somewhat comparable to the flow around a cylinder vibrating in line with the oncoming flow, a case studied e.g. by Ongoren and Rockwell [24].

Due to the combination of symmetric forcing and the antisymmetric structure of the natural wake, the frequency range where lock-in occurs is different from the antisymmetric case. For antisymmetric forcing, lock-in with minimum interaction parameter occurs when the flow is excited with the Strouhal frequency. In contrast, lock-in at symmetric excitation takes place first for frequencies slightly larger or smaller than the Strouhal frequency.

Symmetric forcing can establish symmetric vortex streets of different size depending on interaction parameter and forcing frequency. Examples of flow visualizations and numerical calculations are given in Fig. 10.

IV. OUTLOOK

We report about the present status of our EBLC programme. This programme is aimed to take benefit of the main property of electromagnetic boundary layer control: its flexibility with respect to the geometrical arrangement of magnets/electrodes and the electrical feeding system. For the future we see the following most interesting scientific questions and applications of EBLC:

- Up to which Re a flow stabilization can be reached with DC-currents by an optimized magnet/electrode configuration?

- Will the use of suitable AC currents really lead to an energetic break-even in the turbulent region at higher Re, as the studies on oscillating cylinders imply?
- Which energetic optimization is possible by means of some reactive concept based on some feedback control strategy?
- What is the practical interest in terms of simple and cost-effective realizations of EBLC-actions for flow manoevrability or lift production?

Our investigations are aimed to give answers to these questions.

V. ACKNOWLEDGEMENT

Financial support from "Deutsche Forschungsgemeinschaft" under Grant INK 18/A1-1 is gratefully acknowledged.

VI. REFERENCES

1. A. Gailitis and O. Lielausis, "On a possibility to reduce the hydrodynamical resistance of a plate in an electrolyte", *Applied Magnetohydrodynamics. Reports of the Physics Institute* **12**, (Prikladnaya Magnitogidrodinamika. Trudy Instituta Fiziki, 12), Riga, pp. 143-146 (in Russian), 1961.

2. Proc. "International Workshop on Electromagnetic Boundary Layer Control (EBLC) for Saltwater Flows", Dresden, July 7-8, 1997

3. J.C.S. Meng "Seawater Electromagnetics: A new Frontier", *Magnetohydrodynamics* **30** no. 4, 1994, pp. 401-418.

4. P.S. Klebanoff "Characteristics of turbulence in a boundary layer with zero pressure gradient", NACA-Report 1247, 1954.

5. D.M. Nosenchuck and G.L. Brown "Discrete Spatial Control of Wall Shear Stress in a Turbulent Boundary Layer", in: Near-Wall Turbulent Flows, R.M.C. So, C.G. Speziale and B.E. Launder (Eds.), Elsevier, 1993, p. 689-698.

6. D.M. Nosenchuck, G.L. Brown, H.C. Culver, T.I. Eng and I.S: Huang "Spatial and Temporal Characteristics of Boundary Layers Controlled with the Lorentz Force", 12th Australian Fluid Mechanics Conference, Sydney, 1995.

7. D.M. Nosenchuk "Direct Turbulent Boundary Layer Control on an Axisymmetric Body using the Lorentz force", 4th AIAA Shear-Flow Control Conference, 1996.

8. C. Henoch and J. Stace, "Experimental investigation of a salt water turbulent boundary layer modified by an applied streamwise magnetohydrodynamic body force", *Phys. Fluids*, Vol. **7**, No. 6, pp.1371-1383, 1995.

9. M.V. Morkovin "Panoramic View of Changes in Vorticity Distribution in Transition Instabilities and Turbulence" *1st ASME and JSME Joint Fluids Eng. Conf.* Portland , OR, June 23-27, 1991

10. C. Crawford and G.E. Karniadakis "Reynolds stress analysis of EMHD-controlled wall turbulence. Part I Streamwise Forcing", Phys. Fluids 9 no. 3 pp.788-806, 1997.

11. K.S. Choi, P.E. Roach, J.R. De Bisschop and B.R. Clayton "Active Control of Turbulent Boundary Layer by Spanwise Wall Oscillations", EUROMECH Colloquium 261, Berlin, March 1997.

12. J. Jimenez, A. Pinelli "Wall Turbulence: How it works and how to damp it", AIAA 97-2112, 1997.

13. J. Kim, "Boundary Layer Control for Drag Reduction: Taming Turbulence", Proc. "International Workshop on Electromagnetic Boundary Layer Control (EBLC) for Saltwater Flows", Dresden, July 7-8, 1997;

14. A.. Tsinober and A.G. Shtern, "On the possibility to increase the stability of the flow in the boundary layer by means of crossed electric and magnetic fields", *Magnitnaya Gidrodinamica*, No.2, pp.152-154 (in Russian) 1967.
Nerets, Y. and Shtern, A., Experimental investigation of a possibility to increase the stability of flow in the boundary layer, 6-th Riga MHD Conf. Riga, pp.85--87 (in Russian), 1968.

15. H. Schlichting and K. Gersten, "Grenzschicht-Theorie", Springer, 9th edition, Berlin 1997.

16. E. Grinberg, "On determination of properties of some potential fields",*Applied Magnetohydrodynamics. Reports of the Physics Institute* vol. 12, (Prikladnaya Magnitogidrodinamika. Trudy Instituta Fiziki, 12), Riga, pp.147--154 (in Russian), 1961.

17. T. Weier, G. Gerbeth, G. Mutschke, O. Lielausis, E. Platacis, "Experiments on cylinder wake stabilization in an electrolyte solution by means of electromagnetic forces localized on the cylinder surface", ", to appear in *Experimental Thermal and Fluid Science*, 1998.

18. G. Mutschke, G. Gerbeth, V. Shatrov and A. Tomboulides, "Two- and three-dimensional instabilities of the cylinder wake in an aligned magnetic field", Phys. Fluids **9** (1997) p.3114-3116.

19. S. Taneda "Visual Observations of the Flow past a Circular Cylinder Performing a Rotatory Oscillation" *Journal of the Physical Society of Japan* vol.45, no. 3, pp.1038-1043, 1978.

20. P.T. Tokumaru and P.E. Dimotakis "Rotary oscillation control of a cylinder wake" *J. Fluid Mech.*, vol. 224, pp.77-90, 1991.

21. D. Shiels, A. Leonard and A. Stagg "Computational Investigation of drag reduction on an rotationally oscillating cylinder" *2nd Int. Workshop on Vortex Flows and related numerical Methods*, Montreal, Canada, August 20-24, 1995.

22. L.G. Pack and R.D. Joslin "Overview of Active Flow Control at NASA Langley Research Center" *SPIE's 5th Int. Symp. On Smart Structures and Materials*, San Diego, California, March 1-5, 1998

23. G.Em. Karniadakis and G.S. Triantafyllou "Frequency Selection and asymptotic states in laminar wakes" *J. Fluid Mech.*, vol. 199, pp. 441-469, 1989

24. A. Ongoren and D. Rockwell "Flow structure from an oscillating cylinder. Part 2 Mode competition in the near wake" *J. Fluid Mech.*, vol 191, pp.225-245

ANALYSIS AND FINITE ELEMENT SIMULATION OF MHD FLOWS, WITH AN APPLICATION TO SEAWATER DRAG REDUCTION [1]

A. J. Meir
Department of Mathematics
Auburn University, AL 36849
ajm@math.auburn.edu

P. G. Schmidt
Department of Mathematics
Auburn University, AL 36849
pgs@math.auburn.edu

Abstract. Much research effort has recently been devoted to the electromagnetic control of saltwater flows, exploiting the macroscopic interaction of saltwater with electric currents and magnetic fields. This interaction is governed by the equations of viscous incompressible MHD, essentially, the Navier-Stokes equations coupled to Maxwell's equations. A major problem in the analysis and numerical solution of these equations is the fact that while the Navier-Stokes equations are posed in the fluid domain, Maxwell's equations are generally posed on all of space. Consequently, electric and magnetic fields do not satisfy standard boundary conditions, but jump or continuity relations on the surface of the fluid domain (and other interfaces). Frequently the resulting difficulties are circumvented by prescribing more or less artificial boundary conditions.

In this paper we present a novel formulation of the MHD equations that avoids some inherent difficulties of more traditional approaches by employing the electric current density rather than the magnetic field as the primary electromagnetic variable. This formulation leads to initial-boundary value problems for a system of integro-differential equations in the fluid domain and lends itself naturally to the use of finite-element based discretization techniques. As a first application we describe a mixed finite-element method for the numerical solution of a class of stationary MHD flow problems and report on the computational simulation of a simple drag reduction experiment.

I. INTRODUCTION

It has long been known that the flow of an electrically conducting fluid, such as seawater, is affected by Lorentz forces, induced by the interaction of electric currents and magnetic fields in the fluid. Only recently has it been demonstrated that such Lorentz forces can be used to control the flow and to attain specific engineering design goals such as flow stabilization, suppression or delay of flow separation, reduction of near-wall turbulence and skin friction, drag reduction and thrust generation (see, for example, [4, 9, 10] and the references cited therein).

The theory that describes the macroscopic interaction of an electrically conducting fluid with electric currents and magnetic fields is magnetohydrodynamics (or MHD). Assuming the fluid to be viscous, incompressible, and finitely conducting, the governing equations are the Navier-Stokes and pre-Maxwell equations, coupled via the Lorentz force and Ohm's law. While the Navier-Stokes equations are posed in the fluid domain, Maxwell's equations are generally posed on all of space, and typically both interior and exterior fields must be determined. Only under special circumstances, most notably in the presence of perfectly conducting walls, is it legitimate to confine attention to the body of conducting fluid and to neglect its electromagnetic interaction with the outside world. In general this interaction is of critical importance; in fact, it constitutes what mostly distinguishes MHD from ordinary hydrodynamics and is a source of challenging mathematical and computational problems.

Traditionally, the MHD equations are formulated as a system of evolution equations for the fluid velocity and the magnetic field, along with an auxiliary equation for the electric field outside the fluid region. The fact that the magnetic field extends to all of space and may exhibit jump discontinuities across interfaces separating media with different electromagnetic properties causes analytical as well as computational difficulties, which are frequently circumvented by prescribing more or less artificial boundary conditions. In [5–8] and [12] we developed a novel approach to viscous incompressible MHD that avoids some intrinsic difficulties of the traditional method by employing fluid velocity and electric current density (rather than fluid velocity and magnetic field) as the primary variables. This "velocity-current formulation" exploits the fact that while magnetic fields may extend throughout space, the unknown currents inducing those fields are typically carried by conductors of finite extent. If we consider, for example, a single body of conducting fluid and assume all external field sources to be known, the only unknown current flows in the fluid region itself. In this case, the velocity-current formulation allows us to perform all computations on the fluid domain while still accounting exactly for the effects of the universal electromagnetic field. In general, the velocity-current formulation leads to a system of evolution equations for the fluid velocity and the unknown current density in the fluids and adjacent solid conductors, along with an auxiliary linear div-curl system, which can usually be solved analytically in terms of singular integrals.

The velocity-current formulation lends itself naturally to the use of finite-element based discretization techniques and provides a theoretical framework for the development of efficient computational tools for the simulation of a wide variety of MHD flow problems, including the electromagnetic control of seawater flow. While the method has not yet been applied on an industrial scale, it has been shown to be effective in the analysis and numerical solution of a class of stationary MHD flow problems (see [8]). In the following we describe the general approach (Section II), derive a mixed variational formulation for the stationary case (Section III), discuss a finite-element method based on this formulation (Section IV), and report on the computational simulation of a simple drag reduction experiment (Section V). Despite the academic nature of this simulation, it illustrates the potential usefulness of our approach in solving a variety of MHD flow control and design problems.

II. THE VELOCITY-CURRENT FORMULATION

We are concerned with the flow of a viscous, incompressible, electrically conducting fluid, confined to a bounded region of space and interacting with various body forces, electric currents, and electromagnetic fields. Under the assumptions of the MHD approximation, the flow is governed by the Navier-Stokes equations, posed in the fluid domain, and the pre-Maxwell equations, posed on all of space; both are coupled via the Lorentz force and Ohm's law. As discussed in the introduction, we seek to formulate the problem as a system of evolution equations for the fluid velocity $\mathbf{u}$ and the electric current density $\mathbf{J}$ in the fluid; both are solenoidal vector fields, depending on time t and position x.

The evolution of the velocity field is governed by the Navier-Stokes equations, that is, the momentum balance

$$\rho \mathbf{u}_t - \eta \Delta \mathbf{u} + \rho(\mathbf{u} \cdot \nabla)\mathbf{u} + \nabla p - \mathbf{J} \times \mathbf{B} = \mathbf{F}_{\text{ext}} \tag{1}$$

along with the continuity equation

$$\nabla \cdot \mathbf{u} = 0\,, \tag{2}$$

reflecting the incompressibility of the fluid. Here ρ and η denote the (constant) density and viscosity of the fluid; $\mathbf{F}_{\text{ext}}$ is a given external body force; and p is the scalar pressure, an auxiliary unknown that plays the role of a Lagrange multiplier associated with the divergence constraint (2). Equations (1) and (2) are coupled to Maxwell's equations through the Lorentz force, $\mathbf{J} \times \mathbf{B}$, and Ohm's law,

$$\mathbf{J} = \sigma(\mathbf{E} + \mathbf{u} \times \mathbf{B})\,, \tag{3}$$

where $\mathbf{E}$ and $\mathbf{B}$ denote the (unknown) electric and magnetic fields; σ is the (constant) electric conductivity of the fluid. Additional currents $\mathbf{J}_{\text{ext}}$ may

[1] This material is based upon work supported by the National Science Foundation under Grants DMS-9404440 and DMS-9625096.

be flowing in external conductors, possibly connected to the fluid domain via electrodes on the surface. The total current distribution,

$$\tilde{\mathbf{J}} = \mathbf{J} + \mathbf{J}_{\text{ext}} = \begin{cases} \sigma(\mathbf{E} + \mathbf{u} \times \mathbf{B}) & \text{in the fluid,} \\ \mathbf{J}_{\text{ext}} & \text{in the exterior,} \end{cases}$$

must satisfy the continuity equation

$$\nabla \cdot \tilde{\mathbf{J}} = 0\,,$$

reflecting the conservation of charge.

In order to obtain an evolution equation for the current density, we need to represent $\mathbf{E}$ and $\mathbf{B}$ in terms of $\mathbf{J}$. To begin with, we write the magnetic field as

$$\mathbf{B} = \mathbf{B}_{\text{ext}} + \mathcal{B}(\tilde{\mathbf{J}})\,,$$

where $\mathbf{B}_{\text{ext}}$ is an applied field, possibly generated by permanent or electromagnets surrounding the fluid domain, while $\mathcal{B}(\tilde{\mathbf{J}})$ is the field induced by $\tilde{\mathbf{J}} = \mathbf{J}_{\text{ext}} + \mathbf{J}$. Adopting the quasi-stationary form of Maxwell's equations, as is the custom in MHD, we obtain $\mathcal{B}(\tilde{\mathbf{J}})$ as the solution of

$$\nabla \times \mu^{-1}\mathcal{B}(\tilde{\mathbf{J}}) = \tilde{\mathbf{J}} \quad \text{and} \quad \nabla \cdot \mathcal{B}(\tilde{\mathbf{J}}) = 0\,,$$

where μ denotes the magnetic permeability. For simplicity we assume the fluid as well as all materials outside to be nonmagnetic so that μ is the permeability of the vacuum.

Next we introduce vector potentials for the (solenoidal) vector fields $\mathbf{B}_{\text{ext}}$ and $\mathcal{B}(\tilde{\mathbf{J}})$, that is, vector fields $\mathbf{A}_{\text{ext}}$ and $\mathcal{A}(\tilde{\mathbf{J}})$ satisfying

$$\nabla \times \mathbf{A}_{\text{ext}} = \mathbf{B}_{\text{ext}} \quad \text{and} \quad \nabla \cdot \mathbf{A}_{\text{ext}} = 0\,,$$

$$\nabla \times \mathcal{A}(\tilde{\mathbf{J}}) = \mathcal{B}(\tilde{\mathbf{J}}) \quad \text{and} \quad \nabla \cdot \mathcal{A}(\tilde{\mathbf{J}}) = 0\,.$$

Since we have $\nabla \times \mu^{-1}\mathcal{B}(\tilde{\mathbf{J}}) = \tilde{\mathbf{J}}$ and since μ is assumed to be constant, $\mathcal{A}(\tilde{\mathbf{J}})$ satisfies

$$\nabla \times \nabla \times \mathcal{A}(\tilde{\mathbf{J}}) = \mu\tilde{\mathbf{J}} \quad \text{and} \quad \nabla \cdot \mathcal{A}(\tilde{\mathbf{J}}) = 0\,,$$

or equivalently,

$$-\Delta\mathcal{A}(\tilde{\mathbf{J}}) = \mu\tilde{\mathbf{J}}\,.$$

Under a suitable radiation condition at infinity, this equation has a unique solution,

$$\mathcal{A}(\tilde{\mathbf{J}}) = \mu\mathcal{L}(\tilde{\mathbf{J}}) = \mu\mathcal{L}(\mathbf{J}_{\text{ext}}) + \mu\mathcal{L}(\mathbf{J})\,,$$

where (formally) $\mathcal{L} = (-\Delta)^{-1}$. Similarly,

$$\mathbf{A}_{\text{ext}} = \mathcal{L}(\nabla \times \mathbf{B}_{\text{ext}}) = \nabla \times \mathcal{L}(\mathbf{B}_{\text{ext}})\,.$$

We note that $\mathcal{L}$ is a weakly singular integral operator, given by

$$\mathcal{L}(\mathbf{f})(x) = \frac{1}{4\pi}\int_{\mathbf{R}^3} \frac{\mathbf{f}(y)}{|x-y|}\,dy\,,$$

for any sufficiently regular vector field $\mathbf{f}$ with sufficiently fast decay at infinity, and that

$$\nabla \times \mathcal{L}(\mathbf{f})(x) = -\frac{1}{4\pi}\int_{\mathbf{R}^3} \frac{x-y}{|x-y|^3} \times \mathbf{f}(y)\,dy\,.$$

The resulting representation of the magnetic field,

$$\mathbf{B} = \mathbf{B}_{\text{ext}} + \mathcal{B}(\tilde{\mathbf{J}}) = \mathbf{B}_{\text{ext}} + \mu\nabla \times \mathcal{L}(\mathbf{J}_{\text{ext}}) + \mu\nabla \times \mathcal{L}(\mathbf{J})\,, \qquad (4)$$

is commonly called the Biot-Savart law.

Turning to the electric field $\mathbf{E}$, we observe that according to Faraday's law,

$$\nabla \times \mathbf{E} = -\mathbf{B}_t\,.$$

Since $\mathbf{B} = \nabla \times \mathbf{A}$ with $\mathbf{A} = \mathbf{A}_{\text{ext}} + \mathcal{A}(\tilde{\mathbf{J}})$, it follows that $\nabla \times (\mathbf{E} + \mathbf{A}_t) = 0$ and thus, $\mathbf{E} + \mathbf{A}_t = -\nabla\phi$ for some scalar potential ϕ. But

$$\begin{aligned} \mathbf{A}_t &= \mathbf{A}_{\text{ext},t} + \mathcal{A}(\tilde{\mathbf{J}})_t \\ &= \nabla \times \mathcal{L}(\mathbf{B}_{\text{ext},t}) + \mu\mathcal{L}(\mathbf{J}_{\text{ext},t}) + \mu\mathcal{L}(\mathbf{J}_t) \end{aligned}$$

and thus,

$$\mathbf{E} = \mathbf{E}_{\text{ext}} - \mu\mathcal{L}(\mathbf{J}_t) - \nabla\phi\,,$$

where

$$\mathbf{E}_{\text{ext}} = -\nabla \times \mathcal{L}(\mathbf{B}_{\text{ext},t}) - \mu\mathcal{L}(\mathbf{J}_{\text{ext},t})\,. \qquad (5)$$

Substituting this into Ohm's law (3), we obtain

$$\mathbf{J} = \sigma(\mathbf{E}_{\text{ext}} - \mu\mathcal{L}(\mathbf{J}_t) - \nabla\phi + \mathbf{u} \times \mathbf{B})$$

or equivalently,

$$\mu\mathcal{L}(\mathbf{J}_t) + \sigma^{-1}\mathbf{J} + \nabla\phi - \mathbf{u} \times \mathbf{B} = \mathbf{E}_{\text{ext}}\,. \qquad (6)$$

This is the desired evolution equation for the current density $\mathbf{J}$ in the fluid domain. Analogous to the pressure p in the Navier-Stokes equations, the scalar potential ϕ plays the role of a Lagrange multiplier associated with the divergence constraint

$$\nabla \cdot \mathbf{J} = 0\,. \qquad (7)$$

Obviously the system of equations (1)–(2) and (6)–(7), with $\mathbf{B}$ and $\mathbf{E}_{\text{ext}}$ given by (4) and (5), is *closed* only if the external current distribution $\mathbf{J}_{\text{ext}}$ is assumed to be known. If this is not the case, Equations (6)–(7) must be solved in a larger region of space, including the fluid and adjacent external conductors (with $\mathbf{u} = 0$ outside the fluid, of course). It should be noted, however, that $\mathbf{J}_{\text{ext}}$ enters the equations only via the induced magnetic field, $\mu\nabla \times \mathcal{L}(\mathbf{J}_{\text{ext}})$. In many applications the effect of this field on the fluid motion will be negligible. In fact, the applied magnetic field $\mathbf{B}_{\text{ext}}$ is typically much stronger than *any* induced field, so that it may well be reasonable to neglect induction effects altogether. Formally, this amounts to setting $\mu = 0$ in (4)–(6), in which case Equation (6) becomes quasi-stationary.

The system of equations (1)–(2) and (6)–(7) must be supplemented with initial conditions for $\mathbf{u}$ and $\mathbf{J}$ and suitable boundary conditions for $(\mathbf{u}, p)$ and $(\mathbf{J}, \phi)$. Let Ω denote the fluid domain, Γ its surface, and $\mathbf{n}$ the outward unit normal vector field on Γ. The simplest physically reasonable and mathematically feasible boundary conditions are $\mathbf{u} = 0$ and $\mathbf{J} \cdot \mathbf{n} = 0$ on Γ. Here we allow for both mass and current flux across Γ, which leads to inhomogeneous Dirichlet or Neumann type boundary conditions. Specifically, we prescribe the *velocity* $\mathbf{u}$ on an open subset Γ_1 of Γ and the *stress* $\eta\left(\nabla\mathbf{u}+(\nabla\mathbf{u})^T\right)\cdot\mathbf{n} - p\,\mathbf{n}$ on its complement $\Gamma_2 = \Gamma\setminus\overline{\Gamma_1}$; we prescribe the *current flux* $\mathbf{J} \cdot \mathbf{n}$ on an open subset Γ_3 of Γ and the *electric potential* ϕ on its complement $\Gamma_4 = \Gamma \setminus \overline{\Gamma_3}$:

$$\mathbf{u} = \mathbf{g}_1 \quad \text{on } \Gamma_1, \qquad \eta\left(\nabla\mathbf{u} + (\nabla\mathbf{u})^T\right)\cdot\mathbf{n} - p\,\mathbf{n} = \mathbf{g}_2 \quad \text{on } \Gamma_2,$$

$$\mathbf{J} \cdot \mathbf{n} = g_3 \quad \text{on } \Gamma_3, \qquad \phi = g_4 \quad \text{on } \Gamma_4.$$

In certain cases, the boundary data $\mathbf{g}_1$, $\mathbf{g}_2$, g_3, g_4 must satisfy compatibility conditions. For example, if $\Gamma_2 = \emptyset$, then $\mathbf{g}_1 \cdot \mathbf{n}$ must have mean zero on Γ (since $\nabla \cdot \mathbf{u} = 0$ in Ω); if $\Gamma_4 = \emptyset$, then g_3 must have mean zero on Γ (since $\nabla \cdot \mathbf{J} = 0$ in Ω).

Summarizing, our problem is the following: Given the fluid domain Ω (a bounded region of space with sufficiently regular boundary $\Gamma = \overline{\Gamma_1} \cup \overline{\Gamma_2} = \overline{\Gamma_3} \cup \overline{\Gamma_4}$), given the positive parameters ρ, η, μ, and σ, given the external fields $\mathbf{F}_{\text{ext}}$, $\mathbf{J}_{\text{ext}}$, $\mathbf{B}_{\text{ext}}$, and $\mathbf{E}_{\text{ext}} = -\nabla \times \mathcal{L}(\mathbf{B}_{\text{ext},t}) - \mu\mathcal{L}(\mathbf{J}_{\text{ext},t})$, given compatible boundary data $\mathbf{g}_1$, $\mathbf{g}_2$, g_3, and g_4, and given initial values $\mathbf{u}_0$ and $\mathbf{J}_0$, find vector fields $\mathbf{u} = \mathbf{u}(t, x)$, $\mathbf{J} = \mathbf{J}(t, x)$ and scalar fields $p = p(t, x)$, $\phi = \phi(t, x)$ such that the following equations are satisfied with $\mathbf{B} = \mathbf{B}_{\text{ext}} + \mu\nabla \times \mathcal{L}(\mathbf{J}_{\text{ext}}) + \mu\nabla \times \mathcal{L}(\mathbf{J})$:

$$\rho\mathbf{u}_t - \eta\Delta\mathbf{u} + \rho(\mathbf{u} \cdot \nabla)\mathbf{u} + \nabla p - \mathbf{J} \times \mathbf{B} = \mathbf{F}_{\text{ext}} \quad (t > 0,\ x \in \Omega),$$

$$\nabla \cdot \mathbf{u} = 0 \quad (t > 0,\ x \in \Omega),$$

$$\mu \mathcal{L}(\mathbf{J}_t) + \sigma^{-1}\mathbf{J} + \nabla\phi - \mathbf{u} \times \mathbf{B} = \mathbf{E}_{\text{ext}} \quad (t > 0,\ x \in \Omega),$$

$$\nabla \cdot \mathbf{J} = 0 \quad (t > 0,\ x \in \Omega),$$

$$\mathbf{u} = \mathbf{g}_1 \quad (t > 0,\ x \in \Gamma_1),$$

$$\eta\left(\nabla\mathbf{u} + (\nabla\mathbf{u})^T\right) \cdot \mathbf{n} - p\,\mathbf{n} = \mathbf{g}_2 \quad (t > 0,\ x \in \Gamma_2),$$

$$\mathbf{J} \cdot \mathbf{n} = g_3 \quad (t > 0,\ x \in \Gamma_3), \qquad \phi = g_4 \quad (t > 0,\ x \in \Gamma_4),$$

$$\mathbf{u} = \mathbf{u}_0 \quad (t = 0,\ x \in \Omega), \qquad \mathbf{J} = \mathbf{J}_0 \quad (t = 0,\ x \in \Omega).$$

Under mild regularity assumptions on the data, this problem has a weak solution $(\mathbf{u}, \mathbf{J}, p, \phi)$, defined for all time $t > 0$. If the boundary data are sufficiently small (or if the viscosity η and resistivity σ^{-1} of the fluid are sufficiently large), the solution remains bounded as $t \to \infty$. For further details and a rigorous proof (if only in the case $\Gamma_2 = \Gamma_4 = \emptyset$), the reader is referred to [12].

III. A VARIATIONAL FORMULATION FOR THE STATIONARY PROBLEM

As a first step towards the numerical analysis and finite-element approximation of the full, time-dependent problem described in Section II, we consider the steady-state version where data and unknowns are independent of time. In this case Equations (1)–(2) and (6)–(7) reduce to

$$-\eta\Delta\mathbf{u} + \rho(\mathbf{u} \cdot \nabla)\mathbf{u} + \nabla p - \mathbf{J} \times \mathbf{B} = \mathbf{F}_{\text{ext}}\,, \tag{8}$$

$$\nabla \cdot \mathbf{u} = 0\,, \tag{9}$$

$$\sigma^{-1}\mathbf{J} + \nabla\phi - \mathbf{u} \times \mathbf{B} = \mathbf{E}_{\text{ext}}\,, \tag{10}$$

$$\nabla \cdot \mathbf{J} = 0\,, \tag{11}$$

all posed in the fluid domain Ω and supplemented with boundary conditions on the surface $\Gamma = \overline{\Gamma_1} \cup \overline{\Gamma_2} = \overline{\Gamma_3} \cup \overline{\Gamma_4}$:

$$\mathbf{u} = \mathbf{g}_1 \quad \text{on } \Gamma_1, \qquad \eta\left(\nabla\mathbf{u} + (\nabla\mathbf{u})^T\right) \cdot \mathbf{n} - p\,\mathbf{n} = \mathbf{g}_2 \quad \text{on } \Gamma_2, \tag{12}$$

$$\mathbf{J} \cdot \mathbf{n} = g_3 \quad \text{on } \Gamma_3, \qquad \phi = g_4 \quad \text{on } \Gamma_4. \tag{13}$$

As before, the magnetic field is given by

$$\mathbf{B} = \mathbf{B}_{\text{ext}} + \mu\nabla \times \mathcal{L}(\mathbf{J}_{\text{ext}}) + \mu\nabla \times \mathcal{L}(\mathbf{J})\,. \tag{14}$$

On physical grounds, $\mathbf{E}_{\text{ext}}$ should be zero in the stationary case, but for reasons of symmetry in the equations we allow for an arbitrary field $\mathbf{E}_{\text{ext}}$. We assume that Ω is a bounded Lipschitz domain and that the subsets Γ_i of the surface Γ are non-empty, open Lipschitz surfaces with $\Gamma_1 \cap \Gamma_2 = \emptyset$, $\overline{\Gamma_1} \cup \overline{\Gamma_2} = \Gamma$ and $\Gamma_3 \cap \Gamma_4 = \emptyset$, $\overline{\Gamma_3} \cup \overline{\Gamma_4} = \Gamma$. (The subsequent analysis would remain valid, with only minor modifications, if one of the sets Γ_1, Γ_2 and/or one of the sets Γ_3, Γ_4 was empty.)

We will seek weak solutions $(\mathbf{u}, \mathbf{J}, p, \phi)$ of Equations (8)–(14) with

$$\mathbf{u} \in \mathbf{X}_1 := \mathbf{H}^1(\Omega), \quad \mathbf{J} \in \mathbf{X}_2 := \mathbf{L}^2(\Omega),$$

$$p \in M_1 := L^2(\Omega), \quad \phi \in M_2 := H^1(\Omega).$$

In addition to the above, we will need the subspaces

$$\tilde{\mathbf{X}}_1 := \{\mathbf{v} \in \mathbf{X}_1 \mid \mathbf{v} = 0 \text{ on } \Gamma_1\}$$

and

$$\tilde{M}_2 := \{\psi \in M_2 \mid \psi = 0 \text{ on } \Gamma_4\}.$$

Here and in the sequel, $L^2(\Omega)$ denotes the space of square-integrable scalar functions on Ω, and $H^1(\Omega)$ is the subspace of $L^2(\Omega)$ comprised of functions with square-integrable first-order derivatives. Both $L^2(\Omega)$ and $H^1(\Omega)$ are Hilbert spaces with norms given by

$$\|f\|_{L^2(\Omega)} := \left(\int_\Omega |f|^2\right)^{1/2}$$

and

$$\|f\|_{H^1(\Omega)} := \left(\|f\|^2_{L^2(\Omega)} + \|\nabla f\|^2_{\mathbf{L}^2(\Omega)}\right)^{1/2}$$

Bold-face type is used for the corresponding spaces of vector functions.

The following assumptions on the data guarantee that all the equations are meaningful (in the weak sense):

$$\mathbf{F}_{\text{ext}} \in \mathbf{L}^2(\Omega), \quad \mathbf{E}_{\text{ext}} \in \mathbf{L}^2(\Omega),$$

$$\mathbf{J}_{\text{ext}} \in \mathbf{L}^2(\mathbf{R}^3 \setminus \overline{\Omega}), \quad \mathbf{B}_{\text{ext}} \in \mathbf{H}^1(\Omega),$$

$$\mathbf{g}_1 \in \mathbf{H}^{1/2}(\Gamma_1), \quad \mathbf{g}_2 \in \mathbf{H}^{-1/2}(\Gamma_2),$$

$$g_3 \in H^{-1/2}(\Gamma_3), \quad g_4 \in H^{1/2}(\Gamma_4).$$

The space $H^{1/2}(\Gamma_i)$, for $1 \le i \le 4$, consists of the traces (or generalized boundary values) on Γ_i of functions in $H^1(\Omega)$, and $H^{-1/2}(\Gamma_i)$ is the dual of $H^{1/2}(\Gamma_i)$. These are Hilbert spaces with norms derived from that of $H^1(\Omega)$. Again, bold-face type is used for the corresponding spaces of vector functions.

To derive a weak or variational form of the problem at hand, we multiply Equations (8) and (10) by test functions $\mathbf{v} \in \tilde{\mathbf{X}}_1$ and $\mathbf{K} \in \mathbf{X}_2$, respectively, and Equations (9) and (11) by test functions $q \in M_1$ and $\psi \in \tilde{M}_2$, respectively. We then integrate over Ω, perform several integrations by parts, regroup terms, and add the equations obtained from (8) and (10) and those obtained from (9) and (11). This procedure results in two equations of the form

$$\begin{aligned} a_0\big((\mathbf{u}, \mathbf{J}), (\mathbf{v}, \mathbf{K})\big) + a_1\big((\mathbf{u}, \mathbf{J}), (\mathbf{u}, \mathbf{J}), (\mathbf{v}, \mathbf{K})\big) \\ + b\big((\mathbf{v}, \mathbf{K}), (p, \phi)\big) = \ell_0(\mathbf{v}, \mathbf{K}) \end{aligned} \tag{15}$$

and

$$b\big((\mathbf{u}, \mathbf{J}), (q, \psi)\big) = \ell_1(q, \psi)\,, \tag{16}$$

where a_0 (a bilinear form), a_1 (a trilinear form), b (a bilinear form), ℓ_0 and ℓ_1 (linear forms) are given by

$$\begin{aligned} &a_0\big((\mathbf{v}_1, \mathbf{K}_1), (\mathbf{v}_2, \mathbf{K}_2)\big) \\ &\quad := \frac{\eta}{2}\int_\Omega \left(\nabla\mathbf{v}_1 + (\nabla\mathbf{v}_1)^T\right) : \left(\nabla\mathbf{v}_2 + (\nabla\mathbf{v}_2)^T\right) + \sigma^{-1}\int_\Omega \mathbf{K}_1 \cdot \mathbf{K}_2 \\ &\qquad + \int_\Omega \Big(\big(\mathbf{K}_2 \times \mathbf{B}_0\big) \cdot \mathbf{v}_1 - \big(\mathbf{K}_1 \times \mathbf{B}_0\big) \cdot \mathbf{v}_2\Big)\,, \end{aligned}$$

where $\mathbf{B}_0 := \mathbf{B}_{\text{ext}} + \mu\nabla \times \mathcal{L}(\mathbf{J}_{\text{ext}})$, for $(\mathbf{v}_1, \mathbf{K}_1), (\mathbf{v}_2, \mathbf{K}_2) \in \mathbf{X}_1 \times \mathbf{X}_2$,

$$\begin{aligned} &a_1\big((\mathbf{v}_1, \mathbf{K}_1), (\mathbf{v}_2, \mathbf{K}_2), (\mathbf{v}_3, \mathbf{K}_3)\big) \\ &\quad := \frac{\rho}{2}\int_\Omega \Big(\big((\mathbf{v}_1 \cdot \nabla)\mathbf{v}_2\big) \cdot \mathbf{v}_3 - \big((\mathbf{v}_1 \cdot \nabla)\mathbf{v}_3\big) \cdot \mathbf{v}_2\Big) \\ &\qquad + \mu\int_\Omega \Big(\big(\mathbf{K}_3 \times (\nabla \times \mathcal{L}(\mathbf{K}_1))\big) \cdot \mathbf{v}_2 - \big(\mathbf{K}_2 \times (\nabla \times \mathcal{L}(\mathbf{K}_1))\big) \cdot \mathbf{v}_3\Big)\,, \end{aligned}$$

for $(\mathbf{v}_1, \mathbf{K}_1), (\mathbf{v}_2, \mathbf{K}_2), (\mathbf{v}_3, \mathbf{K}_3) \in \mathbf{X}_1 \times \mathbf{X}_2$,

$$b\big((\mathbf{v}, \mathbf{K}), (q, \psi)\big) := -\int_\Omega (\nabla \cdot \mathbf{v})q + \int_\Omega \mathbf{K} \cdot (\nabla\psi)\,,$$

for $(\mathbf{v}, \mathbf{K}) \in \mathbf{X}_1 \times \mathbf{X}_2$, $(q, \psi) \in M_1 \times M_2$,

$$\ell_0(\mathbf{v}, \mathbf{K}) := \int_\Omega \mathbf{F}_{\text{ext}} \cdot \mathbf{v} + \int_\Omega \mathbf{E}_{\text{ext}} \cdot \mathbf{K} + \int_{\Gamma_2} \mathbf{g}_2 \cdot \mathbf{v}\,,$$

for $(\mathbf{v}, \mathbf{K}) \in \mathbf{X}_1 \times \mathbf{X}_2$, and

$$\ell_1(q, \psi) := \int_{\Gamma_3} g_3 \psi \,,$$

for $(q, \psi) \in M_1 \times M_2$.

Routine arguments show that finding a weak solution $(\mathbf{u}, \mathbf{J}, p, \phi)$ of Equations (8)–(14) is equivalent to solving the following variational problem.

Problem (P)**.** Find $\mathbf{u} \in \mathbf{X}_1$ with $\mathbf{u} = \mathbf{g}_1$ on Γ_1, $\mathbf{J} \in \mathbf{X}_2$, $p \in M_1$, and $\phi \in M_2$ with $\phi = g_4$ on Γ_4 such that Equations (15) and (16) are satisfied for all $(\mathbf{v}, \mathbf{K}) \in \tilde{\mathbf{X}}_1 \times \mathbf{X}_2$ and $(q, \psi) \in M_1 \times \tilde{M}_2$, respectively.

After homogenization of the essential boundary conditions for $\mathbf{u}$ and ϕ, Problem (P) reduces to a mixed variational problem in the sense of the Ladyzhenskaya-Babuska-Brezzi theory (see, for example, [2, Chapter IV.1]). This allows us to prove the well-posedness of Problem (P), at least under a small-data assumption.

Theorem 1. If the data $\mathbf{F}_{\text{ext}}$, $\mathbf{E}_{\text{ext}}$, $\mathbf{J}_{\text{ext}}$, $\mathbf{B}_{\text{ext}}$ and $\mathbf{g}_1$, $\mathbf{g}_2$, g_3, g_4 are sufficiently small (or if the viscosity η and resistivity σ^{-1} are sufficiently large), then Problem (P) has a unique solution $(\mathbf{u}, \mathbf{J}, p, \phi)$, which depends continuously on the data and parameters of the problem.

Roughly speaking, Theorem 1 guarantees the existence, uniqueness, and stability of a steady solution to the MHD equations in the case of low Reynolds and magnetic Reynolds numbers. For a much more precise statement of the theorem, including specific bounds on the allowable size of the data (relative to the parameters of the problem), we refer to [8].

IV. FINITE-ELEMENT DISCRETIZATION AND ERROR ESTIMATES

In order to discretize Problem (P), we choose finite-dimensional approximations $\mathbf{X}_1^h$, $\mathbf{X}_2^h$, M_1^h, and M_2^h of the spaces $\mathbf{X}_1 := \mathbf{H}^1(\Omega)$, $\mathbf{X}_2 := \mathbf{L}^2(\Omega)$, $M_1 := L^2(\Omega)$, and $M_2 := H^1(\Omega)$. Furthermore, we set $\tilde{\mathbf{X}}_1^h := \{\mathbf{v}^h \in \mathbf{X}_1^h \mid \mathbf{v}^h = 0 \text{ on } \Gamma_1\}$ and $\tilde{M}_2^h := \{\psi^h \in M_2^h \mid \psi^h = 0 \text{ on } \Gamma_4\}$ and choose approximate essential boundary data $\mathbf{g}_1^h \in \{\mathbf{v}^h|_{\Gamma_1} \mid \mathbf{v}^h \in \mathbf{X}_1^h\}$ and $g_4^h \in \{\psi^h|_{\Gamma_4} \mid \psi^h \in M_2^h\}$. Here h is a discretization parameter, for example, the meshsize of a triangulation of the domain Ω. We assume that the spaces $\mathbf{X}_i^h$ and M_i^h approximate $\mathbf{X}_i$ and M_i in the sense that the error of best approximation of a function in $\mathbf{X}_i$ or M_i by elements of $\mathbf{X}_i^h$ or M_i^h tends to 0 as $h \to 0$; of course, we also assume that $\mathbf{g}_1^h \to \mathbf{g}_1$ and $g_4^h \to g_4$ (in the respective trace spaces). We then consider the following finite-dimensional approximation of Problem (P).

Problem (P^h)**.** Find $\mathbf{u}^h \in \mathbf{X}_1^h$ with $\mathbf{u}^h = \mathbf{g}_1^h$ on Γ_1, $\mathbf{J}^h \in \mathbf{X}_2^h$, $p^h \in M_1^h$, and $\phi^h \in M_2^h$ with $\phi^h = g_4^h$ on Γ_4 such that the equations

$$\begin{aligned} a_0\big((\mathbf{u}^h, \mathbf{J}^h), (\mathbf{v}^h, \mathbf{K}^h)\big) + a_1\big((\mathbf{u}^h, \mathbf{J}^h), (\mathbf{u}^h, \mathbf{J}^h), (\mathbf{v}^h, \mathbf{K}^h)\big) \\ + b\big((\mathbf{v}^h, \mathbf{K}^h), (p^h, \phi^h)\big) = \ell_0(\mathbf{v}^h, \mathbf{K}^h) \end{aligned} \tag{17}$$

and

$$b\big((\mathbf{u}^h, \mathbf{J}^h), (q^h, \psi^h)\big) = \ell_1(q^h, \psi^h) \tag{18}$$

are satisfied for all $(\mathbf{v}^h, \mathbf{K}^h) \in \tilde{\mathbf{X}}_1^h \times \mathbf{X}_2^h$ and $(q^h, \psi^h) \in M_1^h \times \tilde{M}_2^h$, respectively.

Under certain technical conditions on the finite-dimensional spaces $\mathbf{X}_i^h$ and M_i^h, an analog of Theorem 1 holds for Problem (P^h), and we obtain an optimal-order estimate for the discretization error (see [8] for details).

Theorem 2. If the data $\mathbf{F}_{\text{ext}}$, $\mathbf{E}_{\text{ext}}$, $\mathbf{J}_{\text{ext}}$, $\mathbf{B}_{\text{ext}}$ and $\mathbf{g}_1$, $\mathbf{g}_2$, g_3, g_4 are sufficiently small (or if the viscosity η and resistivity σ^{-1} of the fluid are sufficiently large) and if h is sufficiently small, then both Problem (P) and Problem (P^h) have unique solutions $(\mathbf{u}, \mathbf{J}, p, \phi)$ and $(\mathbf{u}^h, \mathbf{J}^h, p^h, \phi^h)$, respectively. Moreover, the discretization error (that is, the distance between $(\mathbf{u}, \mathbf{J}, p, \phi)$ and $(\mathbf{u}^h, \mathbf{J}^h, p^h, \phi^h)$ in the norm of the product space $\mathbf{X}_1 \times \mathbf{X}_2 \times M_1 \times M_2$) is of the same order as the sum of the error of best approximation of $(\mathbf{u}, \mathbf{J}, p, \phi)$ by elements of $\mathbf{X}_1 \times \mathbf{X}_2 \times M_1 \times M_2$ plus the error in the approximate boundary data, $\|\mathbf{g}_1 - \mathbf{g}_1^h\|_{\mathbf{H}^{1/2}(\Gamma_1)} + \|g_4 - g_4^h\|_{H^{1/2}(\Gamma_4)}$. In particular, $(\mathbf{u}^h, \mathbf{J}^h, p^h, \phi^h) \to (\mathbf{u}, \mathbf{J}, p, \phi)$ as $h \to 0$.

Theorem 2 and general results of finite-element theory suggest that Problem (P^h) will be a k-th order approximation of Problem (P) (for some positive integer k) if we use appropriate piecewise polynomial approximations of degree k for the velocity and electric potential and of degree $k-1$ for the pressure and current density. Assuming, for simplicity, that the domain Ω is a polyhedron and that we are given a regular decomposition of $\overline{\Omega}$ into simplicial or rectangular elements, we may approximate $H^1(\Omega)$ and $L^2(\Omega)$ by the spaces $\mathcal{P}_2^h$ and $\mathcal{P}_1^h$ of continuous piecewise quadratics (or triquadratics) and continuous piecewise linears (or trilinears) on tetrahedra (or rectangular parallelepipeds), respectively, and then set $\mathbf{X}_1^h := \mathcal{P}_2^h \times \mathcal{P}_2^h \times \mathcal{P}_2^h$ and $M_1^h := \mathcal{P}_1^h$. These so-called Taylor-Hood type velocity-pressure pairs are widely used in computational fluid dynamics and well understood (see, for example, [1, Chapter VI.6] or [3, Chapter 3]); in particular, they satisfy all the technical conditions needed to prove Theorem 2, the most important of which is the so-called LBB-condition.

In view of the above choices of velocity-pressure pairs, it is natural to set $M_2^h := \mathcal{P}_2^h$. In order to satisfy the LBB-condition, the space $\mathbf{X}_2^h$ should then contain the gradients of all continuous piecewise quadratics (on tetrahedra) or triquadratics (on rectangular parallelepipeds). Thus, in the case of a *simplicial* triangulation, we choose for $\mathbf{X}_2^h$ the subspace of $\mathbf{L}^2(\Omega)$ comprised of all vector functions on Ω whose components are (generally discontinuous) piecewise linears. When using *rectangular* elements, we let $\mathbf{X}_2^h := \mathbf{X}_{2,1}^h \times \mathbf{X}_{2,2}^h \times \mathbf{X}_{2,3}^h$ and choose for $\mathbf{X}_{2,i}^h$ the tensor product of the space of (generally discontinuous) piecewise linears in the i-th variable and the space of continuous piecewise biquadratics in the remaining two variables. Note that in any case, $\mathbf{X}_2^h$ contains $\mathcal{P}_1^h \times \mathcal{P}_1^h \times \mathcal{P}_1^h$. Pairs of spaces like $\mathbf{X}_2^h$ and M_2^h are commonly used in connection with so-called primal mixed methods (see, for example, [11, Section 12]).

With the above choices of finite-element spaces, the error of best approximation of the exact solution of Problem (P) will be of order h^2 provided that the exact solution is sufficiently regular (that is, if $\mathbf{u} \in \mathbf{H}^2(\Omega)$, $\mathbf{J} \in \mathbf{H}^1(\Omega)$, $p \in H^1(\Omega)$, $\phi \in H^2(\Omega)$). Approximate essential boundary data can be chosen in such a way that the error in those is of the same order. For example, if $\mathbf{g}_1$ and g_4 are sufficiently smooth, one can take for $\mathbf{g}_1^h$ and g_4^h the Lagrange interpolants of $\mathbf{g}_1$ and g_4 in the respective trace spaces of $\mathbf{X}_1^h$ and M_2^h. In general, independent of the smoothness of $\mathbf{g}_1$ and g_4, one can utilize generalized interpolants of Scott-Zhang type (see [13, Section 5]. In any case, Theorem 2 then guarantees that the solution of Problem (P^h) will approximate the exact solution of Problem (P) with an error of order h^2.

Several methods suggest themselves naturally for solving the discrete problem (P^h). Most straightforward is a simple linearization-iteration scheme where one lags the first argument $(\mathbf{u}^h, \mathbf{J}^h)$ of the trilinear form a_1. In the situation of Theorem 2, this scheme converges globally, that is, for every initial guess $(\mathbf{u}_0^h, \mathbf{J}_0^h)$. Despite the presence of the nonlocal operator $\mathcal{L}$, the resulting linear systems are sparse and can be solved either directly or iteratively. Intermediate computations of the induced magnetic field $\mu\nabla \times \mathcal{L}(\mathbf{J})$ are expensive, but can be handled efficiently, for example, with fast multi-pole methods.

Further speed-up may be achieved through the use of multi-level methods. In [5], for example, we describe a simple two-level algorithm, which yields optimal-order approximations by first solving the nonlinear problem (P^h) on a rather coarse grid (with $h \sim H$, say) and then solving a linearization of (P^h) on a much finer grid (with $h \sim H^2$). Finally, parts of the method are inherently parallelizable — a feature that will have to be exploited in order to deal with industrial-strength applications.

V. NUMERICAL EXPERIMENT

We implemented the method, as described, to simulate MHD flow around a circular cylinder in a channel with square cross section (see Figure 1). The flow domain was discretized by first mapping it to a rectangular channel with a rectangular cavity and then decomposing the latter into cubes of equal size (see Figures 2 and 3). In view of the remarks about suitable finite-element spaces in Section IV, we used standard triquadratic Lagrange

elements for the velocity and electric potential, standard trilinear Lagrange elements for the pressure. For the i-th component of the current density, we chose Hermite elements with nine nodes, namely, those nodes of the principal lattice of degree two (on the reference cube) that are not on faces perpendicular to the i-th coordinate axis; two degrees of freedom were associated with each such node a, namely, $f \mapsto f(a)$ and $f \mapsto \partial_i f(a)$. This choice is convenient in constructing a basis for the somewhat nonstandard space $\mathbf{X}^h_{2,i}$. We used Lagrange interpolation to approximate the essential boundary data and employed the simple iteration scheme described in Section IV to solve Problem (P^h).

We prescribed a parabolic inflow velocity profile at the left end of the channel, zero velocity on the channel walls and on the cylinder surface, and zero stress on the outflow boundary (the right end of the channel). A permanent magnet, generating a dipole field $\mathbf{B}_{\text{ext}}$, was positioned along the cylinder axis (north pole facing the front), and a pair of electrodes was located on the down-stream part of the cylinder surface, one near the top, the other near the bottom. On the electrodes we specified the electric potential (negative on the upper, positive on the lower one); on all other boundaries we required zero current flux. No external body forces, external currents, or external electric fields were accounted for.

Since the experiment was anyway of an academic nature, we set all parameters equal to one. Moreover, all non-zero data (inflow velocity, applied magnetic field, and boundary values of the electric potential) were roughly of order one. We first solved the problem without magnetism and electricity; Figure 4 shows the resulting (purely hydrodynamic) velocity field. We then repeated the computation with magnetism and electricity switched on. The resulting velocity field, depicted in Figure 5, reveals a significant change in the flow pattern in the wake of the cylinder. In both cases, we also computed the total force acting on the cylinder, that is, the integral of the stress over the cylinder surface. In both cases, this force is parallel to the channel axis, but its direction is reversed when magnetism and electricity are switched on. The numerical values obtained were +230 versus -148. Most of the change in the total force is due to a reversal of the pressure gradient near the cylinder. Computing only the skin friction component, we found a drag reduction from 56 to 17.

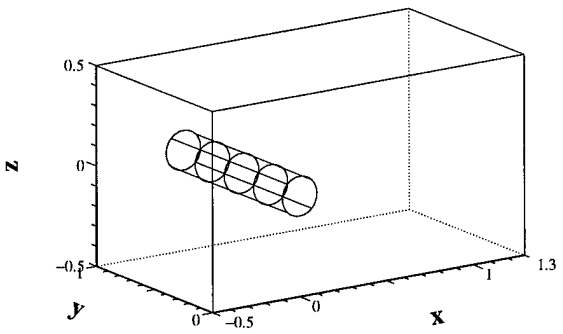

Fig. 1. The channel and cylinder.

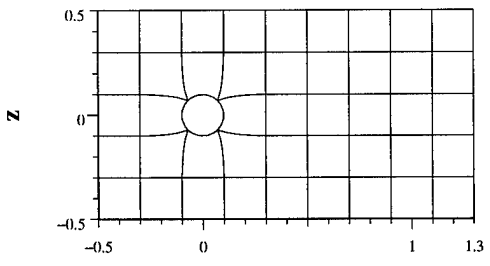

Fig. 2. Physical grid.

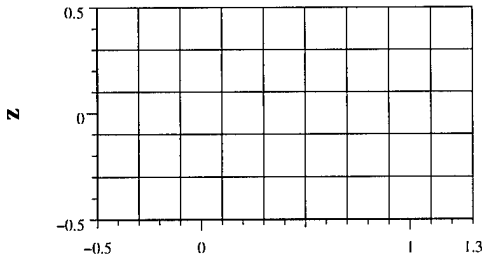

Fig. 3. Logical grid.

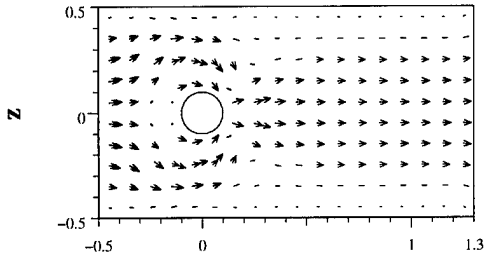

Fig. 4. Velocity field.

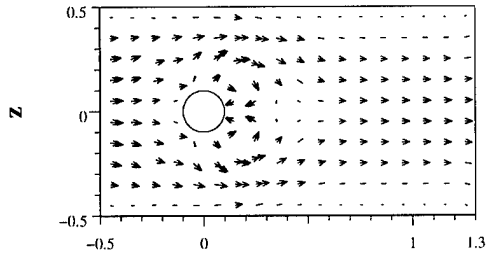

Fig. 5. Velocity field with MHD.

VI. CONCLUDING REMARKS

A novel formulation of the equations of viscous incompressible MHD was presented that allows for realistic boundary and interface conditions and accounts for the electromagnetic interaction of the fluid with the outside world while restricting computations to the region occupied by the fluid (and possibly, adjacent solid conductors). A mixed variational method was developed for the corresponding steady-state problem, which lends itself naturally to a finite-element discretization. The method was successfully implemented and tested by simulating a simple drag reduction experiment. The method can be used to solve a variety of MHD flow control and design problems, where the controls are applied magnetic fields, electric currents, and electric potentials. In its present implementation, the method is limited to the simulation of steady, laminar flows in the case of low Reynolds and magnetic Reynolds numbers, but the approach is potentially applicable to the simulation of unsteady and turbulent flows as well.

VII. REFERENCES

1. F. Brezzi and M. Fortin, Mixed and Hybrid Finite Element Methods, Springer, New York, 1991.
2. V. Girault and P.-A. Raviart, Finite Element Methods for Navier-Stokes Equations, Theory and Algorithms, Springer, New York, 1986.
3. M. D. Gunzburger, Finite Element Methods for Viscous Incompressible Flows, Academic Press, Boston, 1989.
4. C. Henoch and J. Stace, Experimental investigation of a salt water turbulent boundary layer modified by an applied streamwise magnetohydrodynamic body force, *Physics of Fluids*, Vol. 7 (1995), pp. 1371–1383.
5. W. J. Layton, A. J. Meir, and P. G. Schmidt, A two-level discretization method for the stationary MHD equations, *Electronic Transactions on Numerical Analysis*, Vol. 6 (1997), pp. 198–210.
6. A. J. Meir and P. G. Schmidt, A velocity-current formulation for stationary MHD flow, *Applied Mathematics and Computation*, Vol. 65 (1994), pp. 95–109.
7. A. J. Meir and P. G. Schmidt, Variational methods for stationary MHD flow under natural interface conditions, *Nonlinear Analysis, Theory, Methods and Applications*, Vol. 26 (1996), pp. 659–689.
8. A. J. Meir and P. G. Schmidt, Analysis and numerical approximation of a stationary MHD flow problem with nonideal boundary, *SIAM Journal on Numerical Analysis*, to appear.
9. J. C. S. Meng, P. J. Hendricks, and J. D. Hrubes, Superconducting electromagnetic thrusters, *Sea Technology*, Vol. 33 (1992), pp. 29–39.
10. J. C. S. Meng, C. W. Henoch, and J. D. Hrubes, Seawater electromagnetohydrodynamics: A new frontier, *Magnetohydrodynamics*, Vol. 30 (1994), pp. 401–418.
11. J. E. Roberts and J.-M. Thomas, Mixed and hybrid methods, in: Handbook of Numerical Analysis, Vol. II, Finite Element Methods (Part 1), P. G. Ciarlet and J. L. Lions, Eds., North-Holland, Amsterdam, 1991, pp. 523–639.
12. P. G. Schmidt, A Galerkin method for time-dependent MHD flow with nonideal boundaries, *Communications in Applied Analysis*, to appear.
13. L. R. Scott and S. Zhang, Finite element interpolation of nonsmooth functions satisfying boundary conditions, *Mathematics of Computation*, Vol. 54 (1990), 483–493.

LORENTZ FORCE MODELING IN EMHD TURBULENCE CONTROL: DNS STUDIES

Y. Du, C. H. Crawford, G. E. Karniadakis
Center for Fluid Mechanics
Division of Applied Mathematics
Brown University

email: (Y. Du - ydu@cfm.brown.edu); (G. Karniadakis - gk@cfm.brown.edu)

Abstract - In this work we analyze high-resolution numerical data bases for a turbulent channel flow of a weakly conducting fluid and one channel wall covered with electro-magnetic tiles. First, we investigate different approaches of modeling the Lorentz force produced by the tiles, and address the question of effective force penetration. We then present results from different simulations corresponding to various ways of force pulsing by turning *on-and-off* the electrodes. A single case of 5% drag reduction was found but most of the other cases considered resulted in drag increase. Structures associated with drag reduction and drag increase were also visualized.

I. INTRODUCTION

In classical MHD turbulence a magnetic field present in the flow can suppress turbulence fluctuations leading even to flow re-laminarization and significant drag reduction ([13], [14]). The exact result depends on the direction of the magnetic field and the interaction parameter $I = \frac{\sigma B_0^2 L}{\rho U}$ where B_0, U, L are scales for the magnetic field, the velocity field, and the length, and σ, ρ are the electrical conductivity and density of the fluid, respectively. However, in MHD flows with a weakly conducting fluid (e.g. sea water or ionized gas) the induced magnetic and electric fields are negligible. Therefore in order to affect the flow an externally imposed electric field is necessary, and this is the case of Electro-Magneto-Hydro-Dynamics or EMHD that we study in this paper. Unlike MHD, however, where the Lorentz force is a body force, in EMHD the Lorentz force is effectively a surface force and the greater it penetrates into the fluid the greater its effect. This is a fundamental and crucial difference between MHD and EMHD turbulence control.

In EMHD flows the magnetic Reynolds number $R_m = \sigma \mu_0 U L$ is low, of the order of 10^{-5} or smaller for seawater, and the only non-negligible Lorentz force is due to the current, i.e. $\mathbf{F}_L \propto \sigma E B$. The corresponding interaction parameter is then $I_a = \frac{\sigma E B L}{\rho U^2}$ and for typical parameters in EMHD control $I_a \leq 1$. It is thus obvious that in EMHD the magnetic and electric fields are not affected by the flow and can be computed using the equations of electrostatics. The Lorentz force can be pre-computed and then introduced in the Navier-Stokes equations at every time step or appropriately corrected for time-dependent behavior in cases the electrodes are turned *on-and-off*. A crucial aspect of modeling the Lorentz force in EMHD is boundary conditions on the magnetic and electric fields on the magnets and electrodes and the rest of the surfaces. The size of the substrates of magnets is important, edge effects are important but also the simple question as to exactly what is to be specified at the surface a potential value or its flux cannot be readily answered.

In this work we present results from a simulation study that started five years ago [10] in numerical modeling of EMHD turbulence control for different electro-magnetic tile configurations. The numerical results seem to be in disagreement with experimental results reported in [6] and [7] and at least one source for those differences should perhaps be attributed to inadequate models for the Lorentz force used in the simulations. Specifically, we address the question of force penetration as a function of the size and spacing of the tiles and we consider other important effects. We then present results from spectral element DNS corresponding to tiles and conditions matching the experimental configuration of [6] where a nominally normal to the surface Lorentz force is produced if a pair of electrodes is placed in a direction perpendicular to a pair of magnets to form the basic electromagnetic tile. An array of such tiles are then used on the controlled surface with some or all of the tiles activated.

II. FORCE MODELING

In order to address the question of the effectiveness of the Lorentz force on flow modification we examine the effective penetration of the force from the surface into the fluid. To this end, we first consider a simple configuration consisted of alternating strips of electrodes and magnets in the streamwise direction. We then consider a different configuration consisted of electrodes and magnets placed perpendicular to each other. We want to examine how different modeling assumptions employed to compute the electro-magnetic fields as well as different configurations affect the force penetration.

Force Penetration

The afore mentioned first configuration was proposed in [1] and was tested experimentally in [3] and numerically in [11]. However, in [2] an ideal case was considered where the electrodes and magnets overlapped. Specifically, the potential equations for the $\vec{E}$ and $\vec{B}$ fields were employed

$$\nabla^2 \Phi_j = 0 \quad (1a)$$

$$\nabla^2 \Phi_B = 0 \quad (1b)$$

with Neumann boundary conditions on the electrodes and magnets of the form

$$-\frac{\partial \Phi_j}{\partial y} = j_y|_{y=0} \quad (2a)$$

$$= j_0 cos(\tfrac{\pi}{2a}x) \quad (2b)$$

$$-\frac{\partial \Phi_B}{\partial y} = -B_y|_{y=0} \quad (2c)$$

$$= B_0 sin(\tfrac{\pi}{2a}x) \quad (2d)$$

$$\Phi_j, \Phi_B \longrightarrow 0 \quad as \quad y \longrightarrow \infty \quad (2e)$$

where a is the width of electrode/magnet and also the distance between electrodes and magnets of opposite polarization (see Figure 1). The exact solution is

$$\Phi_j = -\frac{2a}{\pi} j_0 e^{-\frac{\pi}{2a}y} cos(\frac{\pi}{2a}x) \quad (3a)$$

$$\Phi_B = \frac{2a}{\pi} B_0 e^{-\frac{\pi}{2a}y} sin(\frac{\pi}{2a}x) \quad (3b)$$

The only component of Lorentz force is in the streamwise direction, i.e.

$$F_x = j_z B_y - j_y B_z = \Phi_{j,z}\Phi_{B,y} - \Phi_{j,y}\Phi_{B,z} = -j_0 B_0 e^{-\frac{\pi}{a}y} \quad (4)$$

λ	Dirichlet	Neumann	DN	Mixed
Simulation	1/4	1/2	1/8	1/8
Exact B	1/8	1/2		1/8

Table I: Force penetration length for alternating strips of electrodes/magnets.

which obviously penetrates into the fluid a distance a, half of the distance that both the electric and magnetic fields penetrate.

In practice, however, such a configuration is not possible and instead discrete tiles of magnets and electrodes are used which correspond to approximately constant fields at the surface (see Figure 1).

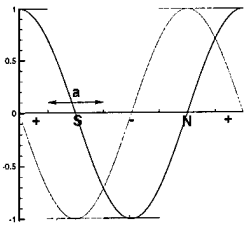

Figure 1: Boundary functions used to describe the fields on the surface of electrodes/magnets. Ideal case is shown by sin and cos functions, and realistic case is shown by piecewise constants.

Solving the same potential equations and using also Neumann boundary conditions in a finite domain of height $2h$ we obtain

$$\begin{aligned}\Phi_E = & \sum_{k=0}^{\infty} C_k [e^{\frac{(2k+1)\pi}{2a}y} \\ & + e^{\frac{(2k+1)\pi}{2a}(2h-y)}] cos\frac{(2k+1)\pi}{2a}x \\ \Phi_B = & \sum_{k=0}^{\infty} D_k [e^{\frac{(2k+1)\pi}{2a}y} \\ & + e^{\frac{(2k+1)\pi}{2a}(2h-y)}] sin\frac{(2k+1)\pi}{2a}x\end{aligned} \quad (5)$$

where

$$\begin{aligned}C_k = & \frac{8j_0 a}{\pi^2}\frac{(-1)^k}{(2k+1)^2} \\ & \times \frac{1}{e^{\frac{(2k+1)\pi h}{a}}-1} cos\frac{(2k+1)\pi}{4} \\ D_k = & \frac{8B_0 a}{\pi^2}\frac{(-1)^k}{(2k+1)^2} \\ & \times \frac{1}{1-e^{\frac{(2k+1)\pi h}{a}}} sin\frac{(2k+1)\pi}{4}\end{aligned} \quad (6)$$

Both the electric and magnetic fields decay exponentially as before in the idealized case, however it is difficult from the expressions above to infer force decay and thus the effective force penetration.

To measure the penetration length we match the force profile from the edge between an electrode and a magnet to the exponential curve $e^{-\frac{\pi}{a\lambda}y}$, where a is the length of a single electrode or magnet, and λ the **force penetration factor**; for the idealized case we have $\lambda = 1$. We then numerically compute the fields and the corresponding Lorentz force and measure λ from different simulations corresponding to different boundary conditions. The electric and magnetic fields we obtained numerically match the analytical expressions above within machine accuracy but it is easier to compute the force numerically.

The results of some of the cases we considered are shown in Table I. Here "Dirichlet" corresponds to using Dirichlet boundary conditions for the potentials, "Neumann" to Neumann boundary conditions, "DN" to Dirichlet boundary conditions for Φ_E and Neumann boundary conditions for Φ_B, and "Mixed" means that for both Φ_E and Φ_B Dirichlet boundary conditions are specified over electrodes/magnets, and Neumann boundary conditions are specified in other regions. Case "Exact B" corresponds to calculating the potential for magnetic $\vec{B}$ field as:

$$\Phi_B(\underline{\mathbf{x}}) = \frac{\mu_M}{4\pi}\oint_S \frac{\vec{n'}\cdot\vec{\mathbf{M}}(\underline{x'})dx'}{|\underline{x}-\underline{x'}|} \quad (7)$$

where S is the surface of magnets, $\vec{n}$ the unit normal to S, and $\vec{\mathbf{M}}$ the permanent magnetization. For the calculation in table I, we take the height of the magnet to be 3 times the length of the magnet.

Edge Effects

The functions one specifies on the boundary could also play an important role in the final force distribution. For example, even if we specify constant values of the potential or its flux on the magnets or electrodes it is important to account for edge effects associated with the finite size of the electrodes and magnets. To obtain an approximate measure of such an effect we calculated the Lorentz force using three different functions on the boundary. The first one is constant, the second one is a 4th order polynomial which is zero at the edges, and the third one is a function with 50% value increase near the edges (see Figure 2).

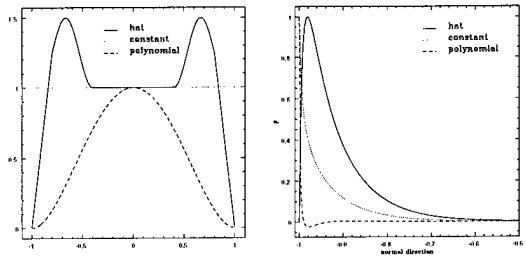

Figure 2: LEFT: Functions used for boundary conditions; RIGHT: Lorentz force profiles corresponding to three different boundary functions.

We see in Figure 2 that the force profile (taken at an electrode/magnet edge) is quite different for the three cases and that the corresponding penetration length is also very different.

Substrate Effects

From equation (7) we see that the exact dimensions of the magnets could also influence the force penetration. For the simplification of a two-dimensional magnet that we consider we can vary the cross-section of the magnet corresponding to different aspect ratios $\alpha = \frac{height}{a}$ and use different α values in equation (7).

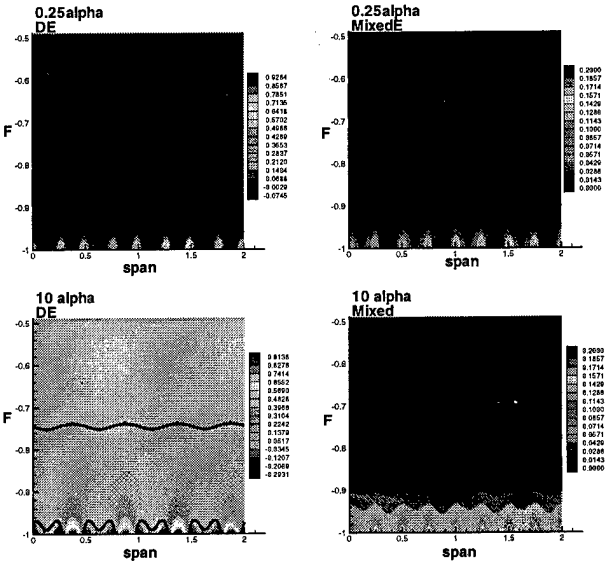

Figure 3: Force contour and 1% contour line for streamwise tiles with $a = 0.5$.

In Figure 3 we see that for different values of α the force distri-

bution and the shape of 1% contour line (defining an approximate penetration length) can vary substantially.

General Tile Configurations

The results presented so far are for tiles of alternating electrodes and magnets all in the same direction and suggest that the maximum force penetration length is a, i.e. the size of the electrodes, and such penetration can hardly be achieved for realistic conditions. We examine next general electromagnetic tiles where the electric and magnetic fields are "nominally" perpendicular to each other. Such tiles have been used in experimental studies reported in [6], [8], [9]) and [5].

The first computational work was reported in [10] for the tiles shown in Figure 4. With such configurations, the Lorentz

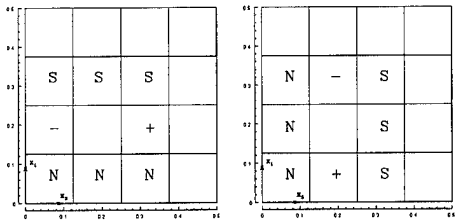

Figure 4: LEFT: Tile 1; RIGHT: Tile 2. We assume that the flow is in the x_1 direction.

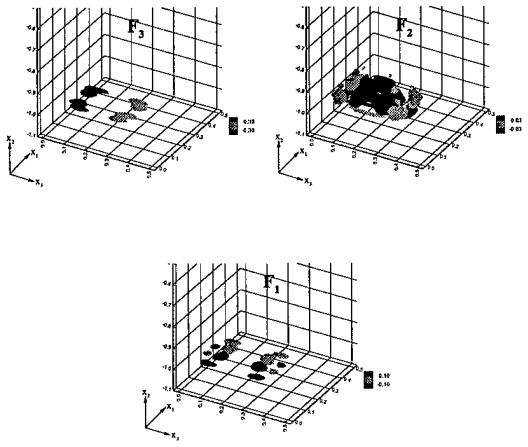

Figure 5: Force contours for Tile 1. Dirichlet boundary conditions are used in computing the electric and magnetic fields.

force field generated is strongly three-dimensional as shown in Figure 5. It is interesting to note that the maximum magnitude of the *normal* force F_2 is approximately one order smaller than the larger *horizontal* force component. This distribution corresponds to prescribing Dirichlet conditions for the magnetic and electric potentials. However, if we instead prescribe Neumann conditions we obtain a force distribution with magnitudes approximately the same for all three components. We will discuss this comparison in some more detail later.

For these general tiles, we have more than one length scales to consider such as the spacing of electrodes and magnets as well as their sizes. We consider next some other configurations with the objective to investigate the effect of such parameters on the overall force penetration. Figure 6 shows the footprint of normal Lorentz force component on the bottom wall. The upper left plot corresponds to Tile 2; the upper right plot shows a case in which the two electrodes are much closer together; the lower left plot shows a case using two-dimensional magnets; and the lower right plot shows a tile configuration designed at Naval Underwater Warfare Center [4]. The results for the four cases are obtained by solving the Laplacian equation for Φ_E and Φ_B using Neumann boundary conditions. We see that the force distribution is different for different cases but it is directed towards the surface

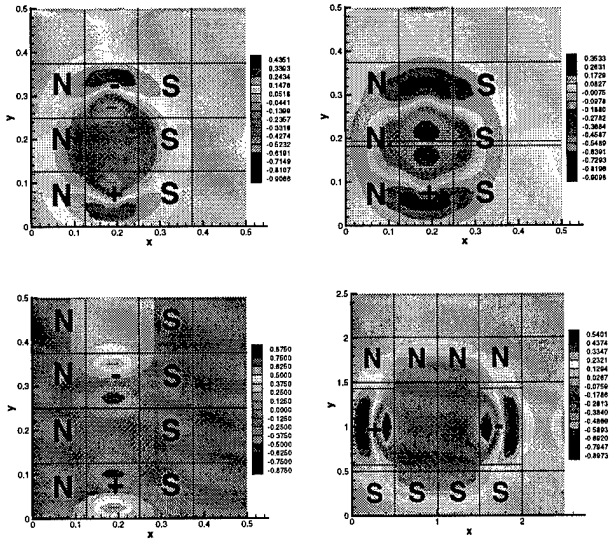

Figure 6: Footprints of normal Lorentz force component.

λ	D	N	DN	Mixed
Simulation	1	1	1	2
$2D$ magnets	1	1	1	2
Close electrodes	1	1	1	1
NUWC	1	1	1	1

Table II: Force penetration parameter for general tiles corresponding to different boundary conditions. The larger the parameter λ the larger the force penetration.

at the center of each tile. The 1% iso-surface of F_{normal} resembles a dome over the center of the tile. We have summarized the results in terms of the penetration parameter λ by matching the decay of F_{normal} to $e^{-\frac{\pi}{a\lambda}y}$, where a is the maximum of the distance between the edges of two electrodes and that between edges of two magnets.

III. DIRECT NUMERICAL SIMULATIONS

We have performed spectral element simulations of a channel turbulent flow with one wall (the lower) covered with electromagnetic tiles as shown in Figure 7. Details of the simulation as well as extensive validation with standard benchmarks can be found in [10]. Here we summarize some representative results (see table III).

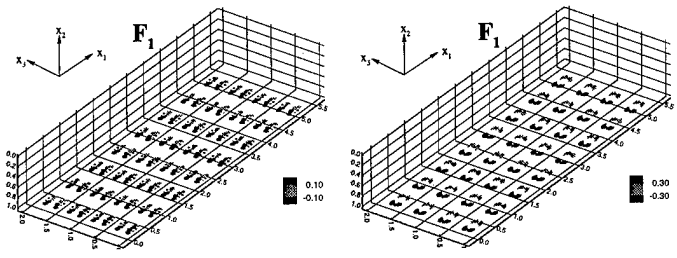

Figure 7: Streamwise component of Lorentz force for LEFT: Tile 1; RIGHT: Tile 2

Static Control

We first performed simulations with all tiles permanently activated; the initial conditions corresponded to a fully-developed turbulent flow when the Lorentz force was turned on. In Figure

Case	$I_{applied}$	E	B	$Re_\tau(l)$	$Re_\tau(u)$
no control	none	none	none	145.7	143.7
Tile 1	1.1	100V/m	0.2T	162	148.4
Tile 2	1.1	100V/m	0.2T	152	146.1

Table III: Summary of the cases studied using electro-magnetic tiles on the lower wall of a canonical channel.

8 we present the drag force on the controlled wall as a function of time for both types of tiles we discussed earlier and compare them with the uncontrolled case. We see that the averaged drag value is higher for the Tile 1 configuration than for the Tile 2. When we plot the instantaneous streamwise vorticity field (Figure 9, we see that the value of ω_x is larger for Tile 1 than for Tile 2 corresponding to larger source of vorticity ($\nabla \times F_3$) and consequently larger drag force.

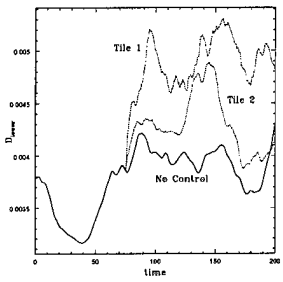

Figure 8: Drag history for Tile 1 and Tile 2.

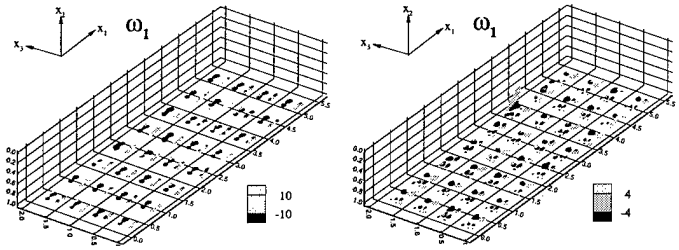

Figure 9: Streamwise vorticity for run using LEFT: Tile 1; RIGHT: Tile2.

Simultaneous Pulsing Control

Next we investigated the drag history for conditions corresponding to turning the electrodes *on-and-off*. The pulsing signal is as shown in Figure 10. To evaluate the effect that the boundary conditions for the electric and magnetic fields have on the Lorentz force distribution and consequently on turbulence modification, we performed simulations first using Dirichlet boundary conditions, and then using Neumann boundary conditions for Φ_E and Φ_B. In Figure 11 and Figure 12 we present the corresponding drag force histories. The simulation using Neumann boundary conditions predicts a lower averaged drag than the corresponding case with Dirichlet conditions. In fact, the Neumann case gives about 5% drag reduction while the Dirichlet case gives about 2% drag increase.

Four-Phase Pulsing Control

We have also investigated different pulsing patterns including four-phase and polarized-four-phase pulsing (see Figure 13). In the four-phase case, the tiles marked "1" are first activated followed by those marked "2", "3" and "4". Then the pattern repeats back to "1", etc. In the polarized-four-phase case, the only difference is that those tiles marked by negative integers are pulsed with $-\vec{F}$.

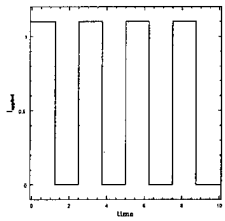

Figure 10: Temporal pulsing pattern used for the time-dependent force case. Shown is the interaction parameter $I_{applied}$ versus non-dimensional time.

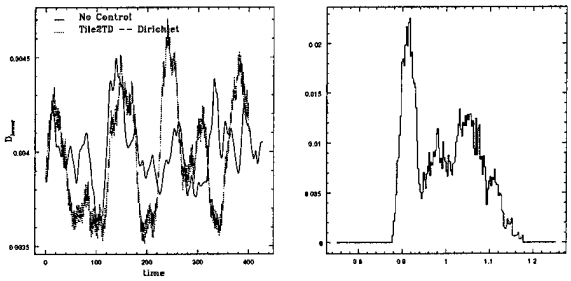

Figure 11: Drag history for Tile 2 with Dirichlet force: LEFT – drag history; RIGHT – drag pdf, normalized with averaged no-control value.

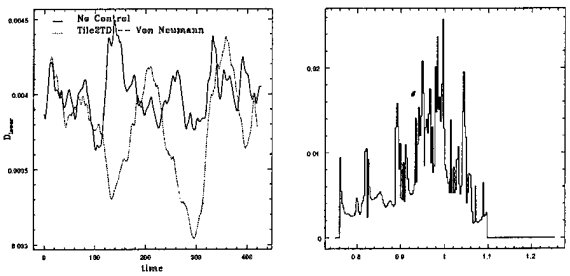

Figure 12: Drag for Tile 2 run with Neumann force: LEFT – drag history; RIGHT – drag pdf, normalized with averaged no-control value.

4	2	4	2	4	2	4	2
3	1	3	1	3	1	3	1
2	4	2	4	2	4	2	4
1	3	1	3	1	3	1	3

4phase

4	-2	4	-2	4	-2	4	-2
3	-1	3	-1	3	-1	3	-1
2	-4	2	-4	2	-4	2	-4
1	-3	1	-3	1	-3	1	-3

4phase.pola

Figure 13: Pulsing pattern: LEFT – four-phase; RIGHT – polarized-four-phase. Tiles with the same (or opposite number) are *on* or *off* at the same time instance.

The drag history over the controlled wall is shown in Figure 14 for the four-phase case and in Figure 15 for the polarized-four-phase case. Neither case exhibits any net drag reduction.

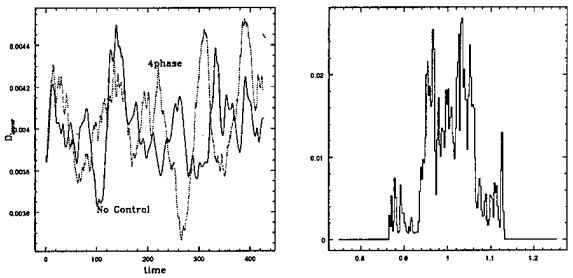

Figure 14: Four-phase: LEFT – drag history; RIGHT– drag pdf. Both are normalized with averaged value of no-control case.

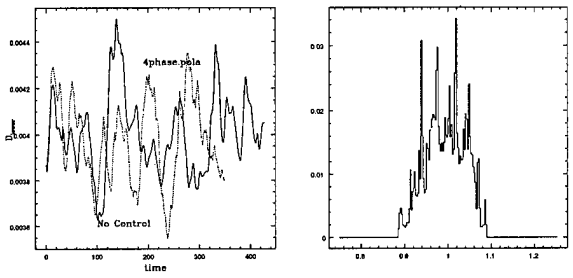

Figure 15: Polarized-four-phase: LEFT – drag history; RIGHT– drag pdf. Both are normalized with averaged value of no-control case.

Structures and Mechanisms

Figure 16 shows the averaged shear stress over a single tile in the four-phase case. In particular, the upper left plot shows

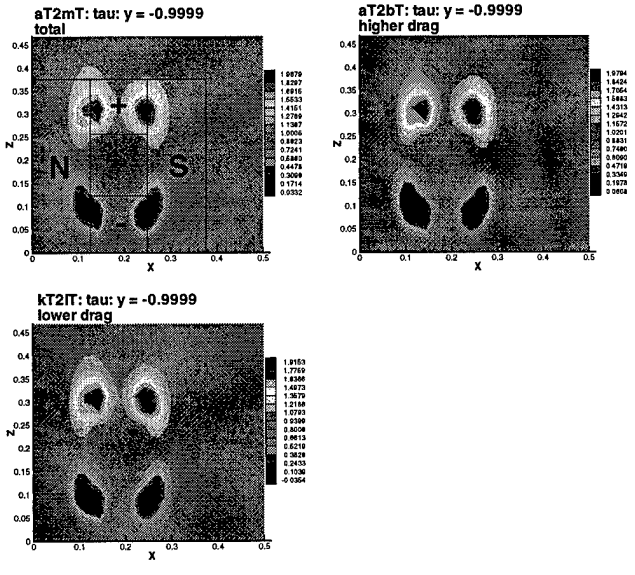

Figure 16: Averaged shear stress over a single tile normalized with the averaged value of no-control case.

shear stress averaged over the entire duration of the simulation, the upper right plot shows shear stress averaged over the first 50 time units which corresponds to higher averaged drag, and the lower left plot shows shear stress averaged over the time period from 250 to 300. It is evident that there are strong pockets of very large shear almost twice the averaged value as well as pockets of very small shear reduced by as much as 97% or even becoming negative during periods of lower than the average drag. The distribution of instantaneous shear stress is shown in Figure 17 and it is very similar with an apparent spatial periodicity. The shear stress value is normalized by the average value of the no-control case. Again, we can see that there are pockets of higher

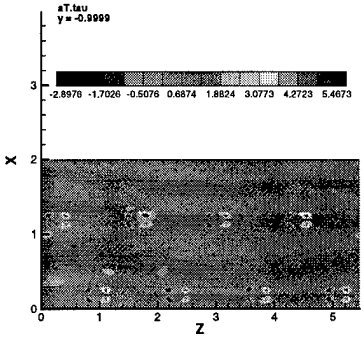

Figure 17: Instantaneous shear stress on the controlled wall.

shear and pockets of lower shear over the region where the tiles are, but most of the region outside tiles shows values like the average shear of the non-controlled case.

To identify flow structures associated with such regions of high and low shear we examine velocity distribution at a streamwise plane that cuts through a pair of low-high shear regions. In Figure 18, we have isolated such a region and magnified the scale to more clearly see such structures. It is clear that drag reduction corresponds to regions of reverse flow, which however are followed by regions of high-speed fluid impinging on the wall (sweep - Q4 events) that induce high shear.

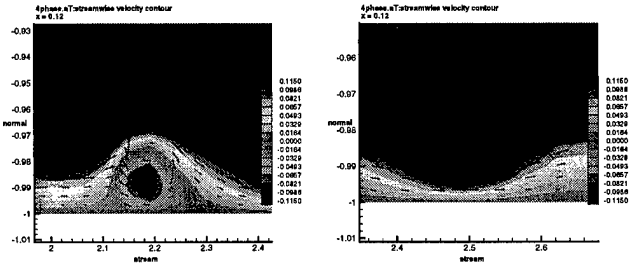

Figure 18: Blowup of previous figure: LEFT – burst; RIGHT – sweep.

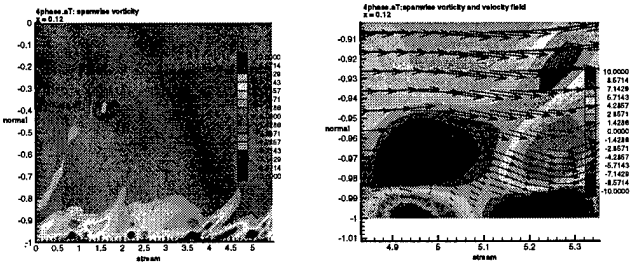

Figure 19: Instantaneous vorticity field: LEFT – contour; RIGHT – blowup.

IV. DISCUSSION

The results of the present work suggest that there is significant variation in the distribution of the Lorentz force due to electro-magnetic tiles that form the controlling surface. The issue is primarily the choice of boundary conditions, especially for the current (or electric field) on the electrode surface. We have seen that prescribing the value of the electric potential on the electrode surface results in a force penetration length quite different than prescribing the normal derivative of the potential, i.e. the normal component of the electric field. Typically, we approximate these surface distributions as constants but that assumption seems to be in contrast with recent experimental results. For weakly ionized gases we can perhaps incorporate Poisson-Boltzmann equations to model the charge and corresponding current distribution around the electrodes but for sea water it is not clear what assumptions to make regarding the current distribution in the immediate vicinity and surfaces of electrodes.

The Lorentz force distribution and the controlling pulsing pattern are key elements in suppressing effectively turbulence in EMHD applications. We have performed here, via spectral direct numerical simulations, several simulations of turbulent channel flow with one of the walls covered by electro-magnetic tiles. From the various configurations we examined we found that if all tiles are permanently and simultaneously activated a drag increase occurs which is higher if the current is in the spanwise direction (TILE 1). This is consistent with the force distribution and associated streamwise vorticity, which is higher in TILE 1. Introducing a pulsing scheme may or may not result in drag reduction and we have presented a case for which a net 5% drag reduction occurs but most cases simulated resulted in net drag increase.

Finally, we analyzed flow structures associated with instances of drag decrease and drag increase and found that pockets of instantaneous flow reversal are responsible for the former while sweep events are responsible for the latter. What has been speculated as two-dimensional "rollers" corresponding to spanwise vorticity ([15], [16], [6], [7]) are in fact local three-dimensional structures. Our current data suggest that attention should be paid to the relative size of structures corresponding to the aforementioned pockets of flow reversal which seem to be of the order of 5 to 10 wall units. That size, however, depends critically on the Lorentz force penetration length.

References

[1] Tsinober A. Turbulent drag reduction versus structure of turbulence. *Proceedings of the 2nd IUTAM symposium on Structure of Turbulence and Drag Reduction.* Zurich, Switzerland, 1989.

[2] Tsinober A. MHD flow drag reduction. *Viscous Drag Reduction In Boundary Layers*, Progress in Astronautics and aeronautics, Vol. 123, edited by D. M. Bushnell and L. N. Heiner.

[3] Henoch C. and Stace J. Experimental investigation of a salt water turbulent boundary layer modified by an applied streamwise magnetohydrodynamic body force. *Phys. Fluids* 1(7):1371, 1995.

[4] Henoch C. Private correspondence.

[5] Bandyopadhyay P. R. and Castano J. M. Micro-tiles for electromagnetic turbulence control in saltwater-preliminary investigations. *Symposium on Turbulence Modification and Drag Reduction*, ASME Summer Meeting, 1996. Invited paper.

[6] Nosenchuck D. M. and Brown G. L. Discrete spatial control of wall shear stress in a turbulent boundary layer. *International Conference on Near-Wall Turbulent Flows, Tempe Arizona*, edited by C. G. Speziale and B. E. Launder (1993).

[7] Nosenchuck D. M. Boundary layer control using the Lorentz force. *http://connector.bsl.prc.com/emtc/emtc.htm.*

[8] Eng T. I. A laminar boundary layer response to an electromagnetic forcing. Master's thesis, Princeton University, May 1995.

[9] Culver H. C. M. An experimental investigation of a laminar boundary layer subject to an applied Lorentz force. Master's thesis, Princeton University, January 1996.

[10] Crawford C. H. Direct numerical simulation of near-wall turbulence: passive and active control. Ph D's thesis, Princeton University, May 1996.

[11] Crawford C. H. and Karniadakis G. E. Reynolds stress analysis of EMHD-controlled wall turbulence.Part I. Streamwise forcing. *Phys. Fluids*, 1(9):788, 1997.

[12] Jackson J. D. Classical electrodynamics. John Wiley & Sons, 1975.

[13] Reed C. B. and Lykoudis P. S. The effect of a transverse magnetic field on shear turbulence. *Journal of Fluid Mechanics*, 89:147, 1987.

[14] Gardner R. A. and Lykoudis P. S. Magneto-fluid-mechanic pipe flow in a transverse magnetic field. Part I. Isothermal flow. *Journal of Fluid Mechanics*, 47:737.

[15] Donovan J. F., Kral L. D. and Cary A. W. Characterization of a Lorentz force actuator. *28th AIAA Fluid Dynamics Conference, 4th AIAA Shear Flow Control Conference.* June 29 - July 2, 1997, Snowmass Village, CO.

[16] Kral L. D. and Donovan J. F. Numerical simulation of turbulence control using electromagnetic forces. *Proceedings of the 1996 ASME Fluids Engineering Conference Forum on Control of Transitional and Turbulent Flows.* July 7-11, 1996, San Deigo, CA.

Fundamental Studies on Active Control of Large Scale Coherent Structures in Channel Turbulence.

Peter L. O'Sullivan and Sedat Biringen,
Department of Aerospace Engineering,
University of Colorado at Boulder,
Boulder, CO 80309-0429.

Abstract

The current work focuses on the spatio-temporal evolution of large scale coherent structures in the turbulent boundary layer of a plane channel both with and without EMHD control. The control actuator design we have used is closely based on designs developed by Bandyopadhyay The aim of this study is to learn more about the correlation of wall shear stress with the passage of large-scale quasi-streamwise vortices which are widely believed to be the key flow structures responsible for strong turbulent ejection events. The heuristic concept behind the microtile designs that we have simulated apparently does not yield a successful drag reduction strategy (for the passive case) and hence we must determine how the applied Lorentz forces are interacting with advecting flow structures (e.g., hairpin vortices). We performed an active control simulation conditioned on the passage of a strong ejection event but obtained no reduction in skin friction. Based on some short-time simulations we found that the flow structures undergo merely a spatial phase-shift when advecting above a single control actuator. During this interaction of the applied Lorentz force with the flow, the Reynolds stress is unchanged. It appears that the applied Lorentz force interacts linearly with near-wall structures and that the structures are simply decelerated or accelerated with little change in their topology.

I. INTRODUCTION

In this paper we are concerned with the problem of controlling turbulent flows. Primarily we are interested in achieving viscous drag reduction although numerous other control objectives may be tackled by a similar approach to the one discussed here. The background for the current work lies in prior attempts by us to realize skin friction reduction via passive control using electromagneto-hydro-dynamic (EMHD) forces in turbulent channel flows of saltwater [1, 2]. Using passive control with both static and temporally pulsed Lorentz forces based upon experimental microtile configurations developed by Bandyopadhyay and co-workers [3] we obtained $\mathcal{O}(1\%)$ net skin friction reductions. However, we also obtained $\mathcal{O}(\pm 10\%)$ localized deviations in time-averaged skin friction in the vicinity of the EMHD microtile actuators. These findings indicate firstly that passive control performs very poorly at low Reynolds numbers (using the designs that we studied). Secondly, the results indicate that an active control scheme may succeed in reducing skin friction given the capability of the microtile actuators to effect significant localized control. In the following sections we briefly summarize the model and numerics for the EMHD control simulations and refer the reader to [2] for greater detail and information on our prior work.

For electrically conducting fluids it is possible to mediate a controlling force *within* the fluid medium. This can be accomplished by imposing external electric and magnetic fields in such a way that their cross product (that is the Lorentz force) acts in a prescribed manner. Saltwater (e.g., seawater) is an example of a weakly conducting fluid (the conductivity is approximately $5 - 6$ Si/m (or Ω^{-1}/m) in SI units). Nevertheless, the Lorentz force which can be generated with electric and magnetic fields of reasonable magnitude is large enough that a viable controlling force may be obtained. One advantage of such a control strategy for saltwater flows is that it may be possible to "tune" the force to act only in certain regions of the flow. The main drawback on the other hand is that the electrical power consumption requirements may be prohibitively large and ultimately offset any fluid dynamic gains (e.g., drag reduction).

A number of recent research efforts have been made into EMHD turbulence control. Nosenchuck and Brown [4] performed experiments by injecting an electrolyte into a non-conducting pure water turbulent boundary layer. They employed a "tile" design and reported a dramatic (almost complete) reduction in turbulence intensity and equally dramatic reduction in skin friction. Their results have as yet to be widely reproduced in general saltwater flows. Bandyopadhyay and Castano [3] modified the tile design by reducing the physical dimensions (to $\mathcal{O}(1)$ mm) and flush-mounting the surface with more "microtiles" per unit area. Once again it has been difficult experimentally to produce reliable, reproducible data [5]. Henoch and Stace [6] performed experiments using a longitudinal strip design with a single component (streamwise) Lorentz force. At low Reynolds numbers they obtained an increase in drag although at high Re they did obtain slight reductions in skin friction. Crawford and Karniadakis [7] performed numerical simulation analogs of the Henoch and Stace experiments and corroborated the slight net increases in skin friction at low Re.

Bandyopadhyay [3] has developed a number of Lorentz force actuators based on silicon microfabrication which are similar to the design of Nosenchuck and Brown [4]. The electrodes and magnets in these "microtiles" have dimensions of $\mathcal{O}(1)$ mm. This new design has a resultant Lorentz force which is three-dimensional (or possibly quasi-two-dimensional). The magnets and electrodes were rectangular and square respectively in his original design, i.e., they are finite in extent and occupy a small fraction of the area of the controlled surface (as opposed to the streamwise strips design). There is a twofold benefit to this type of design. Firstly, the power consumption is reduced compared to that of longitudinal strips. Secondly, the vertical extent of the force, or penetration depth, can be tuned by adjusting the separation between the electrodes. In this way, the length scales of the actuator force can be matched to those of a fully developed turbulent flow. Also, the orientation of the microtiles can be altered to produce dissimilar control schemes based on the differing circulation patterns set up by the re-oriented Lorentz force. Finally, the microtiles can be pulsed in time (and/or phase-sequenced in space). Pulsing has three benefits: reduced power, reduced corrosion of electrode surfaces and the possible favorable resonance with turbulent flow structures.

In a preliminary computational investigation of the effect of these microtiles on a laminar channel flow, Hatay et al. [1] found that the microtile design can generate a secondary vortical flow with feasible input power requirements. At low to moderate electric and magnetic field strengths secondary flows of significant strength were presented. The microtile engendered a flow structure consisting of counter-rotating streamwise vortices above the wall. The induced velocity at the "center" of the actuator was wall-wards which is consistent with the original guiding ideas behind the design. Hatay et al. [1] also showed computationally that when pulsing the Lorentz force, the flow showed a fast response time.

In our earlier work [2] we took the original microtile design of Bandyopadhyay and Castano [3] and performed direct numerical simulations of fully developed turbulence in a canonical channel flow. We studied the effects of EMHD control for this case and for a number of pulsing frequencies in order to investigate Bandy-

opadhyay's hypothesis of a resonance mechanism for the EMHD control based on the length and time scales of the resultant Stokes' layer created by the Lorentz force. We experimented with the electrode spacing to focus and amplify the Lorentz force and we also performed simulations with a 90°-rotated version of the microtile. This last numerical experiment was in the spirit of recent experiments by Jung *et al.* [8] and Laadhari *et al.* [9] which have shown that an oscillatory spanwise wall motion can lead to dramatic reductions in skin friction. We note however that these wall oscillations have no streamwise dependence whereas our simulations do have a sinusoidal dependence on the streamwise direction – i.e., the analogy is strictly in a localized sense. Finally we studied the effect of increasing the magnitude of the Lorentz force.

The outcome of our earlier work was that passive EMHD control was ineffective (for the designs that we used at low Re). However, the reasonably strong localized deviations in skin friction gave us cause for more in-depth study of the spatio-temporal behavior/interaction of the applied Lorentz force with advecting large-scale turbulent flow structures in the boundary layer. The heuristic concept behind the microtile actuator design is that the wall-normal component of Lorentz force inhibits the uplifting motion of typical second quadrant ejection events which characterize turbulent "bursts". It is clear that this argument, while appealing, does not work satisfactorily because it ignores the three dimensionality of the Lorentz force and its (possibly) adverse effects. We note here that, as yet, it is unknown whether or not the microtile Lorentz force does in fact inhibit ejections of low momentum fluid particles.

The first simulation we report on is a long-time active control simulation based on the uv-quadrant detection scheme developed by Alfredsson and Johansson [10]. This simulation serves as an extension of our earlier work. In order to gain insight into the EMHD turbulence control problem we have also performed two short-duration numerical simulations ($\Delta t^+ \approx 32$) of fully developed channel turbulence using identical initial conditions. The first objective is to perform flow visualizations on the uncontrolled case to determine the validity of the hairpin vortex structure as the underlying predominant turbulence structure. By this we mean that there is evidence to support a somewhat more complex picture of the vortex dynamics rather than a picture which contains only isolated, independent hairpins. Secondly, we want to illuminate the instantaneous flow response to the applied EMHD control by observing the modification of advecting coherent structures in the vicinity of the EMHD actuators.

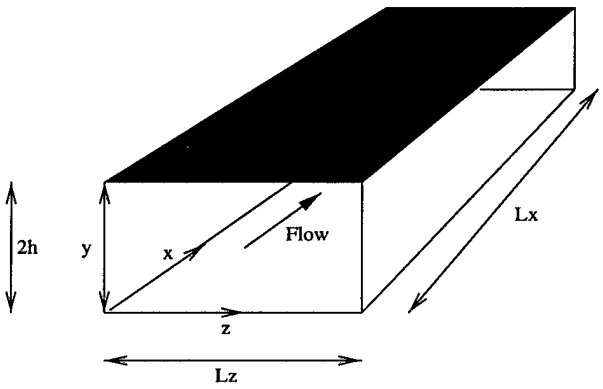

Figure 2: Schematic of flow geometry and co-ordinate system.

II. COMPUTATIONAL MODEL

The channel geometry is depicted in Fig. (2). The Navier-Stokes equations (plus Lorentz body force) are non-dimensionalized by the channel half-height, h, the kinematic viscosity, ν, and the bulk velocity, u_B. Periodic boundary conditions are assumed in the horizontal, (x, z)-, directions and no slip at the upper and lower channel walls. The "box size" is $L_x \times L_z$. The microtile design that we have used is shown in Fig. (3). Notice from this figure that a single tile comprises a diagonally situated ***pair*** of Lorentz force actuators.

The Lorentz force is given by

$$\mathbf{F} = \mathbf{J} \times \mathbf{B}$$

where $\mathbf{J}$ is the current density (measured in Amps/m^2) and $\mathbf{B}$ is the magnetic induction (measured in Tesla). All induced electric and magnetic fields are neglected from the outset but have been verified *a posteriori* to be dynamically inconsequential. In this case we find from elementary EM theory $\mathbf{J}$ in turn is given by

$$\mathbf{J} = \sigma \mathbf{E} \times \mathbf{B} = -\sigma \nabla V \times \mathbf{B}$$

where σ is the electrical conductivity of the fluid measured in Siemen per meter (Si = Ohm^{-1}), $\mathbf{E}$ is the applied electric field and V is the electric potential.

We have invoked the static MHD approximation in which the EM fields are completely decoupled from the fluid velocity and whose time-dependence is taken as steady or instantaneous. From Maxwell's equations we find

$$\nabla^2 V = \nabla^2 B_y = 0$$

which are solved with prescribed Dirichlet data for the microtile distribution of V and B_y. The surface electric and magnetic distributions for V and B_y, respectively, are modelled as smoothed hyperbolic tangent step functions. The remaining components of $\mathbf{B}$ are computed algebraically from Maxwell's equations. Details of the Lorentz force computation can be found elsewhere [1, 2]. The Lorentz force is computed in a pre-processing step assuming periodicity in x and z and then incorporated as a body force in the momentum equations. Note that due to the symmetry (in both x and z) of both the electrodes and magnets in each actuator configuration there is zero net volumetric body force in the x and z directions. That is, the Lorentz force does not induce any spatial mean motion in (x, z).

In Fig. (3) we present a schematic diagram of the microtile design used in this work. A vector plot of the Lorentz force for this tile design is shown in Fig. (4). The plot is taken at a z-location half-way between the magnets of a single actuator. The force field is predominantly wall-ward over the "inner" region of the actuator, i.e., the region between each pair of electrodes. However, one can also clearly see the upward force outside this region especially at the fore and aft edges of the electrodes where the direction of $\mathbf{E}$ is reversed.

III. NUMERICAL METHODS

The surface V and $\mathbf{B}$ fields are non-dimensionalized by a reference voltage, V_0, and magnetic induction, B_0. The resulting non-dimensional incompressible Navier-Stokes equations are then given by

$$\nabla \cdot \mathbf{u} = 0$$

and

$$\partial_t \mathbf{u} + \nabla \cdot \mathbf{u}\mathbf{u} = F(t)\delta_{i1} - \nabla p + \frac{1}{Re_B}\nabla^2 \mathbf{u} + N_B\,(\mathbf{E} \times \mathbf{B})$$

where $Re_B = u_B h/\nu$, $F(t)$ represents the force required to maintain a constant mass flux throughout the flow domain and the interaction parameter, N_B, is given by

$$N_B = \frac{\sigma V_0 B_0}{\rho u_B^2}.$$

The corresponding interaction parameter scaled on inner variables we denote by N_τ with

$$N_\tau = \frac{\sigma V_0 B_0}{\rho u_\tau^2} = N_B (u_B/u_\tau)^2.$$

Our code employs a de-aliased Fourier Galerkin method in (x, z) and fourth order accurate finite differences in y (on a cosine-stretched grid). The code also uses a staggered mesh in y in order to

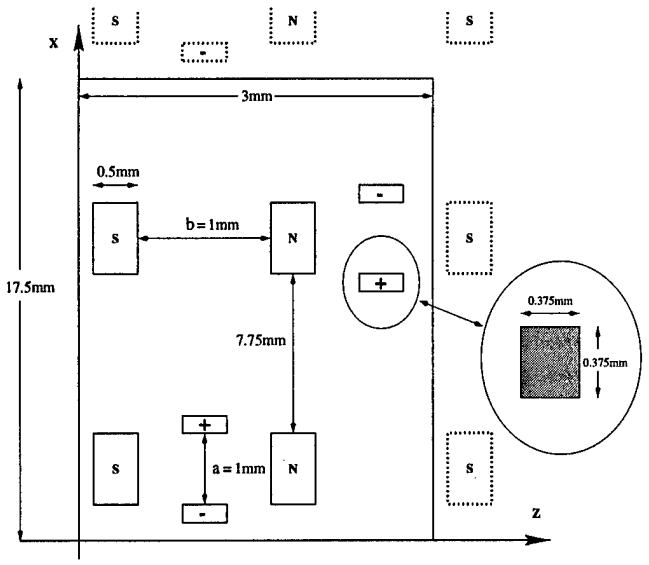

Figure 3: Schematic of microtile dimensions (millimeters) for EMHD control case (not to scale). A single tile consists of a pair of diagonally situated actuators.

keep divergence errors to less than 10^{-10} within each cell. The spatial resolution was $64\times80\times96$ points in the streamwise, wall-normal and spanwise directions, respectively, The solution was advanced in time using the second order accurate Adams-Bashforth/Crank-Nicolson scheme with $\Delta t = 0.0025h/u_B$.

The microtile dimensions and channel height are based closely on typical experimental specifications except that the electrode spacing has been reduced in order to amplify the Lorentz force. The dimensions L_x and L_z were then chosen so that the non-dimensional box lengths would be close to $2\pi \times \pi$ which was found to be sufficiently large for spatial de-correlation. These dimensions lead to the non-dimensional box size of approximately $(6.09 \times 2 \times 3.13)$. The Reynolds number was set to $Re_B = 3,140$ (constant mass flux) with resultant $Re_\tau \approx 196.6$ and $Re_Q \approx 3,689$. In terms of wall unit scaling, $y^+ = yu_\tau/\nu$, the dimensions of the domain are $(1197\times393\times598)y^+$. The horizontal grid resolution is $(\Delta x^+, \Delta z^+) \approx (19, 6)$ and $(\Delta y^+_{min}, (\Delta y^+_{max}) \approx (0.15, 7.72)$. The simulations we report on were initialized with a fully developed turbulent flow field in each case.

IV. EVENT DETECTION

Alfredsson and Johansson [10] developed an experimental technique for reliably and robustly detecting turbulent "events" in which the uv-quadrant analysis is performed on single point X-wire data. We have performed a similar analysis but rather using instantaneous spatial data. Their uv-quadrant analysis detects an event whenever

$$-u'v' \geq Hu_{rms}v_{rms}$$

where H is a positive constant threshold and u', v' are the streamwise and wall-normal fluctuating velocities. Alfredsson and Johansson performed this test at a height of $y^+ \approx 50$ above the wall. This detection scheme isolates strong second (Q2) and fourth quadrant (Q4) turbulent signals. In the current study we have found $H = 5$ (compared with $H = 4$ of Alfredsson and Johansson) to be a good cut-off for "strong" events and we also located our detection "probe" at $y^+ \approx 30$. Note that the values for u_{rms}, v_{rms} were obtained in prior fully turbulent steady state simulations.

In Fig. (5) we have plotted the spatial distribution of the top ten events detected using this scheme. The rank of each event is shown alphabetically with A denoting the strongest event. Event I

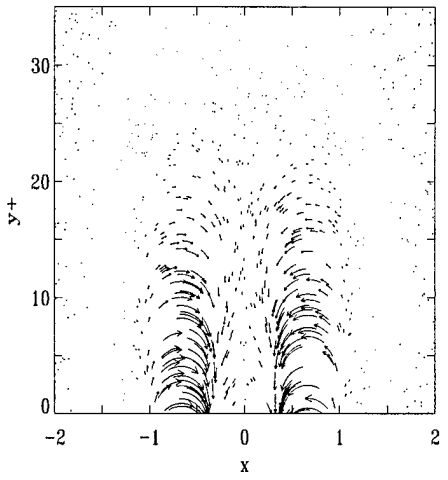

Figure 4: Vector plot of the non-dimensional Lorentz force for the UV cases along the centerline of a single actuator. The z-location of this view is half-way between the magnets. The x-coordinate is measured in millimeters while the vertical coordinate is in wall units. $N_B = 0.0894$.

is the only Q4 event among these ten. The striking feature of this figure is that six of the events are closely aligned in the spanwise direction.

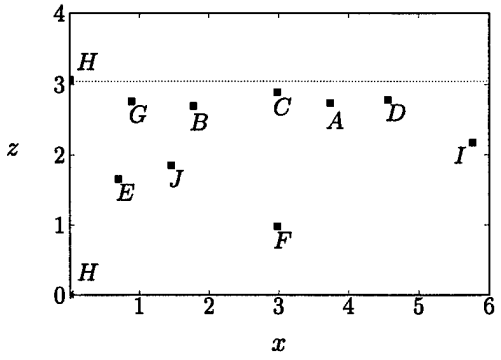

Figure 5: Turbulent events detected with the uv-quadrant scheme for an instantaneous flow realization at $Re_B = 3,140$. The letter beneath each symbol denotes the ranking of each event with A being the strongest. Note that event I is a Q4 event and that H is shown twice because of periodicity. The dotted line indicates the spanwise period of the computational domain.

In ranking the detected events we recursively searched the flow field for the maximum Reynolds stress and then excluded a control volume centered around this point from subsequent event detection searches. We chose the dimensions of the control volume based on the length scales of typical bursts obtained by Alfreddson and Johansson. At $Re_\tau \approx 197$ this gives a control volume with dimensions $206 \times 53 \times 154y^+$ in x, y, z. The individual control volumes for detected events are permitted to overlap. From Fig. (5) we see that with this detection scheme, e.g., events A, C and D are separated by approximately 0.8 units in x which is approximately $160y^+$. We have measured the advection speed of these events to be around $9.5u_\tau$ which leads to a temporal separation of $17t^+$ ($t^+ = tu_\tau^2/\nu$). Alfredsson and Johansson found the duration of uv peaks to be approximately $2 - 4t^+$ although this time scaled neither with inner nor outer variables. The low Reynolds number in the current DNS also does not permit us to conclusively say that events A, C and D are distinct based on just the uv peak separations.

V. VORTEX GROUPS

In Fig. (6) we have plotted three side views of the perturbation vorticity magnitude at the same instant as that of Fig. (5). The middle view is aligned at the same spanwise location as the strongest Q2 event, denoted by A in Fig. (5). The streamwise extent in the figures is the total computational domain size, L_x. The vertical extent is $2.5y^+ \leq y \leq 54y^+$ - we have excluded the wall vorticity from the images for clarity. The vertical direction has also been stretched by a factor of 3 in order to see the structures more easily. In the middle image ($z^+ = 0$) we can see three closely situated inclined vortices near $x^+ = 0$ (by vortices, in this context, we merely mean regions of high vorticity magnitude which *might* be, and probably are, vortices in the more accurate sense of the word). The approximate distance between these structures in this image is $125y^+$. The two close spanwise neighbors of this middle view are presented to give some idea of the spatial structure of these vortices. The lowest image (at $z^+ = +13$) demonstrates even more convincingly that these inclined vortices are advecting as a group. This bottom image in particular shows that these inclined vortices can in fact lie above one another (e.g., the two structures at the left of the bottom image). In this case, the mutual vortex induction will be strong enough to link the two structures.

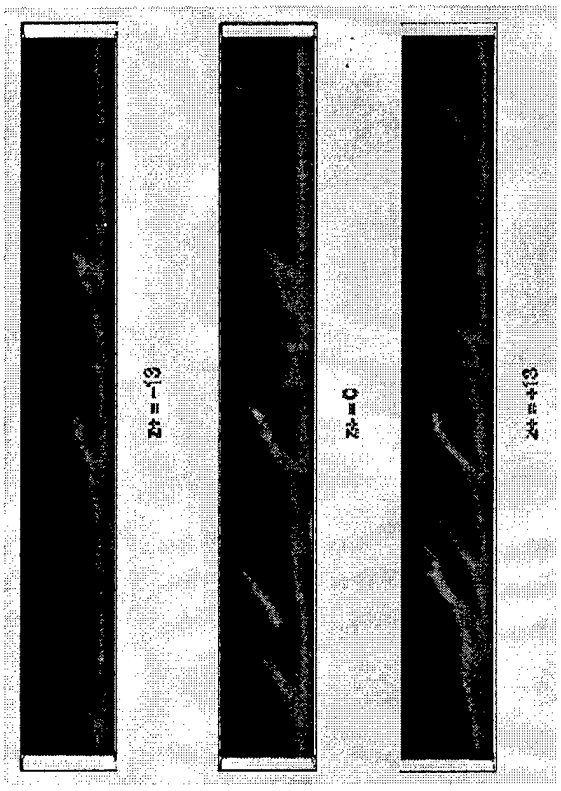

Figure 6: Three side views of perturbation vorticity magnitude during a characteristic burst event. The middle view is at the spanwise location of maximal ejection strength; the streamwise location is in the center of the figure. The top and bottom plots are equivalent side views at spanwise locations of $z = \pm 13y^+$ from the center plot, respectively.

If two hairpin vortices occur in close streamwise proximity at the same spanwise location then the mutual induction will likely lead to the classic leap-frogging interaction. If three or more hairpins are aligned in the streamwise direction then the "sandwiched" vortices will be largely in equilibrium due to the equal and opposite vortex induction of the leading and trailing hairpins. The leading hairpin will be spatially compressed and retarded while the trailing hairpin will be spatially enlarged and accelerated just as in leap-frogging. In addition to the Biot-Savart induction the mean flow itself will add to this effect by simple differential advection in the wall-normal direction. There is visual evidence in the bottom image of Fig. (6) for this scenario: the three inclined structures at the left are such that the trailing vortex is "taller" than the leading vortex. In summary, we infer that a turbulent burst is related to the passage of a group of vortices which act in concert rather than as separate structures. A more quantitative measure of this assertion would be given by computing the two point correlations for a large number of similar bursts. This calculation is left for future work for now. If indeed hairpins advect in groups then this more complex structural arrangement will have ramifications for turbulence control. In particular, actuators designed with the aim of introducing equal and opposite vorticity at the wall (via EMHD or any other means) will need to address the issue of complex near-wall quasi-streamwise vortices (involving overlaid, intertwined or braided streamwise vortices from the legs of a group of hairpin vortices).

V. ACTIVE CONTROL

Using the event detection scheme described in section we performed a long time integration employing an (artificial) active control scheme. That is, we activated a single EMHD actuator if and when a strong Q2 event was detected at some distance upstream. The EMHD actuators are those shown in Fig. (3) and the interaction parameter was set at $N_B = 0.089, N_\tau = 22.04$ ($\sigma = 6, V_0 = 6, B_0 = 0.6$) just as in previous passive control simulations [2]. Whenever a Q2 event was detected (sampling every $4t^+$ approximately), the nearest downstream actuator was turned on while all other actuators were turned off. The purpose of this simulation was to see if an active control scheme would yield any improvements over the previous passive case. In Fig. (7) we have plotted the running time average velocity gradient at the lower controlled wall. The angled brackets denote an average over the x and z directions and the previous $770t^+$. The total duration of this run was approximately $9,700t^+$ but we have omitted the early transient data from the figure.

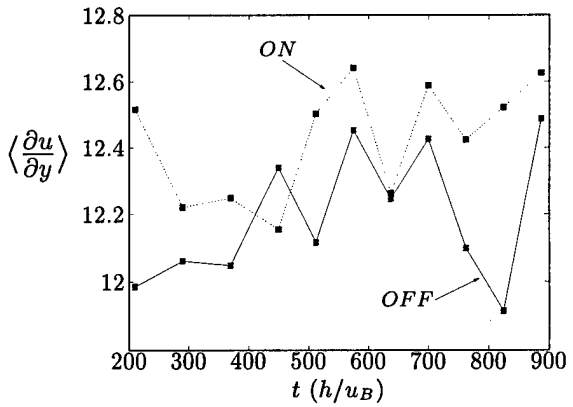

Figure 7: Running time average velocity gradient at lower (controlled) wall with active control scheme.

From this figure we can see clearly that there is no reduction in mean wall shear and possibly in fact a slight increase. This result is surprising given our earlier findings of small but consistent skin friction reductions using passive control with similar EMHD actuator designs. In the following sections we explore in more depth the flow response to the applied control in order to better understand why the control is not achieving drag reduction.

VI. INSTANTANEOUS FLOW RESPONSE

Given the outcome of the active control simulation described above we performed a short-duration simulation with EMHD control turned on statically while again performing the spatial event detection scheme. The x, z-locations of detected events with control ON turned out to be extremely similar to those with control OFF. However, a certain number of the detected Q2 events did undergo a significant alteration when control was applied. In Fig. (8) we have plotted the x-location of the strongest Q2 event versus time with control both ON and OFF. For the uncontrolled case we see a characteristic linear advection but in the controlled case we observe a short deceleration/acceleration of the peak Reynolds stress location. Subsequently the two event locations coincide almost identically.

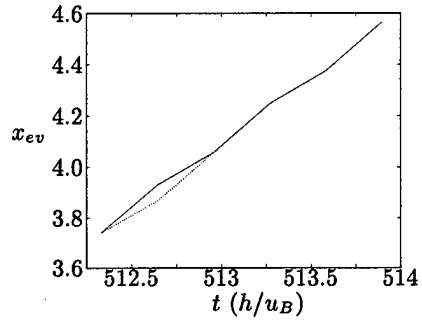

Figure 8: Streamwise location of strongest Q2 event *vs.* time for short-duration simulations. Solid curve is for control OFF; dotted curve is for control ON (static force).

For this pair of (comparable) events we also saved records (in time) of the instantaneous fluctuation velocity which is shown in Fig. (9). We see that at the second detection time the v' velocity is decreased by 30% while the (negative) u' velocity is increased in magnitude by over 40%. In spite of these substantial modifications to the flow the Reynolds stress remains approximately constant and ultimately the controlled flow rejoins the uncontrolled flow. Furthermore, we have performed flow visualizations of the vortical structures in both the uncontrolled and controlled flows in the comparable control volumes for similar detected events. In the visualizations we have found that the vortical structures in the buffer region are essentially unchanged in shape but are shifted in the streamwise direction. There is some alteration in vorticity in the viscous sublayer in the vicinity of the EMHD actuator. Overall, based on this and several other visualizations of event structures, we believe that the current EMHD actuators are not significantly changing the large-scale vortical structures but rather inducing a streamwise phase shift in space as the structures advect above the control actuator.

In Fig. (10) we have plotted the percentage change in skin friction for a spatial region centered about one single turbulent ejection both with and without EMHD control. The detection location (of locally maximal Reynolds stress) is at $(x^+, z^+) = (0, 0)$ in the figure. We can see a very striking pattern of skin friction modification in the left hand side of this figure where we also see three very clear "footprints" of the EMHD actuators. We note that this footprint is very similar to the long-time average footprints obtained in our earlier work [2]. This instantaneous image of the local flow modification reinforces two aspects of the current control actuator under study. First, the actuators can effect a significant localized flow modification: the maximum reduction in local wall shear stress between these two equivalent ejection events is -22% and the maximum increase is $+27\%$. Second, the average change in wall shear between these two events (averaged over the control volume) is extremely small at -0.2% which is statistically insignificant.

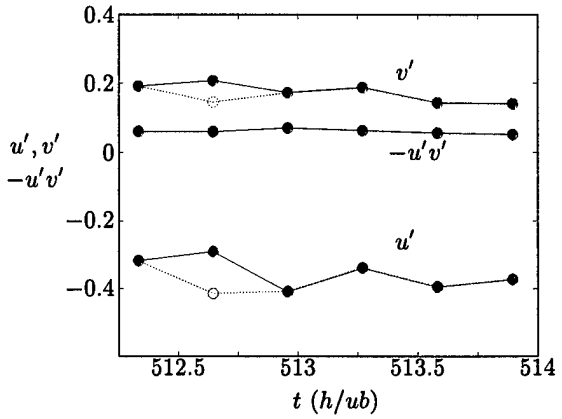

Figure 9: Fluctuating streamwise and wall-normal velocity and Reynolds stress for strongest detected Q2 events with control OFF (solid, filled) and ON (dotted, unfilled).

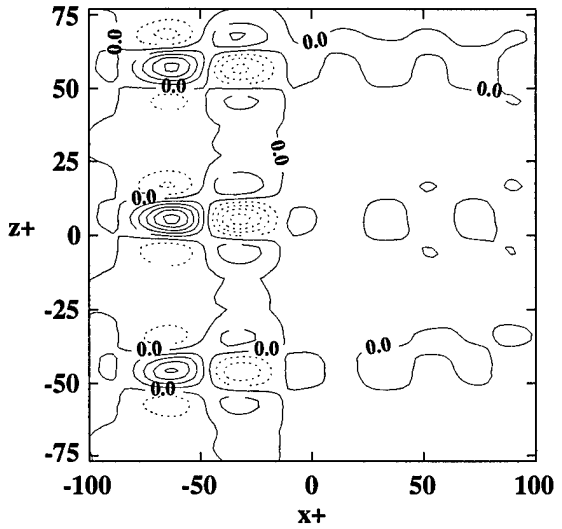

Figure 10: Contours of percentage change in skin friction for control OFF/ON for a single turbulent ejection event. Contour spacing is 5% and negative contours are indicated with dotted curves. The x, z axes are given in wall units centered about the detection location.

VII. CONCLUSIONS

We have implemented a rational active control scheme using EMHD microtile actuators with no reduction in skin friction. The control activation was based on the uv-detection scheme developed by Alfredsson and Johansson [10]. We have also performed short-duration passive control simulations in order to ascertain the instantaneous flow response to the applied Lorentz force controllers. We discovered that the particular design we have investigated induces a deceleration/acceleration phase shift during the advection of strong Q2 ejection events above the EMHD actuators. We compared time series for control volumes centered around the location of a number of ejection events both with and without EMHD control. Despite the fact that the control had a significant effect on the fluctuating velocity this effect was subsequently reversed with essentially no change in Reynolds stress during the passage of the ejection structure. Although significant localized deviations in skin friction on the order of $15 - 18\%$ were found to occur and spatial mean skin friction within a control volume could change by $\pm 4 - 5\%$

we observed almost no net change in (spatial) mean wall shear. In flow visualizations we did not observe significant changes in streamwise vortical structure apart from the spatial phase shifting. These results together with the antisymmetric spatial Lorentz force distribution (of the design considered) leads us to conclude that the control is ineffective. The reason appears to be that the applied Lorentz force interacts linearly with passing flow structures and then reverses the interaction as the structure advects above the downstream half of the actuator. A possible improvement in the design might be to reverse the polarity of the electrodes during this second half of the passage above an actuator. This should have the effect of reinforcing the initial effect of the actuator rather than undoing it.

At a more fundamental level the work we have described here indicates that a somewhat more complex picture of vortex dynamics in the boundary layer is appropriate. Although hairpin vortices are ubiquitous they appear to occur in groups very frequently. Therefore a rational control scheme should most likely be predicated on controlling these trains of hairpin vortices rather than single isolated and independent vortices. Further research needs to be done to substantiate this picture more firmly and possibly develop a better rational control principle.

Finally, we surmise that in view of this more complex vortex structure of turbulent bursts it may be more prudent for EMHD control to utilize a simpler Lorentz force actuator than the one considered here. For example, it is possible to take the uni-directional force actuator developed by Henoch and Stace [6] but to use finite electrodes and magnets rather than producing a global Lorentz force in the streamwise direction. In this approach it would be possible to generate a highly directional Lorentz force that could be used to act directly upon the low speed streaks (since the Lorentz force has an exponential decay with y). The persistence of low speed streaks is well documented [11], a fact which may be exploitable for EMHD control in particular. An analogous spanwise force could also be applied which could be used to produce oppositely-signed streamwise vorticity conditioned upon the occurrence of aligned, strong near-wall streamwise vorticity. Both of these methods would bypass the three dimensional character of the Lorentz force generated by the microtile designs that we have studied here. This simpler but localized EMHD actuator based on a single component Lorentz force will be the focus of a future investigation.

ACKNOWLEDGEMENTS

We wish to thank Dr. Patrick Purtell for his continued interest in this research. We are also grateful to Dr. Bandyopadhyay at NUWC Division, Newport, RI for many lively and fruitful discussions related to this research. This work has been supported by the Office of Naval Research under grant number DOD N00014-95-1-0419. Partial funding was also available from NSF Grant No. ECS-9725504. Computations were performed on a Cray C916 at the US Army Corps of Engineers, Waterways Experiment Station, Vicksburg, MS.

References

1. F. F. Hatay, P. L. O'Sullivan, S. Biringen & P. R. Bandyopadhyay. Numerical Simulation of Secondary Flows in Channels Driven by Applied Lorentz Forces. *AIAA J. of Thermal Physics and Heat Transfer*, **11** (3) pp.446–453, 1997.
2. P. L. O'Sullivan & S. Biringen. Direct Simulations of Low Reynolds Number Turbulent Channel Flow with EMHD Control. *Physics of Fluids*, **10** (5) pp.1169–1181, 1998.
3. P. R. Bandyopadhyay & J. M. Castano. Micro-tiles for electromagnetic turbulence control in saltwater–preliminary investigations. In *Symposium on Turbulence Modification and Drag Reduction*, ASME Summer Meeting, 1996. Invited paper.
4. D. M. Nosenchuck & G. L. Brown. Discrete Spatial Control of Wall Shear Stress in a Turbulent Boundary Layer. In R. M. C. So, C. G. Speziale & B. E. Launder, eds. , *Near-Wall Turbulent Flows*, pp. 313–343. Elsevier, 1993. Proceedings of an International Conference on Near-Wall Turbulent Flows held at Arizona State University, Tempe, AZ, March 15-17, 1993.
5. P. R. Bandyopadhyay, 1997. (Private communication).
6. C. Henoch & J. Stace. Experimental investigation of a salt water turbulent boundary layer modified by an applied streamwise magnetohydrodynamic body force. *Physics of Fluids*, **7** (6) pp.1371–1383, 1995.
7. C. H. Crawford & G. E. Karniadakis. Reynolds stress analysis of EMHD-controlled wall turbulence. Part I. Streamwise Forcing. *Physics of Fluids*, **9** (3) pp.788–806, 1997.
8. W. J. Jung, N. Mangiavacchi & R. Akhavan. Suppression of turbulence in wall-bounded flows by high-frequency spanwise oscillations. *Physics of Fluids* **A**, **4** (8) pp.1605–1607, 1992.
9. F. Laadhari, L. Skandaji & R. Morel. Turbulence reduction in a boundary layer by a local spanwise oscillating surface. *Physics of Fluids*, **6** (10) pp.3218–3220, 1994.
10. P. H. Alfredsson & A. V. Johansson. On the detection of turbulence-generating events. *Journal of Fluid Mechanics*, **139** pp.325–345, 1984.
11. C. R. Smith & Metzler. The characteristics of low-speed streaks in the near-wall region of a turbulent boundary layer. *Journal of Fluid Mechanics*, **129** pp.27–54, 1983.

Interactive Electro-Magnetohydrodynamic Control of Near-Wall Streaks

Stephen R. Snarski
529 Audubon Rd., Kohler, WI 53044

An electro-magnetohydrodynamic transducer array that can be operated in both passive (electromagnetic induction velocity sensor) and active (magnetohydrodynamic force actuator) modes to detect and subsequently manipulate the turbulent velocity field associated with near-wall, high- and low-speed streaks is presented. By examining the physics of the passive and active modes, it is shown that both modes are characterized by the same spatial field function which can be tuned to respond directly to the characteristic spanwise wavelength of the near-wall streaks. Because the near-wall streaks are the most reliable indicator of the preburst turbulence production process, this device would be an ideal candidate for use in an interactive (feedback) turbulence control scheme in electrically conducting (e.g., seawater) turbulent boundary layers. Experiments are being planned to validate the predicted transducer characteristics and to initiate the development of a feedback control algorithm.

1. INTRODUCTION

Electromagnetic turbulence control has recently become an active area of research in pursuits to reduce drag in seawater applications (Nosenchuck and Brown [1], ONR [2], Bandyopadhyay [3], Henoch and Stace [4], Crawford and Karniadakis [5]). Due to the intrinsic relationship which exists between electric and magnetic fields and moving conducting fluids, these approaches attempt to reduce drag by globally applying an electromagnetic (or magnetohydrodynamic) body force to the flow to alter the fundamental structure of the boundary layer. Although such global control strategies have revealed overall reductions in turbulence levels and drag, the net savings after the cost of the required energy expenditure is considered makes these approaches impractical.

Another equally active area of research is interactive turbulence control. Rather than apply some global forcing function to the boundary layer, these approaches attempt to reduce drag by selectively targeting, sensing, and subsequently manipulating some turbulent structure or event in the flow through the use of a closed-loop feedback control system which attempts to maintain an unstable system in a stable state by making small time-dependent adjustments (based on pertinent measurements of some kind) to one of the parameters governing the system's behavior (Gad-el-Hak [6], Moin and Bewley [7]). Proposed control schemes typically involve the use of a large surface matrix of micro-machined sensors and actuators (microelectromechanical systems, or MEMS) to sense some targeted wall perturbation (e.g., fluctuating wall pressure or wall shear transducers) associated with turbulence generating events near the wall and to subsequently modulate the event with an actuator located downstream from the sensor before it breaks down (e.g., resonant membranes, micro-flaps, aspiration ports). Although recent experiments conducted with wall-based shear sensors and a resonant membrane have shown promising reductions in fluctuating velocity and wall pressure rms levels (Rathnasingham and Breuer [8]), actuator frequency response and power consumption is considered a major limiting factor for practical application of real-time MEMS-based control schemes. Researchers at Stanford have recently, however, reported the development of MEMS-based actuators with millisecond rise times and power consumptions in the milliwatt range (Kumar and Reynolds [9]) -- well below the estimated 0.018W per element requirement to break even (Gad-el-Hak [6]). Nevertheless, the inherent mechanical problems associated with using a large matrix of micro-mechanical devices (e.g., mechanical failure, fouling) in harsh seawater environments still needs to be addressed.

Because of the low energy consumption, high frequency response, low fouling potential, and lack of moving parts associated with electromagenetic devices, a natural solution would be to merge the electromagnetic and interactive turbulence control methodologies. Although some attempts have been made to do just that (Bandyopadhyay [3], Meng [10], Singh and Bandyopadhyay [11]), the proposed schemes still rely upon MEMS devices to sense the targeted flow perturbation. Furthermore, these approaches, much like their purely MEMS-based counterparts, rely upon a feedback control methodology which senses a flow perturbation (wall pressure, wall shear) whose correlation and phase relationship to the flow structure being controlled (ejections, sweeps, vortical structures) is only partially understood. As suggested by Gad-el-Hak [6], because the near-wall low-speed streaks are the most visible, reliable and detectable indicators of the preburst turbulence production process (see Section 2), the most natural control scheme would be one which detects low velocity near the wall and then removes (i.e., accelerates) the low-speed region before it breaks down. However, for this approach to be successful, a reliable means to both sense and manipulate the near-wall velocity field is required. This paper is a direct response to this need.

What is proposed and examined in this study is a nonobtrusive electro-magnetohydrodynamic transducer (Snarski [12]) that can be used in both passive (electromagnetic induction) and active (magneto-hydrodynamic force) modes to sense and manipulate the velocity of the near-wall fluid. Because the sensor and actuator functions are combined into a single device that detects and manipulates the same flow variable (i.e., streamwise velocity), a direct coupling exists between the drag reduction methodology and the fundamental near-wall turbulence physics.

This paper is organized as follows. In Section 2, the structure of turbulent boundary layers relevant to this study are reviewed. In Section 3, the physics of both the passive and active transducer modes are described and used to develop a closed form analytical solution for the sensor spatial sensitivity function and actuator force field. The main theme of the paper is in Section 4, which describes the operational characteristics of using an array of such devices for interactive control of near-wall streaks by examining the wavenumber response of the transducer array. Implementation and scaling considerations are also discussed as well as planned proof-of-concept experiments that will be conducted in a laminar salt-water boundary layer with artificially generated streaks. Conclusions are provided in Section 5.

2. TURBULENT BOUNDARY LAYER STRUCTURE AND THE ROLE OF NEAR-WALL STREAKS

In general terms, two types of coherent structures or organized motions can be defined in the turbulent boundary layer (see Snarski and Lueptow [13]). The first are large-scale motions that emanate from the outer portions of the boundary layer, scale with the boundary layer thickness δ, and have an influence across the entire boundary layer. The second is a quasi-cyclical, ordered sequence of events in the near-wall region known as the burst-sweep cycle. Although a complete understanding of the cause-and-effect relationships between the near-wall and outer flow structure is not universally agreed upon (Robinson [14], Kline and Robinson [15]) what is certain is that the majority of turbulence production in the boundary layer occurs during the bursting process. This process, originally visualized and measured by Kline et al. [16], is initially marked by the formation of streaks of relatively low- and high-speed fluid very near the wall as conceptually illustrated in Fig. 1. As the streaks convect downstream, the low-speed regions gradually lift away from the wall until at some downstream location where they move abruptly away from the wall in what is termed an ejection. At this point, the low-speed streaks undergo rapid oscillations that ultimately lead to a complete break-up of the structure known as bursting. Following the burst, an in-rush or sweep of fluid toward the wall has been observed, hence, the name burst-sweep cycle. It is generally believed that the near-

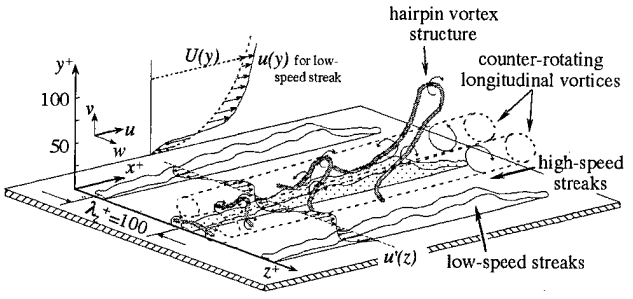

Figure 1. Conceptual illustration of the near-wall streaks and vortex structures beneath a turbulent boundary layer.

wall streaks are the consequence of a redistribution of streamwise momentum resulting from the formation and growth of hairpin vortex structures and counter-rotating vortices near the wall

The ensemble averaged character of the near-wall streaky structure is conceptually illustrated in Fig. 1. Indicated in the figure are the coordinate system $\boldsymbol{x} = \{x, y, z\}$ and the corresponding components of the turbulent boundary layer velocity field $\boldsymbol{u} = \{u, v, w\}$ consisting of mean (time-averaged) and fluctuating (zero-mean) quantities of the form $\{U(\boldsymbol{x}) + u'(\boldsymbol{x},t), v'(\boldsymbol{x},t), w'(\boldsymbol{x},t)\}$, where the prime denotes the fluctuating quantity. Low- and high-speed streaks thus correspond to the conditions $u' < 0$ and $u' > 0$, respectively. All variables with a superscript "+" have been nondimensionalized with the viscous length scale ν/u_τ (e.g., $y^+ = yu_\tau/\nu$), where ν is the kinematic viscosity, $u_\tau^2 = \tau_w/\rho$ is the friction velocity, τ_w is the mean wall shear stress, and ρ is the fluid density. Typically, $u_\tau \sim 0.04 U_\infty$ where U_∞ is the free-stream velocity exterior to the boundary layer. As shown in Fig. 1, the low-speed (or high-speed) streaks have a well defined average spanwise spacing of $\lambda_z^+ \approx 100$ and are concentrated very near the wall ($y^+ < 40$). Because streak lengths are typically $x^+ \sim 1000$, the x-scale in Fig. 1 has been compressed for clarity. The spanwise variation in streamwise velocity $u'(z)$ as well as the inflectional velocity profile $u(y) = U(y) + u'(y)$ associated with the streaks are indicated. The velocity perturbation of the low- and high-speed streaks is typically one half the local mean velocity $|u'| \sim 0.5U$ where at this region of the flow $U \sim 10u_\tau$. Taking as an example an underwater vehicle moving at $U_\infty = 10$ m/s, the friction velocity is $u_\tau = 0.4$ m/s and the viscous length is $\nu/u_\tau = 2.5$ μm such that the streaks have a mean spacing of $\lambda_z = 0.25$ mm, convection velocity of $U_s = 4$ m/s, and perturbation velocity of $u_s' = \pm 2$ m/s.

Because the majority of turbulence production in the boundary layer occurs during the bursting process and bursts are always preceded by low-speed near-wall streaks, removing the streaks as they form, before they lift from the wall, should act to stabilize the near-wall flow and hence control (or at least delay) the production of turbulence in the boundary layer. Because the most definitive indicator of streak formation is a spanwise variation in streamwise velocity $u'(z)$ near the wall ($y^+ < 40$), the goal becomes one of finding a reliable means to sense and manipulate the form of the near-wall streamwise velocity profile (i.e., accelerate the low-speed streaks and decelerate the high-speed streaks). As discussed in the next two sections, the electro-magnetohydrodynamic transducer accomplishes this goal.

3. EMHD TRANSDUCER PHYSICS

The electro-magnetohydrodynamic (EMHD) transducer geometry considered here is illustrated in Fig. 2 relative to the turbulent boundary layer velocity field $\boldsymbol{u} = \{u, v, w\}$. As shown, the EMHD transducer consists of a pair of electrodes of opposite polarity that are mounted parallel to each other in the streamwise direction and flush with the wall with streamwise length $x = 2c$ and spanwise separation $z = 2a$. Mounted beneath the electrodes is a permanent magnet of length $x = 2d$ and width $z = 2b$ oriented such that the net magnetic flux lines $\boldsymbol{B}$ above the face of the magnet point up into the fluid (i.e., north pole top, south pole bottom). Depending upon the voltage condition at the electrodes, the transducer can be operated in either a passive (open-circuit) sensor mode or in an active (applied voltage) actuator mode. The physics of these two transducer modes are described below.

3.1 Passive Mode: Electromagnetic Induction (EMI) Velocity Sensor

The passive mode of operation of the EMHD transducer or electromagnetic induction (EMI) velocity sensor is illustrated in Fig. 2 following the initial work of Langston and Kasper [17] later extended by Snarski [18]. The principle of operation pivots around the process of Faraday induction in which the motion of a conducting fluid of velocity $\boldsymbol{u}(\boldsymbol{x},t)$ through a magnetic field $\boldsymbol{B}(\boldsymbol{x})$ induces an electric field in the fluid according to $\boldsymbol{E}(\boldsymbol{x},t) = \boldsymbol{u}(\boldsymbol{x},t) \times \boldsymbol{B}(\boldsymbol{x})$. If we concern ourselves with just the fluctuating part of the signal (i.e., a.c. couple the sensor electronics), this can be written $\boldsymbol{E}'(\boldsymbol{x},t) = \boldsymbol{u}'(\boldsymbol{x},t) \times \boldsymbol{B}(\boldsymbol{x})$ ($u' < 0$ is illustrated in Fig. 2). Because this electromagnetic induction process occurs at all points in the fluid at which there exists a velocity and magnetic field, the potential difference $\varphi_{12}(t) = \varphi_1(t) - \varphi_2(t)$ measured between a pair of electrodes at the wall is the integral effect of the induced electric fields throughout the flow, or (Shercliff [19], Bevir [20])

$$\varphi_{12}(t) = \int_{\Re} \left(\boldsymbol{u}'(\boldsymbol{x},t) \times \boldsymbol{B}(\boldsymbol{x})\right) \bullet \boldsymbol{j}_v(\boldsymbol{x}) d^3\boldsymbol{x} \quad , \tag{1}$$

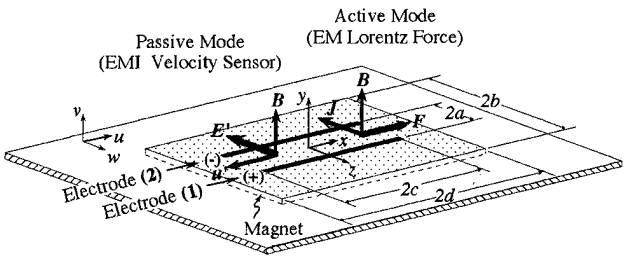

Figure 2. EMHD transducer mounted flush with wall beneath a turbulent boundary layer illustrating passive and active modes of operation.

where $\boldsymbol{j}_v(\boldsymbol{x})$, referred to as the virtual current density, is the current density field per unit current that would be produced if a current was passed through the electrodes with no flow present. Because $\boldsymbol{j}_v(\boldsymbol{x})$ is determined entirely by the electrode shape and electrical boundary conditions, it can be interpreted according to Eq. (1) as a receiving function that maps the induced electric field in the fluid to a voltage at the electrodes. Although $\boldsymbol{B}(\boldsymbol{x})$ in Eq. (1) is the total magnetic field consisting of the applied magnetic field and a secondary magnetic field induced by the motion of the conducting fluid, for low conductivity flows of interest hear the induced magnetic field can be neglected (Branover [21]).

Using vector identities, Eq. (1) can be written in the form

$$\varphi_{12}(t) = \int_{\Re} \boldsymbol{u}'(\boldsymbol{x},t) \bullet \boldsymbol{h}(\boldsymbol{x}) d^3\boldsymbol{x} \quad , \tag{2}$$

where

$$\boldsymbol{h}(\boldsymbol{x}) = \boldsymbol{B}(\boldsymbol{x}) \times \boldsymbol{j}_v(\boldsymbol{x}) \quad , \tag{3}$$

and $\Re$ represents the entire half space above the wall $(|x|, |z| < \infty, y > 0)$. Equation (2) illustrates that the output voltage of the EMI sensor results from a volume integral of velocity fluctuations throughout the boundary layer weighted by an electromagnetic field term $\boldsymbol{B}(\boldsymbol{x}) \times \boldsymbol{j}_v(\boldsymbol{x})$. Because Eq. (2) is merely the input-output relation for a linear space-time system (Strawderman [22]), $\boldsymbol{h}(\boldsymbol{x})$ as defined by Eq. (3) represents the spatial sensitivity distribution function, or Greens function, for the EMI sensor. Thus, to understand the response characteristics of the sensor, one only needs to evaluate the character of $\boldsymbol{h}(\boldsymbol{x})$.

Although closed form solutions for all three components of the electric and magnetic fields in Eq. (3) can be determined by evaluating Maxwell's equations for the electrode and magnet geometry in Fig. 2 (Snarski [18]), several assumptions can be introduced which simplify the ensuing analysis and greatly clarify the pertinent sensor characteristics. First, by assuming that the electrodes are long relative to their separation ($c >> a$) such that electrode end effects can be neglected, then $j_{v_x} << j_{v_y}, j_{v_z}$ such that the current density vector field is essentially 2-dimensional and spatially uniform along the length of the electrodes, or $\boldsymbol{j}_v(\boldsymbol{x}) = \{0, j_{v_y}(y,z), j_{v_z}(y,z)\}$ for $|x| \le c$. If it is also assumed that the magnet dimensions are large relative to the electrode dimensions ($d >> c$, $b >> a$), then $B_y >> B_x, B_z$ in the vicinity of the electrodes such that the magnetic vector field is essentially one-dimensional and spatially uniform in planes parallel to the wall, or $\boldsymbol{B}(\boldsymbol{x}) = \{0, B_y(y), 0\}$ for $|x| << d$, $|z| << b$. As a result, Eq. (3) reduces to

$$\boldsymbol{h}(\boldsymbol{x}) = \boldsymbol{i}\left[B_y(\boldsymbol{x}) j_{v_z}(\boldsymbol{x})\right] \quad , \tag{4}$$

such that the induced electric field is produced by only the streamwise velocity fluctuations, or

$$\varphi_{12}(t) = \int_{\Re} u'(\boldsymbol{x},t) h(\boldsymbol{x}) d^3\boldsymbol{x} \quad , \tag{5}$$

where $h(\boldsymbol{x}) = |\boldsymbol{h}(\boldsymbol{x})|$. Experimental verification for the form of Eq. (5) has been provided by the measurements of Towe [23] which illustrated that the electrodes act to vectorize the sensor response such that the output is produced essentially by just the velocity fluctuations aligned with the electrodes. Additionally, measured voltage spectra for an EMI sensor in a

fully developed turbulent pipe flow by Keith and Abraham [24] obtained over a range of Reynolds numbers collapse well with a scaling valid for turbulent velocity fluctuations indicating that a linear relationship exists between the sensor output and streamwise velocity as indicated by Eq. (5). Finally, dimensional analysis of the full 3-dimensional solution also indicates that the contributions to the sensor output from u' are at least an order of magnitude greater than contributions resulting from either w' or v' (Snarski [18]).

The virtual current density field $j_{v_z}(x)$ in Eq. (4) can be obtained from the Poisson solution for the voltage field $\psi(x)$ produced by a line-sink/line-source pair at the wall, or

$$\psi(x) = \frac{i}{4\pi\sigma} ln\left[\frac{y^2+(z+a)^2}{y^2+(z-a)^2}\right], \tag{6}$$

and Ohm's law in the form

$$J_z(x) = \sigma E_z(x) = -\sigma\frac{\partial\psi(x)}{\partial z}, \tag{7}$$

where i is the current per unit electrode length (A/m), σ is the fluid electrical conductivity (mho) and $E_z(x)$ is the spanwise electric field in the fluid (V/m). By definition, the virtual current density field is $j_{v_z}(x) = J_z(x)/I$ where I is the electrode current (A). Using an exponential function to describe the decay of the magnetic field with distance from the wall of the form $B_o\, exp[-y/\lambda_B]$ (T) and taking the voltage field to be uniform along the length of the electrodes (consistent with the assumption $c >> a$), we can substitute $i = I/2c$ for $|x| \le c$ and $i = 0$ for $|x| > c$ such that Eq. (4) with Eqs. (6) and (7) becomes

$$h(x) = -\frac{B_o e^{-\frac{y}{\beta a}}}{4\pi c}\left[\frac{z+a}{y^2+(z+a)^2} - \frac{z-a}{y^2+(z-a)^2}\right], \quad |x| \le c, \tag{8}$$

and $h(x) = 0$ elsewhere. In Eq. (8), $\beta \equiv \lambda_B / a$ represents the penetration depth λ_B of the magnetic field into the fluid relative to that of the electric field which is proportional to a (Snarski [18]).

Equation (8) is plotted in the nondimensionalized form $h^*(x) = ach(x)/B_o$ in Fig. 3(a) as a function of y/a and z/a. A value of $\beta = 100$ is assumed consistent with a typical turbulent boundary layer application (see Section 4.2). Fig. 3(a) illustrates that the EMI sensor weights the fluctuations near the electrodes much more heavily than those further out in the flow and that the sensor contains negative and positive sensitivities between and outside of the electrodes, respectively. These properties which are a direct result of the dipole character of the virtual current field as shown in Fig. 3(b) are in agreement with measurements of the spatial response function of an EMI sensor similar to that shown in Fig. 2 by Bruno, et al. [25]. Figure 3 thus indicates that although the EMI sensor output is produced by velocity fluctuations throughout the boundary layer, it is dominated by contributions from velocity fluctuations near the wall. In addition, because the sign of the contribution to the output depends upon the spanwise position of the fluctuation relative to the electrodes, the EMI sensor acts as a spatial filter with maximum output occurring for spatial disturbances with a preferred spanwise wavelength. Details and the resulting implications of these sensor characteristics to the proposed interactive control scheme are discussed in Section 4.

3.2 Active Mode: Magnetohydrodynamic (MHD) Force Actuator

The active mode of operation of the EMHD transducer is also illustrated in Fig. 2. As with the passive mode, the principle of operation stems around the process of Faraday induction except here the interaction of mutually orthogonal applied magnetic $B(x)$ and electric $E(x)$ fields induces a magnetohydrodynamic (MHD) force on the fluid according to

$$F_{MHD}(x,t) = \frac{1}{\rho} J(x,t) \times B(x), \tag{9}$$

where

$$J(x,t) = \sigma[E(x) + u(x,t) \times B(x)], \tag{10}$$

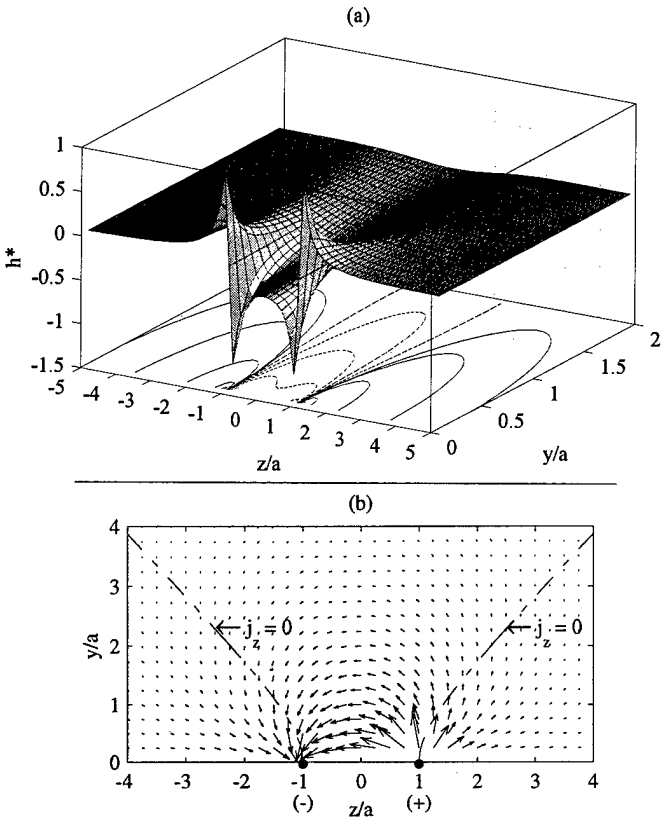

Figure 3. (a) Nondimensionalized spatial sensitivity distribution for the EMHD transducer for $|x| \le c$ and $\beta = 100$, Eq. (8), (b) virtual current density vector field $j_v(y,z) = -\sigma\nabla\psi(y,z)$.

and ρ is the fluid density (kg/m^3). The first term in Eq. (10) is the applied electric field produced by applying a voltage across the electrodes. The second term is the induced electric field resulting from the interaction of the flow field with the magnetic field. Except for high speed flows with very strong magnetic fields, the second term can generally be neglected. For example, with $E \sim V_{12}/2a$ (Eq. 7), $V_{12} = 0.5$ V, $2a = 0.25$ mm, $U = 10$ m/s, and $B_O = 1$T (e.g., a typical turbulent boundary layer application, see Section 4.2) $UB/E \sim 10^{-3}$. Thus, neglecting the induced electric fields in Eq. (10) and neglecting second order end effects as was done in connection with Eq. (4), then $J_x << J_y, J_z$ and $B_y >> B_x, B_z$ such that the induced MHD force acts only in the axial direction,

$$F_{MHD}(x) = i\left[-\frac{1}{\rho} J_z(x) B_y(x)\right], \tag{11}$$

or with Eq. (4),

$$F_{MHD}(x) = -\frac{I_{12}}{\rho} h(x), \tag{12}$$

where $F_{MHD}(x) = |F_{MHD}(x)|$ and I_{12} is the applied electrode current defined as positive if current flows from electrode (1) to (2) in Fig. 2 and negative if current flow is reversed. Strictly speaking, $F_{MHD}(x)$ for the interactive turbulence control application is still a function of time since it is not a steady-state input but one that is modulated on and off by the control scheme. However, because of the largely resistive character of EM devices, the transducer response can be assumed instantaneous without any loss of generality. From Eq. (12), it is clear that the MHD force field produced by the active transducer mode is functionally equivalent to the spatial sensitivity distribution for the passive transducer mode given by Eq. (8) and plotted in Fig. 3. As a result, the MHD force produced by the electrodes is concentrated near the wall and spatially distributed in such a way as to produce a maximum effect at a particular spanwise wavelength. The implications of these force field characteristics are discussed further in the next section.

4. INTERACTIVE EMHD CONTROL OF NEAR-WALL STREAKS

4.1 EMHD Array Physics

Both the spatial sensitivity function for the passive EMI sensor mode and the induced axial force field for the active MHD actuator mode of a single pair of electrodes are described by Eq. (8), shown plotted in Fig. 3. As stated earlier, because the function $h(\boldsymbol{x})$, referred to herein as the EMHD spatial field function, has positive and negative values to either side of the electrodes, the transducer will respond strongly to particular wavelengths in the flow. This effect can be illustrated more clearly by examining the character of the function $h(\boldsymbol{x})$ in wavenumber space. For the EMI sensor mode, the input-output relation given by Eq. (5) can be written in wavenumber-frequency space as (Strawderman [22])

$$\Phi_{\varphi}(\boldsymbol{k},\omega) = G(\boldsymbol{k})\Phi_{u}(\boldsymbol{k},\omega) \ , \tag{13}$$

where $\Phi_{\varphi}(\boldsymbol{k},\omega)$ and $\Phi_{u}(\boldsymbol{k},\omega)$ are the wavenumber-frequency spectra of the EMI sensor and turbulent velocity field, respectively, $\boldsymbol{k} = \{k_x, k_y, k_z\}$ is the wavenumber vector, ω is the circular frequency, and $G(\boldsymbol{k})$ is the wavenumber response for the sensor defined by

$$G(\boldsymbol{k}) = |H(\boldsymbol{k})|^2 \ , \tag{14}$$

$$H(\boldsymbol{k}) = \int_{-\infty}^{\infty} h(\boldsymbol{x}) e^{-i\boldsymbol{k}\bullet\boldsymbol{x}} d^3\boldsymbol{x} \ . \tag{15}$$

Because according to Eq. (13) the output spectrum of the sensor is simply the product of the spectrum of the streamwise turbulent velocity field and the sensor wavenumber response, $G(\boldsymbol{k})$ provides a clear representation of what components of the input field contribute to the sensor output. If $G(\boldsymbol{k}) = 1$, the spectral components are measured without distortion while if $G(\boldsymbol{k}) = 0$, the turbulent field components are suppressed completely.

Evaluating Eqs. (14) and (15) with Eq. (8), the nondimensionalized wavenumber response for the EMI sensor is given by

$$G^*(\boldsymbol{k}) \equiv \frac{G(\boldsymbol{k})}{(B_o a)^2} = \frac{\sin^2(k_x c)}{(k_x c)^2} \frac{\sin^2(k_z a)}{\left[(k_y a)^2 + \left(\beta^{-1} + |k_z a|\right)^2\right]} \ . \tag{16}$$

Because the spatial distribution of the MHD force field produced by the active mode is given by $h(\boldsymbol{x})$, Eq. (16) also provides a direct representation of the wavenumber characteristics of the applied force field. Equation (16), shown plotted in Fig. 4 at $k_x c = 0$ and $\beta = 100$, characterizes the relative level at which the EMHD transducer interacts with various wall-normal and spanwise wavenumbers (or wavelengths, $\lambda_i = 2\pi/k_i$) in the flow. As is illustrated, the transducer responds most strongly to a selective band of spanwise wavenumbers $|k_z a| \sim \pi/2$ due to the combined effects of cancellation of low spanwise wavenumbers resulting from the positive and negative sensitivities (e.g., electrodes) in the spanwise direction and attenuation of the high wavenumbers resulting from the finite spanwise dimensions of the transducer. This result suggests that the transducer can be tuned to respond to selective wavelengths in the flow such as the mean streak spacing. The effect can be greatly enhanced however by considering an array of transducers.

For an array of n transducers ($n + 1$ electrodes) connected in parallel and centered about $z = 0$ with each electrode separated by $z = 2a$, the EMHD spatial field function for the array $h_{array}(\boldsymbol{x})$ and the associated nondimensionalized wavenumber response $G^*_{array}(\boldsymbol{k})$ become,

$$h_{array}(\boldsymbol{x}) = -\left[\frac{z+na}{y^2+(z+na)^2} + 2\sum_{j=1}^{n-1}(-1)^j \frac{z+(n-2j)a}{y^2+\left[z+(n-2j)a\right]^2} + (-1)^n \frac{z-na}{y^2+(z-na)^2}\right] \frac{B_o e^{-\frac{y}{\beta a}}}{4\pi c}, \quad |x| \le c, \tag{17}$$

and

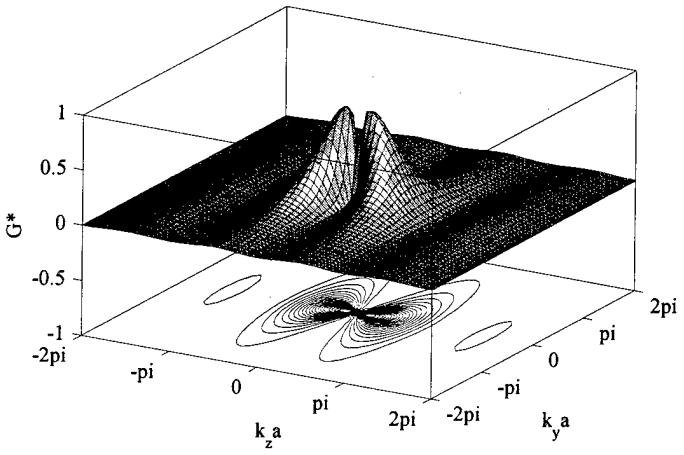

Figure 4. Wavenumber response for the EMHD transducer at $k_x c = 0$ and $\beta = 100$, Eq. (16).

$$G^*_{array}(\boldsymbol{k}) \equiv \frac{G_{array}(\boldsymbol{k})}{(n-1)^2 (B_o a)^2} = \frac{G^*(\boldsymbol{k})}{(n-1)^2} \left[\sum_{j=1}^{n} (-1)^j e^{-i2(j-1)k_z a}\right]^2 \ , \tag{18}$$

where $G^*(\boldsymbol{k})$ in Eq. (18) is given by Eq. (16). Equation (17), in the form $h^*_{array} = a c h_{array} / B_o$, and Eq. (18) are plotted in Figs. 5 and 6, respectively, for the case $n = 5$ corresponding to 6 electrodes. As can be seen, by the addition of just two more electrode pairs, the sign of the EMHD spatial field function in Fig. 5 alternates uniformly in the spanwise direction throughout the entire spanwise domain of the array. As a result, the array wavenumber response in Fig. 6 is dominated by the single spanwise wavenumber $|k_z a| = \pi/2$ corresponding to the spanwise wavelength $\lambda_z = 4a$ in Fig. 5. This implies that the EMHD transducer array can be tuned to respond directly to the near-wall streaks if the electrode half-spacing a is set equal to one quarter of the mean streak spacing $\lambda_z^+ = 100$, or $a^+ = 25$.

Although the specified electrode spacing will assure that the transducer array responds to the spanwise wavelength of the streaks, the array will only be able to efficiently sense and manipulate the streaks if the EMHD spatial field function $h(\boldsymbol{x})$ predominantly acts in the region near the wall occupied by the streaks ($y^+ < 40$). This can be shown to be the case by integrating $h(\boldsymbol{x})$ as a function of y, as shown in Fig. 7 normalized by the total integrated value for four values of the magnet strength parameter ($\beta = 1, 10, 100, \infty$). Because the effect of increasing $\beta = \lambda_B / a$ is to increase the penetration depth of the magnetic field into the fluid, increasing β causes the effect of the EMHD transducer to extend further from the wall. However, even for the case $\beta = \infty$ corresponding to the limiting case of extremely high magnet strength and very close electrode spacing (i.e., the magnetic field does not decay in the region in which the electrodes have an effect on the flow), the region $y^+ < 40$ corresponding to $y/a < 1.6$ for $a^+ = 25$ accounts for over 60% of the total integrated value. As a result, the EMHD transducer's zone of influence will be predominantly that region of the flow occupied by the near-wall streaks, as required.

Support for this near-wall influence of the transducer indicated in Fig. 7 can be found in the work of Henoch and Stace [4] in which they experimentally investigated the use of a steady, globally applied streamwise MHD force to control the shape of the mean velocity profile and hence the ability of the boundary layer to resist transition. In all cases examined, the effect of the MHD force on the mean velocity profile never exceeded much beyond $y/a = 1.2$, consistent with what would be expected from Fig. 7 and the value of $\beta \approx 1$ used in their experiments. Although Keith and Abraham [24] attempted to deduce the locations in the boundary layer in which the primary contributions to the EMI sensor output occur by examining the scaling behavior of the various frequency ranges of their measured voltage spectra ($\beta = 1.2$-7.1), their scaling results were inconclusive due to the spatial averaging and filtering effects at high and low frequencies described by Eq. (13).

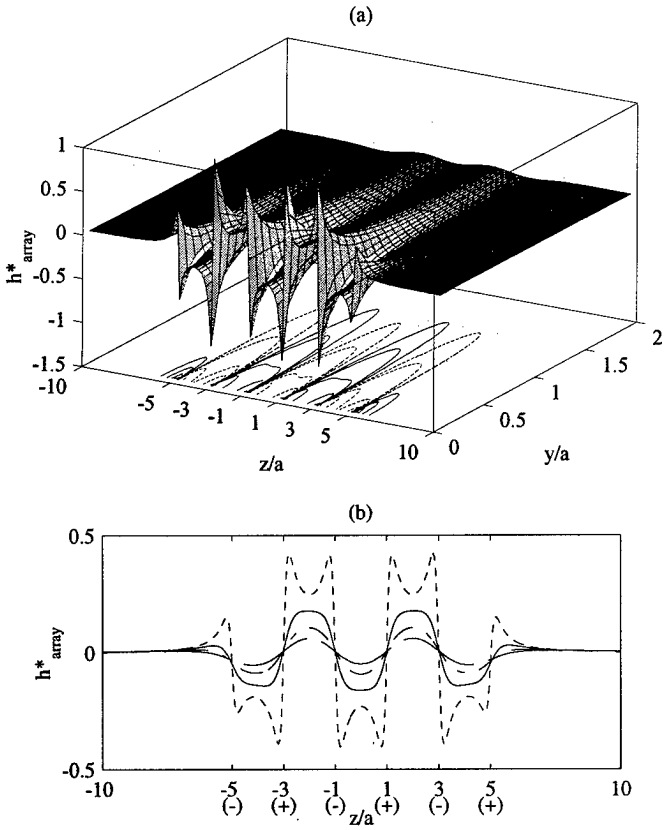

Figure 5. Nondimensionalized EMHD array spatial field function for $|x| \le c$, $b = 100$, and $n = 5$, Eq. (17); (a) surface plot in (y-z)-plane, (b) line plots at $y/a = 0.2$ (- - -), 0.6 (—), 1.0 (- · -), and 1.4 (– –).

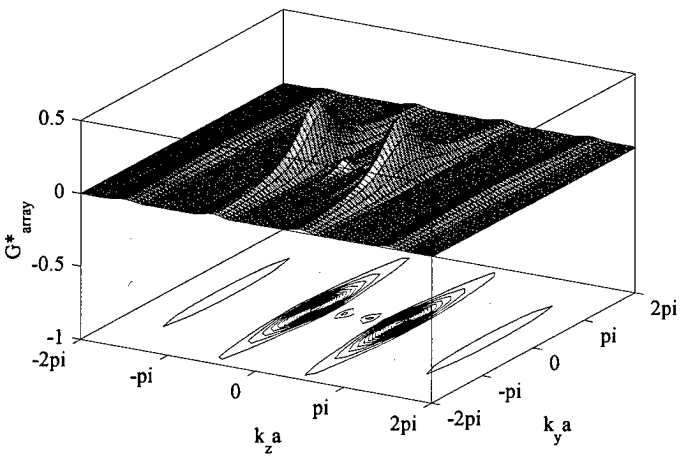

Figure 6. Wavenumber response for the EMHD array for $k_x c = 0$, $\beta = 100$, and $n = 5$, Eq. (18).

4.2 Implementation and Scaling Considerations

The EMHD interactive control scheme proposed here is conceptually illustrated in Fig. 8. Although the number of transducers in the full array would need to be large enough to cover the spanwise extent of the boundary surface under control, sub-arrays of transducers with spanwise extents which scale with the spanwise coherence length of the mean streak spacing would likely be used as individual array elements (e.g., $2na \sim \delta$). For convenience, 5 transducers (6 electrodes) are shown in Fig. 8. The control scenario involves first detecting the existence of a spanwise variation in streamwise velocity $u'(z)$ associated with the near-wall streaks by measuring the open-circuit voltage induced across the electrodes (passive EMI sensor mode), φ_{12}. For the streak orientation shown in the figure (i.e., low-speed streak between the reference electrodes (1) and (2)), the induced passive response according to Eq. (5) and as illustrated in Fig. 8 is $\varphi_{12} \approx \int u'(z)h(z)dz > 0$. When the magnitude of this sensor output exceeds some pre-established threshold level representative of a developing streak, the EMHD transducer would be switched to an active mode by applying a voltage $V_{12} = V_1 - V_2$ across the electrodes of appropriate polarity to attenuate the velocity perturbation and stabilize the near-wall flow (i.e., to accelerate the low-speed fluid and decelerate the high-speed fluid). Because a low-speed streak resides between the reference electrodes in Fig. 8, the sign of $V_1 - V_2$ must be such to produce a positive MHD force in this region. Since the applied MHD force between the reference electrodes and the applied electrode voltage are related through Eqs. (7) and (11) according to

$$F_{MHD} = \frac{\sigma B_y}{\rho}\frac{\partial \psi}{\partial z} \approx \frac{\sigma B_o}{\rho}\frac{V_1 - V_2}{2a} \quad , \tag{19}$$

the required condition is $V_1 - V_2 > 0$. This voltage is also consistent with the required sign of the applied current field $I_{12} > 0$ in Eq. (12) necessary to produce the force field $F_{MHD}(z) \sim -h_{array}(z)$ that is required to remove the spanwise variation in streamwise velocity. If the streaks were oriented opposite to that shown in Fig. 8 (i.e., high-speed streak between reference electrodes), the induced passive and required active responses would be $\varphi_{12} < 0, V_1 - V_2 < 0$, $I_{12} < 0$, and $F_{MHD}(z) \sim h_{array}(z)$. It should be pointed out that because the mean streak spacing is a predictable function of the free stream velocity, the array could be operated at a large number of discrete flow speeds by grouping other than adjacent electrodes, provided the spacing of adjacent electrodes is established from the largest anticipated flow speed. Also, if full arrays of electrodes were appropriately spaced in x, one could theoretically delay the production of turbulence indefinitely.

Although the required polarity of the applied voltage is straight forward, the goal of the interactive control scheme or feedback control algorithm is to apply just enough energy to counteract the spanwise perturbation in the near-wall streamwise velocity profile. This requires being able to relate the magnitude and duration of the applied voltage to the magnitude of the detected velocity perturbation (as calibrated from the EMI sensor output, see Section 4.3) in the feedback control algorithm. An order of magnitude estimate of the voltage required to stabilize the flow can be obtained by examining the magnitude of the required applied MHD force relative to the inertial forces associated with accelerating or decelerating the near-wall fluid, or the ratio

$$N_t = \frac{F_{MHD}}{\partial u_s' / \partial t} \sim \frac{\sigma}{\rho u_s'}\frac{B_o}{2a}\left(V_{12}\Delta t\right) \quad , \tag{20}$$

where Δt is the duration of the applied voltage and u_s' is the perturbation velocity of the near-wall streaks we wish to remove. The variable N_t represents an imposed interaction parameter similar to those defined by Henoch and Stace [4] and Crawford and Karniadakis [5] but referenced here to the unsteady rather than steady inertial force $\sim \rho u_\tau^2 / \delta$ since our goal is to apply an impulse $F_{MHD}\Delta t$ to remove the streak momentum $\rho u_s'$ rather than apply a steady state force field to alter the global character of the boundary layer.[1] In the experimental work of Henoch and Stace [4], they found that an imposed interaction parameter of 0.03 was sufficient to effect a desirable change in the mean velocity profile with minimum drag reductions occurring for a value of 0.3. Because the goal here is again to apply small adjustments to small perturbations in the near-wall velocity field, even smaller values may be required.

Because the perturbation in the near-wall flow must be removed before it convects out of the electrode control volume, it is necessary to impose the condition $\Delta t < 2c / U_s$ where $U_s \approx 10u_\tau$ is the convection velocity of the near-wall streaks. In addition, because it is desirable to attenuate the streaks early in their development, a velocity perturbation of $u_s' \sim u_\tau$ is assumed (see Section 2). Then, considering as an example a seawater vehicle (ρ = 1000 kg/m^3, σ = 4 mho, $\nu = 10^{-6}$ m^2/s) moving at

[1] Although Crawford and Karniadakis [5] did study computationally the effect of time-dependent forcing, their forcing was periodic (pulsed) and not intended to be coupled with any near-wall turbulence phenomena.

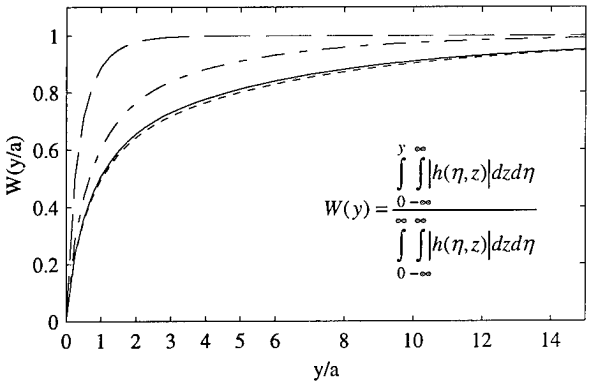

Figure 7. Integrated normalized value of EMHD spatial field function as a function of *y/a* for b = 1 (– –), 10 (- · -), 100 (—), and ∞ (- - -).

U_∞ = 10 m/s ($u_\tau \approx 0.4$ m/s) with a magnetic field induction of B_O = 1T (e.g., Neodymium Iron-Boron magnet), and imposing an electrode half-separation of a^+=25 (i.e., a = 0.125 mm for above conditions) as discussed in Section 4.1, the required electrode voltage and duration are

$$V_{12} \sim 10\frac{\rho u_\tau^2}{\sigma}\left[\frac{N_t}{B_o(c/a)}\right] = 400\left[\frac{N_t}{(c/a)}\right] \quad \text{(V)} \ , \qquad (21)$$

and

$$\Delta t \sim 0.2\frac{\upsilon}{u_\tau^2}\left[a^+(c/a)\right] = 3.125\times10^{-5}(c/a) \quad \text{(s)} \ . \qquad (22)$$

To proceed, an appropriate value for *c/a* is required. This can be obtained by considering the per element power requirements P, equivalent to the product of the applied voltage V_{12}, electrode current density $J_z \sim \sigma V_{12}/2a$, and effective flow area through which the current acts ~4*ac*, or

$$P \sim 200\frac{\rho\nu u_\tau}{\sigma}\left[\frac{N_t^2 a^+}{B_o^2(c/a)}\right] = 80\left[\frac{N_t^2}{(c/a)}\right] \quad \text{(W)} \ . \qquad (23)$$

Assuming P = 0.01 W (satisfying 0.018W requirement established by Gad-el-Hak [6] for an interactive control schemes to achieve a net savings) and an imposed interaction parameter of N_t = 0.1, Eq. (23) yields *c/a* = 80 (c = 10 mm) such that the required voltage and duration are V_{12} = 0.5 V and Δt = 2.5 ms. Reducing the power requirement to 0.001W results in c/a = 800 (c = 10 cm), V_{12} = 0.05 V and Δt = 25 ms.

As a final note, an exponential fit to measurements of the magnetic field produced by a neodymium boron magnet with B_O = 0.3T (Kasper et al [26]) yields λ_B = 7.2 mm such that $\beta = \lambda_B/a$ = 58 for the above example. Because larger values of B_o and hence β would likely be used in any interactive turbulence control scheme and since the form of the EMHD field function in Fig. 7 does not change much for β > 100, a value of β = 100 was used throughout this paper.

4.3 Experimental Validation

Although experimental results exist in the literature which support the passive and active EMHD transducer physics presented here, no attempt has been made to use the transducer for the direct detection or manipulation of streaks. As a result, experiments will be undertaken by the author in a laminar saltwater channel flow using artificially generated low- and high-speed streaks to validate the predicted performance characteristics. The low- and high-speed streaks will be generated with the use of mixing tabs developed by Gretta and Smith [27] that have been shown to produce flow structures similar to what is observed in a fully developed turbulent boundary layer as shown in Fig. 9a. The response characteristics of the passive sensor mode will be evaluated by varying the wavenumber content and perturbation magnitude of the near-wall velocity field through systematic variation of the tab separation Δz and tab-to-electrode separation Δx, respectively, indicated in Fig. 9b and 9c. Variations in Δx will also be used to evaluate the required electrode

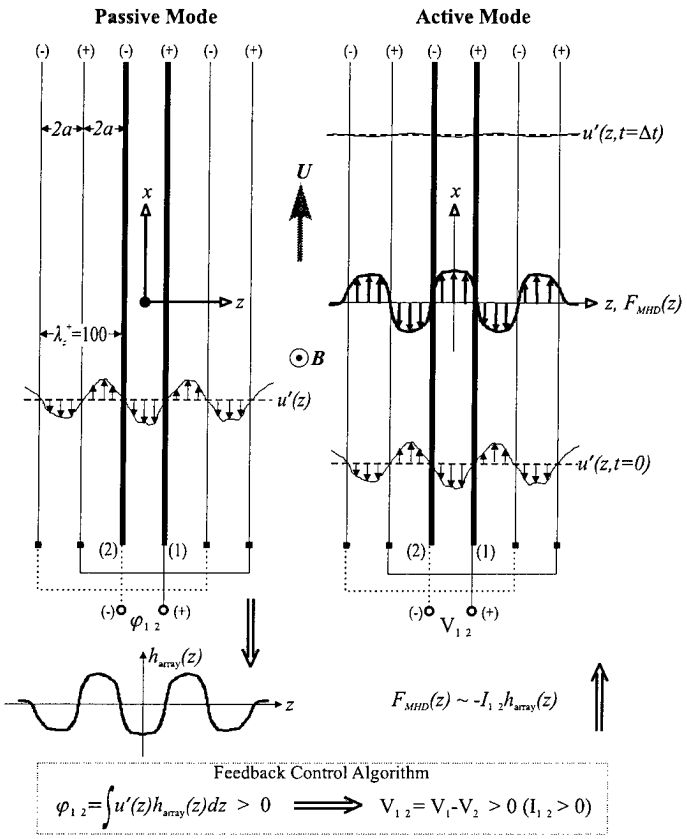

Figure 8. Interactive EMHD turbulence control scheme to detect and manipulate near-wall low- and high-speed streaks.

voltage necessary to eliminate a given spanwise variation level in streamwise velocity produced by the tabs. Although the MHD force field derived from the potential field solution in Fig. 5(a) has a finite value at $y = z = 0$, the real force field is known to decay exponentially to zero at the wall (Tsinober [28]). This behavior of $F_{MHD}(y)$ will be addressed in future modelling efforts and is thus illustrated in Fig. 9c. Particle image velocimetry, wall pressure, and hot film measurements will be used to characterize the effect of the applied MHD force field on near-wall velocity field, fluctuating wall pressure and wall shear levels. The results of this work will then be used as the basis for developing an appropriate feed-back control algorithm.

5. CONCLUSIONS

A nonobtrusive electromagnetohydrodynamic transducer array that can both detect and manipulate the near-wall streamwise velocity field associated with low- and high-speed streaks has been presented. Owing to the intrinsic relationships which exist between electric and magnetic fields and moving conducting fluids, the passive (electromagnetic induction velocity sensor) and active (magnetohydrodynamic force actuator) modes of the transducer are both characterized by the same spatial field function which can be tuned to respond to the spanwise wavelength $\lambda_z^+ = 100$ and near-wall domain $y^+ < 40$ of the streaks by suitable choice of electrode separation, $2a$. Because the near-wall streaks are the most reliable indicator of the preburst turbulence production process, this device would be an ideal candidate for use in an interactive turbulence control scheme in electrically conducting (e.g., seawater) turbulent boundary layers. Since the same device is used to sense and manipulate the same flow variable (i.e., streamwise velocity) at the same spatial location, a direct coupling exists between the drag reduction methodology and the fundamental near-wall turbulence physics. Initial estimates also indicate that effective drag reduction can occur with per array element power inputs in the milliwatt range. Experiments are being planned to calibrate the sensor output, quantify the electrode voltage required to remove the streaks, and lay the foundation for developing a feedback control algorithm.

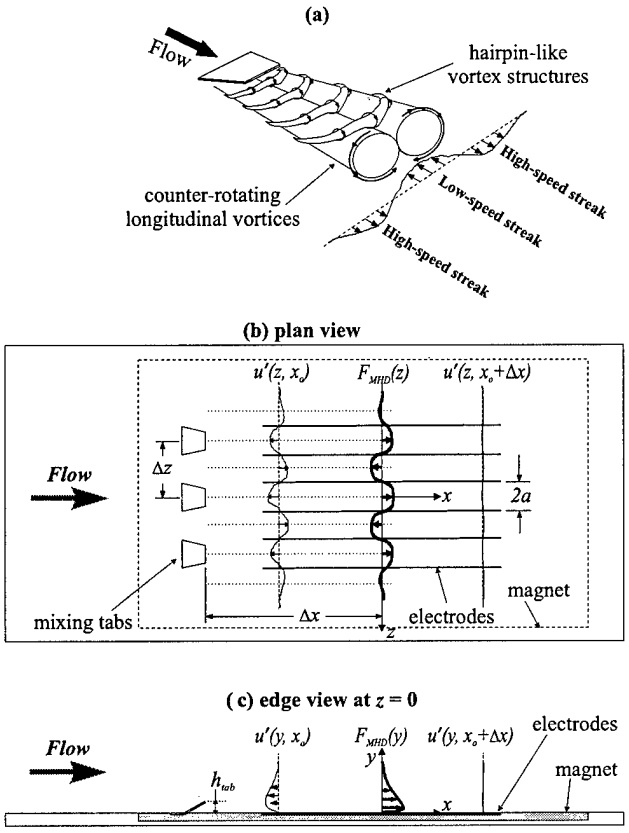

Figure 9. Planned EMHD experiments: (a) development of vortex structures and streaks in wake of mixing tab (Gretta and Smith [27]), (b) plan view of tabs and EMHD array in laminar salt water channel, (c) edge view at location of low-speed streak ($z = 0$).

ACKNOWLEDGMENTS

This work was initially supported by the Naval Undersea Warfare Center (NUWC) Division Newport, RI Independent Research (IR) Program during the authors tenure at NUWC Detachment New London, CT. The IR Program is funded by the Office of Naval Research.

REFERENCES

1. D.M. Nosenchuck and G.L. Brown, "Discrete Spatial Control of Wall Shear Stress in a Turbulent Boundary Layer," *Near-Wall Turbulent Flows*, ed. R.M.C. So, C.G. Speziale and B.E. Launder, Elsevier Publishers, Amsterdam, pp. 689-698, 1993.

2. *ONR Workshop on Electromagnetic Flow Control (EFC)*, org. L. P. Purtell, Naval Surface Warfare Center, Carderock, MD, 19 May 1994.

3. P.R. Bandyopadhyay, "Development of a Microfabricated Surface for Turbulence Diagnostics and Control," *Application of Microfabrication to Fluid Mechanics*, ASME FED-Vol. 197, 1994.

4. C. Henoch and J. Stace., "Experimental Investigation of a Salt Water Turbulent Boundary Layer Modified by an Applied Streamwise Magnetohydrodynamic Body Force," *Phys. Fluids*, Vol. 7, No. 6, pp. 1371-1383, 1995.

5. C.H. Crawford and G.E. Karniadakis, "Reynolds Stress Analysis of Emhd-Controlled Wall Turbulence. Part I. Streamwise forcing," *Phys. Fluids*, Vol. 9, No. 3, pp. 788-806, March 1997.

6. M. Gad-el-Hak, "Interactive Control of Turbulent Boundary Layers: A Futuristic Overview," *AIAA Journal*, Vol. 32, No. 9, p. 1753, 1994.

7. P. Moin and T. Bewley, "Feedback control of turbulence," *Appl. Mech. Review*, Vol. 47, S3, 1994.

8. R. Rathnasingham and K.S. Breuer, "System Identification and Control of a Turbulent Boundary Layer," *Phys. Fluids*, Vol. 9, No. 7, pp. 1867-1869, July 1997.

9. S.M. Kumar and W.C. Reynolds, "Characteristics of MEMS Based Actuators for Flow Control," presented at *American Physical Society, 50th Annual Meeting of the Division of Fluid Dynamics*, 25 Nov. 1997.

10. J.C.S. Meng,, "Electromagnetic Control Based on Micro-Turbulence Phenomenology," *Flow Noise Modeling, Measurement, and Control*, ASME NCA-Vol. 19, FED-Vol. 230, pp. 39-54, 1995.

11. S.N. Singh and P.R. Bandyopadhyay, "Linear Feedback Control of Boundary Layer Using Electromagnetic Microtiles," *ASME - J. Fluids Eng.*, Vol. 119, pp. 852-858, Dec. 1997.

12. S.R. Snarski, *Device for Interactive Turbulence Control in Boundary Layers*, Patent Application, Navy Case #77883, 15 Jul 96.

13. S.R. Snarski and R.M. Lueptow, "Wall Pressure and Coherent Structures in a Turbulent Boundary Layer on a Cylinder in Axial Flow," *J. Fluid Mech.*, Vol. 286, pp. 137-171, 1995.

14. R.L. Robinson, "A Review of Vortex Structures and Associated Coherent Motions in Turbulent Boundary Layers.," *Structure of Turbulence and Drag Reduction IUTAM Symposium, Zurich, Switzerland, 1989*, Springer-Verlag Berlin, pp. 23-50, 1990.

15. S.J. Kline and S.K. Robinson, "Quasi-coherent Structures in the Turbulent Boundary Layer: Parts I & II.," in *Near-wall turbulence: Proceedings of the 1988 Zoran Zaric Memorial Conference*, ed. S.J. Kline and N.H. Afgan, Hemisphere, New York, pp. 200-247, 1990.

16. S.J. Kline, W.C. Reynolds, F.A. Schraub, and P.W. Runstadler, "The Structure of Turbulent Boundary Layers," *J. Fluid Mech.* Vol. 30, part 4, pp. 741-773, 1967.

17. L. S. Langston and R.G. Kasper, "Analysis of an Electromagnetic Boundary Layer Probe for Low Magnetic Reynolds Number Flows," *ASME -J. Fluids Eng.*, Vol. 115, Dec. 1993.

18. S.R. Snarski, *The Response of an Electromagnetic Induction Sensor to Isotropic Turbulence*, NUWC-NPT Tech. Report 10809, Naval Undersea Warfare Center Detachment, New London, CT, 15 Mar 95.

19. J.A. Shercliff, *The Theory of Electromagnetic Flow Measurement*, Cambridge University Press, Cambridge, 1962.

20. M.K. Bevir, "The Theory of Induced Voltage Electromagnetic Flowmeters", *J. Fluid Mech.* , Vol. 43, part 3, pp. 577-590, 1970.

21. H. Branover, *Magnetohydrodynamics Flow in Ducts*, John Wiley & Sons, New York, 1978.

22. W.A. Strawderman, *Wavevector-frequency Analysis with Applications to Acoustics*, U.S. Government Printing Office, SN008-047-00408-7, Naval Undersea Warfare Center Detachment, New London, CT, 1994.

23. B.C. Towe, *Underwater Electromagnetic Turbulent Velocimeter*, NUSC Contractor Report, Contact N66604-89-M-B873, Naval Underwater Systems Center, New London, CT, 15 Sep 89.

24. W.L. Keith and B.M. Abraham, *Spectral Measurements From an Electromagnetic Boundary Layer Probe in a Turbulent Pipe Flow*, NUWC-NPT TR 10755, Naval Undersea Warfare Center, New London, CT, 1994.

25. A.B. Bruno, R.G. Kasper, and B.C. Towe, *Development of Underwater Electromagnetic Velocimeter*, NUWC-NL Technical Document 10065, Naval Undersea Warfare Center, New London, CT, 16 June 1992.

26. R.G. Kasper, A.B. Bruno, and L.S. Langston, *Preliminary Underwater Electromagnetic Turbulence Measurements*, NUSC Technical Document 8909, Naval Underwater Systems Center, New London, CT, 1991.

27. W.J. Gretta and Smith, "The Flow Structure and Statistics of a Passive Mixing Tab," *J. Fluids Eng.*, Vol. 115, pp. 255-263, 1993.

28 A. Tsinober, "MHD Flow Drag Reduction," in *Viscous Drag Reduction in Boundary Layers*, ed. D.L. Bushnell, AIAA, 1990.

Turbulent Drag Reduction Methods: Biology Based Drag Reduction

DOLPHIN DRAG REDUCTION: MYTH OR MAGIC

James A. Fein
Office of Naval Research
800 North Quincy Street
Arlington, VA 22217
feinj@onr.navy.mil

Abstract - The swimming performance of dolphins has been the inspiration for numerous proposed drag reduction techniques, including compliant coatings and riblets. Speculation has focused on the existence of laminar flow in order to explain the difference between the available power and the measured swimming speeds. Gray first postulated the paradox between power and speed capability in 1936 with his claims based on a dolphin swimming speed of 10.3 m/s. This survey paper explores the basis for that paradox, which are the measurements of dolphin speed used by Gray and others. The reliability and error margins of the early measurements are discussed. The range of realistic speed values of up to 8.3 m/s for very short durations and half that for longer periods is established for both captive and wild dolphins. This is well within the dolphins' capabilities based on available muscle mass without any exotic drag reduction. Thus Gray's Paradox may be attributed to incorrect data for dolphin swim speed. Marine mammals other than dolphins are discussed, although data is much less plentiful for whales. The conclusion is that there is no reason to believe, based on the swimming speed data, that dolphins have frictional drag reduction systems or techniques. In order to establish extraordinary performance of biological creatures, swim speed data must be repeatable, have acceptable error bounds and points that lie far from the majority of the data should be rejected. This recommendation will impact the level of data required to establish the existence of other seawater drag reduction mechanisms as well. In conclusion, while dolphins are streamlined swimming organisms that may avoid some form drag and some wave drag, there is no evidence that they reduce skin friction drag or that they postpone transition from laminar to turbulent flow.

I. BACKGROUND

The supposed drag reduction attributes of dolphins and other marine mammals have been the source of speculation for some time. The interest related to translating those attributes for use in increasing the speed or endurance of ships, weapons and underwater vehicles. The dolphin is a biological system that is an evolution driven compromise for survival. Its shape, skin, body fat distribution and other characteristics have favored adaptations that efficiently solve problems of regulating temperature, finding food and avoiding danger. It is reasonable to assume that since mobility and speed are important in avoiding predators, the dolphin may have unusual attributes that allow high-speed swimming.

In this century, the speculation can be said to have begun with the well-known *Gray's Paradox*. Gray (1), writing in 1936 in the Journal of Experimental Biology, states, "*If the resistance of an actively swimming dolphin is equal to that of a rigid model towed at the same speed, the muscles must be capable of generating energy at a rate at least seven times greater than that of other types of mammalian muscle.*" Gray goes on to identify the proposition that the rhythmic movements of the dolphin in some way prevent the fluid from generating turbulence along the body. Furthermore, if the flow is free of turbulence, the horsepower per pound of muscle agrees closely with other mammal muscles. Thus Gray not only proposed the paradox, but also identified the first theory to explain it. He speculated that laminar flow existed along the body.

The solutions to Gray's Paradox have centered on explanations of the muscle power available in dolphins and on the fluid mechanics of the drag producing boundary layer. Fluid mechanical explanations have included various mechanisms to maintain laminar flow and/or turbulent drag reduction. Techniques considered include polymer surface chemistry, surface ridges such as riblets, compliant coatings, surface folds and subsurface energy absorption. There is no satisfactory explanation for other accounts of even higher swimming speeds by an assortment of observers.

This paper will not add to the speculation, but will examine the original source of the paradox, the speed measurements for dolphin swimming. It will be demonstrated that the early measurements used by Gray and others do not stand up to scrutiny. The later, much lower, swimming speed measurements can be explained without unusual physical mechanisms. There is still a great deal of misinformation about dolphin swim speeds and drag reduction abilities as demonstrated by the proposals received at Office of Naval Research that still refer to Gray's Paradox.

II. EARLY MEASUREMENTS

It is a well-accepted postulate in science, going back to Ockham's razor, that the simplest explanation that fits the facts is to be preferred. A corollary is that a very high level of experimental verification and documentation should back up extraordinary claims. Claims of very fast swimming by dolphins (and other marine creatures) which require unusual physical explanations, should be established by high quality data and rigorous error analysis. The early speed estimates are described in Table I, with discussion below.

Gray's Measurement:

Gray's Measurement (1) consists of the following quotation from his work, "*The velocity of a rapidly moving dolphin has seldom been determined with great accuracy, and no doubt it has often been exaggerated. The following observation made by Mr. E. F. Thompson whilst in the Indian Ocean is therefore of interest. A dolphin swimming approximately 30 ft. from the side of the ship passed the ship in the direction of stern to bow in just under 7.0 sec. As timed by a stopwatch: the length of the ship was 136 ft. and its speed was logged at 8.5 knots. This dolphin must therefore have been traveling at 20 knots (=33 ft/sec)*", (or 10.3 m/s). The rest of his arguments related to laminar flow and muscle power are all based on this single observation. First it is clear that the measurement is not Gray's, but Mr. Thompson's. Gray was nowhere near the observation himself and offers nothing in terms of the credibility of the observer. There is no information on the accuracy of the various components of the measurement. For example, while the length of the ship may be given some credence, the calibration of the ship's speed log is unknown. Particularly suspect is the stop watch measurement which by necessity must have been taken from one location. This would require estimates of the time the dolphin crossed the stern and then the bow plane of the ship. It is unlikely that the observer ran along the side with the dolphin since that would have required an unimpeded deck and sprinter running speed by Mr. Thompson. A system of multiple observers and hand signals is possible but no less fraught with error. The speed log and the timing could be expected to have a combined error of at least + or - 10%. The overall uncertainty of the measurement would be greater. The largest source of error, however, is the proximity of the dolphin to the side of the ship. If the dolphin came within the boundary layer or detached separated flow field of the ship, which, for a blunt bow freighter, could be 30 feet from the ship at the stern, the animal would have been swimming through water that was moving forward with a significant velocity. This would invalidate the measurement. If the dolphin were farther from the ship, say 50 to 60 feet, the errors in timing the run would be exaggerated. Another problem that creates uncertainty is that the measurement seems to be taken only once. It is unclear whether other measurements were taken that gave lower speeds or if this was the single measurement. Either way, the case for an over 10 m/s swimming speed is weak.

Measurements of Johannessen and Harder (2):

This publication of 1960 is the second common source of high-speed measurements for dolphin swimming. The authors did not make the observations themselves but asked the navigation officer, Mr. Anderson, of the *S.S. Monterey*, a freighter traveling from California to Australia. The publication has a number of anecdotal observations. One is that while the ship was traveling at 9.8 to 10.8 m/s, dolphins would swim alongside for periods of up to 2 minutes. This can be

explained by the dolphins utilizing the ship boundary layer and in fact it is noted that some of the animals rode the bow wave of the ship during the encounters. There are five other observations of groups of 1 to 500 animals going from 7.2 to 20.6 m/s. Four of them are for dolphin species and estimate speeds of 7.2 to 9.3 m/s. In most cases the animals were a quarter to a half-mile away from the ship. The other is a single animal, a killer whale, going 10.3 to 20.6 m/s. The speed range of 7 to 9 m/s for the dolphins is close to the well-established values of later researchers. The killer whale data point was taken as the animal approached the ship head on with no fixed reference frame for a measurement. There is no mention of an empirical technique for any of the observations, so the data points must be considered estimates, which can be affected greatly by the distances and the moving observer.

There is an additional anecdotal report in the paper, a private communication from William von Winkle of what is today NUWC, *"that a school of blackfish had been observed circling a Navy vessel, which was cruising at 22 knots, for several days at a time."* Again there is no speed calibration, current information or quantitative data. Dr. von Winkle is a scientist and his observations are more credible than those of non-scientists. However the estimate of 11.3 m/s at a duration of several days is far higher than any other more exact measurement made on either whales or dolphins. This single data point also does not address the motivation of the animals, which appears to be non-existent. Blackfish, also known as pilot whales is a dolphin species that is larger than common dolphins, but smaller than most whales. It was hunted extensively by the early whalers, which relied on sail or rowing power to overtake the whales. The indirect evidence that these animals were not capable of speeds of over 11 m/s and durations of several days, is that these animals were often taken and greatly reduced in numbers during the whaling era (3).

It is whaling experience that provides the key data for establishing the swimming speeds of whales. In whale hunting the animal's motivation is clear. The importance of any mechanism to increase speed is also clear. Humans are one predator where extraordinary speed would have been an effective strategy for survival. The blackfish described in Murphy (3) cannot outrun the sail powered whalers and instead use the strategy of diving and reemerging in a different direction. This sometimes works, but often fails as the evidence of 40 or more blackfish taken by a single ship testifies. While the clipper ships reached 10.3 m/s, the whaling ships rarely went over half that speed and the oar and sail powered longboats were even slower. For larger whales the data is also clear. Gawn (4) and Kermack (5) both document maximum whale swimming speeds based on the known speeds of the powered catcher boats used in the 1940s to overtake them. For large blue and fin whales, the maximum speeds for 10 minutes were estimated to be 10.3 m/s. For any longer duration the speeds did not exceed 7.7 m/s in any case. See Gawn (4) for a good discussion of the muscle power available to large whales. The incidents where whales were able to tow ships are discussed. More recently Williamson (6) accompanied Japanese whalers and recorded a 8.2 m/s top speed for up to 10 minutes for blue, fin, sei, bryde, and minke whales. There was anecdotal information from the whalers that an occasional blue or fin whale could reach 10.3 m/s for short durations. Humpback, gray, right and sperm whales had a top speed of only 4.1 m/s. If marine mammals had a drag reduction mechanism, it could be expected that the larger species would have a higher top speed. These top speeds for the largest whales, which are well within the capabilities of the animals' muscles with a fully turbulent boundary layer, are a strong argument for no special mechanisms.

Kellogg's Results:

Another reference that is frequently sighted is Kellogg (7). Kellogg's article is a collection of information on characteristics of marine mammals. It is not a scholarly paper and it offers no information to back up its swimming speed claims. He gives a blue whale swim speed of 7.2 m/s, a long snout dolphin (near ships) swim speed of 6.2 to 7.7 m/s and a *delphinius* species dolphin swim speed of 7.7 to 9.3 m/s with no additional details. This is slightly below the Gray estimate and may be based on it or on other anecdotal estimates. There is no reason to give any credibility to the estimates in Kellogg.

Dolphins riding the bow wave of ships:

Dolphins are recorded to have ridden on the bow wave of ships from ancient times. In Woodcock (8), this behavior is described and attributed to a laminar flow mechanism that is based on Gray's analysis. Perry, Acosta and Kiceniuk (9) conducted experiments to show that there is plenty of forward velocity flow on the wave front in the bow region of a ship to allow the dolphin to ride the flow field. That dolphins are capable of sensing flow fields and getting a 'free ride' has been demonstrated many times by the marine mammal training and physiology communities. This explains some of the high speeds observed when dolphins are swimming near a ship or in its wake.

Lang's Measurements:

Prior to 1960 the dolphin swim speed estimates were based on sparse data subject to exaggeration and influenced by moving observers and the flow field of the moving ship. Dr. Tom Lang of the Naval Laboratory conducted the most extensive series of measurements of dolphin swimming hydrodynamics during the 1960s. These experiments with captive animals spanned a number of species and techniques and are documented in Lang and Daybell (10), Lang and Norris (11) and Lang and Pryor (12). Published in 1963, Lang and Daybell (10) explores the fluid phenomena of the swimming by attaching drag and turbulence inducing collars, conducting studies of dolphin forms in the towing tank and analyzing the propulsive power available. To quote from the abstract of (10), *"Results of the tests indicated no unusual physiological or hydrodynamic phenomena: power values were comparable to human performance. These results, however, are in conflict with observations of unusual sea-animal performance reported in the open literature."* The tests were conducted in seawater in the former Convair Corporation tank in San Diego. The top speed of the *lagenorhynchus* porpoise in the tow tank in 35 runs was only 7.7 m/s. However Lang and Daybell could not explain the high swimming speeds reported by others in the open literature and thus looked for flaws in their own work. One concern was the size of the tow tank. This led to the next series of his experiments. He moved to an open test range at Coconut Island in Kaneohe Bay, Hawaii.

An important factor in the research of Lang and Norris (11) and Lang and Pryor (12) was that the animals were trained to go fast. In all three sets of experiments the animals showed significant improvement after repeatedly undergoing the trial. This implies that wild dolphins do not utilize unusual speed, but that like trained athletes they could improve their speed by exercising the muscles involved in fast swimming. With a *stenella* dolphin in Lang and Pryor, instantaneous speed measurements were made along the swimming course. In over 300 data runs there were three instantaneous top speeds of over 10.3 m/s. The maximum was 11.1 m/s. These data points were taken by comparing frame to frame camera data and not averaged over any length. As instantaneous points they are interesting, but not conclusive, because they were reached only once during the run and the average speed over the few seconds around that point was 20% lower or no more than about 8 m/s. There is a good chance that the camera system or the analysis failed during these few data points as the massive bulk of the data was at much lower values and all sustained measurements were also lower. The often quoted dolphin speed for this experiment is 11.1 m/s, when a speed based on the vast majority of the data points would be much lower. An interesting observation in Lang and Pryor is, *"An alternate check of top speed was made in an oceanarium at Sea Life Park, where two S. attenuata were trained with four spinner porpoises to swim at high speed around a 70 m path circling a small island in the park. The animals appeared to travel at extremely high speed, but reduction of the data showed top speeds of only 7.7 to 8.3 m/s."* In Lang and Norris (11), a *tursiops* species was tested under similar conditions. For very short durations (frame to frame) a top speed of 7 to 8.3 m/s was observed. For longer durations an average of about 3 m/s was noted.

Other Speed Claims:

A number of reference works on marine mammals also repeat some of the early high speeds. These claims can be traced back to the work of References (1) or (2) and thus do not have to be treated separately. There is some Russian research on the implications of dolphin swimming speed. The researchers tend to repeat the speed claims of Gray and the other anecdotal observers and throw in some unsubstantiated results from the 1930s in Russia as well. They assume laminar flow and other mechanisms exist, then study them.

III. RECENT MEASUREMENTS

In the last 20 years there have been a number of experiments that utilize more accurate speed measurement techniques

and larger numbers of data points than the previous results. Many of these results and the implications of the results on the fluid dynamics issues of drag reduction can be found in Fish and Hui (13). They find that there is no evidence of unusual frictional drag reduction mechanisms with dolphins. Each potential mechanism such as compliant damping, dermal ridges, secretions and heating is discussed and found unsubstantiated. Adequate metabolic output for the likely swimming speed is found within the animal's normal muscle abilities. Williams et al. (14) and van Oossanen and Oosterveld (15) present arguments about the amount of energy available. Since about twice as much power is required to travel at a sustained 10 m/s than at 8 m/s, the inflated swim speeds can be a crucial factor in the analysis. Reference (15) finds that at 8 m/s there is sufficient power from the muscles to overcome the turbulent drag. Reference (14) documents that the cost of a dolphin swimming is $1/12^{th}$ the power required by a human swimmer at the same speed. More recent results in the U.S. address a number of the controversial issues with credible data and will be discussed in what follows.

Laminar Flow Mechanisms:

One of the issues that continues to be subject to controversy was addressed conclusively by Lang and Daybell (10). This was the existence of laminar flow where turbulence should be present. For example the careful use of collars to trip the boundary layer at speeds of up to 4 m/s, led to the conclusion, *"The boundary layer is probably about 20% laminar."* This is similar to underwater bodies in the same speed and size regime where Reynolds Number at the point of transition is roughly 1 to 2 million based on the distance from leading edge to transition point. (See Streeter (16).) Other factors such a smoothness and pressure gradient due to shaping come into play, but will not affect this value much. This approximate transition location was verified by Rohr et al. (17) through the use of Bioluminescent Marine Plankton. Lang and Daybell make a further observation, *"Also, small particles suspended in the water can produce turbulence where laminar would otherwise exist."* If other researchers had noted this a great deal of effort in seawater drag reduction might have been avoided.

Captive animals:

There has been much concern about the speed capability of wild versus captive animals. A definitive study in that regard has been made by Rohr et al. (18). They took data on a wide range of both wild and captive animals using digital cameras with fixed reference planes for accurate measurements and many repeat runs to determine swimming speeds. The circumstances were quite different, ranging from aircraft driving schools of animals to captive animals being released in shallow water. Motivation was at least reasonable given that the early data indicating high swimming speeds had no motivation at all. The conclusion was that the captive dolphins were as fast as or faster than the wild animals. This confirms the early evidence that captive animals can be trained to swim faster. In general, captive animals are healthy and well fed. Captive animals can be trained to swim fast to jump high to get even more performance. Wild animals often have scars on the head from encounters with predators or other dolphins that would defeat any frictional resistance reduction anyway. Even among the captive animals, the analysis of 930 speed runs shows a maximum short duration speed of 8.15 m/s, as shown in Table II. The average speed for the distance of the run was around 6 m/s. No overall average speed for the run exceeded 7 m/s. For the wild dolphins, over 1000 runs were analyzed and the maximum velocity was found to be 6.7 m/s, with an overall average of 4.18 m/s, as shown in Table III. Because of the digital camera technique all the durations for the analysis were on the order of 1 to 2 seconds.

Duration:

The short durations associated with the higher dolphin speed numbers raises an interesting issue. There is a large difference between the power that can be exerted over a one-second period and that over a 1 minute period. A very short time speed burst would be of little value to an animal since it would not create a very large distance between the animal and its predator. A distance generated by a 2 m/s burst over 1 second would be about one body length. Any hydrodynamic phenomena that would be leading to such a burst would have to act over the length of the animal and that in itself would take a significant fraction of a second to take effect. This makes it even less likely that a burst is due to hydrodynamic effects and more likely that it is due to a short-term oxygen deficit. The short-term exertion involved in a jump is a good example of the levels that can be reached.

Quality and Quantity of Data:

It is worthwhile to contrast two published papers on the swimming speed of *tursiops trucatus.* One is Lockyer and Morris (19) and the other is Wursig and Wursig (20). Reference (19) gives a couple very high speed points out of a total of 12 data points. The observational technique is prone to subjective interpretation of the position of markers and the start and stop times. These points are questionable since the distance traveled was estimated from charts and the observation was taken from a considerable distance looking down from a cliff. No attempt is made to repeat the clearly extraordinary data point of 15 m/s for a duration of 20 seconds. The efforts of Reference (20) are for the same species, but taken over a long period with over 1000 measurements. Theodolites from two positions recorded the animals at specified time intervals to give a triangulation of the position and the time interval (usually 30 seconds). There is still some inherent error in the technique, but the credibility of the results is enhanced by the quantity of the data points. Recorded speeds did not exceed 6 m/s and averages were less than 5 m/s. The animals were engaged in normal behaviors such as chasing prey and did not interact with a ship.

The implication is that the extraordinary speed observations are for cases with sparse data and crude measurement techniques. The outlying points are quoted as the speed capability instead of being thrown out as bad data. In some cases the expectation of high-speed results may have colored the estimates being made. This naturally led to a misunderstanding about dolphin speed and power capability and led to a great deal of research directed at finding the 'secret' of the dolphin. In the future, drag reduction researchers should be especially aware of the pitfalls of believing sparse data showing unusual capabilities. It is the first concern when an unexplainable, but very promising data point is claimed, to repeat the experiment in a neutral facility or with neutral observers. This must be undertaken before a scale up or follow-on research effort is approved. Extraordinary results always should require an extraordinary level of proof.

IV. FUTURE RESEARCH ISSUES

While the dolphin does not possess a frictional drag reduction mechanism, there are still interesting naval architecture issues involved with the biological system. One is the mechanism for the dolphins' jumping ability. They seem to be able to jump higher than the swimming speed alone can explain. This is noted in Reference (18). Another interesting research direction is the area of wave drag reduction through body shaping and particularly the way the body changes shape during propulsion. The dolphin usually swims near the surface because it needs to breathe air. Thus its swimming should be optimized to be efficient close to the surface. This may be tied to the dolphin's up/down rather than side to side propulsive motion that fish possess. In Reference (17) it is noted that the swim speeds of the dolphins were significantly higher in deep rather than shallow water. Also, the usual dolphin swimming speeds correspond to a length Froude number of close to one. Advanced computational modeling might be able to shed some light on these issues.

V. CONCLUSIONS

Dolphins and other marine mammals are well adapted to swimming in the ocean. Their bodies are streamlined and their physiology takes into account the heat and respiratory constraints of living in the sea. The dolphins swim fast, but do not exceed what they would be capable of doing without exotic drag reduction mechanisms. The range of realistic swim speed values is up to 8.3 m/s for very short durations and half that for longer periods. These speed levels seem to hold for both captive and wild dolphins. Thus Gray's Paradox is based on incorrect data for swim speed of marine mammals. The evidence is that the amount of laminar flow is about what would be expected for that range of Reynold's Number and not prolonged in any way. Thus there is no reason to believe, based on the swimming speed data, that dolphins have frictional drag reduction systems or techniques.

In order to establish extraordinary performance of biological creatures, swim speed data must be repeatable, have acceptable error bounds and points that lie far from the majority of the data should be rejected. This recommendation will impact the level of data required to establish the existence of other seawater drag reduction mechanisms as well. In conclusion, while dolphins are

streamlined swimming organisms that may avoid some form drag and some wave drag, there is no convincing evidence that they reduce skin friction drag or that they postpone transition from laminar to turbulent flow.

VI. ACKNOWLEDGMENT

This paper is dedicated to the late Dr. Arthur E. Bisson. Dr. Bisson was interested in this subject and urged me to see that the correct values for dolphin swimming speeds became widely known. The technical discussions and advice from Dr. J. Rohr and Prof. F. Fish are greatly appreciated. This paper was prepared under the ONR Research Opportunities for Program Officers Program.

VII. REFERENCES

1. Gray, J., 'Studies in Animal Locomotion VI: The Propulsive Power of the Dolphin,' **Journal of Experimental Biology**, V13: p 192-199, 1936.

2. Johannessan, C.L. and J.A. Harder, 'Sustained Swimming Speeds of Dolphins,' **Science**, V132: p1550-1551, 1960.

3. Murphy, Robert C., **Logbook for Grace**, TimeLife Books, 1947

4. Gawn, R. W. L., 'Aspects of the Locomotion of Whales,' **Nature**, V161: p44-46, 1948.

5. Kermack, K. A., 'The Propulsive Powers of Blue and Fin Whales,' **Journal of Experimental Biology**, v25: p 237-240, 1948.

6. Williamson, G. R., 'The True Body Shape of Roqual Whales,' **Journal of Zoology**, London, V167: p 277-286, 1972.

7. Kellogg, R., 'Whales, Giants of the Sea,' **National Geographic**, V 67, 1940

8. Woodcock, A. H., 'The Swimming of Dolphins,' **Nature**, V161: p 602, 1948.

9. Perry, B. and A. Acosta and T. Kiceniuk, 'Simulated Wave Riding Dolphins,' **Nature**, V192: p148-150, 1961.

10. Lang, T.G. and D.A. Daybell, 'Porpoise Performance Tests in a Seawater Tank,' NOTS Technical Publication 3063, Naval Ordnance Test Station, China Lake, CA, 1963

11. Lang, T. G. and K. S. Norris, 'Swimming Speed of a Pacific Bottlenose Porpoise,' **Science**, V151: p588-590, 1966.

12. Lang, T. G. and K. Pryor, 'Hydrodynamic Performance of Porpoises (*Stenella Attentuata*),' **Science**, V152: p 531-533, 1966.

13. Fish, F. and C.A. Hui, 'Dolphin Swimming - A Review,' **Mammal Review**, V21: p181-195, 1991.

14. Williams, T. and W. Friedl, M. Fong, R. Yamada, P. Sedivy, J. Haun, 'Travel at Low Energetic Cost by Swimming and Wave-Riding Dolphins,' **Nature**, V355: p 821-823, 1992.

15. van Oossanen, P. and M. Oosterveld, 'Hydrodynamic Resistance Characteristics of Humans, Dolphins, and Ship Forms,' **Schiffstechnik**, V36:p 31-48, 1989.

16. Streeter, V. L., **Fluid Mechanics**, McGraw Hill, 1966.

17. Rohr, J. and M. Latz, E. Hendricks, J. Nauen, 'Experimental Approaches Towards Interpreting Dolphin-Stimulated Bioluminescence,' Journal **of Experimental Biology**, (in Press).

18. Rohr, J. and E. Hendricks, L. Quigley, F. Fish, J. Gilpatrick, J. Scardino-Ludwig, 'Swimming Observations of Captive and Free-Ranging Dolphins', SPAWARS Systems Center Technical Report 1769, 1998.

19. Lockyer, C. and R. Morris, 'Observations on Diving Behavior and Swimming Speeds in wild Juvenile *Tursiops truncatus*,' **Aquatic Mammals**, V13: p31-35, 1987.

20. Wursig, B. and M. Wursig, 'Behavior and Ecology of the Bottlenose Dolphin, *Tursiops trucatus*, in the South Atlantic,' **Fishery Bulletin**, V77, No. 2, 1979.

Table I. Early speed observations for dolphin species.

Species	Speed (m/s)	Methodology	Speed Classification	Reference
"Dolphin"	10.3	Stopwatch	Along Ship (7s)	1
"Dolphin"	7.2 to 9.3	Ship Estimation	Various	2
Globicephala	11.3	Ship Estimation	Maximum Sustained	2
Orcinus Orca	15.5	Ship Estimation	Maximum Sustained	2
Delphinus delphi	9.3	Unknown	?	7
Tursiops truncatus	15	Cliff Estimation	Burst	19
Tursiops truncatus	8.3	Theodolite Tracking	Burst	20
Tursiops truncatus	1.7	Theodolite Tracking	Average Cruising	20
Tursiops truncatus	4.2	Cliff Estimation	Average Cruising	19
Tursiops truncatus	7.01 to 8.3	Trained in Captivity	Burst (7.5-10s)	11
Tursiops truncatus	6.09	Trained in Captivity	Maximum Sustained	11
Tursiops truncatus	3.08	Trained in Captivity	Average Cruising	11

Table II. Summary of trained captive dolphin swimming speed. (Ref. 18)

Dolphin ID	Species	All Velocity Data		
		# of Observations	Max Vel m/s	Avg Vel m/s
1	*Tursiops truncatus*	97	7.74	6.52
2	*Tursiops truncatus*	68	6.67	5.45
3	*Tursiops truncatus*	111	6.79	5.72
4	*Tursiops truncatus*	26	7.49	6.71
5	*Tursiops truncatus*	142	8.15	6.55
6	*Tursiops truncatus*	189	7.76	6.39
1 to 6	*Tursiops truncatus*	633	8.15	6.24
7	*Delphinus delphi*	103	8.0	6.67
8	*Pseudorca crassidens*	191	8.0	6.38

Table III. Summary of wild dolphin (*Delphinus capensis*) photogrammetric speed measurements. (Ref. 18)

Pass	# of Observations	Maximum Velocity (m/s)	Velocity Range (m/s)	Duration Of Pass (s)	Average Speed Duration (s)
1	80	6.60	2.69 to 6.60	18.6	1.44
2	106	5.89	2.49 to 5.89	15.2	1.24
3	310	6.70	3.07 to 6.70	18.4	1.42
4	377	5.56	2.27 to 5.56	14.2	1.23
5	171	5.78	2.40 to 5.78	18.4	1.48
1 to 5	1044	6.60	2.27 to 6.60	513.2	1.34

HYDRODYNAMICS OF WAVE-LIKE CURVATURE ON BODIES OF SWIMMING ANIMALS

Rudolf Bannasch
Technische Universität Berlin
FG Bionik & Evolutionstechnik
Ackerstrasse 71-76
D-13355 Berlin, Germany
E-mail: bannasch@fb10.tu-berlin.de

Abstract - Experimental studies on live penguins and measurements with life-sized models of their trunk in a water tank revealed extremely low drag coefficients. An axisymmetric body based on the body geometry of three medium sized penguin species was found to be an excellent low-drag laminar body by drag measurements in a water tank. When the transition from laminar to turbulent flow was triggered at 5 % of the body length, the surface drag coefficients remained even lower than those of a turbulent flat plate of equal length, and they declined at a higher rate with increasing Reynolds numbers. Viscous drag was reduced by the characteristic "stepwise" pressure and velocity distribution developed along the multiply curved (wave-like) outlines of that body. Turbulent velocity fluctuations in the boundary layer remained at a low level even in the rigid model. Flow visualization experiments on live penguins showed the wavy contour to be most efficient in conjunction with a compliant wall. In most cases, a regular pattern of transverse waves (wave length 2 -3 cm) was observed over the plumage. Since most flying and swimming vertebrates have wavy body contours, comparative studies on the development of the respective proportions with size progression will be useful.

I. INTRODUCTION

Evolutionary adaptation of animals to sustained fast flying and swimming has faced the same tasks as engineering of modern aircraft, cars, ships and submarines, namely to transport a given body mass or volume with minimum costs and to maintain optimal maneuverability under changing flow conditions. Contrary to engineering, nature had a huge experimental ground. Over millions of years, a wealth of designs have been created, tested and optimized. The sometimes spectacular achievements of animal locomotion in air and water can be explained only by optimal combinations of mechanically highly efficient propulsion systems and extraordinary (complex) drag reduction measures. Here, engineers can still learn from nature.

Indeed, a comparison of the costs of transport of animal flight with that of aircraft and helicopter in a dimensionless way shows that nature has found much more economic solutions [1]. But animals fly at quite low Reynolds numbers ranging from just under 200 for small insects to less than 10^6 for the fastest large birds. Scaling rules predict that they may not deal with the same flow and drag problems as does engineering. In the aquatic environment, however, at least the fastest swimmers may encounter flow regimes comparable to those of technical bodies (e.g. subsonic aircraft, small ships and submarines). But, due to the enormous diversity in life styles, feeding and survival strategies, principles of force generation and the many other functions incorporated in the animal's body, many details and structural solutions to the problem of natural drag reduction still remain undiscovered or ill-understood.

This paper focuses on mechanisms of hydrodynamic drag reduction. Apart from other mechanisms widely used in nature (like polymer ejection, drag reducing surfaces etc.), shape optimization represents the basic and most important factor for drag reduction.

II. LAMINAR VERSUS TURBULENT BODIES

As early as 1800 Cayley (cited in [2]) had proposed to take the shape of the trout as an model for the (future) design of aircraft fuselages. About one hundred years later, streamlining led, indeed, to fish-like designs, for example in the Parseval-17 airship. For such huge constructions, the prevention of flow separation represented the most important consideration.

In the sixties, Hertel [2, 3] concluded that the body geometry of trout, tuna, sharks, dolphins and blue whale, in comparison to technical profiles, represent "laminar-flow spindles". He used this as an argument to replace the "transport tubes" of commercial aircraft by laminar fuselages since the latter offer the largest volume for the lowest drag. However, it is obvious that Hertel was not interested in the details of the natural design. For example, in considering the shape of dolphins, he totally ignored the rostrum and smoothed out the slightly wave-like contour of the body by superimposition of a low drag NACA profile. Strictly speaking, Hertel did just show that the existing engineering knowledge could help to estimate natural shapes, but he did not study natural phenomena experimentally.

In fact, our knowledge about the boundary layer development in fast swimming animals is rather poor. For the most part, conclusions have been made solely on the base of technical analogies.

Experimental studies of the fluid dynamic properties of live swimming animals are crucial. Their flexible bodies are adaptable to particular flow conditions. In fish and dolphins the body is strongly involved in the process of thrust generation, and is thus exposed to highly unsteady effects which can hardly be reproduced experimentally. For the most part, studies with rigid models have been rather disappointing, and various numerical approaches to discover the secrets of the dolphin swimming, namely to solve Gray's Paradox [4], led to controversial results. Some authors [5, 6] reject the existence of any drag reducing mechanisms in dolphins, but concluded that these animals are more powerful than assumed before. Others [7] contend that the hydrodynamic efficiency of the fluke has been largely overestimated. After respective correction it turned out that, Gray was right. These animals must be able to use special methods for drag reduction. Apart from the ability to delay considerably the laminar-turbulent transition in the boundary layer by compliant wall effects [8 - 10] possibly in conjunction with polymer secretion from the eye [11] to keep the turbulence at a low level, drag reduction was referred by Romaneko [7] mainly to favorable pressure gradients actively generated by the wave-like body motion. He had conducted first measurements on the pressure fluctuation and wall shear stress on live animals.

However, the laminar hypothesis might be not applicable to all marine animals. Sharks seems to have developed another mechanism for drag reduction. Their skin was found to reduce turbulent wall shear stress by its "riblet" structure [12 - 14].

Earlier results of Russian scientists summarized by Aleyev [15] and recently reconsidered by Videler [1] point to a further interesting mechanism of drag reduction used in nature. In swordfish, the rostrum forms a long and slender pre-body (blade), which was found both to reduce the dynamic pressure peak at the frontal part of the main body and to smooth the pressure distribution further downstream. It may also reduce the wall shear stress by increasing the local Reynolds numbers downstream. But most interesting, due to its rough surface, it is likely to stimulate an early transition from laminar to "micro-turbulent" turbulent flow. Videler's conclusion that the boundary layer can be kept in that state by the following concave-convex shape of the head, and the theoretical assumption that such a "micro-turbulent boundary layer" may behave like a laminar one, clearly require experimental confirmation. Nevertheless - apart from sharks – the swordfish gives another example for the early development of a turbulent boundary layer in marine animals. Moreover, it represents a first indication of turbulence management by a multiply curved body profile in nature.

III. THE PENGUIN PHENOMENON

As examples of shape optimization for fluid-dynamic purposes, penguins are a particularly interesting group of animals. Derived from highly evolved flying birds, they changed to aquatic life and became the best adapted birds to wing-propelled diving and swimming. After several studies conducted on different penguin species in zoos had pointed to excellent hydrodynamic properties [16, 17, 18], a comprehensive approach to the marine ecology, energetics, swimming and diving performances of penguins was developed in the framework of the German Antarctic Expeditions [19 – 23].

Telemetry showed that medium sized penguins (body length 0,65 – 0,70 m in the swimming posture) can swim more than 100 km per day and dive to maximum depths of ca. 450 m. Their preferred travel speed ranges from 2 to 3 m/s, and the maximum speed is about 4,5 m/s. The larger Emperor penguins are somewhat faster, and can reach a maximum speed above 7 m/s.

Field metabolic studies supplied evidence for low energy consumption in under-water locomotion. Assuming the energy content of krill to be 3700 kJ/kg, 1 kg of that food would allow for example a 4 kg Adélie penguin to travel up to 200 km. One may try to illustrate this result in technical terms: if this penguin would be able to utilize benzine (46700 kJ/kg) instead of krill, 1 l of this fuel would suffice for a ca. 2500 km long trip in the cold ice sea!

These data point to high mechanical efficiency of the propulsion system and to particularly high achievements in body drag reduction, since the biochemistry of the flight muscles does not differ from that of other birds. Unlike in fish and dolphins, the penguin's trunk does not contribute to thrust production; trunk oscillations during a wing beat cycle are moderate. Therefore, the spindle-like penguin trunk may well serve as live example for how energy may be saved by shape optimization of stiff bodies. Our aim was to study this experimentally.

IV. PENGUIN BODY GEOMETRY

For a complex of morpho-functional studies including also hydrodynamic investigations, ten individuals were collected from each of the three pygoscelid species: Gentoo (*Pygoscelis papua*), Adélie (*P. adeliae*) and Chinstrap penguin (*P. antarctica*). After measuring body mass, body length, maximum girth, that individual of each specues which was closest to the mean values was mounted in swimming posture and frozen. Then, models in glass fiber reinforced plastic were made [24].

The geometry of the casts (without wings) was compared to that of the original penguins. No differences were found, and even very small details of the plumage were copied. The contours of the three models (from the dorsal and lateral view) were drawn to the same scale with the body length taken as a standard reference (Fig. 1).

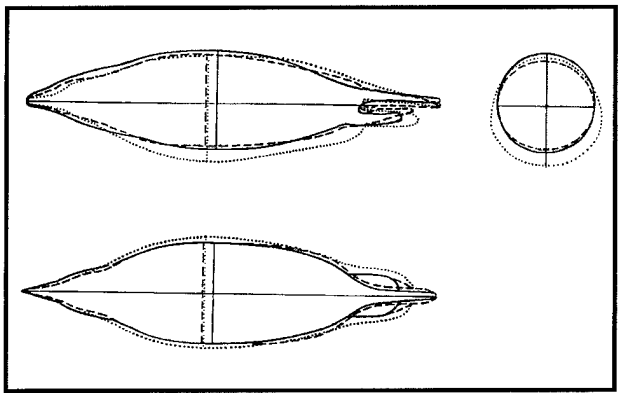

Fig. 1 Geometry of the penguin bodies (three projections): Solid line: Adelie, dashed line: Chinstrap, dotted line: Gentoo penguin.

Table 1 Geometry of penguin bodies. A frontal area [m^2], d diameter of the frontal area [m], l body length [m], x_d abscissa of the maximum thickness [m], l/d length to thickness ratio, x_d / l maximum thickness position.

Species	l/d	x_d/l	A	$d=\sqrt{(4A/\pi)}$
P. antarctica	4,54	0,44	0,01959	0,158
P. adeliae	4,35	0,47	0,02083	0,163
P. papua	4,00	0,44	0,02706	0,186
body of revolution	4,237	0,443	0,02147	0,165

The body shapes of the three species resemble one another in being spindles with high values of maximum thickness position and thickness ratio (see also Table 1). A small degree of dorso-ventral asymmetry was evident from the lateral view (Fig. 1 above). At the position of maximum thickness, the cross section was almost circular. Overall, the geometry of the penguin bodies would characterize them as laminar-flow spindles (sensu Hertel [2, 3]. However, the structure of the beak and a certain roughness at the beginning of the plumage suggests that the transition from laminar to turbulent boundary layer may be triggered in the very frontal part of the body, and moreover the "wave-like" outlines of the forebody look somewhat unusual.

Based on the arithmetic means of the respective diameters at 70 points along the axis, an axisymmetric body of revolution (Table 1, Fig. 2) was turned on a lathe.

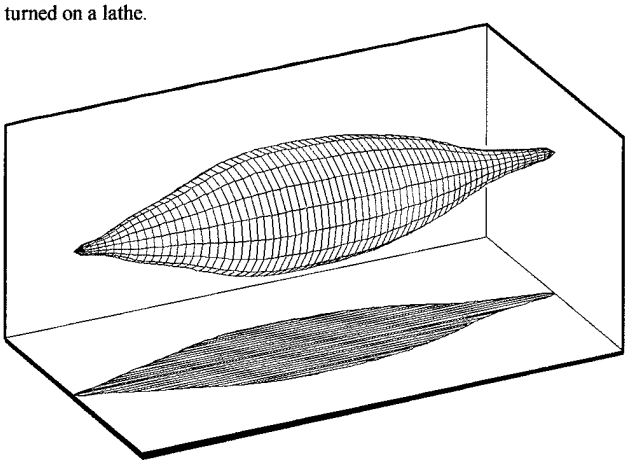

Fig. 2 Body of rotation derived from the penguin data

V. FLOWVISUALISATION AND DRAG MEASUREMENTS

Visualisation experiments in a smoke-wind tunnel showed a smooth flow around the penguin body (Fig. 3). Even at a free stream velocity of 11 m/s (which corresponds to 0,7 m/s in Antarctic seawater) separation occurred only in the tail region. Some increase of the velocity caused a downstream shift of the point of detachment and thereby a reduction in the diameter of the wake. It can be predicted, that at the normal travel speed of penguins (ca.2 - 2,5 m/s) flow separation at the body surface does not occur at all.

Fig. 3 Model of a Gentoo penguin in the smoke-wind tunnel (steam velocity 11 m/s)

In order to cover the range of Reynolds numbers used by the respective penguin species in their natural environment, drag measurements were conducted in the large circulating tank of the Versuchsanstalt für Wasserbau und Schiffbau (VWS; the Berlin Model Basin). In the test section (8 m long and 5 m wide) wall effects were excluded. The water depth was adjusted to 1.5 m by elevation of the floor. The turbulence in the circulating tank was relatively high. The turbulence factor was 1.8 - 2.0 (determined by means of the critical Reynolds number of an ideal sphere). The penguin models were fixed to steel bars (length 1 m, diameter 15 mm) placed in the long axis of the body. The end of the bar was attached to a vertical rod encapsulated by a low drag cowling, and the rod was attached to a balance. The models were submerged to a depth of 75 cm. This was much deeper than 3 times the vertical height of the body in a swimming position, which is a depth below which drag augmentation by surface effects is negligible [2].

Fig. 4 shows the frontal drag coefficients c_{Df} of the penguin models plotted against Reynolds numbers Re_d (using the diameter d as reference length). All three models showed a very similar characteristic best approximated by a logarithmic function $c_{Df} = 11.975\ \mathrm{Re_d}^{-0,4434}$ (correlation coefficient R = -0,943, p = 0,001).

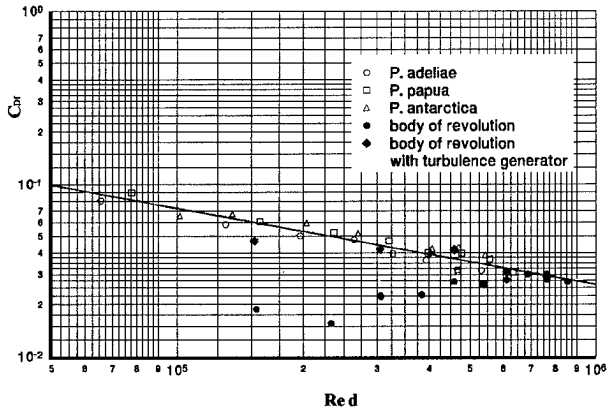

Fig. 4 Frontal drag coefficients plotted against Reynolds numbers. In this graph, Re was calculated by using the maximum diameter d as reference length.

At lower *Re*, the results coincided with those of other authors [17], but the best values (c_{Df} = 0,03) obtained from the Adélie and Gentoo models at $Re_{d,max}$ (flow velocity 4,5 m/s) were surprisingly low.

The body of revolution showed an opposite tendency. Starting with lowest values (just under 0,02 !) the c_{Df} declined first to 0,0156 (at $Re_d = 2{,}331 \cdot 10^5$). Thereafter it increased to finally 0.03 and then decreased again following the regression line of the original penguin models. This was clearly an effect of transition from laminar to turbulent flow in the boundary layer. To prove this experimentally, a 1 mm thick wire ring was attached to the nose of the body in order to trigger the transition at 5 % of the body length. Thereafter, the body of revolution showed nearly the same characteristics observed in the penguin models (Fig. 4). From this similarity we concluded that the boundary layer in our penguin models must also have been turbulent. At this stage, we could not answer the question about applicability to live animals, but the axisymmetric penguin-like body seemed to offer promising perspectives for technical applications.

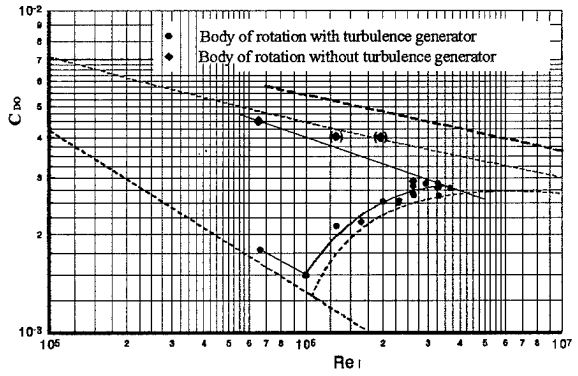

Fig. 5 Surface drag coefficients of the body of rotation plotted against Reynolds numbers. Note that in this graph Re was calculated by using the body length *l* as reference length. The two values in brackets should be neglected (artificial drag increase due to unfavourable Froude numbers in the test section). Dotted lines: laminar (below) and turbulent (above) flat plate. Dashed line on top: turbulent bodies with a length to thickness ratio of 4.2, cf. [25].

To compare the results obtained from the body of rotation to those reported in [25], the surface drag coefficients c_{DO} were plotted against Reynolds numbers using the body length *l* as characteristic length (Fig. 5). Most surprising, in the turbulent case the surface drag coefficients of our axisymmetric body remained even lower than those of a turbulent flat plate of equal length, and with increasing Reynolds numbers they declined at a higher rate. Drag coefficients were some 30-35 % lower than those reported for the best turbulent technical bodies [25].

VI. SOME INSIGHTS INTO THE MECHANISM OF DRAG REDUCTION

1. Unusual pressure and velocity distribution along the contour of the axisymmetric penguin-body

Together with students of the Institut für Luft- und Raumfahrttechnik der TU Berlin, another (hollow) model of the body of rotation was built and equipped with pressure holes. We had to cut off the tail of the body to facilitate connection of the tubes glued inside the holes to a pressure transducer (via a scanivalve) outside of the test section. The pressure distribution was determined in a wind tunnel at various flow velocities. Additional comparative measurements were carried out on both bodies of rotation with an external static pressure sonde (diameter: 1 mm),

Fig. 6 shows the distribution of the dimensionless pressure coefficients c_P obtained experimentally by both methods in comparison with potential flow calculations (panel method without consideration of the displacement thickness).

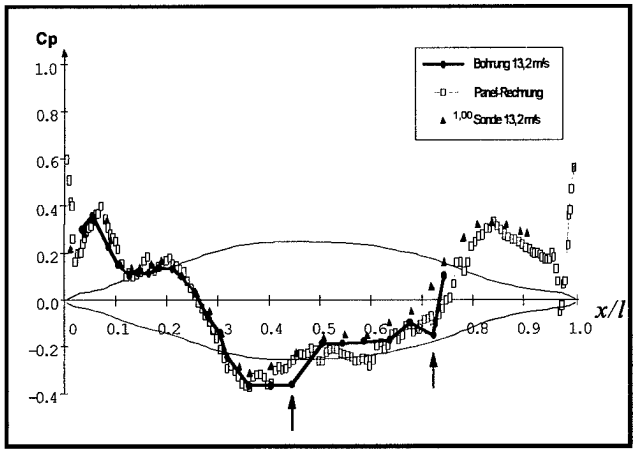

Fig. 6 Pressure distribution, experimental and numerical data.

Apart from small deviations at the points indicated by arrows (probably two defective pressure holes), the results coincide well for the frontal part of the body. At the rear, the differences became somewhat larger since each method implied certain disadvantages. The general tendency, however, was similar in all three approaches.

Contrary to conventional bodies, where the pressure continuously decreases towards and increases beyond the maximum girth position, a more stepwise pressure distribution was found in the present case,. Most remarkable were the roughly similar gradients (slopes) along the forehead, the beginning of the trunk, and - with the opposite sign - also at the end of the trunk. Consequently over the convex areas, the flow was accelerated or decelerated at a nearly constant rate, respectively. Over the intervening slender (concave) parts, the pressure - and consequently also the flow velocity - remained nearly constant (plateau). This unusual pressure fluctuation can be described by a secondary wave superimposed on the main curve. The wave length increased in correspondence with the local Reynolds number. It should be noted, however, that at the beak, the depression in the pressure distribution changed to a plateau when the transition from laminar to turbulent flow was triggered at that point by a wire ring. The downstream pressure distribution was not altered by this measure.

The relatively good coincidence of the experimental results with those obtained from potential flow calculations indicates a low pressure drag. The total drag of the given body seems to be mostly due to friction.

2. Paint flow visualisation

To get some insight into the development of the near wall flow pattern, the paint flow method was used. The body of rotation was evenly painted with a mixture of petroleum, oil acid and titanium white and exposed then to an air stream of 20 m/s ($Re_l = 9.3\ \ 10^5$). This was the maximum speed allowed by the free steam wind tunnel of our department. After evaporation of the oil, the remaining titanium gave an impression of the flow pattern at the surface of that multiple curved body. Fig. 7 shows the

result from two different experiments (without and with turbulence generator at the base of the beak).

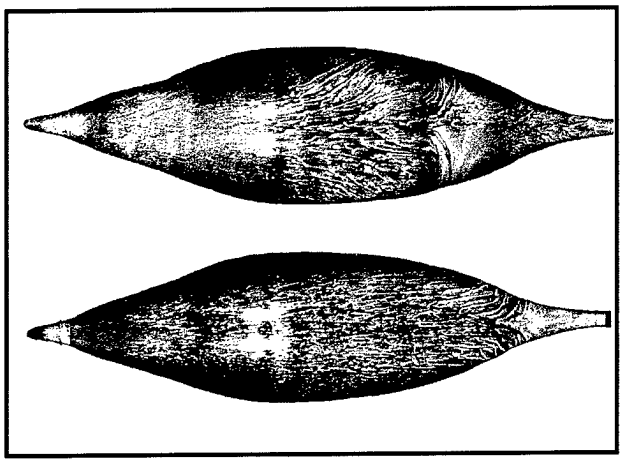

Fig. 7 Paint-flow visualisation on the body of rotation without (above) and with turbulence generator (below). Top view in both cases.

In the picture without turbulence generator (Fig. 7 above), three main zones can be distinguished. In the frontal part (up to ca. 40% of the body length), the flow was stepwise accelerated and remained laminar. The tiny structure of the pigments indicates a relatively high wall shear stress. Friction was highest over the convex parts (tip of the beak, forehead, frontal part of the trunk). However, some relaxation of the boundary layer (increase of the structures imprinted) could be observed along the concave parts at the origin of the beak and in the neck region. The second zone reaches from ca. 40 to 70 % of the body length. Here, the flow seemed to be still laminar, but the structures imprinted grew very fast. The diverging paint flow lines indicate a considerable relaxation of the boundary layer. Especially at the sides of the body, the pigments were driven in an oblique direction since gravity started to dominate over the friction forces. Finally, with a sharp border, a (probably) laminar detachment zone with turbulent reattachment at the tail was formed.

Possibly in the present visualisation experiment, the wind velocity was too low to keep the flow fully attached. It was also possible that the rear of the body was not optimally shaped. When constructing the axisymmetric body, we did not know how to deal with the feet. Finally, that part was smoothed by hand. The design was, however, not that bad. At the tail, the flow reattached, and a drag penalty due to an unbalanced pressure distribution could be avoided. Otherwise the extremely low drag coefficients (C_{DO} = 0.018) measured at similar Reynolds numbers in the water tank could hardly be explained.

The picture changed completely when the turbulence generator (wire ring) was placed at the nose of the body (Fig. 7 below). The concentration of titanium white pigments at the base of the beak marked a stationary ring vortex generated by the wire. The respective separation area had a sharp border. In the first experiment, a similar patch was formed in that area, but its margins were blurred; possibly a ring vortex or laminar detachment bubble was also formed at the end of the beak without turbulence generator. However, due to the laminar reattachment it did not influence the flow pattern downstream. But in the second case, the flow reattached turbulently. Although larger disturbances were immediately dampened out due to the flow acceleration at the following convex forehead, certain microstructures introduced into the boundary layer by the wire ring survived. The paint flow pattern increased in size continuously but rather slowly. Even at the end of the body, these structures remained much smaller than in the experiment without a turbulence generator. The influence of gravity on the direction of the paint flow was less pronounced, implying that the wall shear stress was higher. Since the boundary layer contained more energy, the detachment zone was shifted towards the tail of the body. This picture corresponds well with Fig. 3 (smoke visualisation on the cast of an original Gentoo penguin).

In general, the paint flow pattern obtained in the second experiment suggests a certain similarity with the structure of the plumage in real penguins, in which the size of the feathers increases from the head towards the end of the body at a similar rate. It might be worth noting here also that the microstructure of the penguin plumage is somewhat reminiscent of the riblet pattern known from the shark skin to reduce the turbulent wall shear stress [14].

3. Hot-wire anemometry

Further insights into the near wall flow at the penguin-like body of rotation were gained by using hot-wire anemometry in the large (closed) wind tunnel of the Hermann-Föttinger Institut für Thermo- und Fluiddynamik der TU Berlin. Here, we could obtain a flow velocity of 25 m/s at which the Reynolds number (Re_l = $1{,}2 \cdot 10^6$) corresponded to that preferably used by the pygoscelid penguins in the Antarctic Sea (mean travel speed: 2.3 m/s in saltwater at 4 °C).

Owing to the limited experimental time provided, detailed investigations could be conducted only on the flow around the wave-like frontal part of the body. Fig. 8 shows the velocity distribution in the outer flow field.

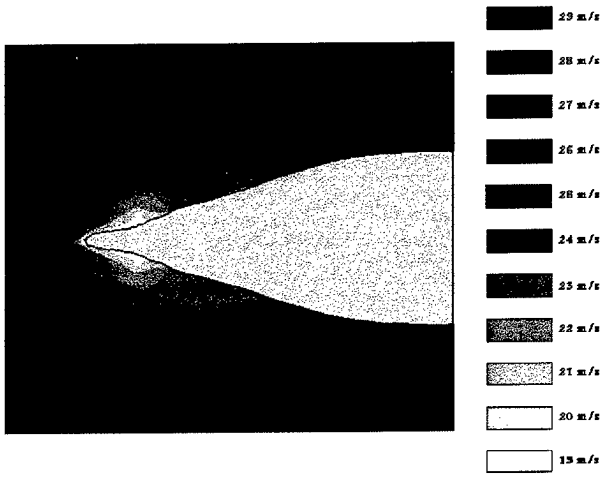

Fig. 8 Velocity distribution in the outer flow around the frontal part of the axisymmetric penguin body.

In this picture, the stagnation point was not well marked. It lay close to the tip of the beak. Generally, the influence of the body on the flow field in front remained moderate. A zone of decelerated flow was vertically extended over the concave part of the beak. Following a short acceleration over the convex forehead, the flow velocity near the wall remained nearly constant at the neck. This corresponds to the first pressure plateau in Fig. 6. At about 26 % of the body length, the free stream velocity was reached (no variation with distance from the body surface). This was the point where the pressure curve crossed the abscissa (Fig. 6). Downstream, a zone of hypervelocity was developed, with as expected, centre at the thickest part of the body.

The effect of this unusual flow pattern on the velocity profiles within the boundary layer is shown in Fig. 9. Most remarkable in both experiments (without and with turbulence generator) was that the thickness of the boundary layer increased suddenly at the base of the beak and thereafter remained nearly constant. In the laminar case, the S-shaped velocity profiles C-F might suggest the flow was close to separating. That would point to extremely low friction in this area.

It was evident from the doubly curved profile C that a shallow separation bubble was formed at the base of the beak (see discussion of the paint flow experiment).

When the body was equipped with the turbulence generator, the boundary layer was about three times thicker than in the laminar case, and the velocity profiles were more rounded. The unusual shape of profile C can be explained as a registration of the wake of the wire which was, obviously, somewhat too large (diameter of the wire in this case: 2 mm). The downstream profiles were no longer S-shaped.

The turbulence profiles shown in Fig. 10 support the ideas developed from the paint flow experiments. The huge disturbances introduced by the wire ring serving as turbulence generator (profile C) were quickly dampened out. Further downstream the turbulent velocity fluctuations were considerably reduced and were restricted to a relatively thin layer near the wall. Although the overall frequency spectrum was quite broad, at the maximum thickness position of the body a definite peak was observed at 3.1 kHz.

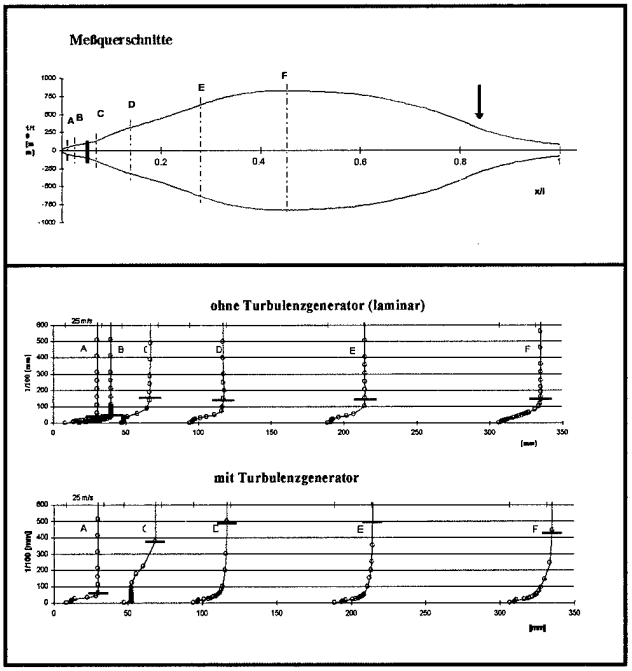

Fig. 9 Velocity profiles in the boundary layer at the wavy frontal part of the body measured by hot-wire anemometry. The horizontal lines indicate the boundary layer thickness corresponding to 99 % of the velocity of the outer flow. Top: position of the measuring points; middle: velocity profiles without turbulence generator; bottom: with turbulence generator.

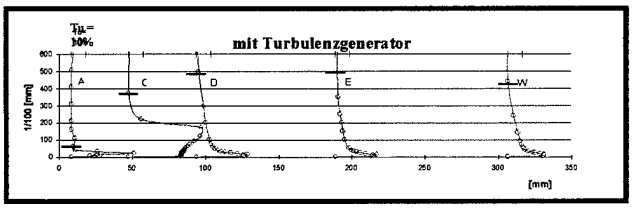

Fig. 10 Turbulence profiles. Transition was stimulated at ca. 5% of the body length. Points of measurement same as indicated in Fig. 9. $Tu = \sqrt{\overline{u'^2}}/U_\infty$, with $\overline{u'}$ mean of the turbulent velocity fluctuation, U_∞ free stream velocity, cf. [26].

When an early transition was stimulated, the magnitude of the velocity fluctuation within the boundary layer was much lower at the end of the body than in the case of natural transition (Fig. 11). Although in the last experiment, the flow velocity was higher, so that the detachment zone at the end of the body was likely to disappear, the result coincided well with the pictures observed in the paint flow experiments.

Apart from the 99 % thickness, the boundary layer is characterised also by the displacement thickness δ_1 and the momentum thickness δ_2 [26]. Our investigations focused only on the frontal part of the penguin-like body of rotation, but even here remarkable differences from those of a flat plate and conventional streamlined bodies could be observed. In the axisymmetric penguin body, the development of δ_1 and δ_2 was in general analogous to that of the 99 % thickness. At the end of the beak, all three boundary layer thickness parameters suddenly increased to values 1.5 – 2.0 times higher than those of the flat plate at a similar distance from the leading edge. In the body of rotation, the first pressure step seemed to generate boundary layer conditions which can be found on a flat surface only at considerably higher local Reynolds numbers, and in usual (three-dimensional) bodies even later. This mechanism may contribute to a drastic reduction of the local wall shear stress. But it involves also a certain risk. At the pressure step at the end of the beak, δ_2 did not jump as much as δ_1. Consequently, the shape parameter H_{12} ($H_{12} = \delta_1 / \delta_2$) showed a peak at this point. In the laminar as well as in the turbulent case, it considerably exceeded the respective values known to be crucial in view of flow detachment from a flat surface. Downstream that point, the shape parameter recovered to values slightly below the critical ones (laminar case), or became even more stable (in the turbulent case).

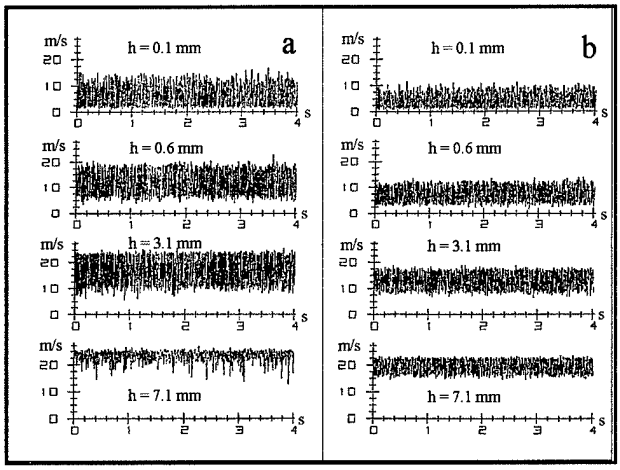

Fig. 11 Velocity fluctuations at the rear of the body (position: see arrow in Fig. 9). a (left side): without and b (right side) with turbulence generator; h distance from the body surface (from top to bottom: 0.1 mm, 0.6 mm, 3.1 mm, and 7.1 mm).

It should also be noted that the nose of the test body might have been less optimally shaped than the asymmetrical beak of a real penguin. It was possible that the separation bubble observed in our experiments was an artefact resulting, on the one hand, from the means of the contour co-ordinates being used and, on the other hand form the large diameter of the wire ring attached. So, there seems to be some potential for further optimisation of the artificial body.

Independent investigations of the wake of the axisymmetric penguin body conducted in another wind tunnel using hot-wire anemometry as well as studies on a somewhat smaller model in a circulating water tank by means of Laser-Doppler-Anemometry supported the very low drag coefficients of the given body shape.

The penguin body seems to be evolved to get use from several drag reducing mechanisms in combination. At the tip of the beak, the only way to reduce the effect of the unavoidably high friction on the total drag is to keep the diameter, and thereby the wetted surface, small. Since the transition causes a peak in the wall shear stress, it might effective to trigger the transition while the circumference is still small. The drag penalty resulting from early onset of turbulence might be moderate since, simultaneously, much stress is taken out by making the boundary layer thicker. Here, one may question the advantage of an early increase of the boundary layer thickness since the total drag equals the momentum loss at the end of the body. Unfortunately, we could not systematically study what really happened at the rear or in the wake of the penguin-like body. However, at the position of the maximum diameter, all three thickness parameters of the boundary layer were about half to two thirds of the values for a flat plate. The convex forehead serves as a kind of high-pass filter allowing only a certain micro-turbulence to survive. Keeping the boundary layer at a nearly constant thickness, then, may help to restrict the frequency band. Ideally (and hypothetically) this "tuning" mechanism may restrict the turbulent pressure and velocity fluctuations to those best controllable by the dampening properties of a compliant body surface. Although, this has to be verified experimentally; there is every indication that this mechanism plays an important role in drag reduction of life penguins.

VII. FLOW-VISUALIZATION IN LIFE PENGUINS

During our last Antarctic expeditions, special hydrodynamic studies were carried out on live penguins swimming in a 21 m long still water tank (cross section ca. 1x 1 m). For this purpose, a novel method for flow visualization in live animals with controlled dye ejection from underneath of the plumage was developed. In combination with conventional video and high-speed video analyses, fundamental insights into the details of the boundary layer development in various flow conditions and into its interaction with the vortex system generated by the wings could be obtained. These visualization experiments confirmed that transition occurred in the most frontal part of the bird's body. However, the boundary layer never became „chaotic" further downstream. In most cases, a quite regular

wavelike pattern (wave length 2 -3 cm with only the amplitude increasing towards the end of the body) was formed. The waves had a velocity of approx. 95 % of the swimming speed, and appeared to be nearly stationary in the fluid (Fig. 12).

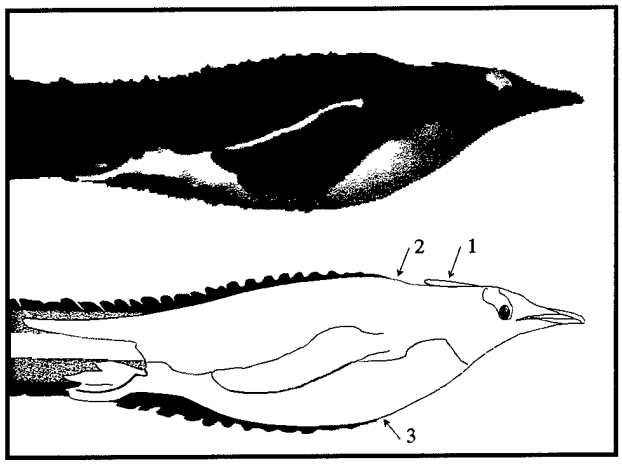

Fig. 12 Boundary layer visualisation in a live Gentoo penguin. Above: a single picture printed out from video records. Below: Scheme obtained from the entire sequence. 1 air bubble, 2 and 3 indicate the places of dye application. Note the quite regular pattern of the intermittent flow.

Corresponding to the change in sense of wing circulation during each stroke phase, the waves became more pronounced on the dorsal and ventral side of the body during the up-stroke and down-stroke, respectively. By means of the high-speed video (250 frames per second), the formation of closed looped roll cells could be observed in the boundary layer of an Adélie penguin gliding at a relatively low speed (ca. 1.2 m/s) (Fig. 13).

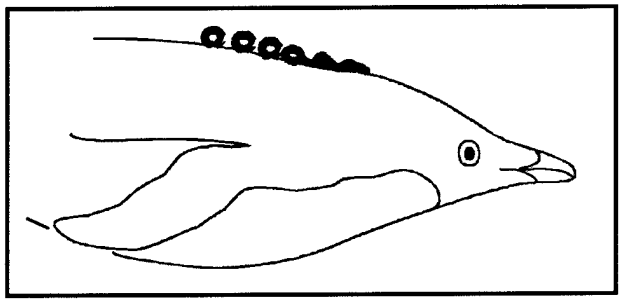

Fig. 13 Schematic graph of a rare high-speed video picture showing the development of ring structures in the boundary layer of an Adelie penguin.

Apart from passive mechanisms (multiple curvature effects, compliance and microstructure of the plumage) possibly responsible for maintaining boundary layer turbulence an overall low level, the flow visualization experiments showed that the structure of the near wall flow can be managed by a number of active mechanisms. Tiny adjustments of the body shape (changes in the position of the head, neck, feet and tail) and thereby of the pressure and velocity distribution had a remarkable influence on the flow pattern.

Additionally in some cases, in the beginning of diving, some parts of the body became covered by a thin film of air that reduces the wall shear stress locally to an absolute minimum. These areas corresponded well to those characterized by a low pressure gradient in the earlier model experiments. For the most part, the air was squeezed out of the plumage. The most persistent air bubble was the one in the neck (see Fig. 12), which was frequently renewed by exhalation, and was subjected to oscillation. At this location a vortex seems to be formed which is assumed to underlie the same oscillation. This could be a possible explanation for the mechanism generating the running wave observed further downstream in the boundary layer.

Based on the pictures on the boundary layer development in life penguins, one may speculate that the early generation of coherent vortex structures might be an effective measure to stabilize the near-wall flow, and to prevent "chaotic" developments even at the end of the body. The special pressure distribution along the wavy contour of the body and the compliance of the surface of the plumage seem to be the mechanisms to control this process.

Finally, it should be mentioned that an extraordinary measure to drastically reduce body drag temporarily could be a sudden ejection of large amounts of air bubbles by the bird. Occasionally, the saturation of the boundary layer with gas bubbles can be observed when the animals try to achieve extreme acceleration e.g. during escape reactions or before jumping out of the water.

VIII. DISCUSSION AND OUTLOOK

The possibility to reduce viscous drag by alternating concave-convex surfaces has been explored experimentally and theoretically in the NASA Langley Research Centre [27 –29]. Most interesting in the present context are the experiments with nose bodies. These experiments were aimed to make application of the fact that compared to a flat surface, the effect of streamwise convex curvature is to reduce skin friction, and the level remains lower even after the curvature is removed. However, the axial distribution of the cross-sectional area ratio was found to be critical to separation. A solution to this problem was found by implementing the drag reduction concept over several short fetches of curvatures instead of a single long fetch. In result, a three-stage nose body was developed (Fig. 14).

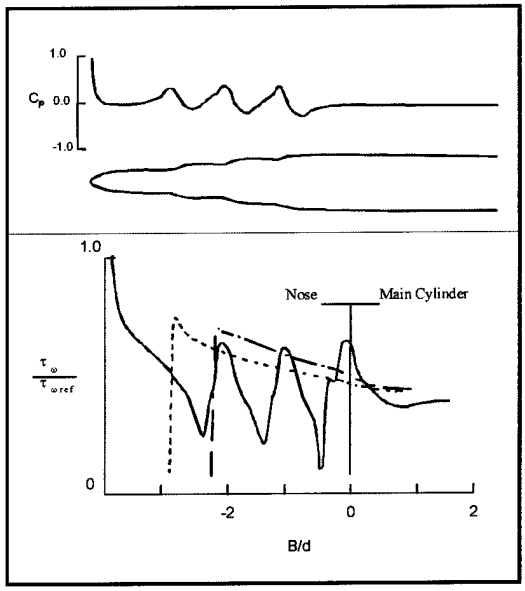

Fig. 14 Computed surface pressure distribution (above), and wall shear stress (below) in a three-stage nose body (solid line) compared with equivalent-area (dashed line) and equivalent-volume (chain line) half-elliptic noses (redrawn from [27]).

Thus, the application of the convex curvature concept led to a structural solution quite similar to that developed by nature in 40 million years of evolution. The respective proportions of the three stages in the frontal part of the penguin body were, however, different from that of the three-stage nose body, and a local pressure increase was observed only at the end of the beak. But even this part of the pressure curve changed to a plateau when a turbulence generator was attached to the model. In the "natural" design, the convex parts were connected not by cylinders but by concave sections. In order to take advantage of the "memory effect" along these parts, it might be more effective to maintain the flow velocity constant instead of decelerating it before acceleration follows in the next stage. With the exception of maximum girth position, the surface flow velocity vector include always a component directed perpendicularly to the axis of the body. If maintaining this constant as well, the local cross-sectional area must change also along the intervening sections. In this way, the length to thickness ratio and thereby the surface to volume ratio of the body can be reduced. The design of respective axisymmetric bodies seems to be a good way to obtain a better understanding of wave-like curvature effects.

Recently, some numerical approaches have proved the Evolution Strategy [30, 31] to be an appropriate method to achieve optimisation in a parallel way as used by nature. The first attempt in this direction was made by Pinebrook already in 1982 [32]. Fig. 15 shows the result of an optimisation experiment aimed to minimise the drag of a turbulent body of revolution at $Re = 10^8$. The transition from laminar to turbulent flow was fixed at 3 % of the body length.

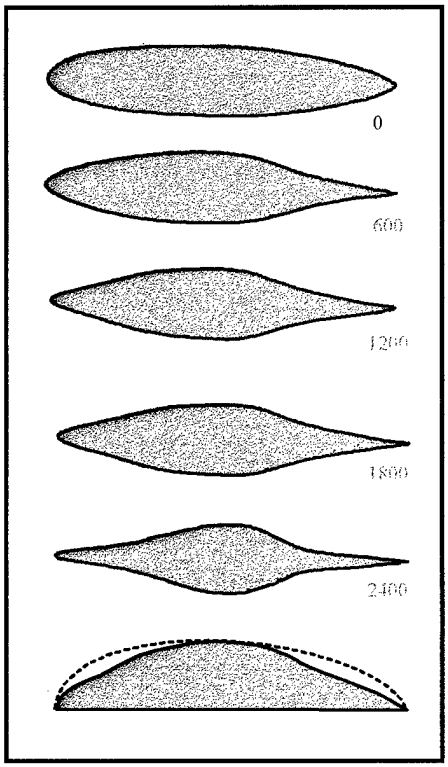

Fig. 15 Evolution of an axisymmetric body profile in the process of numerical shape optimisation (after [32]). Reynolds number 10^8; the numbers indicate the respective generation; below: profile of a thick body; dotted line: initial shape, solid line: final shape.

In Pinebrook's approach, the body contour was described by only 20 contur points equidistant with respect to the central axis. These points were varied, with the restriction that the maximum diameter and the fineness ratio were maintained. Compared to the initial shape, the body drag could be (numerically) reduced by 20 - 30 %, After 600 generations, a tuna-like shape, and thereafter a spindle somewhat reminiscent of the penguin shape with a well pronounced tail and a more pointed nose was developed. Obviously, most of the drag reduction resulted from reduction of the body surface. In consequence, the bodies lost a considerable part of their volume.

In a new approach developed in co-operation with the University of Stuttgart those undesirable effects could be avoided. The task was to find the optimal shape for a given volume under any (given) flow conditions. Some results obtained from an early version of that CFD programme were published [33]. Meanwhile, the programme could be improved further. However, based on the calculation methods implemented as yet, multiple curvature effects did simply not occur even in these simulations. In a numerical evaluation of the penguin-like body, the shape of the drag curve (see Fig. 4 and 5) could be confirmed. The curve was, however, shifted to drag coefficients ca. 20 % higher than those obtained experimentally. Validation experiments are in preparation to find out whether the measurements were incorrect or the turbulence model used in the calculation was insufficient for the this particular application.

Nevertheless, since most of the higher evolved flying and swimming animals show wavy body contours, comparative studies on the curvature development with size progression seem to be promising. Fig. 16 shows a comparison of the outlines from three different sized penguin species.

In these three species, the body length (in the swimming posture) changes at a ration of ca. 1 : 2 : 3, and – considering that they swim at different speeds, and the kinematic viscosity in their marine environment varies with temperature and salinity - the preferably used Reynolds numbers vary at a ratio of about 1 : 2 : 4, respectively. The Little penguin has a slender beak and a relatively big head, whereas the contour wave in the forebody of the Emperor is more extended, and its amplitude increases with length. The shape of the Gentoo seems to be an intermediate stage between these two examples. The superimposition of the contours shows that where the one curve has a maximum, the next one has a minimum, and so on.. This comparison suggests that there might be some distinct ("harmonic") solutions to that kind of shape adaptation.

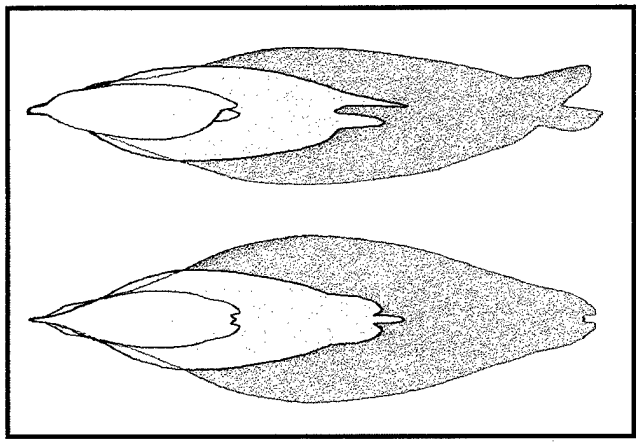

Fig. 16 Comparison of the body contours: Little, Gentoo and Emperor penguin, above: side view, below: top view.

Considering further, that a certain dorso-ventral asymmetry is evident in the body shape of mostly all animals adapted to fast sustained swimming, the understanding of the wave-like curvature concept in a three dimensional way, may eventually lead to completely new and even more "organic" designs in engineering. To find the "composition rules" (the author believes that they exists) will be particularly useful for example to better integrate cockpits etc. into the shape of the fuselage.

IX. ACKNOWLEDGEMENT

The studies on Antarctic penguins were supported by grants from the Deutsche Forschungsgemeinschaft (MZ-AD 24/11, BA 1291/3 1-4). We thank also the Alfred-Wegener-Institut für Polar- und Meeresforschung, Hanseatic Cruises, Plancius-Oceanwide, and Quark Expeditions for the logistic support of our expeditions. The experiments with the body of rotation were enabled by a grant from the Volkswagen-Stiftung. Thanks to all participants of the INTAS project 94-3737 for the many useful discussions.

X. REFERENCES:

1. J. Videler "Comparing the cost of flight: Aircraft designers can still learn from nature" In: W. Nachtigall (ed.): *BIONA-report 8 (1. Bionik-Kongress, Wiesbaden)*, Akad.Wiss. u. Lit., Mainz: G.Fischer, Stuttgart, New York, 1992: 53-72.
2. H. Hertel "Struktur - Form – Bewegung" Krausekopf: Mainz, 1963.
3. H. Hertel "Biologic-technical research on structure, form and movement" In: G.Bugliarello (ed.): *Bioengeneering - an engeneering view.* Proc. Symp. Engin. Signif. Biol. Sci., San Francisco, 1968: 07-143..
4. J. Gray "Studies in Animal Locomotion. VI The Propulsive power of the Dolphin" *J. exp. Biol.* 13, 1936: 192-199.
5. F.E. Fish and C.A. Hui "Dolphin swimming - a review". *Mamm. Rev.* 21, 1991: 181-195.
6. F.E. Fish "Power output and propulsive efficiency of swimming bottlenose dolphins (Tursiops truncatus)", *Ibid*, 1993, 185: 179-193.
7. E.V. Romanenko "Hydrodynamics", In V.E. Sokolov and E.V. Romanenko (eds.) *The Black Sea Bottlenose Dolphin*, Nauka, Moscow, 1997: 621-649 (in Russian).
8. M.O. Kramer "Boundary layer stabilization by distributed damping" *J. Am. Soc. Nav. Eng.* Febr. 1960: 25-33.
9. P.W. Carpenter "Status of transition delay using compliant walls" In: D.M. Bushnell and J.N. Hefner, (eds.): *Viscous drag reduction in boundary layers. AIAA*, New York, 1990: 79-113.
10. V. V. Babenko, M. V. Kanarskij and V. I. Korobov "The boundary layer in elastic plates" Naukova Dumka, Kiew, 1993 (in Russian).

11. E.T. Uskova, V. C. Raevskij, L.I. Momot and I.A. Uskov (1975) "Comparative studies on the hydrodynamic efficiency of polyethylenoxid suspensions and skin secrets of marine animals" *Bionika 9*, Naukova Dumka, Kiew, 1975: 90-92 (in Russian).
12. W.-E. Reif "Squamation and ecology of sharks" *Courier Forschungs-institut Senckenberg, Frankfurt/M.*, Nr. 78, 1985.
13. W.-E. Reif and A. Dinkelacker "Hydrodynamics of the squamation in fast swimming harks" *Neues Jahrbuch für Geologie und Paläontologie. Abhandlungen* Band 164,. E. Schweizerbart'sche Verlagsbuchhandlung, Stuttgart, 1982: 184-187.
14. M. Bruse, D.W. Bechert, J.G.Th. van der Hoeven, W. Hage and G. Hoppe "Experiments with conventional and with novel adjustable drag-reducing surfaces" In: R.M.C. So, C.G. Speziale and B.E. Launder (eds.): *Near-wall turbulent flow*. Elsevier Science Publishers B.V. 1993: 719-738.
15. Y.G. Aleyev "Nekton" The Hague: Dr. W. Junk b.v., 1977.
16. B. D. Clark and W. Bemis "Kinematics of swimming of penguins at Detroit Zoo" *J. Zool., Lond.*, 188, 1979: 411-428.
17. W. Nachtigall and D. Bilo "Strömungsanpassung des Pinguins beim Schwimmen unter Wasser" *J. Comp. Physiol.* 137, 1980: 17-26.
18. C.A. Hui "Swimming in Penguins" Diss. Univ. Calif., Los Angeles, 1983.
19. B.M. Culik "Energy expenditur of Adelie penguins" In: P. Dann, I. Norman and P. Reilly (eds.): *The Penguins*. Surrey Beatty & Sons Pty Limited, Chipping Norton, Australia, 1995: 177-195.
20. B.M. Culik, R.P. Wilson and R. Bannasch "Under-water swimming at low energetic cost by Pygoscelid penguins" *J. exp. Biol.* 197, 1994: 65-78.
21. R. Bannasch "Schwimm- und Tauchleistungen der Pinguine" *Milu* 6, 1985: 295-308.
22. R. Bannasch "Hydrodynamics of penguins - an experimental approach" In: P. Dann, I. Norman and P. Reilly (eds.): *The Penguins*. Surrey Beatty & Sons Pty Limited, Chipping Norton, Australia, 1995: 141-171.
23. R. Bannasch "Widerstandsarme Strömungskörper - Optimalformen nach Patenten der Natur" In: W. Nachtigall & A. Wisser (eds.): *BIONA-report 10*, Akad. Wiss. u. Lit., Mainz: G. Fischer, Stuttgart, Jena, New York, 1996: 151-176.
24. R. Bannasch and J. Fiebig "Herstellung von Pinguinmodellen für hydrodynamische Untersuchungen" *Der Präparator*, Bochum 38 (1), 1992: 1-5.
25. S.F. Hoerner "Fluid-dynamic drag" 2nd edition. Bricktown New Jersy. Hoerner, S. F., 1965.
26. H. Schlichting "Grenzschicht-Theorie" Verlag G. Braun. Karsruhe, 1982.
27. P.R. Bandyopadhyay "Viscous drag reduction of a nose body" *AIAA J.* 27, 1989: 274-282.
28. P.R. Bandyopadhyay "Convex curvature concept of viscous drag reduction" In: D.M. Bushnell and J.N. Hefner (eds.): *Viscous drag reduction in boundary layers*. Vol. 123, 1990: 285-324.
29. P.R. Bandyopadhyay and A. Ahmed "Turbulent boundary layers subjected to multiple curvatures and pressure gradients" *J. Fluid Mech.* 246, 1993: 503-527.
30. I. Rechenberg "Evolutionsstrategie" Problemata, Frommann-Holzboog. Stuttgart, 1973.
31. I. Rechenberg "Evolutionsstrategie '94" Problemata, Frommann-Holzboog, Stuttgart, 1994.
32. W.E. Pinebrook "Drag minimization on a body of revolution" Dissertation.University of Houston, 1982.
33. Th. Lutz, H. Schweyher, S. Wagner and R. Bannasch "Shape optimization of axisymmetric bodies in incompressible flow". *Proc. 2nd Int. Airship Conf., Stuttgart / Friedrichshafen, 3.-4.Juli 1996*: 211-224.

Imaginative solutions by marine organisms for drag reduction

Frank E. Fish

Department of Biology, West Chester University, West Chester, PA 19383 USA

Both machines and animals must contend with the same physical laws that regulate their design and behavior. Many animals demonstrate high levels of performance with respect to movement through water, and therefore, may be useful as model systems to analyze novel mechanisms for drag reduction that are superior to engineered solutions. A survey of various animals demonstrates that they have evolved a number of morphological and behavioral drag-reducing mechanisms. Although more complex, these mechanisms act similarly to analogous engineered solutions for movement when submerged and across the air-water interface.

We were lying upon the back of a sort of submarine boat, which appeared (as far as I could judge) like a huge fish of steel. (Jules Verne, *Twenty Thousand Leagues Under The Sea*)

INTRODUCTION

The idea that new technologies can be developed from observation of nature has been long standing. Indeed, nature has served as the inspiration for various technological developments including flight and robotics [1, 2, 3]. Copying nature by the biomimetic approach attempts to seek common solutions from engineering and biology for increased efficiency and specialization [4]. It is no accident that the shape of modern submarines, fish, and marine mammals are so closely matched. Parallels between natural and engineered designs occur because both are selected for a range of performance constrained by the same physical forces.

Analysis of locomotor specializations in animals holds for engineers the possibility that animals can be used as solutions to design problems for reduction in energy input, whether in their construction or in the performance of work. Any mechanism that allows for increased energy economy use can provide an important advantage to the survival of an animal. It is viewed that evolution (descent with modification) through the Darwinian process of "natural selection" has fostered improvements in design which have culminated in adaptations for high speed and efficiency [4, 5]. Because natural selection chooses from a wide range of design and performance possibilities as dictated through the genetic code and functional demand of the environment, a variety of possible solutions to engineering problems may be investigated. The diverse morphological specializations exhibited by animals may be targeted by engineers for technology transfer and effectively reduce the time of development of innovative technological solutions.

However, the use of animal models for design improvements is not without criticism. Strict adherence to biological designs is considered to rarely produce any practical results and can impede the development of engineered systems [6, 7]. Airplanes do not flap their wings like birds for lift and ships do not undulate like fish for propulsion. The reason that the duplication of biological systems has been limited is due to evolutionary and material constraints.

Animals are functionally multifaceted (i. e., they move, feed, reproduce) and must compromise optimal solutions for specialized functions to perform adequately rather than maximally [8, 9]. The biotic and abiotic environments of the time that a new design evolves dictates its selection without anticipation for potential future purpose and effectiveness. Both superior and poor designs with respect to present time may be lost if they did not function adequately in past environments or if they were accidentally lost due to chance events. In addition, animals have evolved along lines of common descent with shared developmental patterns which restricts possible solutions. Radical redesigns are not permitted to expedite enhancing performance; instead, it is existing designs which are modified. Although swimming in whales would be more efficient if these animals remained submerged like fish (see below), their common evolutionary history with other air-breathing mammals requires that they periodically return to the water surface to fill their lungs despite increased energy cost.

Animals are further limited by the variety of structural materials available. Animals are composed of either fibers, such as collagen, chitin, and keratin, or composites, such as bone and cartilage [10]. Compared to manufactured materials, like metals, ceramics and glasses, biological materials are generally weaker and less stiff. Furthermore, movements are generated through forceful contraction of the muscles transmitted to a jointed skeleton by tendonous connections. The arrangement of the contractile machinery precludes the use of rotational movements so ubiquitous in engineered systems [8]. Therefore, biological systems suffer lower efficiency due to periodic accelerations over a propulsive cycle.

Despite these concerns, the realization of new and superior designs to reduce drag based on animal systems has been tantalizing, although elusive [7, 11, 12]. Aquatic animals are considered superior in their capabilities to technologies produced from nautical engineering [2]. Speeds over 11 m/s (>21 kts) have been attained by dolphins [13], whereas fish display speeds as high as 20 m/s (39 kts) and can accelerate at 40-50 m/s^2 [11, 14]. Such high levels of performance were assumed to be dependent on adaptations which reduced drag.

This report explores the specialized adaptations used by aquatic animals for drag reduction. These adaptations are compared with analogous engineered solutions. Comparison of biological and mechanical systems can provide insight into the effectiveness of each system and help direct engineers toward innovative applications of biological systems. For a full appreciation of the topic, this survey includes discussion of mechanisms which are considered valid, fallacious, and speculative.

DRAG COMPONENTS

A previous review of biological drag reduction by Bushnell and Moore [5] examined three types of drag (form drag, skin-friction drag, and drag-due-to-lift) for organisms totally immersed in a fluid, whether air or water. The present review examines how organisms reduce their drag in an aqueous environment for fully submerged bodies and bodies operating at the air-water interface.

The primary component of drag experienced by aquatic animals varies in accordance with (1) flow conditions around the animal and in its boundary layer, (2) proximity to the air-water interface, and (3) the relative predominance of inertial, gravitational, and viscous forces. Because of the interest in rapid motion in water and application of biological designs to large structures, the discussion will focus on conditions encompassing high Reynolds numbers (Re), expressed as:

$$Re = U L / \upsilon \quad (1)$$

where U is the velocity, L is a characteristic linear distance (e.g., body length), and υ is kinematic viscosity, which is equal to 1.044×10^{-6} m^2/s for sea water at 20°C. At high Re, inertial forces predominate over viscous forces. Of particular interest is the range of $Re > 10^5$, where transition from laminar to turbulent flow conditions can occur. Gravitational forces predominate when animals swim near or pierce the water surface. The ratio of inertial forces to gravitational forces experienced by a body moving at or close to a fluid/fluid interface is given by the dimensionless Froude number, F_L, as:

$$F_L = U/(g L_W)^{1/2} \quad (2)$$

where g is the gravitational acceleration, 9.8 m/s^2, and L_W is the waterline length along the longitudinal axis of the body.

For submerged bodies, minimum drag is associated with purely frictional drag with laminar boundary conditions (Fig. 1). To maintain a laminar boundary layer, the surface of the body should be smooth and the configuration of the body should promote a large favorable (negative) pressure gradient [15]. This gradient occurs when the pressure is decreasing along the streamline from the leading edge toward the trailing edge by gradually increasing the thickness of the

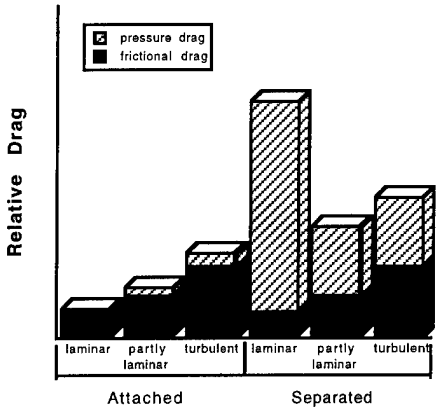

Fig. 1. Relative drag associated with boundary conditions. Redrawn from [11].

body. A large region with a favorable pressure gradient is achieved by positioning the maximum thickness of the body posteriorly. However at high Re (> 10^5), transition from laminar to turbulent boundary conditions can occur. The result of this transition is an increase in the frictional drag due to an increase in boundary layer thickness.

Pressure or form drag is produced from pressure difference in the flow outside the boundary layer arising from changing flow velocities around the body. The pressure differential from leading to trailing edges of the body is the source of the force [11]. Streamlining minimizes drag by reducing the magnitude of the pressure gradient over the body [7].

Pressure drag is also dependent on the interaction of the boundary layer and pressure gradient. Boundary layer separation generally occurs in the region posterior of the maximum thickness of the body. In this region an adverse pressure gradient develops with high pressure located posteriorly. At a point along the gradient, fluid in the boundary layer does not have sufficient momentum to overcome the increasing pressure and separation occurs. Premature separation along the body as opposed to near the trailing edge will produce a broad wake with substantial energy loss. Separation is more likely to occur with laminar boundary conditions. This results in higher drag with laminar conditions than with a turbulent boundary layer (Fig. 1). Separation is delayed in a turbulent boundary layer, because momentum is transferred vertically due to increased mixing within the layer [15].

Wave drag occurs when an animal swims at or near the water surface acting as a displacement hull [16, 17, 18]. Kinetic energy from the animal's motion is transferred into potential energy in the upward displacement of water in the formation of surface waves. This energy loss can be substantial at a maximum of five times the frictional drag when the body is at a relative depth of 50% of the maximum diameter of the body and $F_L = 0.5$ [17, 19, 20].

Speed at the water surface is constrained by the formation of surface waves [18, 21, 22]. As an animal swims faster, constructive interference from bow and stern waves trap it in a trough, ultimately limiting further increases in speed [23, 24]. To move faster, the animal would have to literally swim uphill, which is energetically very costly. This effective speed limit for a conventional displacement hull, such as a ship or duck, is called the hull speed, U_h [21]. Hull speed depends on L_W with longer bodies having higher hull speeds. U_h is calculated as:

$$U_h = (g\, L_W/2\, \pi)^{1/2} \qquad (3).$$

Spray drag or surface interference drag is created by water piled up along the forebody of a surface-piercing strut or foil and being shot into the air [19]. At high F_L, spray drag is approximately 26% of total drag for a surface-piercing flat plate and 30% for a strut with a blunt trailing edge [19]. The best design to reduce spray drag is a pointed leading edge and long forebody region relative to the maximum thickness (Fig. 2).

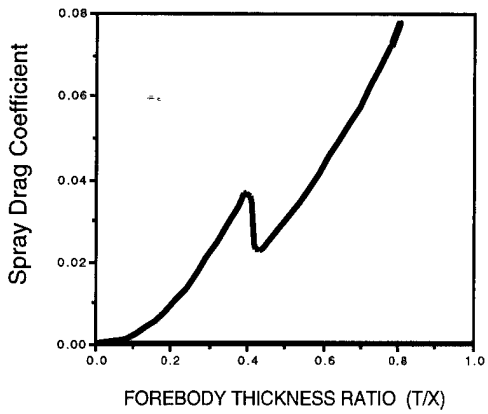

Fig. 2. Relationship between spray drag and forebody thickness ratio based on [19].

The induced drag component is produced from vorticity generated by lifting hydrofoils (e.g., fins, flippers, flukes). When the hydrofoil is canted at an angle to the water flow (i.e., angle of attack), a lift is generated due to deflection of the fluid and pressure difference between the two surfaces of the hydrofoil [5, 11]. The pressure difference induces the formation of longitudinal tip vortices resulting in energy dissipation [7, 11]. The induced drag coefficient (C_{Di}) is determined as:

$$C_{Di} = C_L{}^2/\pi AR \qquad (4)$$

where CL is the coefficient of lift and AR is the aspect ratio. AR is an indicator of the geometry of the hydrofoil and is calculated as:

$$AR = S^2/A = S/C \qquad (5)$$

in which S is the hydrofoil span, A is the maximum projected area of the hydrofoil, and C is the chord. As AR increases, the hydrofoil planform becomes long and narrow. Equation 4 suggests that hydrofoils with high AR will experience a low induced drag.

BIOLOGICAL SOLUTIONS FOR DRAG REDUCTION

A variety of engineered solutions and possible animal mechanisms for drag reduction exist for each of the drag components presented above. Animals reduce drag by utilizing secreted materials, anatomical features, and behavioral patterns.

Friction Drag

Mucus

The addition of dilute solutions of long-chain polymers into flow is well established as a means of drag reduction [25]. The conditions necessary are (1) turbulent or pulsed laminar flow in the boundary layer, (2) the polymer is linear and soluble, (3) the polymer has a molecular weight of 50,000 or more, and (4) the density and viscosity of the fluid from the surface outwards must be constant [25, 26]. The mucus secreted by fish over the body surface is considered to meet these conditions. The mucus is a combination mucopolysaccharides, nucleic acids, proteins, and surfactants in the form of lipids, phospholipids and lipoproteins [5].

The undulatory or oscillatory movements of fish during swimming indicates turbulent or pulsed flow for which mucus could be effective in reducing drag [25, 26]. Measurements of dilute solutions of fish mucus in turbulent pipe flow exhibited as much as 66% reduction in friction drag [25, 27]. The mucus is believed to reduce the velocity gradient over the fish and thus decrease viscous shear stress and reduce the rate of momentum transfer from the free-stream flow to the surface of the fish [26]. The mucus also may fill in irregularities to improve streamlining [28]. However, no association was found between amount of drag reduction and species of fish which swim at high speeds. Even snails, which are not noted for speed, produce a mucus that reduces drag [25].

Secretions from dolphins have been examined also for drag reducing abilities, although with no success. Secretions from the

dolphin eye fail to produce any drag-reducing effect [29]. Likewise, the high density of epidermal cells shed from dolphin skin have little effect, although the composition of these cells is considered similar to a mucopolysaccharide [29, 30]. High rates of skin sloughing may aid in minimizing drag by preventing fouling by encrusting organisms [31].

Riblets

The development of riblets to reduce turbulent skin friction came in part from the study of shark scales or dermal denticles [32]. Riblets are streamwise microgrooves that act as fences to break up spanwise vortices, and reduce the surface shear stress and momentum loss. Fast swimming sharks have scales that are different from other sharks. These scales have flat crowns and sharp ridges oriented longitudinally with rounded valleys [33, 34, 35, 36]. Although the ridges are discontinuous due to the distribution of the scales, a 7-8% drag reduction is possibly as measured for continuous riblets [32, 37]. The streamwise surface grooves of scallop shells also indicate the use of riblets [38]. The optimal riblet spacing is present in those scallops demonstrating the greatest swimming ability. Small ridges on the epidermis of dolphins had been hypothesized to stabilize longitudinal vortices [39, 40], but the geometry of the ridges with rounded edges does not suggest an effective analogy with riblets [12].

Viscous dampening

By far, arguments surrounding the investigation and application of mechanisms for viscous dampening by dolphins have been the most contentious [7, 12]. The controversy, known as Gray's Paradox, was the result of an estimation of the power output, based on calculation of drag with turbulent boundary conditions, for a rapidly swimming dolphin. The estimated drag power could not be reconciled with the available power generated by the muscles [41]. Gray's resolution to the problem was that the drag on the dolphin would have had to be lower by maintenance of a fully laminar boundary layer, despite Re above transition. Gray proposed a mechanism to laminarize the boundary layer by accelerating the flow over the posterior half of the body (see boundary layer acceleration below). However, the basic premise of Gray's Paradox was flawed, because the observation of the dolphin swimming speed was for a sprint (7 sec) and Gray used measurements of muscle power output for sustained performance of human oarsmen, which are lower than power outputs for burst activities [12].

Gray's Paradox, however, endured and was invigorated by the work of Max Kramer [42, 43, 44]. Kramer claimed that a laminar boundary layer without separation could be achieved at high Re by coating a torpedo with an artificial skin based on the skin of a dolphin. The dolphin integument is composed of a smooth, hairless epidermal surface forming an elastic membrane [45] and is anchored to the underlying dermis by longitudinal dermal crest with rows of papillae, which penetrate the lower epidermis [29, 40, 43, 44, 45]. Kramer's analogous skin was composed of a heavy rubber diaphragm supported by rubber studs with the intervening spaces filled with a viscous silicone fluid [42]. It was hypothesized that the coating would dampen out perturbations in the flow and prevent or delay transition. When a portion of a towed body anterior of the maximum thickness was coated, a 59% reduction in drag was achieved at $Re=15x10^6$ compared to a rigid reference model with fully turbulent flow. These results suggested the "dolphin's secret" and a resolution to Gray's Paradox [43].

In what has been characterized as "enthusiastic optimism" and "Pentagon and Kremlin paranoia" [7], research on dolphin hydrodynamics and compliant coatings was accelerated during the 1960s [12, 45, 46]. Attempts to verify Kramer's results subsequently failed [46, 47], although some success in reducing skin friction was possible with other compliant coatings [48, 49]. It was suggested that a compliant coating would reduce drag by controlling turbulence in the boundary layer rather than delaying transition [46]. It would be more important in minimizing total drag by delaying separation than to delay transition in the boundary layer.

The structure of the skin and blubber layer of dolphins is highly organized and complex [40, 50]; thus, the analogy with the compliant skin proposed by Kramer may be only superficial and have little functional similarity. When swimming at high speed or for bursts, dolphins exhibit prominent skin folds [51]. Similar speed-induced skin folds were shown to add to drag when observed on naked women swimming or towed at 2-4 m/s [45]. The possession of a thick skin, which could make the induced folds, is attributed also to turbulent boundary conditions for the beluga whale (*Delphinapterus leucas*) [36].

Drag measurements of gliding dolphins and rigid models indicated that the boundary layer was largely turbulent [13, 16, 36, 39,45, 52]. This was verified by low-speed, flow visualization studies on dolphins using dye or bioluminescence [53, 54, 55]. The fluid layer against the body, inferred to represent the boundary layer, thickened anterior of the dorsal fin. The inferred transition anterior to the dorsal fin corresponded with a local Re of about $3x10^6$, and was confirmed from measurements of turbulent pulsations on a live dolphin [45]. The boundary layer remained attached up to the flukes for gliding animals [55], but separated anterior of the flukes for an actively swimming dolphin [53]. Similar observations were made on seals swimming through bioluminescence [56]. Seals swim in a matter analogous to dolphins [57].

As indicated from flow visualization experiments on dolphins, differences in boundary layer flow occur between actively swimming and gliding animals. This implies that viscous dampening may be under active control when the animal is oscillating its flukes. Experiments using remote pressure sensors in the boundary layer of an actively swimming dolphin indicated that although agitated the boundary layer did not become completely turbulent [58]. Although the degree of turbulence and the pressure were determined to decrease over the posterior portion of the body, these results may not be associated with viscous dampening as has been hypothesized [36, 59]. Indeed there is no evidence to suggest that viscous dampening of the skin should be any more likely when the animal is oscillating its flukes as opposed to gliding [12]. A substantial amount of time during swimming may be occupied by gliding when low drag would be beneficial.

As originally proposed by Gray [41], acceleration of the boundary layer due to propulsive fluke actions could account for the results of flow visualization and pressure studies [53, 58]. Estimates of drag on actively swimming dolphins based on kinematics and hydrodynamic models have indicated turbulence due to high drag values [11, 52, 60, 61]. Such high drags are consistent with estimates for actively swimming animals which can be 2-5 times the greater than drag values of equivalent rigid bodies [62].

Dynamic dampening

The network of subdermal canals and pores in the skin of fish suggests use of a suction mechanism to stabilize the boundary layer and prevent separation [63, 64]. In the trachipterid fish, *Desmodema*, the placement of maximum thickness is at 7% of total length. This will result in a negative pressure gradient over the majority of the body. The pore and canal system is believed to redistribute fluid from high to low pressure regions. Engineered systems using boundary layer suction achieved 66-100% laminar flow [65].

Boundary layer acceleration

Injection of high momentum fluid into the boundary layer has the capacity to delay both transition and separation [11]. The effluent from the gills of fish could potentially introduce kinetic energy into the boundary layer [28, 66]. Flow visualization in fish, however, has shown the pulsed flow during active respiration increases turbulence [45, 66]. The location of the gill slits anterior of the maximum thickness of fish (i.e., position of lowest pressure) would enhance respiratory flow rather than surface flow. During passive or ram ventilation in scombrid fish, the mouth and gill coverings are kept open so that water can continuously flow over the gills without pumping. The constant swimming motion of the fish maintains the flow. Ram ventilation does not prevent turbulence, but it appears to extend the laminar region of the boundary layer by 13-100% [45].

Re-acceleration of the boundary layer as fluid was accelerated from the oscillating flukes of dolphins was proposed originally as the resolution to Gray's Paradox [41]. Calculations of the dynamic pressure distribution over an actively swimming dolphin indicate the extension of a favorable pressure gradient over the total body with a steep pressure reduction in the region of the peduncle and flukes [59]. This mechanism seems to have greater potential for boundary layer stabilization in the dolphin than maintenance of laminar flow with viscous dampening. A similar mechanism may operate in cephalopods (e.g., squid, octopus). Water flowing into the inlet of the mantle cavity during inhalation and during exhalation through the siphon when jetting could accelerate the boundary layer [45].

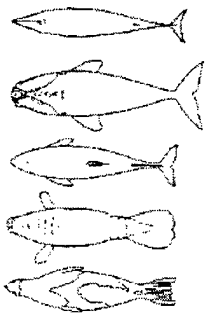

Fig. 3. Representative body shapes of marine mammals. From top to bottom: minke whale (*Balaenoptera acutorostrata*), right whale (*Eubalaena glacialis*), harbor porpoise (*Phocoena phocoena*), Florida manatee (*Trichechus manatus*), and harp seal (*Phoca groenlandica*).

Boundary layer heating

Warm-bodied animals, such as marine mammals, scombrid fishes, and laminid sharks, have the capacity to use heat conducted from the body surface to decrease water viscosity [66, 67]. Dolphins exhibit a temperature differential between the water and skin surface of 9°C which would reduce viscosity by 11% [12]. A maximum temperature difference of 15°C for tuna would provide a 14% decrease in friction drag as long as the boundary layer was heated instantaneously [11]. Although plausible, this method of drag reduction is unlikely due to the short amount of time (0.1 s) that the water would be in contact with the body [66].

Pressure Drag

Fusiform shape

It is surprising that although G. Cayley (circa 1800) considered the fusiform design of the dolphin to be a body of least resistance, this design was not embraced for submarine hulls until the USS Albacore in 1953. Drag is minimized primarily by streamlining the shape of the body and the appendages. The streamlined profile of these structures is characterized by a rounded leading edge and a slowly tapering tail (Fig. 3). This design delays separation which occurs closer to the trailing edge, resulting in a smaller wake and reduced pressure drag.

An indication of the streamlining of a body is the Fineness Ratio (FR = ratio of maximum length to maximum thickness) [11]. Bodies of rotation demonstrate minimum drag in a range of FR of 3-7 [17, 68, 69]. Based on airship design, the optimal FR is 4.5 which provides the minimum drag for the maximum volume [68]. Fast swimming fishes, penguins and aquatic mammals are well streamlined with body dimensions within the optimal range of FR [11, 57, 70, 71].

In engineered 'laminar' profiles, the position of the maximum thickness is located posteriorly to reduce drag by maintenance of an extended favorable pressure gradient and laminar boundary flow [11]. The shape of a dolphin and a sea lion have been likened to a NACA 66-018 airfoil [17, 72], whereas, tuna display similarities with the NACA 67-021 [17]. Indeed, most rapidly swimming aquatic animals have displaced the maximum thickness posteriorly [17, 45]. The maximum thickness of fast swimming fish and marine mammals is located at 0.3-0.7 of the body length [12, 17, 45, 66, 72].

Abrupt departures from a streamlined shape are avoided through use of integumentary structures. Blubber in marine mammals contours the body along its longitudinal axis [56, 71]. In addition, blubber streamlines the caudal peduncle in dolphins to reduce its drag in the flukes' plane of oscillation [12] and provides a streamlined shape to the appendages [73, 74]. Hair and feathers also can be used with their entrapped air layers to contour the body [70, 75, 76]. The lack of arrector pili muscles in seals and sea otters permits the pelage to lie flat in water, minimizing resistance to swimming [77]. When models of a seal with and without hair covering were compared, a reduction in drag with the hair covering occurred at velocities of 8-10 m/s [78]. However, it was noted that these speeds are not normal for seals and the results may not be ecologically relevant [79].

Despite the presumption of the teardrop, fusiform shape as the optimal design for drag reduction, a number of aquatic animals have anterior projecting beaks, bills, and rostrums. In part, the departure from a smoothly rounded head in these animals may be a function of their feeding morphology requiring grasping jaws. However, the alternating concave and convex profile of the forebody may induce a stepwise, gradual pressure change which can reduce skin friction in animals [70, 80, 81]. The relatively small surface area of the anterior projection in conjunction with a reduced pressure gradient [45,82] can decrease drag.

Redirection of flow about dorsal spines of some sharks would aid in preventing flow separation and increased pressure drag. The spines are found on the leading edge of the dorsal fins. Because there is a gap between the spines and the fins, the combination could act in a manner analogous to slotted wings as the body laterally undulates during swimming, canting the dorsal fins at an angle to the flow [83].

Burst-and-coast swimming is a behavioral strategy that exploits the lower drag of a rigid, non-flexing animal compared to when it is actively swimming [62]. Animals rarely swim steadily. Many animals swim intermittently using a two-phase periodic behavior of alternating accelerations (burst phase) interspersed with periods of glides (coast phase) [84, 85]. Estimates of energy savings were projected from 24% to over 50% for fish using this behavior [86, 87].

Vortex generators

Large-scale vortices can be generated around the bodies and appendages of animals to influence flow and reduce drag [5, 11]. Alternate vortices shed from around the head of swimming fish were postulated to act as rigid pegs [88]. The Vortex Peg Hypothesis suggested that the fish pushed off the vortices reducing swimming effort and that the drag was virtually zero by reclaiming energy from the vortices [11, 53, 88]. This hypothesis was considered unlikely, because the velocity difference between the fish and vortices was too great to make the system efficient [11].

However, anteriorly generated vortices and vortices generated from the undulation of the caudal fin can interfere with each other to increase locomotor efficiency [53, 89, 90]. The opposing rotations of the anterior vortices generated as a Kármán vortex street and the thrust-type vortices (reverse Kármán vortex street) can destructively interfere [90]. This interference produced enhanced efficiency when the sites of vortex generating were optimally spaced.

Leading edge bumps were identified as possible drag reducing devices [5]. Leading edge bumps are found on the head of hammerhead sharks and pectoral flipper of humpback whales, which are used as lifting surfaces during maneuvers [91, 92]. On the humpback whale flipper, the bumps are evenly spaced over the majority of the span [91]. These bumps were hypothesized to generate vorticity to postpone stall at high angles of attack. This function may be analogous to strakes which change the stall characteristics of aircraft wings by generating vorticity [19, 93]. Vortex generators are most effective for increasing lift and reducing drag when the boundary layer has been tripped [94]. Turbulent boundary conditions would be likely for humpback whale flippers which operate near Re = 2×10^6 [91].

Turbulizers

Induction of turbulence by roughness and surface projections within the boundary layer can ultimately reduce total drag by delaying boundary layer separation [11]. Sculpturing on the shells of cephalopods (ammonoids and nautiloids) had a positive hydrodynamic effect when immersed in the boundary layer, but sculpturing which extended outside of the boundary layer had a negative effect [95]. For fish, the presence of scales, rough surfaces, and spiny projections has been likened to a tripping device to stabilize the boundary layer [5, 11, 45, 6496]. In mullet, *Mugil saliens*, scale development is correlated with body size and Re [45, 96]. At Re less than 10^3, the fish has no scales; whereas at 3×10^5, rough ctenoid scales appear on the body behind the head. The ctenoid scales have a comblike edge. these scales are believed to produce microturbulence. Ctenoid scales are replaced, however, with smoother cycloid scales above 10^6, where transition would normally occur.

The elongate rostrum of the swordfish, *Xiphias gladius*, has a rough surface with craters and bumps [82]. Because the sword can reach a length of 40-45% of body length, at high swimming speeds, the critical Re for transition would be reached before the head. Thus, separation would be avoided from the body of the fish, despite the anterior position of the maximum thickness which is just posterior of the head [45, 82].

Drafting

Various animals travel in highly organized formations. This behavior has been hypothesized to reduce drag and enhance locomotor performance of individuals. Formation movement generally is accepted for automotive and cycling competitions [97, 98, 99], which use the techniques of "drafting" or "slipstreaming". Wind tunnel measurements on cars demonstrated a 37-48% reduction in drag when following closely behind another vehicle [97, 100]. Trailing cyclists in a pace line experience a 38% reduction in wind resistance [98] and an energy savings of 62% when drafting behind a more massive body, such as a truck [99].

For animals, formation swimmers influence the flow of water around adjacent individuals. Vorticity generated by anterior individuals provides momentum to the water. If a trailing animal is oriented parallel and is moving in the same direction to the tangential velocity of the vortex, the body will experience a reduction in its relative velocity. Because the drag is directly proportional to the velocity squared, a decrease in the relative velocity can decrease drag and the associated energy expenditure. Vorticity is shed into the wake of a passive body as two rows of counter-rotating vortices (i.e., Kármán vortex street) where the optimal position for drag reduction is directly behind another body [101]. Although similar in pattern to the Kármán vortex street, a thrust-type vortex system has the opposite rotation of the vortices. In this system which is generated by an oscillating foil, the optimal orientation is diagonally [102].

Queues of spiny lobsters (*Panulirus argus*) in water were shown to sustain less drag per individual than a single lobster traveling at the same speed [103]. The reduction in energetic cost per individual in a queue was a direct function of queue size. Ducklings which swim behind the mother in single-file experience a 7.8-43.5% decrease in energy cost with increased savings for larger groups [101]. In addition, the duckling at the end of the formation appears to received the largest energetic savings [Fish, 1995]. Drag reduction in single-file formation is associated with small spacings between individuals (< one body length) [97, 100, 104].

Thrust-type vortices produced by fish provide drag reduction in diamond-shaped formations [86, 102]. Trailing fish experience a relative velocity 40-50% of the free stream velocity and a reduction of the force generated for swimming by a factor of 4 to 6. However, the decrease in relative velocity is not maintained with each successive row of trailing fish due to destructive interference.

Wave Drag

Bow structure

Bulbous bows on displacement hulls reduce wave drag by 60% by canceling most of the wave pattern created at the bow and avoiding energy loss by wave breaking [105, 106]. Semiaquatic mammals (e.g., beaver, muskrat, water opossum) swim on the water surface while holding their forelimbs under the chin [22, 107]. Such as configuration of the limbs may effectively act like a bulbous bow, although this has not been examined.

Hydroplaning

Relatively few animals swim at the water surface for extended periods. As a displacement hull, surface swimming animals encounter high energy costs and limitations to speed from wave drag. Despite the small size of ducklings which places severe limitations on swimming velocity due to hull speed, speeds above hull speed are accomplished by replacing the displacement hull configuration with a planing hull [18]. The motion of a planing hull has been described as "hydroplaning" or "skimming" [108]. With the hull inclined with a positive angle of trim, a positive pressure develops under the hull creating a vertical "dynamic lift" component which at high speeds may be greater than buoyancy [105, 109].

Several factors contribute to the relatively low drag of planing. (1) The increase in trim angle raises the bow from the water decreasing the amount of wetted surface area reducing skin friction [108, 109]. (2) Above hull speed water does not have time to respond to the pressure disturbance and the water surface is effectively smoothed [105, 108, 110]. (3) Wave drag is largely eliminated by lifting the hull, although spray drag will increase [19, 105, 109].

At F_L = 0.6-1.0, a hull is semiplaning such that it is supported by both hydrodynamic (dynamic lift) and hydrostatic (buoyant lift) forces [105, 109]. Above F_L = 1, the hull is supported entirely by dynamic lift (planing). Mallard ducklings (*Anas platyrhynchos*) can burst at $F_L > 1$ effectively planing on the water surface [18]. Steamer ducks (*Tachyeres* spp.) include three large, flightless species which hydroplane continuously over distances of 1 km and at speeds up to 6.67 m/s (F_L = 3) over the water surface using their feet and wings [18, 111].

Spray Drag

Two bat species (*Noctilio leporinus, Pizonyx vivesi*) are adapted for catching and eating fish [112, 113]. The bats use their echolocation to detect fish by ripples or breaks on the water surface and then drag their feet through the water to gaff the fish with their claws. To reduce drag, the toes and claws are laterally compressed with a reversed fusiform cross-section [114]. Although a typical fusiform shape works effectively for fully immersed bodies, this shape should be avoided at the air-water interface [20]. At high Froude numbers ($F_L < 0.5$), spray drag can be a significant proportion of the total drag, whereas wave drag is insignificant [19]. For the fishing bats, where $F_L > 270$, the reversed fusiform design with a long forebody region relative to the claw thickness can reduce spray drag [19, 114]. An analogous design is observed in the lower mandible of the black skimmer (*Rhyncops nigra*), which catches fish at the water surface with its beak [115]. Application of this mechanism, however, is limited to linear motion, because the reversed fusiform design will incur premature separation with increased drag and loss of lift during turning maneuvers.

Induced Drag

The design of the appendages (e.g., fins, flukes, flippers) determines the magnitude of the induced drag. Well-performing appendages maximize the ratio of lift (L) to drag (D) generated by their action [11]. An increase in the maximum L/D with increasing size is achieved by increasing span more rapidly than the square-root of planar area, thereby increasing AR [68, 116, 117, 118, 119]. High AR and tapering of the appendages reduces tip vorticity and induced drag [11, 119, 120, 121]. The fastest swimming fish and marine mammals have propulsors with AR ranging from 3.4-8.7 [57]. AR above 8-10 provides little further advantage and may be structurally limited [11].

Induced drag also is limited by the sweep angle of the appendage. A tapered wing with sweptback or crescent design could reduce the induced drag by 8.8% compared to a wing with an elliptical planform [117]. Induced drag can be reduced with a swept wing planform with a root chord greater than the chord at the tips giving a triangular shape [122, 123]. This optimal shape approximates the planform of animals which swim with a lunate propulsor, including scombrid fishes, laminid sharks, extinct ichthyosaurs, cetaceans, and phocid seals [11, 57, 62, 118].

Flight

A behavioral strategy to minimize drag is to leave the water entirely. Many aquatic animals leap clear of the water to travel through the air to reduce the energy required for locomotion and avoid predation. In certain cases the animals take a ballistic trajectory, such as dolphins, seals, sea lions, penguins, and fish [124, 125, 126], whereas others have modified lifting surfaces to extend the flight over long distances, such as flying squid and flying fish [127, 128].

Porpoising consists of rhythmic, serial leaps in which the animal leaves and re-enters the water nose-first during continuous swimming. Models of porpoising predict that at high velocities the energy to leap a given distance is lower than the energy to swim [124, 129]. Below some critical speed, however, the opposite is assumed. As obligate air-breathers, marine mammals and penguins must swim in close proximity to the surface despite increased drag [17, 71]. Porpoising permits these animals to breath while simultaneously reducing locomotor energy costs [125, 130].

CONCLUDING REMARKS

Progress in technologies concerned with drag reduction comes from the discovery and refinement of new designs. A diversity of drag reducing mechanisms are exhibited by aquatic animals in association with their habits and restrictions on body design. Both machines and animals must contend with the same physical laws that regulate their design and behavior. Although animal mechanisms have been recognized mainly after an engineered solution was developed, the analogy simply demonstrates functional similarity and close

examination of the biological mechanism may indicate possible pathways for improvements in engineered designs. In comparison to engineers who can limit variables in their systems, the problem for biologists has been that the systems they study are complex. More than two hundred years ago, the British philosopher David Hume pondered the complexity of biological organisms as:

All these various machines, and even their most minute parts, are adjusted to each other with an accuracy which ravishes into admiration all men who have ever contemplated them. The curious adapting of means to ends, throughout all nature, resembles exactly, though it much exceeds, the productions of human contrivance.

As matters of energy economy and greater speeds are desired in engineered systems [5], imaginative solutions for drag reduction from nature may serve as the inspiration for new technologies. The union between biologists and engineers and use of modern computational approaches [131, 132] promise an understanding of biological systems and modifications fitted to an engineered application.

ACKNOWLEDGMENTS

I would like to express my appreciation to the organizers of this symposium for their invitation to attend. This review is based in part on research performed with support from National Science Foundation grant number DCB-9117274 and the Office of Naval Research grant number N00014-95-1-1045.

REFERENCES

1. Jakab, P. L. 1990. *Visions of a flying machine.* Smithsonian Institution Press, Washington.
2. Triantafyllou, G. S. and Triantafyllou, M. S. 1995. An efficient swimming machine. *Sci. Amer.*, 272:64-70.
3. Bandyopadhyay, P. R. and Donnelly, M. J. 1997. The swimming hydrodynamics of a pair of flapping foils attached to a rigid body. *Tenth Internat. Symp. Unmanned Untethered Submersible Tech.: Proc. Sp. Ses. Bio-Eng Res. Related to Autonomous Underwater Vehicles.* Pp. 27-43.
4. Vincent, J. 1990. *Structural biomaterials.* Princeton Univ. Press, Princeton.
5. Bushnell, D. M. and Moore, K. J. 1991. Drag reduction in nature. *Ann. Rev. Fluid Mech.*, 23:65-79.
6. Harris, J. S. 1989. An airplane is not a bird. *Invention & Technology*, 5: 18-22.
7. Vogel, S. 1994. *Life in moving fluids.* Princeton University Press, Princeton.
8. Katz, S. L and Jordan, C. E. 1997. A case for building integrated models of aquatic locomotion that couple internal and external forces. *Tenth Internat. Symp. Unmanned Untethered Submersible Tech.: Proc. Sp. Ses. Bio-Eng Res. Related to Autonomous Underwater Vehicles.* Pp. 135-152.
9. Webb, P. W. 1997. Designs for stability and maneuverability in aquatic vertebrates: What can we learn. *Tenth Internat. Symp. Unmanned Untethered Submersible Tech.: Proc. Sp. Ses. Bio-Eng Res. Related to Autonomous Underwater Vehicles.* Pp. 85-108.
10. Alexander, R. McN. 1985. The ideal and the feasible: physical constraints on evolution. *Biol. J. Linn. Soc.*, 26:345-358.
11. Webb, P. W. 1975. Hydrodynamics and energetics of fish propulsion. *Bull. Fish. Res. Bd. Can.*, 190:1-158.
12. Fish, F. E. and Hui, C. J. 1991. Dolphin swimming - a review. *Mamm. Rev.*, 21:181-195.
13. Lang, T. G. 1975. Speed, power, and drag measurements of dolphins and porpoises. *In* T. Y. Wu, C. J. Brokaw and C. Brennen (eds.), *Swimming and flying in nature*, Vol. 2, pp. 553-571. Plenum Press, New York.
14. Magnuson, J. J. 1978. Locomotion by scombrid fishes: hydrodynamics, morphology and behaviour. *In* W. S. Hoar and D. J. Randall (eds.), *Fish physiology*, vol. 7, pp. 239-313. Academic Press, London.
15. Katz, J. and Plotkin, A. 1991. *Low-speed aerodynamics: from wing theory to panel methods.* McGraw-Hill, New York.
16. Lang , T. G. and Daybell, D. A. 1963. Porpoise performance tests in a seawater tank. *Nav. Ord. Test Sta. Tech. Rep.* 3063.
17. Hertel, H. 1966. *Structure, form, movement.* Reinhold, New York.
18. Aigeldinger, T. L. and Fish, F. E. 1995. Hydroplaning by ducklings: Overcoming limitations to swimming at the water surface. *J. Exp. Biol.*, 198:1567-1574.
19. Hoerner, S. F. 1965. *Fluid-Dynamic Drag.* Published by author, Brick Town, New Jersey.
20. Marchaj, C. A. 1991. *Aero-hydrodynamics of sailing.* International Marine Publishing, Camden, Maine.
21. Prange, H. and Schmidt-Nielsen, K. 1970. The metabolic cost of swimming in ducks. *J. Exp. Biol.*, 53:763-777.
22. Fish, F. E. 1982. Aerobic energetics of surface swimming in the muskrat *Ondatra zibethicus. Physiol. Zool.*, 55:180-189.
23. Vogel, S. 1988. *Life's devices.* Princeton University Press, Princeton.
24. Denny, M. W. 1993. *Air and water.* Princeton University Press, Princeton.
25. Hoyt, J. W. 1975. Hydrodynamic drag reduction due to fish slimes. *In* T. Y. Wu, C. J. Brokaw, and C. Brennen (eds.), *Swimming and flying in nature*, Vol. 2, pp. 653-672. Plenum Press, New York.
26. Daniel, T. L. 1981. Fish mucus: In situ measurements of polymer drag reduction. *Biol. Bull.*, 160:376-382.
27. Rosen, M. W. and Cornford, N. E. 1971. Fluid friction of fish slimes. *Nature*, 234:49-51.
28. Breder, C. M. 1926. The locomotion of fishes. *Zoologica* (N.Y.), 4:159-256.
29. Sokolov, V., Bulina, I, and Rodionov, V. 1969. Interaction of dolphin epidermis with flow boundary layer. *Nature*, 222:267-268.
30. Harrison, R. J. and Thurley, K. W. 1972. Fine structural features of delphinid epidermis. *J. Anat.*, 111: 498-499.
31. Gucinski, H. and Baier, R. E. 1983. Surface properties of porpoise and killer whale skin *in vivo. Amer. Zool.*, 23:959.
32. Walsh, M. J. 1990. Riblets. *Prog. Astro. Aero.*, 123:203-261.
33. Pershin, S. V., Chernyshov, L. F., Kozlov, L. F., Koval, A. P., and Zayets, V. A. 1976. Patterns in the integuments of fast-swimming fishes. *Bionika*, 10:3-21.
34. Reif, W.-E. 1978. Protective and hydrodynamic function of the dermal skeleton of elasmobranchs. *Neues Jahrb. Geol. Paläotol.*, 157:133-141.
35. Reif, W.-E. and Dinkelacker, A. 1982. Hydrodynamics of the squamation in fast swimming sharks. *Neues Jahrb. Geol. Paläotol.*, 164:184-187.
36. Pershin, S. V. 1988. *Fundamentals of hydrobionics.* Sudostroyeniye Publ., Leningrad.
37. Reidy, L. W. 1987. Flat plate drag reduction in a water tunnel using riblets. NOSC Tech. Rep. 1169.
38. Anderson, E. J., MacGillivray, P. S., and DeMont, M. E. 1997. Scallop shells exhibit optimization of riblet dimensions for drag reduction. *Biol. Bull.* 192:341-344.
39. Purves, P. E., Dudok van Heel, W. H., and Jonk, A. 1975. Locomotion in dolphins Part I: Hydrodynamic experiments on a model of the bottle-nosed dolphin, *Tursiops truncatus*, (Mont.). *Aqu. Mamm.*, 3:5-31.
40. Yurchenko, N. F. and Babenko, V. V. 1980. Stabilization of the longitudinal vortices by skin integuments of dolphins. *Biophysics*, 25:309-315.
41. Gray, J. 1936. Studies in animal locomotion VI. The propulsive powers of the dolphin. *J. Exp. Biol.*, 13:192-199.
42. Kramer, M. O. 1960. Boundary layer stabilization by distributed damping. *J. Amer. Soc. Nav. Eng.*, 72:25-33.
43. Kramer, M. O. 1960. The dolphins' secret. *New Sci.*, 7:1118-1120.
44. Kramer, M. O. 1965. Hydrodynamics of the dolphin. *In* V. T. Chow (ed.), *Advances in Hydroscience*, Vol. 2 ., pp. 111-130. Academic Press, New York.
45. Aleyev, Yu. G. 1977. *Nekton.* Junk, The Hague.
46. Riley, J. J., Gad-el-Hak, M. and Metcalfe, R. W. 1988. Compliant coatings. *Ann. Rev. Fluid Mech.*, 20:393-420.
47. Landahl, M. T. 1962. On stability of a laminar incompressible boundary layer over a flexible surface. *J. Fluid Mech.*, 13:609-632.
48. Blick, E. F. and Walters, R. R. 1968. Turbulent boundary-layer characteristics of compliant surfaces. *J. Aircraft*, 5:11-16.
49. Gad-el-Hak, M. 1987. Compliant coatings research: A guide to the experimentalist. *J. Fluid. Struct.*, 1:55-70.

50. Toedt, M. E., Reuss, L. E., Dillaman, R. M., and Pabst D. A. 1997. Collagen and elastin arrangements in the blubber of common dolphin (*Delphinus delphis*). *Amer. Zool.*, 37:56A.
51. Essapian, F. S. 1955. Speed-induced skin folds in the bottle-nosed porpoise, *Tursiops truncatus*. *Breviora Mus. Comp. Zool.*, 43:1-4.
52. Lang, T. G. and K. Pryor. 1966. Hydrodynamic performance of porpoises (*Stenella attenuata*). *Science*, 152:531-533.
53. Rosen, M. W. 1961. Experiments with swimming fish and dolphins. *Amer. Soc. Mech. Eng. Paper* 61-WA-203.
54. Latz, M. I., Rohr, J. and Hoyt, J. 1995. A novel flow visualization technique using bioluminescent marine plankton - Part I: Laboratory studies. *IEEE J. Ocean. Eng.*, 20:144-147.
55. Rohr, J., M. I. Latz, E. Hendricks, and J. C. Nauen. 1995. A novel flow visualization technique using bioluminescent marine plankton - Part II: Field studies. *IEEE J. Ocean. Eng.*, 20:147-149.
56. Williams, T. M. and Kooyman, G. L. 1985. Swimming performance and hydrodynamic characteristics of harbor seals *Phoca vitulina*. *Physiol. Zool.*, 58:576-589.
57. Fish, F. E., Innes, S., and Ronald, K. 1988. Kinematics and estimated thrust production of swimming harp and ringed seals. *J. Exp. Biol.*, 137:157-173.
58. Romanenko, E. V. 1976. Acoustics and hydrodynamics of certain marine animals. *Sov. Phys. Acoust.*, 22:357-358.
59. Romanenko, E. V. 1981. Distribution of dynamic pressure over the body of an actively swimming dolphin. *Sov. Phys. Dokl*, 26:1037-1038.
60. Videler, J. and Kamermans, P. 1985. Differences between upstroke and downstroke in swimming dolphins. *J. Exp. Biol*, 119:265-274.
61. Fish, F. E. 1993. Power output and propulsive efficiency of swimming bottlenose dolphins (*Tursiops truncatus*). *J. Exp. Biol.*, 185:179-193.
62. Lighthill, J. 1975. *Mathematical biofluiddynamics*. Soc. Ind. Appl. Math., Philadelphia.
63. Walters, V. 1963. The trachipterid integument and an hypothesis on its hydrodynamic function. *Copeia*, 1963:260-270.
64. Bone, Q. 1972. Buoyancy and hydrodynamic functions of integument in the castor oil fish, *Ruvettus pretiosus* (Pisces: Gempylidae). *Copeia*, 1972:78-87.
65. AbdulNour, B. S. and Mueller, M. K. 1993. Hybrid laminar flow over wings enhanced by continuous boundary-layer suction. *SAE Tech. Paper* 931386.
66. Walters, V. 1962. Body form and swimming performance in scombrid fishes. *Am. Zool.*, 2:143-149.
67. Lang, T. G. 1966. Hydrodynamic analysis of cetacean performance. *In* K. S. Norris (ed.), *Whales, Dolphins and Porpoises*, pp. 410-432. Univ. of California Press, Berkeley.
68. von Mises, R. 1945. *Theory of flight*. Dover, New York.
69. Hess, J. L. 1976. On the problem of shaping an axisymmetric body to obtain low drag at large Reynolds numbers. *J. Ship Res.*, 20:51-60.
70. Bannasch, R. 1995. Hydrodynamics of penguins - an experimental approach. *In* P. Dann, I Norman, and P. Reilly (eds.), *The penguins: Ecology and management*, pp. 141-176. Surrey Beatty and Sons, Norton, NSW.
71. Fish, F. E. 1993. Influence of hydrodynamic design and propulsive mode on mammalian swimming energetics. *Aust. J. Zool.*, 42:79-101.
72. Feldkamp, S. D. 1987. Swimming in the California sea lion: Morphometrics, drag and energetics. *J. Exp. Biol.*, 131:117-135.
73. Felts, W. J. L. 1966. Some functional and structural characteristics of cetaceans flippers and flukes. *In* K. S. Norris (ed.), *Whales, Dolphins and Porpoises*, pp. 255-276. University of California Press, Berkeley.
74. Lang, T. G. 1966. Hydrodynamic analysis of dolphin fin profiles. *Nature*, 209:1110-1111.
75. Sokolov, W. 1962. Adaptations of the mammalian skin to the aquatic mode of life. Nature, 195:464-466.
76. Mordvinov, Yu. E. and Kurbatov, B. V. 1972. Influence of hair cover in some species of Phocidae upon the value of general hydrodynamic resistance. *Zool. Zh.*, 51:242-247.
77. Ling, J. K. 1970. Pelage and molting in wild mammals with special reference to aquatic forms. *Quart. Rev. Biol.*, 45:16-54.
78. Romanenko, E. V., Sokolov, V. E., and Kalinichenko, N. M. 1973. Hydrodynamic patterns of hair cover in *Phoca sibirica*. *Zool. Zh.*, 52:1537-1542.
79. Kooyman, G. L. 1989. *Diverse divers: physiology and behavior*. Springer-Verlag, Berlin.
80. Bandyopadhyay, P. R. 1989. Viscous drag reduction of a nose body. *AIAA Journal*, 27:274-282.
81. Bandyopadhyay, P. R. and Ahmed, A. 1993. Turbulent boundary layers subjected to multiple curvatures and pressure gradients. *J. Fluid Mech.*, 246:503-527.
82. Videler, J. J. 1995. Body surface adaptations to boundary-layer dynamics. *In* C. P. Ellington and T. J. Pedley (eds.), *Biological fluid dynamics*, pp. 1-20. Soc. Exp. Biol., Cambridge.
83. Maisey, J. G. 1979. Finspine morphogenesis in squalid and heterodontid sharks. *Zool. J. Linn. Soc.*, 66:161-183.
84. Videler, J. J. and Weihs, D. 1982. Energetic advantages of burst-and-coast swimming of fish at high speeds. *J. Exp. Biol.*, 97:169-178.
85. Weihs, D. and Webb, P. W. 1983. Optimization of locomotion. *In* P. W. Webb and D. Weihs (eds.), *Fish biomechanics*, pp. 339-371. Praeger, New York.
86. Weihs, D. 1974. Energetic advantages of burst swimming of fish. *J. Theor. Biol.*, 48:215-229.
87. Fish FE, Fegely, J, Xanthopoulos CJ. 1991. Burst-and-coast swimming in schooling fish (*Notemigonus crysoleucas*) with implications for energy economy. *Comp. Biochem. Physiol.*, 100A:633-637.
88. Rosen, M. W. 1959. Water flow about a swimming fish. *U.S. Nav. Ord. Test Sta Tech. Publ.* 2298:1-96.
89. Triantafyllou, G. S., Triantafyllou, M. S., and Gosenbaugh, M. A. 1993. Optimal thrust development in oscillating foils with application to fish propulsion. *J. Fluids Struct.*, 7:205-224.
90. Gopalkrishnan, R., Triantafyllou, M. S., Triantafyllou, G. S., and Barrett, D. 1994. Active vorticity control in a shear flow using a flapping foil. *J. Fluid Mech.*, 274:1-21.
91. Fish, F. E. and Battle, J. M. 1995. Hydrodynamic design of the humpback whale flipper. *J. Morph.*, 225:51-60.
92. Nakaya, K. 1995. Hydrodynamic function of the head in the hammerhead sharks (Elasmobranchii: Sphrynidae). *Copeia*, 1995:330-336.
93. Shevell, R. S. 1986. Aerodynamic anomalies: Can CFD prevent or correct them? *J. Aircraft*, 23:641-649.
94. Bragg, M. B. and Gregorek, G. M. 1987. Experimental study of airfoil performance with vortex generators. *J. Aircraft*, 24:305-309.
95. Chamberlain, J. A., Jr. and Westermann, G. E. G. 1976. Hydrodynamic properties of cephalopod shell ornament. *Paleobiology*, 2:316-331.
96. Videler, J. 1993. *Fish swimming*. Chapman and Hall, London.
97. Romberg, G. F., Chianese, F., Jr., and Lajoie, R. G. 1971. Aerodynamics of race cars in drafting and passing situations. *Soc. Auto. Eng.* Paper 710213.
98. Kyle, C. R. 1979. Reduction of wind resistance and power output of racing cyclists and runners traveling in groups. *Ergonomics*, 22:387-397.
99. Hagberg, J. M. and McCole, S. D. 1990. The effect of drafting and aerodynamic equipment on energy expenditure during cycling. *Cycling Sci.*, 2:19-22.
100. Zabat, M., Frascaroli, S., and Browand, F. K. 1994. Drag measurements on 2, 3 and 4 car platoons. *Soc. Auto. Eng.* Paper 940421.
101. Fish, F. E. 1994. Energy conservation by formation swimming: metabolic evidence from ducklings. *In* L. Maddock, Q. Bone, and J. M. V. Rayner (eds.), *Mechanics and physiology of animal swimming*, pp. 193-204. Cambridge University Press, Cambridge.
102. Weihs, D. 1973. Hydromechanics of fish schooling. *Nature*, 241:290-291.
103. Bill, R. G. and Herrnkind, W. F. 1976. Drag reduction by formation movement in spiny lobsters. *Science*, 193:1146-1148.
104. Fish, F. E. 1995. Kinematics of ducklings swimming in formation: Energetic consequences of position. *J. Exp. Zool.*, 272:1-11.
105. Saunders, H. E. 1957. *Hydrodynamics in ship design*. Soc. Nav. Arch. Mar. Eng., New York.

106. Wehausen, J. V. 1973. The wave resistance of ships. *In* C. S. Yih (ed.), *Advances in applied mechanics*, Vol. 13, pp. 93-245. Academic Press, New York.
107. Fish, F. E. 1993. Comparison of swimming kinematics between terrestrial and semiaquatic opossums. *J. Mamm.*, 74:275-284.
108. Hammitt, A. G. 1975. *Technical yacht design*. Van Nostrand Reinhold, New York.
109. Marchaj, C. A. 1964. *Sailing theory and practice*. Dodd, Mead and Co., New York.
110. Taylor, D. W. 1933. *The speed and power of ships*. Ransdell Inc., Washington, D. C.
111. Livezey, B. C. and Humphrey, P. S. 1983. Mechanics of steaming in steamer-ducks. *Auk*, 100:485-488.
112. Bloedel, P. 1955. Hunting methods of fish-eating bats, particularly *Noctilio leporinus*. *J. Mamm.*, 36:390-399.
113. Suthers, R. 1965. Acoustic orientation by fish-catching bats. *J. Exp. Biol.*, 158:319-348.
114. Fish, F. E., Blood, B. R., and Clark, B. D. 1991. Hydrodynamics of the feet of fish-catching bats: Influence of the water surface on drag and morphological design. *J. Exp. Zool.*, 258:164-173.
115. Withers, P. C. and Timko, P. L. 1977. The significance of ground effect to the aerodynamic cost of flight and energetics of the black skimmer (*Rhyncops nigra*). *J. Exp. Biol.*, 70:13-26.
116. Lighthill, J. 1977. Introduction to scaling of aerial locomotion. *In* T. J. Pedley (ed.), *Scale effects in animal locomotion*, pp. 365-404. Academic Press, London.
117. van Dam, C. P. 1987. Efficiency characteristics of crescent-shaped wings and caudal fins. *Nature*, 325:435-437.
118. Bose, N., Lien, J., and Ahia, J. 1990. Measurements of the bodies and flukes of several cetacean species. *Proc. Roy. Soc. Lond.* B, 242:163-173.
119. Daniel, T., Jordan, C., and Grunbaum, D. 1992. *In* R. McN. Alexander (ed.), *Advances in comparative & environmental physiology 11: Mechanics of animal locomotion*, pp. 17-49. Springer-Verlag, Berlin.
120. Rayner, J. M. V. 1985. Vorticity and propulsion mechanics in swimming and flying animals. *In* J. Riess and E. Frey (eds.), *Konstruktionsprinzipen lebender und ausgestorbener Reptilien*, pp. 89-118. University of Tubingen, Tubingen, F.R.G.
121. Webb, P. W., and Buffrénil, V. de. 1990. Locomotion in the biology of large aquatic vertebrates. *Trans. Amer. Fish. Soc.*, 119:629-641.
122. Küchermann, D. 1953. The distribution of lift over the surface of swept wings. *Aero. Quart.*, 4:261-278.
123. Ashenberg, J. and Weihs, D. 1984. Minimum induced drag of wings with curved planform. *J. Aircraft*, 21:89-91.
124. Au, D. and Weihs, D. 1980. At high speeds dolphins save energy by leaping. *Nature*, 284:548-550.
125. Hui, C. A. 1987. The porpoising of penguins: an energy-conserving behavior for respiratory ventilation? *Can. J. Zool.*, 65:209-211.
126. Williams, T. M. 1987. Approaches for the study of exercise physiology and hydrodynamics in marine mammals. *In* A. C. Huntley, D. P. Costa, G. A. J. Worthy, and M. A. Castellini (eds.), *Approaches to marine mammal energetics*, pp. 127-145. Spec. Publ. Soc. Mar. Mamm. No. 1.
127. Fish, F. E. 1990. Wing design and scaling of flying fish with regard to flight performance. *J. Zool., Lond.*, 221:391-403.
128. Azuma, A. 1992. *The biokinetics of flying and swimming*. Springer-Verlag, Tokyo.
129. Blake, R. W. 1983. Energetics of leaping in dolphins and other aquatic animals. *J. Mar. Biol. Assoc. UK.*, 63:61-71.
130. Hui, C. A. 1989. Surfacing behavior and ventilation in free-ranging dolphins. *J. Mamm.*, 70:833-835.
131. Liu, H., Wassersug, R. J., and Kawachi, K. 1996. A computational fluid dynamics study of tadpole swimming. *J. Exp. Biol.*, 199:1245-1260.
132. Moin, P. and Kim, J. 1997. Tackling turbulence with supercomputers. *Sci. Amer.*, 276:62-68.

ON BIOLOGICAL FOUNDATIONS OF DOLPHIN'S CONTROL OF HYDRODYNAMIC RESISTANCE REDUCTION

V. Babenko, A. A. Yaremchuk
Professor, Dr.Tech.Sc., Head of Department
Department of Hydrobionics and Boundary Layer Control
8/4, Zheliabov str., 252057, Kiev, Ukraine
E-mail: vb@bionics.kiev.ua

Abstract - The comparative analysis of the heat emission rating of a man and a dolphin has been carried out. Deficiencies in biopower estimation on the basis of oxygen consumption are shown. The comparative analysis of microvibration components of the skin of man and dolphin is carried out.

In the course of comparative analysis of human's and dolphin's skin surface microvibrations the authors calculated microvibration velocity as the product of the circular frequency and amplitude, according to the records of microvibrations of swimmer skin and of dolphin's (namely, Tursiops truncatus) skin, listed in the work [1]. Average velocity values thus obtained are: for human body - 0,35 mm/s, for dolphin in water - 1,88 mm/s, for dolphin in the air - 1,13 mm/s. Dolphin's vibration velocity in the air is 3,2 times greater than that of human's, and in the water - 5,4 times. As long as mean power of vibration process is proportional to the square of velocity, corresponding power relation looks even more impressive: 10.2 times in the air and 29.2 times in the water. The reason for such excess of vibration power is,evidently, the quality of dolphin's skin surface. But there is something else here - it should be noted,that vibrations of dolphin's skin in the water have higher frequency and greater velocity than vibrations in the air. From the pure mechanical point of view the fact looks incredible: a transition of vibrating surface from the low-viscosity medium (air) to the high-viscosity medium (water) should not expand the frequency range of vibrations. The explanation of the phenomenon may be an adaptive electromagnetic control of vibrations.

Results of electric potentials distribution measurements for the skin surface of a dolphin are listed in the work [2]. The average potential, calculated on the basis of this distribution, is 170 mV. For human body similar technique of measurements gives 18 mV for common points and 57 mV for bioactive points. Such evident excess - about 9.4 times - of dolphin's average potential over human's one has morphological explanation - more powerful peripheral nervous system of a dolphin. However, there is a supposition about very good heat insulation of a dolphin by adipose tissue. In such case the skin surface must be lean in heat energy,that makes nervous system control highly problematic, due to well-known sharp decline of nerve-pulse propagation speed in case of heat-leaning. To check the latter, comparative analysis of dolphin's and swimmer's skin heat emission was carried out. Thermal losses analysis was based on Sirle technique for cylindrical model of heat source. With such a model for the boundary surface there was found:

$$t^{\circ}_{p} - t^{\circ}_{oc} = t^{\circ}_{c} - \frac{p_l}{\pi(\lambda_1 + \lambda_2)} ln \frac{D_p}{D_c} \qquad (1)$$

where t°_{p}, D_p - temperature and diameter of the boundary surface, respectively, t°_{c}, D_c - temperature and diameter of heat-emitting cylinder, t°_{oc} - surrounding medium temperature, p_l - heat power line density, λ_1, λ_2 - thermal conductivities of the source medium and surrounding medium, respectively.

Dolphin skin thermal conductivity is known to be [3] $\lambda_{11} \approx 0.209$ $Wm^{-1}K^{-1}$. Remarkable, that human nonvascular skin, as well as adipose tissues thermal conductivity have just the same value - 0.209 $W\,m^{-1}\,K^{-1}$ [4], while for muscular tissues at normal blood flow $\lambda_{13} \approx 0.532$ $W\,m^{-1}\,K^{-1}$. Conseguently, thermal conductivity of adipose tissues is only 2.5 times less than that of muscular tissues and equal to the skin conductivity. Therefore , wide-spread supposition,regarding heavy heat insulation of a dolphin by adipose tissues is incorrect. For D_c, that corresponds underskin adipose tissue boundary, and D_p=0.3 m, t°_{p}-t°_{oc}=0.54°C, t°_{c}=37°C from (1) we get p_l=246 W/m, that fits the value of heat flux density about 390 W/m^2 , thus disproving the existence of dolphin skin heat leaning.

To compare heat emission capacity of dolphin and that of swimmer, let us analyse the known records of investigations of human heat emission. Results of investigations of heat emission of various parts of human body at rest both for radiant and convective constituents are listed in the work [5]. By averaging the results for various body parts, one can get average heat flux density about 62 W/m^2, that corresponds to overall power of the whole skin surface about 250 W. Furtermore, results of investigations of swimmer body heat emission are listed in the work [6]. These results show that in unsteady-state heat exchange in water temperature range from 15°C up to 27°C thermal losses of swimmer are proportional to the temerature difference between skin and water and in some cases exceed 10 kW. Transition to a steady-state heat exchange takes 7 - 10 min, the heat flux density of a steady state being in the range from 250 W/m^2 up to 800 W/m^2, that yields total losses for the whole skin surface from 1 kW to 3.2 kW. The average value of this power is just 2.1 kW. Therefore, heat flux density of a dolphin, calculated previously,fits the range of swimmer's skin heat flux density.

Estimation of power of basic methabolysm N_o as well as active methabolysm N_a for warm-blooded animals and humans is known [1, 7] to be based on oxygen consumption either of the organism as a whole or that reduced to the unit of weight. By such estimation, values of N_o=100 W and N_a=2.2 kW were obtained in the work [1]. Comparison of methabolysm power estimations, based on oxygen consumption, and previously calculated power losses for just one constituent (heat emission) shows evident underestimation of power losses in calculations, based on oxygen consumption data. Such result is hardly unexpected,takting into account the following:

1. The main process of energy transformation - the oxidizing cycle (e. g. tricarboxylic acid cycle) of warm-blooded animals goes on without oxygen. The latter takes part in reaction only on final stages of phosphorylization [7].
2. According to well-known hypothesis, thermal energy that is released on a final stage of the phosphrylization is spent on maintainence of body thermal conditions. There is a remarkable correspondence of active methabolysm power (2.2 kW), derived from oxygen consumption, and average power of thermal losses of a swimmer, that equals 2.1 kW.
3. QO_2 has nothing to do with oxygen methabolysm of separate organs and tissues of an organism. Table 1 shows data from [7], concerning oxygen supply of human's organs and tissues, wherefrom one can see that, muscles, for instance, having the largest relative mass, consume rather small portion of oxygen.

Summing up all stated above, we may conclude, that, on our opinion, it is incorrect to use oxygen consumption in a quantitative estimation of bioenergetics of the whole being. Such estimates should be used for comparison of separate bioenergetic processes only.

According to experimental data, the frequency of dolphin skin vibrations occupies the range from 11 Hz to 16 Hz. On the other hand, analysis of change of mucles contraction force as a function of electrostimulation pulses frequency [8] shows just that range as a range of rather high speed of increase of muscle contraction force with increase of stimulation frequency. Increase of stimulation frequency above 20 Hz results in eventual halting of contraction force increase, while muscle fatiguability intensifies quickly. Thus micrvibrations frequency range corresponds to optimal one from the point of view of energetical output of muscle tissue.

Field force analysis of electromagnetic interaction between dolphin skin and surrounding water medium was based on Maxwell - Tamm equation for non-unifofm medium [9,10]. In accordance with the equaction volume density of electric forces $\mathbf{f}_0$ is

$$f_0 = \rho E_c - \frac{1}{2} E_c^2 \, grad\, \varepsilon + \frac{1}{2} grad\left(E_c^2 \delta_c \frac{\partial \varepsilon}{\partial \delta_c} \right) \qquad (2),$$

wherein ρ - charge volume density, E_c - electric field intensity, ε - dielectric constant, , δ_c - medium density.

To analyse the contribution of the equation [2] second component an order of dielectric constant gradient intensity has to be evaluated. The said gradient has to be considered on the interface of water medium and dolphin skin surface. Considering the direction of normal to the boundary, approximation can be used.

$$\left|grad\,\varepsilon\right| = \frac{\varepsilon_0(\varepsilon_2 - \varepsilon_1)}{l_{12}} \qquad (3)$$

wherein ε_0 - dielectric constant, ε_2, ε_1 - absolute dielectric constants of dolphin skin and water medium respectively, l_{12} - transition zone width.

Results of examinations of absolute dielectric constants of skin,musscle and other tissues are listed in [4,11,12]. Approximation of these records for frequency range below 10 kHz yields a frequency funcion.

$$\varepsilon_2 \approx 7{,}91 \cdot 10^6 / f^{1/2} \qquad (4)$$

Extremely high level of ε_2 for low frequencies has biophysical explanation [11,12], and substances with such level of ε_2 are called energetically saturated ones. At the same time, such level of dielectric constant of artificial substanses may be the end of a very long technological road. For water medium at low frequencies dielectric constant $\varepsilon_1 \approx 80$, i.e. $\varepsilon_2 >> \varepsilon_1$.

To estimate the value of l_{12} in (3), two premises may be used.: firstly, external layer of epidermis hinder water molecules, and, secondly, to form such medium factor as dielectric constant, at least one layer of water molecules is necessary. That defines the choice of l_{12} value as a figure that equals to maximal size of water moleculae, i. e. 0,138 nm [13, 14].

Surface electric field intensity in regions of heightened hydrodynamic resistance can be as high as E = 1 mV/mm. Then for f = 10 Hz modulus of the second component of (2) $|\mathbf{f}_0`|$=80 kH/m$^3$, and for f=20 Hz we get $|\mathbf{f}_0`|$=57 kH/m^3. Such force action causes changes in water moleculaes construction structure in the near proximity of dolphin skin, that, consequently, leads to decline of hydrodynamic resistance.

When a dolphin is transfered from the air into sea water, that has low conductivity, leveling of different areas of skin surface occurs, and, on the other hand, there is an increase of field intensity due to appearence of crumples on the boundary lines. That explains paradoxal increase of frequency range of microvibrations, noted previously.

Analysis, thus carried out, makes the basis for entire explanation of mechanism of electromagnetic control of a dolphin skin surface.

Table

Tissues	Skeletal muscle	Skin	Digestive organs	Liver	Brain	Heart	Kidney	Lungs
Weight of organ in % from the total body weight	40	10	4	2	4	0,4	0,4	1,4
Consumption of O_2 at rest in % from QO_2	25	2	19	20	15	9	5	4

REFERENCES

1. S. V. Pershin «Basis of a hydrobionics». - Leningrad: Sudostroenie, 1988. - 264 pp.
2. O. V. Nechaeva, V. N. Plehanov, V. G. Hadzginski «Peculiarity of potentials distribution on skin surface of dolphins» Bionica. - 1973. 7, -p. 79-83.
3. D. A. Parry «The Structure of Whale Blubber, and a Discussion of its Thermal Properties» Quart. J. Microsc. Sc. -1949. -N1. -P. 273-1279.
4. «Biophysical characteristics of human's tissues». The reference book / V. A. Berezovski, N. N. Kolotilov - Kiev: Naukova dumka, 1990 -224 pp.
5. M. A. Arakelan «Device for determination of radiant and convective components of heat exchange in the industrial environment» Heat measurement, energy- and resources saving. - Kiev: Institute of energy saving problems, 1989. -p. 17-27.
6. O. A. Geraschenko «Basis of heat measurement». - Kiev: Naukova dumka, 1971. -191 pp.
7. L. D. Lukyanova, B. S. Balmuhanov, A. T. Ugolev «Depended on oxygen processes in a cell and its functional condition». - Moskwa: Nauka, 1982. -301 pp.
8. R. Plonsy, R. Barr «Bioelectricity: Quantative approach».- Moskva: Mir,1964. 366 pp.
9. K. Shimoni «Electroengineering theory». - Moskva: Mir, 1964. 773 pp.
10. I. E. Tamm «Basics of electrical theory». - Moskva: Nauka,1989.-504 pp.
11. W. R. Adey «Frequency and energetic windows in weak electromagnetic fields influence on a living tisssue» TIIER.- 1980. -N 1. - pp. 140-148.
12. H. P. Schwan, K. P. Foster «Influence of high-frequency fields on biological systems» TIIER.-1980.-N1. -pp. 121-132.
13. V. I. Klasssen «Water systems magnetization». - Moskva: Himia,1982. - pp.
14. U. I. Ergin «Electrolytic solutions structure and magneticproperties». -Moskva: Nauka, 1983. - 183 pp.

HYDROBIONICS PRINCIPLES OF DRAG REDUCTION

Viktor V. Babenko

Department of Hydrobionics and Boundary Layer Control, Professor, Dr.Tech.Sc., Head of Department, 8/4, Zheliabov str., 252057, Kiev, Ukraine, E-mail: vb@bionics.kiev.ua

The principles of hydrodynamical drag reduction based on insight to drag-reduction adaptations of Nectons were developed. Presented are the two methods used in nature. The first is based on adaptations in skin cover. It is an analog of viscous-elastic active coating for friction drag reduction. The second consists in use of swordfish sword with polymer feed.

It was demonstrated for the first time in [3] and then confirmed in [6, 9], on the basis of a set biological and hydrodynamic experimental and theoretical studies, with use of modeling, that the cetacean integument has self-adjusting properties during active swimming with regard to damping perturbations in the boundary layer, and that it effectively performs the function of a hydrodynamically active cover that diminishes drag reduction appreciably. This effect is attributable to change in physicomechanical parameters of a specially [or particularly] developed integument, with papillary and ridged microstructure of one layer and other layers, with profuse blood supply and innervation. The mechanical characteristics of the functionally specific integument of cetaceans are regulated by means of the vascular system, as well as change in the animal's metabolism in different modes of nonstationary swimming, in connection with the function of the bendeng and oscillatory propulsion complex. Let us note that live dolphins are characterized by a wide range of vasomotor variability-dilation and constriction of blood vessels.

A model of the delphinid integument was constructed on the basis of a mehanical model of a skin section rendered in the form of a Voigt-Kelvin viscoelastic element with additional links and a corresponding differential equation for oscillation dynamics. The dimensionless parameters of modeling were established, which take into consideration such extremely important features of the skin as active oscillating mass, oscillation frequency and related damping [3, 4]. Some of these characteristics were determined from measurements of live +dolphins, which made it possible to conduct a numerical analysis of modeling parameters and demonstrate their optimum values with an expernal load in the boundary layer conforming to specific speeds of swimming. A comprehensive study was made of the question of actively oscillating mass of the delphinid integument, and a reltionship was demonstrated between thickness of skin layers and typical thicknesses of boundary layer [2].

A conprehensive study was also made of elasticity of the integyment of live dolphins [1]. Measurements of elasticity of the skin of three Black Sea dolphin species-common dolphin, bottlenosed dolphin and porpoise-revealed that the modulus of elasticity depends on the dolphin species, its conditioning and condition of the animal during the experiment. Experiments have showm that, by tensing the cutaneous muscle dolhhins can alter integumental elasticity by almost two times. The distribution of values for the elasticity modulus of the skin over the body of two dilphinid species in different states is illustrated in Figure 1.

The coefficients of absorption of disturbance energy [perturbation energy] by the delphinid integument were measured and, for comparison,sheets of different materials. The value of the coefficient was determined according to relative height of bouncing of solid spheres differing in mass. It was found that, in live dolphins, the coefficient of absorption of disturbance energy by the integument depends on the magnitude of this energy, and it has a maximum of 95% in the area of disturbance energies +corresponding to the order of energy of turbulent pulsations in the boundary layer. The absorption coefficient is lower in a sick dolphin and does not exceed 80%, it is no more than 70% in a dolphing right after death. The absorption coefficient is about 80% for elastomers [elastoplastic] and only 40-50% for construction materials, where the pattern of relative energy of perturbation changes to the opposite.

Self-regulation of skin damping in ceraceans during active swimming has the reverse effect on the hydrodynamic boundary later, with change in nature of pulsations, speed and pressure. Measurements of pulsation of velocities in the dolphin's boundary layer, at Reynolds numbers $Re>2.7\cdot10^6$, revealed that there is extension of the transitional mode of flow [current] and pulsations drop virtually to a level that in close to streamline mode. It has been demonstrated that there are different degrees of turbulence in the boundary layer of the dolphin and rigid model (Figure 2), which increases all the more with some increase invelocity and Reynolds number alogues of integument were developed for comprehensive laboratory studies and explanation of physical patterns in the boundary layer with flow-around [7, 8, 10, 13]. There was experimental confir mation of the possibility of encrease in hydrodynamic stability of flow in a streamline boundary layer of water by use of viscoelastic damping surfaces. It was found that there was a decrease in build-up of perturbed motion,increase in Reynolds number for loss of stability, increased length of transient zone, as compared to a hard surface. The Gertlerian vortices formed in the transitional zone become more stable. Enlargement of the viscous sublayer, decrease in maximum pulsation rates and redistribution of these parameters over the thickness of the boundary layer, decrease in local Reynolds shear stresses were found on elastic surfaces in the turbulent boundary layer. This is indicative of substantisl structural change in flow in the boundary layer on an elastic surface, such as (and more effectively) the integument of cetaceans. Bioenergetic calculations of drag reduction (Figure 3) were made for four delphinid species: porpoese-smallest of the delphinids with moderate speed, common dolphinaverage in size and swift, killer whalelargest high-speed species- and white whale, which is swift, killer whalelargest high-speed species-and white whale, which is a large, slowswimming delphinid. Maximum decline of drag reduction was determined, according to the calculations, for the common dolphin. Taking hydrodynamic distinctions of the gill system of swordfish into consideration, a model was developed to experimentally check interaction of gills with the rostrum [5]. Its construction and methods of investigation in the biohydrodynamic unit, as well as results of testing models with xiphoid [sword-shaped] tips differing in length, without simulating the function of the gill system, are described in [9]. We first filled the disposable container with waterm which flowed under compressed air pressure through the slit in the model, turning on an electric stopwatch [timer]. Duration of fluid injection was determined when interpreting the oscillograms, in addition to timer reading. Similarly, injections of other types of fluids were made through the nose slits with attach ment to the model of an ogive-shaped (OT), short (SXT) and elongated (LXT) xiphoidshaped tips. The oscillograms of model drag reduction were interpreted by means of calibration lines. In addition, the results of fluid injection into stationary water were also recorded on the oscillograms.

Figure 4 illustrates the results of measu ring drag reduction in models with different tips using aqeuous solutions of polyethy lene oxide (PEO) through the slit. Without injection of PEO solution, the coefficient of model drag reduction with C_x a sword shaped tip increased, as compared to OT, although there was insignificant increase in size if wet surface. These experiments simulated flow-around of swordfish with the mouth closed and gill slits open. When the gill slits are also closed, it is possible to lower drag reduction by 10-12%, according to the results of tests on the model [9]. Positions 7 and 9 in Figures 4 and 5, respectively, indicate injection of a PEO solution prepared before the experiments at an average rate of Q=59 cc/s, while 8 and 10 in Figures 2 and 3, respectively, show injection of solution prepared 7 days before the tests, with Q=49 cc/s. As compared to the OT, the efficacy of injection of PEO solution increases with increase in size of the ensiform tip and it depends less on Q (curves in Figure 2 with SXT, Q=34 cc/s, and with LXT, Q=45 cc/s). These experiments simulate dissolution of slime in the gill system of swordfish, regulation of flow through the gill slits, as well as the case of a broken sword or, shorter one as, for example, in a sailfish.

Subsequently, analysis of the obrained results was made with consideration of subtraction from model drag reduction of hydrodynamic characteristics measured in stationary flow (Figure 5). The results of experiments on a model with OT revealed that injection of freshly prepared polymer solution with concentration C=0.1‰ (curve 9) had the greatest effect on lowering drag reduction.

Maximum decrease in drag reduction was obtained with Reynolds numbers where the rate of injection was commensurate with free-stream velocity (the region of minimum curves in Figure 5). Beyond this range of Reynolds numbers, an increase in rate [outlay] was a secondary factor and did not affect the value of C_x.

Replacement of PEO solution (curve 13) with synthetic glue solution in the same concentration (curve 12) led to appreciable decrease in efficacy of injection through the slit. Let us not that the nature of the curves is determined by the fact that, at different flow-around velocities, air pressure in the system of injection of polyner solytion underwent virtually no change, which produced an inconsistency between velocities of injection and free stream flow, with increase in the latter parameter and decrease in efficacy of injection.

Experiments on a model with SXT and LXT revealed that injection of the polymer was the most effective with SXT at C=0.15‰, and with LXT at $Re<10^6$ with C=0.1‰, and with $Re<10^6$ with C=0.05‰. Unlike the experiments with an OT, the inconsistency between rate of injection and free-stream flow did not have such a strong influence on efficacy of injection, while the range of effecacy extended and shifted to the range of high Reynolds numbers. As compared to OT, SXT and LXT led to increase in absolute value of decline of C_x, as well as reduction of C_x, at which better results are observed.

REFERENCES

1 BABENKO V."Investigation of Elasticity of Live Dolphinid Skin," BIONIKA, No 13, 1979, pp 43-52.

2. Idem,"Vibrating Mass of Delphinid Integument," Ibid, No 14, 1980, pp 21-27.
3. BABENKO V., KOZLOW L. and PERSHIN S."Variable Damping of Dolphin Skin at Different Swimming Speeds," Ibid, No 6, 1972, pp 42-52.
4. BABENKO V., KOZLOW L., PERSHIN S. et.al."Self-Regulation of skin damping in cetaceans during active swimming,"BIONICA, No 16, 1986, pp 3-10.
5. BABENKO V., KOZLOW L." Hydrodynamic functions of swordfish gill system," Ibid, pp 11-15.
6. BABENKO V."Hydrobionics principles of drag reduction," in «High speed body motion in water», AGARD report 827, 1988, pp 3-1 - 3-14.
7. KANARSKIY M., BABENKO V., KOZLOW L. "Experimental Investigation of Turbulent Boundary Layer on Elastic Surface," in "Stratifitsirovannyye i turbulentnyye techeniya" [Stratified and Turbulent Flow], Kiev, Naukova dumka, 1979, pp 59-67.
8. KOZLOW L., BABENKO V. "Experimental Studies of Boundary Layer," Kiev, Naukova Dumka, 1978, 184 pages.
9. KOZLOV L., BABENKO V., PERSHIN S."Self-Adjustment of Skin Damping During Active Swimming of Some Cetaceans," BIONICA, No12, 1978, pp 55-58.
10. KOZLOV L., SHAKALO V."Some Results of Measuring Velocity Pulsations in Delphinid Boundary Layer," BIONICA, No 7, 1973, pp 50-52.
11. KAYAN V., PYATETSKIY V. " Hydrodynamic Characteristics of Bottlenosed Dolphin in Different Modes of Acceleration," Ibid, No 12, 1978, pp 48-55.
12. ROMANENKO Ye. "Fundamentals of Statistical Biohydrodynamics," Moscow, Nauka, 1976, 167 pages.
13. YURCHENKO N., BABENKO V., KOZLOV L. "Experimental Study of Gertlerian Instability in Boundary Layer," in"Stratifitsirovanyye i turbulentnyye techeniya", Kiev, Naukova dunka, 1979, pp 50-59.

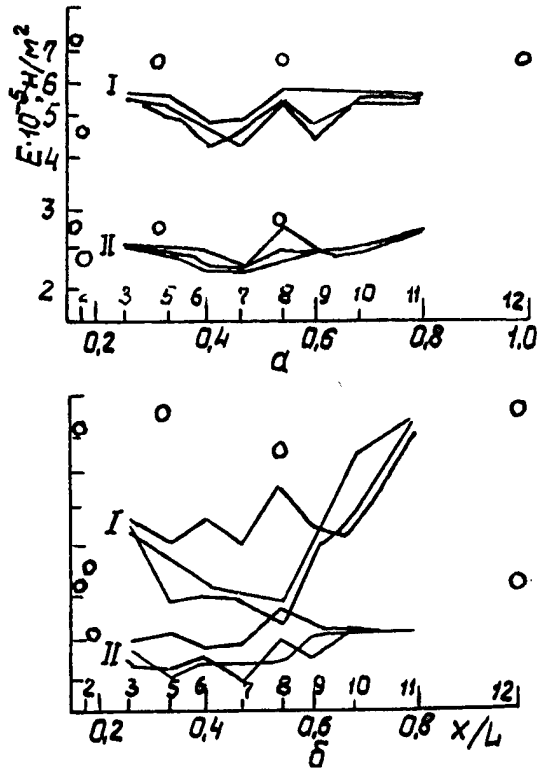

Figure 1. Distribution of values for modulus of elasticity of dolphin skin along body, measured in different longitudinal sections [1]
a - common dolphin;
b - bottlenosed dolphin;
I - just caught and excited dolphin;
II - trained and calm dolphin (same animals)

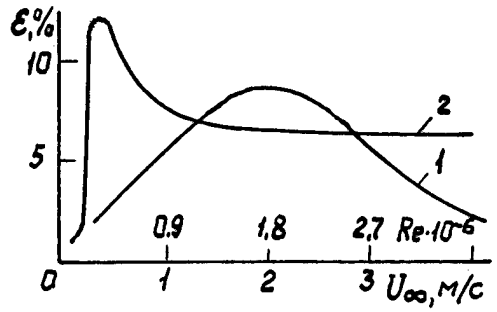

Figure 2. Comparative turbulence in boundary layer of swimming bottlenosed dolphin (1) and towed rigid model of solid of revolution (2) in function of Reynolds numder

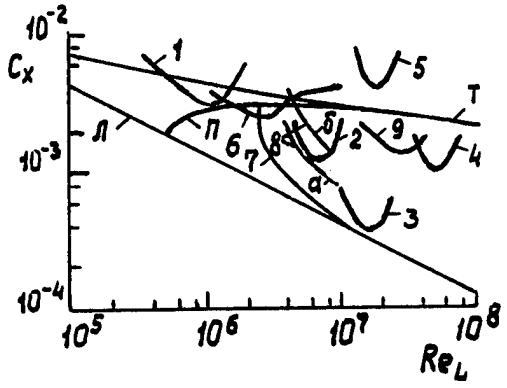

Figure 3. Coefficients of hydrodynamic drag as a function of Reynolds number for dolphins and solids[11,12]: 1 - common porpoise towing carcasses; 2 - porpoise; 3 - common dolphin; 4 - killer whale; 5 - white whale-bioenergetic calculations for active swimming at sea; 6 - rigid model of dottlenoseddolphin, hydrodynamic calculations made on computer; 7, 8 - Bottlenosed dolphin, experiment-passive swimming by inertia in tank (a-positive acceleration, b - negative); 9 - surfacing of streamled rigid "Dolphin" model; L - laminar, Tr - transitional and T - turbulent flowing around the rigid plate

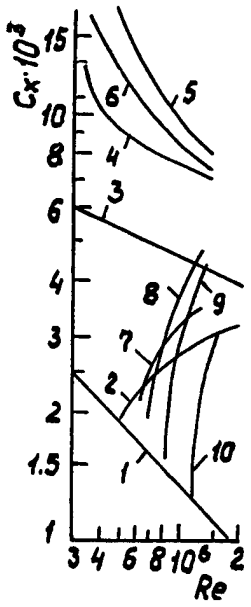

Figure 4. Value C_x as a function of Reynolds number with different-shaped rostral parts of model. 1, 2, 3 - drag of smooth longitudinally streamlined flat plate, with laminar, transitional and turbulent boundary layers, respectively [9]; 4, 5, 6 - model drag with OT, SXT, LXT [9]; with injection of aqueous PEO in concentration of 0.1%; 7, 8 - with OT; 9 - with SXT; 10 - with LXT

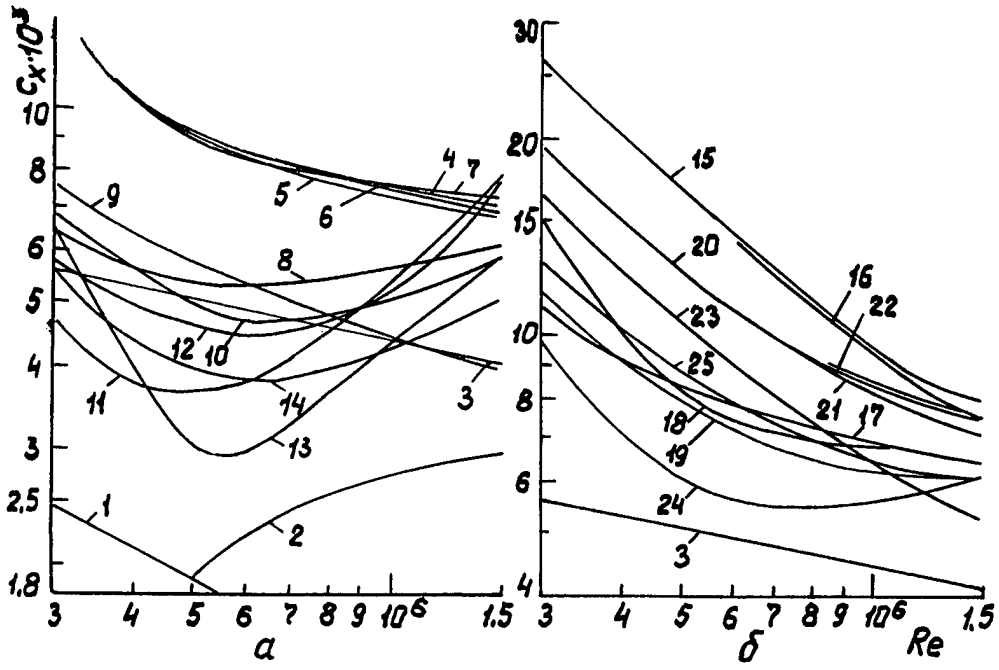

Figure 5. Effect of injection of PEO on drag on model with OT (a), with SXT and LXT (b). a: 1, 2, 3 - same as in Figure 2; 4 - standard [8]; injection of water at average rate: 5 - 57,6 cc/s; 6 - 71 cc/s; 7 - 73 cc/s; injection of PEO concentration & rate: 8 - 0.05%, 54 cc/s; 9 - 0.1%, 59 cc/s; 10 - 0.1%, 49 cc/s; 11 - 0.15%, 54 cc/s; 12 - 0.1%, 80 cc/s 13 - 0.1%, 84 cc/s; 14 - 0,1%, 100 cc/s;

b: model with SXT: 15 - standard [8]; 16 - water injection, 51 cc/s; PEO injection: 17) 0.05%, 47 cc/s; 18 - 0.1%, 34 cc/s; 19 - 0.15%, 28 cc/s; model with LXT: 20 - standard [8]; 21 - water injection, 51 cc/s; 22 - " - " 70 cc/s; PEO injection: 23 - 0.05%, 50 cc/s; 25 - 0.15%, 38 cc/s

PHASED VORTEX SEEDING FOR THRUST MODULATION IN A RIGID CYLINDER WITH FLAPPING FOIL THRUSTERS

Promode R. Bandyopadhyay
John M. Castano,
William Nedderman and
Daniel Thivierge

Naval Undersea Warfare Center
Newport, RI 02841
bandyopadhyay@c80.npt.nuwc.navy.mil

ABSTRACT

A biologically inspired approach to the propulsion of a rigid cylinder is taken. Here, thrust, drag and precision maneuvering of the entire cylinder are viewed in an integral generic framework. The dynamics in such an approach is controlled by deterministic unsteady vortex dynamics. Recently, it has been demonstrated experimentally that such vortex dynamics can be used to produce vectored jets which can provide thrust, drag or maneuvering cross-stream forces and moments to a rigid cylinder. In the present work, it is further shown experimentally that, a phased vortex seeding from the nose of the cylinder can be used to finely modulate, within ± 5-10%, the thrust produced by a pair of flapping foils mounted at the tail of a rigid cylinder.

INTRODUCTION

NUWC is engaged in the study of aquatic locomotion with a goal to apply the knowledge to underwater vehicles. While the works of Lighthill, Wu, Webb, Ellington, Bainbridge and Triantafyllou, to name only a few, have contributed to the understanding of the mechanism of fish propulsion, the application to engineering remains a serious challenge (see citations in Ref. 3).

The NUWC work is described in Refs. 1 - 6. The following summarizes the experience: the biologically based mechanisms need to be applied to rigid bodies as opposed to flexible bodies; the emphasis should be on precision maneuvering and low speed application, rather than the production of pure axial propulsion; production of all forces, viz., thrust, drag and cross-stream maneuvering forces should be viewed in an integral manner because they have a common production mechanism. The NUWC work has also led to the exploration of a new area, viz., biologically-inspired maneuvering of small underwater bodies. The studies indicate that the maneuvering and control of man made vehicles like aircraft are based on moments, while those of biologically based engineering vehicles would be force based. In the latter, this makes brisk maneuvering, which has a low time constant, feasible.

A remarkable feature of the locomotion of a fish like aquatic animal is the production of large unsteady forces. This can be seen by comparing Figs. 1 and 7. In the former, the steady drag levels at 20 cm/s are less than 1/100 th of the peak unsteady forces due to a pair of flapping foils attached to a rigid cylinder, shown in the latter figure. The drag values in Fig. 1 are 1/50 th of the time mean thrust values shown in Fig. 7. Although these biologically based mechanisms give us an impressive level of force, their necessity in an aquatic animal is probably due to the amenability of their origin, viz., an unsteady deterministic vortex shedding, to active control. This makes precision maneuvering, defined as quick acceleration and deceleration, and rapid turning compared to body length, feasible.

The development of a biologically based dual flapping foil device attached to a rigid body, for the generation of axial and cross-stream forces on a rigid cylinder at low speeds is described in Refs. 1 and 3. In these works, the hydrodynamics of the flapping motion of the tail fins is reproduced in an engineering rigid bodied cylindrical model. The present is a follow on work. Here, the motivation has been to understand the role of the head movement of a fish and to apply again in the context of a rigid cylinder. In the literature, Lighthill and others have speculated on the drag reducing, or thrust enhancing role of vortices shed due to the head movement of a fish. It is less ambiguous to carry out this investigation in a rigid cylinder, because therein it is possible to isolate the head movement from the effects of the sinuous motion of the body of a fish.

The hydrodynamic foundation of the dual flapping foil device attached to the tail of a rigid cylinder is given in Bandyopadhyay & Donnelly (1997). The dynamic measurements of axial forces and cross-stream moments, as well as the detailed phase-matched measurements of vorticity-velocity vectors of the vortex shedding process have been reported. The results are compared with theories and others' measurements. Two modes of flap oscillation are considered: waving and clapping. In the waving mode, the flaps move in phase, and in the clapping mode, they are out of phase. In the present work, a new set of tiny vortices are shed from the nose area and they are allowed to convect downstream and interact with those being shed by the flapping foils in waving mode (Fig. 2). Dynamic balance measurements are then carried out to determine the modulating influence of the nose vortex seeding.

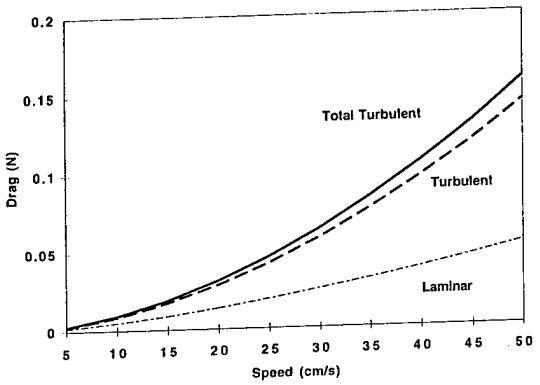

Figure 1. Estimated steady state drag on the basic cylinder model shown in Fig. 2.

EXPERIMENTS:

The model is shown schematically in Fig. 2. Figure 3 is a photograph of the model. The model is 76 mm in diameter and about 1 m in length. The tail has a circular to flat transition section at the end of which two 76 mm x 76 mm flaps are attached. There is a fixed divider plate in between. The entire cylinder floats and the model is strut mounted. A six component dynamic balance is mounted at the strut cylinder junction. The balance (ATI Inc.) measures the strain in a monolithic structure containing three symmetrically placed beams. Temperature compensation and water proofing are provided. A balance with high moment range had to be chosen. The axial force resolution is 0.24 N. Data collected with the balance in the past has compared favorably with theories (Bandyopadhyay & Donnelly 1997; Bandyopadhyay *et al.* 1997c). Two magnetic actuators are used to oscillate the tail flaps and two LVDTs are used to measure their phase. A third actuator is used to oscillate a 1 mm thin plate near the nose.

This nose slider protrudes out of the cylinder surface alternately at port and starboard sides. Figure 4 shows the distribution of nose

slider protrusion against actuator voltage. The maximum protrusion is 3-4 mm in the working range of 12 V. This is probably of the order of the local thickness of the boundary layer which is presumably laminar at flow speeds of around 20 cm/s. At a nose slider frequency of 3.65 Hz and speeds of 20 - 40 cm/s, a Strouhal number based on the slider protrusion of 3 - 4 mm varies between 0.274 and 0.73. The nose slider vortex shedding is probably optimum in this Strouhal number range (Fig. 9a).

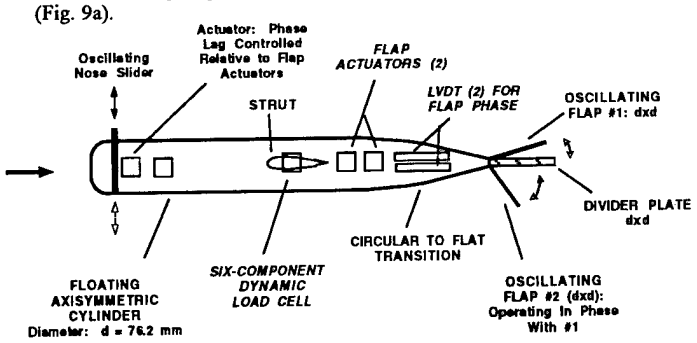

Figure 2. Schematic of Model. A software operated digital controller is used to select the phase lag of the nose slider actuator relative to the two flap actuators which operate in phase, called waving mode here (as opposed to clapping mode where they operate in anti-phase).

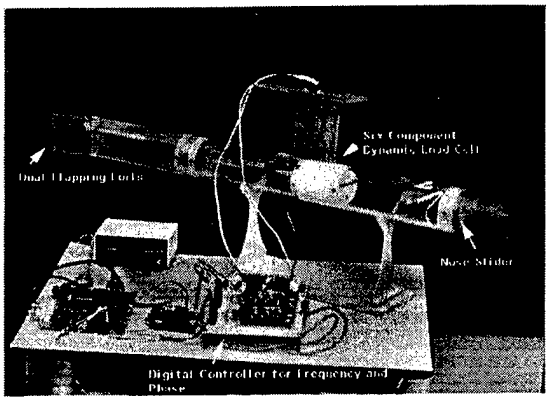

Figure 3. Photograph of model and digital controller of actuators.

The experiments were carried out at flap frequencies between 2.6 and 6.2 Hz and flow speeds of upto 1.5 m/s. A computer driven controller was built to operate the actuators (Fig. 3). All three actuators were operated at the same frequency. The phase of the nose actuator was digitally shifted with respect to the flaps by means of a software. The flap actuators operated in phase. The drag balance was operated by a second computer. A third computer was used to monitor the tunnel characteristics in real time and for acquisition of all data, namely the balance output, flap phase, actuator currents and voltages and their phase, and flow speed. The balance signals were digitized at 250 Hz and the other signals at 8Khz. The balance trace was ensemble averaged over 5 cycles of flap oscillations and then a three-point averaging was performed to further filter out. The flow speed was measured both by a Pitot tube located in the test section near the tail of the model and also from the pressure drop along the tunnel nozzle. The experiments were carried out in the NUWC Low Speed Water Tunnel. The test section is 30 cm x 30 cm in cross-section and the length is about 3 m. The tunnel is noisy at low speeds. Close tracking of flow speed with a sensitive Pitot tube mounted in the test section is required for accuracy. This is particularly in view of the fact that the mechanism on hand is exquisitely Strouhal number dependent. A perforated metal plate was placed in the latter experiments downstream of the test section to improve the flow steadiness at low speeds.

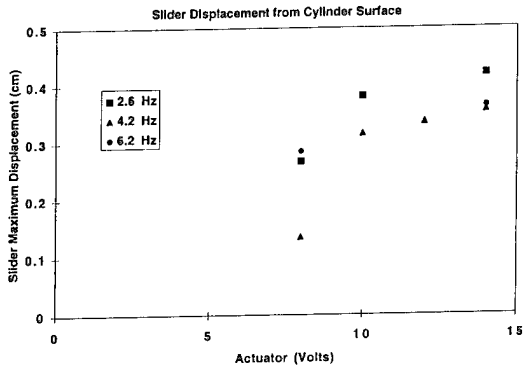

Figure 4. Variation of nose slider depth with actuator voltage (horizontal axis: Volts) and frequency.

PRELIMINARY EXPERIMENTS:

Preliminary measurements of axial forces are shown in Fig. 5 where the ensemble averaged traces are compared for nose slider on/off cases. The time lag in the on-case is zero with respect to the tail flaps. Mainly the peak levels of thrust, and to a lesser extent the drag values as well, are enhanced by the nose vortex seeding. The time integrated values increase in the on-case, but they are still barely above zero and are within the uncertainties of measurements. The effect of a lag in nose vortex shedding is shown in Fig. 6. Particularly the thrust peaks are highest at a lag of 300 degrees and lowest at 120 degrees. The difference between the two lags is 180 degrees which suggests that an exquisitely phase-dependent mechanism is involved.

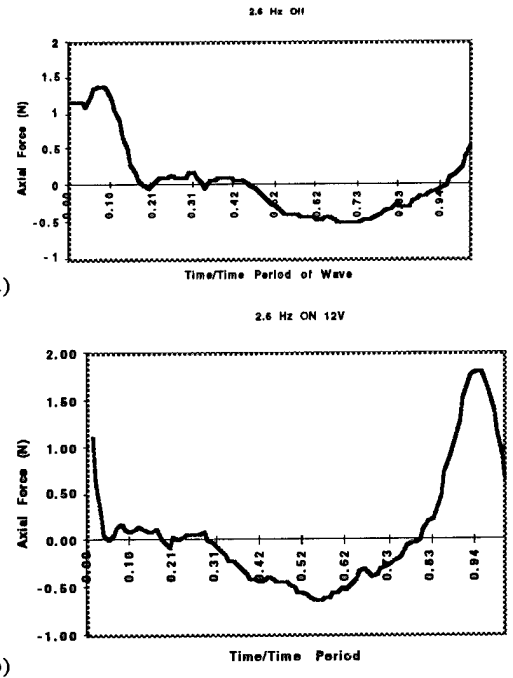

Figure 5. Ensemble averaged trace of axial force on the model. Tail flap St = 0.25 - 0.35. Nose slider: (a) off, (b) on.

(a)

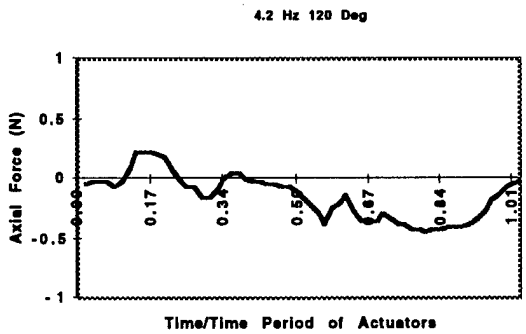

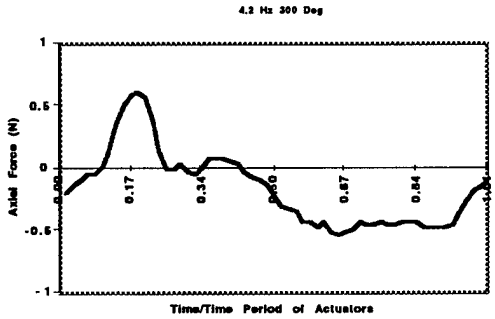

(b)

Figure 6. Effect of phase lag of nose slider on axial force. Tail flap *St* = 0.13. Lag: (a) 120 deg, (b) 300 deg.

RESULTS AND DISCUSSION:

The preliminary results suggested that the nose vortex seeding did have a temporal effect on the axial forces. However, it was necessary to repeat the experiments at a Strouhal number where the net axial force was clearly a thrust. Also, a perforated plate was installed in the downstream end of the test section to steady the low speed streams. These later results are shown in Figs. 7 & 8. Figure 7 shows the temporal effects of phase lag of nose vortex seeding. The thrust peak is highest at 300 deg and lowest at 120 deg. The effects of phase lag on the time integrated thrust levels are shown in Fig. 8 at three Strouhal numbers. The Strouhal number St is defined as $\frac{fA}{U}$, where f and A are frequency and amplitude of oscillation of the tips of the flapping foils and U is the freestream speed. A sinusoidal effect of lag on net thrust is present. The net thrust is enhanced around 120 deg and reduced at 300 deg. The integrated effect is opposite to the effects on peak values of thrust and drag.

Because the mechanism on hand is exquisitely dependent on Strouhal number, care had to be taken in tracking the freestream speed. Recall that a perforated plate was installed in the test section to achieve steady freestream speeds in the later runs. The speeds and Strouhal numbers are 16.2 - 21.0 cm/s and 0.6 - 0.46 in Fig. 8a, 27.4 - 30.5 cm/s and 0.375 - 0.337 in Fig. 8b, and 36.0 - 37.8 cm/s and 0.276 - 0.263 in Fig. 8c, respectively. The speed variation between runs, thus was within 5% at a nominal speed of 40 cm/s, which increased to 20% at lower speeds of 20 cm/s. The measurements reported in Fig. 8 are for those runs where the freestream speed remained nearly constant over several successive runs. At that condition, the Pitot readings were at worst, within 5% from that obtained from the nozzle pressure drop. The scatter can probably be reduced by holding the freestream speed more accurately.

The data has a considerable amount of scatter, but Fig. 8a still indicates that the net thrust is slightly enhanced compared to the off case. No attempt has been made to optimize the protrusion of the nose slider for thrust enhancement, but the possibility of further enhancement remains.

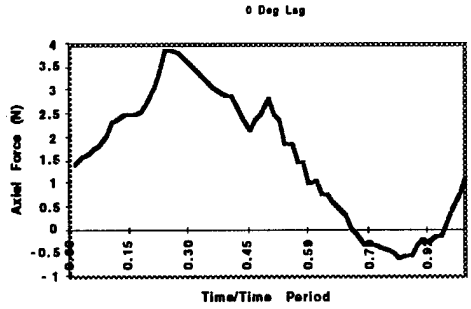

(a)

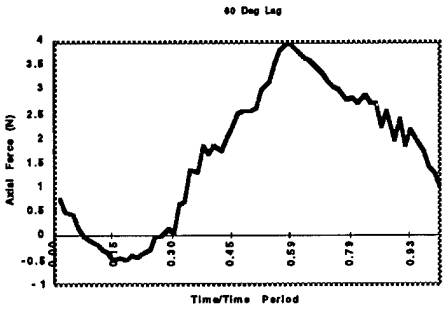

(b)

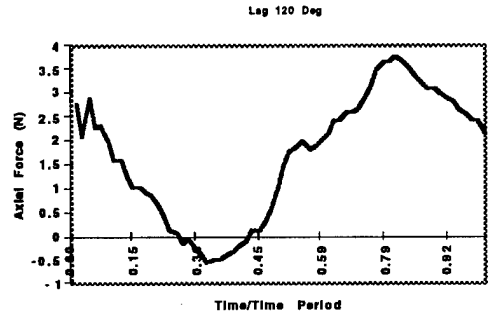

(c)

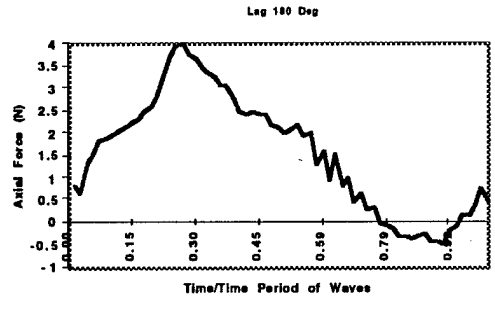

(d)

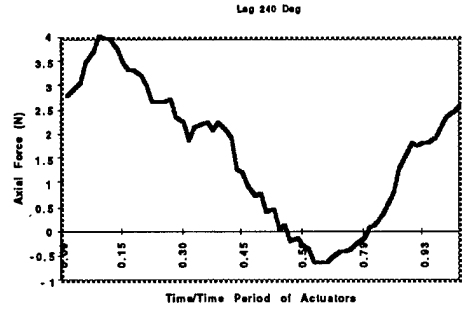

(e)

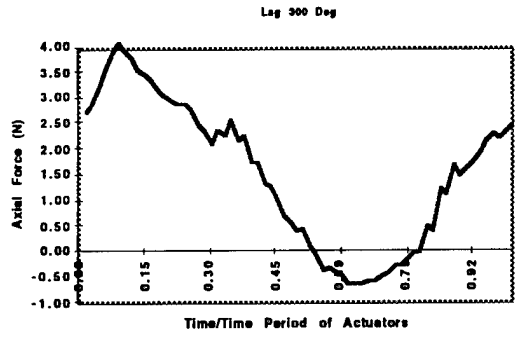

(f)

Figure 7. Ensemble averaged time trace of axial force on the model. (a) Nose slider phase lag: 0 deg; (b) 60 deg; (c) 120 deg; (d) 180 deg; (e) 240 deg; (f) 300 deg.

MECHANISM OF THRUST MODULATION:

Several questions arise: (1) what is the mechanism of thrust modulation? (2) is there any viscous drag reduction over the cylinder involved? (3) how are the presumably tiny nose vortices surviving a distance of 1 m? (4) how relevant are the results to fish locomotion? A hypothesis of flow mechanism given below attempts to provide qualitative answers to these questions.

A starting point would be the question: what is the trajectory of the shed nose vortex? Earlier dye flow visualization and phase-matched laser doppler measurements of vorticity and velocity vectors of the vortex shedding from the flapping foils at the tail is instructive (Bandyopadhyay & Donnelly 1997). They indicated that the shed vortices do not propagate along the tangent at the trailing edge. In a similar manner, in Fig. 9a, it is hypothesized that the shed vortices from an oscillating surface-normal plate would track at a higher elevation than that from a non-moving obstruction would. This would allow the vortices not to interact with the cylinder boundary layer and to survive longer. As sketched in Fig. 9b, the vortices might undergo a pairing process increasing their spacing and survivability. The seed vortices then interact with those formed by the oscillating flaps. Further pairing could ensue. Negative vortices marked A, B & C on the port side could have a common induction due to proximity with the positive vortex D and give rise to a downstream vectored jet over the phase 0 - 180 deg. This could be followed by an agglomerated induction of similar but negative vortices from the starboard side. The net interaction results in the *modulation of the vector of the jets between pairs of vortices* which is the source of the axial force. The mechanism is thus primarily rotational and inviscid.

(a)

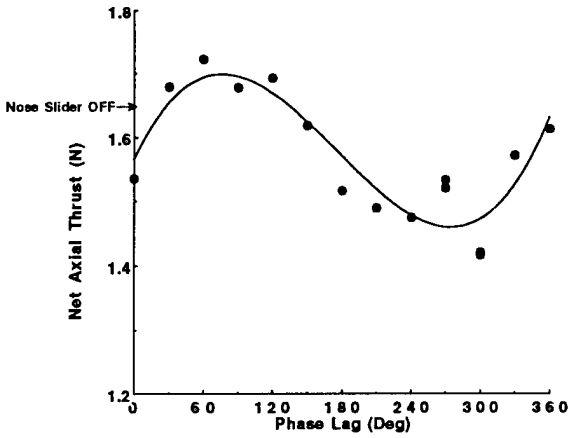

(b)

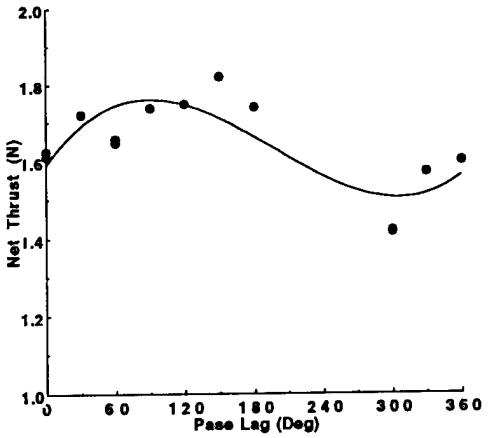

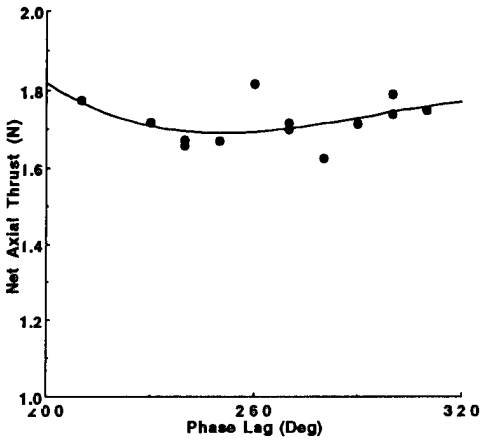

(c)

Figure 8. Variation of time-averaged axial thrust with phase lag of nose slider. Speed, Frequency & Tal Flap *St*: (a) 16.2 - 21.0 cm/s, 3.77 Hz & 0.6 - 0.46; (b) 27.4 - 30.5 cm/s; 3.64 Hz & 0.375 - 0.337; (c) 36 - 38 cm/s; 3.65 Hz & 0.276 - 0.263.

The present work suggests that if the head movement of a fish truly sheds vortices, then the body waving may be a mechanism to ensure the survivability of these vortices in the presence of cross currents so that eventually they become available to modulate the thrust produced by the caudal fins. If the propulsion of novel underwater bodies is based on the jets produced by discrete deterministic vortex shedding, then that would open up the possibility of exquisite maneuverability via phase-matched vortex seeding from other appendages. Further work is necessary to determine if the vortex seeding can be optimized for significant enhancement of net thrust.

CONCLUDING REMARKS:

The dual flapping foil maneuvering device for small cylinders has been demonstrated earlier in the laboratory. A reasonable documentation and understanding of the mechanism of production of axial and cross-stream forces and moments have been reported. In the present work, the effect of a phased vortex seeding from the nose on axial forces is studied. It is shown that such vortex seeding can modulate the axial force in a fine range, within ± 5-10%, if operated at the correct Strouhal numbers.

(a)

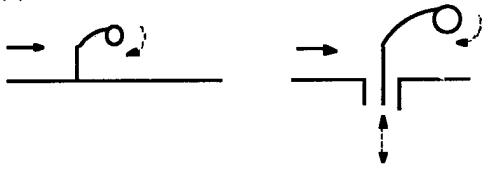

(b)

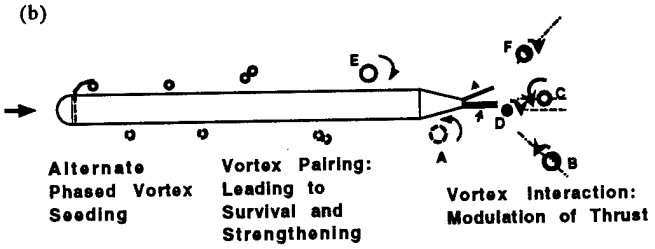

Figure 9. Schematics of mechanism: (a) effect of unsteadiness of a vorticity source on vortex trajectory, and (b) mechanism of thrust modulation.

Future work needs to be carried out to determine the optimizing effects of increasing nose slider protrusion over the cylinder surface and the upstream location of the nose slider with respect to the flapping foils and Strouhal number. The measurements need to be verified in a water tunnel where the low speeds are more accurately held constant, the effects of environmental disturbances determined and the modulation effects need to be verified in an unbounded surrounding. Perhaps, much can be learned by simulating the vortex interactions numerically.

The viscous drag reduction of a turbulent boundary layer involves phenomena that are only partly deterministic; the vortices involved are rather small physically and a great deal of randomness in space and time is present. Bodies with flapping foil mechanism, on the other hand do not have these as primary limitations - force modulation is largely an inviscid process. The optimization process appears to be more tractable when an inviscid phenomena of large deterministic vortices is involved. Biologically based thrust modulation is an alternative to conventional approaches to the drag reduction of turbulent boundary layers. Conventional propulsors also involve an inviscid mechanism, deterministic vortex shedding and the production of jets, much as flapping foils do. It might be worth treating the propulsion and drag of a conventional underwater vehicle in an integral manner. Then, upstream seeding of large deterministic vortices to supplant the turbulent boundary layer structures and achieve an overall enhancement of thrust in presence of the propulsor is worth exploring. In other words, integrating certain cylinder drag reduction methodologies with rotating in-situ propulsors, is a new twist to drag reduction research that can be learned from bilocomotion.

ACKNOWLEDGMENTS

The support of ONR (Dr. T. McMullen) and NUWC IR (Dr. S. Dickinson) is gratefully acknowledged.

REFERENCES

1. Bandyopadhyay, P. R., Castano, J. M., Nedderman, W., Donnelly, M. Zeiger. M 1996 "A Small Maneuvering Device for Energetic Environment," (edited and captioned; 6 minutes) Video, *NUWC Newport, RI.*

2. Bandyopadhyay, P. R., Castano, J. M., Rice, J. Q. Philips, R. B., Nedderman, W. H. & Macy, W. K. 1997a "Low-speed Maneuvering Hydrodynamics of Fish and Small Underwater Vehicles" **ASME Jou. Fluids Engrg.**, V119, pp. 136-144.

3. Bandyopadhyay, P. R. & Donnelly, M. J. 1997 "The Swimming Hydrodynamics of a Pair of Flapping Foils Attached to a Rigid Body", AGARD Meeting on *High-Speed Underwater Bodies*, to be held at Kiev, Ukraine, Sept. 1-3, 1997, pp. 1.1-1.17.

4. Bandyopadhyay, P. R., Nedderman, W. H., Castano, J. M. & Thivierge, D. 1997b "Phased Vortex Shedding for Enhancement of Thrust of a Cylinder," (edited and captioned; 7 minutes) Video, *NUWC Newport, RI.*.

5. Bandyopadhyay, P. R., Nedderman, W. H., Dick, J. & Castano, J. M. 1997c "Loads on Biologically-Inspired Winged Bodies Under Surface Waves", **ASME Jou. Fl. Engrg.**, (submitted).

6. Bandyopadhyay, P. R., Singh, S. & Chockalingam, F., 1998 "A Theoretical Control Study of the Biologically-Inspired Maneuvering of a Small Vehicle Under a Free Surface Wave," *Jou. Fluids Engrg.* (subjudice).

Drag Reduction and Turbulence Control in Swimming Fish-like Bodies

M.J. Wolfgang[1], S.W. Tolkoff[1], A.H. Techet[1], D.S. Barrett[1], M.S. Triantafyllou[1]
D.K.P. Yue[1], F.S. Hover[1], M.A. Grosenbaugh[2], & W.R. McGillis[2]

[1]Department of Ocean Engineering
Massachusetts Institute of Technology
Cambridge, Massachusetts 02139

[2]Department of Applied Ocean Physics and Engineering
Woods Hole Oceanographic Institution
Woods Hole, Massachusetts 02543

Experimental measurements on the *RoboTuna* demonstrate that the power required to propel a swimming streamlined, fish-like body is smaller than the power needed to tow the body at the same speed. The lateral motion of the swimming body is a traveling wave with wavelength λ and amplitude varying quadratically along the length. Parametric studies show sensitivity of drag reduction to the principal parameters, most importantly the Strouhal number and the phase speed of the body wave. Numerical power estimates using an inviscid boundary-integral numerical scheme are in good agreement with the experimental data. Wake flow visualization and near-body digital particle image velocimetry (DPIV) reveal mechanisms contributing to the observed drag reduction.

1 Introduction

Unsteady flow control offers the possibility of advancing the efficiency of marine propulsion technology by shifting the paradigm of conventional propulsion methods. Unsteady propulsion techniques offer several distinct advantages over conventional steady propulsion methods: unsteady foil motion can achieve high lift coefficient [1] and is an efficient thrust production mechanism [2,3]. Additionally, oscillating foils can effectively manipulate oncoming vorticity [4] and recapture energy from these disturbances [5].

Ffowcs-Williams & Zhao [6] and Tokomaru & Dimotakis [7] have shown that efficient flow control can be achieved by unsteady motion of a body in the fluid. In addition, periodic forcing of a flow has been studied by several investigators, with important implications on efficient propulsion. Imposing harmonic rotary oscillations of a cylinder in an oncoming stream can result in a reduction in wake width [8], with maximum influence on the flow when the frequency is close to the Strouhal frequency [7]. Boundary layer turbulence suppression was observed by [9] in the flow around a flexible plate in an oncoming stream, as long as the phase speed of the plate's traveling wave c_p exceeds the free stream velocity U.

The swimming motions of a fish are rhythmic hence causing unsteady flow. They have evolved over millions of years, and as a result, fish swimming dynamics provide an ideal framework to investigate drag reduction and vorticity control mechanisms, in addition to the implications on innovative marine vehicle design. Outstanding maneuvering and propulsive performance by fish has been reported [10,11], causing interest in fish swimming dynamics. Studies by Lighthill [12] and Wu [13,14] have shed light to the inviscid hydromechanics of fish-like propulsion. In this paper, we investigate the effects of unsteady propulsion and flow control on drag reduction in streamlined bodies. Gray [15] first reported a discrepancy between the power required to propel a rigid dolphin and the available muscular power which is smaller by a factor of seven (*Gray's paradox*). However, Gray's conclusions have remained controversial for over sixty years due to the difficulty in obtaining reliable force measurements from live fish.

We chose to develop a robotic mechanism, which can emulate very closely the swimming of the tuna [16,17]. Measurements of the hydrodynamic forces and the swimming kinematics on the flexible robot have shown that at Reynolds number of about 10^6, drag can be reduced by 50% or more. Dye visualization techniques are utilized in experiments with the robotic tuna, in order to elucidate mechanisms of vorticity control by the tail in the wake. Boundary layer modification along the length of the swimming fish is studied quantitatively using digital particle image velocimetry (DPIV) [18,19]. Additionally, an inviscid numerical method has been developed to model the fish swimming dynamics, based on a boundary-integral approach. The numerics provide reasonable estimates of the power needed for fish-like swimming, which indeed compare well with the experimental robotic fish data for the power expended by the motors.

2 Experimental Apparatus

2.1 Robotic design and construction

The hull of the *RoboTuna* has the shape of a bluefin tuna (*thunnus thynnus*), including the tail fin. The length of the robot is $L = 1.25m$. The mechanism is attached to a carriage in the Ocean Engineering Testing Tank Facility at MIT in a water tank with dimensions 35 m by 2.5 m by 1.25 m. The robot is submerged at mid-depth of the tank to avoid free surface and bottom interference. The body sections of the RoboTuna are approximately elliptical, and the maximum transverse dimensions are: height 0.30 m and width 0.21 m. A set of eight anodized aluminum links support the structure shown in Figure 1, showing the basic outline of the mechanism. The eight rigid links are capable of rotating about a single axis. Flexing of the hull is achieved by affixing sets of densely-packed plastic ribs transversely on stainless steel backbones running between the ends of adjacent links. An impermeable skin structure, one inch thick, consisting of layers of filter foam and tensioned thin latex sheets is used, contained on both sides by conformal Lycra skin.

The links are activated by six brushless motors, 3 HP each. The second link is rigidly attached to the carriage and the first and third links are coupled to move in anti-phase, hence there are six degrees of freedom. Strings and pulleys transmit the motion to individual links. Pairs of cables (or tendons) are channeled down the centerline of the frame, one set per motor. The first two links use a block and tackle mechanism which allows developing high torque. The remaining four links use direct drive actuation because of space limitations. We will refer to six *joints*, numbered sequentially from the front joint 0 (activating the coupled first and third links) to the tail joint 5 (activating the tail-fin).

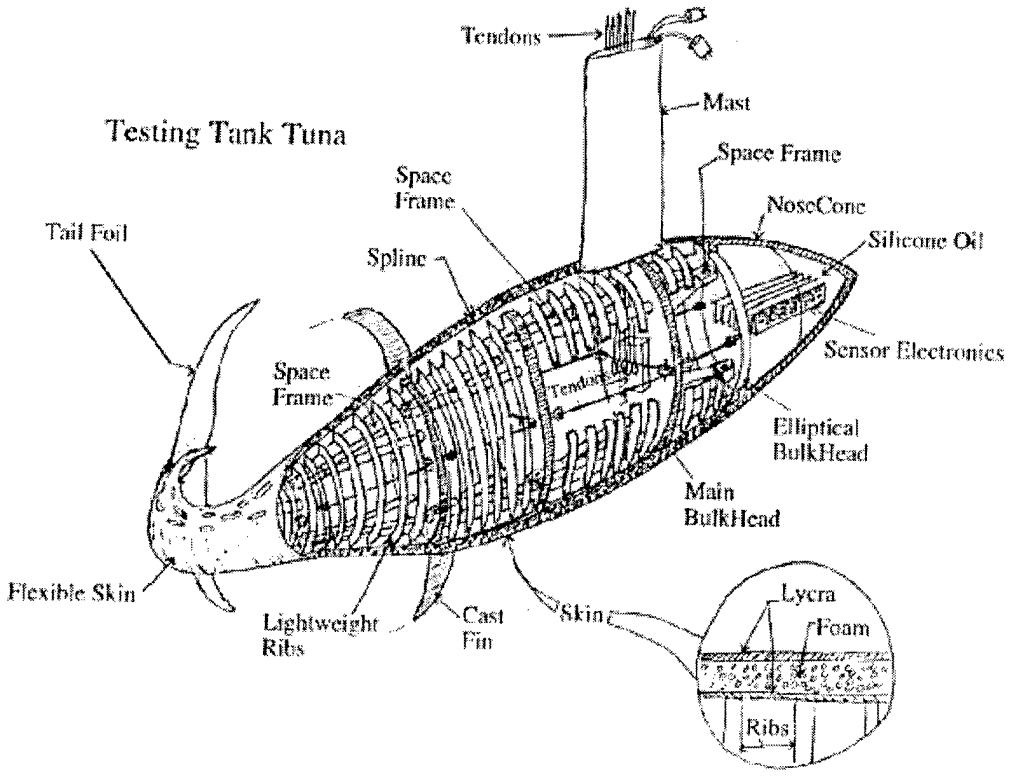

Figure 1: Lateral schematic view of the robotic fish-like mechanism and the supporting streamlined strut which attaches to the tow carriage. Skin cutaways reveal the bulkhead and framing structure.

Load cells (*Entran elf-tc500*) are mounted on the twelve actuating strings to measure the transmitted forces. Displacement sensors (*ETI servomount precision potentiometers*) provide accurate link motion measurements. These measurements allow detailed evaluation of the power transmitted to the mechanism. Also, the axial force transmitted by the streamlined strut on the carriage is measured by two force transducers, for redundancy, a load cell (*Entran elf-tc1000*) and a Kistler quartz force transducer.

2.2 Calibration and operation

After the sensors were calibrated, we conducted an extensive set of experiments to verify the accuracy of energy and power measurements and to assess the internal losses in the mechanism. Weights were hung through wires from the tail of the RoboTuna and motions of the robot were commanded, while measuring the forces and motions of the actuating strings. In addition the motions and forces acting on the strings supporting the hanging weights were directly measured (calibration apparatus). We conducted tests both with slow motions (static tests) and fast oscillating motions (dynamic tests).

All verification tests were conducted by commanding each link separately to move through a certain rotation. The motion resulted in a motion of the tail and hence of the hanging weight, which was directly measured. The motion of the tail as estimated from the motor motion agrees to within 5% with the directly measured motion; the difference is attributed to the partial flexibility of the robot. The error in the force measurements was below 10%, the error reducing for links near the tail where the weights were hung. We conclude that for swimming experiments the expected discrepancy is below 5%, since the force is distributed along the length and not concentrated in a single point.

Next, the energy required to produce a commanded motion by each link was compared to the energy expended by the motors. Each link was commanded to move through a certain distance at a slow speed, while known weights were hung from the calibration apparatus. The potential energy change associated with this motion was compared to the power expended by the motors over a known time interval. Deviations were generally within 12%, with the highest recorded discrepancies again for links furthest away from the tail. Internal losses in the mechanism result consistently in measuring higher motor energy than the actual potential energy. Finally, known weights were hung from the calibration apparatus, and each individual link was commanded to oscillate at a constant amplitude and at a frequency 1 Hz. The power utilized by the motors was averaged over 10 cycles and compared to the power recorded by the force and motion transducers of the calibration apparatus. Results agreed generally to within 15%, with higher discrepancies further away from the tail. Hence, the dynamic error estimates represent an upper bound, particularly for the links further away from the tail, since in the swimming experiments fluid forces are distributed along the entire body. We estimate that the actual power losses are on the order of 5%, similar to errors found for links close to the tail.

2.3 Swimming kinematics

We selected the motions of the robot to be close to the actual motions observed in live tuna [20]. The backbone motion consists of a smooth, purely sinusoidal, amplitude-modulated traveling wave, and the wave travels along the body length with a phase speed $c_p = \omega/k$, which in general may differ from the swimming speed U. The transverse backbone wave motion $y(x,t)$, where x is measured along the backbone of the fish, is given the form:

$$y(x,t) = a(x)\sin(kx - \omega t) \tag{1}$$

where $k = 2\pi/\lambda$ is the wavenumber, corresponding to wavelength λ, ω is the circular frequency of oscillation, and $a(x)$ is the amplitude

envelope, given as:

$$a(x) = c_1 x + c_2 x^2 \tag{2}$$

where c_1 and c_2 are adjustable parameters. c_1 is independently varied, while c_2 is chosen to achieve a specific value of the double-amplitude of motion, denoted by A, at the tail. The distance x is measured from the edge of the second link, which is rigidly attached to the towing strut, and is non-dimensionalized by the body length. Typically, the phase speed $c_p = \omega/k$ is larger than the forward speed U, while the wavelength λ is close in value to the body length. The frequency scaling of data observed in fish is based on the wake Strouhal law [21,22], i.e. keeping constant the non-dimensional parameter St:

$$St = fA/U \tag{3}$$

where f is the frequency of oscillation in Hertz and A is the average lateral excursion of the tail fin.

3 Unsteady Swimming Experiments

3.1 Definitions

In conventional marine propulsion studies, where the main body is rigid and the propulsor is a relatively small device, the thrust of the propulsor can be measured directly at the interface between the body and the propulsor. Hence the drag of the body can be also found: in self-propulsion tests it is equal to the propulsor thrust. This is impossible to do with a flexible hull swimming body, where the body and the propulsor are nearly indistinguishable. Hence, we must estimate the drag of an actively swimming body as follows.

Let U denote the speed at which the body is moving and T_A the average thrust provided by the propulsor; D_A denotes the average drag. By conservation of energy, the average power provided by the motors, P_p, can be written as the sum of the useful power $P_E = T_A\ U$ (used to propel the body)and power losses P_l and P_w:

$$P_p = P_E + P_l + P_w \tag{4}$$

where all quantities are time–averaged; P_l denotes the transmission losses from the motors to the propulsor; P_w denotes the energy wasted in the wake (such as, for example, the rotational energy imparted to the fluid by a screw-propeller).

For a self-propelled body $T_A = D_A$. Hence:

$$P_p = D_A U + P_l + P_w \tag{5}$$

Both P_l and P_w are positive, hence concluding:

$$D_A \leq P_p/U \tag{6}$$

We define the ratio P_p/U as the *upper estimate of body drag*, D_u:

$$D_u = P_p/U \tag{7}$$

If D_o denotes the drag of the towed rigid body, **drag reduction is defined to occur when $D_u < D_o$.**

If the mechanism is not self-propelled, then it is producing a net axial force, the mast force F_n. Then, one substitutes $T_A = F_A + D_A$, where F_A is the time average of the mast force, to find for a net-force-producing mechanism, forced to move at constant speed U:

$$D_A \leq D_u \tag{8}$$

$$D_u = P_p/U - F_A \tag{9}$$

The criterion for drag reduction is conservative, hence the utility of D_u as a gauge of drag reduction depends on having small transmission losses and high hydrodynamic efficiency.

3.2 Experimental flapping body drag and power

The calculation of an upper-bound of the flapping body drag, D_u, is based on (9), involving two quantities: the measured mast force F_A; and the motor power P_p, which is found using the force and motion data of the string actuators as described in the following.

Two strings are connected to each motor, resulting in a total of twelve strings. For the jth motor the first string is pulled in (paid out) with velocity V_j while registering force F_{1j}, and the second string is paid out (pulled in) with equal velocity V_j while registering force F_{2j}. The forces represent the tensions measured on the string and are always positive; hence the net input power from the jth motor is $P_j = F_{1j}\ V_j - F_{2j}\ V_j = (F_{1j} - F_{2j})\ V_j$. We define the jth joint force as $F_j = F_{1j} - F_{2j}$ and then the instantaneous input power is found as $P_j = F_j\ V_j$. The overall instantaneous power is calculated as the sum of the input power in all six joints and then integrated to find the average power absorbed. An average over several cycles was calculated after steady state was achieved.

The mast force, as measured in the present set of experiments, i.e. at the top of the mast, contains: the drag of the strut, the interaction drag between the flexible mechanism and the mast, and the drag of the mechanism including the attached fins and the tail. In order to obtain estimates of the drag coefficient on the body alone, the drag of these components (correction drag) must be measured and then used to correct the measured axial force. For this reason, we measured experimentally, as function of speed, the drag of all appendages.

We provide detailed measurement data for a typical case, with a Reynolds number based on the body length $Re = UL/\nu = 800,000$ and with a Strouhal number of $St = 0.273$. The flow was stimulated to be turbulent, tripped by a ring at the interface between the rigid nose cone and the flexing body, as well as the rough Lycra cloth of the skin structure. Figure 2 provides the measured forces and velocities of the six joints as functions of time after steady-state conditions have been established. Run parameters for this case, with length scales nondimensionalized by body length (BL): $St = 0.273$, $U = 0.656\ BL/s$, wavelength $\lambda = 1.08\ BL$, tail circular frequency $\omega = 8.095\ rad/s$, tail tip double amplitude $A = 0.139\ BL$, tail angle of attack $\alpha = 21.0°$, and the phase angle between angular pitch and lateral heave of the tail at the attachment point $\phi = 97.7°$. The phase speed for this backbone waveform is $c_p = 1.39\ BL/s$.

Figure 3 provides the mast force and total power measurements. The measured total average power in this case was $P_F = 2.04\ W$ and the net average thrust $T_A = 1.98\ N$. The drag of the rigid system at the same speed was measured to be $D_o = 1.66\ N$, including the drag of the appendages, which include: the submerged part of the mast, the tail fin and two smaller fins attached on the body, as well as interaction drag. First we use a propulsive index, which does not require subtraction of a correction drag: we find that $(T_A + D_o)U = 2.55\ W$; hence $(T_A + D_o)U\ /\ P_p = 1.25 > 1$, and we can confirm drag reduction. In this case, the tail requires small but positive power. The upper bound estimate of the moving body drag is obtained using (9), after correcting for the drag of the appendages. Separate experiments established the drag of the mast, after streamlining the lower edge to avoid edge drag. The drag of the support mast is then subtracted from both the flexing body and rigid body values of drag in determining the drag reduction, and although other interference effects are not easily measurable, the drag reduction realized is 47.94%.

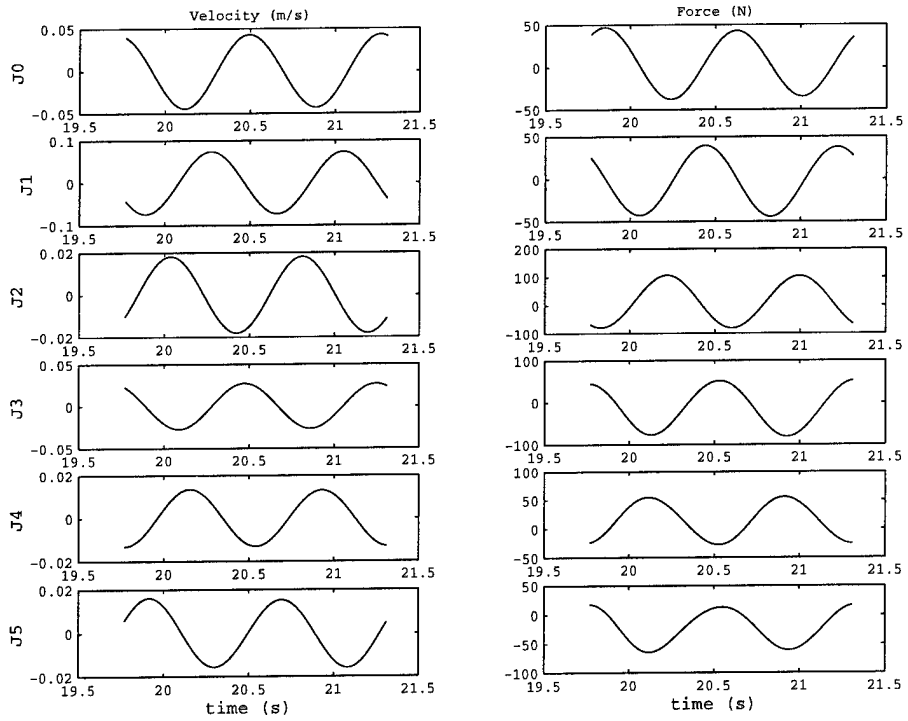

Figure 2: Force and velocity time history records for the individual joints. $St = 0.273$.

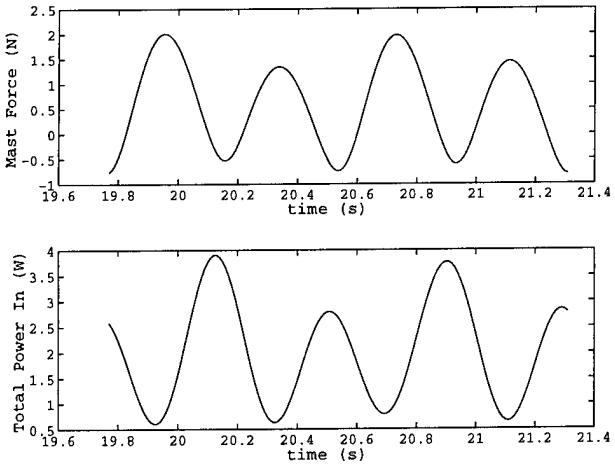

Figure 3: Total mast force and total input power time history records. Mean total input power 2.04 W. $St = 0.273$.

We have investigated speeds ranging from 0.5 to 1.0 m/s, which are the speeds allowed by the limits of our current equipment: length of tank, time to settle down transients, capability of the skin structure to support lateral pressure. The results were repeatable within 4% and consistent. Transition to turbulence through stimulation was complete in terms of its effects on the drag coefficient of the rigid body at speeds higher than 0.6 m/s, so a speed of $U = 0.7$ m/s was chosen to investigate the sensitivity of drag reduction to parametric change, since it provided sufficiently long time records for accurate power and drag estimation.

3.4 Sensitivity to parametric variation

Through comprehensive testing, we have been able to show that there is strong parametric dependence on the qualitative and quantitative form of the data. Six principal parameters were varied to investigate their dependence on performance: (a) Strouhal number, St; (b) tail nominal angle of attack, α; (c) phase angle at the tail between lateral and angular motions, ψ; (d) amplitude of motion at the tail, A; and (e) body wavelength, λ; and (f) amplitude coefficient kinematic parameter c_1 (2).

Over six hundred experiments were conducted, concentrating in parametric combinations where drag reduction was found to be the largest. After several genetic iterations, about three hundred experiments resulted in conditions of self-propulsion, i.e. zero average mast force. The dependence of drag reduction on the principal parameters for self-propulsion, because of its direct relevance on fish propulsion, is found as follows:

- Strouhal number, St: There are two peaks of maximum drag reduction, one at about $St = 0.19$ and a second at about $St = 0.31$.
- Tail nominal angle of attack, α: A high angle of attack was found to provide highest drag reduction in most cases, between 20 and 28 degrees.
- Tail phase angle, ψ: Values in the range of 80 to 100 degrees provide maximum drag reduction.
- Tail tip double amplitude A: Drag reduction is relatively insensitive to this parameter.
- Body wavelength, λ: A wavelength comparable to the body length is found to provide maximum drag reduction.
- Kinematic parameter c_1: Drag reduction is relatively insensitive to this parameter.

These results are generally in agreement with the flapping foil experiments of Anderson *et al.* [3]. Vorticity control is a principal mechanism through which flapping foils achieve high efficiency [3], and also recover energy from oncoming vortical flow [5]; this is also the reason why the Strouhal number, which governs the dynamics of the shed vorticity, is a principal parameter in the present experiments.

All experiments which exhibit drag reduction share one common characteristic: the phase speed of the traveling wave imposed on the body c_p was larger than the forward speed U, identical with the conclusions of Taneda [9] that turbulence suppression and drag

reduction are seen in the flow around a two-dimensional flexible sheet in a uniform flow undergoing periodic traveling wave transverse oscillation. This is the single parametric condition that seems to be unrelated to wake management and indicative drag reduction on the body itself.

We can see from Figure 4 that drag reductions of up to 70% within the range considered are observed.

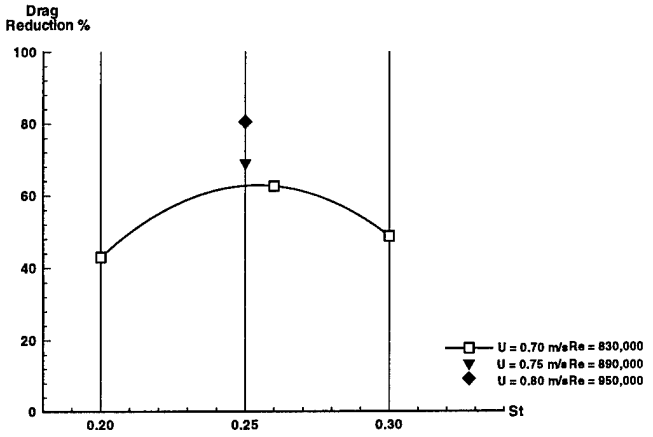

Figure 4: Apparent drag reduction as function of Strouhal number for a range of Reynolds numbers.

4 Drag Reduction Mechanisms

4.1 Discussion

The drag reduction realized must be caused exclusively by the actively-controlled transverse motion. From the parametric studies and the aggregate of force and power data, we can conclude the most plausible mechanisms contributing to this drag reduction include a laminarization of the boundary layer and vorticity control by the tail fin.

Taneda [9] realized laminarization of the boundary layer in his experiments with a flexible rectangular sheet undergoing periodic traveling wave oscillations within an oncoming stream, at Reynolds numbers up to 3×10^6. He observed that when the phase speed of the traveling wave c_p exceeded that of the free stream speed U, separation was delayed or absent and turbulence was suppressed. By estimating the wall stress, he concluded that wall stress, and hence drag, diminished as c_p/U increased.

In all cases where substantial drag reduction was observed in our experiments, the phase velocity of the traveling wave c_p exceeded the swimming velocity U, in complete agreement with the experiments of Taneda. The similarity between our three-dimensional and Taneda's quasi-two-dimensional results is not coincidental. DPIV visualization tests around live fish by Anderson [23] and around the robotic mechanism described herein, have shown that the flow patterns around the body of the fish at mid-depth, within a plane parallel to the direction of lateral motion, are qualitatively similar to the two-dimensional patterns predicted theoretically for an undulating plate by Wu [13,14]. Substantial spanwise, body-bound traveling vorticity develops, which is shed by the time it reaches the caudal peduncle, forming large vortices, which are then manipulated by the tail to form a propulsive reverse Kármán street. Similarly, these results are upheld by the numerical simulations of Cheng, *et al.* [24], for a three-dimensional flapping plate.

Additionally, flapping tail parameters such as the Strouhal number must be within optimal, narrow, parameter ranges to achieve substantial overall drag reduction, due to the tail's role as an efficient unsteady lifting surface [3] and in manipulating vorticity generated by the unsteady flapping of the body. Vorticity control [5] mechanisms are basic to the manipulation of body-generated vorticity by the tail in live fish [23], and explains the sensitivity of the drag reduction to variations in Strouhal number.

The present results seem also to confirm the basic premise in Gray's paradox [15], i.e. that fish-like propulsion must be associated with drag reduction, albeit at a lower Reynolds number than for the dolphins considered by Gray.

4.2 Further experiments

To further elucidate the mechanisms discussed above, further experimental methods have been developed to visualize both the wake and near-body flows of the experimental mechanism. To study the flow around the tail fin and the subsequent wake dynamics, and dye injection system has been fitted into the robotic hull. Fluorescent dye is injected at a point close to the caudal peduncle at the tail's mid-span, and a blacklight is used to illuminate the dye as it is manipulated by the motions of the robotic tail. A dye-injection system similar to this is shown in Triantafyllou & Triantafyllou [17].

Our other goal is to illuminate and characterize the near-hull flow structure within the boundary layer. Flow visualizations and quantitative measurements with digital particle image velocimetry (DPIV) are the first measurements of this type that may quantify the details of boundary layer laminarization. To achieve these results, a laser particle imaging system has been set up in the MIT Testing Tank Facility (Figure 5). A plane of the flow, near the centerline of the fish, is illuminated using a laser beam fanned to form a plane sheet. The surrounding fluid is uniformly seeded with neutrally buoyant fluorescent particles (diameter $\approx$ 40 to 70 μm) which reflect wavelengths in the range of 560-580 nm. Ten to twenty particles per interrogation window were sufficient to ensure good correlations [19].

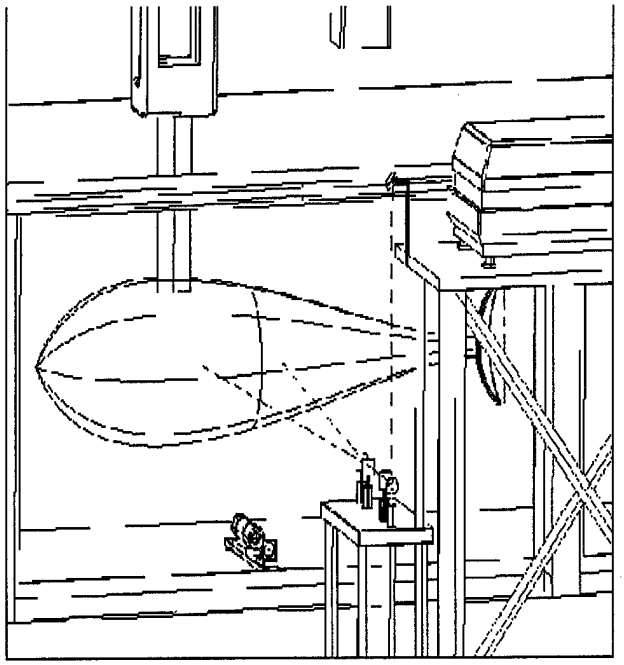

Figure 5: Schematic view of digital particle image velocimetry (DPIV) setup for boundary layer investigation. The pulsed laser beam is directed through a set of optics external to the tank and fanned into a sheet. The laser sheet illuminates a plane of fluid perpendicular to the fish body at mid-depth. An underwater CCD camera and mirror samples the particle images.

The laser used to illuminate the flow field is a dual cavity pulsed Nd:YAG laser from Spectra Physics, Inc., designed specifically for PIV applications. The laser is capable of delivering 400 mJ/pulse of green (532 nm) light at 15 Hz. The beam is passed through a series of optics which fan the light into a larger sheet on the order of 1 *mm* thick. The laser timing is controlled through a four-channel timing box and is synched with the vertical drive on a high resolution, black and white CCD video camera, Texas Instruments MULTICAM MC1134P, which is used to capture the particle motion. The camera records the flow with a maximum pixel resolution of 1134 x 480 pixels at a standard frame rate of 30 Hz. Dual field exposure renders full vertical resolution with no interlace. The video from the CCD camera is stored real-time by a MuTech Frame grabber into 128 Mb Ram on a 133 MHz Pentium Processor PC. The camera placement is fixed with respect to the testing tank, and focused on the illuminated plane. Experiments were conducted using both the stationary YAG pulse laser with a camera fixed to the floor of the tank, and a carriage mounted laser diode with a camera that moved with the robot.

5 Computational Results

The experimental results suggest that significant reduction in body drag is achievable through fish-like propulsion. Because the power measured by the motors is principally influenced by inviscid hydrodynamic mechanisms in the absence of large form-drag, inviscid numerical methods may provide accurate estimates of the necessary propulsive power, provided the vorticity shed from sharp trailing edges (such as the tail fin) is properly modeled and accounted for. In this manner, we may further investigate the mechanisms of large-scale vorticity control by simulation of the flow kinematics and forces around a three-dimensional body under the same conditions used in the experiments.

We consider a flexible, streamlined body equipped with a sharp trailing-edge, rigid caudal fin. We study through simulation the problem of this body starting from rest to reach a constant horizontal velocity U while undergoing periodic undulations about its mean line within an inviscid, incompressible fluid. A thin shear layer wake is continuously shed from the trailing edge of the caudal fin as time proceeds. The flow, with the exception of the thin wake, is assumed to be irrotational, allowing for the existence of a velocity potential $\varphi(\vec{x}, t)$. All time and length scales are chosen to be nondimensional with respect to the body length $\ell = 1$ and swimming speed $U = 1$. A three-dimensional numerical panel method based on Green's theorem is employed to find the velocity potential on the body and in the wake.

The surface of a body similar to the robotic mechanism described above is numerically represented by quadrilateral panels. The body, excluding the caudal fin, employs $O(2,000)$ panels, and the caudal fin is gridded with $O(1,000)$ panels. The motion of the body is described by (1) and (2), identical to that of the flexible, fish-like robot. The tail follows the path of the caudal peduncle but pivots with oscillatory angular motion of amplitude α and arbitrary phase angle with respect to the lateral motion ϕ. The simulation starts with the body in a flexed position, and the caudal fin wake is shed continuously in time as the fish begins to move. After several periods of the motion, transients associated with initial conditions are eliminated, and steady-state wake structure, motions and forces are achieved. The time step depends on the Strouhal number and the frequency of the backbone wave, but is typically chosen around $dt = 0.05$. The wake and body panels are desingularized as described by Krasny [25] with radius $\delta = 0.025$ to eliminate the short-wavelength instability, and the wake generally contains up to $O(10,000)$ panels at the conclusion of the simulation. The evolving wake structure behind the fish compares well qualitatively with dye visualization experiments performed in the wake of the *Robotuna*, such as those illustrated in Triantafyllou & Triantafyllou [17].

Power time histories for both the experimental runs and the numerical simulations can be found in Figure 6. The case is identical to the one detailed previously in Section 3.2, with a Strouhal number $St = 0.273$, which achieved an experimental drag reduction of 47.94%. The time records compare well qualitatively, revealing a second harmonic in the time history of the power expended. In addition, quantitative agreement is good under the assumptions made. Flexibility of the experimental apparatus was shown to have affected the exact timing among the robotic links and may have caused deviations in the overall power time record. Also, natural resonances in the mechanical system and mechanical losses are expected to cause some deviations between theory and experiment. However, despite the simplifying assumptions inherent in the numerical method and the unmodeled mechanical behavior and losses, the difference in the mean power between theory and experiment is only 17.6%, with an 88.4% numerically computed propulsive efficiency.

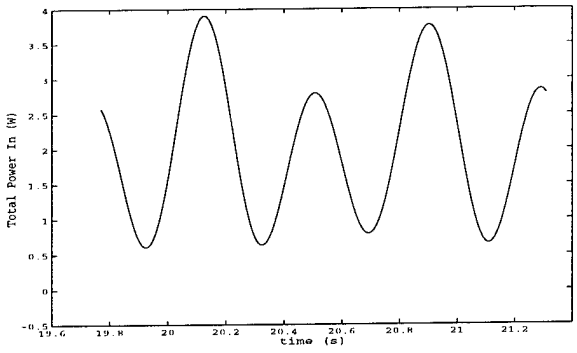

(a) Experimental

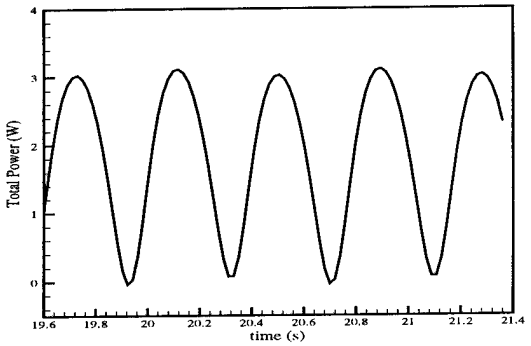

(b) Numerical

Figure 6: Total power into the fluid for straight-line swimming. The mean power deviation between the (a) experimental (2.04 W) and the (b) numerical (1.68 W) time history power records is 17.6%. Run parameters are identical to those of the case shown in Section 3.2.

6 Conclusions

Drag on a swimming flexible body is found to be smaller than the drag on the same body towed rigid. The maximum drag reduction recorded was in excess of 70%, at Reynolds number 10^6 with turbulence stimulation. Drag reduction is particularly sensitive to the speed of the traveling wave over the body, which must exceed the speed of travel, and the Strouhal number which must be within a range which varies with the specific thrust developed and lies between $St = 0.12$ and 0.35.

Numerical simulations were performed with an inviscid boundary integral scheme for arbitrary body geometry and motions, employing a desingularized infinitesimal wake sheet to model the nonlinear dynamics of the wake vorticity. Numerical predictions for the power expended by a body similar to the robotic apparatus undergoing identical movements were in good qualitative and quantitative agreement with experimental measurements.

We propose that the combination of two flow control mechanisms are plausible contributors to the drag reduction realized: *(a)* laminarization of the boundary layer as a result of body flexing in the form of a traveling wave; *(b)* vorticity control by the tail, which manipulates body–shed vorticity to create a propulsive reverse Kármán street. Using experimental techniques such as dye visualization in the wake and near-body DPIV, we can further elucidate the principals leading to boundary layer laminarization and wake vorticity control.

ACKNOWLEDGMENTS

Financial support of the Office of Naval Research under contract N00014-96-1-1141 monitored by P. Purtell, T. McMullen & J. Fein; the Office of Naval Research under grants N00014-89-J-3186 and N00014-93-1-0774; the Advanced Research Project Agency under contract N00014-94-1-0735; and the Sea Grant Program under Grant Number NA46RG0434 is gratefully acknowledged.

REFERENCES

1. I. Gursul & C.M. Ho "High aerodynamic loads on an airfoil submerged in an unsteady stream", *AIAA Journal*, **30**:1117–1119, 1992.
2. K. Streitlien, G.S. Triantafyllou, & M.S. Triantafyllou "Efficient foil propulsion through vortex control", *AIAA Journal*, **34**(11):2315–2319, 1996.
3. J.M. Anderson, K. Streitlien, D.S. Barrett & M.S. Triantafyllou "Oscillating foils of high propulsive efficiency", *J. Fluid Mech.*, **360**:41–72, 1998.
4. M.M. Koochesfahani & P. Dimotakis "A cancellation experiment in a forced turbulent shear layer", *AIAA 88-3713-CP*, 1988.
5. R. Gopalkrishnan, M.S. Triantafyllou, G.S. Triantafyllou & D.S. Barrett "Active vorticity control in a shear flow using a flapping foil", *Journal of Fluid Mechanics*, **274**:1–21, 1994.
6. J.E. Ffowcs-Williams & B.C. Zhao "The active control of vortex shedding", *J. Fluids Struct.*, **3**:115–122, 1989.
7. P.T. Tokomaru & P.E. Dimotakis "Rotary oscillation control of a cylinder wake", *Journal of Fluid Mechanics*, **224**:77–90, 1991.
8. S. Taneda "Visual observations of the flow past a circular cylinder performing a rotary oscillation", *J. Phys. Soc. Japan*, **45**:1038–1043, 1978.
9. S. Taneda "An experiment on the flow around a waving plate", *J. Phys. Soc. Japan*, **36**:1683–1689, 1974.
10. Y. Aleyev, *Nekton*, W. Junk: The Netherlands, 1977.
11. D.G. Harper & R.W. Blake "Fast-start performance of rainbow trout (*Salmo gairdneri*) and Northern Pike (*Esox Lucius*)", *J. Exp. Biol.*, **150**:321–342, 1990.
12. J. Lighthill, *Mathematical Biofluiddynamics*, SIAM: Philadelphia, 1975.
13. T.Y. Wu "Swimming of a waving plate", *Journal of Fluid Mechanics*, **10**:321–344, 1961.
14. T.Y. Wu "Hydromechanics of swimming propulsion. Part 1. Swimming of a two dimensional flexible plate at variable forward speeds in an inviscid fluid", *Journal of Fluid Mechanics*, **46**:337–355, 1971.
15. J. Gray "Studies in animal locomotion VI: The propulsive powers of the dolphin", *J. Exp. Biol.*, **13**:192–199, 1936.
16. D.S. Barrett & M.S. Triantafyllou "The design of a flexible hull undersea vehicle propelled by an oscillating foil", *9th International Symposium on Unmanned Untethered Submersible Technology*, September 1995.
17. M.S. Triantafyllou & G.S. Triantafyllou "An efficient swimming machine", *Scientific American*, **272**(3):64–70, 1995.
18. J.R. Adrian "Particle imaging techniques for experimental fluid mechanics", *Ann. Rev. Fluid Mech.* **23**:261–304, 1991.
19. C.E. Willert & M. Gharib "Digital particle image velocimetry", *Exp. Fluids* **10**:181–193, 1991.
20. H.L. Fierstine and V. Walters "Studies in locomotion and anatomy of scombroid fishes", *Mem. Soc. South. Calif. Acad. Sci.*, **6**:1–31, 1968.
21. M.S. Triantafyllou, G.S. Triantafyllou & R. Gopalkrishnan "Wake mechanics for thrust generation in oscillating foils", *Phys. Fluids A*, **3**:2835–2837, 1991.
22. G.S. Triantafyllou, M.S. Triantafyllou & M.A. Grosenbaugh "Optimal thrust development in oscillating foils with application to fish propulsion", *J. Fluids Struct.*, **7**:205–224, 1993.
23. J.M. Anderson "Vortex control for efficient propulsion", *PhD Thesis*, Joint Program, Massachusetts Institute of Technology & Woods Hole Oceanographic Institution, 1996.
24. J.Y. Cheng, L.X. Zhuang & B.G. Tong "Analysis of swimming three-dimensional waving plates", *Journal of Fluid Mechanics*, **232**:341–355, 1991.
25. R. Krasny "Desingularization of periodic vortex sheet roll-up", *Journal of Computational Physics*, **65**:292–313, 1986b.

FLOW SEPARATION CONTROL BY MEANS OF FLAPPING FOILS

M.F. Platzer
Naval Postgraduate School, Monterey, CA, USA
J.C.S. Lai
Australian Defence Force Academy, Canberra' Australia
C.M. Dohring
German Armed Forces University, Munich, Germany

Abstract - A sinusoidally flapping foil adds energy to the flow which manifests itself in the form of a jet flow downstream of the flapping foil. This effect is greatly enhanced if the foil is flapping close to a solid surface. Therefore, flapping foils can be used for boundary layer control if positioned close to a surface or in the near wake of a body. In this paper, the authors' recent flow visualization and laser-doppler experiments are described. They comprise the flow past single flapping foils, the flow past a foil which is flapping in close proximity to a flat plate, the flow over a backward-facing step with a flapping foil in the recirculatory flow region, and the effect of a flapping foil flow on trailing edge flow separation.

I. INTRODUCTION

Our interest in the flow physics of flapping airfoils derives from several fundamental and applied aspects. As first recognized by Knoller (1909) and Betz (1912), a flapping airfoil generates thrust. This Knoller-Betz effect was first confirmed experimentally by Katzmayr (1922). The first theoretical investigations of the aerodynamics of flapping airfoils were based on flat-plate airfoil theory, notably those of Birnbaum (1924), von Karman and Burgers (1935) and Garrick (1936), who showed that the propulsive efficiency of flapping airfoils is rather poor (not exceeding 50 percent) unless the airfoil is flapping rather slowly. Schmidt (1965) proposed the tandem airfoil arrangement and demonstrated experimentally that a stationary airfoil positioned in the wake of a flapping airfoil nearly doubles the propulsive efficiency of the single flapping airfoil because the stationary airfoil converts the vortical energy generated by the flapping airfoil into additional thrust. This experimental finding was confirmed by Bosch (1978) who showed by means of an oscillatory flat-plate analysis that a sinusoidally flapping airfoil upstream of a stationary airfoil increases the propulsive efficiency of such an arrangement to almost 100 percent. However, little information was available in the literature about the precise flow characteristics generated by flapping airfoils.

Therefore, we first endeavoured to identify the nature of the vortical wakes generated by flapping airfoils. We then attempted to investigate the effect of a flapping airfoil on the flat-plate boundary layer flow, on the flow over a backward-facing step, and on the flow separation downstream of an airfoil with a cusped or semi-circular trailing edge.

It is the objective of this paper to summarize the major results obtained in these experiments and to draw some conclusions concerning the potential of flapping foils for flow control. For the analysis of the experimental results we used both potential and viscous flow methods. Therefore, we first give a description of these analysis tools and then describe the experimental approach.

II. COMPUTATIONAL APPROACHES

Unsteady Panel Code

The unsteady panel code models the wake by releasing a discrete vortex at each time step equal in magnitude and opposite in direction to the change in circulation about the airfoil from the previous time step. After release the vortex is convected downstream, influencing and being influenced by the airfoil and the other discrete wake vortices. In order to enable visualization of the unsteady wake formation and evolution an interactive graphics animation interface was developed which greatly facilitates the understanding of the vortex shedding phenomena. Further details are given by Platzer et al (1993), Jones et al (1996), Jones & Center (1996), Teng and Pang (1988).

Navier-Stokes Code

The Navier-Stokes code is based on the strong conservation-law form of the compressible two-dimensional, thin-layer Navier-Stokes equations in a curvilinear coordinate system. Additional details are described by Tuncer & Platzer (1996).

III. EXPERIMENTAL APPROACH

Water Tunnel Tests

The experiments were carried out in the Naval Postgraduate School water tunnel facility. This tunnel is a closed circuit, continuous flow facility with a contraction ratio of 6:1. The test section is 38 cm wide, 51 cm high, and 150 cm long. The flow velocity can be set in a range from O to 0.5 m/s. The flapping excitation of the airfoil was induced by a vertical shaker which was mounted on the top of the test section. The frequency could be adjusted continuously from 5 Hz to 30 Hz. The amplitude could be varied from zero to a maximum value which depended on the chosen frequency. The LDV measurements were performed with a dual beam frequency shifted 300 mW Argon Ion laser with a beam separation of 50 mm, a focal length of 350 mm and back scatter receiving optics.

IV. RESULTS

Wakes Shed from Single Flapping Airfoils

Qualitative and quantitative comparisons of the wake structures shed from a flapping (plunging) NACA 0012 airfoil of 10 cm chord length are shown in Figure 1. The reduced flapping frequency is defined as

$$k = 2\Pi f c/U$$

where f is the frequency of oscillation, c is the airfoil chord, and U is the flow velocity. If this reduced frequency is multiplied with the non-dimensional flapping amplitude h/c a non-dimensional maximum plunge velocity can be defined as $v_p = k(h/c)$.

Figure 1 shows the vortical wake produced by an airfoil which is flapping sinusoidally with a non-dimensional amplitude of h/c = 0.2 at a reduced frequency of 3.0. The flow velocity is 10.5 cm/s yielding a Reynolds number of 1040. It is seen that the wake is symmetric about the center line, and the wake vortices are evenly spaced. Note that the upper vortices are counter-clockwise and the lower ones are clockwise. Such a vortex pattern is indicative of a thrust producing pattern. This symmetric wake behavior is also observed for lower frequencies' the only difference being the vortical wave length. However, as the non-dimensional plunge velocity is reduced below values of 0.2, the measured time-averaged wake velocity profiles show the velocity defects indicative of drag. At non-dimensional plunge velocities of approximately 0.2 the vortices are aligned along a straight line as shown in Figure 2. At values in excess of 0.2 one observes counterclockwise upper vortices and clockwise lower vortices and the wave length becomes shorter. However, there is an upper non-dimensional plunge velocity limit beyond which the vortical wake pattern changes from a symmetric pattern to an asymmetric one because the large eddies begin to pair up and travel away from the centerline. Tests with three different airfoil chords showed that this pairing and switching to an asymmetric wake occurs at a non-dimensional plunge velocity greater than approximately 0.75. Additional details on the jet characteristics of plunging airfoils have recently been given by Lai and Platzer (l998a).

Before discussing the asymmetric wake behavior it is instructive to examine the symmetric case. In Figure 3 the results of computations of the time-averaged velocity profiles upstream and downstream of a flapping airfoil are shown using the unsteady panel code. The non-dimensional flapping amplitude is 0.1. The profiles are

depicted at three different locations, 0.5 chord lengths upstream and 1.5 and 3 chord lengths downstream of the airfoil leading edge. The reduced frequency is 10. It can be seen that the airfoil produces a jet profile downstream of the trailing edge and that the maximum jet velocity exceeds the free-stream value by a factor of 2.4. The flapping airfoil therefore imparts a momentum increase to the fluid which manifests itself as airfoil thrust. It is also interesting to observe the amount of flow which is captured by the flapping foil, as manifested by the velocity distribution upstream of the leading edge. It is seen that the capturing area extends to roughly three chord lengths above and below the airfoil. In Figure 4 a comparison is given between the computed and measured time-averaged velocity profile at 0.75c downstream of an airfoil, flapping at a reduced frequency of S.4 with a non-dimensional flapping amplitude of 0.088. It is seen that there is good agreement between the measurement and the computation.

If the product of reduced frequency and non-dimensional flapping amplitude is increased beyond a critical value, such that the non-dimensional maximum plunge velocity becomes approximately O.75, the vortical wake pattern becomes asymmetric, as shown in Figure 5. The vortical wake is deflected either upward or downward and therefore generates not only thrust but also a finite average lift. This experimentally observed asymmetric vortex pattern is also found in the numerical computations using the unsteady panel code. The inclination of the vortex pattern (up or down) is determined by the starting conditions used in the panel code. The qualitative agreement between the numerical and experimental wake structures is excellent. Even the small remnants of vorticity, visible at the bottom of Figure 5, that break off from the vortex pairs at higher frequencies are consistent in both approaches.

Wall Effect

Dohring et al (1996) and Dohring (1998) showed that another interesting effect occurs if the airfoil executes a pure flapping oscillation in close proximity to a flat plate. Figure 6 presents a comparison of the measured time-averaged velocity distribution 0.75 chord length downstream of the trailing edge of a 20 mm chord airfoil which executes a flapping oscillation with a nondimensional flapping amplitude of 0.088 at a reduced frequency of 57 (based on free-stream velocity). It is seen that there is a significant velocity increase as the airfoil is positioned closer to the wall (4 mm rather than 8.5 mm). Also shown, for comparison, is the velocity distribution without the flat plate. The leading edge of the airfoil was located 100 mm downstream of the leading edge of the flat plate. Therefore the airfoil was embedded in the laminar boundary layer of the flat plate.

This flow behavior could be confirmed with Navier-Stokes calculations. Dohring et al (1996) and Dohring (1998) provided detailed flowfield calculations and showed that the thrust increases as the non-dimensional airfoil distance from the wall is decreased to values less than 1.5.

This wall effect can also be simulated to some extent by the inviscid unsteady panel code. It is well known that the aerodynamic characteristics of an airfoil flying close to the ground can be calculated by placing an image airfoil and computing the inviscid flow over the two-airfoil combination. Similarly, the ground effect on a flapping airfoil can be computed with the two-airfoil code described by Pang (1988) if the two airfoils are flapping in counter-phase. The application of this code again showed that there is a significant thrust increase generated by each airfoil if they are flapping in close proximity to each other. Furthermore, the thrust increases nonlinearly with reduced frequency. These results are quite consistent with the measurements and the Navier-Stokes calculations.

Flow Separation Control

Another series of experiments was performed to investigate the effectiveness of flapping airfoils to suppress the flow separation caused by the flow over a stationary airfoil with either a cusped or rounded trailing edge as shown in Figure 7. The stationary airfoil had a chord length of 28 cm and a maximum thickness of 4.5 cm. The flapping airfoils had chord lengths of either 2 cm or 10 cm. The gap between the trailing edge of the stationary airfoil and the leading edge of the flapping airfoil was varied between 0.5 to 2 cm. Dye injection was used to observe the wake flow characteristics. The flapping amplitude and frequency were increased until complete flow reattachment was achieved. It was found that the important controlling parameter is the non-dimensional plunge velocity. This is seen in Figure 8 where for the stationary airfoil with cusped trailing edge and a gap of 2 cm between the stationary and the flapping airfoil of 10 cm chord reattachment occurred as soon as the plunge velocity exceeded a value of 4.35. Other more detailed results are documented by Dohring (1998). Figure 9 shows the effectiveness of the 2 cm flapping airfoil, oscillating with a reduced frequency of $k = 100$ and a non-dimensional amplitude of $h/c = 0.038$ to suppress the flow separation behind the rounded trailing-edge airfoil.

Control of Backward Facing Step Flow

Figure 10 depicts the experimental set-up which was used for the experiment to demonstrate the effectiveness of a flapping airfoil to control the extent of the recirculatory flow region caused by the flow over a backward-facing step. The step height was 3 cm and the step width 38 cm. The plate upstream of the step was 91 cm. The free water surface was 42 cm above the upper plate. The free-stream velocity was 0.32 m/s, giving a Reynolds number (based on step height) of 12,700. The flapping airfoil was a NACA 0012 foil with a chord length of 1 cm. Laser-doppler measurements were carried out to measure the mean streamwise velocity and streamwise turbulence intensity distributions which are documented by Lai et al (1997). Figure lla shows the streamlines for backward-facing step flow without flapping foil control. Reattachment occurs between 5 and 6 non-dimensional step heights, a value in agreement with other experiments. Figure llb shows the effect of the flapping airfoil on the size of the recirculation flow region. The airfoil was located at 1.83 non-dimensioanl step heights downstream from the corner and 0.2 step heights above the downstream plate. It is seen that the recirculation region is reduced to about one third its original size.

Additional Results

For additional detailed results about the jet characteristics generated by airfoils which are flapping in a free-stream or in still air we refer to the papers by Lai and Platzer (l998a, l998b). Furthermore, the performance limits of flapping airfoils were determined with a Navier-Stokes code. The objective of this study was to identify the dynamic stall boundary of flapping airfoils. It was found that the main controlling parameter is again the nondimensional plunge velocity. For details we refer to Tuncer et al (1998).

V. SUMMARY & OUTLOOK

Birnbaum was the first one to refer to the sinusoidally flapping (plunging) airfoil as a flapping-foil propeller and to point out that it can be regarded as the two-dimensional equivalent of the conventional propeller. In our recent experimental and computational investigations we have endeavoured to provide specific information about the performance characteristics of flapping-foil propellers. It was found that the main controlling parameter is the non-dimensional plunge velocity. The flapping foil starts to produce thrust as soon as the plunge velocity exceeds values of approximately 0.2. It could also be shown that there exists a favorable wall or ground effect which can be used for purposes of boundary layer propulsion. Also, it could be shown that flow separation could be suppressed completely or, as in the case of flow over a backward-facing step, the recirculatory flow region could be reduced significantly. Because of the necessity to exceed a critical value of non-dimensional plunge velocity, the effectiveness of the flapping-foil propeller is limited to relatively small free-stream velocities unless high flapping frequencies and/or large chord lengths are used. Further studies are needed to explore the potential of flapping-foil propellers for drag reduction by means of flow separation control.

VI. ACKNOWLEDGMENT

The authors gratefully acknowledge the support of the Office of Naval Research (Dr. Peter Majumdar and Dr. Edwin Rood), of the Naval Research Laboratory (Mr. Kevin Ailinger), and of the Naval Postgraduate School Internal Research Program.

VII. REFERENCES

Betz, A., "Ein Beitrag zur Erklaerung des Segelfluges", Z. f. Flugtechnik und Motorluftschiffahrt, Vol. 3, 1912, pp. 269-272, 1912

Birnbaum, W., "Der Schlagfluegelpropeller und die kleinen Schwingungen elastisch befestigter Tragfluegel", Zeitschrift fuer Flugtechnik und Motorluftschiffahrt, Vol. 15, pp. 128-134, 1925

Bosch, H., "Interfering Airfoils in Two-Dimensional Unsteady Incompressible Flow," AGARD CP-227, 1978

Dohring, C.M., Platzer, M.F., Jones, K.D., Tuncer, I.H., Computational and Experimental Investigation of the Wakes Shed from Flapping Airfoils and their Wake Interference/Impingement Characteristics", AGARD-CP-584, Paper No. 33, November 1996

Dohring, C.M., "Der Schub des schlagenden Fluegels und seine Anwendung zur GrenzechichUbeeinflussung-eine experimentelle und numerische Untersuchung", Doctoral Dissertation, German Armed Forces University, Munich, Germany, May 1998

Garrick, I.E., "Propulsion of a Flapping and Oscillating Airfoil," NACA Report 567, 1936

Jones, K.D. and Center, K.B. 1996, "Numerical Wake Visualization for Airfoils Undergoing Forced and Aeroelastic Motions," AIAA Paper 96-0055, January 1996

Jones, K.D., C.M. Dohring, Platzer, M.F., "Wake Structures behind Plunging Airfoils: A Comparison of Numerical and Experimental Results," AIAA Paper 96-0078, January 1996

Katzmayr, R., "Effect of Periodic Changes of Angle of Attack on Behaviour of Airfoils," NACA TM 147, 1922

Knoller, R., "Die Gesetze des Luftwiderstandes," Flug- und Motortechnik (Wien), Vol. 3, No. 21, pp. 1-7, 1909

Lai, J.C.S., Yue, J.W., Platzer, M.F., "Control of Backward Facing Step Flow Using a Flapping Airfoil", ASME Fluids Engineering Division Summer Meeting, FEDSM97-3307, Vancouver, Canada, 22-26 June 1997

Lai, J.C.S. and Platzer, M.F., (l99Sa) "The Jet Characteristics of a Plunging Airfoil", AIAA Paper 98-0101, January 12-15, 1998

Lai, J.C.S. and Platzer, M.F., (l99Bb) "The Jet Characteristics of a Plunging Airfoil in Still Air, ASME Fluids Engineering Division Summer Meeting, Washington, D.C., 20-25 June 1998

Pang, C.K., "A Computer Code for Unsteady Incompressible Flow past Two Airfoils," Aeronautical Engineer's Thesis, Naval Postgraduate School, Monterey, CA, September 1988

Platzer, M.F., Neace, K.S., Pang, C.K., "Aerodynamic Analysis of Flapping Wing Propulsion," AIAA Paper 93-0484, 1993

Schmidt, W., "Der Wellpropeller, ein neuer Antrieb fur Wasser-, Land-, und Luftfahrzeuge," Zeitschrift fur Flugwissen-schaften, Vol. 13, pp. 472-479, 1965

Teng, N.H., "The Development of a Computer Code for the Numerical Solution of Unsteady, Inviscid, and Incompressible Flow over an Airfoil," Master's Thesis, Naval Postgraduate School, Monterey, CA, June 1987

Tuncer, I.H. and Platzer, M.F., "Thrust Generation due to Airfoil Flapping," AIAA Journal, Vol. 34, No. 2, pp. 324-331, 1996

Tuncer, I.H., Ekaterinaris, J.A., Platzer, M.F., "A Novel Viscous Inviscid Interaction Method for Unsteady Low-Speed Airfoil Flows, AIAA Journal, Vol. 33, No. 1, pp. 151-154, January 1995

Tuncer, I.H., Walz, R., Platzer, M.F., "A Computational Study on the Dynamic Stall of a Flapping Airfoil", AIAA Paper 98-2519, June 1998

von Karman, T. and Burgers, J.M., "Aerodynamic Theory, " Vol. 2, Springer Berlin, pp. 280-310, 1935

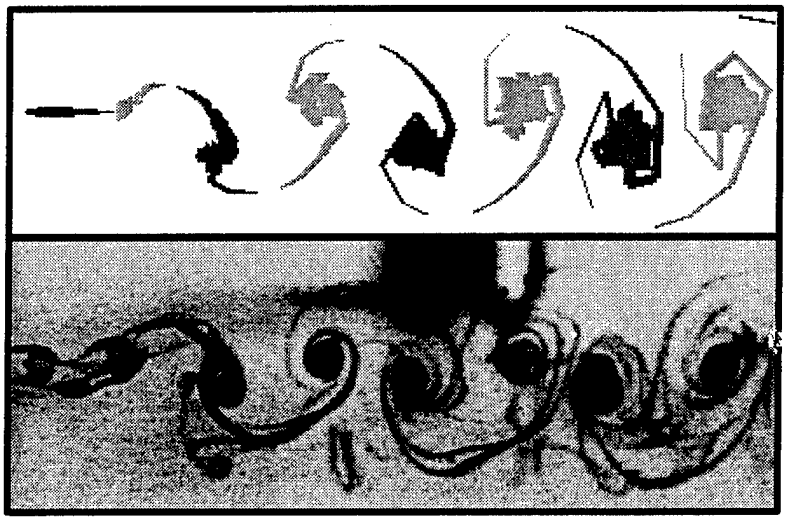

Fig. 1 Wake Comparison
The upper figure shows the panel code computed wake.
The lower figure shows the wake flow visualization

Fig.2 Zero-Drag Vortex Street

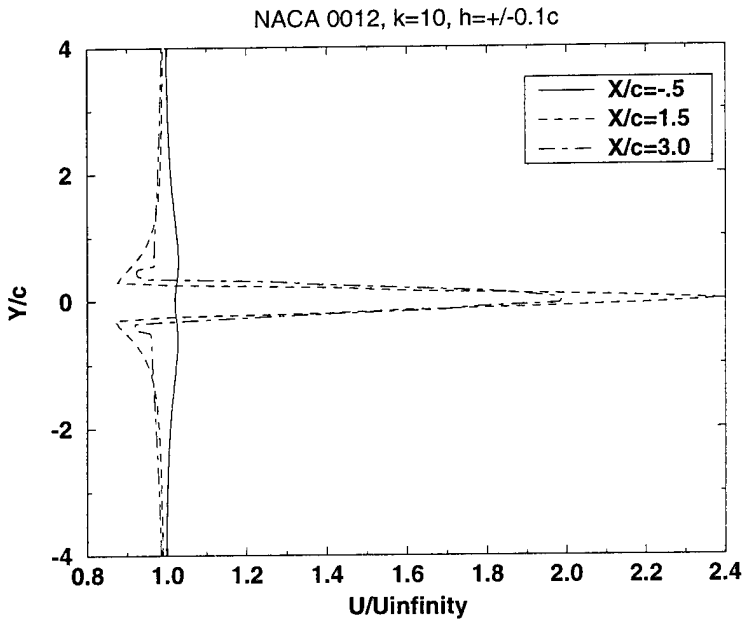

Fig. 3 Computed Velocity Profiles

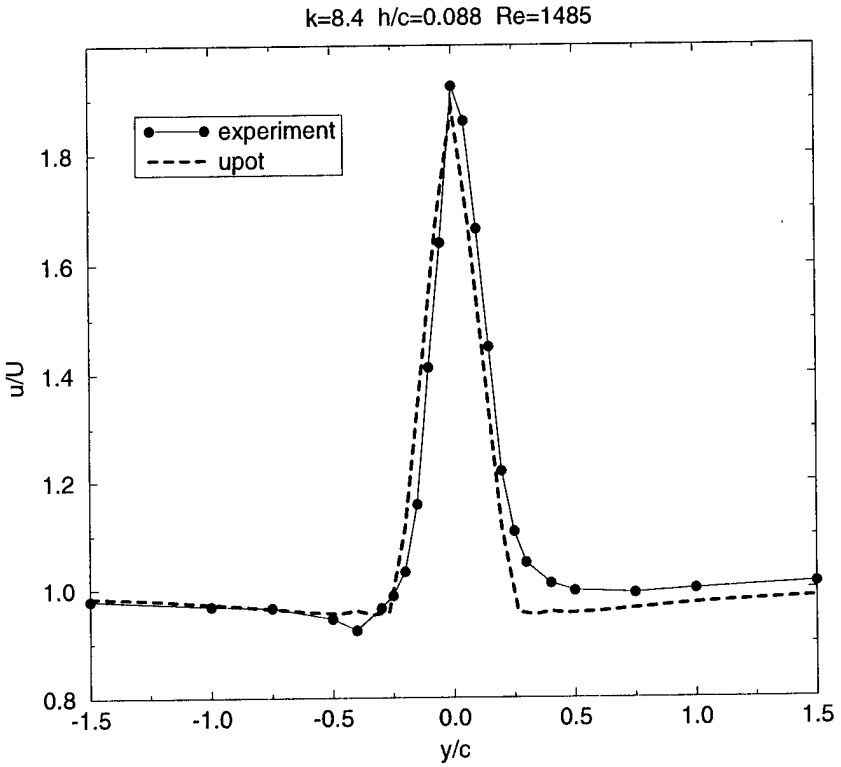

Fig. 4 Comparison of Measured and Computed Time-Averaged Velocity Profiles

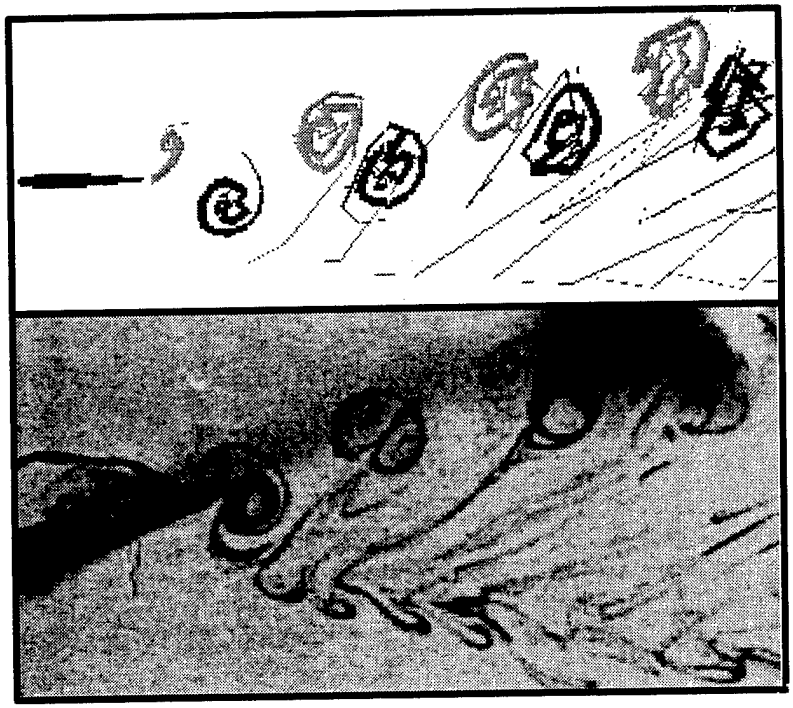

Fig. 5 Asymmetric Wake Comparison
(upper figure: panel code, lower figure: visualization)

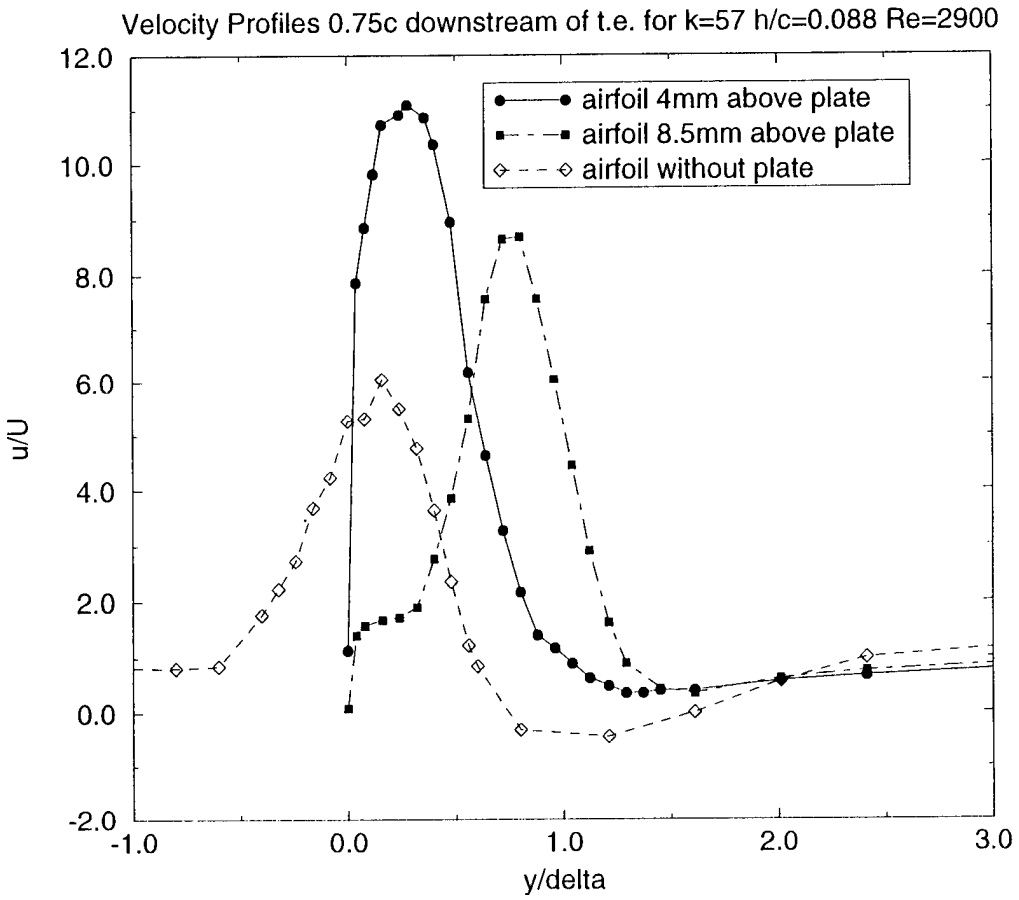

Fig. 6 Measured Velocity Profiles

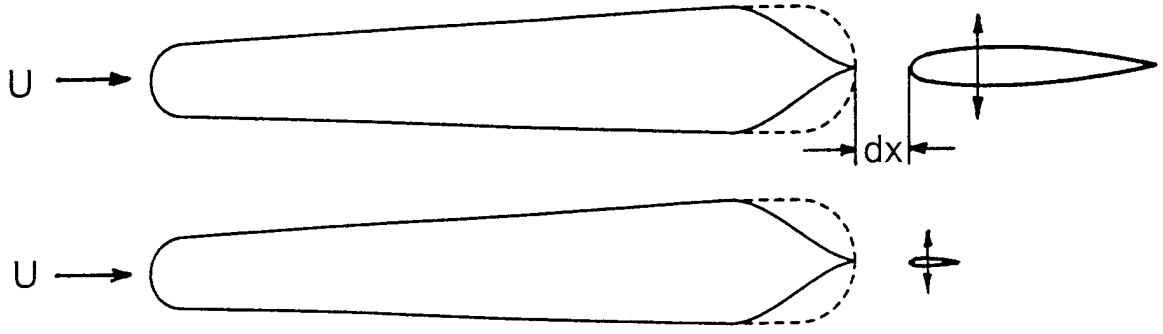

Fig. 7 Experimental Set-up

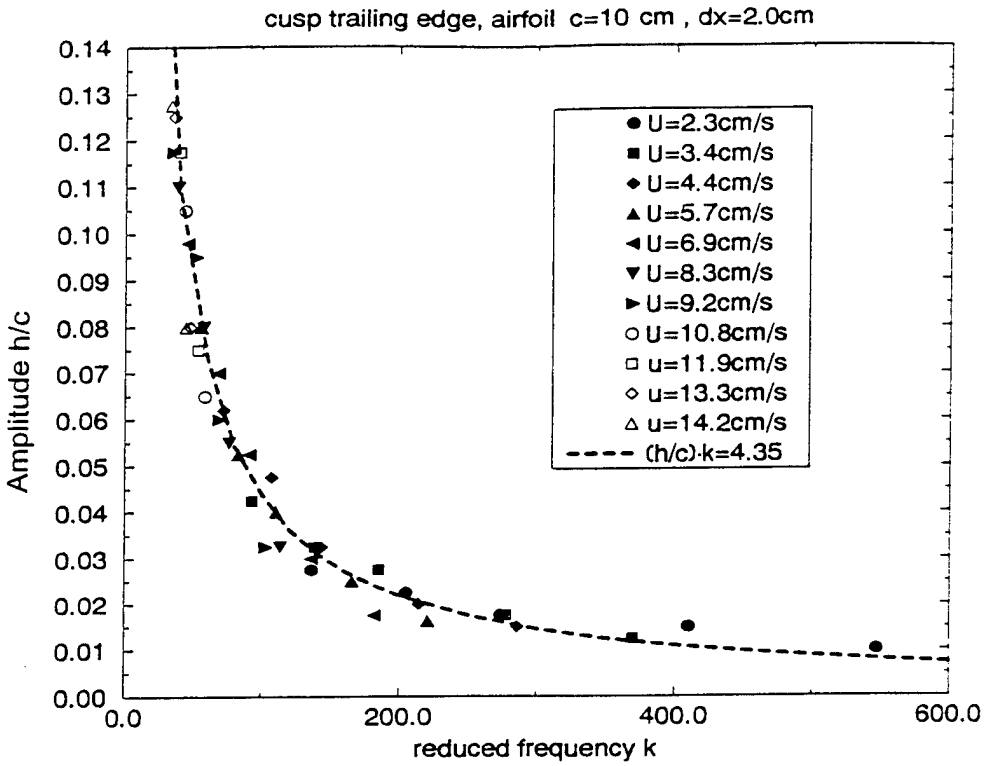

Fig.8 Flow Separation Control Boundary

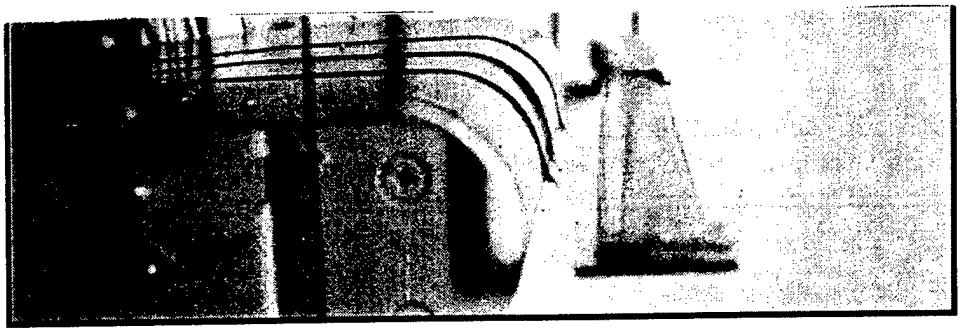

Fig. 9 Visualization of Flow Control

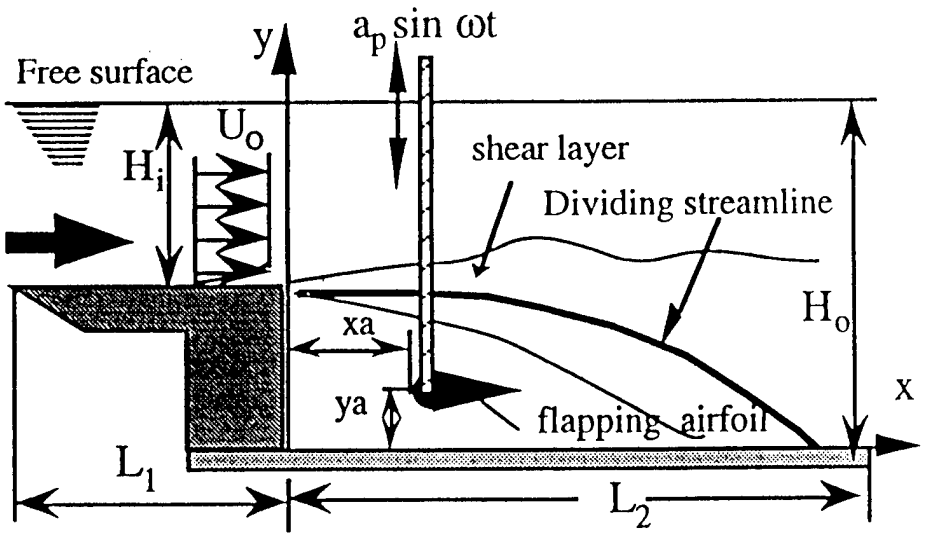

Fig. 10 Experimental Set-up

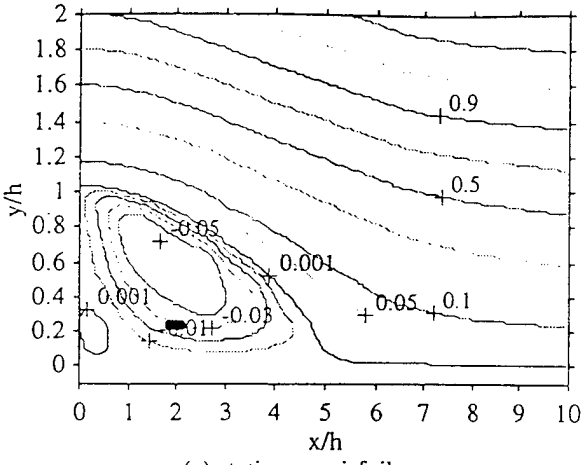

(a) stationary airfoil

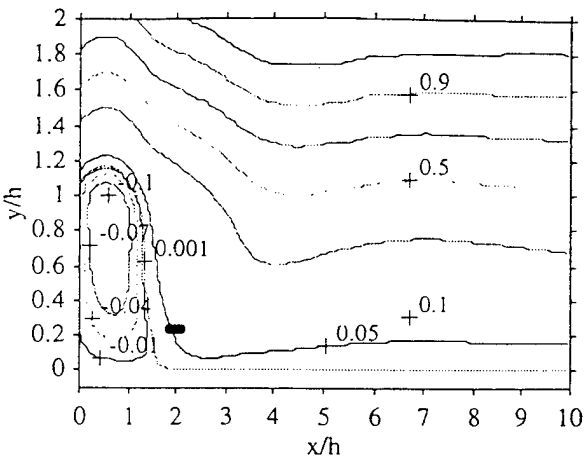

(b) airfoil flapping at 20 Hz with amplitude 0.123c.

Fig. 11 Flow over Backward-Facing Step (without and with flapping foil control)

THE VORTICITY CONTROL UNMANNED UNDERSEA VEHICLE— A BIOLOGICALLY INSPIRED AUTONOMOUS VEHICLE

Jamie M. Anderson
Charles Stark Draper Laboratory
555 Technology Square, MS 23
Cambridge, MA 02139
jamie@draper.com

Abstract - Recent interest in improving the operating performance of unmanned undersea vehicles (UUVs) has led to the notion of mimicking the form and function of fish and marine mammals. Often, capabilities of the biological systems far exceed those of modern engineered vehicles with conventional power supplies and propulsors. Of particular interest are the possible energetic benefits and the improved maneuvering characteristics of fish-like propulsion. In this paper we describe the first autonomous mission-scale fish-like vehicle in development at Draper Laboratory, the Vorticity Control UUV (VCUUV). Named after the flow control mechanisms inherent in fish swimming, the VCUUV mimics the form and movement of a large yellowfin tuna. Designed and built as a proof of concept test platform, the VCUUV will provide unambiguous measurements of the power required to swim and maneuver like a tuna. Drag reduction will be investigated by comparing the power consumed during swimming and that required for straight coasting at the same speed.

I. INTRODUCTION

Fish swimming propulsion has recently gained wide attention in the underwater vehicle community as a viable alternative to traditional marine propulsors. Fish possess many abilities which are desirable for unmanned undersea vehicles (UUVs): they are able to cruise great distances, maneuver well in cluttered environments and accelerate and decelerate quickly. Although the form and movement of fish and cetaceans vary widely across species, the fundamental swimming movements of many "swimmers" such as tunas, sharks, dolphins, *etc.*, are notably similar [1] which suggests that nature has evolved optimal propulsive interaction with water.

Many use the phrase "swim like a fish" to describe superior interaction with the aquatic environment, that is, high propulsion and maneuvering proficiency. The secret to fish swimming performance appears to lie in the use of unsteady flow mechanisms (such as a highly vortical wake) to achieve both steady swimming and unsteady maneuvers. Propulsion and steering are integrated into one system which performs well over a wide range of speed.

The utility of bio-propulsion and maneuvering is apparent when one considers the current UUV missions of interest as illustrated in Figure 1. Today's missions are challenging in that they often require long transit, long duration on site, loitering without loss of power, movement in close proximity to objects for docking, tagging, *etc.*, and operation in dynamic environments such as shallow waters near the beach zone. Vorticity control propulsion and maneuvering may prove to be essential in realizing these missions in that fish-like maneuverability may not be as energetically taxing as conventional means of generating large side forces (such as thrusters) in varying conditions. For example, fish can loiter at zero speed and rapidly accelerate in nearly any direction. Blake *et al.* [2] report turning radii of tunas of less than half a body length, which outperforms conventional vehicle systems by an order of magnitude.

A common misconception of the bio-propulsion concept is that possible improved efficiency and maneuvering capability is not worthwhile when compared to the required displacement for the propulsion system. However, experience has shown that attempts to achieve both long range and highly maneuverable rigid body UUV's have met with disappointment, largely due to the need for both propulsion and maneuvering systems that rarely operate together effectively. Cross-axis thrusters, for instance, are both heavy and detract from useful vehicle displacement, and can only be used at zero speed without concern of control nonlinearities (that can even include control reversal). For high speed maneuvers, for which thrusters are useless, a rigid body UUV must also have a conventional propulsor and control surfaces which cannot produce turning diameters less than several vehicle lengths.

By comparison, bio-propulsion can provide both efficient propulsion and maneuvering at any speed with modest investment in vehicle displacement. For example, the Vorticity Control UUV (VCUUV) propulsion system occupies only 23% of the total displacement (32% of the envelope displacement due to some free-flood volume). *Thunniform* (tuna) morphology and kinematics allow this modest propulsion system displacement with excellent steady swimming and maneuvering performance.

The *Thunniform* model possesses several advantages for use on an underwater vehicle system. As with other carangiform fishes, the propulsion and maneuvering movements are localized to the last 30-40% of the body length and are moderate in amplitude. Tuna caudal fin peak-to-peak excursions rarely exceed 15 to 20% of the body length [3]. The localized tail motion allows the forward body be used as a rigid housing for energy, intelligence, payload, *etc.*, without the complexity of flexible pressure hulls or the power required to move them. The tuna's fusiform forward body has nearly elliptical sections within which internal arrangements are more easily made than with cylindrical sections. The body is low drag but contains significant packaging space.

For the underwater surveillance mission, biologically inspired vehicles may be able to inspect an object of interest more closely, rapidly avoid if necessary and precisely place objects if desired, without loss of efficient survey speed and range. Vorticity control propulsion and maneuvering provides the range and speed of conventional low drag hulls driven by propellers, with the added capability of ship-deployed remotely operated vehicles which can precisely maneuver in a location of interest.

II. BACKGROUND

In recent years, researchers at the Massachusetts Institute of Technology have investigated rigid flapping foils (combined translation with simultaneous heave and pitch) as a means of generating large propulsion forces at very high efficiencies. Anderson *et al.* [4] have demonstrated propulsive efficiencies in excess of 85% with proper selection of the Strouhal number, angle of attack, heave amplitude ratio and the phasing of the combined motions. Flow visualization studies with live fish have shown that the propulsion and maneuvering performance of fishes is related to their ability to control their wake vorticity. Contrary to drag producing bodies, fish generate an oscillatory wake consisting of alternating vortices arranged in a jet pattern. Manipulation of wake vorticity appears to be a dominant factor affecting the propulsive performance of fish [5].

The MIT research has culminated in the development of *Robotuna*, a 1.2 *m* biologically inspired tow tank model built to study propulsive efficiency and how it relates to body movement [6]. *Robotuna* was exercised in the MIT Ocean Engineering Testing Tank by prescribing a set of kinematic parameters (angular deflections of each joint, tow speed, phase relationships) and measuring the net power transmitted to the linkages and the reaction force between the tuna and carriage. Optimal

motion was defined as that set of motion parameters that produced no net force on the carriage (self propelled status) with minimum input energy.

The *Robotuna* project has demonstrated that significant "apparent" drag reduction can be achieved even without careful tuning of the drive mechanism. The observed drag reduction is referred to as "apparent" because in a towed experiment, it is not possible to discriminate between thrust and drag in a single measurement. The input power of the swimming *Robotuna* was compared to the "dead fish" (straightened body and towed) power. An estimated thrust power ratio (mean drag power of "dead fish" over the mean input power of the swimming fish) of 1.27 and an apparent drag reduction of 49% were achieved [6]. This demonstrates that vorticity control for the most part, is a macro effect that can be readily applied to an engineered vehicle without fine tuning the body shape, skin surface smoothness and compliance and fin shape.

III. VCUUV SYSTEM DESCRIPTION

At the Charles Stark Draper Laboratory, the next generation of flexible hull robots is in development. The Vorticity Control Unmanned Undersea Vehicle (VCUUV) is a freely swimming, tuna-shaped vehicle built to demonstrate tuna-like swimming and maneuvering. Constructed as a proof-of-concept demonstration of vorticity control propulsion, the VCUUV serves as a mission-scale exercise in design and packaging as well as a research platform with which we can quantify the energetics of swimming.

Although the first VCUUV prototype is not intended as an ocean going vehicle, the vehicle does contain all of the necessary components of autonomy: onboard energy, actuation and control. The vehicle will be operated in shallow, controlled environments where the propulsion system performance can be quantified. Critical vehicle issues addressed in the VCUUV project including sizing of actuators, design of articulated body, pressure hull design, and on-board intelligence, sensors and power are described in detail by Anderson and Kerrebrock [7, 8].

The VCUUV will operate in swimming pool depths (< 10 *m*), at speeds up to one body length per second (3.9 knots) which approaches the typical cruising speed of yellowfin tunas (1-2 body lengths per second) [9]. Preliminary tests will be done at the lower speed of 2.6 knots for direct comparisons with the MIT *Robotuna* studies.

System Characteristics

The need to demonstrate a fieldable vehicle which can serve as a research tool has driven both the mechanical and electrical system designs. The following requirements were imposed on the prototype vehicle design:

Mechanical system:

- Independent control of profile (phase and amplitude of each link) at variable frequencies and vehicle speeds
- Near neutral buoyancy in articulated tail
- Minimum speed of 2.5 knots
- 2 body length turning diameter
- Minimum mission duration of 3 hours
- Swimming pool missions in depths less than 10 *m*

Sensors:

- Measurement of vehicle location and orientation as a function of input kinematics
- Measurement of propulsive power (*i.e.*, tail linkage velocity and force)
- Measurement of tail linkage position

Control:

- Closed loop control of tail linkage position
- Stable depth and heading

The key parameters in *Thunniform* steady swimming are the vehicle speed, oscillation frequency and amplitude, propulsive wavelength, shape parameters which describe the envelope of transverse motion, tail phasing and angle of attack [6].

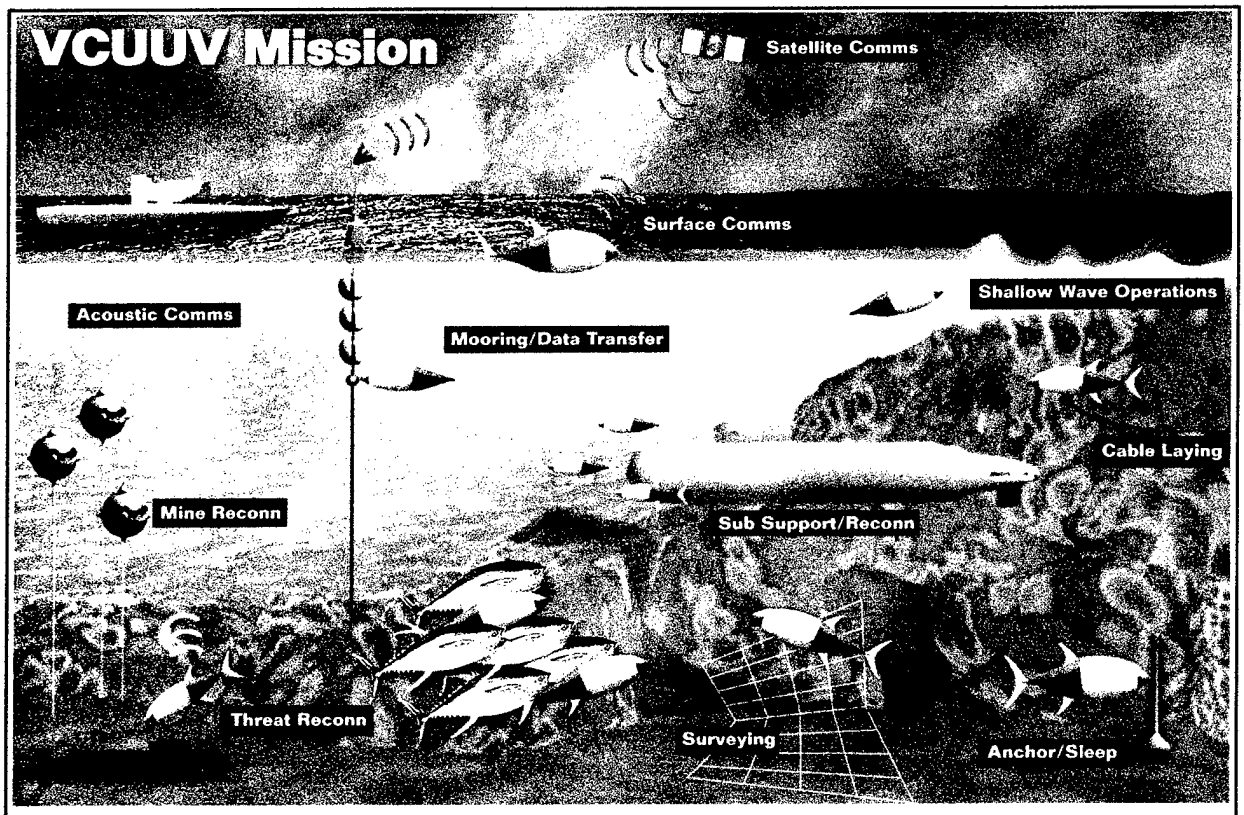

Figure 1: Vorticity control propulsion mission advanced concept

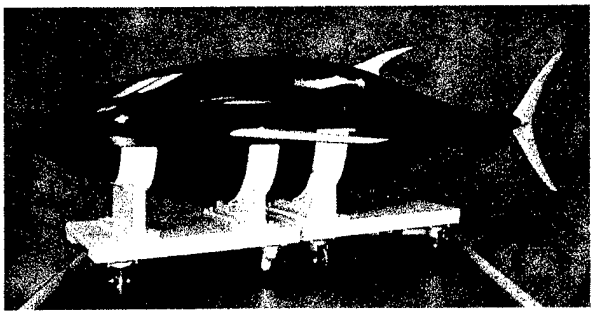

Figure 2: Draper Laboratory Vorticity Control UUV

For steady straight swimming, a traveling propulsive wave is required which moves from head to tail with increasing amplitude near the tail. The kinematics are described in detail by Barrett [6], Dewar and Graham [3] and Anderson and Kerrebrock [7, 8]. Turning kinematics are less understood and consequently, the VCUUV design has most of its design margin in the turning requirements (amplitudes and loading conditions).

Table 1 summarizes the VCUUV prototype characteristics. The vehicle is 8 feet (2.4 *m*) long and displaces approximately 300 *lb* (1334 *N*). The forward half of the vehicle is comprised of rigid pressure hull while the aft portion is articulated and freely flooded. The pressure hull houses all of the dry components including batteries, electronics (computer, sensors, etc.), hydraulic power plant and payload (Figures 2 and 3).

The articulated tail structure consists of a planar, four degree of freedom robot arm that acts upon a tuna-shaped flexible exostructure. The entire tail area is freely flooded with an impermeable skin which prevents exchange of water across the envelope boundary. Three equal length links and the caudal fin are independently actuated with hydraulic cylinders integrated into the links themselves.

The tail exostructure converts the discrete movements of the underlying robot linkage to the smooth, fluid movements of a fish tail. The key elements of the exostructure are rigid buoyant foam "ribs" which are shaped like hollowed out tuna "steaks" and are connected to one another by flexible splines. The splines produce smooth curvature along the tail envelope which simulates a linkage of much higher resolution (as though there are a greater number of links). At three locations along the tail, a follower rod mechanism transmits the hydrodynamic loads on the exostructure to the actuation linkage.

The structure-fluid interface is a dermal layer of overlapping scales which prevent transverse folds between the ribs similar to their function in real fish. The outermost layer consists of neoprene rubber that is bonded to lycra on both sides. This "skin" prevents water movement across the boundary while maintaining an extremely smooth flexible surface which is nearly impermeable to water.

Table 1: VCUUV System Summary

Component	Description
Pressure hull	Carbon graphite/epoxy with aluminum mating surface
Computer and actuator control	PC104 486, DSP, hard drive
Sensors	3 accelerometers, 3 rate gyros, compass, pressure (depth), cylinder displacement and force, leak detectors, internal temperature
Actuators	Recirculating hydraulic system for tail linkage, motors for pectoral fins
Energy	Sealed lead acid batteries, 60 VDC, 800 W-hr
Communications	Ethernet through umbilical when attached status indicator lights

The largest and most heavily loaded fin on the vehicle is the rigid caudal fin which is the primary propulsive actuator. The fin shape was determined by averaging direct measurement of our cast yellowfin tuna and measurements made from photographs of freshly caught fish. The cross section was determined by sectioning the cast caudal fin in multiple locations..

As in actual tunas, dive plane control (and buoyancy adjustment) will be provided by means of two pectoral fins located near the midbody. Real tunas (which are negatively buoyant) use the pectoral fins for speed dependent buoyancy adjustment. At low speeds, the fins are fully splayed for maximum lift; as the speed increases, the fin sweepback angle is increased until the fins are fully adducted, effectively reducing the lifting area [3].

The VCUUV pectoral fins are positioned in the same place as real tuna pectoral fins, slightly forward of the center of gravity. Thus, the pectoral fins act as canards. Unlike actual tunas which can articulate their pectoral fins in pitch and sweep angle, the VCUUV pectoral fins will only pitch, controlled by torquemotors located inside the pressure hull. For simplicity, the pectoral fin shapes are swept and tapered NACA 0015 sections roughly matching the chord and span of actual tuna fins. Because of the large metacentric height of the vehicle, pectoral fin lift will cause little change in the vehicle attitude which allows us to control both depth and buoyancy with the same actuation system.

Two rigid keel like fins (dorsal and anal) attached just aft of the hull/tail interface are included for stability and are constructed in the same manner as the caudal fin. The remaining fins are not included in the VCUUV as they are not critical in straight swimming and maneuvering: two forward ventral fins, the first dorsal fin (may be added later for maneuvering stability), and the finlets along the tail.

Electronics and control

At this time the VCUUV is not intended to demonstrate advanced autonomy; thus, it will initially operate in an open loop, pre-programmed capacity to demonstrate simple swimming and turning, not sophisticated intelligence such as in-flight trajectory planning or obstacle avoidance. However, our system components (processor, guidance sensors, etc.) have been selected with an eye towards future capabilities in complex missions and control.

The center of the electronics system is a PC104 486 computer which monitors sensor input, vehicle status, logs data, *etc.*. The tail actuators are controlled with a dedicated digital signal processor (DSP). The sensor suite includes conventional underwater vehicle sensors required for autonomous operation: inertial measurements of all accelerations and rates, depth (pressure), heading (compass), and auxiliary sensors for vehicle status (temperature in the hull and leak detection). High bandwidth sensing for linkage control (hydraulic cylinder position, hydraulic pressure, motor speed) are directly input to the DSP which controls tail articulation. In addition, hydraulic force is measured at the point of application so that propulsive efficiency can be directly measured.

Initially, only the tail linkage will be operated under closed loop control. In this configuration, the vehicle will be tested with a variety of open loop commands to characterize the propulsor in straight swimming and maneuvering. System identification techniques will be used to detail the input-output relationships necessary to attain closed loop trajectory control.

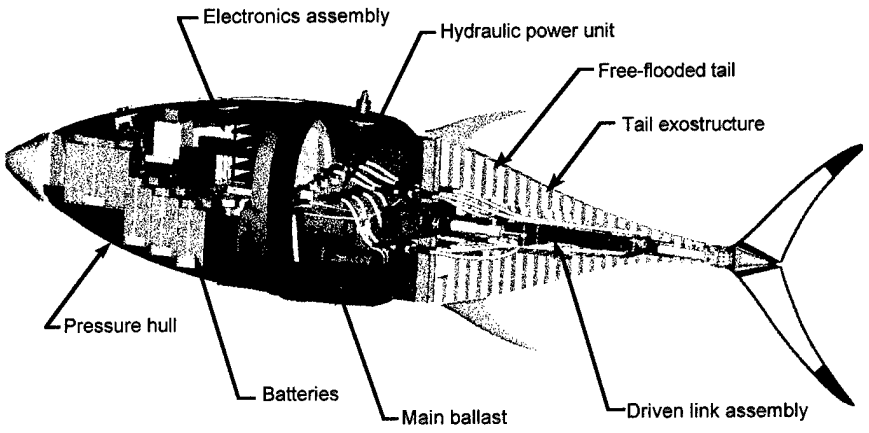

Figure 3: VCUUV System Layout

IV. TECHNICAL PROGRESS

At this writing, the VCUUV has completed system integration and preliminary testing. The first swimming test in April, 1998, was very successful (Figure 4); the vehicle propelled itself forward in a very stable manner without yaw, pitch or roll oscillations.

Extended experiments are planned for Spring and Summer, 1998, during which the following specific studies will be performed:

- Straight swimming with the MIT *Robotuna* self propelled optimal motion parameters. Loads, power and efficiency of straight, steady swimming will be quantified. Results will be compared to steady drag power estimated by deceleration studies around the steady swimming speed.
- Sensitivity study of optimal motion. Performance sensitivity to frequency, angle of attack, propulsive wave speed and amplitude of motion will be assessed.
- Speed trials in straight swimming. Stability, controllability and energetics will be quantified while varying tail oscillation frequency only.
- Maneuvering studies. Turn rate as a function of vehicle speed will be measured by applying bias curvatures to the body during steady swimming. The energetic cost of maneuvering will be quantified.

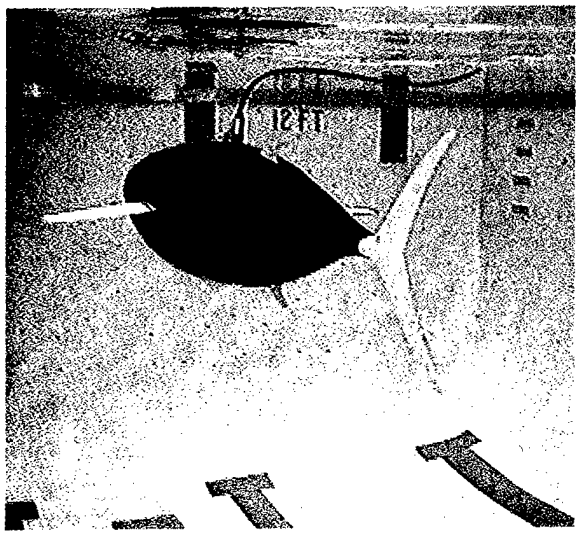

Figure 4: VCUUV Testing

V. SUMMARY

The Draper Laboratory VCUUV is the first autonomously operated fish-like UUV that is realistically sized for real world missions and payload and able to move with arbitrary *Thunniform* kinematics. The fish propulsion paradigm offers order of magnitude improvement in maneuvering capability which is required for today's challenging UUV missions in dynamic, cluttered environments. The VCUUV prototype will prove the concept while serving as a research testbed. Lessons learned from the VCUUV can be applied to new vehicles mechanically optimized to achieve fish-like capabilities in engineered vehicles.

VI. ACKNOWLEDGMENTS

This project is funded internally by the Charles Stark Draper Laboratory.

VII. REFERENCES

1. Triantafyllou, MS and Triantafyllou, GS (1995), "An Efficient Swimming Machine", *Scientific American,* March, 1995.

2. Blake, RW, Chatters, LM and P Domenici (1995), "Turning radius of yellowfin tuna (*Thunnus albacares*) in unsteady swimming manoeuvres", *J. Fish Biology*, v. 46, pp 536-538.

3. Dewar, H and Graham, JB (1994), "Studies of tropical tuna swimming performance in a large water tunnel, Part III: Kinematics", *Journal of Experimental Biology,* Vol 192, pp 45-59.

4. Anderson, JM, Streitlien, K, Barrett, DS and MS Triantafyllou (1998), "Oscillating Foils of High Propulsive Efficiency", *Journal of Fluid Mechanics*, Vol 360, 1998.

5. Anderson, JM (1996), "Vorticity Control for Efficient Propulsion", *Ph.D. Thesis, Massachusetts Institute of Technology/Woods Hole Oceanographic Institution Joint Program.*

6. Barrett, DS (1996), "Propulsive efficiency of a flexible hull underwater vehicle", *Ph.D. Thesis, Massachusetts Institute of Technology.*

7. Anderson, JM and PA Kerrebrock, (1997a), "The Vorticity Control Unmanned Undersea Vehicle—An Autonomous Vehicle Employing Fish Swimming Propulsion and Maneuvering", *Proc. 10th Int. Symp on Unmanned Untethered Submersible Technology*, Durham, NH, 7-10 Sept, 1997, pp 189-195.

8. Anderson, JM, Kerrebrock, PA and MS Triantafyllou (1997b), "Concept Design of a Flexible-Hull Unmanned Undersea Vehicle", *Proc. of the 7th Int. Offshore and Polar Engineering Conference*, Honolulu, USA, May 25-30, 1997 (Vol. II), pp 82-88.

9. Magnuson, JJ (1978), "Locomotion by Scombrid Fishes: Hydromechanics, Morphology and Behavior", in *Fish Physiology*, Vol. VII, Academic Press, Inc.

A Fast-Starting and Maneuvering Vehicle, the ROBOPIKE

John Muir Kumph
Massachusetts Institute of Technology
77 Massachusetts Ave. Room 48-015
Cambridge, MA 02139
ninjo@mit.edu

M.S. Triantafyllou
Massachusetts Institute of Technology
77 Massachusetts Ave. Room 5-323
Cambridge, MA 02139
mistetri@mit.edu

March 20, 1998

ABSTRACT

We describe the biomimetic development of an autonomous flexible-hull vehicle, 81 *cm* in length, capable of emulating the fast-start and rapid maneuvering performance of live fish. The design was based on: the geometrical body characteristics and swimming kinematics of a chain pickerel (*Esox Niger*); principles of vorticity control; and experience and data obtained in the development and testing of the *RoboTuna*. The development of the vehicle required experimenting with novel actuation and skin structure support devices, which resulted in a functional prototype capable of fish-like agility.

1 Introduction

An 81 *cm* long robotic fish-like vehicle was developed to test design ideas about fast-starting and rapidly turning vehicles employing vorticity control. The design used the process of *biomimesis* to arrive at its hull shape and kinematic requirements. The goal of biomimesis is to use biological inspiration to engineer machines capable of emulating outstanding animal performance. By building this vehicle we have identified the principal design characteristics that give fish their superior performance capabilities. We will use this information to develop novel and simple technology to equip vehicles with outstanding maneuvering capabilities. The design was modelled after the chain pickerel (*Esox Niger*), a small pike closely related to the northern pike (*Esox Lucius*), which have superb fast-starting capabilities (Harper & Blake 1990). The vehicle (see Figure 1) was built and tested at MIT in the Ocean Engineering Testing Tank Facility (Towing Tank).

There has been an increasing interest in the development of fish-like vehicles for two reasons. First, it has now become possible for advanced electromechanical and control technology to be purchased off-the-shelf, so that the building of a small, experimental underwater craft can be undertaken at reasonable cost. Second, there has been a growing interest in alternative propulsion schemes for small craft because conventional propulsion and, especially, maneuvering technology has reached a level of maturity that does not allow rapid progress.

Observation of live fish and cetaceans reveals that they have achieved high swimming performance by employing a completely different paradigm, substantially flexing their hull and using rapidly moving fins. It is our aim at the MIT Towing Tank to discover the physical mechanisms of fish swimming, and develop simple technology to implement these mechanisms to improve vehicle agility.

Previous work in the field of fish hydrodynamics has centered in two areas. Some researchers have developed theoretical models of fish propulsion which offer insight into the physics of fish swimming (Lighthill 1975; Wu 1961, 1971). Others have studied the mechanics and fluid mechanics of live fish, to discover models of fish locomotion (Gray 1968, Rosen 1963, Harper & Blake 1991).

Our research takes a different approach, by constructing biomimetically a fish-like robot, which allows a detailed study of the flow around a body swimming exactly like a fish; but also allows arbitrary variation of the principal parameters to reverse-engineer nature's solutions and assess the sensitivity and impact of the parameters involved. Finally, testing technological devices of various degrees of complexity allows the eventual development of simple technological solutions properly suited to engineering vehicles, but closely emulating the performance of live organisms.

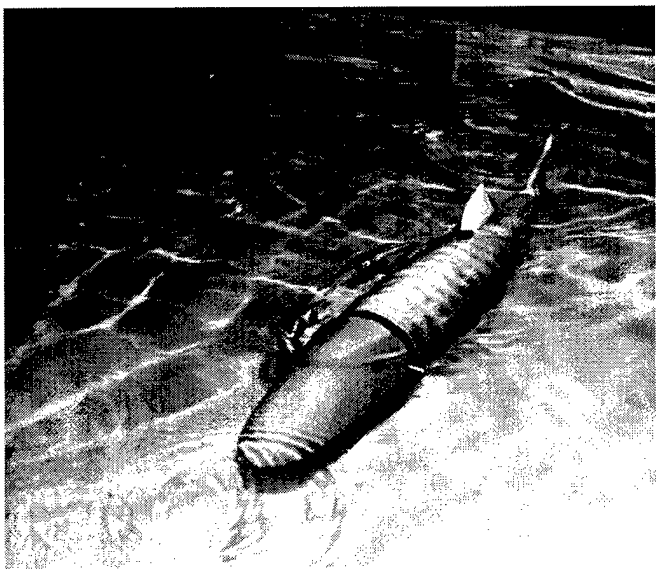

Figure 1: The robotic pike swims in the MIT towing tank.

1.1 Vorticity Control

A maneuvering streamlined rigid hull vehicle generates a substantial drag wake. This occurs because the flow separates as the angle of attack between its longitudinal axis and the incoming velocity exceeds a certain value, first generating symmetric helical vortices and ultimately alternatively shedding vortices.

Fast-starting and maneuvering fish bend their body to form a curvature that travels along the body length, thus generating body-bound vorticity. This vorticity is shed just anterior to the caudal peduncle generating pairs of large-scale free vortices, which cause maneuvering forces. To avoid generating drag wakes, the body vorticity must be manipulated by the tail which switches each shed vortex from one side of the fish to the other; hence shed vortices become propulsive. This is the essence of vorticity control as applied to maneuvering (Anderson 1996, Triantafyllou et al. 1996).

The body bending must be asymmetrical with respect to the plane of symmetry of the fish in order to generate side forces: A C-shape and an S-shape curving of the body classifies often-observed fish fast starts (Harper & Blake 1990); the former corresponds to mild fast-starts and the latter to rapid starts, reaching peak accelerations in excess of 200 m/s^2.

As a first step we decided to perform mild maneuvers. Hence,

the vehicle was designed to bend in a C-shape, travel the curvature down the body and then use the tail to control the forming eddies.

2 Design

When building a biomimetic robot, the intent is to emulate the performance of live fish and not to copy the detailed structures of living organisms, which are very complex, and not necessarily suitable for existing technology. One of the basic principles that has emerged from our work so far, however, is that *embedded in the complexity of living organisms are basic principles, the identification of which leads to emulating their performance.* Significant simplification of the developed technology is possible once these principles are understood.

Still, one realizes that animals have evolved over millions of years and have developed materials, structures and control systems that are best-suited for their mode of operation, and which are hard to replicate with our present technology. Hence the simplification process that will allow biomimetic development of fish-like vehicles requires extensive work and continuous introduction of the newest materials and methodologies. Biotechnology seems to offer enticing solutions in the near future for actuation and for building skin structures.

For example, simply trying to copy the articulated wings of a bird to achieve agile flight leaves out a host of other technologies of birds such as adaptive flight control, vision, and extremely high power-to-weight ratio muscles. A successful biomimesis of agile bird flight may require leaps of our technology. A more positive example is the successful biomimesis of walking creatures (G. Pratt 1995). These machines use biological inspiration to uncover successful design ideas grounded in classical physics. Once these design ideas have become understood, they become another possibility for the design engineer to use in his or her quest to optimize any design.

By studying live fish, theoretical fluid dynamics, and testing the *RoboTuna* (D. Barrett & M. Triantafyllou 1995, D. Barrett 1996, J. Anderson 1996) we concluded that the outstanding performance of fish is obtained through vorticity control, achievable through their body morphology and, especially, close control of their kinematics. Other contributing factors, such as small-scale skin control and polymer injection, appear to be secondary compared to vorticity control.

¿From the outset it was our aim to build a mechanical fish which would have the same shape and movements of live fish. Thus we could test various hypotheses about fish locomotion repeatably and with close attention to details in the flow. In order for the system to achieve the kinematics of maneuvering live fish it is preferable to implement a free-swimming design, because an external support would interfere with the dynamics of the robot. This posed novel problems compared to the *RoboTuna*, which this paper addresses. All the power actuation and control needed to be placed on the mechanism. And it was necessary to control the depth and attitude of the robot during swimming. The first part of the design revolved around two central goals: to have reliable actuation and to create a flexible hull which could undulate in the way fish do. Once the hull and actuators were selected, performance was maximized with the constraints that the robot needed to be self-powered and neutrally buoyant.

2.1 Hull Shape and Materials

The external shape of the mechanism is modelled after a chain pickerel that is 56 *cm* long. We digitized a taxidermist's model of the fish and corrected the computer model to make it symmetric about the vertical plane and geometrically fair. This was to correct for errors in the casting of the physical model. Inspection of live pike shows that the fish is indeed symmetric and has a faired body, except at the mouth where there is a slight saddle shape.

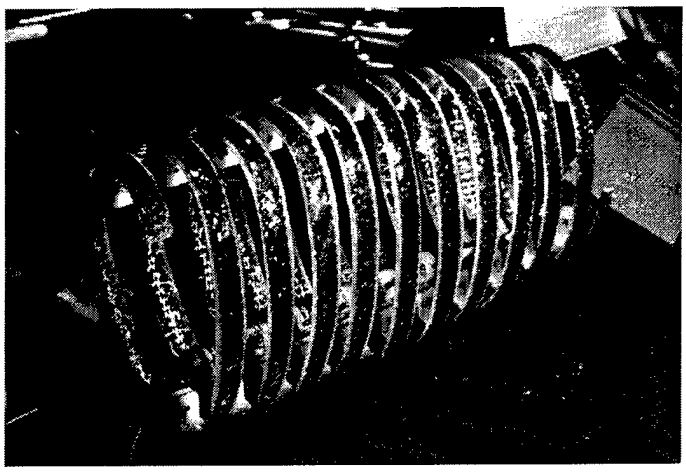

Figure 2: First section of the spiral wound spring before assembly with the rest of the mechanism. There are two splines attached at the top and bottom of the spring which constrain this to act like a flexure bearing.

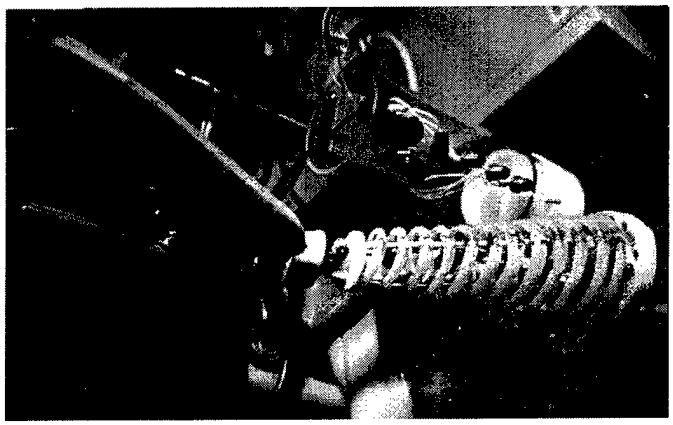

Figure 3: Tail assembly of the robotic fish shows the spiral wound fiberglass spring.

The vehicle hull is fabricated from two sections of fiberglass spiral wound spring which supports a skin of latex, lycra, and steel mesh. See Figures 2 and 3 for the first and second spiral spring sections. This spirally wound spring is attached to splines made of fiberglass (first body section) or delrin (second body section). These splines act as constraints so that the spirally wound springs essentially become two in-line flexure bearings. The machine inside the hull pushes and pulls at the hull to make it bend.

It was decided to use a flooded hull design for this robot because of the difficulty in making a reliable and accessible flexible sealed hull. This design decision created the requirement that any components in the flooded hull would need to be waterproof or water compatible. Because the head of the fish did not need to flex (we eliminated the mouth capability in our robot), that part of the fish could be made dry so that electronics could easily be housed there.

After the hull was digitized, the hull was filled with mechanisms that make the hull undulate like a fish. Because of the limitations in motor technology, it was decided in this first implementation to try to make the fish undulate in the same shapes as live fish, but at a slower rate, using vorticity control principles to scale timing in actuation of the kinematics. This effectively relaxes the control problems for implementing the fish kinematics. Off-the-shelf

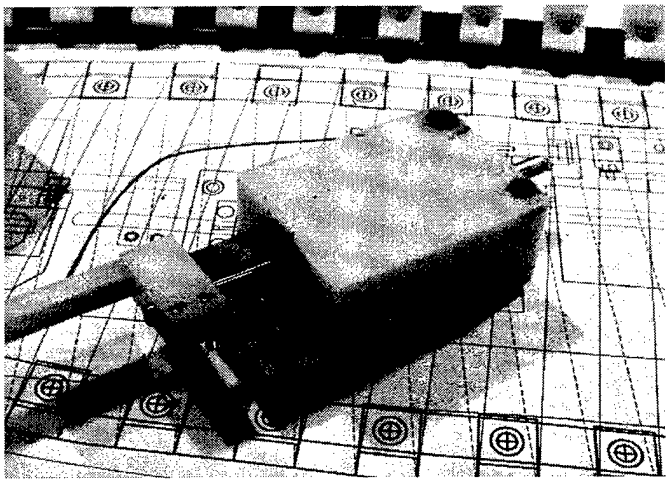

Figure 4: Assembled servo box doesn't show the actual servo or servo faceplate but does show the output shaft and transmission for the first body segment.

motors, which have the power to achieve the extremely powerful movements of fish would be too heavy for this size vehicle. Assuming that strict hydrodynamic scaling is achieved, so that drag forces are prevented from building up, the recorded motions of the present vehicle can be scaled up to be used in new vehicles equipped with more powerful motors.

2.1.1 Actuation

We selected model airplane servo motors because of their ease of control, i.e. a pulse width modulated signal sets their command position, and the fact that they are small in size and light -weight.

To seal the servo motors, a face plate was epoxied to the model airplane servo, and the lower half of the servo was sealed with epoxy. A box with mechanical feedthroughs, and a sealing surface was bolted to the faceplate on the servo. This arrangement also allowed for a transmission to be housed in the servo box (see Figure 4).

Three servos were selected as the minimum number to create the shapes used by fish in C-shaped starts and turns. The minimum size hull that would fit the three servos and associated equipment was estimated at 81 *cm*; hence the computer-generated hull shape was scaled up from 56 *cm* to 81 *cm*.

Two small servos were installed to control pectoral fins on the robot to actively control depth and attitude of the vehicle. We did not implement ventral fins because it appeared that they were not used in forward swimming, turning, and starting (our main areas of study).

The articulation of the hull is performed by two servos, while the third servo controls the pitch angle of the caudal fin. Each servo is individually controlled and the transmission was selected so that there is no kinematic coupling between the servos. The transmission between the servos and the hull is specialized for each section of the fish.

2.1.2 Transmission

Our goal for the articulation of the fish is to bend the first two body segments and to control the pitch on the caudal fin. The first body segment does not need to flex more than 30°, while the second body segment needed to flex as much as 180° of arc length. These requirements led to drastically different transmission and linkage designs.

For the pitch on the caudal fin a simple revolute joint was used. However, the hull near the tail of the fish has small available volume

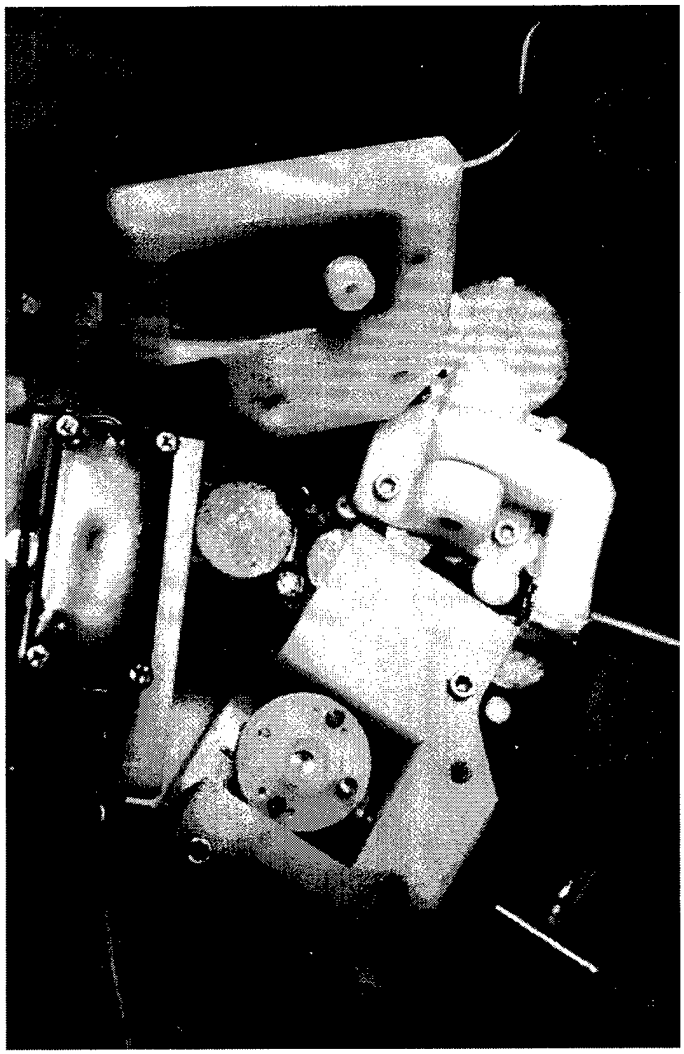

Figure 5: Bulkhead behind head shows the layout of the pectoral fin servos and how they are packaged into this area. The servos are epoxied to their faceplates and the faceplates are bolted and sealed to the servo housings which also house a mitre gear to redirect the servo shaft's movement out of the hull to the pectoral fin shaft.

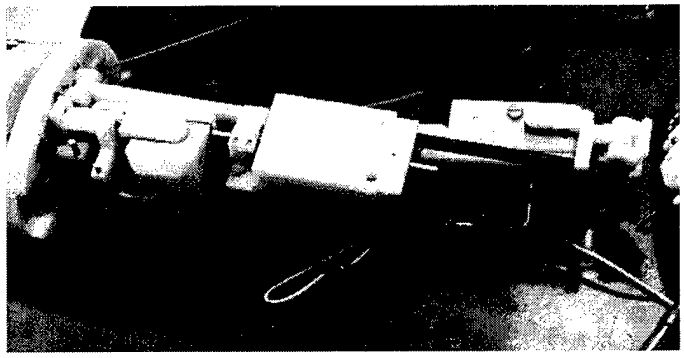

Figure 6: Servo assembly of robot before placement of the spiral wound spring shows the location of the three servos which drive the body.

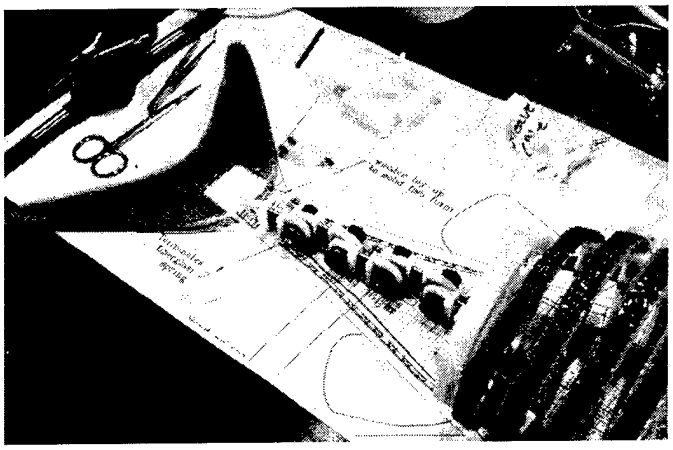

Figure 7: This construction picture of the tail linkage shows the individual links which are driven from a single servo.

and it is not possible to put a motor near the tail. Also, because of the bending of the body it was not possible to use a simple linkage running between the tail and the tail servo. A pulley and sheave mechanism running down the centerline of the body was deemed too complex, while hydraulics at this small scale are very difficult to implement. Fortunately, data from the RoboTuna project showed that the amount of power used by the caudal fin joint is very low in contrast to the other joints. This meant that a relatively inefficient transimission for this joint would not adversely affect the overall system efficiency. A simple pull-pull cable mechanism utilizing cable housing (such as employed in bicycle brakes) was selected for this axis. This let us put the servo for the caudal fin far from the tail area. A waterproofed servo with a dual rotary to linear conversion supplies the motion for this pull-pull cable motion.

For the second body segment, the one requiring up to 180° of flexing, a more complex system was required. It was important to control the shape of the tail, so a simple haptic mechanism, modelled after a human finger, could not be used. Instead a mechanism which bent into a tight arc was needed. A series of joints was chosen to approximate the arc, and one motor was needed to control all the joints. If one ran separate linkages or cables to each joint, the mechanism would be very complex. In order to simplify this section of the fish, each joint was coupled to the previous joint's motion. One difficulty of this mechanism is that since one is superimposing joint on top of joint, the cumulative error (backlash and/or compliance) can become large. The other difficulty of this mechanism is that one motor is controlling a long segment of the fish, so there is a lot of amplification of the motion, resulting in a small amount of available force at the end of the linkage. A waterproofed rotary servo supplies the motion for this series of joints. A series of cables is used to transmit the motion from joint to joint.

The first body segment requires only 30° of flexing. This can be done by bending a spline with an applied moment at the end of the spline. This is achieved with a linear contraction and expansion of a linkage running between the end of the segment. A waterproofed servo with a rotary to linear conversion is used for this segment.

To control the pectoral fins two small model airplane servos were used. For packaging reasons, it was necessary to use a mitre gear box to control the shafts of the pectoral fins.

2.2 Fins

The pectoral fins, dorsal, and anal fins are all made from RTV silicone rubber. The rubber used is rated at shore A 40, making these fins flexible. The profile of these fins was obtained from the fiberglass model of the chain pickerel and drawings of the fish. The cross section of the fins was not accurately reproduced (due the the section being very thin). By inspecting natural fish, it was seen that reproducing the extremely thin fins of fish would be very difficult. A NACA 12 section was chosen because it has been reported to be employed by many fish for their fins and tails. The caudal fin is rigid unlike the other fins. This is because the caudal fin, being the main propulsor, was designed using the experience from oscillating foils (Triantafyllou et. al. 1996).

2.3 Power and Electronics

The head of the fish is the only large dry space and contains electronics of control and communication. A 68332 based computer is mounted along with a radio modem which allows communication over short distances through the water. This allows one to control the robot, monitor the status of the machine, or send new programs to the computer while it is in the water without a tether.

Batteries are rubber encapsulated NiCd rechargeables. There is 12V at 1.5 Ah of energy when fully charged. This should be enough for at least 1 hour worth of continuous testing.

2.4 Stability

When observing live fish, it is not obvious whether the system is open-loop stable, or whether the fish is using some form of control to keep its body to swimming straight. The lack of horizontal stabilizing fins in the rear of the fish's body suggests that the depth control of the fish is open-loop unstable. Our robot will have the same hydrodynamic stability characteristics of the chain pickerel because it has the same morphology and kinematics.

Because of the articulation of the hull, certain unusual weight distribution requirements exist. The hull of the robot changes shape as it oscillates, hence it is important to distribute the weight inside so that the articulation of the vehicle does not create an adverse separation of the center of mass (C.O.M.) and center of buoyancy (C.O.B.) This requires that any component with a different density than water have enough space near it to allow it to be trimmed and become neutrally buoyant.

The pectoral fins of a fish act like the hydroplanes on a submarine controlling dive rate, but without the rear stabilizing fins of a submarine there is little counter moment to stop the rate of pitching. If the C.O.M. and C.O.B. are separated, then there is a small moment against the pectoral fins. However, testing showed that separating the C.O.M. and C.O.B., such as is done in traditional marine vehicles, has undesirable consequences.

The symmetric caudal fin has a center of lift in the middle of the fin. If the C.O.M. is not horizontal with the center of lift of the foil, then a rolling moment is placed on the robot. Pectoral, dorsal, and anal fins will act as roll stabilizers in this configuration, but this roll moment is a side effect of making the vehicle passively stable. We want to minimize the roll moment while keeping the robot passively stable. However, with the robot barely stable (statically), the pectoral fins will make the fish dynamically unstable in pitch because of the lack of stabilizing rear fins. The simplest solution for initial testing is to eliminate depth control by making the robot slightly positively buoyant. This constrains the mechanism to operate near the free surface.

3 Control

The control of the mechanical fish implemented for the series of tests presented here consists of an open-loop series of waveforms. To avoid having to control depth, the tests presented here were all performed with the fish made slightly buoyant.

The model airplane servos have an on-board proportional controller which allows us to send command positions to the actuators.

The onboard computer sends position commands to the servos and the servos respond by flexing the body. By sending a traveling wave profile down the body, the robotic body undulates and swims forward. For fast-starting, one can simply send a traveling wave down the body, just as in regular swimming. Vorticity control principles, however, supported by literature on fish kinematics (Harper & Blake 1990) suggests a far more effective way: By bending the body into a C-shape and then traveling this shape downstream along the body while springing back out into a normal swimming motion, a rapid start can be achieved. This C-shape start is depicted in Figure 8. For turning, the normal forward swimming undulation is interrupted by a similar large flexing of the body.

The "C" shaped start utilizes vorticity control to obtain a high starting thrust. Looking at Figure 8 one sees the body and hydrokinematics of this start. In frames 1-4 the fish winds up its body and creates a vortex ultimately controlled by its tail. In frame 5 the fish sheds this vortex as its tail reverses direction. And in frames 6-8 creates a vortex of opposite sign, thus finishing the creation of a large thrust dipole.

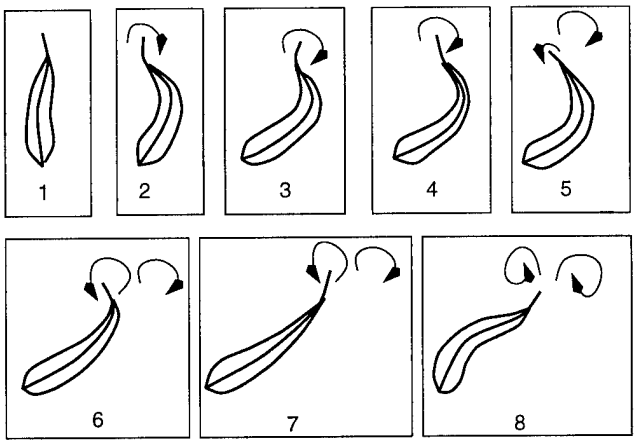

Figure 8: Sequence of pictures of major vorticity as fish executes C shaped start.

4 Testing

Testing was performed initially at the Towing Tank and then later at IS Robotics, Somerville MA. The first tests revolved around getting the robot to swim in a straight line. These first tests were performed without the pectoral fins installed. The robot was made slightly buoyant so that it was constrained near the free surface. And example of such testing is shown in Figure 9. Swimming forward was shown to be stable in yaw.

The next series of tests was performed to investigate the starting and turning performance of the machine. Testing revealed that the "C" shaped start used by the northern pike and trout (see Harper & Blake 1990) was much more effective at accelerating the machine to full speed than simply starting the forward swimming motion. Acceleration was increased by an order of magnitude over starting motion with the steady state traveling wave profile.

While this series of tests did not measure performance precisely it did prove the concept of flapping foil propulsion. The maximum forward speed of this system was 1 m/s or slightly more than a body length per second. The testing also showed that articulation of the main propulsor has serious benefits for fast start performance.

For turning, our tests showed that the turning was much higher performance than if we just used the caudal fin as a rudder. However, testing continued to show that the skin was too stiff for turning maneuvers as tight as a pike. We are currently implementing a much more flexible skin which will not constrain the body's flexing as much.

Figure 9: Testing swimming performance at the MIT Towing Tank.

5 Future Work

We have planned extensive testing of the vehicle involving quantitative measures of the performance of the vehicle, as well as flow visualization. Since the essence of success is the formation of body-bound vortices and their ultimate control by the tail, flow visualization using digital particle image velocimetry (DPIV) is the tool of choice to optimize vehicle performance.

Next, stronger motors and a more compliant skin will be installed to allow for faster maneuvers. A second set of actuators, designed for rapid delivery of power will also be implemented to allow for very rapid maneuvering. This will parallel the use in live fish of red muscle for long periods of slow swimming, versus using white muscle for short periods of burst activity.

More important to the performance of the vehicle than better motors and more compliant skin, is the optimization of swimming, turning, and starting. Since we have built a system with many parameters,optimizing the performance of this machine will require a strategic search of the possibilities. This kind of strategic search

was also used on *RoboTuna* to determine the best forward swimming parameters.

Additionally, this vehicle will be a testbed for miniature unmanned underwater vehicle technology. One of the driving thrusts for this research is the desire to make small highly capable UUV's and so a natural progression of this research is to make it more autonomous.

ACKNOWLEDGMENTS

Financial support of the Office of Naval Research under contracts N00014-96-C-0328 (subcontract to IS Robotics) monitored by T. McMullen, and N00014-96-1-1141 monitored by P. Purtell, T. McMullen & J. Fein; the Sea Grant Program under Grant Number NA46RG0434; and Draper Laboratory IR&D funding, is gratefully acknowledged.

6 References

1. Aleev Y., 1977, "Nekton", Publisher: Junk, The Hague.

2. Anderson J.M., 1996, "Vortex Control for Efficient Propulsion", *PhD Thesis*, Joint Program, Massachusetts Institute of Technology & Woods Hole Oceanographic Institution.

3. D.S. Barrett & M.S. Triantafyllou, "The design of a flexible hull undersea vehicle propelled by an oscillating foil", *9th International Symposium on Unmanned Untethered Submersible Technology*, September 1995.

4. D.S. Barrett, 1996, "Forces and efficiency of a flexible hull vehicle", *PhD Thesis*, Massachusetts Institute of Technology.

5. Bennett M.B., Ker R.F., Alexander R.M., 1987, "Elastic properties of structures in the tails of cetaceans (phocaena and lagenorhynchus) and their effect on the energy cost of swimming", J. Zoology, 211, pp. 177-192.

6. Domenici P. & Blake R.W., 1997, "The kinematics and performance of fish fast-start swimming", *J. exp. Bio.*, **200**, 1165-1178.

7. Gray J., 1968, "Animal Locomotion", Weidenfeld & Nicolson, London.

8. Harper D.G. and Blake R.W., 1990, "Fast-start Performance of Rainbow Trout (Salmo gairdneri) and Northern Pike (Esox Lucius)", Journal of Experimental Biology, Vol. 150, pp. 321-342.

9. Harper D.G. and Blake R.W., 1991, "Prey capture and the fast-start performance of northern pike (*Esox Lucius*)", *J. exp. Biol.*, **155**, 175-192.

10. Lighthill J., 1975, *Mathematical Biofluiddynamics*, SIAM, Philadelphia.

11. Rosen M. W., 1963, "Flow Visualization Experiments with a Dolphin", U.S. Naval Ordnance Test Station, NAVWEPS Report 8062, NOTS TP 3065, China Lake, California.

12. M.S. Triantafyllou, D.S. Barrett, D.K.P. Yue, J.M. Anderson, M.A. Grosenbaugh, K. Streitlien & G.S. Triantafyllou, 1996, "A New Paradigm of Propulsion and Maneuvering for Marine Vehicles" *Transactions of the Society of Naval Architects and Marine Engineers*, **104**, 81-100.

13. Wu T.Y., 1961, "Swimming of a waving plate", *Journal of Fluid Mechanics*, **10**, 321-344.

14. Wu T.Y., 1971, "Hydromechanics of swimming propulsion. Part 1. Swimming of a two dimensional flexible plate at variable forward speeds in an inviscid fluid", *Journal of Fluid Mechanics*, **46**, 337-355.

INDEX BY AUTHOR

Adrian, R. - *University of Illinois at Urbana-Champaign* 33
Amfilokhiev, W. - *Saint Petersburg State Marine Technical University* 305
Amonlirdviman, K. - *Massachusetts Institute of Technology* 135
Anderson, J. - *Charles Stark Draper Laboratory* 479
Babenko, V. - *National Academy of Sciences, Kiev* 113, 319, 451, 453
Balachandar, S. - *University of Illinois at Urbana-Champaign* 33
Bandopadhyay, P. - *Naval Undersea Warfare Center Division Newport* 373, 457
Bannasch, R. - *Technische Universität Berlin* 435
Barrett, D. - *Massachusetts Institute of Technology* 463
Benilov, A. - *Stevens Institute of Technology* 205
Biringen, S. - *University of Colorado at Boulder* 413
Bogdevich, V. - *Siberian Branch of the Russian Academy of Sciences* 327
Botton, V. - *PAMIR Team LEGI* 389
Branover, H. - *Ben-Gurion University of the Negev* 109, 379
Breidenthal, R. - *University of Washington* 127
Breuer, K. - *Massachusetts Institute of Technology* 135
Brown, G. - *Princeton University* 369
Bushnell, D. - *NASA - Langley Research Center* 7
Cantwell, B. - *Stanford University* 29
Carpenter, P. - *University of Warwick* 185
Casper, J. - *Newport News Shipbuilding* 53
Castano, J. - *Naval Undersea Warfare Center Division Newport* 335, 373, 457
Chkhetiana, O. - *Ben-Gurion University of the Negev* 109
Choi, K.S. - *University of Nottingham* 13, 229
Clayton, B. - *University of Nottingham* 229
Cotel, A. - *University of Manitoba* 127
Crawford, C. - *Brown University* 99, 407
Dahlburg, R. - *Naval Research Laboratory* 131
Dhanak, M. - *Florida Atlantic University* 237
Dohring, C. - *German Armed Forces University* 471
Du, Y. - *Brown University* 407
Eidelman, A. - *Ben-Gurion University of the Negev* 109, 379
Fan, X. - *Princeton University* 369

Fein, J. - *Office of Naval Research* 429
Fey, U. - *MHD Dept., Forschungszentrum Rossendorf* 395
Fish, F. - *West Chester University* 443
Fitzgerald, E. - *The Johns Hopkins University* 211
Fitzgerald, J. - *Kildare Corporation* 211, 215
Forestier, B. - *I.R.P.H.E., France* 83
Gad-el-Hak, M. - *University of Notre Dame* 197
Gasljevic, K. - *University of California at Santa Barbara* 281
Gerbeth, G. - *MHD Dept., Forschungszentrum Rossendorf* 395
Giovannelli, G. - *I.R.P.H.E., France* 83
Golbraikh, E. - *Ben-Gurion University of the Negev* 109, 379
Grosenbaugh, M. - *Woods Hole Oceanographic Institution* 463
Guin, M. - *The Johns Hopkins University* 313
Handler, R. - *Naval Research Laboratory* 131
Hanson, J. - *The Johns Hopkins University* 163
Holliday, D. - *Tracor Aerospace* 149
Hover, F. - *Massachusetts Institute of Technology* 463
Hoyer, K. - *University of California at Santa Barbara* 281
Hoyt, J.W. - *San Diego State University* 1
Ivanyuta, Y. - *A.N. Krylov Central Research Institute* 295
Karniadakis, G. - *Brown University* 99, 407
Kato, H. - *The University of Tokyo* 313
Kodama, Y. - *Ship Research Institute, Tokyo* 331
Koryenna, L. - *Institute of Hydromechanics of Ukrainian National Academy of Sciences* 257
Kovach, B. - *Florida Institute of Technology* 169
Kowalski, T. - *University of Rhode Island* 289
Kulik, V. - *Russian Academy of Sciences, Novosibirsk* 299
Kumph, J. - *Massachusetts Institute of Technology* 485
Kwa, T. - *Tao Systems, Inc.* 53
Lai, J. - *Australian Defence Force Academy* 471
LaTorre, R. - *University of New Orleans* 319
Lielausis, O. - *Institute of Physics Riga* 395
Lin, Z. - *The Ohio State University* 277
Madigosky, W. - *A&T, Inc.* 219
Maltzev, L. - *Siberian Branch of the Russian Academy of Sciences* 327
Maluga, A. - *Siberian Branch of the Russian Academy of Sciences* 327
Mangalam, S. - *Tao Systems, Inc.* 53
Marmanis, H. - *Brown University* 99
Martin, J. - *Kildare Corporation* 215
Matthys, E. - *University of California at Santa Barbara* 281

Mazaev, K. - *Saint Petersburg State Marine Technical University* 305
McGillis, W. - *Woods Hole Oceanographic Institution* 463
Meir, A. - *Auburn University* 401
Meng, J. - *Naval Undersea Warfare Center Division Newport* 341, 359
Merkulov, V. - *Siberian Branch of the Russian Academy of Sciences* 263, 385
Mochizuki, S. - *Yamaguchi University* 121
Modert, E. - *Kildare Corporation* 215
Moghadam, H. - *Newport News Shipbuilding* 53
Moiseev, S., - *Space Research Institute, Moscow* 109, 379
Mutschke, G. - *MHD Dept., Forschungszentrum Rossendorf* 395
Myska, J. - *Czech Academy of Sciences* 277
Nedderman, W. - *Naval Undersea Warfare Center Division Newport* 373,457
Nigon, R. - *Naval Surface Warfare Center, Carderock Division* 53
O'Sullivan, P. - *University of Colorado at Boulder* 413
Osaka, H. - *Yamaguchi University* 121
Pfouts, R. - *Tao Systems, Inc.* 53
Philips, R. - *Naval Undersea Warfare Center Division Newport* 335
Platacis, E. - *Institute of Physics Riga* 395
Platzer, M. - *U.S. Naval Postgraduate School* 471
Pognant, M. - *MS L.A.I.A.T. - Université de Toulon* 83
Posdziech, O. - *Inst. Aerospace Eng., TU Dresden* 395
Progrebnyak, V. - *Ecological Center of Scientific and Applied Researches* 295
Rathnasingham, R. - *Massachusetts Institute of Technology* 135
Riahi, D. - *University of Illinois at Urbana-Champaign* 225
Rivir, R. - *Wright-Patterson Airforce Base* 143
Rossi, L. - *PAMIR Team LEGI* 389
Russell, S. - *Naval Surface Warfare Center, Carderock Division* 63
Sandberg, W. - *Naval Research Laboratory* 131
Sarma, G. - *Tao Systems, Inc.* 53
Savchenko, Y. - *Institute of Hydromechanics of Ukrainian National Academy of Sciences* 249
Schmidt, P. - *Auburn University* 401
Schultz, M. - *Florida Institute of Technology* 175
Semonov, B. - *Siberian Branch, Russian Academy of Sciences* 189, 269
Semonova, A. - *Siberian Branch, Russian Academy of Sciences* 189
Si, C. - *Florida Atlantic University* 237
Sirovich, L. - *Brown University* 131
Smith, C. - *Lehigh University* 39
Smits, A. - *Princeton University* 89
Snarski, S. - *Kohler, WI* 419
Stace, J. - *Naval Undersea Warfare Center Division Newport* 335

Swain, G. - *Florida Institute of Technology* 155, 169, 175
Takahashi, Y. - *IHI, Ltd.* 313
Tardu, S. - *Laboratoire des Ecoulements Géophysiques et Industriels* 241
Techet, A. - *Massachusetts Institute of Technology* 463
Thibault, J.P. - *PAMIR Team LEGI* 389
Thivierge, D. - *Naval Undersea Warfare Center Division Newport* 373,457
Tolkoff, S. - *Massachusetts Institute of Technology* 463
Triantafyllou, M. - *Massachusetts Institute of Technology* 463, 485
Uberall, H. - *Catholic University of America* 219
Uhlman, J. - *Naval Undersea Warfare Center Division Newport* 341
Waleffe, F. - *University of Wisconsin-Madison* 47
Wallace, M. - *Newport News Shipbuilding* 53
Watanabe, K. - *Tokyo Metropolitan University* 19
Weier, T. - *MHD Dept., Forschungszentrum Rossendorf* 395
Wolfgang, M. - *Massachusetts Institute of Technology* 463
Yaremchuk, A. - *National Academy of Sciences, Kiev* 451
Yue, D. - *Massachusetts Institute of Technology* 463
Yurchenko, N. - *National Academy of Sciences, Kiev* 143
Zagarola, M. - *Creare, Inc.* 89
Zakharenkov, M. - *Central Aero-Hydrodynamic Institute* 73
Zakin, J. - *The Ohio State University* 277